Transactions of the ASME®

Technical Editor, LEWIS T. WHEELER (1997)

Department of Mechanical Engineering,
University of Houston,
Houston, TX 77204-4792

APPLIED MECHANICS DIVISION

Chairman, J. W. HUTCHINSON
Secretary, L. ANAND
Associate Technical Editors,
R. ABEYARATNE (1994)
T. R. AKYLAS (1994)
D. M. BARNETT (1996)
S. A. BERGER (1994)
I. M. DANIEL (1996)
W. J. DRUGAN (1997)
G. J. DVORAK (1995)
E. J. HAUG, JR. (1996)
J. T. JENKINS (1996)
S. KYRIAKIDES (1997)
S. LICHTER (1995)
W. K. LIU (1996)
X. MARKENSCOFF (1994)
D. M. PARKS (1995)
J. N. REDDY (1995)
W. N. SHARPE, JR. (1996)
S. W. SHAW (1997)
C. F. SHIH (1995)
M. SHINOZUKA (1997)
M. TAYA (1996)

BOARD ON COMMUNICATIONS

Chairman and Vice-President
R. D. ROCKE

Members-at-Large
T. BARLOW, N. H. CHAO, A. ERDMAN,
G. JOHNSON, L. KEER, W. MORGAN,
E. M. PATTON, S. PATULSKI, R. E. REDER,
S. ROHDE, R. SHAH, F. WHITE,
J. WHITEHEAD

OFFICERS OF THE ASME
President, P. J. TORPEY
Exec. Director
D. L. BELDEN
Treasurer
R. A. BENNETT

PUBLISHING STAFF
Mng. Dir., Publ.,
CHARLES W. BEARDSLEY
Managing Editor,
CORNELIA MONAHAN
Production Editor,
JUDITH SIERANT
Production Assistant,
MARISOL ANDINO

Transactions of the ASME, Journal of Applied Mechanics (ISSN 0021-8936) is published quarterly (Mar., June, Sept., Dec.) for $185.00 per year by The American Society of Mechanical Engineers, 345 East 47th Street, New York, NY 10017. Second class postage paid at New York, NY and additional mailing office. POSTMASTER: Send address changes to Transactions of the ASME, Journal of Applied Mechanics, c/o THE AMERICAN SOCIETY OF MECHANICAL ENGINEERS, 22 Law Drive, Box 2300, Fairfield, NJ 07007-2300.

CHANGES OF ADDRESS must be received at Society headquarters seven weeks before they are to be effective. Please send old label and new address.

PRICES: To members, $40.00, annually: to nonmembers, $185.00. Add $30.00 for postage to countries outside the United States and Canada.

STATEMENT from By-Laws. The Society shall not be responsible for statements or opinions advanced in papers or ... printed in its publications (B7.1, Par. 3).

COPYRIGHT © 1994 by The American Society of Mechanical Engineers. Authorization to photocopy material for internal or personal use under circumstances not falling within the fair use provisions of the Copyright Act is granted by ASME to libraries and other users registered with the Copyright Clearance Center (CCC) Transactional Reporting Service provided that the base fee of $3.00 per article is paid directly to CCC, Inc., 222 Rosewood Drive Danvers, MA 01923. Request for special permission or bulk copying should be addressed to Reprints/Permission Department.

INDEXED by Applied Mechanics Reviews and Engineering Information, Inc. Canadian Goods & Services Tax Registration #126148048

Journal of Applied Mechanics

Published Quarterly by The American Society of Mechanical Engineers

VOLUME 61 • NUMBER 4 • DECEMBER 1994

TECHNICAL PAPERS

755 Localized and Propagation of Instabilities in Long Shallow Panels Under External Pressure
T. L. Power and S. Kyriakides

764 Post-buckling Behavior of Beams Under Contact Constraints
M. Adnan, I. Sheinman, and E. Altus

773 The Folding of Triangulated Cylinders: Part I, Geometric Considerations
S. D. Guest and S. Pellegrino

778 The Folding of Triangulated Cylinders: Part II, The Folding Process
S. D. Guest and S. Pellegrino

784 Two New Universal Relations in Nonlinear Elasticity and Some Related Matters
M. Aron and S. Aizicovici

788 Stability Analysis of A Spinning Elastic Disk Under a Stationary Concentrated Edge Load
Jen-San Chen

793 The Annular Taylor Column (94-WA/APM-6)
W. E. Scott

797 The Interface Anticrack and Green's Functions for Interacting Anticracks and Cracks/Anticracks
X. Markenscoff, Luqun Ni, and J. Dundurs

803 The Stress Field and Intensity Factor due to Crazes Formed at the Poles of a Spherical Inhomogeneity
Z. M. Xiao and K. D. Pae

809 External Circular Crack Under Normal Load: A Complete Solution
V. I. Fabrikant, B. S. Rubin, and E. N. Karapetian

815 Mixed Modes I and II Concrete Fracture: An Experimental Analysis
Z. K. Guo, A. S. Kobayashi, and N. M. Hawkins

822 Analysis of Vickers Hardness by the Finite Element Method
Y. Murakami and K. Matsuda

829 Interfacial Zener-Stroh Crack (94-WA/APM-1)
H. Fan

835 Antiplane Elastic Wave Scattering From a Curved Randomly Rough Crack (94-WA/APM-4)
A. Boström, P. A. Jansson, and P. Olsson

843 Eigenfunction Expansion and Higher Order Weight Functions of Interface Cracks
Y.-Z. Chen and N. Hasebe

850 Switching Phenomenon of a Bathtub Vortex
M. Shiraishi and T. Sato

855 Equations of Motion of Two-Phase Variable Mass Systems With Solid Base
F. O. Eke and S.-M. Wang

861 Free Vibrations of Laminated Composite Noncircular Thin Cylindrical Shells (94-WA/APM-11)
K. Suzuki, G. Shikanai, and A. W. Leissa

872 Geometrically Nonlinear Stress-Deflection Relations for Thin Film/Substrate Systems With a Finite Element Comparison (94-WA/APM-10)
C. B. Masters and N. J. Salamon

879 Nonlinear Spatial Equilibria and Stability of Cables Under Uniaxial Torque and Thrust (94-WA/APM-3)
C. L. Lu and N. C. Perkins

887 A Perturbation Method for Inverse Frequency Modification of Discrete, Undamped Systems (94-WA/APM-12)
M. J. Smith and S. G. Hutton

893 Doubly Asymptotic Approximations for Submerged Structures With Internal Fluid Volumes: Formulation
T. L. Geers and P. Zhang

900 Doubly Asymptotic Approximations for Submerged Structures With Internal Fluid Volumes: Evaluation
T. L. Geers and P. Zhang

907 An Approximate Technique for Dynamic Elastic-Plastic Analysis
F. Giambanco, M. Lo Bianco, and L. Palizzolo

914 A Global Extremum Principle in Mixed Form for Equlibrium Analysis With Elastic/Stiffening Materials: A Generalized Minimum Potential Energy Principle
J. E. Taylor

919 Finite Element Analysis of Thermoelastic Contact Stability
T. Yeo and J. R. Barber

923 A Theoretical Study on the Application of Optical Caustics to High-Temperature Creep Fracture Mechanics
J. L. Ding and Y. G. Chen

930 An Analytical Model to Predict Optimal Material Properties in the Context of Optimal Structural Design
M. P. Bendsøe, J. M. Guedes, R. B. Haber, P. Pederson, and J. E. Taylor

(Contents continued on Outside Back Cover)

Downloaded 04 May 2010 to 171.66.16.52. Redistribution subject to ASME license or copyright; see http://www.asme.org/terms/Terms_Use.cfm

938 **Transient Hygrothermal Stress Induced in Two-Dimensional Problems by Nonlinear Theory of Coupled Heat and Moisture** (94-WA/APM-7)
T.-C. Chen and B.-H. Hwang

944 **Theoretical and Experimental Analysis of the Forced Response of Sagged Cable/Mass Suspensions**
S.-P. Cheng and N. C. Perkins

949 **Bending Vibrations of Rotating Nonuniform Timoshenko Beam With an Elastically Restrained Root** (94-WA/APM-8)
S. Y. Lee and S. M. Lin

956 **Automation and Assessment of Augmented Lagrangian Algorithms for Frictional Contact Problems** (94-WA/APM-5)
T. L. Laursen and V. G. Oancea

964 **Vibrations of Transversely Isotropic Finite Circular Cylinders**
K. T. Chau

971 **Load Transfer From a Finite Cylindrical Fiber Into an Elastic Half-Space** (94-WA/APM-9)
V.-G. Lee and T. Mura

BRIEF NOTES

Stagnation Point Flow With Suction: An Approximate Solution 976
P. D. Ariel

Thermoelastic Problem of a Dissimilar Anisotropic Solids With a Rigid Line Inclusion 978
C. K. Chao and R. C. Chang

Stability of Harmonic Waves in a Periodic System and the Radiation Condition 980
P. E. Barbone

Rigid-Body Rotation and Crack-Tip Opening Displacement at the Tip of a Kinked Crack in an Infinite Plate 983
A. Bhattacharya

Identification of Mechanical Parameters in a Porous Elastically Deformable Medium by Compression-Relaxation Test 985
S. Naïli, O. Le Gallo, and D. Geiger

Zero Drag of a Thin Wing Moving in an Elastic Medium at the Rayleigh Speed 988
G. P. Cherepanov

990 Influential Functions for a Layered Medium Subjected to a Finite Distributed Source
Ruichong Zhang and Yan Yong

992 The Complete Stress Field due to a Dislocation Located Anywhere in Two Bonded Quarter Planes
P. Kelly, D. A. Hills, and D. Nowell

994 A Note on Interface Cracks With and Without Friction in Contact Zone
X. Deng

996 Exact Stresses Between Axisymmetric Bodies in Contact Having Quartic Profiles
Chin-Tu Lu and M. D. Bryant

998 Post-buckling Behavior of Stiffened Cross-Ply Cylindrical Shells
M. Savoia and J. N. Reddy

1000 Analytical Solution of Hill's Equation
Y. Pala

1001 Materials With Negative Poisson's Ratio: A Qualitative Microstructural Model
N. Phan-Thien and B. L. Karihaloo

DISCUSSION

1005 **A Conservation Theorem for Constrained Multibody Systems, by J. T. Wang—Discussion by J. G. Papastavridis with Author's Closure**

BOOK REVIEW

1007 ***Biomechanics: Mechanical Properties of Living Tissues,* 2nd ed., by Y. C. Fung . . .** Reviewed by **S. C. Cowin**

ERRATA

796 **The Buckling of an Elastic Layer Bonded to an Elastic Substrate in Plane Strain, by T. W. Shield, K. S. Kim, and R. T. Shield and published in the June 1994 issue of the *Journal of Applied Mechanics***

886 **Thermodynamics of Duffing's Oscillator, by V. Berdichevsky, A. Ozbek, and W. W. Kim and published in the Sept. 1994 issue of the *ASME Journal of Applied Mechanics***

955 **On the Double Cantilever Beam Specimen for Mode-1 Interface Delamination, by B. Balendran and published in the June 1994 issue of the *Journal of Applied Mechanics***

ANNOUNCEMENTS AND SPECIAL NOTES

783 Thermal Stresses '95—Announcement

849 19th International Congress of Theoretical and Applied Mechanics—Announcement

871 International Symposium on Recent Advances in Constitutive Laws for Engineering Materials—Announcement

906 Books Received by the Office of the Technical Editor

918 Change of Address Form

1004 Symposium on Recent Developments in Theories of Viscoplasticity—Announcement

1008 Worldwide Mechanics Meetings List

1010 Information for Authors

1011 1994 Author Index

1014 Plasticity '95—Announcement

Downloaded 04 May 2010 to 171.66.16.52. Redistribution subject to ASME license or copyright; see http://www.asme.org/terms/Terms_Use.cfm

Localization and Propagation of Instabilities in Long Shallow Panels Under External Pressure

T. L. Power

S. Kyriakides
Mem. ASME.

Engineering Mechanics Research Laboratory,
Department of Aerospace Engineering
and Engineering Mechanics,
The University of Texas at Austin,
Austin, TX 78712

This paper discusses the response of long, shallow, elastic panels to uniform pressure loading. Under quasi-static conditions, the deformation of such panels is initially uniform along their length, and their response has the nonlinearity and instabilities characteristic of shallow arches. Shallower panels deform symmetrically about the midspan and exhibit a limit load instability. For less shallow panels, the response bifurcates into an unsymmetric mode before the limit load is achieved. A formulation and a solution procedure are developed and used to analyze the response of such panels beyond first instability. It is demonstrated in both cases that following the first instability the deformation ceases to be axially uniform and localizes to a region a few arch spans in length. A drop in pressure accompanies this localized collapse and causes unloading in the remainder of the panel. Subsequent deformation is confined to this region until membrane tension arrests the local collapse. Further deformation can occur at a constant pressure and takes the form of spreading of the collapsed region along the length of the panel. The lowest pressure at which this can take place (propagation pressure) can be significantly lower than the pressure associated with first instability.

Introduction

This paper is concerned with the response and inherent instabilities in long, shallow, cylindrical panels under uniform pressure loading. Under quasi-static loading, the initial response of such panels has the nonlinearity and instabilities characteristic of shallow arches. Membrane deformations induced by the pressure cause a progressive softening of the response of the structure which for shallower panels results in a limit load instability (point *b* in the pressure-volume change response in Fig. 1(*a*)). For less shallow panels, this nonlinear response, which is symmetric about the midspan, is interrupted by a bifurcation-type instability. Consequently, the structure buckles into an unsymmetric mode before reaching the limit load (point *b* in Fig. 1(*b*)). In both types of panels the deformation remains axially uniform until the onset of the first instability. Our objective here is to explore the behavior of such panels beyond their first instability.

The response of arches (narrow strip rather than a long panel) beyond first instability is well understood (see Timoshenko, 1935; Biezeno, 1938; Marguerre, 1938; Fung and Kaplan, 1952; Hoff and Bruce, 1954; Gjelsvik and Bodner, 1962;

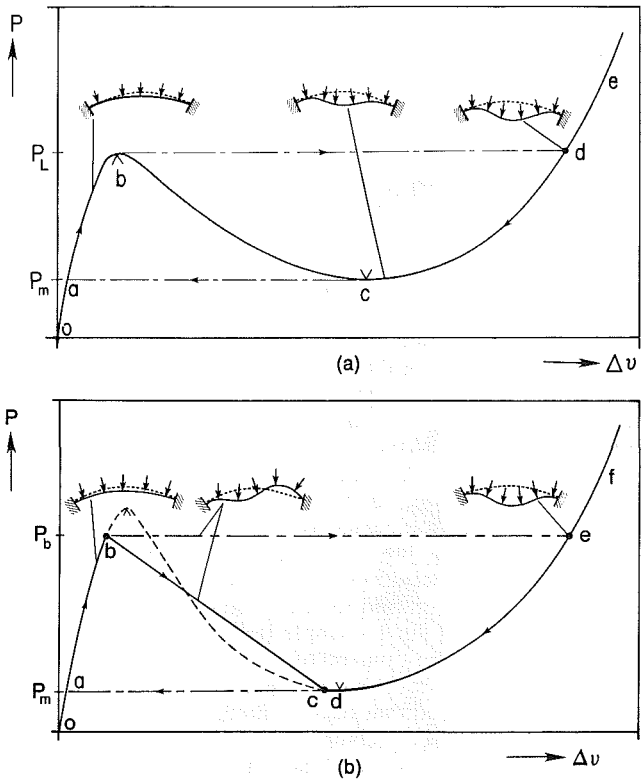


Fig. 1 (*a*) **Pressure-volume change response for arch which buckles symmetrically;** (*b*) **pressure-volume change response for arch which bifurcates into an unsymmetric mode for part of the response**

Contributed by the Applied Mechanics Division of THE AMERICAN SOCIETY OF MECHANICAL ENGINEERS for publication in the ASME JOURNAL OF APPLIED MECHANICS.

Discussion on this paper should be addressed to the Technical Editor, Professor Lewis T. Wheeler, Department of Mechanical Engineering, University of Houston, Houston, TX 77204-4792, and will be accepted until four months after final publication of the paper itself in the ASME JOURNAL OF APPLIED MECHANICS.

Manuscript received by the ASME Applied Mechanics Division, Mar. 8, 1993; final revision, May 24, 1993. Associate Technical Editor: A. K. Noor.

Copyright © 1994 by ASME
Downloaded 03 May 2010 to 171.66.16.20. Redistribution subject to ASME license or copyright; see http://www.asme.org/terms/Terms_Use.cfm

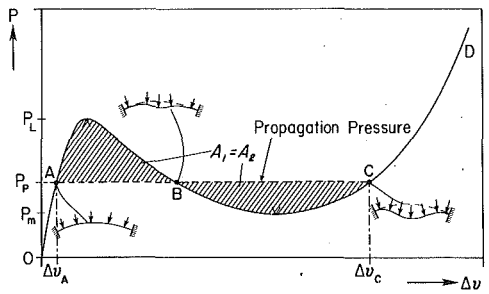


Fig. 2 Maxwell construction for a long shallow panel under uniform pressure

Schreyer and Masur, 1966 and others). Beyond the limit load and under "displacement-controlled" loading, the deformation of the arch in Fig. 1(*a*) grows at a decreasing load, and in the process, the curvature of part of the structure reverses sign. Eventually, further increase in deformation requires membrane stretching. This has a stiffening effect and leads to an upturn in the required load as shown in the figure. If, however, the pressure is prescribed, the structure, upon reaching the limit pressure (P_L), "snaps" from equilibrium point *b* to *d*. Unloading from point *d* to pressure P_m takes place along *dc*. Upon reaching P_m, the structure "snaps" to point *a* on the initial ascending branch. (This snapping back and forth is known as the oil-can effect.)

In the case of the less shallow arch shown in Fig. 1(*b*), the unsymmetric mode of deformation is preferred from point *b* to point *c* on the response. At the bifurcation pressure (P_b), the structure buckles into an unsymmetric mode. In fact, under displacement-controlled loading, the response follows the straight line joining the bifurcation points *b* and *c* (see Schreyer and Masur, 1966). Under pressure-controlled loading, the arch will snap from *b* to *e*. In the process, the unsymmetric deformation yields to a symmetric one, represented by equilibrium point *e*. Again, if the structure is unloaded from *e* to pressure P_m, path *ed* is followed. At *d*, the arch snaps back to point *a* on the prebuckling equilibrium branch. Thus, for prescribed pressure loading, the main difference between the prebuckling response of the two types of arches shown in Fig. 1 is that the maximum pressure reached is P_b rather than P_L.

The preferred mode of behavior is governed by the arch shallowness parameter

$$\lambda = \alpha^2 \frac{R}{t} \tag{1}$$

where 2α is the circular arch span angle, R its radius and t its wall thickness.

The pressure-volume response of both of these types of arches after the first instability has a negative slope. Thus, in the case of a long panel with this same arch as its cross-section, alternate post-buckling branches become available due to the effect of length. Due to the decreasing pressure, localized modes of deformation become energetically preferable to axially uniform collapse. That is, following the onset of the first instability, the deformation ceases to be uniform along the length of the panel. If the pressure is allowed to drop after first buckling (as would occur in volume-controlled pressurization), the buckle can be expected to remain local.

Kyriakides (1993) used a simple experimental apparatus to demonstrate the development of a localized instability in a long, shallow, cylindrical panel loaded by uniform pressure. He also demonstrated that once formed, the local buckle can spread (propagate) at a pressure which is much lower than that required to initiate the instability in a geometrically intact structure. This demonstration experiment will be reviewed below. This work (see also Kyriakides and Arseculeratne, 1993) also showed that the lowest pressure at which such instabilities

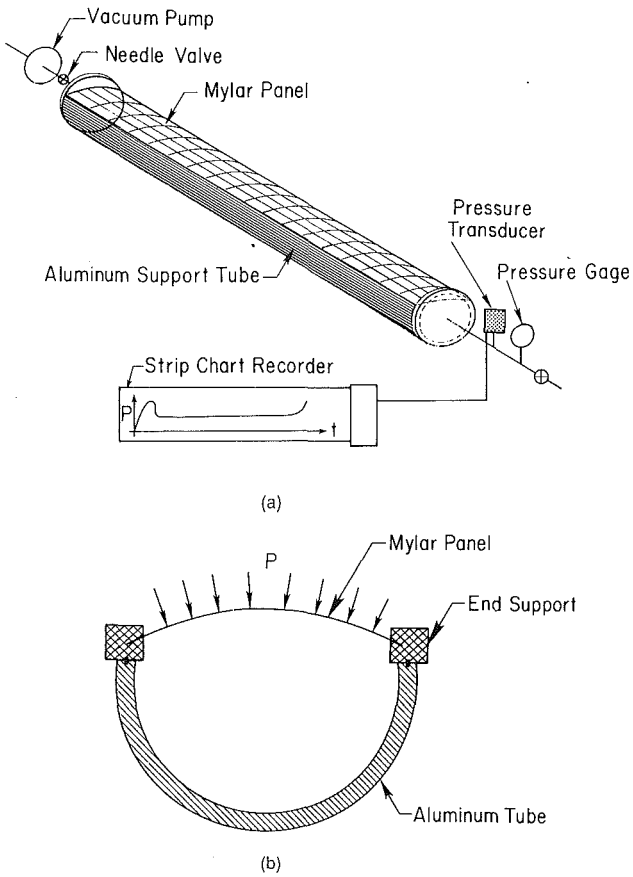


Fig. 3 (*a*) Experimental apparatus used to demonstrate the initiation and propagation of buckles in long panels; (*b*) cross-section of experimental apparatus

will propagate (propagation pressure) can be calculated exactly through an energy balance which utilizes the two-dimensional (axially uniform) response of such panels. This results in the so-called *Maxwell construction* (see Ericksen, 1975; Chater and Hutchinson, 1984; Kyriakides, 1993) shown schematically in Fig. 2. If the two-dimensional response is evaluated using the lowest-order admissible nonlinear kinematics (shallow shell kinematics, see Schreyer and Masur, 1966) the Maxwell construction results in the following closed-form expression for the propagation pressure:

$$P_P = \frac{1}{12} \frac{E}{1-\nu^2} \left(\frac{\pi}{\alpha}\right)^2 \left(\frac{t}{R}\right)^3. \tag{2}$$

In the present work, we use specialized analyses to establish the onset of localized instabilities in long panels and to examine their growth and transformation into propagating buckles. All aspects of the problem are studied in the quasi-static setting. The results are also used to confirm the validity of the propagation pressure yielded by the Maxwell construction.

Experiment

The simple test apparatus used by Kyriakides (1993) to demonstrate the initiation and steady-state propagation of buckles in long panels is shown schematically in Fig. 3. A long shallow panel was formed by bending a strip of thin mylar sheet into the cross-section shown in Fig. 3(*b*). The edges of the mylar strip were positioned and bonded into oblique slits cut into two long metal end support beams. The two end beams were mounted onto a U-shaped aluminum support structure which was made by removing the top of a 4-in. diameter aluminum tube. The arrangement is such that the mylar has a circular arch shape with $R/t = 228$ and an arch parameter $\lambda = 44.7$.

Downloaded 03 May 2010 to 171.66.16.20. Redistribution subject to ASME license or copyright; see http://www.asme.org/terms/Terms_Use.cfm

The tubelike structure, whose ends are closed with flanges, has a length of 10 ft (3 m). External pressure loading was applied by evacuating the air inside the closed tube with a vacuum pump. The pressure was monitored with an electrical pressure transducer and was recorded on a strip-chart recorder.

A typical pressure-time history and some of the major features observed during such an experiment are shown schematically in Fig. 4. Pressurization starts at time t_o. Initially, the structure deformed uniformly along its length with a relatively stiff response. For the parameters of this panel, the first instability was unsymmetric buckling (as in Fig. 1(*b*)). Figure 5(*a*) shows the onset of unsymmetric buckling in the panel (we note that this was influenced significantly by geometric imperfections as well as residual stresses present in the demonstration structures used). Soon after the onset of unsymmetric deformation, the structure collapsed dynamically (t_1) and developed a local buckle which was symmetric about the midspan and extended over a length of approximately 7–8 times the arch span (see Fig. 5(*b*)). Under the loading conditions used, the snap-through buckling produced a significant pressure transient. Once formed, the geometry of the local buckle could be frozen by interrupting the evacuation of air from the closed tube (i.e., after t_2). Once the local buckle was fully developed, further propagation of the buckle occurred at a well-defined pressure which was significantly lower than the pressure recorded at the initiation of local collapse. The buckle propagated in both directions until it reached one of the ends. Propagation continued on the other side until the whole panel was collapsed. The rate of propagation of the buckle was controlled by controlling the rate at which the closed system was evacuated. Figure 5(*c*) shows the transition between the buckled and unbuckled sections during such an experiment. Once the buckle reached both ends of the panel (t_4), further deformation required a significant increase in the pressure and was uniform along the length of the structure. The initial maximum pressure recorded is known as *initiation pressure* (P_I) and the pressure at which the collapse propagated is the *propagation pressure* (P_P) of the structure.

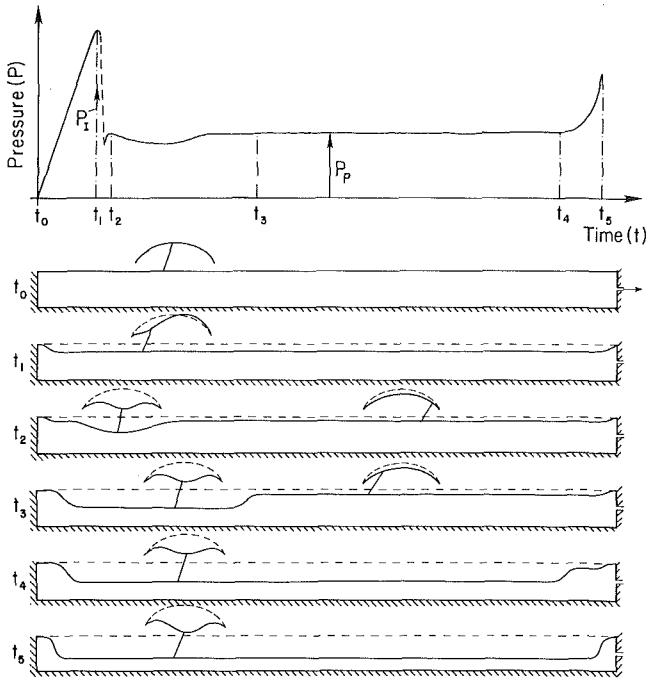


Fig. 4 Schematic representation of the history of an experiment in which a buckle is initiated and propagated in a long panel

Analysis

We consider a circular cylindrical panel of radius R, span angle 2α, thickness t ($\ll R$), and overall length $2L$ subjected to uniform pressure loading (P) over its entire surface as shown in Fig. 6. The panel material is taken to be linearly elastic with Young's modulus E and Poisson's ratio ν. Without loss of generality, the plane $x_1 = 0$ is assumed to be a plane of symmetry. We will consider panels with low values of λ for which deformations remain symmetric about the midspan and panels with higher values of λ which exhibit unsymmetric bifurcation buckling. For symmetric deformations, the plane $x_2 = 0$ is another plane of symmetry and only the darkly shaded portion ($0 \le x \le L$, $0 \le \theta \le \alpha$) of the panel in Fig. 6 is analyzed. For unsymmetric deformations, the problem domain is $0 \le x \le L$, $-\alpha \le \theta \le \alpha$.

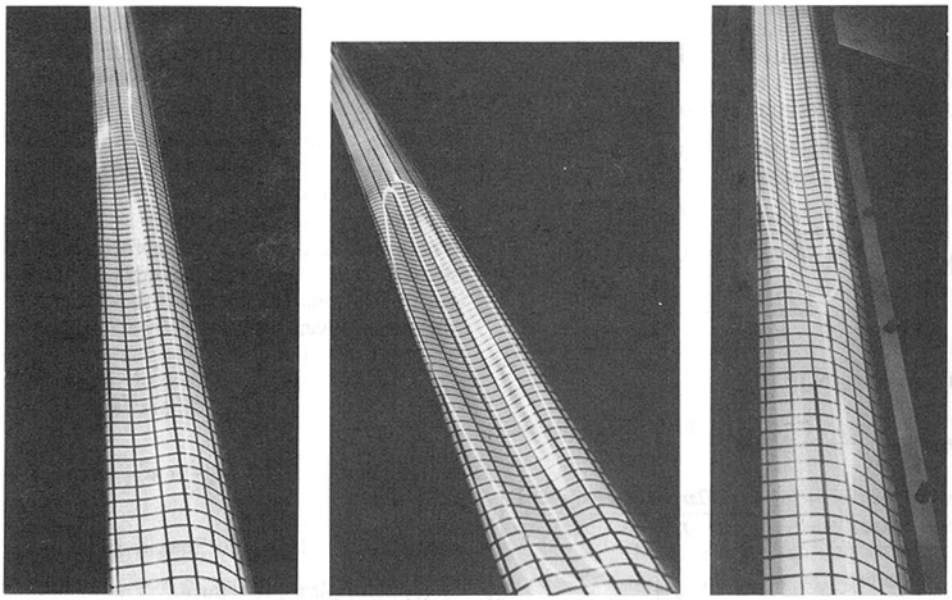


Fig. 5(*a*) Fig. 5(*b*) Fig. 5(*c*)

Fig. 5 Photographs of deformed panel. Fig. 5(*a*) unsymmetric buckle; Fig. 5(*b*) local symmetric buckle; Fig. 5(*c*) transition region between collapsed and uncollapsed portions.

Downloaded 03 May 2010 to 171.66.16.20. Redistribution subject to ASME license or copyright; see http://www.asme.org/terms/Terms_Use.cfm

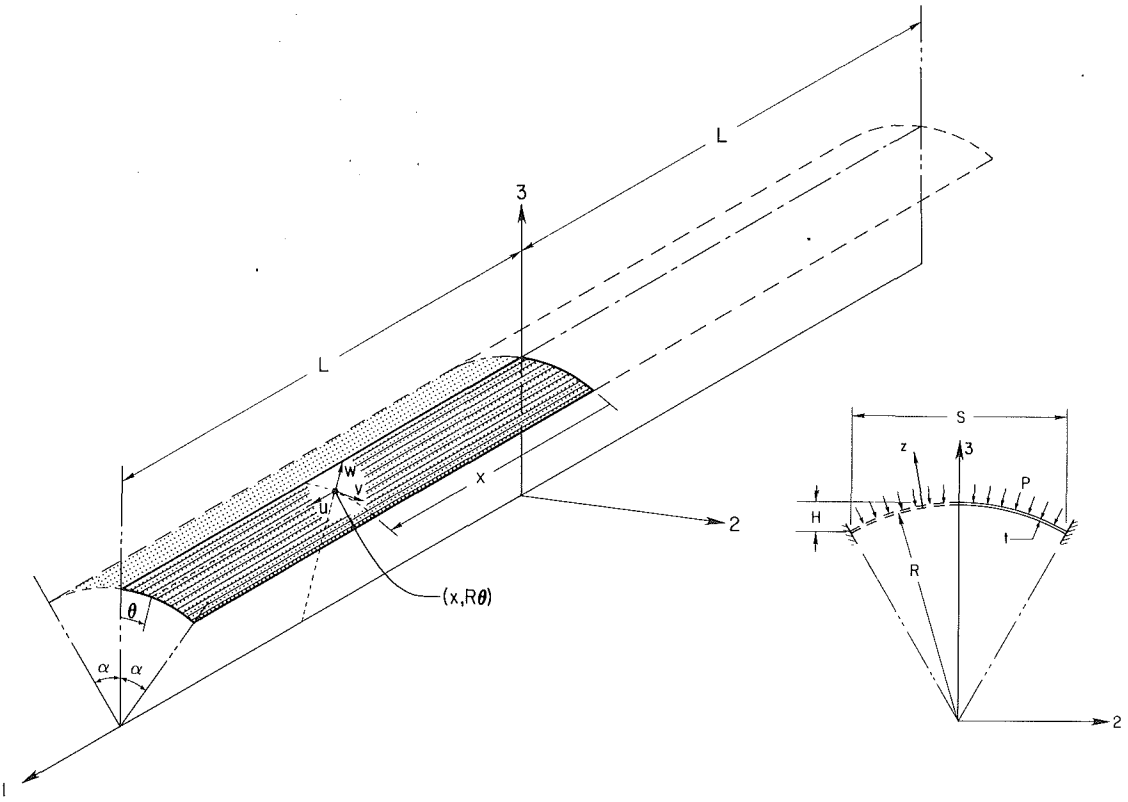


Fig. 6 Geometry of analyzed panel

(a) Kinematics. Sanders (1963) nonlinear shell kinematics with the assumption of small membrane strains are adopted. The particular form of the strain-displacement equations used (specialized for circular cylindrical geometry) was utilized by Dyau and Kyriakides (1993) in their studies of localization of collapse in long metal tubes. Points on the undeformed mid-surface are identified by $(x, R\theta)$, and axial, circumferential, and radial displacements are denoted by u, v, and w, respectively. The strain at any point in the panel is approximated by

$$\epsilon_{\alpha\beta} = (E_{\alpha\beta} + zK_{\alpha\beta})/(A_\alpha A_\beta)^{1/2} \tag{3}$$

where $E_{\alpha\beta}$ and $K_{\alpha\beta}$ are the membrane strains and curvatures, respectively, and z is the coordinate normal to the midsurface (see inset in Fig. 6). Here, $A_1 = 1$ and $A_2 \approx (1 + z/R)$. The strains are related to the displacements through

$$E_{xx} = u_{,x} + \frac{1}{2}[u_{,x}^2 + v_{,x}^2 + w_{,x}^2],$$

$$E_{\theta\theta} = \frac{w + v_{,\theta}}{R} + \frac{1}{2}\left(\frac{u_{,\theta}}{R}\right)^2 + \frac{1}{2}\left(\frac{v_{,\theta} + w}{R}\right)^2 + \frac{1}{2}\left(\frac{w_{,\theta} - v}{R}\right)^2,$$

$$E_{x\theta} = \frac{1}{2}\left[\frac{u_{,\theta}}{R} + v_{,x} + u_{,x}\frac{u_{,\theta}}{R} + v_{,x}\frac{v_{,\theta} + w}{R} + w_{,x}\frac{w_{,\theta} - v}{R}\right],$$

$$K_{xx} = -[u_{,xx}N_x + v_{,xx}N_\theta + w_{,xx}N_z],$$

$$K_{\theta\theta} = -\left[\frac{u_{,\theta\theta}}{R^2}N_x + \frac{v_{,\theta\theta} + 2w_{,\theta} - v}{R^2}N_\theta + \frac{w_{,\theta\theta} - 2v_{,\theta} - w - R}{R^2}N_z + \frac{1}{R}\right],$$

$$K_{x\theta} = -\left[\frac{u_{,x\theta}}{R}N_x + \frac{v_{,x\theta} + w_{,x}}{R}N_\theta + \frac{w_{,x\theta} - v_{,x}}{R}N_z\right], \tag{4}$$

where N_i are the components of the normal to the deformed panel mid-surface given by

$$N_x \cong v_{,x}\frac{w_{,\theta} - v}{R} - w_{,x}\frac{w + v_{,\theta}}{R} - w_{,x},$$

$$N_\theta \cong w_{,x}\frac{u_{,\theta}}{R} - u_{,x}\frac{w_{,\theta} - v}{R} - \frac{w_{,\theta} - v}{R},$$

$$N_z \cong 1 + u_{,x} + \frac{w + v_{,\theta}}{R} + u_{,x}\frac{w + v_{,\theta}}{R} - v_{,x}\frac{u_{,\theta}}{R}. \tag{5}$$

(b) Principle of Virtual Work. Equilibrium of the structure was enforced through the principle of virtual work (PVW) which for uniform, lateral pressure loading may be expressed as follows:

$$\int_0^L \int_{0,(-\alpha)}^{\alpha} [N_{\alpha\beta}\delta E_{\alpha\beta} + M_{\alpha\beta}\delta K_{\alpha\beta}]Rd\theta dx = -P\delta\Delta v^\dagger \tag{6}$$

where $N_{\alpha\beta}$ and $M_{\alpha\beta}$ are the force and moment intensities, related to $E_{\alpha\beta}$ and $K_{\alpha\beta}$ through the usual isotropic linearly elastic relationships, and Δv is the change in volume underneath the panel, given by

$$\Delta v = \int_0^L \int_{0,(-\alpha)}^{\alpha} \left[w + \frac{1}{2}(wu_{,x} - w_{,x}u) + \frac{1}{2R}(w^2 + wv_{,\theta} - w_{,\theta}v + v^2)\right]Rd\theta dx \tag{7}$$

(see Pearson, 1956 and Sewell, 1965).

(c) Solution Procedure. The structure was discretized using the following expansions for the displacements:

†The limits of integration in parentheses are used in the unsymmetric case.

Downloaded 03 May 2010 to 171.66.16.20. Redistribution subject to ASME license or copyright; see http://www.asme.org/terms/Terms_Use.cfm

$$u = R \sum_{m=1}^{M} \sin \frac{m\pi x}{L} \left\{ \sum_{n=1}^{N_s} c_{mn} \left[\cos\left(\frac{2n-1}{2} \frac{\pi\theta}{\alpha} \right) \right] + \sum_{n=1}^{N_a} g_{mn} \left[\sin \frac{n\pi\theta}{\alpha} \right] \right\},$$

$$v = R \sum_{m=1}^{M} \cos \frac{(m-1)\pi x}{L} \left\{ \sum_{n=1}^{N_s} b_{mn} \left[\sin \frac{n\pi\theta}{\alpha} \right] + \sum_{n=1}^{N_a} h_{mn} \left[\frac{\alpha}{\mu_n} \cos\left(\mu_n \frac{\theta}{\alpha} \right) + \frac{\theta^2}{2\alpha} \mu_n \cos \mu_n - \alpha \left(\frac{\mu_n}{2} + \frac{1}{\mu_n} \right) \cos \mu_n \right] \right\},$$

$$w = R \sum_{m=1}^{M} \cos \frac{(m-1)\pi x}{L} \left\{ \sum_{n=1}^{N_s} a_{mn} \frac{1}{2} \left[(-1)^{n+1} + \cos \frac{n\pi\theta}{\alpha} \right] + \sum_{n=1}^{N_a} f_{mn} \left[\sin\left(\mu_n \frac{\theta}{\alpha} \right) - \frac{\theta}{\alpha} \mu_n \cos \mu_n \right] \right\} \quad (8)$$

where μ_n are the positive roots of $\tan \mu_n = \mu_n$. These functions satisfy fixed conditions along the boundaries $\theta = \pm\alpha$ and exhibit symmetry in x. In addition, $w_{,x}$ vanishes at the boundaries $x = \pm L$. The first summation in each displacement component models deformation symmetric in θ, whereas the second summation models deformation antisymmetric in θ. Thus, for the symmetric case, f_{mn}, g_{mn}, and h_{mn} are set to zero. The number of axial half waves (M) used was typically 2–3 times the L/S ratio for a given geometry, and the number of circumferential half waves (both N_s and N_a) was taken to be 6. These values were determined adequate by convergence studies. Integration was performed by Gaussian quadrature. The panel was loaded incrementally by prescribing either the displacement $w(0, 0)$ or the change in volume underneath the panel, Δv, depending on the current nature of the response. The nonlinear equations resulting from Eqs. (3)–(8) were solved using the Newton-Raphson method.

Results and Discussion

Due to the obvious differences in the ways instabilities are initiated and localize for panels with different values of λ, we will discuss separately the behavior of panels with low enough values of λ to deform symmetrically about the midspan and that of panels which deform unsymmetrically. The panels analyzed have $R/t = 480$; various values of λ are achieved by varying the angle α.

(a) Symmetric Initiation and Propagation of Collapse. The features of the response of panels which buckle and collapse symmetrically about the midspan will be discussed by way of an example with $\lambda = 5.6$. For this case, the primary response (axially uniform and symmetric) exhibits bifurcations into unsymmetric modes on the descending portion following the limit load. The events that we will discuss precede these instabilities and thus their effect is irrelevant to our discussion. The calculated primary pressure-volume change response of such a panel with a length of 20 spans is shown in Fig. 7 where the following normalizations are adopted:

$$\bar{P} = \frac{P}{\frac{E}{12(1-\nu^2)} \left(\frac{\pi}{\alpha} \right)^2 \left(\frac{t}{R} \right)^3} \quad \text{and} \quad \Delta\bar{v} = -\frac{1}{\alpha^3} \frac{\Delta v}{R^2 L}. \quad (9)$$

This response is stable up to the limit pressure (identified by "^"). Due to the negative slope of the primary response beyond the limit load, it is easy to visualize that localized modes of collapse may be preferable to axially uniform collapse. The unstable nature of this part of the response can indeed be easily verified by conducting a linearized bifurcation check. This was done as summarized in the Appendix and involved the following buckling modes which are symmetric about the midlength of the panel:

$$\tilde{u} = \sin \frac{m\pi x}{L} \sum_{n=1}^{N} B_n \cos\left(\frac{2n-1}{2} \frac{\pi\theta}{\alpha} \right), \quad m = 1, 2, 3 \ldots$$

$$\tilde{v} = \cos \frac{m\pi x}{L} \sum_{n=1}^{N} C_n \sin \frac{n\pi\theta}{\alpha},$$

$$\tilde{w} = \cos \frac{m\pi x}{L} \sum_{n=1}^{N} A_n \left[(-1)^{n+1} + \cos \frac{n\pi\theta}{\alpha} \right]. \quad (10)$$

The first bifurcation point identified corresponds to $m = 1$ and occurs at $\Delta\bar{v} = 0.1430$, very soon after the limit pressure at $\Delta\bar{v} = 0.1426$. Subsequent bifurcation points, with progressively higher values of m, occur at increasingly higher values of $\Delta\bar{v}$. The first four bifurcation points are identified with Roman numerals in the inset of Fig. 7.

The onset of instability is affected by the length of the panel. This is demonstrated in Fig. 8 which shows expanded views

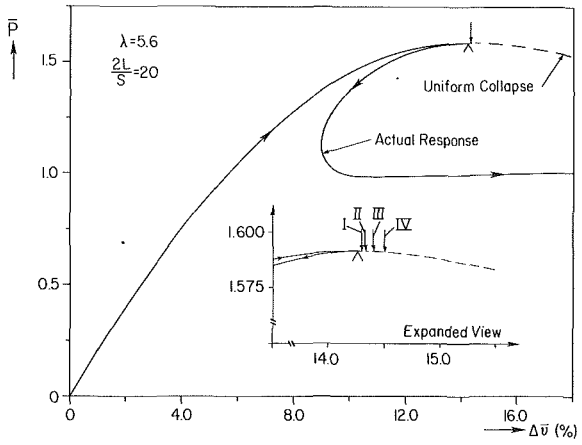


Fig. 7 Calculated pressure-volume change response for $\lambda = 5.6$

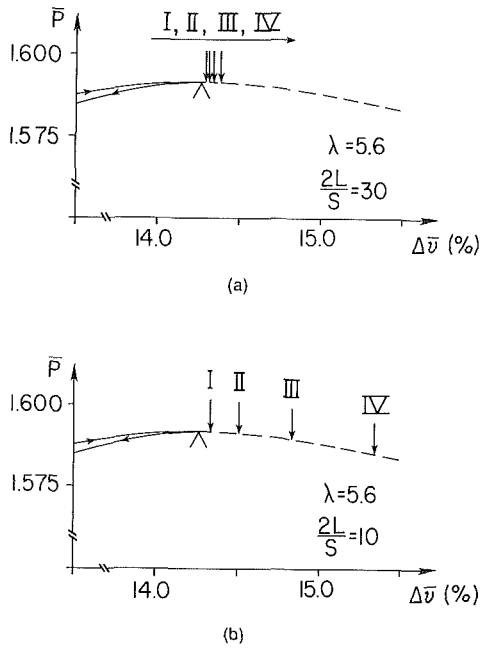


Fig. 8 Expanded view of critical region of pressure-volume change response for $\lambda = 5.6$; (*a*) 2L = 30S; (*b*) 2L = 10S

Downloaded 03 May 2010 to 171.66.16.20. Redistribution subject to ASME license or copyright; see http://www.asme.org/terms/Terms_Use.cfm

of the response in the region of the limit load for two additional panels with lengths of $2L = 30S$ and $10S$. Comparing the positions of the bifurcation points of the three cases, we observe that decreasing the length of the panel has the effect of delaying the onset of the first bifurcation point and increases the distance between subsequent bifurcation points. Conversely, for a very long panel, the limit load is an accumulation point. Thus, the limit load can be viewed as the critical point of the primary response.

This type of behavior has been observed before in other problems characterized by natural limit load instabilities such as necking of bars under uniaxial tension (Hutchinson and Miles, 1974) and bulging of internally pressurized tubes (Kyriakides and Chang, 1991).

The actual response of the structure following the first instability is also included in Fig. 7. It can be seen that the response beyond the bifurcation point reverses direction, that is, both the volume change and the pressure decrease, forming a cusp-like shape. A more complete view of the actual postbuckling response is shown in Fig. 9 which includes a sequence of deformed configurations of the line $\theta = 0$. The configurations are identified on the $P - \Delta v$ response by numbered points. On the ascending part of the response (⓪-③) the panel deforms uniformly along the length. The line $\theta = 0$ is seen in Fig. 9(*b*) to remain straight as it deflects downward. At point ③ the volume under the arch has been reduced significantly. Beyond point ③, a localized mode of deformation appears. In the case shown, the region of the panel around midlength is seen to experience local collapse while the overall pressure required for equilibrium decreases. Configurations ④ to ⑨ clearly show the growth of local collapse. Full views of some of the deformed configurations identified in Fig. 9 are presented in Fig. 10 (rendered from the solution

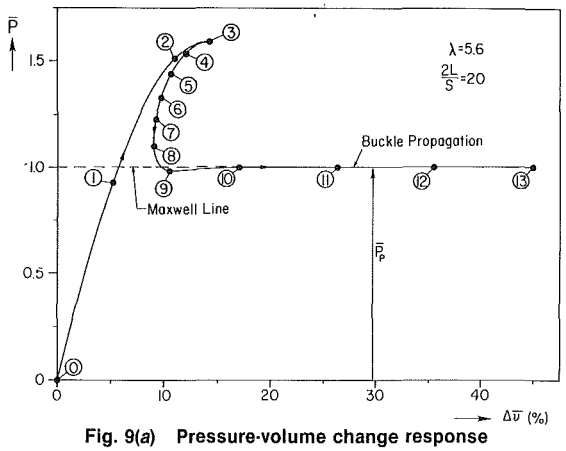


Fig. 9(*a*) Pressure-volume change response

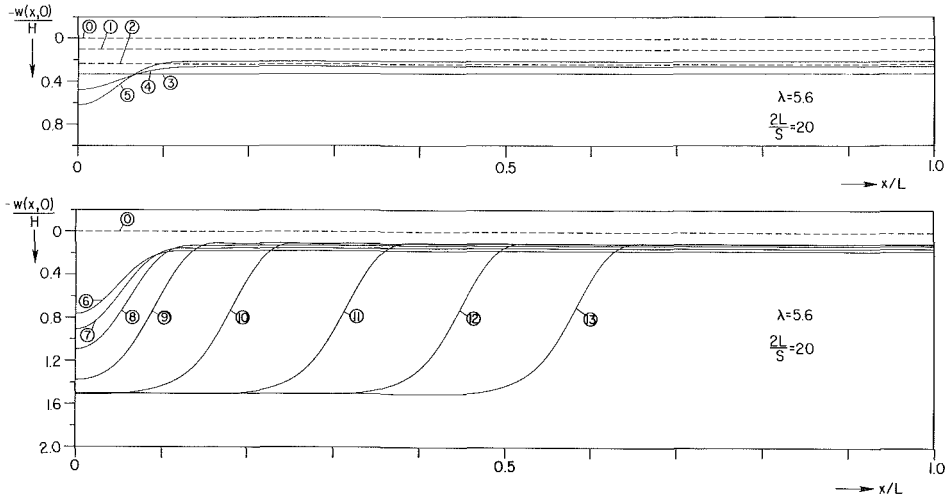


Fig. 9(*b*) Deformed configurations of generator $\theta = 0$

Fig. 9 Panel analysis: $\lambda = 5.6$, $2L = 20S$

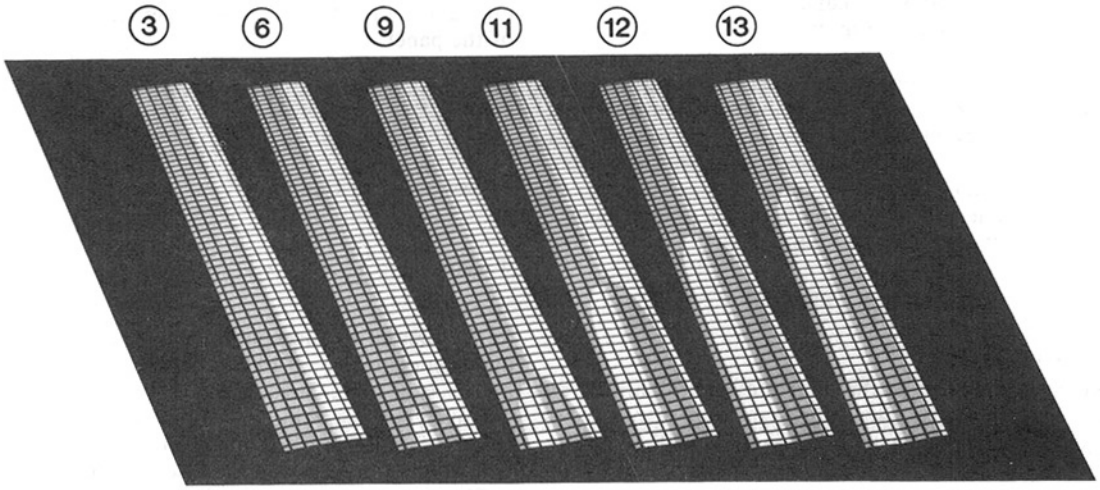


Fig. 10 Sequence of calculated configurations for panel of Fig. 9 showing symmetric initiation and propagation of collapse

Downloaded 03 May 2010 to 171.66.16.20. Redistribution subject to ASME license or copyright; see http://www.asme.org/terms/Terms_Use.cfm

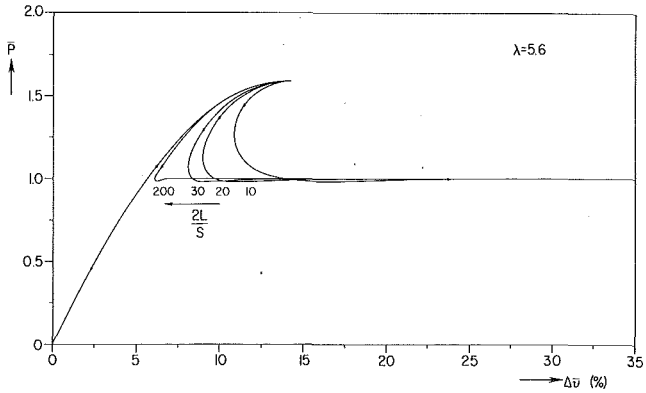


Fig. 11 Calculated pressure-volume change responses for λ = 5.6 and various panel lengths

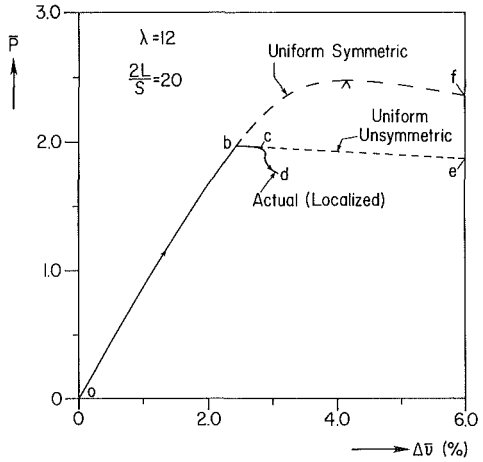


Fig. 12 Calculated pressure-volume change response for λ = 12

using the *SunVision* image processing system). It is interesting to observe that away from the collapsing region the panel deforms uniformly, unloading (as a result of the decreasing pressure) along a path (③-⓪) that corresponds to the one followed during loading. Thus, away from the localized collapse, the line $\theta = 0$ is seen to move upward, indicating an increase in the volume under this region of the panel.

This dichotomy in behavior between the collapsing section and the remainder of the structure is responsible for the cusp-like nature of the overall response shown in Figs. 7 and 9. For longer panels, like the case analyzed, the increase in volume under the section which is unloading is much larger than the decrease in volume under the collapsing section. This results in the net volume change shown in the figures.

The localization process is eventually arrested by membrane tension in the most collapsed region. With this region stabilized, further collapse will occur in adjacent less deformed sections until they become stabilized in turn. Thus, beyond ⑨, the localization of collapse gives way to propagation of collapse along the panel. By configuration ⑩, this propagation reaches a steady state in which a well-defined transition region, or front (actually one on either side of the collapsed region) has formed, joining the collapsed and uncollapsed parts of the structure. Thus, further decrease of the volume under the panel results in propagation (⑩-⑬) of the front which progressively engulfs uncollapsed sections and leaves collapsed sections in its wake. The value of pressure which accommodates this steady-state propagation corresponds exactly to that predicted by the Maxwell construction discussed in the introduction and given approximately by (2).

The propagation of the front will continue until the whole length of the panel is collapsed as discussed in the experimental section. In the case shown in the figure, the calculation was interrupted at configuration ⑬.

As in other structures exhibiting localization, the overall length of the panel affects the initial part of the calculated response (see Kyriakides and Chang, 1991). Figure 11 shows a comparison of the $P - \Delta v$ responses of panels with the same cross-section for lengths of 10, 20, 30, and 200 spans. The size of the cusp which follows the limit load is seen to grow with the length of the panel. In fact, for a very long panel, the cusp portion of the response follows (in reverse) almost the same path as that followed in the initial uniform part of the response. The reason for this is that for such a long panel the volume decrease in the locally collapsing section is small compared to the volume change in the rest of the panel which is experiencing unloading. Quite clearly, in volume-controlled pressurization of such panels, the cusp-like parts of the calculated response would not be realized. Instead, upon reaching the limit load, the response would experience a dynamic drop from the limit pressure to the propagation pressure.

(b) Unsymmetric Initiation and Symmetric Propagation of Collapse. The characteristics of the response of panels which bifurcate from the primary symmetric response into an unsymmetric mode before the natural limit load is achieved will be discussed through an example with $\lambda = 12$ and a length of 20 spans. The calculated response for this geometry, in the neighborhood of the first instability, is shown in Fig. 12. Initially, (path *ob*) the panel deformation is uniform along the length and symmetric about the midspan. The bifurcation into unsymmetric deformation occurs at *b* and corresponds to $(\bar{P}, \Delta\bar{v}) = (1.970, 0.0244)$. The bifurcation mode is axially uniform and is given by

$$\tilde{w} = A\left[\sin\left(\mu\frac{\theta}{\alpha}\right) - \left(\mu\frac{\theta}{\alpha}\right)\cos\mu\right] \tag{11}$$

where μ is the lowest positive root of $\tan\mu = \mu$ (see Schreyer and Masur, 1966). If the unsymmetric postbifurcation deformation were constrained to be axially uniform, the calculated response would follow path *be* in the figure. This path has a negative slope and rejoins the primary response as shown schematically in Fig. 1(*b*). Due to this negative slope, we can again expect localized modes to be preferable to continued axially uniform collapse. Indeed, *bcd* represents the response calculated when the unsymmetric deformation is allowed to localize. Due to the finite length of the panel analyzed, significant departure from path *be* is delayed until point *c*. Again, localized deformation is accompanied by a rather abrupt drop in pressure, but for this length, $\Delta\bar{v}$ remains monotonically increasing.

In the interest of making the problem more realistic, we consider the same panel geometry but introduce a small initial imperfection corresponding to the unsymmetric buckling mode (11). The calculated $P - \Delta v$ response is shown in Fig. 13 together with sets of cross-section configurations for locations A and B which are identified in the inset. Full views of the deformed configurations corresponding to points ① to ⑥ on the response are shown in Fig. 14. The panel initially deforms in a primary symmetric fashion (⓪-①). In the neighborhood of the unsymmetric bifurcation of the perfect problem, the imperfection activates axially uniform, unsymmetric deformations clearly shown in configurations ② in Fig. 13 (note also the off-center position of the shade boundary in Fig. 14).

The response develops a limit load at ② beyond which the deformation starts to localize. In the process, the deformation of a section of the panel at midlength experiences continued growth at a dropping overall pressure, while the remainder of the panel unloads. This difference is clearly illustrated in Fig. 13 by comparing the cross-section configurations of locations A and B corresponding to ③ (see also Fig. 14). As localization continues, the shape of the most deformed cross-section is seen to become progressively more symmetric. Local deformation

Downloaded 03 May 2010 to 171.66.16.20. Redistribution subject to ASME license or copyright; see http://www.asme.org/terms/Terms_Use.cfm

is eventually arrested by membrane tension, and the collapse, which by this time has become symmetric, starts to propagate along the panel. For long panels, the propagation of the collapse can occur in a steady-state fashion and has essentially the same features as those of the symmetric case discussed in Section (a). The propagation pressure again corresponds to that predicted by the Maxwell construction ($\bar{P}_P = 1.0046$).

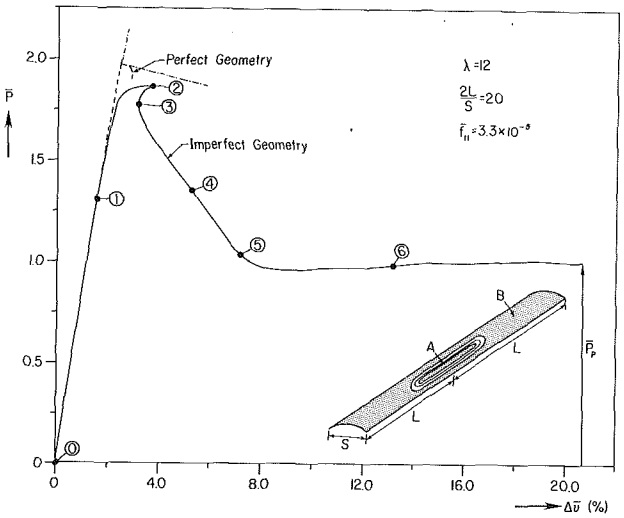


Fig. 13(*a*) Pressure-volume change response

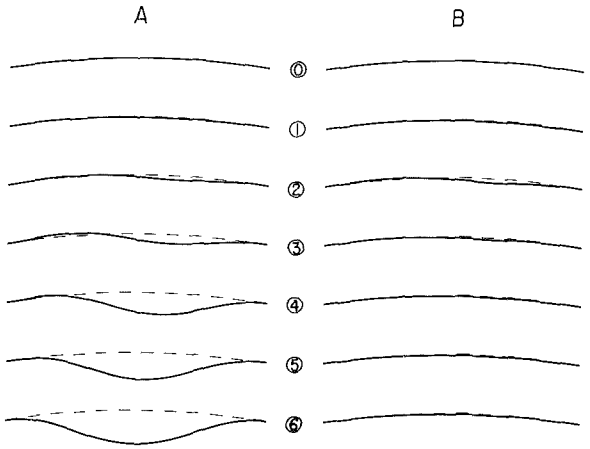


Fig. 13(*b*) Sequence of cross-section configurations at A and B (displacements amplified 2 ×)

Fig. 13 Panel analysis: λ = 12, 2*L* = 20*S*, with uniform unsymmetric initial imperfection

Summary and Conclusions

It has been demonstrated that, in addition to the classical limit load and bifurcation buckling instabilities, long panels can also develop propagating buckles. Once initiated, such buckles will propagate as long as the pressure is higher than the propagation pressure. In general, the propagation pressure is significantly lower than the classical critical pressures associated with the perfect structure.

The objective of the present work was to demonstrate that in such structures the classical instabilities trigger localization of collapse and the initiation of propagating buckles. In the case of panels with lower values of the arch parameter λ, the critical instability of geometrically perfect panels is the limit pressure of the primary symmetric response. In has been shown that following the load maximum the symmetric deformation localizes to a section a few panel spans long, while the remainder of the panel unloads uniformly. The pressure-volume change response follows a cusp-like shape until the localized collapse is arrested by membrane tension. Following this, and under prescribed volume loading, the collapse can propagate along the length at the propagation pressure.

In the case of panels with higher values of λ, the primary symmetric response is interrupted by a bifurcation into an axially uniform, unsymmetric mode before the limit pressure is reached. It has been shown that soon after its onset, this mode of deformation also localizes to a section a few panel spans long. As the deformation progresses, the unsymmetric local deformation gradually yields to a symmetric one. Local deformation is eventually arrested by membrane tension and the collapse can then propagate down the panel.

The propagation pressure of elastic panels exhibiting either type of behavior can be calculated exactly by the Maxwell construction and is given approximately by Eq. (2).

The main requirements for the existence of the type of behavior described are that the structure have a local up-down-up load-deformation response, as those shown in Fig. 1, and that it be long (see Kyriakides, 1993). Thus, long panels with other arch geometries, boundary conditions and load distributions can be expected to exhibit similar localized and propagating instabilities.

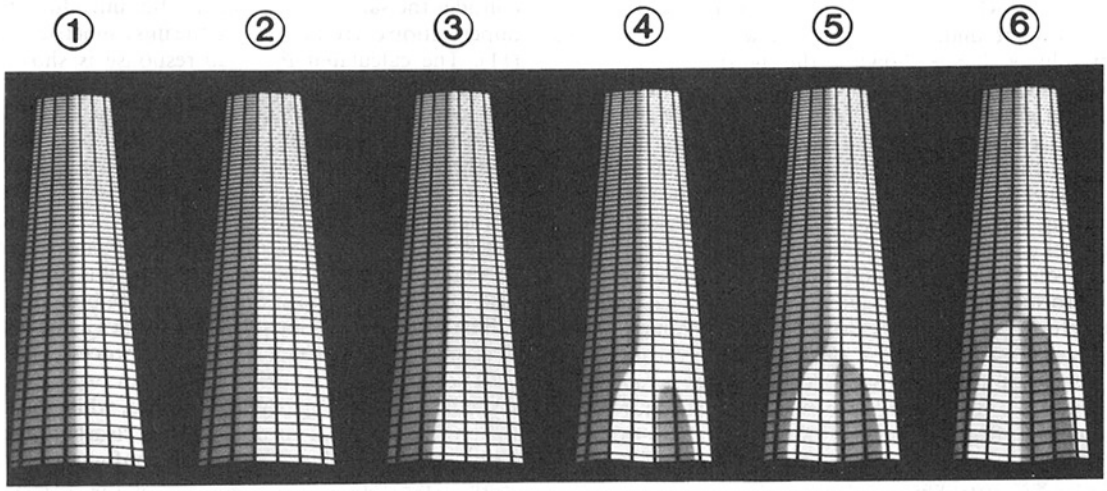


Fig. 14 Sequence of calculated configurations for panel of Fig. 13 showing unsymmetric initiation of collapse followed by symmetric propagation

Downloaded 03 May 2010 to 171.66.16.20. Redistribution subject to ASME license or copyright; see http://www.asme.org/terms/Terms_Use.cfm

Acknowledgment

The work was supported in part by the Office of Naval Research through grant N-00014-91-J-1103 and by the University of Texas at Austin.

References

Biezeno, C. B., 1938, "Das Durchschlagen Eines Schwach Gekrummten Stabes," *Zeitschrift fur Angewandte Mathematik und Mechanik*, Vol. 18, pp. 21–30.

Chater, E., and Hutchinson, J. W., 1984, "On the Propagation of Bulges and Buckles," ASME JOURNAL OF APPLIED MECHANICS, Vol. 51, pp. 269–277.

Dyau, J. Y., and Kyriakides, S., 1993, "On the Localization of Collapse in Cylindrical Shells Under External Pressure," *International Journal of Solids and Structures*, Vol. 30, pp. 463–482.

Ericksen, J. L., 1975, "Equilibrium of Bars," *Journal of Elasticity*, Vol. 5, pp. 191–201.

Fung, Y. C., and Kaplan, A., 1952, "Buckling of Low Arches or Curved Beams of Small Curvature," *NACA TN* 2840.

Gjelsvik, A., and Bodner, S. R., 1962, "The Energy Criterion and Snap Buckling of Arches," *ASCE Journal of the Engineering Mechanics Division*, Vol. 88, No. 4, pp. 87–134.

Hoff, N. J., and Bruce, V. G., 1954, "Dynamic Analysis of the Buckling of Laterally Loaded Flat Arches," *Journal of Mathematics and Physics*, Vol. 32, pp. 276–288.

Hutchinson, J. W., and Miles, J. P., 1974, "Bifurcation Analysis of the Onset of Necking in an Elastic/Plastic Cylinder Under Uniaxial Tension," *Journal of the Mechanics and Physics of Solids*, Vol. 22, pp. 61–71.

Kyriakides, S., 1993, "Propagating Instabilities in Structures," *Advances in Applied Mechanics*, Vol. 30, J. W. Hutchinson and T. Y. Wu, eds., Academic Press, Boston, MA, pp. 67–189.

Kyriakides, S., and Arseculeratne, R., 1993, "Propagating Instabilities in Long Shallow Panels," *ASCE Journal of Engineering Mechanics*, Vol. 119, No. 3, pp. 570–583.

Kyriakides, S., and Chang, Y.-C., 1991, "The Initiation and Propagation of a Localized Instability in an Inflated Elastic Tube," *International Journal of Solids and Structures*, Vol. 27, pp. 1085–1111.

Marguerre, K., 1938, "Uber die Anwendung der Energetischen Methode auf Stabilitatsprobleme," DVL 252–262; also *NACA TM* 1138, 1947.

Pearson, C. E., 1956, "General Theory of Elastic Stability," *Quarterly of Applied Mathematics*, Vol. 14, pp. 133–144.

Sanders, J. L., 1963, "Nonlinear Theories for Thin Shells," *Quarterly of Applied Mathematics*, Vol. 21, pp. 21–63.

Sewell, M. J., 1965, "On the Calculation of Potential Functions Defined on Curved Boundaries," *Proceedings of the Royal Society of London*, Vol. A286, pp. 402–411.

Schreyer, H. L., and Masur, E. F., 1966, "Buckling of Shallow Arches," *ASCE Journal of the Engineering Mechanics Division*, Vol. 92, pp. 1–19.

Timoshenko, S., 1935, "Buckling of Flat Curved Bars and Slightly Curved Plates," ASME JOURNAL OF APPLIED MECHANICS, Vol. 2, pp. A17–A27.

APPENDIX

Bifurcation Into Axially Nonuniform Shape

At any calculated equilibrium state on the primary response, (symmetric, axially uniform) the second variation ($\delta^2 V$) of the potential energy associated with the bifurcation modes (10) may be evaluated. Vanishing of $\delta^2 V$ indicates loss of stability of the uniform configuration. We define $\tilde{\mathbf{q}}$ as

$$\tilde{\mathbf{q}} = [A_1, A_2, \ldots, A_N, B_1, B_2, \ldots, B_N, C_1, C_2, \ldots, C_N]^T \tag{A1}$$

where A_i, B_i and C_i are the mode coefficients in (10). The second variation of the potential energy of the panel may then be expressed as

$$\begin{aligned}\delta^2 V = \int_0^L \int_0^\alpha \Big\{ & \tilde{N}_{\alpha\beta,i}\tilde{E}_{\alpha\beta,j} + \tilde{M}_{\alpha\beta,i}\tilde{K}_{\alpha\beta,j} \\ & + N^0_{xx}(\tilde{\phi}_{1,i}\tilde{\phi}_{1,j} + \tilde{\phi}_{,i}\tilde{\phi}_{,j}) + N^0_{\theta\theta}(\tilde{\phi}_{2,i}\tilde{\phi}_{2,j} + \tilde{\phi}_{,i}\tilde{\phi}_{,j}) \\ & + P\Big[(\tilde{u}_{,xi}\tilde{w}_{,j} - \tilde{u}_{,i}\tilde{w}_{,xj}) + \frac{1}{R}(\tilde{v}_{,i}\tilde{v}_{,j} + \tilde{v}_{,\theta i}\tilde{w}_{,j} \\ & - \tilde{v}_{,i}\tilde{w}_{,\theta j} + \tilde{w}_{,i}\tilde{w}_{,j}) \Big] \Big\} R\,d\theta\,dx\,\tilde{q}_i\tilde{q}_j \end{aligned} \tag{A2}$$

where $(\ )^0$ corresponds to the values in the primary equilibrium state, and derivatives with respect to $\tilde{q}_i$ are denoted by $(\ )_{,i}$. Implicit in the derivation of Eq. (A2) are Sanders' (1963) nonlinear strain-displacement relations for moderate rotations. These relationships, when linearized, yield

$$\begin{aligned} \tilde{E}_{xx} &= \tilde{u}_{,x} + \phi^0_1\tilde{\phi}_1 + \phi^0\tilde{\phi}, \\ \tilde{E}_{\theta\theta} &= \frac{1}{R}(\tilde{v}_{,\theta} + \tilde{w}) + \phi^0_2\tilde{\phi}_2 + \phi^0\tilde{\phi}, \\ \tilde{E}_{x\theta} &= \frac{1}{2}\left[\left(\tilde{v}_{,x} + \frac{1}{R}\tilde{u}_{,\theta} \right) + \phi^0_1\tilde{\phi}_2 + \phi^0_2\tilde{\phi}_1 \right], \\ \tilde{K}_{xx} &= \tilde{\phi}_{1,x}, \\ \tilde{K}_{\theta\theta} &= \frac{1}{R}\tilde{\phi}_{2,\theta}, \\ \tilde{K}_{x\theta} &= \frac{1}{2}\left[\frac{1}{R}\tilde{\phi}_{1,\theta} + \tilde{\phi}_{2,x} + \frac{1}{R}\tilde{\phi} \right] \end{aligned} \tag{A3}$$

where

$$\tilde{\phi}_1 = -\tilde{w}_{,x}, \quad \tilde{\phi}_2 = \frac{1}{R}(\tilde{v} - \tilde{w}_{,\theta}) \text{ and } \tilde{\phi} = \frac{1}{2}\left(\tilde{v}_{,x} - \frac{1}{R}\tilde{u}_{,\theta} \right).$$

Equation (A2) then reduces to the quadratic form $\delta^2 V = \tilde{\mathbf{q}}^T\mathbf{H}\tilde{\mathbf{q}}$. Thus, loss of stability of the primary response is indicated by the vanishing of the determinant of $\mathbf{H}$.

Downloaded 03 May 2010 to 171.66.16.20. Redistribution subject to ASME license or copyright; see http://www.asme.org/terms/Terms_Use.cfm

Post-buckling Behavior of Beams Under Contact Constraints

N. Adan
Faculty of Civil Engineering.

I. Sheinman
Faculty of Civil Engineering.

E. Altus
Faculty of Mechanical Engineering.

Technion-Israel Institute of Technology,
Technion City, Haifa 32000 Israel

An analytical model of the post-buckling behavior of a beam under contact constraints was derived. Experiments were carried out in order to characterize the various phenomenon involved in the problem. Two experiments with symmetric response with various contact surface and initial imperfection, and one experiment of asymmetric behavior were chosen for validation of the analytical results. The theory is based on a nonlinear kinematic approach and on the moving boundary procedure. The nonlinear equations are derived by the variational principle and solved through truncated approximating functions. A modification of an "arc-length" procedure was developed for solving the equation which incorporates the snapping effect. A comprehensive parametric study of the dominant parameters (distance between the beam and the contact surface, initial imperfections, contact location, magnitude of the contact forces, etc.) is carried out through numerical examples. Very good agreement with experimental results for the various phenomena involved in the problem was obtained for a clamped beam.

1 Introduction

The nonlinear behavior of structures with contact constraints has an important role in many engineering applications, and has consequently become the subject of numerous publications (for example, Kikuchi and Oden, 1988). By contrast, few deal with buckling under contact (Kanto and Yagawa, 1990) and very few are concerned with the post-buckling behavior in these circumstances. Recently, in the context of the finite element method, several studies of nonlinear behavior with contact constraints have been performed (see, for example, Simo et al., 1986; Stein et al., 1990). These rather concentrate on the numerical procedure, and since finite element representation of contact problems involves hundreds of degrees-of-freedom, it is unsuitable for parametric study. Post-buckling situations with contact constraints are highly relevant in composite laminated structures (Chang and Kutlu, 1989), one of whose most problematic aspects is multiple separation of layers (so-called delamination) under the action of service factors, with resulting local instability of the sublaminates. Such instability does not necessarily reduce the ultimate load and usually the laminate is capable of carrying on in a post-buckling mode under higher loading (Sheinman and Soffer, 1991) which is where the contact constraints come into play. The effect of interply contact is specially pronounced in realistic cases of multiple delamination, and an advanced analytical tool is necessary for insight into the nonlinear contact response.

In view of the complexity of post-buckling analysis of structures with contact constraints, validation of the adapted model is an essential task. The goal of this investigation is better understanding of the constrained nonlinear behavior including the buckling, post-buckling, and snapping effects. For that purpose, an experimental study of a compressed clamped beam against a contact surface was carried out on the basis of which an analytical model was constructed and its results compared with the experimental findings.

The analytical model consists of highly nonlinear equations derived by the variational principle on the generalized potential energy containing moving boundary parameters. The constraints were introduced via the Lagrange Multiplier function of the contact distance and slope of the displacement curves. Using truncated series functions, the resulting nonlinear partial differential equations were converted into a sequence of nonlinear algebraic ones. Since these equations are characterized by limit points followed by snapping, a suitable modified "arc length" method was developed for the pre- and post-limit behavior. A parametric study of the contact distance and imperfection shape and amplitude was also carried out. Very good agreement with the experimental results was obtained.

Basic Phenomena

The basic phenomena involved in buckling and post-buckling behavior under contact constraints is demonstrated through a simple, yet representative model, shown in Fig. 1. The model consists of an imperfect beam located near a rigid smooth surface. The imperfection function is represented by $\overline{w}(x)$ and $d(x)$ defines the surface. The beam is subjected to compression induced either by a load N^* or by an end-shortening displace-

Contributed by the Applied Mechanics Division of THE AMERICAN SOCIETY OF MECHANICAL ENGINEERS for publication in the ASME JOURNAL OF APPLIED MECHANICS.

Discussion on this paper should be addressed to the Technical Editor, Professor Lewis T. Wheeler, Department of Mechanical Engineering, University of Houston, Houston, TX 77204-4792, and will be accepted until four months after final publication of the paper itself in the ASME JOURNAL OF APPLIED MECHANICS.

Manuscript received by the ASME Applied Mechanics Division, May 26, 1992; final revision, Sept. 20, 1993. Associate Technical Editor: A. K. Noor.

Copyright © 1994 by ASME
Downloaded 03 May 2010 to 171.66.16.20. Redistribution subject to ASME license or copyright; see http://www.asme.org/terms/Terms_Use.cfm

ment u^*. As the compression is applied, the beam deflects freely until contact between the beam and the surface occurs. From that point onward, the displacements are constrained by the surface, resulting in a different nonlinear response pattern.

In order to characterize the complete equilibrium path of the constrained beam and locate the basic phenomena involved, the above contact model was experimentally set and investigated. Experimental characterization of the various stages which the structure undergoes has a crucial importance for its analytical modeling, because it indicates the points in which the solution is prone to diverge. Furthermore, due to the complexed nature of the structural response, experimental validation of analytical results is of great importance.

A schematic of the apparatus set-up for the model is given in Fig. 2: the compression machine (1) induces an end-shortening displacement in a constant rate while monitoring the axial force in the specimen; the clips (2) are designed to provide complete clamped conditions (measured buckling loads in a free-buckling test indicate values of 98 percent of the theoretical load); the specimen (3) and contact surface (4) are polished and greased to prevent friction, the midspan transverse displacement is monitored by an electromagnetic LVDT gauge chosen to minimize the lateral resistance.

Experiments performed for various contact surfaces show two distinct types of post-buckling behavior, namely symmetric and asymmetric responses. In the following, the phenomena is explained qualitatively, noting that quantitative results are presented later.

Figure 3 shows characteristic equilibrium paths for straight contact surface ($d(x) = \text{const}$). The points $s_1 - s_6$ and $a_1 - a_6$ on the symmetric and asymmetric response paths, respectively, indicate transitions between characteristic stages of response. The point "o" indicates the imperfect, preloading state. The first part of both equilibrium curves follow the familiar nonlinear path of imperfect beams under compression. This part of the curve is asymptotic to the classical buckling load level $N = N_{cr}$.

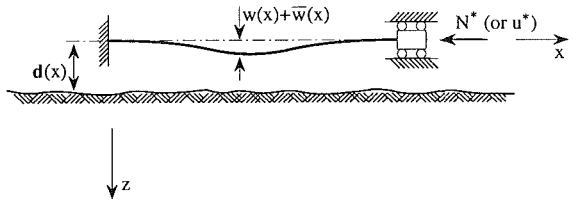


Fig. 1 Beam model for buckling under contact constraints

Transition to the constrained response pattern in the symmetric case, marked by s_1, takes place as contact occurs in the midspan. The transition point is characterized by a sharp increase in the axial stiffness. The contact point which occurs at this point is retained until a straight contact zone begins to form and spread symmetrically to the supports (s_3). At this point, indicated by s_2, a distinct change in the axial stiffness is reflected in the axial force versus the end shortening ($N-u$) curve. Between s_2 and s_3, the contact forces are concentrated at the two end points of the contact line. As the end-shortening is further increased, the axial force increases up to a limit point, s_4, where the straight middle portion of the beam snaps. The equilibrium path of the dynamic snap buckling, as reflected in the $N-w$ curve, is characterized by a nonstable

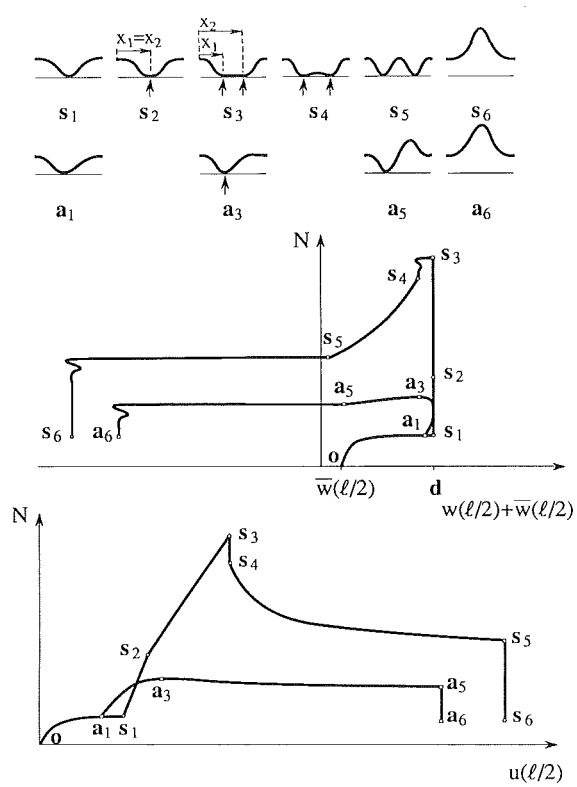


Fig. 3 Characteristic load-midspan displacement and load-end shortening for symmetric and asymmetric structural response

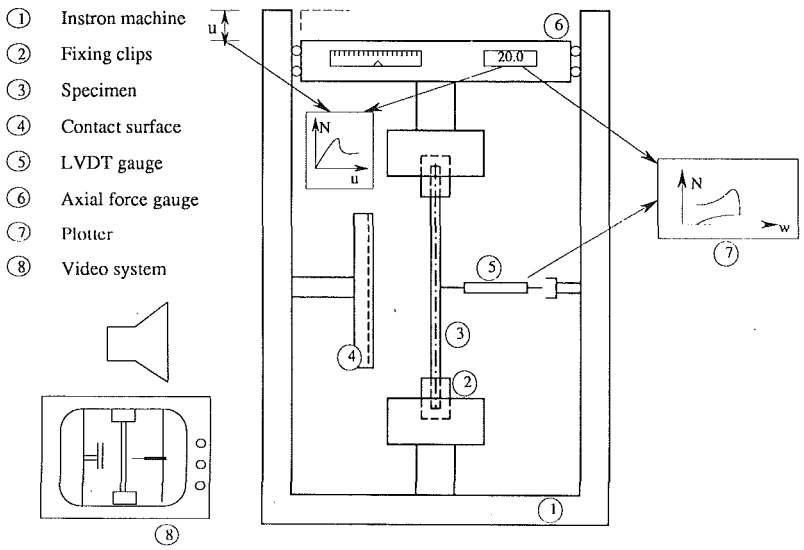


Fig. 2 Schematic test set-up

Downloaded 03 May 2010 to 171.66.16.20. Redistribution subject to ASME license or copyright; see http://www.asme.org/terms/Terms_Use.cfm

deflection with a nearly constant axial force, followed by a sharp drop in the axial force with oscillating deflections decaying to the static equilibrium state, s_4. In the next stage, the distance between the contact points enlarges, the axial force decreases, and the deformed beam gradually takes the shape of the third buckling mode. At the equilibrium state, s_5, in which the shape is close to the third mode, the beam snaps to the opposite side of the load axis. Then it stabilizes with the shape and axial force of the first buckling mode, at position s_6. From this point onwards, the beam follows the unconstrained nonlinear path in an opposite direction to the initial response.

The more common behavior, however, is the asymmetric response. The contact occurs in an eccentric point, marked on the path by a_1. As the constrained response is considerably stiffer than the free one, further increase in the induced end-shortening displacement results in a sharp rise in the axial force and transition of the (single) contact point. The axial force reaches a maximum value at point a_3 and then decreases in a "smooth" manner. The contact point moves further towards the support, and the beam takes a shape close to the second buckling mode. Dynamic snap-back occurs at position a_5, and again the beam stabilizes in the shape of the first mode on the opposite side.

Analytical Formulation

The model is based on the Kirchoff-Love assumption, expressed by

$$u(x, z) = u(x) - z w_{,x}(x)$$

$$w(x, z) = w(x)$$

$$\epsilon(x, z) = \epsilon(x) + z\chi(x) \tag{1}$$

where x, z are the natural global coordinates (see Fig. 1), u, w are the axial and transverse displacements, respectively, and ϵ, χ are the axial strain and change of curvature. $(\ )_{,x}$ denotes derivation with respect to the x-coordinate.

Resorting to the Von-Karman kinematic approach, the strain at the reference surface and change of curvature for imperfect model (represented by $\overline{w}(x)$) is given by

$$\epsilon(x) = u_{,x} + \frac{1}{2} w_{,x}(w_{,x} + 2\overline{w}_{,x})$$

$$\chi(x) = -w_{,xx}. \tag{2}$$

In the framework of these assumptions, under contact conditions, the necessary equations of geometric compatibility for every contact point are

$$w(x) + \overline{w}(x) = d(x)$$

$$w_{,x} + \overline{w}_{,x}(x) = d_{,x}(x). \tag{3}$$

The nonlinear equilibrium equations of the constrained system are derived by means of a variational principle applied on the functional which consists of the total potential of the system π_p and geometric compatibility constraints π_c,

$$\delta\pi = \delta\pi_p + \delta\pi_c. \tag{4}$$

The total potential energy is given by

$$\pi_p = \frac{1}{2}\int_0^l [(N\epsilon + M\chi) - \rho(n_x^* u + q_z^* w)]dx - \rho[N^* u + S^* w + M^* w_{,x}]|_{x=0}^{x=l}. \tag{5}$$

N, M are the axial force and bending moment, respectively; ρ is the loading parameter, n_x^*, q_z^* are the external applied distributed axial and transverse loading; and N^*, S^*, M^* are the external axial force, shear force, and bending moment applied at the boundaries.

The functional π_c, which is used for imposing the geometrical compatibility through the Lagrange Multiplier Technique, is given by

$$\pi_c = \int_{x_1}^{x_2} [\Lambda^{(1)}(w + \overline{w} - d) + \Lambda^{(2)}(w_{,x} + \overline{w}_{,x} - d_{,x})]dx. \tag{6}$$

$\Lambda^{(1)}$ and $\Lambda^{(2)}$ are the Lagrange multipliers function of x and the unknown moving boundaries x_1 and x_2 which are intermediate (changing) location points of contact throughout the displacement process.

The equilibrium equations are obtained by using the boundary terms (x_1 and x_2) as additional variation parameters (see Kerr, 1976) and employing the following variational principle (Eq. 4):

$$\delta\pi = \int_0^l \left\{ A\left[u_{,x} + \frac{1}{2} w_{,x}(w_{,x} + 2\overline{w}_{,x})\right][\delta u_{,x} + (w_{,x} + \overline{w}_{,x})\delta w_{,x}] - Dw_{,xx}\delta w_{,xx} - \rho(n_x^*\delta u + q_z^*\delta w) + (w + \overline{w} - d)\delta\Lambda^{(1)} + \Lambda^{(1)}\delta w + (w_{,x} + \overline{w}_{,x} - d_{,x})\delta\Lambda^{(2)} + \Lambda^{(2)}\delta w_{,x}\right\} dx - \rho[N^*\delta u + S^*\delta w + M^*\delta w_{,x}|_{x=0}^{x=l} - [\Lambda^{(1)}(w + \overline{w} - d) + \Lambda^{(2)}(w_{,x} + \overline{w}_{,x} - d_{,x})]\delta x_1|_{x=x_1} + [\Lambda^{(1)}(w + \overline{w} - d) + \Lambda^{(2)}(w_{,x} + \overline{w}_{,x} - d_{,x})]\delta x_2|_{x=x_2} = 0. \tag{7}$$

A, D are the standard axial and bending stiffness, respectively.

The unknown variables are the displacement functions u, w; the contact generalized force functions are $\Lambda^{(1)}$, $\Lambda^{(2)}$, and the moving boundary variables are x_1 and x_2.

Solution Procedure

The solution strategy undertaken for the nonlinear equations (derived from Eq. (7)) is discretization of the unknown functions into truncated series followed by iterative procedure based on the Newton-Raphson method. Since the nonlinear behavior is characterized by a snap-through phenomenon rather than by bifurcation points, a special modified algorithm of a constant arc-length method is implemented.

The displacement and contact force functions are first approximated as follows:

$$u(x) = \sum_{j=0}^{Nu} u_j g_j(x)$$

$$w(x) = \sum_{j=1}^{Nw} w_j f_j(x)$$

$$\overline{w}(x) = \sum_{j=1}^{Nw} \overline{w}_j f_j(x)$$

$$\Lambda^{(i)}(x, x_1, x_2) = \sum_{k=1}^{Nf} \lambda_k^{(i)} h_k(x, x_1, x_2); \quad i = 1, 2. \tag{8}$$

The axial displacement approximating function g_j ($j = 0, 1 \ldots Nu$) consists of the linear function and a series of symmetric and antisymmetric compatible nonlinear functions. Here these functions are derived from an Airy Stress function (see the Appendix).

The transverse displacement functions f_j are composed of the compatible buckling modes of the beam:

$$f_j(\xi) = C_1 + C_2\xi + C_3\sin(\beta_j\xi) + C_4\cos(\beta_j\xi)$$

$$j = 1, 2 \ldots Nw, \tag{9}$$

Downloaded 03 May 2010 to 171.66.16.20. Redistribution subject to ASME license or copyright; see http://www.asme.org/terms/Terms_Use.cfm

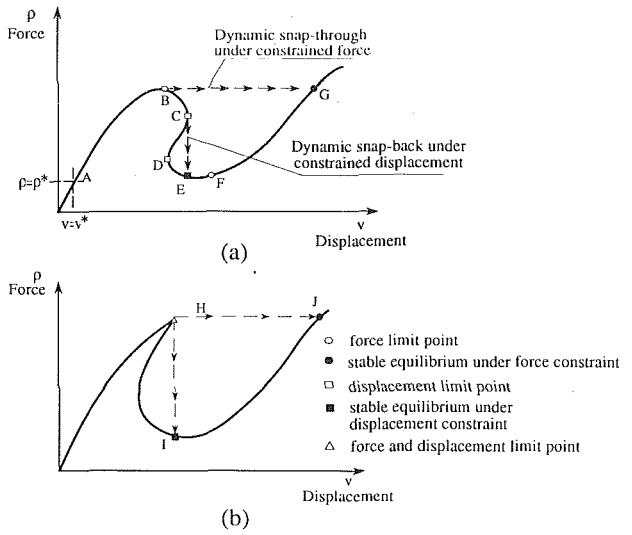


Fig. 4 Equilibrium path characterized by limit points; (*a*) limit point for load and displacement, (*b*) simultaneous limit point for load and displacement

where $\xi = x/l$. β_j are the eigenvalues of the characteristic buckling equations and C_i are determined by the boundary conditions (see Sheinman and Frostig, 1991).

The contact force approximation functions are composed of Dirac contact point functions:

$$h_1(x, x_1, x_2) = \delta(x - x_1)$$

$$h_2(x, x_1, x_2) = \delta(x - x_2); \tag{10a}$$

of linear distribution functions

$$h_3(-x, x_1, x_2) = (x - x_1)/l_c$$

$$h_4(x, x_1, x_2) = (x_2 - x)/l_c \tag{10b}$$

where $l_c = x_2 - x_1$;
and of nonlinear distributed functions:

$$h_5(x, x_1, x_2) = \sin(n\pi(x - x_1)/l_c$$

$$h_6(x, x_1, x_2) = \cos(n\pi(x_2 - x)/l_c \; n = 1, 2 \ldots . \tag{10c}$$

Note that in the case of a straight contact surface and small initial imperfections, the Kirchoff-Love hypothesis yield point contact only, so only h_1 and h_2 should be used.

Substitution of the approximation functions (Eqs. (8)) into the variational equation (Eq. (7)) yields the following nonlinear algebraic set of equations:

$$(\delta U_p): \quad EU_p \equiv \rho G_1(p) + \sum_{m=1}^{Nu} U_m G_2(m, p) + \sum_{m=1}^{Nw}\sum_{n=1}^{Nw} w_m(w_n + 2\overline{w}_n)\, G_4(m, n, p) = 0$$

$$(p = 0, 1, 2 \ldots Nu)$$

$$(\delta w_p): \quad Ew_p \equiv \rho F_1(p) + \sum_{m=0}^{Nu}\sum_{n=1}^{Nw} u_m(w_n + \overline{w})F_2(m, n, p) + \sum_{m=1}^{Nw} w_m F_3(m, p) + \sum_{m=1}^{Nw}\sum_{n=1}^{Nw}\sum_{l=1}^{Nw} w_m(w_n + \overline{w}_n)(w_l + 2\overline{w}_l) \times F_4(m, n, 1, p) + \sum_{k=1}^{Nf}\sum_{i=1}^{2} \lambda_k^{(i)} H_l^{(i)}(k, p) = 0$$

$$(p = 1, 2 \ldots Nw)$$

$$(\delta\lambda_k^{(i)}): \quad E\lambda_k^{(i)} \equiv \sum_{n=1}^{Nw} (w_n + \overline{w}_n)\, H_1^{(i)}(k, n) - H_2^{(i)}(k) = 0$$

$$(i = 1, 2; \; k = 1, 2 \ldots Nf)$$

$$(\delta x_1): \quad Ex_1 \equiv \sum_{k=1}^{Nf}\sum_{i=1}^{2} \lambda_k^{(i)} \left[\sum_{n=1}^{Nw} (w_n + \overline{w}_n)\, H_{31}^{(i)}(k, n) - H_{41}^{(i)}(k) \right] = 0$$

$$(\delta x_2): \quad Ex_2 \equiv \sum_{k=1}^{Nf}\sum_{i=1}^{2} \lambda_k^{(i)} \left[\sum_{n=1}^{Nw} (w_n + \overline{w}_n)\, H_{32}^{(i)}(k, n) - H_{42}^{(i)}(k) \right] = 0. \tag{11}$$

The coefficients G, F, H which are functions of g_i, f_i, and h_i and their derivatives are given in Adan (1991).

The system of nonlinear equations (Eqs. (11)) contain ($Nu + Nw + 2Nf + 3$) equations with ($Nu + Nw + 2Nf + 4$) unknowns. The extra equation needed to complete the system is a constraint equation dictating external force or displacement.

Special attention is given to the application of external constraints since the equilibrium path of the constrained structure exhibits limit point and snap buckling phenomena. A schematic description of these phenomena is given in Fig. 4. Limit points and snap buckling under constrained load or displacement is depicted in Fig. 4(*a*): point B is a limit point under constrained load $\rho = \rho^*$ and snap-through occurs to point G where stable equilibrium is resumed. Under constrained displacement $v = v^*$, snap-back buckling occurs between the limit point C to the stable equilibrium point E. Solution procedures which dictate the parameter (force or displacement) undergoing a limit point will fail near the limit point. The difficulties in the solution are even more pronounced when limit points for load and displacement are close or even overlap as demonstrated in Fig. 4(*b*).

The "arc-length" method (Riks 1972, 1979) is used to derive a suitable modified method for the solution of the unknown vector ($X^T = [\rho, u, w, \lambda^{(i)}, x_{(i)}]$) which contains additional unknowns (i.e., $\lambda^{(i)}$ and $x_{(i)}$) not accounted for in the original algorithm. If one treats the additional unknowns as generalized displacements and include them in the original procedure, the solution diverges in the neighborhood of the limit point. The changes needed to obtain convergence are based on the following distinction between parameter types:

(a) primary parameters ("action" parameters)—which are independent necessary conditions—u, w;
(b) secondary parameters ("reaction" parameters)—which are dependent on the primary parameters—ρ, $\lambda^{(i)}$;
(c) geometric parameters—the intermediate variable contact boundary values x_1, x_2.

The dependence between coupled primary and secondary parameters is expressed as a product between them in the functional. If two coupled primary and secondary parameters reach a limit point simultaneously (or close to it), the procedure will fail since the formulation does not allow for a nonmonotonic change in both action and reaction. An example of such a point is illustrated in Fig. 4(*b*) where the coupled parameters ρ, v reach a common limit. Therefore, the required change is to exclude the secondary (and geometrical) parameters from the original arc-length constant equation. It should also be noted that the widely used two-step algorithm known as "Modified Riks Procedure" (see, for example, Crisfield 1981, 1983; Bathe and Dvorkin, 1983) designed to maintain the symmetry of the stiffness matrix also fails here, since it uses the secondary load parameter ρ as control parameter.

The nonlinear system equations, which include the modified

Downloaded 03 May 2010 to 171.66.16.20. Redistribution subject to ASME license or copyright; see http://www.asme.org/terms/Terms_Use.cfm

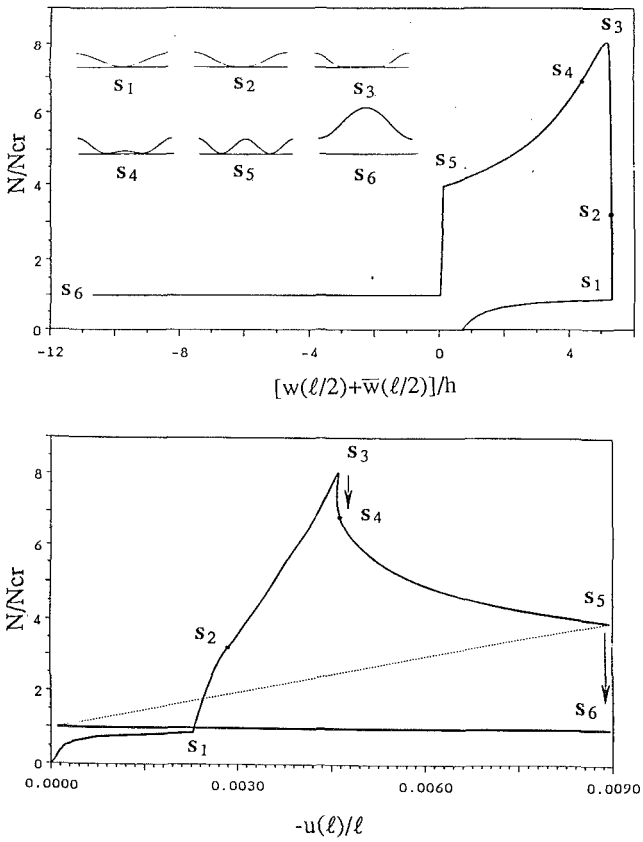


Fig. 5 Analytical load-midspan displacement and load-end shortening curves for symmetric response

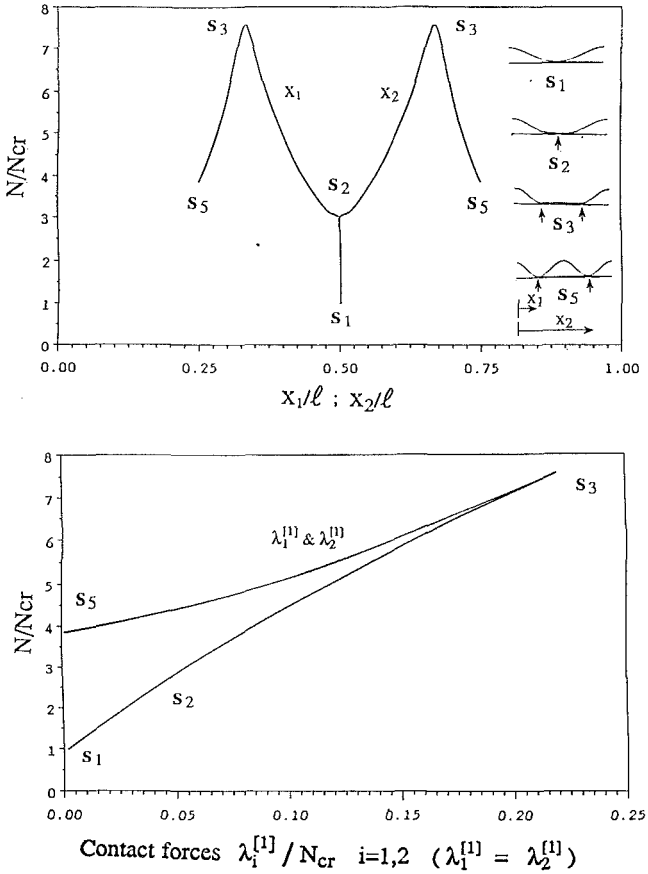


Fig. 6 Analytical contact points coordinates and contact forces for symmetric response

arc-length constraint equation (Eq. (11)), are solved iteratively by the Newton-Raphson method. The contact constraint equations (Eqs. (11*c*,*d*,*e*)) are introduced only once penetration has been detected in the iteration process.

Results and Parametric Study

The above analysis was implemented into a general purpose computer code. The coefficient integrals are calculated exactly, using REDUCE symbolic compiler (Hearn, 1987). An energetic norm is used with a convergence error of 10^{-5}. The code is used for a parametric study of the model, with the data of specimen which were investigated experimentally. The specimen consists of a AL7075-T6 (Aluminium) strut of a rectangular cross-section, with the following data: span l = 393 mm; width b = 12.5 mm; height h = 2.2 mm; elasticity modulus 70 GPa; Poisson ratio ν = 0.33. This specimen was analyzed in the symmetric and asymmetric behavior patterns and then validated by experimental results.

Analysis of the symmetric response type is carried out with eight (Nw = 8) transverse displacement approximating functions. These functions include the first seven symmetric buckling modes of the problem, and one antisymmetric mode needed to prevent singularity of the coefficient matrix when symmetric contact constraints are applied. The axial nonlinear displacements are approximated by 14 antisymmetric functions (Nu = 14). The contact forces are described by two Dirac-Delta functions, which are close to the actual contact force distribution for small imperfections and a straight contact surface. The initial imperfection needed to generate the nonlinear solution is formed by a combination of the two first symmetric buckling modes.

Load-displacement curves for $d(x)$ = const. = 11.7 mm; $\overline{w}_1 = 0$; $\overline{w}_3 = 0.1$ mm are shown in Fig. 5, while the variation in magnitude and location of the contact forces is shown in Fig. 6. The shape of the deflected beam in the transition points $s_1 - s_6$ is visualized in Figs. 5 and 6. Penetration of the beam into the contact surface occurs at point s_1 (N/N_{cr} = 0.882; N_{cr} being the classical buckling load), where the contact constraints are introduced. The solution converges to a single centric contact point. At s_2 (N/N_{cr} = 2.401) the curvature of the beam at the contact point becomes zero, and the contact spreads to two separate points. As the end shortening displacement is increased further, the contact points spread apart forming a straight middle zone. The contact forces increase and the limit point s_3 is detected for N/N_{cr} = 8.941; the curves exhibit a sharp change of slope and one can see that the load, axial displacement, and contact forces reach a limit simultaneously. The equilibrium states between s_3 and s_4 are unstable and buckling is expected as demonstrated in Fig. 5. Then the contact forces decrease, and when nulled at point s_5 the contact constraints are deactivated. The solution "jumps" from point s_5 (N/N_{cl} = 3.95, x_1/l = 0.251, x_2/l = 0.749), which is very close to the third buckling mode, to an unconstrained first mode configuration (N/N_{cr} = 1.001). The axial force values are only close to the exact mode counterparts because of the initial imperfection. Further increase in the end-shortening displacement (without change in the axial force), to a point where the axial displacement is equal to its value at s_5, defines the configuration s_6 after the second snap. From the point onward, the nonlinear solution follows the usual path for unconstrained beams.

The asymmetric response is analyzed with Nu = 19, Nw = 9. As the beam has no symmetry, both symmetric and antisymmetric functions should be used. The imperfection function is combined by $\overline{w}_1$ = 0.8 mm (symmetric); $\overline{w}_2$ = 0.6 mm (antisymmetric). The distance of the contact surface is assumed to be $d(x)$ = 11.7 mm. The resulting equilibrium path is given

Downloaded 03 May 2010 to 171.66.16.20. Redistribution subject to ASME license or copyright; see http://www.asme.org/terms/Terms_Use.cfm

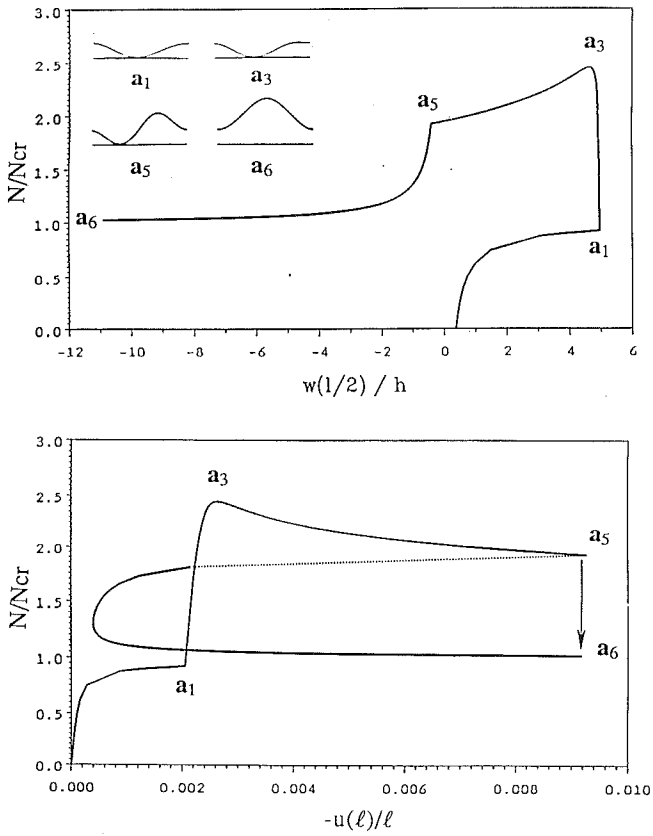
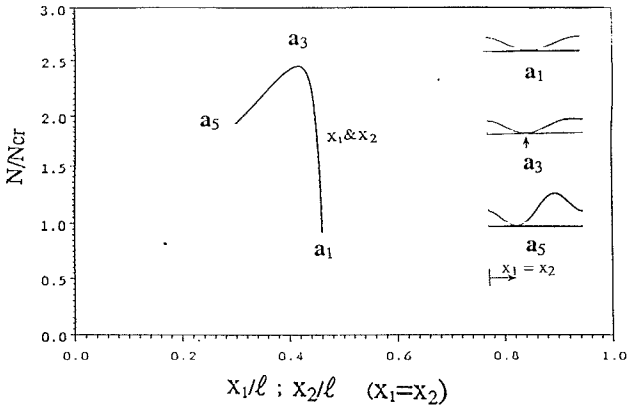


Fig. 7 Analytical load-midspan displacement and load end-shortening curves for asymmetric response



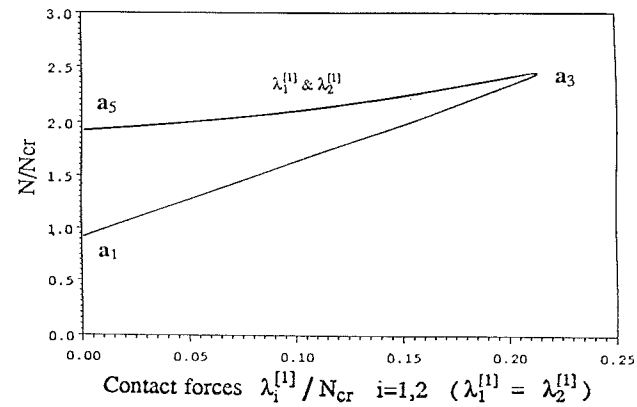


Fig. 8 Analytical contact point coordinates and contact forces for asymmetric response

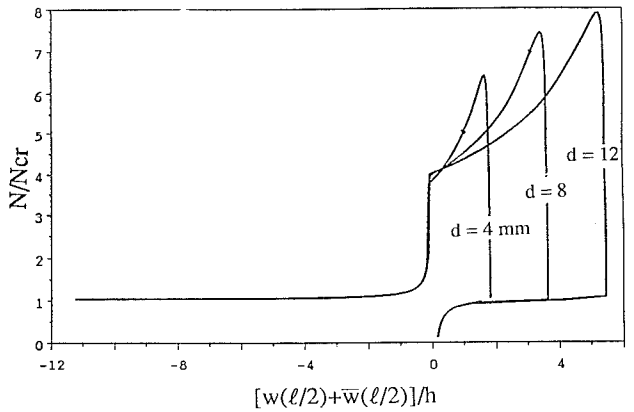
in Fig. 7, while the variation in magnitude and location of the contact forces is described in Fig. 8. The contact occurs at position a_1 ($N/N_{cr} = 0.932$, $x_1/l = x_2/l = 0.461$). It is pointed out that two contact points (and forces) are assumed in every solution step, and their unification to a single contact point results automatically in the iteration process. As the end-shortening displacement increases further, contact remains at a single point (unlike in the symmetric behavior) which moves towards the support. The load limit point occurs at $N/N_{cr} = 2.464$ followed by a monotonic decrease in the axial force. The contact force is nulled as ($N/N_{cr} = 1.940$, $x_1/l = x_2/l = 0.297$), which is very close to the second buckling mode (characterized by $N/N_{cr} = 2.046$, $x_1/l = x_2/l = 0.302$). As the contact constraints are deactivated, the solution "jumps" to a non-constrained configuration. The axial force continues to decrease and the point a_6 ($N/N_{cr} = 1.034$) defines the position to which the beam would have snapped in dynamic process.

The effect of the contact surface distance $d(x)$ is studied through a symmetric case with $\overline{w}_1 = 0.3$ mm; $\overline{w}_3 = 0.3$ mm, by setting $d(x) = 4$, 8, and 12 mm. As seen from the results given in Fig. 9, two characteristics of the response are mainly affected:

(a) As d increases, the load N/N_{cr} in which the limit point s_3 occurs, increases.

(b) Snap buckling (from point s_3 to s_4) is more pronounced for a smaller distance. If d is large enough ($d = 12$ mm for instance), the snap does not occur, and the displacements through the limit points change in a stable manner.

The initial imperfection, which is also a major parameter in the problem, is studied through an asymmetric example with $\overline{w}_1 = 0.8$ mm; $\overline{w}_2 = 0.01$, 0.4, 0.8 and 1.2 mm. The results are shown in Fig. 10. One can see that the smaller the imperfection, the higher the load level of the limit point a_3. Occurrence and magnitude of the snap buckling from a_3 to a_4 is also



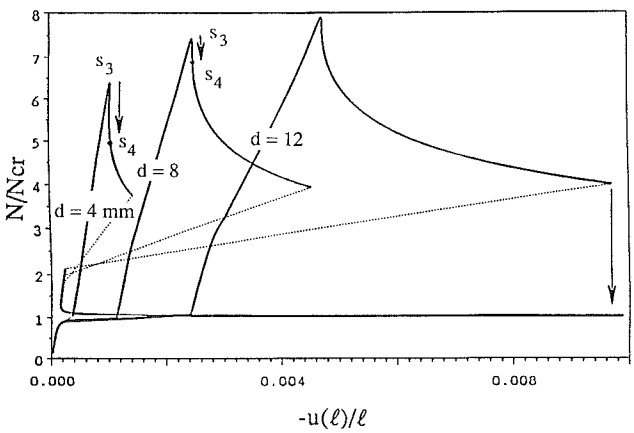


Fig. 9 Effect of contact distance (d) between the beam and contact surface for symmetric response

Downloaded 03 May 2010 to 171.66.16.20. Redistribution subject to ASME license or copyright; see http://www.asme.org/terms/Terms_Use.cfm

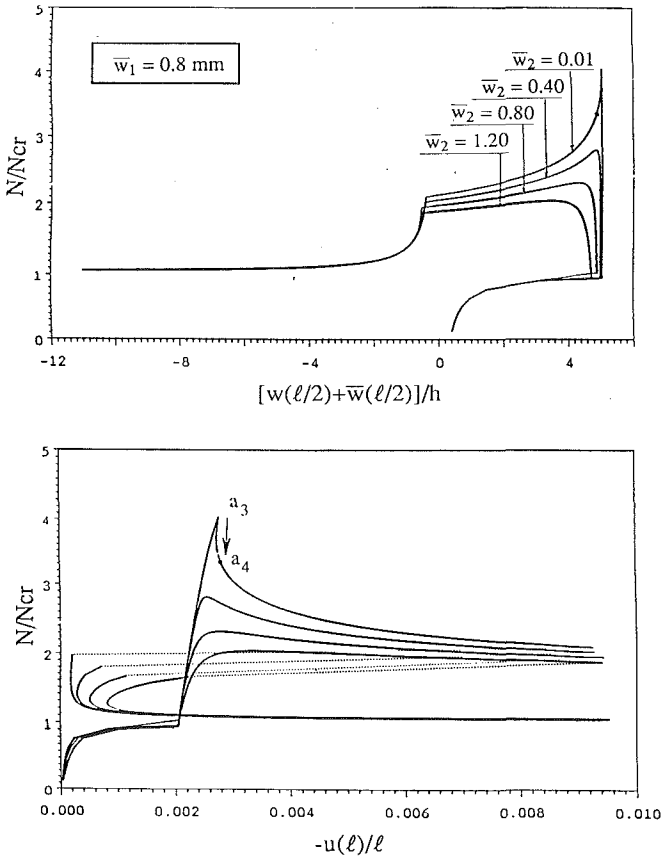


Fig. 10 Effect of the initial imperfection $\overline{w}_2$ on the asymmetric response

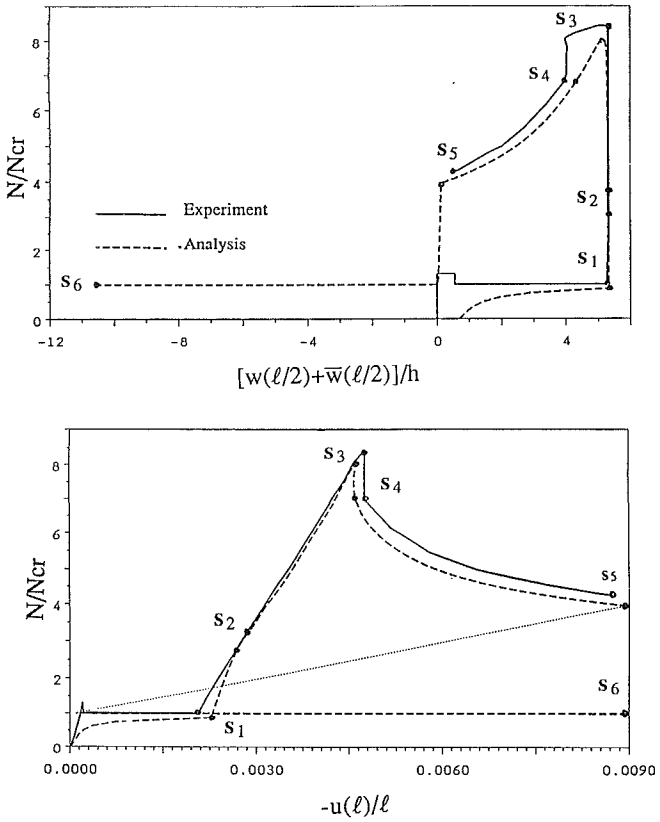


Fig. 11 Comparison between experiment and analysis for symmetric response for d = 11.7 mm

affected—for small imperfection snap does occur, while for larger magnitudes it does not occur at all.

Experimental Validation

Three experiments are chosen for validation of the analytical results. The experiments consist of two cases of symmetric response with various contact surfaces and initial imperfections, and one asymmetric case.

In the first experiment, near-zero imperfection was measured in the center of the specimen. The imperfection coefficients taken for this case are $\overline{w}_1 = 0$ for zero imperfection in the middle length and $\overline{w}_3 = 0.1$ mm, which is the small disturbance needed for generation of the nonlinear symmetric solution. The experimental results versus analysis are presented in Fig. 11. The experiment starts with zero transverse displacement. Buckling occurred at $N/N_{cr} = 1.3$, followed by a sharp drop in the axial force to $N/N_{cr} = 0.99$. After contact occurred the splitting of the contact forces in the analysis (s_2) takes place when $N/N_{cr} = 3.401$. The experimental counterpart, localized by a change of slope of the axial load versus end shortening ($N-u$) curve, took place at $N/N_{cr} = 3.1$. The limit point in the experiment occurs at $N/N_{cr} = 8.42$ while the analysis predicts $N/N_{cr} = 8.04$. These differences demonstrate the imperfection sensitivity of the phenomenon. The discrepancies between the curves between s_3 and s_4 is explained by the dynamic nature of snap buckling (experimental) in contrast to the static analysis. From s_4 onwards the experimental and analytic paths are parallel. The second snap s_5 occurred in the experiment at $N/N_{cr} = 4.24$, while the analytic counterpart is 3.95. Due to the relatively large distance (d = 11.7 mm), the inertia forces cause separation between the gauge and the beam during the snap buckling—so the path beyond s_5 was not recorded. However, the value $N/N_{cr} = 0.99$ was recorded for point s_6, where the beam reached static equilibrium. The analytic value of the force at this point is $N/N_{cr} = 1.001$, and the total displacement at the center is $w(l/2) + \overline{w}(l/2) = 2.028d$. This corresponds to the theoretical value $\overline{w} = 2d$, when considering a snap from the third buckling mode to the first mode assuming the beam remains at the same length ($u_x \ll 1/2\ w,_x^2$).

For the second example, a smaller contact distance d = 4.0 mm was set. The initial imperfection measured was $\overline{w}(l/2) = 0.3$ mm. (The coefficients of the initial imperfection set for the analysis are $\overline{w}_1 = \overline{w}_3 = 0.3$ mm.) The results are shown in Fig. 12. A very good correlation is seen up to s_3. Beyond that point, an uncharacteristic behavior was encountered in the experiment: the system snapped from the limit position s_3 directly to the first mode position s_6 without going through the characteristic stages s_4, s_5. That can be explained by the analytic results: due to the relatively small contact surface distance d, the snap buckling from s_3 to s_4 is very pronounced (see Fig. 9 and parametric study). Thus, point s_4 in this case is close to point s_5 on the path, and the inertia forces, developed in the experiment are large enough for a continuous dynamic transition between s_3 to s_6 without arrest. Very good agreement is obtained in the displacement and axial force at the point of arrest s_6.

The third example, with d = 11.7 mm and $\overline{w}_1 = 0.8$ mm, $\overline{w}_2 = 0.6$ mm exhibit an asymmetric response. The correlation up to point a_3, as seen from Fig. 13, is in good agreement. Beyond that point both the experiment and analysis show monotonic behavior, but the experimental axial forces are approximately ten percent higher than the analytic results. This discrepancy is explained by the imperfection sensitivity of the system. The correlation of the end-shortening displacement at a_5, in which the snap buckling occurred, is approximately 97 percent. Good agreement in the end-shortening values, which

Downloaded 03 May 2010 to 171.66.16.20. Redistribution subject to ASME license or copyright; see http://www.asme.org/terms/Terms_Use.cfm

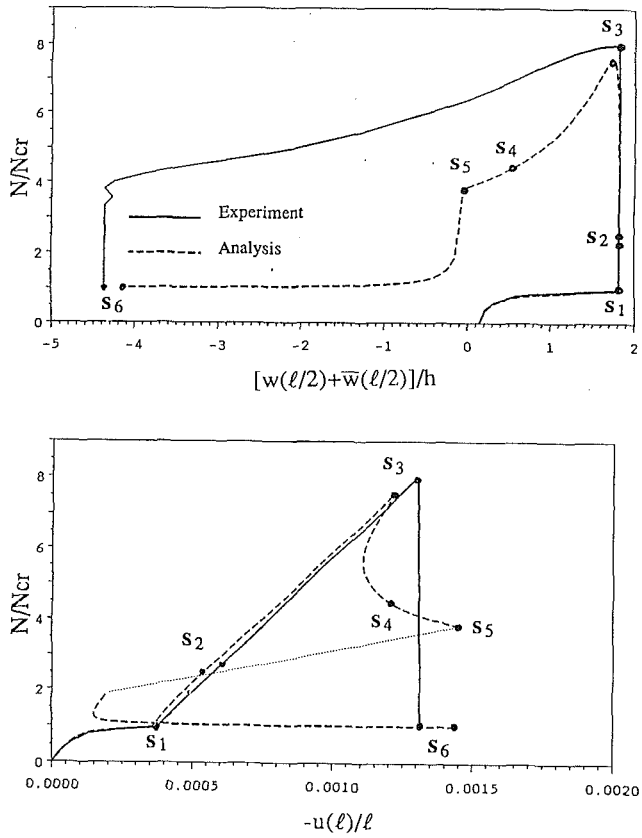


Fig. 12 Comparison between experiment and analysis for symmetric response for d = 4.0 mm

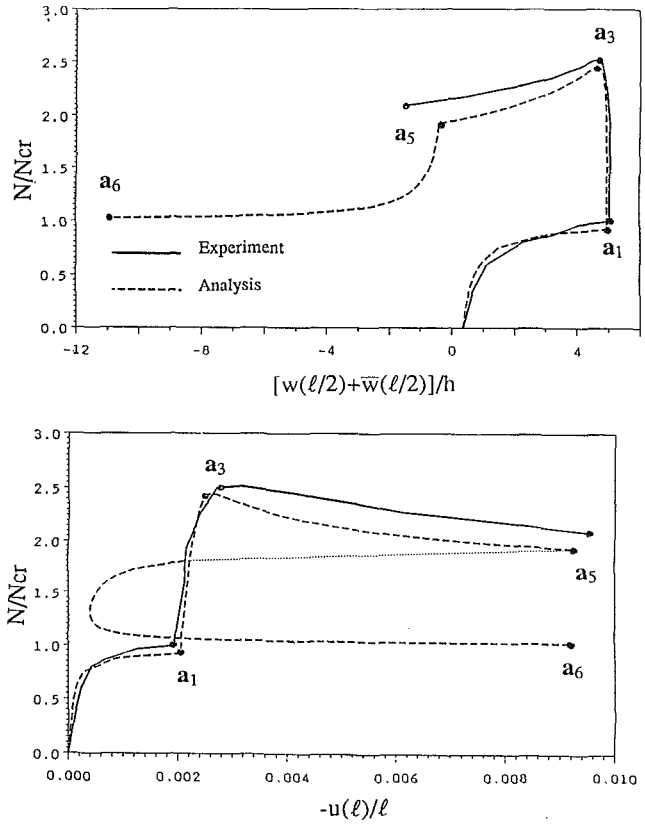


Fig. 13 Comparison between experiment and analysis for asymmetric response for d = 11.7 mm

represents an integral of the displacement, shows that the discrepancy in the midspan transverse displacement $\overline{w}(l/2)$ expresses a local phenomenon, as caused by deviation between actual and assumed imperfection.

Conclusion

Post-buckling of beams in the presence of contact constraints is studied experimentally and analytically. Experiments were conducted in order to characterize the various phenomenon involved in the problem. An analytic nonlinear model was constructed using a variational principle. The contact constraints are applied through the Lagrange Multipliers technique. The constraints functional, defined over the variable contact region, is formulated as a moving intermediate boundary variational problem. A modified "arc-length" algorithm was derived to converge the solution beyond the limit points for forces and displacements. A comprehensive parametric study of the dominant parameters (distance between the beam and the contact surface; initial imperfections, contact location; magnitude of the contact forces, etc.) is carried out through numerical examples. The various stages, typical to symmetric and asymmetric response patterns, are reproduced and explained. Very good correlation is encountered between experimental and analytic results. This nonlinear model can be used successfully in many engineering phenomena involving contact, one of which is the behavior of multidelaminated composite structures, whose behavior may be governed by interply contact.

Acknowledgment

The study was financed in part by the VPR Foundation at the Technion.

References

Adan, M., 1991, "Buckling of Multiply Delaminated Composite Laminates," Ph.D. Thesis, Technion—Israel Institute of Technology, Haifa, Israel.

Bathe, K. J., and Dvorkin, E. N., 1983, "On the Automatic Solution of Nonlinear Finite Element Equations," *Computers & Structures*, Vol. 17, pp. 871-879.

Chang, F., and Kutlu, Z., 1989, "Collapse Analysis of Composite with Multiple Delaminations," *Proc. AIAA/ASME/ASCE/AHS/ASC SDM 80th Conf.*, Alabama, pp. 989-999.

Crisfield, M. A., 1981, "A Fast Incremental/Iterative Solution Procedure that Handles Snapthrough," *Computers & Structures*, Vol. 13, pp. 55-62.

Crisfield, M. A., 1983, "An Arc-length Method Including Line Searches and Accelerations," *Int. J. Num. Meth. Engng.*, Vol. 19, pp. 1269-1289.

Hearn, A. C., 1987, *REDUCE-User Manual*, Version 3.3, The Rand Corporation, CP78, Santa Monica, CA.

Kerr, A. P., 1976, "On the Deviation of Well Posed Boundary Value Problems in Structural Mechanics," *Int. J. Solids Structures*, Vol. 12, pp. 1-11.

Kikuchi, N., and Oden, J. T., 1988, *Contact Problems in Elasticity: A Study of Variational Inequalities and Finite Element Methods*, SIAM, Philadelphia, PA.

Kanto, Y., and Yagawa, G., 1990, "A Dynamic Contact Buckling Analysis by the Penalty Finite Element Method," *Int. J. Num. Meth. Engng.*, Vol. 29, pp. 755-774.

Riks, E., 1972, "The Application of Newton's Method to the Problem of Elastic Stability," ASME Journal of Applied Mechanics, Vol 39, pp. 1060-1066.

Riks, E., 1979, "An Incremental Approach to the Solution of Snapping and Buckling Problems," *Int. J. Solids Structures*, Vol. 15, pp. 529-551.

Sheinman, I., and Soffer, M., 1991, "Post-buckling Analysis of Composite Delaminated Beams," *Int. J. Solids Structures*, Vol. 27, No. 5, pp. 639-646.

Sheinman, I., and Frostig, Y., 1991, "Nonlinear Analysis of Stiffened Laminated Panels with Various Boundary Conditions," *J. of Composite Materials*, Vol. 25, No. 6, pp. 634-649.

Simo, J. C., Wriggers, P., Schweizerhof, K. H., and Taylor, R. L., 1986, "Finite Deformation Post-buckling Analysis Involving Inelasticity and Contact Constraints," *Int. J. for Numerical Methods in Engineering*, Vol. 23, pp. 779-800.

Stein, E., Wagner, W., and Wriggers, P., 1990, "Nonlinear Stability Analysis of Shell and Contact-problems Including Branch-switching," *Computational Mechanics*, Vol 5, pp. 428-446.

Downloaded 03 May 2010 to 171.66.16.20. Redistribution subject to ASME license or copyright; see http://www.asme.org/terms/Terms_Use.cfm

APPENDIX

Axial Displacements Approximating Functions

The axial displacement functions are given by

$$g_j(\xi) = \xi - \frac{1}{\beta_j}\left[\sin(\beta_j\xi) + \gamma_j \cos(\beta_j\xi)\right] - \frac{1}{2}\beta_j\gamma_j\xi^2 + \frac{\gamma_i}{\beta_j} \quad \text{(A1)}$$

where $\xi = x/l$ is the nondimensional axial coordinate.

These displacement functions consists of a linear function and a truncated series of symmetric and asymmetric compatible nonlinear functions derived by integrating the Airy Stress function (see Sheinman and Frostig, 1991)

$$F_j(\xi) = 1 - \cos(\beta_j\xi) + \gamma_j[\sin(\beta_j\xi) - \beta_j\xi]$$

$$\gamma_j = (\cos\beta_j - 1)/(\sin\beta_j - \beta_j). \quad \text{(A2)}$$

β_j are the roots of the characteristic equation

$$\sin\frac{\beta_j}{2}\left(\tan\frac{\beta_j}{2} - \frac{\beta_j}{2}\right) = 0. \quad \text{(A3)}$$

Compatibility is achieved through the intergration constant γ_j/β_j which zeros thè function at $\xi = 0$.

The symmetric functions of (A1) (see Fig. 5(*a*)) are derived by $\tan\beta_j/2 - \beta_j/2 = 0$, while their asymmetric (Fig. 5(*b*)) $\sin\beta_j/2$ and $\gamma_j = 0$ ($j = 1, 3, 5 \ldots$). Note that for symmetric bending, only the asymmetric axial displacement should be taken.

Downloaded 03 May 2010 to 171.66.16.20. Redistribution subject to ASME license or copyright; see http://www.asme.org/terms/Terms_Use.cfm

The Folding of Triangulated Cylinders, Part I: Geometric Considerations

S. D. Guest

S. Pellegrino

Department of Engineering,
University of Cambridge,
Trumpington Street,
Cambridge, CB2 1PZ, U.K.

This study was inspired by a model of a triangulated cylindrical shell made by C. R. Calladine during an investigation of the mechanics of biological structures. The model consisted of identical triangular panels on a helical strip and had a small-displacement internal inextensional mechanism. It is shown that many triangulated cylinders broadly similar to Calladine's model can be folded down to a compact stack of plates: only small strains, whose magnitude can be made arbitrarily small by the choice of suitable design parameters, are imposed during folding. A general geometric formulation of the problem is presented and then, assuming that the folding process is uniform, the folding properties of any triangulated cylinder of this generic type are discussed.

1 Introduction and Some Simple Examples

The work described in this paper is part of a series of related projects in the area of deployable structures whose general aim is the development of simple and effective concepts. An overview of recent work in this field has been compiled by Kwan (1991); other concepts which have emerged from recent work at Cambridge can be seen in Kwan, You, and Pellegrino (1993) and Guest and Pellegrino (1992).

The present study was inspired by a cardboard model of a triangulated cylindrical shell made by C. R. Calladine during an investigation of the mechanics of biological structures. This model consisted of identical triangular panels on a helical strip and had a small-displacement internal inextensional mechanism. We decided to explore the possibility of transforming its small-displacement mechanism into a large-displacement motion by which a triangulated cylindrical shell could be folded down to a compact stack of plates. Quite quickly we found many arrangements that would allow this: only small strains, whose magnitude can be made as small as required by choosing suitable design parameters, are imposed during folding. Recently we have found a more general way of approaching the problem, which considers all possible triangulated cylinders of the same generic type.

In this paper, after describing the general configuration of a triangulated cylinder based on one or more helical strips, we identify those particular configurations which are suitable for folding. Our estimates of strain levels in the plates will be based on the simplifying assumptions that the folding process is uniform and that only one side of each triangle can change its length. Based on the insight gained from this approach, in a separate paper (Guest and Pellegrino, 1994) we have removed these assumptions and simulated the folding process of some particular cylinders. Before considering the fully general case in the next sections, we introduce the problem by discussing briefly some specific examples.

Figure 1 shows photographs of the folding of a particular triangulated cylinder when a flat plate on the top is gradually pushed down. In Fig. 1(*a*) the model is nearly fully extended; only a few triangular plates have been packaged. Then, as a small axial force is applied to the top plate, more and more triangles become part of the prismatic stack at the top of the cylinder and, in Fig. 1(*c*), only a few triangles are still extended. The packaged configuration of this particular cylinder is a heptagonal prism. All cylinders made from isosceles triangles, like this one, fold down to prisms. They are a special case for which the general parameter n—defined in Section 2—becomes equal to one plus the number of sides in the packaged configuration. Hence, the triangulated cylinder of Fig. 1 has $n=8$.

In this paper it is assumed that the plates have negligible thicknesses.

Figure 2 shows line drawings of triangulated cylinders with $n=6$, 7, and 8. As for all cylinders considered in this paper, they are *strain-free both in their fully extended and fully folded configurations*. In each cylinder all triangles are identical, and their sides are denoted by a, b, and c. These particular cylinders are made from isosceles triangles and hence their geometry is quite easy to analyze. For example, for $n=7$ all corners of the triangles in the packaged configuration coincide with the corners of a hexagon, as shown in Fig. 2(*b.ii*). Thus, the lengths of sides a and b, $l_a=l_b$, are related to the length of side c, l_c, by the relationship

Contributed by the Applied Mechanics Division of THE AMERICAN SOCIETY OF MECHANICAL ENGINEERS for publication in the ASME JOURNAL OF APPLIED MECHANICS.

Discussion on this paper should be addressed to the Technical Editor, Professor Lewis T. Wheeler, Department of Mechanical Engineering, University of Houston, Houston, TX 77204-4792, and will be accepted until four months after final publication of the paper itself in the ASME JOURNAL OF APPLIED MECHANICS.

Manuscript received by the ASME Applied Mechanics Division, Aug. 13, 1992; final revision, Apr. 27, 1993. Associate Technical Editor: F. Y. M. Wan.

Copyright © 1994 by ASME

Downloaded 03 May 2010 to 171.66.16.20. Redistribution subject to ASME license or copyright; see http://www.asme.org/terms/Terms_Use.cfm

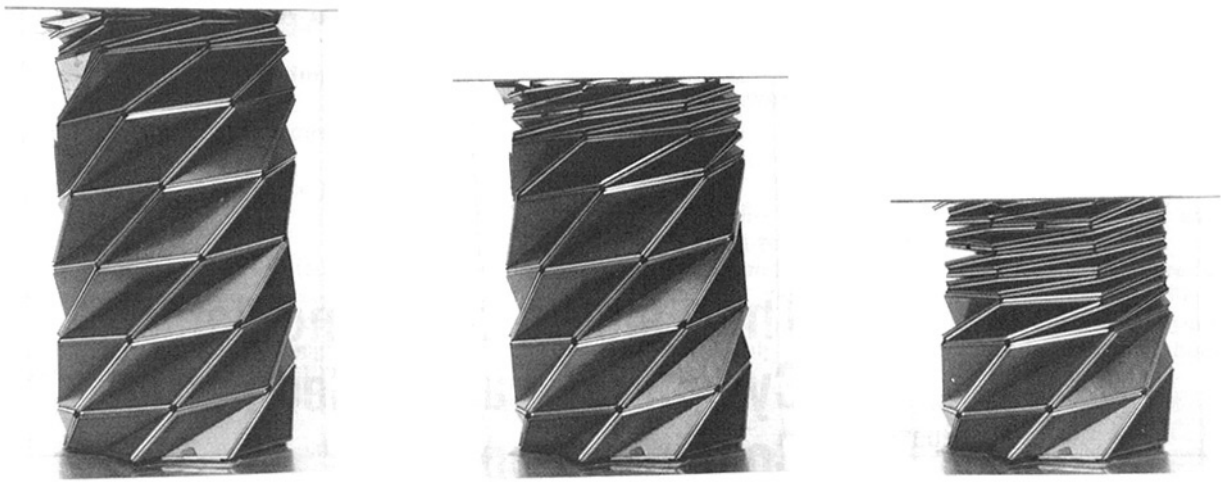


Fig. 1(*a*) Fig. 1(*b*) Fig. 1(*c*)

Fig. 1 Folding sequence of triangulated cylinders with $m=1$, $n=8$, $l_b/l_a=1$, $l_c/l_a=1.802$. The model shown has Al-alloy plates and flexible plastic hinges; its fully extended height is approximately 250 mm.

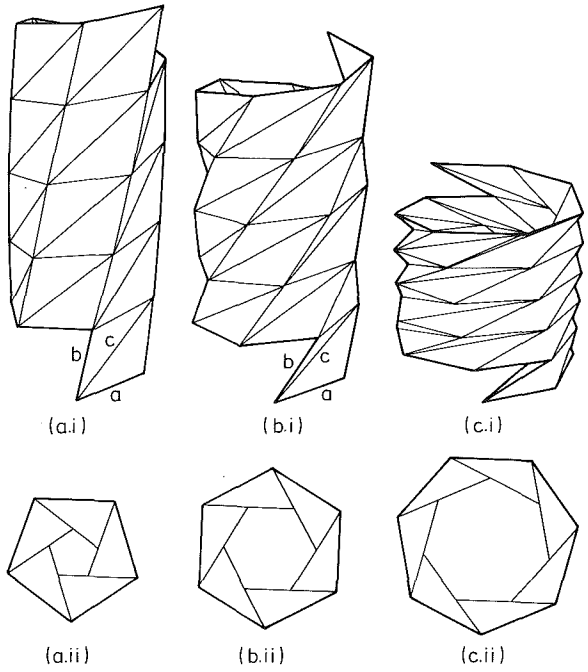


Fig. 2 Triangulated cylinders with $m=1$ and (*a*) $n=6$, (*b*) $n=7$, and (*c*) $n=8$. (*i*) Fully extended, side view. (*ii*) Fully folded, plan view. All cylinders have $l_b/l_a=1$.

$$l_c=2\sin\left(\frac{\pi}{2}-\frac{\pi}{n-1}\right)l_a=2\sin\left(\frac{\pi}{3}\right)l_a=\sqrt{3}\,l_a. \qquad (1)$$

To make a simple model of this cylinder, one draws on a sheet of thin card three sets of straight, parallel lines: the a and b lines are equi-distant and at an angle of $\pi/3$; the c lines go through the points of intersection of a and b lines. Then the sheet is folded along these lines: upwards along a and b lines, downwards along c lines. Finally, two opposite edges of the sheet are glued together to form the cylinder shown in Fig. 2(*b.i*). We have made card model cylinders of this sort for $n=7$, as described above, and also for $n=6$ and $n=8$. The axial force required to fold these models is quite small and the strains are sufficiently small that the models can survive substantially undamaged a small number of folding/unfolding cycles. However, it quickly becomes clear that the strains imposed by folding become lower as the value of n is increased. This observation has been confirmed by detailed computations (see Guest and Pellegrino, 1994) but now, having used these specific examples purely for illustration, we are ready to begin a proper investigation of the geometric design of triangulated cylinders, with the aim of identifying their folding properties.

The layout of the paper is as follows. Section 2 introduces the generic configuration in terms of three sets of helices lying on a cylindrical surface. These helices define the corners of the triangles forming the faceted cylinder. General expressions for the side lengths of the triangles are derived in terms of the helix parameters. With these tools, Section 3 examines the folding properties of a range of cylinders. Section 4 concludes the paper by discussing ways in which the results of Section 3 could be used to advantage in the design of foldable cylinders with different mechanical properties.

2 Geometry of Triangulated Cylinders

A general description of triangulated cylinders made from identical triangular plates arranged on helical strips, like those of Figs. 1 and 2, can be based on the observation that the nodes of the triangulated cylinders lie on the intersection of three sets of helices, as shown in Fig. 3. The helices are described by the sides of the triangles which are closest to them, i.e., they are called the a, b, and c helices.

All helices in one set are identical, apart from a rotation about the axis of the helix. A full set can be defined as a single helix with multiple starts. Each set of helices can be described by the following three parameters (Coxeter, 1980):

(*i*) the number of helices in the set, i.e., the number of starts of the helix (for example, in Fig. 3 the a helix has one start, the b helix seven starts, and the c helix eight starts);
(*ii*) the radius, which has the same value for all helices of Fig. 3 since they all lie on the same circular cylindrical surface;
(*iii*) the angle that the helix makes with a plane perpendicular to the axis of the helix. This angle can be greater than $\pi/2$, for a left-handed helix.

The positions of the nodes, and hence the configuration of a triangulated cylinder, are fully defined by any two of the three helices described above, as the third has to pass through the intersections of the other two. We shall use the a and b helices to describe a triangulated cylinder, therefore it is necessary to give the parameters defining these helices. They are

r = the radius;
α, β = the angles that the a and b helices, respectively, make with a plane perpendicular to their axis;

Downloaded 03 May 2010 to 171.66.16.20. Redistribution subject to ASME license or copyright; see http://www.asme.org/terms/Terms_Use.cfm

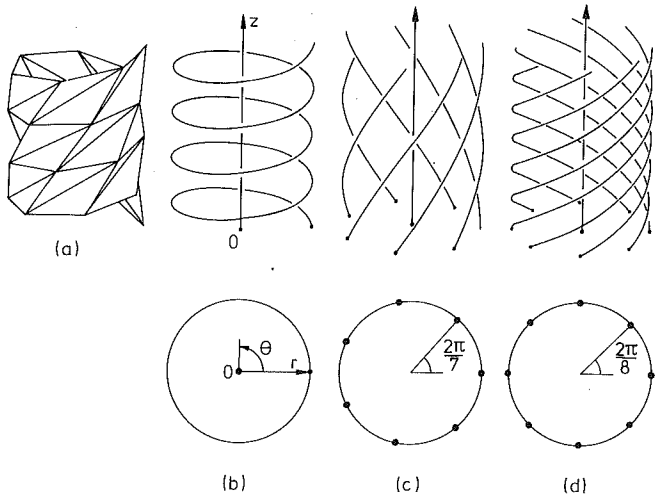


Fig. 3 Geometric definition of nodes of triangulated cylinder (*a*) in terms of three sets of helices, side, and plan views; (*b*) single-start *a*-helix, $m=1$; (*c*) seven-start *b*-helix, $n=7$; (*d*) eight-start *c*-helix, $m+n=8$. The first start of all helices is at (r, 0, 0).

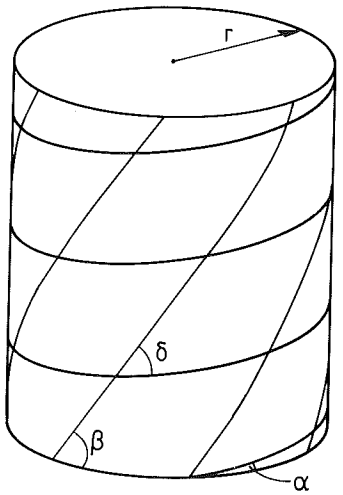


Fig. 4 Coordinate cylinder and parameters defining *a* and *b* helices

m, n = the number of starts of the a and b helices, respectively.

The parameters r, α, β are shown in Fig. 4. The a helix has the equation

$$z = r\theta \tan \alpha. \tag{2}$$

Similarly, the first start of the b helix is defined by

$$z = r\theta \tan \beta \tag{3}$$

and the second start by

$$z = r\left(\theta - \frac{2\pi}{n}\right)\tan \beta, \tag{4}$$

which gives $z=0$ when $\theta = 2\pi/n$. Note that in Eqs. (2)–(4) $0 < \theta < +\infty$: a complete turn of a helix corresponds, obviously, to an increase in the value of θ by 2π.

We define a nodal numbering system where nodes are numbered along the a helices: node (i, j) is the jth node on the ith start of the a helix.

The next task is obtaining the coordinates of enough neighbors of node (1, 1) to be able to calculate the three side lengths of the triangles. The cylindrical coordinate system to be used, O, r, θ, z, is defined in Fig. 3(b): node (i, j) has coordinates $(r, \theta_{i,j}, z_{i,j})$. We define $\theta_{i,j}$ such that $0 \le \theta_{i,j} < 2\pi$ and hence

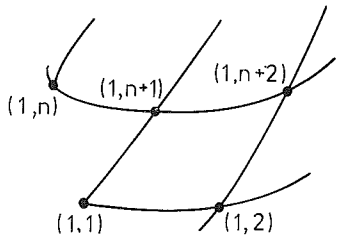


Fig. 5(*a*)

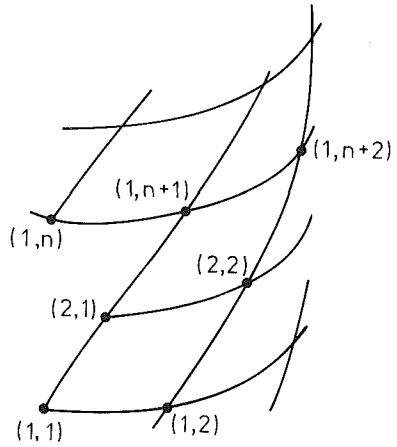


Fig. 5(*b*)

Fig. 5 Neighbors of mode (1,1) for a triangulated cylinder with (*a*) $m=1$ and (*b*) $m=2$. The *c* helices are not shown.

suitable multiples of 2π will be added to it when it is substituted into Eqs. (2)–(4). Node (1, 1) has coordinates (r, 0, 0).

For simplicity, the case $m=1$ will be considered first. Figure 5(a) shows that the θ-coordinates needed are those of nodes (1, 2), (1, $n+1$), and (1, $n+2$).

At node (1, 2) the a helix and the second start of the b helix intersect and so, from Eqs. (2) and (4),

$$r\theta_{1,2}\tan\alpha = r\left(\theta_{1,2} - \frac{2\pi}{n}\right)\tan\beta$$

which gives

$$\theta_{1,2} = \frac{2\pi}{n(1-k)} \tag{5}$$

where

$$k = \frac{\tan\alpha}{\tan\beta}. \tag{6}$$

At node (1, $n+1$) the second turn of the a helix and the first start of the b helix intersect and so, from Eqs. (2), (3)

$$r(\theta_{1,n+1} + 2\pi)\tan\alpha = r\theta_{1,n+1}\tan\beta$$

giving

$$\theta_{1,n+1} = \frac{2k\pi}{1-k}. \tag{7}$$

From Fig. 5(a), $\theta_{1,n+2} = \theta_{1,2} + \theta_{1,n+1}$ and therefore

$$\theta_{1,n+2} = \frac{2(1+kn)\pi}{n(1-k)}. \tag{8}$$

For cases where $m>1$ the nodes connected to node (1, 1) are those shown in Fig. 5(b). The expression for $\theta_{1,2}$ remains that of Eq. (5). The expression for $\theta_{1,n+1}$ does not change either, but it is now $\theta_{2,1}$ which is required, and so from Fig. 5(b)

$$\theta_{2,1} = \frac{\theta_{1,n+1}}{m} = \frac{2k\pi}{m(1-k)}. \tag{9}$$

Downloaded 03 May 2010 to 171.66.16.20. Redistribution subject to ASME license or copyright; see http://www.asme.org/terms/Terms_Use.cfm

Also

$$\theta_{2,2}=\theta_{1,2}+\theta_{2,1}=\frac{2(m+nk)\pi}{mn(1-k)}. \tag{10}$$

All relevant θ-coordinates are now defined. The next, final step is to calculate the side lengths l_a, l_b, and l_c in terms of the parameters defining the helices. In general, the distance l between node (1,1) and a node with coordinates (r, θ, z) is

$$l=\sqrt{\left(2r\sin\frac{\theta}{2}\right)^2+z^2}$$

For node (1,2), $l=l_a$, $\theta=\theta_{1,2}$, and—from Eq. (2)—$z=r\theta_{1,2}\tan\alpha$, hence

$$l_a=\sqrt{\left(2r\sin\frac{\pi}{n(1-k)}\right)^2+\left(\frac{2\pi r}{n(1-k)}\tan\alpha\right)^2}. \tag{11}$$

Similarly, for node $(1,n+1)$ if $m=1$, or node (2,1) if $m>1$, $l=l_b$ and $\theta=\theta_{1,n+1}$, or $l=l_b$ and $\theta=\theta_{2,1}$, respectively. The z-coordinate is

$$z=\frac{n}{m}z_{1,2}=\frac{n}{m}r\theta_{1,2}\tan\alpha$$

hence

$$l_b=\sqrt{\left(2r\sin\frac{k\pi}{m(1-k)}\right)^2+\left(\frac{2\pi r}{m(1-k)}\tan\alpha\right)^2}. \tag{12}$$

Similarly, for node $(1,n+2)$ if $m=1$, or node (2,2) if $m>1$, $l=l_c$ and $\theta=\theta_{1,n+2}$, or $l=l_c$ and $\theta=\theta_{2,2}$, respectively, and

$$z=\left(1+\frac{n}{m}\right)z_{1,2}=\frac{m+n}{m}r\theta_{1,2}\tan\alpha$$

hence

$$l_c=\sqrt{\left(2r\sin\frac{(m+nk)\pi}{mn(1-k)}\right)^2+\left(\frac{2(m+n)\pi r}{mn(1-k)}\tan\alpha\right)^2}. \tag{13}$$

Given the parameters which define the helices of a triangulated cylinder, it is possible to work out the side lengths of the triangular panels from Eqs. (11)-(13). Equally, it is possible to work backwards and, given a set of side lengths l_a, l_b, and l_c, and the topological parameters m, n, to work out the parameters of a corresponding set of helices.

There is one final condition, the inner edges of the triangles cannot cross the z-axis without penetrating each other. Because during folding all triangles move inwards, this condition is most severe in the fully folded state where it can be shown that

$$\frac{l_b}{l_a}\le\frac{\sin\dfrac{(n-2)\pi}{2(m+n)}}{\sin\dfrac{(m+2)\pi}{2(m+n)}}. \tag{14}$$

The equality sign corresponds to the c sides lying along diameters of the coordinate cylinder.

3 Folding Properties

The results of Section 2 can be used to select particular layouts of triangulated cylinders which are suitable for folding, i.e., where both the extended and folded configurations are strain-free, and to gain insight into the folding process. A key assumption is made, that the folding process is uniform, i.e., that all triangles remain identical throughout the folding process. This assumption may appear rather restrictive, particularly because Fig. 1 shows clearly that the deformation pattern in any partially packaged configuration is not uniform: it consists of a fully folded region, at the top, of a fully extended region, at the bottom, and of an intermediate "transition" region. If any strains are induced by folding, one would expect them to be in the transition region and, obviously, this localization cannot be captured if it is assumed that all triangles remain identical. This restriction has been removed in a separate investigation (Guest and Pellegrino, 1994).

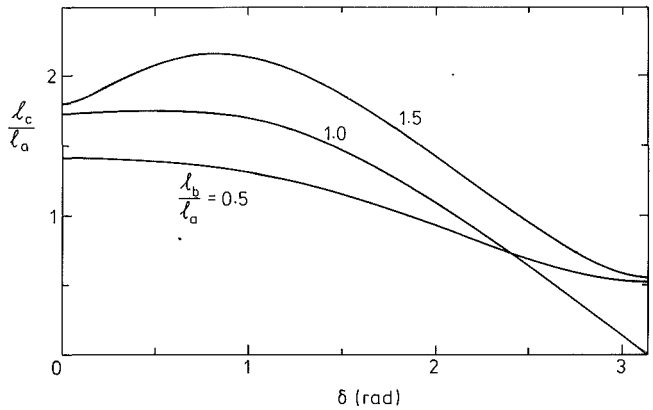


Fig. 6(*a*)

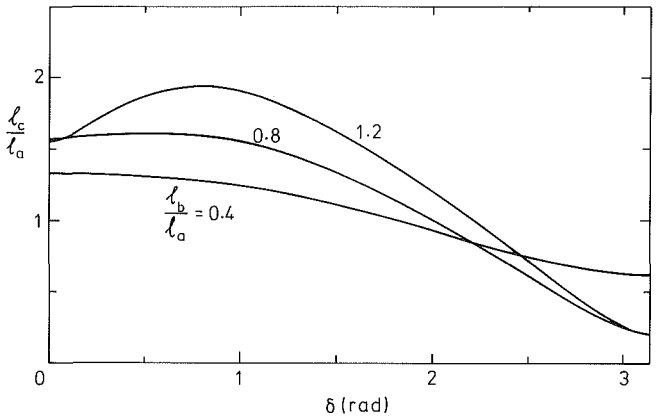


Fig. 6(*b*)

Fig. 6 Plots of l_c/l_a versus δ for triangulated cylinders with (*a*) $m=1$ and (*b*) $m=2$; $n=7$ in both cases

The simplest way of approaching the problem is to investigate the geometric configurations of cylinders with $l_b/l_a=$ constant. This is equivalent to assuming that all deformation can be modeled in terms of changes of l_c only. With these hypotheses, the folding properties of any particular type of triangulated cylinder, defined by l_b/l_a, m, and n can be investigated most effectively on a plot of l_c/l_a versus δ, where

$$\delta=\beta-\alpha \tag{15}$$

(see Fig. 4). Obviously, $0\le\delta<\pi$: configurations with $\delta=0$ have zero height and will be referred to as fully folded. All plots presented in this section have been obtained by solving numerically the nonlinear system of four Eqs. (11)–(13), (15) for the four unknowns r/l_a, α, β, and l_c/l_a, given l_b/l_a, m, n, and δ. The function "fsolve," available in Matlab (The Math Works, 1989), has been used. No closed-form solution has been searched for.

Figure 6(*a*) shows a plot of l_c/l_a versus δ for triangulated cylinders with $m=1$, $n=7$ and for three different values of l_b/l_a. Consider initially the case $l_b/l_a=0.5$. The figure shows that l_c decreases monotonically as δ increases. Indeed, this is the type of behavior that would be expected if all triangles were in a plane, rather than being wrapped in a tube. Within obvious limits, any value of l_c/l_a is associated with a unique configuration of the cylinder. The case $l_b/l_a=1$ (isosceles triangles) is much more interesting since now l_c/l_a initially increases with δ and then, having reached a maximum, starts

Downloaded 03 May 2010 to 171.66.16.20. Redistribution subject to ASME license or copyright; see http://www.asme.org/terms/Terms_Use.cfm

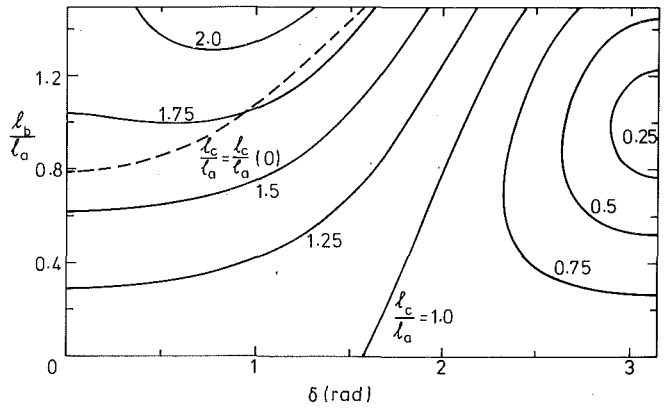


Fig. 7(*a*)

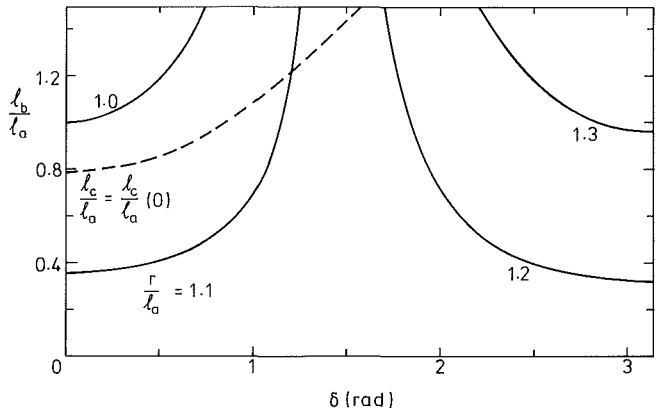


Fig. 7(*b*)

Fig. 7 Contour plots of (*a*) l_c/l_a and (*b*) r/l_a for triangulated cylinders with $m=1$ and $n=7$

decreasing. This can be explained by the effect of the curvature of the cylindrical surface, on which all corner nodes lie, becoming significant. In this case any triangulated cylinder with $l_c/l_a \geq \sqrt{3}$ admits two different, totally unstrained configurations. In particular, $l_c/l_a = \sqrt{3}$ gives one configuration where $\delta = 0$ and one where $\delta = 0.867$. This is the same cylinder which has been analyzed, by much simpler means, in the Introduction. The third curve in Fig. 6(*a*), for the case $l_b/l_a = 1.5$ shows similar behavior, but this time there is a much more marked maximum. This curve shows that triangulated cylinders with $l_b/l_a = 1.5$ and $l_c/l_a = 1.800$ are strain-free both when fully folded ($\delta = 0$) and when extended ($\delta = 1.587$); however, going from one configuration to the other requires large deformations.

Similar considerations apply to other triangulated cylinders. For example, Fig. 6(*b*) shows similar curves for the case $m=2$, $n=7$. Note that the three curves in this figure refer to lower values of l_b/l_a than in the case $m=1$ because the upper limit on l_b/l_a, Eq. (14), is a little lower.

A more general way of plotting data for the case $m=1$, $n=7$ is a contour plot of l_c/l_a for the full range of δ and l_b/l_a, Fig. 7(*a*). A broken line marks those configurations of the cylinder which admit also a strain-free folded configuration with $\delta = 0$. These are the configurations on which we are focusing in this paper. The value $l_b/l_a = 0.788$ is the lowest possible for fully foldable cylinders. Also note that the contour $l_c/l_a = 1.75$, for example, indicates that cylinders with $l_b/l_a = 1.039$ require fairly small strains to go from $\delta = 0$ and $\delta = 0.940$ because the dimple in the contour is rather flat. The contour $l_c/l_a = 1.64$ (not shown) is even flatter, thus allowing δ to vary in the range 0–0.4 with less than 0.1 percent variation in l_b/l_a. Finally, note that the upper limit on l_b/l_a is 1.497, from Eq. (14). Figure 7(*b*) plots the corresponding values of r/l_a: folding, i.e., decreasing δ always implies a reduction of r.

4 Discussion

The general geometric formulation of Section 2 together with the sample plots presented in Section 3 are very powerful tools for the design of foldable tubes. With this approach one can go well beyond the fairly intuitive foldable cylinders presented in the Introduction, all of which had $m=1$ and $l_b/l_a = 1$. Obviously, having the freedom to alter these two parameters can be very useful in the design of foldable cylinders that have to meet some specified requirements. With the hypothesis that l_a and l_b remain constant during folding, while l_c varies, preliminary estimates of strains during folding are easy to obtain (see Fig. 6). More detailed estimates of strains, axial force, shape and length of transition region, etc., are available in Guest and Pellegrino (1994).

Although this paper has concentrated on cylinders which are strain-free both when fully deployed and fully packaged, it should be noted that it is also possible to design cylinders which accumulate elastic strain energy during folding and release it during deployment. This property could be useful for some particular applications, e.g., self-deploying cylinders.

An interesting feature of the plots in Fig. 6 is that they identify some special triangulated cylinders whose l_c/l_a is an analytical maximum. For example, the special configuration of a cylinder with $m=1$, $n=7$ and $l_b/l_a = 1.5$ occurs for $\delta = 0.839$ and hence $l_c/l_a = 2.162$ (see Fig. 6(*a*)). Any cylinder made to be strain-free in such a configuration can change its δ by an infinitesimal amount without any first-order changes of length in the triangular panels. Indeed, Calladine's model, referred to in Section 1, had this property and our analysis has produced a whole group of cylinders with the same property as a by-product. It is well known, see Calladine (1978) for example, that special, singular configurations of an assembly of pin-jointed bars are obtained when the length of one bar, or a group of bars, is maximum. One might expect that the configurations corresponding to the maxima of Fig. 6 should have such property, but they do not. This is because only uniform configurations were considered in the analysis leading to the plots in Fig. 6 and hence the maxima of l_c/l_a are, indeed, the largest when this constraint is enforced. However, if this constraint is removed nonuniform configurations with larger l_c/l_a can be obtained. This has been verified by careful computations based on Pellegrino (1993).

Acknowledgments

We thank Prof. C. R. Calladine for advice and comments on an earlier version of this paper, and Mr. S. Vincer of ITW Irathane International for assistance in the manufacture of the model shown in Fig. 1. We acknowledge, with thanks, financial support from British Aerospace (Space Systems) Ltd. and SERC (S.D.G.), and the award of ESA Fellowship (S.P.).

References

Calladine, C. R., 1978, "Buckminster Fuller's Tensegrity Structures and Clerk Maxwell's Rules for the Construction of Stiff Frames," *International Journal of Solids and Structures*, Vol. 14, pp. 161–172.

Coxeter, H. S. M., 1980, *Introduction to Geometry*, 2nd ed., John Wiley and Sons, New York.

Guest, S. D., and Pellegrino, S., 1992, "Inextensional Wrapping of Flat Membranes," *Proc. First International Seminar on Structural Morphology*, R. Motro and T. Wester, eds., Montpellier, La Grand Motte, pp. 203–215.

Guest, S. D., and Pellegrino, S., 1994, "The Folding of Triangulated Cylinders, Part II: The Folding Process," ASME JOURNAL OF APPLIED MECHANICS, Vol. 61, pp. 778–783.

Kwan, A. S. K., 1991, "A Pantographic Deployable Mast," Ph.D. dissertation, University of Cambridge, Cambridge, U.K.

Kwan, A. S. K., You, Z., and Pellegrino, S., 1993, "Active and Passive Cable Elements in Deployable Masts," *International Journal of Space Structures*, Vol. 8, pp. 29–40.

Pellegrino, S., 1993, "Structural Computations with the Singular Value Decomposition of the Equilibrium Matrix," *International Journal of Solids and Structures*, Vol. 30, pp. 3025–3035.

The Math Works, 1989, Matlab User's Guide.

Downloaded 03 May 2010 to 171.66.16.20. Redistribution subject to ASME license or copyright; see http://www.asme.org/terms/Terms_Use.cfm

S. D. Guest

S. Pellegrino

Department of Engineering,
University of Cambridge,
Trumpintgon Street,
Cambridge, CB2 1PZ, U.K.

The Folding of Triangulated Cylinders, Part II: The Folding Process

In the first paper of this series we have introduced a class of foldable triangulated cylinders. In this paper we consider three particular examples of these cylinders and analyse computationally the way they fold. We show that this process is nonuniform and that it consists of two phases. The first unsteady phase involves the gradual buildup of strain energy in a "shape transition region." In the second phase the transition region moves toward the bottom of the cylinder under almost zero force. Although the behavior of the three example cylinders is qualitatively similar, the peak force on the cylinder, as well as the peak strain, have different magnitudes, in agreement with a result in our first paper.

1 Introduction

In Guest and Pellegrino (1994), henceforth referred to as Part I, we have examined the folding properties of triangulated cylinders like that shown in Fig. 1. By considering a uniform folding mode, which is a simplification of the mode observed in physical experiments, we obtained preliminary estimates of the strains imposed on a triangulated cylinder during folding. In this paper we restrict our attention to a particular type of cylinder which, in terms of the geometric parameters introduced in Part I, have $m = 1$ and $l_b/l_a = 1$ and hence can be packaged "flat" into prismatic stacks of plates. We consider three cylinders of this type, with $n = 6$, 7, and 8, and analyze computationally the way they fold when pressed down by a flat plate. Our prime interest, of course, is in the level of straining induced by this process and also the force required to fold a cylinder. We are also interested in the shape of the transition region immediately ahead of the fully packaged region, and the decay pattern of the strain field. Such information is needed for the design, manufacture, and testing of foldable cylinders. Indeed, only after obtaining some preliminary results of the investigation reported in this paper was it possible to manufacture the Al-alloy cylinder which is shown in Fig. 1 of Part I.

In the next section we set out our computational approach which can handle the inextensional mechanisms present at the end of a triangulated cylinder (activated only during the early stages of folding), and also the variable boundary conditions due to the unilateral support conditions imposed by the loading plate. Then, in Section 3 we present and discuss the results obtained for a cylinder with $n = 7$, which folds down to a hexagonal prism, and compare its response to that of cylinders with $n = 6$ and $n = 8$: all cylinders have $m = 1$ and $l_b/l_a = 1$. Although the folding process is fundamentally the same for all of them, it turns out that the peak strains, the peak force on the loading plate, etc., tend to become smaller as n increases.[1]

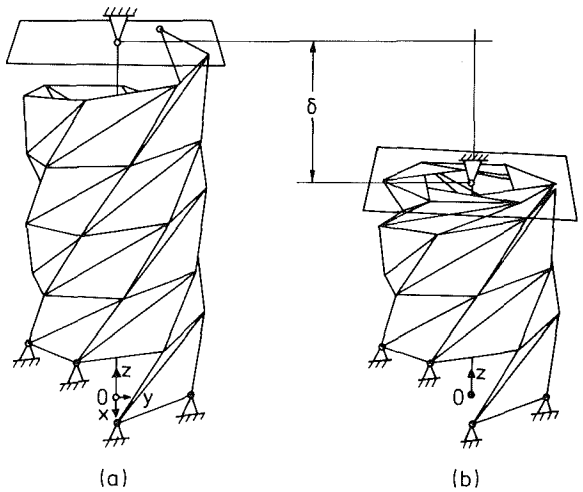


Fig. 1 Triangulated cylinder with $m = 1$, $n = 7$, $l_b/l_a = 1$, and $l_c/l_a = \sqrt{3}$, folded by moving down a rigid plate; (*a*) fully extended configuration, $k = 1$; (*b*) partially folded configuration, $k = 12$. The bottom n nodes of the cylinder are fully restrained. The coordinate system O, x, y, z has the z-axis aligned with the axis of the cylinder; the bottom node lies in the x-y plane.

Contributed by the Applied Mechanics Division of THE AMERICAN SOCIETY OF MECHANICAL ENGINEERS for publication in the ASME JOURNAL OF APPLIED MECHANICS.

Discussion on this paper should be addressed to the Technical Editor, Professor Lewis T. Wheeler, Department of Mechanical Engineering, University of Houston, Houston, TX 77204-4792, and will be accepted until four months after final publication of the paper itself in the ASME JOURNAL OF APPLIED MECHANICS.

Manuscript received by the ASME Applied Mechanics Division, Aug. 13, 1992; final revision, Apr. 27, 1993. Associate Technical Editor: F. Y. M. Wan.

[1] A number of cylinders have now been tested. Many features of their behavior agree with the results presented here, but some other interesting features have also emerged. They will be discussed in a third paper in this series.

Copyright © 1994 by ASME
Downloaded 03 May 2010 to 171.66.16.20. Redistribution subject to ASME license or copyright; see http://www.asme.org/terms/Terms_Use.cfm

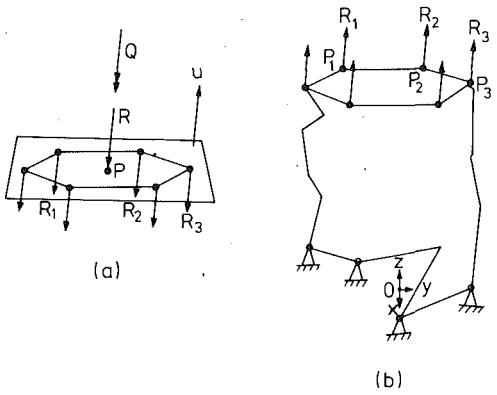


Fig. 2 (*a*) Forces acting on the top plate; (*b*) the corresponding forces on the top k nodes of the cylinder

2 The Algorithm

A simple analytical model of a triangulated cylinder is a truss structure having linear elastic bars of equal cross-section along the edges of the triangles and connected at the nodes by frictionless pin-joints. There are three types of bars, *a*, *b*, *c*, lying on the edges labeled thus in Fig. 3 of Part I. The bottom n nodes of the structure are fully fixed. The structure is compressed by a frictionless, rigid plate which is connected to a rigid foundation at a single point. To simulate the folding process, this point is gradually drawn towards the bottom end of the structure. For simplicity, the thickness of the triangular plates making up the cylinder is neglected.

This model can capture key aspects of the folding process, such as the formation of a shape transition region under gradually increasing force, and its propagation under constant force, which have been observed experimentally. It is also useful to make comparisons between triangulated cylinders with different parameters.

The algorithm presented here is based on a Force Method approach, hence it requires that the overall equilibrium, compatibility, and flexibility matrices be available for any given configuration of the cylinder. These matrices are obtained by assembling the basic matrices of two types of elements, the pin-jointed bars and the rigid loading plate. Of course, there is no difficulty in setting up the matrices for a pin-jointed bar (Livesley, 1975). But the loading plate is not a standard element and we shall briefly explain how to set up the three matrices required, in the hypothesis that all forces acting on the loading plate are orthogonal to it.

Let us consider the loading plate shown in Fig. 2(*a*), whose current configuration is defined by the position of point P and by the unit normal vector $\mathbf{u}$. The plate is acted upon by k interaction forces between the plate and the k joints of the cylinder in contact with it. Equal and opposite forces act upon the top k joints of the cylinder, as shown in Fig. 2(*b*). The plate is also acted upon by a force of magnitude R and a couple of magnitude Q, applied to it by the foundation through the connecting hinge at P. All of these forces, as well as the vector representing Q, are orthogonal to the plate, i.e., parallel to $\mathbf{u}$. In addition to point P, let us define k points on the plate, P_1, ..., P_k; an interaction force of magnitude R_i passes through point P_i. Only compressive R_i's—i.e., opposite to those shown in Fig. 2—are physically meaningful and, although no restrictions on their sign will be imposed in this study, this is a point worth considering in future work.

Although, in general, there are six independent equations of equilibrium for a rigid body, in this particular case—because the plate is under the action of a system of parallel forces—two equations of force equilibrium are identically satisfied. Hence, we need to consider only the equilibrium of forces in the u-direction, which yields the matrix equation

$$[1 \ \ldots \ 1 \ 1] \begin{bmatrix} R_1 \\ \cdots \\ R_k \\ R \end{bmatrix} = 0 \tag{1}$$

and the equilibrium of moments about any point. Because of the kinematic implications of these equations (see below) it is easiest to take moments about a set of axes parallel to x, y, and z (defined in Fig. 2(*b*)) and passing through P. The three moment components of the interaction force at P_i are $(P_i - P) \times (-\mathbf{u})R_i$, hence the three equations of moment equilibrium for the plate can be written in the form

$$[(P_1-P)\times\mathbf{u} \ \ldots \ (P_k-P)\times\mathbf{u} \ \mathbf{u}] \begin{bmatrix} R_1 \\ \cdots \\ R_k \\ Q \end{bmatrix} = \begin{bmatrix} 0 \\ 0 \\ 0 \end{bmatrix}. \tag{2}$$

The r.h.s. of Eq. (1) and (2) have been set directly equal to zero because there are no external forces acting on the plate. Note that the reactions R and Q have been put among the internal forces because their values are not known a priori.

By assembling together Eqs. (1) and (2) we obtain a system of four equations in $k + 2$ generalized stresses, whose 4 by $k + 2$ coefficient matrix is the equilibrium matrix $\mathbf{A}_p$ for the plate:

$$\begin{bmatrix} 1 & \ldots & 1 & 1 & 0 \\ & & & 0 & \\ (P_1-P)\times\mathbf{u} & \ldots & (P_k-P)\times\mathbf{u} & 0 & \mathbf{u} \\ & & & 0 & \end{bmatrix} \begin{bmatrix} R_1 \\ \cdots \\ R_k \\ R \\ Q \end{bmatrix} = \begin{bmatrix} 0 \\ 0 \\ 0 \\ 0 \end{bmatrix}. \tag{3}$$

The transpose of $\mathbf{A}_p$ relates the kinematic variables corresponding to the static variables in Eq. (3) (Livesley, 1975). The $k + 2$ generalized strains, corresponding to the vector on the l.h.s. of Eq. (3), are the extensions e_i of the "connectors" between the plate and the top k joints of the cylinder, together with the u-displacement of point P, d_{Pu}, and the plate rotation ϕ about the u-axis. The four generalized displacements are d_{Pu}, α, β, γ. The variable d_{Pu} appears both as internal and external and so it should be no surprise that the corresponding kinematic equation is a simple identity. The variables α, β, γ are the small rotations of the plate about the x, y, and z-axis, respectively. The system of kinematic equations is

$$\begin{bmatrix} 1 & & (P_1-P)\times\mathbf{u} & \\ \ldots & & \ldots & \\ 1 & & (P_k-P)\times\mathbf{u} & \\ 1 & 0 & 0 & 0 \\ 0 & & \mathbf{u} & \end{bmatrix} \begin{bmatrix} d_{Pu} \\ \alpha \\ \beta \\ \gamma \end{bmatrix} = \begin{bmatrix} e_1 \\ \ldots \\ e_k \\ d_{Pu} \\ \phi \end{bmatrix} \tag{4}$$

The third matrix is straightforward: because the plate and its foundation are rigid all entries in the $k + 2$ by $k + 2$ flexibility matrix $\mathbf{F}_p$ must be zero.

Note that the above formulation, with four external variables, is not the most compact, only two variables are really needed. The size of all three matrices for the plate could be reduced by two rows and two columns, at the expense of a few extra computations.

The matrices derived above are assembled together with the matrices for the pin-jointed bars to form the overall matrices for the cylinder. Let N be the total number of nodes in the cylinder and B the total number of bars. Because the bottom n nodes are fully fixed to a rigid foundation, the corresponding $3n$ equilibrium equations need not be considered. At the top of the cylinder the k nodes in contact with the rigid plate do

Downloaded 03 May 2010 to 171.66.16.20. Redistribution subject to ASME license or copyright; see http://www.asme.org/terms/Terms_Use.cfm

not need any special treatment, apart from noting that each of these joints is subject to an interaction force of magnitude R_i, as shown in Fig. 2(*b*), as well as to the axial forces in the bars connected to it. Hence, there are $3(N - n) + 4$ equilibrium equations in $B + k + 2$ generalized stresses σ and the overall equilibrium matrix $\mathbf{A}$ has size $3(N - n) + 4$ by $B + k + 2$. Similarly, the generalized strain vector ϵ has size $B + k + 2$, while the generalized displacement vector $\mathbf{d}$ has size $3(N - n) + 4$; the flexibility matrix $\mathbf{F}$ has size $B + k + 2$ by $B + k + 2$.

With these tools, the folding of a triangulated cylinder can be analyzed. One begins by setting up the cylinder in its fully extended configuration (as in Section 2 of Part I but w.r.t. the Cartesian coordinate system defined in Fig. 1(*a*)). The loading plate is set initially parallel to the *x-y* plane and the connection point P has coordinates $P = (0, 0, z_p)$, where z_P is also the z-coordinate of the top node of the cylinder. Obviously, at the beginning this is the only node which is in contact with the loading plate, hence $k = 1$.

To compute the folding sequence, the value of z_P is decreased in small steps; note that δ, the overall shortening of the cylinder, see Fig. 1(*b*), is equal to the difference between the initial z_P and its current value. In each step the starting configuration is based on the shape of the cylinder computed at the end of the previous step, only z_P is changed. Obviously, this imposes some strains in the k connectors between the plate and the cylinder and, because they are rigid, these strains must be relieved through suitable displacements. Note that, with this approach, the folding of the cylinder is achieved simply by moving one of its boundaries, i.e., without applying any external forces (the force on the loading plate is treated as an internal force, thus simulating a *displacement controlled test*). If the imposed strains are compatible they produce, of course, only a displacement from the current configuration. This is always the case at the beginning of the folding process and, indeed, at this point the configuration of the loading plate is not uniquely defined. In our simulations, a unique configuration is selected by minimizing the generalized displacement. In general, though, the imposed strains have an incompatible component which sets up a state of self-stress in the system. The calculation of the effects of these strains is geometrically nonlinear because (i) the plate is free to rotate about any in-plane axis (although no u-rotation is allowed), and (ii) it is fairly sensitive to small geometry changes. A further source of nonlinearity is the variability of k, discussed below.

For each value of z_P, our algorithm performs a series of Newton-Raphson iterations to find the new shape of the cylinder and the corresponding value of R. Initially, the displacement $\mathbf{d}^0$ from the current configuration is set to zero and the initial strain $\Delta\epsilon_o$ involves strains in the k connectors only. In iteration i, the system is in the trial configuration defined by $\mathbf{d}^{i-1}$. The strains $\Delta\epsilon_o$ are given, for the bars, by the difference between current trial length and initial, unstrained length. The extensions of the k plate-cylinder connectors are equal to the distance between the top k joints and the loading plate. The overall equilibrium matrix $\mathbf{A}^i$ is formed in this configuration and, after computing the Singular Value Decomposition of $\mathbf{A}^i$, the stresses $\Delta\sigma$ and displacements $\Delta\mathbf{d}$ induced by $\Delta\epsilon_o$ are found (Pellegrino, 1993). Finally, a new trial configuration is obtained from

$$\mathbf{d}^i = \mathbf{d}^{i-1} + \Delta\mathbf{d}.$$

The iteration stops when $\Delta\mathbf{d}$ is sufficiently small. If any nodes of the cylinder have gone past the plate, k is incremented by 1 and a new series of Newton-Raphson iterations is started. Finally, the shape of the cylinder is updated.

3 Simulation of the Folding Process

Let us consider the triangulated cylinder shown in Fig. 1(*a*). It has $m = 1$, $n = 7$, $l_b/l_a = 1$, and $l_c/l_a = \sqrt{3}$. According to Part 1, an unrestrained cylinder with these parameters has two strain-free configurations: one fully folded, the other fully extended. Figure 1(*a*) shows the fully extended configuration.

This cylinder will be modelled as a pin-jointed truss, as discussed in Section 2: the total numbers of joints and bars are $N = 36$ and $B = 86$; bars joining two fully restrained nodes have been taken out. All bars have equal axial stiffness AE. In the extended configuration node 1 (at the bottom of the cylinder) has $z = 0$, while node 36 (at the top of the cylinder) has $z = 4.175\ l_a$. The bottom $n = 7$ nodes are fully restrained: the z-coordinate of the last restrained node is $0.716\ l_a$. Clearly the folding of the cylinder cannot go past this point. The rigid plate at the top of the cylinder is set initially in contact with node 36, hence $z_P = 4.175\ l_a$ and $k = 1$. At this stage $\delta = 0$. Starting from this configuration we have lowered the plate by decreasing z_P in steps of $l_a/100$.

Results from a simulation involving approximately 300 steps are shown in Figs. 3-4. Figure 3(*a*) shows dimensionless plots of the force R and the strain energy U in the cylinder. The cylinder begins to fold under zero force, hence remaining strain-free, until $k = 4$. Then R starts increasing until, when $k = 8$, it reaches a peak and then falls off. Subsequently, R periodically oscillates around zero. The strain energy increases considerably when k goes from 3 to 9, but then remains approximately constant. In fact the strain energy plots show a slow increase, due to end effects in the top part of the cylinder, since the fully folded region does not yet contain enough bars to allow the natural decay of strain to take place.

Fig. 3(*b*) shows some more details of the steady state regime; the periodic variation of R is directly related to changes in k. R is negative, i.e., tensile, just before a new node comes into contact with the plate and there is a sudden stiffness increase caused by the activation of an extra constraint, which corresponds to an increment in the value of k. As δ is increased, R increases until a limit point, it then decreases until the beginning of a new cycle. Note that in our simulation R is negative at the beginning and at the end of a cycle, which is unrealistic. In practice, a small spring-back of the folded region is likely to occur.

The folding cylinder is a continuously softening system, with

$$\frac{d^2R}{d\delta^2} < 0$$

wherever this quantity is defined, but the system is periodically stiffened as new nodes come into contact with the top plate. Although unusual, this behavior has some similarities to the axial crushing of cellular materials (Gibson and Ashby, 1988).

Next, we look at strain variation during steady-state folding. For a clear picture of strain distribution it is best to consider the axial strain ϵ_c in the 28 c bars, plotted in Fig. 3(*c*). As the plate is pushed down, the most significant part of the strain field, say $\epsilon_c > 10^{-3}$, simply translates from right to left, i.e., from the top towards the bottom of the cylinder. However, a region involving compressive strains gradually builds up in the wake of the shape-transition region and the strain energy associated with it is responsible for the slow strain energy increase discussed earlier.

The most significant feature of Fig. 3(*c*) is the peak strain attained: here $\epsilon_{c\,\max} = 8.7 \cdot 10^{-3}$. Similar plots are obtained for the a and b bars, whose (compressive) peak strains are $5.0 \cdot 10^{-3}$ and $6.9 \cdot 10^{-3}$, respectively.

Figure 3(*d*) shows strain plots, again for the c bars only, (i) just after a node has come into contact with the plate, (ii) when R reaches its peak, and (iii) just before a new mode comes into contact with the plate. Here, $k = 14$ throughout. Note that the peak strain remains essentially unchanged during this cycle.

Figure 3(*e*) shows the orientation of the loading plate by means of plots of the x, y, and z-components of $\mathbf{u}$. The plate normal essentially describes a small conical motion about the

Downloaded 03 May 2010 to 171.66.16.20. Redistribution subject to ASME license or copyright; see http://www.asme.org/terms/Terms_Use.cfm

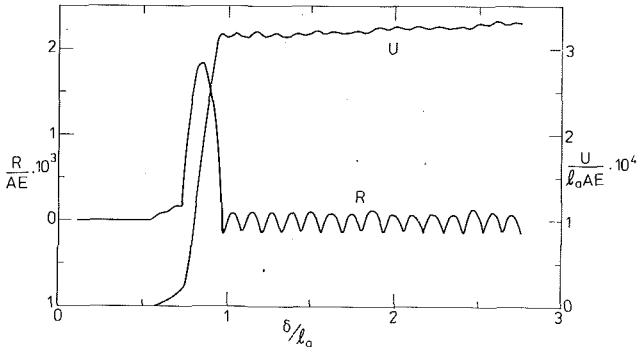


Fig. 3(*a*)

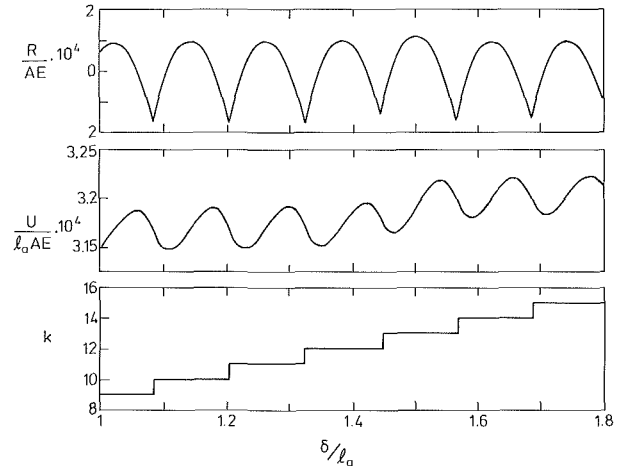


Fig. 3(*b*)

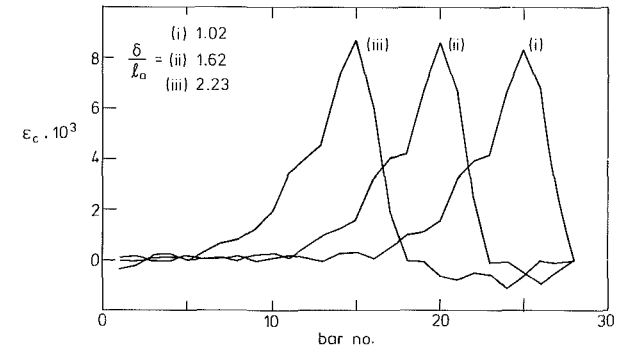


Fig. 3(*c*)

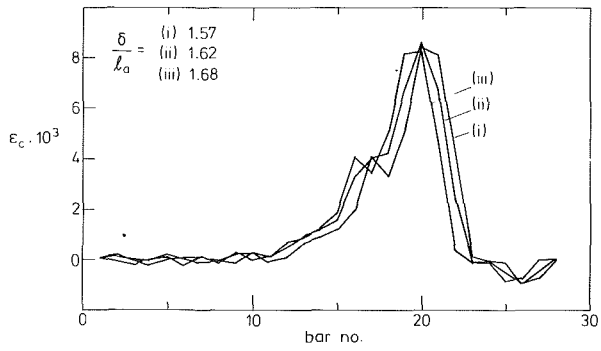


Fig. 3(*d*)

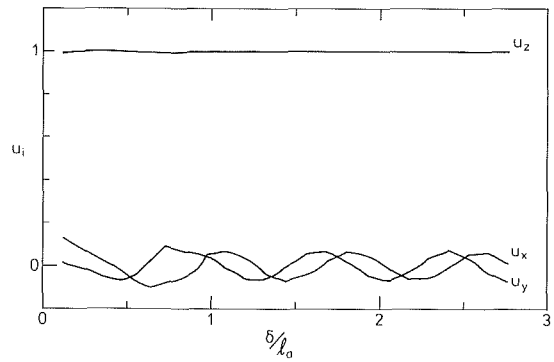


Fig. 3(*e*)

Fig. 3 Folding of cylinders with $m = 1$, $n = 7$, $l_b/l_a = 1$, and $l_c/l_a = \sqrt{3}$; (*a*) plots of R and U in the cylinder; (*b*) detailed data for steady-state phase; (*c, d*) ϵ_c during steady-state folding. Bars take the number of their bottom node, and nodes are numbered going up on the *a* helix. Discrete values have been joined, for legibility; (*e*) three components of u.

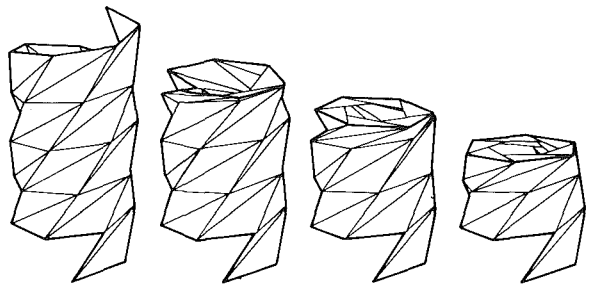


Fig. 4 Fully extended view of cylinder with $m = 1$, $n = 7$, $l_b/l_a = 1$, and $l_c/l_a = \sqrt{3}$, followed by three snapshots from the folding sequence

z-axis. Figure 4 shows four snapshots from the simulation process, including the initial configuration.

Next, we compare the behavior of the three cylinders shown in Fig. 2 of Part I, to gain further insight into the folding process. One of them is the triangulated cylinder examined above, with $m = 1$, $n = 7$, $l_b/l_a = 1$, and $l_c/l_a = \sqrt{3}$. The two other cylinders also have $m = 1$ and $l_b/l_a = 1$: the first has $n = 6$ and $l_c/l_a = 1.618$; the second has $n = 8$ and $l_c/l_a = 1.802$.

The folding of these two cylinders has been analyzed by the technique described above. For $n = 6$ we have considered a pin-jointed truss with $N = 31$ and $B = 74$. In the fully extended configuration $z_P = 4.912\ l_a$. To initiate the correct folding pattern, the simulation had to start with three nodes in contact with the plate. If a smaller number is chosen, the top plates start folding outwards and quickly the process comes to halt. Figure 5(*a*) shows plots of the force R and of the strain energy U. As for $n = 7$, there is a large force peak and a corresponding increase in strain energy soon after the beginning of the process; afterwards, R oscillates around zero and U remains approximately constant. Figure 5(*b*) shows the strain field in the c bars; as in Fig. 3(*c*) the most significant part of the strain field simply translates from right to left. Qualitatively these results are the same as for the earlier cylinder, but the key difference between the cases $n = 6$ and $n = 7$ is in the magnitudes of forces and strains: $R_{\max}$ and $\epsilon_{c\,\max}$ are, respectively, 14 and 4 times higher for $n = 6$ than for $n = 7$.

For the case $n = 8$ we have considered a pin-jointed truss with $N = 49$ and $B = 122$ which, when fully extended, has $z_P = 2.818\ l_a$. Starting from this position the plate has been lowered gradually: the folding behavior of this cylinder, see Fig. 6, is essentially identical to the earlier cases. Note that the trend towards lower forces and strains continues: $R_{\max}$ and $\epsilon_{c\,\max}$ are, respectively, 150 and 17 times higher for $n = 7$ than for $n = 8$. The complete set of values is available in Table 1.

Downloaded 03 May 2010 to 171.66.16.20. Redistribution subject to ASME license or copyright; see http://www.asme.org/terms/Terms_Use.cfm

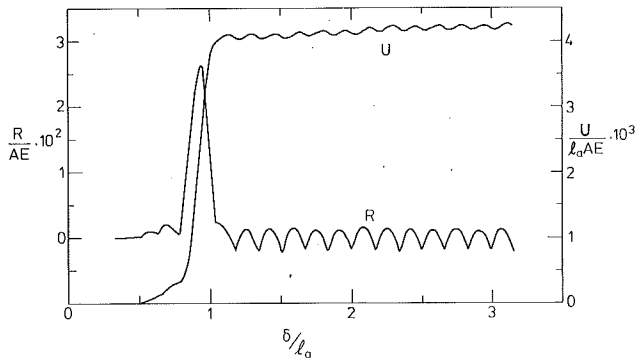


Fig. 5(*a*)

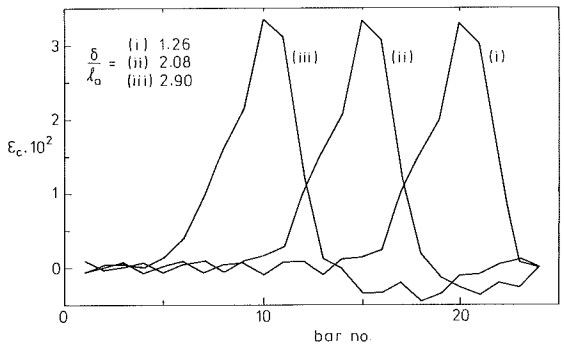


Fig. 5(*b*)

Fig. 5 Folding of cylinders with $m = 1$, $n = 6$, $l_b/l_a = 1$, and $l_c/l_a = 1.618$

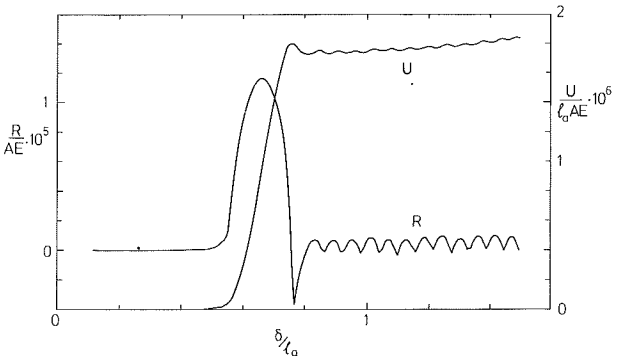


Fig. 6(*a*)

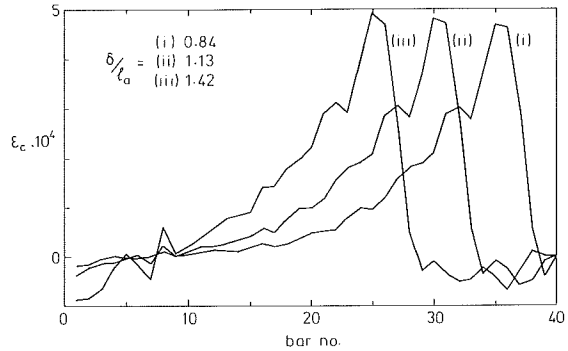


Fig. 6(*b*)

Fig. 6 Folding of cylinders with $m = 1$, $n = 8$, $l_b/l_a = 1$, and $l_c/l_a = 1.802$

4 Discussion

Before discussing the results obtained in this paper it is necessary to comment on the validity of the assumptions behind our approach, namely that a triangulated cylinder can be modeled as a simple pin-jointed truss and that plate thickness can be neglected. Although more complex models could be considered, we think that it would be pointless to do this in a purely conceptual study. More detailed models would need to be firmly based on the mechanical features of a particular triangulated cylinder. For example, in the model shown in Fig. 1 of Part I the plates are connected by thin plastic links which are very flexible in comparison with the plates, and the deformation of such a system is concentrated in these connections. If, on the other hand, more traditional mechanical hinges are used, the effects of joint tolerance would have to be considered. Finally, the pin-jointed truss model assumes that the connections between plates offer no resistance to bending. If this is not the case there would have to be a larger strain energy increase during folding, but we do not expect higher peak strains. Regarding the second assumption, we expect that plate thickness does not play a significant role because its effects do not accumulate in this case unlike, e.g., the wrapping of a membrane around a central hub (Guest and Pellegrino, 1992).

The simulations presented in Section 3 have revealed that the folding of a triangulated cylinder consists of two phases. The first unsteady phase involves a gradual buildup of strain energy under a large applied force, which might provide an effective self-locking feature. During this phase a shape transition region from the fully extended to the fully folded part of the cylinder is formed and, once the energy barrier that prevents folding has been overcome, a second steady-state phase of the process begins. During this phase the shape transition region moves towards the bottom of the cylinder under almost zero force. These observations agree qualitatively with the behavior of several models, including that shown in Fig. 1 of Part I and many card models.

Table 1 ϵ_{max} and R_{max} in cylinders with $m = 1$ and $l_b/l_a = 1$

n	$\lvert\varepsilon_a\rvert_{max}$	$\lvert\varepsilon_b\rvert_{max}$	$\lvert\varepsilon_c\rvert_{max}$	R_{max}/AE
6	$2.0\cdot10^{-2}$	$2.7\cdot10^{-2}$	$3.6\cdot10^{-2}$	$2.6\cdot10^{-2}$
7	$5.0\cdot10^{-3}$	$6.9\cdot10^{-3}$	$8.7\cdot10^{-3}$	$1.8\cdot10^{-3}$
8	$3.5\cdot10^{-4}$	$4.1\cdot10^{-4}$	$5.2\cdot10^{-4}$	$1.2\cdot10^{-5}$

In the three cylinders which have been analyzed in this paper both the peak force and peak strain decrease rapidly as n increases, as noted in Section 3, but the role played by this particular parameter should not be overvalued. The aim of the present study was a characterization of the general folding behavior of triangulated cylinders for which we selected three cylinders that fold down to simple prisms. Although a detailed investigation of design parameters is beyond the scope of the present investigation, it can be noted that the key factor determining peak force and peak strain is the size of the geometric incompatibility shown in, e.g., Fig. 6 of Part I. The particular combination of the parameters m, n, l_b/l_a, and l_c/l_a which leads to it is not very significant. Thus, for example, a similar range of ϵ_{max} and R_{max} to that obtained here, for $n = 6, 7, 8$ but $m = 1$ and $l_b/l_a = 1$, could be obtained with constant n, by varying l_b/l_a.

Finally, it is interesting to compare the present simulations of the folding process with the approach pursued in Part I. A comparison has been made in Table 2 for the case $m = 1$, $n = 7$, $l_b/l_a = 1$, and $l_c/l_a = \sqrt{3}$. The table gives also "modified" peak strains, estimated in the spirit of Part I but allowing all bar lengths to vary simultaneously with constant ratios l_c/l_a and l_b/l_a. Note that these simplified estimates are higher than

Downloaded 03 May 2010 to 171.66.16.20. Redistribution subject to ASME license or copyright; see http://www.asme.org/terms/Terms_Use.cfm

Table 2 Comparison of predictions in Part I and Part II, for cylinders with $m = 1$, $n = 7$, $l_b/l_a = 1$, and $l_c/l_a = \sqrt{3}$

	$\lvert\epsilon_a\rvert_{max}$	$\lvert\epsilon_b\rvert_{max}$	$\lvert\epsilon_c\rvert_{max}$
Part 1	0	0	$2.5 \cdot 10^{-2}$
Part 1 (modified)	$1.2 \cdot 10^{-2}$	$1.2 \cdot 10^{-2}$	$1.3 \cdot 10^{-2}$
Part 2	$5.0 \cdot 10^{-3}$	$6.9 \cdot 10^{-3}$	$8.7 \cdot 10^{-3}$

the predictions obtained with the present method, hence "safe" for preliminary design of foldable cylinders.

Acknowledgments

We thank Prof. C. R. Calladine for comments on an earlier version of this paper. We acknowledge, with thanks, financial support from British Aerospace (Space Systems) Ltd. and SERC (S.D.G.), and the award of an ESA Fellowship (S.P.).

References

Gibson, L. J., and Ashby, M. F., 1988, *Cellular Solids: Structure & Properties*, Pergamon Press, Oxford, U.K.

Guest, S. D., and Pellegrino, S., 1992, "Inextensional Wrapping of Flat Membranes," *Proc. First International Seminar on Structural Morphology*, R. Motro, ed., Montpellier, La Grand Motte, Sept. 7–11, pp. 203–215.

Guest, S. D., and Pellegrino, S., 1994, "The Folding of Triangulated Cylinders, Part I: Geometric Considerations," ASME JOURNAL OF APPLIED MECHANICS, Vol. 61, pp. 773–777.

Livesley, R. K., 1975, *Matrix Methods of Structural Analysis*, 2nd ed., Pergamon Press, Oxford, U.K.

Pellegrino, S., 1993, "Structural Computations with the Singular Value Decomposition of the Equilibrium Matrix," *International Journal of Solids and Structures*, Vol. 30, pp. 3025–3035.

Downloaded 03 May 2010 to 171.66.16.20. Redistribution subject to ASME license or copyright; see http://www.asme.org/terms/Terms_Use.cfm

M. Aron
School of Mathematics and Statistics,
University of Plymouth,
Drake Circus,
Plymouth PL4 8AA, U.K.

S. Aizicovici
Department of Mathematics,
Ohio University,
Athens, OH 45701-2979

Two New Universal Relations in Nonlinear Elasticity and Some Related Matters

Two inequalities which for certain deformation classes may be viewed as universal relations are shown to hold for two distinct subclasses of unconstrained rubberlike solids. The inequalities express the fact that the mean stress corresponding to any purely distortional deformation originating from a given ground state is dominated by (and, respectively, dominates) the mean stress in that ground state. Also discussed is a case in which the deformations involved are necessarily homogeneous.

1 Introduction

Mathematical statements which connect the stress and strain associated with certain deformations but which are independent of the properties of materials that belong to a specified class are known as universal relations. The universal relations are relevant to the experimental process as a material found to violate them cannot belong to the class of materials for which they are known to hold.

Perhaps the best known relation of this type is Rivlin's pioneering universal relation which is valid for all isotropic elastic solids subject to a simple shear deformation (Truesdell and Noll, 1965, Sec. 54). Other universal relations have been obtained by Currie and Hayes (1982), Wineman and Gandhi (1984), Beatty (1987a, b), Rajagopal and Wineman (1987) and Aron (1994). The relation derived in the latter holds for a certain class of isotropic elastic solids (that include the harmonic media (John, 1960)) subject to plane deformations for which J, the determinant of the deformation gradient $\mathbf{F}$, is a constant greater than one. This new relation differs from the ones found previously first because it is expressed as an inequality rather than as an equation and secondly because it connects the stress and strain associated with two different states of deformation namely $\mathbf{F}$ and $\sqrt{J}\,\mathbf{1}$, where $\mathbf{1}$ denotes the identity tensor.

In this paper we establish two universal relations of the kind obtained by Aron (1994) which, in particular, are valid for two distinct subclasses of unconstrained rubberlike solids subject to plane deformations with J = constant. These relations express the fact that the mean stress corresponding to any purely distortional deformation originating from a given ground state is dominated by (and, respectively, dominates) the mean stress in that ground state. Amongst the materials under consideration there are some of the materials of Blatz-Ko type (1962) and a subclass of the class of materials of Ogden type (1972).

According to a theorem of Ericksen (1955) the homogeneous deformations (which are characterized by the condition that $\mathbf{F}$ = constant) are the only deformations possible in all unconstrained elastic solids subject to boundary tractions alone. While the class of deformations with J = constant includes, besides all homogeneous deformations, some deformations which are not homogeneous we show here that in contrast to harmonic materials (see Aron, 1990), the plane nonhomogeneous deformations with constant strain invariants are not possible (with zero body forces) in a class of materials that includes the rubberlike solids mentioned above.

2 Preliminaries

Consider a homogeneous, isotropic, elastic solid which, in a reference configuration, occupies the region Ω of the Euclidean space R^2. In a typical deformation the particle $\mathbf{X} \in \Omega$ is displaced to $\mathbf{x}(\mathbf{X}) \in R^2$.

The deformation gradient

$$\mathbf{F} \equiv \nabla \mathbf{x}, \tag{1}$$

whose determinant satisfies

$$J \equiv \det \mathbf{F} > 0, \tag{2}$$

can be represented uniquely in the form

$$\mathbf{F} = \mathbf{VQ} \tag{3}$$

where $\mathbf{Q}$ is a proper orthogonal tensor and $\mathbf{V}$ is a symmetric, positive-definite tensor. The principal stretches λ_i, $i = 1, 2$, are defined to be the eigenvalues of $\mathbf{V}$. Clearly,

$$\mathbf{B} \equiv \mathbf{V}^2 = \mathbf{FF}^T \tag{4}$$

where $\mathbf{F}^T$ denotes the transpose of $\mathbf{F}$.

For the materials under consideration there exists a reference configuration such that the response function relating

Contributed by the Applied Mechanics Division of THE AMERICAN SOCIETY OF MECHANICAL ENGINEERS for publication in the JOURNAL OF APPLIED MECHANICS.

Discussion on this paper should be addressed to the Technical Editor, Professor Lewis T. Wheeler, Department of Mechanical Engineering, University of Houston, Houston, TX 77204-4792, and will be accepted until four months after final publication of the paper itself in the JOURNAL OF APPLIED MECHANICS.

Manuscript received by the ASME Applied Mechanics Division, Oct. 23, 1992; final revision, Aug. 6, 1993. Associate Technical Editor: R. Abeyaratne.

Copyright © 1994 by ASME
Downloaded 03 May 2010 to 171.66.16.20. Redistribution subject to ASME license or copyright; see http://www.asme.org/terms/Terms_Use.cfm

the (in-plane) Cauchy stress tensor $\mathbf{T}$ to the deformation gradient is given by

$$\mathbf{T} = \psi_0 \mathbf{I} + \psi_1 \mathbf{B} \tag{5}$$

where ψ_0, ψ_1 are scalar-valued functions of the invariants of $\mathbf{B}$ defined by

$$I \equiv \text{trace}\,\mathbf{B} \equiv \text{tr}\,\mathbf{B} = \lambda_1^2 + \lambda_2^2, \quad J \equiv \sqrt{\det \mathbf{B}} = \lambda_1 \lambda_2. \tag{6}$$

When a stored-energy function $W \equiv W(\mathbf{F})$ exists it can be shown that

$$W = W(\lambda_1, \lambda_2) = \hat{W}(I, J) \tag{7}$$

and

$$\psi_0 = \frac{\partial \hat{W}}{\partial J} = \frac{1}{\Delta}(\lambda_1 W_2 - \lambda_2 W_1), \tag{8}$$

$$\psi_1 = \frac{2}{J}\frac{\partial \hat{W}}{\partial I} = \frac{1}{J\Delta}(\lambda_1 W_1 - \lambda_2 W_2), \tag{9}$$

where

$$\Delta \equiv \lambda_1^2 - \lambda_2^2, \quad W_i \equiv \frac{\partial W}{\partial \lambda_i}, \quad i = 1, 2. \tag{10}$$

The equilibrium condition in the absence of body forces is

$$\text{Div}(J\mathbf{T}\mathbf{F}^{-T}) = \mathbf{0}, \tag{11}$$

where Div denotes the divergence operator with respect to $\mathbf{X}$ and $\mathbf{F}^{-T}$ is the inverse of the transpose of $\mathbf{F}$.

The principal stresses t_i, $i = 1, 2$, are the eigenvalues of $\mathbf{T}$. From (5), (8), and (9) we find that

$$t_i = \frac{\lambda_i}{J} W_i \tag{12}$$

so that, at conformal deformations ($\lambda_1 = \lambda_2 \equiv \lambda$) we have

$$t_1 = t_2 = \lambda^{-1} W_1(\lambda, \lambda) \equiv t. \tag{13}$$

The mean stress is defined by

$$\bar{T} \equiv \frac{1}{2}(t_1 + t_2). \tag{14}$$

If the reference configuration is a natural state ($t(1) = 0$) the classical pressure-compression inequality (Truesdell and Noll, 1965, Sec. 51), which is the requirement that the volume of an unconstrained isotropic solid should be decreased by pressure but increased by tension, takes the form

$$t(\lambda)(\lambda - 1) > 0 \quad \text{for} \quad \lambda \neq 1. \tag{15}$$

3 Lower and Upper Bounds for the Mean Stress

In a recent paper (Aron, 1991) a class of symmetric functions of two variables $f(\lambda_1, \lambda_2)$ which satisfy the inequality

$$\hat{f}(I, J) \equiv f(\lambda_1, \lambda_2) > f\left(\sqrt{\lambda_1 \lambda_2}, \sqrt{\lambda_1 \lambda_2}\right), \quad \lambda_1 \neq \lambda_2, \lambda_1, \lambda_2 > 0, \tag{16}$$

has been identified. Specifically, it was shown in that paper that the inequality (16) holds provided

$$\frac{\partial \hat{f}}{\partial I}(I, J) = \frac{1}{2\Delta}(\lambda_1 f_1 - \lambda_2 f_2) \neq 0, \text{for } \lambda_1 \neq \lambda_2, \lambda_1, \lambda_2 > 0, \tag{17}$$

and

$$\frac{\partial \hat{f}}{\partial I}(2J, J) = \frac{1}{4}\left[f_{11}(\lambda, \lambda) - f_{12}(\lambda, \lambda) + \frac{f_1(\lambda, \lambda)}{\lambda}\right] > 0, \quad \lambda > 0, \tag{18}$$

where

$$f_{ij} \equiv \frac{\partial^2 f}{\partial \lambda_i \partial \lambda_j}, \quad i, j = 1, 2.$$

When (17) holds but (18) is replaced by

$$\frac{\partial \hat{f}}{\partial I}(2J, J) < 0, \tag{19}$$

a trivial modification of the proof of (16) shows that f satisfies

$$f(\lambda_1, \lambda_2) < f\left(\sqrt{\lambda_1 \lambda_2}, \sqrt{\lambda_1 \lambda_2}\right), \lambda_1 \neq \lambda_2, \lambda_1, \lambda_2 > 0. \tag{20}$$

The implications of the assumption that $f \equiv W$, the stored-energy function of an isotropic elastic solid, have been discussed by Ericksen (1981) and Aron (1991). In this case (17) is implied by the Baker-Ericksen inequality (Baker and Ericksen, 1954) whereas (18) can be shown to be a necessary condition for the infinitesimal stability of $\lambda\mathbf{I}$ ($\lambda = \text{const.}$, $\lambda > 0$) under prescribed dead-load boundary tractions (see Ogden, 1984a; 1984b, Sec. 6.2). Both (17) and (18) are then implied by the strong-ellipticity condition (Knowles and Sternberg, 1977). When $f \equiv W \in C^2$ the weaker form of (16), (i.e., (16) where " $>$ " has been replaced by " $\geq$ ") is a consequence of the Legendre-Hadamard condition at $\sqrt{J}\mathbf{I}$ and thus it is a necessary condition for the infinitesimal stability (see Truesdell and Noll, 1965, Sec. 68b) of $\sqrt{J}\mathbf{I}$. This follows from the observation that Legendre-Hadamard condition is equivalent to the rank-one convexity condition (see Knops and Stuart, 1984, for instance) and a representation theorem for deformation gradients due to Chipot and Kinderlehrer (1988, p. 249).

Since the stored-energy function $W(\lambda_1, \lambda_2)$ is a symmetric function of its arguments, so is

$$f(\lambda_1, \lambda_2) \equiv \lambda_1 W_1 + \lambda_2 W_2. \tag{21}$$

Using (16)–(18) and

$$W_1(\lambda, \lambda) = W_2(\lambda, \lambda) \tag{22}$$

we find that

$$\lambda_1 W_1 + \lambda_2 W_2 > 2\sqrt{\lambda_1 \lambda_2}\, W_1\left(\sqrt{\lambda_1 \lambda_2}, \sqrt{\lambda_1 \lambda_2}\right), \lambda_1 \neq \lambda_2, \tag{23}$$

provided

$$\lambda_1 W_1 - \lambda_2 W_2 + \lambda_1^2 W_{11} - \lambda_2^2 W_{22} \neq 0, \quad \lambda_1 \neq \lambda_2, \tag{24}$$

and

$$E(\lambda) > 0 \tag{25}$$

where

$$E(\lambda) \equiv 3W_{11}(\lambda, \lambda) - W_{12}(\lambda, \lambda) + \lambda\left[W_{111}(\lambda, \lambda) - W_{112}(\lambda, \lambda) + \frac{W_1(\lambda, \lambda)}{\lambda^2}\right]. \tag{26}$$

When (24) holds and (25) is replaced by

$$E(\lambda) < 0 \tag{27}$$

we have

$$\lambda_1 W_1 + \lambda_2 W_2 < 2\sqrt{\lambda_1 \lambda_2}\, W_1\left(\sqrt{\lambda_1 \lambda_2}, \sqrt{\lambda_1 \lambda_2}\right), \lambda_1 \neq \lambda_2. \tag{28}$$

Downloaded 03 May 2010 to 171.66.16.20. Redistribution subject to ASME license or copyright; see http://www.asme.org/terms/Terms_Use.cfm

From (12)–(14) we now see that (23) and (28) can be re-written as

$$\overline{T}(\lambda_1, \lambda_2) > t\left(\sqrt{\lambda_1\lambda_2}\right), \quad \lambda_1 \neq \lambda_2, \tag{29}$$

and

$$\overline{T}(\lambda_1, \lambda_2) < t\left(\sqrt{\lambda_1\lambda_2}\right), \quad \lambda_1 \neq \lambda_2, \tag{30}$$

respectively.

Following Flory (1961) and Ogden (1976) we decompose each local homogeneous deformation $\mathbf{F}$ into an equal biaxial stretch (volume change) $\sqrt{J}\mathbf{1}$ followed by an isochoric deformation $\mathbf{A}$, i.e.,

$$\mathbf{F} = \sqrt{J}\mathbf{A}, \tag{31}$$

where

$$\mathbf{A} \equiv \frac{1}{\sqrt{J}}\mathbf{F} \tag{32}$$

satisfies

$$\det \mathbf{A} = 1. \tag{33}$$

We then find that the inequality (29) expresses the fact that the mean stress in any purely distortional deformation $\mathbf{A}$ originating from the ground state $\sqrt{J}\mathbf{1}$ is greater than the mean stress in the ground state $\sqrt{J}\mathbf{1}$. Evidently, an analogous interpretation also holds for the inequality (30).

For materials defined by (24) and (25) we now infer (on combining (29) and (15)) that in a state of pressure in mean (i.e., $\overline{T} \leq 0$) there is a volume reduction ($J < 1$); conversely, in the case of a volumetric expansion ($J > 1$), there is a state of tension in mean ($\overline{T} > 0$). Similarly, for materials characterized by (24) and (27) we deduce (on combining (30) and (15)) that in a state of tension in mean (i.e., $\overline{T} \geq 0$) there is a volumetric expansion ($J > 1$); and conversely, in the case of a volumetric contraction ($J < 1$), there is a state of pressure in mean ($\overline{T} < 0$). We also note that when $\mathbf{F}$ is isochoric and $t(1) = 0$, (29) and (30) reduce to $\overline{T} > 0$ and $\overline{T} < 0$, respectively.

4 The Universal Relations

The class of materials which we now consider are elastic solids with a stored-energy function in plane strain given by

$$W = \lambda_1^\alpha + \lambda_2^\alpha + h(J) \tag{34}$$

where $\alpha \neq 0$ is a constant. When $\alpha > 0$ the above coincides with a subclass of the class of materials introduced by Ogden (1972) and as such it includes, among others, the compressible Mooney-Rivlin and neo-Hookean stored-energy functions ($\alpha = 2$; see Ciarlet and Geymonat, 1982; Christensen, 1988), the compressible Varga stored-energy function ($\alpha = 1$; see Haughton, 1987) and the Blatz-Ko stored-energy function for solid polyurethane rubbers ($\alpha = 2$; see Blatz and Ko, 1962). When $\alpha < 0$ (34) includes the stored-energy function for foam polyurethane rubbers ($\alpha = -2$) introduced by Blatz and Ko (1962).

Since

$$\lambda_1 W_1 - \lambda_2 W_2 = \alpha(\lambda_1^\alpha - \lambda_2^\alpha) \neq 0, \quad \text{for } \lambda_1 \neq \lambda_2, \tag{35}$$

and

$$W_{11}(\lambda, \lambda) - W_{12}(\lambda, \lambda) + \frac{W_1(\lambda, \lambda)}{\lambda} = \alpha^2\lambda^{\alpha-2} > 0, \quad \lambda > 0, \tag{36}$$

it is clear that W satisfies

$$W(\lambda_1, \lambda_2) > W\left(\sqrt{\lambda_1\lambda_2}, \sqrt{\lambda_1\lambda_2}\right), \quad \lambda_1 \neq \lambda_2. \tag{37}$$

The stored-energy function (34), however, also satisfies (24) whereas $E(\lambda)$ (see (26)) is given in this case by

$$E(\lambda) = \alpha^3\lambda^{\alpha-2}. \tag{38}$$

According to the discussion in the previous section therefore, the stress associated with any deformation in materials characterized by (34) where $\alpha > 0$ ($\alpha < 0$) must necessarily satisfy (29) ((30)), irrespective of the choice of the material constant α and of the material function h. Thus, if in a laboratory experiment it is found that (29) ((30)) is violated, then it can be concluded that the material involved in the experiment does not belong to the class (34) where $\alpha > 0$ ($\alpha < 0$).

As an experiment of this nature involves the measurement of $t(\sqrt{\lambda_1\lambda_2})$, it is clear that the conformal deformation $\sqrt{\lambda_1\lambda_2}\,\mathbf{1}$ must be an equilibrium solution. A nonhomogeneous conformal deformation, however, is possible in the absence of body forces if and only if the corresponding stress field $t(\sqrt{\lambda_1\lambda_2})$ is independent of the stretch parameter $\sqrt{\lambda_1\lambda_2}$ in which case the classical pressure-compression condition (15) is violated (Aron, 1988). For this reason, in an experiment aimed at checking whether either (29) or (30) is satisfied, the specimen must be subject to deformations $\mathbf{F}$ such that $J = \det \mathbf{F} =$ constant. The class of deformations that obey this condition includes all homogeneous deformations, all isochoric deformations, as well as deformations which are neither homogeneous nor isochoric (see Podio-Guidugli, Vergara Caffarelli and Virga, 1986, for a relevant example; Aron, 1991 and Horgan, 1992 have shown independently that the deformation considered by these authors is possible, in the absence of body forces, in all unconstrained materials of Varga type).

5 Deformations With Constant Principal Stretches

Among the plane nonhomogeneous, nonconformal, deformations with $J =$ constant there are deformations for which both principal stretches are constant. An example of such a deformation, due to Fosdick, is cited by Truesdell and Noll (1965, Sec. 91). Other examples are due to Varley and Day (1966). Here we show that these deformations are not possible in isotropic elastic solids for which (see (9)) $\psi_1 \neq 0$ and which are subject to boundary tractions alone. In particular (see (35) and (36)), they are not possible in materials whose stored-energy function has the form (34). As remarked in Section 3, the condition $\psi_1 \neq 0$ is implied by the stronge-ellipticity condition and, for $\lambda_1 \neq \lambda_2$, also by the Baker-Ericksen inequality which is the requirement that in a deformation process of an isotropic solid the greater principal stress should occur in the direction of the greater principal stretch, i.e.,

$$(t_1 - t_2)(\lambda_1 - \lambda_2) > 0, \quad \text{for } \lambda_1 \neq \lambda_2. \tag{39}$$

To prove this result we show that a plane, nonconformal deformation with constant principal stretches which is in equilibrium in the absence of body forces in an isotropic elastic solid with $\psi_1 \neq 0$, is necessarily homogeneous. To this end we first note that, on account of (4), (5), (8), and (9), the equilibrium condition (11) can be written in the form

$$\operatorname{Div}\left(J\frac{\partial W}{\partial J}\mathbf{F}^{-T}\right) + 2\operatorname{Div}\left(\frac{\partial W}{\partial I}\mathbf{F}\right) = \mathbf{0}. \tag{40}$$

On assuming that I and J ($I \neq 2J$) are constants and on making use of (see, Ogden, 1984b, Chapters 1 and 2, for instance)

$$\operatorname{Div}(\phi\mathbf{F}) = \phi \operatorname{Div}\mathbf{F} + \mathbf{F}^T\operatorname{Grad}\phi \tag{41}$$

and

Downloaded 03 May 2010 to 171.66.16.20. Redistribution subject to ASME license or copyright; see http://www.asme.org/terms/Terms_Use.cfm

$$\mathrm{Div}(J\mathbf{F}^{-T}) = \mathbf{0}, \tag{42}$$

we find that (40) reduces to

$$\frac{\partial W}{\partial I}\mathrm{Div}\,(\mathbf{F}) = \mathbf{0}. \tag{43}$$

As, by assumption $\dfrac{\partial W}{\partial I} \neq 0$ the latter yields

$$\mathrm{Div}(\mathbf{F}) = \mathbf{0} \tag{44}$$

whose component form is (see (1))

$$x_{i,kk} = 0, \quad i,k = 1,2, \tag{45}$$

where the summing convention over repeated indices has been adopted and where $,k$ denotes the partial derivative with respect to X_k. For the remainder of this proof we follow Ogden (1984b, Sec. 5.2.1). Since Grad I = Grad $[\mathrm{tr}(\mathbf{F}\mathbf{F}^{\mathrm{T}})]$ = $\mathbf{0}$, we have

$$x_{i,k}x_{i,km} = 0, \quad m = 1,2, \tag{46}$$

which, by differentiation, leads to

$$x_{i,km}x_{i,km} + x_{i,k}x_{i,kmm} = 0. \tag{47}$$

On combining (45) and (47) we obtain

$$x_{i,km}x_{i,km} = 0, \tag{48}$$

which shows that $x_{i,k}$ = constant.

References

Aron, M., 1988, "A Note on Undistorted States of Isotropic Elastic Solids," *J. Elasticity*, Vol. 19, pp. 179–187.

Aron, M., 1990, "On the Stability of Varley-Day Solutions for Harmonic Materials," *Quart. Appl. Math.*, Vol. 48, pp. 455–461.

Aron, M., 1991, "On a Minimum Property in Nonlinear Elasticity," *Int. J. Engng. Sci.*, Vol. 29, pp. 1471–1478.

Aron, M., 1994, "Some Estimates for the Maximum Shear Stress in Plane, Isotropic Elasticity," *Quart. Appl. Math.*, Vol. 52, pp. 545–551.

Baker, M., and Ericksen, J. L., 1954, "Inequality Restricting the Form of the Stress-Deformation Relations for Isotropic Elastic Solids and Reiner-Rivlin Fluids," *J. Wash. Acad. Sci.*, Vol. 44, pp. 33–35.

Beatty, M. F., 1987a, "Topics in Finite Elasticity: Hyperelasticity of Rubber, Elastomers, and Biological Tissues—With Examples," ASME *Appl. Mech. Rev.*, Vol. 40, pp. 1699–1987.

Beatty, M. F., 1987b, "A Class of Universal Relations in Isotropic Elasticity Theory," *J. Elasticity*, Vol. 17, pp. 113–121.

Blatz, P. J., and Ko., W. L., 1962, "Application of Finite Elasticity to the Deformation of Rubbery Materials," *Trans. Soc. Rheol*, Vol. 6, pp. 223–251.

Chipot, M., and Kinderlehrer, D., 1988, "Equilibrium Configurations of Crystals," *Arch. Ration. Mech. Anal*, Vol. 103, pp. 237–277.

Ciarlet, P. G., and Geymonat, G., 1982, "Sur les Lois de Comportament en Elasticité Non-Linéaire Compressible," *C. R. Acad. Sci. Paris Sér. II*, Vol. 295, pp. 423–426.

Christensen, R. M., 1988, "A Two Material Constant, Nonlinear Elastic Stress Constitutive Equation Including the Effect of Compressibility," *Mech. Mater*, Vol. 7, pp. 155–162.

Currie, P. K., and Hayes, M., 1982, "On Non-Universal Finite Elastic Deformations," *Proc. IUTAM Symp. on Finite Elasticity*, D. E. Carlson and R. T. Shield, eds., Martinus Nijhoff, The Hague, pp. 143–150.

Ericksen, J. L., 1955, "Deformations Possible in Every Compressible, Isotropic, Perfectly Elastic Material," *J. Math. Phys.*, Vol. 34, pp. 126–128.

Ericksen, J. L., 1981, "Some Simpler Cases of the Gibbs Problem for Thermoelastic Solids," *J. Thermal Stresses*, Vol. 4, pp. 13–30.

Flory, P. J., 1961, "Thermodynamic Relations for High Elastic Materials," *Trans. Faraday Soc*, Vol. 57, pp. 829–838.

Haughton, D. M., 1987, "Inflation and Bifurcation of Thick-Walled Compressible Elastic Spherical Shells," *IMA J. Appl. Math*, Vol. 39, pp. 259–272.

Horgan, C. O., 1992, "Void Nucleation and Growth for Compressible Non-Linearly Elastic Materials: an Example," *Int. J. Solids Structures*, Vol. 29, pp. 279–291.

John, F., 1960, "Plane Strain Problems for a Perfectly Elastic Material of Harmonic Type," *Commun. Pure Appl. Math.*, Vol. 13, pp. 239–296.

Knops, R. J., and Stuart, C. A., 1984, "Quasiconvexity and Uniqueness of Equilibrium Solutions in Nonlinear Elasticity," *Arch. Ration. Mech. Anal.*, Vol. 86, pp. 233–249.

Knowles, J. K., and Sternberg, E., 1977, "On the Failure of Ellipticity of the Equations for Finite Elastostatic Plane Strain," *Arch. Ration. Mech. Anal.*, Vol. 63, pp. 321–335.

Ogden, R. W., 1972, "Large Deformation Isotropic Elasticity: On the Correlation of Theory and Experiment for Compressible Rubber-Like Solids," *Proc. Roy. Soc. London*, Vol. A328, pp. 567–583.

Ogden, R. W., 1976, "Volume Changes Associated with the Deformation of Rubber-Like Solids," *J. Mech. Phys. Solids*, Vol. 24, pp. 323–338.

Ogden, R. W., 1984a, "On Non-Uniqueness in the Traction Boundary —Value Problem for a Compressible Elastic Solid," *Quart. Appl. Math.*, Vol. 41, pp. 337–344.

Ogden, R. W., 1984b, *Non-Linear Elastic Deformations*, Ellis Horwood, Chichester, U.K.

Podio-Guidugli, P., Vergara Caffarelli, G., and Virga, E. G., 1986, "Cavitation and Phase Transition of Hyperelastic Fluids," *Arch. Ration. Mech. Anal*, Vol. 92, pp. 121–136.

Rajagopal, K. R., and Wineman, A. S., 1987, "New Universal Relations for Nonlinear Isotropic Elastic Materials," *J. Elasticity*, Vol. 17, pp. 75–83.

Truesdell, C., and Noll, W., 1965, "The Non-Linear Field Theories of Mechanics," *Encyclopedia of Physics*, S. Flugge, ed., Vol. III/3, Springer-Verlag, New York.

Varley, E., and Day, A., 1966, "Equilibrium Phases of Elastic Materials at Uniform Temperature and Pressure," *Arch. Ration. Mech. Anal.*, Vol. 22, pp. 253–269.

Wineman, A. S., and Gandhi, M., 1984, "On Local and Global Universal Relations in Elasticity," *J. Elasticity*, Vol. 14, pp. 97–102.

Downloaded 03 May 2010 to 171.66.16.20. Redistribution subject to ASME license or copyright; see http://www.asme.org/terms/Terms_Use.cfm

Stability Analysis of a Spinning Elastic Disk Under a Stationary Concentrated Edge Load

Jen-San Chen
Associate Professor,
Department of Mechanical Engineering,
National Taiwan University,
Taipei, Taiwan 107

The natural frequencies and stability of a spinning elastic disk subjected to a stationary concentrated edge load are investigated both numerically and analytically. It is found that a stationary, conservative, compressive edge load decreases the natural frequencies of the forward and backward traveling waves, but increases the natural frequency of the so-called reflected wave. It is also found that the significance of the effect of the conservative edge load on the natural frequencies and stability of the spinning disk is solely through the transverse component of the edge load on the boundary, and not through the membrane stress field it produces inside the disk. In addition, the compressive edge load induces a stationary-type instability before the critical speed, and induces a merged-type instability after the critical speed when a reflected wave meets a forward or a backward wave. The expression for the derivative of the eigenvalues of the spinning disk with respect to the edge load is derived to verify the numerical results.

Introduction

Transverse stability is a critical constraint in the optimal design and operation of computer disk drives and circular saws. In computer disk drives, excessive transverse vibrations degrade the signal from the read/write head and can destroy the disk by a "head-crash." In the wood cutting process, saw blade vibrations result in greater kerf loss and can warp the saw permanently through overheating. Initiated by Lamb and Southwell in 1921, early research on spinning disk dynamics was concerned with verifying the critical speed theory and the effects of thermally induced membrane stress field on the natural frequencies of the spinning disk. References to these works can be found in Mote and Szymani (1978). In the past 20 years much attention has been focused on identifying the characteristic instabilities induced by the interaction between a spinning disk and a stationary load system, which represents the recording head suspension in computer disk drives or saw guides in circular saws (Iwan and Moeller, 1976; Hutton et al., 1991; Shen and Mote, 1991; Ono et al., 1991).

One unique feature in circular saw applications is the stationary concentrated in-plane load applied at the outer rim of the spinning disk during the cutting operation. The buckling analysis of a stationary circular disk subjected to general stationary in-plane loads is a classical problem that has been thoroughly studied. Srinivasan and Ramamurti (1980) considered the in-plane dynamic behavior of a stationary disk subjected to a spinning concentrated in-plane load at the outer boundary. They did not study the dynamic response associated with the bending of the disk. Regarding the effects of a concentrated edge load on the natural frequencies and stability of a spinning disk, there are two papers (Carlin et al., 1975; Radcliffe and Mote, 1977) in the literature. Carlin et al. (1975) first wrote the equation of motion for a nonrotating disk with axisymmetric in-plane stresses due to tensioning and asymmetric stresses due to a stationary concentrated normal edge load. In order to account for the effects of the disk rotation, they then superposed the axisymmetric stresses due to the centrifugal force to the membrane stress field induced by tensioning and the edge load. They found that the effects of these centrifugal stresses on blade stiffness are negligible. Radcliffe and Mote (1977) extended the work of Carlin et al. by considering a general concentrated edge load with both normal and tangential components, and were concerned primarily with the critical speed instability. Neither stationary-type nor merged-type instability is induced by their loadings. Since the equations of motion used in these two papers are nongyroscopic, they do not correspond to either a spinning disk-stationary edge load system (Iwan and Moeller, 1976), nor a stationary disk-spinning edge load system (Iwan and Stahl, 1973). On the contrary, their concentrated edge loads appear to be spinning along with the spinning disk, i.e., there is no relative motion between the disk and the edge load in the circumferential direction. Therefore these models do not represent the loading that occurs in the normal cutting process. The effects of a stationary concentrated edge load of the type that occurs in cutting on the natural frequen-

Contributed by the Applied Mechanics Division of THE AMERICAN SOCIETY OF MECHANICAL ENGINEERS for publication in the ASME JOURNAL OF APPLIED MECHANICS.

Discussion on this paper should be addressed to the Technical Editor, Professor Lewis T. Wheeler, Department of Mechanical Engineering, University of Houston, Houston, TX 77204-4792, and will be accepted until four months after final publication of the paper itself in the ASME JOURNAL OF APPLIED MECHANICS.

Manuscript received by the ASME Applied Mechanics Division, July 15, 1992; final revision, Apr. 28, 1993. Associate Technical Editor: F. Y. M. Wan.

Copyright © 1994 by ASME
Downloaded 03 May 2010 to 171.66.16.20. Redistribution subject to ASME license or copyright; see http://www.asme.org/terms/Terms_Use.cfm

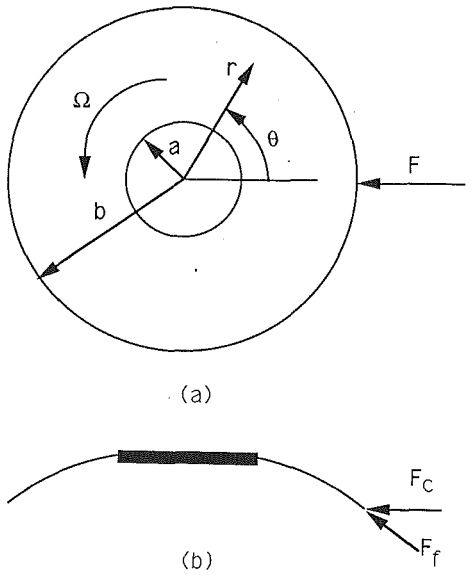


Fig. 1 A spinning disk subjected to a stationary edge load

cies and stability of a spinning disk evidently have not been studied before.

In the present paper we consider a spinning flexible annular disk clamped at the inner radius and subjected to a stationary concentrated edge load at the outer rim. Both follower and conservative edge loads are considered. A finite element procedure based on Galerkin's method is employed to calculate the eigenvalues of the system. Finally, the expression for the derivative of the eigenvalues of the spinning disk with respect to the edge load is derived to verify the numerical results.

Equation of Motion

Figure 1(*a*) shows a circular disk, which is clamped at the inner radius $r = a$ and subjected to a concentrated normal compressive force F at the outer radius $r = b$. The disk is rotating with constant speed Ω, while the edge load is circumferentially stationary in the space. The magnitude of the edge load remains the same when the disk vibrates laterally. The equation of motion of the system, in terms of the transverse displacement w and with respect to the stationary coordinate system (r, θ), is

$$\rho h\left(w_{,tt} + 2\Omega w_{,t\theta} + \Omega^2 w_{,\theta\theta}\right) + D\nabla^4 w + \mathbf{L}w + \hat{\mathbf{L}}w = 0 \quad (1)$$

where

$$D = \frac{Eh^3}{12(1-\nu^2)}.$$

The standard subscript notation for partial derivative is used here. The parameters ρ, h, E, and ν are the mass density, thickness, Young's modulus, and Poisson ratio of the disk, respectively. $\mathbf{L}$ is the membrane operator associated with the axisymmetrical stress field due to the centrifugal force, and $\hat{\mathbf{L}}$ is the membrane operator associated with the asymmetric stress field due to the normal edge load F at $r = b$, $\theta = 0$,

$$\mathbf{L} = -\frac{h}{r}\left[\frac{\partial}{\partial r}\left(r\sigma_r\frac{\partial}{\partial r}\right) + \frac{\partial}{\partial\theta}\left(\frac{1}{r}\sigma_\theta\frac{\partial}{\partial\theta}\right)\right]$$

$$\hat{\mathbf{L}} = -\frac{h}{r}\left[\frac{\partial}{\partial r}\left(r\hat{\delta}_r\frac{\partial}{\partial r} + \hat{\delta}_{r\theta}\frac{\partial}{\partial\theta}\right) + \frac{\partial}{\partial\theta}\left(\hat{\delta}_{r\theta}\frac{\partial}{\partial r} + \frac{1}{r}\hat{\sigma}_\theta\frac{\partial}{\partial\theta}\right)\right].$$

Membrane stresses σ_r and σ_θ are due to the centrifugal force and are proportional to Ω^2. $\hat{\sigma}_r$, $\hat{\delta}_{r\theta}$, and δ_θ can be calculated by following a standard procedure described in Coker and Filon (1957), and the solutions are given in Carlin et al. (1975).

We consider two types of normal edge load F denoted as F_c and F_f (Celep, 1979, 1982), as shown in Fig. 1(*b*). F_c is a conservative force, whose direction and magnitude remains the same when the disk vibrates laterally. F_f is a follower force, which is always tangent to the radial slope of the disk at $r = b$, $\theta = 0$. In the case when $F = F_c$, the boundary conditions for Eq. (1) are

$$w = 0, \quad w_{,r} = 0 \qquad \text{at} \quad r = a \quad (2a)$$

$$\mathbf{B}_1 w + F_c\hat{\mathbf{B}}_1 w = 0, \quad \mathbf{B}_2 w = 0 \quad \text{at} \quad r = b \quad (2b)$$

where the boundary operators are defined as

$$\mathbf{B}_1 = \frac{\partial}{\partial r}\left(\frac{\partial^2}{\partial r^2} + \frac{\partial}{r\partial r} + \frac{\partial^2}{r^2\partial\theta^2}\right) + \frac{1-\nu}{r^2}\left(\frac{\partial^3}{\partial r\partial\theta^2} - \frac{\partial^2}{r\partial\theta^2}\right)$$

$$\hat{\mathbf{B}}_1 = \frac{\delta(\theta)}{bD}\frac{\partial}{\partial r}$$

$$\mathbf{B}_2 = \frac{\partial^2}{\partial r^2} + \frac{\nu}{r}\left(\frac{\partial}{\partial r} + \frac{\partial^2}{r\partial\theta^2}\right).$$

$\delta(:)$ is the Dirac delta function. Therefore the edge load F_c affects the natural frequencies and stability of the spinning disk through two avenues: one is the membrane operator $\hat{\mathbf{L}}$ associated with the membrane stress field induced by F_c, and the other is the boundary operator $\hat{\mathbf{B}}_1$ associated with the transverse component of F_c at $r = b$, $\theta = 0$. In the case when $F = F_f$, on the other hand, the boundary conditions are the same as in Eqs. (2*a*,*b*), except that the term associated with boundary operator $\hat{\mathbf{B}}_1$ in (2*b*) disappears. Therefore F_f affects the natural frequencies and stability of the spinning disk only through the membrane operator $\hat{\mathbf{L}}$ associated with the membrane stress field induced by F_f.

Galerkin's Method

A particular solution of Eq. (1) is assumed to be in the form of a Fourier sine and cosine series expansion as follows:

$$w = \sum_{l=0}^{L}\left[G_l(r,t)\cos l\theta + K_l(r,t)\sin l\theta\right]. \quad (3)$$

After substituting Eq. (3) into Eq. (1), we obtain a set of partial differential equations for the functions $G_l(r,t)$ and $K_l(r,t)$. By a finite element numerical analysis based on Galerkin's method with third-order polynomial shape functions (Ono and Maeno, 1987), we can transform these differential equations with respect to r into matrix algebraic equations for the state vector at the nodes of the elements. From the viewpoints of both computing efficiency and accuracy, the number of elements in the radial direction and the maximum number of nodal diameters are chosen to be 6 and 3, respectively. The material properties of the disk used in the calculation are: $\rho = 7.84 \times 10^3$ kg/m^3, $E = 203 \times 10^9$ N/m^2, $\nu = 0.27$, $h = 1.02$ mm (0.04 in.), $a = 101.6$ mm (4 in.), and $b = 203.2$ mm (8 in.).

Effects of Membrane Operator $\hat{\mathbf{L}}$

We first examine the case when $F = F_f$. The boundary conditions on w of this case are exactly the same as those of the freely spinning disk (without any edge load). Figures 2 and 3 show the relation between the eigenvalues $\lambda = \alpha + i\omega$ of the zero-nodal-circle modes and one-nodal-circle modes, respectively, of the spinning disk and the rotation speed Ω. ω is the natural frequency of the spinning disk, and positive α means the mode is unstable. The dashed lines are the results

Downloaded 03 May 2010 to 171.66.16.20. Redistribution subject to ASME license or copyright; see http://www.asme.org/terms/Terms_Use.cfm

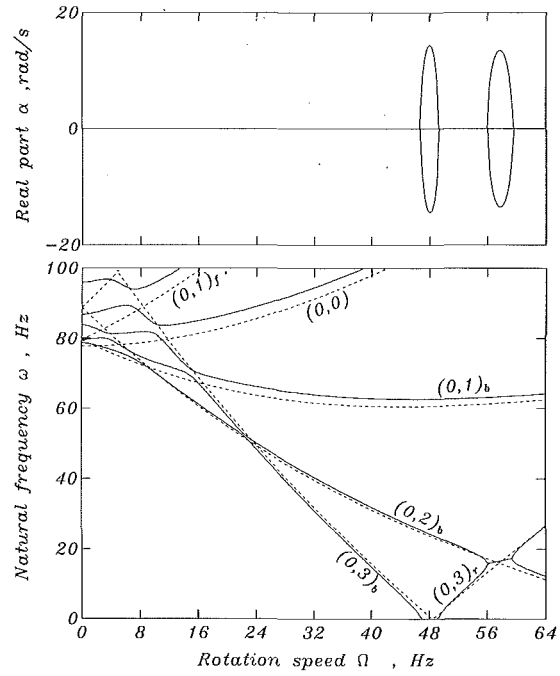


Fig. 2 Effects of follower edge load $F_f b/D = 21$ on the eigenvalues of zero-nodal-circle modes

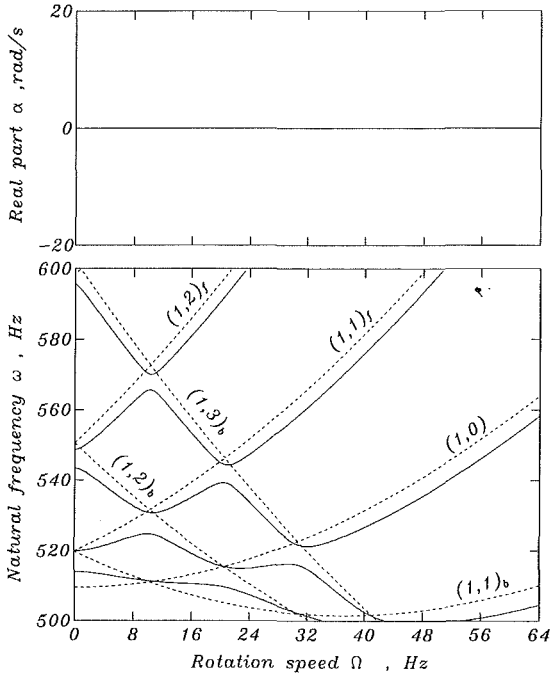


Fig. 3 Effects of follower edge load $F_f b/D = 21$ on the eigenvalues of one-nodal-circle modes

for the freely spinning disk, while the solid lines are the results for a disk under $F_f = 2000$ N (or nondimensional edge load $F_f b/D = 21$).

For a freely spinning disk the eigenvalues $\lambda_{mn} = \lambda^0_{mn}$ are all purely imaginary, i.e., $\lambda^0_{mn} = \mathrm{i}\,\omega_{mn}$, where ω_{mn} are real. The corresponding eigenfunctions are complex and assume the form

$$w^0_{mn} = R_{mn}(r)e^{\pm \mathrm{i}n\theta}, \quad n = 0, 1, 2, \ldots \tag{4}$$

in which R_{mn} is a real-valued function of r. The eigenfunction corresponding to $\bar{\lambda}^0_{mn}$ is $\bar{w}^0_{mn}$, where overbar means complex conjugate. If we consider only the positive ω_{mn}, then w^0_{mn} in Eq. (4) with $+in\theta$ is a backward traveling wave with n nodal diameters and m nodal circles, which is also denoted by $(m, n)_b$. Similarly, w^0_{mn} with $-in\theta$ is a forward traveling wave $(m, n)_f$. The critical speed Ω_c for the mode (m, n) is defined as the rotation speed at which ω_{mn} of the backward traveling wave $(m, n)_b$ is zero. For Ω greater than Ω_c, this mode is a forward traveling wave, and is called a "reflected wave," denoted by $(m, n)_r$.

It is noted from Fig. 3 and other data in the higher frequency range that F_f tends to decrease the natural frequencies of the forward and backward traveling waves with nodal circle(s). However, as shown in Fig. 2, F_f tends to increase the natural frequencies of most of the zero-nodal-circle modes. Regarding the stability, Fig. 2 shows that F_f induces a stationary-type instability (an unstable mode with zero natural frequency) before the critical speed, and a merged-type instability (two unstable modes with the same natural frequencies) after the critical speed when the backward traveling wave $(0, 2)_b$ meets the reflected wave $(0, 3)_r$.

Since the effects of the follower load are through the operator $\hat{\mathbf{L}}$ in the differential equation, we can follow a procedure described in Chen and Bogy (1992a) to calculate the derivative of the eigenvalue λ_{mn} with respect to the edge load F_f,

$$\frac{\partial \lambda_{mn}}{\partial F_f} = \frac{i\langle w^0_{mn}, \hat{\mathbf{L}} w^0_{mn}\rangle}{4\pi(\omega_{mn} \pm n\Omega)F_f \int_a^b R^2_{mn}(r) r dr} \tag{5}$$

where the inner product between two complex functions w_1 and w_2 is defined as

$$\langle w_1, w_2\rangle = \int_{-\pi}^{\pi}\int_a^b \bar{w}_1 w_2 r dr d\theta.$$

Since the inner product in the numerator of Eq. (5) is proportional to F_f, the derivative itself is independent of F_f. It is noted that the denominator in Eq. (5) is positive for a forward and a backward traveling wave, but is negative for a reflected wave (Chen and Bogy, 1992a). After integration by parts, we can calculate

$$\langle w_{mn}, \hat{\mathbf{L}} w_{mn}\rangle = \frac{1}{\rho}\int_{-\pi}^{\pi}\int_a^b \left[\left(\frac{\partial R_{mn}}{\partial r}\right)^2 r\hat{\sigma}_r + n^2 R^2_{mn}\frac{\hat{\sigma}_\theta}{r}\right] dr d\theta + \frac{F_f R_{mn}(b)}{\rho h}\frac{\partial R_{mn}(b)}{\partial r}. \tag{6}$$

While the integral term is primarily negative because the edge load is compressive, the boundary term, i.e., the second term on the right-hand side of Eq. (6), is always positive. For the numerical example in Figs. 2 and 3 we can verify by additional calculations that for the modes with nodal circle(s), the absolute value of the integral term is larger than the boundary term. On the other hand, for most of the zero-nodal-circle modes the boundary term is dominant, and the natural frequencies of the forward and the backward traveling waves tend to increase upon the application of the follower edge load.

Effects of Boundary Operator $\hat{\mathbf{B}}_1$

We next examine the case when the edge load is conservative, i.e., $F = F_c$. In this case, the edge load affects the natural frequencies and stability of the disk through both the membrane operator $\hat{\mathbf{L}}$ and the boundary operator $\hat{\mathbf{B}}_1$. When the conservative edge load with the same magnitude of the follower load in the last section, i.e., $F_c b/D = 21$, is applied, the disk will buckle (in the sense that the lowest natural frequency vanishes) even when the disk is not spinning. In order to understand how the natural frequencies of the disk change as the conservative edge load varies, we apply a

Downloaded 03 May 2010 to 171.66.16.20. Redistribution subject to ASME license or copyright; see http://www.asme.org/terms/Terms_Use.cfm

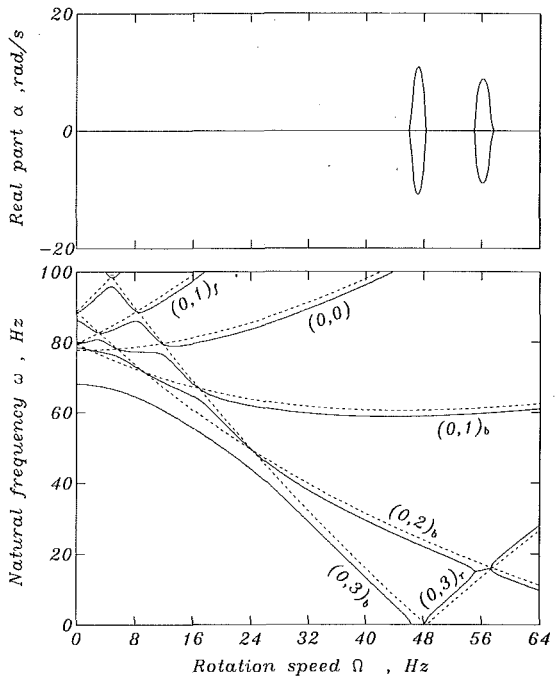


Fig. 4 Effects of conservative edge load $F_c b / D = 3.5$

smaller conservative edge load. Figure 4 shows the effects of $F_c b/D = 3.5$ on the eigenvalues of the system.

It is found that the conservative edge load decreases the natural frequencies of the forward and the backward traveling waves, and increases the natural frequency of the reflected wave. At the intersection point between two dashed curves, i.e., the degenerate eigenvalues of the freely spinning disk, one of the eigenvalues remains unchanged while the other decreases upon the application of F_c. It is also found that even though the magnitude of F_c in Fig. 4 is only one sixth the magnitude of F_f in Fig. 2, the stationary-type instability in Fig. 4 is as significant as that in Fig. 2. The conservative edge load also induces a merged-type instability when the reflected wave $(0,3)_r$ meets the backward wave $(0,2)_b$ on the left-hand side of the intersection point between these two dashed curves.

When a conservative tensile edge load with the same magnitude is applied, additional calculations show that it exhibits the opposite effects, i.e., a tensile edge load increases the natural frequencies of the forward and backward traveling waves, but decreases the natural frequency of the reflected wave. In addition, it induces a stationary-type instability just above the critical speed, and induces a merged-type instability on the right-hand side of the intersection between the dashed curves $(0,3)_r$ and $(0,2)_b$.

Additional eigenvalue calculations show that including or excluding the membrane effect $\hat{\mathbf{L}}$ alters the results by less than five percent. So, the significance of F_c on the natural frequencies and stability of the spinning disk is solely through the boundary operator $\hat{\mathbf{B}}_1$, and not through the membrane operator $\hat{\mathbf{L}}$.

If we concentrate on the effects of $\hat{\mathbf{B}}_1$ alone, we can obtain some physical insight into the stationary-type and merged-type instabilities induced by F_c by the following analysis. Assume that the spinning disk is vibrating in a backward traveling mode,

$$w = R_{mn}(r)\cos(n\theta + \omega_{mn}t + \epsilon_{mn})$$

where ϵ_{mn} is a constant phase. The velocity of the transverse direction of a particle on the spinning disk at position $r = b$, $\theta = 0$ is

$$\dot{w} = -(\omega_{mn} + n\Omega)R_{mn}(b)\sin(\omega_{mn}t + \epsilon_{mn}).$$

The transverse component of the edge load is $F_c(\partial w/\partial r)$. The work done by the edge load over one cycle from time t_1 to t_2 is

$$-\frac{1}{2}F_c(\omega_{mn} + n\Omega)R_{mn}(b)\frac{\partial R_{mn}(b)}{\partial r}\int_{t_1}^{t_2}\sin 2(\omega_{mn}t + \epsilon_{mn})dt.$$

This work is zero when the natural frequency ω_{mn} is not zero. On the other hand, this work can be positive or negative, depending on the phase ϵ_{mn} when $\omega_{mn} = 0$. This explains why instability occurs when the conservative edge load is present and the natural frequency of the mode becomes zero.

Regarding the merged-type instability, we assume that the disk is vibrating in the combination of a backward traveling wave w_{mn} and a reflected wave w_{pq},

$$w_{mn} = R_{mn}(r)\cos(n\theta + \omega_{mn}t + \epsilon_{mn})$$

and

$$w_{pq} = R_{pq}(r)\cos(q\theta - \omega_{pq}t + \epsilon_{pq})$$

where the natural frequencies ω_{mn} and ω_{pq} are assumed to be positive. It is shown in the previous paragraph that the work done on the mode shape w_{mn} by its corresponding transverse component $F_c(\partial w_{mn}/\partial r)$ is zero. However, the work done by the other force component $F_c(\partial w_{pq}/\partial r)$ over one cycle is

$$-\frac{1}{2}F_c(\omega_{mn} + n\Omega)R_{mn}(b)\frac{\partial R_{pq}(b)}{\partial r} \times \int_{t_1}^{t_2}\sin\left[(\omega_{mn} - \omega_{pq})t + \epsilon_{mn} - \epsilon_{pq}\right]dt.$$

In the case when $\omega_{mn} \neq \omega_{pq}$, this work is zero. On the other hand, when $\omega_{mn} = \omega_{pq}$, this work can be positive or negative. This explains why instability occurs when the conservative edge load is present and two frequency loci merge together.

It is emphasized here that while this simple analysis can explain why instability occurs when the natural frequency becomes zero (stationary-type) or when two natural frequencies are identical (merged-type), it does not provide explanations of why the natural frequencies tend to vanish or merge together. To provide explanations for these mechanisms, we need to study the mathematical structure of modal interactions in a manner similar to that described in Chen and Bogy (1992b).

Derivatives of Eigenvalues With Respect to F_c

We derive in this section the expression for the derivative of the eigenvalues with respect to F_c. With this analytical expression we can verify the numerical results regarding the effects of F_c on the natural frequencies of the spinning disk. Since we have shown that the boundary operator $\hat{\mathbf{B}}_1$ is much more important than the membrane operator $\hat{\mathbf{L}}$ in this regard, and the effect of $\hat{\mathbf{L}}$ alone is discussed in the previous section, we exclude $\hat{\mathbf{L}}$ here from the equation of motion for simplicity. After substituting the separable solution $w = w_{mn}e^{\lambda_{mn}t}$ into the equation of motion, we can write the equation for the eigenvalue problem in the operator form as

$$\lambda_{mn}^2\mathbf{M}w_{mn} + \lambda_{mn}\mathbf{G}w_{mn} + \mathbf{K}w_{mn} = 0 \qquad (7)$$

in which

$$\mathbf{M} = 1, \quad \mathbf{G} = 2\Omega\frac{\partial}{\partial\theta}, \quad \mathbf{K} = \frac{D\nabla^4}{\rho h} + \Omega^2\frac{\partial^2}{\partial\theta^2} + \frac{\mathbf{L}}{\rho h}.$$

The boundary conditions are the same as in Eqs. (2*a*, *b*). For a freely spinning disk, i.e., $F_c = 0$, Eq. (7) assumes the form

$$(\lambda_{mn}^0)^2\mathbf{M}w_{mn}^0 + \lambda_{mn}^0\mathbf{G}w_{mn}^0 + \mathbf{K}w_{mn}^0 = 0 \qquad (8)$$

Downloaded 03 May 2010 to 171.66.16.20. Redistribution subject to ASME license or copyright; see http://www.asme.org/terms/Terms_Use.cfm

and the boundary conditions are the same as in Eqs. $(2a, b)$, except that the operator $\hat{\mathbf{B}}_1$ disappears. The difference between eigenpair (λ_{mn}, w_{mn}) in Eq. (7) and $(\lambda^0_{mn}, w^0_{mn})$ in Eq. (8) is due to the boundary perturbation $F_c\hat{\mathbf{B}}_1 w$. This difference vanishes as F_c approaches zero.

Following a procedure described in Stakgold (1979), we first differentiate Eq. (7) and boundary conditions $(2a, b)$ with respect to F_c, and then set $F_c = 0$,

$$2\lambda^0_{mn}\lambda_{mn,F_c}\mathbf{M}w^0_{mn} + \left(\lambda^0_{mn}\right)^2\mathbf{M}w_{mn,F_c} + \lambda_{mn,F_c}\mathbf{G}w^0_{mn} + \lambda^0_{mn}\mathbf{G}w_{mn,F_c} + \mathbf{K}w_{mn,F_c} = 0 \quad (9)$$

$$w_{mn,F_c} = 0, \quad w_{mn,F_cr} = 0 \quad \text{at} \quad r = a$$

$$\mathbf{B}_1 w_{mn,F_c} + \hat{\mathbf{B}}_1 w^0_{mn} = 0, \quad \mathbf{B}_2 w_{mn,F_c} = 0 \quad \text{at} \quad r = b.$$

We multiply the conjugate of Eq. (8) by w_{mn,F_c} and Eq. (9) by $\bar{w}^0_{mn}$, subtract and integrate over the annular region. After recognizing that $(\lambda^0_{mn})^2 = (\bar{\lambda}^0_{mn})^2$ we obtain

$$\frac{\partial\lambda_{mn}}{\partial F_c} = -\frac{iR_{mn}(b)\dfrac{\partial R_{mn}(b)}{\partial r}}{4\pi\rho h(\omega_{mn} \pm n\Omega)\displaystyle\int_a^b R^2_{mn}(r)rdr} \quad (10)$$

The numerator on the right-hand side of Eq. (10) is always positive. The denominator, on the other hand, is positive for a forward and a backward traveling wave, but is negative for a reflected wave. Therefore the derivative is negative for a forward and a backward wave, and is positive for a reflected wave. This verifies our numerical results showing that the conservative compressive edge load tends to decrease the natural frequencies of the forward and backward traveling waves, and tends to increase the natural frequency of the reflected wave.

Conclusions and Discussions

The effects of a stationary edge load on the natural frequencies and stability of a spinning elastic disk are examined both numerically and analytically. The results of these analyses can be summarized as follows:

(1) The stationary, conservative, compressive edge load tends to decrease the natural frequencies of the forward and backward traveling waves, but tends to increase the natural frequency of the reflected wave. In addition, it induces a stationary-type instability before the critical speed, and induces a merged-type instability after the critical speed when a reflected wave meets a forward or a backward wave.

(2) Numerical analysis shows that the significance of the conservative edge load on the natural frequencies and stability of the spinning disk is solely through the transverse component of the edge load on the boundary, and not through the membrane stress field inside the disk.

(3) The derivative of the eigenvalues of a spinning elastic disk with respect to the conservative edge load verifies the numerical results regarding the effects of the edge load on the natural frequencies of the spinning disk.

The goal in circular saw research has been to improve the stability of the spinning saw blade during cutting operation. As we have pointed out the edge load induces a stationary-type instability before the critical speed. In order to raise the operation speed of the circular saw, it becomes necessary to eliminate the instabilities induced by the edge load. In the wood cutting industry, it has been a common practice to use saw guides and a floating central collar to achieve a more stable operation. A theoretical analysis of the stabilizing effects of the saw guides and a floating collar, when the edge load is present, is important in designing new circular saws and should be undertaken.

Acknowledgments

The results presented here were obtained in the course of research supported by a grant from the National Science Council of the Republic of China.

References

Carlin, J. F., Appl, F. C., Bridwell, H. C., and Dubois, R. P., 1975, "Effects of Tensioning on Buckling and Vibration of Circular Saw Blades," ASME *Journal of Engineering for Industry*, Vol. 2, pp. 37–48.

Celep, Z., 1979, "Axially Symmetric Stability of a Completely Free Circular Plate Subjected to a Non-Conservative Edge Load," *Journal of Sound and Vibration*, Vol. 65, No. 4, pp. 549–556.

Celep, Z., 1982, "Vibration and Stability of a Free Circular Plate Subjected to Non-Conservative Loading," *Journal of Sound and Vibration*, Vol. 80, No. 3, pp. 421–432.

Chen, J.-S., and Bogy, D. B., 1992a, "Effects of Load Parameters on the Natural Frequencies and Stability of a Flexible Spinning Disk with a Stationary Load System," ASME JOURNAL OF APPLIED MECHANICS, Vol. 59, Part 2, pp. S230–S235.

Chen, J.-S., and Bogy, D. B., 1992b, "Mathematical Structure of Modal Interactions in a Spinning Disk-Stationary Load System," ASME JOURNAL OF APPLIED MECHANICS, Vol. 59, Part 1, pp. 390–397.

Coker, E. G., and Filon, L. N. G., 1957, *A Treatise on Photo-Elasticity*, Cambridge University Press, London.

Hutton, S. G., Chonan, S., and Lehmann, B. F., 1987, "Dynamic Response of a Guided Circular Saw," *Journal of Sound and Vibration*, Vol. 112, No. 3, pp. 527–539.

Iwan, W. D., and Moeller, T. L., 1976, "The Stability of a Spinning Elastic Disk With a Transverse Load System," ASME JOURNAL OF APPLIED MECHANICS, Vol. 43, pp. 485–490.

Iwan, W. D., and Stahl, K. J., 1973, "The Response of an Elastic Disk With a Moving Mass System," ASME JOURNAL OF APPLIED MECHANICS, Vol. 40, pp. 445–451.

Lamb, H., and Southwell, R. V., 1921, "The Vibration of a Spinning Disk," *Proceedings of the Royal Society*, London, Vol. 99, pp. 272–280.

Mote, C. D., Jr., and Szymani, R., 1978, "Circular Saw Vibration Research," *The Shock and Vibration Digest*, Vol. 10, No. 6, pp. 15–30.

Ono, K., Chen, J.-S., and Bogy, D. B., 1991, "Stability Analysis for the Head-Disk Interface in a Flexible Disk Drive," ASME JOURNAL OF APPLIED MECHANICS, Vol. 58, No. 4, pp. 1005–1014.

Ono, K., and Maeno, T., 1987, "Theoretical and Experimental Investigation on Dynamic Characteristics of a 3.5-Inch Flexible Disk Due to a Point Contact Head," *Tribology and Mechanics of Magnetic Storage Systems*, Vol. 3, SP.21 (STLE), pp. 144–151.

Radcliffe, C. J., and Mote, C. D., Jr, 1977, "Stability of Stationary and Rotating Discs Under Edge Load," *International Journal of Mechanical Science*, Vol. 19, pp. 567–574.

Shen, I.-Y., and Mote, C. D., Jr., 1991, "On the Mechanisms of Instability of a Circular Plate Under a Rotating Spring-Mass-Dashpot System," *Journal of Sound and Vibration*, Vol. 148, No. 2, pp. 307–318.

Srinivasan, V., and Ramamurti, V., 1980, "Dynamic Response of an Annular Disk to a Moving Concentrated, In-Plane Edge Load," *Journal of Sound and Vibration*, Vol. 72, No. 2, pp. 251–262.

Stakgold, Ivar, 1979, *Green's Functions and Boundary Value Problems*, John Wiley and Sons, New York.

Downloaded 03 May 2010 to 171.66.16.20. Redistribution subject to ASME license or copyright; see http://www.asme.org/terms/Terms_Use.cfm

The Annular Taylor Column

W. E. Scott
Department of Engineering Science,
The University of Tennessee,
Knoxville, TN 37916

*A study is made of the time evolution of the flow generated by an annulus (*a *disk with a hole in it) of inner, outer radii* a *and* b *(*a ≪ b*), impulsively set into motion and rising at an infinitesimal Rossby number along the axis of rotation of a uniformly rotating, unbounded mass of inviscid, incompressible fluid. The result is that a Taylor column in the form of an annular cylinder of inner, outer radii* a *and* b*, does evolve, with all the properties a Taylor column should possess. As a consequence, possibly the first engineering application of the Taylor column is suggested.*

Introduction

The Taylor column (Proudman, 1916; Taylor, 1923) is a well-researched phenomenon experimentally (Long, 1953; Hide and Ibbottson, 1966, 1969; Maxworthy, 1968, 1970, 1982), analytically (Grace, 1922, 1923, 1927; Stewartson, 1952, 1953, 1957, 1958; Jacobs, 1964; Bretherton, 1967; Hocking, Moore, and Walton, 1979), and numerically (Dennis et al., 1982, 1983). Hence, the physics of the phenomenon is reasonably well understood and helps account for several meteorological and oceanographic processes. On the other hand, it remains an anomaly, a curiosity, seemingly having no exploitable engineering application or relevance. Perhaps for that reason there are no studies of Taylor column generation by anything other than spheres, cylinders, and disks. Hence, the present work involving the time development of the flow generated by an axially moving annulus rotating with the fluid is one small step toward filling that void in the Taylor column literature; and the properties of this column suggest, possibly, the first engineering application of the Taylor column.

Since the original mathematical analyses that predicted a Taylor column for disks, spheres, and cylinders were analytical rather than numerical, which, of course, demanded the neglect of viscosity, the author here, in this analytical attempt, also ignores viscosity.

Analysis

In Fig. 1, instead of letting the annulus rise slowly with a velocity U such that $U/2\Omega b \ll 1$ (i.e., small Rossby number), take the annulus as rotating with the fluid but otherwise at rest as the fluid flows past it with velocity U. Hence (Greenspan, 1968), the governing equation for the rotationally symmetric flow development is

$$[\partial^2(\partial^2/\partial r^2 - \partial/r\partial r + \partial^2/\partial z^2)/\partial t^2) + 4\Omega^2\partial^2/\partial z^2]\Psi = 0 \quad (1)$$

where Ψ, a stream function, is such that the velocity $\mathbf{v}$ can be written

$$\mathbf{v} = (u, v, w) = (\partial\Psi/r\partial z, v, -\partial\Psi/r\partial r). \quad (2)$$

In terms of the Laplace transform of Eq. (1) (see Sarma, 1957, for a discussion of how the initial conditions can be incorporated into the definition of Ψ), the appropriate solution of Eq. (1) is

$$\Psi^{\pm}(r, z, s) = -Ur^2/2s + \int_0^\infty rA_k^{\pm}J_1(kr/b)\exp(\mp kzs/b\sqrt{(s^2+4\Omega^2)}dk \quad (3)$$

where s is the Laplace transform variable and where the upper signs go together and refer to the region above the annulus and where the lower signs go together and refer to the region beneath the annulus.

Invoking the assumption of continuity in u and w at $z = 0$ for $0 < r < a$ and $b < r < \infty$, one has

$$\partial\Psi^+/r\partial r = \partial\Psi^-/r\partial r, \; z = 0, \; 0 < r < a \quad (4)$$

$$\partial\Psi^+/r\partial r = \partial\Psi^-/r\partial r, \; z = 0, \; b < r < \infty \quad (5)$$

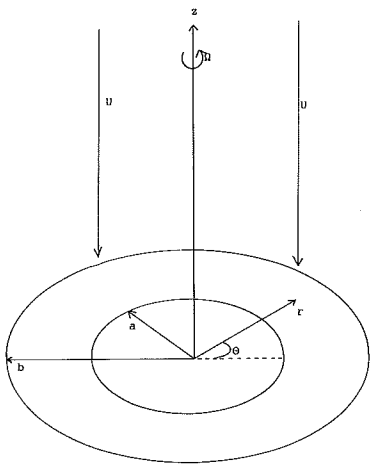


Fig. 1 Geometry of the flow past an annulus in a rotating fluid

Contributed by the Applied Mechanics Division of The American Society of Mechanical Engineers for presentation at the International Mechanical Engineering Congress and Exhibition, the Winter Annual Meeting of The ASME, Chicago, IL, Nov. 6–11, 1994.

Discussion on this paper should be addressed to the Technical Editor, Professor Lewis T. Wheeler, Department of Mechanical Engineering, University of Houston, Houston, TX 77204-4792, and will be accepted until four months after final publication of the paper itself in the ASME Journal of Applied Mechanics.

Manuscript received by the ASME Applied Mechanics Division, Dec. 11, 1992; final revision, Dec. 6, 1993. Associate Technical Editor: S. Lichter.

Paper No. 94-WA/APM-6.

Copyright © 1994 by ASME
Downloaded 03 May 2010 to 171.66.16.20. Redistribution subject to ASME license or copyright; see http://www.asme.org/terms/Terms_Use.cfm

$$\partial\Psi^+/r\partial z=\partial\Psi^-/r\partial z,\ z=0,\ 0<r<a \tag{6}$$

$$\partial\Psi^+/r\partial z=\partial\Psi^-/r\partial z,\ z=0,\ b<r<\infty. \tag{7}$$

Finally, for $z = 0$, $a < r < b$, $w = 0$. Hence,

$$\vartheta\Psi^+/r\vartheta r=\vartheta\Psi^-/r\vartheta r=0,\ a<r<b,\ z=0. \tag{8}$$

From these boundary conditions, $A_k^+ = A_k^- = A_k$, and expression (3) becomes

$$\Psi^{\pm}=-Ur^2/2s+\int_0^{\infty} rA_kJ_1(kr/b)\exp(\mp kzs/b\sqrt{(s^2+4\Omega^2)}dk \tag{9}$$

where the A_k are to be found from the triple integral equations for $z = 0$

$$\int_0^{\infty} kA_kJ_1(kr/b)dk=0,\ 0<r<a \tag{10}$$

$$\int_0^{\infty} kA_kJ_1(kr/b)dk=0,\ b<r<\infty, \tag{11}$$

$$\int_0^{\infty} A_kJ_1(kr/b)dk=Ur/2s,\ a<r<b. \tag{12}$$

This set of triple integral equations (Eqs. (10), (11), (12)), which appear nowhere else in the fluid dynamics literature in so far as the author can determine, will be solved for the A_k by following rather closely Cooke's (1972) solution for the electric field due to a charged disk with a hole in it, a problem that defied an analytic solution until 1972. It should not be surprising, then, that since Eq. (12) is more complex than Cooke's corresponding expression (in which the right-hand side is a constant), the analysis here is considerably more complex. We thus find it convenient to set $kA_k = C_k$ and to consider instead the set

$$\int_0^{\infty} C_kJ_1(kr/b)dk=0,\ 0<r<a \tag{13}$$

$$\int_0^{\infty} C_kJ_1(kr/b)dk/k=Ur/2s,\ a<r<b \tag{14}$$

$$\int_0^{\infty} C_kJ_1(kr/b)dk=0,\ b<r<\infty. \tag{15}$$

We now follow Cooke and attempt to convert this set of triple integral equations into a single Abel-type integral equation, the well-known solution of which will be used to arrive at a single, nonhomogeneous linear integral equation of the second kind, the solution of which will yield C_k.

Consider, then, the integrals in Eqs. (13) and (15). If these integrals were also zero in $a < r < b$, then, obviously, C_k would be zero. Hence, assuming $C_k \neq 0$, there follows

$$\int_0^{\infty} C_kJ_1(kr/b)dk=f(r)=\int_0^{\infty} k(C_k/k)J_1(kr/b)dk,\ a<r<b. \tag{16}$$

Taking, now, the Hankel transform of the expression on the right, one gets

$$C_k/k=\int_0^{\infty} (r/b)f(r)J_1(kr/b)dr/b = \int_a^b (r/b)f(r)J_1(kr/b)dr/b \tag{17}$$

since $f(r) = 0$ in $0 < r < a$ and $b < r < \infty$. So, if one can find $f(r)$, one has C_k and, hence, A_k. To that end, we now derive an equation for $f(r)$ independent of the expressions in Eq. (16) by substituting the expression in Eq. (17) into Eq. (14). Hence

$$\int_a^b \xi f(\xi)d\xi\int_0^{\infty} J_1(k\xi/b)J_1(kr/b)dk=Urb^2/2s,\ a<r<b. \tag{18}$$

We now manipulate this equation into the form of an Abel's integral equation for which the solution is well known. That is, if

$$G(r)=\int_a^r f(x)dx/\sqrt{(r^2-x^2)}, \tag{19}$$

then

$$f(x)=(2/\pi)(d/dx)\int_a^x rG(r)dr/\sqrt{(x^2-r^2)}. \tag{20}$$

Since there are no infinite integrals in these expressions, one rewrites Eq. (18) as

$$\int_a^r f(\xi)d\xi\int_0^{\infty} J_1(k\xi/b)J_1(kr/b)dk + \int_r^b f(\xi)d\xi\int_0^{\infty} Jo1(k\xi/b)J_1(kr/b)dk=Urb^2/2s \tag{21}$$

where, in the first term, $\xi < r$, and, in the second term, $\xi > r$. One now uses these conditions and Watson (1952, Eq. (8) p. 401) to replace the infinite integrals by finite ones. Hence, Eq. (21) can be written

$$\int_a^r f(\xi)d\xi\int_0^{\xi} x^2dx/(\sqrt{(\xi^2-x^2)}(r^2-x^2)+\int_r^b f(\xi)d\xi\int_0^r x^2dx/\sqrt{(\xi^2-x^2)}(r^2-x^2)=\Pi Ubr^2/4s. \tag{22}$$

In order to get this in the form of an Abel integral equation for $G(r)$ (see Eq. (19)) from which one can get $f(r)$ (see Eq. (20)), one inverts the order of integration along with the requisite changes in the limits (see Dirichlet's theorem). Hence, one can rewrite Eq. (22) as

$$\int_a^r x^2dx/\sqrt{(r^2-x^2)}\int_x^b f(\xi)d\xi/\sqrt{(\xi^2-x^2)} + \int_0^a x^2dx/\sqrt{(r^2-x^2)}\int_a^b f(\xi)d\xi/\sqrt{(\xi^2-x^2)} = U\Pi r^2b/4s,\ a<r<b \tag{23}$$

which can be written

$$\int_a^r x^2G(x)dx/\sqrt{(r^2-x^2)}=U\Pi r^2b/4s - \int_o^a y^2dy/\sqrt{(r^2-y^2)}\int_a^b f(\xi)d\xi/\sqrt{(\xi^2-y^2)} \tag{24}$$

where $G(x) = \int_x f(\xi)d\xi/\sqrt{(\xi^2 - x^2)}$.
Hence

$$f(\xi)=-(2/\Pi)(d/d\xi)\int_{\xi}^b xG(x)dx/\sqrt{(x^2-\xi^2)}. \tag{25}$$

There then follows, from Eqs. (19) and (20),

Downloaded 03 May 2010 to 171.66.16.20. Redistribution subject to ASME license or copyright; see http://www.asme.org/terms/Terms_Use.cfm

$$x^2G(x) = (2d/\Pi dx)\int_a^x [U\Pi r^2 b/4s$$

$$-\int_0^a y^2 dy/\sqrt{(r^2-y^2)}g(y)]rdr/\sqrt{(x^2-r^2)} \quad (26)$$

where $g(y) = \int_a^b f(\xi)d\xi/\sqrt{(\xi^2 - y^2)}$.
Hence, for $a/b \ll 1$,

$$G(x) \approx Ub(1-2a^2b/\Pi^2x^3)/s; \quad (27)$$

and, from Eq. (25),

$$f(\xi) \doteq 2Ub[\xi + 2a^2/\xi]/\Pi s\sqrt{(b^2-\xi^2)}. \quad (28)$$

Finally, from Eq. (17).

$$C_k/k = [U\sqrt{(2/k)}/\pi s]\{b\Gamma(1/2)[J_{3/2}(k) - J_{3/2}(ka/b)]$$

$$+ (2a^2\sqrt{\pi}/b)[H_{1/2}(k) - H_{1/2}(ka/b)]\}, \quad (29)$$

where the H's are Struve functions. It follows, then, from the inverse Laplace transform of expression (9),

$$\Psi^{\pm} = -Ur^2/2 + \int_0^{\infty} (2\pi i)^{-1}\int_{\Upsilon - i\infty}^{\Upsilon + i\infty} (C_k/k)\exp[st \mp kzs/b\sqrt{(s^2}$$

$$+ 4\Omega^2)]rJ_1(kr/b)dkds, \quad (30)$$

and this is the stream function for the flow past the annulus. It will now be analyzed to see if it corresponds to a Taylor column stream function.

In expression (30), note that there are branch points at $s = \pm 2\Omega i$. Hence, one evaluates this integral via the Cauchy integral theorem and the contour shown in Fig. 2. If done carefully, there results, for large times,

$$\Psi^{\pm} = -Ur^2/2 \pm \int_0^{2\Omega bt/z} [2Ub\Gamma(1/2)/\pi\sqrt{(2k)}]\{J_{3/2}(k)$$

$$- J_{3/2}(ka/b)\}rJ_1(kr/b)dk \pm \{4Ua^2/kb\sqrt{(2\pi)}\}\int_0^{2\Omega bt/z}\{[1$$

$$- \cos k - (1-\cos(ka/b))]/\sqrt{(a/b)}\}rJ_1(kr/b)dk. \quad (31)$$

Note that, for $t \to \infty$, this stream function becomes steady and independent of z, i.e., the stream function becomes two dimensional, which, of course, is the Proudman theorem.

It is a straightforward exercise (Greenspan, 1968) to show that this stream function is indeed that for flow past an annular taylor column, with all the properties such a flow should possess, i.e., no axial or radial flow in $a < r < b$, opposing directions of the swirl velocity v above, beneath the annulus, and Stewartson layers at $r = a, b$. As a further check on this stream function, the use of it to calculate the Taylor column drag D (Stewartson, 1958) on the annulus yields

$$D = 16\rho\Omega Ub^3[1 - 3a^2/(2b^2) + a^4/(2b^4)]/3 \quad (32)$$

which, for $a = 0$, yields the well-known Stewartson result for a rising sphere or disk of radius b.

If the above results hold for a/b not small (and the determination of $G(x)$ for such a case is a tedious process that will require the analytical evaluation of finite integrals involving products of Bessel functions, elliptic functions, Struve functions, and hypergeometric functions, none of which is tabulated or appears in integral tables or software packages), then the engineering application (possibly the first) of the Taylor column phenomenon proposed in the following paragraph is tenable.

An Engineering Application of the Taylor Column Phenomenon

If launching of the spin-stabilized liquid-filled artillery projectile in Fig. 3 results in its being dynamically unstable due to the presence of inertial waves (Scott, D'Amico, 1973, and the references cited therein), then it is proposed to allow an annulus to move along a centrally located wire in the liquid-filled cavity (Fig. 4). The purpose of the annulus is to destroy the inertial waves that cause the instability, an instability that is due to the numerical equality of the frequency of the circumferentially travelling inertial waves, and the nutational frequency of the artillery projectile. The destruction of the inertial waves is caused by the developing Taylor column, the associated two dimensionality of which produces an environment that precludes inertial waves (see Greenspan, 1968, and his proof that inertial waves can exist only if the fluid motion is three-dimensional).

Based on the analysis herein, it would seem that there are four serious objections to this proposal. They are as follows:

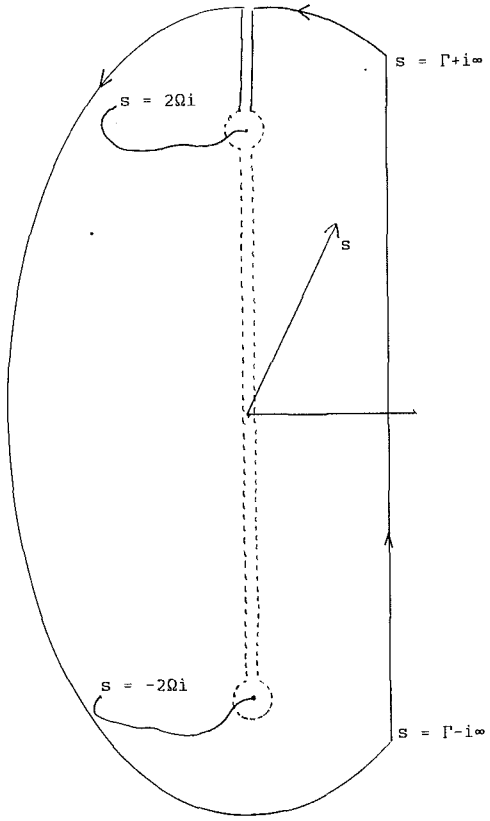


Fig. 2 Geometry for the contour integration of Eq. (30)

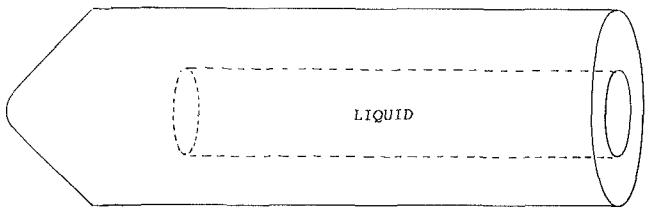


Fig. 3 A liquid-filled artillery projectile

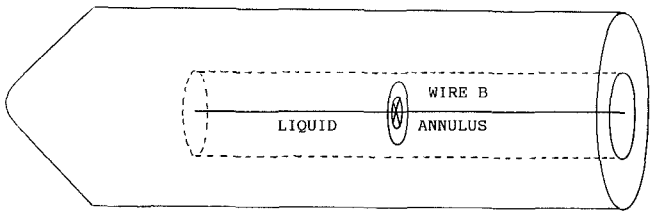


Fig. 4 The mechanism for stabilizing a dynamically unstable projectile when the instability is due to inertial waves

Downloaded 03 May 2010 to 171.66.16.20. Redistribution subject to ASME license or copyright; see http://www.asme.org/terms/Terms_Use.cfm

(1) The analysis herein is for an unbounded fluid, whereas the fluid in the artillery shell is cylindrically bounded.

(2) The analysis herein ignores the spin-up regime.

(3) The analysis herein assumes $t = \infty$ in Eq. (31).

(4) The analysis herein neglects viscosity and all its ramifications for time-dependent rotating flows.

In the absence of an analysis which addresses these issues in comprehensive manner, it is noted that Hocking, Moore, and Walton (1979) and Scott (1985) show, respectively, that the ends and walls of the container do not preclude Taylor column development. In addition, Greenspan (1968) shows that both the spin-up process and the Taylor column development are well along toward completion after only several revolutions of the container. Finally, Hocking, Moore, and Walton (1979) show that viscosity does not impede Taylor column development; and, as well, Scott and D'Amico (1973) show that viscosity does not destroy inertial waves—it merely shifts their frequency slightly.

References

Bretherton, F. P., 1967, "Time Dependent Motion of a Cylinder Moving in an Unbounded Rotating or Stratified Fluid," *Jour. Fl. Mech.*, Vol. 28, p. 545.

Dennis, S., Ingham, D., and Singh, S., 1982, "Slow Translation of a Sphere in a Rotating, Viscous Fluid," *Jour. Fl. Mech.*, Vol. 117, p. 251.

Cooke, J., 1972, "Triple Integral Equations," *Quar. J. Mech. & Appl. Math.*, Vol. 16, p. 193.

Grace, S., 1923, "Free Motion of a Sphere in a Rotating Liquid Parallel to the Axis of Rotation," *Proc. Roy. Soc. London*, Vol. A102, p. 89.

Grace, S., 1926, "On the Motion of Sphere in a Rotating Liquid," *Proc. Roy. Soc. London*, Vol. A113, p. 46.

Grace, S., "A Spherical Source in a Rotating Liquid," *Proc. Roy. Soc. London*, Vol. A105, p. 532.

Greenspan, H., 1968, *The Theory of Rotating Fluids*, Cambridge University Press, New York.

Heikes, K., and Maxworthy, T., 1982, "Observations of Inertial Waves in a Homogeneous Rotating Fluid," *Jour. Fl. Mech.*, Vol. 123, p. 319.

Hide, R., and Ibbetson, A., 1966, "A Flow Past a Sphere in a Rotating Fluid," *Icarus*, Vol. 5, p. 279.

Hide, R., and Ibbetson, A., 1968, "On the Slow Transverse Flow Past Obstacles in a Rapidly Rotating Fluid," *Jour. Fl. Mech.*, Vol. 32, p. 251.

Hocking, L., Moore, D., and Walton, I., 1979, "The Drag on a Sphere Moving Axually in a Long Rotating Container," *Jour. Fl. Mech.*, Vol. 90, p. 781.

Jacobs, S., 1964, "The Taylor Column Problem," *Jour. Fl. Mech.*, Vol. 20, p. 581.

Long, R., 1952, "The Flow of a Liquid Past a Barrier in a Rotating Spherical Shell," *J. Meteorology*, Vol. 9, p. 187.

Long, R., 1953, "Steady Motion Around a Symmetrical Obstacle Moving Along the Axis of a Rotating Liquid," *J. Meteorology*, Vol. 10, p. 197.

Maxworthy, T., 1970, "The Flow Created by a Sphere Moving Along the Axis of a Rotating, Slightly Viscous Liquid," *Jour. Fl. Mech.*, Vol. 40, p. 453.

Proudman, J., 1916, "On the Motion of Solids in a Liquid Possessing Vorticity," *Proc. Roy. Soc. London*, Vol. A92, p. 408.

Sarma, L., 1958, "Slow Motion of a Paraboloid of Revolution in a Rotating Fluid," *Jour. Fl. Mech.*, Vol. 3, p. 408.

Scott, W., and D'Amico, W., 1973, "Amplitude Dependent Behavior of a Liquid Filled Gyroscope," *Jour. Fl. Mech.*, Vol. 60, p. 751.

Scott, W., 1985, "Taylor Column Genesis, and Sidewall Drag, in a Rapidly Rotating Liquid," *Physics of Fluids*, Vol. 28, p. 416.

Stewartson, K., 1952, "On the Slow Motion of a Sphere Along the Axis of a Rotating Fluid," *Proc. Camb. Phil. Soc.*, Vol. 48, p. 169.

Stewartson, K., 1953, "On the Slow Motion of an Ellipsoid in a Rotating Fluid," *Quart. Jour. Math & Appl. Mech.*, Vol. 6, p. 141.

Stewartson, K., "On the Free Motion of an Ellipsoid in a Rotating Fluid," *Quart. Jour. Math & Appl. Mech.*, Vol. 11, p. 231.

Stewartson, K., 1958, "On the Motion of a Sphere Along the Axis of a Rotating Fluid," *Quart. Jour. Math. & Appl. Mech.*, Vol. 11, p. 39.

Taylor, G. I., 1923, "Experiments on the Motion of Solid Bodies in Rotating Fluids," *Proc. Roy. Soc. London*, Vol. A102, p. 39.

Downloaded 03 May 2010 to 171.66.16.20. Redistribution subject to ASME license or copyright; see http://www.asme.org/terms/Terms_Use.cfm

ERRATUM

Erratum on "The Buckling of an Elastic Layer Bonded to an Elastic Substrate in Plane Strain," by T. W. Shield, K. S. Kim, and R. T. Shield, published in the June 1994 issue of ASME JOURNAL OF APPLIED MECHANICS, Vol. 61, pp. 231–235.

On page 234, the term outside the brackets on the right hand side of Eq. (17) should be $\Omega_c^2/12$ so that Eq. (17) should read:

$$\epsilon_c = \frac{\Omega_c^2}{12}\left\{3+\frac{(1-2\nu)}{(1-\nu)}\,\Omega_c+\frac{2}{3}\,\Omega_c^2+\frac{(3-4\nu)}{12(1-\nu)^2}\,\Omega_c^2\right\}\left\{1+\frac{\Omega_c^2}{6}\right\}^{-1}.$$

Copyright © 1994 by ASME
Downloaded 03 May 2010 to 171.66.16.20. Redistribution subject to ASME license or copyright; see http://www.asme.org/terms/Terms_Use.cfm

The Interface Anticrack and Green's Functions for Interacting Anticracks and Cracks/Anticracks

X. Markenscoff
Fellow ASME

Luqun Ni
Department of Applied Mechanics and Engineering Sciences, University of California, La Jolla, CA 92093

J. Dundurs
Northwestern University, Evanston, IL 60208
Fellow ASME

Solution is obtained for an anticrack—a bonded rigid lamella inclusion—at the interface between two isotropic elastic solids. The problem is formulated in terms of distributed line-loads at the anticrack which constitute the Green's functions and the system of the governing coupled integral equations is solved analytically in closed form for the cases of uniform biaxial tension and of anticracks loaded by concentrated forces or moment. Solutions are also obtained by the interaction of an interface anticrack with a first-order singularity (concentrated force and dislocation) and second-order singularity (doublet of forces) at the interface. In the latter case the limit as the second-order singularity approaches the tip of the anticrack does not exist, but neither can a finite limit be obtained by rescaling as in the homogeneous material. The solution of the interface anticrack exhibits the oscillatory singularities that appear at interface cracks which indicates that the overlapping of the displacement on the crack faces is not the reason for this anomalous behavior. Moreover, it should be pointed out that the material condition that the stress does not exhibit oscillatory behavior is not the same as for interface cracks: for anticracks it is $\kappa_1 (1-\beta) = \kappa_2 (1+\beta)$ *while for cracks it is* $\beta = 0$.

Introduction

The properties of interfaces have received increased attention in recent years with the main focus on interface cracks. Interface rigid line inclusions (anticracks) are also stress concentrators and they can be analyzed by an analogous methodology as the interface cracks. Interface anticracks exhibit the same oscillatory singularities as interface cracks (Williams, 1959). While it was possible to remove the oscillatory singularity in interface cracks by removing the displacement overlapping at the crack faces, it is obviously not possible to mend the oscillatory behavior here, since no overlapping is taking place, and the displacement is continuous everywhere. It should also be pointed out that the condition that the material constants need to satisfy for nonoscillatory behavior is $\kappa_1 (1-\beta) = \kappa_2 (1+\beta)$ while for cracks it is $\beta = 0$. Thus, the materials with $\beta = 0$ cannot be called nonpathological, since they will exhibit pathological behavior if they contain anticracks. Solutions for anticracks have been obtained by considering the anticracks as limits of rigid ellipsoidal inclusions (Wang, Zhang, and Chou, 1985) and for interface anticracks by complex variable formulation (Ballarini, 1991) in the case of an interface anticrack in uniform biaxial tension. Anisotropic line inclusions at interfaces have been treated by Wu (1990).

Here the solution for interface anticracks is obtained on the basis of Green's functions, which are distributed line loads p_x and p_y on the anticracks, as in Dundurs and Markenscoff (1989b) for homogeneous media. The method for treating anticracks as distributed line loads has indeed a physical meaning. This is also manifested by looking at the two situations when the anticrack (an $r^{-1/2}$ singularity) interacts with an approaching concentrated force or a dislocation, both r^{-1} singularities.The two limits are different: the anticrack absorbs the approaching force and the limit is $\sim r^{-1/2}$, while it does not absorb the approaching dislocation and the limit is $\sim r^{-1}$. The "dual" is true for cracks: the crack absorbs the dislocation but does not absorb the concentrated force. Thus considering cracks as distributed dislocations and anticracks as distributed forces is not only a mathematical method of treating the problem, but also represents the physics of it.

The governing integral equations for the line loads p_x, p_y are formulated so that the extensional strain and the change of curvature due to the externally applied loading be cancelled on the anticrack. Obviously this formulation extends to curved anticracks as well. The system of the ensuing two coupled integral equations is first solved analytically for the case of uniform biaxial loading and of anticracks loaded by concentrated forces F_x, F_y and a concentrated couple applied on them. These solutions naturally involve translation and rotation of the anticrack. The solutions for the interaction of an interface anticrack with a first-order singularity at the interface (con-

Contributed by the Applied Mechanics Division of THE AMERICAN SOCIETY OF MECHANICAL ENGINEERS for publication in the ASME JOURNAL OF APPLIED MECHANICS.

Discussion on this paper should be addressed to the Technical Editor, Professor Lewis T. Wheeler, Department of Mechanical Engineering, University of Houston, Houston, TX 77204-4792, and will be accepted until four months after final publication of the paper itself in the ASME JOURNAL OF APPLIED MECHANICS.

Manuscript received by the ASME Applied Mechanics Division, Dec. 26, 1991; final revision, July 13, 1993. Associate Technical Editor: L. M. Keer.

Copyright © 1994 by ASME
Downloaded 03 May 2010 to 171.66.16.20. Redistribution subject to ASME license or copyright; see http://www.asme.org/terms/Terms_Use.cfm

centrated force F_x, F_y, and dislocation b_x, b_y) and a second-order singularity (force doublet) are also obtained. When a second-order singularity such as force doublet, dipole of dislocations, center of dilatation or shear approaches the tip of the interface anticrack the limit diverges, which is a very unintuitive behavior since it makes the interaction of the anticrack with an expanding inclusion inordinately strong. In contrast to the homogeneous material (Dundurs and Markenscoff, 1989a, b), the pathology cannot be removed by the rescaling of the doublet, due to the logarithmic terms in the solution. Since the fields of the interactions of an interface anticracks with a force and a dislocation are obtained, these provide the Green's function for the interactions of two (or more) anticracks or anticracks and cracks.

Formulation of the Governing Equations

The fields due to concentrated forces P_x, P_y, normal and in the direction of the interface, respectively, have been obtained by Dundurs and Markenscoff (1991). In particular, the quantities needed for the formulation of the anticrack equations are the strains $\partial u_y/\partial y$ $(0, y)$ and $\partial u_x/\partial y$ $(0, y)$, since the total extensional strain and the change of curvature on the anticrack must vanish. For a load P_y applied at the origin along the interface, they are

$$\frac{\partial u_x}{\partial y}(0, y)=\frac{P_y}{4m}[-\kappa_2(1+\beta)+\kappa_1(1-\beta)]\delta(y) \tag{1a}$$

$$\frac{\partial u_y}{\partial y}(0, y)=\frac{P_y}{4\pi m}[-\kappa_2(1+\beta)-\kappa_1(1-\beta)]\frac{1}{y} \tag{1b}$$

where $$m=\frac{\mu_1(\kappa_2+1)(1-\beta^2)}{1-\alpha}=\frac{\mu_2(\kappa_1+1)(1-\beta^2)}{1+\alpha}.$$

For a concentrated force P_x normal to the interface

$$\frac{\partial u_x}{\partial y}(0, y)=\frac{-P_x}{4\pi m}[\kappa_1(1-\beta)+\kappa_2(1+\beta)]\frac{1}{y} \tag{2a}$$

$$\frac{\partial u_y(0, y)}{\partial y}=\frac{P_x}{4\pi m}[\kappa_2(1+\beta)-\kappa_1(1-\beta)]\,\delta(y). \tag{2b}$$

For distributed line loads p_x, p_y these strains are

$$4m\frac{\partial u_x}{\partial y}(0, y)=[\kappa_2(1+\beta)+\kappa_1(1-\beta)]\frac{1}{\pi}\int_{-a}^{a}\frac{p_x(\zeta)d\zeta}{\zeta-y}-[\kappa_2(1+\beta)-\kappa_1(1-\beta)]p_y(y) \tag{3a}$$

$$4m\frac{\partial u_y(0, y)}{\partial y}=[\kappa_2(1+\beta)-\kappa_1(1-\beta)]p_x(y)+[\kappa_2(1+\beta)+\kappa_1(1-\beta)]\frac{1}{\pi}\int_{-a}^{a}\frac{p_y(\zeta)d\zeta}{\zeta-y}. \tag{3b}$$

In the above relations κ_1, κ_2 are the Kolosoff constants for the two elastic solids, α and β are the Dundurs parameters (Dundurs, 1969), $\Gamma=\mu_2/\mu_1$ the ratio of the two shear moduli. The values of the left-hand sides of the above equations are determined from the applied loading and the resulting equations constitute the governing equations for the anticrack. We solve the system analytically for the following cases of applied loading.

(a) Uniform Biaxial Tension T_x, $T_y^{(1)}$, $T_y^{(2)}$ (Fig. 1). The applied tractions must satisfy the jump conditions along the interface (Dundurs, 1990). Since the stresses are homogeneous only the equality of the longitudinal stretch along the interface remains to be satisfied, i.e.,

$$(1-\alpha)T_y^{(2)}=(1+\alpha)\,T_y^{(1)}-2(\alpha-2\beta)T_x \tag{4}$$

which guarantees equality of the interfacial strains $E_{yy}^{(1)}$ and $E_{yy}^{(2)}$ where

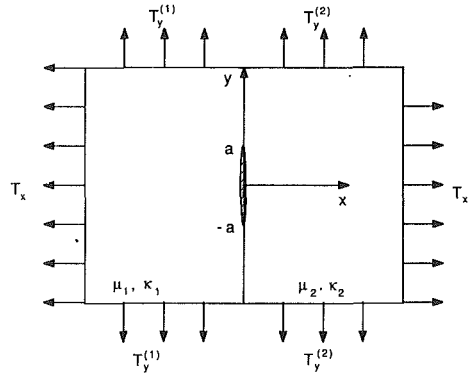


Fig. 1 Uniform biaxial tension T_x, $T_y^{(1)}$, $T_y^{(2)}$

$$E_{yy}^{(1)}=E_{yy}^{(2)}\equiv E_{yy}^{i}(0, y)=\frac{1}{8\mu_i}[(\kappa_i+1)T_y^{(i)}-(3-\kappa_i)T_x]\equiv E_{yy}\ (i=1, 2). \tag{5}$$

Since the total strain $\partial u_x/\partial y$ along the anticrack must equal the constant angle of rotation ω of the anticrack, while the total extension strain $\partial u_y/\partial y$ must vanish at the anticrack faces, the governing equations are:

$$\frac{1}{\pi}\int_{-a}^{a}\frac{p_x(\zeta)}{\zeta-y}d\zeta-Bp_y(y)=\frac{4m\omega}{\kappa_2(1+\beta)+\kappa_1(1-\beta)} \tag{6a}$$

$$\frac{1}{\pi}\int_{-a}^{a}\frac{p_y(\zeta)}{\zeta-y}d\zeta+Bp_x(y)=-\frac{4mE_{yy}}{\kappa_2(1+\beta)+\kappa_1(1-\beta)} \tag{6b}$$

with

$$B=\frac{\kappa_2(1+\beta)-\kappa_1(1-\beta)}{\kappa_2(1+\beta)+\kappa_1(1-\beta)}=\frac{\Gamma\kappa_1(\kappa_2-1)-\kappa_2(\kappa_1-1)}{\Gamma\kappa_1(\kappa_2+1)+\kappa_2(\kappa_1+1)}.$$

The system of Eqs. (6*a*), (6*b*) involves three undetermined constants (two from the integral equations and ω), which are determined from the equilibrium conditions on the anticrack.

$$\int_{-a}^{a}p_x(\zeta)d\zeta=\int_{-a}^{a}p_y(\zeta)d\zeta=0,\ \int_{-a}^{a}\zeta p_x(\zeta)d\zeta=0 \tag{7}$$

The system of the coupled Eqs. (6*a*), (6*b*) is written equivalently

$$\frac{1}{\pi}\int_{-1}^{1}\frac{\mathbf{p}(\eta)d\eta}{\eta-s}-B\begin{pmatrix}0&-1\\1&0\end{pmatrix}\mathbf{p}(s)=A\begin{pmatrix}\omega\\-E_{yy}\end{pmatrix} \tag{8}$$

with

$$A=\frac{4m}{\kappa_2(1+\beta)+\kappa_1(1-\beta)}$$

and can be decoupled as in (Ni and Nemat-Nasser, 1991) by diagonalizing the matrix B in (8) to give

$$\frac{1}{\pi}\int_{-1}^{1}\frac{\mathbf{k}(\eta)}{\eta-s}d\eta+B\begin{pmatrix}-i&0\\0&i\end{pmatrix}\mathbf{k}(s)=\frac{A}{2}\begin{pmatrix}\omega-iE_{yy}\\-E_{yy}-i\omega\end{pmatrix} \tag{9}$$

$$\mathbf{k}(s)\equiv U^{-1}\mathbf{p}(s)\ \text{and}\ U=\begin{pmatrix}1&-i\\i&1\end{pmatrix} \tag{10}$$

with solutions

$$k_1(s)=\frac{iA(E_{yy}-i\omega)}{2\sqrt{1-B^2}}\left(\frac{1+s}{1-s}\right)^{M}\left[1-\frac{2M}{(1+s)}\right] \tag{11a}$$

$$k_2(s)=\frac{iA(-\omega+iE_{yy})}{2\sqrt{1-B^2}}\left(\frac{1+s}{1-s}\right)^{M}\left[1-\frac{2\overline{M}}{(1+s)}\right] \tag{11b}$$

$$M=\frac{1}{2}+\frac{i}{2\pi}\ln\left(\frac{1+B}{1-B}\right),$$

Downloaded 03 May 2010 to 171.66.16.20. Redistribution subject to ASME license or copyright; see http://www.asme.org/terms/Terms_Use.cfm

or in terms of the line loads

$$p_x(y)=\frac{A}{\sqrt{1-B^2}\sqrt{a^2-y^2}}[(\omega y+2\gamma_o E_{yy}a)\cos t - (E_{yy}y-2\gamma_o\omega a)\sin t] \quad (12a)$$

$$p_y(y)=\frac{A}{\sqrt{1-B^2}\sqrt{a^2-y^2}}[(-E_{yy}y+2\omega\gamma_o)\cos t - (\omega y+2\gamma_o E_{yy}a)\sin t] \quad (12b)$$

$$\gamma_o=\frac{1}{2\pi}\ln\left|\frac{\kappa_1(1-\beta)}{\kappa_2(1+\beta)}\right|$$

$$t=\gamma_o\ln\left|\frac{a+y}{a-y}\right|.$$

With the additional use of (7c) it is found that $\omega=0$. It is obvious from (12) that if material coefficients of the two phases satisfy $\kappa_1(1-\beta)/\kappa_2(1+\beta)=1$, then the anticrack exhibits only square root singularity and not an oscillatory one in agreement with Ballarini (1991). In order to calculate the stress field due to the line loads p_x and p_y we need to compute the integrals

$$\int_{-a}^{a}\frac{p_y(\zeta)d\zeta}{\zeta-y} \text{ and } \int_{-a}^{a}\frac{p_x(\zeta)d\zeta}{\zeta-y}$$

which involve integrals of the type

$$\int_{-a}^{a}\frac{\zeta^j\cos t(\zeta)}{\sqrt{a^2-\zeta^2}(\zeta-y)}d\zeta \text{ and } \int_{-a}^{a}\frac{\zeta^j\sin t(\zeta)d\zeta}{\sqrt{a^2-\zeta^2}(\zeta-y)}$$

$$j=0,\ 1 \text{ and } t(\zeta)=\gamma_o\ln\left|\frac{a+\zeta}{a-\zeta}\right|.$$

We have

$$\int_{-a}^{a}\frac{\cos t(\zeta)d\zeta}{\sqrt{a^2-\zeta^2}(\zeta-y)}=-\frac{\pi B}{\sqrt{a^2-\zeta^2}}\sin t$$

$$\int_{-a}^{a}\frac{\sin t(\zeta)d\zeta}{\sqrt{a^2-\zeta^2}(\zeta-y)}=\frac{\pi B}{\sqrt{a^2-y^2}}\cos t$$

$$\int_{-a}^{a}\frac{\zeta\cos t(\zeta)d\zeta}{\sqrt{a^2-\zeta^2}(\zeta-y)}=2\pi\sqrt{1-B^2}-\frac{\pi B}{\sqrt{a^2-y^2}}\sin t$$

$$\int_{-a}^{a}\frac{\zeta\sin t(\zeta)d\zeta}{\sqrt{a^2-\zeta^2}(\zeta-y)}=\frac{\pi By}{\sqrt{a^2-y^2}}\cos t. \quad (13)$$

Apparently, the solution for the stress field of interface anticracks contains oscillatory singularities of the type that appear in interface cracks (Williams, 1959). This oscillatory behavior cannot be removed as in the case of the interface crack (Comninou, 1978) since there is no overlapping of the displacement that is taking place. The oscillatory singularity seems to be a property of the inability of the interface of the two solids to accommodate the square root singularity of the crack (anticrack) in a more smooth way.

(b) An Anticrack Loaded by Concentrated Forces and Moment Applied on the Anticrack (Fig. 2). In this case the governing equations are

$$\frac{1}{\pi}\int_{-a}^{a}\frac{\hat{p}_x(\zeta)d\zeta}{\zeta-y}-B\hat{p}_y(y)=\tilde{\omega} \quad (14a)$$

$$\frac{1}{\pi}\int_{-a}^{a}\frac{\hat{p}_y(\zeta)d\zeta}{\zeta-y}+B\hat{p}_x(y)=0 \quad (14b)$$

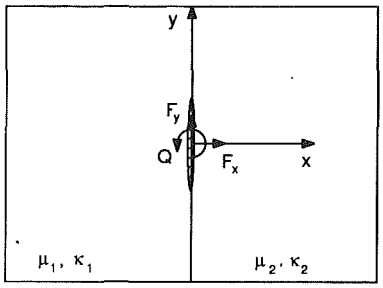


Fig. 2 An anticrack loaded by concentrated forces and moment

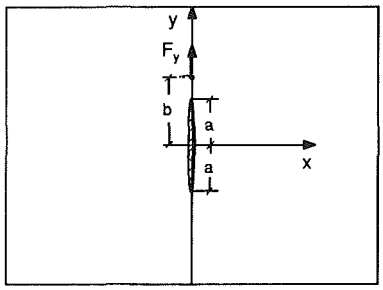


Fig. 3 An anticrack interacting with a force and dislocation at the interface

where $\hat{p}_x(y)=p_x(y)+F_x\delta(y)$, $\hat{p}_y(y)=p_y(y)+F_y\delta(y)$, $\tilde{\omega}=4m\omega/[\kappa_2(1+\beta)+\kappa_1(1-\beta)]$ and with the side conditions

$$\int_{-a}^{a}p_x(\zeta)d\zeta=F_x,\ \int_{-a}^{a}p_y(\zeta)d\zeta=F_y$$

and (15)

$$\int_{-a}^{a}\zeta p_x(\zeta)d\zeta=Q.$$

The three side conditions (15) are used to determine ω and the two constants that arise from the integration of the integral equations. The solution to (14), obtained similarly as before, is

$$\hat{p}_x(y)=\frac{1}{\sqrt{1-B^2}\sqrt{a^2-y^2}}\times\left\{\left[\tilde{\omega}y+\frac{F_x}{\pi}\right]\cos t+\left[2a\gamma_o\tilde{\omega}+\frac{F_y}{\pi}\right]\sin t\right\} \quad (16a)$$

$$\hat{p}_y(y)=\frac{1}{\sqrt{1-B^2}\sqrt{a^2-y^2}}\times\left\{\left[2a\gamma_o\tilde{\omega}+\frac{F_y}{\pi}\right]\cos t-\left[\tilde{\omega}y+\frac{F_x}{\pi}\right]\sin t\right\} \quad (16b)$$

with

$$\tilde{\omega}=\frac{2(Q-2a\gamma_o F_y)}{a^2\pi(1+4\gamma_o^2)} \quad (16c)$$

(c) An Anticrack Interacting With a Force F_y at the Interface. If the force F_y is applied at their interface at a point with $y=b$, $|b|<a$, the problem is reduced to the previously discussed case of a loaded anticrack; so we discuss the case $|b|>a$. (Fig. 3).

The integral equations are

$$\frac{1}{\pi}\int_{-a}^{a}\frac{p_x(\zeta)d\zeta}{\zeta-y}-Bp_y(y)=\tilde{\omega} \quad (17a)$$

Downloaded 03 May 2010 to 171.66.16.20. Redistribution subject to ASME license or copyright; see http://www.asme.org/terms/Terms_Use.cfm

$$\frac{1}{\pi}\int_{-a}^{a}\frac{p_y(\zeta)d\zeta}{\zeta-y}+Bp_x(y)=\frac{-F_y}{\pi}\frac{1}{b-y}. \tag{17b}$$

The solution of the above system is

$$p_x(y)=\frac{\tilde{\omega}}{\sqrt{1-B^2}}\left(\frac{a+y}{a-y}\right)^{1/2}\cos t+\frac{c_1}{a+y}\left(\frac{a+y}{a-y}\right)^{M}+\frac{ic_2}{a+y}\left(\frac{a+y}{a-y}\right)^{M}-\frac{D}{\pi\sqrt{1-B^2}(b-y)}\operatorname{Im}\left[\left(\frac{a+y}{a-y}\right)^{M}\times\left|\frac{a+b}{b-a}\right|^{(-M)}\right] \tag{18a}$$

$$p_x(y)=\frac{-\tilde{\omega}}{\sqrt{1-B^2}}\left(\frac{a+y}{a-y}\right)^{1/2}\sin t+\frac{ic_1}{a+y}\left(\frac{a+y}{a-y}\right)^{M}+\frac{c_2}{a+y}\left(\frac{a+y}{a-y}\right)^{M}-\frac{D}{\pi\sqrt{1-B^2}(b-y)}\operatorname{Re}\left[\left(\frac{a+y}{a-y}\right)^{M}\times\left|\frac{a+b}{b-a}\right|^{(-M)}\right] \tag{18b}$$

$$M=\frac{1}{2}+i\gamma_o$$

with the constants $\tilde{\omega}$, c_1, c_2 determined from the side conditions (7). Introducing (7) into (18) yields

$$p_x(y)=\frac{\tilde{\omega}y}{\sqrt{1-B^2}\sqrt{a^2-y^2}}\cos t+\frac{2a\gamma_o\tilde{\omega}}{\sqrt{1-B^2}\sqrt{a^2-y^2}}\sin t+\frac{F_y}{\pi\sqrt{1-B^2}\sqrt{a^2-y^2}}\left[\sin t-\sqrt{\frac{b-a}{b+a}}\sin(t-t_o)\right]-\frac{F_y}{\pi\sqrt{1-B^2}(b-y)}\sqrt{\left(\frac{a+y}{a-y}\right)\left(\frac{b-a}{b+a}\right)}\sin(t-t_o) \tag{19a}$$

$$p_y(y)=\frac{-\tilde{\omega}y\sin t}{\sqrt{1-B^2}\sqrt{a^2-y^2}}+\frac{2a\gamma_o\tilde{\omega}\cos t}{\sqrt{a^2-y^2}\sqrt{1-B^2}}+\frac{F_y}{\pi\sqrt{1-B^2}\sqrt{a^2-y^2}}\left[\cos t-\sqrt{\frac{b-a}{b+a}}\cos(t-t_o)\right]-\frac{F_y}{\pi\sqrt{1-B^2}(b-y)}\sqrt{\left(\frac{a+y}{a-y}\right)\left(\frac{b-a}{b+a}\right)}\cos(t-t_o) \tag{19b}$$

where

$$t=\gamma_o\ln\left|\frac{a+y}{a-y}\right|$$

$$t_o=\gamma_o\ln\left|\frac{a+b}{a-b}\right|$$

$$\tilde{\omega}=-\frac{4aF_y\gamma_o+2F_y(b-a)\sqrt{b-a/b+a}\sin t_o}{a^2(1+4\gamma_o^2)\pi}. \tag{19c}$$

If the limit of (19) is taken as the force F_y approaches the tip of the anticrack, i.e., as $b\to a$, then it is found that the limit coincides with the solution of the loaded anticrack by a force F_y obtained in (16). Thus the r^{-1} singularity of the force disappears and the $r^{-1/2}$ singularity of the anticrack remains as the force approaches the tip of the anticrack from the outside. We can thus say that "the anticrack absorbs the concentrated force" and the dual that "the crack absorbs the dislocation" (Zener-Stroh crack).

(d) An Anticrack Interacting With a Force F_x at the Interface. If a force F_x is applied at $y=b$ the governing equations are

$$\frac{1}{\pi}\int_{-a}^{a}\frac{p_x(\zeta)}{\zeta-y}d\zeta-Bp_y(y)=\frac{-F_x}{(b-y)\pi}+\tilde{\omega} \tag{20a}$$

$$Bp_x(y)+\frac{1}{\pi}\int_{-a}^{a}\frac{p_y(\zeta)}{(\zeta-y)}d\zeta=0 \tag{20b}$$

with equilibrium conditions

$$\int_{-a}^{a}p_x\,d\zeta=\int_{-a}^{a}p_y\,d\zeta=\int_{-a}^{a}\zeta p_x\,d\zeta=0. \tag{21}$$

The solution is

$$p_x(y)=\frac{\tilde{\omega}[y\cos t+2a\gamma_0\sin t]}{\sqrt{1-B^2}\sqrt{a^2-y^2}}+\frac{F_x}{\pi\sqrt{1-B^2}\sqrt{a^2-y^2}}\left\{\sqrt{\frac{b-a}{b+a}}\cos(t-t_0)-\cos t\right\}-\frac{F_x}{\pi\sqrt{1-B^2}(b-y)}\sqrt{\left|\frac{b+a}{a-y}\right|\left|\frac{b-a}{b+a}\right|}\cos(t-t_0) \tag{22a}$$

$$p_y(y)=\frac{\tilde{\omega}[-y\sin t+2a\gamma_o\cos t]}{\sqrt{1-B^2}\sqrt{a^2-y^2}}+\frac{F_x}{\pi\sqrt{1-B^2}\sqrt{a^2-y^2}}\left\{\sin t-\sqrt{\frac{b-a}{b+a}}\sin(t-t_0)\right\}+\frac{F_x}{\pi\sqrt{1-B^2}(b-y)}\sqrt{\left|\frac{a+y}{a-y}\right|\left|\frac{b-a}{b+a}\right|}\sin(t-t_0) \tag{22b}$$

$$\tilde{\omega}=\frac{-2F_x[b-(b-a)\sqrt{b-a/b+a}\cos t_0+4a\gamma_0\sqrt{b-a/b+a}\sin t_0]}{\pi a^2(1+4\gamma_o^2)}$$

where

$$t=\gamma_0\ln\left|\frac{a+y}{a-y}\right|\quad t_0=\gamma_0\ln\left|\frac{a+b}{a-b}\right|$$

$$\gamma_0=\frac{1}{2\pi}=\frac{1}{2\pi}\ln\left|\frac{\kappa_1(1-\beta)}{\kappa_2(1+\beta)}\right|.$$

(e) An Anticrack Interacting With a Dislocation b_x at the Interface. For a dislocation $b_x\neq 0$, $b_y=0$ at the interface applied at the point $y=b$ the governing equations are

$$\frac{1}{\pi}\int_{-a}^{a}\frac{p_x(\zeta)}{\zeta-y}d\zeta-Bp_y(y)=\frac{-4m}{[\kappa_2(1+\beta)+\kappa_1(1-\beta)]}\frac{\partial u_x}{\partial y}(0,y)+\tilde{\omega} \tag{23a}$$

$$Bp_x(y)+\frac{1}{\pi}\int_{-a}^{a}\frac{p_y(\zeta)}{\zeta-y}d\zeta=\frac{-4m}{[\kappa_2(1+\beta)+\kappa_1(1-\beta)]}\frac{\partial u_y}{\partial y}(0,y) \tag{23b}$$

Downloaded 03 May 2010 to 171.66.16.20. Redistribution subject to ASME license or copyright; see http://www.asme.org/terms/Terms_Use.cfm

with the forcing function

$$\frac{\partial u_y}{\partial y}(0, y) = -\frac{Ab_x}{2\pi}\frac{1}{y-b} \qquad \frac{\partial u_x}{\partial y}(0, y) = 0. \tag{24}$$

The solution is

$$p_x(y) = \frac{\tilde{\omega}\cos t}{\sqrt{1-B^2}\sqrt{a^2-y^2}} + \frac{\sin t[D_1/\pi + 2a\gamma_0\tilde{\omega}_1]}{\sqrt{1-B^2}\sqrt{a^2-y^2}} - \frac{\sin(t-t_0)D_1\sqrt{b^2-a^2}}{\pi\sqrt{1-B^2}\sqrt{a^2-y^2}(b-y)} \tag{25a}$$

$$p_y(y) = \frac{-\tilde{\omega}\, y \sin t}{\sqrt{1-B^2}\sqrt{a^2-y^2}} + \frac{\cos t}{\sqrt{1-B^2}\sqrt{a^2-y^2}}\left[\frac{D_1}{\pi} + 2a\gamma_0\tilde{\omega}_1\right] - \frac{\cos(t-t_0)D_1\sqrt{b^2-a^2}}{\pi\sqrt{1-B^2}\sqrt{a^2-y^2}(b-y)} \tag{25b}$$

with

$$D_1 = \frac{-2mAb_x}{\kappa_2(1+\beta)+\kappa_1(1-\beta)},$$

$$\tilde{\omega} = \frac{-2D_1[2a\gamma_0 + (b-a)\sqrt{b-a/b+a}\sin t_0]}{a^2(1+4\gamma_0^2)\pi}.$$

(f) An Anticrack Interacting With a Dislocation b_y at the Interface. For a dislocation $b_x = 0$, $b_y \neq 0$ at $y = b$ the forcing function at the right-hand side of (23*a*), (23*b*) are

$$\frac{\partial u_x}{\partial y}(0, y) = \frac{Ab_y}{2\pi}\frac{1}{y-b} \qquad \frac{\partial u_y}{\partial y}(0, y) = 0 \tag{26}$$

and the solution is

$$p_x(y) = \frac{\tilde{\omega}[y\cos t + 2a\gamma_0 \sin t]}{\sqrt{1-B^2}\sqrt{a^2-y^2}} + \frac{D_2}{\pi\sqrt{1-B^2}\sqrt{a^2-y^2}}\left[\sqrt{\frac{b-a}{b+a}}\cos(t-t_0) - \cos t\right] - \frac{D_2}{\pi\sqrt{1-B^2}\sqrt{(b-y)}}\sqrt{\frac{(a+y)(b-a)}{(a-y)(b+a)}}\cos(t-t_0) \tag{27a}$$

$$p_y(y) = \frac{\tilde{\omega}[-y\sin t + 2a\gamma_0\cos t]}{\sqrt{1-B^2}\sqrt{a^2-y^2}} + \frac{D_2}{\pi\sqrt{1-B^2}\sqrt{a^2-y^2}}\left[\sin t - \sqrt{\frac{b-a}{b+a}}\sin(t-t_0)\right] + \frac{D_2}{\pi\sqrt{1-B^2}(b-y)}\sqrt{\frac{(a+y)(b-a)}{(a-y)(b+a)}}\sin(t-t_0) \tag{27b}$$

where

$$\tilde{\omega} = \frac{2D_2[-b + (b-a)\sqrt{b-a/b+a}\cos t_0 - 4a\gamma_0\sqrt{b-a/b+a}\sin t_0]}{\pi a^2(1+4\gamma_o^2)}$$

$$D_2 = \frac{-2mAb_y}{\kappa_2(1+\beta)+\kappa_1(1-\beta)}.$$

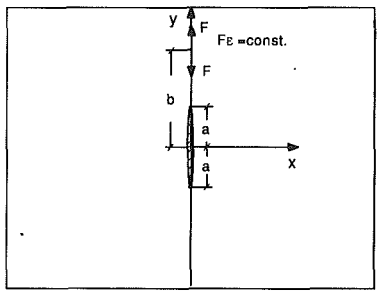


Fig. 4 Interaction of an anticrack with a second-order singularity at an interface

(g) Interaction of an Anticrack With a Second-Order Singularity at an Interface (Fig. 4). An interface can admit second-order concentrated action singularities that are uniquely defined and which are either self-equilibrated or not. These singularities have been obtained by (Markenscoff, Dundurs, Ye, 1992). Here we consider the interation of the anticrack with a doublet of forces at the interface. If the strength of the doublet is $F_y\epsilon$ = constant and it is located at $y = b > a$, then the solution is obtained by differentiation of the solution for a point force F_y at b (obtained in the previous section) with respect to b. The results are

$$p_x = \frac{-2(F_y\epsilon)}{a^2(1+4\gamma_o^2)\pi}\frac{(b-a)^{1/2}}{(b+a)^{3/2}} \times \frac{(y\cos t + 2a\gamma_o\sin t)\,[(b+2a)\sin t_o - 2a\gamma_o\cos t_o]}{\sqrt{1-B^2}\sqrt{a^2-y^2}} - \frac{(F_y\epsilon)}{\pi\sqrt{1-B^2}\sqrt{a^2-y^2}} \times \frac{[a\sin(t-t_o) + 2a\gamma_o\cos t(t-t_o)]}{(a+b)^{3/2}(b-a)^{1/2}}\frac{(a+b-2y)}{b-y} + \frac{(F_y\epsilon)}{\pi\sqrt{1-B^2}\sqrt{a^2-y^2}}\sqrt{\frac{b-a}{b+a}}\frac{a-y}{(b-y)^2}\sin(t-t_o) \tag{28a}$$

$$p_y = \frac{-2(F_y\epsilon)(b-a)^{1/2}}{a^2(1+4\gamma_o^2)\pi(b+a)^{3/2}} \times \frac{(2a\gamma_o\cos t - y\sin t)((b+2a)\sin t_o - 2a\gamma_o\cos t_o)}{\sqrt{1-B^2}\sqrt{a^2-y^2}} - \frac{(F_y\epsilon)}{\pi\sqrt{1-B^2}\sqrt{a^2-y^2}} \times \left[\frac{a\cos(t-t_o) - 2a\gamma_o\sin(t-t_o)}{(a+b)^{3/2}(b-a)^{1/2}}\right]\frac{(a+b-2y)}{(b-y)} + \frac{(F_y\epsilon)}{\pi\sqrt{1-B^2}\sqrt{a^2-y^2}}\sqrt{\frac{b-a}{b+a}}\frac{a-y}{(b-y)^2}\cos(t-t_o). \tag{28b}$$

It is obvious from Eqs. (20) that the solution diverges as $b \to a$ as in Dundurs and Markenscoff (1989a). However, this diverenge cannot be removed by rescaling and setting $F_y\epsilon/(b-a)^{1/2}$ = constant as in Dundurs and Markenscoff (1989a)

Downloaded 03 May 2010 to 171.66.16.20. Redistribution subject to ASME license or copyright; see http://www.asme.org/terms/Terms_Use.cfm

since the distance $(b-a)$ appears uncoupled from the load in sin t_0, where

$$t_o = \gamma_o \ln \left| \frac{a+b}{b-a} \right|,$$

unless of course

$$\gamma_o = 0.$$

(h) Interface Cracks from Interface Anticracks. The solution to crack problems can be obtained from that of anticrack problems in homogeneous elastic solids as first observed by Dundurs (1989) and proved by Markenscoff (1993). This is done by setting the Kolosoff constant $\kappa = -1$. The crack faces will be stress-free if the rotation of the anticrack is zero at $\kappa = -1$. It is observed here that such a reduction can go through also for two materials and that the interface crack solution may be obtained from that of an anticrack by setting $\kappa_1 = \kappa_2 = -1$.

Also, the combination that removes oscillatory singularities at anticracks $\kappa_1(1-\beta) = \kappa_2(1+\beta)$ naturally yields $\beta = 0$ for $\kappa_1 = \kappa_2 = -1$, which is the material combination that removes the oscillatory singularities for cracks.

Conclusion

The solution of an anticrack directly loaded by forces and moment are new solutions that involve the rotation of the anticrack as a rigid body. The solution for a force and a dislocation at an interface in the presence of an anticrack provide the Green's function for solving any number of interacting cracks and anticracks at an interface.

Interesting physical properties of the solution are manifested with the anticrack absorbing one first-order singularity (the force) while not another (the dislocation). This is easily explained in the context of the formulation of the problem of the anticrack as a distribution of line loads $p_x(y)$, $p_y(y)$.

The interaction of the anticrack with a force doublet (or other second-order singularities, such as centers of dilatation and dipoles of dislocations) produces infinite stress everywhere as the tip of the anticrack is approached, which is a very unintuitive behavior.

Acknowledgment

This research was supported by the National Science Foundation grant #MSS-90002804 and by the U.S. Army Research Office DAAL-03-86-K-0169 to the University of California, San Diego.

References

Ballarini, R., 1991, "A Rigid Inclusion at a Bimaterial Interface," *Engineering Fracture Mechanics*, in press.

Comninou, M., 1978, "The Interface Crack," ASME JOURNAL OF APPLIED MECHANICS, Vol. 45, pp. 287–292.

Dundurs, J., 1969, Discussion of a paper by D. B. Bogy, ASME JOURNAL OF APPLIED MECHANICS, pp. 650–652.

Dundurs, J., 1989, "Cavities Vis-a-Vis Rigid Inclusions and Some Related Results in Plane Elasticity," ASME JOURNAL OF APPLIED MECHANICS, Vol. 56, pp. 786–790.

Dundurs, I., and Markenscoff, X., 1989a, "A Green's Functions Formulation of Anticracks and Their Interaction With Load-Induced Singularities," ASME JOURNAL OF APPLIED MECHANICS, Vol. 56, pp. 550–554.

Dundurs, J., and Markenscoff, X., 1989b, "The Sterberg-Koiter Conclusion and Other Anamalies of the Concentrated Couple," ASME JOURNAL OF APPLIED MECHANICS, Vol. 56, pp. 240–245.

Dundurs, J., 1990, "Boundary Conditions at Interfaces," *Micromechanics and Inhomogeneity*, G. J. Weng, et al., Springer-Verlag, New York.

Markenscoff, X., 1993, "On the Dundurs Correspondence Between Cavities and Rigid Inclusions," ASME JOURNAL OF APPLIED MECHANICS, Vol. 60, pp. 260–264.

Markenscoff, X., Dundurs, J., and Ye, W., 1992, "Elastic Singularities at Bimaterial Interfaces," Vol. AMD-148, *Defects in an Elasticity in the Characterization of Crystalline Solids*, ASME, New York, pp. 93–96.

Ni, L., and Nemat-Nasser, S., 1991, "Interface Crack in Anisotropic Dissimilar Materials: An Analytic Solution," *Journal of the Mechanics and Physics of Solids*, Vol. 39, pp. 113–144.

Wang, Z. Y., Zhang, H. T., and Chou, Y. T., 1985, "Characteristics of the Elastic Field of a Rigid Line in Homogeneity," ASME JOURNAL OF APPLIED MECHANICS, Vol. 52, pp. 818–822.

Williams, M. L., 1959, "The Stresses Around a Fault or Crack in Dissimilar Materials," *Bulletin Seismology Society of America*, Vol. 49, pp. 199–204.

Wu, K.-C., 1990, "Line Inclusions at Anisotropic Bimaterial Interface," *Mechanics of Materials*, Vol. 10, pp. 173–183.

Downloaded 03 May 2010 to 171.66.16.20. Redistribution subject to ASME license or copyright; see http://www.asme.org/terms/Terms_Use.cfm

The Stress Field and Intensity Factor due to Crazes Formed at the Poles of a Spherical Inhomogeneity

Z. M. Xiao
School of Mechanical and Production Engineering, Nanyang Technological University, Nanyang Avenue, Singapore 2263, Republic of Singapore

K. D. Pae
Department of Mechanical and Aerospace Engineering, Rutgers University, Piscataway, NJ 08855-0909

The problem of two penny-shaped crazes formed at the top and the bottom poles of a spherical inhomogeneity has been investigated. The inhomogeneity is embedded in an infinitely extended elastic body which is under uniaxial tension. Both the inhomogeneity and the matrix are isotropic but have different elastic moduli. The analysis is based on the superposition principle of the elasticity theory and Eshelby's equivalent inclusion method. The stress field inside the inhomogeneity and the stress intensity factor on the boundary of the craze are evaluated in the form of a series which involves the ratio of the radius of the penny-shaped craze to the radius of the spherical inhomogeneity. Numerical examples show the interaction between the craze and the inhomogeneity is strongly affected by the elastic properties of the inhomogeneity and the matrix. The conclusion deduced from the numerical results is in good agreement with experimental results given in the literature.

1 Introduction

Experimental studies of craze initiation in glassy polymers which are toughened by spherical particles have been carried out by Wang et al. (1971) and Dekkers and Heikens (1983). Wang and his co-workers (1971) showed that when the embedded particle is harder than the matrix (e.g., polystyrene (PS) matrix containing a steel ball), crazes are formed near the top and bottom poles of the ball; while when the particle is softer (a rubber ball) than the matrix, the craze first occurs at the equator of the ball. The further experiments done by Dekkers and Heikens (1983) showed that the interfacial adhesion between the inclusion and the matrix plays a crucial role for the position where the crazes appear. They investigated the craze formation around glass beads dispersed in a PS matrix. The clear photographs obtained in their experiments show that in the case of excellent interfacial adhesion, the crazes form near the poles of the inclusion. With poor interfacial adhesion the crazes form at the interface between the pole and equator.

The problem we study is the case in which the crazes are formed on the top and the bottom poles of a spherical particle. The theoretical analysis is based on the assumption that perfect bonding exists between the inclusion and the matrix so that both the filler and the matrix obey elastic stress-strain relations. Eshelby's notation (1961) is followed here; i.e., an inclusion with different elastic moduli than the matrix is called an "inhomogeneity" and a region with eigenstrains existing but having the same elastic moduli as the matrix is called an "inclusion." According to the analysis given by Walton and Weitsman (1984), a penny-shaped craze can be treated as a crack which contains parallel fibrils connecting its opposite surfaces. The fibrils inside the craze are handled as continuously distributed, one-dimensional springs. Therefore, our problem is reduced to studying the interaction between cracks and an inhomogeneity. We shall briefly review the papers on this subject. Because of the mathematical difficulties most of the studies have been limited to two dimensions. The interaction between a crack and a circular inhomogeneity in a sheet under tension was studied by Tamate (1968) and an exact solution was obtained. Hsu and Shivakumar (1976) investigated the interaction between an elastic circular inclusion and two symmetrical placed colinear cracks. The problem of a crack located between two rigid inclusions was studied by Sendeckyj (1974). A few papers concerned with the interaction of a crack and a cavity (a special kind of inhomogeneity) in a three-dimensional space have been published. Srivastava and Mahajan (1970) determined the stress distribution in an infinite solid containing a spherical cavity and an external crack. Hiral and Satake (1980) solved the problem involving a penny-shaped crack located between two spherical cavities in an infinite solid. Recently Xiao and Pae (1991) investigated the interaction between a spherical inhomogeneity and a penny-shaped crack,

Contributed by the Applied Mechanics Division of THE AMERICAN SOCIETY OF MECHANICAL ENGINEERS for publication in the ASME JOURNAL OF APPLIED MECHANICS.

Discussion on this paper should be addressed to the Technical Editor, Professor Lewis T. Wheeler, Department of Mechanical Engineering, University of Houston, Houston, TX 77204-4792, and will be accepted until four months after final publication of the paper itself in the ASME JOURNAL OF APPLIED MECHANICS.

Manuscript received by the ASME Applied Mechanics Division, Jan. 13, 1992; final revision, Nov. 13, 1992. Associate Technical Editor: X. Markenscoff.

Copyright © 1994 by ASME
Downloaded 03 May 2010 to 171.66.16.20. Redistribution subject to ASME license or copyright; see http://www.asme.org/terms/Terms_Use.cfm

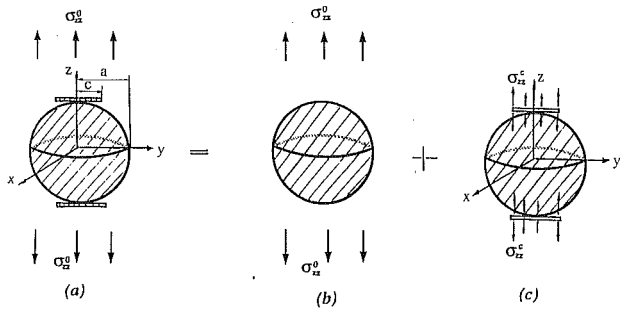


Fig. 1 The superposition process

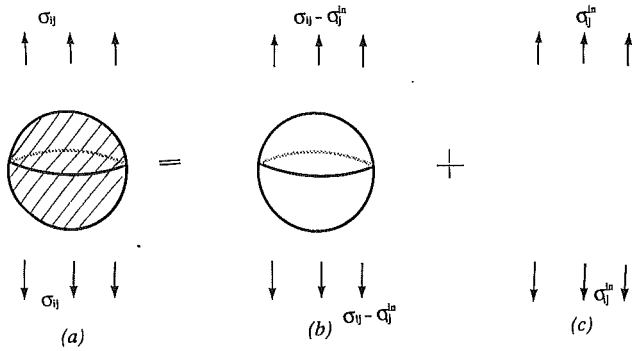


Fig. 2 Tanaka-Mura's Alternative Method

and obtained an analytical solution to the stress field and the stress intensity factor of the crack.

In this paper an approximate three-dimensional analytical solution for our problem is obtained. The radius of the inhomogeneity is denoted by a and the radius of the crazes by c. What we are interested in is an early period of craze formation such that $c/a = \delta \leq 1/3$. The stress intensity factors on the boundary of the crazes are evaluated by dropping the terms with the sixth or higher order of δ. The stress field inside the spherical inhomogeneity is obtained by neglecting the terms with the fifth or higher order of δ.

2 Superposition Process

The physical model of the problem is shown in Fig. 1(a). The inhomogeneity is embedded in an infinitely extended elastic matrix. The stress applied at infinity is $\sigma_{zz}^0 =$ constant. The inhomogeneity and the matrix are isotropic and have the elastic moduli C_{ijkl} and C_{ijkl}^0, respectively. We choose the center of the spherical inhomogeneity as the origin of the coordinate system. The planes of the penny-shaped crazes are perpendicular to the z-axis and the centers of the crazes are on the z-axis. The superposition of the elasticity theory is applied. When the crazes are removed, the stress distribution at the craze domain in the z-direction in Fig. 1(b) is supposed to be σ_{zz}^{c0}. We then exert this σ_{zz}^{c0} to the top and the bottom surfaces of the crazes in Fig. 1(c). The original problem is thus decomposed into two configurations shown in Fig. 1(b) and 1(c). By a process to be described later, the crazes in Fig. 1(c) are transformed to cracks and σ_{zz}^{c0} is changed to σ_{zz}^{c}. The stress σ_{zz}^{c} is to be determined.

The stress field σ_{ij}^{in} inside the inhomogeneity in Fig. 1(b) is determined by Eshelby (1961):

$$\sigma_{xx}^{in} = \sigma_{yy}^{in} = \frac{1}{3}\left[\frac{\kappa_1}{\alpha_0(\kappa_1 - \kappa_0) + \kappa_0} - \frac{\mu_1}{\beta_0(\mu_1 - \mu_0) + \mu_0}\right]\sigma_{zz}^0$$

$$\sigma_{zz}^{in} = \left[\frac{2}{3}\frac{\mu_1}{\beta_0(\mu_1 - \mu_0) + \mu_0} + \frac{1}{3}\frac{\kappa_1}{\alpha_0(\kappa_1 - \kappa_0) + \kappa_0}\right]\sigma_{zz}^0$$

where κ_1, μ_1, and κ_0, μ_0 are the bulk and shear moduli of the inhomogeneity and the matrix, respectively, and

$$\alpha_0 = \frac{1}{3}\frac{1 + \nu_0}{1 - \nu_0}, \quad \beta_0 = \frac{2}{15}\frac{4 - 5\nu_0}{1 - \nu_0},$$

in which ν_0 is the Poisson's ratio of the matrix.

The stress field outside the inhomogeneity in Fig. 1(b) is rather complex. An alternative method proposed by Tanaka and Mura (1982) to evaluate the elastic stress distribution for points exterior to the inhomogeneity is adopted. The process of solving the problem is illustrated in Fig. 2. The figure shows that the problem of a spherical inhomogeneity in a matrix under σ_{ij} applied at infinity is the sum of the problem of a spherical void in a matrix under $\sigma_{ij} - \sigma_{ij}^{in}$ and the problem of the matrix under σ_{ij}^{in}. The stress distribution $\sigma_{ij} - \sigma_{ij}^{in}$ at infinity in Fig. 2(b) for our problem is given by

$$\sigma_{zz} = \sigma_{zz}^0 + \sigma_{zz}^{in}, \quad \sigma_{xx} = \sigma_{yy} = -\sigma_{xx}^{in} = -\sigma_{yy}^{in}.$$

This stress distribution can be decomposed into a uniaxial tension in the z-direction as $\sigma_{zz}^1 = \sigma_{zz}^0 - \sigma_{zz}^{in} + \sigma_{xx}^{in}$ and a hydrostatic pressure as $\sigma_{zz}^2 = \sigma_{xx}^2 = \sigma_{yy}^2 = -\sigma_{xx}^{in}$. By using Timoshenko's elastic solution (1934) of the problem of a spherical void in an infinite body under uniaxial tension, and adding the stress field of the hydrostatic pressure, the stress σ_{zz} on $z = a$ plane for Fig. 2(b) is obtained as

$$\sigma_{zz}(z = a) = \sigma_{zz}^1\left\{1 + \frac{5(1 - 2\nu_0)a^3}{2(7 - 5\nu_0)(a^2 + r^2)^{3/2}} + \frac{a^3\left[(41 + 20\nu_0)a^2 - (1 - 5\nu_0)r^2\right]}{a(7 - 5\nu_0)(a^2 + r^2)^{5/2}} - \frac{165a^7}{2(7 - 5\nu_0)(a^2 + r^2)^{7/2}} + \frac{105a^9}{2(7 - 5\nu_0)(a^2 + r^2)^{9/2}}\right\} + \sigma_{zz}^2\left[1 - \frac{a^3(2a^2 - r^2)}{2(a^2 + r^2)^{5/2}}\right] \quad (1)$$

where $r^2 = x^2 + y^2$. Our aim is to find the stress in the craze zone. So we let $r \leq c$. Equation (1) is expanded into a series of r/a. The terms whose order are equal or higher than δ^6 are dropped. By substituting σ_{zz}^1 and σ_{zz}^2 with their expression, Eq. (1) becomes

$$\sigma_{zz}(z = a) = \sigma_{zz}^0\left[B\left(\frac{r}{a}\right)^2 + C\left(\frac{r}{a}\right)^4\right] + O(\delta^6), \quad (2)$$

in which B and C are constants as

$$B = \frac{\mu_1}{\beta_0(\mu_1 - \mu_0) + \mu_0} - \frac{\kappa_1}{\alpha_0(\kappa_1 - \kappa_0) + \kappa_0} - \frac{3 + 15\nu_0}{7 - 5\nu_0}\frac{(\beta_0 - 1)(\mu_1 - \mu_0)}{\beta_0(\mu_1 - \mu_0) + \mu_0}, \quad (3)$$

$$C = \frac{15}{8}\left[\frac{\kappa_1}{\alpha_0(\kappa_1 - \kappa_0) + \kappa_0} - \frac{\mu_1}{\beta_0(\mu_1 - \mu_0) + \mu_0}\right] + \frac{4(24 + 7\nu_0)}{7 - 5\nu_0}\frac{(\beta_0 - 1)(\mu_1 - \mu_0)}{\beta_0(\mu_1 - \mu_0) + \mu_0}. \quad (4)$$

By combining Fig. 2(b) and Fig. 2(c), the stress in the z-direction at $z = a$ in Fig. 2(a) or Fig. 1(b) in the craze region is obtained as

$$\sigma_{zz}^{c0} = \sigma_{zz}^0\left[A + B\left(\frac{r}{a}\right)^2 + C\left(\frac{r}{a}\right)^4\right] + O(\delta^6). \quad (5)$$

This is the stress which is applied to the top and bottom

Downloaded 03 May 2010 to 171.66.16.20. Redistribution subject to ASME license or copyright; see http://www.asme.org/terms/Terms_Use.cfm

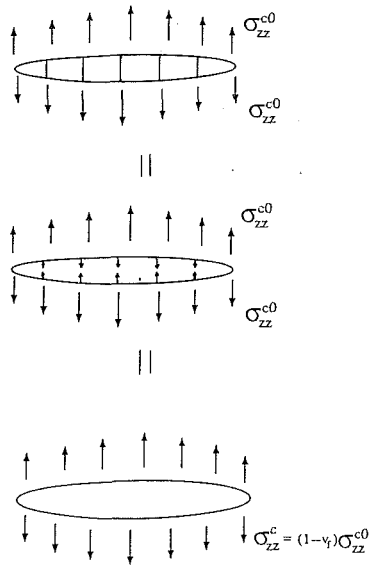


Fig. 3 The process to make a craze equivalent to a crack

surfaces of the crazes in Fig. 1(c) and A is a constant given by

$$A = \frac{2}{3}\frac{\mu_1}{\beta_0(\mu_1 - \mu_0) + \mu_0} + \frac{1}{3}\frac{\kappa_1}{\alpha_0(\kappa_1 - \kappa_0) + \kappa_0}. \quad (6)$$

In the absence of detailed experimental results, we follow Walton and Weitsman's (1984) method to transform a craze equivalent to a crack. The process is shown in Fig. 3. The tensile stress in the parallel craze fibrils is assumed to equal the local applied stress σ_{zz}^{c0}. We then cut off the fibrils and replace them by the fibril stress at the position of the fibrils. This discrete fibril stress is then incorporated into the continuously distributed stress along the craze surfaces but the magnitude of the stress becomes $v_f\sigma_{zz}^{c0}$, in which v_f is the volume fraction of the fibrils inside the craze. Therefore, the craze can be treated as a crack but the stress exerted on the surfaces of the crack should be changed to

$$\sigma_{zz}^{c} = \tau\sigma_{zz}^{0}\left[A + B\left(\frac{r}{a}\right)^2 + C\left(\frac{r}{a}\right)^4\right] + O(\delta^6), \quad (7)$$

where $\tau = 1 - v_f$ is a constant determined by the volume fraction of craze fibrils within a craze.

3 The Stress Field Inside the Inhomogeneity

By using the superposition method, our original problem can be changed to the problem of two penny-shaped cracks located on the poles of the spherical inhomogeneity as shown in Fig. 1(c). We let the equations for the cracks to be

$$\frac{x^2}{c^2} + \frac{y^2}{c^2} + \frac{z \mp a}{a_3^2} = 1 \quad \text{and} \quad a_3 \to 0.$$

Eshelby's equivalent inclusion method (1961) is adopted here. The cracks and the inhomogeneity are treated to have the same elastic moduli as the matrix by introducing so-called eigenstrains (Mura, 1982) ϵ_{ij}^{*c} and ϵ_{ij}^{*s} inside the cracks and the domain of the spherical inhomogeneity, respectively. Moschovidis and Mura (1975) studied the interaction between two ellipsoidal inhomogeneities in an infinite matrix by equivalent inclusion method. They performed the numerical calculations by taking the eigenstrains inside the inhomogeneities to be polynomials of degree zero and of degree one in the position coordinates. Here we also adopt the eigenstrain ϵ_{ij}^{*s} inside the spherical inhomogeneity to be a linear function of the coordinates. In a similar problem Xiao and Pae (1991) proved that all the nonlinear terms dropped in ϵ_{ij}^{*s} have the order of δ^5, here $\delta = c/a$. Since our problem is symmetric about the z-axis and the x-y plane, the linear term of the position vector in ϵ_{ij}^{*s} should be zero. Therefore ϵ_{ij}^{*s} is constant over the spherical domain when the terms with order of δ^5 are dropped. One important conclusion obtained by Moschovidis and Mura (1975) and also by Xiao and Pae (1991) is that when the distance between the centers of any two ellipsoidal inhomogeneities is greater than four times that of the largest axis of the ellipsoids, the interaction between them is negligible. For our problem, the two cracks can be considered as ellipsoidal inhomogeneities whose elastic moduli are zero. The distance between the center of them is $2a$, which is greater than $4c$. The interaction between the cracks is thus neglected. We only need to consider the interaction between the cracks and the spherical inhomogeneity. According to the equivalent inclusion method, ϵ_{ij}^{*s} is to satisfy the following equation:

$$C_{ijkl}^{1}\left(u_{k,l}^{0} + u_{k,l}^{pt}\right) = C_{ijkl}^{0}\left(u_{k,l}^{0} + u_{k,l}^{pt} - \epsilon_{kl}^{*s}\right),$$

or

$$C_{ijkl}^{1}\left(\epsilon_{kl}^{0} + \epsilon_{kl}^{pt}\right) = C_{ijkl}^{0}\left(\epsilon_{kl}^{0} + \epsilon_{kl}^{pt} - \epsilon_{kl}^{*s}\right). \quad (8)$$

Here C_{ijkl}^{1} and C_{ijkl}^{0} are the elastic moduli of the inhomogeneity and the matrix, respectively. ϵ_{ij}^{0} is the strain field inside the domain of the inhomogeneity when the inhomogeneity is removed, while the cracks exists. ϵ_{ij}^{pt} is the perturbation term caused by the inhomogeneity. When σ_{ij}^{*s} is constant, ϵ_{ij}^{pt} is related to ϵ_{ij}^{*s} by Eshelby tensor (1961):

$$\epsilon_{ij}^{pt} = S_{ijkl}\epsilon_{ij}^{*s}.$$

Substituting this result into (8), the eigenstrain ϵ_{ij}^{*s} is obtained as

$$\epsilon^{*s} = -\left[(\mathbf{C}^1 - \mathbf{C}^0)\mathbf{S} + \mathbf{C}^0\right]^{-1}(\mathbf{C}^1 - \mathbf{C}^0)\epsilon^0. \quad (9)$$

The strain ϵ_{ij}^{0} can be obtained through the derivative of the displacement u_k^0, which is given by

$$u_i^0(\mathbf{r}) = \oint_{S_{c1}+S_{c2}} G_{ij}(\mathbf{r} - \mathbf{r}')C_{jklm}^{0}\epsilon_{lm}^{*c}n_k ds' \quad (10)$$

where ϵ_{ij}^{*c} is the eigenstrain inside the crack zone and S_{c1} and S_{c2} are the surfaces of the cracks. $G_{ij}(\mathbf{r} - \mathbf{r}')$ is the Green's tensor function (Mura, 1982) which may be written for our problem as

$$G_{ij}(\mathbf{R}) = \frac{A_1}{R}\delta_{ij} + \frac{A_2}{R^3}R_iR_j, \quad (11)$$

where

$$\mathbf{R} = \mathbf{r} - \mathbf{r}', \quad A_1 = \frac{3 - 4\nu_0}{16\pi\mu_0(1 - \nu_0)},$$

$$A_2 = \frac{1}{16\pi\mu_0(1 - \nu_0)}.$$

In (9), if ϵ_{ij}^{*s} is constant, ϵ_{ij}^{0} should be constant. Thus u_k^0 should be a linear function of the coordinates. By expanding the Green's function $G_{ij}(\mathbf{R})$ in (10) into a series of the coordinates and keep linear terms, we obtain

$$u_{0i}(\mathbf{r}) = \lim_{a_3 \to 0}\int\int_{\Omega} 4A_1\frac{z}{a^3}\sqrt{1 - \frac{x'^2 + y'^2}{c^2}}\, a_3 C_{i3lm}^{0}\epsilon_{lm}^{*c}dx'dy' + O(\delta^5), \quad (12)$$

in which Ω is the domain $x'^2 + y'^2 \le c^2$. All the terms with the order of δ^5 or higher are dropped in the above equation. Since the term z/a^3 inside the integration in (12) has the order of δ^2, we only need to maintain the terms of degree zero and degree one of δ in ϵ_{lm}^{*c} to calculate $u^0i(\mathbf{r})$. The

Downloaded 03 May 2010 to 171.66.16.20. Redistribution subject to ASME license or copyright; see http://www.asme.org/terms/Terms_Use.cfm

eigenstrain ϵ_{lm}^{*c} in the crack domain is determined by σ_{zz}^{c} and the effect of the spherical inhomogeneity. We will show later by Fig. 4 that the effect of the inhomogeneity on the cracks in Fig. 1(*c*) has the order of δ^3, which contributes terms with order of $O(\delta^3)$ to ϵ_{ij}^{*c}, and thus can be neglected in determining $u_i^0(\mathbf{r})$ by (12). From (7), $\sigma_{zz}^{c} = \tau A \sigma_{zz}^{0} + O(\delta^2)$, which means that only $\tau A \sigma_{zz}^{0}$ can influence ϵ_{lm}^{*c} with the zeroth order term of δ. Here A is the constant given in (6).

According to Mura (1982), the eigenstrain caused by a constant stress $\tau A \sigma_{zz}^{0}$ exerted on the top and the bottom surface of a penny-shaped crack is given by

$$\lim_{a_3 \to 0} \epsilon_{33}^{*} = \text{constant} = \frac{2(1-\nu_0)c}{\mu_0 \pi} \tau A \sigma_{zz}^{0},$$

$$\text{and other } \epsilon_{ij}^{*} = 0.$$

Thus, for our problem we get

$$\epsilon_{33}^{*c} = \frac{2(1-\nu_0)c}{\mu_0 \pi} \tau A \sigma_{zz}^{0} + O(\delta^2),$$

$$\text{and other } \epsilon_{ij}^{*c} = O(\delta^2).$$

Substituting this result into (12), we obtain

$$u_i^0 = \tau A \frac{2(1-\nu_0)(3-4\nu_0)}{3\pi(1-2\nu_0)} \frac{\sigma_{zz}^{0}}{\mu_0} \left(\frac{c}{a}\right)^3 z \delta_{i3} + O(\delta^5). \quad (13)$$

By taking the derivative of the above equation, we can easily find

$$\epsilon_{33}^{0} = \tau A \frac{2(1-\nu_0)(3-4\nu_0)}{3\pi(1-2\nu_0)} \frac{\sigma_{zz}^{0}}{\mu_0} \left(\frac{c}{a}\right)^3 + O(\delta^5),$$

$$\text{other } \epsilon_{ij}^{0} = 0. \quad (14)$$

Noting that the real strain field inside the inhomogeneity is $\epsilon_{kl}^{0} + \epsilon_{kl}^{pt}$, the stress field inside the inhomogeneity of Fig. 1(*c*) is

$$\sigma'^{s} = \mathbf{C}^1(\epsilon^0 + \epsilon^{pt}) = \mathbf{C}^1(\epsilon^0 + \mathbf{S}\epsilon^{*s}). \quad (15)$$

Substituting (14) and (9) into (15), we obtain

$$\sigma_{11}'^{s} = \sigma_{22}'^{s} = A_3 \left(\frac{c}{a}\right)^4 \tau \sigma_{zz}^{0} \left[\frac{\kappa_1}{\alpha_0(\kappa_1-\kappa_0)+\kappa_0} - \frac{\mu_1}{\beta_0(\mu_1-\mu_0)+\mu_0} \frac{1-2\nu_0}{1+\nu_0}\right] + O(\delta^5), \quad (16)$$

$$\sigma_{33}'^{s} = A_3 \left(\frac{c}{a}\right)^4 \tau \sigma_{zz}^{0} \left[\frac{\kappa_1}{\alpha_0(\kappa_1-\kappa_0)+\kappa_0} + \frac{2\mu_1}{\beta_0(\mu_1-\mu_0)+\mu_0} \frac{1-2\nu_0}{1+\nu_0}\right] + O(\delta^5), \quad (17)$$

$$\sigma_{ij}'^{s} = O(\sigma^5) \quad \text{when} \quad i \neq j,$$

where

$$A_3 = \frac{4(1-\nu_0^2)(3-4\nu_0)}{9\pi(1-2\nu_0)^2} A. \quad (18)$$

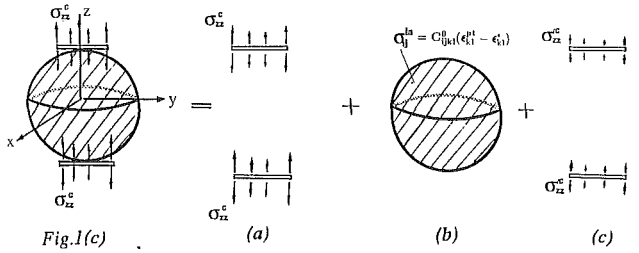


Fig. 4 The decomposition to find the stress intensity factor on the crack boundary

Adding the stress field inside the inhomogeneity in Fig. 1(*b*) to (16) and (17), we obtain the stress field inside the spherical inhomogeneity for our original problem Fig. 1(*a*) as

$$\sigma_{xx}^{s} = \sigma_{yy}^{s} = \sigma_{zz}^{0}\left[S_0 + S_1\left(\frac{c}{a}\right)^3\right] + O(\delta^5), \quad (19)$$

$$\sigma_{zz}^{s} = \sigma_{zz}^{0}\left[S_2 + S_3\left(\frac{c}{a}\right)^3\right] + O(\delta^5),$$

$$\sigma_{ij}^{s} = O(\delta^5) \quad \text{when} \quad i \neq j \quad (20)$$

where $\delta = c/a$, S_0, S_1, S_2, and S_3 are constants given by

$$S_0 = \frac{1}{3}\left[\frac{\kappa_1}{\alpha_0(\kappa_1-\kappa_0)+\kappa_0} - \frac{\mu_1}{\beta_0(\mu_1-\mu_0)+\mu_0}\right] \quad (21)$$

$$S_1 = \tau A_3 \left[\frac{\kappa_1}{\alpha_0(\kappa_1-\kappa_0)+\kappa_0} - \frac{\mu_1}{\beta_0(\mu_1-\mu_0)+\mu_0} \frac{1-2\nu_0}{1+\nu_0}\right] \quad (22)$$

$$S_2 = A = \frac{2}{3} \frac{\mu_1}{\beta_0(\mu_1-\mu_0)+\mu_0} + \frac{1}{3} \frac{\kappa_1}{\alpha_0(\kappa_1-\kappa_0)+\kappa_0} \quad (23)$$

$$S_3 = \tau A_3 \left[\frac{\kappa_1}{\alpha_0(\kappa_1-\kappa_0)+\kappa_0} + \frac{2\mu_1}{\beta_0(\mu_1-\mu_0)+\mu_0} \frac{1-2\nu_0}{1+\nu_0}\right]. \quad (24)$$

4 The Stress Intensity Factor on the Craze Boundary

According to (8) and (15), the stress field inside the inhomogeneity of Fig. 1(*c*) can be expressed as $C_{ijkl}^{0}(\epsilon_{kl}^{0} + \epsilon_{kl}^{pt} - \epsilon_{kl}^{*s})$. We further decompose the problem in Fig. 1(*c*) into those of Fig. 4(*a*), Fig. 4(*b*), and Fig. 4(*c*). The stress applied inside the inhomogeneity in Fig. 4(*b*) is $C_{ijkl}^{0}(\epsilon_{kl}^{pt} - \epsilon_{kl}^{*s})$. The stress $\sigma_{zz}'^{c}$ applied on the crack surfaces in Fig. 4(*c*) is the stress in the crack domain of Fig. 4(*b*). Later we will find that $\sigma_{zz}'^{c}$ has the order of δ^3. By the same analysis we have carried out in Section 3 the stress field in the domain of the spherical inhomogeneity in Fig. 4(*c*) is found to have the order of δ^6 which can be neglected. Noting that the stress field in the domain of the inhomogeneity in Fig. 4(*a*) is $c_{ijkl}^{0}\epsilon_{kl}^{0}$, in which ϵ_{kl}^{0} is given in (14). Therefore Fig. 1(*c*) is equivalent to the sum of Fig. 4(*a*), Fig. 4(*b*), and Fig. 4(*c*).

In order to find $\sigma_{zz}'^{c}$, Tanaka and Mura's (1982) alternative method is again applied here. Equation 4(*b*) is equivalent to the sum of a spherical void in the matrix under the stress $-C_{ijkl}^{0}(\epsilon_{kl}^{pt} - \epsilon_{kl}^{*s})$ applied at infinity, and the infinite matrix under the stress $C_{ijkl}^{0}(\epsilon_{kl}^{pt} - \epsilon_{kl}^{*s})$. By the same process we used in Section 2, we find

$$\sigma_{zz}'^{c} = \tau \sigma_{zz}^{0}\left[A'\left(\frac{r}{a}\right)^3 + B'\left(\frac{r}{a}\right)^5\right] + O(\delta^6), \quad (25)$$

where $r = \sqrt{x^2 + y^2}$, A' and B' are constants given by

Downloaded 03 May 2010 to 171.66.16.20. Redistribution subject to ASME license or copyright; see http://www.asme.org/terms/Terms_Use.cfm

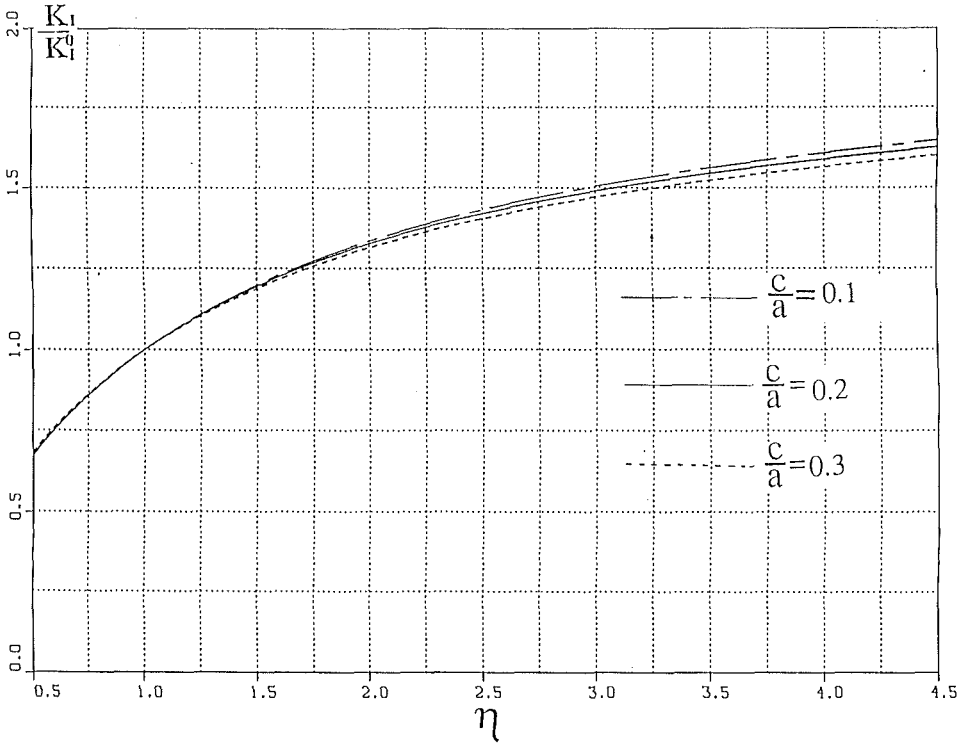


Fig. 5 The relative stress intensity factor K_I/K_{I0} on the boundary of the crazes

$$A' = A_3\left[\frac{\kappa_1}{\alpha_0(\kappa_1-\kappa_0)+\kappa_0} + 2\frac{1-2\nu_0}{1+\nu_0}\frac{\mu_1}{\beta_0(\mu_1-\mu_0)+\mu_0} - 3\frac{1-\nu_0}{1+\nu_0}\right], \quad (26)$$

$$B' = A_3\left[-3\frac{\kappa_1}{\alpha_0(\kappa_1-\kappa_0)+\kappa_0} + 30\frac{1-2\nu_0}{7-5\nu_0}\frac{\mu_1}{\beta_0(\mu_1-\mu_0)+\mu_0} + 9\frac{5\nu_0-1}{7-5\nu_0}\right], \quad (27)$$

in which A_3 is the constant given in (18). We define a stress σ_{zz}^{ct} as the sum of $\sigma_{zz}^{\prime c}$ and σ_{zz}^{c}, i.e.,

$$\sigma_{zz}^{ct} = \sigma_{zz}^{\prime c} + \sigma_{zz}^{c} = \tau\sigma_{zz}^{0}\left[A + B\left(\frac{r}{a}\right)^2 + A'\left(\frac{r}{a}\right)^3 + C\left(\frac{r}{a}\right)^4 + B'\left(\frac{r}{a}\right)^5\right] + O(\delta^6). \quad (28)$$

Since there is no crack in Fig. 4(b), the stress intensity factor on the boundary of the cracks in Fig. 1(c) is the sum of that in Fig. 4(a) and that in Fig. 4(c) and is obtained (1969) by

$$K_I = \frac{2}{\sqrt{\pi c}}\int_0^c \frac{\sigma_{zz}^{ct} r}{\sqrt{c^2-r^2}}dr = 2\tau\sqrt{\frac{c}{\pi}}\,\sigma_{zz}^{0}\left[A + \frac{2}{3}B\left(\frac{c}{a}\right)^2 + \frac{3\pi}{16}A'\left(\frac{c}{a}\right)^3 + \frac{8}{15}C\left(\frac{c}{a}\right)^4 + \frac{5\pi}{32}B'\left(\frac{c}{a}\right)^5\right] + O(\delta^6). \quad (29)$$

A, B, A', C, and B' are constants respectively given in (6), (3), (26), (4), and (27). The stress intensity factor in Fig. 1(b) is zero. Thus the stress intensity factor on the boundary of the crazes for our original problem shown in Fig. 1(a) is given by (29).

Table 1 The variation of K_I/K_{I0} with η and c/a

c/a \ η	0.5	2	∞
0.1	0.681	1.314	1.945
0.2	0.672	1.326	1.989
0.3	0.669	1.335	2.032

5 Numerical Examples

For all our numerical results, we assume the Poisson's ratio ν_0 of the matrix and the Poisson's ratio ν_1 of the spherical inhomogeneity are both equal to 1/3. Then the ratios of the other elastic constants of the inhomogeneity to the matrix are equal and denoted by η, i.e., $\lambda_1/\lambda_0 = \mu_1/\mu_0 = \kappa_1/\kappa_0 = \eta$. The stress field at infinity is σ_{zz}^0 = constant. According to Farrar and Kramer (1981), the volume fraction of the fibrils inside the crazes is taken as 0.25, thus $\tau = 0.75$.

Figure 5 shows the variation of the relative stress intensity factor K_I/K_{I0} with η at a different value of c/a. Here K_{I0} is the stress intensity factor on the boundary of the crazes without the inhomogeneity. When $\eta < 1$, in other words, the inhomogeneity is softer than the matrix, K_I/K_{I0} is found to be less than 1. This indicates that the crazes are more difficult to propagate if they are formed at all at the poles of a softer inhomogeneities. When $\eta > 1$, we find $K_I/K_{I0} > 1$, which means, because of the hard inhomogeneity, the crazes can easily propagate than the case without inhomogeneity. The figure also shows the stress intensity factor are strongly affected by η, the modulus ratio of the inhomogeneity to the matrix. Some special values of K_I/K_{I0} are given in Table 1.

For the case of $c/a = 0.1$, the above table shows that when $\eta = 0.5$, K_I decreases about 30 percent comparing with K_{I0} and when η goes to infinity (in the calculation we take $\eta = 10^7$), K_I increases about 100 percent. Also we can find when $\eta < 1$, K_I/K_{I0} decreases as c/a increases. When $\eta > 1$, K_I/K_{I0} increases as c/a increases. The result indicates that for soft inhomogeneity case the crazes will hardly grow. This clearly shows crazes are not likely to appear at the

Downloaded 03 May 2010 to 171.66.16.20. Redistribution subject to ASME license or copyright; see http://www.asme.org/terms/Terms_Use.cfm

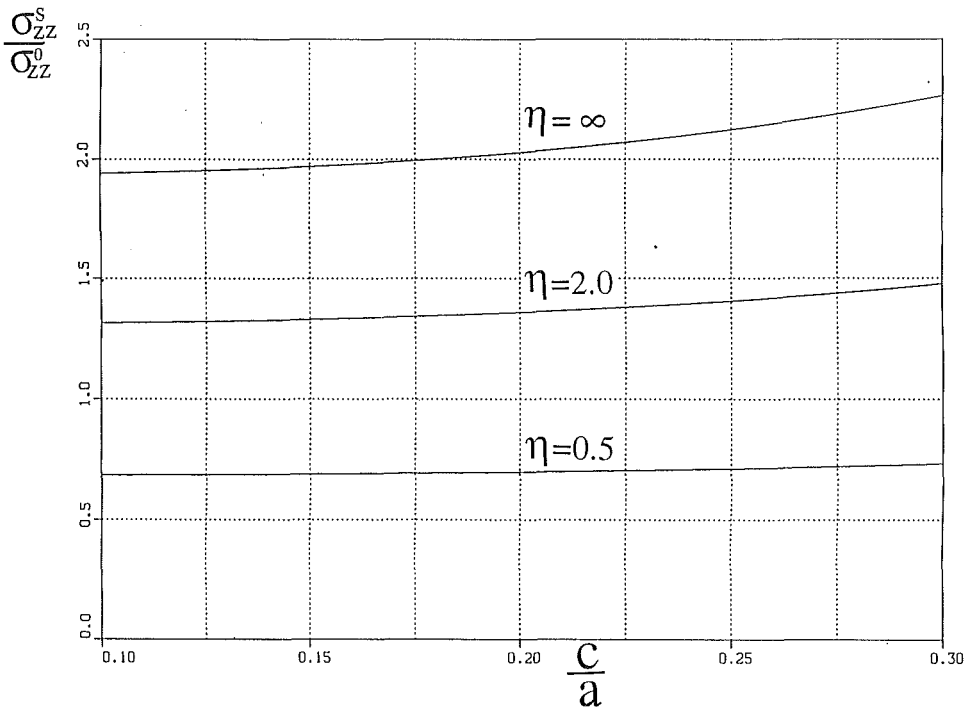


Fig. 6 The stress field $\sigma^s_{zz}/\sigma^0_{zz}$ inside the spherical inhomogeneity

Table 2 The variation of $\sigma^s_{zz}/\sigma^0_{zz}$ with η and c/a

c/a \ η	0.5	2.0	∞
0.1	0.686	1.312	1.935
0.2	0.692	1.334	1.979
0.3	0.710	1.393	2.098

holes of a softer inhomogeneity. In the case of hard inhomogeneity, the craze will propagate easily and catastrophic failure will occur because the stress intensity factor becomes bigger and bigger as the craze length increases.

Since the stress applied at infinity is only in the z-direction, the stress σ^s_{xx} and σ^s_{yy} are much smaller than σ^s_{zz} inside the spherical inhomogeneity. Figure 6 shows the variation of $\sigma^s_{zz}/\sigma^0_{zz}$ with c/a at different η. It is found that, for soft inhomogeneity, σ^s_{zz} is less than σ^0_{zz}. When the inhomogeneity is rigid, i.e., $\eta = \infty$, σ^s_{zz} is about two times of the stress applied at infinity. The figure shows the stress inside the inhomogeneity increases steadily with the craze length but is dominated by the modulus ratio. Some special values of $\sigma^s_{zz}/\sigma^0_{zz}$ are given in Table 2.

6 Conclusion

The interaction between a spherical inhomogeneity and the crazes formed at the poles of the inhomogeneity is investigated. An approximate analytical solution for the stress field inside the inhomogeneity and the stress intensity factor of the craze are evaluated. It is found that if the inhomogeneity is softer than the matrix, the stress intensity factor for polar crazes decreases as the craze length increases and is much lower than that of the case without the inhomogeneity. This result indicates that the propagation of the craze is not likely if the polar crazes are ever initiated. Therefore it can be concluded that no craze is likely to form at the poles for $\eta < 1$. If the inhomogeneity is harder than the matrix, the stress intensity factor increases as the craze length increases and is much higher than that for the case without the inhomogeneity. In this case the craze will propagate rapidly and catastrophic failure of the material will occur. This is consistent with the experimental work done by Wang and his co-workers (1971).

References

Dekkers, M. E. J., and Heikens, D., 1983, "The Effect of Interfacial Adhesion on the Mechanism for Craze Formation in Polystyrene-Glass Bead Composites," *J. Mater. Sci.*, Vol. 18, p. 3281.

Eshelby, J. D., 1961, "Elastic Inclusions and Inhomogeneities," *Progress in Solid Mechanics*, I. N. Sneddon and R. Hill, eds., North-Holland, Amsterdam.

Farrar, N. R., and Kramer, E. J., 1981, "Microstructure and Mechanics of Crazes in Oriented Polystyrene," *Polymer*, Vol. 22, May.

Hiral, H., and Satake, M., 1980, "Stress Analysis of a Penny-Shaped Crack Located Between Two Spherical Cavities in an Infinite Solid," ASME JOURNAL OF APPLIED MECHANICS, Vol. 47, p. 806.

Hsu, Y. C., and Shivakumar, V., 1976, "Interaction Between an Elastic Circular Inclusion and Two Symmetrically Placed Colinear Cracks," *Int. J. Frac. Mech.*, Vol. 12, p. 619.

Moschovidis, Z. A., and Mura, T., 1975, "Two-Ellipsoidal Inhomogeneities by the Equivalent Inclusion Method," ASME JOURNAL OF APPLIED MECHANICS, Vol. 47, p. 847.

Mura, T., 1982, *Micromechanics of Defects in Solid*, Martinus Nijhoff Publishers, Dordrecht, The Netherlands.

Sendeckyj, G. P., 1974, "Interaction of Cracks with Rigid Inclusions in Longitudinal Shear Deformation," *Int. J. Frac. Mech.*, Vol. 10, p. 45.

Sneddon, I. N., and Lowengrub, M., 1969, *Crack Problems in the Classical Theory of Elasticity*, John Wiley and Sons, New York.

Srivastava, K. N., and Mahajan, R. L., 1970, "Distribution of Stress in an Infinite Solid Containing a Spherical Cavity and an External Crack," *Indian J. Tech.*, Vol. 8, p. 398.

Tamate, O., 1960, "The Effect of a Circular Inclusion on the Stresses Around a Line Crack in a Sheet Under Tension," *Int. J. Frac. Mech.*, Vol. 4, p. 257.

Tanaka, K., and Mura, T., 1982, "A Theory of Fatigue Crack Initiation at Inclusions," *Metall. Trans.*, Vol. 13A, pp. 117–123.

Timoshenko, S. P., and Goodier, J. N., 1934, *Theory of Elasticity*, McGraw-Hill, New York.

Walton, J. R., and Weitsman, Y., 1984, "Deformations and Stress Intensities Due to a Craze in an Extended Elastic Material," ASME JOURNAL OF APPLIED MECHANICS, Vol. 51, p. 84.

Wang, T., Matsuo, M., and Kwei, T. K., 1971, "Criteria of Craze Initiation in Glassy Polymers," *J. Applied Physics*, Vol. 42, p. 4188.

Xiao, Z. M., and Pae, K. D., 1991, "The Interaction Between a Penny-Shaped Crack and a Spherical Inhomogeneity," *Acta Mechanica*, Vol. 90, pp. 91–104.

Downloaded 03 May 2010 to 171.66.16.20. Redistribution subject to ASME license or copyright; see http://www.asme.org/terms/Terms_Use.cfm

V. I. Fabrikant[1]
5525 Trent Avenue, Apt. 504,
Cote-St.-Luc, Montreal H4W 2B8,
Canada

B. S. Rubin
Department of Mathematics,
Hebrew University,
Jerusalem, Israel

E. N. Karapetian[2]
45 Brittany, Apt. 307,
T.M.R., Montreal H3P 1A3, Canada

External Circular Crack Under Normal Load: A Complete Solution

For the first time, a complete solution in terms of elementary functions is given to the problem of a transversely isotropic elastic space weakened by an external circular crack and subjected to arbitrary normal loading applied symmetrically to both crack faces. A complete field of displacements and stresses due to a concentrated loading is given for both transversely isotropic and purely isotropic cases. The method of solution is based on the results published earlier by the first author.

Introduction

The great majority of the crack problems solved deals with the stresses and displacements in the plane $z = 0$ only. There are just a few complete solutions published (Sneddon, 1951; Elliott, 1949; Westman, 1965) where explicit expressions are given for the field of displacements and stresses for the simplest axisymmetric problems (a circular punch and penny-shaped crack). The explicit expressions for the field of displacements due to an elliptic crack can be found in (Kassir and Sih, 1975). Knowledge of complete solutions is indispensable for consideration of more complicated problems of crack interactions, influence of external loads on punches and cracks, etc. By using the reciprocal theorem, many new results can be obtained, like, for example, the stress intensity factors due to an arbitrarily located force.

We present here a *complete* solution to the problem of an external circular crack in a transversely isotropic elastic space, subjected to an arbitrary normal loading. All the relevant Green's functions are given explicitly in terms of elementary functions. The interaction between an arbitrarily located force and the crack is considered by using the reciprocal theorem. The crack opening displacement and the Mode I stress intensity factor is derived in terms of elementary functions.

The case of an isotropic body weakened by an external circular crack is solved as a limiting case of the transversely isotropic one. The explicit expressions for the fields of displacements and stresses are presented. Some particular cases are given in a graphical form.

General Solution

Consider a transversely isotropic elastic body which is characterized by five elastic constants A_{ik} defining the following stress-strain relationships:

$$\sigma_x = A_{11}\frac{\partial u_x}{\partial x} + (A_{11} - 2A_{66})\frac{\partial u_y}{\partial y} + A_{13}\frac{\partial w}{\partial z},$$

$$\sigma_y = (A_{11} - 2A_{66})\frac{\partial u_x}{\partial x} + A_{11}\frac{\partial u_y}{\partial y} + A_{13}\frac{\partial w}{\partial z},$$

$$\sigma_z = A_{13}\frac{\partial u_x}{\partial x} + A_{13}\frac{\partial u_y}{\partial y} + A_{33}\frac{\partial w}{\partial z},$$

$$\tau_{xy} = A_{66}\left(\frac{\partial u_x}{\partial y} + \frac{\partial u_y}{\partial x}\right), \quad \tau_{yz} = A_{44}\left(\frac{\partial u_y}{\partial z} + \frac{\partial w}{\partial y}\right),$$

$$\tau_{zx} = A_{44}\left(\frac{\partial w}{\partial x} + \frac{\partial u_x}{\partial z}\right). \tag{1}$$

The equilibrium equations are

$$\frac{\partial \sigma_x}{\partial x} + \frac{\partial \tau_{xy}}{\partial y} + \frac{\partial \tau_{zx}}{\partial z} = 0, \quad \frac{\partial \tau_{xy}}{\partial x} + \frac{\partial \sigma_y}{\partial y} + \frac{\partial \tau_{yz}}{\partial z} = 0,$$

$$\frac{\partial \tau_{zx}}{\partial x} + \frac{\partial \tau_{yz}}{\partial y} + \frac{\partial \sigma_z}{\partial z} = 0. \tag{2}$$

Substitution of (1) in (2) yields

[1]Current address: Prisoner No. 167932D, Donnacona Correctional Facility, 1538 Rte. 138, Donnacona, Quebec G0A 1T0, Canada.

[2]Current address: Department of Mechanical Engineering, Tufts University, Medford, MA 02155.

Contributed by the Applied Mechanics Division of THE AMERICAN SOCIETY OF MECHANICAL ENGINEERS for publication in the ASME JOURNAL OF APPLIED MECHANICS.

Discussion on this paper should be addressed to the Technical Editor, Professor Lewis T. Wheeler, Department of Mechanical Engineering, University of Houston, Houston, TX 77204-4792, and will be accepted until four months after final publication of the paper itself in the ASME JOURNAL OF APPLIED MECHANICS.

Manuscript received by the ASME Applied Mechanics Division, Aug. 17, 1992; final revision, Aug. 16, 1993. Associate Technical Editor: E. F. Shih.

Copyright © 1994 by ASME
Downloaded 03 May 2010 to 171.66.16.20. Redistribution subject to ASME license or copyright; see http://www.asme.org/terms/Terms_Use.cfm

$$A_{11}\frac{\partial^2 u_x}{\partial x^2}+A_{66}\frac{\partial^2 u_x}{\partial y^2}+A_{44}\frac{\partial^2 u_x}{\partial z^2}+(A_{11}-A_{66})\frac{\partial^2 u_y}{\partial x\partial y}+(A_{13}+A_{44})\frac{\partial^2 w}{\partial x\partial z}=0,$$

$$A_{66}\frac{\partial^2 u_y}{\partial x^2}+A_{11}\frac{\partial^2 u_y}{\partial y^2}+A_{44}\frac{\partial^2 u_y}{\partial z^2}+(A_{11}-A_{66})\frac{\partial^2 u_x}{\partial x\partial y}+(A_{13}+A_{44})\frac{\partial^2 w}{\partial x\partial z}=0,$$

$$A_{44}\left[\frac{\partial^2 w}{\partial x^2}+\frac{\partial^2 w}{\partial y^2}\right]+A_{33}\frac{\partial^2 w}{\partial z^2}+(A_{44}+A_{13})\left[\frac{\partial^2 u_x}{\partial x\partial z}+\frac{\partial^2 u_y}{\partial y\partial z}\right]=0. \quad (3)$$

Introduce complex tangential displacements $u = u_x + iu_y$ and $\bar{u} = u_x - iu_y$. This will allow us to reduce the number of equations in (3) by one, and to rewrite these equations in a more compact manner, namely,

$$\frac{1}{2}(A_{11}+A_{66})\Delta u+A_{44}\frac{\partial^2 u}{\partial z^2}+\frac{1}{2}(A_{11}-A_{66})\Lambda^2\bar{u}+(A_{13}+A_{44})\Lambda\frac{\partial w}{\partial z}=0,$$

$$A_{44}\Delta w+A_{33}\frac{\partial^2 w}{\partial z^2}+\frac{1}{2}(A_{13}+A_{44})\frac{\partial}{\partial z}(\bar{\Lambda}u+\Lambda\bar{u})=0. \quad (4)$$

Here the following differential operators were used:

$$\Delta=\frac{\partial^2}{\partial x^2}+\frac{\partial^2}{\partial y^2},\quad \Lambda=\frac{\partial}{\partial x}+i\frac{\partial}{\partial y}, \quad (5)$$

and the overbar everywhere indicates the complex conjugate value. Note also that $\Delta = \Lambda\bar{\Lambda}$. One can verify that Eqs. (4) can be satisfied by

$$u=\Lambda(F_1+F_2+iF_3),\quad w=m_1\frac{\partial F_1}{\partial z}+m_2\frac{\partial F_2}{\partial z}, \quad (6)$$

where all three functions F_k satisfy the equation (Elliott, 1948)

$$\Delta F_k+\gamma_k^2\frac{\partial^2 F_k}{\partial z^2}=0,\quad \text{for } k=1, 2, 3. \quad (7)$$

Introducing the notation $z_k = z/\gamma_k$, for $k = 1, 2, 3$, we may call function $F_k = F(x, y, z_k)$ harmonic. The values of m_k and γ_k are related by the following expressions (Elliott, 1948):

$$\frac{A_{44}+m_k(A_{13}+A_{44})}{A_{11}}=\frac{m_k A_{33}}{m_k A_{44}+A_{13}+A_{44}}=\gamma_k^2,\quad \text{for } k=1, 2$$

$$\gamma_3=\left(\frac{A_{44}}{A_{66}}\right)^{1/2}. \quad (8)$$

Note the property $m_1 m_2 = 1$. The other elastic constant which will be used throughout the paper is

$$H=\frac{(\gamma_1+\gamma_2)A_{11}}{2\pi(A_{11}A_{33}-A_{13}^2)}. \quad (9)$$

Introduce the following in-plane stress components:

$$\sigma_1=\sigma_x+\sigma_y,\quad \sigma_2=\sigma_x-\sigma_y+2i\tau_{xy},\quad \tau_z=\tau_{zx}+i\tau_{yz}. \quad (10)$$

This will simplify expressions (1), namely

$$\sigma_1=(A_{11}-A_{66})(\bar{\Lambda}u+\Lambda\bar{u})+2A_{13}\frac{\partial w}{\partial z},\quad \sigma_2=2A_{66}\Lambda u,$$

$$\sigma_z=\frac{1}{2}A_{13}(\bar{\Lambda}u+\Lambda\bar{u})+A_{33}\frac{\partial w}{\partial z},\quad \tau_z=A_{44}\left(\frac{\partial u}{\partial z}+\Lambda w\right). \quad (11)$$

We have now only four components of stress, instead of six, as it was in (1). The substitution of (6) in (11) yields

$$\sigma_1=2A_{66}\frac{\partial^2}{\partial z^2}\{[\gamma_1^2-(1+m_1)\gamma_3^2]F_1+[\gamma_2^2-(1+m_2)\gamma_3^2]F_2\},$$

$$\sigma_2=2A_{66}\Lambda^2(F_1+F_2+iF_3),$$

$$\sigma_z=A_{44}\frac{\partial^2}{\partial z^2}[(1+m_1)\gamma_1^2F_1+(1+m_2)\gamma_2^2F_2]=-A_{44}\Delta[(1+m_1)F_1+(1+m_2)F_2],$$

$$\tau_z=A_{44}\Lambda\frac{\partial}{\partial z}[(1+m_1)F_1+(1+m_2)F_2+iF_3]. \quad (12)$$

Here we used the fact that each F_k satisfies Eq. (7), and the relation: $A_{11}\gamma_k^2 - A_{13}m_k = A_{44}(1 + m_k)$, (for $k = 1, 2$) which is an immediate consequence of (8). Expressions (6) and (12) give a general solution expressed in terms of three harmonic functions F_k. It is very attractive to express each function F_k through just one harmonic function as follows:

$$F_k(x, y, z)=c_k F(x, y, z_k), \quad (13)$$

where $z_k = z/\gamma_k$, and c_k is an as yet unknown complex constant. As we shall see further, this is possible indeed. All the results obtained in the paper are valid for isotropic solids, provided that we take

$$\gamma_1=\gamma_2=\gamma_3=1,\quad H=\frac{1-\nu^2}{\pi E},\quad A_{66}=A_{44}=\frac{E}{2(1+\nu)}, \quad (14)$$

where E is the elastic modulus and ν is the Poisson coefficient.

Governing Equations

A general solution to the mixed problems in terms of three harmonic functions was given in previous section. We show here that in the case of a flat crack under normal loading, the general solution can be expressed through just *one* such function. Consider a transversely isotropic elastic space weakened by a flat crack S in the plane $z = 0$, with arbitrary pressure p applied to the crack faces. Due to symmetry, the problem can be formulated as follows: find the solution to the set of differential Eqs. (3) for a half-space $z \geq 0$, subject to the mixed boundary conditions on the plane $z = 0$:

$$\sigma_z=-p(x, y),\ \text{for } (x, y)\in S;\quad w=0,\ \text{for } (x, y)\notin S;$$

$$\tau_z=0,\ \text{for } -\infty<(x, y)<\infty. \quad (15)$$

These conditions can be satisfied by a representation in terms of one harmonic function. Let us put, according to (13),

$$F_1(z)=c_1F(z_1),\quad F_2(z)=c_2F(z_2),\quad F_3(z)=0. \quad (16)$$

Expressions of the type $F_1(z)$ and $F(z_1)$, etc., everywhere in the paper should be understood as $F_1(x, y, z)$ and $F(x, y, z_1)$, respectively. The substitution of (16) and the last of expressions (12) in the third condition (15) yields

$$c_1=-c_2\gamma_1/m_1\gamma_2. \quad (17)$$

We can represent the function F as the potential of a simple layer, i.e.,

$$F(\rho, \phi, z)\equiv F(z)=\iint_S\frac{\omega(N)dS}{R(M, N)}, \quad (18)$$

where ω stands for the crack face displacement $w(x, y, 0)$, $R(M, N)$ is the distance between the points $M(\rho, \phi, z)$ and $N(r, \psi, 0)$, and the integration is taken over the crack domain S. Expression (18) satisfies the second condition (15) identically, due to the well-known property of the potential of a simple layer. Inside the crack the same property gives

$$\left.\frac{\partial F}{\partial z}\right|_{z=0}=-2\pi\omega=-2\pi w(x, y, 0). \quad (19)$$

Now expressions (16), (18), (19), and (6) give the second equation for c_1 and c_2:

Downloaded 03 May 2010 to 171.66.16.20. Redistribution subject to ASME license or copyright; see http://www.asme.org/terms/Terms_Use.cfm

$$-m_1c_1/\gamma_1 = -m_2c_2/\gamma_2 = 1/2\pi. \quad (20)$$

The constants c_1 and c_2 are determined from (17) and (20) as

$$c_1 = -\frac{\gamma_1}{2\pi(m_1-1)}, \quad c_2 = -\frac{\gamma_2}{2\pi(m_2-1)}. \quad (21)$$

The potential functions will be given by

$$F_1(z) = -\frac{\gamma_1}{2\pi(m_1-1)} F(z_1), \qquad F_2(z) = -\frac{\gamma_2}{2\pi(m_2-1)} F(z_2). \quad (22)$$

The substitution of (22) and (12) in the first condition (15) leads to the governing integral equation:

$$p(N_0) = -\frac{1}{4\pi^2 H} \Delta \iint_S \frac{\omega(N)dS}{R(N_0, N)}, \quad (23)$$

where, as before, $R(N_0, N)$ stands for the distance between two points N_0 and N, and both N_0, $N \in S$. The following identities were used:

$$m_1m_2 = 1, \quad (m_1-1)/(m_1+1) = 2\pi A_{44} H(\gamma_1-\gamma_2). \quad (24)$$

Green's Functions for an External Circular Crack

Let a be the interior radius of the crack. The exact solution of (23) can be found in Fabrikant (1989) as

$$\omega = \frac{2}{\pi} H \int_0^{2\pi} \int_a^\infty \frac{p(\rho_0, \phi_0)}{R} \tan^{-1}\left(\frac{\eta}{R}\right) \rho_0 d\rho_0 d\phi_0, \quad (25)$$

where

$$R = [\rho^2 + \rho_0^2 - 2\rho\rho_0 \cos(\phi-\phi_0)]^{1/2},$$
$$\eta = (\rho^2-a^2)^{1/2}(\rho_0^2-a^2)^{1/2}/a. \quad (26)$$

In this paper, we do not restrict our attention to the plane $z = 0$: our purpose is to obtain a *complete* solution. We shall call $F(\rho, \phi, z)$, as defined by (18), the main potential function since both functions F_1 and F_2 become easily available, when F is found. The substitution of (25) in (18) allows us to express the main potential function as follows:

$$F(\rho, \phi, z) = \frac{2}{\pi} H \int_0^{2\pi} \int_a^\infty K(\rho, \phi, z; \rho_0, \phi_0) p(\rho_0, \phi_0) \rho_0 d\rho_0 d\phi_0, \quad (27)$$

where the Green's function K reads

$$K(M, N_0) = K(\rho, \phi, z; \rho_0, \phi_0)$$
$$= \int_0^{2\pi} \int_a^\infty \frac{1}{R(N, N_0)} \tan^{-1}\left[\frac{\sqrt{r^2-a^2}\sqrt{\rho_0^2-a^2}}{aR(N, N_0)}\right] \frac{rdrd\psi}{R(M, N)}. \quad (28)$$

Here, $R(\bullet, \bullet)$ denotes the distance between respective points: $M(\rho, \phi, z)$, $N(r, \psi, 0)$, and $N_0(\rho_0, \phi_0, 0)$. Although we cannot compute the integral in (28) in elementary functions, all its derivatives can be expressed in elementary functions, due to the fundamental integrals established in Section 1.6 of Fabrikant (1989). We can write

$$\frac{\partial K}{\partial z} = -\frac{2\pi}{R(M, N_0)} \tan^{-1}\left[\frac{j}{R(M, N_0)}\right], \quad (29)$$

where

$$j = \sqrt{l_2^2-a^2}\sqrt{\rho_0^2-a^2}/a, \quad (30)$$

and the contractions l_1 and l_2 everywhere in the paper stand for $l_1(a)$ and $l_2(a)$, respectively, as they are defined by

$$l_1(t) = \frac{1}{2}\{[(\rho+t)^2+z^2]^{1/2} - [(\rho-t)^2+z^2]^{1/2}\},$$
$$l_2(t) = \frac{1}{2}\{[(\rho+t)^2+z^2]^{1/2} + [(\rho-t)^2+z^2]^{1/2}\}. \quad (31)$$

Note that j tends to η, as defined by (26), for $z \to 0$ and $\rho > a$. Expressions (27) and (29) allow us to write:

$$\frac{\partial F}{\partial z} = -4H \int_0^{2\pi} \int_a^\infty \frac{1}{R(M, N_0)} \tan^{-1}\left[\frac{j}{R(M, N_0)}\right] \times p(\rho_0, \phi_0)\rho_0 d\rho_0 d\phi_0. \quad (32)$$

The integral in (32), although looking difficult to compute even for $p = \text{const}/\rho^2$, can be expressed in elementary functions for any polynomial loading. This becomes evident, if we use the equivalent representations through the L-operator (Fabrikant, 1989):

$$\frac{\partial F}{\partial z} = -8\pi H \int_{l_1}^\rho \frac{dx}{(x^2-\rho^2)^{1/2}} \int_{g(x)}^\infty \frac{\rho_0 d\rho_0}{[\rho_0^2 - g^2(x)]^{1/2}} \times L\left(\frac{x^2}{\rho\rho_0}\right) p(\rho_0, \phi). \quad (33)$$

Here

$$g(x) = x\left[1 + \frac{z^2}{\rho^2-x^2}\right]^{1/2}. \quad (34)$$

Using the change of variables $x = l_1(t)$, $t = g(x)$, expression (33) can be rewritten as follows:

$$\frac{\partial F}{\partial z} = -8\pi H \int_a^\infty \frac{dl_1(t)}{[\rho^2 - l_1^2(t)]^{1/2}} \int_t^\infty \frac{\rho_0 d\rho_0}{(\rho_0^2-t^2)^{1/2}} \times L\left(\frac{l_1^2(t)}{\rho\rho_0}\right) p(\rho_0, \phi). \quad (35)$$

Since the function F vanishes at infinity, it can be determined from (35) in the form

$$F(\rho, \phi, z) = -8\pi H \int_\infty^z dz \int_a^\infty \frac{dl_1(t)}{[\rho^2 - l_1^2(t)]^{1/2}} \times \int_t^\infty \frac{\rho_0 d\rho_0}{(\rho_0^2-t^2)^{1/2}} L\left(\frac{l_1^2(t)}{\rho\rho_0}\right) p(\rho_0, \phi). \quad (36)$$

We can proceed now with the remaining derivatives of the Green's function K, defined by (28). Differentiation of (28) yields

$$\Lambda K(\rho, \phi, z; \rho_0, \phi_0) = -\int_0^{2\pi} \int_a^\infty \frac{\rho e^{i\phi} - re^{i\psi}}{R^3(M, N)} \times \tan^{-1}\left[\frac{\sqrt{r^2-a^2}\sqrt{\rho_0^2-a^2}}{aR(M, N_0)}\right] \frac{rdrd\psi}{R(N, N_0)}. \quad (37)$$

This integral can be computed by the following method:

$$\Lambda K = \int_\infty^z \Lambda \frac{\partial K}{\partial z} dz. \quad (38)$$

Thus we have replaced the two-dimensional integral by a one-dimensional one. The integral in (38) can be computed as indefinite, with the result

$$\int \Lambda \frac{\partial K}{\partial z} dz = \frac{2\pi}{\bar{q}} \left[\frac{z}{R_0} \tan^{-1} \frac{j}{R_0} - \frac{(\rho_0^2-a^2)^{1/2}}{\bar{s}} \tan^{-1} \frac{\bar{s}}{(a^2-l_1^2)^{1/2}}\right]. \quad (39)$$

Substituting the upper and lower limits in (39), we obtain

$$\Lambda K(\rho, \phi, z; \rho_0, \phi_0) = \frac{2\pi}{\bar{q}} \left[\frac{z}{R_0} \tan^{-1} \frac{j}{R_0} - \frac{(\rho_0^2-a^2)^{1/2}}{\bar{s}} \left(\tan^{-1} \frac{\bar{s}}{(a^2-l_1^2)^{1/2}} - \tan^{-1} \frac{\bar{s}}{a}\right) - \tan^{-1} \frac{(\rho_0^2-a^2)^{1/2}}{a}\right], \quad (40)$$

Downloaded 03 May 2010 to 171.66.16.20. Redistribution subject to ASME license or copyright; see http://www.asme.org/terms/Terms_Use.cfm

where Λ is given by (5), j is defined by (30), and

$$\bar{q}=\rho e^{-i\phi}-\rho_0 e^{-i\phi_0},\quad \bar{s}=(\rho\rho_0 e^{-i(\phi-\phi_0)}-a^2)^{1/2},$$

$$R_0=R(M, N_0)=[\rho^2+\rho_0^2-2\rho\rho_0\cos(\phi-\phi_0)+z^2]^{1/2}. \quad (41)$$

The other derivatives, which will be needed for the complete solution, are

$$\frac{\partial^2}{\partial z^2}K(\rho, \phi, z; \rho_0, \phi_0)=2\pi\left\{\frac{z}{R_0^3}\tan^{-1}\left(\frac{j}{R_0}\right)-\frac{j}{z(R_0^2+j^2)}\left[\frac{l_2^2-\rho^2}{l_2^2-l_1^2}-\frac{z^2}{R_0^2}\right]\right\}, \quad (42)$$

$$\frac{\partial}{\partial z}\Lambda K(\rho, \phi, z; \rho_0, \phi_0)=2\pi\left\{\frac{\rho e^{i\phi}-\rho_0 e^{i\phi_0}}{R_0^3}\tan^{-1}\left(\frac{j}{R_0}\right)+\frac{j}{R_0^2+j^2}\left[\frac{\rho e^{i\phi}-\rho_0 e^{i\phi_0}}{R_0^2}-\frac{\rho e^{i\phi}}{l_2^2-l_1^2}\right]\right\}, \quad (43)$$

$$\Lambda^2 K(\rho, \phi, z; \rho_0, \phi_0)=2\pi\left\{\frac{(\rho_0^2-a^2)^{1/2}}{\bar{q}\bar{s}}\left(\frac{2}{\bar{q}}+\frac{\rho_0 e^{i\phi_0}}{\bar{s}^2}\right)\times\left[\tan^{-1}\left(\frac{\bar{s}}{(a^2-l_1^2)^{1/2}}\right)-\tan^{-1}\left(\frac{\bar{s}}{a}\right)\right]-\frac{z(3R_0^2-z^2)}{\bar{q}^2R_0^3}\tan^{-1}\left(\frac{j}{R_0}\right)+\frac{(\rho_0^2-a^2)^{1/2}(a^2-l_1^2)^{1/2}\rho_0 e^{i\phi_0}}{\bar{q}\bar{s}^2[l_1^2-\rho\rho_0 e^{-i(\phi-\phi_0)}]}-\frac{zj}{R_0^2+j^2}\left[\frac{q}{\bar{q}R_0^2}-\frac{\rho^2 e^{2i\phi}}{(l_2^2-l_1^2)(\rho^2-l_1^2)}\right]+\frac{2}{\bar{q}^2}\tan^{-1}\frac{(\rho_0^2-a^2)^{1/2}}{a}+\frac{(\rho_0^2-a^2)^{1/2}a}{\bar{q}\bar{s}^2\rho e^{-i\phi}}\right\}. \quad (44)$$

This concludes the general solution to the problem of an external circular crack subjected to an arbitrary pressure. Formulae (29) and (40)–(44) are the main results of this section.

Point Force Loading of an External Circular Crack

Consider an external circular crack opened by two equal concentrated forces P applied in opposite directions at the points $(\rho_0, \phi_0, 0^{\pm})$, $\rho_0 > a$. Formulae (6), (12), (22), (29), and (40)–(44) give a complete solution for the field of displacements and stresses in elementary functions, namely,

$$u=\frac{2}{\pi}HP\left[\frac{\gamma_1}{m_1-1}f_1(z_1)+\frac{\gamma_2}{m_2-1}f_1(z_2)\right], \quad (45)$$

$$w=\frac{2}{\pi}HP\left[\frac{m_1}{m_1-1}f_2(z_1)+\frac{m_2}{m_2-1}f_2(z_2)\right], \quad (46)$$

$$\sigma_1=\frac{2P}{\pi^2(\gamma_1-\gamma_2)}\left\{\left[\frac{\gamma_1}{(m_1+1)\gamma_3^2}-\frac{1}{\gamma_1}\right]f_3(z_1)-\left[\frac{\gamma_2}{(m_2+1)\gamma_3^2}-\frac{1}{\gamma_2}\right]f_3(z_2)\right\}, \quad (47)$$

$$\sigma_2=\frac{4}{\pi}HA_{66}P\left[\frac{\gamma_1}{m_1-1}f_4(z_1)+\frac{\gamma_2}{m_2-1}f_4(z_2)\right], \quad (48)$$

$$\sigma_z=\frac{P}{\pi^2(\gamma_1-\gamma_2)}[\gamma_1 f_3(z_1)-\gamma_2 f_3(z_2)], \quad (49)$$

$$\tau_z=\frac{P}{\pi^2(\gamma_1-\gamma_2)}[f_5(z_1)-f_5(z_2)], \quad (50)$$

where

$$f_1(z)=-\frac{1}{\bar{q}}\left[\frac{z}{R_0}\tan^{-1}\frac{j}{R_0}-\frac{(\rho_0^2-a^2)^{1/2}}{\bar{s}}\times\left(\tan^{-1}\frac{\bar{s}}{(a^2-l_1^2)^{1/2}}-\tan^{-1}\frac{\bar{s}}{a}\right)-\tan^{-1}\frac{(\rho_0^2-a^2)^{1/2}}{a}\right], \quad (51)$$

$$f_2(z)=\frac{1}{R_0}\tan^{-1}\left(\frac{j}{R_0}\right), \quad (52)$$

$$f_3(z)=-\frac{z}{R_0^3}\tan^{-1}\left(\frac{j}{R_0}\right)+\frac{j}{z(R_0^2+j^2)}\left[\frac{l_2^2-\rho^2}{l_2^2-l_1^2}-\frac{z^2}{R_0^2}\right], \quad (53)$$

$$f_4(z)=-\left\{\frac{(\rho_0^2-a^2)^{1/2}}{\bar{q}\bar{s}}\left(\frac{2}{\bar{q}}+\frac{\rho_0 e^{i\phi_0}}{\bar{s}^2}\right)\times\left[\tan^{-1}\left(\frac{\bar{s}}{(a^2-l_1^2)^{1/2}}\right)-\tan^{-1}\left(\frac{\bar{s}}{a}\right)\right]-\frac{z(3R_0^2-z^2)}{\bar{q}^2R_0^3}\tan^{-1}\left(\frac{j}{R_0}\right)+\frac{(\rho_0^2-a^2)^{1/2}(a^2-l_1^2)^{1/2}\rho_0 e^{i\phi_0}}{\bar{q}\bar{s}^2[l_1^2-\rho\rho_0 e^{-i(\phi-\phi_0)}]}-\frac{zj}{R_0^2+j^2}\left[\frac{q}{\bar{q}R_0^2}-\frac{\rho^2 e^{2i\phi}}{(l_2^2-l_1^2)(\rho^2-l_1^2)}\right]+\frac{2}{\bar{q}^2}\tan^{-1}\frac{(\rho_0^2-a^2)^{1/2}}{a}+\frac{(\rho_0^2-a^2)^{1/2}a}{\bar{q}\bar{s}^2\rho e^{-i\phi}}\right\}, \quad (54)$$

$$f_5(z)=-\left\{\frac{\rho e^{i\phi}-\rho_0 e^{i\phi_0}}{R_0^3}\tan^{-1}\left(\frac{j}{R_0}\right)+\frac{j}{R_0^2+j^2}\left[\frac{\rho e^{i\phi}-\rho_0 e^{i\phi_0}}{R_0^2}-\frac{\rho e^{i\phi}}{l_2^2-l_1^2}\right]\right\}. \quad (55)$$

It is reminded that $R_0 = [\rho^2 + \rho_0^2 - 2\rho\rho_0 \cos(\phi - \phi_0) + z^2]^{1/2}$. The expression (49) for σ_z simplifies when $z = 0$ and $\rho < a$, namely,

$$\sigma_z=\frac{P}{\pi^2}\frac{(\rho_0^2-a^2)^{1/2}}{(a^2-\rho^2)^{1/2}[\rho^2+\rho_0^2-2\rho\rho_0\cos(\phi-\phi_0)]}. \quad (56)$$

Defining the stress intensity factor

$$k_1=\lim_{\rho\to a}[(a-\rho)^{1/2}\sigma_z],$$

the following result may be obtained from (56):

$$k_1=\frac{P}{\pi^2(2a)^{1/2}}\frac{(\rho_0^2-a^2)^{1/2}}{a^2+\rho_0^2-2a\rho_0\cos(\phi-\phi_0)}. \quad (57)$$

One can write for an arbitrarily distributed pressure

$$k_1=\frac{1}{\pi^2(2a)^{1/2}}\int_0^{2\pi}\int_a^{\infty}\frac{(\rho_0^2-a^2)^{1/2}p(\rho_0, \phi_0)\rho_0 d\rho_0 d\phi_0}{a^2+\rho_0^2-2a\rho_0\cos(\phi-\phi_0)},$$

which corresponds to the well-known result (Cherepanov, 1974).

Concentrated Load Outside a Circular Crack

Consider a tranversely isotropic space weakened by an external circular crack of radius a in the plane $z = 0$. Let a concentrated force P be applied at an arbitrary point (ρ, ϕ, z) in the Oz direction. The crack faces are stress-free. Let us find the crack-opening displacement and the opening mode stress intensity factor k_1.

Consider the second system in equilibrium: two unit concentrated forces Q applied normally to the crack faces in opposite directions at the points $(\rho_0, \phi_0, 0^{\pm})$. Denote the normal displacement in the space due to the forces Q by w_Q, while w_P is the crack opening displacement due to force P. Note that the term "crack-opening displacement" is used here to denote the difference between the normal displacements of the crack

Downloaded 03 May 2010 to 171.66.16.20. Redistribution subject to ASME license or copyright; see http://www.asme.org/terms/Terms_Use.cfm

faces. Application of the reciprocal theorem to the two systems yields

$$Qw_P = Pw_Q$$

which gives the crack-opening displacement

$$w_P(\rho_0, \phi_0) = \frac{2}{\pi} HP\left[\frac{m_1}{m_1-1} f_2(z_1) + \frac{m_2}{m_2-1} f_2(z_2)\right], \quad (58)$$

with f_2 defined by (52). The stress intensity factor can be determined by

$$k_1(\phi_0) = \frac{1}{8\pi H} \lim_{\rho_0 \to a} \frac{w_P(\rho_0, \phi_0)}{(a-\rho_0)^{1/2}} = \frac{P}{2(2a)^{1/2}\pi^2}\left[\frac{m_1}{m_1-1} f_6(z_1) + \frac{m_2}{m_2-1} f_6(z_2)\right],$$

where

$$f_6(z) = (l_2^2 - a^2)^{1/2}/r_a^2, \quad r_a^2 = \rho^2 + a^2 - 2\rho a \cos(\phi - \phi_0) + z^2. \quad (59)$$

The stress intensity factor vanishes as z tends to zero for $\rho \le a$.

In the case of an isotropic body, expression (58) transforms into

$$w_P(\rho_0, \phi_0) = \frac{P}{\pi^2 \mu}\left\{\frac{1-\nu}{R_0}\tan^{-1}\left(\frac{j}{R_0}\right) - \frac{1}{2}\left[\frac{j}{R_0^2 + j^2}\left(\frac{l_2^2-\rho^2}{l_2^2-l_1^2} - \frac{z^2}{R_0^2}\right) - \frac{z^2}{R_0^3}\tan^{-1}\left(\frac{j}{R_0}\right)\right]\right\}. \quad (60)$$

Here μ is the shear modulus, and ν is Poisson's ratio.

Solution for an Isotropic Body

The case of an isotropic body can be obtained as a limiting case of transversely isotropic solution, subject to the conditions in (14). The limits were computed according to the L'Hospital rule. The following scheme was used:

$$\lim_{\gamma_1 \to \gamma_2 \to 1} \sum_{k=1}^{2} \frac{\gamma_k}{m_k - 1} f(z_k) = -\frac{(1-2\nu)f(z) + zf'(z)}{2(1-\nu)}, \quad (61)$$

$$\lim_{\gamma_1 \to \gamma_2 \to 1} \sum_{k=1}^{2} \frac{m_k}{(m_k-1)} f(z_k) = \frac{2(1-\nu)f(z) - zf'(z)}{2(1-\nu)}, \quad (62)$$

$$\lim_{\gamma_1 \to \gamma_2 \to 1} \frac{1}{\gamma_1 - \gamma_2} \sum_{k=1}^{2} (-1)^{k+1}\left[\frac{\gamma_k}{\gamma_3^2(m_k+1)} - \frac{1}{\gamma_k}\right] f(z_k) = \frac{1}{2}[(1+2\nu)f(z) + zf'(z)], \quad (63)$$

$$\lim_{\gamma_1 \to \gamma_2 \to 1} \frac{1}{\gamma_1 - \gamma_2} \sum_{k=1}^{2} (-1)^{k+1}\gamma_k f(z_k) = f(z) - zf'(z), \quad (64)$$

$$\lim_{\gamma_1 \to \gamma_2 \to 1} \frac{1}{\gamma_1 - \gamma_2} \sum_{k=1}^{2} (-1)^{k+1} f(z_k) = -zf'(z). \quad (65)$$

Here the following relationships were used:

$$\lim_{\gamma_1 \to \gamma_2 \to 1} m_1 = 1, \quad \lim_{\gamma_1 \to \gamma_2 \to 1}\left[\frac{\partial m_1}{\partial \gamma_1}\right] = 2(1-\nu), \quad (66)$$

and the symbol ($'$) indicates differentiation with respect to z.

In the case of an isotropic body, formulae (45)–(55) transform into

$$u = \frac{P(1+\nu)}{\pi^2 E}\left\{(1-2\nu)\frac{1}{\bar{q}}\left[\frac{z}{R_0}\tan^{-1}\frac{j}{R_0} - \tan^{-1}\frac{(\rho_0^2-a^2)^{1/2}}{a} - \frac{(\rho_0^2-a^2)^{1/2}}{\bar{s}}\left(\tan^{-1}\frac{\bar{s}}{(\alpha^2-l_1^2)^{1/2}} - \tan^{-1}\frac{\bar{s}}{\alpha}\right)\right]\right.$$
$$\left. + \frac{z}{\bar{q}}\left[\frac{R_0^2-z^2}{R_0^3}\tan^{-1}\frac{j}{R_0} + \frac{j}{R_0^2+j^2}\left(\frac{l_2^2-\rho^2}{l_2^2-l_1^2} - \frac{z^2}{R_0^2}\right) - \frac{l_1(\rho_0^2-a^2)^{1/2}(\rho^2-l_1^2)^{1/2}}{(l_1^2 - \rho\rho_0 e^{-i(\phi-\phi_0)})(l_2^2-l_1^2)}\right]\right\}, \quad (67)$$

$$w = \frac{P(1+\nu)}{\pi^2 E}\left\{\left[\frac{2(1-\nu)}{R_0} + \frac{z^2}{R_0^3}\right]\tan^{-1}\frac{j}{\bar{R}_0} - \frac{j}{R_0^2+j^2}\left(\frac{l_2^2-\rho^2}{l_2^2-l_1^2} - \frac{z^2}{R_0^2}\right)\right\}, \quad (68)$$

$$\sigma_1 = -\frac{P}{\pi^2}\left\{(1+2\nu)\left[\frac{z}{R_0^3}\tan^{-1}\frac{j}{R_0} - \frac{j}{z(R_0^2+j^2)}\left(\frac{l_2^2-\rho^2}{l_2^2-l_1^2} - \frac{z^2}{R_0^2}\right)\right]\right.$$
$$+ z\left[\frac{R_0^2-3z^2}{R_0^5}\tan^{-1}\frac{j}{\bar{R}_0} + \frac{j}{R_0^2(R_0^2+j^2)}\left(\frac{2(l_2^2-\rho^2)}{l_2^2-l_1^2} - \frac{3z^2}{R_0^2} + 1\right)\right.$$
$$- \frac{j\rho^2}{(R_0^2+j^2)(l_2^2-l_1^2)^2}\left(\frac{2(\rho^2+z^2-a^2)}{l_2^2-l_1^2} - 1\right)$$
$$\left.\left. + \frac{2j^3}{z^2(R_0^2+j^2)^2}\left(\frac{l_2^2-\rho^2}{l_2^2-l_1^2} + \frac{z^2}{j^2}\right)\left(\frac{l_2^2-\rho^2}{l_2^2-l_1^2} - \frac{z^2}{R_0^2}\right)\right]\right\}, \quad (69)$$

$$\sigma_2 = \frac{P}{\pi^2}\left\{(1-2\nu)\left[\frac{(\rho_0^2-a^2)^{1/2}}{\bar{q}\bar{s}}\left(\frac{2}{\bar{q}} + \frac{\rho_0 e^{i\phi_0}}{\bar{s}^2}\right)\right.\right.$$
$$\times\left(\tan^{-1}\frac{\bar{s}}{(a^2-l_1^2)^{1/2}} - \tan^{-1}\frac{\bar{s}}{a}\right) - \frac{z(3R_0^2-z^2)}{\bar{q}^2 R_0^3}\tan^{-1}\frac{j}{R_0}$$
$$+ \frac{2}{\bar{q}^2}\tan^{-1}\frac{(\rho_0^2-a^2)^{1/2}}{a} + \frac{(\rho_0^2-a^2)^{1/2}(a^2-l_1^2)^{1/2}\rho_0 e^{i\phi_0}}{\bar{q}\bar{s}^2(l_1^2 - \rho\rho_0 e^{-i(\phi-\phi_0)})}$$
$$\left. - \frac{zj}{R_0^2+j^2}\left(\frac{q}{\bar{q}R_0^2} - \frac{\rho^2 e^{2i\phi_0}}{(l_2^2-l_1^2)(\rho^2-l_1^2)}\right) + \frac{(\rho_0^2-a^2)^{1/2}a}{\bar{q}\bar{s}^2\rho e^{-i\phi}}\right]$$
$$+ z\left[\frac{(\rho_0^2-a^2)^{1/2}}{\bar{q}}\left(\frac{2}{\bar{q}} - \frac{2\rho_0 e^{i\phi_0}}{l_1^2 - \rho\rho_0 e^{-i(\phi-\phi_0)}}\right)\right.$$
$$\times\frac{l_1(\rho^2-l_1^2)^{1/2}}{(l_1^2 - \rho\rho_0 e^{-i(\phi-\phi_0)})(l_2^2-l_1^2)}$$
$$- \frac{3(R_0^2-z^2)^2}{\bar{q}^2 R_0^5}\tan^{-1}\frac{j}{R_0} - \frac{j}{R_0^2+j^2}\left(\frac{4R_0^2-2z^2}{\bar{q}^2R_0^2}\left(\frac{l_2^2-\rho^2}{l_2^2-l_1^2} - \frac{z^2}{R_0^2}\right)\right.$$
$$+ \frac{(R_0^2-z^2)^2}{\bar{q}^2R_0^4} - \frac{\rho^2 e^{2i\phi}}{(l_2^2-l_1^2)^2} + \frac{4l_1^2(l_2^2-\rho^2)e^{2i\phi}}{(l_2^2-l_1^2)^3}\Big)$$
$$\left.\left. + \frac{2j^3}{(R_0^2+j^2)^2}\left(\frac{l_2^2-\rho^2}{l_2^2-l_1^2} + \frac{z^2}{j^2}\right)\left(\frac{q}{\bar{q}R_0^2} - \frac{\rho^2 e^{2i\phi}}{(l_2^2-l_1^2)(\rho^2-l_1^2)}\right)\right]\right\}, \quad (70)$$

$$\sigma_z = -\frac{P}{\pi^2}\left\{\frac{z}{R_0^3}\tan^{-1}\frac{j}{R_0} - \frac{j}{z(R_0^2+j^2)}\left(\frac{l_2^2-\rho^2}{l_2^2-l_1^2} - \frac{z^2}{R_0^2}\right)\right.$$
$$- z\left[\frac{R_0^2-3z^2}{R_0^5}\tan^{-1}\frac{j}{R_0} + \frac{j}{R_0^2(R_0^2+j^2)}\left(\frac{2(l_2^2-\rho^2)}{l_2^2-l_1^2} - \frac{3z^2}{R_0^2} + 1\right)\right.$$
$$- \frac{j\rho^2}{(R_0^2+j^2)(l_2^2-l_1^2)^2}\left(\frac{2(\rho^2+z^2-a^2)}{l_2^2-l_1^2} - 1\right)$$
$$\left.\left. + \frac{2j^3}{z^2(R_0^2+j^2)^2}\left(\frac{l_2^2-\rho^2}{l_2^2-l_1^2} + \frac{z^2}{j^2}\right)\left(\frac{l_2^2-\rho^2}{l_2^2-l_1^2} - \frac{z^2}{R_0^2}\right)\right]\right\}, \quad (71)$$

Downloaded 03 May 2010 to 171.66.16.20. Redistribution subject to ASME license or copyright; see http://www.asme.org/terms/Terms_Use.cfm

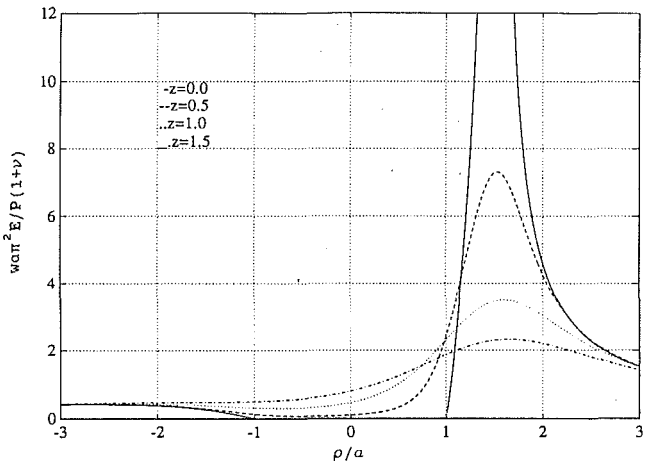


Fig. 1 Normal displacement distribution in an isotropic body

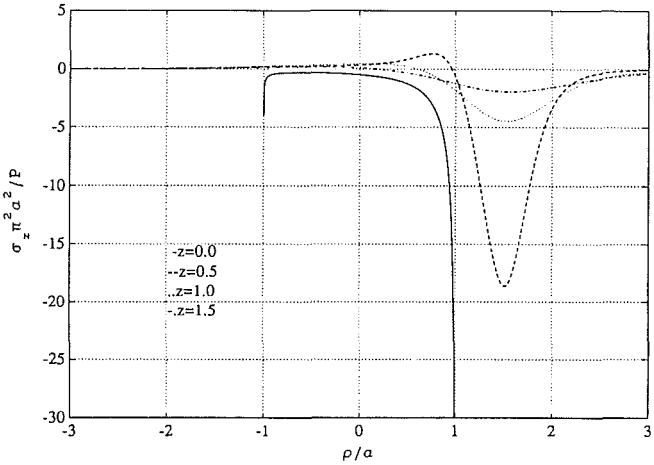


Fig. 2 Normal stress distribution in an isotropic body

$$\tau_z = \frac{P}{\pi^2}\left\{\frac{jq}{R_0^2(R_0^2+j^2)}\left[\frac{2(l_2^2-\rho^2)}{l_2^2-l_1^2}-\frac{3z^2}{R_0^2}\right]\right.$$
$$-\frac{2j^3}{(R_0^2+j^2)^2}\left[\frac{l_2^2-\rho^2}{l_2^2-l_1^2}+\frac{z^2}{j^2}\right]\left(\frac{q}{R_0^2}-\frac{\rho e^{i\phi}}{l_2^2-l_1^2}\right)$$
$$\left.-\frac{j\rho e^{i\phi}}{R_0^2+j^2}\left[\frac{l_2^2-\rho^2}{(l_2^2-l_1^2)^2}-\frac{2z^2(l_1^2+l_2^2)}{(l_2^2-l_1^2)^3}\right]-\frac{3z^2q}{R_0^5}\tan^{-1}\frac{j}{R_0}\right\}. \quad (72)$$

Numerical computations were performed for the field of normal displacements and normal stresses, with the Poisson coefficient $\nu = 0.2$. The field of normal displacements due to a pair of concentrated forces applied at the crack faces in opposite direction at the points $(1.5a, 0, 0^+)$ and $(1.5a, 0, 0^-)$, is given in Fig. 1 as a function of ρ/a for a set of different values of z. Similar data for the normal stresses are presented in Fig. 2.

Acknowledgment

The reported research was supported by a grant from the Natural Sciences and Engineering Research Council of Canada. The second author was supported in part by the National Council of Israel (Grant No. 032-7251).

References

Cherepanov, G. P., 1974, *Mechanics of Brittle Fracture*, Nauka, Moscow (English translation: McGraw-Hill, 1979).

Elliott, H. A., 1948, "Three-Dimensional Stress Distribution in Hexagonal Aeolotropic Crystals," *Proceedings of the Cambridge Philosophical Society*, Vol. 44, pp. 522–533.

Elliott, H. A., 1949, "Axial Symmetric Stress Distributions in Aeolotropic Hexagonal Crystals: The Problem of the Plane and Related Problems," *Proceedings of the Cambridge Philosophical Society*, Vol. 45, pp. 621–630.

Fabrikant, V. I., 1989, *Applications of Potential Theory in Mechanics: Selection of New Results*, Kluwer Academic, Dordrecht, The Netherlands.

Kassir, M. K., and Sih, G. C., 1975, *Three-Dimensional Crack Problems*, Vol. 2 (Mechanics of Fracture), Noordhoff International Publishing, Leyden.

Sneddon, I. N., 1951, *Fourier Transforms*, McGraw-Hill, New York.

Westmann, R. A., 1965, "Asymmetric Mixed Boundary-Value Problem of the Elastic Half-Space," ASME JOURNAL OF APPLIED MECHANICS, Vol. 32, pp. 411–417.

Downloaded 03 May 2010 to 171.66.16.20. Redistribution subject to ASME license or copyright; see http://www.asme.org/terms/Terms_Use.cfm

Z. K. Guo
Predoctoral Research Associate II.

A. S. Kobayashi
Professor,
Fellow ASME.

Department of Mechanical Engineering,
University of Washington,
Seattle, WA 98195

N. M. Hawkins
Professor and Head,
Department of Civil Engineering,
University of Illinois at Urbana-Champaign,
Champaign, IL 61820-6219

Mixed Modes I and II Concrete Fracture: An Experimental Analysis

The development of the fracture process zone associated with subcritical crack growth in a three-point bend concrete specimen with an off-centered, single-edged precrack was monitored with moire interferometry. The applied load and the crack opening and sliding displacements together with a finite element model of the concrete specimen were used to determine the crack closing stress due to aggregate bridging. Under this mixed-mode fracture, aggregate interlocking increased the crack closing stresses in the fracture process zone and hence the load carrying capacity of the concrete specimen. The dissipated energy rate in the fracture process zone also increased with aggregate interlocking.

1 Introduction

While it may be argued that mixed mode, i.e. combined modes I and II, crack extension is not possible in brittle metals and polymers, aggregate bridging and interlocking forces in a fracturing concrete structure could influence the otherwise dominant mode I crack-tip state of stress and could result in a mixed-mode crack extension. For example, Swartz et al. (1988) measured the average total fracture energy under mixed-mode concrete fracture and showed that it was "eight to ten times those obtained for mode I tests of the same size concrete beam." Jenq and Shah (1988, 1989) compared the theoretically predicted failure angles using maximum circumferential stress, maximum energy release rate, and minimum strain energy density criteria, all of which are based on linear elastic fracture mechanics with those measured experimentally in three-point bend and four-point shear mixed-mode tests of concrete fracture specimens and concluded that the differences between the failure angles predicted by these three criteria were indistinguishable. Linear elastic fracture mechanics with modification was also used by Davies (1989) to study shear fracture of symmetrically notched mortar cubes and by Wong and Miller (1989) to study mixed-mode fracture of early-aged concrete beam specimens. Their results showed that mode I crack propagation prevailed in those concrete fracture specimens which were otherwise loaded in mixed modes I and II condition. Using mixed-mode fracture tests of double-edge notched concrete specimens, Nooru-Mohamed and van Mier (1989) observed shear softening thus contradicting Walraven (1981) and Reinhardt and Walraven (1982) who reported increased interface shear with increased interface slip in concrete.

Recent studies using displacement-controlled double-edge notched specimens by Hillerborg (1989) and Hassanzadeh (1991) showed increased interface shear stress with increased interface slip which varied with the applied normal versus shear displacement relations. In a particular linear loading relation between the applied normal and shear displacements, the interface shear stress initially increased and then decreased with increasing interface slip, thus showing the highly load-path dependence of the interface shear stress versus slip relation. Nooru-Mohamed also showed that the failure modes in double-edge notched fracture specimen subjected to mixed-mode loading is load path-dependent and therefore the interface shear stress versus interface slip could not be a material property.

In all of the foregoing studies, the starter crack was a machined notch which was subjected to either pure mode I or mixed modes I and II loading. Aggregate bridging and interlocking in the fracture process zone, which trails the natural crack tip, would only be possible with crack growth from the machined notch tip. Without the influence of the fracture process zone, the crack would otherwise propagate under the dominant influence of the mode I crack-tip stress field as shown by Liaw et al. (1990).

The most common mixed-mode fracture in concrete structures is the diagonal tension failure of a reinforced concrete beam. That cracking usually develops from flexural cracks generated by fracture along the tension edge of the beam. Those initial cracks extend perpendicularly from the edge of the beam, with their depths depending on the applied moments, and then kinks only after extending beyond the reinforcement. Since aggregate bridging and interlocking exist in these crack prior to kinking, the kinking angle as well as the

Contributed by the Applied Mechanics Division of THE AMERICAN SOCIETY OF MECHANICAL ENGINEERS for publication in the ASME JOURNAL OF APPLIED MECHANICS.

Discussion on this paper should be addressed to the Technical Editor, Professor Lewis T. Wheeler, Department of Mechanical Engineering, University of Houston, Houston, TX 77204-4792, and will be accepted until four months after final publication of the paper itself in the ASME JOURNAL OF APPLIED MECHANICS.

Manuscript received by the ASME Applied Mechanics Division, Sept. 14, 1992; final revision, Sept. 7, 1993. Associate Technical Editor: W. N. Sharpe, Jr.

Copyright © 1994 by ASME
Downloaded 03 May 2010 to 171.66.16.20. Redistribution subject to ASME license or copyright; see http://www.asme.org/terms/Terms_Use.cfm

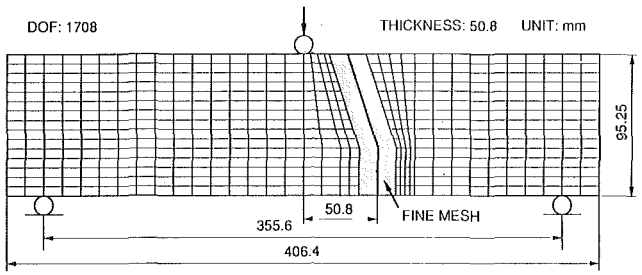


Fig. 1 Finite element method model of concrete specimen

subsequent crack extension could be influenced by the resultant interfacial crack closing and shearing forces.

The purpose of this study was to quantify the bridging and the interlocking forces in the fracture process zone trailing a stably growing crack in plain concrete beam specimens under offset loading conditions.

2 Experimental Procedure

2.1 Specimen. The dimensions of the three-point bend specimens, which were used in this study, are shown in Fig. 1. Five specimens were made using steel molds and a high early strength Portland cement, a rounded glacial outwash aggregate of 6.4 mm maximum size and sand, both of which were obtained locally. The concrete strength at the time of the test, as determined from the tests on 150 × 300 mm cylinders, was 48 MPa. A shallow notch of 0.3-mm width and 19-mm depth was machined in the bottom of the specimen. An orthogonal moire diffraction grating of 600 lines/mm was attached to the specimen using the Post procedure (1993). The specimen, with the machined crack centrally located, was then subjected to symmetric mode I loading in the moire interferometry setup and the crack was extended about an additional 12.7 mm by stable crack growth.

2.2 Test Procedure. Mixed-mode loading was then applied by rearranging the loading points so that the notch was offset from the central loading point by 50.8 mm. While this loading arrangement provide a simple modeling of diagonal tension fracture of concrete beams, it does not provide the flexibility of imposing varying load plots, such as those used by Hillerborg (1989), Hassanzadeh (1991), and Nooru-Mohamed (1992). The test procedure consisted of applying an incrementally increased load-point displacement, photographing the moire fringes and recording the applied load and displacements. Figure 2 shows the four-beam moire interferometry setup used to record the horizontal, u_x, and the vertical, u_y, displacements in a 95 × 95 mm area surrounding the stably growing crack. The reflected first-order diffraction from the oblique incident light of 18 deg provided a fringe multiplication of two and thus an effective sensitivity of 1200 lines/mm was achieved in this optical setup. The crack-opening and crack sliding displacements, along the slanted crack were computed from the moire patterns related to the horizontal and vertical displacements. Load-point displacements were increased until the microcrack tip, which was located using the moire fringe pattern, had almost penetrated through the depth of the specimen.

3 Numerical Analysis

A hybrid experimental-numerical procedure was used to quantify the resultant surface tractions acting in the fracture process zone and to determine the resistance curves, i.e., variations in K_{IR} and K_{IIR} with stable crack growth. Figure 1 shows a typical finite element model of the concrete specimen and its kinked crack. The entire specimen had to

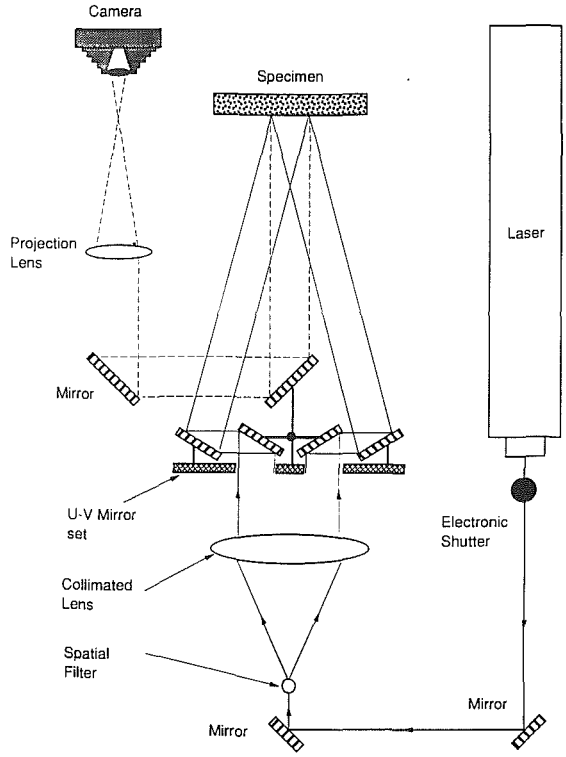


Fig. 2 Moire interferometry setup for concrete fracture test

be modeled for this mixed-mode fracture analysis, as in the analysis by Liaw et al. (1990), due to the lack of symmetry in the loading geometry. Since the boundary conditions were completely prescribed from the experimental data, the solution to this finite element method boundary value problem should have provided the desired answers directly as in the analysis by Guo et al. (1993). In practice, the relative displacement field obtained from the finite-sized moire grating did not provide the absolute displacements which had to be prescribed along the finite element method model of the kinked crack. Thus the time-consuming inverse analysis (Liaw, 1990; Yon et al., 1991) was used in this study.

The numerical procedure consisted of determining the crack closing stress due to aggregate bridging and the crack shearing stress due to aggregate interlocking under a prescribed load. This analysis was initiated with the crack closing stress versus crack opening displacement relation of Guo et al. (1993), to which a similar crack shearing stress versus crack sliding displacement relation was adjoined, and then prescribing the appropriate normal and tangential nodal forces corresponding to the crack opening displacement and crack sliding displacement computed from the measured u_x and u_y, respectively, along the fracture process zone. The length of this fracture process zone is governed by the maximum crack opening displacement in the crack closing stress versus crack opening displacement relation used. Through a trial and error process, the computed u_x and u_y displacements during the kinked crack extension were matched with their measured counterparts. Reinhardt et al. (1987) had suggested that the resultant crack closing stress versus crack opening displacement and the crack closing stress versus crack sliding displacement relations could be interrelated and thus one of our objectives was to quantify this interrelation. The sum of the work done by the crack closing stress acting on the crack opening displacement and the crack shearing stress acting on the crack sliding displacement for unit crack extension represents the energy dissipation rate in the fracture process zone. The energy release

Downloaded 03 May 2010 to 171.66.16.20. Redistribution subject to ASME license or copyright; see http://www.asme.org/terms/Terms_Use.cfm

rate was computed directly by incrementing the crack-tip one finite element node and then computing the difference in release energies in the specimen prior to, and after, that incremental crack extension.

The modes I and II stress intensity factors, K_I and K_{II}, were computed from the energy release rate and the crack-tip, crack opening displacement and crack sliding displacement. These K_I and K_{II} are the resultant stress intensity factors which incorporate the surface tractions, i.e., crack closing stress and crack shearing stress, acting on the crack surface in the FPZ. First, the finite element model was numerically calibrated for accurate stress intensity factor determination by using known K_I and K_{II} solutions. Then the energy release rate, G, was obtained from the finite element analysis of the fracture specimen with the prescribed crack closing stress and crack shearing stress in the fracture process zone. This total G is related to the K_I and the K_{II} in the presence of the fracture process zone by

$$\frac{K_I^2(1-\nu^2)}{E} + \frac{K_{II}^2(1-\nu^2)}{E} = G \tag{1}$$

where E and ν are the modulus of elasticity and Poisson ratio, respectively.

K_I and K_{II} are also related to the crack-tip crack opening displacement and crack sliding displacement at the node adjacent to the crack tip through

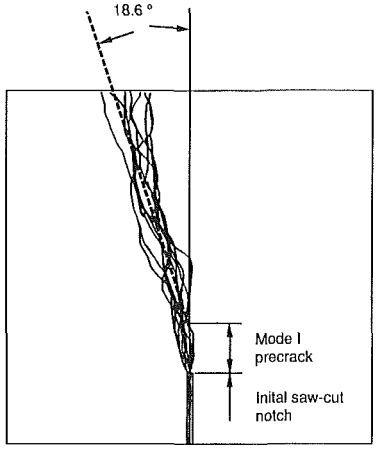


Fig. 3 Kinked crack paths in five concrete fracture specimens

$$\frac{K_I}{K_{II}} = \frac{\text{crack opening displacement}}{\text{crack sliding displacement}}. \tag{2}$$

These two equations were used to compute the resistance curves for K_I and K_{II} or the changes in K_I and K_{II} with stable crack growth.

4 Results

4.1 Experimental Results. A total of five concrete specimens were tested for stable crack growth under mixed-mode fracture. The kinked crack paths for these specimens are shown in Fig. 3. The undulations in the crack paths, which is not normally observed in metal fracture specimens, are caused by the aggregates dispersed throughout the thickness of the specimen. For the same reason, a difference of about one aggregate diameter was observed between the crack paths on the front and the back surfaces of the specimen. For finite element method modeling, the averaged crack paths, as indicated by the broken line in Fig. 3, was used in the numerical analysis.

Figure 4 shows the averaged measured load versus computed load-line displacement relations for all five specimens. It was necessary to use the computed rather than the measured load-line displacements since the latter, which was recorded on one side of the specimen only, did not represent the actual deflections due to uneven local crushing along the load line through the thickness of the specimen.

Figure 5 shows a typical pair of moire interferometry patterns corresponding to the horizontal and vertical displacement fields of u_x and u_y, respectively, of a kinked crack in a three-point bend specimen. Figure 6 is a composite figure showing the averaged u_x and the averaged u_y variations along the initial and the kinked crack with increasing crack extension. The u_x and the u_y are plotted in terms of the averaged distance measured along the vertical and kinked crack paths. The circles in this figure are the averaged displacements obtained from moire interferometry and the continuous curves are computed results obtained from finite element method modeling.

4.2 Numerical Results. Figure 7 shows the crack closing stress versus crack opening displacement relation which provided the best fit between the measured and the computed u_x and u_y. Also shown is the crack closing stress versus crack

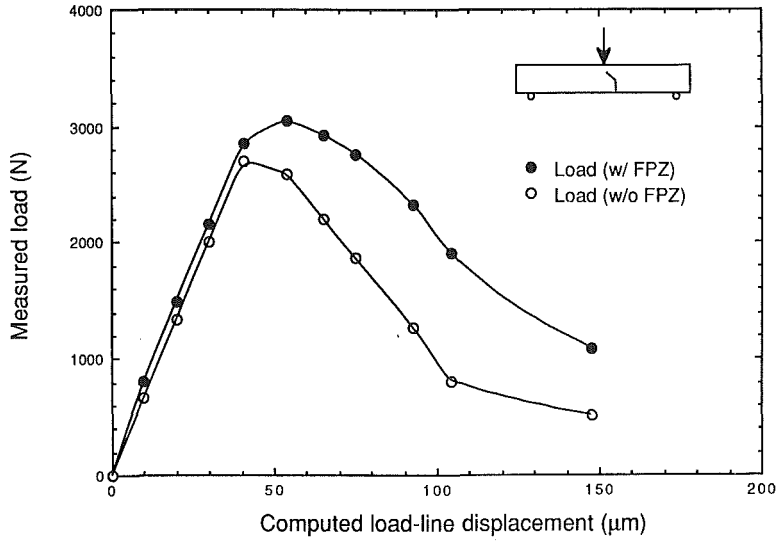


Fig. 4 Averaged load and displacement variations with kinked crack extension

Downloaded 03 May 2010 to 171.66.16.20. Redistribution subject to ASME license or copyright; see http://www.asme.org/terms/Terms_Use.cfm

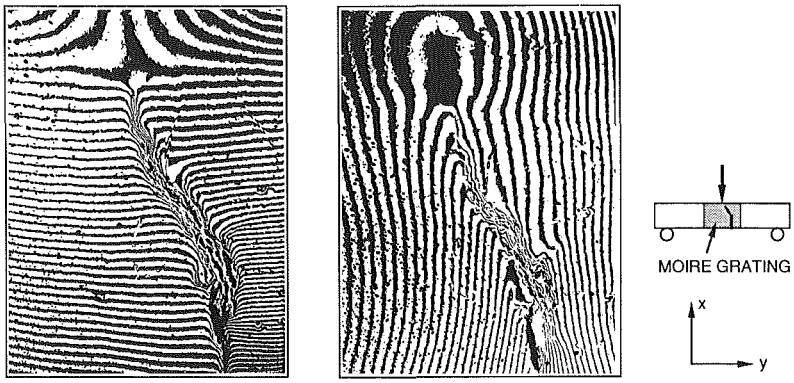


Fig. 5 Typical u_x- and u_y-moire patterns

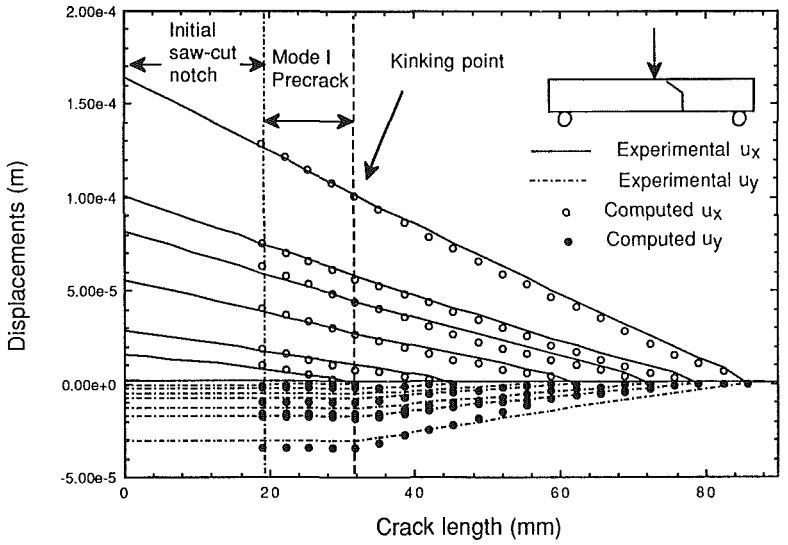


Fig. 6 Measured and computed u_x and u_y displacements

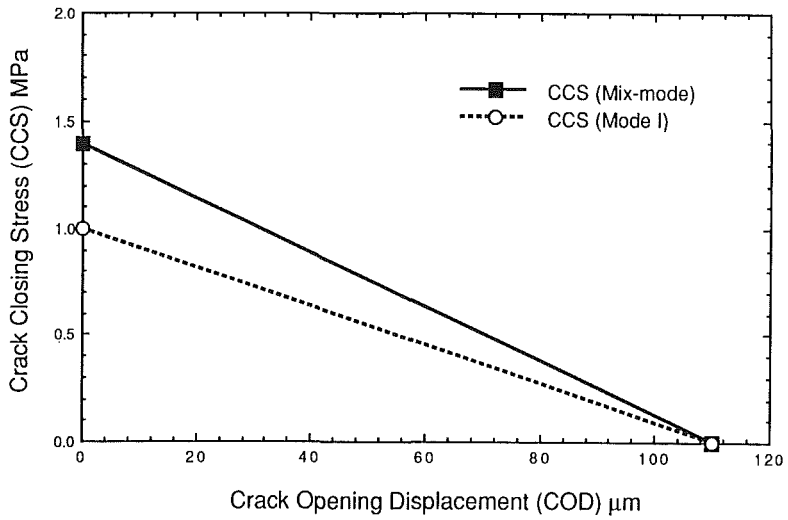


Fig. 7 Constitutive relations governing the fracture pressure zone

opening displacement relation obtained from identical concrete fracture specimens which were tested under mode I loading. The crack closing stress increased under mixed-mode loading condition. It thus appears that there is an additional friction generated by the interlocking force which affected the crack closing stress versus crack opening displacement relation through an increased crack closing stress. The linear crack closing stress versus crack opening displacement relation, which provided the best fit between the numerical and the experimental u_x and u_y, differs with the trilinear relation obtained by Liaw et al. (1990) for a nonsingular fracture model. The present model is based on linear elastic fracture mechanics and thus characterizes concrete fracture with a single parameter, i.e., the stress intensity factor, with the attendant fracture process zone.

Conspicuously missing from Fig. 7 is the associated crack

Downloaded 03 May 2010 to 171.66.16.20. Redistribution subject to ASME license or copyright; see http://www.asme.org/terms/Terms_Use.cfm

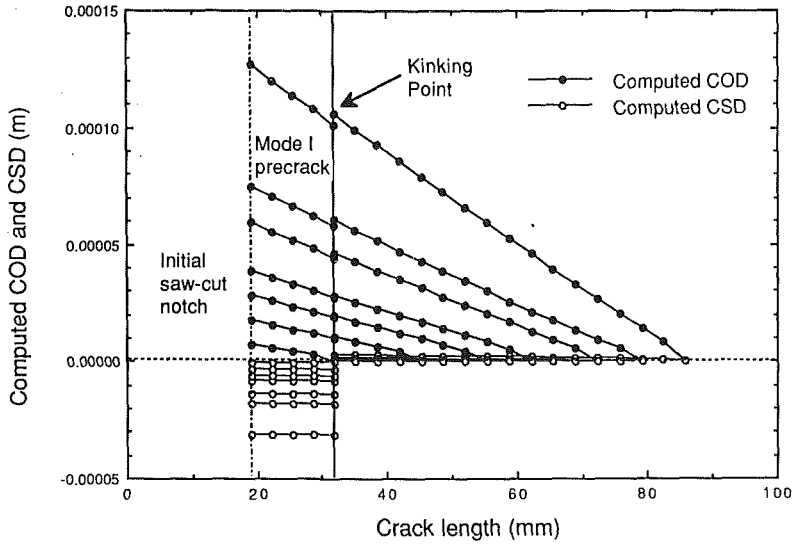


Fig. 8 Computed crack opening displacement (COD) and crack sliding displacement (CSD)

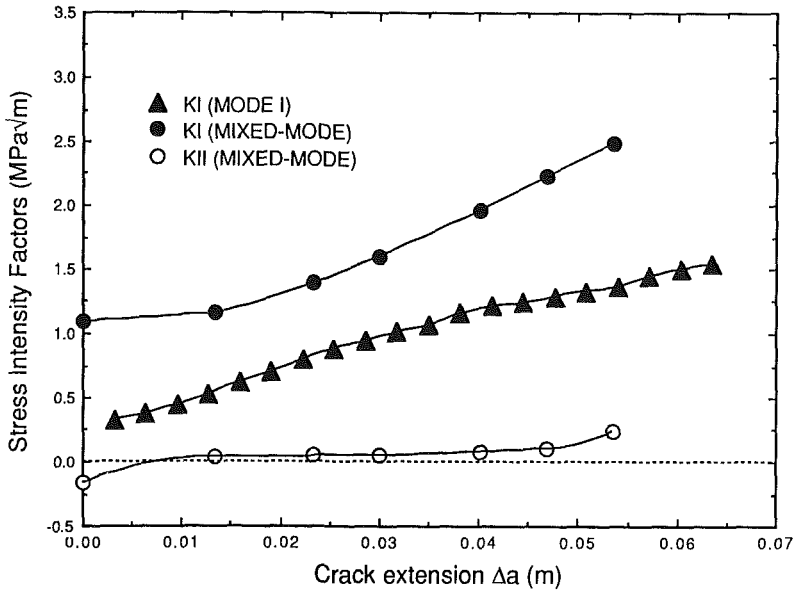


Fig. 9 Variations in stress intensity factors with crack extension

shearing stress versus crack sliding displacement relation which was not needed for the best fit between the computed and measured crack opening displacements and crack sliding displacements. A rationale for neglecting the crack shearing stress, despite the evidences to the contrary (Davies, 1989; Nooru-Mohamed and van Mier, 1989; Reinhardt and Walraven, 1982), is that aggregate interlocking could be greatly reduced if not totally eliminated with the mode I opening of the precrack surface. The crack sliding displacement along the kinked crack surface was negligible since the crack, after kinking, propagated in mode I. Thus aggregate interlocking, which obviously dominates pure mode II loading of a concrete fracture specimen, is relatively ineffective in the presence of mode I or under combined mode I and II loading.

The corresponding computed crack opening displacements and crack sliding displacements at different crack length are shown in Fig. 8. The crack sliding displacements along the kinked portion of the crack are negligible, but are appreciable along the vertical portion of the crack. The constant crack sliding displacements for a given crack length in this region indicates a vanishing normal strain, ϵ_{yy}, in this free corner at the mouth of the precrack.

Figure 9 shows the variations of stress intensity factors, K_I and K_{II}, with crack extension, which was measured from the precracked tip. The reduction in K_{II} as the crack extends, shows that the crack extends in essentially the mode I condition as expected of brittle material. Also shown in Fig. 9 is the K_I, which was determined previously by Guo et al. (1992), for mode I loading. The substantial difference between the K_I curves for pure mode I and mixed-mode loading show, as expected, that the resistance curve, K_{IR}, is not a material property.

Figure 10 shows the energy partitions, which were output directly from the finite element code, in the three-point bend concrete specimen. The partitioned energy was then used to compute the energy release and dissipation rates with crack extension of Fig. 11. The energy dissipation rate relates only to the fracture process zone and does not include rates due to other energy sinks, such as microcracking ahead of the crack tip, crushing at the load and support points and aggregate-mortar debonding. The energy release rate represents the resistance curve for this mixed-mode fracture process. Using identical concrete fracture specimens, Guo et al. (1992) showed that the energy dissipation rate remains constant

Downloaded 03 May 2010 to 171.66.16.20. Redistribution subject to ASME license or copyright; see http://www.asme.org/terms/Terms_Use.cfm

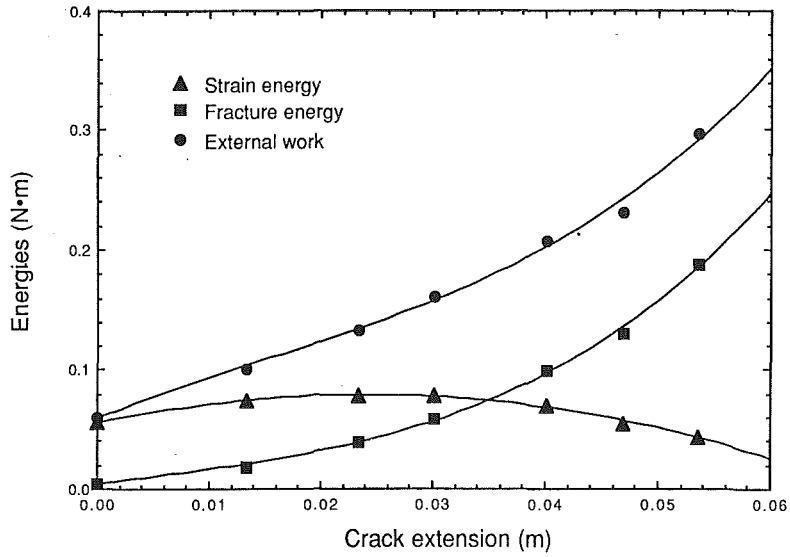


Fig. 10 Energy participation in concrete bend specimens

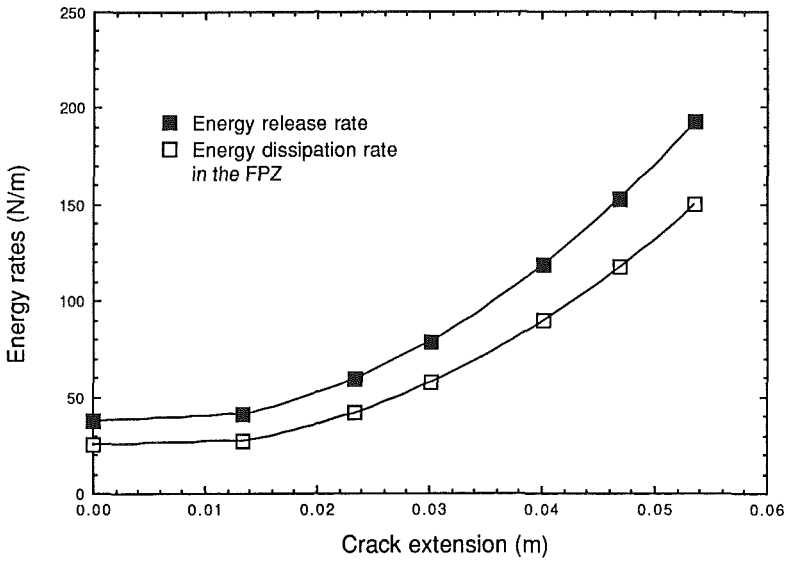


Fig. 11 Energy rates in three-point bend concrete specimens

after the fracture process zone is fully developed. Figure 11 shows that this not the case. As shown by Guo et al. for mode I concrete fracture, the energy dissipation rate at the fracture process zone continues to be the dominant component of the energy release rate in mixed-mode concrete fracture.

5 Discussion

Figure 4 shows two average load versus load-line displacement curves for all five specimens, one with and one without a fracture process zone. The correct curve, of course, is that with the fracture pressure zone included in computing the load-line displacement. For comparison, the computation was repeated with the computed load-line displacement applied to the concrete specimen without the fracture process zone. Figure 4 shows that the resultant load carrying capacity for a given load-line displacement is reduced 20 percent for the peak load and in excess of 50 percent for the strain-softening region when the fracture process zone is not included in the estimation. This result underscores the additional role of the fracture process zone in increasing the load carrying capacity and the post-peak stiffness of a fractured concrete beam.

Table 1 Measured and predicted kinking angles of concrete specimens

Measured kinking angle	18.6°
Predicted kinking angle	17.4°
Error	5.9%

The stress intensity factors in Fig. 9 were used to predict the crack kinking angle in the presence of mixed-mode loading. As shown in Table 1, the maximum circumferential stress criterion (Erdogan and Sih, 1963) provided a reasonable estimation of the crack kinking angle.

As in all inverse analyses, the uniqueness of the results are in doubt although the authors believe that much of such uncertainty was removed by matching the crack opening displacements and crack sliding displacements. These crack-tip parameters, i.e., the crack opening displacement and the crack sliding displacement, are more sensitive to changes in the fracture process zone than the remotely measured applied load, loadline displacements and isolated measurements by crack opening displacement and crack sliding displacement gages. In fact, previous analysis showed that the

Downloaded 03 May 2010 to 171.66.16.20. Redistribution subject to ASME license or copyright; see http://www.asme.org/terms/Terms_Use.cfm

computed and measured u_x's and u_y's could be matched with a sizable crack shearing stress versus crack sliding displacement relation contrary to that shown in Fig. 8. It was only when the predicted crack kinking angle using the computed K_I and K_{II} deviated substantially with the measured angle that the data was reanalyzed. This finding demonstrated the need for exhaustive cross checking of the results which are generated by an inverse analysis. As described above, the present results provide excellent agreement between the measured and computed crack kinking angles which is just one more evidence supporting the reasonableness of the crack closing stress versus crack opening displacement and the crack shearing stress versus crack sliding displacement models in this study.

6 Conclusions

1 Crack closing stress versus crack opening displacement relation due to crack bridging in an off-set three-point bend concrete specimen was obtained.

2 For a given crack opening displacement, the crack closing stress increased under mixed-mode loading.

3 The dominant energy dissipation mechanism in concrete fracture in the crack bridging is the trailing fracture process zone.

4 Under mixed-mode loading, the crack extended with vanishing K_{II}.

5 The fracture process zone increased the load carrying capacity of the concrete fracture specimen.

Acknowledgment

This research was supported by the US Air Force Office of Scientific Research Grant AFOSR-91-0218 and National Science Foundation Grant MSM-892287. The authors wish to thank Drs. Spencer T. Wu and Jim C. I. Chang, AFOSR, and Dr. Ken Chong, NSF, for their continuing support and encouragement during the course of this investigation.

References

Davies, J., 1989, "Study of Shear Fracture," *Fracture of Concrete and Rock: Recent Developments*, S. P. Shah, S. E. Swartz, and B. Barr, eds., Elsevier, Amsterdam, pp. 438–446.

Erdogan, F., and Sih, G. C., 1963, "On the Crack Extension in Plates under Plane Loading and Transverse Shear," *J. Basic Eng.*, Vol. 85, pp. 519–527.

Guo, Z. K., Yon, J.-H., Hawkins, N. M., and Kobayashi, A. S., 1993, "Fracture Energy Dissipation Mechanism of Concrete," to be published in *Fracture Mechanics*, 23rd Symposium, ASTM.

Hassanzadeh, M., 1991, "Consideration Regarding Fracture Zone Response to Simultaneous Normal and Shear Displacement," *Analysis of Concrete Structure by Fracture Mechanics*, L. Elfgren and S. P. Shah, eds., Chapman and Hall, London, pp. 44–54.

Hillerborg, A., 1989, "Mixed Mode Fracture in Concrete," *Advances in Fracture Research*, K. Salama, K. Ravi-Chandar, D. M. R. Taplin, P. Rama Rao, eds., Vol. 3, Pergamon Press, pp. 2259–2268.

Jenq, Y. S., and Shah, S. P., 1988, "Mixed Mode Fracture of Concrete," *International Journal of Fracture*, Vol. 38, pp. 123–142.

Jenq, Y. S., and Shah, S. P., 1989, "On the Fundamental Issues of Mixed Mode Concrete Crack Propagation in Concrete," *Fracture of Concrete and Rock: Recent Developments*, S. P. Shah, S. E. Swartz, and B. Barr, eds., Elsevier, Amsterdam, pp. 27–38.

Liaw, B. M., Jeang, F. L., Hawkins, N. M., and Kobayashi, A. S., 1990, "Fracture Process Zone for Mixed Mode Concrete Fracture," *ASCE Journal of Engineering Mechanics*, Vol. 116, No. 7, pp. 1560–1579.

Nooru-Mohamed, M. B., and van Mier, J. G. M., 1989, "Fracture of Concrete under Mixed-Mode Loading," *Fracture of Concrete and Rock, Recent Developments*, S. P. Shah, S. E. Swartz, and B. Barr, eds., Elsevier, Amsterdam, pp. 458–467.

Nooru-Mohamed, M. B., 1992, "Mixed-Mode Fracture of Concrete: An Experimental Approach," Ph.D. thesis submitted to Delft University of Technology, The Hague Cataloging in Publication Data, -151.

Post, D., 1993, "Moire Interferometry," *Handbook of Experimental Mechanics*, 2nd rev. ed., A. S. Kobayashi, ed., Prentice-Hall, Englewood Cliffs, NJ, pp. 297–364.

Reinhardt, H. W., and Walraven, J. C., 1982, "Cracks in Concrete Subjected to Shear," *ASCE Journal of Structure Division*, Vol. 108, No. 1, pp. 207–224.

Reinhardt, H. W., Cornelissen, L. W., and Hordijk, D. A., "Mixed Mode Fracture Tests on Concrete," *Fracture of Concrete and Rock*, S. P. Shah and S. E. Swartz, eds., Springer-Verlag, New York, pp. 117–130.

Swartz, S. E., Lu, L. W., Tang, L. D., and Refai, T. M., 1988, "Mode II Fracture Parameter Estimates for Concrete from Beam Specimens," *Experimental Mechanics*, Vol. 28, No. 2, pp. 146–153.

Walraven, J. C., 1981, "Fundamental Analysis of Aggregate Interlock," *ASCE Journal of Structure Division*, Vol. 107, No. 11, pp. 2245–2270.

Wong, W., and Miller, R. A., 1990, "Mixed Mode Fracture at Early Age," *Micromechanics of Failure of Quasi-brittle Materials*, S. P. Shah, S. E. Swartz, and M. L. Wang, eds., pp. 166–175.

Yon, J.-H., Hawkins, N. M., and Kobayashi, A. S., 1991, "Fracture Process Zone in Dynamically Loaded CLWL-DCB Specimens," *ACI Materials Journal*, Vol. 88, No. 5, pp. 470–479.

Downloaded 03 May 2010 to 171.66.16.20. Redistribution subject to ASME license or copyright; see http://www.asme.org/terms/Terms_Use.cfm

Analysis of Vickers Hardness by the Finite Element Method

Y. Murakami
Department of Mechanical Science and Engineering, Faculty of Engineering, Kyushu University, Hakozaki, Fukuoka 812, Japan
Mem. ASME

K. Matsuda
Department of Mechanical Engineering, Kyushu Institute of Technology, Kitakyushu 804, Japan

A particular formulation of the three-dimensional finite element method specifically for analyzing the Vickers hardness test is established. The Vickers hardness of 0.46 percent carbon steel and 70/30 brass is calculated using the proposed method using the stress-strain curve obtained from a tensile test. The calculated values correlate well with the experimental results for 0.46 percent steel and 70/30 brass. In addition, the analysis predicts the extension of the plastic zone induced by indentation, the stresses at the maximum load, and the residual stresses present after complete removal of the load. At the maximum load there are no tensile stresses in the vicinity of the indenter. However, after removal of the load, large tensile residual stresses are present on the diagonal edge beneath the indentation in the direction perpendicular to the diagonal edge. These results imply that it is necessary to reconsider the accuracy and validity of the conventional indentation method used for the determination of K_{Ic} *for brittle materials such as ceramics.*

1 Introduction

For many years, Vickers hardness testing of ductile materials has been used to measure hardness, one of the basic mechanical properties. Recently, the Vickers hardness testing technique has been considered as a possible method for the determination of additional material properties in brittle materials such as the fracture toughness, K_{Ic}. In addition, it may also be used to evaluate the strength of thin coatings and the measurement of near surface residual stresses.

However, to date there are 19 published formulae (Ponton and Rowlings, 1989)) relating the measured micro-indentation-induced crack length with K_{Ic}. This abundance of different formulae is due to the fact that the Vickers hardness test has never been completely analyzed. Such an analysis forms the subject of this paper.

The correlation of the Vickers hardness with other mechanical properties has been studied mostly by experiment only (Tabor, 1951; Yoshizawa, 1967; Westbrook and Conrod, 1973). There have been a few theoretical and analytical studies (Perrott, 1977; Chiang, Marshall, and Evans, 1982; Tanaka, 1984; Yoshino and Yamada, 1984; Mura, Yamashita, Mishima, and Hirose, 1989), however, these do not appear to satisfy the exact boundary conditions and their accuracy is insufficient for analysis of the Vickers hardness test Hv for engineering materials.

An accurate numerical analysis is necessary for a systematic investigation of the effects of the mechanical properties on Hv and thus gain a thorough understanding of the related phenomena.

Although the development of the finite element method has progressed over the years, indentation problems such as the Vickers hardness test cannot be solved using conventional commercial finite element method software as commercial programs are unable to simulate interface contact problems to the accuracy required for this particular purpose. For this reason the finite element method solutions for the Vickers hardness test have yet to be published despite many demands from experimental researchers.

In this paper, a particular formulation for indenting the specimen with a diamond pyramid is established. An accurate analysis of the Vickers hardness requires a special formulation of the three-dimensional finite element method based on the strain incremental plastic theory (Prandtl-Reuss equation (Zienkiewicz, 1971)). The Vickers hardness of 0.46 percent carbon steel and 70/30 brass is analyzed by the proposed method.

To confirm the validity of the proposed method, numerical values for indentation diagonal size and hardness are compared with experimental results. Finally, after investigating the stress distribution in the vicinity of the indentation at the maximum load and after unloading, the validity of the conventional indentation method for measuring the fracture toughness K_{Ic} for materials such as ceramics is discussed.

2 Finite Element Formulation for the Vickers Hardness Analysis

2.1 Displacement Boundary Conditions. The Vickers hardness Hv is defined as the load divided by the surface area of a square diamond pyramid indentation with top angle of 136 degrees. Since it is expected that the diamond indenter barely deforms during the hardness test, we regard the indenter as a rigid body.

Contributed by the Applied Mechanics Division of THE AMERICAN SOCIETY OF MECHANICAL ENGINEERS for publication in the ASME JOURNAL OF APPLIED MECHANICS.

Discussion on this paper should be addressed to the Technical Editor, Professor Lewis T. Wheeler, Department of Mechanical Engineering, University of Houston, Houston, TX 77204-4792, and will be accepted until four months after final publication of the paper itself in the ASME JOURNAL OF APPLIED MECHANICS.

Manuscript received by the ASME Applied Mechanics Division, Oct. 30, 1992; final revision, May 22, 1993. Associate Technical Editor: W. N. Sharpe, Jr.

Copyright © 1994 by ASME
Downloaded 03 May 2010 to 171.66.16.20. Redistribution subject to ASME license or copyright; see http://www.asme.org/terms/Terms_Use.cfm

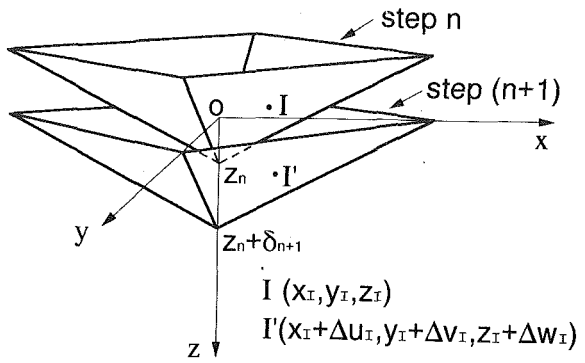


Fig. 1 Displacement boundary condition

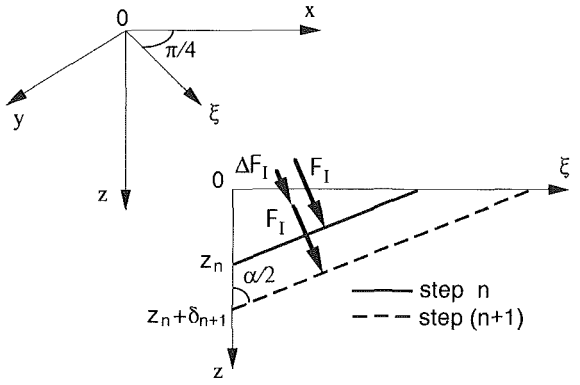


Fig. 2 Load boundary condition

Figure 1 shows the beginning of step n of the indentation process. The equation of the indenter surface can be written as

$$C_x x + C_y y + C_z(z - z_n) = 0 \quad (x \geq 0,\ y \geq 0). \tag{1}$$

At the beginning of step $(n+1)$, the equation of the indenter surface is given by

$$C_x x' + C_y y' + C_z(z' - z_n - \delta_{n+1}) = 0 \tag{2}$$

where δ_{n+1} is the incremental displacement of the indenter in the z-direction in step $n+1$, and C_x, C_y and C_z are the direction cosines of the indenter surface defined by

$$C_x = C_y = \cos(\alpha/2)/\sqrt{2}$$
$$C_z = \sin(\alpha/2). \tag{3}$$

In Fig. 1, I and I' indicate a nodal point on the contact surface of the specimen at steps n and $(n+1)$, respectively. (x_I, y_I, z_I) are the coordinates and $(\Delta u_I, \Delta v_I, \Delta w_I)$ are the incremental displacements of node I. Substituting the coordinates I' $(x_I+\Delta u_I, y_I+\Delta v_I, z_I+\Delta w_I)$ into Eq. (2), gives

$$C_x(x_I+\Delta u_I) + C_y(y_I+\Delta v_I) + C_z(z_I+\Delta w_I - z_n - \delta_{n+1}) = 0. \tag{4}$$

From Eq. (1), the following is obtained:

$$C_x\Delta u_I + C_y\Delta v_I + C_z(\Delta w_I - \delta_{n+1}) = 0. \tag{5}$$

Using Eq. (3),

$$\Delta u_I + \Delta v_I + \beta(\Delta w_I - \delta_{n+1}) = 0$$
$$[\beta = C_z/C_x = C_z/C_y = \sqrt{2}\tan(\alpha/2)]. \tag{6}$$

Equation (6) is therefore the displacement boundary condition.

2.2 Load Boundary Condition. In this situation, the contact surface of the hardness specimen is assumed to be frictionless. Therefore, the pressure at the contact surface acts in the normal direction. Denoting the x, y, and z components of the nodal force of node I by F_{Ix}, F_{Iy}, and F_{Iz} (see Fig. 2), we can write the load boundary condition at the contact surface under the condition of no friction as follows:

$$F_{Ix}/C_x = F_{Iy}/C_y = F_{Iz}/C_z (= F_I). \tag{7}$$

Denoting the incremental nodal force of node I in normal direction by ΔF_I, its x, y, and z-components ΔF_{Ix}, ΔF_{Iy}, and ΔF_{Iz} must satisfy the following condition:

$$\Delta F_{Ix}/C_x = \Delta F_{Iy}/C_y = \Delta F_{Iz}/C_z (= \Delta F_I). \tag{8}$$

Substituting Eq. (3) into (8), gives

$$\Delta F_{Ix} = \Delta F_{Iy} = \Delta F_{Iz}/\beta. \tag{9}$$

Equation (9) is therefore the incremental load boundary condition at the contact surface.

2.3 Formulation of Incremental Loading Process. Considering the incremental loads ΔF_{Ix}, ΔF_{Iy}, and ΔF_{Iz}, the simultaneous equations for nodes at the contact surface can be written as follows:

$$\begin{bmatrix} \vdots & \vdots & \vdots \\ \cdots\ k_{3I-2,3I-2} & k_{3I-2,3I-1} & k_{3I-2,3I}\ \cdots \\ \cdots\ k_{3I-1,3I-2} & k_{3I-1,3I-1} & k_{3I-1,3I}\ \cdots \\ \cdots\ k_{3I,3I-2} & k_{3I,3I-1} & k_{3I,3I}\ \cdots \\ \vdots & \vdots & \vdots \end{bmatrix} \begin{Bmatrix} \vdots \\ \Delta u_I \\ \Delta v_I \\ \Delta w_I \\ \vdots \end{Bmatrix} = \begin{Bmatrix} \vdots \\ \Delta F_{Ix} \\ \Delta F_{Iy} \\ \Delta F_{Iz} \\ \vdots \end{Bmatrix} \tag{10}$$

where k's are the finite element method incremental elastic-plastic stiffness matrix components. The equation for the remaining nodes are the same as those which are used in conventional finite element method. From Eq. (9), the line $(3I)$ in Eq. (10) is divided by $-\beta(=-\sqrt{2}\tan(\alpha/2))$ and added to the lines $(3I-2)$ and $(3I-1)$, ΔF_{Ix} and ΔF_{Iy} can then be eliminated from Eq. (10). The following is obtained:

$$\begin{bmatrix} \vdots & \vdots & \vdots & \vdots \\ k_{3I-2,1}-k_{3I,1}/\beta\ \cdots & k_{3I-2,3I-2}-k_{3I,3I-2}/\beta & k_{3I-2,3I-1}-k_{3I,3I-1}/\beta & k_{3I-2,3I}-k_{3I,3I}/\beta\ \cdots \\ k_{3I-1,1}-k_{3I,1}/\beta\ \cdots & k_{3I-1,3I-2}-k_{3I,3I-2}/\beta & k_{3I-1,3I-1}-k_{3I,3I-1}/\beta & k_{3I-1,3I}-k_{3I,3I}/\beta\ \cdots \\ k_{3I,1}\ \cdots & k_{3I,3I-2} & k_{3I,3I-1} & k_{3I,3I}\ \cdots \\ \vdots & \vdots & \vdots & \vdots \end{bmatrix} \begin{Bmatrix} \vdots \\ \Delta u_I \\ \Delta v_I \\ \Delta w_I \\ \vdots \end{Bmatrix} = \begin{Bmatrix} \vdots \\ 0 \\ 0 \\ \Delta F_{Iz} \\ \vdots \end{Bmatrix}. \tag{11}$$

Replacing the line $(3I)$ of Eq. (11) by the displacement boundary condition (6) gives

$$\begin{bmatrix} \vdots & \vdots & \vdots & \vdots \\ k_{3I-2,1}-k_{3I,1}/\beta\ \cdots & k_{3I-2,3I-2}-k_{3I,3I-2}/\beta & k_{3I-2,3I-1}-k_{3I,3I-1}/\beta & k_{3I-2,3I}-k_{3I,3I}/\beta\ \cdots \\ k_{3I-1,1}-k_{3I,1}/\beta\ \cdots & k_{3I-1,3I-2}-k_{3I,3I-2}/\beta & k_{3I-1,3I-1}-k_{3I,3I-1}/\beta & k_{3I-1,3I}-k_{3I,3I}/\beta\ \cdots \\ \cdots 0 \cdots & 1.0 & 1.0 & \beta\ \cdots 0 \cdots \\ \vdots & \vdots & \vdots & \vdots \end{bmatrix} \begin{Bmatrix} \vdots \\ \Delta u_I \\ \Delta v_I \\ \Delta w_I \\ \vdots \end{Bmatrix} = \begin{Bmatrix} \vdots \\ 0 \\ 0 \\ \beta\delta_{n+1} \\ \vdots \end{Bmatrix}. \tag{12}$$

Downloaded 03 May 2010 to 171.66.16.20. Redistribution subject to ASME license or copyright; see http://www.asme.org/terms/Terms_Use.cfm

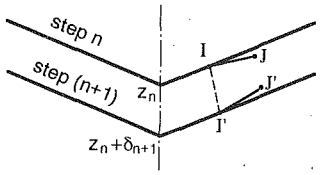


Fig. 3 Correction of the incremental displacement

Thus, Eq. (12) is the final formulation for the analysis of the Vickers hardness, though a sufficiently small incremental displacement δ_n must be given to obtain accurate solutions.

2.4 Particular Numerical Procedure to Satisfy the Conditions of Indenter Contact Surface. Equation (6) is the condition which the nodal displacements at the contact surface must satisfy to maintain the contact surface pyramid. Figure 3 illustrates that node J near the indenter surface at step n enters the indenter domain at step $(n+1)$. In this case

$$x_J+\Delta u_J+y_J+\Delta v_J+\beta(z_J+\Delta w_J-z_n-\delta_{n+1})\geq 0 \qquad (13)$$

is not satisfied. Therefore, a constant m_J is determined which satisfies the following equation:

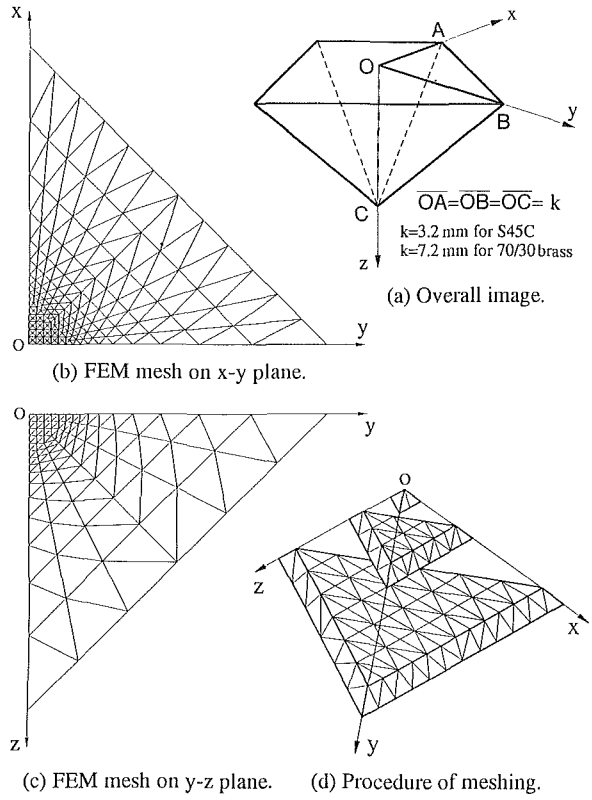
$$x_J+m_J\Delta u_J+y_J+m_J\Delta v_J+\beta(z_J+m_J\Delta w_J-z_n-m_J\delta_{n+1})=0. \qquad (14)$$

The minimum value of m_J for an arbitrary node is denoted $m_{\min}$ and satisfies the relation $0.0<m_{\min}<1.0$. $m_{\min}\delta_{n+1}$ is thus considered as the modified incremental indenter displacement to ensure that the particular node does not penetrate the specimen surface at the end of the step.

2.5 The Finite Element Method Program. A three-dimensional finite element method based on the strain incremental plastic theory Prandtl-Reuss equation (Zienkiewicz (1971)) is used for the numerical analysis of the Vickers hardness test. Unless otherwise stated, the isotropic hardening rule was used for specifying the dependence of the yield condition on plastic strain and deformation history. The deformation of the specimen is determined by adding incremental displacement to the node coordinates. The number of displacement increments during loading and unloading is 335 for 0.46 percent C steel and 295 for 70/30 brass. Therefore, the calculation for a single increment is sufficiently small to obtain accurate solutions by the small strain incremental plastic theory.

2.6 The Finite Element Method Mesh and Boundary Conditions. Figure 4 shows the finite element method mesh, the design of which is based on the particular characteristics of the Vickers indentation test. An inverted pyramid (Fig. 4(*a*)) was used for the initial shape of the specimen. The x and y-axes coincide with the direction of the diagonals of the base surface of the pyramid. The symmetry of the shape ensures that only the region $x\geq 0$, $y\geq 0$ needs to be analyzed. Tetrahedral elements are generally used to compose the total specimen with 581 nodes and 2376 elements. To avoid using a complicated mesh, units of triangular column elements or rectangular parallelepipeds composed with some tetrahedral elements may be used to build the total pyramid. However, if coarse and fine meshes are mixed, flat elements are inevitably produced.

In this analysis, truncated triangular pyramids with tetrahedral elements are initially created. This base layer is then built up to make and piled them up to the total triangular the whole pyramid as shown in Fig. 4(*d*). The volume of individual elements are initially created. This base layer is then built up to make contained in truncated triangular pyramids from the first to sixth stage remains unchanged. Each truncated triangular pyramid above the seventh stage has an equal numbers of elements: 216. Thus, it is possible to change the size of



(a) Overall image.

(b) FEM mesh on x-y plane.

(c) FEM mesh on y-z plane. (d) Procedure of meshing.

Fig. 4 Finite element mesh

truncated triangular pyramids which have close geometrical similarity. If the nodes are numbered in order from the top stage (the coordinate origin), the bandwidth of the stiffness matrix does not change after seven stages. This reduces computer storage requirements.

The symmetric displacement boundary condition for the y-z plane is $\Delta u=0$ and that for z-x plane is $\Delta v=0$. Considering the results of the preliminary calculations (see Sec. 3.1), the boundary conditions for the side plane of the total pyramid (ABC in Fig. 4(*a*)) were considered to be $\Delta u=\Delta v=\Delta w=0$.

3 Numerical Results and Comparison With Experimental Results

To confirm the validity and accuracy of the analytical method, the Vickers hardness of 0.46 percent carbon steel and 70/30 brass is analyzed, and the results compared with experimental results. The state of crack formation around the indentation in ceramics is investigated by considering the stress distribution around the indentation.

3.1 Analysis of the Vickers Hardness of 0.46 Percent C Steel. Figure 5 steel shows the stress-strain curves of 0.46 percent C steel and 70/30 brass in tensile tests. The true stress-logarithmic strain curves are used for the Vickers hardness analysis, and show that the yield stress of 0.46 percent C steel is 337 MPa.

The Hv specimen is cylindrical in shape with a diameter of 15 mm and height of 10 mm. The maximum load $P_{\max}$ is 490 N (50 kgf). Although the shape of the specimen for the analysis is different to that for the experiment, both specimen sizes are much larger than the dimension of indentation and the resulting plastic zone.

The preliminary calculations showed that the difference in boundary conditions at the support with regard to the plane ABC of Fig. 4(*a*) has little effect on the stress distribution except for the elements near the point B. Thus, it is expected

Downloaded 03 May 2010 to 171.66.16.20. Redistribution subject to ASME license or copyright; see http://www.asme.org/terms/Terms_Use.cfm

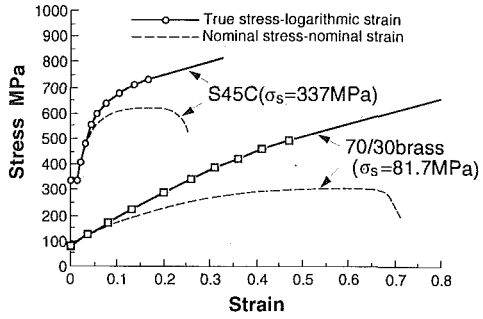


Fig. 5 Stress-strain curve of 0.46 percent C steel and 70/30 brass

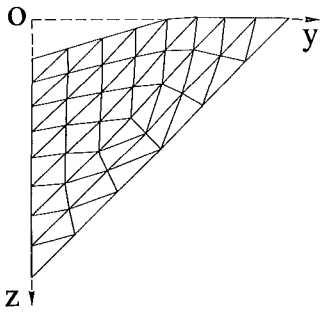


Fig. 6 Deformed shape of element near the origin (0.46 percent C steel, $P = P_{max}$)

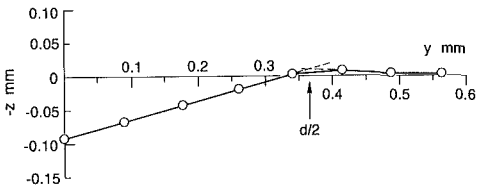


Fig. 7 Shape of diagonal of indentation after unloading (0.46 percent C steel)

that if the specimen size for the analysis is sufficiently larger than the extension of the plastic zone, the analysis should correlate well with the experimental results for the Vickers hardness. In this study, therefore, the displacement boundary condition $\Delta u = \Delta v = \Delta w = 0$ for the plane ABC of Fig. 4(*a*) is adopted.

Figure 6 shows the deformed shape of elements near the origin for $P = P_{max} = 490$ N (50 kgf). Figure 7 shows the shape of the indentation diagonal after unloading. The five nodal points nearest the origin are in contact with the indenter at $P = P_{max}$, and they are approximately in a straight line after unloading. The determination of the indentation size d in the analysis is in a sense somewhat arbitrary; there is no absolute definition of the indentation size in the analysis. In this study, the edge of the indentation was defined as shown in Fig. 7 by the intersection of two lines. The first is the line extended from the center of indentation and the second is the line extended from outside of the indentation. Thus, the Vickers hardness is calculated as follows.

$$Hv = \frac{2P_{max}}{d^2}\sin(\alpha/2) = \frac{2\times 50}{0.734^2}\times 0.9272 = 172 \text{ kgf/mm}^2 \quad (15)$$

To investigate the effect of mesh size on the accuracy of the results, several additional calculations using a fine mesh were performed. The results were almost identical to those already obtained. In the additional calculations, 13 nodal points were in contact with the indenter for 0.46 percent C steel. (In the original calculation, only five nodal points were in contact with the indenter.)

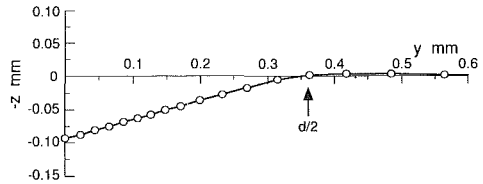


Fig. 8 Shape of diagonal of indentation after unloading by the analysis of fine mesh (0.46 percent C steel)

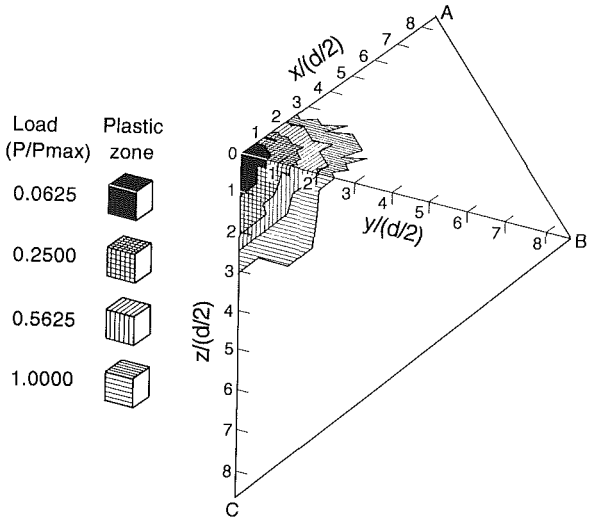


Fig. 9 Extension of plastic zone in 0.46 percent C steel specimen (*d*: diagonal of the indentation)

Table 1 Comparison of calculated results by conventional mesh and fine mesh

	(1/4 specimen)		(0.46%C steel)	
	Nodes	Elements	Hv	Depth of indentation
Original mesh	581	2376	172	0.0923mm
Fine mesh	1169	4968	176	0.0938mm

Figure 8 shows the shape of the indentation diagonal after unloading. The calculations are shown in Table 1. Thus, it may be concluded that the original mesh is sufficient for obtaining accurate results.

Figure 9 shows the extension of the plastic zone in the specimen at several loading steps. The elements which satisfy the Von Mises yield criterion within ±1 percent error are regarded as yielded elements. For the load $P = P_{max}$, the extension of the plastic zone on the specimen surface is 2.5 ~ 2.7 times the diagonal of indentation and the periphery of the plastic zone is almost circular in shape. The depth of the plastic zone is approximately 1.5 times the diagonal of the indentation and 12 times the indentation depth. These types of numerical results will enable one to understand the effect of specimen size and the existence of inhomogeneities near the point of measurement on empirically measured values of Hv. These problems must be addressed in more detail in future research.

Figure 10 shows the stress distribution in the vicinity of the y-axis for $P = P_{max}$. At the center of the contact surface, σ_z is approximately twice the value of σ_y. This result closely resem-

Downloaded 03 May 2010 to 171.66.16.20. Redistribution subject to ASME license or copyright; see http://www.asme.org/terms/Terms_Use.cfm

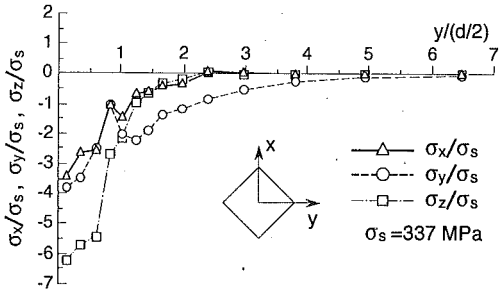


Fig. 10 Stress distribution in the vicinity of *y*-axis (0.46 percent C steel, $P = P_{max}$)

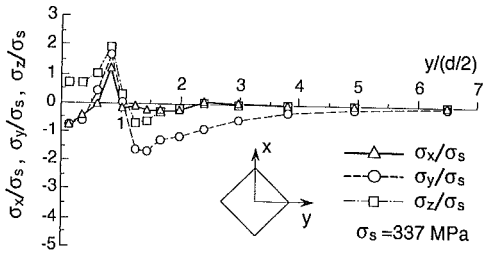


Fig. 11 Residual stress distribution in the vicinity of *y*-axis (0.46 percent C steel)

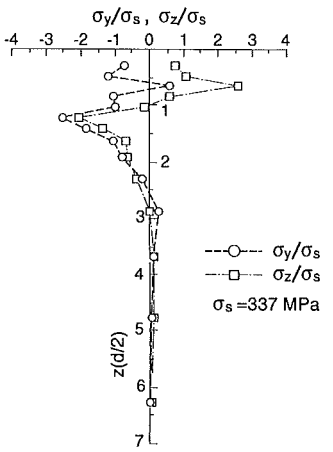


Fig. 12 Residual stress distribution in the vicinity of *z*-axis (0.46 percent C steel)

bles the numerical results of Brinell hardness (Murakami and Yuan, 1990, 1992). However, the maximum values of the three stresses σ_x, σ_y, and σ_z occur at the center of indentation. It should be noted that up to the point of unloading, there are no tensile stresses in the vicinity of the indenter. This is of critical importance regarding the question of whether indentation-induced cracking in ceramics initiates during loading or unloading. (This result was obtained using the mesh shown in Fig. 4.)

Figures 11 and 12 illustrate the distribution of residual stresses in the vicinity of y and z-axis, respectively, after unloading. The residual stresses σ_x and σ_y near the origin are compressive and they become tensile along the diagonal near the indentation edge (see Fig. 11). If these tensile stresses are the cause of crack initiation in ceramics, the crack should be formed during unloading. This is an important condition which must be taken into consideration when the stress intensity factor K of an indentation-induced crack is analyzed.

The comparatively large stresses σ_z in the vicinity of the indentation can be explained by considering the following two points. First, the values of σ_z are not the values at the actual free surface but average values of the elements near the surface.

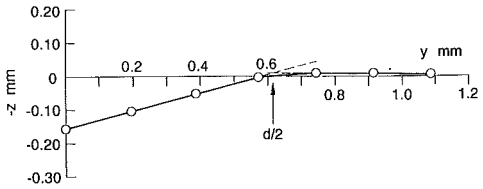


Fig. 13 Shape of diagonal of indentation after unloading (70/30 brass)

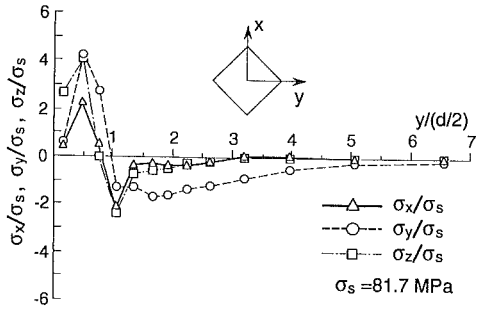


Fig. 14 Residual stress distribution in the vicinity of *y*-axis (70/30 brass)

Secondly, the indentation surface is inclined, thus leading to higher values in the z-direction. The tensile residual stresses σ_z in the vicinity of the z-axis in Fig. 12 are also important in relation to lateral cracks produced by the Vickers indentation test observed in glasses and other ceramics (Marshall and Lawn, 1979; Antis, Chantikal, Lawn, and Marshall, 1981).

3.2 Analysis of the Vickers Hardness of 70/30 Brass. Figure 5 shows the stress-strain curve of 70/30 brass in a tensile test and the true stress-logarithmic strain curve used for the Vickers hardness analysis. The yield stress of 70/30 brass is 81.7 MPa. The applied maximum load P_{max} in the Vickers hardness test and analysis is 490 N (50 kgf). The finite element method mesh pattern is the same as that for 0.46 percent C steel, though the size is approximately twice that for 0.46 percent C steel since the extension of the plastic zone is much greater.

Figure 13 shows the shape of indentation diagonal after unloading. According to Fig. 13, the diagonal of indentation is 1.236 mm and accordingly the Vickers hardness Hv is 60.7 kgf/mm^2.

The extension shape of the plastic zone in the specimen at several loading steps is almost identical to that of 0.46 percent C steel (Fig. 9). The stress distribution in the vicinity of the y-axis for $P = P_{max}$ is also almost identical to that of 0.46 percent C steel (Fig. 10). Figures 14 and 15 illustrate the distribution of residual stresses in the vicinity of the y and z-axes, respectively, after unloading. The residual stresses σ_x and σ_y near the y-axis in the indentation are both tensile.

3.3 Effect of Hardening Rules. The above results are based on isotropic hardening. However, phenomena such as the Bauschinger effect in engineering materials make the results inconsistent with the isotropic hardening rule. Furthermore, the application of alternative hardening rules yields a different set of analytical results.

To investigate the effect of different hardening rules, the Vickers hardness of elastic-linear-hardening materials was analyzed based firstly on the isotropic hardening rule and secondly on the kinematic hardening rule. The yield stress σ_y in the basic stress strain curve is 392 MPa (40 kfg/mm^2) and the plastic strain-hardening modulus H' ($= d\sigma/d\epsilon_p$) is 4900 MPa (500 kgf/mm^2). (Prager's rule (Prager, 1955) was used for the kinematic hardening rule.)

Downloaded 03 May 2010 to 171.66.16.20. Redistribution subject to ASME license or copyright; see http://www.asme.org/terms/Terms_Use.cfm

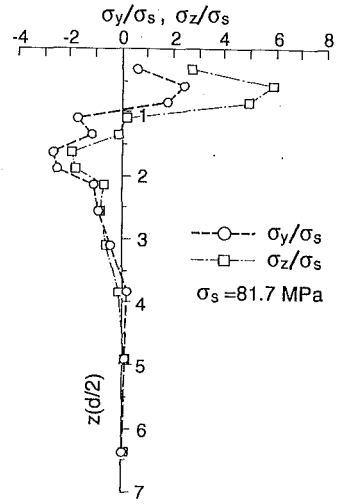


Fig. 15 Residual stress distribution in the vicinity of z-axis (70/30 brass)

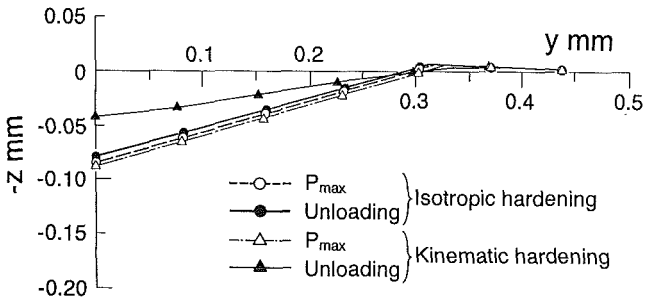


Fig. 16 Comparison of the numerical results based on the isotropic hardening rule and the kinematic hardening rule ($\sigma_s = 392$ MPa, $H' = d\sigma/d\epsilon_p = 4900$ MPa)

Figure 16 shows the analytical results for two hardening results. The indenter displacements for $P = P_{max}$ in the kinematic hardening rule ($\triangle$) are only 3.7 percent higher than that in the isotropic hardening ($\circ$). However, while the recovery of the maximum indentation displacement from $P = P_{max}$ to $P = 0$ is 6.5 percent for the isotropic hardening rule, that for the kinematic hardening rule exceeds 50 percent. These results clearly indicate the remarkable effect that the hardening rules have upon indentation displacement. The experimentally measured depth from the edge of the indentation to the base is 104 μm for 0.46 percent carbon steel and 168 μm for 70/30 brass. The calculated results based on the isotropic hardening rule (100 μm for 0.46 percent carbon steel and 168 μm for 70/30 brass) correlate well with the experimental results. However, it should be noted that the hardening rule has little effect on the analytical values of the Vickers hardness (i.e., less than two percent in the isotropic hardening rule and less than six percent in the kinematic hardening rule).

3.4 Comparison of Numerical Results With Experimental Results. Table 2 compares the numerical and experimental results for 0.46 percent carbon steel and 70/30 brass. For both materials good correlation exists between the numerical and experimental results.

3.5 Tensile Residual Stresses Induced by Indentation and Initiation of Indentation Cracks in Ceramics. As shown in Fig. 11 and Fig. 14, after unloading there is large tensile residual stress in the vicinity of the indentation for 0.46 percent carbon steel and 70/30 brass. The locations of the maximum tensile stress peaks are dependent upon material type and differ slightly for 0.46 percent carbon steel and 70/30 brass. Since exact

Table 2 Comparison of the numerical results with experimental ones of 0.46 percent C steel and 70/30 brass

		Load P_{max}	Diagonal of indentation d (mm)	Vickers hardness Hv
0.46%C steel	Experiment	490N(50kgf)	0.737	171
	Calculation	490N(50kgf)	0.734	172
70/30brass	Experiment	490N(50kgf)	1.229	61.4
	Calculation	490N(50kgf)	1.236	60.7

stress-strain curves (i.e., constitutive equations of ceramics) are not known, it is difficult to determine the location and value of the maximum tensile stress. However, the elastic-plastic response to indentation for metals may be qualitatively applied to ceramics.

The indentation technique for measuring fracture toughness K_{Ic} of brittle materials such as ceramics has been studied by many investigators (Chiang, Marshall, and Evans, 1982; Tanaka, 1984; Lawn and Marshall, 1978; Lankford and Davidson, 1979; Niihara, 1983; Shetty, Wright, Mincer, and Clauer, 1985; Keer, Farris, and Lee, 1986; Li, Ghosh, Kobayashi, and Bradt, 1989; Yingzhi and Hills, 1990; Marshall and Lawn, 1979; Antis, Chantikal, Lawn, and Marshall, 1981). However, since the exact stress state around the indentation with cracks is not known, many equations for the determination of K_{Ic} were proposed by combining dimensional analysis for the indentation crack and K_{Ic} values measured using the standard fracture mechanics techniques. The K_{Ic} equations based on the Lawn, Evans, and Marshall model (Lawn, Evans, and Marshall, 1980) and the internal inclusion model (Tanaka, Kitahara, Ichinose, and Iimura, 1984) were also proposed. In addition, there are reports (Keer, Farris, and Lee, 1986; and Li, Ghosh, Kobayashi, and Bradt, 1989) of an elastic numerical analysis in which the indentation load is replaced by a concentrated point force. Nevertheless, it should be noted that most of these models assume that indentation cracks are formed at the loading process rather than the unloading process (Lankford, 1979). However, some reports (Marshall and Lawn, 1979; Antis, Chantikal, Lawn, and Marshall, 1981) indicate that the behavior of the materials during the unloading process cannot be ignored when considering crack formation.

The question as to whether it is the loading or unloading process which has the more critical effect on crack formation was investigated experimentally. The plastic replicas taken from the vicinity of indentation at $P = P_{max}$ and after unloading ($P = 0$) were compared.[1] Figures 17(a) and (b) show the photographs of two plastic replicas at $P = P_{max}$ and after unloading. These indicate that the crack initiated at the unloading process. Therefore, it may be concluded that the residual tensile stress during the unloading process has an important effect on the behavior of crack initiation and also upon its subsequent arrest. However, the authors have recently observed crack initiation during the loading process in some other ceramics. Thus, the phenomena during micro-indentation and the response of ceramics would appear to be very complicated.

Since material properties influence the distribution of residual stresses, it seems possible that the equations proposed by many investigators for the determination of K_{Ic} based on the size of the crack formed around the indentation and the max-

[1] In the soft state (immediately after being dipped in solution) the plastic replica is spread around the diamond indenter at $P = P_{max}$. Once the plastic replica has rehardened, the diamond indenter is removed and the specimen is unloaded. Thus, it is possible to observe the behavior of the specimen at maximum load, though the center of the replica is vacant (as shown in Fig. 17(a)). A second plastic replica is then spread over the indentation, once the material has been unloaded. In this way, it is possible to observe the state of the crack formation during the process of unloading.

Downloaded 03 May 2010 to 171.66.16.20. Redistribution subject to ASME license or copyright; see http://www.asme.org/terms/Terms_Use.cfm

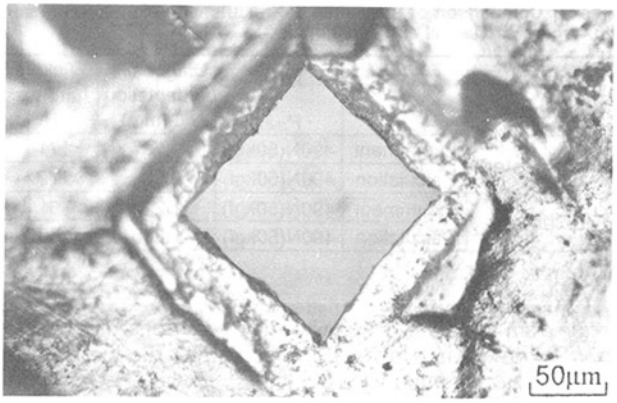


Fig. 17(*a*) Photograph of plastic replica of $P = P_{max}$ (20 kgf)

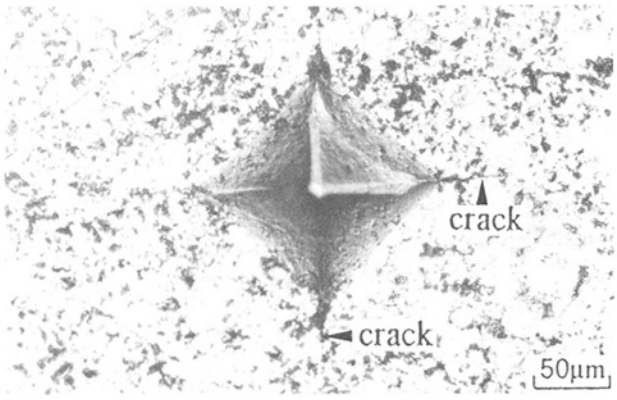


Fig. 17(*b*) Photograph of plastic replica after unloading

Fig. 17 State of crack formation of Al_2O_3-TiC under the Vickers hardness test

imum load could be applicable to just one specific material. Thus, for the determination of K_{Ic} of ceramics by the so-called "micro-indentation method," it might be necessary in some cases to closely study the position and timing of crack formation.

4 Conclusion

(1) A particular formulation of the three-dimensional finite element method for the Vickers hardness test is established.

(2) The Vickers hardness of 0.46 percent carbon steel and 70/30 brass are analyzed by the proposed method. The calculated values show good correlation with the experimentally measured hardness.

(3) At the maximum load of indentation process there is no tensile stress in the vicinity of the indenter. However, after removal of the load, large tensile residual stresses are induced at the diagonal edge beneath the indentation. These results imply that crack initiation in ceramics during the indentation test may occur mainly during the unloading process. Therefore, the validity of the so-called micro-indentation method for the determination of K_{Ic} of ceramics must be carefully reconsidered.

Acknowledgments

The authors wish to express their thanks to Prof. T. N. Farris, Purdue University, for the useful discussion on this paper and for his kindness in revising the English manuscript.

References

Anstis, G. R., Chantikul, P., Lawn, B. R., and Marshall, D. B., 1981, "A Critical Evaluation of Indentation Techniques for Measuring Fracture Toughness: I. Direct Crack Measurements," *J. Am. Ceram. Soc.*, Vol. 64, pp. 533–538.

Chiang, S. S., Marshall, D. B., and Evans, A. G., 1982, "The Response of Solids to Elastic/Plastic Indentation. I. Stresses and Residual Stresses," *J. Appl. Phys.*, Vol. 53, pp. 298–311.

Keer, L. M., Farris, T. N., and Lee, J. C., 1986, "Knoop and Vickers Indentation in Ceramics Analyzed as a Three-Dimensional Fracture," *J. Am. Ceram. Soc.*, Vol. 69, No. 5, pp. 392–396.

Lankford, J., and Davidson, D. L., 1979, "The Crack Initiation Threshold in Ceramic Materials Subject to Elastic/Plastic Indentation," *J. Materials Sci.*, Vol. 14, pp. 1662–1668.

Lawn, B. R., Evans, A. G., and Marshall, D. B., 1980, "Elastic/Plastic Indentation Damage in Ceramics: The Median/Radial Crack System," *J. Am. Ceram. Soc.*, Vol. 63, pp. 574–581.

Lawn, B. R., and Marshall, D. B., 1978, *Fracture Mechanics of Ceramics*, Vol. 3, edited by R. C. Bradt, D. P. H. Hasselman, and F. F. Lange, Plenum, New York, pp. 205–209.

Li, Z., Ghosh, A., Kobayashi, A. S., and Bradt, R. C., 1989, "Indentation Fracture Toughness of Sintered Silicon Carbide in the Palmqvist Crack Regime," *J. Am. Ceram. Soc.*, Vol. 69, pp. 904–911.

Marshall, D. B., and Lawn, B. R., 1979, "Residual Stress Effects in Sharp Contact Cracking, Part 1. Indentation Fracture Mechanics," *Journal of Materials Science*, Vol. 14, pp. 2001–2012.

Mindlin, R. D., 1936, "Force at a Point in the Interior of a Semi-Infinite Solids," *Physics*, Vol. 7, pp. 195–202.

Mura, T., Yamashita, N., Mishima, T., and Hirose, Y., 1989, "A Dislocation Model for Hardness Indentation Problems—I," *Int. J. Engng. Sci.*, Vol. 27, pp. 1–9.

Murakami, Y., and Yuan, L. P., 1990, "Analysis of Brinell Hardness by the Finite Element Method (Particular Formulation and Comparison with Experimental Results)," submitted to *Int. J. Solids & Structures*.

Murakami, Y., and Yuan, L. P., 1992, "Finite Element Method (FEM) Analysis of Elastic-Linear-Hardening Materials and Comparison with Measurement on Commercial Materials," *ASTM Journal of Testing and Evaluation*, Vol. 20, pp. 15–24.

Niihara, K., 1983, "A Fracture Mechanics Analysis of Indentation-induced Palmqvist Crack in Ceramics," *J. Materials Sci. Letters*, Vol. 2, pp. 221–223.

Perrott, C. M., 1977, "Elastic-Plastic Indentation: Hardness and Fracture," *Wear*, Vol. 45, pp. 293–309.

Ponton, C. B., and Rawlings, R. D., 1989, "Dependence of the Vickers Indentation Fracture Toughness on the Surface Crack Length," *British Ceram. Trans. J.*, Vol. 88, pp. 83–90.

Prager, W., 1955, "Theory of Plasticity: A Survey of Recent Achievement," *Proc. Inst. Mech. Eng.*, Vol. 169, pp. 41–57.

Shetty, D. K., Wright, I. G., Mincer, P. N., and Clauer, A. H., 1985, "Indentation Fracture of WC-Co Cermets," *J. Materials Sci.*, Vol. 20, pp. 1873–1882.

Tabor, D., 1951, *The Hardness of Metals*, Oxford University Press, London.

Tanaka, K., 1984, "Evaluation of Elastic/Plastic Indentation Stress to Determine Fracture Toughness," *Trans. Japan Inst. Metals*, Vol. 48, pp. 1157–1162 (in Japanese).

Tanaka, K., Kitahara, Y., Ichinose, Y., and Iimura, T., 1984, "Fracture Analysis of Single Crystal Manganese Zinc Ferrites Using Indentation Flaws," *Acta Metall.*, Vol. 32, pp. 1719–1729.

Westbrook, J. H., and Conrad, H., 1973, *The Science of Hardness Testing and Its Research Applications*, American Society for Metals, Metals Park, Ohio.

Yingzhi, L., and Hills, D. A., 1990, "The Analysis of Three-Dimensional Cracks Generated by Sharp Indentation," *J. Mech. Phys. Solids*, Vol. 38, pp. 255–272.

Yoshino, T., and Yamada, M., 1984, "FEM Analysis of Elastic Indentation Stress of Pyramidal Indenter," *Tran. Japan Soc. Mech. Engrs.*, Vol. 50, pp. 1628–1636 (in Japanese).

Yoshizawa, T., 1967, *The Hardness Testing and Its Application*, Shokabo Press, Tokyo (in Japanese).

Zienkiewicz, O. C., 1971, *The Finite Element Method in Engineering Science*, McGraw-Hill, London.

Downloaded 03 May 2010 to 171.66.16.20. Redistribution subject to ASME license or copyright; see http://www.asme.org/terms/Terms_Use.cfm

Interfacial Zener-Stroh Crack

Hui Fan
Division of Applied Mechanics
School of Mechanical and
Production Engineering,
Nanyang Technological University,
Nanyang Avenue,
Singapore 2263, Republic of Singapore

Zener-Stroh crack is formed via coalescing dislocations piled up against an obstacle such as an interface of bimaterial. The crack is loaded by the total number of dislocations entered it, while the well-known Griffith crack is loaded by the stress traction acting on the crack surfaces. In the present paper, a Zener-Stroh crack at the interface of an anisotropic elastic bimaterial is formulated with recent improvements in two dimensional anisotropic elasticity and interfacial Griffith crack. Many interesting features of the Zener-Stroh crack are drawn from the present study and compared with those of the Griffith crack.

1 Introduction

It is probably known that, like the more famous Griffith crack, the Zener-Stroh crack was also named after its first two researchers, Zener and Stroh. Zener proposed in 1947 that dislocations in pileup stopped at an obstacle could coalesce into a crack (as shown in Fig. 1). Besides Zener, Koehler and Cottrell (see review by Weertman, 1986) were also among the pioneers who modeled this kind of cracks based on experimental observations. It was Stroh (1954) who made the first analytical study on this crack. His calculation predicted that about 1000 dislocations were needed to initiate a Zener crack from a dislocation pileup. In a follow-up paper (1955), he reduced the number of dislocation to the order of 100 by considering multislip planes. Most importantly, from the modern fracture mechanics point of view, he calculated a critical crack length via a Griffith-like energy consideration. The name of Zener-Stroh crack, coming from the above history, will be adopted in the present paper.

The Zener-Stroh crack differs from the well-known Griffith crack in terms of boundary conditions along the crack surfaces. The boundary conditions for a Zener-Stroh crack are written as

$$\mathbf{t}=0, \tag{1a}$$

$$\int_{-a}^{a}[\mathbf{u}]'dx=\mathbf{b}_T, \tag{1b}$$

for $y = 0$, $-a < x < a$. Equation (1a) is the traction-free condition on the crack surfaces; Eq. (1b) states that the net Burgers vector is nonzero. As a comparison, the boundary conditions for a Griffith crack are

$$\mathbf{t}=\bar{\mathbf{t}}, \tag{2a}$$

$$\int_{-a}^{a}[\mathbf{u}]'dx=0 \tag{2b}$$

where $\bar{\mathbf{t}}$ is the prescribed traction on the crack surfaces.

As a central topic of fracture mechanics, the Griffith crack has been thoroughly studied from all aspects. When people mention crack, they imply the Griffith crack. On the other hand, the Zener-Stroh crack has not been paid enough attention as an important topic of fracture mechanics. The reason is probably that the Griffith crack is observed at all levels of engineering structures, while the Zener-Stroh crack is usually of the size of micron (μm) or submicron which is the level of material science and micromechanics. Due to wide applications of modern materials, such as inhomogeneity reinforced composite and ceramic materials, microcracks in the order of submicron become more and more important to the understanding of failure mechanisms as well as the macroscopic properties of the materials. People begin to realize that cracks in the order of submicron may have different nature from those of bigger size. Furthermore, it has been noticed that the Griffith crack theory is not suitable to explain some failure phenomena related to very small cracks, for example, crack initiation and early stage of crack propagation in fatigue (Weertman, 1986). These impetuses lead to the current study of the Zener-Stroh crack.

In the present paper, recent development of two-dimensional anisotropic elasticity is employed to study Zener-Stroh crack which was treated by Stroh (1954) in a homogeneous isotropic medium. Without having a complete concept of modern fracture mechanics, Stroh (1954) used an energy formulation which was analogous to the Griffith theory to obtain the critical crack length. It will be shown in Section 3 that his global energy consideration can also be converted to the crack-tip energy release rate proposed by Irwin via the concept of stress intensity factors. As a more generalized case, an interfacial Zener-Stroh crack is discussed in the following sections. The discussion is motivated by observations that the Zener-Stroh crack can be initiated by piled-up dislocations at grain boundaries (Fig. 1). When an interfacial crack is concerned, people may immediately think of crack-tip oscillatory behavior. Although the

Contributed by the Applied Mechanics Division of THE AMERICAN SOCIETY OF MECHANICAL ENGINEERS for presentation at the International Mechanical Engineering Congress and Exhibition, the Winter Annual Meeting of The ASME, Chicago, IL, Nov. 6–11, 1994.

Discussion on this paper should be addressed to the Technical Editor, Professor Lewis T. Wheeler, Department of Mechanical Engineering, University of Houston, Houston, TX 77204-4792, and will be accepted until four months after final publication of the paper itself in the ASME JOURNAL OF APPLIED MECHANICS.

Manuscript received by the ASME Applied Mechanics Division, Mar. 29, 1993; final revision, Aug. 20, 1993. Associate Technical Editor: C. F. Shih.

Paper No. 94-WA/APM-1.

Copyright © 1994 by ASME
Downloaded 03 May 2010 to 171.66.16.20. Redistribution subject to ASME license or copyright; see http://www.asme.org/terms/Terms_Use.cfm

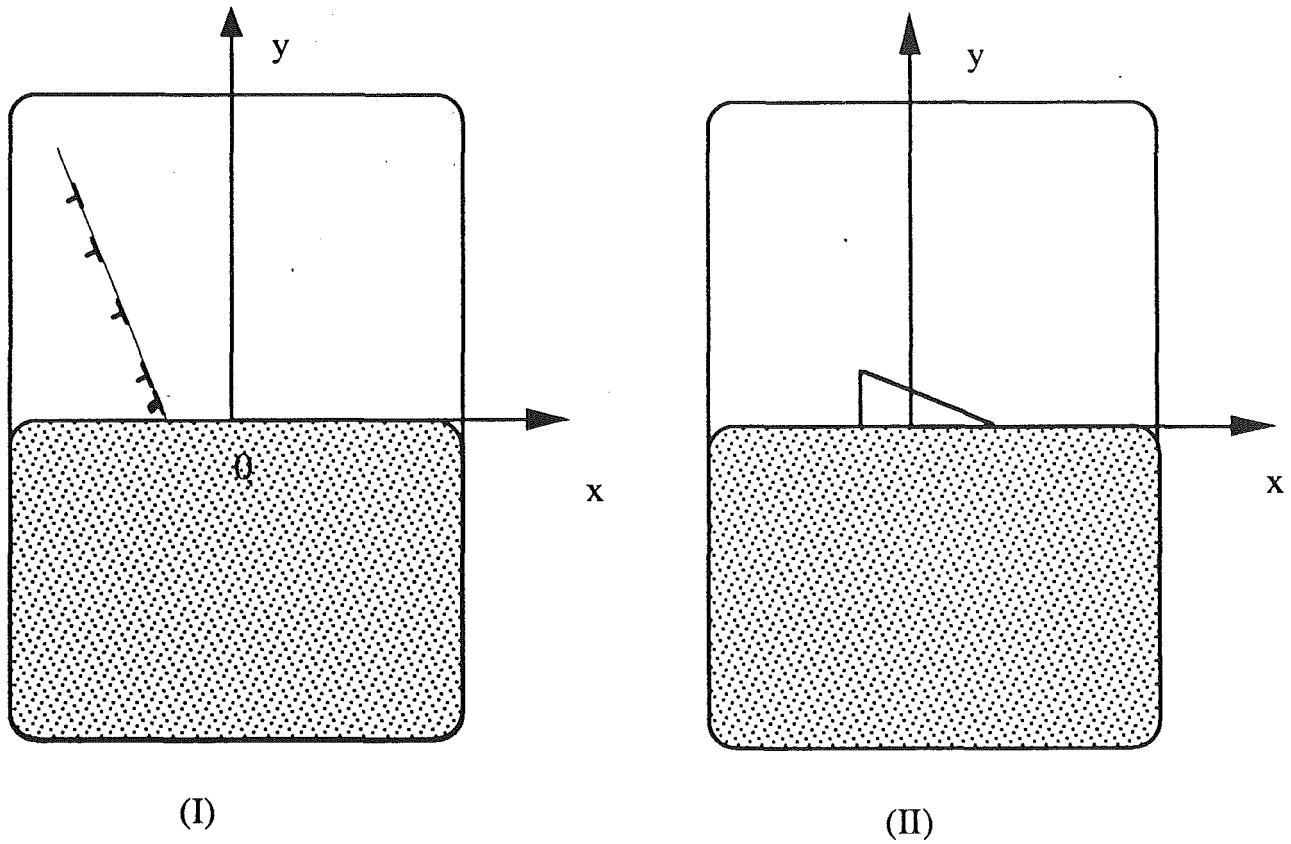


Fig. 1 Dislocation pile-up (I) coalesces into a Zener-Stroh crack

interface crack-tip oscillatory behavior was found a long time ago (Williams, 1959), the structure of the crack-tip field in an anisotropic bimaterial is a recent development. The understanding of this behavior has reached an agreeable stage due to extensive studies conducted recently (see the review article by Hutchinson and Suo, 1992). The Zener-Stroh crack tip is expected to show the same oscillation as that of the Griffith crack because the crack-tip oscillatory behavior is independent from the whole-field solution. Therefore, we will adopt some recent works, such as Suo (1990) and Gao et al. (1992), on crack-tip oscillatory behavior in the following sections without any more detailed discussion on this topic. Our attention will be focused on the new issues brought up by the Zener-Stroh crack.

2 Stroh's Formulation for Anisotropic Elasticity

Since Zener-Stroh cracks are often formed at grain boundaries, anisotropy becomes essential in the present study. The two-dimensional anisotropic elasticity can be treated by either the Lehknitskii (1961) or Stroh (1958) formulation. However, Stroh's matrix notation provides more compactness and clearness comparing to Lehknistkii's notation. It has been shown that Stroh formulation is more efficient for some anisotropic problems, such as dislocation and wave propagation. Therefore, we shall follow the Stroh's scheme in the present study. Besides, it is nice to see that Stroh's anisotropic elasticity notation serves as a powerful tool to analyze the crack named after him.

Stroh's formalism for the anisotropic elasticity has been intensively extended since its original proposition by Eshelby et al. (1953). The compactness of the matrix notation attracted researchers in the field of surface waves (e.g., Barnett and Lothe, 1985) and more recently interfacial cracks (e.g., Ting, 1992). A detailed review of this formalism is beyond the scope of the present paper. A brief derivation of the anisotropic elasticity along Stroh's formalism is presented as follows.

A linear anisotropic elastic medium is described as

$$\epsilon_{ij}=\frac{1}{2}\,(u_{i,j}+u_{j,i}), \tag{3a}$$

$$\sigma_{ij}=C_{ijkl}\epsilon_{kl}, \tag{3b}$$

$$\sigma_{ij,j}=0, \tag{3c}$$

where u_i, ϵ_{ij}, and σ_{ij} are, respectively, displacement, strain, and stress. Substituting the first two relations into the equilibrium equation, we have

$$C_{ijkl}u_{k,lj}=0. \tag{4}$$

It is assumed that

$$u_k=a_k f(z) \text{ with } z=x+py. \tag{5}$$

Equation (4) thus becomes

$$(C_{i1k1}+p(C_{i1k2}+C_{i2k1})+p^2C_{i2k2})a_k=0. \tag{6}$$

A nonzero solution of a_k requires that

$$\det(C_{i1k1}+p(C_{i1k2}+C_{i2k1})+p^2C_{i2k2})=0. \tag{7}$$

It was proven that all roots of the above equation cannot be real because of the positive definiteness of the strain energy density. Also

$$p_i=\bar{p}_{i+3}, \quad \mathrm{Im}\,p_i>0, \quad (i=1,2,3)$$

where the bar denotes the complex conjugate.

In general, we can write the displacement and stress as

$$u_i=2\mathrm{Re}\left(\sum_{j=1}^{3}A_{ij}f_j(z_j)\right), \tag{8a}$$

$$\sigma_{2i}=2\mathrm{Re}\left(\sum_{j=1}^{3}L_{ij}f_j'(z_j)\right), \tag{8b}$$

Downloaded 03 May 2010 to 171.66.16.20. Redistribution subject to ASME license or copyright; see http://www.asme.org/terms/Terms_Use.cfm

$$\sigma_{1i} = -2\mathrm{Re}\left(\sum_{j=1}^{3} L_{ij} p_j f_j'(z_j)\right), \tag{8c}$$

where

$$z_j = x + p_j y, \quad \mathbf{A} = (\mathbf{a}_1, \mathbf{a}_2, \mathbf{a}_3),$$

and

$$L_{ij} = \sum_{k=1}^{3} (C_{i2k1} + p_j C_{i2k2}) A_{kj}. \tag{9}$$

Each of the **a**'s is determined by the eigenvalue problem (Eqs. (6) and (7)) up to a complex-valued normalization constant.

When the roots p_j are distinct, Stroh (1958) proved that the matrices **A** and **L** are nonsingular. With this property, another matrix is defined as

$$\mathbf{B} = i\mathbf{A}\mathbf{L}^{-1}. \tag{10}$$

Based on the expressions of **A** and **L**, Stroh proved that matrix **B** is a Hermitian. The dynamic version of matrix **B** was introduced in surface wave propagation studies. Chadwick and Smith (1977), Barnett, Lothe, and their co-workers (e.g., Barnett and Lothe, 1985) have been active researchers in this field. More detailed results and reviews of the matrix **B** can be found in their papers.

Besides the Stroh's matrix notation presented above, the analytic continuation approach for anisotropic elasticity is employed in the following sections. Recently, Suo (1990) and Gao et al. (1992) showed that this approach is efficient to deal with joint half-space anisotropic elastic problems when they studied interfacial crack. Fan and Keer (1994) also used this approach in the analysis of a contacted anisotropic half-space. All these results are expressed in elegant and compact forms.

3 Interfacial Zener-Stroh Crack

With the expression (8) and referring to Fig. 1(*b*), stress continuation along the interface ($y = 0$) is written as

$$\mathbf{L}_1\mathbf{f}_1'(x) + \overline{\mathbf{L}_1\mathbf{f}_1'(x)} = \mathbf{L}_2\mathbf{f}_2'(x) + \overline{\mathbf{L}_2\mathbf{f}_2'(x)}, \tag{11}$$

which is followed by

$$\mathbf{L}_1\mathbf{f}_1'(z) = \overline{\mathbf{L}_2\mathbf{f}_2'(\bar{z})} \quad z \in S_1, \tag{12a}$$

$$\mathbf{L}_2\mathbf{f}_2'(z) = \overline{\mathbf{L}_1\mathbf{f}_1'(\bar{z})} \quad z \in S_2. \tag{12b}$$

With these relations, the displacement jump and traction $t_i(x) = \sigma_{2i}(x)$ along $y = 0$ are expressed as

$$i[\mathbf{u}]'(x) = \mathbf{H}\mathbf{L}_1\mathbf{f}_1'(x) - \overline{\mathbf{H}}\mathbf{L}_2\mathbf{f}_2'(x) \tag{13a}$$

$$\mathbf{t}(x) = \mathbf{L}_1\mathbf{f}_1'(x) + \mathbf{L}_2\mathbf{f}_2'(x), \tag{13b}$$

where

$$\mathbf{H} = \mathbf{B}_1 + \overline{\mathbf{B}_2}. \tag{14}$$

By defining a new function

$$\mathbf{h}(z) = \begin{cases} \mathbf{L}_1\mathbf{f}_1'(z) & \text{if } z \in S_1 \\ \mathbf{H}^{-1}\overline{\mathbf{H}}\mathbf{L}_2\mathbf{f}^2(z) & \text{if } z \in S_2 \end{cases}, \tag{15}$$

and having noted that **H** is a positive definite Hermitian (Barnett and Lothe, 1985), we have

$$i\mathbf{H}^{-1}[\mathbf{u}]'(\mathbf{x}) = \mathbf{h}^+(x) - \mathbf{h}^-(x) \tag{16}$$

$$\mathbf{t}(\mathbf{x}) = \mathbf{h}^+(x) + \overline{\mathbf{H}}^{-1}\mathbf{H}\mathbf{h}^-(x). \tag{17}$$

Equations (11) to (17) were presented by Suo (1990) for an interfacial Griffith crack. It has been proved that $\mathbf{H} = \overline{\mathbf{H}}$ is the necessary and sufficient condition for nonoscillation at the crack tip (Qu and Bassani, 1989; Suo, 1990). As the first step to the present discussion, let us consider the case $\mathbf{H} = \overline{\mathbf{H}}$ where the stress intensity factor can be defined in a conventional manner.

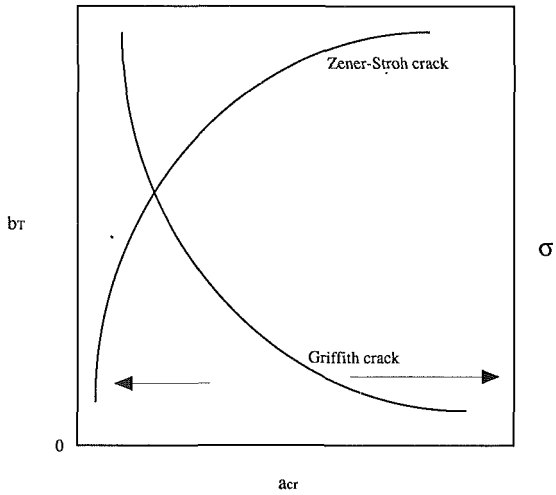


Fig. 2 Dependence of critical crack length on the loadings

(i) $\mathbf{H} = \overline{\mathbf{H}}$. The Hilbert problem for a Zener-Stroh crack under $\mathbf{H} = \overline{\mathbf{H}}$ is presented as

$$i\mathbf{H}^{-1}[\mathbf{u}]'(\mathbf{x}) = \mathbf{h}^+(x) - \mathbf{h}^-(x) = 0, \quad x \notin (-a, a) \tag{18}$$

$$\mathbf{t}(\mathbf{x}) = \mathbf{h}^+(x) + \mathbf{h}^-(x) = 0, \quad x \in (-a, a), \tag{19}$$

with

$$\int_{-a}^{a} [\mathbf{u}]'(x)dx = \int_{-a}^{a} -i\mathbf{H}(\mathbf{h}^+(x) - \mathbf{h}^-(x))dx = \mathbf{b}_T, \tag{20}$$

where $\mathbf{b}_T$ is the total Burgers vector inside the crack. The solution of the homogeneous Hilbert problem is written as

$$\mathbf{h}(z) = \mathbf{Q}(z^2 - a^2)^{-1/2}. \tag{21}$$

The vector **Q** is determined by considering that the crack is equivalent to a super dislocation with Burgers vector b_T to the far field, i.e.,

$$\mathbf{h}(z) \to \frac{\mathbf{Q}}{z} \quad \text{as} \quad |z| \to \infty. \tag{22}$$

From the solution of an interface dislocation Eq. (A7), one has

$$\mathbf{Q} = \mathbf{H}^{-1}\mathbf{b}_T/2\pi. \tag{23}$$

The stress intensity factor, **k**, of the Zener-Stroh crack is introduced by considering

$$\mathbf{t}(r) = (2\pi r)^{-1/2}\mathbf{k} \tag{24}$$

where r is the distance measured from the crack tip. With Eq. (8*b*) and Eq. (21), the stress intensity factor is obtained as

$$\mathbf{k} = \{K_{II}, K_I, K_{III}\}^T = \frac{\mathbf{H}^{-1}\mathbf{b}_T}{\sqrt{\pi a}}. \tag{25}$$

It has to be mentioned that the stress intensity factor of a Zener-Stroh crack is inversely proportional to $\sqrt{a}$, while the stress intensity factor of a Griffith crack is proportional to $\sqrt{a}$.

Without the stress intensity factor concept, Stroh (1954) found the crack propagation criterion via energy consideration which is the same as the Griffith theory. Following this idea, let us consider that the self-energy caused by the Zener-Stroh crack is approximated by the self-energy of a super-dislocation with Burger's vector $\mathbf{b}_T$ (Eq. (A8)).

$$U_{\text{self}} = \frac{1}{2\pi}\mathbf{b}_T^T\mathbf{H}^{-1}\mathbf{b}_T \ln\frac{R}{\alpha a} \tag{26}$$

where α is a constant. The total energy of the system is

$$U_{\text{total}} = U_{\text{self}} + 4a\gamma_s \tag{27}$$

Downloaded 03 May 2010 to 171.66.16.20. Redistribution subject to ASME license or copyright; see http://www.asme.org/terms/Terms_Use.cfm

where $\gamma_s = \gamma_1 + \gamma_2 - \gamma_{12}$ is the energy needed to break the interface. Then, the crack propagation criterion is set as

$$\frac{\partial U_{\text{total}}}{\partial a} = \frac{-1}{2\pi} \mathbf{b}_T^T \mathbf{H}^{-1} \mathbf{b}_T \frac{1}{a} + 4\gamma_s = 0, \tag{28}$$

which gives a critical crack length

$$a_{cr} = \frac{\mathbf{b}_T^T \mathbf{H}^{-1} \mathbf{b}_T}{8\pi\gamma_s}. \tag{29}$$

It is not difficult to verify that this a_{cr} corresponds to a minimum point of the energy function by taking the second order derivatives of U_{total}. Therefore, a_{cr} is a stable crack length. The relations between critical crack length and loadings (b_T for Zener-Stroh crack and σ for Griffith crack) are schematically shown in Fig. 2.

For a Griffith crack, Irwin realized that the energy release rate should be connected with crack-tip parameters by

$$G = \frac{1}{2\Delta} \int_0^{\Delta} \mathbf{t}^T (\Delta - r) \mathbf{d}(r) dr \tag{30}$$

where Δ is an arbitrary length.

For a Zener-Stroh crack, the energy release rate and stress intensity factor are also related via Eq. (30). This statement can be verified as follows. Substituting crack-tip stress $\mathbf{t}$ of Eq. (24) and the displacement jump behind the crack tip

$$\mathbf{d}(r) = (2r/\pi)^{1/2} \mathbf{H}\mathbf{k}$$

into Eq. (30), one obtains

$$G = \frac{1}{4} \mathbf{k}^T \mathbf{H}\mathbf{k}. \tag{31}$$

Checking Eq. (31) from the global consideration, i.e., solving $\mathbf{b}_T$ from Eq. (25) and substituting it into Eq. (28), one reaches the same result as Eq. (31).

Before we proceed the formulation for more generalized case, $\mathbf{H} \neq \overline{\mathbf{H}}$, let us summarize the key points revealed from the above discussion.

1 The critical Zener-Stroh crack length is stable, while the critical Griffith crack length is unstable. This issue will be discussed further in the next section.

2 The critical crack length of a Zener-Stroh crack increases as loading b_T increases, while the critical length of a Griffith crack decreases as loading σ increases.

3 The dependence of $\mathbf{k}$ on $1/\sqrt{a}$ implies that propagation of a small crack is controlled by Zener-Stroh crack mechanism.

These conclusions are also expected to be true for a more generalized interface crack where $\mathbf{H} \neq \overline{\mathbf{H}}$.

(ii) $\mathbf{H} \neq \overline{\mathbf{H}}$. An interface crack associated with this condition shows the so-called oscillatory behavior at the crack tip as discussed by many articles. Qu and Bassani (1989), Suo (1990), and Gao et al. (1992) are, among others, recent contributors to this subject. Recall the Hilbert problem defined in Eq. (16) and (17), the solution of this interfacial crack can be obtained by considering an eigenvalue problem as follows:

$$\overline{\mathbf{H}}^{-1} \mathbf{H}\mathbf{r} = \lambda \mathbf{r} \quad \text{or} \quad (\mathbf{H} - \lambda \overline{\mathbf{H}})\mathbf{r} = 0. \tag{32}$$

The eigenvalue λ of the above equation is obtained from

$$\det(\mathbf{H} - \lambda \overline{\mathbf{H}}) = 0. \tag{33}$$

By the definitions of the $\mathbf{H}$ (Eq. (14)), $\mathbf{B}_1$ and $\mathbf{B}_2$ (Eq. (10)), Eq. (33) is converted to a standard form which was discussed by Ting (1986):

$$\det(\mathbf{W} + i\delta \mathbf{D}) = 0 \tag{34}$$

where

$$\delta = \frac{1-\lambda}{1+\lambda}, \quad \mathbf{W} = \mathbf{W}_2 - \mathbf{W}_1, \quad \mathbf{D} = \mathbf{D}_2 + \mathbf{D}_1 \tag{35}$$

$$\mathbf{B}_1 = \mathbf{D}_1 + i\mathbf{W}_1, \quad \mathbf{B}_2 = \mathbf{D}_2 + i\mathbf{W}_2. \tag{36}$$

The eigenvalues were obtained by Ting (1986) as

$$\delta_{1,2} = \pm \left(\frac{1}{2} \operatorname{tr}[\mathbf{W}\mathbf{D}^{-1}]^2 \right)^{1/2}, \quad \delta_3 = 0. \tag{37}$$

If we write

$$\overline{\mathbf{H}}^{-1} \mathbf{H} = \mathbf{R} \Lambda \mathbf{R}^{-1}, \tag{38}$$

where $\mathbf{R}$ is formed by three independent eigenvectors of Eq. (32), Eq. (17) is then decoupled as

$$\hat{\mathbf{t}}(\mathbf{x}) = \hat{\mathbf{h}}^+(x) + \Lambda \hat{\mathbf{h}}^-(x). \tag{39}$$

where

$$\hat{\mathbf{t}} = \mathbf{R}^{-1}\mathbf{t}, \quad \hat{\mathbf{h}} = \mathbf{R}^{-1}\mathbf{h}$$

and

$$\Lambda = \operatorname{diag}(\lambda_1, \lambda_2, 1). \tag{40}$$

The solution of the potential function $\hat{\mathbf{h}}$ is obtained as

$$\begin{aligned} \hat{h}_1(z) &= Q_1^*(z-a)^{-1/2+i\epsilon}(z+a)^{-1/2-i\epsilon} \\ \hat{h}_2(z) &= Q_2^*(z-a)^{-1/2-i\epsilon}(z+a)^{-1/2+i\epsilon} \\ \hat{h}_3(z) &= Q_3^*(z-a)^{-1/2}(z+a)^{-1/2} \end{aligned} \tag{41}$$

where

$$\epsilon = \frac{1}{2\pi} \ln |\lambda_1|$$

is called the oscillation index. The vector $\mathbf{Q}^*$ is obtained via

$$\mathbf{R}\mathbf{Q}^* = \mathbf{H}^{-1}\mathbf{b}_T/2\pi, \tag{42}$$

which is given by considering the far-field limit.

A nonzero ϵ causes the crack-tip singularity oscillation. In order to dismiss the material penetration at crack tip, a near-tip zone (e.g., a contact zone proposed by Cominnou, 1977) has to be considered. It has been realized that this contact zone is so small that Eq. (41) is still valid outside this contact zone and the stress intensity factor can be defined. From Eq. (41), with definition Eq. (8*b*), one has

$$\mathbf{t}(x) = 2\operatorname{Re}(\mathbf{r}_1 \hat{h}_1(x) + \mathbf{r}_2 \hat{h}_2(x) + \mathbf{r}_3 \hat{h}_3(x)) \tag{43}$$

along the crack line. It has been proved from Eq. (32) that (e.g., Fan and Keer, 1994)

$$\mathbf{R} = \{\mathbf{r}_1, \mathbf{r}_2, \mathbf{r}_3\} = \{\mathbf{r}, \bar{\mathbf{r}}, \mathbf{r}_3\}. \tag{44}$$

Then, substituting Eq. (44) into Eq. (43) and taking Eq. (41) with $z \to a + r$, it follows that

$$\begin{aligned} \mathbf{t}(r) = r^{-1/2} &(\mathbf{r}(Q_1^* + \overline{Q}_2^*) r^{i\epsilon} (2a)^{-1/2-i\epsilon} \\ &+ \bar{\mathbf{r}}(Q_2^* + \overline{Q}_1^*) r^{-i\epsilon} (2a)^{-1/2+i\epsilon} + \mathbf{r}_3 (Q_3^* + \overline{Q}_3^*)(2a)^{-1/2}). \end{aligned} \tag{45}$$

Comparing Eq. (45) with Suo's (1990) definition,

$$\mathbf{t}(r) = (2\pi r)^{-1/2} (\mathbf{r} K r^{i\epsilon} + \bar{\mathbf{r}} \overline{K} r^{-i\epsilon} + \mathbf{r}_3 K_3), \tag{46}$$

it is easy to have the stress intensity factor for the Zener-Stroh crack as

$$K = (Q_1^* + \overline{Q}_2^*)(2a)^{-1/2-i\epsilon}(2\pi)^{1/2} \tag{47a}$$

$$K_3 = (Q_3^* + \overline{Q}_3^*)(2a)^{-1/2}(2\pi)^{1/2}. \tag{47b}$$

Since the crack-tip analysis for the interface crack has been presented by Suo (1990), the energy release rate is quoted here without detailed derivation

$$G = \bar{\mathbf{r}}^T (\mathbf{H} + \overline{\mathbf{H}}) \mathbf{r} |K|^2 / (4 \cosh^2 \pi\epsilon) + \frac{1}{8} \bar{\mathbf{r}}_3^T (\mathbf{H} + \overline{\mathbf{H}}) \mathbf{r}_3 K_3^2. \tag{48}$$

4 Griffith-Zener-Stroh Crack

As a more generalized case, a crack may be loaded with external stress and nonzero dislocations inside it. We may call it the Griffith-Zener-Stroh crack. Obviously, the stress intensity factor of a Griffith-Zener-Stroh crack depends on both the stress acting on the crack surfaces and the dislocations

Downloaded 03 May 2010 to 171.66.16.20. Redistribution subject to ASME license or copyright; see http://www.asme.org/terms/Terms_Use.cfm

entered the crack. The solution of the Hilbert problem for a Griffith-Zener-Stroh crack,

$$i\mathbf{H}^{-1}[\mathbf{u}]'(\mathbf{x}) = \mathbf{h}^{+}(x) - \mathbf{h}^{-}(x) \tag{16}$$

$$\mathbf{t}(\mathbf{x}) = \mathbf{h}^{+}(x) + \overline{\mathbf{H}}^{-1}\mathbf{H}\mathbf{h}^{-}(x), \tag{17}$$

is easily obtained by superposition of the Griffith and Zener-Stroh crack solutions. For $\mathbf{H} = \overline{\mathbf{H}}$, one has

$$\mathbf{h}(z) = \frac{\chi(z)}{2\pi i}\int_{-a}^{a}\frac{\mathbf{t}(x)dx}{\chi^{+}(x)(x-z)} + \mathbf{Q}(z^2-a^2)^{-1/2} \tag{49}$$

where

$$\chi(z) = (z^2-a^2)^{1/2}.$$

It is noted that the dislocations that formed the Griffith crack are equivalent to a super-dislocation dipole to the far field. Thus, the leading term of $\mathbf{h}(z)$ still tends to $1/z$ as $z \to \infty$ since a dislocation dipole only contributes to $1/z^2$ term as $z \to \infty$. In turn, the constant $\mathbf{Q}$ is the same as the one in Section 3 because the leading term of the solution remains the same.

The stress intensity factor apparently consists of two terms: $\mathbf{k} = \{K_{II}, K_I, K_{III}\}^T =$

$$-\frac{1}{\sqrt{\pi a}}\int_{-a}^{a}\left(\sqrt{\frac{a+\xi}{a-\xi}}\right)\mathbf{t}(\xi)d\xi + \frac{\mathbf{H}^{-1}\mathbf{b}_T}{\sqrt{\pi a}}. \tag{50}$$

For the case of uniform stress distribution on the crack surfaces, $\mathbf{t}(x) = -\mathbf{t}_0$, the integral on the left-hand side of the above formula can be obtained in a closed form, and the stress intensity factor is then written as

$$\mathbf{k} = \mathbf{t}_0\sqrt{\pi a} + \frac{\mathbf{H}^{-1}\mathbf{b}_T}{\sqrt{\pi a}}. \tag{51}$$

Generally speaking, increasing stress loading tends to make the crack more like a Griffith one, while increasing net Burgers vector tends to keep the crack a Zener-Stroh one. It is interesting to see that, for a given crack length a, the crack may be controlled by the Zener-Stroh mechanism in the ith mode if

$$t_{0i}\pi a \ll H_{ij}^{-1}b_{Tj}, \tag{52}$$

and meanwhile the crack is characterized as a Griffith crack in other modes if

$$t_{0k}\pi a \gg H_{kj}^{-1}b_{Tj}, \tag{53}$$

where $k \neq i$.

For the Griffith-Zener-Stroh crack, the Irwin's expression Eq. (31) is more efficient than the Stroh's global formulation Eq. (28) when we calculate the critical crack length. Substituting Eq. (51) into Eq. (31), it follows that

$$G = \frac{1}{4}(\pi a\mathbf{t}_0^T\mathbf{H}\mathbf{t}_0 + 2\mathbf{t}_0^T\mathbf{b}_T + \mathbf{b}_T^T\mathbf{H}^{-1}\mathbf{b}_T/\pi a). \tag{54}$$

The critical crack length is then obtained from the condition $G = G_{cr}$, i.e.,

$$\pi a_{cr} = \frac{1}{\mathbf{t}_0^T\mathbf{H}\mathbf{t}_0}\left((2G_{cr} - \mathbf{t}_0^T\mathbf{b}_T) \pm \sqrt{(2G_{cr} - \mathbf{t}_0^T\mathbf{b}_T)^2 - (\mathbf{t}_0^T\mathbf{H}\mathbf{t}_0)(\mathbf{b}_T^T\mathbf{H}^{-1}\mathbf{b}_T)}\right). \tag{55}$$

The minus sign corresponds to the stable equilibrium crack length (Zener-Stroh); while the plus sign corresponds to the unstable equilibrium crack length (Griffith). However, if

$$(2G_{cr} - \mathbf{t}_0^T\mathbf{b}_T)^2 < (\mathbf{t}_0^T\mathbf{H}\mathbf{t}_0)(\mathbf{b}_T^T\mathbf{H}^{-1}\mathbf{b}_T), \tag{56}$$

there is no equilibrium crack length, the crack will propagate catastrophically (Weertmean, 1986). These three cases, Eqs. (55) and (56), are depicted in Fig. 3 from which some interesting discussion can be made as follows.

Refer to Fig. 3(a) and recall Fig. 2, increasing σ moves a_{cr+} in Fig. 3(a) toward a_{cr-}; on the other hand, accumulated dislocations push a_{cr-} toward a_{cr+}. As the limit of this moving, the situation in Fig. 3(b) is finally reached. This mechanism provides alternative explanations for the following two widely observed phenomena. First, it explains why material fails at a stress level far below the so-called theoretical stress. Due to inevitable pre-existed b_T or stress-induced dislocation accumulation, a nonzero a_{cr-} sets a bottom line for a_{cr+}. The material fractures when the stress reaches the level at which $a_{ar+} = a_{cr-}$. It is seen that this stress is a finite number which depends on materials constants ($\mathbf{H}$ in Eq. (55)) and the number of dislocations. Secondly, fatigue failure can be explained qualitatively by this mechanism. For a given cyclic stress level σ which is lower than the static fracture stress, the dislocation b_T accumulates as the cycle number increases (for example, Mura and Nakasone, 1990). Increased b_T moves a_{cr-} toward a_{cr+} until the stage in Fig. 3(b) is reached. The consequence is that the material fails at the cyclic stress which is far below the static limit. Figure 3(c) is interpreted as that for a given pre-existing b_T (damaged material); that is a stress level above which the material fails immediately.

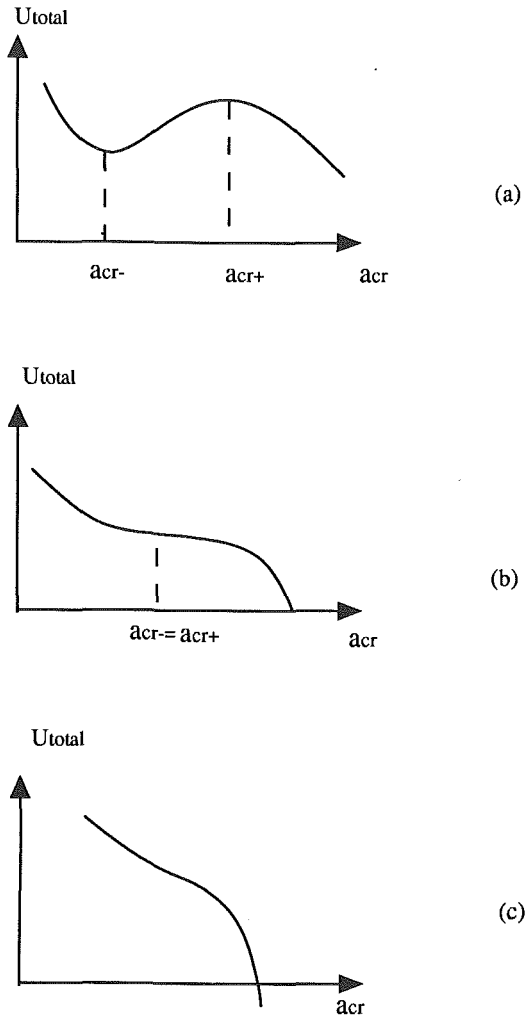


Fig. 3 Energy of a Griffith-Zener-Stroh crack

For the case of complex $\mathbf{H}$, formulation is more complicated due to the oscillatory behavior. However, similar results as above can be expected.

Downloaded 03 May 2010 to 171.66.16.20. Redistribution subject to ASME license or copyright; see http://www.asme.org/terms/Terms_Use.cfm

5 Summary and Concluding Remarks

A Zener-Stroh crack at the interface of two anisotropic half-spaces is formulated via the Stroh formalism and the analytic continuation approach. Major attention is focused on the differences between the Zener-Stroh crack and the Griffith one. It is noted that the Zener-Stroh crack is displacement loaded, which leads to a stable critical crack length; while the Griffith crack is stress loaded, which leads to an unstable critical crack length. Roughly speaking, short crack behaviors are controlled by the Zener-Stroh mechanism and longer crack behaviors are controlled by the Griffith theory. The quantitative description of a crack being "short" or "long" has to do with the material properties and loading levels (see Eqs. (52) and (53)).

Besides the physical dual properties between these two cracks, the Zener-Stroh and Griffith cracks also play counterpart roles in their mathematical formulation. Weertman (1986) pointed out that the Zener-Stroh crack and Griffith crack form a complementary pair from mathematics point of view based on his dislocation density formulation. The present formulation shows that the Zener-Stroh crack solution is simply a solution of a homogeneous Hilbert problem, while the Griffith crack solution is that of the nonhomogeneous Hilbert problem. A generalized solution is presented in Section 4 for a Griffith-Zener-Stroh crack. From this solution, stability of a crack in a whole range is discussed (Eq. (55) and Fig. 3).

It has been shown that the introduction of the Zener-Stroh crack provides us a new angle to look at the mechanisms of failure phenomena. More applications of the Zener-Stroh crack are expected in the field of micromechanics and fracture mechanics. I hope that the present paper can shed some light on this subject.

References

Barnett, D. M., and Lothe, J., 1985, "Free Surface (Rayleigh) Waves in Anisotropic Elastic Half Space: The Surface Impendance Method," *Proceedings of the Royal Society of London*, Vol. A402, pp. 135–152.

Chadwick, P., and Smith, G. D., 1977, *Advances in Applied Mechanics*, Vol. 17, Academic Press, San Diego, CA.

Comninou, M., 1977, "The Interface Crack," ASME JOURNAL OF APPLIED MECHANICS, Vol. 44, pp. 631–636.

Eshelby, J. D., Read, W. T., and Shockley, W., 1953, "Anisotropic Elasticity with Applications to Dislocation Theory," *Acta Metall.*, Vol. 1, pp. 251–259.

Gao, H., Addudi, H., and Barnett, D. M., 1992, "Interfacial Crack-Tip Field in Anisotropic Elastic Solids," *Journal of the Mechanics and Physics of Solids*, Vol. 40, No. 2, pp. 393–416.

Fan, H., and Keer, L. M., 1994, "Two-Dimensional Contact on an Anisotropic Elastic Half-Plane," ASME JOURNAL OF APPLIED MECHANICS, Vol. 61, pp. 250–255.

Hutchinson, J. W., and Suo, Z., 1992, *Advances in Applied Mechanics*, Vol. 29, Academic Press, San Diego, pp. 64–192.

Lekhnitskii, S. G., 1961, *Theory of Elasticity of an Anisotropic Body*, Holden Day, San Francisco, CA.

Mura, T., and Nakasone, Y., 1990, "A Theory of Fatigue Crack Initiation in Solids," ASME JOURNAL OF APPLIED MECHANICS, Vol. 57, pp. 1–6.

Qu, J., and Bassani, J. L., 1989, "Cracks on Bimaterial and Bicrystal Interface," *Journal of the Mechanics and Physics of Solids*, Vol. 37, pp. 417–434.

Qu, J., and Li, Q. Q., 1991, "Interfacial Dislocation and its Application to Interface Cracks in Anisotropic Bimaterials," *Journal of Elasticity*, Vol. 26, pp. 169–195.

Sou, Z., 1990, "Singularities, Interfaces and Cracks in Dissimilar Anisotropic Media," *Proceedings of the Royal Society of London*, Vol. A427, pp. 331–358.

Stroh, A. N., 1954, "The Formation of Cracks as a Results of Plastic Flow," *Proceedings of the Royal Society of London*, Vol. A223, pp. 404–414.

Stroh, A. N., 1955, "The Formation of Cracks in Plastic Flow II," *Proceedings of the Royal Society of London*, Vol. A232, pp. 548–560.

Stroh, A. N., 1958, "Dislocation and Crack in Anisotropic Elasticity," *Philosophical Magazine*, Vol. 3, pp. 625–646.

Ting, T. C. T., 1986, "Explicit Solution and Invariance of the Singularities at an Interface Crack in Anisotropic Composite," *International Journal of Solids and Structures*, Vol. 22, pp. 965–983.

Ting, T. C. T., 1992, "Interface Cracks in Anisotropic Elastic Bimaterials—A Decomposition Principle," *International Journal of Solids and Structures*, Vol. 29, pp. 1989–2003.

Weertman, J. R., 1986, "Zener-Stroh Crack, Zener-Hollomon Parameter, and Other Topics," *Journal of Applied Physics*, Vol. 60, No. 6, pp. 1877–1887.

Williams, M. L., 1959, "The Stress Around a Fault or Crack in Dissimilar Media," *Bulletin of the Seismological Society of America*, Vol. 49, pp. 199–204.

Willis, J. R., 1971, "Fracture Mechanics of Interface Crack," *Journal of the Mechanics and Physics of Solids*, Vol. 19, pp. 353–368.

APPPENDIX

A Dislocation at the Interface of a Bimaterial

This solution has been discussed in many articles. Cited here is Suo's (1990) formulation via the complex variable approach. Assuming that the dislocation is embedded in the lower space (S_2), the complex potential is written as

$$\mathbf{f}(z)=\begin{cases}\mathbf{f}_1(z) & \text{if } z\in S_1\\ \mathbf{f}_0(z)+\mathbf{f}_*(z) & \text{if } z\in S_2,\end{cases} \tag{A1}$$

where $\mathbf{f}_0(z)$ is the solution of a dislocation in an infinite homogeneous space, i.e.,

$$f_{oj}(z)=q_j \ln (z-s_j) \tag{A2}$$

$$\mathbf{q}=\mathbf{L}^{-1}(\mathbf{B}+\bar{\mathbf{B}})^{-1}\mathbf{b}/2\pi. \tag{A3}$$

Stress traction and displacement continuities along the interface ($y = 0, -\infty < x < \infty$) lead to

$$\mathbf{f}_1(z)=\mathbf{L}_1^{-1}\mathbf{H}^{-1}(\bar{\mathbf{B}}_2+\mathbf{B}_2)\mathbf{L}_2\mathbf{f}_0(z) \quad z\in S_1, \tag{A4}$$

$$\mathbf{f}_*(z)=\mathbf{L}_2^{-1}\bar{\mathbf{H}}^{-1}(\bar{\mathbf{B}}_2-\mathbf{B}_1)\overline{\mathbf{L}\mathbf{f}_0(\bar{z})} \quad z\in S_2. \tag{A5}$$

When the dislocation sits on the interface of the bimaterial, the foregoing result is simplified as

$$\mathbf{L}_1\mathbf{f}_1(z)=\bar{\mathbf{L}}_2\overline{\mathbf{f}_2(\bar{z})}=\frac{1}{2\pi}\mathbf{H}^{-1}\mathbf{b}\ln z. \tag{A6}$$

Furthermore, the traction along the interface is

$$\mathbf{t}(x)=\frac{1}{2\pi}\left(\frac{\mathbf{H}^{-1}}{x+0i}+\frac{\bar{\mathbf{H}}^{-1}}{x-0i}\right)\mathbf{b}. \tag{A7}$$

This form was introduced by Willis (1971). Recently, Qu and Li (1991) revisited this problem since it is a basic block of the interface crack solution. The strain energy of a dislocation at the interface is calculated as

$$U=\frac{1}{2}\mathbf{b}^T\int_r^R \mathbf{t}(x)dx=\frac{1}{2\pi}\mathbf{b}^T\mathbf{H}^{-1}\mathbf{b}\ln\frac{R}{r}. \tag{A8}$$

This equation has been used in Eq. (26) where the equilibrium Zener-Stroh crack length is obtained.

Downloaded 03 May 2010 to 171.66.16.20. Redistribution subject to ASME license or copyright; see http://www.asme.org/terms/Terms_Use.cfm

Antiplane Elastic Wave Scattering From a Curved Randomly Rough Crack

A. Boström

P.-Å. Jansson

P. Olsson

Division of Mechanics,
Chalmers University of Technology,
S-412 96 Göteborg,
Sweden

The problem of scattering of antiplane elastic waves from a rough crack is solved by means of an extension of the null field approach. The extension consists of the expansion of certain matrix elements in terms of a small parameter followed by an analytical ensemble averaging. The geometry is taken to be two-dimensional, and the scatterer is a curved crack with a small random roughness. Both effects due to overall curvature and effects due to surface roughness are thus included in the analysis. It is assumed that the roughness is one where the height has less effect on the scattering than does the gradient (this is satisfied whenever the correlation length of the surface roughness is much smaller than the curvature of the crack), and some numerical results are given for this case. However, it is a straightforward extension of the analysis to consider cases where the height effects are included.

Introduction

The scattering of elastic waves from cracks is a field of study which has a number of important applications in nondestructive testing and characterization of materials. The present paper deals with a problem which lies at the intersection of this and another important subject, namely the theory of scattering from rough surfaces. The latter subject also has many applications, some of them in ultrasonic nondestructive testing. The reader is referred to the book by Ogilvy (1991) for a recent review of the literature on scattering from randomly rough surfaces. Ogilvy (1989) demonstrates clearly the relevance for nondestructive testing of studying the scattering properties of rough defects. Kirchhoff theory, which has perhaps been the most common approach to the scattering problem for rough surfaces, is used by Ogilvy (1989). Lewis (1990) provides an example of another approach, using a Green function technique.

The problem considered in the following sections is a two-dimensional problem of scattering of "horizontally" polarized shear waves in an isotropic solid. The applications we have in mind are such which involve ultrasonic waves in nondestructive testing. (It could be argued that the antiplane wave case is far from typical in ultrasonic nondestructive testing, but apart from it primarily forming a test case for the approach as such, we should mention that it is the case of antiplane waves with respect to the crack rather than with respect to the probe that is considered.) We consider an ultrasonic wave which is scattered off a rough curved crack in the otherwise homogeneous solid.

Chapter 9 of the book by Ogilvy (1991) provides a summary of what is known about the scattering properties of rough surfaces. A number of unresolved problems are also listed. One of these concerns the role of edge diffraction in determining the scattered field for finite-sized surfaces, and another the effects of nonplanar reference surfaces. We touch upon both of these questions in the problem we consider: The crack is curved; for simplicity it is assumed to form a circular arc. In addition to this overall curvature we introduce a roughness on a scale which is taken to be much smaller than the extension of the crack, but, more importantly, much smaller than the wavelength of the elastic waves with which we insonify the crack. In our analysis we include the stochastic contribution to the edge effects. To indicate the importance of this contribution we for comparison give some numerical results where the stochastic part of the edge effects has been suppressed.

The sense in which the roughness is small will be made precise in the following sections, but we indicate here that the case which will receive the most attention in this paper is that where the influence of the roughness manifests itself mostly through its slope, rather than through its height perturbation.

The problem which we solve is the direct scattering problem for this type of scatterer; i.e., we wish to determine the scattered field from a knowledge of the incident field and the properties of the crack. This type of problem for the much simpler case of antiplane wave scattering from a semi-infinite or finite planar two-dimensional crack has been dealt with extensively in the literature. It is well known that for the semi-infinite case the

Contributed by the Applied Mechanics Division of THE AMERICAN SOCIETY OF MECHANICAL ENGINEERS for presentation at the International Mechanical Engineering Congress and Exhibition, the Winter Annual Meeting of The ASME, Chicago, IL, Nov. 6-11, 1994.

Discussion on this paper should be addressed to the Technical Editor, Professor Lewis T. Wheeler, Department of Mechanical Engineering, University of Houston, Houston, TX 77204-4792, and will be accepted until four months after final publication of the paper itself in the ASME JOURNAL OF APPLIED MECHANICS.

Manuscript received by the ASME Applied Mechanics Division, Apr. 13, 1993; final revision, Oct. 26, 1993. Associate Technical Editor: S. K. Datta.

Paper No. 94-WA/APM-4.

Copyright © 1994 by ASME

Downloaded 03 May 2010 to 171.66.16.20. Redistribution subject to ASME license or copyright; see http://www.asme.org/terms/Terms_Use.cfm

scattering problem can be solved exactly in terms of Fresnel integrals, and the finite case can be solved by means of integral equation techniques, see e.g., Achenbach et al. (1982). The method of solution we have adopted for the present problem is the so-called null-field approach (sometimes called the T matrix method, for a number of reasons an unfortunate designation). The book edited by Varadan and Varadan (1980) provides a number of examples of problems to which this method has been applied in various branches of scattering theory. More specifically relevant to our treatment are the papers by Boström and Olsson (1987) and by Olsson (1986, 1990) on scattering by nonplanar cracks, as well as the paper by Olsson et al. (1990) on scattering from inclusions covered by thin coatings. In the present paper, as well as in a previous paper by Jansson (1993), the idea of Olsson et al. (1990) of expanding the matrix elements of the null-field expression for the transition matrix in terms of a small parameter describing the perturbation of a simpler scatterer is utilized.

However, interesting as it might be in itself, we are not primarily interested in the scattering from a certain, specified "deterministic" crack, but rather in the scattering properties of a *randomly* rough crack. This could be obtained by solving numerically the scattering problems for a "large" number of specific rough cracks, picked from a certain ensemble (cf. Ogilvy, 1988, 1991). The result for a randomly rough crack could then be found by averaging the results from the specific cracks. In the book by Ogilvy (1991) this is called the numerical simulation technique. As in the paper by Jansson (1993), dealing with acoustic scattering from a rough sound-soft sphere, we instead adopt what is called the analytical averaging technique (cf. Ogilvy, 1991) where we assume a certain correlation function for the local height of the roughness. The roughness is then described in terms of the parameters of the correlation function used. In the present case, such parameters are the root-mean-square height and the correlation length. All averaging is performed analytically, and we thus only have to solve one scattering problem, as opposed to the large number of such which we would have had to consider had we instead adopted the numerical simulation approach.

In order to be able to solve the problem by means of the null-field approach, we need to complete the curve describing the crack into a closed curve, where different boundary conditions apply over different parts of the curve. For reasons of continuity we endow the entire closed curve with the same roughness as the crack. A complication for closed curves (as for closed surfaces in the three-dimensional case) is the fact that correlation functions such as the exponential or the gaussian, while often being perfectly acceptable for a scatterer of infinite extension, lead to difficulties in the form of delta function behavior. However, as we shall demonstrate, this can easily be overcome by a slight modification of the gaussian correlation function, a modification which does not alter its short-range behavior.

1 Formulation and Null-Field Solution

The scattering problem we consider is the following: Inside an otherwise homogeneous and isotropic elastic solid a nonplanar crack is situated. The crack, which in addition to having an overall curvature is endowed with a small scale roughness, is insonified by an ultrasonic wave. Given the incident sound field and the geometry of the crack, we want to compute the scattered sound. We here only consider a two-dimensional geometry (cf. Fig. 1) so that the shape and relative location of the intersection of the crack with any plane parallel to a fixed plane is assumed to be constant. The curve C_o which forms the intersection between the crack and one of the planes is furthermore assumed to be almost a circular arc of radius a, i.e., with ϵ being a small dimensionless parameter,

$$C_o: \quad r(\varphi) = a(1 + \epsilon h(\varphi)), \quad -\varphi_o \le \varphi \le \varphi_o \tag{1}$$

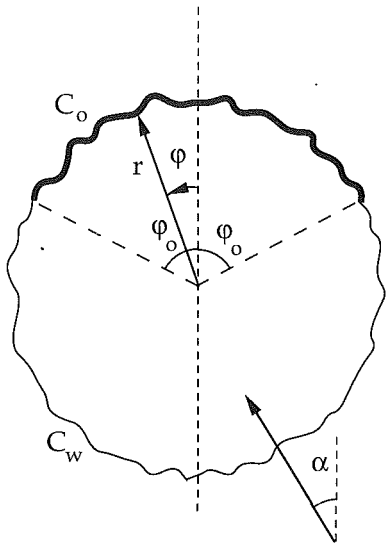


Fig. 1 The two-dimensional geometry of the crack. C_o is the curve representing the crack. C_w is a fictitious curve introduced to form a closed curve C, encircling the origin. α is the angle of incidence of the planar wave considered in Section 4.

where r and φ are polar coordinates in the plane, and h is a continuously differentiable function describing the shape of the small scale roughness of the crack. Note that we assume the crack to be a "mathematical" crack. Both sides of the crack are thus described by the same curve. As noted by Ogilvy (1991), almost all studies of scattering from "slightly" rough surfaces carry the assumption that the mean scattering surface is planar; the present study (as well as the one by Jansson, 1993) contains the combined effects of an overall curvature and a microstructure in the form of a surface roughness. It should be noted that the simplifying assumption of almost circularity is not necessary for the analysis of the present paper to carry through (cf. Boström and Olsson, 1987; Olsson, 1986, 1990). However, it allows us to compute the matrix elements analytically, which is a definite advantage. In Section 2 we will specify the assumptions on the parameter ϵ and the function h. Here it will suffice to assume that ϵ is "sufficiently" small for us to be able to make Taylor expansions in ϵ.

We take the incident wave to be a time harmonic antiplane wave, i.e., a shear wave of horizontal polarization, the displacement being directed in the z direction, normal to the $r\varphi$ plane. The time factor is $\exp(-i\omega t)$, and we suppress it throughout. The component of the displacement vector of the incident wave normal to the $r\varphi$ plane is denoted by u^i. The incident as well as the scattered wave u^s satisfy the same equation as does the total field u, the scalar Helmholtz equation

$$\nabla^2 u + k^2 u = 0, \tag{2}$$

where ∇^2 is the two-dimensional Laplacian and k is the shear wave number in the solid.

The elementary outgoing wave solutions of Eq. (2) are

$$\psi_m(\mathbf{r}) = \frac{1}{2} H_m(kr) e^{im\varphi}, \quad m \in \mathbf{Z} \tag{3}$$

and the corresponding regular functions are given by

$$\phi_m(\mathbf{r}) = \frac{1}{2} J_m(kr) e^{im\varphi}, \quad m \in \mathbf{Z} \tag{4}$$

Here H_m is the cylindrical Hankel function of the first kind, and J_m is the cylindrical Bessel function (and $\mathbf{Z}$ is the set of integers). In terms of these solutions, we can expand the incident and scattered fields:

Downloaded 03 May 2010 to 171.66.16.20. Redistribution subject to ASME license or copyright; see http://www.asme.org/terms/Terms_Use.cfm

$$u^i = \sum_{m=-\infty}^{\infty} a_m \phi_m \tag{5}$$

$$u^s = \sum_{m=-\infty}^{\infty} f_m \psi_m \tag{6}$$

where Eq. (5) holds from the origin out to the closest source point of the incident sound field (we take this to be at some distance from the origin which is greater than $\max\{r:\mathbf{r} \in C_o\}$; in the numerical examples, where we treat plane wave incidence, the sources lie at infinity). Equation (6), on the other hand, holds outside the circumscribed circle (centered at the origin) of C_o. The free space Green function $G(\mathbf{r}, \mathbf{r}') = iH_0(k|\mathbf{r} - \mathbf{r}'|)/4$ corresponding to Eq. (2) is similarly expanded as

$$G(\mathbf{r}, \mathbf{r}') = i \sum_{m=-\infty}^{\infty} (-1)^m \phi_m(k\mathbf{r}_<)\psi_{-m}(k\mathbf{r}_>) \tag{7}$$

where the minus sign in the index can be moved to the other function. $\mathbf{r}_<$ is either $\mathbf{r}$ or $\mathbf{r}'$, depending on which of them have the lesser modulus, and similarly for $\mathbf{r}_>$ and the greater modulus. The boundary conditions imposed on the normal derivative of the total field on the outer (+) and inner (−) side of C_o are

$$\left(\frac{\partial u}{\partial n}\right)_+ = 0, \quad \left(\frac{\partial u}{\partial n}\right)_- = 0 \quad \text{on } C_o \tag{8a,b}$$

which implies vanishing traction on the crack surface. Following the same procedure as Boström and Olsson (1987) and Olsson (1986, 1990) we now introduce a curve C_w (w for "welded") which together with C_o forms a closed, positively oriented curve C, the latter being a perturbed circle centered at the origin. This could be construed as extending the definition of the function $h(\varphi)$ in Eq. (1) to take values also for φ in the range outside of the one corresponding to C_o, in such a manner that h is continuously differentiable and periodic with period 2π. To employ the null-field approach we need a closed curve, and to take the edge effects into account we need a curve with continuous tangent vector. On C_w we have the boundary conditions

$$u_+ = u_-, \quad \left(\frac{\partial u}{\partial n}\right)_+ = \left(\frac{\partial u}{\partial n}\right)_- \text{ on } C_w. \tag{9a,b}$$

The scattered field is generated from the crack-opening displacement, and can be expressed as a line integral along C_o:

$$u^s(\mathbf{r}) = \int_{C_o} (u_+(\mathbf{r}') - u_-(\mathbf{r}')) \frac{\partial G(\mathbf{r}, \mathbf{r}')}{\partial n'} ds', \quad \mathbf{r} \text{ not on } C_o \tag{10}$$

where the line element is given by

$$ds' = a[1 + 2\epsilon h(\varphi') + \epsilon^2(h'(\varphi')^2 + h(\varphi')^2)]^{1/2} d\varphi'. \tag{11}$$

The incident field inside C is given by a similar expression, but involving also an integral along the entire curve C:

$$u^i(\mathbf{r}) = -\int_{C_o} (u_+(\mathbf{r}') - u_-(\mathbf{r}')) \frac{\partial G(\mathbf{r}, \mathbf{r}')}{\partial n'} ds' - \int_C \left[u_-(\mathbf{r}') \frac{\partial G(\mathbf{r}, \mathbf{r}')}{\partial n'} - G(\mathbf{r}, \mathbf{r}') \left(\frac{\partial u(\mathbf{r}')}{\partial n'}\right)_- \right] ds', \quad \mathbf{r} \text{ inside } C. \tag{12}$$

Equations (10) and (12) have been derived by means of an integral representation theorem in which the boundary conditions have been inserted (cf. the derivation by Olsson, 1990). A further integral relation, derived in the same manner, which we will find useful is the following:

$$\int_C u_-(\mathbf{r}') \frac{\partial G(\mathbf{r}, \mathbf{r}')}{\partial n'} ds' - \int_{C_w} G(\mathbf{r}, \mathbf{r}') \left(\frac{\partial u(\mathbf{r}')}{\partial n'}\right)_- ds' = 0, \quad \mathbf{r} \text{ outside } C \tag{13}$$

which provides a relation between the total displacement field on the inside of C and the traction on the welded part of C.

In a manner closely reminiscent of the procedure of Boström and Olsson (1987) and Olsson (1986, 1990) we now introduce an auxiliary field v, defined on the curve C:

$$v(\mathbf{r}) = \begin{cases} \dfrac{1}{Z_o(\mathbf{r})} (u_+(\mathbf{r}) - u_-(\mathbf{r})), & \mathbf{r} \in C_o \\ \dfrac{1}{Z_w(\mathbf{r})} \dfrac{1}{k} \left(\dfrac{\partial u(\mathbf{r})}{\partial n}\right)_-, & \mathbf{r} \in C_w. \end{cases} \tag{14}$$

Here the two functions $Z_o(\mathbf{r})$ and $Z_w(\mathbf{r})$ are introduced so as to make $v(\mathbf{r})$ a continuous function on C. This means that the factors must incorporate the edge conditions at the crack edges, taking the location and slope into account. Many different choices are possible, but for technical reasons (see below) we prefer

$$Z_o(\mathbf{r}) = [ka(\varphi_o^2 - \varphi^2)]^{1/2}, \quad -\varphi_o \le \varphi \le \varphi_o \tag{15}$$

$$Z_w(\mathbf{r}) = \left[\frac{\varphi_o(\pi - \varphi_o)}{4ka(\varphi - \varphi_o)(2\pi - \varphi_o - \varphi)[1 + 2\epsilon h(\varphi) + \epsilon^2(h'(\varphi)^2 + h(\varphi)^2)]} \right]^{1/2}, \quad \varphi_o \le \varphi \le 2\pi - \varphi_o. \tag{16}$$

In order to discretize our problem we approximate the surface fields u_- and v in the following manner:

$$u_- = \sum_{m=-\infty}^{\infty} \alpha_m \phi_m \tag{17}$$

$$v = \sum_{m=-\infty}^{\infty} \beta_m e^{im\varphi}. \tag{18}$$

The reason for choosing the regular wave functions as the expansion system for u_- is to simplify the matrix relations between the expansion coefficients in Eqs. (5), (6), (17), and (18) (see below). Strictly speaking, Eqs. (17) and (18) are (if C is not a perfect circle) sequence approximations, where the coefficients in general depend on the truncation, but this technicality will not be discussed further here.

Inserting the expansions Eqs. (5), (6), (7) and the surface field approximations Eqs. (17) and (18) into the integral relations Eqs. (10), (12), and (13), and picking field points inside the inscribed or outside the circumscribed circle, as appropriate (cf. Boström and Olsson, 1987, and Olsson, 1990, for more details), we obtain three matrix equations:

$$\mathbf{a} = \boldsymbol{\alpha} - iQ\boldsymbol{\beta} \tag{19a}$$

$$\mathbf{f} = iR\boldsymbol{\beta} \tag{19b}$$

$$P\boldsymbol{\alpha} = S\boldsymbol{\beta}. \tag{19c}$$

Here the letters $\mathbf{a}$, $\mathbf{f}$, $\boldsymbol{\alpha}$, and $\boldsymbol{\beta}$ stand for column vectors formed from the sequences of coefficients a_m, f_m, etc. Note that in Eq. (19a) the $\boldsymbol{\alpha}$ vector is not premultiplied by any matrix; this is a consequence of our choice of expansion system for u_-. The matrices Q, R, P, and S are given by

$$Q_{mm'} = (-1)^m \int_{C_o} \frac{\partial \psi_{-m}}{\partial n} Z_o e^{im'\varphi} ds \tag{20}$$

$$R_{mm'} = (-1)^m \int_{C_o} \frac{\partial \phi_{-m}}{\partial n} Z_o e^{im'\varphi} ds \tag{21}$$

Downloaded 03 May 2010 to 171.66.16.20. Redistribution subject to ASME license or copyright; see http://www.asme.org/terms/Terms_Use.cfm

$$P_{mm'} = (-1)^m \int_C \frac{\partial \phi_{-m}}{\partial n} \phi_{m'} ds \tag{22}$$

$$S_{mm'} = (-1)^m k \int_{C_w} \phi_{-m} Z_w e^{im'\varphi} ds. \tag{23}$$

For a given ("deterministic") shape of the crack, the scattering problem is now solved by eliminating the surface field coefficients from Eqs. (19*a*)–(19*c*) and solving for f in terms of a,

$$\mathbf{f} = T\mathbf{a} \tag{24}$$

where the transition matrix T is given by

$$T = -R(PQ + iS)^{-1}P. \tag{25}$$

It is worthwhile to compare the expression in Eq. (25) to the corresponding one obtained by, e.g., Boström and Olsson (1987). By choosing to expand the interior field rather than the exterior one, we have eliminated the need for double matrix inversions in the expression for the transition matrix, an improvement over Boström and Olsson (1987). Apart from suggesting a slightly better way of solving the scattering problem in the latter paper, it entails a considerable simplification in the present context, where we aim at making a Taylor expansion of the T matrix.

The Taylor expansion of the transition matrix is given by

$$T = T_0 + \epsilon k a T_1 + (\epsilon k a)^2 T_2 + O((\epsilon k a)^3) \tag{26}$$

where ϵka must be assumed to be small to enable us to expand the Bessel and Hankel functions entering in the matrix elements (cf. Eqs. (43)–(49) below). (This assumption is not specific to the present approach (cf. Ogilvy, 1991).) The matrices T_i, i = 0, 1, 2, can be expressed in terms of the corresponding coefficients Q_i, R_i, P_i, and S_i in Taylor expansions, similar to Eq. (26), of the matrices Q, R, P, and S. Introducing the matrix

$$A_0 = (P_0 Q_0 + iS_0)^{-1}, \tag{27}$$

the matrices T_0, T_1, and T_2 are given by

$$T_0 = -R_0 A_0 P_0 \tag{28a}$$

$$T_1 = -R_0 A_0 P_1 + R_0 A_0 (P_0 Q_1 + P_1 Q_0 + iS_1) A_0 P_0 - R_1 A_0 P_0 \tag{28b}$$

$$\begin{aligned} T_2 = &-R_0 A_0 P_2 - R_2 A_0 P_0 - R_1 A_0 P_1 + R_0 A_0 (P_0 Q_1 + P_1 Q_0 \\ &+ iS_1) A_0 P_1 + R_1 A_0 (P_0 Q_1 + P_1 Q_0 + iS_1) A_0 P_0 \\ &- R_0 A_0 (P_0 Q_1 + P_1 Q_0 + iS_1) A_0 (P_0 Q_1 + P_1 Q_0 + iS_1) A_0 P_0 \\ &+ R_0 A_0 (P_0 Q_2 + P_1 Q_1 + P_2 Q_0 + iS_2) A_0 P_0. \end{aligned} \tag{28c}$$

While explicit expressions for the matrices could now be given, we will instead proceed to take the random nature of the roughness into account. This amounts to computing averages of the matrices involved, and to do so we must make a statistical description of the crack surface. This is the topic of the next section.

2 Statistical Description of the Surface

In Section 1, Eq. (1), we gave a description of the crack shape C_o in terms of a small parameter ϵ and a function h giving the deviation from a circular arc. Later, when introducing the "fictitious" curve C_w to form a closed curve C together with C_o, we extended the domain of definition of the function h to the entire unit circle. Thus C is the star-shaped curve

$$C: \quad r(\varphi) = a(1 + \epsilon h(\varphi)), \quad -\varphi_o \le \varphi \le 2\pi - \varphi_o \tag{29}$$

where h is continuously differentiable and periodic with period 2π.

As stated above we assume that the deviation of C from a circle of radius a is small. This amounts to restricting ϵh to be small compared to unity. To give a description of the roughness we now furthermore assume that the roughness is ergodic. This means that any statistical average, taken over many different parts of the curve C, is equivalent to an average taken over many different curves in a certain ensemble of allowed curves: Ensemble averaging and spatial averaging lead to the same statistics. As a consequence of this, the probability that the deviation from the circle at a certain point φ falls in a certain range $\epsilon a\, dh$ around $\epsilon a h$ is independent of φ. The deviation is assumed to be randomly distributed around the average 0, with ϵa being the RMS height of the deviation. Denoting ensemble averaging by $\langle \cdot \rangle$, we thus have

$$\langle h(\varphi) \rangle = 0, \quad \langle h(\varphi)^2 \rangle = 1. \tag{30a, b}$$

It can be noted that from the first of these relations we obtain $\langle h'(\varphi) \rangle = 0$.

We also need to introduce a correlation function to describe the length scale over which changes in height occur. This function depends only on the distance between two points along the unperturbed curve; i.e., in this case on the angle between the radii to the two points. There are some types of correlation functions in common use which are not very useful to employ in the present context. Consider the exponential and the Gaussian correlation functions (Ogilvy, 1991): both of these lead to discontinuities in the first derivatives (and thus delta function behavior in the higher derivatives) of the correlation function at the endpoints of the angular interval. We must ensure that the correlation function is periodic of period 2π in the difference between the angular coordinates, and since it is still desirable to have, e.g., a Gaussian correlation at small angular distances, the natural assumption seems to be

$$\langle h(\varphi) h(\varphi') \rangle = \exp\left[-\frac{a^2}{\lambda_c^2} (1 - \cos(\varphi - \varphi')) \right]. \tag{31}$$

Here λ_c is the correlation length, a quantity related to the average distance between two consecutive peaks on the curve C. By differentiation of Eq. (31) it is a simple matter to compute quantities like $\langle h'(\varphi)^2 \rangle$, which is related to the average slope of the deviation.

The correlation function in Eq. (31) has a simple Fourier expansion. In the following sections we will, however, only need the expansion of the function which describes the slope correlation:

$$\langle h'(\varphi) h'(\varphi') \rangle = \sum_{n=-\infty}^{\infty} \xi_n e^{in(\varphi - \varphi')} \tag{32}$$

where

$$\xi_n = n^2 \exp(-a^2/\lambda_c^2) I_n(a^2/\lambda_c^2). \tag{33}$$

Here $I_n(x) = i^{-n} J_n(ix)$ is a modified Bessel function of the first kind.

For fixed a/λ_c, the Fourier coefficients in this expansion behave like

$$\xi_n \sim \frac{\lambda_c e^{-a^2/\lambda_c^2}}{a\sqrt{\pi e}} \left(\frac{ea^2}{2\lambda_c^2 |n|} \right)^{|n| + 1/2} \quad \text{as } n \to \infty \tag{34}$$

and thus decay rapidly for large n. Had we instead used a Gaussian correlation function, the corresponding expansion of the slope correlation function would have had Fourier coefficients which were $O(1)$ as $n \to \infty$. This reflects the delta function behavior mentioned earlier.

As stated in the Introduction, we will in this paper concentrate on the case where the more important contributions to the modification in scattering behavior of the crack comes from the change in slope due to the roughness, rather than the case where the height change is of comparable or greater importance. The more general case is a straightforward extension which follows from the equations already given, at the price of some more unwieldy formulae in the expressions for the T_i in the next section.

Forming the ensemble average of T in Eq. (26) involves

Downloaded 03 May 2010 to 171.66.16.20. Redistribution subject to ASME license or copyright; see http://www.asme.org/terms/Terms_Use.cfm

finding the averages of the T_i in Eqs. (28*a*)–(28*c*). Forming these averages, we need to compare the three correlations $\langle h(\varphi)h(\varphi')\rangle$, $\langle h'(\varphi)h(\varphi')\rangle$, and $\langle h'(\varphi)h'(\varphi')\rangle$ in order to find the conditions under which the influence of the latter of these represents the larger contribution. As the functions decay rapidly for larger angular separations, we need only consider comparatively small values of $\varphi - \varphi'$, and for such values we have

$$\langle h(\varphi)h(\varphi')\rangle \approx \exp\left[-\frac{a^2}{2\lambda_c^2}(\varphi-\varphi')^2\right] \tag{35a}$$

$$\langle h'(\varphi)h(\varphi')\rangle \approx -\frac{a^2}{\lambda_c^2}(\varphi-\varphi')\exp\left[-\frac{a^2}{2\lambda_c^2}(\varphi-\varphi')^2\right] \tag{35b}$$

$$\langle h'(\varphi)h'(\varphi')\rangle \approx \frac{a^2}{\lambda_c^2}\left\{1-\frac{a^2}{\lambda_c^2}(\varphi-\varphi')^2\right\}\exp\left[-\frac{a^2}{2\lambda_c^2}(\varphi-\varphi')^2\right]. \tag{35c}$$

If we make the assumption that

$$\lambda_c \ll a \tag{36}$$

which, if φ_o is $O(1)$, amounts to saying that the correlation length is much smaller than the extent of the crack, we see that the first of the correlations, Eq. (35*a*), can be neglected in comparison to the other two. If it were not for the fact that the second factor in the right member of Eq. (35*c*) had a zero for a small angular difference, we could immediately draw the conclusion that also $\langle h'(\varphi)h(\varphi')\rangle$ could be neglected in comparison to $\langle h'(\varphi)h'(\varphi')\rangle$. Forming the ratio between the right members in Eqs. (35*c*) and (35*b*), we find that it can be written as

$$F(x)=\frac{\eta^2x^2-1}{x}, \text{ where } \eta=\frac{a}{\lambda_c}\gg 1 \text{ and } x=(\varphi-\varphi'). \tag{37}$$

The length of the interval where $F(x)$ is smaller than η, say, is of the order of $1/\eta$. Thus, as long as Eq. (36) holds, we can in fact neglect both (35*a*) and (35*b*) in comparison to (35*c*). One implication of this is that the analysis in the following section is somewhat simplified, as we can then neglect all those terms in the Taylor expansions up to the second order, which involve at least one factor $h(\bullet)$.

There is, however, one more assumption which we need to make, which involves the relative size of the two parameters ϵ and η. The maximum value of $\langle h'(\varphi)h'(\varphi')\rangle$ is of the order of η^2, so T_2 contains an implicit factor η^2. We assume (cf. Ogilvy, 1991; Jansson, 1993), that

$$\epsilon\eta \ll 1 \tag{38}$$

which ensures that the corrections to the scattering from the smooth crack (i.e., the unperturbed circular arc) are small. The interpretation of Eq. (38) is that the root-mean-square height should be much less than the correlation length.

3 The Averaged Transition Matrix

Under the assumptions of the previous sections, we can obtain the ensemble averaged transition matrix from Eqs. (26)–(28). Loosely speaking, this is done by deleting all terms proportional to h in the expressions, replacing all occurances in the matrix products of $\langle h'(\varphi)h'(\varphi')\rangle$ by the expansion Eq. (32), and finally splitting the factor $\exp[in(\varphi-\varphi')]$ in this expansion into two, each entering in the appropriate matrix element (cf. Jansson, 1993, where the terms in the corresponding expansion is split into spherical harmonics). This yields

$$\langle T\rangle = \langle T_0\rangle + \epsilon ka\langle T_1\rangle + (\epsilon ka)^2\langle T_2\rangle + O((\epsilon ka)^3) \tag{39}$$

where

$$\langle T_0\rangle = T_0 = -R_0(P_0Q_0+iS_0)^{-1}P_0 \tag{40}$$

and, in fact,

$$\langle T_1\rangle = 0 \tag{41}$$

while

$$\begin{aligned}\langle T_2\rangle = \sum_n \xi_n[&-R_0A_0(P_0Q_{1n}+P_{1n}Q_0)A_0\\ &\times(P_0Q_{1,-n}+P_{1,-n}Q_0)A_0P_0+R_0A_0P_{1n}Q_{1,-n}A_0P_0\\ &+R_0A_0(P_0Q_{1n}+P_{1n}Q_0)A_0P_{1,-n}\\ &-R_{1n}A_0P_{1,-n}+R_{1n}A_0(P_0Q_{1,-n}+P_{1,-n}Q_0)A_0P_0].\end{aligned} \tag{42}$$

The sum over n in Eq. (42) originates in the expansion Eq. (32), and ξ_n is given by Eq. (33). The various matrices are given by

$$[Q_0]_{mm'} = \begin{cases}\dfrac{\pi}{2}(ka)^{3/2}H_m'(ka)\dfrac{\varphi_o}{m'-m}J_1((m'-m)\varphi_o), & m\neq m'\\ \dfrac{\pi}{2}(ka)^{3/2}H_m'(ka)\dfrac{\varphi_o^2}{2}, & m=m'\end{cases} \tag{43}$$

$$[Q_{1n}]_{mm'} = \begin{cases}\dfrac{im\pi\varphi_o}{2(n+m'-m)}(ka)^{-1/2}H_m(ka)J_1((n+m'-m)\varphi_o), & n\neq m-m'\\ \dfrac{im\pi\varphi_o^2}{2}(ka)^{-1/2}H_m(ka), & n=m-m'\end{cases} \tag{44}$$

$$[R_0]_{mm'} = \begin{cases}\dfrac{\pi}{2}(ka)^{3/2}J_m'(ka)\dfrac{\varphi_o}{m'-m}J_1((m'-m)\varphi_o), & m\neq m'\\ \dfrac{\pi}{2}(ka)^{3/2}J_m'(ka)\dfrac{\varphi_o^2}{2}, & m=m'\end{cases} \tag{45}$$

$$[R_{1n}]_{mm'} = \begin{cases}\dfrac{im\pi\varphi_o}{2(n+m'-m)}(ka)^{-1/2}J_m(ka)J_1((n+m'-m)\varphi_o), & n\neq m-m'\\ \dfrac{im\pi\varphi_o^2}{2}(ka)^{-1/2}J_m(ka), & n=m-m'\end{cases} \tag{46}$$

$$[P_0]_{mm'} = \delta_{mm'}\frac{\pi}{2}kaJ_m'(ka)J_m(ka) \tag{47}$$

$$[P_{1n}]_{mm'} = \delta_{n,m-m'}\frac{i\pi}{2}mJ_m(ka)J_{m'}(ka)/(ka) \tag{48}$$

Downloaded 03 May 2010 to 171.66.16.20. Redistribution subject to ASME license or copyright; see http://www.asme.org/terms/Terms_Use.cfm

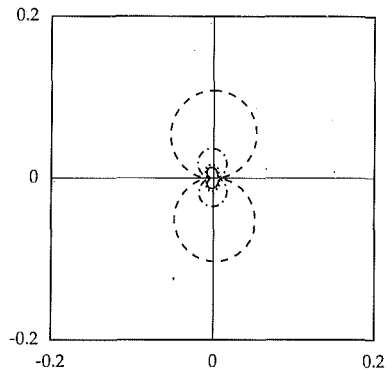


Fig. 2(*a*) Polar plot of the scattered far-field amplitude versus the scattering angle for $\alpha = 90$ deg, $ka = 1$, $\lambda_c/a = 0.1$, and for $\epsilon = 0$ (—), $\epsilon = 0.02$ (· · · ·), $\epsilon = 0.05$ (- · - · -), $\epsilon = 0.1$ (- - - -)

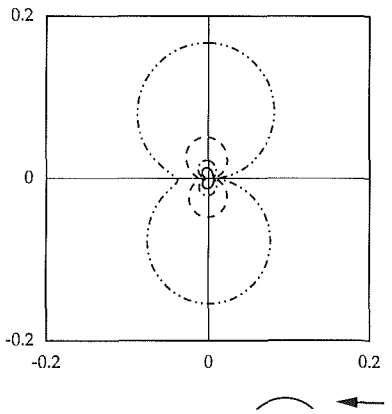


Fig. 2(*b*) Polar plot of the scattered far-field amplitude versus the scattering angle for $\alpha = 90$ deg, $ka = 1$, $\lambda_c/a = 0.2$, and for $\epsilon = 0$ (—), $\epsilon = 0.05$ (- · - · -), $\epsilon = 0.1$ (- - - -), $\epsilon = 0.2$ (- · - · - · -)

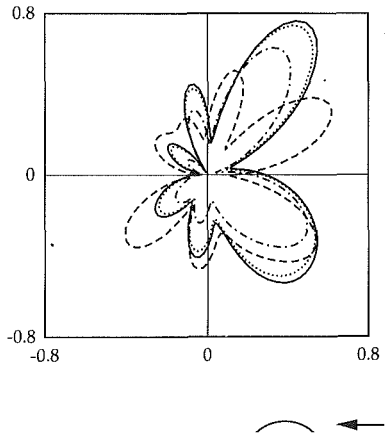


Fig. 2(*c*) Polar plot of the scattered far-field amplitude versus the scattering angle for $\alpha = 90$ deg, $ka = 10$, $\lambda_c/a = 0.1$, and for $\epsilon = 0$ (—), $\epsilon = 0.02$ (· · · ·), $\epsilon = 0.05$ (- · - · -), $\epsilon = 0.1$ (- - - -)

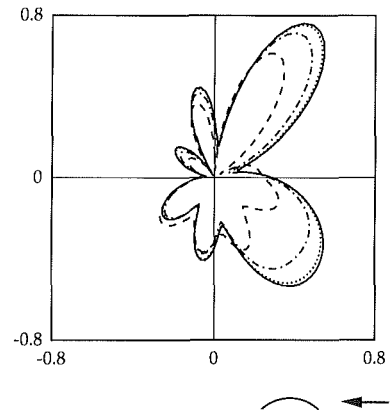


Fig. 2(*d*) Polar plot of the scattered far-field amplitude versus the scattering angle for $\alpha = 90$ deg, $ka = 10$, $\lambda_c/a = 0.2$, and for $\epsilon = 0$ (—), $\epsilon = 0.02$ (· · · ·), $\epsilon = 0.05$ (- · - · -), $\epsilon = 0.1$ (- - - -)

$$[S_0]_{mm'} = (-1)^{m'-m}\frac{\pi}{4}[ka\varphi_o(\pi-\varphi_o)]^{1/2} \times J_m(ka)J_0((m'-m)(\pi-\varphi_o)). \quad (49)$$

The relative simplicity of the above formula is due to several facts. One of these is our judicious choice of the functions Z_o and Z_w. The particular choice we made has, among other things, the pleasant property of cancelling the factor containing h' in the line element of the matrix S. This makes $\langle S_2\rangle$ vanish in the present context. If we are interested in how large a part of the correction to T_0 is due to the stochastic edge effects, we only need to insert one additional term in the expression for $\langle T_2\rangle$. This extra term contains a modified $\langle S_2\rangle$. The modification of $\langle S_2\rangle$ can be described in simple terms as taking the second-order term in an expansion of Eq. (23) but with Z_w replaced by

$$Z_w^*(\mathbf{r}) = \left[\frac{\varphi_o(\pi-\varphi_o)}{4ka(\varphi-\varphi_o)(2\pi-\varphi_o-\varphi)}\right]^{1/2} \quad (50)$$

after which ensemble averaging is performed. The $\langle S_2\rangle$ obtained in this manner is just $1/(2ka)$ times the expression for S_0 in Eq. (49), and the additional term in $\langle T_2\rangle$ is simply $iR_0A_0\langle S_2\rangle A_0P_0$.

4 Numerical Results

The scattered field u^s can be calculated from Eqs. (6), (3), and (24). Taking the incident field to be a plane wave of amplitude u_0 and angle of incidence α (cf. Fig. 1), we obtain

$$u^s = u_0\sum_{nn'} T_{nn'}i^{n'}H_n(kr)\exp(i(n\varphi-n'\alpha)). \quad (51)$$

The far field is obtained by replacing $H_n(kr)$ by the asymptotic expression $(2/\pi kr)^{1/2}\exp(i(kr - n\pi/2 - \pi/4))$. Hence, the averaged far-field amplitude is given by

$$\langle u^s\rangle \sim u_0\frac{\exp(ikr)}{(kr)^{1/2}}f(\varphi) \quad (52)$$

where

$$f(\varphi) = \frac{1-i}{\sqrt{\pi}}\sum_{nn'}\langle T_{nn'}\rangle i^{n'-n}\exp(i(n\varphi-n'\alpha)) \quad (53)$$

is the far-field amplitude of the scattered field.

Expanding the averaged T matrix according to Eq. (39) we obtain the corresponding expansion of the averaged scattered field, i.e.,

$$\langle u^s\rangle = u_0^s + (\epsilon ka)^2\langle u_2^s\rangle + O((\epsilon ka)^4). \quad (54)$$

The scattered field given by Eq. (53) has been calculated numerically using Eqs. (40)–(49) for various values of the frequency, the angle of incidence, the small parameter ϵ, and the correlation length λ_c. In all cases the opening angle $2\varphi_0$ is chosen to be 60 deg.

In Figs. 2(*a–d*) the magnitude of the far-field amplitude is plotted as a function of the scattering angle φ for $ka = 1$ and 10, $\lambda_c/a = 0.1$ and 0.2 and for various values of ϵ. The orientation of the crack and the direction of the incident wave are indicated in the diagrams. Due to convergence problems it has not been possible to decrease the correlation length further. The angle of incidence $\alpha = 90$ deg in all cases. The solid curve corresponds to the case $\epsilon = 0$; i.e., the smooth crack. Obviously, the effect of roughness is very important

Downloaded 03 May 2010 to 171.66.16.20. Redistribution subject to ASME license or copyright; see http://www.asme.org/terms/Terms_Use.cfm

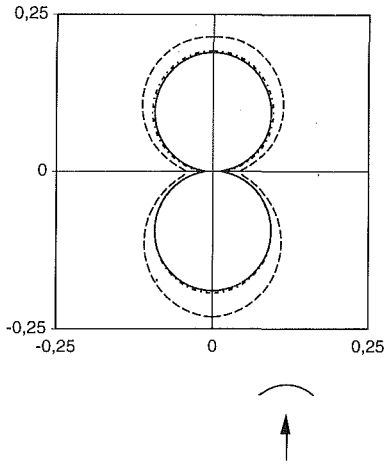


Fig. 3(*a*) Polar plot of the scattered far-field amplitude versus the scattering angle for $\alpha = 0$ deg, $ka = 1$, $\lambda_c/a = 0.1$, and for $\epsilon = 0$ (—), $\epsilon = 0.02$ (· · · ·), $\epsilon = 0.05$ (- • - • -), $\epsilon = 0.1$ (- - - -)

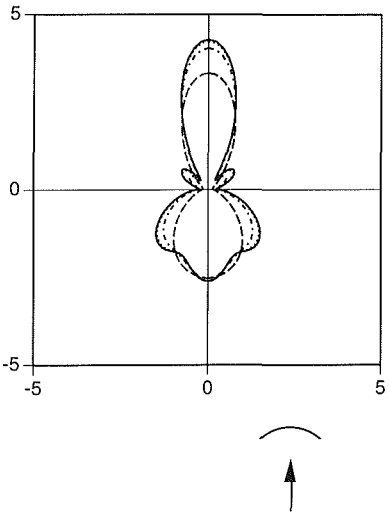


Fig. 3(*b*) Polar plot of the scattered far-field amplitude versus the scattering angle for $\alpha = 0$ deg, $ka = 10$, $\lambda_c/a = 0.1$, and for $\epsilon = 0$ (—), $\epsilon = 0.02$ (· · · ·), $\epsilon = 0.05$ (- • - • -), $\epsilon = 0.1$ (- - - -)

here, especially at low frequencies. Not surprisingly, the significance of roughness is seen to increase with a decreasing correlation length.

Figures 3(*a–b*) show similar results for $\alpha = 0$ deg and $\lambda_c/a = 0.1$. We note that the relative effect of roughness compared to the case of the smooth crack is less spectacular than in Figs. 2. The absolute effect, however, is not negligible, especially not for $ka = 10$.

The back-scattered far-field is obtained by taking $\varphi = \alpha + \pi$ in Eq. (52). Some numerical results are presented in Figs. 4(*a–b*) where $ka = 1$ and 10, and $\lambda_c/a = 0.1$.

The numerical results are strictly valid only as long as the conditions $\epsilon ka \ll 1$ and $\epsilon \ll \lambda_c/a$ are fulfilled. It is obvious that in some of the cases presented in Figs. 2–4 this is not true. In fact, one or even both of the small parameters ϵka and $\epsilon a/\lambda_c$ are equal to unity for the curve corresponding to the maximum value of ϵ in each diagram. Even though these results cannot be expected to be correct from a quantitative point of view they have been included, since they are believed to give an indication of what happens in the case of a crack with considerable roughness.

To ensure convergence, the indices m and n of Eqs. (43)–(49) in most cases have to run from -90 to 90 and -50 to 50, respectively. Increasing the ranges even more will cause

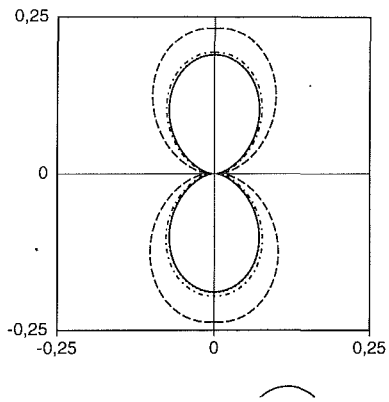


Fig. 4(*a*) Polar plot of the back-scattered far-field amplitude versus the angle of incidence for $ka = 1$, $\lambda_c/a = 0.1$, and for $\epsilon = 0$ (—), $\epsilon = 0.02$ (· · · ·), $\epsilon = 0.05$ (- • - • -), $\epsilon = 0.1$ (- - - -)

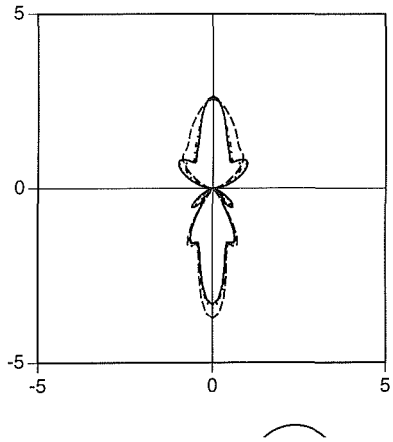


Fig. 4(*b*) Polar plot of the back-scattered far-field amplitude versus the angle of incidence for $ka = 10$, $\lambda_c/a = 0.1$, and for $\epsilon = 0$ (—), $\epsilon = 0.02$ (· · · ·), $\epsilon = 0.05$ (- • - • -), $\epsilon = 0.1$ (- - - -)

Table 1 The relative amplitude $(|\langle u^s \rangle| - |u_0^s|)/|u_0^s|$ of the back-scattered far-field for various values of the angle of incidence and for $ka = 5.0$, $\lambda_c/a = 0.1$, $\epsilon = 0.01$

α	Stochastic edge effects not included	Stochastic edge effects included
0 deg	$-0.414 \cdot 10^{-3}$	$-0.412 \cdot 10^{-3}$
45 deg	$-0.371 \cdot 10^{-2}$	$-0.367 \cdot 10^{-2}$
90 deg	$-0.791 \cdot 10^{-2}$	$-0.789 \cdot 10^{-2}$
135 deg	$0.736 \cdot 10^{-2}$	$0.770 \cdot 10^{-2}$
180 deg	$0.469 \cdot 10^{-3}$	$0.479 \cdot 10^{-3}$

the matrix inversion routine to become unstable. Consequently, due to the numerical restrictions, our calculations are limited to low frequencies and not too small values of the correlation length.

In order to investigate the effect of stochastic edge effects we have studied a few particular cases without including these effects. In Table 1 the relative amplitude of the back-scattered far field is given for various values of the angle of incidence. It is clear that the stochastic edge effects are very small, at most about four percent, in this case. This remark seems to be of general validity (we have checked it for a few more cases).

5 Discussion

In the present paper we have considered the two-dimensional antiplane scattering problem for rough nonplanar cracks, in

Downloaded 03 May 2010 to 171.66.16.20. Redistribution subject to ASME license or copyright; see http://www.asme.org/terms/Terms_Use.cfm

particular for the case where the slope perturbation has greater effect on the scattering than has the height perturbation. Most cracks are, of course, more or less rough—it all depends on what length scale you are studying—and more or less nonplanar. The present analysis has a relevance for the study of "real" cracks in the sense that it provides tools by which one could, e.g., study the relative importance of curvature and roughness effects. But of course the analysis can and should be extended in several directions. We have already indicated that a straightforward extension is to include height effects. To include P and SV waves (i.e., compression and shear waves which have their polarization in the plane of propagation), and even to extend the analysis to the full three-dimensional case is, at least in principle, easy to do. In the two and three-dimensional cases alike, there are limitations on the size and shape of the unperturbed crack (cf. Boström and Olsson, 1987; Olsson, 1986, 1990). Another limitation seems to be that given by Eq. (38), i.e., that the root-mean-square height should be in some sense smaller than the correlation length. This means that we cannot treat cracks which are so-called deep scatterers, having a root-mean-square height greater than (or equal to) the correlation length.

An issue which is in need of some consideration is the question of which model should be used to model the roughness of a real crack as accurately as desirable. Different types of cracks should possibly be modeled by means of different statistical tools. The surface roughness of a crack produced by intergranular stress corrosion possibly differs from that of a fatigue crack, not only in root-mean-square height and correlation length, but even in the type of correlation function. Changing the correlation function would in the formalism of the present paper correspond to taking another set of ξ_n than those given by Eq. (33).

In the present study we have touched upon the question of the importance of the stochastic contribution to the edge effects. This is definitely one which should be studied further. In our study we have only included the effect of a stochastic edge slope. Apart from allowing a stochastic displacement in the normal direction, which is straightforward, one could possibly include also a random perturbation of the angle φ_o.

Acknowledgments

This project was financially supported by the Swedish Research Council for Engineering Sciences, and this is gratefully acknowledged.

References

Achenbach, J. D., Gautesen, A. K., and McMaken, H., 1982, *Ray Methods for Waves in Elastic Solids with Applications to Scattering by Cracks*, Pitman, London.

Boström, A., and Olsson, P., 1987, "Scattering of Elastic Waves by Nonplanar Cracks," *Wave Motion*, Vol. 9, pp. 61–76.

Jansson, P.-Å., 1993, "Acoustic Scattering by a Rough Sphere," *Journal of the Acoustical Society of America*, Vol. 93, pp. 3032–3042.

Lewis, P. A., 1990, "Scattering of Elastic Waves by Rough Cracks," *Elastic Waves and Ultrasonic Nondestructive Evaluation*, S. K. Datta, J. D. Achenbach, and Y. S. Rajapakse, eds., North-Holland, Amsterdam.

Ogilvy, J. A., 1988, "Computer Simulation of Acoustic Wave Scattering from Rough Surfaces," *Journal of Physics D: Applied Physics*, Vol. 21, pp. 260–277.

Ogilvy, J. A., 1989, "Model for the Ultrasonic Inspection of Rough Defects," *Ultrasonics*, Vol. 27, pp. 69–79.

Ogilvy, J. A., 1991, *Theory of Wave Scattering from Random Rough Surfaces*, Adam Hilger, Bristol, U.K.

Olsson, P., 1986, "Elastodynamic Scattering by Fluid-Filled Nonplanar Cracks," *Journal of Nondestructive Evaluation*, Vol. 5, pp. 161–168.

Olsson, P., 1990, "Elastodynamic Scattering From Pennyshaped and Nonplanar Flaws With Dissipation and Restoring Forces," ASME JOURNAL OF APPLIED MECHANICS, Vol. 57, pp. 661–666.

Olsson, P., Datta, S. K., and Boström, A., 1990, "Elastodynamic Scattering From Inclusions Surrounded by Thin Interface Layers," ASME JOURNAL OF APPLIED MECHANICS, Vol. 57, pp. 672–676.

Varadan, V. K., and Varadan, V. V., eds., 1980, *Acoustic, Electromagnetic and Elastic Wave Scattering—Focus on the T-matrix Approach*, Pergamon, New York.

Downloaded 03 May 2010 to 171.66.16.20. Redistribution subject to ASME license or copyright; see http://www.asme.org/terms/Terms_Use.cfm

Yi-Zhou Chen
Division of Engineering Mechanics,
Jiangsu University of Science
and Technology,
Zhenjiang, Jiangsu, 212013, China

Norio Hasebe
Department of Civil Engineering,
Nagoya Institute of Technology,
Gokiso-cho, Showa-ku, Nagoya 466, Japan

Eigenfunction Expansion and Higher Order Weight Functions of Interface Cracks

In this paper the properties of the eigenfunction expansion form in the interface crack problem of plane elasticity are discussed in detail. After using the Betti's reciprocal theorem to the cracked dissimilar bonded body, several path-independent integrals are obtained. All the coefficients in the eigenfunction expansion form, including the K_1 and K_2 values, and the J-integral can be related to corresponding path independent integrals. Possibility for formulating the weight function is also suggested.

1 Introduction

There has been a resurgence of interest in the elastic interface crack problem, for which the characteristic oscillating stress singularity was determined by Williams (1959). Works by Huchinson, Mear, and Rice (1987), Rice (1988), Mukai, Ballarini, and Miller (1990), and Hasebe, Okumura, and Nakamura (1990) provide examples of recent contributions.

The interface crack problem in plane elasticity was first studied by Williams (1959). Williams used an eigenfunction expansion technique to solve the interface crack problem and discovered complex singularities and rapidly oscillating stresses near the crack tip. Williams also estimated the oscillatory region to be very small. It has been pointed out that the near-tip fields that have been derived for this problem (Williams, 1959; Erdogan, 1963; Sih and Rice, 1964) are not complete. Using a complex variable function formulation, Rice (1988) gave a complete series solution that includes integer order terms. Using the Airy stress function in plane elasticity, the integer order terms in the eigenfunction form was also obtained by Symington (1987). In the isotropic case, the terms in the eigenfunction expansion form with negative eigenvalues was discussed by Rice (1974), and was named an outer Williams expansion. It is easy to see that the eigenfunction expansion form with the negative eigenvalues must be defined in a region where a small region in the vicinity of the crack tip has been excluded. A practical usage of the term with negative eigenvalue can be also found in the work of Bueckner (1973). Also, the properties of the eigenfunction expansion form, including both the positive and negative eigenvalues in the isotropic case, was investigated by Chen (1985).

The fracture analysis of an interface crack has been complicated by the oscillatory feature of a near-tip deformation field. Despite this complication, Rice (1988) has argued that the oscillatory solution can still be used to characterize the interface crack field since the contact zone size is extremely small for a broad range bimaterial and loading configuration.

The weight function analysis in the crack problem was earlier proposed by Bueckner (1970) and Rice (1972). On account of the elastic strain energy variation with respect to (a) the crack length under the fixed displacement condition and (b) the generalized displacement, a perfect differential form is obtained (Rice, 1972). As an important consequence of the obtained perfect differential, the weight function formulation for crack problem was completed. In an isotropic case, Rice (1972) showed that the weight functions could be determined by differentiating known elastic displacement field solutions with respect to crack length. Also, after considering the released energy in the process of a crack extension and using the Betti's reciprocal theorem to two stress fields, the weight function for the crack problem is also obtainable (Sham and Zhou, 1989; Chen, 1989). In the meantime it was proved that the fundamental fields proposed by Bueckner (1973) and the fields generated by an incremental crack growth are identical (Rice, 1989).

Following the notion proposed by Bueckner (1973), the higher order weight function formulation was introduced by Sham (1989). Its merit is to provide a way for finding the higher order expansion coefficients in fracture analysis. Alternatively, after using the properties of the eigenfunction expansion form including both the positive and negative eigenvalues, the weight function formulation was discussed by Chen (1985).

Recently, Gao (1991) showed that, other than a few material constants, the interface weight function is completely parallel to its homogeneous counterpart developed by Bueckner (1973) and Rice (1972). Stern and co-workers (Stern, 1979; Hong and Stern, 1978) developed a concept of "com-

Contributed by the Applied Mechanics Division of THE AMERICAN SOCIETY OF MECHANICAL ENGINEERS for publication in the ASME JOURNAL OF APPLIED MECHANICS.

Discussion on this paper should be addressed to the Technical Editor, Professor Lewis T. Wheeler, Department of Mechanical Engineering, University of Houston, Houston, TX 77204-4792, and will be accepted until four months after final publication of the paper itself in the ASME JOURNAL OF APPLIED MECHANICS.

Manuscript received by the ASME Applied Mechanics Division, Oct. 12, 1992; final revision, Oct. 26, 1993. Associate Technical Editor: C. F. Shih.

Copyright © 1994 by ASME
Downloaded 03 May 2010 to 171.66.16.20. Redistribution subject to ASME license or copyright; see http://www.asme.org/terms/Terms_Use.cfm

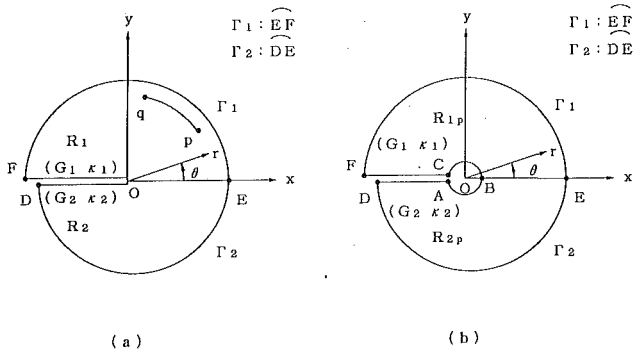


Fig. 1 Region near crack tip; (*a*) for a physical problem, (*b*) for defining the eigenfunction expansion form including the negative eigenvalues

plementary elastic state" to evaluate the stress intensity factor for cracked dissimilar materials. Following Rice's (1972) notion of reciprocal relations among energetic forces on a crack tip and other interacting defects, the interface weight function method was developed by Gao (1991). The interface crack problem can also be analyzed by means of the concept of mismatch (Gao, 1991). It is shown that the near-tip oscillation of an interface may be understood from the viewpoint of interface mismatch that results from the cracking. An alternative approach can be formulated following that of Bueckner (1973) in searching for a fundamental field whose potential functions behave as $z^{-1/2+i\epsilon}$ near a crack tip.

Except for the above contributions, the following investigations concerning the interface crack problem and the weight function formulation are worth citing. The weight function theory for three-dimensional elastic crack analysis was developed by Rice (1985), and Gao and Rice (1986, 1987). In particular, the perturbation approach is suggested to find the first-order variation of the stress intensity factor provided that the crack front can be approximated by a regular boundary. These works have been summarized in Rice (1989). Using the concepts of fundamentals fields and elastic reciprocity, the weight function theory in antiplane elasticity for notches composed of two dissimilar materials was developed by Sham and Bueckner (1988).

In this paper, the properties of the eigenfunction expansion form in the interface crack problem is also discussed. Meantime, several facts can be found from the following analysis:

(a) In the case of using the Betti's reciprocal theorem, a path-independent integral $W(u_{i(\alpha)}, \sigma_{ij(\alpha)}, u_{i(\beta)}, \sigma_{ij(\beta)})$ which starts at a point of the lower face of the interface crack and ends at a point of upper face can be defined. The integral W depends on two stress fields: $u_{i(\alpha)}$, $\sigma_{ij(\alpha)}$ and $u_{i(\beta)}$, $\sigma_{ij(\beta)}$. W is a subtraction of two works along a curve; the one is the work done by the displacement of the α stress field to the traction of the β stress field and the other is the work done by the displacement of the β stress field to the traction of the α stress field. The α stress field and the β stress fields mentioned above are some particular solution of elasticity and satisfy the traction-free condition along the crack faces. It has been shown that only some particular pairs of the stress fields derived from the eigenfunction expansion form have a contribution to the integral W. This property likes the similar property in the orthogonal function series.

(b) Using the obtained properties of the eigenfunction expansion form, all the coefficients in the eigenfunction expansion form can be expressed by corresponding path-independent integrals and the well-known J-integral is also obtainable.

(c) Also using the properties of the eigenfunction expansion form in the interface crack problem, a possibility for formulating the weight function method is suggested.

2 Properties of the Eigenfunction Expansion Form

The eigenfunction expansion form in the interface crack problem has been discussed in many references. By the use of the complex variable function method in plane elasticity the eigenfunction expansion form can be easily obtained. The obtained results can be found from the following works: Williams (1959), Symington (1987), Rice (1988).

The complex variable function method for plane elasticity proposed by Muskhelishvili (1953) is used as indicated below. According to this method, the stresses $(\sigma_{xx}, \sigma_{yy}, \sigma_{xy})$, the resultant forces (X, Y), and the displacements (u, v) can be described by two complex potentials $\phi(z)$ and $\omega(z)$

$$\sigma_{xx} + \sigma_{yy} = 4\mathrm{Re}[\Phi(z)]$$

$$\sigma_{yy} - i\sigma_{xy} = \Phi(z) + (z - \bar{z})\overline{\Phi'(z)} + \overline{\Omega(z)} \quad (1)$$

$$P = -Y + iX = \phi(z) + (z - \bar{z})\overline{\phi'(z)} + \overline{\omega(z)} \quad (2)$$

$$2G(u + iv) = \kappa\phi(z) - (z - \bar{z})\overline{\phi'(z)} - \overline{\omega(z)} \quad (3)$$

where $\Phi(z) = \phi'(z)$ and $\Omega(z) = \omega'(z)$, G is the shear modulus, $\kappa = 3 - 4\nu$ for the plane-strain problem, $\kappa = (3 - \nu)/(1 + \nu)$ for the plane-stress problem, and ν is Poisson's ratio.

We seek the form of solution in region R ($R = R_1 + R_2$, Fig. 1(*a*)) surrounding a traction-free interface crack. The elastic constants and the complex potentials are denoted by G_1, κ_1, $\phi_1(z)$, $\omega_1(z)$ and G_2, κ_2, $\phi_2(z)$, $\omega_2(z)$ for upper and lower planes, respectively. From Eqs. (2) and (3), the continuation condition of the resultant force and displacement gives rise to the following relations:

$$\phi_1^+(x) + \overline{\omega_1^+(x)} = \phi_2^-(x) + \overline{\omega_2^-(x)} \quad (x > 0) \quad (4)$$

$$G_2\left(\kappa_1\phi_1^+(x) - \overline{\omega_1^+(x)}\right) = G_1\left(\kappa_2\phi_2^-(x) - \overline{\omega_2^-(x)}\right) \quad (x > 0). \quad (5)$$

Also, the traction-free condition along the upper and lower crack faces leads to

$$\phi_1^+(x) + \overline{\omega_1^+(x)} = 0 \quad (x < 0) \quad (6)$$

$$\phi_2^-(x) + \overline{\omega_2^-(x)} = 0 \quad (x < 0). \quad (7)$$

From Eqs. (4)–(7), the following eigenfunction expansion form was obtained by Rice (1988):

$$\phi_1(z) = e^{-\pi\epsilon}z^{1/2-i\epsilon}f(z) + D_1g(z) \quad (z \in R_1 \text{ or } R_{1p}) \quad (8)$$

$$\omega_1(z) = e^{\pi\epsilon}z^{1/2+i\epsilon}\bar{f}(z) - D_1\bar{g}(z) \quad (z \in R_1 \text{ or } R_{1p}) \quad (9)$$

$$\phi_2(z) = e^{\pi\epsilon}z^{1/2-i\epsilon}f(z) + D_2g(z) \quad (z \in R_2 \text{ or } R_{2p}) \quad (10)$$

$$\omega_2(z) = e^{-\pi\epsilon}z^{1/2+i\epsilon}\bar{f}(z) - D_2\bar{g}(z) \quad (z \in R_2 \text{ or } R_{2p}) \quad (11)$$

where

$$f(z) = \sum_{n=-\infty}^{\infty} \frac{a_n}{n + 1/2 - i\epsilon}z^n \quad (12)$$

$$g(z) = \sum_{n=-\infty}^{\infty} e_nz^n \quad (13)$$

and

$$\epsilon = \frac{1}{2\pi}\ln\left(\frac{C_1}{C_2}\right)$$

$$C_1 = G_1 + \kappa_1G_2$$

$$C_2 = G_2 + \kappa_2G_1 \quad (14)$$

Downloaded 03 May 2010 to 171.66.16.20. Redistribution subject to ASME license or copyright; see http://www.asme.org/terms/Terms_Use.cfm

$$D_1 = 2G_1\frac{\kappa_2 + 1}{C_1 + C_2}$$
$$D_2 = 2G_2\frac{\kappa_1 + 1}{C_1 + C_2} \tag{15}$$

It is easy to see that the obtained eigenfunction expansion form contains two parts. The first part is composed of the complex eigenvalue and the second of integer eigenvalue. Differing from the eigenfunction expansion form previously suggested, the terms with the negative values of n in the $f(z)$ and $g(z)$ are also included in summation. The displacements must be finite for the bonded materials, and thus, in Eqs. (12) and (13), we can conclude that

(a) the terms corresponding to $n > 0$ for both functions $f(z)$ and $g(z)$ are physically possible in the region R ($R = R_1 + R_2$, Fig. 1(a)) and the term of $n = 0$ in $g(z)$ represents a rigid motion of body.

(b) the terms corresponding to $n < 0$ for both functions $f(z)$ and $g(z)$ are only physically possible in the region R_p ($R_p = R_{1p} + R_{2p}$, Fig. 1(b)), where a small region with contour ABC has been excluded. We shall soon prove that the terms corresponding to $n < 0$ have many uses in the following analysis.

Now the first property of the eigenfunction expansion form can be reached as follows. If the displacements u and v are derived from one term (with the eigenvalue $n + 1/2 - i\epsilon$ for the first part, or n for the second part) of the eigenfunction expansion form in Eqs. (8)–(11), then $u_* = \partial u/\partial x$ and $v_* = \partial v/\partial x$ is also a term (with the eigenvalue $n - 1/2 - i\epsilon$ for the first part, or $n - 1$ for the second part) of the eigenfunction expansion form in Eqs. (8)–(11). The exception is the case of $n = 0$ in the second part of the eigenfunction expansion form.

The following proof is carried out for a term of the first part of the eigenfunction expansion form defined in the upper half-plane. In fact, from the above formulation we have

$$2G_1(u + iv) = \kappa_1\phi_1(z) - (z - \bar{z})\overline{\phi_1'(z)} - \overline{\omega_1(z)} \quad (z \in R_{1p}) \tag{16}$$

where

$$\phi_1(z) = e^{-\pi\epsilon}\frac{a_n}{n + 1/2 - i\epsilon}z^{n+1/2-i\epsilon} \quad (z \in R_{1p})$$
$$\omega_1(z) = e^{\pi\epsilon}\frac{\bar{a}_n}{n + 1/2i\epsilon}z^{n+1/2+i\epsilon} \quad (z \in R_{1p}), \tag{17}$$

Then we can get

$$2G_1(u_* + iv_*) = 2G_1\left(\frac{\partial u}{\partial x} + i\frac{\partial v}{\partial x}\right) = \kappa_1\phi_1'(z) - (z - \bar{z})\overline{\phi_1''(z)} - \overline{\omega_1'(z)} \tag{18}$$

and rewrite the above equation in the form

$$2G_1(u_* + iv_*) = \kappa_1\phi_{1*}(z) - (z - \bar{z})\overline{\phi_{1*}'(z)} - \overline{\omega_{1*}(z)} \tag{19}$$

where

$$\phi_{1*}(z) = \phi_1'(z) = e^{-\pi\epsilon}a_n z^{n-1/2-i\epsilon}$$
$$\omega_{1*}(z) = \omega_1'(z) = e^{\pi\epsilon}\bar{a}_n z^{n-1/2+i\epsilon} \tag{20}$$

Clearly, the above complex potential belongs to one term of the first part of the eigenfunction expansion form with the eigenvalue $n - 1/2 - i\epsilon$. Similar proof can be performed for the case of a lower half-plane. Also, it is easy to prove the same property for the case of the second part of the eigenfunction expansion form.

Before discussing the second property of the eigenfunction expansion form, the following result obtained by Bueckner (1973) is useful. If there are two cases of a deformation state in-plane elasticity, namely, $u_{i(\alpha)}$, $\sigma_{ij(\alpha)}$ and $u_{i(\beta)}$, $\sigma_{ij(\beta)}$, which are derived from the complex potentials $\phi_{(\alpha)}(z)$, $\omega_{(\alpha)}(z)$ and $\phi_{(\beta)}(z)$, $\omega_{(\beta)}(z)$, respectively, then the following integral can be defined:

$$2GW_{pq} = 2G\int_{pq}(u_{i(\alpha)}\sigma_{ij(\beta)} - u_{i(\beta)}\sigma_{ij(\alpha)})n_j ds \tag{21}$$

where p and q are two points in the elastic plane (Fig. 1(a)). Clearly, by the use of the Betti's reciprocal theorem (Sokolnikoff, 1956), the above integral is path independent. After some manipulation, the above integral can be evaluated by the following equation:

$$2GW_{pq} = (\kappa + 1)\text{Im } H(z)|_p^q + \text{Im } R|_p^q \tag{22}$$

where

$$H(z) = \int h(z)dz$$
$$h(z) = -\omega_\alpha(z)\phi_\beta'(z) + \omega_\beta(z)\phi_\alpha'(z) \tag{23}$$

$$R = -\kappa P_\alpha\overline{P_\beta} + (\kappa + 1)(P_\alpha - \phi_\alpha)\left(\overline{P_\beta} - \overline{\phi_\beta}\right) \tag{24}$$

and P_α, P_β are the resultant force functions derived from the α and the β stress fields, respectively.

For convenience to get the derivation cited below, the following definition is used. A particular stress field is called the eigenstress field in this paper. It is defined in a dissimilar bonded region as shown in Fig. 1(b) and satisfies (a) all the governing equations of plane elasticity, (b) the displacement and traction continuations along the bonded line ($x > 0$, $y = 0$), (c) the traction-free condition along the upper and lower faces of the crack. Clearly, for any pairs of the α and the β stress fields which belong to the eigenstress field, the following path-independent integral is obtainable:

$$W = \int_{\Gamma_2+\Gamma_1}(u_{i(\alpha)}\sigma_{ij(\beta)} - u_{i(\beta)}\sigma_{ij(\alpha)})n_j ds \tag{25}$$

where Γ_2 is any integration path starting at any point D of the lower crack face, and Γ_1 is any integration path ended at any point F of the upper crack face (Fig. 1(b)). Obviously, each term in the eigenfunction expansion form can serve as the eigenstress field mentioned above. In the following, three types of integral (25) will be investigated.

(a) In the first case, both the α and the β stress fields are taken from the first part of the eigenfunction expansion form in Eqs. (8)–(11). It is assumed that the α stress field ($u_{i(\alpha)}$, $\sigma_{ij(\alpha)}$) is derived from the following complex potentials:

$$\phi_1(z) = e^{-\pi\epsilon}\frac{a_n}{n + 1/2 - i\epsilon}z^{n+1/2-i\epsilon} \quad (z \in R_{1p})$$
$$\omega_1(z) = e^{\pi\epsilon}\frac{\bar{a}_n}{n + 1/2 + i\epsilon}z^{n+1/2+i\epsilon} \quad (z \in R_{1p})$$
$$\phi_2(z) = e^{\pi\epsilon}\frac{a_n}{n + 1/2 - i\epsilon}z^{n+1/2-i\epsilon} \quad (z \in R_{2p})$$
$$\omega_2(z) = e^{-\pi\epsilon}\frac{\bar{a}_n}{n + 1/2 + i\epsilon}z^{n+1/2+i\epsilon} \quad (z \in R_{2p}). \tag{26}$$

and the β stress field ($u_{i(\beta)}$, $\sigma_{ij(\beta)}$) is derived from the following complex potentials:

$$\phi_1(z) = e^{-\pi\epsilon}\frac{b_m}{m + 1/2 - i\epsilon}z^{m+1/2-i\epsilon} \quad (z \in R_{1p})$$
$$\omega_1(z) = e^{\pi\epsilon}\frac{\bar{b}_m}{m + 1/2 + i\epsilon}z^{m+1/2+i\epsilon} \quad (z \in R_{1p})$$

Downloaded 03 May 2010 to 171.66.16.20. Redistribution subject to ASME license or copyright; see http://www.asme.org/terms/Terms_Use.cfm

$$\phi_2(z) = e^{\pi\epsilon}\frac{b_m}{m+1/2-i\epsilon}z^{m+1/2-i\epsilon} \quad (z \in R_{2p})$$

$$\omega_2(z) = e^{-\pi\epsilon}\frac{\bar{b}_m}{m+1/2+i\epsilon}z^{m+1/2+i\epsilon} \quad (z \in R_{2p}). \quad (27)$$

After using Eqs. (21)–(24), we can get

$$W = \int_{\Gamma_2+\Gamma_1}(u_{i(\alpha)}\sigma_{ij(\beta)} - u_{i(\beta)}\sigma_{ij(\alpha)})n_j ds = \begin{cases} 0 & \text{if } n+m+1 \neq 0 \\ H_1 & \text{if } n+m+1 = 0 \end{cases} \quad (28)$$

where

$$H_1 = -\frac{(C_1+C_2)\pi}{G_1G_2}\mathrm{Re}\left[\frac{a_n\overline{b_m}}{n+1/2-i\epsilon}\right]. \quad (29)$$

(b) In the second case, both the α and the β stress fields are taken from the second part of the eigenfunction expansion form in Eqs. (8)–(11). It is assumed that the α stress field $(u_{i(\alpha)}, \sigma_{ij(\alpha)})$ is derived from the following complex potentials:

$$\phi_1(z) = D_1e_nz^n \quad (z \in R_{1p})$$
$$\omega_1(z) = -D_1\overline{e_n}z^n \quad (z \in R_{1p})$$
$$\phi_2(z) = D_2e_nz^n \quad (z \in R_{2p})$$
$$\omega_2(z) = -D_2\overline{e_n}z^n \quad (z \in R_{2p}) \quad (30)$$

and the β stress field $(u_{i(\beta)}, \sigma_{ij(\beta)})$ is derived from the following complex potentials:

$$\phi_1(z) = D_1f_mz^m \quad (z \in R_{1p})$$
$$\omega_1(z) = -D_1\overline{f_m}z^m \quad (z \in R_{1p})$$
$$\phi_2(z) = D_2f_mz^m \quad (z \in R_{2p})$$
$$\omega_2(z) = -D_2\overline{f_m}z^m \quad (z \in R_{2p}) \quad (31)$$

After using Eqs. (21)–(24), we can get

$$W = \int_{\Gamma_2+\Gamma_1}(u_{i(\alpha)}\sigma_{ij(\beta)} - u_{i(\beta)}\sigma_{ij(\alpha)})n_j ds = \begin{cases} 0 & \text{if } n+m \neq 0 \\ H_2 & \text{if } n+m = 0 \end{cases} \quad (32)$$

where

$$H_2 = -\frac{4n\pi C_1C_2}{G_1G_2(C_1+C_2)}\mathrm{Re}(e_n\overline{f_m}). \quad (33)$$

(c) In the third case, the α stress field is taken from the first part of the eigenfunction expansion form in Eqs. (8)–(11), and β stress field is taken from the second part of the eigenfunction expansion form in Eqs. (8)–(11). It is assumed that the α stress field $(u_{i(\alpha)}, \sigma_{ij(\alpha)})$ is derived from the complex potentials shown by (26), and the β stress field $(u_{i(\beta)}, \sigma_{ij(\beta)})$ is derived from the complex potentials shown by (31). After using Eqs. (21)–(24), in any case of n and m in Eqs. (26) and (31), we can get

$$W = \int_{\Gamma_2+\Gamma_1}(u_{i(\alpha)}\sigma_{ij(\beta)} - u_{i(\beta)}\sigma_{ij(\alpha)})n_j ds = 0. \quad (34)$$

From Eqs. (28), (32), and (34) we see that only some particular pairs in the eigenfunction expansion form have a contribution to the path-independent integral (25).

3 Path-Independent Integrals

As mentioned above, if some pairs of the stress fields which belong to the eigenstress field are taken in Eq. (25), the relevant path-independent integrals can be obtained. Several important cases are cited below.

(a) We take the α stress field $(u_{i(\alpha)} = u_i, \sigma_{ij(\alpha)} = \sigma_{ij})$ as a physical stress field caused by some tractions acting on the boundary of the cracked dissimilar body. Therefore, the corresponding complex potential takes the form shown by (8)–(11), and the functions $f(z)$ and $g(z)$ will be

$$f(z) = \sum_{n=0}^{\infty}\frac{a_n}{n+1/2-i\epsilon}z^n$$
$$g(z) = \sum_{n=0}^{\infty}e_nz^n. \quad (35)$$

In addition, we choose the following the β stress field: $u_{i(\beta)} = \partial u_i/\partial x$ and $\sigma_{ij(\beta)} = \partial\sigma_{ij}/\partial x$. Using the properties of the eigenfunction expansion form mentioned above, it is easy to see that only one pair, which consists of one term with the eigenvalue $1/2 - i\epsilon$ in the α stress field and another term with the eigenvalue $-1/2 - i\epsilon$ in the β stress field, has a contribution to the integral (25). After using the well-known relation (Rice, 1988)

$$K_1 - iK_2 = 2\sqrt{2\pi}a_0 - \cosh(\pi\epsilon), \quad (36)$$

a simple derivation leads to the following path-independent integral:

$$W = \int_{\Gamma_2+\Gamma_1}\left(u_i\frac{\partial\sigma_{ij}}{\partial x} - \frac{\partial u_i}{\partial x}\sigma_{ij}\right)n_j ds = \pi\left(\frac{\kappa_1+1}{G_1} + \frac{\kappa_2+1}{G_2}\right)(a_0\overline{a_0}) = \left(\frac{\kappa_1+1}{G_1} + \frac{\kappa_2+1}{G_2}\right)\frac{K_1^2+K_2^2}{8[\cosh(\pi\epsilon)]^2}. \quad (37)$$

Also, after making integration by part and using the properties of the eigenstress field (Chen, 1985), Eq. (37) can be rewritten in a form

$$J = \frac{W}{2} = \int_{\Gamma_2+\Gamma_1}\left(Udy - \frac{\partial u_i}{\partial x}\sigma_{ij}n_j ds\right) = \left(\frac{\kappa_1+1}{G_1} + \frac{\kappa_2+1}{G_2}\right)\frac{K_1^2+K_2^2}{16[\cosh(\pi\epsilon)]^2}. \quad (38)$$

where U is the strain energy density. An approach for determining the individual stress intensity factor from Eq. (38) was suggested by Yau and Wang (1984).

(b) We take the α stress field $(u_{i(\alpha)} = u_i, \sigma_{ij(\alpha)} = \sigma_{ij})$ as a physical stress field caused by some tractions acting on the boundary of the cracked dissimilar body, and let the β stress field be derived from the following complex potential:

$$\phi_1(z) = e^{-\pi\epsilon}g_{-k}z^{-k+1/2-i\epsilon} \quad (z \in R_{1p})$$
$$\omega_1(z) = e^{\pi\epsilon}\bar{g}_{-k}z^{-k+1/2+i\epsilon} \quad (z \in R_{1p})$$
$$\phi_2(z) = e^{\pi\epsilon}g_{-k}z^{-k+1/2-i\epsilon} \quad (z \in R_{2p})$$
$$\omega_2(z) = e^{-\pi\epsilon}\bar{g}_{-k}z^{-k+1/2+i\epsilon} \quad (z \in R_{2p}) \quad k = 1, 2, \ldots. \quad (39)$$

After using the properties of the eigenfunction expansion form mentioned above, it is easy to see that only one pair, which consists of one term with the eigenvalue $k - 1/2 - i\epsilon$ in the α stress field and the β stress field, has a contribution to the integral (25). A simple derivation leads to the following path-independent integral:

Downloaded 03 May 2010 to 171.66.16.20. Redistribution subject to ASME license or copyright; see http://www.asme.org/terms/Terms_Use.cfm

$$W = \int_{\Gamma_2+\Gamma_1} (u_i \sigma_{ij(\beta)} - u_{i(\beta)} \sigma_{ij}) n_j ds$$
$$= \frac{(C_1 + C_2)\pi}{G_1 G_2} \mathrm{Re}(a_{k-1} \overline{g_{-k}}). \quad (40)$$

Also, some particular cases are cited as follows:

$$W = \frac{(C_1 + C_2)\pi}{G_1 G_2} \mathrm{Re}(a_{k-1}) \quad (\text{if } g_{-k} = 1, k = 1, 2, \ldots)$$
$$W = \frac{(C_1 + C_2)\pi}{G_1 G_2} \mathrm{Im}(a_{k-1}) \quad (\text{if } g_{-k} = i, k = 1, 2, \ldots)$$
$$W = \frac{(C_1 + C_2)\sqrt{\pi} K_1}{2\sqrt{2} G_1 G_2 \cosh(\pi\epsilon)} \quad (\text{if } k = 1, g_{-1} = 1)$$
$$W = -\frac{(C_1 + C_2)\sqrt{\pi} K_2}{2\sqrt{2} G_1 G_2 \cosh(\pi\epsilon)} \quad (\text{if } k = 1, g_{-1} = i). \quad (41)$$

(c) We take the α stress field ($u_{i(\alpha)} = u_i$, $\sigma_{ij(\alpha)} = \sigma_{ij}$) as a physical stress field caused by some tractions acting on the boundary of the cracked dissimilar body, and let the β stress field be derived from the following complex potential:

$$\phi_1(z) = D_1 h_{-k} z^{-k} \quad (z \in R_{1p})$$
$$\omega_1(z) = -D_1 \overline{h_{-k}} z^{-k} \quad (z \in R_{1p})$$
$$\phi_2(z) = D_2 h_{-k} z^{-k} \quad (z \in R_{2p})$$
$$\omega_2(z) = -D_2 \overline{h_{-k}} z^{-k} \quad (z \in R_{2p}) \quad k = 1, 2, \ldots. \quad (42)$$

After using the properties of eigenfunction expansion form mentioned above, it is easy to see that only one pair, which consists of one term with the eigenvalue k in the α stress field and the β stress field, has a contribution to the integral (25). A simple derivation leads to the following path-inde pendent integral:

$$W = \int_{\Gamma_2+\Gamma_1} (u_i \sigma_{ij(\beta)} - u_{i(\beta)} \sigma_{ij}) n_j ds$$
$$= -\frac{4k\pi C_1 C_2}{(C_1 + C_2) G_1 G_2} \mathrm{Re}(e_k \overline{h_{-k}}). \quad (43)$$

Also, some particular cases are cited here:

$$W = -\frac{4k\pi C_1 C_2}{(C_1 + C_2) G_1 G_2} \mathrm{Re}(e_k) \quad (\text{if } h_{-k} = 1, k = 1, 2, \ldots)$$
$$W = -\frac{4k\pi C_1 C_2}{(C_1 + C_2) G_1 G_2} \mathrm{Im}(e_k) \quad (\text{if } h_{-k} = i, k = 1, 2, \ldots). \quad (44)$$

4 Weight Functions

As mentioned above, the pioneer investigations for weight function in crack problem were completed by Bueckner (1970, 1989) and Rice (1972). The higher order weight function formulation was suggested by Sham (1989), and the weight function in the interface crack problem was analyzed by Gao (1991). It is pointed out that the weight function in crack problem likes the Green's function in the solution of Laplace's equation (Courant and Hilbert, 1962). Using the properties of the eigenfunction expansion form, the weight function formulation is also possible. For simplifying statement, the formulation is limited to the traction boundary problem of a cracked body with traction-free crack surfaces.

Below, the α stress field is chosen as the physical stress field, and the β stress field is derived from the following complex potentials:

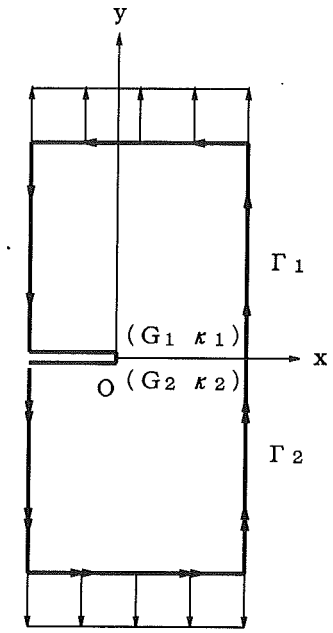


Fig. 2 An example of bounded plate with crack

$$\phi_{1s}(z) = e^{-\pi\epsilon} g_{-1} z^{-1/2-i\epsilon} \quad (z \in R_{1p})$$
$$\omega_{1s}(z) = e^{\pi\epsilon} \overline{g_{-1}} z^{-1/2+i\epsilon} \quad (z \in R_{1p})$$
$$\phi_{2s}(z) = e^{\pi\epsilon} g_{-1} z^{-1/2-i\epsilon} \quad (z \in R_{2p})$$
$$\omega_{2s}(z) = e^{-\pi\epsilon} \overline{g_{-1}} z^{-1/2+i\epsilon} \quad (z \in R_{2p}). \quad (45)$$

From Eqs. (39)–(41), we have the following result:

$$W = \int_{\Gamma_2+\Gamma_1} (u_i \sigma_{ij(\beta)} - u_{i(\beta)} \sigma_{ij}) n_j ds$$
$$= \begin{cases} \dfrac{(C_1 + C_2)\sqrt{\pi} K_1}{2\sqrt{2} G_1 G_2 \cosh(\pi\epsilon)} & (\text{if } g_{-1} = 1) \\ -\dfrac{(C_1 + C_2)\sqrt{\pi} K_2}{2\sqrt{2} G_1 G_2 \cosh(\pi\epsilon)} & (\text{if } g_{-1} = i). \end{cases} \quad (46)$$

For definiteness, the integration pathes Γ_2 and Γ_1 are taken along the outer boundary of the cracked body in Fig. 2. From Eq. (46) we see that, in order to obtain the stress intensity factors at the crack tip, one has to know not only the tractions σ_{ij} but also the displacements u_i along the boundaries Γ_2 and Γ_1. Therefore, it is necessary to solve the traction boundary value problem. In addition, if there are many traction boundary value problems, one has to solve so many problems. The merit of the weight function is that, once a particular boundary value problem is solved, all the boundary value problems with the same geometry can be solved immediately. This idea is universal in mathematical physics.

In the weight function method, the α field is also of the physical stress field, and the β field is derived from the complex potential with the following form:

$$\phi_1(z) = \phi_{1s}(z) + \phi_{1r}(z) \quad (z \in R_{1p})$$
$$\omega_1(z) = \omega_{1s}(z) + \omega_{1r}(z) \quad (z \in R_{1p})$$
$$\phi_2(z) = \phi_{2s}(z) + \phi_{2r}(z) \quad (z \in R_{2p})$$
$$\omega_2(z) = \omega_{2s}(z) + \omega_{2r}(z) \quad (z \in R_{2p}). \quad (47)$$

Two parts are involved in Eq. (47), and the corresponding

Downloaded 03 May 2010 to 171.66.16.20. Redistribution subject to ASME license or copyright; see http://www.asme.org/terms/Terms_Use.cfm

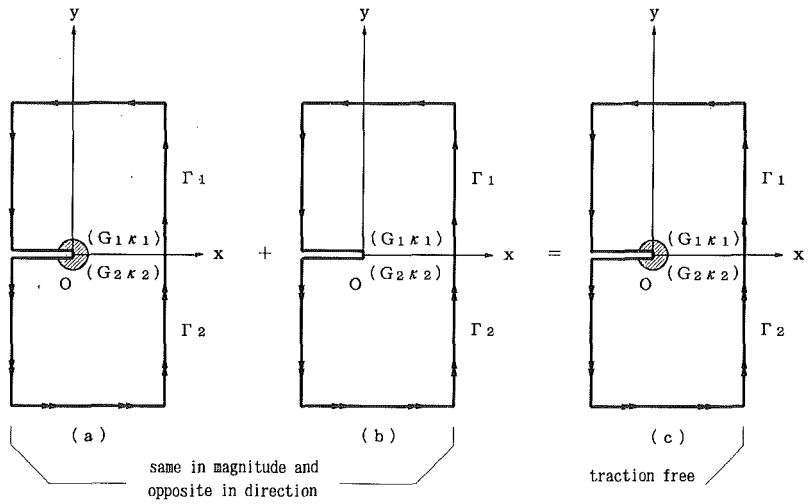


Fig. 3 A model for formulating the weight function approach

loading conditions are shown in Fig. 3(a) and 3(b), respectively. Note that the eigenvalue in Eq. (45) is $-1/2 - i\epsilon$ and its real part is negative. Therefore, the stress field derived from the complex potential $\phi_{1s}(z)$, $\omega_{1s}(z)$ $(z \in R_{1p})$ and $\phi_{2s}(z)$, $\omega_{2s}(z)$ $(z \in R_{2p})$ is a singular stress field in the sense of unbounded displacement in the vicinity of the crack tip. In addition, it has been proved that the traction applied along the pathes Γ_2 and Γ_1 caused by this field is in equilibrium. Thus, we can let the tractions along the Γ_2 and Γ_1 in Fig. 3(b) caused by $\phi_{1r}(z)$, $\omega_{1r}(z)$ $(z \in R_{1p})$ and $\phi_{2r}(z)$, $\omega_{2r}(z)$ $(z \in R_{2p})$ be opposite to those caused by $\phi_{1s}(z)$, $\omega_{1s}(z)$ $(z \in R_{1p})$ and $\phi_{2s}(z)$, $\omega_{2s}(z)$ $(z \in R_{2p})$. The superposition of two loading cases makes the β stress field shown by Fig. 3(c). Clearly, the boundary value problem shown by Fig. 3(b) is a usual problem, and can be solved by any numerical method, for example, the finite element method. After considering the property of the eigenfunction expansion form, Eq. (46) is still valid in this case. Since the traction $\sigma_{ij(\beta)}n_j$ vanishes along the contours Γ_2 and Γ_1, thus, Eq. (46) is reduced to the following equality:

$$W = \int_{\Gamma_2+\Gamma_1} (-u_{i(\beta)}\sigma_{ij}n_j)ds = \begin{cases} \dfrac{(C_1 + C_2)\sqrt{\pi}K_1}{2\sqrt{2}\,G_1G_2\cosh(\pi\epsilon)} & (\text{if } g_{-1} = 1) \\ -\dfrac{(C_1 + C_2)\sqrt{\pi}K_2}{2\sqrt{2}\,G_1G_2\cosh(\pi\epsilon)} & (\text{if } g_{-1} = i). \end{cases} \tag{48}$$

In Eq. (48), $u_{i(\beta)}$ shows the displacement along the boundaries Γ_1 and Γ_2 in Fig. 3(c), and serves the weight function mentioned above. From the above analysis we see that, once the weight function is obtained, the stress intensity factors at the crack tip for all the boundary value problems with the same geometry can be evaluated immediately. In fracture analysis, the original idea of the weight function was proposed by Bueckner (1970, 1973) and Rice (1972).

Obviously, the higher order weight functions in the interface crack problem can be formulated in a similar manner. However, one particular point should be noticed. In the case that the singular field is chosen as $k = 1$ in Eq. (42), the resultant forces applied along the path $\Gamma_2 + \Gamma_1$ in Fig. 3 vanish and the moment applied is equal to $M = 2\pi(D_1 + D_2)\mathrm{Im}(h_{-1})$. This is to say the corresponding weight function exists only if the condition $\mathrm{Im}(h_{-1}) = 0$ is satisfied. This situation is easy to understand since we cannot determine the rotation of the cracked body in the traction boundary value problem. A similar conclusion was found by Sham (1989).

References

Bueckner, H. F., 1970, "A Novel Principle for the Computation of Stress Intensity Factors," *Zeitschrift fur angewandte Mathematik and Mechanik*, Vol. 50, pp. 529–546.

Bueckner, H. F., 1973, "Field Singularities and Related Integral Representations," *Mechanics of Fracture*, G. C. Sih, ed., Vol. 1, pp. 239–314.

Bueckner, H. F., 1989, "Observations on Weight Functions," *Engineering Analysis with Boundary Elements*, Vol. 6, pp. 3–18.

Chen, Y. Z., 1985, "New Path Independent Integrals in Linear Elastic Fracture Mechanics," *Engineering Fracture Mechanics*, Vol. 22, pp. 673–686.

Chen, Y. Z., 1989, "Weight Function Technique in a More General Case," *Engineering Fracture Mechanics*, Vol. 33, pp. 983–986.

Courant, R., and Hilbert, D., 1962, *Methods of Mathematical Physics*, Vol. 2, John Wiley and Sons, New York.

Erdogan, F., 1963, "Stress Distribution in a Nonhomogeneous Elastic Plane with Cracks," ASME JOURNAL OF APPLIED MECHANICS, Vol. 30, pp. 232–236.

Gao, H., and Rice, J. R., 1986, "Shear Stress Intensity Factors for a Planar Crack with Slightly Curved Front," ASME JOURNAL OF APPLIED MECHANICS, Vol. 53, pp. 774–778.

Gao, H., and Rice, J. R., 1987, "Nearly Circular Connections of Elastic Half Spaces," ASME JOURNAL OF APPLIED MECHANICS, Vol. 54, pp. 627–634.

Gao, H., 1991, "Weight Function Analysis of Interface Cracks: Mismach Versus Oscillation," ASME JOURNAL OF APPLIED MECHANICS, Vol. 58, pp. 931–938.

Hasebe, N., Okumura, M., and Nakamura, T., 1990, "Partially Bonded Bimaterial Plane under Tension," *Journal of Engineering Mechanics*, Vol. 116, pp. 2017–2034.

Hong, C., and Stern, M., 1978, "The Computation of Stress Intensity Factors in Dissimilar Materials," *Journal of Elasticity*, Vol. 8, pp. 21–34.

Hutchinson, J. W., Mear, M. E., and Rice, J. R., 1987, "Crack Paralleling an Interface Between Dissimilar Materials," ASME JOURNAL OF APPLIED MECHANICS, Vol. 54, pp. 828–832.

Mukai, D. J., Ballarini, R., and Miller, G. R., 1990, "Analysis of Branched Interface Cracks," ASME JOURNAL OF APPLIED MECHANICS, Vol. 57, pp. 887–893.

Muskhelishvili, N. I., 1953, *Some Basic Problems of Mathematical Theory of Elasticity*, Noordhoff, Groningen.

Rice, J. R., 1972, "Some Remarks on Elastic Crack Tip Stress Fields," *International Journal of Solids and Structures*, Vol. 8, pp. 751–758.

Rice, J. R., 1974, "Limitations to the Small Scale Yielding Approximation for Crack Tip Plasticity," *J. Mech. Phys. Solids*, Vol. 22, pp. 17–26.

Rice, J. R., 1985, "First-order Variation in Elastic Fields Due to Variation in Location of a Planar Crack Front," ASME JOURNAL OF APPLIED MECHANICS, Vol. 52, pp. 571–579.

Rice, J. R., 1988, "Elastic Fracture Mechanics Concept for Interfacial Cracks," ASME JOURNAL OF APPLIED MECHANICS, Vol. 55, pp. 98–103.

Rice, J. R., 1989, "Weight Function Theory for Three-Dimensional Elastic Crack Analysis," *Fracture Mechanics, Perspectives and Directions* (Twentieth Symposium), ASTM-STP-1020, R. P. Wei and R. P. Gangloff, eds., American Society for Testing and Materials, Philadelphia, pp. 29–57.

Sham, T. L., and Bueckner, H. F., 1988, "The Weight Function Theory

Downloaded 03 May 2010 to 171.66.16.20. Redistribution subject to ASME license or copyright; see http://www.asme.org/terms/Terms_Use.cfm

for Piecewise Homogeneous Isotropic Notches in Antiplane Strain," ASME JOURNAL OF APPLIED MECHANICS, Vol. 55, pp. 596–603.

Sham, T. L., 1989, "The Theory of Higher Order Weight Functions for Linear Elastic Plane Problems," *International Journal of Solids and Structures*, Vol. 25, pp. 357–380.

Sham, T. L., and Zhou, Y., 1989, "Weight Function in Two-Dimensional Bodies with Arbitrary Anisotropy," *International Journal of Fracture*, Vol. 40, pp. 13–41.

Sih, G. C., and Rice, J. R., 1964, "The Bending of Plates of Dissimilar Materials with Cracks," ASME JOURNAL OF APPLIED MECHANICS, Vol. 31, pp. 477–482.

Sokolnikoff, 1956, *Mathematical Theory of Elasticity*, McGraw-Hill, New York.

Stern, M., 1979, "The Numerical Calculation of Thermally Induced Stress Intensity Factors," *Journal of Elasticity*, Vol. 9, pp. 91–95.

Symington, M. F., 1987, "Eigenvalues for Interface Cracks in Linear Elasticity," ASME JOURNAL OF APPLIED MECHANICS, Vol. 54, pp. 973–974.

Williams, M. L., 1959, "The Stresses Around a Fault or Crack in Dissimilar Media," *Bull. Seismol. Soc. America*, Vol. 49, pp. 199–204.

Yau, J. F., and Wang, S. S., 1984, "An Analysis of Interface Cracks between Dissimilar Isotropic Materials Using Conservation Integrals in Elasticity," *Engineering Fracture Mechanics*, Vol. 20, pp. 423–432.

Downloaded 03 May 2010 to 171.66.16.20. Redistribution subject to ASME license or copyright; see http://www.asme.org/terms/Terms_Use.cfm

M. Shiraishi

Professor,
Faculty of Engineering,
Ibaraki University,
4-12-1 Nakanarusawa-Machi,
Hitachi 316, Japan
Mem. ASME

T. Sato

NTT Japan Cable Co., Ltd.
2-3-1 Ote-Machi,
Chiyoda-Ku,
Tokyo 100, Japan

Switching Phenomenon of a Bathtub Vortex

Switching phenomenon of the bathtub vortex in a double-orifice water tank is experimentally investigated. This alternation between "vortex flow" and "nonvortex flow" is caused by flow rate differences through the two orifices. The oscillation frequency is experimentally examined by changing the design parameters, such as the orifice size, the distance between two orifices, and the fluid level. A linear relationship is obtained between the frequency and the flow rate difference.

1 Introduction

The vortex which is observed when water is drained from a hole in the bottom of a water tank is a natural phenomenon. This kind of vortex is called a "bathtub vortex" and it grows into an "air-entraining vortex" which has an air core that extends to the drain opening. There are several studies dealing with the origin of the bathtub vortex (Shapiro, 1962; Sibulkin, 1962), the vortex reversal and re-reversal phenomena (Binnie, 1964; Marris, 1967) and the vortex mechanism using Navier-Stokes equations (Akaike and Toyokura, 1970; Granger, 1972). For example, Shapiro explained the rotation of the bathtub vortex on the basis that the earth-rotation-generated vorticity was caused by diffusion of vorticity from the viscous boundary layer at the bottom of the water tank. Sibulkin suggested from his experiments that the boundary layer vorticity was carried down through the bottom opening according to Helmholtz's theorem.

Recently a switching phenomenon of the bathtub vortex has been experimentally observed by the authors when two identical orifices were placed at the bottom of a water tank at a certain distance (Sato, 1987). The flow of the air-entraining bathtub vortex alternatively changes between the two orifices in the form of vortex flow and nonvortex flow. In the present paper, vortex flow means the flow with swirling motion which occurs while the water in a bathtub is being drained out through a bottom orifice. Nonvortex flow therefore means the discharge without swirling motion. "Switching motion" suggests the oscillation behavior of the vortex flow, i.e., the switching motion of the vortex flow between two orifices with a certain frequency although the water is drained out from both orifices during oscillation. The oscillation frequency depends on the orifice size, the distance between the two orifices, and the fluid level.

This paper reports on the discovery of this new phenomenon, mainly from the experimental point of view. According to the flow visualization, the behavior of a bathtub vortex with two discharge holes shows a complicated three-dimensional flow pattern which depends on the design parameters. Velocity measurement using a heat-flux velocity sensor is therefore focused on the flow near the vortex core and its vicinity. As a consequence of this measurement, the switching phenomenon of an air-entraining vortex takes place by the flow rate difference between the two orifices. In other words, a lower velocity distribution around the vortex core causes the switching behavior between the two orifices. The main characteristic of this phenomenon is that the switching is caused by the flow itself, and is not caused by any other energy or additional flow. One application for this phenomenon is as a switching device in an automated system just like a "fluidics device."

2 Switching Mechanism

This section will describe the mechanics of the switching phenomenon. Assume that the fluid level in the water tank is kept constant and that a vortex flow takes place in the left-side orifice A and a nonvortex flow takes place in the right-side orifice B, as shown in Fig. 1. The vortex flow consists of an air-entraining vortex and the diameter of its air core is given by d near the outlet of the orifice A. A bathtub vortex flow has a complicated three-dimensional flow pattern with velocity components of u (peripheral), v (radial), and w (axial), as depicted in Fig. 1. In the orifice inlet, however, the radial velocity component is considerably smaller in comparison with the peripheral velocity component. The air-entraining vortex is therefore mainly composed of the peripheral and axial velocity components.

By neglecting the loss due to viscosity, the following equation is obtained from the energy balance between free surface I and bottom level II, which is just behind the orifice inlet as shown

Contributed by the Applied Mechanics Division of THE AMERICAN SOCIETY OF MECHANICAL ENGINEERS for publication in the ASME JOURNAL OF APPLIED MECHANICS.

Discussion on this paper should be addressed to the Technical Editor, Professor Lewis T. Wheeler, Department of Mechanical Engineering, University of Houston, Houston, TX 77204-4792, and will be accepted until four months after final publication of the paper itself in the ASME JOURNAL OF APPLIED MECHANICS.

Manuscript received by the ASME Applied Mechanics Division, Sept. 17, 1992; final revision, Apr. 22, 1993. Associate Technical Editor: S. Lichter.

Copyright © 1994 by ASME
Downloaded 03 May 2010 to 171.66.16.20. Redistribution subject to ASME license or copyright; see http://www.asme.org/terms/Terms_Use.cfm

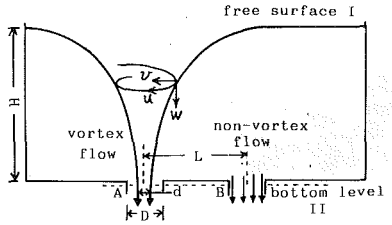


Fig. 1 Switching phenomenon of bathtub vortex

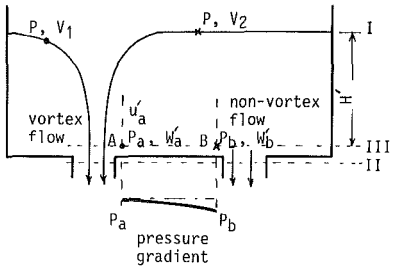


Fig. 2 Assumed pressure gradient between two orifices

in Fig. 1, provided that the velocity component (u, v, w) at the fluid level is small compared with that of the orifice.

$$\rho g H = \frac{1}{2}\rho(u^2 + w^2) \tag{1}$$

where ρ, g, and H denote the density of fluid, the gravitational constant, and the fluid level, respectively.

It is convenient to introduce the circulation Γ, which is described here as

$$\Gamma = ur = \frac{1}{2}du \quad (r\text{: vortex radius from its center}). \tag{2}$$

Then using Eq. (1), the mean axial velocity w_a in orifice A is expressed by

$$w_a = \sqrt{2gH - \frac{4\Gamma^2}{d^2}}. \tag{3}$$

Axial velocity w_b for the nonvortex flow in orifice B is given by the well-known equation, providing that there are no losses due to the orifice shape and the flow exits to atmospheric pressure

$$w_b = \sqrt{2gH}. \tag{4}$$

A comparison of Eqs. (3) and (4) yields

$$w_a < w_b. \tag{5}$$

The effective orifice exit area is therefore less for A than B. This implies that the discharge rate of orifice A is smaller than that of orifice B.

Now, let P_a, u_a', and w_a' be the pressure, peripheral velocity, and axial velocity near the vortex core A at the level III, respectively, as shown in Fig. 2. P_b and w_b' in Fig. 2 denote the pressure and axial velocity for the nonvortex flow B at the same level III. By applying the Bernoulli theorem again at the level I and III, the following equations are obtained for each flow:

$$P + \rho g H' + \frac{1}{2}\rho v_1^2 = P_a + \frac{1}{2}\rho(u_a'^2 + w_a'^2) \tag{6}$$

$$P + \rho g H' + \frac{1}{2}\rho v_2^2 = P_b + \frac{1}{2}\rho w_b'^2 \tag{7}$$

where P is the atmospheric pressure.

By assuming $v_1 \approx v_2$, Eqs. (6) and (7) lead to

$$P_a - P_b = \frac{1}{2}\rho\{w_b'^2 - (u_a'^2 + w_a'^2)\}. \tag{8}$$

As clarified later (Fig. 8), the experimental data show the following relation for the orifice size below 40 mm which is the limitation of the occurrence of the switching phenomenon in this study.

$$w_b'^2 > u_a'^2 + w_a'^2 \tag{9}$$

From Eqs. (8) and (9), the pressure distribution around the two orifices then satisfies

$$P_a > P_b. \tag{10}$$

The vortex flow therefore gradually moves towards the lower pressure side (the right-side orifice B). In other words, the corresponding assumed pressure gradient shown in Fig. 2 between the two orifices gradually bends and finally shifts the vortex flow towards the other side orifice. The flow in orifice A then shows a general nonvortex flow. This behavior is alternatively repeated between A and B, thus generating an oscillating phenomenon of the vortex flow with a certain frequency.

The pressure difference ΔP ($= P_a - P_b$) between the two orifices is of great importance in explaining the switching mechanism. It is quite difficult, however, to estimate ΔP experimentally because of the lack of an adequate sensor which can measure the pressure distribution in the vicinity of the vortex core. We therefore use the flow rate difference between the two orifices instead in this discussion. By introducing the flow rate coefficient α, the flow rates Q_a and Q_b at each orifice can be expressed using Eqs. (3) and (4) as

$$Q_a = \frac{\alpha\pi(D^2 - d^2)}{4}\sqrt{2gH - \frac{4\Gamma^2}{d^2}} \quad \text{(vortex flow at orifice } A\text{)} \tag{11}$$

and

$$Q_b = \frac{\alpha\pi D^2}{4}\sqrt{2gH} \quad \text{(nonvortex flow at orifice } B\text{)}. \tag{12}$$

Thus

$$\Delta Q = Q_b - Q_a. \tag{13}$$

A large value of ΔQ, which implies a large pressure difference ΔP between the two orifices yields a higher oscillation frequency. As discussed later, the design parameters relating to Eq. (13) determine the oscillation frequency f and the experimental data follow a linear equation of the form

$$\log f = a\Delta Q + b \tag{14}$$

where a and b are constants determined by the chosen design parameters.

3 Experimental

3.1 Experimental Apparatus. Experiments were performed using a rectangular acrylic water tank having the dimensions shown in Fig. 3. The water tank is partitioned by a removable center divider (acrylic plate) M_0, and the outlet for each separated tank is initially located at the center of each tank. Water is supplied from an overflow subtank through the main feed pipe using a pump with a maximum flow rate of 180 l/min. The water flows into each tank through six guide plates which are used to stabilize the flows. During filling, the two orifices are closed with stoppers which are removed at the commencement of the experiments. The orifice size D and the distance L between the two orifices are easily changeable by using cassette-type acrylic inserts which have holes ranging from 10 to 50 mm in diameter, 20 mm in spout length, and are from 20 to 100 mm apart. During the experiments, the fluid level is kept constant by a control valve. The direction of the vortex rotation depends on the flow, which is control-

Downloaded 03 May 2010 to 171.66.16.20. Redistribution subject to ASME license or copyright; see http://www.asme.org/terms/Terms_Use.cfm

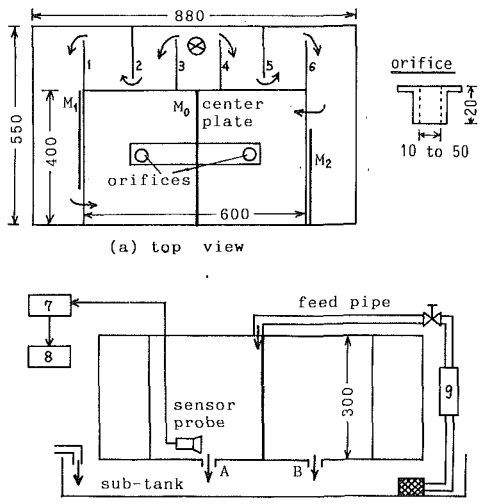


Fig. 3 Experimental apparatus

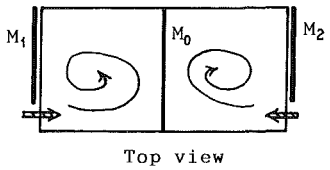


Fig. 4 Counterclockwise and clockwise circulations of vortices

lable by changing the location of plates M_1 and M_2 in Fig. 3(*a*).

The volume flow rate was measured with a graduated cylinder and timer for each flow. Velocity measurements were carried out by using a heat-flux velocity sensor. By changing the sensor probe direction, it can approximately estimate the peripheral (u) and axial (w) velocity components. Practically, the probe was set perpendicular to the direction of vortex rotation for u, and perpendicular to the direction of vortex axis for w.

3.2 Experimental Method. Experiments were conducted under the following condition where an initial dimple vortex or an air-entraining vortex was created in each water tank. The locations of plates M_1 and M_2 shown in Fig. 4 give a counterclockwise circulation in the left-side water tank and a clockwise circulation in the right-side water tank. By removing the center divider, M_0, two vortices behave as a single vortex with a certain circulation. This vortex flow then begins to oscillate between the two orifices based on the distance between them. Experiments were terminated when the fluid level, which can vary from 10 to 300 mm, dropped below 60 mm because the bathtub vortex no longer oscillated for the range of parameters investigated. The center divider plays an important role in making stable initial vortices.

4 Results and Discussion

4.1 Visualization of Switching Phenomenon. A photographic explanation of the switching phenomenon is shown in Fig. 5. Flow visualization was done by photographing a locus of floating aluminum powder. In the divided water tank, two vortices are seen, with a counterclockwise and a clockwise circulations (*a*). By removing the center divider, the two vortices act as a single vortex with a clockwise circulation (*b*). At an adequate distance between the two orifices, this vortex begins to shift from left to right (*c*), and then right to left (*d*).

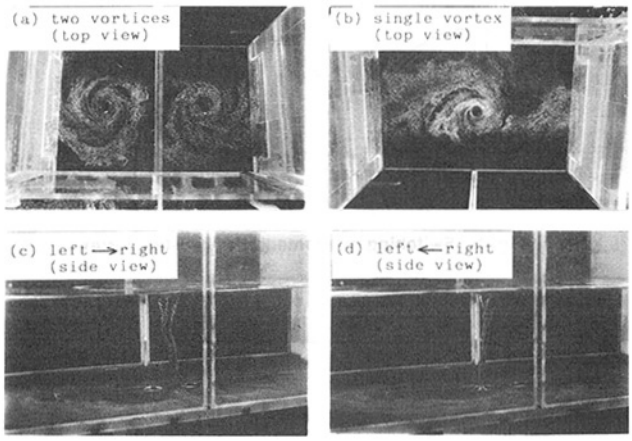


Fig. 5 Switching phenomenon

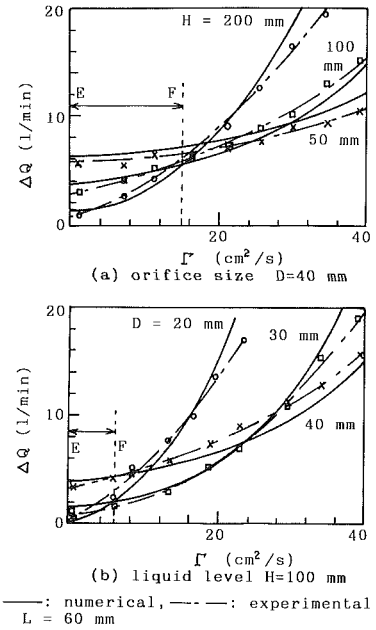


Fig. 6 Circulation Γ versus flow rate difference ΔQ

Other experiments have been performed when the two vortices initially had the same sense. By removing the center divider, in this case, each vortex flow initially showed a turbulent behavior along the boundary of the two vortex flows. In the meantime (after 8 to 12 seconds), they came together and were unified into a single vortex. The direction of rotation was determined by the unbalance of their flow rates into each divided water tank. However, the switching phenomenon was also observed in the same way with Fig. 5. In all of the following experiments, a single vortex behaves with a clockwise circulation after removing the center divider.

4.2 Flow Rate Difference. As mentioned previously, the switching behavior is dependent on the flow rate difference ΔQ given by Eq. (13) which includes the design parameters for the fluid level H and the orifice size D. Figure 6 compares circulation Γ and flow rate difference ΔQ at the orifice distance of L = 60 mm numerically and experimentally. In Fig. 6(*b*), for example, the volume flow rates measured in the vortex flow A and the nonvortex flow B were Q_a = 32.5 l/min and Q_b = 40.2 l/min at D = 30 mm, and Q_a = 62.4 l/min and Q_b = 68.6 l/min at D = 40 mm, respectively. The calculation was performed using measured values of vortex air core d near the orifice outlet and circulation Γ based on Eq. (2). The flow

Downloaded 03 May 2010 to 171.66.16.20. Redistribution subject to ASME license or copyright; see http://www.asme.org/terms/Terms_Use.cfm

Table 1 Measurement result of air-core diameter

D (mm) / H(mm)	30	40
	d mm	d mm
50	9	15
100	6	10
150	4	7
200	3	5

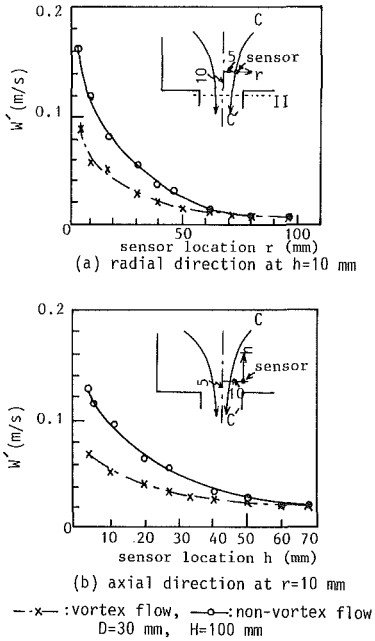


Fig. 7 Distribution of the axial velocity component W'

rate coefficient α is dependent on the orifice design and is difficult to determine theoretically. It was chosen as $\alpha = 0.65$ by using Eq. (12) with representative parameters of $Q_b = 68.6$ l/min, $D = 40$ mm, $H = 100$ mm, and $g = 980$ cm/s^2. The size of the air core was measured with a scale after taking a photograph of the flow pattern through the acrylic orifice. The measurement result is shown in Table 1.

As shown in Fig. 6, the numerical results generally coincide with the experimental results. In Fig. 6(*a*), ΔQ increases with Γ, particularly at high fluid levels. The increase in Γ implies an increase in the peripheral velocity component and, at the same time, a decrease in the axial velocity component from the energy balance, thus generating a large ΔQ (see Eq. (11)). In a small range of Γ (*E-F* in Fig. 6(*a*)), a low fluid level yields a large ΔQ, which will result in a higher oscillation frequency of the bathtub vortex.

Further, as shown in Fig. 6(*b*), ΔQ increases even more with Γ when the orifice size is smaller. This is basically due to the difference in the axial velocity component as d varies. In a small range of Γ(*E-F* in Fig. 6(*b*)), a larger orifice size produces a larger ΔQ, which will also result in a higher oscillation frequency.

4.3 Velocity Distribution of Vortex and Nonvortex Flows. In considering the assumed pressure gradient shown in Fig. 2, the velocity distribution around the vortex and nonvortex flows must be clarified in order to explain the switching mechanism. In particular, the flow around the vortex core (*C-C'* in Fig. 7) and its vicinity is primarily characterized by the axial and peripheral velocity components.

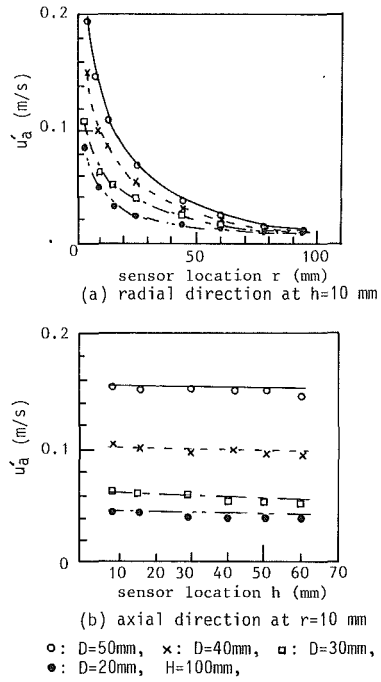


Fig. 8 Distribution of the peripheral velocity component u_a'

Figure 7 illustrates the change in the axial velocity component w': (*a*) in the radial direction r and (*b*) in the axial direction H at a fluid level of 100 mm, with an orifice size of 30 mm. This is the result of an independent experiment with only one orifice open. In Fig. 7(*a*), the horizontal axis r denotes the distance from the orifice center. From Table 1, the air core diameter d in this case is 6 mm at the orifice outlet. As depicted in Fig. 7(*a*), the sensor probe is located about 10 mm above the bottom level II, where the boundary of the vortex core is determined as $r = 5.0$ mm by the photographic observation. Measurement was therefore performed from $r = 5.0$ mm along the fluid level of $h = 10$ mm. The axial velocity in the radial direction exponentially decreases with an increasing r for both vortex and nonvortex flows as demonstrated in Fig. 7(*a*). At the boundary of the vortex core, i.e., $r = 5.0$ mm, the velocity in the nonvortex flow is about two times that of the vortex flow and the velocity difference between the two flows continues up to $r = 65$ mm. These results suggest the validity of the relationship shown in Eq. (5) and further indicate that the switching phenomenon might be expected to depend on the distance between the two orifices, which is confirmed experimentally in Section 4.4.

Figure 7(*b*) shows the measurements made at $r = 10$ mm which is 7 mm outside the boundary of the vortex core near the orifice outlet. The sensor location h, i.e., the horizontal axis in Fig. 7(*b*), was changed from 5 to 70 mm along $r = 10$ mm. It was found from this figure that the velocity of the nonvortex flow is larger than that of the vortex flow and that the velocity difference between the two flows exists from 5 up to 70 mm. This also suggests the occurrence of the switching phenomena. The velocity distribution for the vortex flow approximates that of Granger's simulation results, although it is not presented in this figure.

To verify the relationship given by Eq. (9), the peripheral velocity distribution u for the vortex flow was measured with the same sensor locations with Figs. 7(*a*) and 7(*b*). The results are shown in Fig. 8: (*a*) in the radial direction at $h = 10$ mm and (*b*) in the axial direction at $r = 10$ mm, with orifice sizes ranging from 20 to 50 mm. As expected, the velocity in the radial direction rapidly decreases with r (Fig. 8(*a*)), while that of the axial direction gives almost no change with h at each

Downloaded 03 May 2010 to 171.66.16.20. Redistribution subject to ASME license or copyright; see http://www.asme.org/terms/Terms_Use.cfm

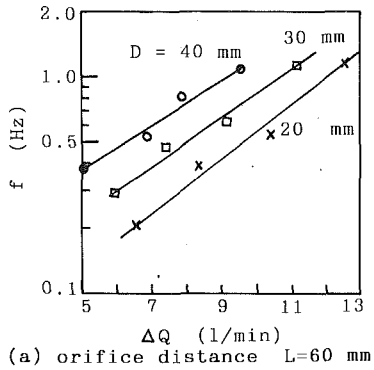


Fig. 9 Flow rate difference ΔQ versus frequency f

orifice size (Fig. 8(*b*)). In case of the orifice size of $D = 30$ mm, for example, the axial velocities for vortex and nonvortex flows are $w_a' = 5.8$ cm/s and $w_b' = 11.1$ cm/s at $h = 10$ mm and $r = 10$ mm, respectively, as illustrated in Fig. 7. From Fig. 8, on the other hand, the peripheral velocity under the same condition with Fig. 7 shows $u_a' = 6.2$ cm/s at the orifice size of $D = 30$ mm. These velocities satisfy the relation given by Eq. (9). We confirmed that the orifice size of $D = 50$ mm did not hold this relation with $w_a' = 12.2$ cm/s, $w_b' = 18.7$ cm/s, and $u_a' = 15.5$ cm/s at $h = 10$ mm and $r = 10$ mm. In other words, the switching phenomenon was not observed for the orifice size of $D = 50$ mm. The limitation of its occurrence was found to be $D \leq 40$ mm with the validity of Eq. (9) in this study.

4.4 Oscillation Frequency. In Sections 4.2 and 4.3, we showed the switching phenomenon from the standpoint of the flow rate and velocity differences between vortex and nonvortex flows. In Fig. 9, the relationship between ΔQ and f is shown for changes in D and L. Figure 9(*a*) indicates that at each orifice size, the increase in ΔQ, i.e., the decrease in H, yields an increase in f which also increases with D. These results coincide with those of Figs. 6 and 7. Further, an increase in L reduces the frequency f, increasing the time to shift, as shown in Fig. 9(*b*). Both figures indicate the linear relationship between $\log f$ and ΔQ as given by Eq. (14), and slope a is nearly independent of the orifice size and the distance between the two orifices.

Other experiments suggest that the occurrence of the switching phenomenon is limited to orifice distances from 30 to 60 mm and to fluid levels from 60 to 200 mm for orifice sizes ranging from 20 to 40 mm. When the fluid level is too high, a very narrow vortex is observed and it flows out from only one side orifice without oscillation. Switching was also observed in a single vortex with a counterclockwise circulation for different locations of plates M_1 and M_2, with behavior quite similar to the phenomenon described above.

5 Conclusion

We investigated the switching behavior of the bathtub vortex experimentally for a double-orifice water tank. This is the alternation of vortex and nonvortex flows between the two orifices with a certain frequency determined by the chosen parameters. The phenomenon observed is based on the flow rate difference between the two flows, which is caused by changes in the fluid level. This implicitly generates a pressure gradient between the two orifices. The oscillation frequency is very low and depends on the orifice size and the distance between the two orifices. The experimental data show a linear relationship between the log of the oscillation frequency and the flow rate difference. A key characteristic of this phenomenon is that the switching behavior is caused by the flow itself and not by any other energy. Several applications of this phenomenon may be considered in the field of automation systems where it could be used just like a fluidics device.

References

Akaike, S., and Toyokura, T., 1970, "Vortex Phenomena in a Water Tank," *Bulletin of the Japan Society of Mechanical Engineers*, Vol. 13, No. 57, pp. 373–381.

Binnie, A. N., 1964, "Some Experiments on the Bath-Tub Vortex," *Journal of Mechanical Engineering Science*, Vol. 6, pp. 256–257.

Granger, R. A., 1972, "A Steady Axisymmetric Vortex Flow," *Geophysical Fluid Dynamics*, Vol. 3, pp. 45–88.

Marris, A. W., 1967, "Theory of Bathtub Vortex," ASME JOURNAL OF APPLIED MECHANICS, Vol. 34, pp. 11–15.

Sato, T., 1987, "A Study on a Switching Phenomenon of Bath-Tub Vortex," MS Thesis, Ibaraki University.

Shapiro, M., 1962, "Bath-Tub Vortex," *Nature*, Vol. 196, No. 4859, pp. 1080–1081.

Sibulkin, M., 1962, "A Note on the Bathtub Vortex," *Journal of Fluid Mechanics*, Vol. 14, Part 1, pp. 21–24.

Downloaded 03 May 2010 to 171.66.16.20. Redistribution subject to ASME license or copyright; see http://www.asme.org/terms/Terms_Use.cfm

F. O. Eke
Assistant Professor,
Mem. ASME

Song-Min Wang
Graduate Research Assistant.

Department of Mechanical and
Aeronautical Engineering,
University of California,
Davis, CA 95616

Equations of Motion of Two-Phase Variable Mass Systems With Solid Base

This paper develops dynamical equations for variable mass systems that can be viewed, at any given instant, as comprising a solid phase and a fluid phase. The equations of translational and rotational motion are presented, and several versions of each are given. It is shown that some versions have major advantages over others because they involve parameters that are relatively easy to estimate in practical problems, and make close-form solutions possible without the usual penalty of drastic simplifying assumptions. A simple rocket example is presented, and shows that instability cannot be ruled out for such systems. It is shown that system and combustion chamber geometry play a crucial role in the attitude stability of such systems.

Introduction

The expression "variable mass system," as used in the context of this paper, refers to mechanical systems that lose and/or gain mass while in motion. Examples of such devices abound in the engineering literature. They include complex systems such as aircraft, rockets, automobiles, and moving robots picking up or letting go of objects, as well as simpler systems such as water sprinkler systems or an inflated balloon with air loss through one or more holes. Variable mass systems can be divided into two classes: those with continuous mass variation and those with discrete mass variation. Rockets, for example, fall in the continuous variable mass class, and robots picking up or releasing objects, or a moving vehicle dropping off some of its payload in discrete chunks, belong to the discrete variable mass system class. The focus of the study presented here is on systems with continuously varying mass, with the additional restriction that such systems comprise a main solid frame or base and a fluid phase, mass variation being a consequence of fluid flow across an imaginary boundary that delimits the system.

Variable mass systems have received a lot of attention in the engineering literature. They have been the subject of at least two Ph.D. dissertations (Hammidi, 1961; Belknap 1970), several journal and conference papers (Meirovitch, 1970; Ge, 1984; etc.) and a number of textbooks (Rosser et al., 1947). Much of the early as well as current work on these systems is motivated by developments in rocketry, which in turn, are promoted by the need for more efficient delivery systems for large space payloads such as missiles and spacecraft.

Figure 1 shows the type of system being considered in this paper. It consists of a main part R that is solid and to which matter (S') is continuously added, and from which matter (S'') is continuously removed while the system as a whole evolves in space. The mass of R does not necessarily remain constant, since parts of R may be "eaten away" by combustion or other processes as time changes. Usually, interest is restricted to the location and orientation of everything inside a closed imaginary shell B that is rigidly attached to R. Thus, the system under consideration is essentially a continuous system with an infinite number of degrees-of-freedom, and, at the same time, its mass is time dependent. To derive equations of motion for the system, two approaches are possible. One can approximate this continuum with a finite number of degrees-of-freedom prior to the formulation of equations of motion, or, one can describe the continuous problem in terms of partial differential equations, then introduce a discretization later. In either case, one must still find

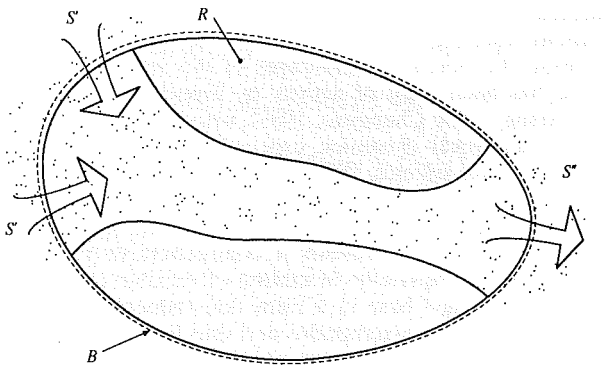


Fig. 1 A general two-phase variable mass system

Contributed by the Applied Mechanics Division of THE AMERICAN SOCIETY OF MECHANICAL ENGINEERS for publication in the ASME JOURNAL OF APPLIED MECHANICS.

Discussion on this paper should be addressed to the Technical Editor, Professor Lewis T. Wheeler, Department of Mechanical Engineering, University of Houston, Houston, TX 77204-4792, and will be accepted until four months after final publication of the paper itself in the ASME JOURNAL OF APPLIED MECHANICS.

Manuscript received by the ASME Applied Mechanics Division, Oct. 9, 1992; final revision, Aug. 27, 1993. Associate Technical Editor: D. J. Inman.

Copyright © 1994 by ASME
Downloaded 03 May 2010 to 171.66.16.20. Redistribution subject to ASME license or copyright; see http://www.asme.org/terms/Terms_Use.cfm

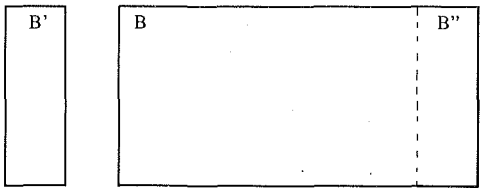


Fig. 2 Early model of variable mass systems

a way to contend with the fact that the mass of the system is variable.

As is well known, the difficulty with the derivation of equations of motion for such systems comes from the fact that the basic principles of classical dynamics (Newton-Euler Equations, Langrange's Equations, etc.) are only valid for systems comprising definite sets of objects each with constant mass. Yet, if attention is to be restricted to B in Fig. 1, as practical considerations demand, then the equations of motion cannot be obtained by direct application of any of the formulations of classical dynamics described above, because the mass of B varies with time. Two main strategies have been developed to circumvent this difficulty. Early researchers viewed the system, at any given instant, as comprising three parts: B, B', and B'' as shown in Fig. 2. Here, B is the main part of the system and is analogous to the closed shell of Fig. 1; B'' represents the part of B that will be lost at a later time, and B' is material that will coalesce with B at a later time. Because this viewpoint keeps track of all the particles of the system, the basic laws of mechanics are applicable and lead to the equations of motion of the system. This approach was developed most fully by Thomson (1963, 1965, 1966), and led to the well-known relations for variable mass systems that still appear in many undergraduate texts in dynamics. The merit of this approach is that it yields relatively simple equations of motion. Its main drawback is that the model utilized is overly simple, so that the resulting equations are not likely to account for many important features of the system. For example, in the case of rockets, this approach implies that the particles leaving the system through the nozzle all have the same velocity relative to the main body of the rocket, and that this relative velocity is parallel to the direction of motion of the rocket. This assumption is obviously at variance with reality, yet, the resulting equations have proven somewhat useful for certain applications.

A second viewpoint is the so-called control volume approach, where everything within the closed region B in Fig. 1 is considered the "system." The system is thus part solid and part fluid, and can lose or gain mass with time. Some of the early proponents of this viewpoint include Leitman (1957) and Thorpe (1962), and this approach has been progressively refined by other investigators (Belknap, 1970; Meirovitch, 1970). The main difficulty with this method so far has been that it leads to a set of equations containing several volume integrals which are difficult to evaluate for real systems without resorting to major simplifying assumptions that compromise the potential advantages of this method. Recently, there has been a lot of activity by investigators (Ge, 1984; Fengxiang, 1989; Chengyao, 1989), who seek to apply methods of analytical dynamics, especially Kane's equations, to variable mass systems. The main shortcoming of some of their work is that it basically views the system as a particle, thus making the results less useful for attitude dynamics studies. This paper presents a comprehensive method for generating the equations of motion of variable mass systems containing a rigid base in a form that reduces the need for drastic simplifying assumptions and thus leads ultimately to a more accurate representation of the behavior of many types of variable mass systems.

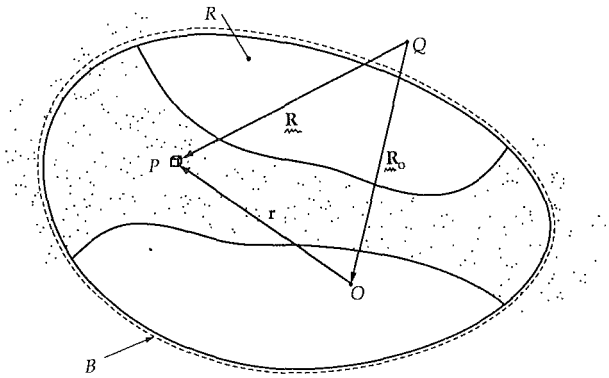


Fig. 3 Control volume model for variable mass systems

Equation Formulation

The system under consideration is shown once more in Fig. 3. One imagines a closed region or closed massless shell that encloses, is rigidly attached to, and moves in space with the solid part, R, of a variable mass system. This region is assumed to maintain a constant shape and thus has a constant volume V_0 and a constant surface area S_0. Everything within the region is considered the "system," and interest is restricted to the motion of the shell and its instantaneous contents. The viewpoint adopted is that, at any instant of time, t, a definite set of material particles is contained within this closed region (labeled B in Fig. 3), and that B and its contents must obey Newton's second law or any other laws of mechanics that one may choose to invoke. Another instant t', B may contain a different set of particles, but, these too must obey the laws of mechanics. Thus, Newton's second law, Lagrange's equations or Kane's equations can be applied instantaneously to everything within the region B to produce equations of motion that will be valid for the system at each instant of time.

Newton's second law applied to the system at any general instant of time, t, yields

$$\mathbf{F} = \int_V \rho \mathbf{a} dV \tag{1}$$

where $\mathbf{F}$ is the resultant external force on the system, $\mathbf{a}$ is the acceleration of a generic point P (see Fig. 3) of the system, in an inertial reference frame, ρ is the mass density, and V is the volume of space that the system occupies at the instant t. There is a subtle but important difference between V and the volume V_0 defined earlier as the constant volume of the region B. V is associated with the particles that happen to be within B at the instant t under consideration, and is identical with V_0 at that instant. At any other instant t', V_0 is unchanged, but V must remain associated with the same particles that were in B at time t. Hence, V may change with time and contains the same particles at all times, whereas V_0 is constant and contains different particles at different times. One important consequence of this is that although the time derivative of a volume integral taken over V can be equated to the integral of the time derivative of the integrand, the same is not true for a volume integral over V_0. The reason is that it is no longer valid, in the case of V_0, to equate the time derivative of a sum to the sum of time derivatives since the summation at different times is taken over different sets of particles. Because it is easier to visualize the motion of particles such as P with respect to the solid base R rather than their absolute motion, it is useful to express Eq. (1) as

$$\mathbf{F} = \int_V \rho \left[\mathbf{a}^0 + \boldsymbol{\alpha} \times \mathbf{r} + \boldsymbol{\omega} \times (\boldsymbol{\omega} \times \mathbf{r})\right] dV + 2\int_V \rho \boldsymbol{\omega} \times \mathbf{v}_r dV + \int_V \rho \mathbf{a}_r dV \tag{2}$$

Downloaded 03 May 2010 to 171.66.16.20. Redistribution subject to ASME license or copyright; see http://www.asme.org/terms/Terms_Use.cfm

where $\mathbf{a}^0$ is the acceleration of an arbitrary point O of R, $\boldsymbol{\omega}$ and $\boldsymbol{\alpha}$ are, respectively, the angular velocity and angular acceleration of R, $\mathbf{r}$ is the position vector from O to P, and $\mathbf{v}_r$ and $\mathbf{a}_r$ are velocity and acceleration of point P in the reference frame R. Another form can be obtained by invoking Reynolds Transport Theorem (Shames, 1982), and using it to expand the last term in Eq. (2) as follows:

$$\int_V \rho \mathbf{a}_r dV = \int_V \rho \frac{{}^B d\mathbf{v}_r}{dt} dV = \frac{{}^B d}{dt} \int_V \rho \mathbf{v}_r dV$$
$$= \frac{{}^B d}{dt} \int_{V_0} \rho \mathbf{v}_r dV + \int_{S_0} \mathbf{v}_r (\rho \mathbf{v}_r \cdot \mathbf{n}) dS \quad (3)$$

where, at any point on the surface of B, $\mathbf{n}$ is a unit normal pointing outwards; also, the left superscript B indicates the reference frame in which the time derivative is to be taken. Taken together, Eqs. (2) and (3) yield

$$\mathbf{F} = m\left[\mathbf{a}^0 + \boldsymbol{\alpha} \times \mathbf{r}^* + \boldsymbol{\omega} \times (\boldsymbol{\omega} \times \mathbf{r}^*)\right]$$
$$+ 2\int_V \rho \boldsymbol{\omega} \times \mathbf{v}_r dV + \frac{{}^B d}{dt} \int_{V_0} \rho \mathbf{v}_r dV + \int_{S_0} \rho \mathbf{v}_r (\mathbf{v}_r \cdot \mathbf{n}) dS \quad (4)$$

where $\mathbf{r}^*$ is the position vector from O to the system's instantaneous mass center. One can arrive at the same vector equation of translational motion by starting with the linear momentum principle, where one equates the sum of the external forces on the system to the time derivative of the linear momentum of the system.

The expression within brackets on the right-hand side of Eq. (4) is the acceleration of the mass center of a fictitious rigid body obtained by freezing the system at the instant under consideration. Hence, the whole of the first term on the right-hand side of Eq. (4) can be viewed as the force due to the rigid body motion of the system. The second term is the Coriolis force, and the third term is a force due to the change in linear momentum of the system when its rigid portion is held stationary in inertial space. As for the last term, we note that in the case of rockets (see for example Fig. 5), $\mathbf{v}_r \cdot \mathbf{n}$ is zero everywhere except at the nozzle exit plane. The surface integral would then produce a force that is directed axially and backwards for axisymmetric velocity distribution. The negative of this term is thus a force that, in general, tends to propel the system forward—the thrust vector. In fact, Eq. (4) can be written without this last term, with the understanding that it is part of the externally applied force $\mathbf{F}$.

The vector equation of attitude motion can be obtained from Eq. (1) by cross-multiplying each side of the equation with $\mathbf{r}$:

$$\mathbf{M} = \int_V \rho \mathbf{r} \times \mathbf{a} dV \quad (5)$$

where $\mathbf{M}$ is the sum of the moments of all external forces about the point O. Following developments similar to those performed above for Eq. (1), it is possible to write Eq. (5) in the form

$$\mathbf{M} = \int_V \rho \mathbf{r} \times \left[\mathbf{a}^0 + \boldsymbol{\alpha} \times \mathbf{r} + \boldsymbol{\omega} \times (\boldsymbol{\omega} \times \mathbf{r}) + 2\boldsymbol{\omega} \times \mathbf{v}_r + \mathbf{a}_r\right] dV$$
$$= m\mathbf{r}^* \times \mathbf{a}^0 + \mathbf{I} \cdot \boldsymbol{\alpha} + \boldsymbol{\omega} \times \mathbf{I} \cdot \boldsymbol{\omega} + 2\int_V \rho \mathbf{r} \times (\boldsymbol{\omega} \times \mathbf{v}_r) dV$$
$$+ \int_V \rho \mathbf{r} \times \mathbf{a}_r dV \quad (6)$$

or as

$$\mathbf{M} = m\mathbf{r}^* \times \mathbf{a}^0 + \mathbf{I} \cdot \boldsymbol{\alpha} + \boldsymbol{\omega} \times \mathbf{I} \cdot \boldsymbol{\omega} + 2\int_V \rho \mathbf{r} \times (\boldsymbol{\omega} \times \mathbf{v}_r) dV$$
$$+ \frac{{}^B d}{dt} \int_{V_0} \rho \mathbf{r} \times \mathbf{v}_r dV + \int_{S_0} \rho (\mathbf{r} \times \mathbf{v}_r)(\mathbf{v}_r \cdot \mathbf{n}) dS \quad (7)$$

after invoking Reynolds Transport Theorem. In Eqs. (6) and (7), $\mathbf{I}$ represents the instantaneous inertia dyadic of the system with respect to the point O of R. Here again, the first three terms on the right-hand side of Eq. (7) capture the rigid-body motion. The contribution of mass variability to the dynamics of the system is embodied in the remaining three terms, which are, respectively, the Coriolis moment, moment due to the change in angular momentum of the system in the reference frame B, and the moment of the thrust vector about point O.

Several investigators who have used the so-called control volume approach in the derivation of equations of motion of variable mass systems have arrived at equations similar in form to Eqs. (4) and (7). Another form of the moment equation will now be developed starting from the angular momentum principle. We define the inertial angular momentum, $\mathbf{H}$, of the system (everything within B in Fig. 3) with respect to the point O as

$$\mathbf{H} = \int_V \rho \mathbf{r} \times \mathbf{v} dV = \int_V \rho \mathbf{r} \times (\mathbf{v}_r + \mathbf{v}_0 + \boldsymbol{\omega} \times \mathbf{r}) dV \quad (8)$$

where $\mathbf{v}$ is the velocity of the generic point P in the inertial reference frame N. Because the point O is neither the mass center of the system nor is it fixed in N, the angular momentum principle for the system has the form (Eke, 1991)

$$\mathbf{M} = \frac{{}^N d\mathbf{H}}{dt} - m\mathbf{v}^* \times \mathbf{v}_0. \quad (9)$$

From Eq. (8),

$$\frac{{}^N d\mathbf{H}}{dt} = \int_V \rho \frac{{}^N d\mathbf{r}}{dt} \times \mathbf{v}_0 dV + \int_V \rho \mathbf{r} \times \frac{{}^N d\mathbf{v}_0}{dt} dV + \frac{{}^B d}{dt} \int_V \rho \mathbf{r}$$
$$\times \mathbf{v}_r dV + \boldsymbol{\omega} \times \int_V \rho \mathbf{r} \times \mathbf{v}_r dV + \frac{{}^B d}{dt} \int_V \rho \mathbf{r} \times (\boldsymbol{\omega} \times \mathbf{r}) dV$$
$$+ \boldsymbol{\omega} \times \int_V \rho \mathbf{r} \times (\boldsymbol{\omega} \times \mathbf{r}) dV. \quad (10)$$

In Fig. 3, point Q is fixed in the inertial frame, N, so that

$$\frac{{}^N d\mathbf{r}}{dt} = \frac{{}^N d}{dt} (\mathbf{R} - \mathbf{R}_0) = \mathbf{v} - \mathbf{v}_0. \quad (11)$$

Equations (10), (11), and Reynolds Transport Theorem then lead to

$$\frac{d\mathbf{H}}{dt} = \int_V \rho \mathbf{v} \times \mathbf{v}_0 dV + \int_V \rho \mathbf{r} \times \mathbf{a}^0 dV + \frac{{}^B d}{dt} \int_{V_0} \rho \mathbf{r} \times \mathbf{v}_r dV$$
$$+ \int_{S_0} \rho (\mathbf{r} \times \mathbf{v}_r)(\mathbf{v}_r \cdot \mathbf{n}) dS + \boldsymbol{\omega} \times \int_V \rho \mathbf{r} \times \mathbf{v}_r dV$$
$$+ \frac{{}^B d}{dt} \int_V \rho \mathbf{r} \times (\boldsymbol{\omega} \times \mathbf{r}) dV + \boldsymbol{\omega} \times \int_V \rho \mathbf{r} \times (\boldsymbol{\omega} \times \mathbf{r}) dV \quad (12)$$

which can be simplified and combined with Eq.(9) to yield

$$\mathbf{M} = m\mathbf{r}^* \times \mathbf{a}^0 + \mathbf{I} \cdot \boldsymbol{\alpha} + \boldsymbol{\omega} \times \mathbf{I} \cdot \boldsymbol{\omega} + \left(\frac{{}^B d\mathbf{I}}{dt}\right) \cdot \boldsymbol{\omega}$$
$$+ \int_{S_0} \rho [\mathbf{r} \times \mathbf{v}_r (\mathbf{v}_r \cdot \mathbf{n})] dS + \boldsymbol{\omega} \times \int_V \rho \mathbf{r} \times \mathbf{v}_r dV$$
$$+ \frac{{}^B d}{dt} \int_{V_0} \rho \mathbf{r} \times \mathbf{v}_r dV. \quad (13)$$

Downloaded 03 May 2010 to 171.66.16.20. Redistribution subject to ASME license or copyright; see http://www.asme.org/terms/Terms_Use.cfm

Note that the inertia dyadic, $\mathbf{I}$, in Eq. (13) is that associated with the volume V (as opposed to the volume V_0). The inertia dyadic, $\mathbf{I}_0$, associated with V_0 can be introduced into this equation by applying the Reynolds Transport Theorem to the second to the last term on the right-hand side of Eq. (12). The result is

$$\mathbf{M} = m\mathbf{r}^* \times \mathbf{a}^0 + \mathbf{I}_0 \cdot \boldsymbol{\alpha} + \boldsymbol{\omega} \times \mathbf{I}_0 \cdot \boldsymbol{\omega} + \left(\frac{{}^B d\mathbf{I}_0}{dt}\right) \cdot \boldsymbol{\omega} + \int_{S_0} \rho[\mathbf{r} \times (\boldsymbol{\omega} \times \mathbf{r})(\mathbf{v}_r \cdot \mathbf{n})]dS + \boldsymbol{\omega} \times \int_V \rho \mathbf{r} \times \mathbf{v}_r dV + \frac{{}^B d}{dt} \int_{V_0} \rho \mathbf{r} \times \mathbf{v}_r dV + \int_{S_0} \rho(\mathbf{r} \times \mathbf{v}_r)(\mathbf{v}_r \cdot \mathbf{n})dS. \quad (14)$$

Actually, $\mathbf{I}$ and $\mathbf{I}_0$ are equal at any given instant, but their time derivatives are different, in general. Equations (7) and (13) must be equivalent. To verify this, we now show that

$$2\int_V \rho \mathbf{r} \times (\boldsymbol{\omega} \times \mathbf{v}_r)dV = \left(\frac{{}^B d\mathbf{I}}{dt}\right) \cdot \boldsymbol{\omega} + \boldsymbol{\omega} \times \int_V \rho \mathbf{r} \times \mathbf{v}_r dV. \quad (15)$$

First, we define the unit dyadic

$$\mathbf{U} = \mathbf{b}_1\mathbf{b}_1 + \mathbf{b}_2\mathbf{b}_2 + \mathbf{b}_3\mathbf{b}_3 \quad (16)$$

where $\mathbf{b}_i$ $(i = 1, 2, 3)$ constitute a dextral set of mutually perpendicular unit vectors fixed in B. The inertia dyadic of the system relative to the point O can be expressed as

$$\mathbf{I} = \int_V \rho[\mathbf{U}(\mathbf{r} \cdot \mathbf{r}) - \mathbf{rr}]dV \quad (17)$$

so that

$$\left(\frac{{}^B d\mathbf{I}}{dt}\right) \cdot \boldsymbol{\omega} + \int_V \rho\boldsymbol{\omega} \times (\mathbf{r} \times \mathbf{v}_r)dV = \left\{\int_V \rho[2\mathbf{U}(\mathbf{v}_r \cdot \mathbf{r}) - \mathbf{v}_r\mathbf{r} - \mathbf{r}\mathbf{v}_r]dV\right\} \cdot \boldsymbol{\omega} + \int_V \rho[(\boldsymbol{\omega} \cdot \mathbf{v}_r)\mathbf{r} - (\boldsymbol{\omega} \cdot \mathbf{r})\mathbf{v}_r]dV = 2\int_V \rho[(\mathbf{v}_r \cdot \mathbf{r})\boldsymbol{\omega} - (\boldsymbol{\omega} \cdot \mathbf{r})\mathbf{v}_r]dV = 2\int_V \mathbf{r} \times (\boldsymbol{\omega} \times \mathbf{v}_r)dV. \quad (18)$$

Hence the two equations are indeed equivalent.

At this point, it is appropriate to discuss the merits and demerits of the two forms of the moment equation given above. Before this is done, we observe that the equations of translational and rotational motion are coupled through the acceleration term, $\mathbf{a}^0$. They can be decoupled simply by solving for $\mathbf{a}^0$ in the translational equation and substituting into the rotational equations. For example, we solve for $m\mathbf{a}^0$ in Eq. (4) and substitute into Eq. (7) to obtain

$$\mathbf{M} - \mathbf{r}^* \times \mathbf{F} = \mathbf{I} \cdot \boldsymbol{\alpha} - m\mathbf{r}^* \times (\boldsymbol{\alpha} \times \mathbf{r}^*) + \boldsymbol{\omega} \times \mathbf{I} \cdot \boldsymbol{\omega} - m\mathbf{r}^* \times [\boldsymbol{\omega} \times (\boldsymbol{\omega} \times \mathbf{r}^*)] + 2\int_V \rho \mathbf{r} \times (\boldsymbol{\omega} \times \mathbf{v}_r)dV - 2\mathbf{r}^* \times \int_V \rho(\boldsymbol{\omega} \times \mathbf{v}_r)dV + \frac{{}^B d}{dt}\int_{V_0} \rho(\mathbf{r} \times \mathbf{v}_r)dV - \mathbf{r}^* \times \frac{{}^B d}{dt}\int_{V_0} \rho\mathbf{v}_r dV + \int_{S_0} \rho(\mathbf{r} \times \mathbf{v}_r)(\mathbf{v}_r \cdot \mathbf{n})dS - r^* \times \int_{S_0} \rho\mathbf{v}_r(\mathbf{v}_r \cdot \mathbf{n})dS \quad (19)$$

or

$$\mathbf{M}^* = \mathbf{I}^* \cdot \boldsymbol{\alpha} + \boldsymbol{\omega} \times \mathbf{I}^* \cdot \boldsymbol{\omega} + 2\int_V \rho\mathbf{p} \times (\boldsymbol{\omega} \times \mathbf{v}_r)dV + \frac{{}^B d}{dt}\int_{V_0} \rho\mathbf{p} \times \mathbf{v}_r dV + \int_{S_0} \rho[\mathbf{p} \times \mathbf{v}_r(\mathbf{v}_r \cdot \mathbf{n})]dS. \quad (20)$$

The position vector $\mathbf{p}$ replaces $\mathbf{r}$, and is measured from the system's instantaneous mass center. Furthermore, the moment $\mathbf{M}^*$ and inertia dyadic $\mathbf{I}^*$ are both now taken about the mass center of the system instead of the point O. The same process converts Eq. (13) to

$$\mathbf{M}^* = \mathbf{I}^* \cdot \boldsymbol{\alpha} + \boldsymbol{\omega} \times \mathbf{I}^* \cdot \boldsymbol{\omega} + \left(\frac{{}^B d}{dt}\mathbf{I}^*\right) \cdot \boldsymbol{\omega} + \int_V \rho\boldsymbol{\omega} \times (\mathbf{p} \times \mathbf{v}_r)dV + \frac{{}^B d}{dt}\int_{V_0} \rho\mathbf{p} \times \mathbf{v}_r dV + \int_{S_0} \rho[\mathbf{p} \times \mathbf{v}_r(\mathbf{v}_r \cdot \mathbf{n})]dS \quad (21)$$

and Eq. (14) to

$$\mathbf{M}^* = \mathbf{I}_0^* \cdot \boldsymbol{\alpha} + \boldsymbol{\omega} \times \mathbf{I}_0^* \cdot \boldsymbol{\omega} + \left(\frac{{}^B d}{dt}\mathbf{I}_0^*\right) \cdot \boldsymbol{\omega} + \int_{S_0} \rho[\mathbf{p} \times (\boldsymbol{\omega} \times \mathbf{p})](\mathbf{v}_r \cdot \mathbf{n})dS + \int_V \rho\boldsymbol{\omega} \times (\mathbf{p} \times \mathbf{v}_r)dV + \frac{{}^B d}{dt}\int_{V_0} \rho(\mathbf{p} \times \mathbf{v}_r)dV + \int_{S_0} \rho[\mathbf{p} \times \mathbf{v}_r(\mathbf{v}_r \cdot \mathbf{n})]dS. \quad (22)$$

Note that $\mathbf{I}_0^*$ is the central inertia dyadic associated with the control volume V_0.

A comparison of Eqs. (20) and (22) indicates, at first glance, that both equations require a complete knowledge of the flow pattern within the fluid phase of the system. Since this is a difficult task in most cases, the evaluation of the several volume integrals is rendered next to impossible. However, for many variable mass systems, it is reasonable to assume that the motion of the fluid phase relative to the solid phase has axial symmetry. In such situations

$$\int_V \rho\mathbf{p} \times \mathbf{v}_r dV = \int_{V_0} \rho\mathbf{p} \times \mathbf{v}_r dV \equiv 0. \quad (23)$$

This is so because, for every particle P of the system with position vector $\mathbf{p}$ and relative velocity $\mathbf{v}_r$, there exists another particle P' of position vector $\mathbf{p}'$ and relative velocity $\mathbf{v}_r'$ such that the vectors $\mathbf{p} \times \mathbf{v}_r$ and $\mathbf{p}' \times \mathbf{v}_r'$ have the same magnitude but opposite directions. And, since axisymmetry also implies that the immediate neighborhoods of P and P' have the same mass density, Eq. (23) follows. This equation immediately leads to

$$\frac{{}^B d}{dt}\int_{V_0} \rho\mathbf{p} \times \mathbf{v}_r dV = 0 \quad (24)$$

and also to

$$\int_V \rho\boldsymbol{\omega} \times (\mathbf{p} \times \mathbf{v}_r)dV = \boldsymbol{\omega} \times \int_V \rho(\mathbf{p} \times \mathbf{v}_r)dV = 0 \quad (25)$$

and

$$\int_{S_0} \rho[\mathbf{p} \times \mathbf{v}_r(\mathbf{v}_r \cdot \mathbf{n})]dS = 0. \quad (26)$$

Hence, the last two terms of Eq. (20) and the last three terms of Eq. (22) vanish. This gives Eq. (22) a tremendous advantage over Eq. (20) because most of the troublesome terms have now dropped out of Eq. (22). The only term in this equation that now contains $\mathbf{v}_r$ is a surface integral over S_0. Since $\mathbf{v}_r \cdot \mathbf{n}$ is zero everywhere except at the nozzle exit plane (in the case of rockets), where it can be approximated rela-

Downloaded 03 May 2010 to 171.66.16.20. Redistribution subject to ASME license or copyright; see http://www.asme.org/terms/Terms_Use.cfm

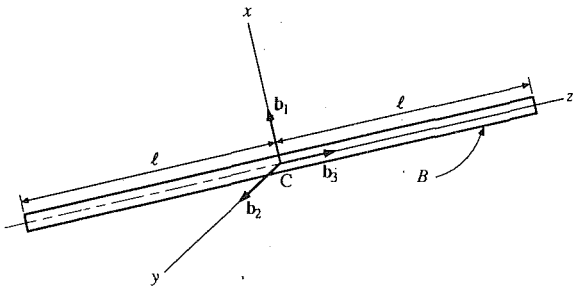


Fig. 4 Burning rod

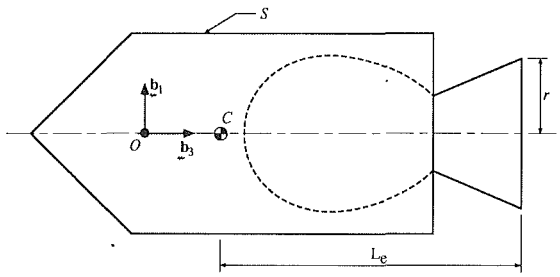


Fig. 5 Spinning rocket

tively well, the surface integral can in fact be evaluated easily. On the other hand, the third term on the right-hand side of Eq. (20) does not vanish under axisymmetric flow conditions, and it requires that $\mathbf{v}_r$ be known everywhere within B. Because several previous investigators have used this form of the moment equation, they have been forced to resort to drastic simplifying assumptions, such as axial flows, in order to make further progress with this equation. Equation (22) is, therefore, clearly superior to Eq. (20) for practical applications.

Applications

The dynamics of a given variable mass system can now be studied with the aid of the various equations developed above. As an illustration, the attitude motion of a burning rod and that of a spinning rocket will now be analyzed with the aid of some of these equations.

Burning Rod. Figure 4 shows a cylindrical rod B of length, $2l$, cross-sectional radius $r(r << l)$, and density ρ, with ρ assumed to have the same value everywhere within the rod. The rod burns in such a way that its external dimensions remain unchanged but its density varies with time. This is somewhat analogous to what happens in a rocket motor, where the external dimensions generally remain unchanged but the material inside the motor casing becomes less dense with time due to combustion. In the case of the rod, we make the additional assumption that the density changes in the same manner everywhere within the rod. Thus, ρ is a function of time, but not of position. The x, y, z axes are arranged as shown in Fig. 4, with the z-axis parallel to the axis of the cylinder, and x and y axes in so-called transverse directions. The origin is attached to point C, the mass center of the rod, and the unit vectors $\mathbf{b}_1$, $\mathbf{b}_2$, $\mathbf{b}_3$ are fixed in B and aligned with the axes as shown.

If, at any given instant, the inertial angular velocity of the rod is

$$\boldsymbol{\omega} = \omega_1\mathbf{b}_1 + \omega_2\mathbf{b}_2 + \omega_3\mathbf{b}_3, \tag{27}$$

then each of the terms on the right-hand side of Eq. (22) can be evaluated as follows:

$$\mathbf{I}^* \cdot \alpha = I\left(\dot{\omega}_1\mathbf{b}_1 + \dot{\omega}_2\mathbf{b}_2\right) + J\dot{\omega}_3\mathbf{b}_3 \tag{28}$$

where I is the central transverse moment of inertia of the rod while J is the axial moment of inertia ($J << I$).

$$\boldsymbol{\omega} \times \mathbf{I}^* \cdot \boldsymbol{\omega} \cong -I(\omega_2\mathbf{b}_1 - \omega_1\mathbf{b}_2)\omega_3 \tag{29}$$

$$\dot{\mathbf{I}}^* \cdot \boldsymbol{\omega} = \dot{I}(\omega_1\mathbf{b}_1 + \omega_2\mathbf{b}_2) + \dot{J} + \omega_3\mathbf{b}_3 \tag{30}$$

Assuming that the products of combustion escape through the ends of the rod, and that $\mathbf{v}_r$ is constant over the ends,

$$\int_{S_0} \rho[\mathbf{p} \times (\boldsymbol{\omega} \times \mathbf{p})](\mathbf{v}_r \cdot \mathbf{n})dS \cong$$

$$-\dot{m}\left[l^2(\omega_1\mathbf{b}_1 + \omega_2\mathbf{b}_2) + 0.5r^2\omega_3\mathbf{b}_3\right]. \tag{31}$$

The other terms vanish because of the axisymmetric nature of the problem. Hence, the equations of attitude motion in a torque-free environment become

$$\dot{\omega}_1 - \omega_2\omega_3 + \delta\omega_1 = 0 \tag{32}$$

$$\dot{\omega}_2 + \omega_1\omega_3 + \delta\omega_2 = 0 \tag{33}$$

and

$$\dot{\omega}_3 + \left[\left(\dot{J} - 0.5\dot{m}r^2\right)/J\right]\omega_3 = 0 \tag{34}$$

where

$$\delta = \left(\dot{I} - \dot{m}l^2\right)/I. \tag{35}$$

Since

$$\dot{J} = 0.5\dot{m}r^2, \tag{36}$$

Eq. (34) leads to

$$\omega_3 = \text{const.} = \Omega. \tag{37}$$

By defining the complex angular velocity

$$\omega_c = \omega_1 + i\omega_2 \tag{38}$$

where

$$i = \sqrt{-1}, \tag{39}$$

Eqs. (32) and (33) can be combined into

$$\dot{\omega}_c + [i\Omega + \delta]\omega_c = 0. \tag{40}$$

Note that a nonburning rigid rod has the same equation, with $\delta = 0$. For a burning rod,

$$\delta = -2\dot{m}/m. \tag{41}$$

Since δ cannot be made equal to zero unless $\dot{m}$ is zero, the attitude behavior of a burning rod will always be different from that of a nonburning rod. Equations (40) and (41) yield

$$\omega_c/\omega_c(0) = [m/m(0)]^2\exp(-i\Omega t). \tag{42}$$

Thus, the burning rod under consideration maintains a stable coning motion, with the cone angle decreasing as the burn progresses.

Spinning Rocket. As a second example, we now consider a solid rocket motor and its payload, shown schematically in Fig. 5. It is assumed that the system is axisymmetric with axisymmetric gas flow inside the combustion chamber. Once more, Eq. (22) is invoked to examine the attitude behavior of such a system in a force-free environment. Because of the gas flow pattern assumed, the last three terms of Eq. (22) vanish. The evaluation of the other terms is straightforward, except for the surface integral, whose determination requires a knowledge of the flow field at the exit plane. Assuming that $\mathbf{v}_r \cdot \mathbf{n}$ is constant over the exit plane, the equations of attitude motion reduce to

$$I\dot{\omega}_1 - (I - J)\omega_2\omega_3 + \left[\dot{I} - \dot{m}\left(L_e^2 + 0.25r^2\right)\right]\omega_1 = 0 \tag{43}$$

$$I\dot{\omega}_2 + (I - J)\omega_1\omega_3 + \left[\dot{I} - \dot{m}\left(L_e^2 + 0.25r^2\right)\right]\omega_2 = 0 \tag{44}$$

and

$$J\dot{\omega}_3 + \left(\dot{J} - 0.5\dot{m}r^2\right)\omega_3 = 0 \tag{45}$$

Downloaded 03 May 2010 to 171.66.16.20. Redistribution subject to ASME license or copyright; see http://www.asme.org/terms/Terms_Use.cfm

where I is the transverse central moment of inertia of the system, J is the axial moment of inertia, and ω_i $(i = 1, 2, 3)$ are the components of the inertial angular velocity of the rocket. Equation (45) is decoupled from the other two, and can be solved to yield

$$\omega_3 = \omega_3(0)\exp\left\{-\int_0^t\left[\left(\dot{J} - 0.5\dot{m}r^2\right)/J\right]dt\right\}. \quad (46)$$

Unlike the case of a rigid axisymmetric body, the spin rate of a variable mass rocket can vary with time.

To study the transverse behavior, the complex transverse angular speed is introduced once more:

$$\omega_c = \omega_1 + i\omega_2. \quad (47)$$

Equations (43) and (44) are combined into

$$\dot{\omega}_c/\omega_c = -\left[\dot{I} - \dot{m}\left(L_e^2 + 0.25r^2\right)/I\right] - i(I - J)\omega_3/I, \quad (48)$$

the solution of which yields

$$\omega_c = \omega_c(0)\exp\left\{-\int_0^t\left(\left[\dot{I} - \dot{m}\left(L_e^2 + 0.25r^2\right)\right]/I\right)dt\right\} \cdot \exp\left\{i\int_0^t\left[(I - J)/I\right]\omega_3 dt\right\}. \quad (49)$$

Thus, the transverse angular velocity oscillates at a variable frequency, and the shape of its envelope is determined by the quantity

$$Q = \int_0^t\left(\left[\dot{I} - \dot{m}\left(L_e^2 + 0.25r^2\right)\right]/I\right)dt. \quad (50)$$

If Q is positive, oscillations decay with time, but, if Q is negative, oscillations grow and the system is unstable. Note that, unlike the case of the burning rod, instability is not ruled out in this case. Since Q is a function of system mass properties and combustion chamber geometry, these parameters are seen to be crucial to attitude stability.

Conclusion

The complete equations of motion of variable mass systems can be derived by instantaneous application of the principles of mechanics to matter contained in judiciously defined enclosures and accounting for mass variation within such enclosures through the use of Reynolds Transport Theorem. It is possible to obtain special versions of the equations of attitude motion which make closed form solutions possible even for relatively complex models. Application of these equations to a model of a solid rocket motor revealed the possibility of unstable lateral motion for such systems.

Acknowledgment

This material is based upon work supported by the National Science Foundation under Award No. MSS-9021549.

References

Belknap, S. B., 1970, "Variable Mass Dynamics for Engineering Systems," Ph.D Dissertation, UCLA.

Chengyao, D., 1989, "Dynamics and Applications of Nonholonomic Variable Mass Systems," Proceedings of the International Conference on Applied Mechanics, Beijing, China, Aug.

Eke, F. O., 1991, "Angular Momentum and Multibody Dynamics," paper No. AAS 91-110, AAS/AIAA Space Flight Mechanics Meeting, Houston, TX, Feb.

Eke, F. O., 1982, "Star 48 Coning Anomaly," JPL Internal Document No. 343-82-989, Oct.

Fengxiang, M., 1989, "Time-Integral Theorems for Variable Mass Nonholonomic Systems," Proceedings of the International Conference on Applied Mechanics, Beijing, China, Aug.

Ge, Z. M., 1984, "Equations of Motion of Nonlinear Nonholonomic Variable Mass System with Applications," ASME Journal of Applied Mechanics, Vol. 51.

Hammidi, I. B., 1961, "The Attitude of a Variable Mass System," Ph.D Dissertation, UCLA, June.

Leitman, G., 1957, "On the Equations of Rocket Motion," *Journal of British Interplanetary Society*, Vol. 16.

Meirovitch, L., 1970, "General Motion of a Variable Mass Flexible Rocket with Internal Flow," *Journal of Spacecraft and Rockets*, Vol. 7, No. 2, pp. 186–195.

Rosser, J. B., Newton, R. R., and Cross, G. L., 1947, *Mathematical Theory of Rocket Flight*, McGraw-Hill, New York.

Shames, I. H., 1982, *Mechanics of Fluids*, 2nd ed., McGraw-Hill, New York.

Thomson, W. T., 1966, "Equations of Motion for the Variable Mass System," *AIAA Journal*, Vol. 4. No. 4.

Thomson, W. T., 1963, *Introduction to Space Dynamics*, John Wiley and Sons, New York, 1963.

Thomas, W. T. and Reiter, G. S., 1965, "Jet Damping of a Solid Rocket: Theory and Flight Results," *AIAA Journal*, Vol. 3, No. 3.

Thorpe, J. F., 1962, "On the Momentum Theorem for a Continuous System of Variable Mass," American Journal of Physics, Vol. 30.

Downloaded 03 May 2010 to 171.66.16.20. Redistribution subject to ASME license or copyright; see http://www.asme.org/terms/Terms_Use.cfm

K. Suzuki
Professor.

G. Shikanai
Research Associate.

Faculty of Engineering,
Yamagata University,
Yonezawa, Japan

A. W. Leissa
Professor,
Department of Engineering Mechanics,
The Ohio State University,
Columbus, OH 43210
Fellow ASME

Free Vibrations of Laminated Composite Noncircular Thin Cylindrical Shells

An exact solution procedure is presented for solving free vibration problems for laminated composite noncircular cylindrical shells. Based on the classical lamination theory, strain energy and kinetic energy functionals are first derived for shells having arbitrary layer stacking sequences. These functionals are useful for a general analysis based upon energy principles. However, in the present work equations of motion and boundary conditions are obtained from the minimum conditions of the Lagrangian (Hamilton's principle). The equations of motion are solved exactly by using a power series expansion for symmetrically laminated, cross-ply shells having both ends freely supported. Frequencies are presented for a set of elliptical cylindrical shells, and the effects of various parameters upon them are discussed.

1 Introduction

Laminated composite shells are becoming increasingly used in structures such as spacecraft, automobiles, pressure vessels and many others because of their high specific strengths and specific stiffnesses. There exist a number of investigations dealing with the free vibrations of laminated composite shallow shells, circular cylindrical shells and conical shells (cf. the publications summarized in Qatu and Leissa (1991a, 1991b), Singh, Zhu and Mirza (1991), and Sivadas and Ganesan (1991).

But to the authors' knowledge, no published papers exist for laminated composite noncircular cylindrical shells, which are among the many important structural components. Furthermore, many works dealing with composite shell vibrations use approximate methods. Suzuki and Leissa (1985, 1986, 1990) analyzed exactly the free vibration characteristics of homogeneous isotropic noncircular cylindrical shells having both ends freely supported.

In the present study, free vibrations of laminated composite noncircular cylindrical shells are studied. Based on the classical lamination theory, equations of motion and boundary conditions are obtained from the minimum conditions of the Lagrangian. The equations of motion are solved exactly by using a power series expansion for symmetrically laminated cross-ply shells having both ends freely supported. The present method is demonstrated for a set of elliptical cylindrical shells, and numerical investigations are performed to show the effects of various parameters upon the frequencies.

2 Analysis

2.1 Stress and Strain Relationships. Let us consider the free vibrations of a laminated noncircular thin cylindrical shell composed of N laminae symmetric about the middle surface. For the shell to be considered here the center line of the cross-section is a smooth curve. The center line, which is the intersection of the middle surface of the shell with the plane $x' =$ const, is shown in Fig. 1. The length of the shell is $l = \mu r_0$ where r_0 is a representative radius, h is the thickness, and the curvature at any point along the center line is $1/\rho$. The coordinate x'-axis is taken along the generator of the middle

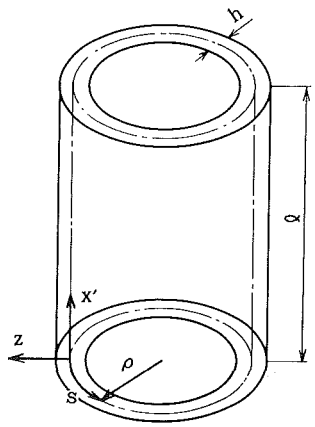


Fig. 1 Coordinates

Contributed by the Applied Mechanics Division of THE AMERICAN SOCIETY OF MECHANICAL ENGINEERS for presentation at the International Mechanical Engineering Congress and Exhibition, the Winter Annual Meeting of The ASME, Chicago, IL, Nov. 6-11, 1994.

Discussion on this paper should be addressed to the Technical Editor, Professor Lewis T. Wheeler, Department of Mechanical Engineering, University of Houston, Houston, TX 77204-4792, and will be accepted until four months after final publication of the paper itself in the ASME JOURNAL OF APPLIED MECHANICS.

Manuscript received by the ASME Applied Mechanics Division, Aug. 4, 1993; final revision, Nov. 17, 1993. Associate Technical Editor: J. N. Reddy.

Paper No. 94-WA/APM-11.

Copyright © 1994 by ASME
Downloaded 03 May 2010 to 171.66.16.20. Redistribution subject to ASME license or copyright; see http://www.asme.org/terms/Terms_Use.cfm

surface, the arc length s measured along the center line of the cross-section (the center line and the generator being orthogonal) and the z-axis in the direction normal to the middle surface (positive outward). Employ a nondimensional coordinate $x = x'/r_0$ and denote the displacements in the x', s, and z directions by $\bar{u}$, $\bar{v}$, and $\bar{w}$, respectively.

The transformation of variable

$$\frac{d\theta}{ds} = 1/\rho = (G/r_0)\Phi(\theta) \tag{1}$$

is now introduced, where θ is a variable that shows an angle between the tangent at the origin of s and the one at any point on the center line, G is a constant determined by the shape of the curve, and $\Phi(\theta)$ is a function of θ. The displacements $\bar{u}$, $\bar{v}$, and $\bar{w}$ are assumed in the form

$$\bar{u} = u(x, \theta, t) + \frac{z}{r_0}\Psi_x(x, \theta, t)$$

$$\bar{v} = v(x, \theta, t) + \frac{z}{r_0}\Psi_\theta(x, \theta, t)$$

$$\bar{w} = w(x, \theta, t) \tag{2}$$

where t denotes the time, and u, v, w, Ψ_x, and Ψ_θ are functions of x, θ, and t. The normal and the shearing strain expressions at any point are obtained from Love (1927):

$$\epsilon_{xx} = \frac{1}{r_0}\frac{\partial \bar{u}}{\partial x}, \quad \epsilon_{\theta\theta} = \frac{1}{\rho + z}\left(\frac{\partial \bar{v}}{\partial \theta} + \bar{w}\right),$$

$$\epsilon_{zz} = \frac{\partial \bar{w}}{\partial z}, \quad \epsilon_{x\theta} = \frac{1}{r_0}\frac{\partial \bar{v}}{\partial x} + \frac{1}{\rho + z}\frac{\partial \bar{u}}{\partial \theta},$$

$$\epsilon_{xz} = \frac{\partial \bar{u}}{\partial z} + \frac{1}{r_0}\frac{\partial \bar{w}}{x}, \quad \epsilon_{\theta z} = \frac{\partial \bar{v}}{\partial z} + \frac{1}{\rho + z}\left(\frac{\partial \bar{w}}{\partial \theta} - \bar{v}\right). \tag{3}$$

The present development is limited to shells sufficiently thin that the effects of shear deformation and rotary inertia may be neglected. Setting ϵ_{xz} and $\epsilon_{\theta z}$ in Eq. (3) equal to zero, one finds

$$\Psi_x = -\frac{\partial w}{\partial x}, \quad \Psi_\theta = G\Phi\left(-\frac{\partial w}{\partial \theta} + v\right). \tag{4}$$

Substituting Eqs. (2) and (4) into ϵ_{xx}, $\epsilon_{\theta\theta}$, ϵ_{zz} and $\epsilon_{x\theta}$ in Eq. (3) yields

$$\epsilon_{xx} = \frac{1}{r_0}\left(\frac{\partial u}{\partial x} - \frac{z}{r_0}\frac{\partial^2 w}{\partial x^2}\right)$$

$$\epsilon_{\theta\theta} = \frac{1}{\rho + z}\left[\frac{\partial v}{\partial \theta} + w - \frac{z}{r_0}\frac{\partial}{\partial \theta}\left\{G\Phi\left(\frac{\partial w}{\partial \theta} - v\right)\right\}\right]$$

$$\epsilon_{zz} = 0$$

$$\epsilon_{x\theta} = \left[\frac{1}{\rho + z}\left(\frac{\partial_{11}}{\partial \theta} - \frac{z}{r_0}\frac{\partial^2 w}{\partial x \partial \theta}\right) + \frac{1}{r_0}\left\{\frac{\partial v}{\partial x} - \frac{z}{r_0}G\Phi\left(\frac{\partial^2 w}{\partial x \partial \theta} - \frac{\partial v}{\partial x}\right)\right\}\right]. \tag{5}$$

Consider now that the materials of each lamina consist of parallel, continuous fibers of one material bonded in a matrix material. Each lamina may be regarded on a macroscopic scale as being homogeneous and orthotropic. The stress-strain relation for the kth lamina may be written as (cf. Whitney, 1987; Vinson and Sierakowski, 1987)

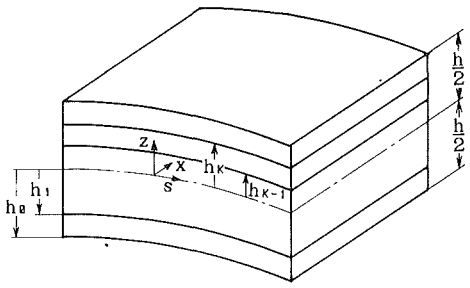


Fig. 2 Cross-sectional view of shell

$$\begin{bmatrix} \sigma_{xx} \\ \sigma_{\theta\theta} \\ \sigma_{x\theta} \end{bmatrix}_k = \begin{bmatrix} \bar{Q}_{11} & \bar{Q}_{12} & \bar{Q}_{16} \\ \bar{Q}_{12} & \bar{Q}_{22} & \bar{Q}_{26} \\ \bar{Q}_{16} & \bar{Q}_{26} & \bar{Q}_{66} \end{bmatrix} \begin{bmatrix} \epsilon_{xx} \\ \epsilon_{\theta\theta} \\ \epsilon_{x\theta} \end{bmatrix}_k \tag{6}$$

where σ_{xx} and $\sigma_{\theta\theta}$ are normal stress components, and $\sigma_{x\theta}$ is a shear stress component. The constants $\bar{Q}_{ij}$ are the elastic stiffness coefficients for the material which are given in Appendix A.

2.2 Lagrangian Formulation for Vibration. The strain energy for the kth lamina is

$$U_k = \frac{1}{2}\int_{h_{k-1}}^{h_k}\int_{\theta_1}^{\theta_2}\int_0^{l/r_0}[\sigma_{xx}\epsilon_{xx} + \sigma_{\theta\theta}\epsilon_{\theta\theta} + \sigma_{x\theta}\epsilon_{x\theta}]r_0(\rho + z)dxd\theta dz \tag{7}$$

where h_k and h_{k-1} are the distances measured from the middle surface to the outer and inner surfaces of the kth laminate, respectively, as shown in Fig. 2. The kinetic energy for each lamina is

$$T_k = \frac{1}{2}\int\int\int \rho^{(k)}\left[\left(\frac{\partial \bar{u}}{\partial t}\right)^2 + \left(\frac{\partial \bar{v}}{\partial t}\right)^2 + \left(\frac{\partial \bar{w}}{\partial t}\right)^2\right]r_0(\rho + z)dxd\theta dz \tag{8}$$

where $\rho^{(k)}$ is the density of the kth lamina per unit volume.

Now define the Lagrangian at any instant of time as follows:

$$L_k = T_k - U_k. \tag{9}$$

The Lagrangian of the entire shell is then found to be

$$L = \sum_{k=1}^{N} L_k \tag{10}$$

where N is the total number of laminae. Substituting Eqs. (2), (5), and (6) into Eqs. (7)–(10) and using the following relations,

$$\int_{h_{k-1}}^{h_k}\frac{1}{\rho + z}dz \doteqdot \frac{H_1}{\rho} - \frac{H_2}{\rho^2} + \frac{H_3}{\rho^3},$$

$$\int_{h_{k-1}}^{h_k}\frac{z}{\rho + z}dz \doteqdot \frac{H_2}{\rho} - \frac{H_3}{\rho^2},$$

$$\int_{h_{k-1}}^{h_k}\frac{z^2}{\rho + z}dz \doteqdot \frac{H_3}{\rho},$$

$$\int_{h_{k-1}}^{h_k}\frac{z^3}{\rho + z}dz \doteqdot \int_{h_{k-1}}^{h_k}\frac{z^4}{\rho + z}dz \doteqdot 0$$

$$H_1 = h_k - h_{k-1}, \quad H_2 = \frac{1}{2}(h_k^2 - h_{k-1}^2),$$

$$H_3 = \frac{1}{3}(h_k^3 - h_{k-1}^3), \quad H_4 = \frac{1}{4}(h_k^4 - h_{k-1}^4), \tag{11}$$

Downloaded 03 May 2010 to 171.66.16.20. Redistribution subject to ASME license or copyright; see http://www.asme.org/terms/Terms_Use.cfm

Eq. (10) becomes

$$-L\Big/\frac{E_0h^3}{2Gr_0^2}=\int\int\Bigg[-\lambda^4\left\{\left(\frac{\partial u}{\partial t}\right)^2+\left(\frac{\partial v}{\partial t}\right)^2+\left(\frac{\partial w}{\partial t}\right)^2\right\}\left(\overline{\rho_1}+\frac{1}{\beta}\,\overline{\rho_2}G\Phi\right)$$
$$+\beta^2\Bigg[A_{11}\left(\frac{\partial u}{\partial x}\right)^2+2A_{12}(G\Phi)\,\frac{\partial u}{\partial x}\left(\frac{\partial v}{\partial\theta}+w\right)$$
$$+A_{22}(G\Phi)^2\left(\frac{\partial v}{\partial\theta}+w\right)^2+A_{66}\left(G\Phi\,\frac{\partial u}{\partial\theta}+\frac{\partial v}{\partial x}\right)^2\Bigg]$$
$$+2\beta^2\Bigg[A_{16}\left(G\Phi\,\frac{\partial u}{\partial x}\,\frac{\partial u}{\partial\theta}+\frac{\partial u}{\partial x}\,\frac{\partial v}{\partial x}\right)+A_{26}\Bigg\{(G\Phi)^2\,\frac{\partial u}{\partial\theta}\left(\frac{\partial v}{\partial\theta}+w\right)$$
$$+G\Phi\,\frac{\partial v}{\partial x}\left(\frac{\partial v}{\partial\theta}+w\right)\Bigg\}\Bigg]$$
$$+\beta\Bigg[B_{11}\left\{G\Phi\left(\frac{\partial u}{\partial x}\right)^2-2\,\frac{\partial u}{\partial x}\,\frac{\partial^2 w}{\partial x^2}\right\}-B_{22}G^2\Phi^2\left(G\Phi\left(\frac{\partial v}{\partial\theta}+w\right)^2\right.$$
$$\left.+2\,\frac{\partial}{\partial\theta}\left(G\Phi\left(\frac{\partial w}{\partial\theta}-v\right)\right)\left(\frac{\partial v}{\partial\theta}+w\right)\right\}$$
$$+B_{66}\Bigg\{3G\Phi\left(\frac{\partial v}{\partial x}\right)^2-(G\Phi)^3\left(\frac{\partial u}{\partial\theta}\right)^2$$
$$+4G^2\Phi^2\,\frac{\partial u}{\partial\theta}\,\frac{\partial^2 w}{\partial x\partial\theta}-4G\Phi\,\frac{\partial v}{\partial x}\,\frac{\partial^2 w}{\partial x\partial\theta}+2G^2\Phi^2\,\frac{\partial u}{\partial\theta}\,\frac{\partial v}{\partial x}\Bigg\}\Bigg]$$
$$+2\beta\Bigg[-B_{12}G\Phi\left\{\frac{\partial u}{\partial x}\,\frac{\partial}{\partial\theta}\left(G\Phi\left(\frac{\partial w}{\partial\theta}-v\right)\right)+\frac{\partial^2 w}{\partial x^2}\left(\frac{\partial v}{\partial\theta}+w\right)\right\}$$
$$+B_{16}\Bigg[G\Phi\left\{2\,\frac{\partial u}{\partial x}\left(\frac{\partial v}{\partial x}-\frac{\partial^2 w}{\partial x\partial\theta}\right)-\frac{\partial u}{\partial\theta}\,\frac{\partial^2 w}{\partial x^2}\right\}-\frac{\partial v}{\partial x}\,\frac{\partial^2 w}{\partial x^2}\Bigg]$$
$$-B_{26}\Bigg[G^2\Phi^2\left(\frac{\partial v}{\partial\theta}+w\right)\left(G\Phi\,\frac{\partial u}{\partial\theta}+2\,\frac{\partial^2 w}{\partial x\partial\theta}-\frac{\partial v}{\partial x}\right)$$
$$+G\Phi\left(\frac{\partial v}{\partial x}+G\Phi\,\frac{\partial u}{\partial\theta}\right)\frac{\partial}{\partial\theta}\left\{G\Phi\left(\frac{\partial w}{\partial\theta}-v\right)\right\}\Bigg]\Bigg]$$
$$+D_{11}\Bigg[\left(\frac{\partial^2 w}{\partial x^2}\right)^2-2G\Phi\,\frac{\partial u}{\partial x}\,\frac{\partial^2 w}{\partial x^2}\Bigg]$$
$$+D_{22}G^2\Phi^2\Bigg[G\Phi\left(\frac{\partial v}{\partial\theta}+w\right)+\frac{\partial}{\partial\theta}\left\{G\Phi\left(\frac{\partial w}{\partial\theta}-v\right)\right\}\Bigg]^2$$
$$+D_{66}G^2\Phi^2\Bigg[3\left(\frac{\partial^2 w}{\partial x\partial\theta}-\frac{\partial v}{\partial x}\right)^2+\left(\frac{\partial^2 w}{\partial x\partial\theta}+G\Phi\,\frac{\partial u}{\partial\theta}\right)^2\Bigg]$$
$$+2D_{12}(G\Phi)\,\frac{\partial^2 w}{\partial x^2}\,\frac{\partial}{\partial\theta}\left\{G\Phi\left(\frac{\partial w}{\partial\theta}-v\right)\right\}$$
$$+2D_{16}G\Phi\left(\frac{\partial^2 w}{\partial x\partial\theta}-\frac{\partial v}{\partial x}\right)\left(2\,\frac{\partial^2 w}{\partial x^2}-G\Phi\,\frac{\partial u}{\partial x}\right)$$
$$+2D_{26}G^2\Phi^2\Bigg[\frac{\partial}{\partial\theta}\left\{G\Phi\left(\frac{\partial w}{\partial\theta}-v\right)\right\}\left(G\Phi\,\frac{\partial u}{\partial\theta}-\frac{\partial v}{\partial x}+2\,\frac{\partial^2 w}{\partial x\partial\theta}\right)$$
$$+G\Phi\left(\frac{\partial v}{\partial\theta}+w\right)\left(G\Phi\,\frac{\partial u}{\partial\theta}+\frac{\partial^2 w}{\partial x\partial\theta}\right)\Bigg]\Bigg]\left(\frac{1}{\Phi}\right)dxd\theta \quad (12)$$

where h is the total shell thickness, ρ_0 and E_0 are a representative material density and elastic modulus, respectively, and

$$\lambda^4=\frac{\rho_0 r_0^4}{E_0h^2},\quad \beta^2=\frac{r_0^2}{h^2},\quad \overline{\rho_1}=\sum_{K=1}^{N}\frac{\rho^{(K)}}{\rho_0}\,(h_K-h_{k-1})/h,$$

$$\overline{\rho_2}=\sum_{K=1}^{N}\frac{\rho^{(K)}}{\rho_0}\,\frac{1}{2}\,(h_K^2-h_{K-1}^2)/h^2,$$

$$A_{ij}=\sum_{K=1}^{N}\frac{\overline{Q}_{ij}}{E_0}\,(h_K-h_{K-1})/h,$$

$$B_{ij}=\sum_{K=1}^{N}\frac{\overline{Q}_{ij}}{E_0}\,\frac{1}{2}\,(h_K^2-h_{K-1}^2)/h^2,$$

$$D_{ij}=\sum_{K=1}^{N}\frac{\overline{Q}_{ij}}{E_0}\,\frac{1}{3}\,(h_K^3-h_{K-1}^3)/h^3. \quad (13)$$

For a cross-ply laminate of orthotropic laminae oriented at either 0 deg or 90 deg to the laminate axes, A_{16}, A_{26}, B_{16}, B_{26}, D_{16}, and D_{26} in Eq. (12) are zero. For shells which are laminated symmetrically with respect to the midsurfaces, $B_{ii}=0$.

2.3 Equations of Motion and Boundary Conditions. Applying Hamilton's principle $\delta\int_{t_1}^{t_2}L\,dt=0$, one obtains

$$-\int_{t_1}^{t_2}\int_{\theta_1}^{\theta_2}[E_1\delta u+E_2\delta v+E_3\delta w]dxd\theta dt$$
$$+\int_{t_1}^{t_2}\int_{\theta_1}^{\theta_2}\left[T_1\delta u+T_2\delta v+T_3\delta w+M_1\delta\left(\frac{\partial w}{\partial x}\right)\right]\Bigg|_{x=0}^{x=\mu}d\theta dt$$
$$+\int_{t_1}^{t_2}\int_{0_1}^{\mu}\left[T_4\delta u+T_5\delta v+T_6\delta w+M_2\delta\left(\frac{\partial w}{\partial\theta}\right)\right]\Bigg|_{\theta=\theta_1}^{\theta=\theta_2}dxdt$$
$$+\int_{t_1}^{t_2}[T\delta w]\Bigg|_{x=0\ \theta=\theta_1}^{x=\mu\ \theta=\theta_2}dt-\int_{\theta_1}^{\theta_2}\int_0^{\mu}\lambda^2\left(\overline{\rho_1}+\frac{1}{\beta}\,\overline{\rho_2}G\Phi\right)$$
$$\times\left[\frac{\partial u}{\partial t}\,\delta u+\frac{\partial v}{\partial t}\,\delta v+\frac{\partial w}{\partial t}\,\delta w\right]\Bigg|_{t=t_1}^{t=t_2}\left(\frac{1}{\Phi}\right)dxd\theta dt=0 \quad (14)$$

where

$$E_1=-\lambda^4\,\frac{\partial^2(u/\Phi)}{\partial t^2}\left(\overline{\rho_1}+\frac{1}{\beta}\,\overline{\rho_2}G\Phi\right)+\beta^2\Bigg[A_{11}\,\frac{\partial^2}{\partial x^2}\,(u/\Phi)$$
$$+G(A_{12}+A_{66})\,\frac{\partial^2 v}{\partial x\partial\theta}+GA_{12}\,\frac{\partial w}{\partial x}+A_{66}G^2\,\frac{\partial}{\partial\theta}\left(\Phi\,\frac{\partial u}{\partial\theta}\right)$$
$$+A_{16}\left(2G\,\frac{\partial^2 u}{\partial x\partial\theta}+\frac{1}{\Phi}\,\frac{\partial^2 v}{\partial x^2}\right)+A_{26}G^2\,\frac{\partial}{\partial\theta}\left\{\Phi\left(\frac{\partial v}{\partial\theta}+w\right)\right\}\Bigg]$$
$$+\beta\Bigg[B_{11}\left(G\,\frac{\partial^2 u}{\partial x^2}-\frac{1}{\Phi}\,\frac{\partial^3 w}{\partial x^3}\right)+B_{12}G^2\,\frac{\partial}{\partial\theta}\left\{\Phi\left(\frac{\partial v}{\partial x}-\frac{\partial^2 w}{\partial x\partial\theta}\right)\right\}$$
$$+B_{16}G\left(2\,\frac{\partial^2 v}{\partial x^2}-3\,\frac{\partial^3 w}{\partial x^2\partial\theta}\right)$$
$$-B_{26}G^3\,\frac{\partial}{\partial\theta}\left\{\Phi^2\left(\frac{\partial v}{\partial\theta}+w\right)+\Phi\,\frac{\partial}{\partial\theta}\left(\Phi\left(\frac{\partial w}{\partial\theta}-v\right)\right)\right\}$$
$$-B_{66}G^2\,\frac{\partial}{\partial\theta}\left\{\Phi\left(G\Phi\,\frac{\partial u}{\partial\theta}+2\,\frac{\partial^2 w}{\partial x\partial\theta}-\frac{\partial v}{\partial x}\right)\right\}\Bigg]$$
$$-D_{11}G\,\frac{\partial^3 w}{\partial x^3}+D_{16}G^2\Phi\left(\frac{\partial^2 v}{\partial x^2}-\frac{\partial^3 w}{\partial x^2\partial\theta}\right)$$
$$+D_{26}G^4\,\frac{\partial}{\partial\theta}\Bigg[\Phi^2\,\frac{\partial}{\partial\theta}\left\{\Phi\left(\frac{\partial w}{\partial\theta}-v\right)\right\}+\Phi^3\left(\frac{\partial v}{\partial\theta}+w\right)\Bigg]$$
$$+D_{66}G^3\,\frac{\partial}{\partial\theta}\left\{\Phi^2\left(G\Phi\,\frac{\partial u}{\partial\theta}+\frac{\partial^2 w}{\partial x\partial\theta}\right)\right\}$$

$$\Phi E_2=-\lambda^4\left(\overline{\rho_1}+\frac{1}{\beta}\,\overline{\rho_2}G\Phi\right)\frac{\partial^2 v}{\partial t^2}+\beta^2\Bigg[G\Phi A_{12}\,\frac{\partial^2 u}{\partial x\partial\theta}+A_{16}\,\frac{\partial^2 u}{\partial x^2}$$

Downloaded 03 May 2010 to 171.66.16.20. Redistribution subject to ASME license or copyright; see http://www.asme.org/terms/Terms_Use.cfm

$$+A_{22}G^2\Phi\frac{\partial}{\partial\theta}\left\{\Phi\left(\frac{\partial v}{\partial\theta}+w\right)\right\}+A_{26}G\Phi\left\{G\frac{\partial}{\partial\theta}\left(\Phi\frac{\partial u}{\partial\theta}\right)+2\frac{\partial^2 v}{\partial x\partial\theta}+\frac{\partial w}{\partial x}\right\}+A_{66}\left(G\Phi\frac{\partial^2 u}{\partial x\partial\theta}+\frac{\partial^2 v}{\partial x^2}\right)\Bigg]$$

$$+\beta\Bigg[B_{12}G\Phi\left(G\Phi\frac{\partial^2 u}{\partial x\partial\theta}-\frac{\partial^3 w}{\partial x^2\partial\theta}\right)+B_{16}\left(2G\Phi\frac{\partial^2 u}{\partial x^2}-\frac{\partial^3 w}{\partial x^3}\right)-B_{22}G^3\Phi\Bigg[\Phi\frac{\partial\Phi}{\partial\theta}\left(\frac{\partial v}{\partial\theta}+w\right)+\frac{\partial}{\partial\theta}\left\{\Phi^2\left(\frac{\partial^2 w}{\partial\theta^2}-\frac{\partial v}{\partial\theta}\right)+\Phi\frac{\partial\Phi}{\partial\theta}\left(\frac{\partial w}{\partial\theta}-v\right)\right\}\Bigg]+B_{26}G^2\Bigg[\Phi^2\left(\frac{\partial^2 v}{\partial x\partial\theta}+\frac{\partial w}{\partial x}\right)-3\Phi\frac{\partial}{\partial\theta}\left\{\Phi\left(\frac{\partial^2 w}{\partial x\partial\theta}-\frac{\partial v}{\partial x}\right)\right\}-\Phi\frac{\partial\Phi}{\partial\theta}\left(\frac{\partial v}{\partial x}+G\Phi\frac{\partial u}{\partial\theta}\right)\Bigg]+B_{26}G\Phi\left[3\frac{\partial^2 v}{\partial x^2}-2\frac{\partial^3 w}{\partial x\partial\theta}+G\Phi\frac{\partial^2 u}{\partial x\partial\theta}\right]\Bigg]$$

$$-D_{12}G^2\Phi^2\frac{\partial^3 w}{\partial x^2\partial\theta}+D_{16}G\Phi\left(G\Phi\frac{\partial^2 u}{\partial x^2}-2\frac{\partial^3 w}{\partial x^3}\right)+D_{22}G^4\Phi^2\frac{\partial\Phi}{\partial\theta}\left[\frac{\partial\Phi}{\partial\theta}\left(\frac{\partial w}{\partial\theta}-v\right)+\Phi\left(w+\frac{\partial^2 w}{\partial\theta^2}\right)\right]$$

$$+D_{26}G^3\Phi\left[\Phi\frac{\partial\Phi}{\partial\theta}\left(G\Phi\frac{\partial u}{\partial\theta}+2\frac{\partial v}{\partial x}-\frac{\partial^2 w}{\partial x\partial\theta}\right)+2\Phi^2\left(\frac{\partial^2 v}{\partial x\partial\theta}-\frac{\partial^3 w}{\partial x\partial\theta^2}\right)\right]+3D_{66}G^2\Phi^2\left(\frac{\partial^2 v}{\partial x^2}-\frac{\partial^3 w}{\partial x^2\partial\theta}\right)$$

$$-\Phi E_3=\lambda^4\left(\overline{\rho_1}+\frac{1}{\beta}\overline{\rho_2}G\Phi\right)\frac{\partial^2 w}{\partial t^2}+\beta^2\Bigg[A_{12}G\Phi\frac{\partial u}{\partial x}+A_{22}G^2\Phi^2\left(\frac{\partial v}{\partial\theta}+w\right)+A_{26}G\Phi\left(G\Phi\frac{\partial u}{\partial\theta}+\frac{\partial v}{\partial x}\right)\Bigg]$$

$$-\beta\Bigg[B_{11}\frac{\partial^3 u}{\partial x^3}+B_{12}G\Phi\left[\frac{\partial}{\partial\theta}\left(G\Phi\frac{\partial^2 u}{\partial x\partial\theta}\right)+\frac{\partial^3 v}{\partial x^2\partial\theta}+2\frac{\partial^2 w}{\partial x^2}\right]+B_{16}\left[3G\Phi\frac{\partial^3 u}{\partial x^2\partial\theta}+\frac{\partial^3 v}{\partial x^3}\right]+B_{22}G^3\Bigg[\Phi^2\Bigg[\Phi\left(\frac{\partial v}{\partial\theta}+w\right)+\frac{\partial}{\partial\theta}\left\{\Phi\left(\frac{\partial w}{\partial\theta}-v\right)\right\}\Bigg]+\Phi\frac{\partial}{\partial\theta}\Bigg[\Phi\frac{\partial}{\partial\theta}\left\{\Phi\left(\frac{\partial v}{\partial\theta}+w\right)\right\}\Bigg]\Bigg]+B_{26}G^2\Phi\Bigg[\Phi\left(G\Phi\frac{\partial u}{\partial\theta}+2\frac{\partial^2 w}{\partial x\partial\theta}-\frac{\partial v}{\partial x}\right)+\frac{\partial}{\partial\theta}\Bigg[\Phi\left\{2\left(\frac{\partial^2 v}{\partial x\partial\theta}+\frac{\partial w}{\partial x}\right)+\frac{\partial}{\partial\theta}\left(\frac{\partial v}{\partial x}+G\Phi\frac{\partial u}{\partial\theta}\right)\right\}\Bigg]\Bigg]+2B_{66}G\Phi\frac{\partial}{\partial\theta}\left\{G\Phi\frac{\partial^2 u}{\partial x\partial\theta}+\frac{\partial^2 v}{\partial x^2}\right\}\Bigg]+D_{11}\left(\frac{\partial^4 w}{\partial x^4}-G\Phi\frac{\partial^3 u}{\partial x^3}\right)+D_{12}G^2\Phi\frac{\partial}{\partial\theta}\left[\Phi\left(2\frac{\partial^3 w}{\partial x^2\partial\theta}-\frac{\partial^2 v}{\partial x^2}\right)\right]+D_{16}G\Phi\left[4\frac{\partial^4 w}{\partial x^3\partial\theta}-2\frac{\partial^3 v}{\partial x^3}-\frac{\partial}{\partial\theta}\left(G\Phi\frac{\partial^2 u}{\partial x^2}\right)\right]+D_{22}G^4\left[\Phi^2+\frac{1}{2}\frac{\partial\Phi^2}{\partial\theta}\frac{\partial}{\partial\theta}+\Phi^2\frac{\partial^2}{\partial\theta^2}\right]\left[\Phi\frac{\partial}{\partial\theta}\left\{\Phi\left(\frac{\partial w}{\partial\theta}-v\right)\right\}+\Phi^2\left(\frac{\partial v}{\partial\theta}+w\right)\right]+D_{26}\Bigg[G^3\Phi^3\left(G\Phi\frac{\partial u}{\partial\theta}+\frac{\partial^2 w}{\partial x\partial\theta}\right)+G^3\Phi\frac{\partial}{\partial\theta}\Bigg[\Phi^2\left(\frac{\partial^2 v}{\partial x\partial\theta}+\frac{\partial w}{\partial x}\right)+\Phi\frac{\partial}{\partial\theta}\left\{\Phi\left(4\frac{\partial^2 w}{\partial x\partial\theta}-3\frac{\partial v}{\partial x}+G\Phi\frac{\partial u}{\partial\theta}\right)\right\}\Bigg]\Bigg]+D_{66}G^2\Phi\frac{\partial}{\partial\theta}\left[\Phi\left\{4\frac{\partial^3 w}{\partial x^2\partial\theta}-3\frac{\partial^2 v}{\partial x^2}+G\Phi\frac{\partial^2 u}{\partial x\partial\theta}\right\}\right] \quad (15)$$

and where

$$T_1=\beta^2\Bigg[A_{11}\frac{\partial}{\partial x}(u/\Phi)+A_{12}G\left(\frac{\partial v}{\partial\theta}+A_{16}\left(G\frac{\partial u}{\partial\theta}+\frac{1}{\Phi}\frac{\partial v}{\partial x}\right)\right]+\beta\Bigg[B_{11}\left\{G\frac{\partial u}{\partial x}-\frac{1}{\Phi}\frac{\partial^2 w}{\partial x^2}\right\}-B_{12}G^2\frac{\partial}{\partial\theta}\left\{\Phi\left(\frac{\partial w}{\partial\theta}-v\right)\right\}+2B_{16}G\left(\frac{\partial v}{\partial x}-\frac{\partial^2 w}{\partial x\partial\theta}\right)\Bigg]-D_{11}G\frac{\partial^2 w}{\partial x^2}-D_{16}G^2\Phi\left(\frac{\partial^2 w}{\partial x\partial\theta}-\frac{\partial v}{\partial x}\right)$$

$$\Phi T_2=\beta^2\Bigg[A_{16}\frac{\partial u}{\partial x}+A_{26}G\Phi\left(\frac{\partial v}{\partial\theta}+w\right)+A_{66}\left(G\Phi\frac{\partial u}{\partial\theta}+\frac{\partial v}{\partial x}\right)\Bigg]+\beta\Bigg[B_{16}\left(2G\Phi\frac{\partial u}{\partial x}-\frac{\partial^2 w}{\partial x^2}\right)+B_{26}\Bigg[G^2\Phi^2\left(\frac{\partial v}{\partial\theta}+w\right)-G^2\Phi\frac{\partial}{\partial\theta}\left\{\Phi\left(\frac{\partial w}{\partial\theta}-v\right)\right\}\Bigg]+B_{66}\left(3G\Phi\frac{\partial v}{\partial x}-2G\Phi\frac{\partial^2 w}{\partial x\partial\theta}+G^2\Phi^2\frac{\partial u}{\partial\theta}\right)\Bigg]+D_{16}G\Phi\left(G\Phi\frac{\partial u}{\partial x}-2\frac{\partial^2 w}{\partial x^2}\right)-D_{26}G^3\Phi^2\frac{\partial}{\partial\theta}\left\{\Phi\left(\frac{\partial w}{\partial\theta}-v\right)\right\}+3D_{66}G^2\Phi^2\left(\frac{\partial v}{\partial x}-\frac{\partial^2 w}{\partial x\partial\theta}\right)$$

$$-\Phi T_3=\beta\Bigg[-B_{11}\frac{\partial^2 u}{\partial x^2}-B_{12}G\Phi\left(\frac{\partial^2 v}{\partial x\partial\theta}+\frac{\partial w}{\partial x}\right)-B_{16}\left(3G\Phi\frac{\partial^2 u}{\partial x\partial\theta}+\frac{\partial^2 v}{\partial x^2}\right)-2B_{26}G^2\Phi\frac{\partial}{\partial\theta}\left\{\Phi\left(\frac{\partial v}{\partial\theta}+w\right)\right\}-2B_{66}G\Phi\left\{\frac{\partial^2 v}{\partial x\partial\theta}+\frac{\partial}{\partial\theta}\left(G\Phi\frac{\partial u}{\partial\theta}\right)\right\}\Bigg]+D_{11}\left(\frac{\partial^3 w}{\partial x^3}-G\Phi\frac{\partial^2 u}{\partial x^2}\right)+D_{12}G^2\Phi\frac{\partial}{\partial\theta}\left\{\Phi\left(\frac{\partial^2 w}{\partial x\partial\theta}-\frac{\partial v}{\partial x}\right)\right\}+D_{16}G\Phi\left\{4\frac{\partial^3 w}{\partial x^2\partial\theta}-2\frac{\partial^2 v}{\partial x^2}-\frac{\partial}{\partial\theta}\left(G\Phi\frac{\partial u}{\partial x}\right)\right\}+D_{26}G^3\Phi\frac{\partial}{\partial\theta}\left[\Phi^2\left(\frac{\partial v}{\partial\theta}+w\right)+2\Phi\frac{\partial}{\partial\theta}\left\{\Phi\left(\frac{\partial w}{\partial\theta}-v\right)\right\}\right]+D_{66}G^3\Phi\frac{\partial}{\partial\theta}\left[\Phi\left\{4\frac{\partial^2 w}{\partial x\partial\theta}-3\frac{\partial v}{\partial x}+G\Phi\frac{\partial u}{\partial\theta}\right\}\right]$$

$$T_4=\beta^2\Bigg[A_{16}G\frac{\partial u}{\partial x}+A_{26}G^2\Phi\left(\frac{\partial v}{\partial\theta}+w\right)+A_{66}G\left(G\Phi\frac{\partial u}{\partial\theta}+\frac{\partial v}{\partial x}\right)\Bigg]+\beta\Bigg[-B_{16}G\frac{\partial^2 w}{\partial x^2}-B_{26}G^3\Phi\left\{\Phi\left(\frac{\partial v}{\partial\theta}+w\right)+\frac{\partial}{\partial\theta}\left(\Phi\left(\frac{\partial w}{\partial\theta}-v\right)\right)\right\}-B_{66}G^2\Phi\left(G\Phi\frac{\partial u}{\partial\theta}+2\frac{\partial^2 w}{\partial x\partial\theta}-\frac{\partial v}{\partial x}\right)\Bigg]$$

Downloaded 03 May 2010 to 171.66.16.20. Redistribution subject to ASME license or copyright; see http://www.asme.org/terms/Terms_Use.cfm

$$+D_{26}G^4\Phi\left[\Phi\frac{\partial}{\partial\theta}\left\{\Phi\left(\frac{\partial w}{\partial\theta}-v\right)\right\}+\Phi^2\left(\frac{\partial v}{\partial\theta}+w\right)\right]$$
$$+D_{66}G^2\Phi^2\left(\frac{\partial^2 w}{\partial x\partial\theta}+G\Phi\frac{\partial u}{\partial\theta}\right)$$

$$T_5=\beta^2\left[A_{12}G\frac{\partial u}{\partial x}+A_{22}G^2\Phi\left(\frac{\partial v}{\partial\theta}+w\right)+A_{26}G\left(G\Phi\frac{\partial u}{\partial\theta}+\frac{\partial v}{\partial x}\right)\right]$$
$$+\beta\left[B_{12}G\left(G\Phi\frac{\partial u}{\partial x}-\frac{\partial^2 w}{\partial x^2}\right)-B_{22}G^2\Phi\left[G\Phi\left(\frac{\partial^2 w}{\partial\theta^2}-\frac{\partial v}{\partial\theta}\right)\right.\right.$$
$$\left.\left.+G\frac{\partial\Phi}{\partial\theta}\left(\frac{\partial w}{\partial\theta}-v\right)\right]-2B_{26}G^2\Phi\left(\frac{\partial^2 w}{\partial x\partial\theta}-\frac{\partial v}{\partial x}\right)\right]$$
$$-D_{12}G^2\Phi\frac{\partial^2 w}{\partial x^2}+D_{26}G^3\Phi^2\left(\frac{\partial v}{\partial x}-\frac{\partial^2 w}{\partial x\partial\theta}\right)$$

$$-T_6=\beta\left[-B_{12}G^2\Phi\frac{\partial^2 u}{\partial x\partial\theta}-2B_{16}G\frac{\partial^2 u}{\partial x^2}\right.$$
$$-B_{22}G^3\Phi\frac{\partial}{\partial\theta}\left\{\Phi\left(\frac{\partial v}{\partial\theta}+w\right)\right\}-B_{26}G^2\Phi\left[3\frac{\partial^2 v}{\partial x\partial\theta}+2\frac{\partial w}{\partial x}\right.$$
$$\left.+\frac{\partial}{\partial\theta}\left(G\Phi\frac{\partial u}{\partial\theta}\right)\right]-2B_{66}G\left(\frac{\partial^2 v}{\partial x^2}+G\Phi\frac{\partial^2 u}{\partial x\partial\theta}\right)\Big]$$
$$+D_{12}G^2\Phi\frac{\partial^3 w}{\partial x^2\partial\theta}+D_{16}G\left(2\frac{\partial^3 w}{\partial x^3}-G\Phi\frac{\partial^2 u}{\partial x^2}\right)$$
$$+D_{22}G^4\Phi\frac{\partial}{\partial\theta}\left[\Phi^2\left(\frac{\partial v}{\partial\theta}+w\right)+\Phi\frac{\partial}{\partial\theta}\left\{\Phi\left(\frac{\partial w}{\partial\theta}-v\right)\right\}\right]$$
$$+D_{26}G^3\left[\Phi^2\left(\frac{\partial^2 v}{\partial x\partial\theta}+\frac{\partial w}{\partial x}\right)\right.$$
$$\left.+\Phi\frac{\partial}{\partial\theta}\left\{\Phi\left(4\frac{\partial^2 w}{\partial x\partial\theta}-3\frac{\partial v}{\partial x}+G\Phi\frac{\partial u}{\partial\theta}\right)\right\}\right]$$
$$+D_{66}G^2\Phi\left[4\frac{\partial^3 w}{\partial x^2\partial\theta}-3\frac{\partial^2 v}{\partial x^2}+G\Phi\frac{\partial^2 u}{\partial x\partial\theta}\right]$$

$$T_7=\beta\left[-2B_{16}G\frac{\partial u}{\partial x}-2B_{26}G^2\Phi\left(\frac{\partial v}{\partial\theta}+w\right)\right.$$
$$\left.-2B_{66}G\left(\frac{\partial v}{\partial x}+G\Phi\frac{\partial u}{\partial\theta}\right)\right]+D_{16}G\left(2\frac{\partial^2 w}{\partial x^2}-G\Phi\frac{\partial u}{\partial x}\right)$$
$$+D_{26}G^3\Phi\left[2\frac{\partial}{\partial\theta}\left\{\Phi\left(\frac{\partial w}{\partial\theta}-v\right)\right\}+\Phi\left(\frac{\partial v}{\partial\theta}+w\right)\right]$$
$$+D_{66}G^2\Phi\left(4\frac{\partial^2 w}{\partial x\partial\theta}-3\frac{\partial v}{\partial x}+G\Phi\frac{\partial u}{\partial\theta}\right)$$

$$\Phi M_1=\beta\left[-B_{11}\frac{\partial u}{\partial x}-B_{12}G\Phi\left(\frac{\partial v}{\partial\theta}+w\right)-B_{16}\left(G\Phi\frac{\partial u}{\partial\theta}+\frac{\partial v}{\partial x}\right)\right]$$
$$+D_{11}\left(\frac{\partial^2 w}{\partial x^2}-G\Phi\frac{\partial u}{\partial x}\right)+D_{12}G^2\Phi\frac{\partial}{\partial\theta}\left\{\Phi\left(\frac{\partial w}{\partial\theta}-v\right)\right\}$$
$$+2D_{16}G\Phi\left(\frac{\partial^2 w}{\partial x\partial\theta}-\frac{\partial v}{\partial x}\right)$$

$$M_2=\beta\left[-B_{12}G^2\Phi\frac{\partial u}{\partial x}-B_{22}G^3\Phi^2\left(\frac{\partial v}{\partial\theta}+w\right)\right.$$
$$\left.-B_{26}G^2\Phi\left(\frac{\partial v}{\partial x}+G\Phi\frac{\partial u}{\partial\theta}\right)\right]$$
$$+D_{12}G^2\Phi\frac{\partial^2 w}{\partial x^2}+D_{22}G^4\Phi^2\left[\Phi\left(\frac{\partial v}{\partial\theta}+w\right)+\frac{\partial}{\partial\theta}\left\{\Phi\left(\frac{\partial w}{\partial\theta}-v\right)\right\}\right]$$
$$+D_{26}G^3\Phi^2\left(G\Phi\frac{\partial u}{\partial\theta}-\frac{\partial v}{\partial x}+2\frac{\partial^2 w}{\partial x\partial\theta}\right). \quad (16)$$

Euler equations (equations of motion) are

$$E_1=E_2=E_3=0. \quad (17)$$

The boundary conditions at $x = 0$ and $x = \mu$ are

$$T_1\delta u=T_2\delta v=T_3\delta w=M_1\left(\frac{\partial w}{\partial x}\right)=0. \quad (18)$$

For boundaries at $\theta = \theta_1$ and $\theta = \theta_2$ they are

$$T_4\delta u=T_5\delta v=T_6\delta w=M_2\delta\left(\frac{\partial w}{\partial\theta}\right)=0. \quad (19)$$

An additional condition to be satisfied at corner is

$$T_7\delta w=0. \quad (20)$$

The last term in Eq. (14) vanishes because of the additional conditions of displacement, $\delta u = \delta v = \delta w = 0$ at $t = t_1$ and $t = t_2$.

Replacing w by $(-w)$ and setting

$$A_{16}=A_{26}=D_{16}=D_{26}=B_{ij}=\overline{\rho_2}=0,$$

$$A_{11}=A_{22}=12,\quad A_{12}=12\nu,\quad A_{66}=12\left(\frac{1-\nu}{2}\right),$$

$$D_{11}=D_{22}=1,\quad D_{12}=\nu,\quad D_{66}=\frac{1-\nu}{2},$$

$$E_0=\frac{E}{12(1-\nu^2)},\quad 12\beta^2=\beta, \quad (21)$$

one finds that Eqs. (14)–(20) correspond with those for a homogeneous isotropic noncircular thin cylindrical shell obtained by Suzuki and Leissa (1985).

2.4 Solutions of the Equation of Motion for Freely Supported Ends. Consider the vibration of a symmetrically laminated cross-ply noncircular cylindrical shell having the curved ends supported by shear diaphragms (or freely supported). As mentioned at the end of Section 2.2, for this lamination type, $A_{16} = A_{26} = D_{16} = D_{26} = 0$, and all $B_{ij} = 0$. The conditions to be imposed at the ends are

$$T_1 = v = w = M_1 = 0 \quad (22)$$

which satisfy Eqs. (18). Equations (22) are exactly satisfied at $x = 0$ and μ by choosing

$$u=u_m(\theta)\cos\frac{m\pi}{\mu}x\sin\omega t,$$

$$v=v_m(\theta)\sin\frac{m\pi}{\mu}x\sin\omega t,$$

$$w=w_m(\theta)\sin\frac{m\pi}{\mu}x\sin\omega t \quad (23)$$

where m is an integer and ω is the circular frequency of vibration. Substituting the displacements (23) into the equations of motion (17) yields the following set of ordinary differential equations:

$$(\alpha_0^4\overline{\rho}_1-k^2\beta^2A_{11})u_m/\Phi+kG(\beta^2A_{12}+k^2D_{11})w_m$$
$$+\beta^2kG(A_{12}+A_{66})\frac{dv_m}{d\theta}+\beta^2G^2A_{66}\frac{d}{d\theta}\left(\Phi\frac{du_m}{d\theta}\right)$$
$$+G^3D_{66}\frac{d}{d\theta}\left\{\Phi^2\left(k\frac{dw_m}{d\theta}+G\Phi\frac{du_m}{d\theta}\right)\right\}=0,$$

Downloaded 03 May 2010 to 171.66.16.20. Redistribution subject to ASME license or copyright; see http://www.asme.org/terms/Terms_Use.cfm

$$(\alpha_0^4\bar{\rho}_1 - k^2\beta^2 A_{66})v_m - k\beta^2 G\Phi(A_{12}+A_{66})\frac{du_m}{d\theta}$$
$$+\beta^2 G^2\Phi A_{22}\frac{d}{d\theta}\left\{\Phi\left(\frac{dv_m}{d\theta}+w_m\right)\right\}$$
$$+G^4\Phi^2 D_{22}\left[\frac{1}{2}\frac{d\Phi^2}{d\theta}\left(w_m+\frac{d^2w_m}{d\theta^2}\right)+\left(\frac{d\Phi}{d\theta}\right)^2\left(\frac{dw_m}{d\theta}-v_m\right)\right]$$
$$+k^2G^2\Phi^2\left[(D_{12}+3D_{66})\frac{dw_m}{d\theta}-3D_{66}v_m\right]=0,$$
$$-kG\Phi(k^2D_{11}+\beta^2A_{12})u_m+(k^4D_{11}-\alpha_0^4\bar{\rho}_1)w_m$$
$$+\beta^2G^2\Phi^2A_{22}\left(\frac{dv_m}{d\theta}+w_m\right)+D_{12}k^2G^2\Phi\frac{d}{d\theta}\left[\Phi\left(v_m-2\frac{dw_m}{d\theta}\right)\right]$$
$$+D_{66}kG^2\Phi\frac{d}{d\theta}\left[\Phi\left\{3kv_m-4k\frac{dv_m}{d\theta}-G\Phi\frac{dU_m}{d\theta}\right\}\right]$$
$$+D_{22}G^4\left(\Phi^2+\frac{1}{2}\frac{d\Phi^2}{d\theta}\frac{d}{d\theta}+\Phi^2\frac{d^2}{d\theta^2}\right)$$
$$\times\left[\Phi\frac{d}{d\theta}\left\{\Phi\left(\frac{dw_m}{d\theta}-v_m\right)\right\}+\Phi^2\left(\frac{dv_m}{d\theta}+w_m\right)\right]=0 \quad (24)$$

where

$$\alpha_0^4=\rho_0\omega^2r_0^4/E_0h^2,\quad \beta=r_0/h,\quad k=m\pi/\mu. \quad (25)$$

Equations (24) are complicated differential equations with variable coefficients, but exact solutions may be obtained by expressing the ellipticity functions $\Phi^2(\theta)$ as infinite power series in θ and assuming solutions for u_m/Φ, v_m, and w_m which are also infinite power series in θ. The solution procedure will be demonstrated here for shells having cross-sections with one or more axes of symmetry.

Let $\theta = 0$ correspond to a symmetry axis and expand Φ^2 as

$$\Phi^2=\Phi_0\sum_{n=0}^{\infty}\zeta_n\theta^{2n}. \quad (26)$$

One can denote Φ^2 as in Eq. (26) for the curves for which the curvatures are expressed as even functions of θ (cf. Suzuki, Takahashi, and Ishiyama, 1978). As an example, consider an ellipse for which the equations are denoted by the rectangular coordinates (ξ_1, ξ_2) as $\xi_1 = a\cos\eta$, $\xi_2 = b\sin\eta$ in which $2a$, $2b$, and η are the major and the minor axes and a parameter, respectively. Setting the representative radius r_0 and the ellipticity of the curve μ_0 as

$$r_0=\sqrt{(a^2+b^2)/2},\quad \mu_0=\frac{a^2-b^2}{a^2+b^2} \quad (27)$$

one obtains

$$\Phi(\theta)=(1+\mu_0\cos 2\theta)^{3/2},\quad \tan\theta=\sqrt{(1+\mu_0)/(1-\mu_0)}\tan\eta$$
$$\frac{1}{G}=1-\mu_0^2,\quad \Phi_0=(1+\mu_0)^3,\quad \zeta_0=1$$
$$\zeta_n=\frac{3\mu_0^3(-1)^n2^{2n}}{(1+\mu_0)^3(2n)!}\left[\frac{1+3^{2n-1}}{4}+\frac{2^{2n-1}}{\mu_0}+\frac{1}{\mu_0^2}\right]. \quad (28)$$

Then Eqs. (24) have two solutions, one in which u_m/Φ and w_m are even functions of θ and v_m is an odd function of θ, and another in which u_m/Φ and w_m are odd functions of θ and v_m is an even function of θ.

(i) In the case that u_m/Φ is an even function of θ, one takes

$$u_m/\Phi=\sum_{n=0}^{\infty}A_n\theta^{2n},\quad v_m=\sum_{n=0}^{\infty}B_n\theta^{2n+1},\quad w_m=\sum_{n=0}^{\infty}C_n\theta^{2n} \quad (29)$$

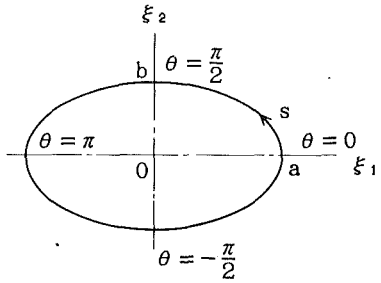


Fig. 3 Elliptical shell

where A_n, B_n and C_n are coefficients which are determined in turn as follows. Substituting Eqs. (29) into Eqs. (24) yields

$$\sum_{n=0}^{\infty}[G^2\Phi_0\zeta_0(2n+1)(2n+2)(\beta^2A_{66}+G^2\Phi_0\zeta_0D_{66})A_{n+1}+f_{na}]\theta^{2n}=0$$
$$\sum_{n=0}^{\infty}[\beta^2G^2\Phi_0\zeta_0(2n+2)(2n+3)A_{22}B_{n+1}+f_{nb}]\theta^{2n+1}=0$$
$$\sum_{n=0}^{\infty}[G^4\Phi_0^2\zeta_0^2D_{22}(2n+1)(2n+2)(2n+3)(2n+4)C_{n+2}+f_{nc}]\theta^{2n}=0 \quad (30)$$

where f_{na}, f_{nb}, and f_{nc} are series defined in Appendix B. If Eqs. (30) hold for any value of θ, the expressions in the brackets of each equation in Eqs. (30) must become zero. Hence, the coefficients A_{n+1}, B_{n+1}, and C_{n+2} $(n \geqq 0)$ are obtained in terms of A_0, B_0, C_0, and C_1, with the last four left undetermined and four independent solutions arise.

(ii) In the case that u_m/Φ is an odd function of θ one takes

$$u_m/\Phi=\sum_{n=0}^{\infty}A_n\theta^{2n+1},\quad v_m=\sum_{n=0}^{\infty}B_n\theta^{2n},\quad w_m=\sum_{n=0}^{\infty}C_n\theta^{2n+1} \quad (31)$$

where A_n, B_n, and C_n are undetermined coefficients. Substituting Eqs. (31) into Eqs. (24) yields

$$\sum_{n=0}^{\infty}[G^2\Phi_0\zeta_0(2n+2)(2n+3)\times(\beta^2A_{66}+G^2\Phi_0\zeta_0D_{66})A_{n+1}+f_{na}]\theta^{2n+1}=0$$
$$\sum_{n=0}^{\infty}[G^2\beta^2\Phi_0\zeta_0(2n+1)(2n+2)A_{22}B_{n+1}+f_{nb}]\theta^{2n}=0$$
$$\sum_{n=0}^{\infty}[G^4\Phi_0^2\zeta_0^2D_{22}(2n+2)\times(2n+3)(2n+4)(2n+5)C_{n+2}+f_{nc}]\theta^{2n+1}=0 \quad (32)$$

where f_{na}, f_{nb}, and f_{nc} are given in Appendix B. From Eqs. (32), the coefficients B_{n+1}, A_{n+1} and C_{n+2} $(n \geqq 0)$ are obtained in turn with A_0, B_0, C_0 and C_1, left undetermined.

In this way, eight independent solutions for the complete problem are obtained. The general solutions of Eqs. (24) are expressed by combining linearly these eight independent solutions. However, when the cross-section is symmetric about $\theta = 0$, the vibrations are divided into a symmetric vibration and an antisymmetric one about the axis of symmetry passing through the axis $\theta = 0$. Then the displacements given by Eqs. (29) are the solutions for the symmetric models of vibration, and those from Eq. (31) are for the antisymmetric modes.

Consider now an elliptical cylindrical shell with cross-section as shown in Fig. 3. The axes of symmetry are the ξ_1-axis passing

Downloaded 03 May 2010 to 171.66.16.20. Redistribution subject to ASME license or copyright; see http://www.asme.org/terms/Terms_Use.cfm

through the points $\theta = 0$, π and the ξ_2-axis passing through the points $\theta = \pm\pi/2$. Vibrations are divided into four symmetry classes (S-S, S-A, A-S, A-A), depending on whether they are symmetric (S) or antisymmetric (A) with respect to the ξ_1 and ξ_2-axes, respectively. These symmetry classes are obtained by utilizing the symmetric functions (29) or the antisymmetric functions (31), and by enforcing the conditions at $\theta = \pi/2$ that either

$$T_4 = v = T_6 = \frac{\partial w}{\partial \theta} = 0 \quad \text{(symmetric)} \tag{33}$$

or

$$u = T_5 = w = M_2 = 0 \quad \text{(antisymmetric)}. \tag{34}$$

3 Numerical Results

Numerical studies are made for elliptical cylindrical shells of symmetric cross-ply laminates. As composite materials, unidirectional graphite fiber-reinforced epoxy (hereafter called G/E) are considered. All layers are taken to be equal thickness. The moduli of elasticity of the materials are taken from Vinson and Sierakowski (1987) and used; $E_{11} = 138$ (GPa), $E_{22} = 8.96$ (GPa), $G_{12} = 7.1$ (GPa), $\nu_{12} = 0.30$. To be specific, the following shell parameters are used; $\mu_0 = 0.2$ ($\sim a/b = 1.22$), β ($= r_0/h$) $= 50$.

The displacement functions u_m, v_m, and w_m are calculated by retaining 70 terms for each of the coefficients A_n, B_n, and C_n in Eqs. (29) and (31). Each of the independent solutions corresponding to each symmetry class was obtained by setting one of the A_0, B_0, C_0, and C_1 equal to unity and the others equal to zero. To show the characteristics of the vibration, the nondimensional frequency parameter α_0^4/β^2 is used where, from Eqs. (25),

$$\frac{\alpha_0^4}{\beta^2} = \frac{\rho_0 \omega^2 r_0^2}{E_0} \tag{35}$$

and E_0 is defined by $E_0 = E_{11}/12(1 - \nu_{12}\nu_{21})$. In the calculations for the results shown hereafter, β and k ($= m\pi l/r_0$) were first chosen, and then a search was conducted for the values of α_0^4/β^2 which satisfy the frequency equations.

The rate of convergence of the solutions varies with the parameters. In general, the convergence becomes slow as β, μ_0, α_0^4/β^2, N, and k become larger. The first two parameters, in particular, have larger influences on the convergence.

Table 1 shows the convergence of the solutions arising from Eqs. (29). In the table are shown the number of terms and converged digits for a representative shell. The convergence for the other four sets of solutions is almost similar.

Figures 4–7 show the frequency curves for the (S-S), (S-A), (A-S), and (A-A) modes of elliptical cylindrical shells having 3, 5, and 9 laminae with stacking sequence (0 deg, 90 deg, 0 deg, · · · · · · , 90 deg, 0 deg) in the case where $\beta = 50$, $\mu_0 = 0.2$. The curves are for the first, second, and third modes of vibration of each symmetry class. From the figures, one finds that the frequency curves generally become higher with increasing the number of laminae N. The frequency curves for the (S-S) and (A-A) modes are similar, as are the ones for (S-A) and (A-S) modes.

Figure 8 shows the frequency curves for the (S-S) and (S-A) modes of elliptical cylindrical shells with three laminae of (90 deg, 0 deg, 90 deg), and Fig. 9 does this for the (A-S) and (A-A) modes. Comparing the figures with Figs. 4–7, one finds that the frequencies for (90 deg, 0 deg, 90 deg) are very much higher than those for (0 deg, 90 deg, 0 deg).

Figures 10 and 11 show the effects of number of laminae and stacking sequence upon the frequencies for (S-S) modes of shells with two length ratios k ($= m\pi l/r_0$) 1 and 3 in the case where $\beta = 50$. As seen from the figures, there are large differences between the data for the stacking sequence (0 deg, 90 deg, 0 deg) and (90 deg, 0 deg, 90 deg) when N is small, but the differences become smaller with an increasing number of laminae. It is interesting to note that, for both types of stacking sequences, some frequencies increase while others decrease as the number of layers (N) increases.

Table 1 Converged digits of functions

(S-S modes, ($\mu = 0.2$, $\alpha_0^4/\beta^2 = 1.0$, $K = 3$)

Functions	$\beta = 50$			
	Number of terms			
	40	50	60	70
U_m	4	5	6	8
V_m	4	5	7	7
W_m	2	5	6	6
W_m^1	4	4	5	6
T_{4m}	4	5	6	8
T_{5m}	3	4	6	7
T_{6m}	4	5	5	6
M_{2m}	4	5	6	8

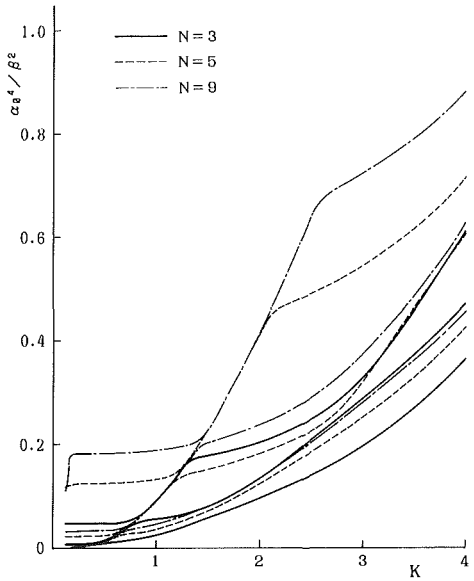


Fig. 4 Frequency curves, (S-S) modes ($\beta = 50$)

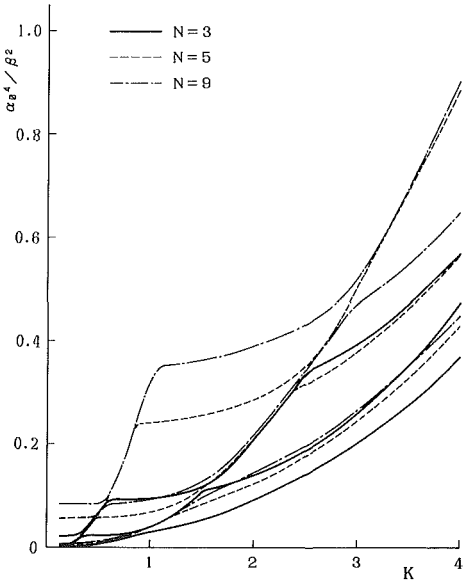


Fig. 5 Frequency curves, (S-A) modes ($\beta = 50$)

Downloaded 03 May 2010 to 171.66.16.20. Redistribution subject to ASME license or copyright; see http://www.asme.org/terms/Terms_Use.cfm

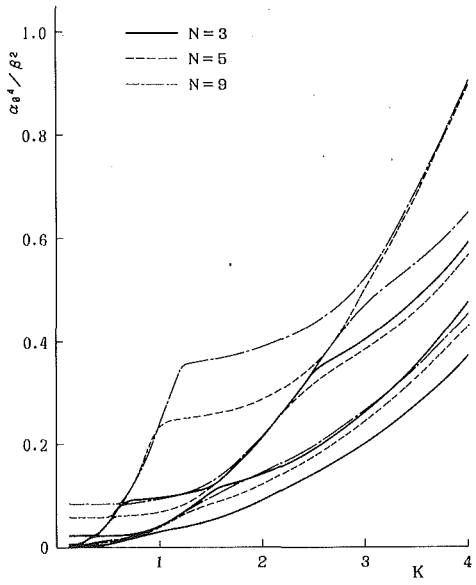


Fig. 6 Frequency curves, (A-S) modes (β = 50)

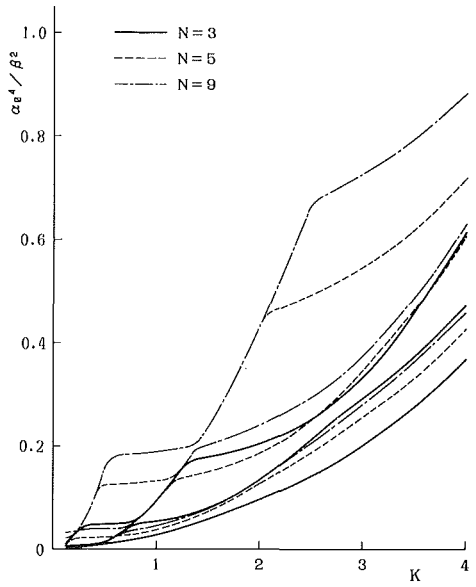


Fig. 7 Frequency curves, (A-A) modes (β = 50)

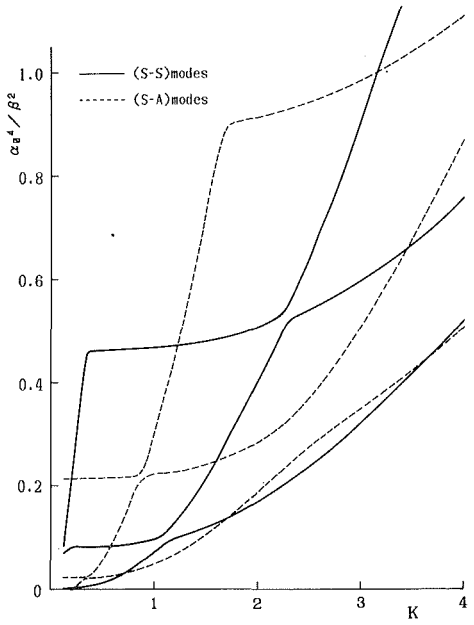


Fig. 8 Frequency curves, (β = 50), N = 3, (90 deg, 0 deg, 90 deg)

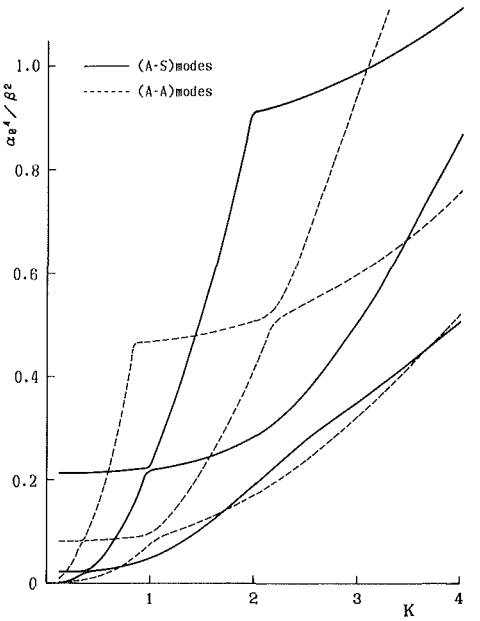


Fig. 9 Frequency curves, (β = 50), N = 3, (90 deg, 0 deg, 90 deg)

4 Conclusions

In this paper, an exact solution procedure has been demonstrated for solving free-vibration problems for laminated composite noncircular thin cylindrical shells. The method is a general one applicable to various noncircular thin cylindrical shells, although limited to symmetrically laminated cross-ply shells having both ends freely supported. As numerical examples, natural frequencies were found for elliptical cylindrical shells, and from the results were clarified the effects of number of laminae and stacking sequence upon the frequencies.

References

Love, A. E. H., 1927, *A Treatise on the Mathematical Theory of Elasticity*, Cambridge University Press, New York.

Qatu, M. S., and Leissa, A. W., 1991a, "Free Vibrations of Completely Free Doubly Curved Laminated Composite Shallow Shells," *Journal of Sound and Vibration*, Vol. 151, pp. 9–29.

Qatu, M., and Leissa, A. W., 1991b, "Natural Frequencies for Cantilevered Doubly-Curved Laminated Composite Shallow Shells," *Composite Structures*, Vol. 17, pp. 227–255.

Singh, A. V., Zhu, L., and Mirza, S., 1991, "On Asymmetric Vibrations of Layered Orthotropic Shells of Revolution," *Journal of Sound and Vibration*, Vol. 148, pp. 265–277.

Sivadas, K. R., and Ganesan, N., 1991, "Vibration Analysis of Laminated Conical Shells with Variable Thickness," *Journal of Sound and Vibration*, Vol. 148, pp. 477–491.

Suzuki, K., and Leissa, A. W., 1985, "Free Vibrations of Non-Circular Cylindrical Shells Having Circumferentially Varying Thickness," ASME JOURNAL OF APPLIED MECHANICS, Vol. 52, pp. 149–154.

Suzuki, K., and Leissa, A. W., 1986, "Exact Solutions for the Free Vibrations of Open Cylindrical Shells with Circumferentially Varying Curvature and Thickness," *Journal of Sound and Vibration*, Vol. 107, pp. 1–15.

Suzuki, K., and Leissa, A. W., 1990, "Analysis of Free Vibrations of Noncircular Thick Cylindrical Shells Having Circumferentially Varying Thickness," *International Journal of Solids and Structures*, Vol. 26, pp. 255–270.

Suzuki, K., Takahashi, S., and Ishiyama, H., 1978, "In-Plane Vibrations of Curved Bars," *Bulletin of the JSME*, Vol. 21, pp. 618–627.

Vinson, J. R., and Sierakowski, R. L., 1987, *The Behaviour of Structures Composed of Composite Materials*, Martinus Nijhoff Publishers, Dordrecht, The Netherlands.

Whitney, J. M., 1987, *Structural Analysis of Laminated Anisotropic Plates*, Technomic Publishing Co., Lancaster, PA.

Downloaded 03 May 2010 to 171.66.16.20. Redistribution subject to ASME license or copyright; see http://www.asme.org/terms/Terms_Use.cfm

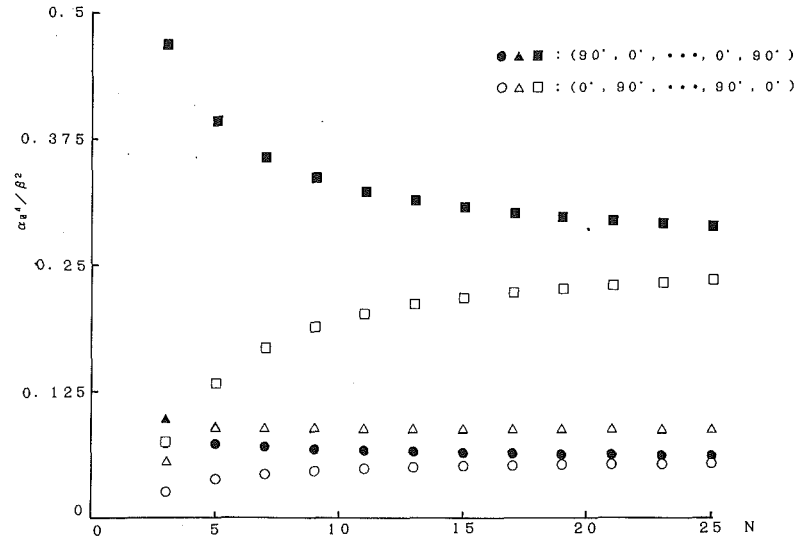


Fig. 10 Effect of number of layers upon the frequencies, (S-S) modes (β = 50.0, K = 1)

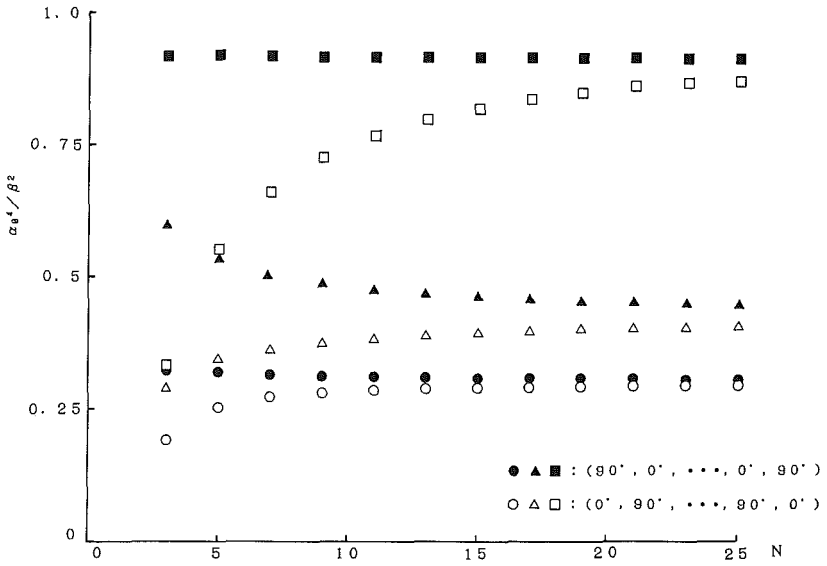


Fig. 11 Effect of number of layers upon the frequencies, (S-S) modes (β = 50.0, K = 3)

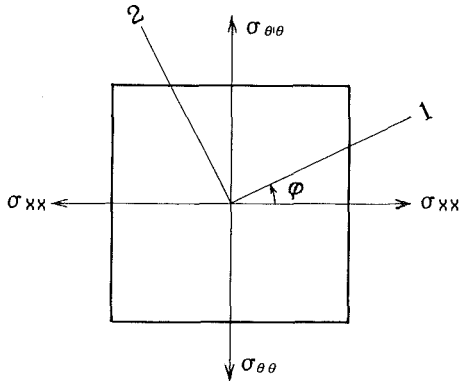


Fig. A1 Coordinate system of lamina

APPENDIX A

$\overline{Q}_{ij}$ in Eqs. (6)

$$\overline{Q}_{11} = Q_{11}m^4 + 2(Q_{12} + 2Q_{66})m^2n^2 + Q_{22}n^4,$$

$$\overline{Q}_{12} = (Q_{11} + Q_{22} - 4Q_{66})m^2n^2 + Q_{12}(m^4 + n^4),$$

$$\overline{Q}_{16} = -mn^3Q_{22} + m^3nQ_{11} - mn(m^2 - n^2)(Q_{12} + 2Q_{66}),$$

$$\overline{Q}_{22} = Q_{11}n^4 + 2(Q_{12} + 2Q_{66})m^2n^2 + Q_{22}m^4,$$

$$\overline{Q}_{26} = -m^3nQ_{22} + mn^3Q_{11} + mn(m^2 - n^2)(Q_{12} + 2Q_{66}),$$

$$\overline{Q}_{66} = (Q_{11} + Q_{22} - 2Q_{12})m^2n^2 + Q_{66}(m^2 - n^2)^2,$$

$$m = \cos\phi,\ n = \sin\phi,$$

$$\overline{Q}_{11} = E_{11}/(1 - \nu_{12}\nu_{21}),$$

$$\overline{Q}_{22} = E_{22}/(1 - \nu_{12}\nu_{21}),$$

$$\overline{Q}_{12} = \nu_{21}E_{11}/(1 - \nu_{12}\nu_{21}),$$

$$\overline{Q}_{66} = G_{12}$$

where E_{11} is the modulus of elasticity of the lamina in the direction of the fibers and E_{22} is the transverse modulus; G_{12} is the shear modulus; and ν_{12} and ν_{21} are Poisson's ratios.

Downloaded 03 May 2010 to 171.66.16.20. Redistribution subject to ASME license or copyright; see http://www.asme.org/terms/Terms_Use.cfm

The principal material axes are labelled 1 and 2, that is the 1 direction is parallel to the fibers, the 2 direction is normal to them. The shell geometric axes are x and θ as depicted in Fig. 3.

APPENDIX B

Terms Contained in Eqs. (30) and (32)

For Eqs. (30),

$$f_{na} = (\alpha_0^4\bar{\rho}_1 - k^2\beta^2 A_{11})A_n + k\beta^2 G(A_{12}+A_{66})(2n+1)B_n$$
$$+ kG(\beta^2 A_{12} + k^2 D_{11})C_n + \beta^2 G^2 \Phi_0 A_{66}(2n+1)$$
$$\times \sum_{p=0}^{n} (n+p+1)\zeta_{n+1-p}A_p$$
$$+ kG^3\Phi_0 D_{66}(2n+1)\sum_{p=0}^{n}\zeta_{n-p}(2p+2)C_{p+1}$$
$$+ G^4\Phi_0^2\zeta_0 D_{66}(2n+1)\sum_{n=0}^{n-1}\zeta_{n-p}(2p+2)A_{p+1}$$
$$+ G^4\Phi_0^2 D_{66}(2n+1)\sum_{q=0}^{n}\zeta_{n-q}\sum_{p=0}^{q}(q+p+1)\zeta_{q+1-p}A_p,$$

$$f_{nb} = (\alpha_0^4\bar{\rho}_1 - k^2\beta^2 A_{66}(B_n + \beta^2 G^2\Phi_0\zeta_0 A_{22}(2n+2)C_{n+1}$$
$$- k\beta^2 G\Phi_0(A_{12}+A_{66})\sum_{p=0}^{n+1}(n+p+1)\zeta_{n+1-p}A_p$$
$$+ \beta^2 G^2\Phi_0 A_{22}\sum_{p=0}^{n}(n+p+1)\zeta_{n+1-p}\{(2p+1)B_p + C_p\}$$
$$+ G^4\Phi_0^2 D_{22}\sum_{q=0}^{p}\Bigg[(C_q + (2q+1)(2q+2)c_{q+1}\}\sum_{p=1}^{n+1-q}p\zeta_p\zeta_{n+1-q-p}$$
$$+ \{-B_q + (2q+2)c_{q+1}\}\sum_{p=1}^{n+1-q}p\zeta_p(n+1-q-p)\zeta_{n+1-q-p}\Bigg]$$
$$+ k^2G^2\Phi_0\sum_{p=0}^{n}\zeta_{n-p}[(2p+2)(D_{12}+3D_{66})C_{p+1} - 3D_{66}B_p],$$

$$f_{nc} = -kG(k^2D_{11}+\beta^2A_{12})\Phi_0\sum_{p=0}^{n}\zeta_{n-p}A_p + (k^4D_{11} - \alpha_0^4\bar{\rho}_1)C_n$$
$$+ G^4\Phi_0^2\zeta_0^2 D_{22}(2n+1)(2n+2)C_{n+1}$$
$$+ \beta^2G^2\Phi_0A_{22}\sum_{p=0}^{n}\zeta_{n-p}[(2p+1)B_p + C_p]$$
$$+ k^2G^2\Phi_0D_{12}\sum_{p=0}^{n}(n+p+1)\zeta_{n-p}[B_p - 2(2p+2)C_{p+1}]$$
$$+ k^2G^2\Phi_0D_{66}\sum_{p=0}^{n}(n+p+1)\zeta_{n-p}[3B_p - 4(2p+2)C_{p+1}]$$
$$- kG^3\Phi_0^2D_{66}\sum_{q=0}^{n}(n+q+1)\zeta_{n-q}\sum_{p=0}^{q+1}(q+p+1)\zeta_{q+1-p}A_p$$
$$+ G^4\Phi_0^2D_{22}\Bigg[(2n+1)(2n+2)\zeta_0\sum_{p=0}^{n}\zeta_{n+1-p}[C_p$$
$$+ (n+p+2)(2p+2)C_{p+1} - (n+1-p)B_p]$$
$$+ \sum_{q=0}^{n}\{2q(n+q)\zeta_{n+1-q} + \zeta_{n-q}\}\sum_{p=0}^{q}\zeta_{q-p}[C_p$$
$$+ (q+p+1)(2p+2)C_{p+1} - (q-p)B_p]\Bigg].$$

For Eqs. (32),

$$f_{na} = (\alpha_0^4\bar{\rho}_1 - k^2\beta^2A_{11})A_n + kG(\beta^2A_{12}+k^2D_{11})C_n$$
$$+ \beta^2kG(2n+2)(A_{12}+A_{66})B_{n+1}$$
$$+ kG^3\Phi_0\zeta_0D_{66}(2n+2)(2n+3)C_{n+1}$$
$$+ \beta^2G^2\Phi_0A_{66}(2n+2)\sum_{p=0}^{n}(n+p+2)\zeta_{n+1-p}A_p$$
$$+ G^4\Phi_0^2\zeta_0D_{66}(2n+2)\sum_{p=0}^{n}(n+p+2)\zeta_{n+1-p}A_p$$
$$+ G^3\Phi_0D_{66}(2n+2)\sum_{q=0}^{n}\zeta_{n+1-q}\Bigg[k(2q+1)C_q$$
$$+ G\Phi_0\sum_{p=0}^{q}(q+p+1)\zeta_{q-p}A_p\Bigg]$$

$$f_{nb} = (\alpha_0^4\bar{\rho}_1 - k^2\beta^2A_{66})B_n + \beta^2G^2\Phi_0\zeta_0(2n+1)A_{22}C_n$$
$$- k\beta^2G\Phi_0(A_{12}+A_{66})\sum_{p=0}^{n}(n+p+1)\zeta_{n-p}A_p$$
$$+ \beta^2G^2\Phi_0A_{22}\sum_{p=0}^{n-1}(n+p+1)\zeta_{n-p}[2p+2)B_{p+1} + C_p]$$
$$+ G^4\Phi_0^2D_{22}\sum_{q=0}^{n}\Bigg[\{(2q+1)C_q - B_q\}$$
$$\times\sum_{p=0}^{n-q}p(n+1-q-p)\zeta_p\zeta_{n+1-q-p}$$
$$+ \{(2q+2)(2q+3)C_{q+1} + C_q\}\sum_{p=0}^{n-q}p\zeta_p\zeta_{n-q-p}\Bigg]$$
$$+ k^2G^2\Phi_0\sum_{p=0}^{n}\zeta_{n-p}[(2p+1)(D_{12}+3D_{66})C_p - 3D_{66}B_p],$$

$$f_{nc} = -kG(k^2D_{11}+\beta^2A_{12})\Phi_0\sum_{p=0}^{n}\zeta_{n-p}A_p$$
$$+ (k^4D_{11} - \alpha_0^4\bar{\rho}_1)C_n$$
$$+ \beta^2G^2\Phi_0A_{22}\sum_{p=0}^{n}\zeta_{n-p}[(2p+2)B_{p+1} + C_p]$$
$$+ G^4\Phi_0^2\zeta_0^2D_{22}(2n+2)(2n+3)C_{n+1}$$
$$+ k^2G^2\Phi_0\sum_{p=0}^{n+1}(n+p+1)\zeta_{n+1-p}[(D_{12}+3D_{66})B_p$$
$$- 2(2p+1)(D_{12}+2D_{66})C_p]$$

Downloaded 03 May 2010 to 171.66.16.20. Redistribution subject to ASME license or copyright; see http://www.asme.org/terms/Terms_Use.cfm

$$- kG^3\Phi_0^2 D_{66}\sum_{q=0}^{n+1}(n+q+1)\zeta_{n+1-q}\sum_{p=0}^{q}(q+p+1)\zeta_{q-p}A_p$$

$$+ G^4\Phi_0^2 D_{22}\sum_{q=0}^{n}\{\zeta_{n-q}+(n+q+1)(2q+1)\zeta_{n+1-q}\}$$

$$\cdot\left[\sum_{p=0}^{q+1}(q+p+1)\zeta_{a+1-p}\{(2p+1)C_p - B_p\}\right.$$

$$\left.+\sum_{p=0}^{q}\zeta_{q-p}\{(2p+2)B_{p+1}+C_p\}\right]$$

$$+ G^4\Delta_0^2\zeta_0 D_{22}(2n+2)(2n+3)\left[\sum_{p=0}^{n+1}(n+p+2)\zeta_{n+2-p}\right.$$

$$\left.\times\{(2p+1)C_p - B_p\}+\sum_{p=0}^{n}\zeta_{n+1-p}\{(2p+2)B_{p+1}+C_p\}\right].$$

Downloaded 03 May 2010 to 171.66.16.20. Redistribution subject to ASME license or copyright; see http://www.asme.org/terms/Terms_Use.cfm

Geometrically Nonlinear Stress-Deflection Relations for Thin Film/Substrate Systems With a Finite Element Comparison

C. B. Masters
411 West Drive
Boalsburg, PA 16827

N. J. Salamon
Professor,
Department of Engineering Science and Mechanics,
The Pennsylvania State University,
227 Hammond Building,
University Park, PA 16802
Mem. ASME

A new higher order geometrically nonlinear relation is developed to relate the deflection of a thin film/substrate system to the intrinsic film stress when these deflections are larger than the thickness of the substrate. Using the Rayleigh-Ritz method, these nonlinear relations are developed by approximating the out-of-plane deflections by a second-order polynomial and midplane normal strains by sixth-order polynomials. Several plate deflection configurations arise in an isotropic system: at very low intrinsic film stresses, a single, stable, spherical plate configuration is predicted; as the intrinsic film stress increases, the solution bifurcates into one unstable spherical shape and two stable ellipsoidal shapes; in the limit as the intrinsic film stress approaches infinity, the ellipsoidal configurations develop into cylindrical plate curvatures about either one of the two axes. Curvatures predicted by this new relation are significantly more accurate than previous theories when compared to curvatures calculated from three-dimensional nonlinear finite element deflection results. Furthermore, the finite element results display significant transverse stresses in a small boundary region near the free edge.

Introduction

A great deal of research is concerned with the intrinsic stresses which develop in a thin film as it is deposited onto a substrate. If the substrate is inflexible, the film's intrinsic stress may cause the film to crack or delaminate, greatly reducing the thin film's usefulness in many microelectronic and optical applications. However, if the substrate is flexible, the intrinsic stresses produce deflections in the film/substrate system which can be measured and used to determine the intrinsic stresses produced in the film during deposition. This technique for calculating intrinsic film stress, known as the beam or plate bending method, typically uses the linear relation of Stoney (1909) or Brenner and Senderoff (1949) to predict initial film stresses from measured beam curvatures (deflections). However, some film/substrate systems such as tantalum on polycarbonate are very flexible and prone to large deflections. Moreover, it has been noted that curvature measurements can be made with much greater accuracy from large deflections (Glang et al., 1965). This supplies the motivation to develop a geometrically nonlinear relation to accurately calculate intrinsic film stress from film/substrate deflection measurements (Masters and Salamon, 1991).

Starting with work by Hyer (1982), a geometrically nonlinear stress-curvature relation for the intrinsic stress in isotropic thin film systems undergoing large deflections was developed by Harper and Wu (1990) and Masters et al. (1990). This relation was derived by modeling the film/substrate system as a two-layer composite plate using nonlinear plate theory. The deformations and midplane normal strains of the thin film/substrate system were approximated by second-order polynomials with unknown coefficients. By minimizing the strain energy of the system, values of these coefficients were found which describe the equilibrium deflection configurations of the plate. For a square plate in which both film and substrate have isotropic material properties, at low stresses a single spherical plate configuration is predicted. At higher stress, however, the solution bifurcates and three equilibrium configurations are predicted: one unstable spherical shape and two stable ellipsoidal shapes. Both spherical and ellipsoidal shapes have been observed experimentally (Fahnline et al., 1991).

Subsequently, the assumptions for this model, that the x-direction midplane normal strain ϵ_x^o varies only with y, the y-direction midplane normal strain ϵ_y^o varies only with x, and the midplane shear strain $\gamma_{xy}^o = 0$, were discovered to be too restrictive. In later work Masters and Salamon (1993) system-

Contributed by the Applied Mechanics Division of THE AMERICAN SOCIETY OF MECHANICAL ENGINEERS for presentation at the International Mechanical Engineering Congress and Exhibition, the Winter Annual Meeting of The ASME, Chicago, IL, Nov. 6-11, 1994.

Discussion on this paper should be addressed to the Technical Editor, Professor Lewis T. Wheeler, Department of Mechanical Engineering, University of Houston, Houston, TX 77204-4792, and will be accepted until four months after final publication of the paper itself in the ASME JOURNAL OF APPLIED MECHANICS.

Manuscript received by the ASME Applied Mechanics Division, June 16, 1993; final revision, Nov. 23, 1993. Associate Technical Editor: J. N. Reddy.

Paper No. 94-WA/APM-10.

Copyright © 1994 by ASME
Downloaded 03 May 2010 to 171.66.16.20. Redistribution subject to ASME license or copyright; see http://www.asme.org/terms/Terms_Use.cfm

atically released these restrictions to determine their limiting effect on the original nonlinear relation. It was found that releasing the restrictions on the normal midplane strains had only a slight effect on the solution, but allowing the shear strain to vary across the plate significantly improved the nonlinear theory. The updated theory also produced improved approximate closed-form geometrically nonlinear equations for calculating intrinsic film stress from plate curvatures.

In this paper, previous nonlinear theories are extended further to produce a model of the thin film/substrate deflection which satisfies the natural boundary conditions for shear (as well as the essential kinematic conditions). The approximation equations on the midplane strains are expanded from the second-order polynomials used in the previous analyses to sixth-order polynomials which allow the shear strain to vary while maintaining the conventional plate theory boundary conditions that the shear components of in-plane force and moment vanish at the free edges. Expanding the deflection approximation from the second-order polynomial used in the previous analysis produced an unwieldy set of equations which could not be solved. While retaining the second-order deflection approximation prevents this theory from representing a complete higher order solution, the results of this analysis show notable improvement over the previous nonlinear theories, particularly in determining the intrinsic stress levels at which bifurcation in shape will occur. The plate curvatures predicted by this theory show good correlation with a three-dimensional nonlinear finite element analysis of the film/substrate system when finite element curvatures are calculated from deflection data at specified points. In agreement with plate theory, examination of the finite element transverse stress results show that these stresses are negligible throughout much of the plate, consequently they do not have a significant effect on the intrinsic film stress and curvature measurement. However, their magnitudes become significant near the free edges.

Plate Theory

The thin film/substrate system is modeled as a thin composite plate. Following classical Kirchhoff plate theory (Ugural, 1981), which assumes that transverse components of strain are negligible, the total strains can be expressed in Cartesian coordinates as

$$\epsilon_x = \epsilon_x^o - z\frac{\partial^2 w}{\partial x^2}, \quad \epsilon_y = \epsilon_y^o - z\frac{\partial^2 w}{\partial y^2}, \quad \gamma_{xy} = \gamma_{xy}^o - 2z\frac{\partial^2 w}{\partial x \partial y} \tag{1}$$

where ϵ^o and γ_{xy}^o denote midplane ($z = 0$) strain, w is the plate deflection, x and y are the in-plane global plate coordinates, and z is the out-of-plane coordinate. When deflections are large compared with the thickness of the plate, but still small compared with the x and y dimensions of the plate, nonlinear terms in the midplane strain definitions involving w cannot be neglected, while the nonlinear terms involving in-plane displacements are assumed negligible. Hence, the midplane strains are defined by the following equations:

$$\epsilon_x^o = \frac{\partial u^o}{\partial x} + \frac{1}{2}\left(\frac{\partial w}{\partial x}\right)^2, \quad \epsilon_y^o = \frac{\partial v^o}{\partial y} + \frac{1}{2}\left(\frac{\partial w}{\partial y}\right)^2,$$

$$\gamma_{xy}^o = \frac{\partial u^o}{\partial y} + \frac{\partial v^o}{\partial x} + \left(\frac{\partial w}{\partial x}\right)\left(\frac{\partial w}{\partial y}\right) \tag{2}$$

where u^o and v^o are x and y-directed midplane displacements.

Using the reduced elastic stiffnesses $\overline{Q}_{ij}$ for a linear material (Agarwal and Broutman, 1980), an equation for the strain energy density U_o^n for each layer n in the plate can be written as

$$U_o^n = \frac{1}{2}\overline{Q}_{11}^n\epsilon_x^2 + \overline{Q}_{12}^n\epsilon_x\epsilon_y + \frac{1}{2}\overline{Q}_{22}^n\epsilon_y^2 + \frac{1}{2}\overline{Q}_{66}^n\gamma_{xy}^2$$

$$- (\overline{Q}_{11}^n\epsilon_x^* + \overline{Q}_{12}^n\epsilon_y^*)\epsilon_x - (\overline{Q}_{12}^n\epsilon_x^* + \overline{Q}_{22}^n\epsilon_y^*)\epsilon_y - \overline{Q}_{66}^n\gamma_{xy}^*\gamma_{xy}$$

$$+ \frac{1}{2}\overline{Q}_{11}^n\epsilon_x^{*2} + \overline{Q}_{12}^n\epsilon_x^*\epsilon_y^* + \frac{1}{2}\overline{Q}_{22}^n\epsilon_y^{*2} + \frac{1}{2}\overline{Q}_{66}^n\gamma_{xy}^{*2}$$

$$+ \sigma_x^*\epsilon_x + \sigma_y^*\epsilon_y + \tau_{xy}^*\gamma_{xy} - \sigma_x^*\epsilon_x^* - \sigma_y^*\epsilon_y^* - \tau_{xy}^*\gamma_{xy}^* \tag{3}$$

where ϵ^*s are the elastic strains (e.g., thermal strains) and σ^*s are the intrinsic stresses. Both are assumed constant in each layer. This equation assumes at most orthotropic material properties in the layers (terms involving $\overline{Q}_{16}$ and $\overline{Q}_{26}$ have been dropped). This analysis assumes that the substrate is completely constrained from bending and stretching during film deposition and the curvature is generated after film deposition is complete and the constraints on the substrate have been released.

Displacement and Strain Fields

The fields are set for a free-free square plate of side lengths L and thickness h having zero deflection and slope at the origin of coordinates in the center and symmetry about the x and y axes. The approximation function for the deflection w is chosen to be

$$w(x, y) = \frac{1}{2}(ax^2 + by^2) \tag{4}$$

where a and b are unknown constants which physically denote curvature about y and x, respectively. This form permits four configurations: spherical ($a = b$); saddle ($a = -b$); and two ellipsoidal shapes ($a > b$ with $b \to 0$ and $a < b$ with $a \to 0$), where the limits are approached as intrinsic stress becomes large.

In choosing approximating polynomials for the midplane shear strains, this analysis begins with the natural boundary conditions on the shear components of in-plane force N_{xy} and moment M_{xy} which must vanish at the free edges:

$$N_{xy} = A_{16}\epsilon_x^o + A_{26}\epsilon_y^o + A_{66}\gamma_{xy}^o + B_{16}\kappa_x + B_{26}\kappa_y + B_{66}\kappa_{xy} = 0$$

$$M_{xy} = B_{16}\epsilon_x^o + B_{26}\epsilon_y^o + B_{66}\gamma_{xy}^o + D_{16}\kappa_x + D_{26}\kappa_y + D_{66}\kappa_{xy} = 0 \tag{5}$$

Here the A_{ij}, B_{ij}, and D_{ij} are composite coefficients defined (in matrix form) by

$$[\mathbf{A}] = \int_{-\frac{h}{2}}^{\frac{h}{2}} [\overline{\mathbf{Q}}^n]dz, \quad [\mathbf{B}] = \int_{-\frac{h}{2}}^{\frac{h}{2}} [\overline{\mathbf{Q}}^n]z dz, \quad [\mathbf{D}] = \int_{-\frac{h}{2}}^{\frac{h}{2}} [\overline{\mathbf{Q}}^n]z^2 dz \tag{6}$$

and the κ's are plate curvatures defined by

$$\kappa_x = -\frac{\partial^2 w}{\partial x^2}, \quad \kappa_y = -\frac{\partial^2 w}{\partial y^2}, \quad \kappa_{xy} = -2\frac{\partial^2 w}{\partial x \partial y}. \tag{7}$$

Since this theory is limited to orthotropic systems, the composite coefficients A_{16}, A_{26}, B_{16}, B_{26}, D_{16}, and D_{26} are zero. Also using the deflection approximation (4) in the curvature definition (7) gives $\kappa_{xy} = 0$. Substituting these into the boundary conditions (5) results in the constraint $\gamma_{xy}^o = 0$ at the free edges. (The other components of in-plane force and moment produce extremely complicated constraint equations and therefore were not considered in this analysis.) It was found by Masters and Salamon (1993) that constraining this midplane shear strain to zero everywhere in the plate proved to be extremely restrictive and that allowing the shear strain to vary across the plate significantly improved the solution. Therefore the polynomials chosen to approximate the midplane strains should satisfy the boundary condition that $\gamma_{xy}^o = 0$ at the free edges yet allow γ_{xy}^o to be nonzero elsewhere in the plate. The lowest order polynomial which will produce a variation in the shear strain while satisfying the boundary condition on shear includes the terms xy, xy^3, x^3y, and x^3y^3. Based on the procedure discussed by Hyer (1982), Harper and Wu (1990), Mas-

Downloaded 03 May 2010 to 171.66.16.20. Redistribution subject to ASME license or copyright; see http://www.asme.org/terms/Terms_Use.cfm

ters et al. (1990), Masters (1992), and Masters and Salamon (1993) for calculating the shear strain equation, to produce these odd power algebraic terms in the midplane shear strain equation, the ϵ_x^o approximation should include the even power terms y^2, x^2y^2, y^4 and x^2y^4; similarly the ϵ_y^o approximation should include the even power terms x^2, x^2y^2, x^4 and x^4y^4. Only the even powers of x and y are included in this approximation because it is assumed that each normal midplane strain is symmetric about the plate's x and y-axes. Consequently, in this expanded analysis a complete even power sixth-order polynomial is chosen to approximate each of the midplane normal strains ϵ_x^o and ϵ_y^o,

$$\epsilon_x^o = a_1 + a_2x^2 + a_3y^2 + a_4x^4 + a_5x^2y^2 + a_6y^4 + a_7x^6 + a_8x^4y^2 + a_9x^2y^4 + a_{10}y^6$$

$$\epsilon_y^o = b_1 + b_2y^2 + b_3x^2 + b_4y^4 + b_5x^2y^2 + b_6x^4 + b_7y^6 + b_8x^2y^4 + b_9x^4y^2 + b_{10}x^6 \quad (8)$$

where a_i and b_i are unknown constants. Substituting Eq. (8) and (4) into the definitions given in Eqs. (2), integrating w.r.t x or y, and specifying that $u^o = 0$ along the y-axis and $v^o = 0$ along the x-axis (based on the symmetry of the plate about the x and y-axes) produces approximating equations for the in-plane deformations u^o or v^o, respectively. Substituting these equations for deformation along with Eq. (4) for w into the midplane shear strain definition (2) yields

$$\gamma_{xy}^o = (2a_3 + 2b_3 + ab)xy + \left(\frac{2}{3}a_5 + 4b_6\right)x^3y + \left(\frac{2}{3}b_5 + 4a_6\right)xy^3 + \frac{4}{3}(a_9 + b_9)x^3y^3 + \left(\frac{2}{5}a_8 + 6b_{10}\right)x^5y + \left(\frac{2}{5}b_8 + 6a_{10}\right)xy^5. \quad (9)$$

Again invoking symmetry with respect to the x and y-axes, the coefficients on the higher order terms in ϵ_x^o and ϵ_y^o are set equal: $a_i = b_i$ for $i = 5$ through 10. Evaluating (9) at the free edges $x = L/2$ and $y = L/2$ and applying the boundary condition that $\gamma_{xy}^o = 0$ at the free edges gives three constraint equations which can be solved for three of the unknowns in terms of the others

$$a_6 = -\frac{1}{6}a_5 - \frac{1}{L^2}(2a_3 + 2b_3 + ab)$$

$$a_9 = \frac{6}{L^4}(2a_3 + 2b_3 + ab), \quad a_{10} = -\frac{1}{15}a_8. \quad (10)$$

Equilibrium Solution

The total strain energy U of the system is (Ugural and Fenster, 1987):

$$U = \int_{-\frac{h}{2}}^{\frac{h}{2}} \int_{-\frac{L}{2}}^{\frac{L}{2}} \int_{-\frac{L}{2}}^{\frac{L}{2}} U_o^n \, dx \, dy \, dz \quad (11)$$

where the integrand is given in (3). In performing the integration the definitions given in (6) are used.

To find the solution for the equilibrium shapes of the film-substrate system, values for the unknown coefficients, a, b, a_i and b_i must be found which will minimize U. Taking the first variation of the total strain energy,

$$\left[\frac{\partial U}{\partial a}\right]\delta a + \left[\frac{\partial U}{\partial b}\right]\delta b + \sum_{i=1}^{10}\left(\left[\frac{\partial U}{\partial a_i}\right]\delta a_i + \left[\frac{\partial U}{\partial b_i}\right]\delta b_i\right) = 0, \quad (12)$$

the individual variations δa, δb, δa_i, and δb_i are arbitrary, therefore their coefficients must each vanish for the entire variation to equal zero. After employing the nine constraints (Eqs. (10) and $a_i = b_i$, $i = 5$ through 10), this generates a system of 13 independent equations in terms of the 13 unknown coefficients in the system. Using the algebraic manipulation

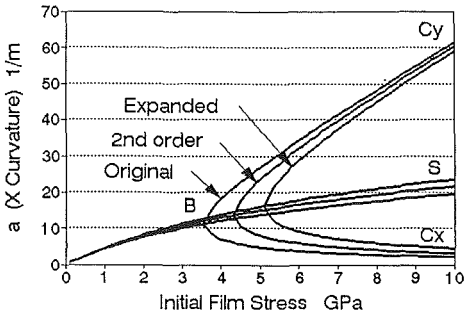


Fig. 1 Curvature versus stress: isotropic nonlinear theoretical solutions

code MACSYMA (1988), these independent equations are obtained by substituting the strain approximations into Eq. (11) via (3). Each of the a_i and b_i coefficients is solved for in terms of a and b. These equations for a_i and b_i are then substituted into the equations $\partial U/\partial a = 0$ and $\partial U/\partial b = 0$. The former is then solved for a in terms of b, and the latter for b in terms of a. The resulting equations for a and b become

$$a = -\frac{G_1b + G_2}{G_3b^2 + G_4}, \quad b = -\frac{H_1a + H_2}{H_3a^2 + H_4} \quad (13)$$

where the G's and H's are given in the Appendix. Solving Eq. (13) for a gives the fifth-order polynomial equation

$$\beta_1a^5 + \beta_2a^4 + \beta_3a^3 + \beta_4a^2 + \beta_5a + \beta_6 = 0 \quad (14)$$

where

$$\beta_1 = H_3^2G_4, \quad \beta_2 = H_3^2G_2, \quad \beta_3 = -H_1H_3G_1 + H_1^2G_3 + 2H_3H_4G_4$$

$$\beta_4 = -H_2H_3G_1 + 2H_3H_4G_2 + 2H_1H_2G_3,$$

$$\beta_5 = -H_1H_4G_1 + H_2^2G_3 + H_4^2G_4$$

$$\beta_6 = -H_2H_4G_1 + H_4^2G_2. \quad (15)$$

The roots of this equation, which are obtained numerically, appear as either 1 or 3 real roots which correspond to 1 or 3 equilibrium deflection shapes. However, because they are derived by setting the first variation of the total strain energy to zero, only configurations which minimize the total strain energy will represent stable solutions. This corresponds to configurations in which the second variation of the total strain energy is positive definite. According to elastic stability theory (Simitses, 1986), the second variation of the strain energy is positive definite if and only if the $k \times k$ Hessian determinant $|\partial^2U/\partial\alpha_i\partial\alpha_j|$, i and $j = 1$ through k, and all of its principle minors are positive definite (k is the total number of unknowns and the α_i's denote a, b, a_i, and b_i). This provides a test for stable shapes.

Theoretical Results

By setting the inelastic strains to zero, $\epsilon_x^* = \epsilon_y^* = 0$, assuming an isotropic intrinsic stress $\sigma_x^* = \sigma_y^* = \sigma^*$ in the film only (no intrinsic stress in the substrate), and varying σ^*, the film/substrate response to a range of intrinsic film stress is examined. The film properties are $E = 186$ GPa and $\nu = 0.34$. The film thickness is 500 Å (.05 μm). The material properties for the substrate are $E = 2.25$ GPa and $\nu = 0.37$. The substrate thickness is 127 μm. It should be noted that the film-to-substrate thickness ratio is less than 0.0004 strengthening the validity of the assumption that the intrinsic film stress is constant. The side dimension of the square plate is $L = 1$ cm.

It can be seen from Fig. 1 that the solution for curvature a is stress dependent and that the "original" lower order theory (Masters et al., 1990 or Harper and Wu, 1990), the second-order theory (Masters and Salamon, 1993) and the present

Downloaded 03 May 2010 to 171.66.16.20. Redistribution subject to ASME license or copyright; see http://www.asme.org/terms/Terms_Use.cfm

"expanded" theory each demonstrate the typical pitchfork bifurcation. Taking the original analysis for example, at intrinsic film stresses below point B, only a spherical solution ($a = b$) is predicted. At stresses above point B, the solution bifurcates producing three possible curvature configurations. The line BC_y represents one of the ellipsoidal curvature configurations for which the curvature is greater about the y-axis of the plate ($a > b$) developing, in the limit as $\sigma^* \to \infty$, into a cylindrical curvature about $y(b \to 0)$. Line BC_x represents the other ellipsoidal curvature configuration in which the curvature is greater about the x-axis ($a < b$) developing, in the limit as $\sigma^* \to \infty$, into a cylindrical curvature about $x(a \to 0)$. Line BS represents a spherical plate curvature where $a = b$. An identical graph for curvature b is obtained by interchanging symbols x and y.

From the stability analysis, it is found that while the spherical curvature predicted at stresses below the bifurcation stress represents a stable configuration, the spherical solution predicted above it is unstable. The two ellipsoidal solutions, either of which is equally prone to occur at stresses above the bifurcation point, both represent stable configurations.

Figure 1 also compares the results of this expanded higher order nonlinear theory to the original and expanded second-order theories over a range of intrinsic film stresses. The spherical solution predictions are nearly identical indicating that extensions of the original analysis offer little improvement to the spherical curvature solution. This is beneficial since both the original and expanded second-order theories offer closed-form equations for calculating intrinsic stress directly from curvature measurements (Fahnline et al., 1991 and Masters and Salamon, 1993). The present higher order theory proves to be too complicated for reduction to closed form. However, as can be seen in Fig. 1, the closed-form equations are only accurate up to the stress at which each solution bifurcates. At higher stresses these lower order solutions differ greatly from the higher order theory.

The intrinsic film stresses shown in these theoretical results are very high. And although some experimentally determined thin film stress results approach these magnitudes (Hudson and Somekh, 1992; Fahnline et al., 1991; and Glang et al., 1965), the theoretical results presented in this paper represent just one possible combination of film and substrate material properties and thicknesses which happen to produce large stresses. It should be noted that this theory can be applied to a wide range of film and substrate property and thickness combinations, correspondingly changing the magnitude of intrinsic film stress at which bifurcation will occur.

Finite Element Model

To verify the accuracy of the theoretical analysis, a thin film/substrate system was analyzed with finite elements using the nonlinear, large deflection capability of the ABAQUS (1991) program. (The benefit of the nonlinear finite element analysis is that it is free of the limiting assumptions imposed upon the theoretical analysis. In particular, while it does model the strains and deformations in each element with piecewise approximations, it does not place limiting restrictions on the deformations or strains over the entire plate.) The film, modeled by a single layer, 8 × 8 mesh of 8-node doubly curved shell elements, lies on top of the substrate which is modeled by a single layer, 8 × 8 mesh of 20-node quadratic displacement brick elements. The material properties used were those previously given for the theoretical analysis. Most results presented are from this model. However, to ensure that the mesh was adequately refined, a 20 × 20 mesh of elements was also analyzed. In order to facilitate the analysis of the transverse shears, the side dimension of each element in this refined mesh was 0.77 times smaller than the previous element in both the x and y directions, creating a bias in element distribution to

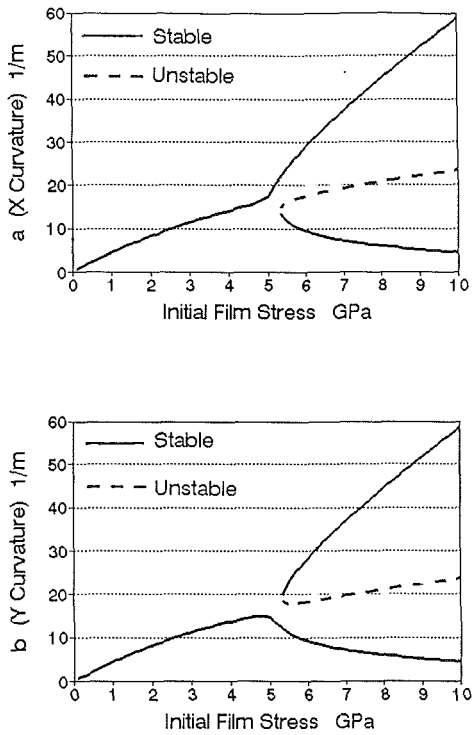


Fig. 2 Curvature versus stress: expanded higher order nonlinear theoretical solution with intrinsic film stress $\sigma_x^* = 1.0025\ \sigma_y^*$

produce a higher concentration of elements in the free edge region. The displacement and stress results were compared with the results of the 8 × 8 mesh at three different stress levels: $\sigma^* = 2.0$ GPa (spherical region), $\sigma^* = 5.2$ GPa (bifurcation region), and $\sigma^* = 8.0$ GPa (ellipsoidal region). Since all comparisons displayed identical results away from the free edge boundary region, the two solutions are convergent and both meshes are acceptable.

The finite element analysis with material isotropy and uniform loading failed to develop the ellipsoidal or cylindrical solutions at high intrinsic stresses; spherical solutions persisted beyond bifurcation. Although the spherical solution predicted by the nonlinear theory beyond bifurcation represents an unstable configuration, it is still a physically possible shape. By introducing slightly unequal intrinsic stresses into the film, under uniformly increasing magnitudes, the finite element solutions are induced through the transition from nearly spherical shapes to ellipsoidal shapes to nearly cylindrical shapes. In order to compare the theory with these finite element solutions, it must be applied to the same problem. For the chosen problem, Fig. 2 demonstrates the theoretical results at each stress level for a film/substrate system in which $\sigma_x^* = 1.0025\ \sigma_y^*$. This slight inequality in the intrinsic film stress components generates curvatures a and b which are slightly unequal below the bifurcation and significantly unequal above it.

Results

Deflection and Curvature. Figure 3 superposes theoretical and finite element results for deflection versus initial film stress for two locations on the plate: $A(x = 0.5$ cm, $y = 0)$ and $B(x = 0, y = 0.5$ cm). The finite element results display the typical pitchfork bifurcation, but are only in reasonable agreement with the second-order and higher order expanded theory. However, points A and B do not reveal the whole story. Since most experiments measure curvature, this issue will be addressed in those terms.

Curvatures are calculated from the finite element deflections

Downloaded 03 May 2010 to 171.66.16.20. Redistribution subject to ASME license or copyright; see http://www.asme.org/terms/Terms_Use.cfm

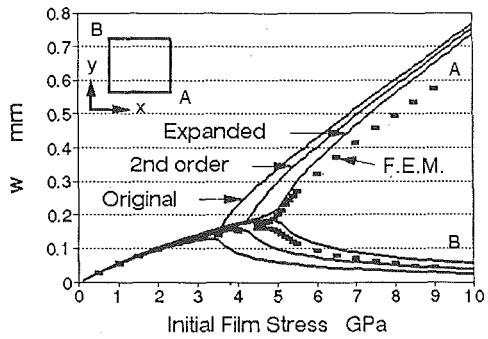


Fig. 3 Deflection versus stress: nonlinear theoretical solutions and finite element results at plate locations A (x = 0.5 cm, y = 0) and B (x = 0, y = 0.5 cm); $\sigma_x^* = 1.0025\ \sigma_y^*$

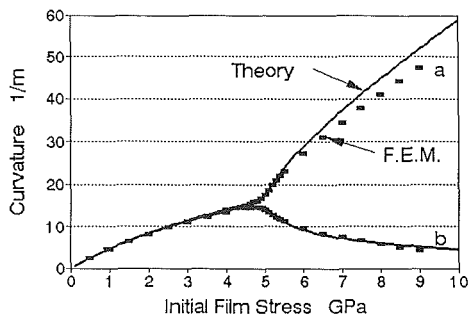


Fig. 5 Curvature versus stress: expanded higher order nonlinear theory and finite element results with a (x curvature) calculated at x = 0.25 cm, y = 0 and b (y curvature) calculated at x = 0, y = 0.25 cm; $\sigma_x^* = 1.0025\ \sigma_x^*$

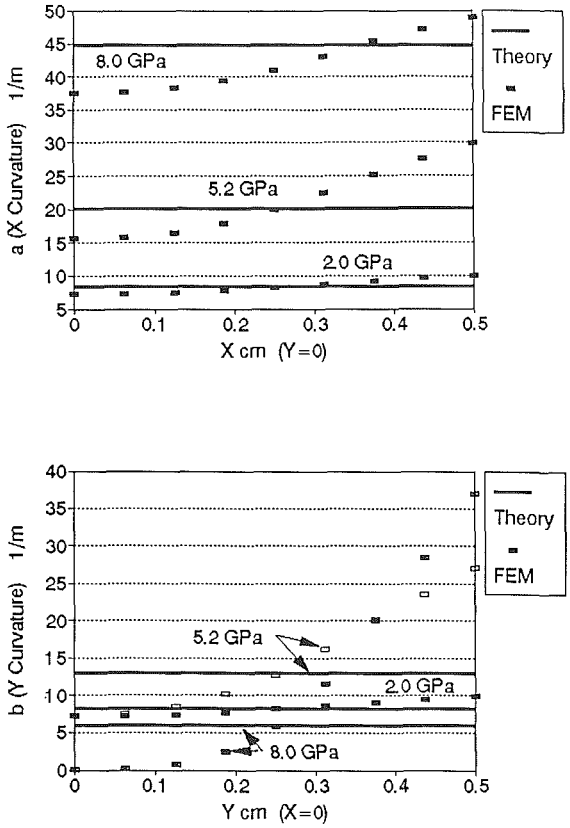


Fig. 4 Expanded higher order nonlinear theory and finite element curvatures; $a = \partial^2 w/\partial x^2$ and $b = \partial^2 w/\partial y^2$ along $y = 0$ and $x = 0$, respectively, at three stress levels: σ^* = 2.0 GPa (spherical region), σ^* = 5.2 GPa (bifurcation region), and σ^* = 8.0 GPa (ellipsoidal region). Solid lines represent the theoretical solution while squares display finite element results.

by substituting interior values into the second-order-accurate central difference expression for the second derivative and free edge values into the second-order-accurate backward difference expression (James et al., 1985). Contrary to the nonlinear theories employed which assume constant curvature everywhere across the plate, the finite element curvatures vary across the plate. This curvature variation is shown in Fig. 4 at three representative stress levels: 2.0 GPa (spherical region), 5.2 GPa (bifurcation region), and 8.0 GPa (ellipsoidal region). These plots demonstrate that for most points, the constant x-curvature a predicted by the theory approximates the finite element x-curvature most accurately near x = 0.25 cm, y = 0 (midway between the center and the edge of the plate along the x-axis). Similarly, the y-curvature b predicted by the theory approximates the finite element y-curvature most accurately near x = 0, y = 0.25 cm (midway between the center and the edge of the plate along the y-axis). If the curvatures are calculated from the finite element results at these particular points over a range of intrinsic film stresses, then as shown in Fig. 5, good agreement is obtained for spherical and the lesser post-bifurcation curvature and improved agreement is obtained for the greater post-bifurcation curvature. Clearly even the expanded higher order theory errs at large curvatures generated by extreme intrinsic stresses.

Transverse Stresses. These theories totally fail to predict transverse (z-component) stresses because they are founded upon classical laminate theory (Agarwal and Broutman, 1980) which assumes them to be negligible. However, the finite element solutions approximate them and representative distributions 26.8 μm below the interface are shown in Figs. 6–8. The transverse normal stress σ_z versus x at y = 0.16 cm, Fig. 6, achieves the largest magnitude near the free edge where layered composite theory predicts it to contain a low-order singularity (Wang and Choi, 1982); σ_z versus y along x = 0.16 cm is similar and not shown. The transverse shear stress τ_{xz} versus x at y = 0.16 cm shown in Fig. 7(a) is an order of magnitude less than σ_z and appears to rise without bound, but in the expanded scale of Fig. 7(b), the trend to satisfy the free edge condition is obvious with an exception at the highest intrinsic stress for which the finite element mesh lacks adequate resolution to capture the return to zero; the distribution along y is of a singular nature, but for the most part is insignificant in magnitude, hence is not shown. The shear stress τ_{yz} versus y at x = 0.16 cm is shown in Fig. 8 over a portion of the expanded scale only. Interestingly its rate of increase with intrinsic stress clearly decreases except very near the free edge. This is because at high intrinsic stress, the dominant curvature is about y (see fig. 5) and as the cylindrical shape is approached, further distortion in the yz-plane is nil away from free edges. Notably τ_{yz} tends toward satisfaction of the free-edge condition and tends to zero as y approaches zero, though not shown; the distribution along x is of a singular nature, but for the most part is insignificant in magnitude, hence is not shown. All transverse stresses display significant activity only within a boundary region 0.01 cm along the free edges and only τ_{xz} persists with low-grade activity into the interior region. If one refers to free edge effects in anisotropic, layered composite research, the latter is in agreement with it, but the former is not; Pipes and Pagano (1970) for extension and Salamon (1978, 1981) for bending report the extent of the boundary region on the order of a layer thickness.

Conclusions

A higher order approximate theory has been developed for calculating curvatures in thin film/substrate systems generated

Downloaded 03 May 2010 to 171.66.16.20. Redistribution subject to ASME license or copyright; see http://www.asme.org/terms/Terms_Use.cfm

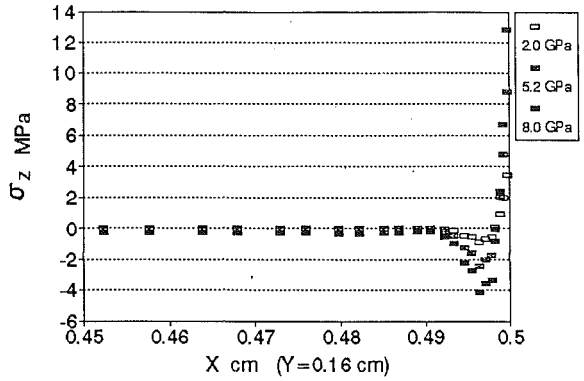


Fig. 6 Finite element results for out-of-plane stress σ_z along y = 0.16 cm and x = 0.16 cm at three stress levels: σ^* = 2.0 GPa (spherical region), σ^* = 5.2 GPa (bifurcation region), and σ^* = 8.0 GPa (ellipsoidal region)

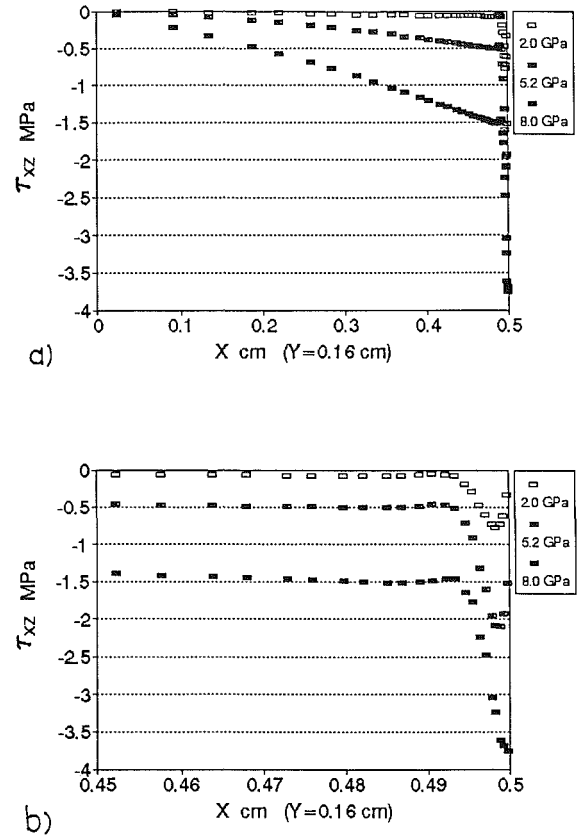


Fig. 7 Finite element results for interlaminar shear stress τ_{xz} along y = 0.16 cm at three stress levels: σ^* = 2.0 GPa (spherical region), σ^* = 5.2 GPa (bifurcation region), and σ^* = 8.0 GPa (ellipsoidal region); (*a*) normal scale, (*b*) expanded scale

by intrinsic stresses in the film. The theory compares well with a full three-dimensional finite element analysis if results are sampled at midpoints on the in-plane, centrally located axes. For system deflections or curvatures, the agreement is excellent in the spherical and bifurcation regimes of response, but grows increasingly less so for high curvatures generated by extreme post-bifurcation intrinsic stresses as the cylindrical regime is approached. For intrinsic stresses decreasing in value from the bifurcation point, a previous second-order theory is also accurate and with further stress reductions, even lower order theories will suffice. The previous lower order theories have the advantage of being in closed form. The high order theory, especially if programmed into a computer, has considerable

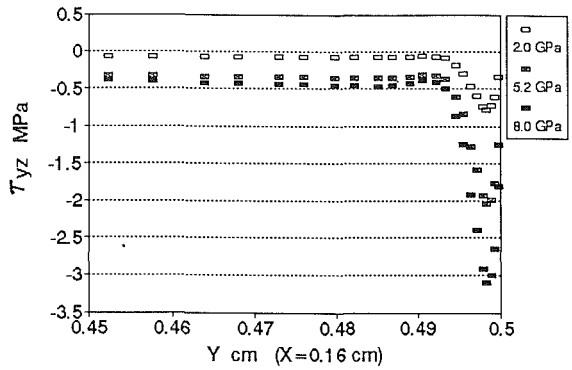


Fig. 8 Finite element results for interlaminar shear stress τ_{yz} along x = 0.16 cm at three stress levels: σ^* = 2.0 GPa (spherical region), σ^* = 5.2 GPa (bifurcation region), and σ^* = 8.0 GPa (ellipsoidal region); expanded scale

advantage over finite element analysis because it is faster and requires significantly less processing power and memory.

However, all previous theories cannot calculate transverse stresses in the system; the finite element method can. Such stresses, though singular, are generally of low order and appreciable magnitudes are confined to a free-edge boundary region of inward extend on the order of the thin film/substrate thickness. Hence they have little effect on intrinsic film stress and curvature measurements, but should be of interest to those dealing with system integrity and failure.

Acknowledgments

The authors thank R. F. Messier for suggesting the original problem, L.J. Pilioine for many useful discussions and especially D. Fahnline for closer interactions. The finite element analysis was conducted through supercomputing grants from both the National Center for Supercomputing Applications and the Cornell Theory Center. C. Masters is grateful for the support of the Academic Computing Fellowship funded through the Pennsylvania State University with partial support from the IBM Corporation.

References

ABAQUS User's Manual, 1991, HKS Inc., Pawtucket, RI.

Agarwal, B. D., and Broutman, L. J., 1980, *Analysis and Performance of Fiber Composites*, John Wiley and Sons, New York.

Brenner, A., and Senderoff, S., 1949, "Calculation of Stress in Electrodeposits from the Curvature of a Plated Strip," National Bureau of Standards No. RP1954, Vol. 42, pp. 105–123.

Fahnline, D. E., Masters, C. B., and Salamon, N. J., 1991, "Thin Film Stress From Nonspherical Substrate Bending Measurements," *Journal of Vacuum Science and Technology A*, Vol. 9, pp. 2483–2487.

Glang, R., Holmwood, R. A., and Rosenfeld, R. L., 1965, "Determination of Stress in Films on Single Crystalline Silicon Substrates," *Review of Scientific Instruments*, Vol. 36, pp. 7–10.

Harper, B. D., and Wu, C. P., 1990, "A Geometrically Nonlinear Model for Predicting the Intrinsic Film Stress by the Bending-Plate Method," *International Journal of Solids and Structures*, Vol. 26, pp. 511–525.

Hudson, C., and Somekh, R. E., 1992, "Stresses in UHV Planar Magnetron Sputtered Films," *Materials Research Society Symposium Proceedings, Thin Films: Stresses and Mechanical Properties III.*, W. D. Nix et al., eds., Materials Research Society, Pittsburgh, PA, Vol. 239, pp. 145–150.

Hyer, M. W., 1982, "The Room-Temperature Shapes of Four-Layer Unsymmetric Cross-Ply Laminates," *Journal of Composite Materials*, Vol. 16, pp. 318–340.

James, M. L., Smith, G. M., and Wolford, J. C., 1985, *Applied Numerical Methods for Digital Computation*, Harper and Row, New York.

MACSYMA Reference Manual, 1988, Version 13, Symbolics Inc., Cambridge, MA.

Masters, C. B., and Salamon, N. J., 1993, "Geometrically Nonlinear Stress-Deflection Relations for Thin Film/Substrate Systems," *International Journal of Engineering Science*, Vol. 31, No. 6, pp. 915–925.

Masters, C. B., 1992, "A Geometrically Nonlinear Stress-Deflection Relation for Thin Film/Substrate Systems," Ph.D. Thesis, The Pennsylvania State University, University Park, PA.

Downloaded 03 May 2010 to 171.66.16.20. Redistribution subject to ASME license or copyright; see http://www.asme.org/terms/Terms_Use.cfm

Masters, C. B., and Salamon, N.J., 1991, "Practical Application of a Geometrically Nonlinear Stress-Curvature Relation," *Materials Research Society Symposium Proceedings, Thin Films: Stresses and Mechanical Properties III*, W. D. Nix et al., ed., Materials Research Society, Pittsburgh, PA, Vol. 239, pp. 293–298.

Masters, C. B., Salamon, N. J., and Fahnline, D. E., 1990, "Deflection Shapes Due to Intrinsic Stress in Thin Films," *Materials Research Society Symposium Proceedings, Thin Films: Stresses and Mechanical Properties II.*, M. F. Doerner et al., ed., Materials Research Society, Pittsburgh, PA, Vol. 188, pp. 21–27.

Pipe, R. Byron, and Pagano, N. J., 1970, "Interlaminar Stresses in Composite Materials under Uniform Axial Extension," *Journal of Composite Materials*, Vol. 4, pp. 538–548.

Salamon, N. J., 1981, "Stress Distribution in Sandwich Beams in Uniform Bending," *Test Methods and Design Allowables for Fibrous Composites,* ASTM STP 734, C. C. Chamis, ed., ASTM, Philadelphia, PA, pp. 166–177.

Salamon, Nicholas J., 1978, "Interlaminar Stresses in a Layered Composite Laminate in Bending," *Fiber Science and Technology*, Vol. 11, pp. 305–317.

Simitses, G. J., 1986, *An Introduction to the Elastic Stability of Structures*, Robert E. Krieger Publishing Company, FL.

Stoney, G. G., 1909, "The Tension of Metallic Films Deposited by Electrolysis," *Proceedings of the Royal Society of London*, Vol. A82, pp. 172–175.

Ugural, A. C., and Fenster, S. K., 1987, *Advanced Strength and Applied Elasticity*, Elsevier, New York.

Ugural, W. C., 1981, *Stresses in Plates and Shells*, McGraw-Hill, New York.

Wang, S. S., and Choi, I.,1982, "Boundary-Layer Effects in Composite Laminates:" ASME JOURNAL OF APPLIED MECHANICS, Vol. 49, "Part 1—Free-Edge Stress Singularities," pp. 541–548; "Part 2—Free-Edge Stress Solutions and Basic Characteristics," pp. 549–560.

APPENDIX

$$G_1 = H_1 = D_{12}k_1 - A_{11}B_{12}B_{22} + A_{12}(B_{11}B_{22} + B_{12}^2) - A_{22}B_{11}B_{12}$$

$$G_2 = (A_{12}B_{12} - A_{22}B_{11})(N_{x\epsilon}^* - N_{x\sigma}^*) + (A_{12}B_{11} - A_{11}B_{12})(N_{y\epsilon}^* - N_{y\sigma}^*) + (M_{x\epsilon}^* - M_{x\sigma}^*)k_1$$

$$G_3 = H_3 = \text{Num/Den}$$

$$G_4 = D_{11}k_1 - A_{11}B_{12}^2 + 2A_{12}B_{11}B_{12} - A_{22}B_{11}^2$$

$$H_2 = (A_{12}B_{22} - A_{22}B_{12})(N_{x\epsilon}^* - N_{x\sigma}^*) + (A_{12}B_{12} - A_{11}B_{22})(N_{y\epsilon}^* - N_{y\sigma}^*) + (M_{y\epsilon}^* - M_{y\sigma}^*)k_1$$

$$H_4 = D_{22}k_1 - A_{11}B_{22}^2 + 2A_{12}B_{12}B_{22} - A_{22}B_{12}^2$$

where

$$k_1 = A_{11}A_{22} - A_{12}^2$$

$$\text{Num} = L^4(A_{11}A_{22} - A_{12}^2)^2\{A_{66}[12745920A_{11}^2A_{12}A_{22}^2 - 452800A_{11}A_{12}^3A_{22} + (A_{11} + A_{22})(9748800A_{11}^2A_{22}^2 - 510160A_{11}A_{12}^2A_{22} + 800A_{12}^4) + (A_{11}^2 + A_{22}^2)(6372960A_{11}A_{12}A_{22} - 187200A_{12}^3) + (A_{11}^3 + A_{22}^3)(3249600A_{11}A_{22} - 156720A_{12}^2)] + 338400A_{11}^3A_{22}^3 - 353794A_{11}^2A_{12}^2A_{22}^2 - 61928A_{11}A_{12}^4A_{22} + (A_{11} + A_{22})(385146A_{11}^2A_{12}A_{22}^2 - 462868A_{11}A_{12}^3A_{22} + 400A_{12}^5) + (A_{11}^2 + A_{22}^2)(225600A_{11}^2A_{22}^2 - 194636A_{11}A_{12}^2A_{22} - 30964A_{12}^4) + (A_{11}^3 + A_{22}^3)(128382A_{11}A_{12}A_{22} - 51060A_{12}^3) + (A_{11}^4 + A_{22}^4)(56400A_{11}A_{22} - 17739A_{12}^2)\}$$

$$\text{Den} = 14400A_{66}[1515200A_{11}^3A_{22}^3 - 604728A_{11}^2A_{12}^2A_{22}^2 + 13472A_{11}A_{12}^4A_{22} + (A_{11} + A_{22})(981112A_{11}^2A_{12}A_{22}^2 - 57168A_{11}A_{12}^3A_{22}) + (A_{11}^2 + A_{22}^2)(920080A_{11}^2A_{22}^2 - 308600A_{11}A_{12}^2A_{22} + 5136A_{12}^4) + (A_{11}^3 + A_{22}^3)(318648A_{11}A_{12}A_{22} - 9360A_{12}^3) + (A_{11}^4 + A_{22}^4)(162480A_{11}A_{22} - 7836A_{12}^2)] + 144[32188780A_{11}^3A_{12}A_{22}^3 - 33635600A_{11}^2A_{12}^3A_{22}^2 + 673600A_{11}A_{12}^5A_{22} + (A_{11} + A_{22})(23151300A_{11}^3A_{22}^3 - 22300360A_{11}^2A_{12}^2A_{22}^2 - 1237550A_{11}A_{12}^4A_{22}) + (A_{11}^2 + A_{22}^2)(16736300A_{11}^2A_{12}A_{22}^2 - 16993100A_{11}A_{12}^3A_{22} + 256800A_{12}^5) + (A_{11}^3 + A_{22}^3)(8187100A_{11}^2A_{22}^2 - 7972745A_{11}A_{12}^2A_{22} - 21050A_{12}^4) + (A_{11}^4 + A_{22}^4)(641910A_{11}A_{12}A_{22} - 255300A_{12}^3) + (A_{11}^5 + A_{22}^5)(282000A_{11}A_{22} - 88695A_{12}^2)]$$

and

$$\{N_\sigma^*\} = \int_{-\frac{h}{2}}^{\frac{h}{2}} \{\sigma^*\}dz, \quad \{N_\epsilon^*\} = \int_{-\frac{h}{2}}^{\frac{h}{2}} [\overline{\mathbf{Q}}^n]\{\epsilon^*\}dz$$

$$\{M_\sigma^*\} = \int_{-\frac{h}{2}}^{\frac{h}{2}} \{\sigma^*\}zdz, \quad \{M_\epsilon^*\} = \int_{-\frac{h}{2}}^{\frac{h}{2}} [\overline{\mathbf{Q}}^n]\{\epsilon^*\}zdz.$$

Downloaded 03 May 2010 to 171.66.16.20. Redistribution subject to ASME license or copyright; see http://www.asme.org/terms/Terms_Use.cfm

Nonlinear Spatial Equilibria and Stability of Cables Under Uni-axial Torque and Thrust

C.-L. Lu
Graduate Student Research Assistant.

N. C. Perkins
Associate Professor,
Mem. ASME.

Department of Mechanical Engineering
and Applied Mechanics,
The University of Michigan,
Ann Arbor, MI 48109-2125

Low tension cables subject to torque may form complex three-dimensional (spatial) equilibria. The resulting nonlinear static deformations, which are dominated by cable flexure and torsion, may produce interior loops or kinks that can seriously degrade the performance of the cable. Using Kirchhoff rod assumptions, a theoretical model governing cable flexure and torsion is derived herein and used to analyze (1) globally large equilibrium states, and (2) local equilibrium stability. For the broad class of problems described by pure boundary loading, the equilibrium boundary value problem is integrable and admits closed-form elliptic integral solutions. Attention is focused on the example problem of a cable subject to uni-axial torque and thrust. Closed-form solutions are presented for the complex three-dimensional equilibrium states which, heretofore, were analyzed using purely numerical methods. Moreover, the stability of these equilibrium states is assessed and new and important stability conclusions are drawn.

1 Introduction

Cables are versatile structural elements that are employed in a wide range of engineering applications. For instance, cables serve as mooring, towing, and haul lines, as umbilicals and tethers; and as electrical and optical signal transmission lines. In all these applications, the overall flexibility of the cable renders it susceptible to large deformations that may impair its performance.

This investigation is motivated in part by an undesirable static response of cables referred to herein as *hockling*. The term hockling follows that used by Rosenthal (1975 and 1976) and describes the formation of an interior loop (Zajac, 1962; Yabuta et al., 1982; Coyne 1990) or kink (Liu, 1975; Ross, 1977; Yabuta, 1984) in an otherwise straight cable.[1] For example, fiber optic cables are susceptible to hockling during ocean deployment. Initially wound on spools, fiber optic cables are paid out with slight residual torsion and significant tension. As the cable lays down on the sea bed, the tension is reduced and the torsion may be sufficiently large to induce a three-dimensional buckling of the cable leading to an interior loop. Upon subsequent retensioning, the loop, if stable, may eventually kink the cable rendering it useless for signal transmission.

The mechanisms responsible for hockling are largely controlled by cable flexure and torsion. Thus, a fundamental problem of interest is the elastic stability of a straight rod subject to steady end torque and thrust; a local analysis of which was first presented by Greenhill in 1883 (Timoshenko and Gere, 1961). Further local analyses of classes of conservative and nonconservative rod elastic stability problems are summarized by Bolotin (1963), Ziegler (1968) and Leipholz (1980). The classical theory of generally curved and twisted rods began with the work of Kirchhoff and Clebsch and is summarized in Love (1944). Antman (1974) provides a comprehensive review of all rational rod theories. The large buckled states of nonlinearly elastic rods under torsion, thrust, and gravity are specifically considered by Antman and Kenney (1981) who employ a director theory for rods.

Investigations specific to cable hockling begin with the analytical study of Zajac (1962) who focuses on the stability of a planar loop to out-of-plane perturbations, the so-called "pop-out" phenomenon. Closed-form instability conditions are found for cable loop segments forming (1) a circle with one complete twist, and (2) a planar, noninflectional elastica. The initiation of a loop in a straight cable is addressed in the study of Liu (1975) who proposed an instability condition based on Greenhill's analysis for cables of infinite length. Considering finite length cables, Rosenthal (1975 and 1976) provides a nonlinear extension to Greenhill's problem by numerically evaluating the large post-buckled equilibrium states of cables with ends unrestrained in rotation. Shortly following, Ross (1977) concludes that Greenhill's result may only provide an

[1] As noted by Myers et al. (1969), Ross (1977) use the term *hockling* to describe a phenomenon also known as *birdcaging* of standard cables (Rosenthal, 1975 and 1976).

Contributed by the Applied Mechanics Division of THE AMERICAN SOCIETY OF MECHANICAL ENGINEERS for presentation at the International Mechanical Engineering Congress and Exhibition, the Winter Annual Meeting of The ASME, Chicago, IL, Nov. 6–11, 1994.

Discussion on this paper should be addressed to the Technical Editor, Professor Lewis T. Wheeler, Department of Mechanical Engineering, University of Houston, Houston, TX 77204-4792, and will be accepted until four months after final publication of the paper itself in the ASME JOURNAL OF APPLIED MECHANICS.

Manuscript received by the ASME Applied Mechanics Division, July 19, 1993. Associate Technical Editor: J. N. Reddy.

Paper No. 94-WA/APM-3.

Copyright © 1994 by ASME
Downloaded 03 May 2010 to 171.66.16.20. Redistribution subject to ASME license or copyright; see http://www.asme.org/terms/Terms_Use.cfm

upper bound to the loading levels required to initiate loop formation. This conclusion, however, follows from the assumptions of an ideal circular cable loop within an infinite cable. By assuming an ideal helical cable shape and ends completely restrained in rotation, Yabuta et al. (1982 and 1984) analyze (1) the formation of a loop in a twisted but otherwise straight cable, and (2) the subsequent pop-out stability of the loop. This same problem was recently addressed by Coyne (1990) who relaxes the assumption of helical cable geometry. Coyne (1990) provides closed-form results for both the looping instability and the pop-out instability using the three-dimensional elastica theory summarized in Love (1944). The same elastica formulation is employed by Tan and Witz (1993) who evaluate the three-dimensional equilibrium states that form in response to terminal moments.

Rosenthal (1975 and 1976) extends the local analysis of Greenhill by numerically evaluating the three-dimensional, post-buckled equilibrium states of cables under uni-axial torque and thrust. The stability of these computed equilibrium states, however, was never assessed and thus the question remains as to whether such states are always attainable. A partial answer is found in the stability analyses of (Maddocks, 1984) and (Perkins and Chirehdast, 1990) who demonstrate that the *planar* loops (formed by planar elasticas under large thrust) are always unstable with respect to out-of-plane disturbances (pop-out) and are frequently unstable with respect to in-plane disturbances. This paper extends these stability results to the complex *spatial* (three-dimensional) elasticas formed under combined uni-axial torque and thrust. Using Kirchhoff rod assumptions, a theoretical model is derived that governs (1) globally large static deformations, and (2) local equilibrium stability. The associated equilibrium boundary value problem is cast in an integrable form that permits the closed-form analysis of the complex, three-dimensional equilibrium states determined numerically in Rosenthal (1975, 1976). The stability of these equilibrium states is assessed leading to new and important stability conclusions.

2 Model for Cable Flexure/Torsion

A continuum model is developed that describes the two-axis flexure and torsion of an elastic cable. Hamilton's principle is employed to derive the equations of motion governing the three-dimensional displacement and rotation of the cable about a generally curved three-dimensional equilibrium state. The equilibrium state is formed in response to the steady external load system shown in Fig. 1(*a*) which consists of the boundary load system ($\mathbf{F}_0$, $\mathbf{F}_L$, $\mathbf{M}_0$, $\mathbf{M}_L$) and the domain load $\mathbf{Q}$. In Fig. 1, $S \in [0, L]$ denotes the arc length coordinate measured along the equilibrium cable centerline χ^i and ($\mathbf{e}_1$, $\mathbf{e}_2$, $\mathbf{e}_3$) is the Cartesian triad fixed at $S = 0$. $\boldsymbol{R}^i(S)$ locates a material point on χ^i and $\boldsymbol{R}^i(L) = D\mathbf{e}_1$ locates that at the right end. In response to a disturbance, the cable centerline deflects to the final configuration illustrated by χ^f in Fig. 1(*b*).

The position vector $\boldsymbol{R}^f(S, T)$ locates a material point on χ^f following the three-dimensional displacement

$$\mathbf{U}(S, T) = U_1(S, T)\mathbf{l}_1^i + U_2(S, T)\mathbf{l}_2^i + U_3(S, T)\mathbf{l}_3^i. \quad (1)$$

Here, $\mathbf{U}(S, T)$ is resolved into components aligned with the Serret-Frenet triad (tangential $\mathbf{l}_1^i$, normal $\mathbf{l}_2^i$, and binormal $\mathbf{l}_3^i$ unit vectors) defined by χ^i and T denotes time.

The cable is modeled as a linearly elastic rod of uniform circular cross-section obeying Kirchhoff assumptions for rod deformation (Love, 1944). These assumptions lead to the following expressions for the curvature components K_2^f (along $\mathbf{l}_2^i$), K_3^f (alone $\mathbf{l}_3^i$), the twist Ω^f (along $\mathbf{l}_1^i$), and the axial strain ϵ^f of χ^f all accurate to second order in the deformation field variables:

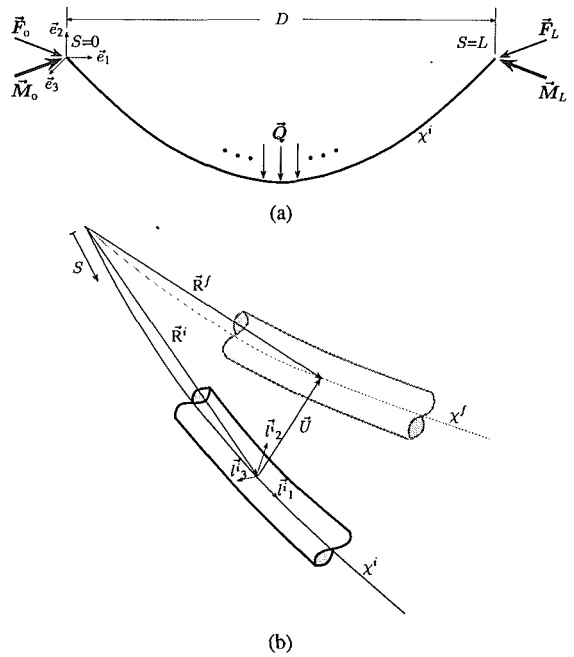


Fig. 1 (*a*) **Cable of length L held in equilibrium under domain loading Q, external end forces F_0 and F_L, and external end moments M_0 and M_L. The equilibrium cable centerline, χ^i, has arc length coordinate S. (*b*) Equilibrium (χ^i) and final (χ^f) configurations of cable centerline. Displacement from χ^i is referenced to Serret-Frenet triad (l_1^i, l_2^i, l_3^i) defined by χ^i.**

$$K_2^f = \frac{M_3^i}{EI} + a_{2,S} - \Gamma^i a_3 + a_{3,S}a_4 - \frac{1}{2}K^i(a_3^2 + a_4^2) + \Gamma^i a_2 a_4 + oh(3),$$

$$K_3^f = -a_{3,S} + K^i a_4 - \Gamma^i a_2 + a_{2,S}a_4 - \Gamma^i a_3 a_4 + oh(3),$$

$$\Omega^f = \frac{M_1^i}{GJ} + a_{4,S} + K^i a_3 + a_{2,S}a_3 - \frac{1}{2}\Gamma^i(a_2^2 + a_3^2) + oh(3),$$

$$\epsilon^f = \frac{F_1^i}{EA} + a_1 + \frac{1}{2}(a_2^2 + a_3^2) + oh(3), \quad (2)$$

where

$$\frac{M_3^i}{EI} = K^i, \ \frac{M_1^i}{GJ} = \Omega^i, \ \frac{F_1^i}{EA} = \epsilon^i,$$

$$a_1 = U_{1,S} - K^i U_2, \ a_2 = U_{2,S} + K^i U_1 - \Gamma^i U_3,$$

$$a_3 = U_{3,S} + \Gamma^i U_2, \ a_4 = U_\theta. \quad (3)$$

In the above, M_1^i and M_3^i represent the equilibrium internal torque and moment along $\mathbf{l}_1^i$ and $\mathbf{l}_3^i$, respectively, and $\mathbf{F}^i$ is the equilibrium internal axial force (along $\mathbf{l}_1^i$). The quantities E, G, A, I, and J represent Young's modulus, the shear modulus, the cross-sectional area, principal area moment and the polar area moment, respectively. In addition, $K^i(S)$ and $\Gamma^i(S)$ denote the principal curvature and geometric torsion of χ^i. The final twist, Ω^f, is the combination of the geometric torsion and the angle of twist, in which $\mathbf{U}_\theta(S, T)$ denotes the (rigid) rotation of the cross-section about $\mathbf{l}_1^i$ (Alexander and Antman, 1982).

The preceding relations are utilized in the following expression for the cable strain energy:

$$\Pi_V = \frac{1}{2}\int_0^L [EA(\epsilon^f)^2 + EI(K_2^f)^2 + EI(K_3^f)^2 + GJ(\Omega^f)^2]dS. \quad (4)$$

The cable kinetic energy becomes

$$\Pi_T = \frac{1}{2}\int_0^L [\rho A(U_{1,T}^2 + U_{2,T}^2 + U_{3,T}^2) + \rho J U_{\theta,T}^2]dS, \quad (5)$$

where ρ is the cable density. The virtual work done by the external loading shown in Fig. 1(*a*) is

Downloaded 03 May 2010 to 171.66.16.20. Redistribution subject to ASME license or copyright; see http://www.asme.org/terms/Terms_Use.cfm

$$\delta W=\int_0^L \mathbf{Q}\cdot\delta\mathbf{U}dS+[\mathbf{F}_0\cdot\delta\mathbf{U}]|_{S=0}+[\mathbf{F}_L\cdot\delta\mathbf{U}]|_{S=L}$$
$$+[\mathbf{M}_0\cdot\{(\delta a_4+a_2\delta a_3)\mathbf{l}_1^i-(\delta a_3+a_4\delta a_2)\mathbf{l}_2^i$$
$$+(\delta a_2+a_1\delta a_2+a_3\delta a_4)\mathbf{l}_3^i\}]|_{S=0}+[\mathbf{M}_L\cdot\{(\delta a_4+a_2\delta a_3)\mathbf{l}_1^i$$
$$-(\delta a_3+a_4\delta a_2)\mathbf{l}_2^i+(\delta a_2+a_1\delta a_2+a_3\delta a_4)\mathbf{l}_3^i\}]|_{S=L}. \quad (6)$$

Equations (4), (5), and (6) are used in Hamilton's principle

$$\int_{T_1}^{T_2}(\delta\Pi_T-\delta\Pi_V+\delta W)dT=0, \quad (7)$$

and lead to the ensuing equilibrium and response problems.

3 Equilibrium Boundary Value Problem

The terms of first order in the deformation field variables in (7) lead to the cable equilibrium equations and the associated boundary terms. Utilizing the nondimensional variables defined in Appendix A, the four equilibrium field equations

$$\kappa\kappa'+p'+\mathbf{q}\cdot\mathbf{l}_1^i=0, \quad (8)$$
$$-\kappa''+p\kappa+\kappa\tau^2-\kappa h\tau+\mathbf{q}\cdot\mathbf{l}_2^i=0, \quad (9)$$
$$-2\kappa'\tau-\kappa\tau'+(\kappa h)'+\mathbf{q}\cdot\mathbf{l}_3^i=0, \quad (10)$$
$$h'=0, \quad (11)$$

govern the equilibrium curvature $\kappa(s)$, geometric torsion $\tau(s)$, internal axial force $p(s)$, and internal torque $h(s)$. The associated boundary terms are

$$[(-p+f_0b_1^0)\delta u_1+(\kappa'+f_0b_2^0)\delta u_2+(\kappa\tau-\kappa h+f_0b_3^0)\delta u_3]|_{s=0}$$
$$+[(-p+f_1b_1^1)\delta u_1+(\kappa'+f_1b_2^1)\delta u_2+(\kappa\tau-\kappa h+f_1b_3^1)\delta u_3]|_{s=1}$$
$$+[(-\kappa+m_0c_3^0)\delta u_2'+(-h+m_0c_1^0)\delta u_\theta]|_{s=0}$$
$$+[(-\kappa+m_1c_3^1)\delta u_2'+(-h+m_1c_1^1)\delta u_\theta]|_{s=1}=0 \quad (12)$$

from which problem specific boundary conditions can be extracted. The following direction cosine definitions are employed in the foregoing equations

$$b_k^0=\cos(\mathbf{F}_0,\mathbf{l}_k^i),\quad b_k^1=\cos(\mathbf{F}_L,\mathbf{l}_k^i),$$
$$c_k^0=\cos(\mathbf{M}_0,\mathbf{l}_k^i),\quad c_k^1=\cos(\mathbf{M}_L,\mathbf{l}_k^i),\quad k=1,2,3. \quad (13)$$

3.1 Integrable Case: Pure Boundary Loading. For the cases of pure bounding loading, ($\mathbf{q}$ = 0), the field Eqs. (8)–(11) are integrable and admit a general, closed-form elliptic integral solution. The integrability of the boundary value problem in this case follows from "Kirchhoff's kinetic analogue" (Love, 1944). To this end, the Eqs. (8)–(11) can be reduced to a single equation in the unknown curvature $\kappa(s)$. Integrating (8), (10), and (11), and then substituting the results into (9) provides the uncoupled equation for the curvature:

$$\kappa''+\left(\frac{1}{2}\kappa^2-d_1+\frac{d_3^2}{4}\right)\kappa-\frac{d_2^2}{\kappa^3}=0. \quad (14)$$

Here, the constants d_1, d_2, and d_3 are first integrals of (8), (10), and (11), given by

$$d_1=p+\frac{1}{2}\kappa^2,\quad d_2=\left(\tau-\frac{h}{2}\right)\kappa^2,\quad d_3=h, \quad (15)$$

respectively. Next, integrating (14) and using the substitution $\sigma=\kappa^2$ leads to the first-order equation

$$(\sigma')^2+\sigma^3+(-4d_1+d_3^2)\sigma^2+8d_4\sigma+4d_2^2=0, \quad (16)$$

where d_4 is a fourth constant of integration. Attention will focus on the fundamental (symmetric) solution for which σ achieves the extremum value σ_m at the midspan s = 1/2; i.e., $\sigma'(1/2)=0$. The five constants (d_1, d_2, d_3, d_4, σ_m) are then related through (16):

$$\sigma_m^3+(-4d_1+d_3^2)\sigma_m^2+8d_4\sigma_m+4d_2^2=0. \quad (17)$$

Substituting $\xi=\sigma_m-\sigma$ into (16) yields the factored form

$$(\xi')^2-\xi(\xi-Y_1)(\xi-Y_2)=0, \quad (18)$$

where

$$Y_{1,2}=\frac{(3\sigma_m-4d_1+d_3^2)\mp\sqrt{(3\sigma_m-4d_1+d_3^2)^2+4\left[\frac{4d_2^2}{\sigma_m}-2\sigma_m^2+\sigma_m(4d_1-d_3^2)\right]}}{2}. \quad (19)$$

The final substitutions of

$$\varphi=\sin^{-1}\sqrt{\frac{\xi}{Y_1}}\ \text{and}\ Y^2=\frac{Y_1}{Y_2}$$

reduce (18) to standard form (Ames, 1968) for which the solution becomes

$$s=\frac{2}{\sqrt{Y_2}}\left[\mathbf{F}\left(Y,\sin^{-1}\sqrt{\frac{\xi}{Y_1}}\right)-\mathbf{F}\left(Y,\sin^{-1}\sqrt{\frac{\xi_0}{Y_1}}\right)\right]. \quad (20)$$

Here,

$$\mathbf{F}\left(Y,\sin^{-1}\sqrt{\frac{\xi}{Y_1}}\right)=\int_0^{\sin^{-1}\sqrt{\frac{\xi}{Y_1}}}\frac{d\varphi}{[1-Y^2\sin^2\varphi]^{1/2}},$$
$$0\le Y\le 1,\quad 0\le\frac{\xi}{Y_1}\le 1 \quad (21)$$

is an incomplete elliptic integral of the first kind, and $\xi_0=\xi(s=0)$. Equation (21) represents a general symmetric solution to (14) involving the five constants d_1, d_2, d_3, d_4, and σ_m. These constants are evaluated through application of problem specific boundary conditions. As a particular example, the existence and stability of equilibria for the prototypical problem of Rosenthal (1975, 1976) are determined presently.

4 Example: Uni-Axial Torque/Thrust

Consider the cable depicted in Fig. 2 which is subject to the *uni-axial* torque/thrust pair. Closed-form equilibrium solutions to this prototypical problem are pursued in Section 4.1 which lead to the complex, three-dimensional equilibrium states determined numerically by Rosenthal (1975, 1976). New insights regarding these equilibrium states are gained through the stability analysis of Section 4.2.

4.1 Equilibrium Analysis. The uni-axial torque/thrust pair is defined $\mathbf{f}_0=f_0\mathbf{e}_1=-\mathbf{f}_1$ and $\mathbf{m}_0=m_0\mathbf{e}_1=-\mathbf{m}_1$. Let ψ denote the angle between $\mathbf{e}_1$ and the end tangent $\mathbf{l}_1^i(0)$ and thus, the direction cosines become $b_k^0=c_k^0=-b_k^1=-c_k^1=n_k$, k = 1, 2, 3, where $n_1=\cos\psi$, $n_2=0$ and $n_3=\sin\psi$. The (natural) boundary conditions for this problem at s = 0

$$\kappa(0)=m_0n_3,\quad h(0)=m_0n_1,\quad p(0)=f_0n_1,$$
$$\kappa'(0)=-f_0n_2,\quad \tau(0)=h(0)-\frac{f_0n_3}{\kappa(0)}, \quad (22)$$

are extracted from (12) and are symmetric to those at s = 1. The five constants (d_1, d_2, d_3, d_4, and σ_m) are evaluated as follows:

1 Two of the three parameters m_0, f_0 and ψ may be chosen arbitrarily (say m_0 and f_0) and an initial guess provided for the

Downloaded 03 May 2010 to 171.66.16.20. Redistribution subject to ASME license or copyright; see http://www.asme.org/terms/Terms_Use.cfm

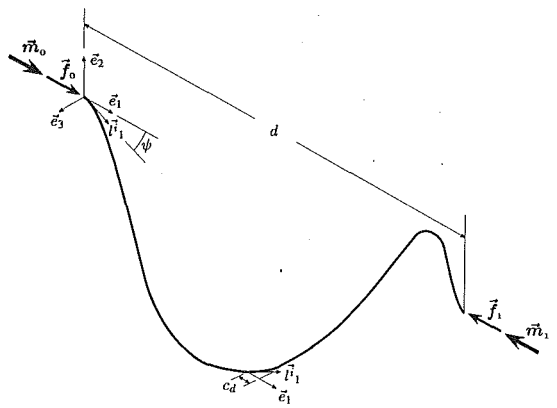


Fig. 2 Cable subject to *uni-axial* torque $\mathbf{m}_0 = m_0\mathbf{e}_1 = -\mathbf{m}_1$ and thrust $\mathbf{f}_0 = f_0\mathbf{e}_1 = -\mathbf{f}_1$ (Rosenthal, 1975, 1976)

third (say ψ). Employing these values of m_0, f_0 and ψ, the boundary values of $\kappa(0)$, $h(0)$, $p(0)$, $\kappa'(0)$ and $\tau(0)$ are evaluated using (22).

2 The constants d_1, d_2, d_3, d_4, and σ_m are calculated by using (15) and (17), and evaluating (16) at $s = 0$. Thus, the additional constants Y, $Y_{1,2}$, and ξ_0 appearing in (20) may also be computed.

3 Final evaluation of (20) at $s = 1/2$ using $\xi(1/2) = 0$, leads to a single nonlinear equation in the original unknown parameter (say ψ). The parameter is evaluated herein using Newton-Raphson iteration. The original four field variables $\kappa(s)$, $h(s)$, $p(s)$, and $\tau(s)$ can now be found by repeated evaluation of (15) and (20). Moreover, the coordinates of the three-dimensional space defining χ^i can also be evaluated through integration of the curvature $\kappa(s)$ and geometric torsion $\tau(s)$ distributions (Rosenthal, 1975, 1976; Hildebrand, 1976).

4.2 Stability Analysis. In Hamilton's principle (7), terms of second order in the deformation field variables lead to the equations of motion linearized about an equilibrium state. In nondimensional form (see Appendix A), the homogeneous equations govern free linear response are as follows:

tangential direction $\mathbf{l}_1^i$:

$$[a_{2,s} + (h-\tau)a_3]_{,s}\kappa - [(p+\tau^2-h\tau)a_2 + \tau a_{3,s}]\kappa + (ra_1)_{,s} = u_{1,tt}, \tag{23}$$

normal direction $\mathbf{l}_2^i$:

$$\begin{aligned} &-[a_{2,s} + (h-\tau)a_3]_{,ss} \\ &\quad -[(p+\tau^2-h\tau-\kappa^2+g\kappa^2)a_3 + (h-\tau)a_{2,s} + g\kappa a_{4,s}]\tau \\ &\quad +[(p+\tau^2-h\tau)a_2 + \tau a_{3,s}]_{,s} + (a_{3,s}+\tau a_2)_{,s}\tau + ra_1\kappa = u_{2,tt}, \end{aligned} \tag{24}$$

bi-normal direction $\mathbf{l}_3^i$:

$$\begin{aligned} &-[a_{2,s} + (h-\tau)a_3]_{,s}\tau \\ &\quad +[(p+\tau^2-h\tau-\kappa^2+g\kappa^2)a_3 + (h-\tau)a_{2,s} + g\kappa a_{4,s}]_{,s} \\ &\quad +[(p+\tau^2-h\tau)a_2 + \tau a_{3,s}]\tau - (a_{3,s}+\tau a_2)_{,ss} = u_{3,tt}, \end{aligned} \tag{25}$$

rotation along $\mathbf{l}_1^i$:

$$g(a_{4,s} + \kappa a_3)_{,s} = ju_{\theta,tt}, \tag{26}$$

where $\kappa(s)$, $h(s)$, $p(s)$, and $\tau(s)$ define the known equilibrium solution satisfying (8)–(12); refer to Section 4.1. The associated boundary terms from Hamilton's principle lead to the boundary conditions

$$u_1 = 0, \quad u_2 = 0, \quad u_3 = 0 \text{ at } s = 0,\ 1, \tag{27}$$

$$a_{2,s} + (h-\tau)a_3 - \kappa a_1 = 0, \quad a_{3,s} - (h-\tau)a_2 = 0,$$
$$ga_{4,s} - (1-g)\kappa a_3 = 0 \text{ at } s = 0,\ 1, \tag{28}$$

on the assumption that the ends of the cable are immobile but otherwise free to rotate *after* the equilibrium state is formed. Use of the separable solutions

$$u_1(s,t) = v_1(s)e^{i\omega t}, \quad u_2(s,t) = v_2(s)e^{i\omega t}$$
$$u_3(s,t) = v_3(s)e^{i\omega t}, \quad u_\theta(s,t) = v_4(s)e^{i\omega t} \tag{29}$$

leads to the following eigenvalue problem governing free response:

$$\boldsymbol{K}\mathbf{V} = \begin{bmatrix} K_{11} & K_{12} & K_{13} & K_{14} \\ K_{21} & K_{22} & K_{23} & K_{24} \\ K_{31} & K_{32} & K_{33} & K_{34} \\ K_{41} & K_{42} & K_{43} & K_{44} \end{bmatrix} \begin{pmatrix} v_1 \\ v_2 \\ v_3 \\ v_4 \end{pmatrix}$$
$$= \omega^2 \begin{bmatrix} 1 & 0 & 0 & 0 \\ 0 & 1 & 0 & 0 \\ 0 & 0 & 1 & 0 \\ 0 & 0 & 0 & j \end{bmatrix} \begin{pmatrix} v_1 \\ v_2 \\ v_3 \\ v_4 \end{pmatrix} = \omega^2 \boldsymbol{M}\mathbf{V}, \tag{30}$$

in which K_{ij} are homogeneous linear differential operators defined in Appendix B. The form of the associated boundary conditions (27) and (28) remain unchanged.

The Galerkin method is employed to numerically determine the eigensolutions using the following comparison function series:

$$v_1(s) = \sum_{l=1}^{n} \alpha_l \phi_{1l}, \qquad v_2(s) = \sum_{l=1}^{n} \beta_l \phi_{2\beta l} + \sum_{l=1}^{n} \gamma_l \phi_{2\gamma l},$$

$$v_3(s) = \sum_{l=1}^{n} \beta_l \phi_{3\beta l} + \sum_{l=1}^{n} \gamma_l \phi_{3\gamma l}, \quad v_4(s) = \sum_{l=1}^{n} \beta_l \phi_{4\beta l} + \sum_{l=1}^{n} \theta_l \phi_{4l}, \tag{31}$$

where

$$\sigma_{1l}(s) = \phi_{2\gamma l}(s) = \phi_{3\beta l}(s) = \sin(l\pi s),$$
$$\phi_{2\beta l}(s) = -\phi_{3\gamma l}(s)$$
$$= \begin{cases} \dfrac{-2(2\tau_0 - h_0)l\pi}{[(l+1)\pi]^2}[1-\cos((l+1)\pi s)]\left(s-\dfrac{1}{2}\right), & \text{when } l \text{ is odd}, \\ \dfrac{(2\tau_0 - h_0)}{l\pi}[1-\cos(l\pi s)], & \text{when } l \text{ is even}, \end{cases}$$
$$\phi_{4l}(s) = \cos((l-1)\pi s),$$
$$\phi_{4\beta l}(s) = \frac{(1-g)\kappa_0}{g}\sin(l\pi s), \tag{32}$$

and $\tau_0 = \tau(0)$ and $h_0 = h(0)$.

Application of the Galerkin method leads to the discrete $4n \times 4n$ eigenvalue problem

$$\boldsymbol{K}^* \begin{pmatrix} \alpha \\ \beta \\ \gamma \\ \theta \end{pmatrix} = \omega^2 \boldsymbol{M}^* \begin{pmatrix} \alpha \\ \beta \\ \gamma \\ \theta \end{pmatrix}, \tag{33}$$

where the elements of the discrete operators $\boldsymbol{K}^*$ and $\boldsymbol{M}^*$ are defined in Appendix B. The eigensolutions are determined numerically. In this formulation, an unstable mode is one for which $\text{Imag}[\omega] < 0$. Despite the fact that this problem is nonconservative (Bolotin, 1963; Leipholz, 1980), all computed instabilities that follow arise through divergence and ω is either purely real (+/− pairs) or imaginary (+/− pairs). Moreover, one rigid-body mode ($\omega = 0$) always exists describing rotation about the $\mathbf{e}_1$ (loading) axis.

4.3 Discussion of Results. In the equilibrium analysis of Section 4.1, the boundary data f_0 and m_0 represent two in-

Downloaded 03 May 2010 to 171.66.16.20. Redistribution subject to ASME license or copyright; see http://www.asme.org/terms/Terms_Use.cfm

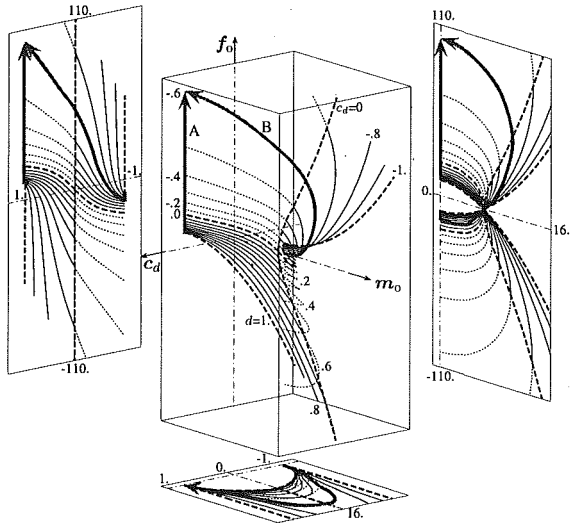


Fig. 3 Equilibrium solutions in the (f_0, m_0, c_d) parameter space. In this example, $r = 3.6 \times 10^5$, $j = 5.56 \times 10^{-6}$, $\nu = 0.3$. Curves of constant end distance (d) are drawn (in 0.1 increments) and distinguish stable (solid) from unstable (dotted) states.

dependent load variables. Two dependent variables, d and c_d, are presently introduced as measures of the deformation field that aid in distinguishing possible equilibrium states. The quantity d measures the separation of the two ends (measured positive to the right from the end $s = 0$). The quantity

$$c_d = \mathbf{e}_1 \cdot \mathbf{l}_1^i \left(\frac{1}{2}\right) \tag{34}$$

measures the projection of the tangent at the midspan onto the loading axis; refer to Fig. 2. Values of these two quantities distinguish three major classes of equilibrium states:

Trivial Equilibrium	$\lvert d\rvert = 1$,	
Planar Equilibria	$\lvert d\rvert < 1$,	$\lvert c_d\rvert = 1$,
Spatial Equilibria	$\lvert d\rvert < 1$,	$\lvert c_d\rvert < 1$.

Moreover, it will be shown that these same two quantities govern the stability of all nontrivial (planar and spatial) equilibrium states.

The computed nontrivial equilibrium states and their stability are summarized in Fig. 3 and discussed in detail in the following. The equilibrium solutions are illustrated by a surface in the (f_0, m_0, c_d) parameter space. Curves of constant end separation (constant d) are shown for the entire range $-1.0 \le d \le 1.0$ (in 0.1 increments) for which solid (dotted) curves designate stable (unstable) states. The boundaries separating stable from unstable states are highlighted by dashed curves. Projections of this surface onto the three coordinate planes highlight significant solution symmetries.

As a check, attention is first focused on the planar equilibria (planar elastica) examined previously by Maddocks (1984) and Perkins and Chirehdast (1990). Consider the loading path marked "A" in Fig. 3 along which f_0 increases (compression) while $m_0 = 0$ and $c_d = 1$. Along this path, the straight cable at $d = 1$ buckles at the Euler buckling load $f_0 = \pi^2$ and passes through the sequence of planar equilibria depicted in Fig. 4(a) for which $1.0 \ge d \ge -0.6$. For all cases in which $d \le 0$, there exists a point of self-intersection and any contact force system at such a point is presently neglected (Maddocks, 1984; Perkins and Chirehdast, 1990). The (dashed) equilibrium corresponding to $d = 0$ ($f_0 \approx 21.55$), separates stable (solid) from unstable (dotted) planar equilibria. This conclusion is drawn from Fig. 4(b) which illustrates the eigenvalues ω associated with critical modes as functions of the end load f_0. For $f_0 \le \pi^2$ and $d = 1$, only the trivial equilibrium exists, the (nonzero) eigenvalues for elastic modes are purely real and repeated, and there exists a single rigid-body mode ($\omega = 0$) describing rotation about the $\mathbf{e}_1$ (loading) axis. A divergence instability is reached at the Euler buckling load, $f_0 = \pi^2$, and a symmetric pair of planar equilibria bifurcate from the trivial equilibrium. Simultaneously, the repeated eigenvalues describing elastic modes unfold for $f_0 > \pi^2$, and are associated with pairs of distinct in-plane and out-of-plane modes. The lowest eigenvalue pair, that shown in Fig. 4(b), vanishes when the two ends of the cable coincide ($d = 0$, $f_0 \approx 21.55$) marking the location of a secondary bifurcation. At this point, the cable possesses three rigid-body modes describing arbitrary (three-dimensional) rotations about the common end pivot. For loads just beyond this point, the planar equilibria are unstable with respect to both out-of-plane and in-plane perturbations (Maddocks, 1984). For the unstable out-of-plane mode, $v_3(s)$ and $v_4(s)$ are antisymmetric functions of s, while $v_1(s) \equiv v_2(s) \equiv 0$. The unstable in-plane mode is one for which $v_1(s)$ is symmetric, $v_2(s)$ is antisymmetric and $v_3(s) \equiv v_4(s) \equiv 0$. As noted in the experiments of Perkins and Chirehdast (1990), these two unstable modes may initiate globally large responses that may ultimately lead to a reversion to the stable equilibrium having the same end separation. Moreover, the unstable out-of-plane mode promotes the "pop-out" response discussed in Coyne (1990). Finally, note that the in-plane mode is restabilized for $f_0 > 100.3$ (Maddocks, 1984).

Pure compressive loading leads to the planar equilibrium forms above that are distinguishable by the single quantity d. The addition of the end moment $\mathbf{m}_0$ shown in Fig. 2 may lead to spatial (three-dimensional) equilibrium forms for which the quantity c_d serves as a measure of out-of-plane deformation. The existence of these spatial equilibria is governed by the (fundamental) buckling condition

$$\left(\frac{m_0}{2}\right)^2 - f_0 = \pi^2, \tag{35}$$

obtained by Greenhill in 1883 (Timoshenko and Gere, 1961) and obtained from the linearized form of the equilibrium boundary value problem, (8)–(12). The trivial equilibrium ($\lvert d\rvert = 1$) remains stable for all load values below the Greenhill condition; i.e., $(m_0/2)^2 - f_0 < \pi^2$. Load values in excess of this condition lead to nonlinear deformations and the nontrivial states summarized in Fig. 3.

As an example, consider the loading path marked "B" in Fig. 3. Like path A, path B begins with the trivial equilibrium and ends with the same planar form ($d = -0.6$). However, path B reaches this planar form through the sequence of planar and spatial forms shown in Fig. 5. Starting from the trivial equilibrium, the cable buckles through the application of increasingly greater compressive loads leading to the stable planar form for which $d = -0.6$ ($f_0 = -12.2$). Next, the moment $\mathbf{m}_0$ is applied and the compressive load is reduced in such a manner as to maintain a constant end separation. In response, a stable spatial form ($c_d > -1$) is born from the planar form ($c_d = -1$). As the compressive load is reduced further (ultimately becoming tensile, $f_0 > 0$), c_d continues to increase. At $f_0 = 49.8$, the tangent at the midspan is orthogonal to the loading axis ($c_d = 0$) and the moment $\mathbf{m}_0$ achieves its maximum value. Any further increase in f_0 leads to an unstable spatial form for which $c_d > 0$. Thus, the condition $c_d = 0$ separates stable from unstable spatial forms. Also at the condition $c_d = 0$, the internal axial force at the midspan vanishes, $p(1/2) = 0$, and the internal torque h at the midspan achieves its maximum value.

The instability above is induced by the unstable mode denoted "Type 1" in Fig. 6. For this particular mode, $v_1(s)$, $v_3(s)$, and $v_4(s)$ are antisymmetric while $v_2(s)$ is symmetric. As the tensile load is increased further, a second instability is induced through the mode labeled "Type 2" in Fig. 6 for which $v_1(s)$, $v_3(s)$, and $v_4(s)$ are symmetric while $v_2(s)$ is

Downloaded 03 May 2010 to 171.66.16.20. Redistribution subject to ASME license or copyright; see http://www.asme.org/terms/Terms_Use.cfm

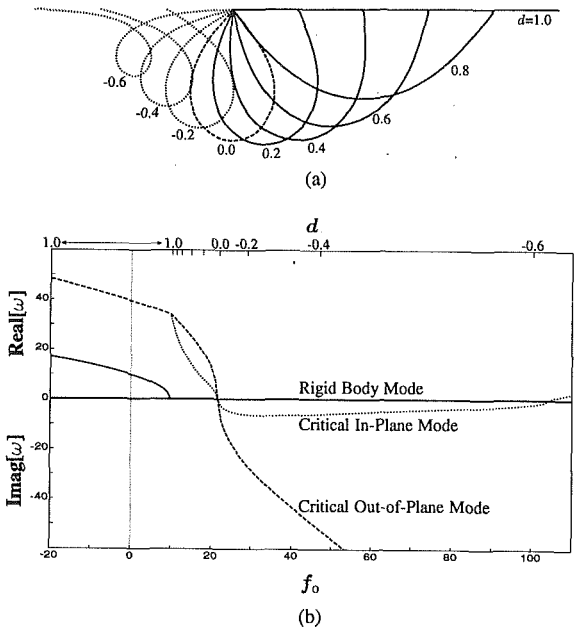


Fig. 4 Stability of planar equilibrium states: (*a*) Loading path *A* in Fig. 3 leads to illustrated sequence of planar equilibria. Solid (dotted) curves designate stable (unstable) equilibrium states separated by the critical equilibrium state (dashed curve, $d = 0$). (*b*) Eigenvalues for critical modes over large range of compressive load values f_0. In this discretization, $n = 20$ terms are used.

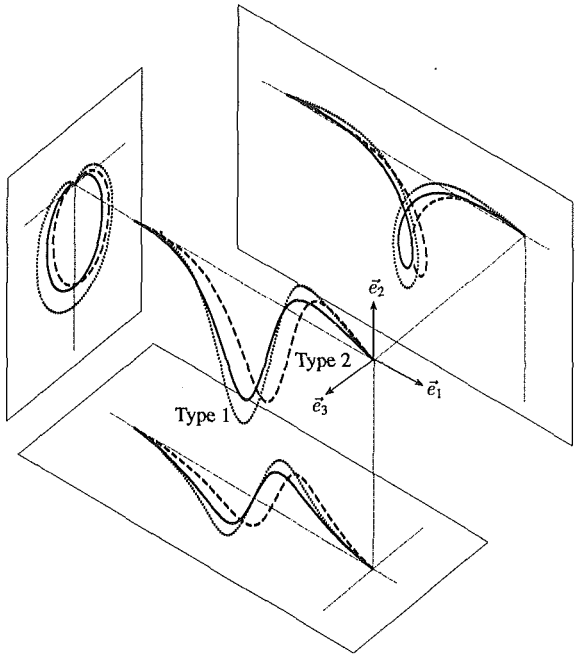
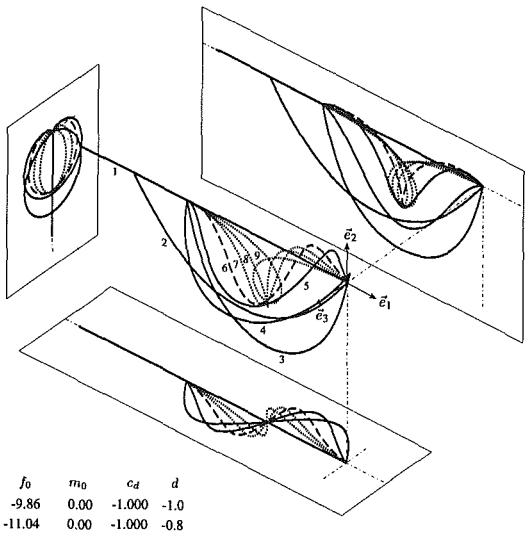


Fig. 6 The two unstable modes of unstable spatial form #7 ($f_0 = 68.00$, $m_0 = 9.57$) of Fig. 5. Solid curve illustrates spatial equilibrium form. Dashed (dotted) curve illustrates Type 1 (Type 2) unstable mode for which v_1, v_3, and v_4 are antisymmetric (symmetric), while v_2 is symmetric (antisymmetric).



State	f_0	m_0	c_d	d
1	-9.86	0.00	-1.000	-1.0
2	-11.04	0.00	-1.000	-0.8
3	-12.20	0.00	-1.000	-0.6
4	-3.20	5.61	-0.658	-0.6
5	22.80	9.09	-0.339	-0.6
6	49.80	10.26	0.000	-0.6
7	68.00	9.57	0.336	-0.6
8	84.00	7.52	0.665	-0.6
9	100.30	0.00	1.000	-0.6

Fig. 5 Spatial equilibria along loading path *B* of Fig. 3, which begins with the trivial equilibrium and ends with the same (unstable) planar form ($d = -0.6$) as path *A*. Solid (dotted) curves designate stable (unstable) equilibrium states separated by the critical equilibrium state (dashed curve, $c_d = 0$).

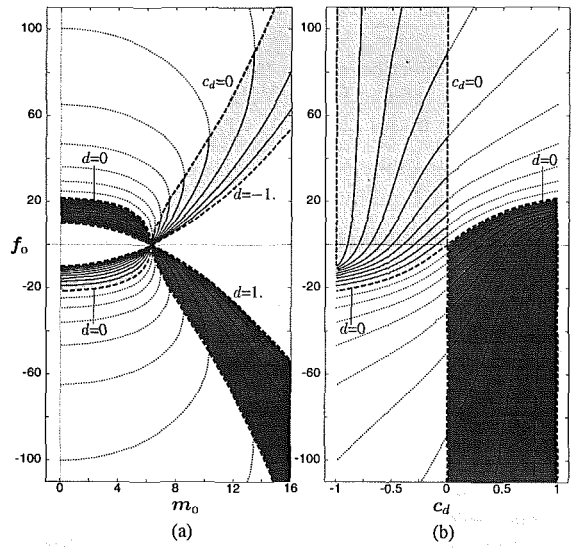


Fig. 7 Stability regions (grey) for nontrivial equilibria viewed in (m_0, f_0) and (c_d, f_0) planes

antisymmetric. These two unstable modes for the spatial form are extensions of the two unstable modes for the planar form. In particular, mode Type 1 (Type 2) possesses the same symmetry characteristics as the unstable out-of-plane (in-plane) mode for the planar form.

4.4 Stability Conclusions. Figure 7 highlights the governing roles played by the two quantities d and c_d. Figures 7(*a*) and 7(*b*) illustrate the stability regions viewed in (f_0, m_0) and (f_0, c_d) planes. Curves of constant end separation are drawn for which solid (dotted) segments designate stable (unstable) states. In addition, the loci of states for which $d = 0$ and $c_d = 0$ are also drawn by dashed curves. Inspection of this figure reveals the following conclusions.

Recall that the curves for $d = \pm 1.0$ define the two branches of the (Greenhill) buckling condition (35). In Fig. 7(*a*), between these two branches, only the trivial solution exists and is stable (unstable) to the left (right) of the intersection point at $m_0 = 2\pi$. Outside these branches, the trivial equilibrium is unstable and coexists with nontrivial equilibria ($|d| < 1$).

The nontrivial equilibrium states of Fig. 7, obtained from the closed-form analysis of Section 4.1, reproduce the numerical solutions obtained by Rosenthal (1975, 1976) using a shooting algorithm. The stability properties of these equilibria, however, were overlooked by Rosenthal and are clearly iden-

Downloaded 03 May 2010 to 171.66.16.20. Redistribution subject to ASME license or copyright; see http://www.asme.org/terms/Terms_Use.cfm

tified in Fig. 7. The *stable* nontrivial equilibria exist outside the boundaries defined by $d = \pm 1.0$ (Greenhill condition) and within the boundaries defined by $d = 0$ and $c_d = 0$. All other (fundamental) spatial and planar equilibrium forms are unstable.

The stability boundary $d = 0$ for spatial forms ($m_0 \neq 0$ in Fig. 7) is an extension of that governing the planar forms (Maddocks, 1984; Perkins and Chirehdast, 1990), and the stability boundaries $d = 0$ and $c_d = 0$ for spatial forms govern the stability of Type 1 modes alone. The spatial forms remain stable with respect to Type 2 modes over a larger range of the loading parameters. Moreover, the stability boundaries for Type 2 modes depend on the cable geometric and material properties. This larger parameter range includes the aforementioned region of restabilization of the planar forms with respect to in-plane perturbations (Type 2 mode); see $f_0 > 100.3$ in Fig. 4.

In summary, the stable regions of all (fundamental) nontrivial equilibrium states are bounded by the existence condition $|d| < 1$ and the two stability boundaries $d = 0$ and $c_d = 0$.

Acknowledgment

The authors gratefully acknowledge the support of the Office of Naval Research under contract number N00014-89-J-3159.

References

Ames, W. F., 1968, *Nonlinear Ordinary Differential Equations in Transport Processes*, Academic Press, New York.

Antman, S. S., 1974, "Kirchhoff's Problem for Nonlinearly Elastic Rods," *Quarterly of Applied Mathematics*, Vol. 32, No. 3, pp. 221–240.

Antman, S. S., and Kenney, C. S., 1981, "Large Buckled States of Nonlinearly Elastic Rods under Torsion, Thrust and Gravity," *Arch. Rational Mech. and Anal.*, Vol. 76, pp. 289–338.

Alexander, J. C., and Antman, S. S., 1982, "The Ambiguous Twist of Love," *Quarterly of Applied Mathematics*, Vol. 40, pp. 83–92.

Bolotin, V. V., 1963, *Nonconservative Problems of the Theory of Elastic Stability*, MacMillan, New York, pp. 119–138.

Coyne, J., 1990, "Analysis of the Formation and Elimination of Loops in Twisted Cable," *IEEE Journal of Oceanic Engineering*, Vol. 15, No. 2, pp. 72–83.

Hildebrand, F. B., 1976, *Advanced Calculus for Applications*, 2nd ed., Prentice-Hall, Englewood Cliffs, NJ, pp. 279–281.

Leipholz, H., 1980, *Stability of Elastic Systems*, Sijthoff and Noordhoff International Publishers BV, Alphen aan den Rijn, The Netherlands.

Liu, F. C, 1975, "Kink Formation and Rotational Response of Single and Multistrand Electromechanical Cables," Tech. Note N-1403, Civil Engineering Laboratory, Naval Construction Batallion Center, Port Hueneme, CA.

Love, A. E. H., 1944, *A Treatise on the Mathematical Theory of Elasticity*, 4th ed., Dover, New York.

Maddocks, J. H., 1984, "Stability of Nonlinearly Elastic Rods," *Arch. Rational Mech. and Anal.*, Vol. 85, pp. 311–354.

Myers, J. J., Holm, C. H., and McAllister, R. F., 1969, *Handbook of Ocean and Underwater Engineering*, McGraw-Hill, New York, pp. 4–43.

Perkins, N. C., and Chirehdast, M., 1990, "Planar Vibration of an Elastica Arch: Theory and Experiment," *Journal of Vibration and Acoustics*, Vol. 112, No. 3, pp. 374–379.

Rosenthal, F., 1975, "Greenhill's Formula and the Mechanics of Cable Hockling," NRL Report 7940, Naval Research Laboratory, Washington, D.C.

Rosenthal, F., 1976, "The Application of Greenhill's Formula to Cable Hockling," ASME JOURNAL OF APPLIED MECHANICS, Vol. 43, No. 4, pp. 681–683.

Ross, A. L., 1977, "Cable Kinking Analysis and Prevention," *Journal of Engineering for Industry*, Vol. 99, No. 1, pp. 112–115.

Tan, Z., and Witz, J. A., 1993, "On the Flexural-Torsional Behavior of a Straight Elastic Beam Subject to Terminal Moments," ASME JOURNAL OF APPLIED MECHANICS, Vol. 60, No. 2, pp. 498–505.

Timoshenko, S. P., and Gere, J. M., 1961, *Theory of Elastic Stability*, 2nd ed., pp. 76–81.

Yabuta, T., Yoshizawa, N., and Kojima, N., 1982, "Cable Kink Analysis: Cable Loop Stability Under Tension," ASME JOURNAL OF APPLIED MECHANICS, Vol. 49, No. 3, pp. 584–588.

Yabuta, T., 1984, "Submarine Cable Kink Analysis," *Bulletin of JSME*, Vol. 27, No. 231, pp. 1821–1828.

Zajac, E. E., 1962, "Stability of Two Planar Loop Elasticas," ASME JOURNAL OF APPLIED MECHANICS, Vol. 29, No. 1, pp. 136–142.

Ziegler, H., 1968, *Principles of Structural Stability*, Blaisdell Publ. Co., Waltham, MA.

APPENDIX A

Nondimensional Parameters

The following nondimensional quantities are introduced:

$$s=\frac{S}{L},\quad t=\frac{T}{\sqrt{\frac{\rho AL^4}{EI}}},\quad r=\frac{AL^2}{I},\quad g=\frac{GJ}{EI},$$

$$j=\frac{J}{AL^2},\quad d=\frac{D}{L},\quad \mathbf{q}=\frac{\mathbf{Q}L^3}{EI},$$

$$f_0=\frac{F_0L^2}{EI},\quad m_0=\frac{M_0L}{EI},\quad f_1=\frac{F_LL^2}{EI},$$

$$m_1=\frac{M_LL}{EI},\quad p=\frac{F_1^iL^2}{EI},\quad \kappa=\mathbf{K}^iL,$$

$$\tau=\Gamma^iL,\quad h=\frac{M_1^iL}{EI},\quad u_1=\frac{U_1}{L},$$

$$u_2=\frac{U_2}{L},\quad u_3=\frac{U_3}{L},\quad u_\theta=U_\theta.$$

Note the parameter $g = GJ/EI = 1/(1 + \nu)$, where ν is Poisson's ratio and, for a circular cable cross-section, $J = 2I$.

APPENDIX B

Stiffness and Mass Operators

The ordinary differential operators comprising $\boldsymbol{K}$ are

$$K_{11}(v) = -(r+\kappa^2)v'' - 2\kappa\kappa' v' - (\kappa'' - s_1\kappa)\kappa v,$$

$$K_{12}(v) = -\kappa v''' + (r+s_2)\kappa v' + (r\kappa' - h_1\kappa\tau')v,$$

$$K_{13}(v) = -h_1\kappa v'' + 3\kappa\tau' v' + (\tau'' - s_1\tau)\kappa v,$$

$$K_{14}(v) = K_{41}(v) = 0,$$

$$K_{21}(v) = -K_{12}(v) + 3\kappa' v'' + 3\kappa'' v' + [\kappa''' + (r-s_2)\kappa' - p'\kappa]v,$$

$$K_{22}(v) = v'''' - s_3 v'' - (p' - 3h_2\tau')v' + [h_2\tau'' - 3\tau'^2 + s_1\tau^2 + (r+g_1\tau^2)\kappa^2]v,$$

$$K_{23}(v) = h_2 v''' - 6\tau' v'' - [4\tau'' - (s_1+s_2+g_1\kappa^2)\tau]v' - (\tau''' - s_3\tau' - p'\tau)v,$$

$$K_{24}(v) = g\kappa\tau v',$$

$$K_{31}(v) = K_{13}(v) - 2h_1\kappa' v' - (h_1\kappa'' - 3\kappa'\tau')v,$$

$$K_{32}(v) = -K_{23}(v) - g_1(2\kappa'\tau + \kappa\tau')\kappa v,$$

$$K_{33}(v) = K_{22}(v) - g_1\kappa^2 v'' - 2g_1\kappa\kappa' v' - (r+g_1\tau^2)\kappa^2 v,$$

$$K_{34}(v) = K_{43}(v) = -g\kappa v'' - g\kappa' v',$$

$$K_{42}(v) = -K_{24}(v) - g(\kappa'\tau + \kappa\tau')v,$$

$$K_{44}(v) = -gv'',$$

where $g_1 = g - 1$, $h_1 = h - 3\tau$, $h_2 = h - 4\tau$, $s_1 = p + \tau^2 - h\tau$, $s_2 = p + 3\tau^2 - 2h\tau$ and $s_3 = p + 6\tau^2 - 3h\tau$.

The elements of the discrete operator $\boldsymbol{K}^*$ are

$$K_{11}^*(i,j) = \int_0^1 \phi_{1j} K_{11}(\phi_{1i})\,ds,$$

$$K_{12}^*(i,j) = \int_0^1 \phi_{1j} K_{12}(\phi_{2\beta i}) + \phi_{1j} K_{13}(\phi_{3\beta i}) + \phi_{1j} K_{14}(\phi_{4\beta i})\,ds,$$

$$K_{13}^*(i,j) = \int_0^1 \phi_{1j} K_{12}(\phi_{2\gamma i}) + \phi_{1j} K_{13}(\phi_{3\gamma i})\,ds,$$

$$K_{14}^*(i,j) = \int_0^1 \phi_{1j} K_{14}(\phi_{4i})\,ds,$$

$$K_{21}^*(i,j) = \int_0^1 \phi_{2\beta j} K_{21}(\phi_{1i}) + \phi_{3\beta j} K_{31}(\phi_{1i}) + \phi_{4\beta j} K_{41}(\phi_{1i})\,ds,$$

Downloaded 03 May 2010 to 171.66.16.20. Redistribution subject to ASME license or copyright; see http://www.asme.org/terms/Terms_Use.cfm

$$K^*_{22}(i,j)=\int_0^1 \phi_{2\beta j}K_{22}(\phi_{2\beta i})+\phi_{3\beta j}K_{32}(\phi_{2\beta i})+\phi_{4\beta j}K_{42}(\phi_{2\beta i})$$
$$+\phi_{2\beta j}K_{23}(\phi_{3\beta i})+\phi_{3\beta j}K_{33}(\phi_{3\beta i})+\phi_{4\beta j}K_{43}(\phi_{3\beta i})$$
$$+\phi_{2\beta j}K_{24}(\phi_{4\beta i})+\phi_{3\beta j}K_{34}(\phi_{4\beta i})+\phi_{4\beta j}K_{44}(\phi_{4\beta i})ds,$$

$$K^*_{23}(i,j)=\int_0^1 \phi_{2\beta j}K_{22}(\phi_{2\gamma i})+\phi_{3\beta j}K_{32}(\phi_{2\gamma i})+\phi_{4\beta j}K_{42}(\phi_{2\gamma i})$$
$$+\phi_{2\beta j}K_{23}(\phi_{3\gamma i})+\phi_{3\beta j}K_{33}(\phi_{3\gamma i})+\phi_{4\beta j}K_{43}(\phi_{3\gamma i})ds,$$

$$K^*_{24}(i,j)=\int_0^1 \phi_{2\beta j}K_{24}(\phi_{4i})+\phi_{3\beta j}K_{34}(\phi_{4i})+\phi_{4\beta j}K_{44}(\phi_{4i})ds,$$

$$K^*_{31}(i,j)=\int_0^1 \phi_{2\gamma j}K_{21}(\phi_{1i})+\phi_{3\gamma j}K_{31}(\phi_{1i})ds,$$

$$K^*_{32}(i,j)=\int_0^1 \phi_{2\gamma j}K_{22}(\phi_{2\beta i})+\phi_{3\gamma j}K_{32}(\phi_{2\beta i})+\phi_{2\gamma j}K_{23}(\phi_{3\beta i})$$
$$+\phi_{3\gamma j}K_{33}(\phi_{3\beta i})+\phi_{2\gamma j}K_{24}(\phi_{4\beta i})+\phi_{3\gamma j}K_{34}(\phi_{4\beta i})ds,$$

$$K^*_{33}(i,j)=\int_0^1 \phi_{2\gamma j}K_{22}(\phi_{2\gamma i})+\phi_{3\gamma j}K_{32}(\phi_{2\gamma i})+\phi_{2\gamma j}K_{23}(\phi_{3\gamma i})$$
$$+\phi_{3\gamma j}K_{33}(\phi_{3\gamma i})ds,$$

$$K^*_{34}(i,j)=\int_0^1 \phi_{2\gamma j}K_{24}(\phi_{4i})+\phi_{3\gamma j}K_{34}(\phi_{4i})ds,$$

$$K^*_{41}(i,j)=\int_0^1 \phi_{4j}K_{41}(\phi_{1i})ds,$$

$$K^*_{42}(i,j)=\int_0^1 \phi_{4j}K_{42}(\phi_{2\beta i})+\phi_{4j}K_{43}(\phi_{3\beta i})+\phi_{4j}K_{44}(\phi_{4\beta i})ds,$$

$$K^*_{43}(i,j)=\int_0^1 \phi_{4j}K_{42}(\phi_{2\gamma i})+\phi_{4j}K_{43}(\phi_{3\gamma i})ds,$$

$$K^*_{44}(i,j)=\int_0^1 \phi_{4j}K_{44}(\phi_{4i})ds.$$

The elements of the discrete operator M^* are

$$M^*_{11}(i,j)=\int_0^1 \phi_{1j}\phi_{1i}ds,$$

$$M^*_{22}(i,j)=\int_0^1 \phi_{2\beta j}\phi_{2\beta i}+\phi_{3\beta j}\phi_{3\beta i}+j\phi_{4\beta j}\phi_{4\beta i}ds,$$

$$M^*_{23}(i,j)=\int_0^1 \phi_{2\beta j}\phi_{2\gamma i}+\phi_{3\beta j}\phi_{3\gamma i}ds,$$

$$M^*_{24}(i,j)=\int_0^1 j\phi_{4\beta j}\phi_{4i}ds,$$

$$M^*_{32}(i,j)=\int_0^1 \phi_{2\gamma j}\phi_{2\beta i}+\phi_{3\gamma j}\phi_{3\beta i}ds,$$

$$M^*_{33}(i,j)=\int_0^1 \phi_{2\gamma j}\phi_{2\gamma i}+\phi_{3\gamma j}\phi_{3\gamma i}ds,$$

$$M^*_{42}(i,j)=\int_0^1 j\phi_{4j}\phi_{4\beta i}ds,$$

$$M^*_{44}(i,j)=\int_0^1 j\phi_{4j}\phi_{4i}ds,$$

and all other elements vanish.

Downloaded 03 May 2010 to 171.66.16.20. Redistribution subject to ASME license or copyright; see http://www.asme.org/terms/Terms_Use.cfm

ERRATUM

Dr. M. Akif Özbek, second author of the paper "Thermodynamics of Duffing's Oscillator," by V. Berdichevsky, M. A. Özbek, and W. W. Kim and published in The ASME JOURNAL OF APPLIED MECHANICS, Vol. 61, Sept. 1994, pp. 670–675, was listed as O. Özbek. Dr. Özbek's name should have been denoted as A. Özbek.

Copyright © 1994 by ASME
Downloaded 03 May 2010 to 171.66.16.20. Redistribution subject to ASME license or copyright; see http://www.asme.org/terms/Terms_Use.cfm

A Perturbation Method for Inverse Frequency Modification of Discrete, Undamped Systems

M. J. Smith
Postdoctoral Fellow.

S. G. Hutton
Professor,
Mem. ASME.

Department of Mechanical Engineering,
University of British Columbia,
Vancouver, BC V6T 1Z4, Canada

A method is described for determining the stiffness and mass modifications required in order to modify the natural frequencies of undamped discrete nongyroscopic vibrating systems in a prescribed manner. The method is based upon a new perturbation formulation. Structural changes are represented by perturbed stiffness and mass matrices defined in terms of linear design parameters of the discrete model. The equations are subject to frequency constraints defined by the analyst, and the modified mode shapes are assumed confined to a subspace of the baseline modes. The proposed method provides a complete solution of the perturbation equations without deleting or approximating coupling terms in the unknowns and is therefore suitable for large and small changes alike. Numerical results demonstrate that the new method is superior to the predictor-corrector method for determining large structural changes and that solutions of a high accuracy can be obtained provided a sufficiently rich subspace of baseline modes is used.

1 Introduction

In the present study, a perturbation method is developed for solving inverse modification problems that arise in free vibration analysis of linear systems. In particular, a new iterative method is described for satisfying frequency constraints. Problems involving mode-shape constraints are left for a further study. In relation to previous work, this method is similar in spirit to the predictor-corrector method of Hoff et al. (1984) in that the perturbation equations are confined to the modal subspace defined by the baseline mode set, and in that solutions are found in terms of structural parameters selected by the analyst that are amenable to direct modification by the designer. The proposed method differs from the predictor-corrector method in that design solutions are calculated without deleting terms from the perturbation equations. As a result, the proposed method is not susceptible to linearization errors, it is more reliable for large design changes, and the resulting mode shapes of the modified structure automatically satisfy orthogonality conditions.

Contributed by the Applied Mechanics Division of THE AMERICAN SOCIETY OF MECHANICAL ENGINEERS for presentation at the International Mechanical Engineering Congress and Exhibition, the Winter Annual Meeting of The ASME, Chicago, IL, Nov. 6–11, 1994.

Discussion on this paper should be addressed to the Technical Editor, Professor Lewis T. Wheeler, Department of Mechanical Engineering, University of Houston, Houston, TX 77204-4792, and will be accepted until four months after final publication of the paper itself in the ASME JOURNAL OF APPLIED MECHANICS.

Manuscript received by the ASME Applied Mechanics Division, Aug. 23, 1993; final revision, Feb. 8, 1994. Associate Technical Editor: D. J. Inman.

Paper No. 94-WA/APM-12.

2 Background

Many developments in dynamic optimization have been based upon sensitivity methods. In this work, first-order approximations to design changes satisfying frequency or mode shape goals are calculated and are generally only suitable for small-magnitude structural modifications. Fox and Kapoor (1968) give the basic first-order sensitivity equations and, along with Nelson (1976), provide methods for calculating eigenvector derivatives. Bohte (1967), Biegler-König (1981), and Friedland et al. (1987) discuss Newton's method solutions of inverse eigenvalue problems. Smith and Hutton (1992) use a Newton's method approach to solve frequency modification problems associated with finite element models; this work involves the repeated solution of first-order sensitivity equations followed by an accurate update of the mode shapes using inverse iteration. Other researchers have investigated the effects of local modifications. Weissenburger (1968) and Pomazal and Snyder (1971) derive expressions describing the frequency change produced by a rank-1 matrix modification which can be used for forward and inverse modification alike. Tsuei and Yee (1989) describe a method for calculating either a single stiffness or lumped mass addition satisfying a prescribed frequency shift.

Another approach comes through the use perturbation methods. Stetson (1976) describes structural matrices of the modified system in terms of the baseline values plus incremental terms. An admixture matrix is used to describe the modified mode shapes; that is, the increment of the ith mode shape is written as a linear combination of all the baseline modes excluding the ith mode. The modified terms are substituted into the decoupled dynamic equations and all nonlinear incremental terms are eliminated. The resulting equation is called the linear

Copyright © 1994 by ASME
Downloaded 03 May 2010 to 171.66.16.20. Redistribution subject to ASME license or copyright; see http://www.asme.org/terms/Terms_Use.cfm

perturbation equation and it describes approximately how structural frequencies and mode shapes change with stiffness and mass matrix changes. Like the sensitivity equation, it is only accurate for small modifications.

Sandström and Anderson (1982) present the same formulation but allow mode shape constraints to be specified explicitly instead of through admixture coefficients. Kim et al. (1983a, 1983b) use an equilibrium formulation of the perturbation equation with all nonlinear terms included. Mathematical programming is applied to the full set of equations to find minimum weight and minimum change solutions. In this approach, the design parameters as well as the unspecified components of the mode shapes are determined by the mathematical program. Consequently, the number of variables can become prohibitively large with complex models. Kim and Anderson (1984) use a dynamic condensation technique to reduce the order of the equilibrium equations before solving.

Hoff et al. (1984, 1985) present a two-stage predictor-corrector algorithm suitable for large structural changes. The predictor phase estimates the structural changes and the perturbed mode shapes using the linear perturbation equation. In the corrector phase, the general perturbation equations, incorporating the estimated mode shape perturbations, are solved to improve on the predictor phase results. At least one frequency constraint must be present to use the predictor-corrector algorithm; if only mode shape changes are specified, the method reduces to the linear analysis of Stetson (1976). To improve the performance with large modifications, Bernitsas and Kang (1991) use the predictor-corrector algorithm incrementally to calculate a sequence of small steps leading to the complete solution. Gans and Anderson (1991) adapted the predictor-corrector method for systems with centrifugal and coriolis forces.

In a parallel development of perturbation methods, Ram and Braun (1991) determine optimal perturbing stiffness and mass matrices for a particular modal subspace. The subsidiary problem is then to relate the optimal perturbation to physical changes in the actual model, but this was not investigated by the authors.

3 Perturbation Equations

The natural modes of a linear, undamped, nongyroscopic discrete structure are determined by the eigenvalue equation,

$$[K-\lambda_i M]\psi_i=0 \quad i=1, 2, \ldots, n, \tag{1}$$

where K and M are the real, symmetric stiffness and mass matrices of size $n \times n$; ψ_i is the ith mode shape and is a vector of length n. The structural eigenvalues are denoted by λ_i; provided K and M are positive definite they are real, positive and, for the purposes of the present study, are assumed to be distinct. However, multiple null eigenvalues are allowed when K is positive semi-definite.

If the structure's mass and stiffness characteristics are modified in some way, the new natural modes are determined by the modified eigenvalue equation,

$$[K+\Delta K-\lambda_i'(M+\Delta M)]\psi_i'=0 \quad i=1, 2, \ldots, n, \tag{2}$$

where ΔK and ΔM denote the changes in the stiffness and mass matrix as a result of such a structural modification and λ_i' and ψ_i' are the ith modified eigenvalue and mode shape of the system. It is convenient to consider a class of modifications in which the topology of the original system is left unchanged. The types of modifications allowed by this assumption are discussed in Section 4.

It is assumed that the modified mode shape ψ_i' can be expressed as a linear combination of the original mode shapes

$$\psi_i'=\sum_{k=1}^{q}\psi_k c_{ik}=\Psi c_i. \tag{3}$$

If a complete set of modes is included in Ψ (i.e., $q = n$), no approximation is involved in the representation of ψ_i'. Otherwise the representation of ψ_i' is approximate in so far as it is confined to a q-dimensional subspace of the modal matrix Ψ.

Premultiplying (2) by Ψ^T gives the following result assuming, without any loss of generality, that the baseline modes are mass normalized:

$$\Psi^T[\Delta K-\lambda_i'\Delta M]\Psi c_i=-(\Lambda-\lambda_i' I)c_i \quad i=1, 2, \ldots, q. \tag{4}$$

The perturbation Eq. (4) is well known and is commonly used in "forward" modification analysis (Baldwin and Hutton, 1985). This equation has the physical interpretation that within the q-dimensional subspace of the baseline modes, the work done by the stiffness and inertia forces of the modified system on the displacements of the unmodified system is zero. Its principal advantage is the reduction of order achieved with the subspace approximation. The baseline modes in Ψ are generally of low frequency; therefore, (4) is capable of giving fairly accurate solutions for the low-frequency modified modes without the computational expense incurred in solving (2) for systems with large n.

It is for these same advantages that (4) is adopted for inverse modification problems. Previous perturbation developments in this area, beginning with Stetson (1976), have premultiplied by the modified instead of the baseline modes. However, since both are described in the same subspace, little is to be gained by premultiplying by the modified modes. Indeed, this merely creates a higher degree of nonlinear coupling among the unknowns, making the equations more difficult to solve. Premultiplying by the baseline modes instead makes the equations tractable, and it is shown in Section 5 that they can be solved without neglecting any terms.

4 Structural Changes

The objective of inverse modification problems considered in the present study is to determine the matrix pair ΔK, ΔM required to satisfy the perturbation Eq. (4) subject to prescribed modal constraints. For any given problem, many combinations of ΔK and ΔM may satisfy the constraints, but not all of these will be physically possible. To obtain a realistic solution, ΔK and ΔM must be defined in terms of a number of physically meaningful "property change" or "design" variables.

Considering ΔK, ΔM to be a perturbation to a finite element model, this representation limits the possible structural change to a combination of the three following types:

- changes to the material properties of the structure;
- resizing of existing elements provided that node locations are left unchanged;
- adding new elements, externally connected springs, or lumped masses to the existing mesh.

The structural changes ΔK and ΔM are described by the summation of elemental changes:

$$\Delta K=\sum_e A_e^T\Delta k_e A_e \tag{5}$$

$$\Delta M=\sum_e A_e^T\Delta m_e A_e \tag{6}$$

where A_e is a matrix that transforms element coordinates to global coordinates.

The element matrices are functions of a number of independently varying "properties." For example, linear properties have element stiffness matrices of the form

$$k_e=(k_e^L)r+k_e^0, \tag{7}$$

where r represents the property variable and k_e^L is the matrix of coefficients. The perturbed element stiffness Δk_e is therefore ness Δk_e is therefore

Downloaded 03 May 2010 to 171.66.16.20. Redistribution subject to ASME license or copyright; see http://www.asme.org/terms/Terms_Use.cfm

$$\Delta k_e = k_e' - k_e = (k_e^L)\Delta r = (k_e^L) r\alpha \tag{8}$$

where α is the fractional change to the property r. Changes to element mass matrices are usually of this type. Nonlinear stiffness properties, such as the depth of a beam element or the thickness of a plate element, may be approximated as linear changes by the use of a Taylor expansion and by limiting the magnitude of the changes. Such a linearized perturbed element stiffness matrix can be expressed as

$$\Delta \tilde{k}_e = \Delta r \left.\frac{\partial k_e}{\partial r}\right|_{r=r_0} \equiv \alpha \left.\frac{\partial (\Delta k_e)}{\partial \alpha}\right|_{\alpha=0} \tag{9}$$

where r_0 denotes the baseline value of the property.

Summing over the m design variables affecting structural elements e and using the linearized expression (9), the total matrix perturbations are expressed as

$$\Delta K = \sum_e \sum_{j=1}^{m} A_e^T \frac{\partial k_e}{\partial r_j} A_e r_j \alpha_j = \sum_{j=1}^{m} (K_r)_j \alpha_j \tag{10}$$

$$\Delta M = \sum_e \sum_{j=1}^{m} A_e^T \frac{\partial m_e}{\partial r_j} A_e r_j \alpha_j = \sum_{j=1}^{m} (M_r)_j \alpha_j. \tag{11}$$

These expressions are generally only valid for linear property changes. For nonlinear changes the formulae are accurate only when the fractional change is small.

5 Solution Method for Frequency Modification Problems

Substituting (10) and (11) into the perturbation Eq. (4) gives

$$\sum_{j=1}^{m} \alpha_j \Psi^T [(K_r)_j - \lambda_i' (M_r)_j] \Psi c_i = -(\Lambda - \lambda_i' I) c_i \qquad i = 1, 2, \ldots, q. \tag{12}$$

Assuming for the present that only one frequency is modified, the ith frequency is prescribed by substituting $\lambda_i' = \lambda_i^*$ in (12), giving

$$\sum_{j=1}^{m} \alpha_j \Psi^T [(K_r)_j - \lambda_i^* (M_r)_j] \Psi c_i = -(\Lambda - \lambda_i^* I) c_i. \tag{13}$$

Equation (13) is a system of q equations in $q - 1 + m$ unknowns ($q - 1$ components of c_i that can be uniquely determined and m design variables). Because of coupling between the unknowns a direct solution of the equations is not possible and therefore an iterative solution is required.

With just one design variable, a unique solution to the frequency modification problem $\lambda_i' = \lambda_i^*$ is possible. For $m = 1$, (13) takes the form

$$\alpha_1 \Psi^T [(K_r)_1 - \lambda_i^* (M_r)_1] \Psi c_i = -(\Lambda - \lambda_i^* I) c_i \tag{14}$$

which is an eigenvalue equation with eigenvalue α_1 and eigenvector c_i. The solution of (14) gives rise to q values of α_1 and a corresponding number of c_i. Each of these solutions corresponds to a case where a different eigenvalue of the modified structure has been given the prescribed value λ_i^*. In practice many of the predicted design changes α_1 may not be physically realistic. A similar result can be obtained if there are m design variables and m prescribed frequencies.

In the more general case when the number of design variables is greater than the number of prescribed frequencies an iterative solution procedure is used. If a single eigenvalue λ_i^* is prescribed, then (13) provides a set of q equations each of which represents the work done by the inertial and stiffness forces of the ith modified mode on the displacements of one of the baseline modes. From this set the ith equation is used to determine the design variables $\alpha = (\alpha_1, \alpha_2, \ldots, \alpha_m)^T$.

$$\sum_{j=1}^{m} \alpha_j \psi_i^T [(K_r)_j - \lambda_i^* (M_r)_j] \Psi c_i = (\lambda_i^* - \lambda_i) c_{ii} \tag{15}$$

By choosing the ith equation, the resulting design solution will seek to change the spectrum such that the ith frequency of the modified mode attains the prescribed value. It may be appreciated that for small changes the forces of the ith modified mode are orthogonal to the displacements of the kth baseline mode ($k \neq i$) and thus the above strategy is appropriate. For large changes it is not possible to state definitively that the proposed equation is optimal. However, numerical experience has shown that the proposed approach works effectively. It was found that with (15) the original order of the modes is consistently preserved in the resulting design solution, although switching in the order of the modes is possible when the modes are closely spaced.

Having determined α from the design equation, the resulting mode shape change is determined by substituting α into the remaining $q - 1$ equations of (13):

$$\sum_{j=1}^{m} \alpha_j \psi_k^T [(K_r)_j - \lambda_i^* (M_r)_j] \Psi c_i + (\lambda_k - \lambda_i^*) c_{ik} = 0 \qquad k = 1, 2, \ldots, q;\ k \neq i. \tag{16}$$

As the vector of admixture coefficients c_i is only specified to within a common factor, one element of c_i must be set to unity so that the other $q - 1$ elements of the vector can be determined from (16). To avoid numerical difficulties, it is advisable to prescribe a unit value to the largest component of c_i, which is usually c_{ii}.

The solution of (15) and (16) can be performed repeatedly until the design solution converges. The solutions steps are summarized as follows, where (t) indicates the current iteration:

1 Let $t = 0$, $c_{ii}^{(0)} = 1$, $c_{ik}^{(0)} = 0$ for $k = 1, 2, \ldots, q$; $k \neq i$.

2 Calculate the design variables satisfying the design Eq. (15); i.e., solve

$$\sum_{j=1}^{m} \alpha_j^{(t+1)} \psi_i^T [(K_r)_j - \lambda_i^* (M_r)_j] \Psi c_i^{(t)} = (\lambda_i^* - \lambda_i) c_{ii}^{(t)} \tag{17}$$

for $\alpha_j^{(t+1)}$, $j = 1, 2, \ldots, m$. Note that if $m = 1$, the solution of this equation is unique. When $m > 1$, the solution is underdetermined and it is necessary to use optimization. A description of the optimization algorithm is given below under the heading "Mathematical Programming."

3 Calculate the eigenvector change satisfying (16) subject to the design modification $\alpha^{(t+1)}$; i.e., solve

$$\sum_{j=1}^{m} \alpha_j^{(t+1)} \psi_k^T [(K_r)_j - \lambda_i^* (M_r)_j] \Psi_i^{(t+1)} - (\lambda_k - \lambda_i^*) c_{ik}^{(t+1)} = 0 \qquad k = 1, 2, \ldots, q;\ k \neq i \tag{18}$$

for $c_i^{(t+1)}$. The $q - 1$ equations of (18) can be solved for $q - 1$ unknowns once a unit value has been prescribed to a single element of $c_i^{(t+1)}$.

4 Set $t = t + 1$ and repeat Steps 2, 3, and 4 until $\alpha^{(t+1)} = \alpha^{(t)}$.

In Step 1, the initial assumption made is that the modified eigenvector is no different from the baseline eigenvector. This is a useful approximation if, of the many possible solutions which may satisfy the equations, the most desirable is the one closest to the baseline.

Mathematical Programming. When $m > 1$, the solution of Step 2 is underdetermined and so a minimum change solution is sought through mathematical programming. In this study, a penalty function method employing a minimum change objective is used. This involves minimizing the functional

$$F^* = \alpha^T \alpha + \mu^{-1/2} R^T R + \mu \sum_{j=1}^{n_g} 1/g_j. \tag{19}$$

Downloaded 03 May 2010 to 171.66.16.20. Redistribution subject to ASME license or copyright; see http://www.asme.org/terms/Terms_Use.cfm

The first term is a measure of the overall change that is to be minimized. Minimum change solutions are often preferable to minimum weight solutions in redesign problems and are less liable to produce pathological solutions (Gans and Anderson, 1991). The second term is an external penalty function where R is the residual of the equality constraints. In this case R is just the residual of the design equation:

$$R = \sum_{j=1}^{m} \alpha_j^{(t+1)} \psi_i^T [(K_r)_j - \lambda_i^* (M_r)_j] \Psi c_i^{(t)} - (\lambda_i^* - \lambda_i) c_{ii}^{(t)}. \quad (20)$$

The third term of F^* is an interior penalty function in which $g_j \geq 0$, $j = 1, 2, \ldots, n_g$ are inequality constraints limiting the feasible domain of the design variables. For instance, $\alpha_j < -1$ are physically impossible, and so

$$\alpha_j + 1 \geq 0 \quad j = 1, 2, \ldots, m \quad (21)$$

are necessary inequality constraints. Further constraints on α can be added as desired. The use of this type of penalty function is discussed by Haftka and Kamat (1985). For it to be successful, the starting point ($\alpha = 0$) must be in the feasible region defined by the inequality constraints g_j, $j = 1, 2, \ldots, n_g$, otherwise the interior penalty function cannot work.

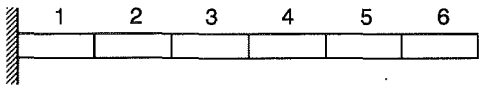
The minimum value of F^* is calculated using a quasi-Newton algorithm with a weak line search and a BFGS update, a description of which is given by Dennis and Schnabel (1983). The factor μ is chosen based on an initial estimate of the minimum of F^*. In the course of the quasi-Newton algorithm, μ is decreased by a factor of 5 after each iteration, progressively deemphasizing the inequality constraints in favor of the equality constraints.

Multiple Frequency Constraints. The above algorithm is easily adaptable for simultaneous multiple frequency constraints. If p frequencies are prescribed, p sets of q equations are obtained by substituting the appropriate index i in (13). One design equation is selected from each set, giving p equations with m unknowns in Step 2. A solution is possible when $m \geq p$, provided the p design equations are independent; a unique solution is possible when $m = p$, and mathematical programming is used when $m > p$. In Step 3, the modified mode shapes are obtained by solving each set of $q - 1$ equations separately. Generally, the number of frequency constraints is small compared to q, and so the number of additional equations is not too large to jeopardize the numerical efficiency of the method.

6 Examples

Two examples are given, the first of which is a simple cantilevered beam that serves to allow an effective comparison of the proposed method with the predictor-corrector method (Hoff et al., 1984, 1985). The second is more complex and is used to illustrate the effect of modal truncation and to make a further comparison of the two methods. Linear property variables are used exclusively in both examples, thus avoiding errors caused by the linearization of the design changes.

Cantilevered Beam; Comparison With the Predictor-Corrector Method. The six-element, 12-degree-of-freedom cantilevered beam in Fig. 1 was analyzed with the finite element program VAST (*VAST User's Manual*, 1990). Three undamped bending modes are retained for use in the perturbation analysis. The objective is to raise the fundamental frequency ($f_1 = 8.26$ Hz) by 10 percent, 50 percent, and 100 percent by changing the second moment of area of the six elements. The resulting fractional changes for the proposed new method and for the predictor-corrector method are given in Table 1. In the first two cases, a single-step of the predictor-corrector method was used to obtain the solutions. But with a frequency shift of 100 percent, single-step solutions violated the $\alpha_j \geq -1$ inequalities. Instead, 19 steps of the predictor-corrector algorithm were executed in which the prescribed eigenvalue was increased in seven-percent increments until a total frequency change of 100 percent was obtained. In all three cases it can be seen that the proposed method satisfies the frequency constraint better than the predictor-corrector method, and gives a design change of smaller absolute magnitude ($\Sigma \alpha_i^2$), thereby better satisfying the minimum change objective.



$f_1 = 8.283$ Hz
$f_2 = 51.92$ Hz
$f_3 = 145.6$ Hz

Fig. 1 Six-element cantilevered beam

Table 1 Design changes for the cantilevered beam with one prescribed frequency

f_1^*/f_1	1.1		1.5		2.0	
	A	B	A	B	A	C
α_1	0.289	0.313	1.727	2.977	4.175	5.639
α_2	0.175	0.152	1.173	0.999	2.918	2.965
α_3	0.086	0.062	0.682	−0.198	1.864	1.040
α_4	0.030	0.023	0.289	0.331	0.904	0.283
α_5	0.005	0.006	0.064	0.268	0.224	0.050
α_6	0.000	0.000	0.003	0.018	0.010	0.002
$\sum \alpha_i^2$	0.123	0.126	4.91	10.08	30.29	41.75
f_1'/f_1	1.100	1.099	1.496	1.436	1.997	1.957

A: Proposed Method
B: Predictor-Corrector (single step)
C: Predictor-Corrector (19 steps, 7% increments)

Table 2 Design changes for the cantilevered beam for two prescribed frequencies

f_1^*/f_1	1.1		1.3		
f_2^*/f_2	1.1		1.1		
	A	B	A	B	C
α_1	0.291	0.330	0.983	1.100	1.158
α_2	0.086	0.097	0.760	−0.060	0.505
α_3	0.193	0.170	0.258	0.798	0.443
α_4	0.222	0.203	−0.142	−0.011	−0.325
α_5	0.087	0.090	−0.120	−0.690	−0.046
α_6	0.005	0.006	−0.009	−0.086	0.026
$\sum \alpha_i^2$	0.186	0.197	1.65	2.32	1.90
f_1'/f_1	1.099	1.106	1.296	1.192	1.289
f_2'/f_2	1.099	1.099	1.095	0.985	1.070

A: Proposed Method
B: Predictor-Corrector (single step)
C: Predictor-Corrector (25 steps, 2% increments)

Similar comparisons can be made for the results in Table 2 where two frequency constraints are applied to the same problem. Two cases are presented: in the first, f_1 and f_2 are both raised by 10 percent; in the second case, these two frequencies are raised by 30 percent and 10 percent, respectively. In the latter case two sets of results for the predictor-corrector method are given, one of which is a single-step solution and the other a 25-step solution with two-percent increments in the prescribed eigenvalue. In all of these results, three baseline modes were retained in the equations. Tables 1 and 2 indicate that the proposed method is more effective than the predictor-corrector method, even when the latter is used step-wise.

The source of error in the predictor-corrector results in

Downloaded 03 May 2010 to 171.66.16.20. Redistribution subject to ASME license or copyright; see http://www.asme.org/terms/Terms_Use.cfm

Tables 1 and 2 is the linearization of the perturbation equations in the predictor phase. This linearization causes nonlinear coupling terms in the equations to be ignored which results in an inaccurate prediction of the modified mode shapes for large structural changes. The predicted mode shapes are used in the corrector phase to get an improved estimate of the structural changes. While the overall change in the mode shapes is not large (the admixture coefficients are listed in Table 3), it does not require a very large mode shape error to significantly affect the accuracy of the frequency. Note that the mode shape change required by the proposed method for shifting f_1 by 50 percent consists of an addition of a component of the second mode whose magnitude is only four percent of the baseline mode.

Note also that the predictor-corrector method predicts twice this change in the second baseline mode. It was found that if the correct mode shape was supplied to the corrector phase equations, results of accuracy equal to that of the proposed method were obtained.

Furthermore, as a result of linearization, modified mode shapes calculated in the predictor phase do not satisfy orthogonality conditions. The predictor-corrector methods have attempted to remedy this by imposing orthogonality constraints in the corrector phase. This is apt to make a naturally underconstrained problem overconstrained, thus necessitating a minimum error rather than a minimum change solution (Hoff et al., 1984). This difficulty is avoided in the proposed method because mode shape changes calculated from (18) automatically satisfy the orthogonality conditions and so the additional constraints are unnecessary.

Because the proposed method uses the full set of available perturbation equations to calculate the admixture coefficients, mode shape errors stemming from linearization are eliminated and the resulting design solution is more accurate. In fact, the new method gives the best accuracy possible with the available set of baseline modes provided a solution can be found; any remaining error in the satisfaction of the frequency constraint is caused by modal truncation. To obtain a more accurate solution, either the redesign solution should be repeated with a larger modal subspace, or else the structure should be fully reanalyzed with the resulting design changes and the redesign solution repeated with the new baseline modes.

Finite Element Container Ship; The Effect of Modal Truncation. As a second example, consider the two-dimensional model of a container ship in Fig. 2. A model of this type is useful for determining the vertical vibration modes of the actual ship. The model contains a total of 447 nodes and 894 degrees-of-freedom and is composed of membrane and bar elements. The membrane elements are used to simulate vertical panels, and the bar elements to simulate the presence of decks and bulkheads. The model is divided into five components and analyzed with a free-interface component mode synthesis method which includes the residual effects of neglected modes. Thirty undamped modes of the ship were accurately determined with this method (Smith, 1993).

The fourth mode (f_4 = .88 Hz), which corresponds to the two-node vertical bending mode of the hull, is to be raised by changing the stiffness of the hull bottom. In the present example, the frequency of this mode is raised by changing the effective elastic modulus of the hull-bottom stiffeners. Three groups of stiffeners belonging to three separate components are identified for modification, as shown in Fig. 2.

First, the three segments are made to change together as a single variable. Figure 3 shows the results of the proposed method for several different baseline mode approximations, along with results obtained by reanalysis with component mode synthesis. The one-mode approximation does not allow any mode shape correction; consequently, the curve is straight and is similar to what is obtained with a first-order sensitivity analysis. Additional modes in the baseline approximation progressively improve the accuracy of the redesigned vessel, and at $q = 30$ the reanalysis results are closely approximated. Even with 30 modes, the order of the perturbation equations is 30 times smaller than the size of the original model, and thus the iterative method described in Section 5 can still be used with great economy.

Secondly, the results for the three segments changing independently with a 30 baseline mode approximation were examined. The predictor-corrector results were calculated using a single equation (the frequency constraint equation) in the corrector phase and by neglecting the orthogonality constraints. Results obtained with the two methods are shown in Fig. 4 over a relatively small range of frequency shift, where α_1, α_2, and α_3 are the fractional changes of the element groups 1, 2, and 3, respectively. Finite element reanalysis with the design changes predicted for $f_4^* = 1.00$ Hz gives

$$\text{Proposed method: } f_4' = 0.995 \text{ Hz} \quad f_4'/f_4 = 1.131$$
$$\text{Predictor-corrector: } f_4' = 0.931 \text{ Hz} \quad f_4'/f_4 = 1.058.$$

The results determined from the proposed method are considerably more accurate than those determined from a single step of the predictor-corrector method. Figure 4 shows that the two methods predict similar design changes only for very small frequency changes, but as the changes become larger, the results for the two methods rapidly diverge. In fact, the size of the design change given by the predictor-corrector method actually begins to decrease when the frequency shift is large enough. This demonstrates that severe errors can result from the linearization of the perturbation equations even when the frequency shift is less than 15 percent as in Fig. 4. To improve the predictor corrector results in such cases, a step-wise solution of the type presented for the cantilevered beam is necessary.

Table 3 Modified mode shape admixture coefficients corresponding to the cantilevered beam results in Table 1

f_1^*/f_1	1.1		1.5		2.0	
	A	B	A	B	A	C
c_{11}	1.000	1.000	0.999	0.997	0.998	0.995
c_{12}	0.012	0.014	0.040	0.081	0.057	0.098
c_{13}	−0.001	−0.001	0.001	−0.008	0.005	0.006

A: Proposed Method
B: Predictor-Corrector (single step)
C: Predictor-Corrector (19 steps, 7% increments)

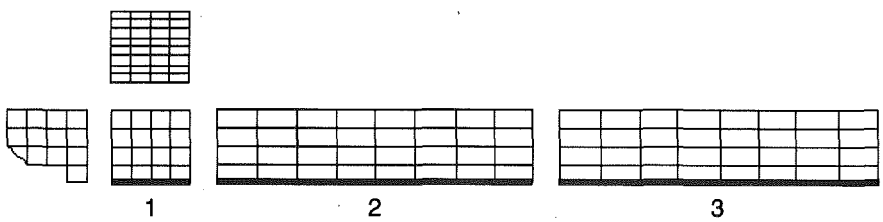


Fig. 2 Substructured container ship model with three groups of bar stiffeners designated for modification

Downloaded 03 May 2010 to 171.66.16.20. Redistribution subject to ASME license or copyright; see http://www.asme.org/terms/Terms_Use.cfm

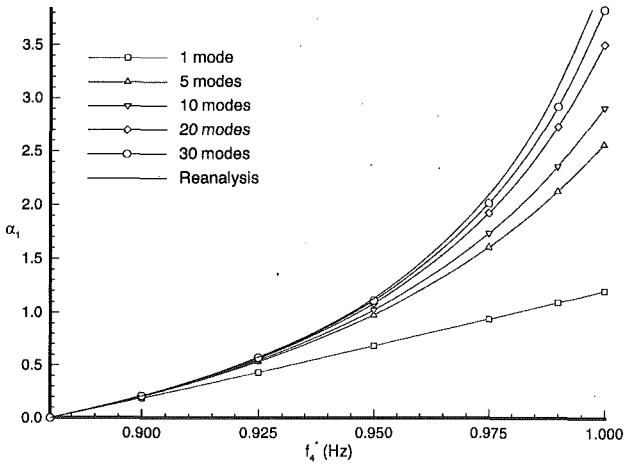


Fig. 3 Single-parameter frequency modification results for the container ship model

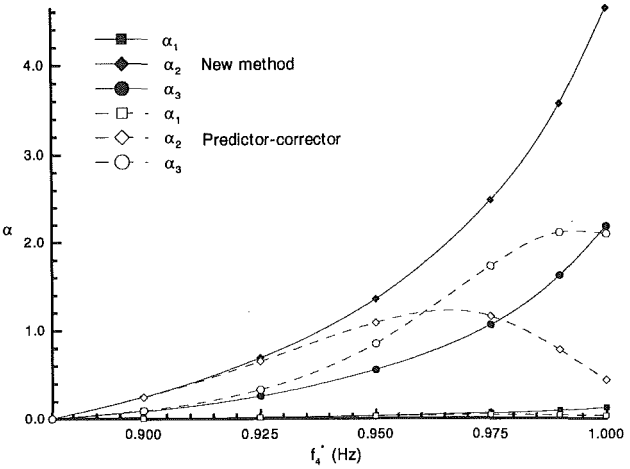


Fig. 4 Three-parameter frequency modification results for the container ship model

7 Summary and Conclusions

In this study, a new perturbation method has been given for frequency modification problems which arise in the design of discrete, undamped structures. In this method, a formulation different from previous methods is used for the perturbation equations. This enables the full set of equations to be solved by an iterative method which is better able to predict large mode shape changes and large design changes of a structure. The accuracy of the method relies on: (1) an accurate representation of the modified modes in a subspace defined by linear combinations of baseline modes; (2) the description of a structural change in terms of a set of linear design parameters which define perturbing stiffness and mass matrices for the system. By maintaining both of these conditions it is shown that accurate results can be obtained over a significant range of prescribed frequencies without resorting to a reanalysis of an intermediate structure. The method is capable of handling multiple frequency constraints and employs optimization for determining underconstrained design changes. Numerical results showed that the new method gives results of superior accuracy for large design changes, when compared to an established predictor-corrector method. The new method produces a solution which not only satisfies the frequency constraint (to within the limit imposed by the truncated baseline mode set), but also gives modified mode shapes that are automatically orthogonal with respect to the modified matrices.

References

Baldwin, J. F., and Hutton, S. G., 1985, "Natural Modes of Modified Structures," *AIAA Journal*, Vol. 23, No. 11, pp. 1737–1743.

Bernitsas, M. M., and Kang, B., 1991, "Admissible Large Perturbations in Structural Redesign," *AIAA Journal*, Vol. 29, No. 1, pp. 104–113.

Biegler-König, F. W., 1981, "A Newton Iteration Process for Inverse Eigenvalue Problems," *Numerische Mathematik*, Vol. 37, pp. 349–354.

Bohte, Z., 1967, "Numerical Solution of the Inverse Algebraic Eigenvalue Problem," *The Computer Journal*, Vol. 10, pp. 385–388.

Dennis, J. E., and Schnabel, R. B., 1983, *Numerical Methods for Unconstrained Optimization and Nonlinear Equations*, Prentice-Hall, Englewood Cliffs, NJ, p. 325.

Fox, R. L., and Kapoor, M. P., 1968, "Rates of Change of Eigenvalues and Eigenvectors," *AIAA Journal*, Vol. 6, No. 12, pp. 2426–2429.

Friedland, S., Nocedal, J., and Overton, M. L., 1987, "The Formulation and Analysis of Numerical Methods for Inverse Eigenvalue Problems," *SIAM Journal of Numerical Analysis*, Vol. 24, No. 3, pp. 634–667.

Gans, H. D., and Anderson, W. J., 1991, "Structural Optimization Incorporating Centrifugal and Coriolis Effects," *AIAA Journal*, Vol. 29, No. 10, pp. 1743–1750.

Haftka, R. T., and Kamat, M. P., 1985, *Elements of Structural Optimization*, Martinus Nijhoff Publishers, Dordrecht, The Netherlands, pp. 139–142.

Hoff, C. J., Bernitsas, M. M., Sandstrom, R. E., and Anderson, W. J., 1984, "Inverse Perturbation Method for Structural Redesign with Frequency and Mode Shape Constraints," *AIAA Journal*, Vol. 22, No. 9, pp. 1304–1309.

Hoff, C. J., and Bernitsas, M. M., 1985, "Dynamic Redesign of Marine Structures," *Journal of Ship Research*, Vol. 29, No. 4, pp. 285–295.

Kim, K., 1983a, "Nonlinear Inverse Perturbation Method in Dynamic Redesign," Ph.D. Thesis, University of Michigan, Ann Arbor, Mich.

Kim, K., Anderson, W. J., and Sandstrom, R. E., 1983b, "Nonlinear Inverse Perturbation Method in Dynamic Analysis," *AIAA Journal*, Vol. 21, No. 9, pp. 1310–1316.

Kim, K., and Anderson, W. J., 1984, "Generalized Dynamic Reduction in Finite Element Dynamic Optimization," *AIAA Journal*, Vol. 22, No. 11, pp. 1616–1617.

Nelson, R. B., 1976, "Simplified Calculation of Eigenvector Derivatives," *AIAA Journal*, Vol. 14, No. 9, pp. 1201–1205.

Pomazal, R. J., and Snyder, V. W., 1971, "Local Modifications of Damped Linear Systems," *AIAA Journal*, Vol. 9, No. 11, pp. 2216–2221.

Ram, Y. M., and Braun, S. G., 1991, "An Inverse Problem Associated with Modification of Incomplete Dynamic Systems," ASME Journal of Applied Mechanics, Vol. 58, pp. 233–237.

Sandström, R. E., and Anderson, W. J., 1982, "Modal Perturbation Methods for Marine Structures," *SNAME Transactions*, Vol. 90, pp. 41–54.

Smith, M. J., and Hutton, S. G., 1992, "Frequency Modification Using Newton's Method and Inverse Iteration Eigenvector Updating," *AIAA Journal*, Vol. 30, No. 7, pp. 1886–1891.

Smith, M. J., 1993, "An Evaluation of Component Mode Synthesis for Modal Analysis of Finite Element Models," Ph.D. Thesis, Department of Mechanical Engineering, University of British Columbia, Vancouver, Canada.

Stetson, K. A., and Palma, G. E., 1976, "Inversion of First-Order Perturbation Theory and Its Application to Structural Design," *AIAA Journal*, Vol. 14, No. 4, pp. 454–460.

Tsuei, Y. G., and Yee, E. K. L., 1989, "A Method for Modifying Dynamic Properties of Undamped Mechanical Systems," ASME *Journal of Dynamic Systems, Measurement, and Control*, Vol. 111, pp. 403–408.

Vibration and Strength Analysis Program (VAST), Version 6.0: User's Manual, 1990, Martec Limited, Halifax, Nova Scotia, Canada.

Weissenburger, J. T., 1968, "Effect of Local Modifications on the Vibration Characteristics of Linear Systems," ASME Journal of Applied Mechanics, Vol. 35, pp. 327–332.

Downloaded 03 May 2010 to 171.66.16.20. Redistribution subject to ASME license or copyright; see http://www.asme.org/terms/Terms_Use.cfm

Doubly Asymptotic Approximations for Submerged Structures With Internal Fluid Volumes: Formulation

T. L. Geers
Fellow ASME.

Peizhen Zhang[1]
Assoc. Mem. ASME.

Center for Acoustics,
Mechanics and Materials,
Department of Mechanical Engineering,
University of Colorado,
Boulder, CO 80309-0427

Doubly asymptotic approximations (DAAs) are approximate temporal impedance relations for a medium in contact with a flexible body. In this paper, the method of operator matching previously used for external acoustic domains is used to develop first- and second-order boundary integral DAAs for internal acoustic domains. Corresponding boundary element forms permit the numerical solution of transient structural acoustics problems with complex geometry. The accuracy of the DAAs is assessed in the following companion paper by comparing DAA and exact solutions for a canonical problem with spherical geometry.

1 Introduction

Treating the transient dynamic interaction between a structure in contact with an acoustic medium is a formidable task. Given the dynamical equations for the structure and a specification of the initial conditions, external dynamic forces, and/or incident-wave field, a *doubly asymptotic approximation* (DAA) provides a link that greatly simplifies the analysis. This simplification allows the analyst to devote most of his/her computational resources to the structural model, which is the focus of interest, by minimizing the resources required for modeling the medium, which is rarely of interest.

In the 1970s, DAAs were first developed to treat the external fluid-structure interaction in underwater shock problems (Geers, 1971, 1974, 1978). These approximations approach exactness in both the early-time/high-frequency and late-time/low-frequency limits: hence the name *doubly asymptotic*. Acoustic DAAs have been incorporated in a variety of production computer programs that are routinely used for engineering analysis (Ranlet, et al., 1977; DeRuntz, et al., 1980; DeRuntz and Brogan, 1980; Neilson, et al., 1981; Vasudevan and Ranlet, 1982; Atkatsh, et al., 1987). In the 1980's, the acoustic DAA methodology was improved (Felippa, 1980a; Geers and Felippa, 1983; Nicolas-Vullierme, 1989) and the DAA concept was extended to elastodynamics and electromagnetics (Underwood and Geers, 1981; Mathews and Geers, 1987; Geers and Zhang, 1988).

In an acoustics context, the general approach has been to regard the pressure and fluid displacement in the medium as the sum of those associated with the incoming incident wave (if there is one) and those associated with the outgoing scattered wave (of which there is always one—if there is no incident wave, the scattered wave is usually called the radiated wave). Compatibility of surface pressures and normal displacements provides all of the remaining relations needed save one: a temporal impedance relation between the scattered-wave pressure and the scattered-wave normal fluid displacement over the surface of the structure in contact with the medium.

The Kirchhoff retarded-potential formula for an acoustic medium provides an exact temporal impedance relation connecting scattered-wave pressure and normal displacement. Unfortunately, this relation constitutes an integral equation over the contact surface that involves field variables with retarded-time arguments; hence it is local neither in space nor in time, and it is complicated. These characteristics mitigate against computational efficiency, prompting the development of simpler relations. *Singly asymptotic approximations* have been developed that apply either at early time or at late time (but not both), but they are not sufficiently robust for diverse application. In contrast, doubly asymptotic approximations for external domains have been found to be efficient and accurate in many applications.

Recently, interest has developed in DAAs for *internal acoustic domains*, principally for application to submerged structures possessing free-flooding areas and fluid-filled tanks. This interest has been motivated by the following factors: (1) internal domains of practical interest often possess exceedingly complex geometries, which make three-dimensional mesh generation for finite element modeling costly and cumbersome; (2) numerical simulations of discontinuous wave fronts through three-dimensional finite element meshes typically contain nonphysical oscillations that compromise the value of the calculations; and (3) an exact boundary element treatment based

[1]Present address: J I Case, Hinsdale, IL 60521.

Contributed by the Applied Mechanics Division of THE AMERICAN SOCIETY OF MECHANICAL ENGINEERS for publication in the ASME JOURNAL OF APPLIED MECHANICS.

Discussion on this paper should be addressed to the Technical Editor, Professor Lewis T. Wheeler, Department of Mechanical Engineering, University of Houston, Houston, TX 77204-4792, and will be accepted until four months after final publication of the paper itself in the ASME JOURNAL OF APPLIED MECHANICS.

Manuscript received by the ASME Applied Mechanics Division, Dec. 9, 1991; final revision, Oct. 18, 1993. Associate Technical Editor: S. K. Datta.

Copyright © 1994 by ASME
Downloaded 03 May 2010 to 171.66.16.20. Redistribution subject to ASME license or copyright; see http://www.asme.org/terms/Terms_Use.cfm

on Kirchhoff's retarded-potential formula would be computationally intensive, typically usurping resources that are needed for accurate structural modeling.

First- and second-order DAAs are formulated herein by the *method of operator matching* (Nicolas-Vullierme, 1989), which is akin to the well-known method of matched asymptotic expansions (see, e.g., Van Dyke, 1964). In the latter, matching is applied to solutions; in the former, matching is applied to equations. Operator matching enjoys the advantage over other DAA formulation methods that it is systematic and unambiguous.

The accuracy of the DAAs formulated in this paper is examined in the following companion paper through specialization to axisymmetric flow inside and outside a spherical surface. The resulting DAA relations are used to determine response histories for a fluid-filled, submerged spherical shell excited by an incident step-wave. These histories are compared with corresponding exact histories for this canonical problem (Zhang and Geers, 1993) to assess DAA accuracy.

2 DAA_1 For an External Acoustic Domain

It is appropriate first to outline the formulation, by the method of operator matching, of the first-order doubly asymptotic approximation for an external acoustic domain. The resulting DAA_1 is that originally formulated heuristically in Geers (1971). In this and subsequent external DAA formulations, the acoustic variables pertain exclusively to the scattered wave.

2.1 Retarded Potential Formula. With the acoustic *pressure* $p(\mathbf{r}, t)$ and fluid *displacement* $\mathbf{u}(\mathbf{r}, t)$ given in terms of a *velocity potential* $\varphi(\mathbf{r}, t)$ as

$$p(\mathbf{r}, t) = \rho\dot{\varphi}(\mathbf{r}, t)$$

$$\dot{\mathbf{u}}(\mathbf{r}, t) = -\nabla\varphi(\mathbf{r}, t) \tag{1}$$

where ρ is the mass density of the fluid, an overdot denotes differentiation in time, and ∇ is the gradient operator. The wave equation for a uniform acoustic fluid is (see, e.g., Pierce, 1981)

$$c^2\nabla^2\varphi = \ddot{\varphi} \tag{2}$$

where c is the speed of sound in the fluid and ∇^2 is the Laplacian operator. With $\mathbf{n}$ as the normal going *into* the fluid at a point on a surface S that bounds the fluid domain, the inward fluid displacement normal to that surface is defined by $u = \mathbf{u} \cdot \mathbf{n}$.

An exact, integral-equation solution to (2) is given by Kirchhoff's retarded potential formula (RPF) (see, e.g., Baker and Copson, 1939; Sobolev, 1964), which may be written for points P and Q on S as

$$2\pi p(P, t) = \int_S \{\rho R_{PQ}^{-1}\ddot{u}(Q, t_R) - R_{PQ}^{-2}\cos\phi_{PQ}[p(Q, t_R) + c^{-1}R_{PQ}\dot{p}(Q, t_R)]\}dS_Q \tag{3}$$

where $R_{PQ} = |\mathbf{r}_P - \mathbf{r}_Q|$, ϕ_{PQ} is the angle between $\mathbf{R}_{PQ}$ and $\mathbf{n}_Q$, and t_R is the *retarded time* $t - c^{-1}R_{PQ}$; the line through the integral sign denotes the Cauchy principle value of the integral (see, e.g., Greenberg, 1978). The constant 2π multiplying $p(P, t)$ on the left side of (3) indicates that the point P is located on a smooth portion of the surface S. If P is not on the surface, but is inside (outside) the fluid domain, the multiplying constant becomes 4π (zero); if S is not smooth at P, but instead has an edge or a corner there, the multiplying constant becomes the value of the solid angle subtended by the edge or corner. It is sometimes convenient formally to incorporate the singular contribution $2\pi p(P, t)$ into the spatial integral of (3) and then take the Laplace transform of the result to obtain

$$\int_S R_{PQ}^{-2}\cos\phi_{PQ}(1 + R_{PQ}s/c)e^{-(R_{PQ}s/c)}p(Q, s)dS_Q = \rho\int_S R_{PQ}^{-1}s^2e^{-(R_{PQ}s/c)}u(Q, s)dS_Q. \tag{4}$$

2.2 First-Order Early-Time/High-Frequency Approximation: ETA_1/HFA_1. Early-time approximations (ETA's) are the inverse Laplace transforms of high-frequency approximations (HFA's) to which (4) reduces when $\bar{R}s/c \gg 1$, where $\bar{R}$ is a characteristic length dimension of the structure; this corresponds in the time domain to $ct/\bar{R} \ll 1$ (Geers, 1975). The first-order ETA for an external acoustic medium was first utilized by Mindlin and Bleich (1953) for a problem in polar coordinates. In a systematic analysis, Felippa (1980a) found the same result for a general smooth surface, which is

$$\text{ETA}_1: \qquad p(P, t) = \rho c\dot{u}(P, t). \tag{5}$$

Thus, by the Laplace transformation, the first-order high-frequency approximation is

$$\text{HFA}_1: \qquad p(P, s) = \rho csu(P, s). \tag{6}$$

A simple way to obtain (5) is to visualize the scattered wave as having propagated only a very short distance away from the smooth surface of the structure. To an observer at a point on or behind the wavefront, the surface looks *flat*, so that $\cos\phi_{pq} \cong 0$ and (3) reduces to

$$2\pi p(P, t) \cong \rho\int_S R_{PQ}^{-1}\ddot{u}(Q, t_R)dS_Q \tag{7}$$

Now construct a local polar coordinate system at P and observe that surface accelerations at points further than the distance ct from P do not contribute to the integral; hence (7) becomes

$$2\pi p(P, t) \cong \rho\int_0^{ct}\int_0^{2\pi} r^{-1}\ddot{u}(r, \theta, t - r/c)rd\theta dr. \tag{8}$$

Next, regard $\ddot{u}$ as approximately constant within the circle $r = ct$ around P and introduce the change of variable $r = c(t - t')$, $dr = -ct'$, so that (8) becomes

$$2\pi p(P, t) \cong 2\pi\rho c\int_0^t \ddot{u}(P, t')dt'. \tag{9}$$

Evaluation of the integral for $\dot{u}(P, 0) = 0$ yields (5).

ETA_1 (HFA_1) is clearly a *spatially local approximation*, stating that each element of the surface S independently generates a plane wave that propagates normally into the fluid. In addition, it applies equally well to either an external or an internal fluid domain. Finally, because ETA_1 (HFA_1) approaches exactness only as $t \to 0$ ($s \to \infty$), it is *singly asymptotic*. In the literature, ETA_1 is often referred to as the *plane wave approximation*.

2.3 First-Order Late-Time/Low-Frequency Approximation: LTA_1/LFA_1. Late-time approximations (LTA's) are the inverse Laplace transforms of low-frequency approximations (LFA's) to which (4) reduces when $\bar{R}s/c \ll 1$, which corresponds in the time domain to $ct/\bar{R} \gg 1$ (Geers, 1975). The first-order LTA for an external acoustic domain was first utilized by Chertock (1972). The corresponding first-order LFA is readily obtained by expanding the exponentials in (4) in a Maclaurin's series as

$$e^{-R_{PQ}s/c} = 1 - R_{PQ}s/c + \frac{1}{2}(R_{PQ}s/c)^2 - \ldots, \tag{10}$$

introducing (10) into (4), and retaining only terms of order s^0 on the left and s^2 on the right. The result is

$$\text{LFA}_1: \qquad \beta^{-1}\gamma p(P, s) = \rho s^2 u(P, s) \tag{11}$$

where the spatial integral operators β and γ are defined by

Downloaded 03 May 2010 to 171.66.16.20. Redistribution subject to ASME license or copyright; see http://www.asme.org/terms/Terms_Use.cfm

$$\beta q(P) \equiv \int_S R_{PQ}^{-1}\, q(Q)\, dS_Q$$

$$\gamma q(P) \equiv \int_S R_{PQ}^{-2} \cos\phi_{PQ}\, q(Q)\, dS_Q. \tag{12}$$

In (11), β^{-1} denotes the inverse of the operator β, i.e., if $q(P)$ produces $p(P) = \beta q(Q)$ through the first of (12), then $p(P)$ produces $q(P)$ through the relation $q(P) = \beta^{-1}p(Q)$. It can be shown that β is invertible. Inverse transformation of (11) yields the first-order late-time approximation

$$\text{LTA}_1\text{:} \qquad \beta^{-1}\gamma p(P, t) = \rho\ddot{u}(P, t). \tag{13}$$

Note that, unlike ETA_1 (HFA_1), LTA_1 (LFA_1) is not spatially local, and that, like ETA_1 (HFA_1), LTA_1 (LFA_1) is singly asymptotic, but in the limit $t \to \infty$ ($s \to 0$) instead of $t \to 0$ ($s \to \infty$).

By taking the Laplace transform of (2), considering $\nabla^2 \sim \overline{R}^{-2}$, and then letting $\overline{R}s/c \to 0$, one obtains Laplace's equation, $\nabla^2\phi = 0$. But this same limiting process turns (4) into (11); correspondingly, (3) turns into (13) for $ct/\overline{R} \to \infty$. Thus LFA_1 and LTA_1 pertain to the irrotational flow of an inviscid, incompressible fluid. In the literature, LTA_1 is often referred to as the *added mass approximation* or *virtual mass approximation*.

2.4 First-Order Doubly Asymptotic Approximation: DAA_1. An examination of (6) and (11) reveals that a relation with one term in $s^0p(P, s)$ and another in $s^1p(P, s)$ on the left, and with one term in $s^2u(P, s)$ on the right, is the most compact relation capable of reducing to the two singly asymptotic relations in the appropriate limits. Hence, as the first step in the method of operator matching, we introduce the DAA_1 *trial equation*

$$[sP_1 + cP_0]p(P, s) = \rho cs^2u(P, s) \tag{14}$$

where P_0 and P_1 are spatial operators (not functions of s!).

For $s \to 0$, we write (14) as

$$[P_0 + O(s)]p(P, s) = \rho s^2u(P, s) \tag{15}$$

and match it to (11) as $s \to 0$, which yields $P_0 = \beta^{-1}\gamma$. For $s \to \infty$, we write (14)

$$[P_1 + O(s^{-1})]p(P, s) = \rho csu(P, s), \tag{16}$$

and match it to (6) as $s \to \infty$, which yields $P_1 = 1$. The introduction of these results into (14) produces the first-order DAA for an external acoustic domain, expressed in transform space as

$$\text{DAA}_1(s)\text{:} \qquad [s + c\beta^{-1}\gamma]p(P, s) = \rho cs^2u(P, s) \tag{17}$$

and in the time domain as

$$\text{DAA}_1(t) \qquad \dot{p}(P, t) + c\beta^{-1}\gamma p(P, t) = \rho c\ddot{u}(P, t) \tag{18}$$

We note that, as might be anticipated, DAA_1 is not a spatially local approximation.

As discussed in Geers and Zhang (1991), a boundary element form of (18) is readily constructed for numerical computation. In that form, p and u become column vectors of nodal quantities, and β and γ become fully populated coefficient matrices. Thus (18) becomes a set of ordinary differential equations, which, upon further development, can be symmetrized.

3 DAA_1 for an Internal Acoustic Domain

Development of the first-order DAA for an internal acoustic domain is complicated by the existence of low-frequency dilatational motion, which does not occur in an external domain. Hence, while ETA_1 (HFA_1) is the same for both internal and external domains, LTA_1 (LFA_1) and thus DAA_1 for the internal domain differ from their external counterparts.

3.1 Equivoluminal and Dilatational Fields for Low-Frequency Motion. We recall the conservation-of-mass equation, the constitutive equation, and the small-perturbation assumption for an acoustic fluid (see, e.g., Pierce, 1981)

$$\frac{\partial\rho}{\partial t} + \nabla\cdot(\rho\dot{\mathbf{u}}) = 0, \quad \frac{\partial p}{\partial t} = c^2\frac{\partial\rho}{\partial t}, \quad \nabla\cdot(\rho\dot{\mathbf{u}}) \cong \rho\nabla\cdot\dot{\mathbf{u}}. \tag{19}$$

These may be combined to yield

$$\nabla\cdot\dot{\mathbf{u}} = -(\rho c^2)^{-1}\frac{\partial p}{\partial t}. \tag{20}$$

In order to accommodate dilatational fluid motion in the internal domain, we take $p(\mathbf{r}, t) = p^d(t)$, so that (20) becomes, after integration in time with quiescent initial conditions,

$$\nabla\cdot\mathbf{u}(\mathbf{r}, t) = -(\rho c^2)^{-1}p^d(t). \tag{21}$$

Note that $p^d(t) = 0$ for an external medium, in order that the boundary condition of zero acoustic pressure at infinity may be satisfied.

Now (21) is an equation that holds at every point in the fluid volume. Hence we may integrate it over the volume and apply the divergence theorem to the left side of the resulting equation to obtain

$$\int_S u(P, t)\, dS_P = (\rho c^2)^{-1}Vp^d(t) \tag{22}$$

where we recall that $u = \mathbf{u}\cdot\mathbf{n}$, and where V is the volume of the internal fluid domain. Let us investigate the nature of the solutions to (22).

First, we take the fluid displacement field as comprised of two parts: $\mathbf{u}(\mathbf{r}, t) = \mathbf{u}^e(\mathbf{r}, t) + \mathbf{u}^d(\mathbf{r}, t)$, where $\mathbf{u}^e(\mathbf{r}, t)$, is the homogeneous solution, i.e., that for which $p^d(t) = 0$, and $\mathbf{u}^d(\mathbf{r}, t)$ is the particular solution produced by $p^d(t)$. On this basis, (22) yields

$$\int_S u^e(P, t)\, dS_P = 0$$

$$\int_S u^d(P, t)\, dS_P = (\rho c^2)^{-1}Vp^d(t). \tag{23}$$

We recognize $\mathbf{u}^e$ and $\mathbf{u}^d$ as linearly independent equivoluminal and dilatational fluid displacement fields, respectively. Similarly, $p(r, t) = p^e(r, t) + p^d(t)$, where $p^e(P, t)$ satisfies a zero-average equation like the first of (23).

Next, we show that u^d is *constant over the surface S* and determine its relationship to p^d. Suppose that

$$u^d(P, t) = u^d(t) + u^v(P, t) \tag{24}$$

in which $u^d(t)$ is the average of $u^d(P, t)$, given by $u^d(t) = \alpha u^d(P, t)$, where α is the *averaging operator* defined as

$$\alpha q(P) \equiv \frac{1}{A}\int_S q(P)\, dS_P \tag{25}$$

in which A is the area of the surface S. Then integration of (24) over S yields

$$\int_S u^v(P, t)\, dS_P = 0 \tag{26}$$

But if u^v satisfies this equation, then, from the first of (23), it must be part of the homogeneous solution u^e rather than part of the particular solution u^d. Thus $u^d(P, t) = u^d(t)$, and the second of (23) yields

$$p^d(t) = \rho c^2(A/V)u^d(t). \tag{27}$$

3.2 First-Order Late-Time/Low-Frequency Approximation: $\text{LTA}_1/\text{LFA}_1$. Determining LFA_1 for an internal acoustic domain requires separate consideration of equivoluminal motion and dilatational motion. For equivoluminal motion,

Downloaded 03 May 2010 to 171.66.16.20. Redistribution subject to ASME license or copyright; see http://www.asme.org/terms/Terms_Use.cfm

where the flow is incompressible, LFA_1 is determined in the same manner as that used for general motion in the external domain, and is given by (cf. (11))

$$\beta^{-1}\gamma p^e(P, s) = \rho s^2 u^e(P, s). \tag{28}$$

Note, however, that γ here pertains to an inward normal, while γ in (11) pertains to an outward normal.

The equivoluminal relation (28) is not valid for dilatational motion, because $\gamma p(P) = 0$ when $p(P)$ is constant over S. This may be shown by introducing into Green's second identity

$$\int_V (p\nabla^2 q - q\nabla^2 p)dV = \int_S \left(p\frac{\partial q}{\partial n} - q\frac{\partial p}{\partial n}\right)dS \tag{29}$$

the particular functions $p = 1$ and $q = 1/R_{PQ'}$. Here, P is any point on S and Q' represents all points in V; Q' is isolated from P by an arbitrarily small hemispherical dimple. In this case, all terms vanish except that produced by the first integrand on the right, yielding

$$\int_S \frac{\partial}{\partial n}(1/R_{PQ})dS = -\int_S R_{PQ}^{-2}\frac{\partial(R_{PQ})}{\partial n}dS$$

$$= -\int_S R_{PQ}^{-2}\cos\phi_{PQ}dS = 0. \tag{30}$$

But, from the second of (12), we recognize the last integral as $\gamma 1$; thus $\gamma p(P) = 0$ when $p(P)$ is constant over S.

To determine LFA_1 for dilatational motion, we take $p(P, s) = p^d(s)$ and $u(P, s) = u^d(s)$, introduce (10) into (4), and retain on both sides all terms through those of order s^2 to obtain

$$\left(0 - \frac{1}{2}(s/c)^2\eta 1\right)p^d(s) = \rho s^2\beta 1 u^d(s) \tag{31}$$

where the spatial operator η is defined as

$$\eta q(P) \equiv \int_S \cos\phi_{PQ}\, q(Q)dS_Q. \tag{32}$$

Because (31) must agree with (27), $\eta 1 = -2(V/A)\beta 1$.

To derive a first-order LFA for general motion in an internal domain, one might simply introduce (10) into (4), retain on both sides all terms through those of order s^2, and premultiply through by β^{-1} to get

$$\left[\beta^{-1}\gamma - \frac{1}{2}(s/c)^2\beta^{-1}\eta\right]p(P, s) = \rho s^2 u(P, s). \tag{33}$$

However, for equivoluminal motion, this expression contains on the left both $O(s^0)$ and $O(s^2)$ terms and therefore doesn't agree with (28); hence it is not a first-order LFA. The correct first-order LFA is

$$LFA_1: \quad [\beta^{-1}\gamma + (s/c)^2 L\alpha]p(P, s) = \rho s^2 u(P, s) \tag{34}$$

where $L = V/A$. For equivoluminal motion, this relation becomes (28) because $\alpha p^e(P, s) = 0$; for dilatational motion, it corresponds to (27) because $\gamma p^d(P, s) = \gamma p^d(s) = 0$, $\alpha p^d(P, s) = \alpha p^d(s) = p^d(s)$, and $u^d(P, s) = u^d(s)$. We note that (34) is spatially nonlocal and singly asymptotic in the limit $s \to 0$. We also note that the first-order late-time approximation LTA_1 is given by the inverse transform of (34).

3.3 First-Order Doubly Asymptotic Approximation: DAA_1. Having gained in Section 2.4 some experience in the method of operator matching, we propose a DAA_1 trial equation that immediately satisfies (6) for $s \to \infty$, viz.,

$$(s + cP_0)p(P, s) = \rho cs(s + cU_0)u(P, s) \tag{35}$$

where P_0 and U_0 are unknown spatial operators.

For *equivoluminal motion* with $s \to 0$, we write (35) as

$$[P_0 + O(s)]p^e(P, s) = \rho s(cU_0 + s)u^e(P, s). \tag{36}$$

The only way in which this can match (34) with $p(P, s) = p^e(P, s)$ is if $U_0 = V_0\alpha$, which annihilates the first term on the right side of (36), and if $P_0 = \beta^{-1}\gamma$.

Next, we consider (35) as it would apply to *dilatational motion* with $s \to 0$. Dividing through by s, and noting that $P_0 p(P, s) = \beta^{-1}\gamma p^d(s) = 0$, and that $U_0 u(P, s) = V_0\alpha u^d(s) = V_0 u^d(s)$, we obtain

$$p^d(s) = \rho c^2 V_0 u^d(s) + O(s). \tag{37}$$

This matches (34) with $p(P, s) = p^d(s)$ only if $V_0 = L^{-1}$.

The introduction of these results into (35) produces the first-order DAA for an internal acoustic domain, expressed in transform space as (cf. (17))

$$DAA_1(s): \quad (s + c\beta^{-1}\gamma)p(P, s) = \rho cs(s + cL^{-1}\alpha)u(P, s) \tag{38}$$

and in the time domain as (cf. (18))

$$DAA_1(t): \quad \dot{p}(P, t) + c\beta^{-1}\gamma p(P, t) = \rho c\ddot{u}(P, t) + \rho c^2 L^{-1}\alpha\dot{u}(P, t). \tag{39}$$

As expected, this is a spatially nonlocal approximation.

A boundary element form of (39) is readily constructed (Geers and Zhang, 1991). In that form, p and u become column vectors, β and γ become fully populated matrices (with γ being singular), and α becomes a rank-one matrix. Thus (39) becomes a set of ordinary differential equations, which can be symmetrized.

4 DAA_2 for an External Acoustic Domain

In the previous sections we formulated first-order DAAs for both external and internal domains. In this section, we derive a second-order DAA for an external domain by the method of operator matching. The corresponding matrix form for boundary element analysis is given in Geers and Zhang (1991).

4.1 Second-Order High-Frequency/Early-Time Approximation: HFA_2/ETA_2. An extension of the development described in Section 2.2 (Felippa, 1980a) yields the second-order high-frequency approximation (cf. (6))

$$HFA_2: \quad [s + c\kappa(P)]p(P, s) = \rho cs^2 u(P, s) \tag{40}$$

where $\kappa(P)$ is the local mean curvature of the surface, which is here defined as positive for a *convex* surface. The second-order early-time approximation ETA_2 is simply the inverse transform of this equation.

An alternate way to obtain (40) (Nicolas-Vullierme, 1989) is to retrieve from acoustic ray theory the following expression for field variation along a scattered ray (see, e.g., Pierce, 1981):

$$\varphi(P, l, s) = \left[\frac{\rho_1\rho_2}{(\rho_1 + l)(\rho_2 + l)}\right]^{1/2} e^{-ls/c}\varphi(P, 0, s) \tag{41}$$

where ρ_1 and ρ_2 are the principal radii of curvature for the surface at point P (positive when convex) and l is the distance along the ray that is perpendicular to the surface at P. From this expression,

$$\frac{d\varphi}{dl}(P, l, s) = -\frac{s}{c}\varphi(P, l, s) - \frac{(\rho_1\rho_2)^{1/2}(\rho_1 + \rho_2 + 2l)}{2(\rho_1 + l)^{3/2}(\rho_2 + l)^{3/2}} e^{-ls/c}\varphi(P, 0, s). \tag{42}$$

Hence, with $su(P, s) = -(d\varphi/dl)(P, 0, s)$ and $p(P, s) = \rho s\varphi(P, 0, s)$, (42) yields

$$\rho cs^2 u(P, s) = \left(s + c\frac{\rho_1 + \rho_2}{2\rho_1\rho_2}\right)p(P, s) \tag{43}$$

which agrees with (40).

Like ETA_1 (HFA_1), ETA_2 (HFA_2) is a local approximation in space, except that it has each element of the surface S independently generating a curved wave that propagates out-

Downloaded 03 May 2010 to 171.66.16.20. Redistribution subject to ASME license or copyright; see http://www.asme.org/terms/Terms_Use.cfm

wardly into the fluid. ETA_2 is often referred to in the literature as the *curved wave approximation*; it was introduced in Haywood (1958) for a problem in cylindrical coordinates and generalized in Bedrosian and Dimaggio (1972).

4.2 Second-Order Low-Frequency/Late-Time Approximation: LFA_2/LTA_2. The derivation of LFA_2 consists merely of extending that of LFA_1, i.e., introducing (10) into (4) and retaining terms of order s^0 and s^1 on the left and s^2 and s^3 on the right. This yields (cf. (11))

$$\text{LFA}_2: \quad \beta^{-1}\gamma p(P, s) = \rho s^2(1 - c^{-1}sA\beta^{-1}\alpha)u(P, s) \tag{44}$$

where α, β, and γ are given in (25) and (12). We observe that the term of order s^1 on the left has vanished identically and that LTA_2 is obtained by inverse transformation of (44).

4.3 Second-Order Doubly Asymptotic Approximation: DAA_2. Pursuing a procedure similar to, but more complicated than, that used for DAA_1, we propose the DAA_2 trial equation

$$(s^2 + csP_1 + c^2P_o)p(P, s) = \rho cs^2(s + cU_o)u(P, s) \tag{45}$$

where P_o, P_1 and U_o are spatial operators to be defined. For $s \to 0$, we write this as

$$[P_o + c^{-1}sP_1 + O(s^2)]p(P, s) = \rho s^2(U_o + c^{-1}s)u(P, s). \tag{46}$$

For $s \to \infty$, we write (45) as

$$[1 + cs^{-1}P_1 + O(s^{-2})]p(P, s) = \rho c(s + cU_o)u(P, s). \tag{47}$$

In order to match (46) to (44) and (47) to (40), we need to invert the operator ensembles either on the left or right of (46) and (47). This leads to four possible solution procedures, which, as might be expected, are equivalent. For example, let us invert the operator on the left side of (46) to obtain, for $s \to 0$,

$$p(P, s) = \rho s^2[1 - c^{-1}sP_0^{-1}P_1 + O(s^2)]P_o^{-1}(U_o + c^{-1}s)u(P, s) \tag{48}$$

because $[1 - c^{-1}sP_o^{-1}P_1 + O(s^2)]P_o^{-1}[P_o + c^{-1}sP_1 + O(s^2)] = 1 + O(s^2)$. Thus, keeping terms of order s^0 and s^1, and then multiplying through by the operator $\beta^{-1}\gamma$, we obtain the result

$$\beta^{-1}\gamma p(P, s) = \rho s^2\beta^{-1}\gamma P_o^{-1}[U_o + c^{-1}s(1 - P_1P_o^{-1}U_o)]u(P, s). \tag{49}$$

Matching this to (44), we find

$$\beta^{-1}\gamma P_o^{-1}U_o = 1$$

$$\beta^{-1}\gamma P_o^{-1}(P_1P_o^{-1}U_o - 1) = A\beta^{-1}\alpha \tag{50}$$

Similarly, we invert the operator on the right side of (47) to obtain

$$s^{-1}[1 - cs^{-1}U_o + O(s^{-2})][1 + cs^{-1}P_1 + O(s^{-2})]p(P, s) = \rho cu(P, s) \tag{51}$$

inasmuch as $s^{-1}[1 - cs^{-1}U_o + O(s^{-2})](s + cU_o) = 1 + O(s^{-2})$. Hence, retaining terms of order s^{-1} and s^{-2}, and then multiplying through by s^2, we obtain

$$[s + c(P_1 - U_o)]p(P, s) = \rho cs^2u(P, s). \tag{52}$$

Matching this to (40), we find

$$P_1 - U_o = \kappa(P) \tag{53}$$

The unknown operators P_o, P_1, and U_o may now be determined by solving (50) and (53) simultaneously. This yields

$$P_o = \chi\beta^{-1}\gamma$$

$$P_1 = \chi + \kappa(P)$$

$$U_o = \chi \tag{54}$$

where

$$\chi = [\beta^{-1}\gamma - \kappa(P)](1 - A\beta^{-1}\alpha\beta^{-1}\gamma)^{-1} \tag{55}$$

The introduction of these results into (45) produces the second-order DAA for an external acoustic domain, expressed in transform space as

$$\text{DAA}_2(s): \quad \{s^2 + cs[\chi + \kappa(P)] + c^2\chi\beta^{-1}\gamma\}p(P, s) = \rho cs^2(s + c\chi)u(P, s) \tag{56}$$

and in the time domain as

$$\text{DAA}_2(t): \quad \ddot{p}(P, t) + c[\chi + \kappa(P)]\dot{p}(P, t) + c^2\chi\beta^{-1}\gamma p(P, t) = \rho c[\dddot{u}(P, t) + c\chi\ddot{u}(P, t)]. \tag{57}$$

This result agrees with that of Nicolas-Vullierme (1989). In his formulation, the term $A\beta^{-1}\alpha\beta^{-1}\gamma$ in (55) is replaced by $A\beta^{-1}\gamma(1/2\pi)\alpha\beta^{-1}\gamma$. This is due to a result obtained previously by Ohayon and Sanchez-Palencia (1983) which, in the present context, states that $\gamma^{-1}\alpha$ reduces to $(1/2\pi)\alpha$. Extending an idea introduced in Felippa (1980b), Nicolas-Vullierme was the first to formulate DAAs by operator matching, making use of the Fourier transform and the method of stationary phase. Although his formulation works well for nonconcave surfaces, it becomes cumbersome for concave surfaces, a circumstance that is disadvantageous for internal domains. This is because high-frequency behavior does not correspond to early-time behavior when an acoustic ray departing along the normal from a surface element intersects another surface element. In the time domain, causality prevents such early-time interaction.

It is possible to obtain approximations that lie between DAA_1 and DAA_2 by matching either two high-frequency terms and one low-frequency term or two low-frequency terms and one high-frequency term. The latter matching, which corresponds to setting $\kappa(P) = 0$ in (55)–(57), has not been found advantageous. However, the former matching, which corresponds to setting $\alpha = 0$ in (55), has been found quite useful because it eliminates inversion of the complicated operator in the expression for χ while exhibiting good performance in evaluation studies (Geers and Felippa, 1983; DeRuntz, 1991; Hasheminejad and Geers, 1991). This one-term-low, two-term-high matching approximation has been termed the *curvature-corrected DAA* (Felippa, 1980b).

4.4 Other Formulations. Matching is not the only way to derive higher-order DAA's. In 1978, Geers formulated a matrix DAA_2 for an external acoustic domain on the basis of "fluid boundary modes." This procedure introduced a free parameter in each modal DAA_2 equation that could be used to optimize its accuracy across the intermediate frequency region. This has not been deemed necessary for external-domain problems, but may be found advantageous for internal domains.

In addition to matched DAA formulations and modal DAA formulations, there are symmetric DAA formulations (Geers and Zhang, 1988). A symmetric formulation was found to be essential in achieving satisfactory performance by a first-order DAA in electromagnetic scattering problems. In the context of acoustic scattering, a symmetric DAA involves accompanying (4) with an equation obtained by taking the partial derivative of (4) with respect to the surface normal.

5 DAA_2 for an Internal Acoustic Domain

We recall from Section 3 that the derivation of DAAs for an internal acoustic domain is complicated by the existence of low-frequency dilatational motion. Thus, LTA_2 for the internal domain differs from its external counterpart, while ETA_2 is the same for both internal and external domains. In this section, we formulate a second-order DAA for an internal domain by operator matching; the corresponding matrix form is given in Geers and Zhang (1991).

5.1 Second-Order Low-Frequency/Late-Time Approximation: LFA_2/LTA_2. LFA_2 for *equivoluminal* motion in an

Downloaded 03 May 2010 to 171.66.16.20. Redistribution subject to ASME license or copyright; see http://www.asme.org/terms/Terms_Use.cfm

internal domain is here determined by the procedure previously utilized in Section 4.2 for general motion in an external domain; it is given by

$$\beta^{-1}\gamma p^e(P, s) = \rho s^2 u^e(P, s) \tag{58}$$

where γ pertains to an inward normal and the inverse of γ does not exist. Note that the term corresponding to the last term in (44) is absent here because $\alpha u^e(P, s) = 0$.

To determine LFA_2 for *dilatational* motion, we replace $p(Q, s)$ by $p^d(s)$ and $u(Q, s)$ by $u^d(s)$ in (4), introduce (10) into (4), and retain on both sides all terms through those of order s^3. We then introduce operator symbols to represent the spatial integrals and recall that $\gamma p^d(s) = 0$ and $\alpha u(P, s) = u^d(s)$. The result is

$$\left[0 - \frac{1}{2}(s/c)^2\eta 1 + \frac{1}{3}(s/c)^3\zeta 1\right] p^d(s) = \rho s^2[\beta 1 - (s/c)A]u^d(s) \tag{59}$$

where the spatial operators β and η have been defined in (12) and (32), and ζ is defined as

$$\zeta q(P) \equiv \int_S R_{PQ} \cos \phi_{PQ}\, q(Q) dS_Q. \tag{60}$$

As discussed in Section 3.2, a naive derivation of LFA_2 for *general* motion in an internal domain consists merely of the introduction of (10) into (4) and the retention on both sides of all terms through those of order s^3. This yields

$$\left[\gamma - \frac{1}{2}(s/c)^2\eta + \frac{1}{3}(s/c)^3\zeta\right] p(P, s) = \rho s^2[\beta - (s/c)A\alpha]u(P, s). \tag{61}$$

Comparing this with (58) and (59), we see that the $O(s^2)$ and $O(s^3)$ terms on the left side are not appropriate for equivoluminal motion but are needed for dilatational motion; hence, we introduce the averaging operator α into these terms to obtain

$$\text{LFA}_2: \quad \left[\gamma + (s/c)^2 L\beta\alpha + \frac{1}{3}(s/c)^3\zeta\alpha\right] p(P, s) = \rho s^2[\beta - (s/c)A\alpha]u(P, s) \tag{62}$$

where we have used the fact that $\eta 1 = -2L\beta 1$, as established in Section 3.2.

5.2 Second-Order Doubly Asymptotic Approximation: DAA_2. To construct a trial equation for the internal DAA_2, we increase the order of the trial equation for the internal DAA_1, (35). Thus we try

$$(s^2 + csP_1 + c^2P_o)p(P, s) = \rho cs(s^2 + csU_1 + c^2U_o)u(P, s) \tag{63}$$

where P_o, P_1, U_o and U_1 are spatial operators to be found. Determining these operators requires separate consideration of equivoluminal motion and the dilatational motion, accompanied by extensive matching.

Let us first examine the trial equation (63) for *equivoluminal motion*. For $s \to 0$, the only way that this equation with $p(P, s) = p^e(P, s)$ and $u(P, s) = u^e(P, s)$ can match (58) is if $U_o = V_o\alpha$, in order that the lowest-order term on the right is $O(s^2)$. Hence, for equivoluminal motion, (63) with $s \to 0$ becomes

$$[P_o + c^{-1}sP_1 + O(s^2)]p^e(P, s) = \rho s^2(U_1 + c^{-1}s)u^e(P, s). \tag{64}$$

For equivoluminal motion with $s \to \infty$, (63) becomes

$$[1 + cs^{-1}P_1 + O(s^{-2})]p^e(P, s) = \rho c(s + cU_1)u^e(P, s). \tag{65}$$

Following the same procedure as that used in Section 4.3 for general motion in an external domain, we determine the spatial operators P_o, P_1, and U_1 by matching (64) to (58) and (65) to (40); the results are

$$P_o = [\beta^{-1}\gamma - \kappa(P)]\beta^{-1}\gamma$$
$$P_1 = \beta^{-1}\gamma$$
$$U_1 = \beta^{-1}\gamma - \kappa(P). \tag{66}$$

We recall that γ here pertains to an inward normal and the inverse of γ does not exist.

We now observe that the preceding development for equivoluminal motion would be unaffected if P_o, P_1, and U_1 were replaced by $P_o + Q_o\alpha$, $P_1 + Q_1\alpha$ and $U_1 + V_1\alpha$, respectively. Hence, remembering that $U_o = V_o\alpha$, we write from (63) the updated trial equation

$$[s^2 + cs(P_1 + Q_1\alpha) + c^2(P_o + Q_o\alpha)]p(P, s) = \rho cs[s^2 + cs(U_1 + V_1\alpha) + c^2V_o\alpha]u(P, s) \tag{67}$$

where P_o, P_1 and U_1 are known, and Q_o, Q_1, V_o and V_1 are unknown.

Let us now examine (67) for *dilatational motion*. With $p(P, s) = p^d(s)$, $\alpha p^d(s) = p^d(s)$, $u(P, s) = u^d(s)$, $\alpha u^d(s) = u^d(s)$ and $\gamma 1 = 0$, (67) may be expressed for dilatational motion as (note (66))

$$[s^2 + csQ_1 + c^2Q_o]p^d(s) = \rho cs\{s^2 + cs[V_1 - \kappa(P)] + c^2V_o\}u^d(s). \tag{68}$$

Unique solutions for Q_o, Q_1, V_o, and V_1 can be found in the R^1 *subspace of dilatational solutions*. Hence, we project (68) into this R^1 subspace by preoperating through by α, which leads to the conclusion that Q_o, Q_1, V_o, and V_1 must be *scalars*. This yields the scalar equation

$$(s^2 + csQ_1 + c^2Q_o)p^d(s) = \rho cs[s^2 + cs(V_1 - \bar{\kappa}) + c^2V_o)]u^d(s) \tag{69}$$

where $\bar{\kappa}$ is the *average curvature* over the surface S. For future use, we write this equation for small s as

$$(c^2Q_o + csQ_1 + s^2)p^d(s) = \rho c^2 s[cV_o + s(V_1 - \bar{\kappa}) + O(s^2)]u^d(s) \tag{70}$$

and for large s as

$$[1 + cs^{-1}Q_1 + O(s^{-2})]p^d(s) = \rho cs[1 + cs^{-1}(V_1 - \bar{\kappa}) + O(s^{-2})]u^d(s). \tag{71}$$

In order to determine Q_o, Q_1, V_o and V_1 by second-order matching, we must also project (62) and (40) onto the R^1 subspace of dilatational solutions. Hence, with $p(P, s) = p^d(s)$ and $u(P, s) = u^d(s)$, we preoperate (62) through by α to obtain LFA_2 for dilatational motion

$$\left[Lb + \frac{1}{3}(s/c)z\right] p^d(s) = \rho c^2[b - (s/c)A]u^d(s) \tag{72}$$

where $b = \alpha\beta 1$ and $z = \alpha\zeta 1$. Then we do the same to (40) to obtain HFA_2 for dilatational motion

$$(1 + cs^{-1}\bar{\kappa})p^d(s) = \rho csu^d(s) \tag{73}$$

We now perform second-order small-s matching of (70) and (72). First, we observe that (70) can match (72) as $s \to 0$ only if $Q_o = 0$, in order that the lowest-order term on the left is $O(s)$. Then we multiply (70) through by $(cV_o)^{-1}[1 - (s/c)V_o^{-1}(V_1 - \bar{\kappa})]$ to obtain

$$\{V_o^{-1}Q_1 + (s/c)V_o^{-1}[1 - V_o^{-1}Q_1(V_1 - \bar{\kappa})] + O(s^2)\}p^d(s) = \rho c^2[1 + O(s^2)]u^d(s). \tag{74}$$

Next, we multiply (72) through by $b^{-1}[1 + (s/c)b^{-1}A]$ to get

$$\left[L + (s/c)b^{-1}\left(V + \frac{1}{3}z\right) + O(s^2)\right] p^d(s) = \rho c^2[1 + O(s^2)]u^d(s) \tag{75}$$

Downloaded 03 May 2010 to 171.66.16.20. Redistribution subject to ASME license or copyright; see http://www.asme.org/terms/Terms_Use.cfm

Matching these two equations through $O(s)$, we find

$$V_o^{-1}Q_1 = L$$

$$V_o^{-1}[1 - V_o^{-1}Q_1(V_1 - \bar{\kappa})] = b^{-1}\left(V + \frac{1}{3}z\right). \quad (76)$$

To perform second-order large-s matching of (71) and (73), we multiply (71) through by $1 - cs^{-1}(V_1 - \bar{\kappa})$; this yields

$$[1 + cs^{-1}(Q_1 - V_1 + \bar{\kappa}) + O(s^{-2})]p^d(s) = \rho cs[1 + O(s^{-2})]u^d(s). \quad (77)$$

Matching this to (73), we find

$$Q_1 - V_1 + \bar{\kappa} = \bar{\kappa} \quad (78)$$

Finally, we solve (76) and (78) simultaneously to obtain

$$Q_1 = Ld$$

$$V_o = d$$

$$V_1 = Ld \quad (79)$$

where

$$d = \frac{1 + \bar{\kappa}L}{L^2 + (V + z/3)/b} \quad (80)$$

Thus, by introducing (66), (79) and $Q_o = 0$ into (67), we obtain the second-order DAA for an internal acoustic domain, expressed in transform space as

$$\text{DAA}_2(s): \quad \{s^2 + cs(\beta^{-1}\gamma + Ld\alpha) + c^2[\beta^{-1}\gamma - \kappa(P)]\beta^{-1}\gamma\}p(P, s) = \rho cs\{s^2 + cs[\beta^{-1}\gamma + Ld\alpha - \kappa(P)] + c^2 d\alpha\}u(P, s) \quad (81)$$

and in the time domain as

$$\text{DAA}_2(t): \quad \ddot{p}(P, t) + c(\beta^{-1}\gamma + Ld\alpha)\dot{p}(P, t) + c^2[\beta^{-1}\gamma - \kappa(P)]\beta^{-1}\gamma p(P, t) = \rho c\{\dddot{u}(P, t) + c[\beta^{-1}\gamma + Ld\alpha - \kappa(P)]\ddot{u}(P, t) + c^2 d\alpha\dot{u}(P, t)\}. \quad (82)$$

6 Conclusion

First- and second-order doubly asymptotic approximations have been formulated for internal and external acoustic domains by the method of operator matching in s-space. Time-dependent first-order DAAs are given by (18) for an external domain and (39) for an internal domain. Time-dependent second-order DAAs are given by (57) for an external domain and (82) for an internal domain. Corresponding matrix forms for boundary element analysis are given in Geers and Zhang (1991). The accuracy of the various DAAs is examined in the following companion paper.

Acknowledgments

This work was sponsored by the Defense Nuclear Agency under Contract DNA001-88-C-0057. The authors thank Drs. Kent Goering, Paul Senseny, and Thomas Tsai for their support and encouragement.

References

Atkash, R., et al., 1987, "Developments for the EPSA Computer Code," DNA-TR-87-155, Defense Nuclear Agency, Washington, DC.

Baker, B. B., and Copson, E. T., 1939, *The Mathematical Theory of Huygen's Principle*, Clarendon Press, Oxford, U.K.

Bedrosian, B., and DiMaggio, F. L., 1972, "Acoustic Approximations in Fluid-Shell Interactions," *J. Eng. Mech. Div., ASCE*, Vol. 98, No. EM3, pp. 731–742.

Chertock, G., 1992, "Transient Flexural Vibrations of Ship-Like Structures Exposed to Underwater Explosions," *J. Acoust. Soc. Am.*, Vol. 48, pp. 170–180.

DeRuntz, J. A., 1991, "Discrete-Element Acoustic Analysis of Submerged Structures with Internal Fluid Volumes," *Structural Acoustics*, R. F. Keltie, et al., eds., NCA-Vol. 12/AMD-Vol. 128, ASME, New York, pp. 139–151.

DeRuntz, J. A., Geers, T. L., and Felippa, C. A., 1980, "The Underwater Shock Analysis Code (USA-Version 3)," DNA 5615F, Defense Nuclear Agency, Washington, DC.

DeRuntz, J. A., and Brogan, F. A., 1980, "Underwater Shock Analysis of Nonlinear Structures, A Reference Manual for the USA-STAGS Code (Version 3)," DNA 5545F, Defense Nuclear Agency, Washington, DC.

Felippa, C. A., 1980a, "A Family of Early Time Approximations for Fluid Structure Interaction," ASME JOURNAL OF APPLIED MECHANICS, Vol. 47, pp. 703–708.

Felippa, C. A., 1980b," Top-down Derivation of Doubly Asymptotic Approximations for Structure-Fluid Interaction Analysis," *Innovative Numerical Analysis for the Engineering Sciences*, edited by R. P. Shaw et al., U.P. of Virginia, Charlottesville, pp. 79–88.

Geers, T. L., 1971, "Residual Potential and Approximate Methods for Three-dimensional Fluid-Structure Interaction Problems," *J. Acoust. Soc. Am.*, Vol. 49, pp. 1505–1510.

Geers, T. L., 1974, "Shock Response Analysis of Submerged Structures," *Shock and Vibration Bulletin*, Vol. 44, Supp. 3, pp. 17–32.

Geers, T. L., 1975, "Transient Response Analysis of Submerged Structures," *Finite Element Analysis of Transient Nonlinear Structural Behavior*, T. Belytschko, et al., eds., AMD-Vol. 14, ASME, New York, pp. 59–84.

Geers, T. L., 1978, "Doubly Asymptotic Approximation for Transient Motions of Submerged Structures," *J. Acoust. Soc. Am.*, Vol. 64, pp. 1500–1508.

Geers, T. L., and Felippa, C. A., 1983, "Doubly Asymptotic Approximations for Vibration Analysis of Submerged Structures," *J. Acoust. Soc. Am.*, Vol. 73, pp. 1152–1159.

Geers, T. L., and Zhang, P., 1988, "Doubly Asymptotic Approximations for Electromagnetic Scattering Problems," *Boundary Element Methods in Applied Mechanics*, M. Tanaka and T. A. Cruse, eds., Pergamon Press, Oxford, U.K. 1988, pp. 357–369.

Geers, T. L., and Zhang, P., 1991, "Doubly Asymptotic Approximations for Internal and External Acoustic Domains: Formulation," *Dynamic Response of Structures to High Energy Excitations*, edited by T. L. Geers and Y. S. Shin, AMD-127/PVP-225, ASME, New York, pp. 13–26.

Greenberg, M. D., 1978, *Foundations of Applied Mathematics*, Prentice-Hall, Englewood Cliffs, NJ, p. 54.

Hasheminejad, M., and Geers, T. L., 1992, "The Accuracy of Doubly Asymptotic Approximations for an Acoustic Half-Space," *J. Vib. Acoust.*, Vol. 114, pp. 555–563.

Haywood, J. H., 1958, "Response of an Elastic Cylindrical Shell to a Pressure Pulse," *Quart. J. Mech. & Appl. Math.*, Vol. 11, Part 2, pp. 129–141.

Mathews, I. C., and Geers, T. L., 1987, "A Doubly Asymptotic, Non-Reflecting Boundary for Ground-Shock Analysis," ASME JOURNAL OF APPLIED MECHANICS, Vol. 54, pp. 489–497.

Milne-Thomson, L. M., 1960, *Theoretical Hydrodynamics*, Macmillan, New York.

Mindlin, R. D., and Bleich, H. H., 1953, "Response of an Elastic Cylindrical Shell to a Transverse, Step Shock Wave," ASME JOURNAL OF APPLIED MECHANICS, Vol. 20, pp. 189–195.

Neilson, H. C., et al., 1981, "Transient Response of a Submerged, Fluid-Coupled, Double-Walled Shell Structure to a Pressure Pulse," *J. Acoust. Soc. Am.*, Vol. 70, pp. 1776–1782.

Nicolas-Vullierme, B., 1989, "A Contribution to Doubly Asymptotic Approximations: An Operator Top-down Approach," *Numerical Techniques in Acoustic Radiation*, NCA-Vol. 6, ASME, New York, pp. 7–13 (see also *J. Vib. Acoust.*, Vol. 113, pp. 409–415 (1991)).

Ohayon, R., and Sanchez-Palencia, 1983, "On the Vibration Problem for an Elastic Body Surrounded by a Slightly Compressible Fluid," R.A.I.R.O. Numerical Analysis, Vol. 17, pp. 311–326.

Pierce, A. D., 1981, *Acoustics: An Introduction to its Physical Principles and Applications*, McGraw-Hill, New York.

Ranlet, D., et al., 1977, "Elastic Response of Submerged Shells with Internally Attached Structures to Shock Loading," *Int. J. Computers and Structures*, Vol. 7, pp. 355–364.

Sobolev, S. L., 1964, *Partial Differential Equations of Mathematical Physics*, Pergamon Press, London, U.K.

Underwood, P. G., and Geers, T. L., 1981, "Doubly Asymptotic, Boundary Element Analysis of Dynamic Soil-Structure Interaction," *Int. J. Solids and Structures*, Vol. 17, pp. 687–697.

Van Dyke, M. D., 1964, *Perturbation Methods in Fluid Mechanics*, Academic Press, New York.

Vasudevan, R., and Ranlet, D., 1982, "Submerged Shock Response of a Linear Elastic Shell of Revolution Containing Internal Structure-Users Manual for the ELSHOK Code," DNA-TR-81-184, Defense Nuclear Agency, Washington, DC.

Zhang, P., and Geers, T. L., 1993, "Excitation of a Fluid-Filled, Submerged Spherical Shell by a Transient Acoustic Wave," *J. Acoust. Soc. Am.*, Vol. 93, pp. 696–705.

Downloaded 03 May 2010 to 171.66.16.20. Redistribution subject to ASME license or copyright; see http://www.asme.org/terms/Terms_Use.cfm

T. G. Geers
Fellow ASME.

Peizhen Zhang[1]
Assoc. Mem. ASME.

Center for Acoustics, Mechanics and Materials,
Department of Mechanical Engineering,
University of Colorado,
Boulder, CO 80309-0427

Doubly Asymptotic Approximations for Submerged Structures With Internal Fluid Volumes: Evaluation

The accuracy of the doubly asymptotic approximations formulated in the previous companion paper is examined through the comparison of DAA and exact transient response histories for a fluid-filled, submerged spherical shell excited by an incident plane step-wave. The numerical results indicate that second-order DAAs are satisfactory for problems of this type.

1 Introduction

In the previous companion paper, first- and second-order doubly asymptotic approximations are formulated for internal and external acoustic domains. Here, those DAAs are evaluated in the context of a canonical problem in spherical coordinates for which exact solutions have been obtained (Zhang and Geers, 1993). Direct comparisons are made between DAA and exact response histories for velocity and strain at several locations on a step-wave-excited, fluid-filled, submerged spherical shell.

Previous DAA evaluations using "exact" solutions to similar transient-response problems in the absence of internal fluid have been performed by Geers (1974, 1978), Huang (1975), and Geers and Yen (1989), for infinite circular cylindrical and spherical shells. The primary conclusion that emerges from these studies is that DAA_2 is robust and accurate for three-dimensional transient-response problems with external acoustic domains. A secondary conclusion is that the application of DAA_1 to such problems and of any DAA to similar two-dimensional problems is limited.

The present evaluation focuses on a three-dimensional axisymmetric problem in which a spherical shell is both filled with and surrounded by the same acoustic fluid. A *nondimensional formulation* is used, with length normalized to a (the mean radius of the shell), time normalized to a/c (where c is the speed of sound in the fluid), and pressure normalized to ρc^2 (where ρ is the mass density of the fluid).

2 Modal DAA Equations for a Spherical Geometry

In this section, modal DAA equations are derived for axisymmetric flow in a spherical geometry. The derivation utilizes velocity potential fields external and internal to a spherical surface, expanding those fields in generalized Fourier series involving Legendre polynomials and spherical Bessel functions. Exact modal equations linking the Laplace transforms of the velocity potentials and their derivatives are first obtained, from which high-frequency and low-frequency approximations are generated. Then modal DAAs of first and second order are formulated by scalar matching (Felippa, 1980; Geers and Felippa, 1983), the scalar form of operator matching, which was employed for general geometries in the previous companion paper.

An alternative to the modal scalar matching procedure consists of introducing Legendre-Fourier series expansions of the pressure and velocity fields into the general DAAs derived in the previous companion paper and then exploiting the orthogonality property of the Legendre functions to obtain modal DAAs. This approach was, in fact, investigated by the authors for the external DAA_1; as expected, it produced the same result as that produced by the modal scalar matching procedure, but was much more tedious. Because the operator matching method yields unambiguous DAAs, modal decomposition followed by DAA formulation yields the same modal DAA as that produced by modal decomposition of the corresponding general DAA.

2.1 Exact Modal Relations. For axisymmetric flow, the acoustic wave equation in spherical coordinates admits solutions of the form (Morse and Ingard, 1968)

$$\varphi(r, \theta, t) = \sum_{n=0}^{\infty} \varphi_n(r, t) P_n(\cos\theta) \tag{1}$$

where r and θ are the radial and meridional coordinates, respectively, $\varphi(r, \theta, t)$ is the velocity potential, and $P_n(\cos\theta)$ is the Legendre polynomial of order n (Abramowitz and Stegun, 1964). By introducing (1) into the wave equation employing the Laplace transform, and utilizing the orthogonality property of Legendre polynomials, one can obtain the following ordinary differential equation for each of the $\varphi_n(r, s)$:

$$\xi^2 \frac{d^2\varphi_n}{d\xi^2} + 2\xi \frac{d\varphi_n}{d\xi} - [\xi^2 + n(n+1)]\varphi_n = 0 \tag{2}$$

where $\xi = rs$.

[1]Present address: JI Case, Hinsdale, IL 60521.

Contributed by the Applied Mechanics Division of THE AMERICAN SOCIETY OF MECHANICAL ENGINEERS for publication in the ASME JOURNAL OF APPLIED MECHANICS.

Discussion on this paper should be addressed to the Technical Editor, Professor Lewis T. Wheeler, Department of Mechanical Engineering, University of Houston, Houston, TX 77204-4792, and will be accepted until four months after final publication of the paper itself in the ASME JOURNAL OF APPLIED MECHANICS.

Manuscript received by the ASME Applied Mechanics Division, Dec. 9, 1991; final revision, Oct. 18, 1993. Associate Technical Editor: S. K. Datta.

Copyright © 1994 by ASME
Downloaded 03 May 2010 to 171.66.16.20. Redistribution subject to ASME license or copyright; see http://www.asme.org/terms/Terms_Use.cfm

The solution to (2) that vanishes as $\xi \to \infty$ is

$$\varphi_n(r, s) = f_n(s) k_n(rs) \tag{3}$$

where $f_n(s)$ is an undetermined function and $k_n(\xi)$ is the nth-order modified spherical Bessel function of the third kind (Abramowitz and Stegun, 1964). The solution to (2) that remains finite at $r = 0$ is

$$\varphi_n(r, s) = g_n(s) i_n(rs) \tag{4}$$

where $g_n(s)$ is again an unknown function and $i_n(\xi)$ is the nth-order modified spherical Bessel function of the first kind (Abramowitz and Stegun, 1964).

2.2 Modal DAA Equations for the External Fluid. The definitions $p = \dot{\varphi}$ and $\mathbf{u} = -\nabla\varphi$ (where a dot denotes partial differentiation in time), along with (1) and (3), yield as the relation between the nth components of nondimensional pressure and radial fluid displacement on the external surface of the unit sphere

$$\frac{k_n'(s)}{k_n(s)} p_n(s) = -s u_n(s) \tag{5}$$

where the single argument s for p_n and u_n denotes $r = 1$, k_n is given by (Abramowitz and Stegun, 1964)

$$k_n(\xi) = \frac{\pi}{2} e^{-\xi} \sum_{m=0}^{n} \Gamma_{nm} \xi^{-(m+1)} \tag{6}$$

k_n' is the derivative of k_n with respect to argument, and $\Gamma_{nm} = (n+m)![2^m m!(n-m)!]^{-1}$.

For $s \to \infty$, long division gives

$$\frac{k_n'(s)}{k_n(s)} = -1 - s^{-1} + O(s^{-2}) \tag{7}$$

and, for $s \to 0$, long division gives

$$\frac{k_0'(s)}{k_0(s)} = -s^{-1} - 1$$

$$\frac{k_n'(s)}{k_n(s)} = -(n+1)s^{-1} + O(s), \quad n > 0. \tag{8}$$

The first- or second-order high-frequency approximation is obtained by keeping terms in (7) through s^0 or s^{-1}, and introducing each result, one at a time, into (5). The two HFAs are

$$\begin{aligned} &\text{HFA}_1^n: && p_n(s) = s u_n(s) \\ &\text{HFA}_2^n: && (s+1) p_n(s) = s^2 u_n(s) \end{aligned} \tag{9}$$

Similarly, the first- or second-order low-frequency approximation is obtained by retaining terms in (8) through s^{-1} or s^0, and introducing each result, one at a time, into (5). The results are

$$\begin{aligned} &\text{LFA}_1^n: && (n+1) p_n(s) = s^2 u_n(s) \\ &\text{LFA}_2^n: && (1+s) p_0(s) = s^2 u_0(s) \\ & && \text{same as LFA}_1^n(s) \text{ for } n > 0. \end{aligned} \tag{10}$$

DDAs will now be derived by scalar matching. As in the previous companion paper, the method consists of selecting the most compact trial equation in transform space that contains an appropriate number of arbitrary coefficients, and then determining those coefficients by forcing the trial equation to fit both the corresponding HFA and LFA for large and small s, respectively.

As will soon be evident, the trial equation for the first-order DAA is

$$(P_1^n s + P_0^n) p_n(s) = s^2 u_n(s) \tag{11}$$

where P_1^n and P_0^n are coefficients to be determined. This equation will match the first of (9) for $s \to \infty$ only if $P_1^n = 1$, and it will match the first of (10) for $s \to 0$ only if $P_0^n = n + 1$. Thus we have the first-order modal DAA in transform space

$$\text{DAA}_1^n(s): \qquad (s+n+1) p_n(s) = s^2 u_n(s) \tag{12}$$

and in the time domain

$$\text{DAA}_1^n(t): \qquad \dot{p}_n(t) + (n+1) p_n(t) = \ddot{u}_n(t). \tag{13}$$

A logical extension of (11) that satisfies HFA_1^n as $s \to \infty$ and LFA_1^n as $s \to 0$ produces the trial equation for the second-order DAA, viz.,

$$[s^2 + P_1^n s + (n+1) P_0^n] p_n(s) = (s^3 + P_0^n s^2) u_n(s). \tag{14}$$

To match $\text{HFA}_2^n(s)$, we divide this equation through by s^2 and divide the second of (9) through by s; then we match the resulting equations through order s^{-1} to obtain $P_0^n = P_1^n - 1$. To match $\text{LFA}_2^n(s)$, we divide (14) through by $(n+1)P_0^n$, divide both of (10) through by $n+1$, and match the resulting equations through order s; this yields $P_1^n = (n+1)$. Thus, introducing these results into (14), we obtain the second-order DAA in transform space as

$$\text{DAA}_2^n(s): \qquad [s^2 + (n+1)s + n(n+1)] p_n(s) = (s+n) s^2 u_n(s) \tag{15}$$

and in the time domain as

$$\text{DAA}_2^n(t): \qquad \ddot{p}_n(t) + (n+1)\dot{p}_n(t) + n(n+1) p_n(t) = \dddot{u}_n(t) + n\ddot{u}_n(t). \tag{16}$$

2.3 Modal DAA Equations for the Internal Fluid. For the internal fluid, the equation analogous to (5) is

$$\frac{i_n'(s)}{i_n(s)} p_n(s) = s u_n(s) \tag{17}$$

where $i_n(s)$ is given by (Abramowitz and Stegun, 1964)

$$i_n(\xi) = \frac{1}{2} \xi^{-(n+1)} \sum_{m=0}^{n} \Gamma_{nm} \xi^{n-m} [(-1)^m - (-1)^n e^{-2\xi}] e^{\xi} \tag{18}$$

and i_n' is the derivative of i_n with respect to argument; we recall that $u_n(s)$ is defined for the internal fluid as *positive inward*. Following the procedure of the previous section, we determine the singly asymptotic approximations by examining (17) as $s \to \infty$ and $s \to 0$.

For $s \to \infty$, long division gives

$$\frac{i_n'(s)}{i_n(s)} = 1 - s^{-1} + O(s^{-2}) \tag{19}$$

and, for $s \to 0$, long division gives

$$\frac{i_n'(s)}{i_n(s)} = n s^{-1} + 2(\gamma_{n1}/\gamma_{no}) s + O(s^3) \tag{20}$$

where

$$\gamma_{nm} = \frac{1}{[1 \cdot 3 \cdot 5 \cdots (2n + 2m + 1)] 2^m m!}. \tag{21}$$

HFA_1^n or HFA_2^n is obtained by keeping terms through s^0 or s^{-1} in (19) and introducing each result, one at a time, into (17). The two HFA's are (c.f., (9))

$$\begin{aligned} &\text{HFA}_1^n: && p_n(s) = s u_n(s) \\ &\text{HFA}_2^n: && (s-1) p_n(s) = s^2 u_n(s). \end{aligned} \tag{22}$$

LFA_1^n or LFA_2^n is obtained by retaining terms in (20) through s or s^2 for $n = 0$ and s^{-1} or s^0 for $n > 0$, and introducing each result, one at a time, into (17). The results are (c.f., (10))

$$\begin{aligned} &\text{LFA}_1^n: && p_0(s) = 3\, u_0(s) \\ & && n p_n(s) = s^2 u_n(s), \quad n > 0 \\ &\text{LFA}_2^n: && \text{same as LFA}_1^n(s). \end{aligned} \tag{23}$$

Downloaded 03 May 2010 to 171.66.16.20. Redistribution subject to ASME license or copyright; see http://www.asme.org/terms/Terms_Use.cfm

Because the LFAs for $n=0$ are distinct from their counterparts for $n>0$, DAA derivations will be performed in pairs. The trial equation for the first-order DAA for $n=0$ is

$$p_0(s) = (U_1^0 s + U_0^0) u_0(s) \tag{24}$$

where U_1^0 and U_0^0 are coefficients to be determined. This equation will match the first of (22) for $s\to\infty$ only if $U_1^0=1$; it will match the first of (23) for $s\to 0$ only if $U_0^0=3$. Thus we have the first-order DAA for $n=0$ in transform space

$$\text{DAA}_1^n(\text{s}) \text{ for } n=0: \quad p_0(s) = (s+3)u_0(s) \tag{25}$$

and in the time domain

$$\text{DAA}_1^n(\text{t}) \text{ for } n=0: \quad p_0(t) = \dot{u}_0(t) + 3u_0(t). \tag{26}$$

The trial equation for the first-order DAA for $n>0$ is

$$(P_1^n s + P_0^n) p_n(s) = s^2 u_n(s). \tag{27}$$

This equation will match the first of (22) for $s\to\infty$ only if $P_1^n=1$, and it will match the second of (23) for $s\to 0$ only if $P_0^n=n$. Thus we have the first-order DAA in transform space

$$\text{DAA}_1^n(s) \text{ for } n>0: \quad (s+n)p_n(s) = s^2 u_n(s) \tag{28}$$

and in the time domain

$$\text{DAA}_1^n(t) \text{ for } n>0: \quad \dot{p}_n(t) + n p_n(t) = \ddot{u}_n(t). \tag{29}$$

For the second-order DAA, the trial equation for $n=0$ is constructed by extending (24) and noting (25), which yields

$$(s+P_0^0)p_0(s) = (s^2 + U_0^0 s + 3P_0^0)u_0(s). \tag{30}$$

To match HFA_2, we divide both this equation and the second of (22) through by s, and then require that the resulting equations match through order s^{-1}. That is, we require $(1+P_0^0 s^{-1})p_0(s) = s[1+U_0^0 s^{-1} + O(s^{-2})]u_0(s)$ to match $(1-s^{-1})p_0(s) = s u_0(s)$ through order s^{-1}; long division and matching yields $U_0^0 = P_0^0 + 1$. To match LFA_2, we divide (30) through by P_0^0 and match through order s^{-1} the resulting equation to the first of (23); this yields $P_0^0 = 2$. With P_0^0 and U_0^0 thus determined, (30) becomes

$$\text{DAA}_2^n(s) \text{ for } n=0: \quad (s+2)p_0(s) = (s^2+3s+6)u_0(s). \tag{31}$$

In the time domain, this equation is

$$\text{DAA}_2^n(t) \text{ for } n=0: \quad \dot{p}_0(t) + 2p_0(t) = \ddot{u}_0(t) + 3\ddot{u}_0(t) + 6u_0(t). \tag{32}$$

Similarly, by referring to (27) and (28), the trial equation for the second-order DAA for $n>0$ is constructed as

$$(s^2 + P_1^n s + nP_0^n)p_n(s) = (s^3 + P_0^n s^2)u_n(s). \tag{33}$$

By following here the same matching procedure as that applied above, we obtain $P_0^n = P_1^n + 1$ and $P_1^n = n$. Thus, introducing these results into (33), we find the second-order internal DAA for $n>0$ in transform space to be

$$\text{DAA}_2^n(s) \text{ for } n>0: \quad [s^2 + ns + n(n+1)]p_n(s) = (s+n+1)s^2 u_n(s) \tag{34}$$

and in the time domain to be

$$\text{DAA}_2^n(t) \text{ for } n>0: \quad \ddot{p}_n(t) + n\dot{p}_n(t) + n(n+1)p_n(t) = \ddot{u}_n(t) + (n+1)\ddot{u}_n(t). \tag{35}$$

3 DAA Analysis of a Fluid-Filled Submerged Spherical Shell

Here, DAA shell-response solutions are obtained for a spherical shell filled with and submerged in an acoustic fluid, and excited by a plane step-wave. The method of separation of variables is used to construct generalized Fourier series solutions with enhanced convergence.

3.1 Shell Equations. A diagram of this canonical problem appears in Fig. 1. The shell material is elastic and isotropic,

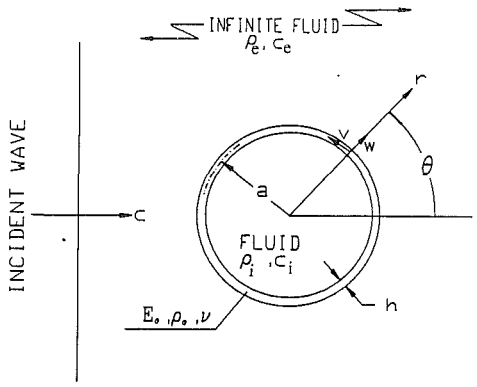


Fig. 1 Geometry of the spherical shell problem

with density ρ_0 and plate velocity $c_0 = [E/(1-\nu^2)]^{1/2}$, where E is Young's modulus and ν is Poisson's ratio. The shell's thickness-to-radius ratio h/a is sufficiently small that thin-shell theory suffices.

Just as the expansions in generalized Fourier series of the internal and external velocity potentials are given by (1), those of the shell displacements are given by

$$v(\theta, t) = -\sum_{n=1}^{\infty} v_n(t) P_{n,\theta}(\cos\theta)$$

$$w(\theta, t) = \sum_{n=0}^{\infty} w_n(t) P_n(\cos\theta) \tag{36}$$

where the θ subscript denotes differentiation with respect to the meridional coordinate. The equations of motion for the nth Fourier component of shell response may be written as (Junger and Feit, 1986)

$$n(n+1)\ddot{v}_n + \lambda_n^{vv} v_n + \lambda_n^{vw} w_n = 0$$

$$\ddot{w}_n + \lambda_n^{vw} v_n + \lambda_n^{ww} w_n = \mu p_n(t) \tag{37}$$

in which $\mu = (\rho/\rho_0)(a/h)$, $p_n(t)$ is the nth Fourier component of net pressure acting radially *outward* on the shell, and

$$\lambda_n^{vv} = n(n+1)(1+\epsilon)\xi_n\gamma_0$$

$$\lambda_n^{vw} = n(n+1)(1+\nu+\epsilon\xi_n)\gamma_0$$

$$\lambda_n^{ww} = [2(1+\nu) + n(n+1)\epsilon\xi_n]\gamma_0 \tag{38}$$

where $\epsilon = (h/a)^2/12$, $\gamma_0 = (c_0/c)^2$, and $\xi_n = n(n+1) - 1 + \nu$.

3.2 Fluid Structure Interaction Equations. The net pressure acting radially outward on the shell is $p_n = p_n^i - p_n^e$, where p_n^i and p_n^e are the pressures exerted by the internal and external fluid, respectively. But p_n^e is the sum of the known incident pressure p_n^0 and an unknown scattered pressure p_n^s. Hence p_n may be expressed as

$$p_n(t) = p_n^i(t) - p_n^0(t) - p_n^s(t). \tag{39}$$

Similarly, geometric compatibility at the inner and outer surfaces of the shell requires that

$$u_n^i(t) = -w_n(t)$$

$$u_n^0(t) + u_n^s(t) = w_n(t). \tag{40}$$

Note that circumferential geometric compatibility is not enforced, as the fluid is inviscid.

3.3 Assembly of the Modal Response Equations. We can now combine (13) for the *scattered wave*, and (26) and (29) for the *internal wave*, with (37), (39), and (40) to eliminate $p_n(t)$, $u_n^i(t)$, and $u_n^s(t)$. The resulting set of DAA_1 response equations is

Downloaded 03 May 2010 to 171.66.16.20. Redistribution subject to ASME license or copyright; see http://www.asme.org/terms/Terms_Use.cfm

$$n(n+1)\ddot{v}_n+\lambda_n^{vv}v_n+\lambda_n^{vw}w_n=0$$

$$\ddot{w}_n+\lambda_n^{vw}v_n+\lambda_n^{ww}w_n+\mu(p_n^s-p_n^i)=-\mu p_n^0$$

$$\ddot{w}_n-\dot{p}_n^s-(n+1)p_n^s=\ddot{u}_n^0$$

$$\dot{w}_0+3w_0+p_0^i=0$$

$$\ddot{w}_n+\dot{p}_n^i+np_n^i=0,\quad n>0. \tag{41}$$

We can then repeat this process using (16), (32) and (35), instead of (13), (26) and (29), respectively. The resulting set of DAA_2 response equations is

$$n(n+1)\ddot{v}_n+\lambda_n^{vv}v_n+\lambda_n^{vw}w_n=0$$

$$\ddot{w}_n+\lambda_n^{vw}v_n+\lambda_n^{ww}w_n+\mu(p_n^s-p_n^i)=-\mu p_n^0$$

$$\dddot{w}_n+n\ddot{w}_n-\ddot{p}_n^s-(n+1)\dot{p}_n^s-n(n+1)p_n^s=\dddot{u}_n^0+n\ddot{u}_n^0$$

$$\ddot{w}_0+3\dot{w}_0+\dot{p}_0^i+2p_0^i+6w_0=0$$

$$\dddot{w}_n+(n+1)\ddot{w}_n+\ddot{p}_n^i+n\dot{p}_n^i+n(n+1)p_n^i=0,\quad n>0. \tag{42}$$

The presence of $\dddot{u}_n^0$ in the third of these equations motivates the replacement of pressure with velocity potentials ($p_n=\dot{\varphi}_n$), followed by integration of the third and last of (42). This produces the computationally advantageous set

$$n(n+1)\ddot{v}_n+\lambda_n^{vv}v_n+\lambda_n^{vw}w_n=0$$

$$\ddot{w}_n+\lambda_n^{vw}v_n+\lambda_n^{ww}w_n+\mu(\dot{\varphi}_n^s-\dot{\varphi}_n^i)=-\mu p_n^0$$

$$\ddot{w}_n-\ddot{\varphi}_n^s+n\dot{w}_n-(n+1)\dot{\varphi}_n^s-n(n+1)\dot{\varphi}_n^s=\ddot{u}_n^0+n\dot{u}_n^0$$

$$\ddot{w}_0+\ddot{\varphi}_0^i+3\dot{w}_0+2\dot{\varphi}_0^i+6w_0=0$$

$$\ddot{w}_n+\ddot{\varphi}_n^i+(n+1)\dot{w}_n+n\dot{\varphi}_n^i+n(n+1)\varphi_n^i=0,\quad n>0. \tag{43}$$

The same substitutions can clearly be used to "smooth" the third and last of (41) also.

Because meridional strain computations are presented herein, it is appropriate to provide the series expression for that quantity. From Junger and Feit (1986),

$$\epsilon_{\theta\theta}(z,\theta,t)=\sum_{n=0}^{\infty}\{w_n(t)P_n(\cos\theta)-[(1+z)v_n(t)+zw_n(t)]P_{n,\theta\theta}(\cos\theta)\} \tag{44}$$

where z is the radial distance from the neutral axis of the shell.

3.4 Enhancement of Modal Convergence. As discussed in Zhang and Geers (1993), the generalized Fourier Series for many response quantities do not converge satisfactorily. Hence, a convergence enhancement technique used in that study is also employed here. It is based on Cesàro summation (Apostol, 1957), but weights the modal components differently. The result is *modified Cesàro summation*, in which, for example, the series for $w(\theta, t)$ in (36) is replaced by

$$w(\theta,t)=\sum_{n=0}^{N}C_nw_n(t)P_n(\cos\theta) \tag{45}$$

where $C_0=C_1=C_2=1$ and $C_n=(N+1-n)/(N-1)$ for $n>2$. For the computations performed herein, $N=8$. The benefits produced by modified Cesàro summation for this problem are illustrated in Zhang and Geers (1993).

4 Numerical Results

Computed transient response histories are presented in this section for a steel spherical shell submerged in water that is excited by a plane step-wave; the shell is first empty, and then it is filled with water. The thickness-to-radius ratio is $h/a=0.01$, the mass-density ratio is $\rho_0/\rho=7.7$, and the sound-velocity ratio is $c_0/c=(13.8)^{1/2}$. Fifth-order Runge-Kutta integration was used to solve the modal response equations. Nine Fourier meridional harmonics were used; the adequacy of this number is demonstrated in Zhang and Geers (1993).

Transient response histories produced by DAA_2 treatments of the fluid-structure interaction are compared with their exact counterparts in Figs. 2 through 7; in these figures, the exact histories are labeled "Acoustic." Results produced by DAA_1 treatments are not shown, as DAA_1s have been found to be substantially inferior to DAA_2s. All of the figures show shell response, in keeping with the premise of the previous companion paper, viz., the structure is the focus of interest. Pressure-history comparisons, as well as DAA_1 histories, appear in Geers and Zhang (1991).

Figure 2 shows *radial velocity* histories (with reversed sign) at $\theta=\pi$ and $\theta=0$ on an *empty* submerged shell. As an indicator of external-DAA_2 performance, velocity histories are also shown that result from applying only the incident-wave pressure to the shell, i.e., histories for which the fluid-structure interaction is ignored; these histories are labeled "No FSI." Figure 3 exhibits Acoustic, DAA_2 and No-FSI *meridional strain* histories (also with reversed sign) on the inner and outer surfaces of the empty shell at $\theta=\pi$; Fig. 4 shows corresponding histories at $\theta=0$. The last two figures illustrate that strain response is predominantly membrane. All three demonstrate that external-DAA_2 accounts for virtually all FSI effects that affect structural response.

Figures 5–7 pertain to the water-filled submerged shell. Figure 5 shows *radial velocity* histories (with reversed sign) at $\theta=\pi$ and $\theta=0$ produced by completely acoustic and completely DAA_2 treatments of external and internal FSI, as well as by acoustic treatment of external FSI and no treatment of internal FSI. The last histories, of course, are merely the empty-shell acoustic histories in Fig. 2. As discussed by Geers and Ju (1994),

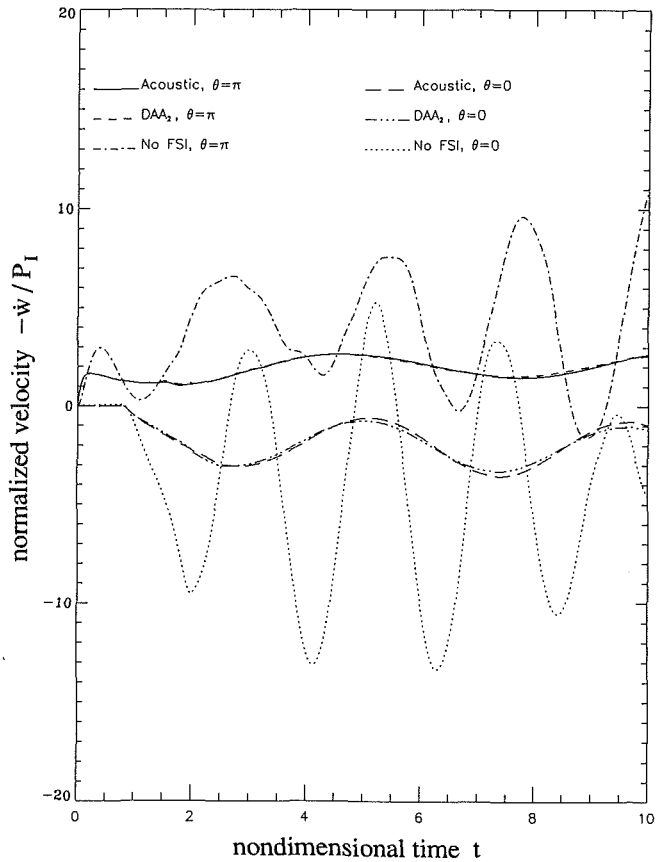


Fig. 2 Radial-velocity histories at two points on a submerged, empty spherical shell

Downloaded 03 May 2010 to 171.66.16.20. Redistribution subject to ASME license or copyright; see http://www.asme.org/terms/Terms_Use.cfm

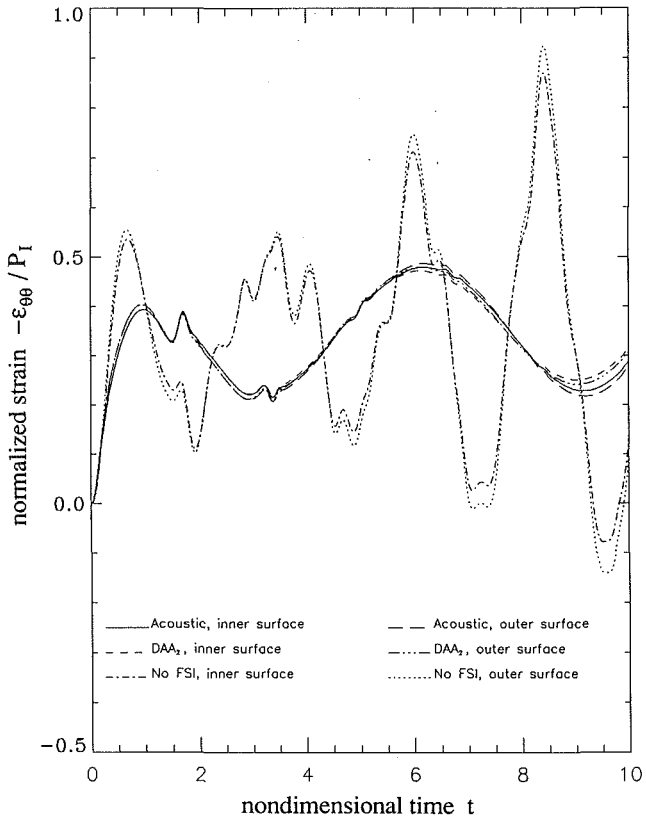


Fig. 3 Meridional-strain histories at $\theta = \pi$ on a submerged, empty spherical shell

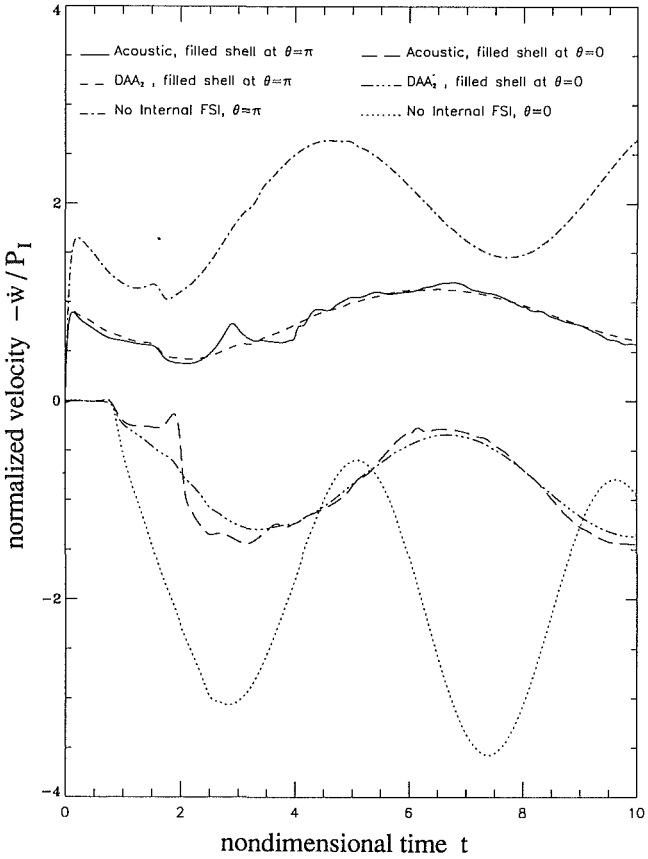


Fig. 5 Radial-velocity histories at two points on a submerged, filled spherical shell

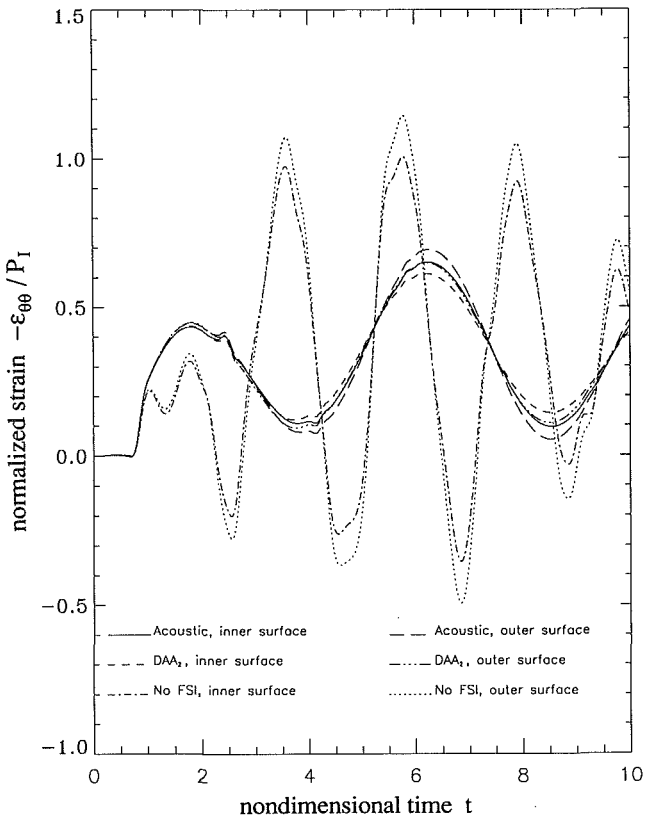


Fig. 4 Meridional-strain histories at $\theta = 0$ on a submerged, empty spherical shell

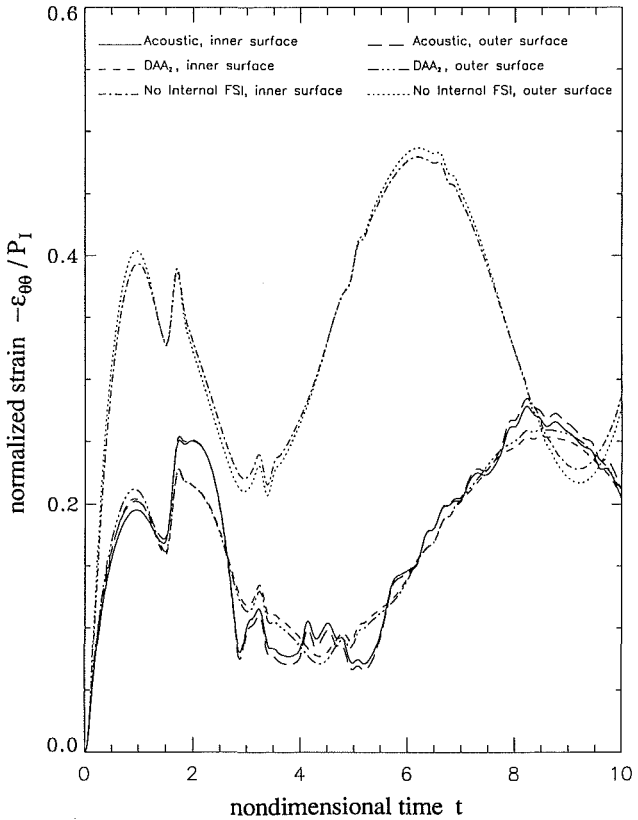


Fig. 6 Meridional-strain histories at $\theta = \pi$ on a submerged, filled spherical shell

Downloaded 03 May 2010 to 171.66.16.20. Redistribution subject to ASME license or copyright; see http://www.asme.org/terms/Terms_Use.cfm

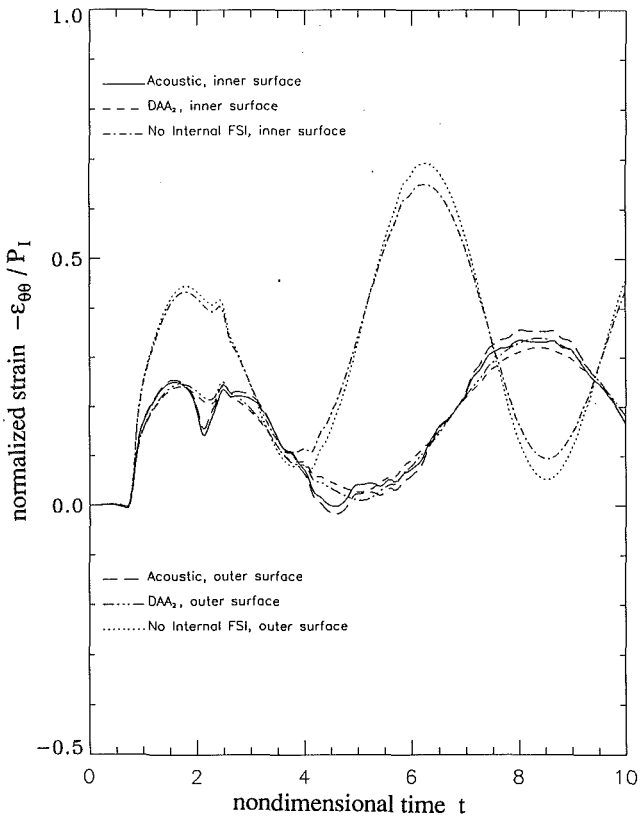


Fig. 7 Meridional-strain histories at $\theta = 0$ on a submerged, filled spherical shell

modal convergence is not complete in the $\theta = 0$ acoustic history during $1 < t < 2$, which prevents comparison of the $\theta = 0$ acoustic and DAA_2 histories during that period.

Figure 6 exhibits Acoustic, DAA_2, and No-Internal-FSI *meridional strain* histories (also with reversed sign) on the inner and outer surfaces of the water-filled shell at $\theta = \pi$. This figure and Fig. 7, which shows corresponding histories at $\theta = 0$, illustrate that strain response is predominantly membrane.

A comparison of Figs. 5–7 with Figs. 2–4 indicates that internal-DAA_2 is not as accurate as external-DAA_2. Whereas external-DAA_2 accounts for virtually all external-FSI effects that affect structural response, internal-DAA_2 fails to account for acoustic transmission and reflection phenomena that affect structural response to some degree. Nevertheless, the discrepancies in Figs. 5–7 between the DAA_2 and Acoustic histories are much smaller than those between the No-Internal-FSI and Acoustic histories. More specifically, maximum discrepancies between the DAA_2 and Acoustic histories, when normalized to peak Acoustic values, are about 20 percent, whereas such discrepancies between No-Internal-FSI and Acoustic histories are about 200 percent. This implies that internal-DAA_2 accounts for roughly 90 percent of the internal FSI effects that affect structural response.

6 Conclusion

The accuracy of the doubly asymptotic approximations given in the preceding companion paper has been examined through a comparison of DAA_2 and exact response histories for empty and fluid-filled, submerged spherical shells excited by a plane step-wave. The shell-response histories of Figs. 2–7 indicate that external-DAA_2 is highly accurate and that internal-DAA_2 is acceptably accurate for transient structural response computation. To improve the accuracy of internal-DAA_2, current research efforts are focusing on two strategies: extension to multiple surfaces of the acoustic ray development in Section 4.1 of the previous companion paper, and utilization of approximate kernels in some of the integrals (Carrier, et al., 1966).

A question of some interest concerns the accuracy of DAA's for nonspherical geometries. An analytical study of an infinite, elastic, circular cylindrical shell structure (Geers, 1974) shows external-DAA_1 to be quite accurate for that geometry. Comparisons of computational and experimental data for a transversely excited, long, elastic, circular cylindrical shell-structure (Littlewood, et al., 1988) show that external-DAA_1 and external-DAA_2 provide nearly the same level of satisfactory accuracy. These results stand in contrast to those for an elastic *spherical* shell (Geers, 1978), which demonstrate that external-DAA_2 is far superior to external-DAA_1, with the former exhibiting very good accuracy.

A recent analysis of an infinite, *inelastic*, circular cylindrical shell (Geers and Yen, 1989), has shown that no existing external DAA is suitable for two-dimensional shock-response analysis of soft structures. This is because no low-frequency added-mass asymptote exists for two-dimensional dilatational motion in an acoustic medium (Whitman, 1972). For such motion, all existing DAAs reduce to the high-frequency plane-wave approximation, which is satisfactory only for dilatationally stiff structures.

The present paper and its predecessor (Geers and Zhang, 1991) are the first to examine the accuracy of internal DAAs, which certainly inhibits a discussion of their applicability to other geometries. Once can argue, however, that the regularity of the spherical geometry, which produces highly coherent internal transmission and reflection, is a severe one in which to evaluate internal-DAA accuracy. The principal applications envisioned for internal DAAs involve highly irregular fluid volumes, which calls for future evaluation studies involving such geometries.

As mentioned in the Introduction of the preceding companion paper, the accuracy of engineering computations that involve finite element modeling of internal acoustic domains is often unacceptable for computationally practical mesh geometries. In addition, the principal errors in previous shock-response computations for complex structures have usually been associated with structural finite element modeling rather than with DAA treatment of the external fluid-structure interaction. It is therefore appropriate to pursue computationally efficient approximate treatments of fluid-structure interaction that introduce uncertainties smaller than or comparable to those that characterize structural modeling.

The FORTRAN program used to generate the numerical results shown in Figs. 2–7 may be obtained from the Shock and Vibration Information Analysis Center, 2711 Jefferson Davis Highway, #600, Arlington, VA 22202-4158, (703) 769-7856. The program (Geers and Ju, 1992) may be useful as a verification tool to developers and users of finite element/boundary element analyzers for this class of problems.

Acknowledgments

This work was sponsored by the Defense Nuclear Agency under Contract DNA001-88-C-0057. The authors express their appreciation to Dr. Kent Goering and to Messrs. Douglas Bruder and Michael Giltrud for their continued interest in doubly asymptotic approximations. The authors also wish to acknowledge the help of Dr. Jianming Chen in the preparation of Figs. 2 through 7.

References

Apostol, T. M., 1957, *Mathematical Analysis: A Modern Approach to Advanced Calculus*, Addison-Wesley, Reading, MA, pp. 378–379.

Abramowitz, M., and Stegun, I. A., eds., 1964, *Handbook of Mathematical Functions*, NBS Appl. Math. Ser. 55, U.S. Dept. of Commerce, Washington, DC.

Downloaded 03 May 2010 to 171.66.16.20. Redistribution subject to ASME license or copyright; see http://www.asme.org/terms/Terms_Use.cfm

Carrier, G. F., Krook, M., and Pearson, C. E., 1966, *Functions of a Complex Variable*, McGraw-Hill, New York, pp. 393–399.

Felippa, C. A., 1980, "Top-down Derivation of Doubly Asymptotic Approximations for Structure-Fluid Interaction Analysis," *Innovative Numerical Analysis for the Engineering Sciences*, R. P. Shaw, et al., eds., U.P. of Virginia, Charlottesville, VA, pp. 79–88.

Geers, T. L., 1974, "Shock Response Analysis of Submerged Structures," *Shock and Vibration Bulletin*, Vol. 44, No. 3, pp. 17–32.

Geers, T. L., 1978, "Doubly Asymptotic Approximations for Transient Motions of Submerged Structures," *J. Acoust. Soc. Am.*, Vol. 63, pp. 1500–1508.

Geers, T. L., and Felippa, C. A., 1983, "Doubly Aysmptotic Approximations for Vibration Analysis of Submerged Structures," *J. Acoust. Soc. Am.*, Vol. 73, pp. 1152–1159.

Geers, T. L., and Ju, T. H., 1994, "A Computer Program for a Canonical Problem in Underwater Shock," *Shock and Vibration*, Vol. 1, pp. 331–337.

Geers, T. L., and Yen, C. L., 1989, "Inelastic Response of an Infinite Cylindrical Shell to Transient Acoustic Waves," ASME JOURNAL OF APPLIED MECHANICS, Vol. 56, pp. 900–909.

Geers, T. L., and Zhang, P., 1991, "Doubly Asymptotic Approximations for Internal and External Acoustic Domains: Evaluation," *Dynamic Response of Structures to High-Energy Excitations*, T. L. Geers and Y. S. Shin, eds., AMD-127/PVP-225, ASME, New York, pp. 27–34.

Huang, H., 1975, "A Qualitative Appraisal of the Doubly Asymptotic Approximation for Transient Analysis of Submerged Structures Excited by Weak Shock Waves," NRL Memorandum Report 3135, Naval Research Laboratory, Washington, DC.

Junger, M. C., and Feit, D., 1986, *Sound, Structures, and Their Interaction*, 2nd ed., MIT Press, Cambridge, MA.

Littlewood, T. S., et al., 1988, "Comparison of Shock Test Data with Computational Predictions: The ONR Cylinder Shock Test Series—Refined Analysis of the Side-On Attack Geometry," TN-AM-88-05, General Dynamics/Electric Boat Division, Groton, CT.

Morse, P. M., and Ingard, K. U., 1968, *Theoretical Acoustics*, McGraw-Hill, New York.

Whitman, A. M., 1972, "Aspect Ratio Effects on the Added-Mass of a Slender Pulsating Cylinder," ASME JOURNAL OF APPLIED MECHANICS, Vol. 39, pp. 1047–1049.

Zhang, P., and Geers, T. L., 1993, "Excitation of a Fluid-Filled, Submerged Spherical Shell by a Transient Acoustic Wave," *J. Acoustic Soc. Am.*, Vol. 93, pp. 696–705.

Downloaded 03 May 2010 to 171.66.16.20. Redistribution subject to ASME license or copyright; see http://www.asme.org/terms/Terms_Use.cfm

F. Giambanco

M. Lo Bianco

L. Palizzolo

Dipartimento di Ingegneria
Strutturale e Geotecnica, DISEG,
Università di Palermo,
Viale delle Scienze,
I-90128 Palermo, Italy

An Approximate Technique for Dynamic Elastic-Plastic Analysis

The possibility of obtaining an approximate sufficiently reliable response for elastic-plastic discretized structures subjected to dynamic load (kinematical and/or mechanical), with a low computational effort, has been considered. A suitable technique to this effect comes from the form of the dynamic influence matrix of imposed plastic strains on self-stresses, which is shaped by adding up a sparse time-dependent matrix and a block diagonal time-independent matrix (which is the sum of two block diagonal matrices). Several cases of practical interest have been studied, among these cases a special one where all the degrees-of-freedom are dynamic. The technique is compared to other approximate techniques. The structures the elements of which have monodimensional elastic domain are considered with special attention.

1 Introduction

Stepwise analysis (see, e.g., Owen, 1980a, b; Wilson et al., 1973; Polizzotto, 1986; Borino et al., 1990) is certainly the most complete and conclusive computational tool in the investigation of elastic-plastic behavior of structures subjected to a given dynamic loading history. It is founded on the space discretization of the structure and on the time discretization of the given loading history; the discretization of the physical problem allows a well-known simplification of the corresponding mathematical problem: the differential equations which describe and govern the continuum analysis problem are transformed into a sequence of linear complementarity algebraical problems which can be solved as such or by solving certain quadratic programming equivalent problems (see, e.g., Polizzotto, 1986; Borino et al., 1990). This procedure, based on the mathematical programming, can be considered as an extension to the dynamic field of tested methods of quasi-static analysis of discrete structures (see, e.g., Maier, 1978; Cohn and Maier, 1979; De Donato and Maier, 1976).

Actually, several efficient programs devoted to the quadratic programming problem solution already exist, but, unfortunately, quadratic programming problem dimensions are sometimes so big, in executing dynamic elastic plastic analysis, to create considerable computational difficulties. A possible way to get over these said difficulties has been found in the so-called element optimization technique (see, e.g., Feijòo, 1986; Feijòo and Zouain, 1987; Borino et al., 1990) which iteratively obtains the solution satisfying, separately, element-by-element yield conditions.

In this paper a simple technique, based on the so-called indirect method (Polizzotto, 1986; Borino et al., 1990; Borino and Polizzotto, 1989) is proposed, which allows us to obtain approximate solutions of the quadratic programming problem relative to the whole structural system by solving more quadratic programming problems, with smaller dimensions, without iterations. This approximate technique comes from the structure of the quadratic programming problem constraint matrix which is the sum of a block diagonal time-independent matrix (which is the sum of two block diagonal matrices) and a sparse matrix whose coefficients depend on the width h of the time step, as well as on the shape function, utilized to model the plastic activations during the same generic time interval. It is possible to prove that the sparse matrix coefficients tend to zero if $h \to 0$. Providing that h is small enough, it is therefore correct to approximate the constraint matrix to a diagonal block one disregarding the entire sparse matrix, or at least the elements out of the diagonal blocks. From this position it follows a computational advantage, i.e., for every step we have to solve several quadratic programming problems with small dimensions instead of one quadratic programming problem with dimensions equal to the sum of dimensions of the smaller problems.

It may be opportune to note that, generally, two different simplificative ipotheses give rise to the approximation of the proposed technique: the first one—essential to this procedure—consists in assuming zero value for the elements of the sparse matrix (or for a part of them), the second one—usually accepted for discrete analysis—consists in modeling the plastic activation during the generic time interval according to a prefixed shape function. The adopted modeling of the plastic activation influences also the sparse matrix coefficient values (for fixed h). In particular, if an impulsive history of plastic activation is adopted, all the sparse matrix coefficients result exactly zero for every width of h (Borino and Polizzotto, 1989); this occurrence partially makes up for an unrealistic plastic activation modelling that implies an elastic behavior of the structure in every instant except the ones which define the time discretization.

The physical meaning of the procedure consists in taking into account—during the current step—the (instantaneous) ef-

Contributed by the Applied Mechanics Division of THE AMERICAN SOCIETY OF MECHANICAL ENGINEERS for publication in the ASME JOURNAL OF APPLIED MECHANICS.

Discussion on this paper should be addressed to the Technical Editor, Professor Lewis T. Wheeler, Department of Mechanical Engineering, University of Houston, Houston, TX 77204-4792, and will be accepted until four months after final publication of the paper itself in the ASME JOURNAL OF APPLIED MECHANICS.

Manuscript received by the ASME Applied Mechanics Division, Mar. 2, 1992; final revision, Sept. 22, 1993. Associate Technical Editor: A. K. Noor.

Copyright © 1994 by ASME
Downloaded 03 May 2010 to 171.66.16.20. Redistribution subject to ASME license or copyright; see http://www.asme.org/terms/Terms_Use.cfm

fect of plastic activation which rises in a plastified element on the other ones with it directly connected only through the elasticity of the structure, and in overlooking the effect (delayed in time) on the other elements connected with it also through the dynamic behavior of the structure.

Sometimes further computational economy is possible in studying some special structure typologies. Actually, if the block diagonal matrix satisfies the Mangasarian conditions (Mangasarian, 1976), the solution of the quadratic programming problems can be obtained by solving the same number of equal order linear programming problems. At other times, the block diagonal matrix structure is so simple that the solution of the quadratic programming problems can be obtained by solving some linear equation systems with further small dimensions, drawn from quadratic programming problems through an appropriate preliminary investigation on the known terms. It is simple to show that the plastic activations obtained by solving the linear equation systems are all positive and such that the inactived constraints are satisfied as an inequality, i.e., the preliminary investigation on the known terms and the following solution of the linear equation systems deduced in this way correspond exactly to the solution of the original linear complimentary problems and so of the equivalent quadratic programming problems. This last case concerns structures constituted by plastic elements with monodimensional domain, independently from the order of the element stiffness matrix, which can be a scalar (truss structures, shear type frames) or a matrix (bending type frames). In these special cases the low computational effort of the procedure allows us to refine the time step almost arbitrarily.

2 Dynamic Elastic-Plastic Analysis

Let us consider a finite element discretized structure, subjected to mechanical loads $\mathbf{f}(t)$ and to imposed strains $\boldsymbol{\vartheta}(t)$; the components of these two vectors are known and depend on time t, for $0 \le t \le t_f$. Adopting the hypothesis of infinitesimal displacements and indicating with a superimposed dot the relevant time derivative, the equations of motion can be expressed as follows:

$$\left.\begin{aligned}&\mathbf{M}\ddot{\mathbf{u}}+\mathbf{V}\dot{\mathbf{u}}+\mathbf{K}\mathbf{u}-\mathbf{B}\mathbf{p}=\mathbf{f}+\mathbf{B}\boldsymbol{\vartheta},\\&\mathbf{Q}=\mathbf{B}^T\mathbf{u}-\mathbf{D}\mathbf{p}-\mathbf{D}\boldsymbol{\vartheta},\end{aligned}\right\}\forall t\in(0,\ t_f) \quad (1),(2)$$

$$\mathbf{u}=\mathbf{u}_o,\quad \dot{\mathbf{u}}=\dot{\mathbf{u}}_o,\quad \mathbf{p}=\mathbf{p}_o,\quad \text{for } t=0 \quad (3)$$

where $\mathbf{M}$, $\mathbf{V}$, and $\mathbf{K}$ are, respectively, the mass, damping, and stiffness matrices of the structure; $\mathbf{D}$ is the plastic mode internal stiffness matrix, B is the so-called pseudo-force matrix, which transforms the strains into nodal equivalent forces; $\mathbf{u}$, $\mathbf{Q}$, and $\mathbf{p}$ are the vectors of the nodal displacements, generalized stresses, and generalized plastic strains of the elements. If the structure is constituted by elastic perfectly plastic material, assuming for the generic finite element an hyperpolyhedric elastic domain, the equations governing the plastic behavior of the elements are

$$\left.\begin{aligned}&\boldsymbol{\varphi}=\mathbf{N}^T\mathbf{Q}-\mathbf{R}\le\mathbf{0},\\&\dot{\mathbf{p}}=\mathbf{N}\dot{\boldsymbol{\lambda}},\quad \dot{\boldsymbol{\lambda}}\ge 0,\quad \boldsymbol{\varphi}^T\dot{\boldsymbol{\lambda}}=0\end{aligned}\right\}\forall t\in[0,\ t_f] \quad (4a,b),(5a\text{-}c)$$

where $\boldsymbol{\varphi}$ is the supervector of the plastic potentials, $\mathbf{N}$ is the matrix of the external unit normals to the elastic domains of the elements, $\mathbf{R}$ is the supervector of the plastic resistances, and $\dot{\boldsymbol{\lambda}}$ is the supervector of the plastic activation coefficients.

When the load history and the initial conditions are known, it is always possible (at least in principle) to obtain the exact elastic-plastic response of the structure by integrating the Eqs. (1)–(5).

Effectively, to obtain the solution it is necessary to discretize the problem also with regard to time, subdividing the time axis into small time intervals usually chosen with the same width h, so that $t_o = 0, t_1, t_2, \ldots, t_n = nh, \ldots, t_f$ are the discretization instants. For every time interval the analysis is developed in two subsequent phases: the first one is linear, and in this phase the elastic response of the structure to the current step initial conditions and load is calculated; the second one is not linear and in this phase the plastic deformation increments of current step are calculated.

The previously mentioned research of the elastic response can be carried out by using the direct or the indirect method.

Here, we adopt the indirect method, founded on the extension to the dynamic field, of the Colonnetti's decomposition principle, which says that the elastic-plastic response to given dynamic loads can be obtained as the sum of two elastic responses: the first one is the response to given load and the second one is the response to unknown plastic deformations, understood as imposed dynamic distortions. This method reaches the exact solution of (1)–(3) utilizing the superimposition of the natural vibration modes (Owen, 1980) which implies a preventive modal analysis of the structure necessary to obtain the essential dynamic features of the structure as the displacement modes $\boldsymbol{\Phi}_i$ (normalized in such a way that $\boldsymbol{\Phi}_i^T\mathbf{M}\boldsymbol{\Phi}_i = 1$), the natural frequencies ω_i, the damping ratios ξ_i, and the reduced frequencies $\omega_i^D = \omega_i \cdot \sqrt{1-\xi_i^2}$, for $i = 1, 2, \ldots, \nu$, with ν freedom degrees of the structure. These quantities make it possible to construct some dynamic operators by which the structure's elastic response history for every $t \in [0, t_f]$ can be calculated. These operators are (Polizzotto, 1986; Borino et al., 1990; Borino and Polizzotto, 1989) the dynamic correction matrix

$$\mathbf{G}(t)=\sum_{i=1}^{\nu}\boldsymbol{\Phi}_i\psi_i\boldsymbol{\Phi}_i^T, \quad (6)$$

where

$$\psi_i=\frac{1}{\omega_i^2}\exp(-\xi_i\omega_i t)\left[\cos\omega_i^D t+\frac{\xi_i\omega_i}{\omega_i^D}\sin\omega_i^D t\right], \quad (7)$$

and the dynamic influence matrices

$$\mathbf{A}(t)=\mathbf{K}^{-1}-\mathbf{G}(t), \quad (8)$$

$$\mathbf{L}(t)=\mathbf{A}(t)\mathbf{B}, \quad (9)$$

$$\mathbf{Z}(t)=\mathbf{B}^T\mathbf{A}(t)\mathbf{B}-\mathbf{D}. \quad (10)$$

The elastic response of the structure can be represented as follows:

$$\mathbf{u}(t)=\mathbf{G}(t)\mathbf{K}\mathbf{u}_o-\dot{\mathbf{G}}(t)\mathbf{M}\dot{\mathbf{u}}_o+\mathbf{A}(t)\mathbf{f}(o)+\mathbf{L}(t)\boldsymbol{\vartheta}(o)+\int_0^t[\mathbf{A}(t-\bar{t})\dot{\mathbf{f}}(\bar{t})+\mathbf{L}(t-\bar{t})\dot{\boldsymbol{\vartheta}}(\bar{t})]d\bar{t}+\mathbf{L}(t)\mathbf{p}_o+\int_0^t\mathbf{L}(t-\bar{t})\dot{\mathbf{p}}(\bar{t})d\bar{t}, \quad (11a)$$

$$\mathbf{Q}(t)=\mathbf{B}^T[\mathbf{G}(t)\mathbf{K}\mathbf{u}_o-\dot{\mathbf{G}}(t)\mathbf{M}\dot{\mathbf{u}}_o]+\mathbf{L}^T(t)\mathbf{f}(o)+\mathbf{Z}(t)\boldsymbol{\vartheta}(o)+\int_0^t[\mathbf{L}^T(t-\bar{t})\dot{\mathbf{f}}(\bar{t})+\mathbf{Z}(t-\bar{t})\dot{\boldsymbol{\vartheta}}(\bar{t})]d\bar{t}+\mathbf{Z}(t)\mathbf{p}_o+\int_0^t\mathbf{Z}(t-\bar{t})\dot{\mathbf{p}}(\bar{t})d\bar{t}. \quad (11b)$$

Introducing the state function vector

$$\mathbf{X}=[\mathbf{u}^T\ \dot{\mathbf{u}}^T]^T \quad (12)$$

and setting

$$\boldsymbol{\Gamma}(t)=\begin{bmatrix}\mathbf{GK} & -\dot{\mathbf{G}}\mathbf{M}\\ \dot{\mathbf{G}}\mathbf{K} & -\ddot{\mathbf{G}}\mathbf{M}\end{bmatrix},\quad \mathbf{W}(t)=\begin{bmatrix}\mathbf{L}\\ \dot{\mathbf{L}}\end{bmatrix}, \quad (13a,b)$$

$$\boldsymbol{\Omega}(t)=\begin{bmatrix}\mathbf{A} & \mathbf{L}\\ \dot{\mathbf{A}} & \dot{\mathbf{L}}\end{bmatrix},\quad \mathbf{F}(t)=\begin{bmatrix}\mathbf{f}\\ \boldsymbol{\vartheta}\end{bmatrix}, \quad (13c,d)$$

$$\boldsymbol{\Pi}(t)=\mathbf{B}^T[\mathbf{GK}\quad -\dot{\mathbf{G}}\mathbf{M}],\quad \boldsymbol{\Lambda}(t)=[\mathbf{L}^T\quad \mathbf{Z}], \quad (13e,f)$$

Downloaded 03 May 2010 to 171.66.16.20. Redistribution subject to ASME license or copyright; see http://www.asme.org/terms/Terms_Use.cfm

Eqs. (11*a*, *b*) become

$$\mathbf{X}(t)=\mathbf{\Gamma}(t)\mathbf{X}_o+\mathbf{\Omega}(t)\mathbf{F}_o+\mathbf{W}(t)\mathbf{p}_o+\int_0^t\mathbf{\Omega}(t-\bar{t})\dot{\mathbf{F}}(\bar{t})d\bar{t}+\int_0^t\mathbf{W}(t-\bar{t})\dot{\mathbf{p}}(\bar{t})d\bar{t},\quad(14a)$$

$$\mathbf{Q}(t)=\mathbf{\Pi}(t)\mathbf{X}_o+\mathbf{\Lambda}(t)\mathbf{F}_o+\mathbf{Z}(t)\mathbf{p}_o+\int_0^t\mathbf{\Lambda}(t-\bar{t})\dot{\mathbf{F}}(\bar{t})d\bar{t}+\int_0^t\mathbf{Z}(t-\bar{t})\dot{\mathbf{p}}(\bar{t})d\bar{t}.\quad(14b)$$

The Eqs. (14*a*, *b*) can be applied in every instant

$$\tau=t-t_{n-1}\quad(t_{n-1}\le t\le t_n)\qquad(15)$$

of the generic nth time interval, assuming as initial conditions of the relevant interval the structure response (in term of displacements, velocities, and plastic strains) at time t_{n-1}; namely

$$\mathbf{X}(\tau)=\mathbf{\Gamma}(\tau)\mathbf{X}_{n-1}+\mathbf{\Omega}(\tau)\mathbf{F}_{n-1}+\mathbf{W}(\tau)\mathbf{p}_{n-1}+\int_0^\tau\mathbf{\Omega}(\tau-\bar{\tau})\dot{\mathbf{F}}(\bar{\tau})d\bar{\tau}+\int_0^\tau\mathbf{W}(\tau-\bar{\tau})\dot{\mathbf{p}}(\bar{\tau})d\bar{\tau},\quad(16a)$$

$$\mathbf{Q}(\tau)=\mathbf{\Pi}(\tau)\mathbf{X}_{n-1}+\mathbf{\Lambda}(\tau)\mathbf{F}_{n-1}+\mathbf{Z}(\tau)\mathbf{p}_{n-1}+\int_0^\tau\mathbf{\Lambda}(\tau-\bar{\tau})\dot{\mathbf{F}}(\bar{\tau})d\bar{\tau}+\int_0^\tau\mathbf{Z}(\tau-\bar{\tau})\dot{\mathbf{p}}(\bar{\tau})d\bar{\tau}.\quad(16b)$$

Defined into the nth time interval the variations of load, of plastic deformation, and of plastic activation intensity,

$$\Delta\mathbf{F}_n=\mathbf{F}_n-\mathbf{F}_{n-1},\qquad(17a)$$

$$\Delta\mathbf{p}_n=\mathbf{p}_n-\mathbf{p}_{n-1},\qquad(17b)$$

$$\mathbf{Y}_n=\lambda_n-\lambda_{n-1},\qquad(17c)$$

the load variation rate is modeled according to a suitable shape function $\mathbf{g}_1(\bar{\tau})$

$$\dot{\mathbf{F}}(\bar{\tau})=\mathbf{g}_1(\bar{\tau})\Delta\mathbf{F}_n,\qquad(18a)$$

the plastic deformation rate and the plastic activation coefficients are modeled according to another suitable shape function $\mathbf{g}_2(\bar{\tau})$

$$\dot{\mathbf{p}}(\bar{\tau})=\mathbf{g}_2(\bar{\tau})\Delta\mathbf{p}_n,\qquad(18b)$$

$$\dot{\lambda}(\bar{\tau})=\mathbf{g}_2(\bar{\tau})\mathbf{Y}_n.\qquad(18c)$$

Setting

$$\hat{\mathbf{\Omega}}(h)=\int_0^h\mathbf{\Omega}(h-\bar{\tau})\mathbf{g}_1(\bar{\tau})d\bar{\tau},\qquad(19a)$$

$$\hat{\mathbf{W}}(h)=\int_0^h\mathbf{W}(h-\bar{\tau})\mathbf{g}_2(\bar{\tau})d\bar{\tau},\qquad(19b)$$

$$\hat{\mathbf{\Lambda}}(h)=\int_0^h\mathbf{\Lambda}(h-\bar{\tau})\mathbf{g}_1(\bar{\tau})d\bar{\tau},\qquad(19c)$$

$$\hat{\mathbf{Z}}(h)=\int_0^h\mathbf{Z}(h-\bar{\tau})\mathbf{g}_2(\bar{\tau})d\bar{\tau},\qquad(19d)$$

and recalling the (5*a*), the (16*a*, *b*) give the response for $t=t_n$ (and $\tau=h$) to the initial conditions, evaluated for $t=t_{n-1}$, and to the variations of load and plastic deformation of current step; i.e.,

$$\mathbf{X}_n=\mathbf{\Gamma}(h)\mathbf{X}_{n-1}+\mathbf{\Omega}(h)\mathbf{F}_{n-1}+\mathbf{W}(h)\mathbf{p}_{n-1}+\hat{\mathbf{\Omega}}(h)\Delta\mathbf{F}_n+\hat{\mathbf{W}}(h)\mathbf{N}\mathbf{Y}_n,\quad(20a)$$

$$\mathbf{Q}_n=\mathbf{\Pi}(h)\mathbf{X}_{n-1}+\mathbf{\Lambda}(h)\mathbf{F}_{n-1}+\mathbf{Z}(h)\mathbf{p}_{n-1}+\hat{\mathbf{\Lambda}}(h)\Delta\mathbf{F}_n+\hat{\mathbf{Z}}(h)\mathbf{N}\mathbf{Y}_n.\quad(20b)$$

In particular, if a piecewise constant modeling of the load variation rates and of the plastic deformation is assumed, calling $\mathbf{I}$ the identity matrix, it results in the following:

$$\mathbf{g}_1=\mathbf{g}_2=\mathbf{g}=\frac{1}{h}\mathbf{I},\qquad(21)$$

$$\hat{\mathbf{\Omega}}=\frac{1}{h}\int_0^h\mathbf{\Omega}(h-\bar{\tau})d\bar{\tau},\quad\hat{\mathbf{\Lambda}}=\frac{1}{h}\int_0^h\mathbf{\Lambda}(h-\bar{\tau})d\bar{\tau},\qquad(22a,b)$$

$$\hat{\mathbf{W}}=\frac{1}{h}\int_0^h\mathbf{W}(h-\bar{\tau})d\bar{\tau},\quad\hat{\mathbf{Z}}=\frac{1}{h}\int_0^h\mathbf{Z}(h-\bar{\tau})d\bar{\tau}.\qquad(22c,d)$$

In order to obtain the elastic response (20*a*,*b*) deduced beginning from (1)–(3) and (5*a*), it is necessary to know $\mathbf{Y}_n$, which must be such in order to satisfy the relationships (4) and (5*b*,*c*) at each instant. Effectively, because of the modeling (18*b*,*c*) arbitrarily adopted into the generic time interval, it is possible to satisfy Eqs. (4) and (5*c*) only in the discretization instants, writing at the end of the nth step

$$\varphi_n=\mathbf{N}^T\mathbf{Q}_n-\mathbf{R}\le\mathbf{0},\qquad(23a)$$

$$\mathbf{Y}_n\ge\mathbf{0},\quad\mathbf{Y}_n^T\varphi_n=0.\qquad(23b,c)$$

Replacing (20*b*) in (23*a*) and setting

$$\mathbf{b}_n=\mathbf{R}-\mathbf{N}^T(\mathbf{\Pi}\mathbf{X}_{n-1}+\mathbf{\Lambda}\mathbf{F}_{n-1}+\mathbf{Z}\mathbf{p}_{n-1}+\hat{\mathbf{\Lambda}}\Delta\mathbf{F}_n),\qquad(24a)$$

$$\mathbf{S}=-\mathbf{N}^T\hat{\mathbf{Z}}\mathbf{N},\qquad(24b)$$

(23) changes into the linear complementarity problem

$$\mathbf{S}\mathbf{Y}_n+\mathbf{b}_n\ge\mathbf{0},\quad\mathbf{Y}_n\ge\mathbf{0},\quad\mathbf{Y}_n^T(\mathbf{S}\mathbf{Y}_n+\mathbf{b}_n)=0,\qquad(25a\text{–}c)$$

the solution of which gives $\mathbf{Y}_n$. Vector $\mathbf{Y}_n$ is often obtained by solving one of the two quadratic programming problems, equivalent to the linear complementarity problem (25):

$$\left.\begin{array}{l}\min\limits_{(Y_n)}\dfrac{1}{2}\mathbf{Y}_n^T\mathbf{S}\mathbf{Y}_n+\mathbf{b}_n^T\mathbf{Y}_n\\ \text{subject to the constraints }\mathbf{Y}_n\ge\mathbf{0}\end{array}\right\}\qquad(26a)$$

$$\left.\begin{array}{l}\min\limits_{(Y_n)}\dfrac{1}{2}\mathbf{Y}_n^T\mathbf{S}\mathbf{Y}_n\\ \text{subject to the constraints }\mathbf{S}\mathbf{Y}_n+\mathbf{b}_n\ge\mathbf{0}\end{array}\right\}.\qquad(26b)$$

3 Elastic-Plastic Approximated Analysis

The high number of components of vector $\mathbf{Y}_n$, also for small structures, gives considerable computational difficulties in solving the linear complementarity problem (25) or the quadratic programming problems (26*a*,*b*). An approximate method to overcome these difficulties has been found out in the so-called element optimization technique (see, e.g., Feijòo, 1986; Feijòo and Zouain, 1987; Borino et al., 1990), which arrives iteratively at the solution of the problem, satisfying element by element the plastic laws.

Another approximated method to solve the problem can be the following one, developed in the general (and also frequent) case in which the structure has ν_d dynamic freedom degrees and ν_s not dynamic freedom degrees with $\nu_d+\nu_s=\nu$. In this case, Eq. (1) breaks in

$$\mathbf{M}_{11}\ddot{\mathbf{u}}_d+\mathbf{V}_{11}\dot{\mathbf{u}}_d+\mathbf{K}_{11}\mathbf{u}_d+\mathbf{K}_{12}\mathbf{u}_s=\mathbf{f}_1+\mathbf{B}_1(\vartheta+\mathbf{p}),\qquad(27a)$$

$$\mathbf{K}_{21}\mathbf{u}_d+\mathbf{K}_{22}\mathbf{u}_s=\mathbf{f}_2+\mathbf{B}_2(\vartheta+\mathbf{p}),\qquad(27b)$$

where $\mathbf{u}_d$ are the ν_d dynamic freedom degrees and $\mathbf{u}_s$ are the ν_s not dynamic freedom degrees. Obtaining $\mathbf{u}_d$ from (27*a*) and $\mathbf{u}_s$ from (27*b*) results in

$$\mathbf{u}_d=\mathbf{K}_{11}^{-1}(-\mathbf{M}_{11}\ddot{\mathbf{u}}_d-\mathbf{V}_{11}\dot{\mathbf{u}}_d-\mathbf{K}_{12}\mathbf{u}_s+\mathbf{f}_1+\mathbf{B}_1(\vartheta+\mathbf{p})),\qquad(28a)$$

$$\mathbf{u}_s=\mathbf{K}_{22}^{-1}(-\mathbf{K}_{21}\mathbf{u}_d+\mathbf{f}_2+\mathbf{B}_2(\vartheta+\mathbf{p})).\qquad(28b)$$

Replacing the (28*b*) into the (27*a*) and the (28*a*) into (27*b*), Eqs. (27) become

$$\mathbf{M}_{dd}\ddot{\mathbf{u}}_d+\mathbf{V}_{dd}\dot{\mathbf{u}}_d+\mathbf{K}_{dd}\mathbf{u}_d=\mathbf{f}_d+\mathbf{B}_d(\vartheta+\mathbf{p}),\qquad(29a)$$

$$\mathbf{M}_{sd}\ddot{\mathbf{u}}_d+\mathbf{V}_{sd}\dot{\mathbf{u}}_d+\mathbf{K}_{ss}\mathbf{u}_s=\mathbf{f}_s+\mathbf{B}_s(\vartheta+\mathbf{p}),\qquad(29b)$$

where

Downloaded 03 May 2010 to 171.66.16.20. Redistribution subject to ASME license or copyright; see http://www.asme.org/terms/Terms_Use.cfm

$$\mathbf{M}_{dd}=\mathbf{M}_{11},\quad \mathbf{M}_{sd}=-\mathbf{K}_{21}\mathbf{K}_{11}^{-1}\mathbf{M}_{11},\qquad (30a,b)$$

$$\mathbf{V}_{dd}=\mathbf{V}_{11},\quad \mathbf{V}_{sd}=-\mathbf{K}_{21}\mathbf{K}_{11}^{-1}\mathbf{V}_{11},\qquad (30c,d)$$

$$\mathbf{K}_{dd}=\mathbf{K}_{11}-\mathbf{K}_{12}\mathbf{K}_{22}^{-1}\mathbf{K}_{21},\quad \mathbf{K}_{ss}=\mathbf{K}_{22}-\mathbf{K}_{21}\mathbf{K}_{11}^{-1}\mathbf{K}_{12},\qquad (30e,f)$$

$$\mathbf{f}_d=\mathbf{f}_1-\mathbf{K}_{12}\mathbf{K}_{22}^{-1}\mathbf{f}_2,\quad \mathbf{f}_s=\mathbf{f}_2-\mathbf{K}_{21}\mathbf{K}_{11}^{-1}\mathbf{f}_1,\qquad (30g,h)$$

$$\mathbf{B}_d=\mathbf{B}_1-\mathbf{K}_{12}\mathbf{K}_{22}^{-1}\mathbf{B}_2,\quad \mathbf{B}_s=\mathbf{B}_2-\mathbf{K}_{21}\mathbf{K}_{11}^{-1}\mathbf{B}_1.\qquad (30i,j)$$

Assuming knowledge of the vector $\mathbf{P}^{(t)}$, the dynamic freedom degrees can be calculated by solving the problem (29*a*); moreover, the nondynamic freedom degrees can be calculated soon after through the (29*b*) or, more suitably, through the (28*b*).

Because the diagonal disposition of the elastic stiffness matrix of the structure, the nonvanishing blocks of which ($\mathbf{K}_{dd}$ and $\mathbf{K}_{ss}$) appear in (29*a*, *b*), the (6), (8), and (10) formulas become, respectively,

$$\mathbf{G}_{dd}(t)=\sum_{i=1}^{\nu_d}\Phi_i\psi_i\Phi_i^T,\qquad (31)$$

$$\mathbf{A}(t)=\mathbf{K}_{dd}^{-1}-\mathbf{G}_{dd}(t),\qquad (32)$$

$$\mathbf{Z}(t)=\mathbf{B}_d^T(\mathbf{K}_{dd}^{-1}-\mathbf{G}_{dd})\mathbf{B}_d+\mathbf{B}_s^T\mathbf{K}_{ss}^{-1}\mathbf{B}_s-\mathbf{D}.\qquad (33)$$

Remarking that

$$\lim_{h\to 0}\left(\frac{1}{h}\int_0^h\psi_i(\tau)d\tau\right)=\frac{1}{\omega_i^2},\quad (i=1,\ 2,\ \ldots,\ \nu_d)\qquad (34)$$

and taking into account Eqs. (31), (32), and (33), one obtains

$$\lim_{h\to 0}\mathbf{G}_{dd}(h)=\mathbf{K}_{dd}^{-1},\qquad (35)$$

$$\lim_{h\to 0}\mathbf{Z}(h)=\mathbf{B}_s^T\mathbf{K}_{ss}^{-1}\mathbf{B}_s-\mathbf{D}.\qquad (36)$$

Utilizing again the piecewise constant modeling (21) for plastic deformations, one also obtains

$$\lim_{h\to 0}\hat{\mathbf{Z}}(h)=\lim_{h\to 0}\mathbf{Z}(h)=\mathbf{B}_s^T\mathbf{K}_{ss}^{-1}\mathbf{B}_s-\mathbf{D}.\qquad (37a,b)$$

Provided that the width h of the elementary time subinterval utilized for discretization of the interval $(o,\ t_f)$ is small enough, compared to the smallest structure natural vibration period which has to be taken into account, Eqs. (37) allow us to set

$$\hat{\mathbf{Z}}\cong\mathbf{B}_s^T\mathbf{K}_{ss}^{-1}\mathbf{B}_s-\mathbf{D}.\qquad (38)$$

The first addendum matrix on the right-hand side of (38) is a block diagonal one, even if some of its diagonal blocks can have dimensions bigger than the diagonal blocks of $\mathbf{D}$. In particular, its diagonal blocks relative to elements with points of connection which converge all on dynamic freedom degrees are zero. In every case, matrix $\hat{\mathbf{Z}}$ is yet a block diagonal one. Because of the block diagonal form of the matrices $\hat{\mathbf{Z}}$ and $\mathbf{N}$, the matrix

$$\mathbf{S}\cong\mathbf{N}^T\mathbf{B}_s^T\mathbf{K}_{ss}^{-1}\mathbf{B}_s\mathbf{N}-\mathbf{N}^T\mathbf{D}\mathbf{N}\qquad (39)$$

is also a block diagonal one, and then the solution of quadratic programming problem (26*a*, *b*) can be obtained solving a greater number of quadratic programming problems with reduced orders.

Suitably refining the time step, the accuracy of the elastic response (20*b*) and the full attendibility of the approximation (39) take reasonably to very good results.

The physical meaning of the Eq. (39) consist of taking into account—during the current step—the (instantaneous) effect of plastic activation which produces in plastified elements on the other ones with them directly connected only through the elasticity of the structure, and in overlooking the effect (delayed in time) on the other elements connected with them also through the dynamic behavior of the structure.

Adopting the formula (38), all the elements of the sparse matrix $\mathbf{B}_d^T(\mathbf{K}_{dd}^{-1}-\mathbf{G}_{dd})\mathbf{B}_d$ are disregarded with respect to those of the matrix $\mathbf{B}_s^T\mathbf{K}_{ss}^{-1}\mathbf{B}_s-\mathbf{D}$. Alternatively, it is possible to disregard only the sparse matrix elements which are outside the diagonal blocks. So, one must have an improvement of the response without any increase of the computational effort.

In the particular case in which $\nu_s=\nu$, Eq. (39) becomes exact, while $\hat{\mathbf{Z}}$ identifies itself with the classic expression of the matrix $\mathbf{Z}$, valid in the static field.

In the particular case in which $\nu_s=0$, Eq. (39) simplifies itself

$$\mathbf{S}\cong-\mathbf{N}^T\mathbf{D}\mathbf{N}.\qquad (40)$$

Since adopting Eq. (40), the plastic laws are satisfied element-by-element, one realizes that, when all the freedom degrees are dynamic, this approximate technique coincides with the element optimization technique, stopped at the first iteration. Compared to this last technique, the proposed technique needs an increase of the computational effort in relation to the necessity of adopting a very small h interval, but on the other hand it allows a decrease of the computational effort because it does not need iterations.

4 Example of Application of the Approximate Analysis to Some Particular Structures

Sometimes the diagonal blocks of matrix $\mathbf{S}$, obtained using the approximation (39), or (40), can satisfy the Mangasarian's conditions (Mangasarian, 1976). In these cases it is possible to make a further computational economy; the solution of quadratic programming problem (26*b*) can be obtained by solving a linear programming problem having the same constraints as the quadratic programming problem and with an objective function suitably chosen (see, e.g., Borino et al., 1990; Giambanco et al., 1990).

In the special case of bending frames, if $\nu_s=0$, the diagonal blocks of the matrix $\mathbf{S}$ have the form

$$\mathbf{U}=\alpha\begin{vmatrix}2&-2&-1&1\\-2&2&1&-1\\-1&1&2&-2\\1&-1&-2&2\end{vmatrix}\qquad (41)$$

or the form

$$\mathbf{U}=\alpha\begin{vmatrix}2&-2\\-2&2\end{vmatrix}\qquad (42)$$

where α is a dimensional constant which depends on the physical and geometrical features of the element to which the block is pertinent. Referring to the structure of formula (41) and denoting with $\mathbf{Y}=[Y_1\ Y_2\ Y_3\ Y_4]^T$ the components of the plastic activation intensity vector $\mathbf{Y}_n$ (23*b*) and with $\mathbf{b}=[b_1\ b_2\ b_3\ b_4]^T$ (24*a*) the opposites of the components of the vector $\mathbf{b}_n$, all relative to the same element to which Eq. (41) refers, the generic linear complementarity problem with reduced dimensions can be written as

$$\alpha\begin{vmatrix}2&-2&-1&1\\-2&2&1&-1\\-1&1&2&-2\\1&-1&-2&2\end{vmatrix}\begin{vmatrix}Y_1\\Y_2\\Y_3\\Y_4\end{vmatrix}\geq\begin{vmatrix}b_1\\b_2\\b_3\\b_4\end{vmatrix},\qquad \begin{matrix}(43a)\\(43b)\\(43c)\\(43d)\end{matrix}$$

$$\mathbf{Y}\geq\mathbf{0},\quad \mathbf{Y}^T(\mathbf{U}\mathbf{Y}-\mathbf{b})=0.\qquad (43e,f)$$

Subject to examination of known coefficients, it is possible to deduce from (43*a*–*d*) one or two equations which, being solved, give the components different by zero of $\mathbf{Y}$, which come out all positive, and such as the constraints (43*a*–*d*) not being satisfied as equality are satisfied as inequality, and also such as the Eqs. (43*e*, *f*) are satisfied, i.e., such as to satisfy the linear complementarity problem (43*a*–*f*).

- *If the known terms are all negative, it is* $\mathbf{Y}=\mathbf{0}$.
- If $b_1>0$ and $b_3>0$, then $Y_1>0$ and $Y_3>0$ (while Y_2

Downloaded 03 May 2010 to 171.66.16.20. Redistribution subject to ASME license or copyright; see http://www.asme.org/terms/Terms_Use.cfm

$= Y_4 = 0$) and it is necessary to choose the Eqs. (43*a*) and (43*c*), satisfied as equality.

- If $b_2 > 0$ and $b_4 > 0$, then $Y_2 > 0$ and $Y_4 > 0$, etc.
- If $b_1 > 0$ and $b_4 > 0$, according to whether $1/2 < b_4/b_1 < 2$, $b_4/b_1 \leq 1/2$, $2 \leq b_4/b_1$, it is, respectively:
  $(Y_1 > 0, Y_4 > 0)$ (while $Y_2 = Y_3 = 0$), and it is necessary to choose Eqs. (43*a*) and (43*d*) satisfied as equality;
  $(Y_1 > 0, Y_4 = 0)$ (while $Y_2 = Y_3 = 0$) and it is necessary to choose (43*a*), satisfied as equality;
  $(Y_1 = 0, Y_4 > 0)$ (while $Y_2 = Y_3 = 0$) and it is necessary to choose Eq. (43*d*), satisfied as equality.
- If $b_2 > 0$ and $b_3 > 0$, according to whether $1/2 < b_3/b_2 < 2$, $b_3/b_2 \leq 1/2$, $2 \leq b_3/b_2$, it is, respectively:

  $(Y_2 > 0, Y_3 > 0)$, etc.; $(Y_2 > 0, Y_3 = 0)$, etc.; $(Y_2 = 0, Y_3 > 0)$, etc.
- If $b_1 > 0$, according to whether $1/2 < -b_3/b_1 < 2$, $-b_3/b_1 \leq 1/2$, $2 \leq -b_3/b_1$, it is, respectively,

  $(Y_2 > 0, Y_3 > 0)$, etc.; $(Y_1 > 0, Y_3 = 0)$, etc.; $(Y_1 = 0, Y_3 > 0)$, etc.
- If $b_2 > 0$, according to whether $1/2 < -b_4/b_2 < 2$, $-b_4/b_2 \leq 1/2$, $2 \leq -b_4/b_2$, it is, respectively,

  $(Y_2 > 0, Y_4 > 0)$, etc.; $(Y_2 > 0, Y_4 = 0)$, etc.; $(Y_2 = 0, Y_4 > 0)$, etc.
- If $b_3 > 0$, according to whether $1/2 < -b_1/b_3 < 2$, $-b_1/b_3 \leq 1/2$, $2 \leq -b_1/b_3$, it is, respectively,

  $(Y_3 > 0, Y_1 > 0)$, etc.; $(Y_3 > 0, Y_1 = 0)$, etc.; $(Y_3 = 0, Y_1 > 0)$, etc.
- If $b_4 > 0$, according to whether $1/2 < -b_2/b_4 < 2$, $-b_2/b_4 \leq 1/2$, $2 \leq -b_2/b_4$, it is respectively,

  $(Y_4 > 0, Y_2 > 0)$, etc.; $(Y_4 > 0, Y_2 = 0)$, etc.; $(Y_4 = 0, Y_2 > 0)$, etc.

The other combinations of $b > 0$ not mentioned are not physically possible.

One can make similar simpler considerations for truss structures and for shear-type frames.

It is clear that, in the particular cases examined, the very low computational effort of procedure allows us to refine the time step practically arbitrarily.

5 Numerical Applications

As an application, the proposed technique has been applied to the steel frame in Fig. 1. F_i $(i = 1, 2)$ are sinusoidally variable loads, i.e., $F_i = \bar{F}_i \sin \bar{\omega}_i t$ $(i = 1, 2)$, with amplitudes $\bar{F}_i$ and circular frequencies $\bar{\omega}_i$. The structure is modeled as a shear-type frame, with rigid beams where masses M_i $(i = 1, 2)$ are distributed, with elastic columns and rigid perfectly plastic hinges (critical sections) located at the extremes of the columns. The structure freedom degrees are the displacements u_i $(i = 1, 2)$ of the beams. Let ξ_i $(i = 1, 2)$ indicate the structure damping ratios. Let J_j, R_j, q_j $(j = 1, 2, \ldots, 6)$ indicate the second area moments, the plastic resistances (yield shear forces) and the plastic deformations (relative displacements of the column extremes) of the columns, respectively.

The dynamic elastic-plastic response of the structure has been studied in three different ways: the first one is the system optimization technique and consists in solving the quadratic programming problem (26*b*) obtaining the exact solution of the time discretized problem; the second one is the well-known element optimization technique broken after eight iterations; the last one is the proposed approximate technique.

The numerical computations were performed for different parameter values. The results relative to two of the studied cases are reported.

The data of the problem for the first case (frame n. 1) are

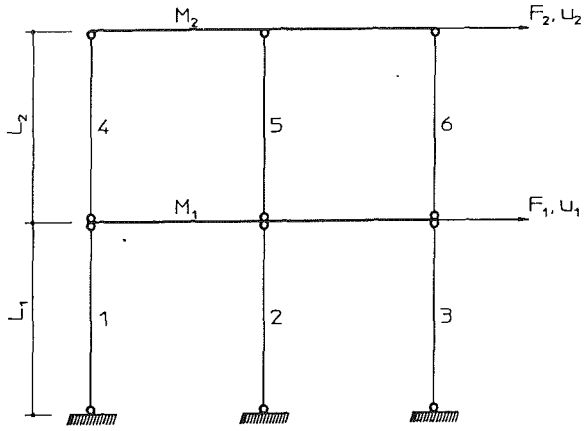


Fig. 1 Shear-type elastic perfectly plastic plane frame: rigid beams (where the masses M_1 and M_2 are distributed) subjected to the sinusoidally variable forces F_1 and F_2 exhibiting the displacements u_1 and u_2, elastic columns, rigid perfectly plastic critical sections where potential hinges are located.

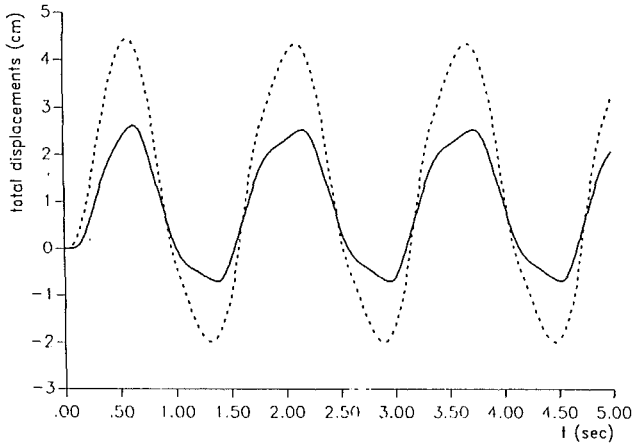


Fig. 2 Elastic-plastic displacement response of the first floor (solid line) and of the second floor (dashed line) for the frame n. 1

$L_1 = L_2 = 350$ cm;
$M_1 = M_2 = 30{,}000$ kg;
$E = 21{,}000{,}000$ N/cm^2;
$J_1 = J_3 = J_4 = J_6 = 2{,}138$ cm^4;
$J_2 = J_5 = 9{,}734$ cm^4;
$R_1 = R_3 = R_4 = R_6 = 19{,}143$ N;
$R_2 = R_5 = 58{,}514$ N;
$\bar{F}_1 = 0.00$ N;
$\bar{F}_2 = 94{,}200$ N;
$\bar{\omega}_2 = 4$ rad/sec;
$\xi_1 = \xi_2 = 0.05$.

One obtains

T_1 = first natural vibration period = 0.6136 sec and
T_2 = second natural vibration period = 0.2344 sec.

Figure 2 shows total displacements of first and second floor, computed for $0 \leq t \leq 5$ sec, and h = time step = 0.01 sec $= T_2/23{,}44$, by means of the three described techniques (the obtained results are practically coincident).

Tables 1, 2, and 3 contain plastic deformations of the six columns, computed for $t = 5$ sec and $h = 0.05$ sec, $h = 0.01$ sec, $h = 0.005$ sec, respectively. It is worth noting the convergency of the approximate technique results towards the system optimization technique results for smaller and smaller h.

The data of the problem for the second case (frame n. 2) are

Downloaded 03 May 2010 to 171.66.16.20. Redistribution subject to ASME license or copyright; see http://www.asme.org/terms/Terms_Use.cfm

$L_1 = L_2 = 350$ cm;
$M_1 = M_2 = 30{,}000$ kg;
$E = 21{,}000{,}000$ N/cm^2;
$J_1 = 6{,}000$ cm^4;
$J_2 = 10{,}000$ cm^4;
$J_3 = J_4 = 4{,}000$ cm^4;
$J_5 = 5{,}000$ cm^4;
$J_6 = 2{,}000$ cm^4;
$R_1 = R_3 = 30{,}000$ N;
$R_2 = 40{,}000$ N;
$R_4 = 15{,}000$ N;
$R_5 = 20{,}000$ N;
$R_6 = 10{,}000$ N;
$\bar{F}_1 = \bar{F}_2 = 50{,}000$ N;
$\bar{\omega}_1 = \bar{\omega}_2 = 12.566$ rad/sec;
$\xi_1 = \xi_2 = 0.05$.

One obtains

T_1 = first natural vibration period = 0.563 sec;
T_2 = second natural vibration period = 0.237 sec.

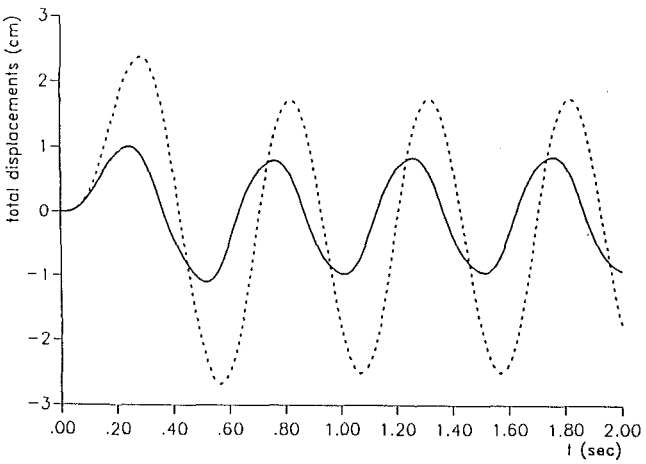


Fig. 3 Elastic-plastic displacement response of the first floor (solid line) and of the second floor (dashed line) for the frame n. 2

Figure 3 shows total displacements of first and second floor, computed for $0 \le t \le 2$ sec, and h = time step = 0.01 sec = $T_2/23{,}70$, by means of the three described techniques (the obtained results are practically coincident).

Tables 4, 5, and 6 contain plastic deformations of the six columns, computed for $t = 2$ sec and $h = 0.05$ sec, $h = 0.01$ sec, $h = 0.005$ sec, respectively. Also in this case the approximate technique results converge towards the system optimization results for smaller and smaller h.

6 Conclusions

It has been shown that the procedure of step-by-step elastic-plastic dynamic analysis can be made in an approximate way, taking advantage of the structure of the constraint matrix, which results from the summation of two time-independent block diagonal matrices (the sum of which is yet a block diagonal matrix) and one sparse matrix, which has elements tending to zero when time step tends to zero.

Table 1

frame structure n. 1
time step $h = 0.05$ sec = $T_2/4.688$
step n. 100; time = 5 sec

	plastic deformations					
Columns	1	2	3	4	5	6
Sys. Opt.	.5233052	.5021912	.5233052	.0925979	-.0211101	.0925979
El. Opt.	.5233049	.5021909	.5233049	.0925984	-.0211097	.0925984
Appr. Tech.	.4991944	.4733710	.4991944	.1015684	-.0102434	.1015684

Table 2

frame structure n. 1
time step $h = 0.01$ sec = $T_2/23.44$
step n. 500; time = 5 sec

	plastic deformations					
Columns	1	2	3	4	5	6
Sys. Opt.	.7835020	.9348778	.7835020	.1920207	.0708545	.1920207
El. Opt.	.7835020	.9348778	.7835020	.1920207	.0708545	.1920207
Appr. Tech.	.7828012	.9340207	.7828012	.1939179	.0719306	.1939179

Table 3

frame structure n. 1
time step $h = 0.005$ sec = $T_2/46.88$
step n. 1000; time = 5 sec

	plastic deformations					
Columns	1	2	3	4	5	6
Sys. Opt.	.7691884	.9720757	.7691884	.1419450	.0418983	.1419450
El. Opt.	.7691884	.9720757	.7691884	.1419450	.0418983	.1419450
Appr. Tech.	.7690686	.9719358	.7690686	.1421209	.0420718	.1421209

Table 4

frame structure n. 2
time step $h = 0.05$ sec = $T_2/4.740$
step n. 40; time = 2 sec

	plastic deformations					
Columns	1	2	3	4	5	6
Sys. Opt.	.0825205	.1368250	0.00	.5662601	.5408765	.3707376
El. Opt.	.0825231	.1368274	0.00	.5662570	.5408741	.3707352
Appr. Tech.	.1426833	.2008264	0.00	.5510534	.5481398	.3780009

Downloaded 03 May 2010 to 171.66.16.20. Redistribution subject to ASME license or copyright; see http://www.asme.org/terms/Terms_Use.cfm

Table 5

frame structure n. 2

time step h = 0.01 sec = T_2 /23.70

step n. 200; time = 2 sec

	plastic deformations					
Columns	1	2	3	4	5	6
Sys. Opt.	-.014706	-.143834	0.00	.0796123	.1221470	.2922859
El. Opt.	-.014706	-.143834	0.00	.0796123	.1221470	.2922859
Appr. Tech.	-.013330	-.144056	0.00	.0809752	.1235102	.2936489

Table 6

frame structure n. 2

time step h = 0.005 sec = T_2 /47.41

step n. 400; time = 2 sec

	plastic deformations					
Columns	1	2	3	4	5	6
Sys. Opt.	-.011373	-.181223	0.00	-.016919	.0256152	.1957541
El. Opt.	-.011373	-.181223	0.00	-.016919	.0256152	.1957541
Appr. Tech.	-.011336	-.181151	0.00	-.016706	.0258286	.1959675

When the time step is small enough, it is allowed to disregard, entirely or in a large part, the elements of sparse matrix, so that the linear complementarity problem which must be solved at the generic step breaks in more but smaller linear complementarity problems with a cut in computational effort. The effected computational experiences have shown that the results obtained by means of the proposed approximate technique are very good when the time step is not greater than about 1/50 of the smallest structure natural vibration period that must be considered (but, even if the time step is not greater than about 1/20 of the smallest structure natural vibration period that must be considered, the results are quite valid, too).

In conclusion, it can be stated that the proposed technique appear effective under the computational viewpoint, particularly when the extreme simplicity of the reduced linear complimentarity problems allows us to refine the time step practically without limit, and without incurring excessive computational effort.

References

Borino, G., and Polizzotto, C., 1989, "A Finite Element Elastic-Plastic Dynamic Analysis by Mathematical Programming," *Proc. FEMSA*, Feb., 8–10, Stellemboschy, South Africa.

Borino, G., Caddemi, S., and Polizzotto, C., 1990, "Mathematical Programming Methods for the Evaluation of Dynamic Plastic Deformations," *Mathematical Programming Methods in Structural Plasticity*, D. L. Smith, ed., Springer-Verlag, New York, Chapter 17, pp. 349–372.

Cohn, M. Z., and Maier, G., eds., 1979, *Engineering Plasticity and Mathematical Programming*, Pergamon Press, New York.

De Donato, O., and Maier, G., 1976, "Historical Deformations Analysis of Elasto-plastic Structures as a Parametric Linear Complementarity," *Meccanica*, Vol. 11, No. 3, pp. 166–171.

Feijòo, R. A., 1986, "Variational Methods in the Theory of Plasticity," Seminar held at the Dept. of Structural and Geotechnical Engineering, University of Palermo, Palermo, Italy.

Feijòo, R. A., and Zouain, N., 1987, "Variational Formulation for Rates and Increments in Plasticity," *Proc. Int. Conf. on Computational Plasticity*, Barcellona, pp. 33–57.

Giambanco, F., Lo Bianco, M., and Palizzolo, L., 1990, "A Bilateral Convergent Bounding Technique for Plastic Deformations," *Meccanica*, Vol. 25, pp. 181–188.

Maier, G., 1978, "Mathematical Programming Methods in Structural Analysis," *Proc. Int. Conf. on Variational Methods in Engineering*, Vol. II, No. 8, Southampton Univ. Press.

Mangasarian, O. L., 1976, "Linear Complementarity Problems Solvable by a Single Linear Program," *Mathematical Programming*, Vol. 10, pp. 263–270.

Owen, D. R. J., and Hinton, E., 1980a, *Finite Elements in Plasticity*, Pineridge Press, Swansea, U.K.

Owen, D. R. J., 1980b, "Implicity Finite Element Methods for the Dynamic Transient Analysis of Solids with Particular Reference to Nonlinear Situations," *Advanced Structural Analysis*, ed. by J. Donea, ed., Applied Science Publs., London, pp. 123–152.

Polizzotto, C., 1986, "Elastoplastic Analysis Method for Dynamic Agencies," *Jour. Eng. Mech. Div., ASCE*, pp. 293–310.

Wilson, E. L., Farhoomand, I., and Bathe, K. J., 1973, "Nonlinear Dynamic Analysis of Complex Structures," *Earth. Eng. and Struct. Dyn.*, Vol. 1, pp. 241–252.

Downloaded 03 May 2010 to 171.66.16.20. Redistribution subject to ASME license or copyright; see http://www.asme.org/terms/Terms_Use.cfm

A Global Extremum Principle in Mixed Form for Equilibrium Analysis With Elastic/Stiffening Materials (a Generalized Minimum Potential Energy Principle)

J. E. Taylor
Department of Aerospace Engineering,
The University of Michigan,
Aerospace Engineering Building,
Ann Arbor, MI 48109-2140

An extremum problem formulation is presented for the equilibrium mechanics of continuum systems made of a generalized form of elastic/stiffening material. Properties of the material are represented via a series composition of elastic/locking constituents. This construction provides a means to incorporate a general model for nonlinear composites of stiffening type into a convex problem statement for the global equilibrium analysis. The problem statement is expressed in mixed "stress and deformation" form. Narrower statements such as the classical minimum potential energy principle, and the earlier (Prager) model for elastic/locking material are imbedded within the general formulation. An extremum problem formulation in mixed form for linearly elastic structures is available as a special case as well.

1 Introduction

In their classical forms the extremum principles available for equilibrium analysis in continuum mechanics are divided into stress or deformation principles, i.e., extremum problem statements expressed in stresses alone or in displacements alone. The familiar "mixed principles" in effect reflect stationarity conditions for saddlepoint problems (established variational models for field problems are discussed broadly in Oden and Reddy, 1976; Arthurs, 1980; Sewell, 1987). The present formulation for this structural analysis is distinctive insofar as it comprises a global extremum problem statement that is not tied to a specific material, and one having both measures of stress and deformations appear as independent variables. The development is described for an arbitrary heterogeneous and anisotropic continuum. Deformation kinematics are assumed to be linear. Stress and deformation fields are represented in the model in a way that provides conveniently for the analysis of systems made up of a *general type of elastic/stiffening material*. This provision relies on a feature of the structure of the problem that facilitates the synthesis of stress-strain relations. Also, since equilibrium mechanics is presented here as a convex optimization problem, the analytical development is described conveniently using well-established results from the mathematics of such problems.

Several known simpler models in continuum mechanics analysis are imbedded within the present formulation. The *minimum potential energy principle*, and models introduced by Prager (1957, 1964) for *ideal locking* and *elastic/locking* materials, are identified as special cases in relation to the more general problem statement. Given these connections, the basic model described in this paper could be interpreted as a generalization of the classical minimum potential energy principle. Also the general model is in a sense complementary to another generalized extremum problem formulation in mixed form (Taylor, 1992, 1993; Taylor and Logo, 1993) that is applicable for global equilibrium analysis of structures formed of materials having arbitrary polygonal-shaped *elastic/softening* properties. It is notable that the two formulations, the model for softening materials and the present one for stiffening structures, are not Lagrangian duals.

2 Background

The cited Prager (1964) model of an elastic/locking material is used in the construction for modeling the general polygonal-shaped elastic stiffening material covered here. In $1D$ the stress-strain relation for elastic locking material has the bilinear form shown in Fig. 1. This relation is summarized in the statement defining strain as

$$\epsilon = \begin{cases} \sigma/E \text{ for } |\epsilon| < \bar{\epsilon} \\ \bar{\epsilon} \text{ sgn } \epsilon \text{ otherwise} \end{cases} \tag{1}$$

where σ represents stress, E stands for elastic modulus, and $\bar{\epsilon}$

Contributed by the Applied Mechanics Division of THE AMERICAN SOCIETY OF MECHANICAL ENGINEERS for publication in the ASME JOURNAL OF APPLIED MECHANICS.
Discussion on this paper should be addressed to the Technical Editor, Professor Lewis T. Wheeler, Department of Mechanical Engineering, University of Houston, Houston, TX 77204-4792, and will be accepted until four months after final publication of the paper itself in the ASME JOURNAL OF APPLIED MECHANICS.
Manuscript received by the ASME Applied Mechanics Division, Jan. 4, 1993; final revision, May 21, 1993. Associate Technical Editor: J. N. Reddy.

Copyright © 1994 by ASME
Downloaded 03 May 2010 to 171.66.16.20. Redistribution subject to ASME license or copyright; see http://www.asme.org/terms/Terms_Use.cfm

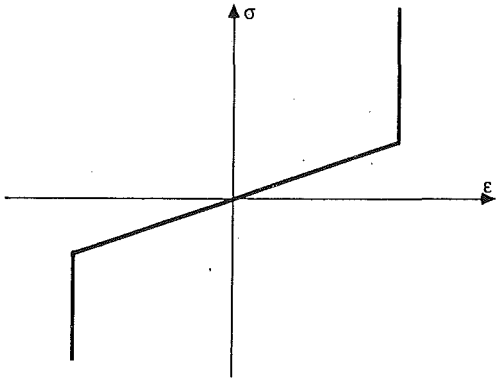


Fig. 1 Stress-strain relation for an *elastic/locking* material

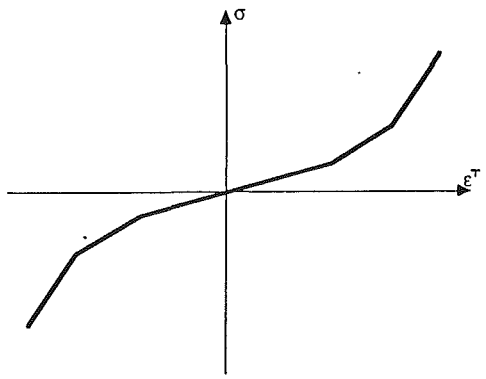


Fig. 2 Stress-total strain relation for the *elastic/stiffening* material

symbolizes a prescribed limit value of strain. Consider now a superposition of strains, so that the total strain, say ϵ^T, is represented via

$$\epsilon^T = \sigma/\tilde{E} + \sum_{\beta=1}^{B} \epsilon^\beta. \tag{2}$$

Here the term $\sigma/\tilde{E}$ stands for a contribution that remains indefinitely linearly elastic, and each constituent term ϵ^β has the properties of the elastic/locking material just described. Of course in mechanical terms this composition of deformations simply corresponds in effect to a set of constituents (each identified with one of the terms in (2)) working in series.

The net effect is a material which in 1*D* has the stress-strain character shown in Fig. 2. The polygonal shape of this stress-strain relation is set quantitatively by the choice of material constants E_β, $\tilde{E}$, and $\bar{\epsilon}_\beta$, where $\beta = 1, 2, \ldots B$. The counterpart for the 3*D* continuum is accomplished (following Prager) with the introduction of a 'locking function," say $h(\epsilon)$, such that $h(\epsilon) - \bar{h} = O$ defines a convex surface in the space of tensor fields ϵ. (Locking function h is expressed in general as a concave, non-negative function of the invariants of the strain tensor ϵ). We do not at present address issues related to a matching of the form of h to the physics of a specific material. At the same time, the *particular form* of the function is not a factor in the development of this paper. A strain state satisfying the condition $h(\epsilon) - \bar{h} < Q$ is considered to be elastic, while for any strain state satisfying $h(\epsilon) - \bar{h} = 0$, i.e., a state corresponding to a "point on the locking surface," the material is said to be locked. The same composition (2) is used for the 3*D* continuum, with each field ϵ^β now being controlled by its own locking function $h_\beta(\epsilon^\beta)$.

The counterpart to (2) for the tensor fields is stated:

$$\underset{\sim}{\epsilon}^T = \underset{\sim}{\mathbf{C}}\underset{\sim}{\sigma} + \sum_{\beta=1}^{B} \underset{\sim}{\epsilon}^\beta. \tag{3}$$

The details necessary for a full characterization of material properties should become clear with a reading of the problem formulation given in the next section. We simply note here that with constitutive tensors $\mathbf{C}$ and $\mathbf{L}_\beta$ and locking bounds $\bar{h}_\beta$ variable over the domain of the structure, and with the form of the locking functions $h^\beta(\epsilon^\beta)$ themselves being variable from constituent to constituent, the simple construction (3) in fact provides for substantial versatility in the modelling of nonlinear composite materials.

In contrast to the behavior identified with the classical elastic/locking concept, it is characteristic of the material described in (2) and (3) that its response evolves in the deformation process toward a limiting linearly elastic state. As a consequence the global response of systems made of the general elastic/stiffening material also has a linearly elastic limit state. In other words, with the "new" material the singular (locking) condition associated with the earlier simple material model is removed at both the local and global levels (local refers to the pointwise constitutive property, while global refers to the overall structural response). As a result, the model for analysis of structural systems described in what follows is valid over the full range of response, from initial linearly elastic behavior through the entire evolution of material stiffening, without limit on the level of load.

3 Formulation for the Continuum

The material properties associated with the elastic/stiffening material introduced in Section 2 are incorporated in the global extremum problem statement partly in explicit form, and partly via the structure of the problem itself. For example, the "locking" property is represented through a local constraint that comprises part of the definition of admissible strain fields. The full characterization of these local properties, as well as satisfaction of the complete set of requirements for equilibrium analysis of the nonlinear continuum, are verified via a mathematical interpretation of the global minimization problem statement. As it applies for the heterogeneous and anisotropic elastic/stiffening material, this global problem formulation is stated:

$[Q]$ $\min_{\alpha,\sigma,\mathbf{u},\epsilon^\beta} \alpha$

Subject to:

$$(C1)\quad \int_\Omega \left[\frac{1}{2} C_{ijkl}\sigma_{ij}\sigma_{kl} + \sum_{\beta=1}^{B} \frac{1}{2} L^\beta_{ijkl}\epsilon^\beta_{ij}\epsilon^\beta_{kl} - \alpha X_i u_i\right] dV - \alpha \int_{\Gamma_t} t_i u_i d\Gamma + \mathbf{E} \le 0$$

$$(C2)\quad h_\beta(\epsilon^\beta_{ij}) - \bar{h}_\beta \le 0 \quad \text{in } \Omega;\ \forall\beta$$

$$(C3)\quad \left[C_{ijkl}\sigma_{kl} + \sum_{\beta} \epsilon^\beta_{ij} - \frac{1}{2}(u_{i,j} + u_{j,i})\right] = 0 \quad \text{in } \Omega;\ \forall i, j$$

Formulation $[Q]$ is the counterpart for continua of the statement given in Taylor and Washabaugh (1994) for discrete structures. Constitutive tensors C_{ijkl} and L^β_{ijkl}, locking bound values $\bar{h}_\beta$, energy bound $\mathbf{E}$, field loads X_i surface tractions t_i, and the definition of region Ω by its boundaries are data. Also, the number B of constituents identified by index β is given, and the l.c. latin subscripts have range 2 or 3 corresponding to the dimension of the continuum (summation convection is implied for the latin indices). Having loads on the system described in terms of a (uniform) load factor α provides for the study of behavior under proportional loading. It can be verified that α is monotone w.r.t. energy bound value $\mathbf{E}$, and so the evolution of structural response under increasing load

Downloaded 03 May 2010 to 171.66.16.20. Redistribution subject to ASME license or copyright; see http://www.asme.org/terms/Terms_Use.cfm

can be established in the form of a set of solutions to [Q] corresponding to an appropriate set of data values for $\mathbf{E}$ (with other data fixed). Note also that with the inclusion in problem [Q] of a statement of strain-displacement relations as an explicit constraint, namely ($C3$), both strain and displacement appear as *independently varying fields*.

An equivalent alternate form for isoperimetric problem [Q] is obtained by interchanging the isoperimetric constraint with the objective function. This alternate problem statement is given by

$$[Q'] \quad \min_{\alpha,\sigma,\mathbf{u},\epsilon} \left\{ \int_\Omega \left[\frac{1}{2} \left(C_{ijkl}\sigma_{ij}\sigma_{kl} + \sum_\beta L^\beta_{ijkl}\epsilon^\beta_{ij}\epsilon^\beta_{kl} \right) - \alpha X_i u_i \right] dV - \alpha \int_{\Gamma_t} t_i u_i d\Gamma \right\}$$

Subject to:

$$(C1') \quad \alpha - \bar{\alpha} \le 0$$

$$\left.\begin{matrix}(C2')\\(C3')\end{matrix}\right\} \text{identical to } (C2) \text{ and } (C3) \text{ of } [Q].$$

Here the value $\bar{\alpha}$ bounding load factor α from above replaces the energy bound $\mathbf{E}$ of problem [Q] in the "data set." The load constraint is active at the solution, and so the bound value $\bar{\alpha}$ in effect represents applied load. Equivalence between [Q] and [Q'] can be expressed as follows. Suppose all data other than $\mathbf{E}$ in [Q] and $\bar{\alpha}$ in [Q'] are the same in the two problems. Then for a given value of $\bar{\alpha}$ there exists a value for $\mathbf{E}$ such that the solutions to the two problems are identical. This equivalence can be verified via a comparison of "necessary conditions."

4 Analysis

Problem [Q] is to be interpreted using basic means available within the subject of mathematics for infinite dimensional convex optimization problems (see, e.g., Clarke, 1983). The objective is to demonstrate that with satisfaction of the necessary conditions for the problem, all the requirements of continuum mechanics analysis for systems composed of the subject constitutively nonlinear media are met. Within conditions customary to the definition of admissible stress and deformation fields, problem [Q] is convex. Symbolizing by Λ, μ_β, and κ_{ij} the multipliers associated with constraints ($C1$) through ($C3$), necessary conditions for an optimal solution reflecting stationarity w.r.t. α, field $\mathbf{u}(x)$, field $\sigma_{ij}(x)$, and fields $\epsilon^\beta_{ij}(x)$, respectively, are stated next:

$$1 - \Lambda \left\{ \int_\Omega X_i u_i dV + \int_{\Gamma_t} t_i u_i d\Gamma \right\} = 0 \tag{4}$$

$$\left.\begin{matrix}\Lambda\alpha X_i + \kappa_{ij,j} = 0 & \text{in } \Omega\\ -\Lambda\alpha t_i + \kappa_{ij} n_j = 0 & \text{on } \Gamma_t\end{matrix}\right\} \tag{5}$$

$$\Lambda\sigma_{ij} - \kappa_{ij} = 0 \quad \text{in } \Omega \tag{6}$$

$$\Lambda L^\beta_{ijkl}\epsilon^\beta_{kl} + \mu^\beta \frac{\partial h\beta}{\partial \epsilon^\beta_{ij}} - \kappa_{ij} = 0 \quad \text{in } \Omega. \tag{7}$$

A solution to problem [Q] must satisfy at the same time the (generalized Kurash-Kuhn-Tucker) conditions:

$$\Lambda \left\{ \int_\Omega \left[\frac{1}{2} C_{ijkl}\sigma_{ij}\sigma_{kl} + \sum_\beta \frac{1}{2} L^\beta_{ijkl}\epsilon^\beta_{ij}\epsilon^\beta_{kl} - \alpha X_i u_i \right] dV - \alpha \int_{\Gamma_t} t_i u_i d\Lambda + E \right\} = 0 \tag{8}$$

$$\mu_\beta [h_\beta(\epsilon^\beta_{ij}) - \bar{h}_\beta] = 0 \quad \text{in } \Omega;\ \forall\beta \tag{9}$$

$$\kappa_{ij} \left[C_{ijkl}\sigma_{kl} + \sum_\beta \epsilon^\beta_{ij} - \frac{1}{2}(u_{i,j} + u_{j,i}) \right] = 0 \quad \text{in } \Omega;\ \forall i, j \tag{10}$$

$$\Lambda \ge 0;\ \mu_\beta \ge 0. \tag{11}$$

Toward an interpretation of the system (4)–(11), note that (4) implies that $\Lambda \neq 0$, whereby (8) requires that the energy constraint ($C1$) is met via equality. Further, the elimination of κ_{ij} between (6) and (7) leads to

$$L^\beta_{ijkl}\epsilon^\beta_{kl} + \tilde{\mu}_\beta \frac{\partial h\beta}{\partial \epsilon^\beta_{ij}} = \sigma_{ij} \quad \begin{matrix}\text{in } \Omega\\ \forall\beta;\ i, j.\end{matrix} \tag{12}$$

(For convenience, symbol $\tilde{\mu}_\beta$ is introduced to stand for μ_β/Λ.) Also, substitution of κ_{ij} from (6) into (5) produces

$$\left.\begin{matrix}\sigma_{ij,j} + \alpha X_i = 0 & \text{in } \Omega\\ \sigma_{ij} n_j - \alpha t_i = 0 & \text{on } \Gamma_t,\end{matrix}\right\} \tag{13}$$

i.e., the condition that the solution stress field must satisfy the (local) equilibrium requirements. Since (13) is free of multipliers, the conditions hold uniformly, independent of other variables appearing in problem [Q]. According to Eq. (10), wherever $\kappa_{ij} \neq 0$ (which by (6) is equivalent to $\sigma_{ij} \neq 0$) the solution total strain ($C_{ijkl}\sigma_{kl} + \Sigma_\beta\, \epsilon_{ij}^\beta$) satisfies the strain-displacement relation. Thus within the (usual) restriction that displacement $u(x)$ is continuous, the solution strain is "compatible." Note that these results hold over the entire domain, and they apply independent of the local "state," i.e., independent of the degree of evolution toward stiffening.

According to complementarity relation (9)

$$\begin{array}{lll} \text{either} & h_\beta - \bar{h}_\beta < 0 \rightarrow \mu_\beta = 0 & (a)\\ \text{or} & \mu_\beta > 0 \rightarrow h_\beta - \bar{h}_\beta = 0 & (b) \quad \text{in } \Omega;\ \forall\beta\\ \text{or} & \mu_\beta = 0 \text{ and } h_\beta - \bar{h}_\beta = 0 & (c) \end{array}$$

(a) and (b) are associated, respectively, with the condition that the βth constituent is elastic or locked, i.e., its strain state lies within the locking surface or on it. Let the intervals in Ω associated with (a) and (b) be identified by $\Omega_{\beta E}$ and $\Omega_{\beta L}$. Clearly (c) is met where these intervals intersect (it may be verified that $\Omega_{\beta E}$ and $\Omega_{\beta L}$ do not overlap). From (12), where a constituent is not locked its response follows the linearly elastic relation, i.e.,

$$L^\beta_{ijkl}\epsilon^\beta_{kl} = \sigma_{ij} \quad \text{in } \Omega_{\beta E};\ \beta \epsilon \Sigma_E. \tag{12'}$$

Here the notation Σ_E is introduced to identify the set of values of β associated with unlocked or elastic constituents. Note that the set designated by Σ_E generally varies over the domain Ω. With strain state for the locked condition symbolized by $\hat{\epsilon}^\beta_{ij}$, (12) requires for the locked constituent

$$L^\beta_{ijkl}\hat{\epsilon}^\beta_{ij} + \tilde{\mu}_\beta \frac{\partial h\beta}{\partial \epsilon^\beta_{ij}} = \sigma_{ij} \quad \text{in } \Omega_{\beta L};\ \beta \epsilon \Sigma_L. \tag{12''}$$

(Σ_L identifies the set of β associated with locked constituents.) It is clear that multiplier $\tilde{\mu}_\beta$ provides for a "statical relaxation" associated with the (kinematic) constraint on ϵ^β_{ij}. Note that the interpretation just given applies for each locking constituent field. Since the fields are controlled independently, generally there may be intersection between intervals $\Omega_{\beta E}$ and $\Omega_{\gamma E}$ for the different (βth and γth) constituents.

In summary, the correspondence between the solution to [Q] and the (typical) requirements for a valid model in continuum mechanics are established. The latter have been identified in part in the form of equilibrium statement (13) and the compatibility relation implied by of (10), and the fact that $\kappa_{ij} = \sigma_{ij} \neq 0$ almost everywhere. Also, it is verified that the local constitutive character implicit in problem statement [Q]

Downloaded 03 May 2010 to 171.66.16.20. Redistribution subject to ASME license or copyright; see http://www.asme.org/terms/Terms_Use.cfm

does in fact correspond to the polygonal elastic/stiffening material model introduced in Section 2.

5 Models Contained Within Statement [Q] (or [Q′])

A number of narrower problem statements are imbedded in [Q], including both familiar and/or known extremum principles as well as apparently unknown specialized forms of the general formulation. As an example, for C_{ijkl} identically zero, problem [Q] is reduced to the statement [Q1] expressed in terms of deformation fields only.

[Q1] $\min_{\alpha,\vec{u},\vec{\epsilon}} \alpha$

Subject to:

$$\int_\Omega \left[\sum_{\beta=1}^{\beta} \frac{1}{2} L^{\beta}_{ijkl} \epsilon^{\beta}_{ij} \epsilon^{\beta}_{kl} - \alpha X_i u_i \right] dV - \alpha \int_{\Gamma_t} t_i u_i d\Gamma + \mathbf{E} \leq 0$$

$$h_\beta(\epsilon^{\beta}_{ij}) - \bar{h}_\beta \leq 0 \quad \text{in } \Omega;\ \forall \beta$$

$$\sum_{\beta=1}^{B} \epsilon^{\beta}_{ij} - \frac{1}{2}(u_{i,j} + u_{j,i}) = 0 \quad \text{in } \Omega;\ \forall i, j.$$

This is a generalized form of Prager's (1964) extremum problem statement for the elastic/locking material. In the case $B = 1$, [Q1] is in fact identical to Prager's model, while for $B > 1$ it amounts to an extension for "polygonal" elastic/locking material properties.

Two distinct other models are produced as limiting cases of [Q1]. Within the one-constituent version of [Q1] (i.e., $B = 1$), in the limit $\bar{h}$ sufficiently large relative to energy bound value E the result is

[Q2] $\min_{\alpha,\vec{u},\vec{\epsilon}} \alpha$

Subject to:

$$\int_\Omega \left[\frac{1}{2} L_{ijkl} \epsilon_{ij} \epsilon_{kl} - \alpha X_i u_i \right] dV - \alpha \int_{\Gamma_t} t_i u_i d\Gamma + \mathbf{E} \leq 0$$

$$\epsilon_{ij} - \frac{1}{2}(u_{i,j} + u_{j,i}) = 0 \quad \text{in } \Omega;\ \forall i, j.$$

The interpretation [Q2] is equivalent to the classical Minimum Potential Energy Principle (this observation might have been made more conveniently working from the general form [Q′]). Consider as another special case the form obtained from [Q1] with $B = 1$ and where all elements of L_{ijkl} equal zero. The result is

[Q3] $\min_{\alpha,\vec{u},\vec{\epsilon}} \alpha$

Subject to:

$$-\int_\Omega \alpha X_i u_i dV - \alpha \int_{\Gamma_t} t_i u_i d\Gamma + \mathbf{E} \leq 0$$

$$h(\epsilon_{ij}) - \bar{h} \leq 0 \quad \text{in } \Omega$$

$$\epsilon_{ij} - \frac{1}{2}(u_{i,j} + u_{j,i}) = 0 \quad \text{in } \Omega \forall i, j$$

is simply a statement of Prager's (1957) model for the ideal-locking material.

As the last example of lesser formulations imbedded within the general form, a reduction from [Q] for $B = 1$, $\mathbf{C} = \mathbf{L}^{-1}$ and with value $\bar{h}$ sufficiently large relative to ϵ (so that the locking constraint is nowhere active) leads to

[Q4] $\min_{\alpha,\vec{\sigma},\vec{\epsilon}\vec{u}} \alpha$

Subject to:

$$\int_\Omega \left[\frac{1}{2} L^{-1}_{ijkl} \sigma_{ij} \sigma_{kl} + \frac{1}{2} L_{ijkl} \epsilon_{ij} \epsilon_{kl} - \alpha X_i u_i \right] dV$$

$$-\alpha \int_{\Gamma_t} t_i u_i d\Gamma + \mathbf{E} \leq 0$$

$$L^{-1}_{ijkl} \sigma_{kl} + \epsilon_{ij} - \frac{1}{2}(u_{i,j} + u_{j,i}) = 0 \quad \text{in } \Omega \forall i, j.$$

This is an extremum principle in mixed stress and deformation form for linearly elastic systems.

6 Discussion

There is a striking contrast between the present formulation for the continuum problem and the material presented by Prager (1964) cited earlier. To summarize the comparison in a few statements:

- The Minimum principle (expressed in deformations alone) given by Prager is imbedded in the present formulation, as indicated above.
- Prager's variational formulation in mixed stress and deformation form is stated as a stationarity principle rather than in the form of an extremum problem statement.

Prager's presentation is easily extended to accommodate a general polygonal elastic/locking model by the simple device of introducing a set of deformation fields (as described in Section 2) instead of just one. However, the extremum problem form [Q] (or its equivalent statement [Q′]) for the elastic/stiffening material is unique to the development described here. As indicated in the Introduction, this formulation, which can be interpreted as a generalized form of Minimum Potential Energy Principle, has a complementary counterpart form that is applicable for the analysis of systems made of elastic/softening (rather than stiffening) materials (Taylor, 1992, 1993; Taylor and Logo, 1993). ("Polygonal stress-strain relations" have been used in earlier works, e.g., Besseling (1984), on the modelling of elastic/softening materials.) The fact that use is made of a superposition of elastic/locking constituents in the one form, and a superposition of elastic/yielding ones in the latter formulation reflects a sort of duality in modelling. Generally such complementarity relationships admit interpretation within the context of ideas of mathematical duality (Luenberger (1992) provides a very readable account of various forms of duality; his discussion is written for vector problems.) As interpreted for the same linearly elastic material, the two extremum principles, still in mixed stress and deformation form, are mathematical duals in a conventional sense and their solutions coincide. However, as noted in the introduction, the two general formulations, one for softening materials and the other for hardening ones are not duals in the usual sense, i.e., they are not Lagrangian duals. Still, availability of these dual forms can be used to advantage, e.g., to obtain complementary information such as bounds on the field variables, and so on.

Aside from their significance as means for modeling the equilibrium analysis of elastic/stiffening systems, formulations [Q] and [Q′] provide an obvious convenience for the development of methods for the numerical solution of such problems. Standard programs for the computational treatment of constrained, convex minimization problems can be used to obtain a solution for arbitrary load in a single application to the computer. Thus, the use of incremental methods for the interpretation of such nonlinear problems, the standard practice in common approaches to their implementation for the computer, is circumvented. On another subject, availability of a convex, global model for *analysis* facilitates the treatment of problems in optimal structural *design*. This is exemplified in presentations on topology and material distribution design, and on optimal modification of material properties for elastic/

Downloaded 03 May 2010 to 171.66.16.20. Redistribution subject to ASME license or copyright; see http://www.asme.org/terms/Terms_Use.cfm

softening trusses (Taylor, 1992; Taylor and Logo, 1993). Similar design problems for structures composed of elastic/stiffening material can be treated in the same way; examples in truss design are described in Taylor (1992, 1993). Following an approach that has elements of the constitutive tensors themselves appear in the role of design variables, it becomes possible in either case to address in a conceptually new way a variety of problems in material design. An example of this approach, described specifically for the design of linear materials for optimal performance, is given in Bendsøe et al. (1994).

Acknowledgment

The author is grateful for support provided by the Mathematics Institute of the Danish Technical University during his stay in Aug. 1992.

References

Arthurs, A. M., 1980, *Complementary Variational Principles*, 2nd ed., Clarendon Press, Oxford, U.K.

Bendsøe, M. P., Guedes, J. M., Haber, R. B., Pedersen, P., and Taylor, J. E., 1994, "On Optimal Material Properties in the Context of Structural Optimization," ASME JOURNAL OF APPLIED MECHANICS, to be published.

Besseling, J. F., 1984, "Models of Metal Plasticity: Theory and Experiment," *Plasticity Today*, A. Sawczuk and G. Bianchi, eds., Elsevier, New York.

Clarke, Frank H., 1983, *Optimization and Nonsmooth Analysis*, John Wiley and Sons, New York.

Luenberger, David G., 1992, "A Double Look at Duality," *IEEE Trans. Auto. Cntrl.*, Vol. 37, No. 10.

Oden, J. T., and Reddy, J. N., 1976, "Variational Methods in Theoretical Mechanics," Springer-Verlag, Heidelberg, Germany.

Prager, William, 1957, "On Ideal Locking Materials," *Trans. Soc. Rheology*, Vol. I, pp. 169–175.

Prager, William, 1964, "On Elastic, Perfectly Locking Materials," *Proc. Eleventh Intrntl Congr. of Appld. Mechs.*, Munich, Germany, Henry Gortler, ed., Springer-Verlag, New York.

Sewell, M. J., 1987, *Maximum and Minimum Principles*, Cambridge University Press, Cambridge, U.K.

Taylor, J. E., 1992, "Truss Topology Design for Elastic/Softening Materials," *Proc. NATO Adv. Res. Workshop: Topology Design of Structures*, Sesimbra, Portugal, June 20–26, 1992, Martin P. Bendsøe and Carlos A. Mota Soares, eds., Kluwer Academic Publishers, The Netherlands.

Taylor, J. E., 1993, "A Global Extremum Principle for the Analysis of Solids Composed of Softening Material," *International J. Solids and Structures*, Vol. 30, No. 15, pp. 2057–2069.

Taylor, J. E., and Janos Logo, 1993, "Analysis and Design of Elastic/Softening Truss Structures Based on a Mixed-Form Extremum Principle," *Proc. NATO/FRG Conf: Optimization of Large Structural Systems*, G. Rozvany, ed., Sept. 23–Oct. 4, 1991, Kluwer Academic Publishers, The Netherlands.

Taylor, J. E., and Washabaugh, 1994, "Analysis and Design of Trussed Structures Made of Elastic/Stiffening Materials," *Structural Optimization*, Vol. 8, No. 1, pp. 1–8.

Downloaded 03 May 2010 to 171.66.16.20. Redistribution subject to ASME license or copyright; see http://www.asme.org/terms/Terms_Use.cfm

Finite Element Analysis of Thermoelastic Contact Stability

Taein Yeo

J. R. Barber

Department of Mechanical Engineering
and Applied Mechanics,
University of Michigan,
Ann Arbor, MI 48109-2125

When heat is conducted across an interface between two dissimilar materials, thermoelastic distortion affects the contact pressure distribution. The existence of a pressure-sensitive thermal contact resistance at the interface can cause such systems to be unstable in the steady-state. Stability analysis for thermoelastic contact has been conducted by linear perturbation methods for one-dimensional and simple two-dimensional geometries, but analytical solutions become very complicated for finite geometries. A method is therefore proposed in which the finite element method is used to reduce the stability problem to an eigenvalue problem. The linearity of the underlying perturbation problem enables us to conclude that solutions can be obtained in separated-variable form with exponential variation in time. This factor can therefore be removed from the governing equations and the finite element method is used to obtain a time-independent set of homogeneous equations in which the exponential growth rate appears as a linear parameter. We therefore obtain a linear eigenvalue problem and stability of the system requires that all the resulting eigenvalues should have negative real part. The method is discussed in application to the simple one-dimensional system of two contacting rods. The results show good agreement with previous analytical investigations and give additional information about the migration of eigenvalues in the complex plane as the steady-state heat flux is varied.

1 Introduction

If heat is conducted across an interface between two elastic bodies, thermoelastic distortion generally affects the contact pressure and the extent of the contact area (Clausing, 1966; Jones et al., 1975). Early solutions of such problems encountered difficulties with existence of solution (Lewis and Perkins, 1968; Barber, 1973), which were later resolved by the use of a more physically realistic boundary condition in which a pressure-dependent thermal resistance exists at the interface (Barber, 1978).

Even with this refinement, the steady-state solution can be nonunique and also in some circumstances unstable (Duvaut, 1979; Shi and Shillor, 1990). Experimental evidence of instability of practical thermoelastic contact systems has been reported for heat exchanger tubes (Srinivasan and France, 1985) and for the solidification of castings (Richmond and Huang, 1977).

Analysis of the stability of thermoelastic contact was first attempted for one-dimensional systems, using linear perturbation methods (Barber et al., 1980; Barber 1981, 1986). The method was later extended to the two-dimensional problem of the contact of two-half planes (Barber, 1987, Zhang and Barber, 1990), making use of the fact that an arbitrary perturbation could be represented as a superposition of spatially sinusoidal terms, each of which could be represented in separated-variable form, thus reducing the problem essentially to one dimension. The same method has been used to consider the problem of a layer of finite thickness in contact with a half-plane (Yeo and Barber, 1991). Difficulties of a different order are encountered when the contact area is bounded, since separated-variable solutions cannot then generally be used. In such cases, methods using series solutions might be envisaged, but it seems likely that a direct numerical treatment would be more efficient. In the present paper, we therefore develop one possible numerical implementation for the perturbation problem and illustrate its use in the simple two-rod geometry of Barber and Zhang (1988).

2 The Finite Element Method

An obvious numerical approach to the problem would be to simulate the transient behavior of the system—for example, using a finite element description of the temperature and stress fields in space and time. Parametric investigation of such a system would then enable stability boundaries to be determined, as well as identifying stable and unstable steady-states, in cases of multiple solution. However, such an effort would be extremely computer-intensive, since (i) the

Contributed by the Applied Mechanics Division of THE AMERICAN SOCIETY OF MECHANICAL ENGINEERS for publication in the ASME JOURNAL OF APPLIED MECHANICS.

Discussion on this paper should be addressed to the Technical Editor, Professor Lewis T. Wheeler, Department of Mechanical Engineering, University of Houston, Houston, TX 77204-4792, and will be accepted until four months after final publication of the paper itself in the ASME JOURNAL OF APPLIED MECHANICS.

Manuscript received by the ASME Applied Mechanics Division, Apr. 7, 1992; final revision, Sept. 21, 1992. Associate Technical Editor: R. M. Bowen.

Copyright © 1994 by ASME

Downloaded 03 May 2010 to 171.66.16.20. Redistribution subject to ASME license or copyright; see http://www.asme.org/terms/Terms_Use.cfm

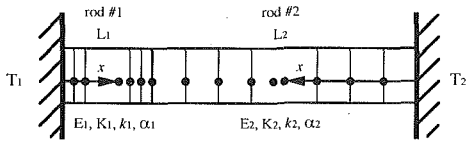


Fig. 1 The two-rod problem

solution of the transient heat conduction equation with reasonably fine meshing involves the use of a very small time increment for numerical stability and convergence and (ii) the additional effect of a very pressure-sensitive boundary condition at the contact interface would create considerable computational difficulties of its own. Similar difficulties are encountered with other numerical implementations of transient thermoelastic contact problems and are documented in (Barber and Zhang, 1988; Azarkhin and Barber, 1986).

A preferable alternative is suggested by the fact that the system (including the boundary conditions) is linear to sufficiently small perturbations from the steady-state. It therefore follows that if we postulate the existence of a separated-variable solution for the perturbation in which the fields grow with time t according to $\exp(bt)$, the exponential term will cancel in the governing equations, leaving a time-independent problem that can be solved by the finite element method. The resulting equations will be homogeneous and will have a nontrivial solution only for certain eigenvalues of b. We can then construct a more general solution to the transient problem as a series of the associated eigenfunctions. Assuming this eigenfunction series to be complete, we can deduce that the system will be stable if and only if all the eigenvalues have negative real part.

2.1 The Two-Rod Problem. The ideas behind the method are best explained in terms of its implementation for the simple two-rod model, which was treated by analytical methods by Barber and Zhang (1988). The results of this latter reference also give a convenient check on the validity of the proposed method.

The system is illustrated in Fig. 1. Two perfectly conducting rigid walls are maintained at constant temperatures T_1, T_2, respectively. Two uniform elastic rods of lengths L_1, L_2 are built into the respective walls and make contact at their free ends. Young's modulus, thermal conductivity, thermal diffusivity and coefficient of thermal expansion for the materials are denoted by E_γ, K_γ, k_γ, α_γ respectively ($\gamma = 1,2$).

Heat flow occurs across the contacting interface at the free ends of the rods through a thermal contact resistance (Shlykov and Ganin, 1964; Cooper et al., 1969; Thomas and Probert, 1970) R, which is assumed to be a continuous function of the contact pressure p. This boundary condition is appropriate to situations in which the steady-state under consideration involves contact between the rods. Steady-states involving separation between the ends of the rods can be subsumed under the same analysis by defining an extension of the concept of contact pressure as in Eq. (7) of Barber and Zhang (1988).

We investigate the circumstances in which a small perturbation from the steady-state can grow with time. Because the perturbation is small, the relation

$$T = QR \tag{1}$$

between the heat flux, Q, at the interface, the temperature difference, T between the free ends of the rods and the contact resistance, R can be linearized, giving

$$\Delta T = Q_0 \Delta R + R_0 \Delta Q, \tag{2}$$

where Q_0, T_0, R_0 denote the corresponding steady-state values and ΔQ, ΔT, ΔR are the perturbations. Noting that $\Delta R = R'(p_0)\Delta p$, we can rewrite (2) as

$$\Delta T = Q_0 R'(p_0)\Delta p + R_0 \Delta Q. \tag{3}$$

Equation (3) is a linear boundary condition and hence the perturbation is governed entirely by linear equations, the nature of which permit a separated-variable solution in which the time variation is of the form $\exp(bt)$ where b is a (possibly complex) constant. We therefore postulate the existence of such a solution and examine the conditions under which it is possible. By analogy with related problems, we anticipate that the problem will reduce to a system of homogeneous linear algebraic equations with a denumerable set of eigenvalues for b. We also anticipate that the corresponding set of eigenfunctions will be complete in the sense that an arbitrary initial condition could be expressed as an eigenfunction expansion. This being the case, the stability of the system will be determined by the condition that all the eigenvalues should have negative real part.

2.2 The Heat Conduction Equation. The governing equations are only time-dependent through the heat conduction equation, which in one dimension takes the form

$$T_{,xx} = \frac{1}{k} T_{,t}. \tag{4}$$

Thus, if we assume the perturbed temperature field has the form

$$T(x,t) = \Theta(x) e^{bt}, \tag{5}$$

the function Θ of the spatial coordinates only must satisfy the equation

$$\Theta_{,xx} - \frac{b}{k}\Theta = 0. \tag{6}$$

To develop a finite element formulation of this equation, we use Galerkin's method (Hughes (1987)). Briefly, we multiply Eq. (6) by an arbitrary function $w(x)$ and integrate over the domain of each rod, obtaining for example

$$\int_0^{L_\gamma} \left(\Theta^\gamma_{,xx} - \frac{b}{k_\gamma}\Theta^\gamma \right) w^\gamma(x)\, dx = 0. \tag{7}$$

This must be satisfied for all functions $w^\gamma(x)$ and a system of equations can be obtained by defining the functions Θ^γ, w^γ in the discrete form

$$\Theta^\gamma(x) = \sum_{i=1}^{n} \Theta_i^\gamma N_i(x); \quad w^\gamma(x) = \sum_{i=1}^{n} w_i^\gamma N_i(x) \tag{8}$$

where $N_i(x)$ is a suitable shape function.

Integrating Eq. (7) by parts, noting that the perturbation Θ^γ must be zero at the wall ($x = 0$) and substituting for Θ^γ, w^γ from (8), we obtain

$$\mathbf{K}^\gamma \mathbf{\Theta}^\gamma + b\mathbf{H}^\gamma \mathbf{\Theta}^\gamma = \mathbf{\Phi}^\gamma \{q_0^\gamma\}; \quad \gamma = 1,2 \tag{9}$$

where the matrices

$$K_{ij}^\gamma = \int_0^{L_\gamma} \frac{\partial N_i}{\partial x}\frac{\partial N_j}{\partial x} dx;$$

$$H_{ij}^\gamma = \int_0^{L_\gamma} \frac{N_i N_j dx}{k_\gamma}; \quad \Phi_i^\gamma = -\frac{N_n(L_\gamma)\,\delta_{in}}{K_\gamma}, \tag{10}$$

δ_{in} is the Kronecker delta and $q_0^\gamma \exp(bt)$ is the perturbation in the outward heat flux at the free end of rod γ. Continuity of heat flux at the interface then demands that $\{q_0^1\} = -\{q_0^2\} \equiv \{q_0\}$.

2.3 The Thermoelastic Contact Problem. An essentially similar formulation can be used for the thermoelastic deformation and contact of the rods. Equilibrium considerations demand that the axial stress, σ_{xx}^γ be independent of x—i.e., $\sigma_{xx,x}^\gamma = 0$ and, using the thermoelastic constitutive law, we can write this condition in the form

$$E_\gamma (u^\gamma_{,xx} - \alpha^\gamma \Theta^\gamma_{,x}) = 0, \tag{11}$$

Downloaded 03 May 2010 to 171.66.16.20. Redistribution subject to ASME license or copyright; see http://www.asme.org/terms/Terms_Use.cfm

where we have already removed a factor $\exp(bt)$, so that u^γ is here to be interpreted such that the axial displacement of the rod is $u^\gamma(x)\exp(bt)$.

The resulting set of equations can be written in the form

$$\mathbf{L}^\gamma \mathbf{u}^\gamma = \mathbf{F}^\gamma \mathbf{\Theta}^\gamma + \mathbf{f}^\gamma\{\sigma_0\} \tag{12}$$

where

$$L_{ij}^\gamma = \int_0^{L_\gamma} \frac{\partial N_i}{\partial x}\frac{\partial N_j}{\partial x}dx;$$

$$F_{ij}^\gamma = \alpha_\gamma \int_0^{L_\gamma} \frac{\partial N_i}{\partial x} N_j dx; \quad f_i^\gamma = \frac{N_n(L_\gamma)\,\delta_{in}}{E_\gamma} \tag{13}$$

and $\sigma_0^\gamma \exp(bt)$ is the perturbation in the traction at the free end of rod γ.

It is convenient to partition this set of equations as

$$\begin{bmatrix} \mathbf{L}_{11}^\gamma & \mathbf{L}_{12}^\gamma \\ \mathbf{L}_{21}^\gamma & \mathbf{L}_{22}^\gamma \end{bmatrix} \begin{Bmatrix} \mathbf{u}_1^\gamma \\ \mathbf{u}_2^\gamma \end{Bmatrix} = \begin{bmatrix} \mathbf{F}_1^\gamma \\ \mathbf{F}_2^\gamma \end{bmatrix} \{\mathbf{\Theta}^\gamma\} + \begin{Bmatrix} \mathbf{f}_1^\gamma \\ \mathbf{f}_2^\gamma \end{Bmatrix} \{\sigma_0\} \tag{14}$$

where $\mathbf{u}_2^\gamma$ is a vector with only one component representing the nodal displacement at the free (contacting) end and $\mathbf{u}_1^\gamma$ is a vector with $(n-1)$ components representing the displacements at the interior nodes.

Since the two rods are in contact at their free ends, we have

$$\mathbf{u}_2^1 = -\mathbf{u}_2^2 = \{u_0\}; \quad \{\sigma_0^1\} = \{\sigma_0^2\} = \{\sigma_0\}. \tag{15}$$

Eliminating $\mathbf{u}_1^\gamma$ from the partitioned Eqs. (14) and using (15), we obtain

$$\left(\mathbf{L}_{21}^\gamma(\mathbf{L}_{11}^\gamma)^{-1}\mathbf{F}_1^\gamma - \mathbf{F}_2^\gamma\right)\mathbf{\Theta}^\gamma + (-1)^\gamma\left(\mathbf{L}_{21}^\gamma(\mathbf{L}_{11}^\gamma)^{-1}\mathbf{L}_{12}^\gamma - \mathbf{L}_{22}^\gamma\right)\{u_0\} = \mathbf{f}_2^\gamma\{\sigma_0\}. \tag{16}$$

We can then eliminate u_0 between the two equations (16 with $\gamma = 1,2$) obtaining

$$\{\sigma_0\} = \mathbf{S}_1\mathbf{\Theta}^1 + \mathbf{S}_2\mathbf{\Theta}^2, \tag{17}$$

where

$$\mathbf{S}_1 = \mathbf{r}\left(\mathbf{r}\mathbf{f}_2^1 + \mathbf{f}_2^2\right)^{-1}\left(\mathbf{L}_{21}^1(\mathbf{L}_{11}^1)^{-1}\mathbf{F}_1^1 - \mathbf{F}_2^1\right);$$

$$\mathbf{S}_2 = \left(\mathbf{r}\mathbf{f}_2^1 + \mathbf{f}_2^2\right)^{-1}\left(\mathbf{L}_{21}^2(\mathbf{L}_{11}^2)^{-1}\mathbf{F}_1^2 - \mathbf{F}_2^2\right) \tag{18}$$

and

$$\mathbf{r} = \left(\mathbf{L}_{21}^2(\mathbf{L}_{11}^2)^{-1}\mathbf{L}_{12}^2 - \mathbf{L}_{22}^2\right)\left(\mathbf{L}_{21}^1(\mathbf{L}_{11}^1)^{-1}\mathbf{L}_{12}^1 - \mathbf{L}_{22}^1\right)^{-1}. \tag{19}$$

2.4 Stability Analysis. To complete the formulation of the stability problem, we must couple the solutions of the heat conduction and thermoelastic problems through the linearized boundary condition (3), which can be written in the matrix form

$$\mathbf{P}\mathbf{\Theta}^1 - \mathbf{P}\mathbf{\Theta}^2 = -Q_0R'\{\sigma_0\} + R_0\{q_0\}, \tag{20}$$

where $\mathbf{P}$ is a $1 \times n$ matrix whose elements are zero except for the nth element which is unity.

Eliminating q_0, σ_0 between Eqs. (9), (17), (20) we finally obtain

$$\begin{bmatrix} R_0\mathbf{K}^1 - Q_0R'\mathbf{\Phi}^1\mathbf{S}_1 - \boldsymbol{\phi}^1\mathbf{P} & -Q_0R'\mathbf{\Phi}^1\mathbf{S}_2 + \mathbf{\Phi}^1\mathbf{P} \\ Q_0R'\mathbf{\Phi}^2\mathbf{S}_1 + \mathbf{\Phi}^2\mathbf{P} & R_0\mathbf{K}^2 + Q_0R'\mathbf{\Phi}^2\mathbf{S}_2 - \mathbf{\Phi}^2\mathbf{P} \end{bmatrix} \times \begin{Bmatrix} \mathbf{\Theta}^1 \\ \mathbf{\Theta}^2 \end{Bmatrix} = b\begin{bmatrix} -R_0\mathbf{H}^1 & 0 \\ 0 & -R_0\mathbf{H}^2 \end{bmatrix} \begin{Bmatrix} \mathbf{\Theta}^1 \\ \mathbf{\Theta}^2 \end{Bmatrix}. \tag{21}$$

This matrix equation constitutes a generalized linear eigenvalue problem for the exponential growth rate b, which is easily solved by standard numerical methods. Instability is indicated by the system having at least one eigenvalue with positive real part.

Table 1

Rod No.	Material	E GPa	K $W/m°C$	k m^2/s	α $°C^{-1}$
1	Stainless steel	190	21	5.93×10^{-6}	14×10^{-6}
2	Aluminum alloy	72	173	67×10^{-6}	22×10^{-6}

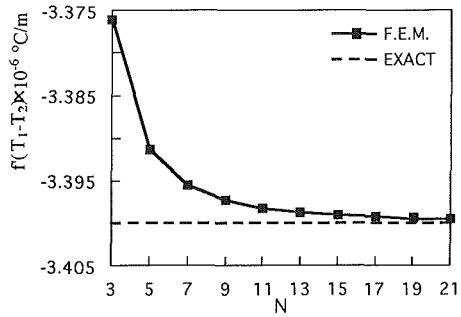


Fig. 2 Convergence of the dimensionless heat flux at the stability boundary for $L_1 = 0.1$ m, $L_2 = 0.25$ m and the steady-state contact resistance $R_0 = L_1/K_1 + L_2/K_2$

3 Results

The principle purpose of the present investigation is to test the viability of the proposed algorithm against previously published analytical results (Barber and Zhang (1988)). The rod lengths and material properties were therefore chosen to be the same as in the earlier paper, the relevant material properties being listed in Table 1. Figure 2 shows the dimensionless heat flux at the stability boundary for $L_1 = 0.1$ m, $L_2 = 0.25$ m, and a steady-state contact resistance equal to the sum of the combined resistances of the two rods—i.e., $R_0 = L_1/K_1 + L_2/K_2$, which corresponds to $f = 0.5$ in the notation of Barber and Zhang (1988). Results are shown for various values of N and compared with the exact value from the earlier analysis. Even with $N = 3$—i.e., using only three linear elements in the discretization of each rod—the stability boundary is predicted with an accuracy of better than 0.5 percent and a modest refinement of the mesh permits this estimate to be improved by an order of magnitude.

Numerical results were obtained over the entire range of parameter values treated by the analytical perturbation method by Barber and Zhang (1988) and in all cases the stability boundary, defined by the minimum steady-state heat flux required for the system to be unstable, agreed within ± 1 percent for $N = 5$.

One advantage of the present method is that it generates values for all the eigenvalues of the discretized problem and therefore permits us to investigate the migration of eigenvalues in the complex plane as the imposed steady-state heat flux is varied. Of course, the discrete problem only has $2N$ eigenvalues, as compared with a denumerably infinite set for the real problem, but the discrete eigenvalues should give good approximations for the lower terms in the set and order of magnitude estimates for those near the truncation limit.[1]

Figure 3 shows the locus of the first eigenvalue for a two-rod system in which stability is determined by migration of an eigenvalue across the imaginary axis (giving oscillatory transient behavior). Notice that the two leading eigenvalues

[1]The agreement between the stability boundary as determined by analytical and numerical methods is a measure of the high degree of accuracy of the lowest eigenvalue in the discrete problem, since this is the term that determines stability of the system.

Downloaded 03 May 2010 to 171.66.16.20. Redistribution subject to ASME license or copyright; see http://www.asme.org/terms/Terms_Use.cfm

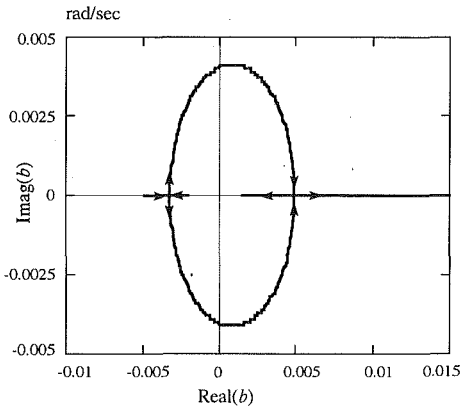


Fig. 3 Migration of the leading pair of eigenvalues, b as the heat flux Q_0 is increased for the case where $L_1 = 0.1$ m, $L_2 = 0.2$ m and the steady-state contact resistance $R_0 = L_1/K_1 + L_2/K_2$

are real and negative at low values of Q_0, but as Q_0 increases, they pass into complex values, cross the imaginary axis into the unstable half-plane and later rejoin the real axis. For the same combinations of rod lengths but the opposite direction of heat flow, the leading eigenvalues remained real for all heat fluxes and the stability boundary was therefore determined by the passage of the first eigenvalue through the origin.

It was found in all cases that at most one pair of eigenvalues passed into the right half-plane as Q_0 increased. All the remaining eigenvalues were located at substantially larger distances from the origin in the left half-plane. Thus, instability is in all cases associated with a single form of perturbation and has (possibly complex) pure exponential growth as long as the perturbation is small enough for the linearity condition to hold.

4 Conclusions

We have shown that by assuming an exponential variation in time for a linear perturbation from the steady-state solution, a finite element discretization can be developed for the spatial variation of the temperature and stress fields, leading eventually to a linear eigenvalue problem for the exponential growth rate. The results agree closely with those obtained by analytical methods for the two-rod problem. Furthermore, since stability is determined by the leading eigenvalue of the system, good accuracy can be obtained using a very modest number of elements. The proposed algorithm therefore presents an attractive approach to finite geometry thermoelastic stability problems in two and three dimensions, where analytical methods would be prohibitively complicated. These applications will be explored in a subsequent publication.

References

Azarkhin, A., and Barber, J. R., 1986, "Thermoelastic Instability for the Transient Contact Problem of Two Sliding Half-Planes," ASME JOURNAL OF APPLIED MECHANICS, Vol. 53, pp. 565–572.

Barber, J. R., 1973, "Indentation of the Semi-Infinite Elastic Solid by a Hot Sphere," *Int. J. Mech. Sci.*, Vol. 15, pp. 813–819.

Barber, J. R., 1978, "Contact Problems Involving a Cooled Punch," *J. Elasticity*, Vol. 8, pp. 409–423.

Barber, J. R., 1981, "Stability of Thermoelastic Contact Problem for the Aldo Model," ASME JOURNAL OF APPLIED MECHANICS, Vol. 48, pp. 555–558.

Barber, J. R., 1986, "Nonuniqueness and Stability for Heat Conduction Through a Duplex Heat Exchanger Tube," *J. Thermal Stresses*, Vol. 9, pp. 69–78.

Barber, J. R., 1987, "Stability of Thermoelastic Contact," *Institution of Mechanical Engineers*, International Conference on Tribology, London, pp. 981–986.

Barber, J. R., Dundurs, J., and Comninou, M., 1980, "Stability Considerations in Thermoelastic Contact," ASME JOURNAL OF APPLIED MECHANICS, Vol. 47, pp. 871–874.

Barber, J. R., and Zhang, R., 1988, "Transient Behavior and Stability for the Thermoelastic Contact of Two Rods of Dissimilar Materials," *Int. J. Mech. Sci.*, Vol. 30, pp. 691–704.

Clausing, A. M., 1966, "Heat Transfer at the Interface Between Dissimilar Metals—The Influence of Thermal Strain," *Int. J. Heat Mass Transfer*, Vol. 9, pp. 791–801.

Cooper, M. G., Mikic, B. B., and Yovanovich, M. M., 1969, "Thermal Contact Conductance," *Int. J. Heat Mass Transfer*, Vol. 12, pp. 279–300.

Duvaut, G., 1979, "Free Boundary Problem Connected with Thermoelasticity and Unilaterial Contact," *Free Boundary Problems*, Vol. 11, Pavia.

Hughes, T. J. R., 1987, *The Finite Element Method*, Prentice-Hall, Englewood Cliffs, NJ, Chapters 1,2.

Jones, A. M., O'Callaghan, P. W., and Probert, S. D., 1975, "Thermal Rectification Due to Distortion Induced by Heat Fluxes Across Contact Between Smooth Surfaces," *J. Mech. Eng. Sci.*, Vol.17, pp. 252–261.

Lewis, D. V., and Perkins, H. C., 1968, "Heat Transfer at the Interface of Stainless Steel and Aluminum—The Influence of Surface Conditions on the Directional Effect," *Int. J. Heat Mass Transfer*, Vol. 11, pp. 1371–1383.

Richmond, O., and Huang, N. C., 1977, "Interface Stability during Unidirectional Solidification of a Pure Metal," *Proc. 6th Canadian Congress of Applied Mechanics*, Vancouver, pp. 453–454.

Shi, P., and Shillor, M., 1990, "Uniqueness and Stability of the Solution to a Thermoelastic Contact Problem," *Euro. J. Appl. Math.*, Vol. 1, pp. 371–387.

Shlykov, Y. P., and Ganin, Ye. A., 1964, "Thermal Resistance of Metallic Contacts," *Int. J. Heat Mass Transfer*, Vol. 7, pp. 921–929.

Srinivasan, M. G., and France, D. M., 1985, "Non-uniqueness in Steady-State Heat Transfer in Prestressed Duplex Tubes—Analysis and Case History," ASME JOURNAL OF APPLIED MECHANICS, Vol. 52, pp. 257–262.

Thomas, T. R., and Probert, S. D., 1970, "Thermal Contact Resistance: The Directional Effect and Other Problems," *Int. J. Heat Mass Transfer*, Vol. 13, pp. 789–807.

Yeo, T., and Barber, J. R., 1991, "Stability of Thermoelastic Contact of a Layer and a Half-Plane," *J. Thermal Stresses*, Vol. 14, pp. 371–388.

Zhang, R., and Barber, J. R., 1990, "Effect of Material Properties on the Stability of Static Thermoelastic Contact," ASME JOURNAL OF APPLIED MECHANICS, Vol. 57, pp. 365–369.

Downloaded 03 May 2010 to 171.66.16.20. Redistribution subject to ASME license or copyright; see http://www.asme.org/terms/Terms_Use.cfm

J. L. Ding
Mem. ASME.

Y. G. Chen

Department of Mechanical and Materials Engineering, Washington State University, Pullman, WA 99164-2920

A Theoretical Study of the Application of the Optical Caustics to High-Temperature Creep Fracture Mechanics[1]

In the current study, a theoretical basis is established for interpreting and correlating the optical caustic patterns with the transition of the crack-tip stress and strain fields under high-temperature creep condition. The theory forms a foundation for a possible experimental method based on optical caustics for characterizing the time-dependent fracture at elevated temperatures. Some numerical simulations of the high-temperature caustic phenomena were also performed based on the proposed theory.

1 Introduction

The understanding and characterization of the behavior of a crack at elevated temperatures are essential for the fracture control of the materials and structures for high-temperature applications. In addition to the nonlinearity involved, the analysis of creep fracture is further complicated by the time dependence of the material behavior. Most of the theoretical creep fracture analysis has been based on the assumption that the creep behavior is dominated by the power-law secondary creep. In this simplified case, the creep rate ($\dot{\epsilon}_{ij}^c$) is given by

$$\dot{\epsilon}_{ij}^c = \frac{3}{2} B \bar{\sigma}^{(n-1)} s_{ij}, \tag{1}$$

where $s_{ij} = \sigma_{ij} - \sigma_{kk}\delta_{ij}/3$, $\bar{\sigma} = (3/2\, s_{ij}s_{ij})^{1/2}$, and B and n are the material constants. Based on the above constitutive equation and the assumption that the elastic part of strain rate can be neglected inside the creep zone, Riedel and Rice (1980) showed that the crack-tip stress and strain fields inside the creep zone with respect to a polar coordinate system (r,θ) fixed at the crack tip were of the following forms:

$$\sigma_{ij} = \left[\frac{C(t)}{BI_n r}\right]^{1/n+1} \tilde{\sigma}_{ij}(\theta), \tag{2}$$

$$\dot{\epsilon}_{ij}^c = B\left[\frac{C(t)}{BI_n r}\right]^{n/n+1} \tilde{\epsilon}_{ij}(\theta) \tag{3}$$

where $\tilde{\epsilon}_{ij}(\theta)$ and $\tilde{\epsilon}_{ij}(\theta)$ are the same dimensionless functions characterizing the angular distribution of strain and stress, respectively, in the HRR singularity field (Hutchinson (1968), Rice and Rosengren (1968)), and I_n is a scalar function of n. The initial value of the crack-tip loading parameter $C(t)$ is the elastic field characterized by the stress intensity factor K; and its steady-state value under the long term or the so-called extensive creep condition is C^*. The definition of C^* is similar to Rice's J integral (1968).

As far as the experimental work is concerned, most of the experiments in this area have been centered around the measurement of the creep crack growth rate and correlation of the data with one of the proposed loading parameters, in general either K or C^*. While creep crack growth tests, which are essentially material tests, have generated some data on material properties for engineering design, they provide little information either on the time dependence of the stress or strain fields of a crack or for the evaluation of the loading parameters at elevated temperatures. It was proposed in 1976 by Landes and Begley to use the load displacement rate data to evaluate C^* as was done for the evaluation of the J integral. A similar approach was later proposed by Saxena (1986) to evaluate $C(t)$ or C_t. In addition to the large number of the specimens and tedious data reduction procedure involved, these approaches still shed little light on the local crack-tip fields at elevated temperatures. To the authors' knowledge, there have been very few experimental techniques available which can be used to directly characterize the time-dependent behavior of a crack at elevated temperatures to either better understand the fracture process or to endorse the results of the theoretical analyses.

In 1964, Manogg introduced the method of caustics to

[1]Presented and included in the proceedings of the symposium on Experimental Mechanics co-sponsored by The ASME Aerospace Division and the Applied Mechanics Division and held during the 1992 ASME Winter Annual Meeting.

Contributed by the Applied Mechanics Division of THE AMERICAN SOCIETY OF MECHANICAL ENGINEERS for publication in the ASME JOURNAL OF APPLIED MECHANICS.

Discussion on this paper should be addressed to the Technical Editor, Professor Lewis T. Wheeler, Department of Mechanical Engineering, University of Houston, Houston, TX 77204-4792, and will be accepted until four months after final publication of the paper itself in the ASME JOURNAL OF APPLIED MECHANICS.

Manuscript received and accepted by the ASME Applied Mechanics Division Sept. 28, 1992. Associate Technical Editor: R. M. McMeeking.

Copyright © 1994 by ASME
Downloaded 03 May 2010 to 171.66.16.20. Redistribution subject to ASME license or copyright; see http://www.asme.org/terms/Terms_Use.cfm

evaluate the stress intensity factor. This method was later developed by Theocaris (1981) and Beinert and Kalthoff (1981) into a very useful tool for studying various static and dynamic linear elastic fracture mechanics problems. More recently, Rosakis et al. (1988) further extended this method to the field of plastic fracture mechanics, e.g., for the evaluation of the J integral. An example of this application can be found in the work by Judy and Sanford (1989).

One major advantage of this method is the direct observation of part of the crack-tip deformation field. It then seems to be a very interesting issue to see whether or not this technique can be applied to high-temperature environments as well. If it can, this technique may be able to shed some light on the transition of the crack-tip fields at elevated temperatures. Furthermore, if the correlation between the caustic pattern and the crack-tip loading parameter can be established, this method may also provide a convenient approach to the experimental determination of these parameters. The current work is an attempt to establish a theoretical basis for interpreting and correlating the caustic patterns with the transition of the crack-tip stress and strain fields. The results of the corresponding experimental study are reported elsewhere (Ding and Chen, 1994).

2 Optical Caustics by Reflection

The physical principle of application of optical caustics to fracture mechanics is well understood. Its details can be found in the review papers by Theocaris (1981), Beinert and Kalthoff (1981), and Rosakis et al. (1988). In order to facilitate the following discussion, a brief description of this method will be given here. The notations adopted follow essentially those used by Rosakis et al. (1988).

When the crack tip of a polished opaque fracture test specimen is illuminated by a laser beam (or a point light source), due to the localized lateral contraction (thickness change), the curved reflecting surface around the crack tip acts as a concave mirror. Virtual extension of the reflected rays will envelop a three-dimensional surface in the backside of the specimen, called caustic. Intersection of the caustic surface with a virtual image plane located at a distance z_0 from the illuminated surface forms a two-dimensional caustic curve surrounding a shadow spot. It can be shown that the light that forms the caustic curve originates from a locus of points, called initial curve, on the specimen surface which surrounds the crack tip. The shadow spot is formed because all the virtual extension of the reflected rays from both inside and outside the initial curve falls to the outside of the caustic curve. The caustic curve can thus also be viewed as a mapped image of the initial curve on the z_0 plane.

The mapping equation based on geometrical optics can be shown to be

$$\mathbf{X} = \mathbf{x} - 2(z_0 - f)\frac{\nabla f}{1 - |\nabla f|^2}, \tag{4}$$

where $\mathbf{x}$ is the position of a point on the reflecting surface, $\mathbf{X}$ is the mapped position on the image plane, and $f = -u$ with u being the out of plane displacement. In most of the practical applications, z_0 is much larger than f and $|\nabla f|^2$ is much smaller than 1, Eq. (4) can then be reduced to

$$\mathbf{X} = \mathbf{x} - 2z_0\nabla f. \tag{5}$$

It can also be shown that for given z_0 and f, the initial curve is described by the following equation:

$$I(x_1,x_2;z_0) = \text{determinant of } [X_{i,j}] = \text{determinant of } [\delta_{ij} - 2z_0 f_{,ij}] = 0. \tag{6}$$

By adjusting the position of the image plane, i.e., the value of z_0, the caustic curves corresponding to different initial curves can be obtained. For the elastic-plastic fracture under small-scale yielding condition. The initial curve can be zoomed well into the HRR singularity field. It is this feature that Rosakis used to evaluate the J integral for characterizing the plastic singularity at the crack tip. The stress intensity factor K can be evaluated in the same way with a caustic curve on a different image plane, or equivalently an initial curve outside the HRR field. Since either K or the J integral is the single loading parameter which characterizes the crack-tip stress and deformation field for different material behavior, the resultant caustic curve or the shadow spot is essentially an image of these loading parameters; and one single measurement, e.g., the size of the caustic curve, should be sufficient for evaluating these parameters.

3 Caustic Patterns Associated with the High-Temperature Crack-Tip Field

According to Eqs. (4) or (5), in order to determine the mapping relation, the crack-tip strain field needs to be determined first. For this purpose, Eq. (3) is integrated with respect to time to yield the time-dependent creep strain at the crack tip, namely,

$$\epsilon_{ij}^c = E(t)\left(\frac{1}{BI_n r}\right)^{n/n+1}\tilde{\epsilon}_{ij}(\theta), \tag{7}$$

where

$$E(t) = B\int_0^t C(t)^{n/n+1}dt. \tag{8}$$

Based on Eq. (7), the out-of-plane displacement can be calculated as

$$f = -u = -\frac{h}{2}\epsilon_{33}^c = \frac{h}{2}E(t)\left(\frac{1}{BI_n r}\right)^{n/n+1}[\tilde{\epsilon}_{rr}(\theta,n) + \tilde{\epsilon}_{\theta\theta}(\theta,n)] = \frac{1}{2}F(t)r^{-n/n+1}\psi, \tag{9}$$

where $\psi = \tilde{\epsilon}_{rr}(\theta,n) + \tilde{\epsilon}_{\theta\theta}(\theta,\mathrm{n})$, and $F(t) = hE(t)(1/BI_n)^{n/n+1}$. The gradient of function f can be shown to be

$$2\nabla f = -F(t)r^{-(2n+1)/(n+1)}\left\{\left[\frac{n}{n+1}\psi\cos\theta + \psi'\sin\theta\right]\mathbf{i} + \left[\frac{n}{n+1}\psi\sin\theta - \psi'\cos\theta\right]\mathbf{j}\right\}. \tag{10}$$

Substituting Eq. (10) into Eq. (5) then yields the following mapping equations:

$$X(t) = x + F(t)z_0 r^{-(2n+1)/(n+1)}\left[\frac{n}{n+1}\psi\cos\theta + \psi'\sin\theta\right] \tag{11}$$

$$Y(t) = y + F(t)z_0 r^{-(2n+1)/(n+1)}\left[\frac{n}{n+1}\psi\sin\theta - \psi'\cos\theta\right] \tag{12}$$

where the prime denotes the derivative with respect to θ.

Substitution of the above mapping equations into Eq. (6) results in a quadratic equation in terms of $r^{(3n+2)/(n+1)}$ with the coefficients depending on ψ, ψ', and ψ'', and the material constant n. The root of the quadratic equation, namely,

$$r^{(3n+2)/(n+1)}(\theta,n) = z_0F(t)R(\theta,n) \tag{13}$$

is the equation for the initial curve, where

Downloaded 03 May 2010 to 171.66.16.20. Redistribution subject to ASME license or copyright; see http://www.asme.org/terms/Terms_Use.cfm

$$R(\theta,n) = \frac{1}{2}\left[\left(\frac{n}{n+1}\right)^2\psi + \psi''\right] + \left\{\left[\left(\frac{n}{n+1}\right)^2\psi + \psi''\right]^2 + 4\frac{2n+1}{n+1}\left[\left(\frac{n}{n+1}\right)^2\psi^2 - \frac{n}{n+1}\psi\psi'' + \frac{2n+1}{n+1}(\psi')^2\right]\right\}^{1/2}, \quad (14)$$

which is the same as that for the HRR field derived by Rosakis et al. (1983). Notice that unlike elastic or plastic fracture, the initial curve varies with time for a fixed experimental setup under creep condition. Substituting Eq. (13) back into the mapping equations again, (11) and (12), results in the equation for the corresponding caustic curve:

$$X = [F(t)z_0R]^{(n+1)/(3n+2)} \times \left[\cos\theta + R^{-1}\left(\frac{n}{n+1}\psi\cos\theta + \psi'\sin\theta\right)\right] \quad (15)$$

$$Y = [F(t)z_0R]^{(n+1)/(3n+2)} \times \left[\sin\theta + R^{-1}\left(\frac{n}{n+1}\psi\sin\theta - \psi'\cos\theta\right)\right] \quad (16)$$

for values of θ in the range $-\pi < \theta < \pi$.

In applying optical caustics to the characterization of the flaws or cracks, usually the maximum transverse diameter D is used as the characteristic dimension. In this case,

$$D(t) = 2\left[\max_\theta \text{ of } Y(t)\right] = 2[F(t)z_0]^{(n+1)/(3n+2)} \times \max_\theta\left\{R^{n+1/3n+2}\left[\sin\theta + R^{-1}\left(\frac{n}{n+1}\psi\sin\theta - \psi'\cos\theta\right)\right]\right\}. \quad (17)$$

The maximum transverse diameter $D(t)/2 = \max_\theta$ of $Y(t)$ can be written as

$$\frac{3n+2}{n+1}\left(\frac{D(t)}{2}\right)^{2n+1/n+1}\frac{\dot{D}(t)}{2} = \max_\theta\left\{\left[\dot{F}(t)z_0R\right] \times\left[\sin\theta + R^{-1}\left(\frac{n}{n+1}\psi\sin\theta - \psi'\cos\theta\right)\right]^{3n+2/n+1}\right\} = \left[\dot{F}(t)z_0\right]\max_\theta\left\{R\left[\sin\theta + R^{-1}\left(\frac{n}{n+1}\psi\sin\theta - \psi'\cos\theta\right)\right]^{3n+2/n+1}\right\}. \quad (22)$$

Since $\dot{F}(t) = h\dot{E}(t)(1/BI_n)^{n/n+1}$ and $\dot{E}(t) = BC(t)^{n/n+1}$, Eq. (22) can also be written as

$$\frac{3n+2}{n+1}\left(\frac{D(t)}{2}\right)^{2n+1/n+1}\frac{\dot{D}(t)}{2} = z_0hB\left(\frac{1}{BI_n}\right)^{n/n+1}C(t)^{n/n+1}\max_\theta\left\{R\left[\sin\theta + R^{-1}\left(\frac{n}{n+1}\psi\sin\theta - \psi'\cos\theta\right)\right]^{3n+2/n+1}\right\}. \quad (23)$$

Based on Eq. (23), $C(t)$ can be expressed as

$$C(t) = \left(\frac{3n+2}{n+1}\right)^{n+1/n}S_n\left(\frac{1}{z_0h}\right)^{n+1/n} \times B^{-1/n}\dot{D}(t)^{n+1/n}D(t)^{2n+1/n}. \quad (24)$$

The coefficient S_n is a function of n only and is given by

$$S_n = \frac{I_n}{\max_\theta\left\{R^{n+1/n}\left[2\sin\theta + \frac{2}{R}\left(\frac{n}{n+1}\psi\sin\theta - \psi'\cos\theta\right)\right]^{3n+2/n}\right\}} \quad (25)$$

Unlike elastic or place fracture, $D(t)$ is directly related to the time integration of the crack-tip loading parameter $C(t)$, i.e., $F(t)$, but not $C(t)$ itself. However, certain correlation can still be obtained with the following approach.

Rewrite Eqs. (15) and (16) as

$$X^{(3n+2)/(n+1)} = [F(t)z_0R]\left[\cos\theta + R^{-1} \times\left(\frac{n}{n+1}\psi\cos\theta + \psi'\sin\theta\right)\right]^{(3n+2)/(n+1)}, \quad (18)$$

$$Y^{(3n+2)/(n+1)} = [F(t)z_0R]\left[\sin\theta + R^{-1} \times\left(\frac{n}{n+1}\psi\sin\theta - \psi'\cos\theta\right)\right]^{(3n+2)/(n+1)}, \quad (19)$$

respectively. Differentiating both sides with respect to time leads to

$$\frac{3n+2}{n+1}\dot{X}X^{2n+1/n+1} = \left[\dot{F}(t)z_0R\right]\left[\cos\theta + R^{-1} \times\left(\frac{n}{n+1}\psi\cos\theta + \psi'\sin\theta\right)\right]^{3n+2/n+1}, \quad (20)$$

and

$$\frac{3n+2}{n+1}\dot{Y}Y^{2n+1/n+1} = \left[\dot{F}(t)z_0R\right]\left[\sin\theta + R^{-1} \times\left(\frac{n}{n+1}\psi\sin\theta - \psi'\cos\theta\right)\right]^{3n+2/n+1}. \quad (21)$$

which is again the same as that for the HRR field derived by Rosakis et al. (1983). A list of the numerical values of S_n for different n's were also given by Rosakis et al. (1983).

Equation (24) reveals an important fact that $C(t)$ in general depends on not only the size but also the rate of change of the size of the shadow spot. In other words, determination of $C(t)$ relies on the knowledge of the time history of both $D(t)$ and $\dot{D}(t)$. It should also be noted that Eq. (24) is a general relation which is valid for both small-scale and large-scale creep conditions.

When the steady-state is reached, $C(t)$ becomes C^* and $E(t)$ is equal to $B(C^*)^{n/n+1}t$. By substituting the above $E(t)$ into Eq. (17), it can be shown that at steady-state, $D(t)$ is a power function of time, namely,

$$D(t) = D^*t^{n+1/3n+2}, \quad (26)$$

where $D^* = [(C^*)^nBS_n^{-n}(z_0h)^{n+1}]^{1/3n+2}$. Equation (26) indicates that by plotting $D(t)$ versus time t on a log-log basis, C^* can be determined by the intercept of the straight line formed by the data on $D(t)$ at the steady-state with the axis of log $t = 0$.

4 Simulation of the Caustic Curves

In order to better understand the caustics phenomena under high-temperature creep condition and provide a basis for comparison with experimental results, a numerical simulation is carried out based on the equations derived above. The simulation is performed for the small-scale creep and large-scale creep conditions, respectively; and is based on an estimated crack-tip loading parameter $C(t)$ and the following

Downloaded 03 May 2010 to 171.66.16.20. Redistribution subject to ASME license or copyright; see http://www.asme.org/terms/Terms_Use.cfm

material constants for the 2219-T3511 aluminum alloy (Ding and Chen, 1994): $E = 71.7$ GPa, $K = 18.9$ MPa$\sqrt{m}$, $J = K^2/E = 4987$ Nm^{-1}, $n = 15$, $B = 0.305 \times 10^{-40}$ MPa^{-15} s^{-1}, $C^* = 1.75 \times 10^{-5}$ Nm^{-1} s^{-1} and $z_0 = 0.147$ m.

4.1 Small-Scale Creep Condition. For small-scale creep condition which is valid during a short time period after the load is applied, an asymptotic solution for $C(t)$ inside the creep zone was derived by Riedel and Rice (1980) as

$$C(t) = \frac{J}{(n+1)t}, \tag{27}$$

where $J = K^2/E$ for the plane stress condition. With this asymptotic solution, Eq. (8) can be integrated with time to yield

$$E(t) = E_1(t) = BJC(t)^{-1/n+1}, \tag{28}$$

and

$$F(t) = hE_1(t)\left(\frac{1}{BI_n}\right)^{n/n+1} = hBJC(t)^{-1/n+1}\left(\frac{1}{BI_n}\right)^{n/n+1}, \tag{29}$$

for small-scale creep condition.

Since $F(t)$ is an explicit function of $C(t)$, $C(t)$ can actually be directly related to $D(t)$ through Eq. (17) as

$$C(t) = S_n\left[\frac{1}{z_0 h(n+1)t}\right]^{n+1/n} B^{-1/n}D(t)^{3n+2/n} \tag{30}$$

or

$$C(t) = S_n^{-n}(z_0 hJ)^{n+1}BD(t)^{-(3n+2)}. \tag{31}$$

However, it should be reminded that Eqs. (30) or (31) is only a special case under the premise that $C(t)$ can indeed be described by Eq. (27) for small-scale creep condition. Of course the practical determination of $C(t)$ by the use of optical caustics and Eq. (24) does not require a prior knowledge on the time dependence of $C(t)$. However, the experiment is certainly a good way to evaluate the theoretical prediction on $C(t)$.

The simulation starts with a dot matrix in the x-y plane with the center located at the crack tip. Each point with a coordinate of (x,y) in the matrix is mapped to the X-Y plane through an appropriate mapping equation. Under small-scale creep condition, the creep zone is surrounded by a K-dominated field. Therefore, in simulating the caustic patterns at any specified time, the corresponding creep zone boundary needs to be determined first. The dots inside the creep zone are then mapped to the X-Y plane through Eqs. (29), (11), and (12); and those outside the creep zone are through the elastic mapping equations (Beinert and Kalthoff, 1981), namely,

$$X = x + 2z_0\frac{\nu h K_I}{2\sqrt{2\pi}Er^{3/2}}\cos\frac{3\theta}{2}, \tag{32}$$

$$Y = y + 2z_0\frac{\nu h K_I}{2\sqrt{2\pi}Er^{3/2}}\sin\frac{3\theta}{2}. \tag{33}$$

The initial curve corresponding to the elastic K field is a circle given by

$$r_0 = \left[\frac{3h\nu K_I z_0}{2E\sqrt{2\pi}}\right]^{2/5}, \tag{34}$$

where ν is the Poisson's ratio which was taken to be 0.33 in the current simulation.

In Riedel and Rice's work (1980), the boundary of the creep zone has been somewhat arbitrarily defined by either equating the effective stress in the creep zone and the

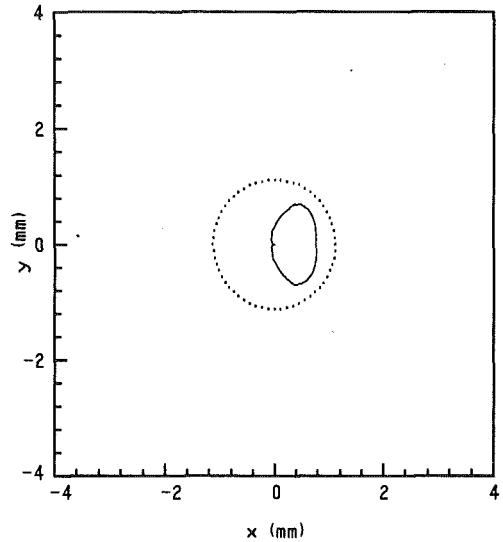


Fig. 1(a1) $t/t_T = 10^{-5}$

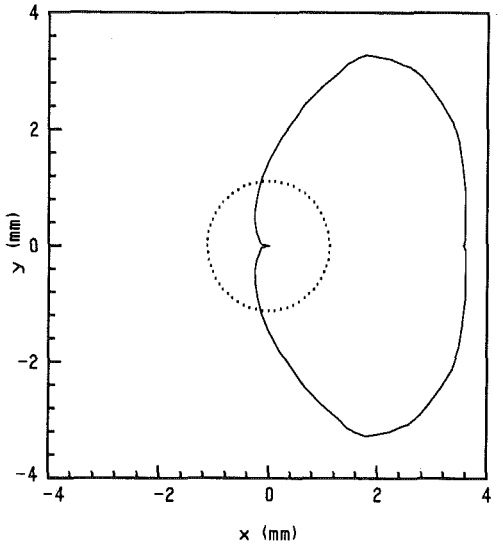


Fig. 1(a2) $t/t_T = 0.5$

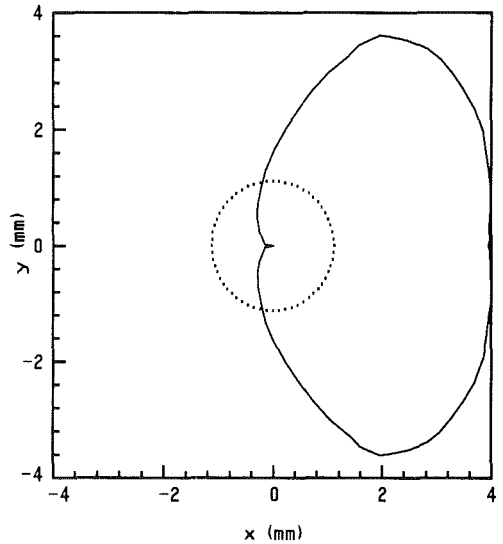


Fig. 1(a3) $t/t_T = 1$

Fig. 1(a) Estimation of the evolution of the creep zone boundaries under small-scale creep condition (solid lines) relative to the position of the initial curve (dotted line) at the beginning of the creep. The estimation was based on $z_0 = 0.147$ m and the following material constants: $n = 15$, $B = 0.305 \times 10^{-40}$ MPa^{-15} s^{-1}, $J = 4987$ Nm^{-1}, $C^* = 1.75 \times 10^{-5}$ Nm^{-1} s^{-1}.

Downloaded 03 May 2010 to 171.66.16.20. Redistribution subject to ASME license or copyright; see http://www.asme.org/terms/Terms_Use.cfm

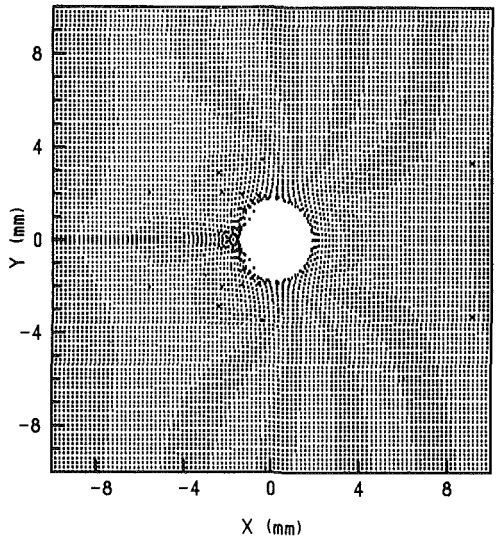


Fig. 1(*b1*) $t/t_T = 10^{-5}$

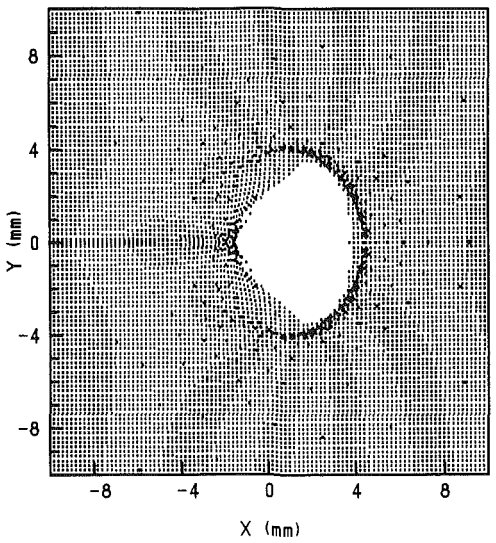


Fig. 1(*b2*) $t/t_T = 0.5$

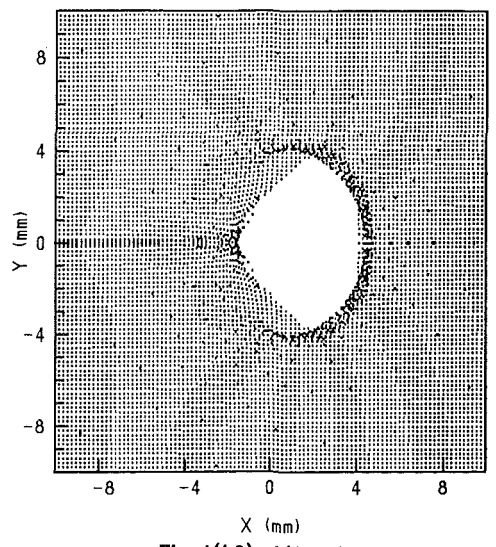


Fig. 1(*b3*) $t/t_T = 1$

Fig. 1(*b*) The caustic patterns corresponding to the crack-tip fields shown in Fig. 1(*a*)

remote elastic stress field; or by equating the effective creep strain in the creep zone and the effective elastic strain in the elastic field. In the current work, the latter definition is used. The evolution of the creep zone boundary (shown as the solid line) at different times with respect to the initial position of the initial curve (shown as the dotted line) is shown in Fig. 1(*a*). The corresponding simulated caustic patterns are shown in Fig. 1(*b*). The time has been normalized with respect to the transition time t_T from small-scale to large-scale creep condition which was defined by Riedel and Rice (1980) as $t_T = J/(n+1)C^*$. Based on the materials constants adopted here, t_T is equal to 1.78×10^7 s. Since the initial crack-tip field at the time of loading is an elastic one, the initial position of the initial curve is in the K field and the shape should be a circle as mentioned earlier. As creep continues, the creep zone will expand and soon reaches the position where the initial curve at the time of loading is located. At this point, the caustic pattern starts to distort from the epicycloid corresponding to the elastic field to the shapes shown in Figs. 1(*b*2) and 1(*b*3). As mentioned earlier, once the initial curve is inside the creep zone, its position is no longer fixed even under constant loading condition.

The caustic patterns shown in Figs. 1(*b*2) and 1(*b*3) do not show a well-defined caustic boundary. There is a dark arc, i.e., where part of the light concentration is, on the right side of the blank area, i.e., shadow region. In other words, the boundary of the shadow region does not coincide with the line of the light concentration. As the creep zone expands, the density of the mapped points in the arc region increases; and the blank area also expands closer to the dark arc. In order to interpret this particular pattern, the caustic pattern shown in Fig. 1(*b*3) was further studied by investigating the mapping from the creep zone and elastic region separately. It was found that the dark arc originated from the points inside the creep zone and the rest of the image including the blank area was from the elastic region. Since this caustic pattern is contributed from both K and $C(t)$, it is probably very difficult to use this pattern to deduce either of them. As also shown in Fig. 1(*a*), it seems that the estimated creep zone can never extend to completely cover the initial curve completely even when $t/t_T = 1$. However, it should be reminded that the above simulation was based on an estimation of the creep zone boundary which may not be very realistic. In reality, the experiment may be set up in such a way that the initial curve is small enough to be completely embedded inside the creep zone soon after the creep has started. This anticipation is based on the fact that in plastic fracture the initial curve can be adjusted to be embedded in the HRR field under small-scale yield condition as demonstrated by Rosakis et al. (1983). In this case, the caustic pattern will have the same shape as that which will be shown in the next section and be analogous to each other, and Eq. (24) can be directly applied to the interpretation of the pattern and data reduction.

4.2 Large-Scale Creep. For the large-scale creep condition, Ehlers and Riedel (1981) proposed the following approximate equation for $C(t)$ based on their finite element analysis, namely,

$$C(t) = C^*\left(1 + \frac{t_T}{t}\right), \tag{35}$$

which has the right short-term and long-term limits for $C(t)$. Substituting Eq. (35) into Eq. (8) then yields the following form for E in terms of the nondimensionized time t/t_T, namely,

$$E\left(\frac{t}{t_T}\right) = E_2\left(\frac{t}{t_T}\right) = Bt_T\int_0^{\frac{t}{t_T}}\left[C^* + \frac{J}{(n+1)t_T t}\right]^{n/n+1} dt. \tag{36}$$

Downloaded 03 May 2010 to 171.66.16.20. Redistribution subject to ASME license or copyright; see http://www.asme.org/terms/Terms_Use.cfm

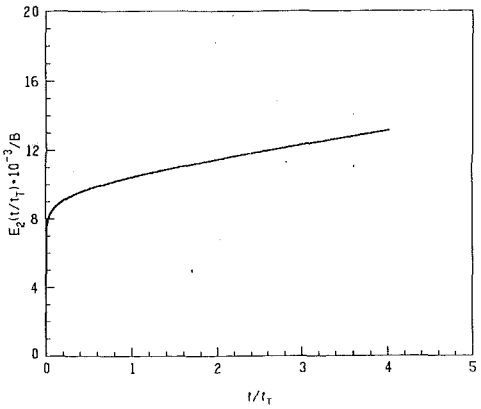


Fig. 2 A typical numerically integrated E_2/B (in $(N/m)^{15/16}$) curve based on the constants described in the caption of Fig. 1(*a*)

Unlike small-scale creep condition, a closed-form solution for E_2 is not available. Figure 2 shows a typical numerically integrated E_2 curve based on the aforementioned materials constants. Because of the singularity of Eq. (35) at $t = 0$, the E_2 curve was calculated by a combination of two integrals, i.e., integral of Eq. (27) from 0 to 0.2 sec and that of Eq. (35) from 0.2 sec to the current time.

Under large-scale creep condition, the elastic K field no longer exists and the initial curve is definitely inside the creep zone. In this case, all the dots in the x-y plane are mapped to the X-Y plane through Eqs. (36), (11), and (12). A simulated result at $t/t_T = 50$ is shown in Fig. 3. Since the mapping equations are essentially the same except for the strength of the creep singularity, the resultant caustic curves at different times should be analogous in shape but different in size. Notice also that the right side of the caustic curve is similar to that of the dark arc shown in Fig. 1(*b*).

As mentioned earlier, even under small-scale creep condition, if the initial curve is completely embedded inside the creep zone, the simulated caustic patterns should have the same shape as shown in Fig. (3). This is again because both small-scale creep and large-scale creep have the same crack-tip field inside the creep zone except for the strength of the singularity.

5 Simulaton of the Time-Dependent Evolution of the Size of the Caustic Curve

Assuming that the initial curve is small enough to be embedded in the creep zone soon after the creep starts, a predicted evolution of the size of the caustic pattern as a function of time is shown in Fig. 4. The prediction is based on Eq. (17) and the E_2 curve described above. As mentioned earlier, as the crack-tip field approaches to the steady-state, the size of the caustic patterns should change as a power function of time.

6 Discussion

The procedure of application of optical caustics to the characterization of the time-dependent fracture is opposite to that of the numerical simulation described above. In the numerical simulation, the resultant caustic patterns are predicted from a given crack-tip field. In the practical application, a record of the caustic patterns as a function of time is obtained from the experiment, which is then coupled with Eq. (24) to retrieve the information related to the crack-tip field, such as the loading parameter. Although there may be some difficulty in interpreting the caustic patterns under small-scale creep condition if they do follow the pattern shown in the later part of Fig. 1(*b*), this difficulty may be

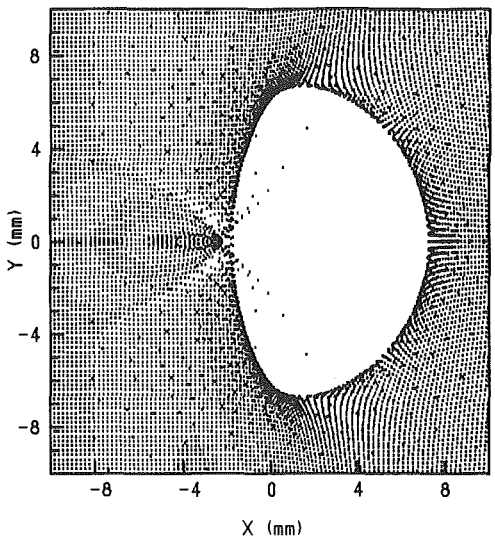


Fig. 3 A simulated caustic pattern under large-scale creep condition at $t/t_T = 50$ based on the constants described in the caption of Fig. 1(*a*)

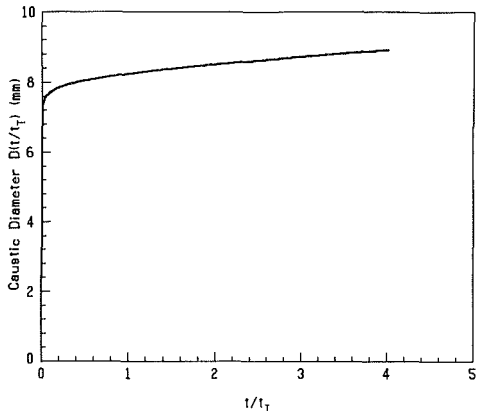


Fig. 4 A simulated evolution of the size of the caustic pattern *D* based on the constants described in the caption of Fig. 1(*a*)

overcome by setting up the experiment in such a way that the initial curve can be made as small as possible. In practical applications, the emphasis of the development of an experimental method should probably be put on the large-scale creep condition anyway because the dominant crack-tip loading parameter for the small-scale creep is the stress intensity factor which can be determined by many well established experimental techniques.

Because of its dependence on the theoretical analysis of the crack-tip fields for interpreting the experimental results, the accuracy of current experimental technique is limited by the two major assumptions adopted in the theoretical analysis, namely, the material model and the plane-stress condition. The current analysis is based on the consideration of secondary creep only which is probably the only case that crack-tip fields under creep condition is reasonably understood. However, at elevated temperatures, the material behavior is generally more complicated than the steady-state creep. Therefore, the accuracy of using Eq. (24) combined with the optical caustics for characterizing the time-dependent fracture can at most be only equal to that of using steady-state creep equation to model the high-temperature material behavior. Another limitation is related to the assumption of the plane stress condition. Determination of the possible error introduced by the finite thickness of the test specimen in contrast to the plane stress condition may need a systematic experimental or numerical investigation.

For high-temperature application, a further experimental

Downloaded 03 May 2010 to 171.66.16.20. Redistribution subject to ASME license or copyright; see http://www.asme.org/terms/Terms_Use.cfm

difficulty may also rise from the possible creep crack growth under constant load, which will of course affect the observed caustic patterns and may make the interpretation more difficult.

7 Conclusion

In the current work, a theoretical foundation has been developed for application of optical caustics to the characterization of the time-dependent fracture of engineering materials at elevated temperatures. Under the assumption that the material behavior is governed by the steady-state creep, it has been shown that the time-dependent crack-tip loading parameter can be determined by the time history of the size and rate of change of the size of the shadow spot through a correlation relation.

Within its limitations, the method of optical caustics does seem to provide a convenient tool for observing the time-dependent crack-tip field and characterizing the crack-tip loading parameter. All that is required in this experimental approach is essentially a record of the size of the caustic curve as a function of time and some basic material constants used in the steady-state creep equations.

Acknowledgments

This work was supported in part by the National Science Foundation under Grants MSS-9015616, and by the Department of Mechanical and Materials Engineering, Washington State University.

References

Beinert, J., and Kalthoff, J. F., 1981, "Experimental Determination of Dynamic Stress Intensity Factors by Shadow Patterns," *Experimental Evaluations of Stress Concentration and Intensity Factors*, G. C. Sih, ed., Martinus Nijhoff, The Hague, pp. 281–330.

Ding, J. L., and Chen, Y. G., 1994, "Characterization of the Time-Dependent Fracture at Elevated Temperatures by Optical Caustics," *Engineering Fracture Mechanics*, Vol. 47, No. 1, pp. 101–120.

Ehler, R., and Riedel, H., 1981, "A Finite Element Analysis of creep Deformation in a Specimen Containing a Macroscopic Crack," *Advances in Fracture Research* (Proc. of the Fifth Int. Conf. on Fracture, Cannes, France), D. Francois et al., eds., Vol. 2, Pergamon Press, Oxford, pp. 691–69.

Hutchinson, J. W., 1968, "Singular Behavior at the End of a Tensile Crack in a Hardening Material," *J. Mech. Phys. Solids*, Vol. 16, pp. 13–24.

Judy, R. W., Jr., and Sanford, R. J., 1989, "Correlation of Optical Caustics with Fracture Behavior of High-Strength Steels," *Nonlinear Fracture Mechanics: Vol. 1—Time-Dependent Fracture*, ASTM STP 995, A. Saxena, J. D. Landes, and J. L. Bassani, eds., pp. 340–357.

Landes, J. D., and Begley, J. A., 1976, "A Fracture Mechanics Approach to Creep Crack Growth," *Mechanics of Crack Growth*, ASTM STP 590, pp. 121–148.

Rice, J. R., 1968, "A Path-Independent Integral and the Approximate Analysis of Strain Concentration by Notches and Cracks," ASME JOURNAL OF APPLIED MECHANICS, Vol. 35, pp. 379–386.

Rice, J. R., and Rosengren, G. F., 1968, "Plane Strain Deformation Near a Crack Tip in Power Law Hardening Materials," *J. of Mech. Phys. Solids*, Vol. 16, pp. 1–12.

Riedel, H., and Rice, J. R., 1980, "Tensile Cracks in Creeping Solids," *Fracture Mechanics*, ASTM STP 700, pp. 112–123.

Rosakis, A. J., Ma, C. C., and Freund, L. B., 1983, "Analysis of the Optical Shadow Spot Method for a Tensile Crack in a Power-Law Hardening Material," ASME JOURNAL OF APPLIED MECHANICS, Vol. 50, pp. 777–782.

Rosakis, A. J., Zehnder, A. T., and Narasimhan, R., 1988, "Caustics by Reflection and Their Application to Elastic-Plastic and Dynamic Fracture Mechanics," *Optical Engineering*, Vol. 20, pp. 596–627.

Saxena, A., 1986, "Creep Crack Growth Under Non-Steady-State Conditions," *Fracture Mechanics*, ASTM STP 905, J. H. Underwood, et al., eds., pp. 185–201.

Theocaris, P. S., 1981, "Elastic Stress Intensity Factors Evaluated by Caustics," *Experimental Evaluations of Stress Concentration and Intensity Factors*, G. C. Sih, ed., Martinus Nijhoff, The Hague, pp. 189–252.

Downloaded 03 May 2010 to 171.66.16.20. Redistribution subject to ASME license or copyright; see http://www.asme.org/terms/Terms_Use.cfm

M. P. Bendsøe
Mathematical Institute,
The Technical University of Denmark,
DK-2800 Lyngby, Denmark

J. M. Guedes
CEMUL,
Instituto Superior Tecnico,
Av. Rovisco Pais,
P-1096 Lisboa Codex, Portugal

R. B. Haber
Department of Theoretical
and Applied Mechanics,
University of Illinois at Urbana-Champaign,
Urbana, IL 61801

P. Pedersen
Department of Solid Mechanics,
The Technical University of Denmark,
DK-2800 Lyngby, Denmark

J. E. Taylor
Department of Aerospace Engineering,
University of Michigan,
Ann Arbor, MI 48109-2140

An Analytical Model to Predict Optimal Material Properties in the Context of Optimal Structural Design

This paper deals with the simultaneous optimization of material and structure for minimum compliance. Material properties are represented in the most general form possible for a (locally) linear elastic continuum, namely the unrestricted set of elements of positive semi-definite constitutive tensors and cost measures based on certain invariants of the tensors. Analytical forms are derived for the optimized material properties. These results, which apply in general, indicate that the optimized material is orthotropic with the directions of orthotropy following the directions of principal strains. The analysis for optimization of the material leads to a reduced structural optimization problem, for which the existence of solutions can be shown and for which effective methods for computational solution can be devised.

1 Introduction

Our goal in this study is to formulate a structural optimization problem in a form that encompasses the design of structural material and to provide some general results from analysis with this problem. The development is restricted to structures comprised of linear elastic material and to small-deformation kinematics. The global design objective is structural compliance. Within the usual limitations for physical materials, material properties are represented in the most general form possible for a linear elastic continuum: the unrestricted set of elements of positive semi-definite constitutive tensors. Given this description of the material, we are able to demonstrate in analytical form the local properties associated with materials that are optimal with respect to the global compliance objective. Topologies associated with the optimum structural distribution of the optimized materials are in effect predicted out of the same treatment of the structural optimization problem.

Optimal design with advanced materials is a subject of recent intensive research. The problem of optimal rotation of orthotropic materials provides a natural starting point for considerations for a more general approach to the concurrent design of material and structure (Pedersen, 1989, 1990). The simultaneous design of material and overall structure has been taken one step further in the recent studies of optimal topology design using homogenization modeling (see, e.g., Allaire and Kohn, 1992; Bendsøe and Kikuchi, 1988; Bendsøe and Mota Soares, 1992; Bendsøe, Diaz, and Kikuchi, 1992; Jog, Haber, and Bendsøe, 1992; Kohn, 1988; Lipton, 1993; Lurie and Cherkaev, 1986). This field relies heavily on the work on regularization of the plate optimal design problem (Cheng and Olhoff, 1982; Lurie, Cherkaev, and Fedorov, 1982). In the work of these papers the structure is assumed to be made up of an arbitrary composition of a strictly limited number of given materials, and for the special case of topology design one of the given materials is void (usually approximated by a very flexible material). The homogenization modeling predicts a ranked set of "microstructures" or "structures with microscale variations" as the optimal material distribution. This shows the relation between topology design and the problem of generating the stiffest microstructures and emphasizes the strong interrelation between the fields of optimal design and materials science (see, e.g., Kohn, 1988; Lipton, 1993; Lurie and Cherkaev, 1986).

Contributed by the Applied Mechanics Division of THE AMERICAN SOCIETY OF MECHANICAL ENGINEERS for publication in the ASME JOURNAL OF APPLIED MECHANICS.
Discussion on this paper should be addressed to the Technical Editor, Professor Lewis T. Wheeler, Department of Mechanical Engineering, University of Houston, Houston, TX 77204-4792, and will be accepted until four months after final publication of the paper itself in the ASME JOURNAL OF APPLIED MECHANICS.
Manuscript received by the ASME Applied Mechanics Division, Dec. 22, 1992; final revision, Aug. 12, 1993. Associate Technical Editor: E. N. Reddy.

Copyright © 1994 by ASME
Downloaded 03 May 2010 to 171.66.16.20. Redistribution subject to ASME license or copyright; see http://www.asme.org/terms/Terms_Use.cfm

In the homogenization method of topology design, the total volume of material, defined at the microlevel, provides a natural cost function for optimization problem formulations. There is no such natural cost function for the general material design formulation we consider here. Instead, we use certain invariants of the stiffness tensor as the measure of cost, thus ensuring that the optimal design solutions are *not* influenced by the choice of reference frame. Moreover, we can express cost and energy in any frame that is suitable for our formulation, a feature that is crucial for the developments stated below.

In the modeling of the optimization problem the parameters which describe the structure can be divided into two sets: the parameters defining the local material tensor and those that describe the specific cost of the material. It is shown that the minimum compliance optimization of a structure with respect to these two sets of parameters can be performed independently. Furthermore, the optimization with respect to the local material tensor parameters can be performed analytically. This results in an optimized, linear material which minimizes the compliance of the applied load, and the optimization of the elasticity tensor can (in any dimension) be performed by considering an equivalent, one-parameter convex sizing problem for a linear zero-Poisson-ratio material. A similar multilevel approach to the analysis of minimum compliance problems has also been used to great effect in the homogenization modeling applied to a locally elastic medium with "holes" (Allaire and Kohn, 1992; Jog, Haber, and Bendsøe, 1992; Lipton, 1993). Results obtained using such models predict nonlinear and nonsmooth optimized materials, however.

The very general framework of optimizing directly on a free parametrization of the material tensor results in developments which provide an attainable global lower bound on the performance of any structure designed for the same loadings, boundary conditions, and ground structure. At the same time, it provides an attainable global upper variational bound on the effective moduli of any elastic material. Also, the considerable simplifications we are able to demonstrate indicates that the broader form of a material design problem, as described and analyzed in this paper, should constitute effective means for studying the global structural optimization problem involving sizing, shape, topology, and material selection.

2 The Problem in Dimension $N = 2$

The problem we consider is an extension of the problem of minimizing the compliance of a structure made of a given material, which has the material properties themselves appear in the role of design variables. We first formulate the problem for a two-dimensional domain Ω.[1]

$$\min_{E,u} l(u) = \int_\Omega fud\Omega + \int_{\Gamma_T} tuds$$

subject to

$$\int_\Omega E_{ijkl}\epsilon_{ij}(u)\epsilon_{kl}(v)d\Omega = l(v) \text{ for all } v \in U$$

$$E \geq 0$$

$$\int_\Omega \Psi(E)d\Omega \leq V \tag{1}$$

We take the minimization over all positive, semi-definite rigidity tensors E_{ijkl} and use the integral over the domain of some invariant $\Psi(E_{ijkl})$ of the rigidity tensor as the measure of cost. In (1) we have written the equilibrium equation in the weak form, using U to denote the space of kinematically admissible trial functions. Note that we treat only a single loading condition, represented by the specified body force f and boundary traction t.

Next, we reformulate problem (1) into a convenient form that emphasizes the role of the material design:

$$\max_{\substack{\text{rigidity } E\geq 0 \\ \int_\Omega \Psi(E)d\Omega}} \min_{u\in U} \Pi(E, u) \tag{2}$$

with

$$\Pi(E, u) = 1/2 \int_\Omega E_{ijkl}\epsilon_{ij}(u)\epsilon_{kl}(u)d\Omega - l(u). \tag{3}$$

In (2), the equilibrium requirement is represented via minimization of the potential energy with respect to deformation. Also, the minimum compliance problem in (2) is stated as a maximization of potential energy with respect to design, since the measure of compliance equals the negative of twice the value of the potential energy at equilibrium. This form of problem statement has been used effectively in studies of optimal rotation of orthotropic materials (Pedersen, 1989), in recent studies of optimal topology design with the so-called rank-2 materials (Allaire and Kohn, 1992; Jog, Haber, and Bendsøe, 1992), as well as in the formulation of conventional "material distribution" design problems (e.g., Prager and Taylor, 1968).

For physical reasons, the possible rigidity tensors in the above design formulation are restricted to the set of positive semi-definite, symmetric (2,2)-tensors. Note that a necessary and sufficient condition for E to be positive semi-definite is that the principal determinants for the quadratic form $E_{ijkl}\epsilon_{ij}\epsilon_{kl}$ are all non-negative (cf. Gantmacher, 1959); i.e., if and only if

$$\begin{aligned} &E_{1111} \geq 0,\ E_{2222} \geq 0,\ E_{1212} \geq 0, \\ &E_{1111}E_{2222} - E_{1122}^2 \geq 0,\ E_{1111}E_{1212} - E_{1112}^2 \geq 0, \\ &\qquad E_{2222}E_{1212} - E_{2212}^2 \geq 0, \\ &E_{1111}E_{2222}E_{1212} + 2E_{1112}E_{2212}E_{1122} - E_{1212}E_{1122}^2 \\ &\qquad - E_{2222}E_{1112}^2 - E_{1111}E_{2212}^2 \geq 0. \end{aligned} \tag{4}$$

As discussed in the Introduction, suitable cost functions must have the property of frame indifference. Since the goal is to optimize the local material properties as well as the global structural response, we choose to consider cost in terms of invariants of the constitutive tensor itself. Specifically, we choose the following two invariants as examples of local cost:

$$\begin{aligned} &\text{Case A:}\quad \Psi_A(E) = E_{ijij} = E_{1111} + E_{2222} + 2E_{1212}, \\ &\text{Case B:}\quad \Psi_B(E) = E_{ijkl}E_{ijkl} = E_{1111}^2 + E_{2222}^2 \\ &\qquad + 2E_{1122}^2 + 4E_{1212}^2 + 4E_{1112}^2 + 4E_{2212}^2, \end{aligned} \tag{5}$$

i.e., respectively, measures of the trace and the Frobenius norm of the (2,2)-tensor E.

For the sake of simplifying the derivation, we introduce cost density functions, ρ_A and ρ_B, defined as

$$\begin{aligned} &\text{Case A:}\quad \rho_A = E_{ijij} = E_{1111} + E_{2222} + 2E_{1212}, \\ &\text{Case B:}\quad \rho_B^2 = E_{ijkl}E_{ijkl} = E_{1111}^2 + E_{2222}^2 + 2E_{1122}^2 \\ &\qquad + 4E_{1212}^2 + 4E_{1112}^2 + 4E_{2212}^2 \end{aligned} \tag{6}$$

and restate the design problem in the form

Case A:

$$\max_{\substack{\text{density } \rho_A \\ 0<\rho_{\min}\leq\rho_A\leq\rho_{\max}<\infty \\ \int_\Omega \rho_A d\Omega \leq V}} \max_{\substack{\text{rigidity } E\geq 0 \\ \Psi_A(E)=\rho_A}} \min_{u\in U} \Pi(\rho_A, E, u) \tag{7}$$

[1] In these expressions and in what follows we use a notation consistent with a Cartesian reference frame; this does not imply a loss of generality.

Downloaded 03 May 2010 to 171.66.16.20. Redistribution subject to ASME license or copyright; see http://www.asme.org/terms/Terms_Use.cfm

Case B:

$$\max_{\substack{\text{density } \rho_B \\ 0<\rho_{\min}\le\rho_B\le\rho_{\max}<\infty \\ \int_\Omega \rho_B^2 d\Omega \le V}} \quad \max_{\substack{\text{rigidity } E\ge 0 \\ \Psi_B(E)=\rho_B^2}} \quad \min_{u\in U} \Pi(\rho_B, E, u). \tag{8}$$

The cost constraints, linear in Case A and quadratic in Case B, are convex in both cases. In (7) and (8) we have introduced upper and lower bounds on the cost densities in order to ensure that the problem is well posed.

As will be shown below, this separation of the design variables provides a separation between the properties of the tensor E that can be optimized locally (at each point in the structure) and those that must be treated as a distributed parameter problem over the full domain.

Problem (1) in a discretized formulation has been studied numerically by Ringertz (1992) using similar cost functions. These investigations are based on the use of an interior point algorithm, with a logarithmic barrier function employed for converting the constraint $E > 0$ to a convex constraint. In the developments to follow, we show that an analytical optimization can reduce the number of free design variables in problems (7) and (8) from 6 in dimension two and 21 in dimension three to only *one* in both dimensions!

We now proceed by interchanging the order of the inner operators in problems (7) and (8), so that as inner problems we obtain

$$\text{Case A:} \quad \max_{\substack{\text{rigidity } E\ge 0 \\ \Psi_A(E)=\rho_A}} \Pi(\rho_A, E, u), \text{ for fixed } \rho_A \text{ and } u \tag{9}$$

$$\text{Case B:} \quad \max_{\substack{\text{rigidity } E\ge 0 \\ \Psi_B(E)=\rho_B^2}} \Pi(\rho_B, E, u), \text{ for fixed } \rho_B \text{ and } u. \tag{10}$$

Note that for a function of two parameters, we have the relation

$$\sup_x \inf_y \varphi(x, y) \le \inf_y \sup_x \varphi(x, y). \tag{11}$$

Therefore, a solution to (9), (10) will give an upper bound on the objective of the inner problems (and thus a lower bound on the compliance). If this bound is attainable, then the interchange is allowed. We shall demonstrate that the lower bound is indeed attainable and that in fact it can be found as an exact analytical solution.

Solving (9) and (10) corresponds to finding the pointwise stiffest material for a given strain field and a given distribution of "density"—this is a standard problem setting in the theory of variational bounds on effective moduli of anisotropic materials and is of interest in its own right. The relation between bounding theorems in materials science and optimum compliance design is well documented in the case of topology design with one given isotropic and linearly elastic material (see, e.g., Kohn, 1988) and has been used to generate analytical expressions for the optimal energy functionals that arise from the introduction of microstructures (Jog, Haber, and Bendsøe, 1992).

In this section we approach the optimization of the strain energy density via a direct parametric study that serves to identify certain features of optimal materials. In the following section, we extend the result to three-dimensional elasticity (actually any dimension) using an alternative geometric approach.

The inner problems (9) and (10) are constrained by the positivity constraints (4) as well as the relations (7) and (8) between the material parameters and the density. We now make use of our frame-independent descriptions of cost and energy to express the strain energy density in the frame of the principal strains.

$$W = 1/2 E_{ijkl}\epsilon_{ij}\epsilon_{kl} = 1/2\{E_{1111}\epsilon_I^2 + E_{2222}\epsilon_{II}^2 + 2E_{1122}\epsilon_I\epsilon_{II}\} \tag{12}$$

Note that this function, the strain energy density which is to be maximized, does not depend on the value of E_{1212}, and as this parameter enters in the cost function for both the cases we consider, we can conclude that the parameter should have value zero. Moreover, it then follows from the conditions (4) that

$$E_{1122} = E_{2212} = E_{1212} = 0. \tag{13}$$

This implies that the optimal material is at each point an orthotropic material, which is co-aligned with the principal strain axes and which has zero shear stiffness. This confirms the results on optimal rotations of orthotropic materials described via a different approach by Pedersen (1989, 1990).

We have reduced our admissible stiffness matrices to the form

$$\begin{pmatrix} E_{1111} & E_{1122} & 0 \\ E_{1122} & E_{2222} & 0 \\ 0 & 0 & 0 \end{pmatrix} \tag{14}$$

for which the conditions (4) reduce to

$$E_{1111} \ge 0, \; E_{2222} \ge 0,$$

$$E_{1111}E_{2222} - E_{1122}^2 \ge 0. \tag{15}$$

For Case A, the parameter E_{1122} is a free parameter for the inner problem, so to maximize the strain energy density this parameter should be chosen as numerically large as possible and with the same sign as $(\epsilon_I\epsilon_{II})$. Thus, the second constraint of (15) must be active. Accordingly, the strain energy density W and the density ρ_A are reduced to

$$W_A' = 1/2\{E_{1111}\epsilon_I^2 + E_{2222}\epsilon_{II}^2 + 2\sqrt{E_{1111}E_{2222}}\,|\epsilon_I\epsilon_{II}|\}$$
$$= 1/2[\sqrt{E_{1111}}\,|\epsilon_I| + \sqrt{E_{2222}}\,|\epsilon_{II}|]^2. \tag{16}$$

Case A:

$$\rho_A = E_{1111} + E_{2222}.$$

In other words, W_A' is obtained when the parameter E_{1122} is eliminated in expression (12) for the strain energy density W, through the equality

$$E_{1122} = \text{sign}(\epsilon_I\epsilon_{II})\sqrt{E_{1111}E_{2222}}. \tag{17}$$

The necessary conditions for optimality of the rigidity tensor for Case B imply that the second constraint of (15) must again be active (this is left to the reader). This means that we can reduce the strain energy density to the same form shown above for Case A. The cost density in this case is given by

$$\rho_B^2 = E_{1111}^2 + E_{2222}^2 + 2E_{1122}^2 = (E_{1111} + E_{2222})^2 \tag{18}$$

and we therefore have the expressions

$$W_B' = 1/2\{E_{1111}\epsilon_I^2 + E_{2222}\epsilon_{II}^2 + 2\sqrt{E_{1111}E_{2222}}\,|\epsilon_I\epsilon_{II}|\}$$
$$= 1/2[\sqrt{E_{1111}}\,|\epsilon_I| + \sqrt{E_{2222}}\,|\epsilon_{II}|]^2. \tag{19}$$

Case B:

$$\rho_B = E_{1111} + E_{2222}.$$

Thus, the minimization of strain energy density leads to identical reduced objective functions for the two cases. The only difference between the two problems at this stage is the way the density enters in the cost constraint.

We continue the maximization of the strain energy density and from here on drop the indexing of the two cases, as they now have the same form. The maximization is performed by expressing E_{1111}, E_{2222} as

$$E_{1111} = x_1^2, \; E_{2222} = x_2^2 \tag{20}$$

so that the optimization with respect to E_{1111}, E_{2222} can be formulated as

$$\max_{\|x\|^2=\rho, x\ge 0} [(|\epsilon_I|, \; |\epsilon_{II}|)\cdot(x_1, x_2)]^2. \tag{21}$$

Downloaded 03 May 2010 to 171.66.16.20. Redistribution subject to ASME license or copyright; see http://www.asme.org/terms/Terms_Use.cfm

This is the problem of finding a positive vector of length $\sqrt{\rho}$ for which the inner product with the vector $(|\epsilon_I|, |\epsilon_{II}|)$ is maximal. The solution is unique and is the obvious one, namely

$$(x_1, x_2) = (|\epsilon_I|, |\epsilon_{II}|) \frac{\sqrt{\rho}}{\sqrt{\epsilon_I^2 + \epsilon_{II}^2}}. \tag{22}$$

The resulting optimal rigidities and the corresponding optimized strain energy density, W'', are

$$E_{1111} = \rho \frac{\epsilon_1^2}{\epsilon_I^2 + \epsilon_{II}^2}, \; E_{2222} = \rho \frac{\epsilon_{II}^2}{\epsilon_I^2 + \epsilon_{II}^2}, \; E_{1122} = \rho \frac{\epsilon_I \epsilon_{II}}{\epsilon_I^2 + \epsilon_{II}^2}$$

$$W'' = 1/2\rho(\epsilon_I^2 + \epsilon_{II}^2). \tag{23}$$

Note that the optimized material is indeed orthotropic, and that the material rigidity tensor has two zero eigenvalues. Thus, the extremization of the strain energy density results in a material which is at the utmost limit of feasibility for satisfying the positivity constraints (4), and the material can only carry strain fields which are direct rescalings of the given strain field for which the optimization was undertaken. This underlines the true optimal nature of the material. Such behavior of extremized materials is also seen in the homogenization method for topology design with one given material. In dimension 2 and for a single loading condition (as here), the optimized materials there have only one zero eigenvalue corresponding to vanishing shear stiffness. The restriction used in the homogenization approach that the composite material should be constructed from some specified elastic material is a penalty that is thus evident in the form of optimized strain energies. Other aspects of extremal composites are also discussed in Cherkaev (1992).

The optimized strain energy density can be expressed as

$$W'' = 1/2\rho(\epsilon_{11}^2 + \epsilon_{22}^2 + 2\epsilon_{12}^2) \tag{24}$$

for the strains in any frame. This result shows that the optimized material has the effective energy of a linearly elastic, isotropic material with zero Poisson ratio. The optimal orthotropic material has isotropic effective properties because its axes of orthotropy are rotated to be co-aligned with the principal strain directions. Note that the corresponding isotropic zero-Poisson-ratio material has a cost which for both Case A and B is three times greater than the optimized material. The optimization of orthotropy thus provides for a considerable improvement on the performance of the material.

The above derivation demonstrates that the fixed-density optimization of problem (2) satisfies

$$\max_{\substack{\text{rigidity } E \geq 0 \\ \Psi(E) = \rho}} \min_{u \in U} \Pi(\rho, E, u)$$

$$\leq \min_{u \in U} \left\{ 1/2 \int_\Omega \rho(\epsilon_{11}^2 + \epsilon_{22}^2 + 2\epsilon_{12}^2) d\Omega - l(u) \right\} \tag{25}$$

for any fixed distribution of density ρ. Now, for a fixed density distribution ρ_0, let u_0 denote the solution to the right-hand-side linear equilibrium problem of (25), and let E^0 denote the corresponding optimal rigidities given by (23). For E^0 we have

$$\min_{u \in U} \Pi(\rho_0, E^0, u) \leq \max_{\substack{\text{rigidity } E \geq 0 \\ \Psi(E) = \rho}} \min_{u \in U} \Pi(\rho_0, E, u), \tag{26}$$

where the left-hand side is solved by u_0. This follows from the fact that the stresses corresponding to u_0 are the same for the zero-Poisson-ratio material and the orthotropic material with the rigidity tensor E^0. In the frame of principal stresses for u_0, we have the stresses

$$\begin{pmatrix} \sigma_{11} \\ \sigma_{22} \\ \sigma_{12} \end{pmatrix} = \begin{pmatrix} \rho \frac{\epsilon_I^2}{\epsilon_I^2 + \epsilon_{II}^2} & \rho \frac{\epsilon_I \epsilon_{II}}{\epsilon_I^2 + \epsilon_{II}^2} & 0 \\ \rho \frac{\epsilon_I \epsilon_{II}}{\epsilon_I^2 + \epsilon_{II}^2} & \rho \frac{\epsilon_{II}^2}{\epsilon_I^2 + \epsilon_{II}^2} & 0 \\ 0 & 0 & 0 \end{pmatrix} \begin{pmatrix} \epsilon_I \\ \epsilon_{II} \\ 0 \end{pmatrix} = \rho \begin{pmatrix} \epsilon_I \\ \epsilon_{II} \\ 0 \end{pmatrix} \tag{27}$$

for the orthotropic material and

$$\begin{pmatrix} \sigma_{11} \\ \sigma_{22} \\ \sigma_{12} \end{pmatrix} = \begin{pmatrix} \rho & 0 & 0 \\ 0 & \rho & 0 \\ 0 & 0 & \rho/2 \end{pmatrix} \begin{pmatrix} \epsilon_I \\ \epsilon_{II} \\ 0 \end{pmatrix} = \rho \begin{pmatrix} \epsilon_I \\ \epsilon_{II} \\ 0 \end{pmatrix} \tag{28}$$

for the zero-Poisson-ratio material. We have thus seen that the right-hand side of (25) equals the left-hand side (25), showing that (25) is in reality an equality and the problem

$$\max_{\substack{\text{rigidity } E \geq 0 \\ \Psi(E) = \rho}} \min_{u \in U} \Pi(\rho, E, u) \tag{29}$$

is a saddle point problem.

We have thus been able to show that the problems (7) and (8) can be reduced to the forms

$$\max_{\text{density } \rho} \min_{u \in U} \left\{ 1/2 \int_\Omega \rho(\epsilon_{11}^2 + \epsilon_{22}^2 + 2\epsilon_{12}^2) d\Omega - l(u) \right\}.$$

Case A: subject to (30)

$$0 < \rho_{\min} \leq \rho \leq \rho_{\max}, \; \int_\Omega \rho d\Omega \leq V.$$

$$\max_{\text{density } \rho} \min_{u \in U} \left\{ 1/2 \int_\Omega \rho(\epsilon_{11}^2 + \epsilon_{22}^2 + 2\epsilon_{12}^2) d\Omega - l(u) \right\}$$

Case B: subject to (31)

$$0 < \rho_{\min} \leq \rho \leq \rho_{\max}, \; \int_\Omega \rho^2 d\Omega \leq V.$$

The reduced problem for Case A is exactly equivalent to the variable-thickness design problem for a sheet made of an isotropic zero-Poisson-ratio material, with the density ρ playing the role of the thickness of the sheet. Case B is a similar problem, but with a rather unusual convex cost that favors intermediate densities. The reduced problems have a very simple form and have been studied in great detail (see, e.g., Taylor, 1969; Rossow and Taylor, 1973). Note that the problems (30), (31) are again saddle point problems (see below), and that the necessary and sufficient conditions of optimality are

$$\text{Case A:} \quad \epsilon_{11}^2 + \epsilon_{22}^2 + 2\epsilon_{12}^2 = 2\Delta \text{ if } \rho_{\min} < \rho < \rho_{\max} \tag{32}$$

$$\text{Case B:} \quad \epsilon_{11}^2 + \epsilon_{22}^2 + 2\epsilon_{12}^2 = 2\Delta\rho \text{ if } \rho_{\min} < \rho < \rho_{\max} \tag{33}$$

where Δ is a Lagrange multiplier for the volume constraint.

The problem of variable thickness-sheet design is one of the few examples of distributed parameter design for which regularization is not needed, either in the form of a relaxation or a restriction of the design space (see, e.g., Bendsøe, 1983). In fact, the existence of optimal solutions in $L^\infty(\Omega)$ (with the weak* topology) can be proved by a fairly straightforward development (see the Appendix). Moreover, a finite element discretization of the variable thickness sheet design problems is of the same form as the equivalent problem for trusses and thus a numerical optimization can make use of the very efficient optimization algorithms devised for truss problems (see Section 3). We also note that numerical experience shows that this type of problems is less prone to develop the "checkerboard-pattern" numerical instabilities associated with some implementations of the homogenization methods (c.f. Jog, Haber, and Bendsøe, 1992; Bendsøe, Diaz, and Kikuchi, 1992).

Downloaded 03 May 2010 to 171.66.16.20. Redistribution subject to ASME license or copyright; see http://www.asme.org/terms/Terms_Use.cfm

3 The Problem in Dimension $N = 3$

The above analysis generalizes to any dimension, of which dimension 3 has special interest. We make use of index notation since the extension of the formulas becomes very cumbersome even in dimension 3. All points of theoretical nature used above hold directly in any dimension, so we are primarily concerned with an algebraic generalization, based on some alternative, simple geometric arguments.

As above, we introduce specific cost functions ρ_A, ρ_B defined as

$$\text{Case A:} \quad \rho_A = E_{ijij}; \quad \text{Case B:} \quad \rho_B^2 = E_{ijkl}E_{ijkl} \tag{34}$$

so that our problem statements (7) and (8) become

Case A:

$$\max_{\substack{\text{density } \rho \\ 0<\rho_{\min}\le\rho_A\le\rho_{\max}<\infty \\ \int_\Omega \rho d\Omega \le V}} \quad \max_{\substack{\text{rigidity } E\ge 0 \\ E_{ijij}=\rho}} \quad \min_{u\in U} \Pi(\rho, E, u). \tag{35}$$

Case B:

$$\max_{\substack{\text{density } \rho \\ 0<\rho_{\min}\le\rho\le\rho_{\max}<\infty \\ \int_\Omega \rho^2 d\Omega \le V}} \quad \max_{\substack{\text{rigidity } E\ge 0 \\ E_{ijkl}E_{ijkl}=\rho^2}} \quad \min_{u\in U} \Pi(\rho, E, u). \tag{36}$$

We first note that in the subproblems

$$\text{Case A:} \quad \max_{\substack{\text{rigidity } E\ge 0 \\ E_{ijij}=\rho}} \Pi(\rho, E, u) \tag{37}$$

$$\text{Case B:} \quad \max_{\substack{\text{rigidity } E\ge 0 \\ E_{ijkl}E_{ijkl}=\rho^2}} \Pi(\rho, E, u) \tag{38}$$

the term (an inner product)

$$(E_{ijkl}\epsilon_{kl})\epsilon_{ij} \tag{39}$$

is maximal if $E_{ijkl}\epsilon_{kl}$ is proportional to ϵ_{ij}, i.e., if ϵ is an eigentensor for the rigidity tensor E. Moreover, in view of (34) and from the requirement that E is positive semi-definite, it follows that ϵ is the only eigentensor for the optimal E with nonzero eigenvalue, and this eigenvalue must be equal to ρ in both Case A and Case B. Thus, the strain energy density for the optimal material has the general expression

$$W'' = 1/2\rho\epsilon_{ij}\epsilon_{ij} \tag{40}$$

for the strains in any frame, corresponding to an isotropic, linear hyperelastic effective medium. However, as we shall see, the optimized material for any fixed strain ϵ is orthotropic for all dimensions N.

The short development above gives the optimized energy but not directly the expressions for the rigidity tensor in the Cartesian tensor basis. For this, we write ϵ in terms of the principal strains $\hat{\epsilon}_K$, $K = 1, 2, 3$. In the frame of reference given by the principal strains, the stiffness tensor is written in matrix form as

$$E = X^T \begin{pmatrix} \rho & 0 & 0 & \\ 0 & 0 & 0 & 0_{3\times 3} \\ 0 & 0 & 0 & \\ & 0_{3\times 3} & & 0_{3\times 3} \end{pmatrix} X \tag{41}$$

where X is an orthogonal transformation from the Cartesian tensor basis to an orthonormal basis of tensors where the first basis tensor is ϵ. Using the notation $\hat{\epsilon} = (\hat{\epsilon}_I, \hat{\epsilon}_{II}, \hat{\epsilon}_{III})$, $\|\hat{\epsilon}\|^2 = \hat{\epsilon}_I^2 + \hat{\epsilon}_{II}^2 + \hat{\epsilon}_{III}^2$ the resulting rigidity matrix is a straightforward generalization of the result for dimension two,

$$E = \begin{pmatrix} E_{3\times 3} & 0_{3\times 3} \\ 0_{3\times 3} & 0_{3\times 3} \end{pmatrix} \tag{42}$$

with the submatrix $E_{3\times 3}$ given by

$$E_{3\times 3} = \frac{\rho}{\|\hat{\epsilon}\|^2}\hat{\epsilon}\hat{\epsilon}^T. \tag{43}$$

Note that the rigidity tensor E given by (42) and (43) satisfies the constraints

$$E_{kkkk}E_{llll} - E_{kkll}^2 \ge 0, \text{ for all } k, l \tag{44}$$

as equalities. Also, the specific cost function ρ can be expressed as $\rho = E_{iiii}$ for both Case A and Case B.

Having thus obtained the optimized strain energy density we can now proceed by repeating ad verbatim the argument for the interchange of the max and min operators in (35) and (36). Also, by a direct generalization the existence proof carries through for the two resulting problems in dimension three as well. The resulting problems are

$$\max_{\text{density } \rho} \quad \min_{u\in U} \left\{ 1/2 \int_\Omega \rho\epsilon_{ij}\epsilon_{ij} d\Omega - l(u) \right\}.$$

Case A: subject to (45)

$$0<\rho_{\min}\le\rho\le\rho_{\max}, \quad \int_\Omega \rho d\Omega \le V.$$

$$\max_{\text{density } \rho} \quad \min_{u\in U} \left\{ 1/2 \int_\Omega \rho\epsilon_{ij}\epsilon_{ij} d\Omega - l(u) \right\}$$

Case B: subject to (46)

$$0<\rho_{\min}\le\rho\le\rho_{\max}, \quad \int_\Omega \rho^2 d\Omega \le V.$$

For problems (45) and (46) we can return to the original form of the minimum compliance problem as stated in (1), taking the development "full circle"

$$\min_{u,\rho} l(u)$$

subject to

$$\int_\Omega \rho\epsilon_{ij}(u)\epsilon_{ij}n(v)d\Omega = l(v) \text{ for all } v\in U$$

$$0<\rho_{\min}\le\rho\le\rho_{\max},$$

$$\text{and} \begin{cases} \text{for case A:} & \int_\Omega \rho d\Omega \le V \\ \text{for case B:} & \int_\Omega \rho^2 d\Omega \le V. \end{cases} \tag{47}$$

4 The Globally Optimal Potential Energy

The reduced problems (45) and (46) formulated above are again saddle point problems. The common objective function is concave in the cost density and convex in the displacements. Also, the cost density is constrained to a compact set of $L^\infty(\Omega)$ (with the weak* topology) and the objective is semi-continuous with respect to this topology as well as the topology of the displacements. This assures the existence of a saddle value of problems (45) and (46) and we can find the optimal compliance values by solving

$$\min_{u\in U} \{1/2\hat{W}_A(\epsilon) - l(u)\}, \text{ where}$$

$$\text{Case A:} \quad \hat{W}_A(\epsilon) = \max_{\substack{\text{density } \rho \\ 0<\rho_{\min}\le\rho\le\rho_{\max} \\ \int_\Omega \rho d\Omega \le V}} \int_\Omega \rho\epsilon_{ij}\epsilon_{ij} d\Omega. \tag{48}$$

$$\min_{u\in U} \{1/2\hat{W}_B(\epsilon) - l(u)\}, \text{ where}$$

$$\text{Case B:} \quad \hat{W}_B(\epsilon) = \max_{\substack{\text{density } \rho \\ 0<\rho_{\min}\le\rho\le\rho_{\max} \\ \int_\Omega \rho^2 d\Omega \le V}} \int_\Omega \rho\epsilon_{ij}\epsilon_{ij} d\Omega. \tag{49}$$

Downloaded 03 May 2010 to 171.66.16.20. Redistribution subject to ASME license or copyright; see http://www.asme.org/terms/Terms_Use.cfm

Here we can derive analytically the solution to the convex inner problems. Introducing a Lagrange multiplier λ for the cost constraints, this optimization results in the following optimized potential energies:

$$\hat{W}_A(\epsilon) = \min_{\lambda \geq 0} \left\{ \int_\Omega \max\{\rho_{\min}(\epsilon_{ij}\epsilon_{ij} - \lambda),\ \rho_{\max}(\epsilon_{ij}\epsilon_{ij} - \lambda)\}\, d\Omega + \lambda V \right\} \tag{50}$$

$$\hat{W}_B(\epsilon) = \int_\Omega \rho \epsilon_{ij}\epsilon_{ij} d\Omega, \text{ where}$$

$$\rho = \begin{cases} \rho_{\min} & \text{if } \rho_{\min} > \dfrac{1}{2\lambda}\epsilon_{ij}\epsilon_{ij} \\ \dfrac{1}{2\lambda}\epsilon_{ij}\epsilon_{ij} & \text{if } \rho_{\min} \leq \dfrac{1}{2\lambda}\epsilon_{ij}\epsilon_{ij} \leq \rho_{\max} \\ \rho_{\max} & \text{if } \rho_{\max} < \dfrac{1}{2\lambda}\epsilon_{ij}\epsilon_{ij} \end{cases} \tag{51}$$

with λ determined by

$$\int_\Omega \rho^2 d\Omega = V.$$

This implies that the design variables can be removed entirely from the problem, and the resulting problems are nonlinear and nonsmooth convex analysis problems.

For the homogenization method for topology design in dimension two, a parallel development to the above is described in Allaire and Kohn (1992) and in Jog, Haber, and Bendsøe (1992). For stress-based formulations in terms of the complementary energy principle it is possible to obtain a reduction similar to (51). However, in a strain-based formulation it is impossible to go beyond the formulation as in (45) and (46) as the homogenization method results in an optimized strain energy that is convex in the cost density.

5 Numerical Implementation

The problem of optimal design of a variable thickness sheet was first solved by Rossow and Taylor (1973) using finite element approximations for discretization of the continuum problem and an optimality criterion approach to solve the optimization problem. We note that problems (45), (46) and (50), (51) can be solved by a number of different algorithms, using a similar discretization based on a finite element approximation of the two fields of interest, namely the displacement field u and the density field ρ.

Introducing the approximations

$$u = u_k Y_k, \quad k = 1, \ldots, N$$

$$\rho = \rho_i \Xi_i, \quad i = 1, \ldots, M \tag{52}$$

of the displacement field u and the density field ρ, with nonnegative basis functions Ξ_i for ρ, we can write discretizations of problem (45)

$$\max_t \min_u \left\{ \frac{1}{2} \sum_{i=1}^M t_i u^T \mathbf{A}_i u - p^T u \right\}$$

subject to

$$0 < t_{\min} \leq t^i_{\min} \leq t_i \leq t^i_{\max} < \infty, \quad i = 1, \ldots, M$$

$$\sum_{i=1}^M t_i = V, \tag{53}$$

of problem (47),

$$\min_{t,u} p^T u,$$

subject to

$$\sum_{i=1}^M t_i u^T \mathbf{A}_i u = p^T u$$

$$0 < t_{\min} \leq t^i_{\min} \leq t_i \leq t^i_{\max} < \infty, \quad i = 1, \ldots, M$$

$$\sum_{i=1}^M t_i = V, \tag{54}$$

and of problem (48),

$$\min_{u,\lambda} \left[\frac{1}{2} \sum_{i=1}^M \max\{t^i_{\min}(u^T \mathbf{A}_i u - \lambda),\ t^i_{\max}(u^T \mathbf{A}_i u - \lambda)\} + \frac{1}{2}\lambda V - p^T u \right]. \tag{55}$$

Here $\mathbf{A} = \sum_{i=1}^M t_i \mathbf{A}_i$ is the stiffness matrix and

$$t_i = b_i \rho_i, \ b_i = \int_\Omega \Xi_i d\Omega > 0$$

$$(\mathbf{A}_i)_{kl} = b_i^{-1} \int_\Omega \Xi_i \epsilon_{pq}(Y_k)\epsilon_{pq}(Y_l) d\Omega, \quad \mathbf{A}_i \geq 0$$

$$p_k = l(Y_k). \tag{56}$$

For element-wise constant approximations of the density, t_i and $\mathbf{A}_i$ are the total element density and the specific element stiffness matrix, respectively.

It is well known (Svanberg, 1984) that the problem (54) is a convex problem in the t's only, i.e., the problem

$$\min_t p^T \left[\sum_{i=1}^M t_i u^T \mathbf{A}_i \right]^{-1} p$$

subject to

$$0 < t_{\min} \leq t^i_{\min} \leq t_i \leq t^i_{\max} < \infty, \quad i = 1, \ldots, M$$

$$\sum_{i=1}^M t_i = V \tag{57}$$

is convex. This fact follows easily from the form (53), as the inner equilibrium problem is a minimization over a set of linear functions in t, the result of which is a concave function (cf. Rockafellar, 1970). This property of convexity also holds for a discretization of problem (46).

Problems (54) and (57) lend themselves to the application of interior point algorithms as described in detail in Ben-Tal and Nemirovskii (1992) and Ringertz (1992). For example, the use of a logarithmic barrier function method has proved useful in these works. Note that for efficiency, sparse matrix techniques have been employed. These methods are readily extendible to the case of quadratic cost as for Case B.

A solution method based on problem (51) operates on the variables t as the only variables, while a different class of specialized algorithms have appeared that work with the displacements only problem (55) (Achtziger et al., 1992; Ben-Tal and Bendsøe, 1993). Again sparse techniques have been employed for these algorithms, in implementations for truss design. Extensions of these methods to the quadratic cost constraint for Case B are currently under development.

A third class of algorithms for the variable thickness sheet design problem is the so-called optimality criterion methods. These methods consist of iteration schemes based directly on the conditions of optimality for the problem statement (54) and these methods have seen widespread use for primarily compliance design (Bendsøe, Diaz, and Kikuchi, 1992; Bendsøe and Kikuchi, 1988; Cheng and Olhoff, 1982; Ped-

Downloaded 03 May 2010 to 171.66.16.20. Redistribution subject to ASME license or copyright; see http://www.asme.org/terms/Terms_Use.cfm

ersen, 1990; Rossow and Taylor, 1973; Rozvany, 1989). It is this method that has been employed to obtain the numerical result presented in this paper.

6 Example

We include numerical results for a simple plane stress model of a medium aspect ratio cantilever to exemplify the type of results that arise from the above optimal design formulation (45) (Case A). The result was generated using a $Q4$ finite element approximation of the displacement field and an element-wise constant approximation of the density field. The optimality criterion method was used for the design optimization. Figure 1 shows the result obtained in terms of the optimal moduli given by Eqs. (23) and we show the spatial variation of the three non-zero moduli, as well as the co-aligned principal directions of material and strains.

Note that a discretization using a $Q4$ finite element approximation of the displacement field and an element-wise constant approximation of the density field for problem (45) is less prone to develop the unstable checkerboard patterns reported for implementations of the homogenization approach for this type of approximation (cf. Bendsøe, Diaz, and Kikuchi, 1992; Jog, Haber, and Bendsøe, 1992). However, mild checkerboard patterns are visible around the tip of the cantilever in the present example. The unstable checkerboard patterns can be avoided by appropriate choice of finite element discretizations of displacements and density, using an analogy with the Stokes flow problem (Jog, Haber, and Bendsøe, 1992). However, this feature is not well understood at this time.

7 Conclusions and Discussion

The results of this paper provide an answer in analytical form to the question "what is the optimal configuration of material throughout a structure consistent with the objective for globally optimal design." Material configuration is represented by the elastic constitutive tensor itself, and so in the absence of (local) constraints on this tensor the results of our study provide a bound on the global objective. (A similarly general form for modeling nonlinear materials is obtained with the use of *a set of* unconstrained constitutive tensors (Taylor, (1992).) In other words, the measure of compliance predicted in the present formulation bounds from below the compliance of like structures, relative to all possible material configurations, i.e., in effect relative to any physical configuration of composite material. Of course this conclusion is limited to structures described via continuum mechanics and, in the present context, made up of locally linearly elastic materials. For present purposes "linear elasticity" is identified with the property that the separate elements of the constitutive tensor are independent of deformation state. Two example problems are treated, each having a distinct frame-invariant form for the material cost function. While local form for the optimal material does *not* depend on the choice of cost function, the spatial distribution of a "density" does depend on this choice.

Results obtained within the assumption of a locally unconstrained configuration of material may be informative toward gaining insight into the nature of efficient local structure. At the same time, clearly it would be useful to consider alternate treatments of the material design problem, forms where the problem statement is modified to provide for modeling of material with practical and/or realizable local structure. The same global formulation suffices for this purpose, but in order to simulate local structure it is necessary to introduce local constraints on the elements of the constitutive tensor. Such constraints would have the effect to penalize impractical or otherwise inadmissible features of local structure. The details of how to match particular local structure to the specific form of local constraints is the subject of another investigation. We simply note that with the appropriate form of constraint it should be possible with the present formulation to model any composite material formed from elastic constituents.

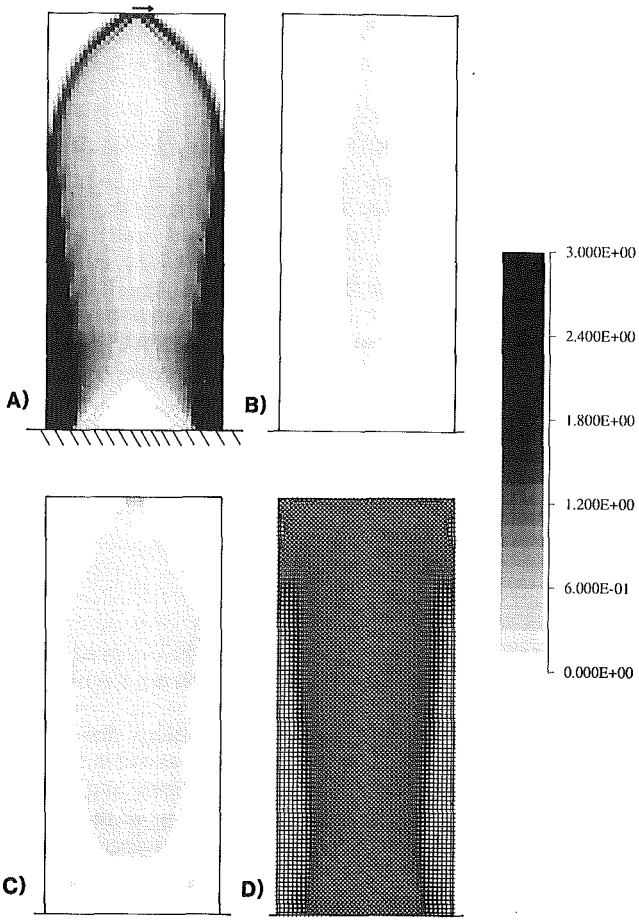


Fig. 1 The optimal design of a 12-by-5 cantilever using an optimized material for the trace cost $E_{1111} + E_{2222} + 2E_{1212}$. The cost constraint V is 6.0 and the cost density ρ is constrained by $0.001 \leq \rho \leq 3.0$. (A) The variation of E_{1111}. (B) The variation of E_{2222}. (C) The variation of E_{1122}. (D) The rotation of the material and the principal strains and the principal stresses.

Acknowledgments

This work was supported in part by the Danish Technical Research Council, through the Programme of Research on Computer Aided Design (MPB, PP). The support of the The Technical University of Denmark (RBH), The Danish Research Academy and INIC (Instituto National de Investigacao Cientifica, Portugal) (JMG), and the Danish Natural Sciences Research Council (JET) is also gratefully acknowledged.

References

Achtziger, W., Bendsøe, M. P., Ben-Tal, A., and Zowe, J., 1992, "Equivalent Displacement Based Formulations for Maximum Strength Truss Topology Design," *IMPACT of Computing in Science and Engineering*, Vol. 4, pp. 315–345.

Allaire, G., and Kohn, R. V., 1993, "Topology Optimization and Optimal Shape Design Using Homogenization," loc. cit. Bendsøe and Mota Soares, pp. 207–218.

Ben-Tal, A., and Bendsøe, M. P., 1993, "A New Method for Optimal Truss Topology Design," *SIAM J. Optimization*, Vol. 3, pp. 322–358.

Ben-Tal, A., and Nemirovskii, A., 1993, "A Interior Point Algorithm for Truss Topology Design," loc. cit. Bendsøe and Mota Soares, pp. 55–70.

Bendsøe, M. P., 1983, "On Obtaining a Solution to Optimization Problems for Solid, Elastic Plates by Restriction of the Design Space," *J. Struct. Mech.*, Vol. 11, pp. 501–521.

Bendsøe, M. P., Diaz, A., and Kikuchi, N., 1993, "Topology and Generalized

Downloaded 03 May 2010 to 171.66.16.20. Redistribution subject to ASME license or copyright; see http://www.asme.org/terms/Terms_Use.cfm

Layout Optimization of Elastic Structures," loc. cit. Bendsøe and Mota Soares, pp. 159–206.

Bendsøe, M. P., and Kikuchi, N., 1988, "Generating Optimal Topologies in Structural Design Using a Homogenization Method," *Comput. Meths. Appl. Mechs. Engrg.*, Vol. 71, pp. 197–224.

Bendsøe, M. P., and Mota Soares, C. A., 1993, *Topology Optimization of Structures*, Kluwer, Dordrecht, The Netherlands.

Cheng, G., and Olhoff, N., 1982, "Regularized Formulation for Optimal Design of Axisymmetric Plates," *Int. J. Solids Struct.*, Vol. 18, pp. 153–170.

Cea, J., and Malanowski, K., 1970, "An Example of a Max-Min Problem in Partial Differential Equations," *SIAM J. Control*, Vol. 8, pp. 305–316.

Cherkaev, A. V., 1993, "Stability of Optimal Structures of Elastic Composites," loc. cit. Bendsøe and Mota Soares, pp. 547–558.

Dacorogna, B., 1989, "Direct Methods in the Calculus of Variations," Springer-Verlag, Berlin.

Gantmacher, F. R., 1959, *The Theory of Matrices*, Vol. I, Chapter 10, Section 4, Chelsea, New York.

Jog, C., Haber, R., and Bendsøe, M. P., 1993, "A Displacement-Based Topology Design Method with Self-Adaptive Layered Materials," loc. cit. Bendsøe and Mota Soares, 1993, pp. 219–238.

Kohn, R. V., 1988, "Recent Progress in the Mathematical Modelling of Composite Materials," *Composite Material Response: Constitutive Relations and Damage Mechanisms*, G. Sih et al., eds., Elsevier, Amsterdam, The Netherlands, 1988, pp. 155–177.

Lipton, R., 1993, "On Implementation of Partial Relaxation for Optimal Structural Compliance Problems," *Optimal Design with Advanced Materials*, P. Pedersen, ed., Elsevier, Amsterdam, The Netherlands, pp. 457–468.

Lurie, K. A., and Cherkaev, A. V., 1986, "The Effective Properties of Composites and Problems of Optimal Design of Constructions," *Uspekhi Mekhaniki*, Vol. 9, No. 2, pp. (in Russian).

Lurie, K. A., Cherkaev, A. V., and Fedorov, A. V., 1982, "Regularization of Optimal Design Problems for Bars and Plates," *JOTA*, Vol. 37, (1982), pp. 499–522 (Part I); Vol. 37 (1982), pp. 523–543 (Part II); and Vol. 42 (1984), pp. 247–282 (Part III).

Pedersen, P., 1989, "On Optimal Orientation of Orthotropic Materials," *Structural Optimization*, Vol. 1, pp. 101–106.

Pedersen, P., 1990, "Bounds on Elastic Energy in Solids of Orthotropic Materials," *Structural Optimization*, Vol. 2, pp. 55–63.

Prager, W., and Taylor, J. E., 1968, "Problems of Optimal Structural Design," ASME JOURNAL OF APPLIED MECHANICS, Vol. 35, pp. 102–106.

Ringertz, U., 1992, "On Finding the Optimal Distribution of Material Properties," The Aeronautical Research Institute of Sweden.

Rockafellar, R. T., 1970, *Convex Analysis*, Princeton University Press, Princeton, NJ.

Rossow, M. P., and Taylor, J. E., 1973, "A Finite Element Method for the Optimal Design of Variable Thickness Sheets," *AIAA J.*, Vol. 11, pp. 1566–1569.

Rozvany, G. I. N., 1989, *Structural Design via Optimality Criteria*, Kluwer Academic Publishers, Dordrecht, The Netherlands.

Svanberg, K., 1984, "On Local And Global Minima in Structural Optimization," *New Directions in Optimum Structural Design*, A. Atrek, R. H. Gallagher, K. M. Ragsdell, and O. C. Zienkiewicz, eds., John Wiley and Sons, New York, pp. 327–341.

Taylor, J. E., 1969, *Maximum Strength Elastic Structural Design, Proc. ASCE*, Vol. 95, pp. 653–663.

Taylor, J. E., 1992, *Truss Topology Design for Elastic/Softening Materials*, loc. cit. Bendsøe and Mota Soares, pp. 451–467.

APPENDIX

Existence of Solutions to Minimum Compliance Design Problems With Linear Rigidity and Convex Cost Function

The variable thickness sheet problem reads

$$\underset{u,\eta}{\text{minimize}}\ l(u)$$

subject to

$$a_\eta(u, v) = l(v), \text{ for all } v \in U,$$
$$\eta \in L^\infty(\Omega),$$
$$\int_\Omega \eta(x)\, d\Omega \le V;\ 0 < \eta_{\min} \le \eta \le \eta_{\max} < \infty$$

where

$$a_\eta(u, v) = \int_\Omega \eta(x) E_{ijkl} \epsilon_{ij}(u) \epsilon_{kl}(v)\, d\Omega,\ u, v \in U,$$
$$H_0^1 \subseteq U \subseteq H^1$$

where E_{ijkl} is the fixed rigidity tensor for a given linearly elastic material and η is the thickness distribution of the sheet. It is a classical result in the field of distributed optimal control that there exists a solution to this problem (Cea and Malanovsky, 1970). This follows from the fact that the admissible thickness functions η belong to a bounded, and thus weak* compact, set in $L^\infty(\Omega)$ and the fact that the compliance, as a function of η given through the equilibrium equation, is a lower weak*-semi-continuous function. The latter property is seen by considering the following calculation for a set of feasible thickness functions η_n, $n \in \mathbf{N} \cup \{0\}$ and corresponding displacements u_n, $n \in \mathbf{N} \cup \{0\}$:

$$\begin{aligned} l(u_n) - l(u_0) &= l(u_n) - 2l(u_0) + l(u_0) \\ &= a_{\eta_n}(u_n, u_n) - 2a_{\eta_n}(u_n, u_0) + a_{\eta_0}(u_0, u_0) \\ &= a_{\eta_n}(u_n - u_0, u_n - u_0) + a_{\eta_0 - \eta_n}(u_0, u_0). \end{aligned}$$

As the bilinear forms $a_\eta(,)$ are uniformly elliptic on our set of admissible designs, it follows that

$$\liminf\ [l(u_n) - l(u_0)] \ge 0 \quad \text{whenever}$$
$$\lim_{n\to\infty} \int_\Omega [\eta_n - \eta_0]\varphi\, d\Omega = 0 \qquad \text{for all } \varphi \in L^1(\Omega).$$

The existence of solutions is easily extended to any problem for which the cost constraint is of the form $\int_\Omega f(\eta)\, d\Omega \le V$., with a convex function f: $\mathbf{R} \to \mathbf{R}$, as such constraints are lower weak*-semi-continuous (see, e.g., Dacorogna, 1989).

Downloaded 03 May 2010 to 171.66.16.20. Redistribution subject to ASME license or copyright; see http://www.asme.org/terms/Terms_Use.cfm

Transient Hygrothermal Stresses Induced in Two-Dimensional Problems by Nonlinear Theory of Coupled Heat and Moisture

Tei-Chen Chen
Associate Professor,
Assoc. Mem. ASME

Bai-Hsing Hwang
Graduate Student.

Department of Mechanical Engineering,
National Cheng Kung University,
Tainan, Taiwan, Republic of China

According to some experimental data, the value of moisture diffusivity for composite and porous materials is strongly dependent on temperature. Therefore, if the temperature variation of the problem is not confined within a small range, this coefficient may not be regarded as a constant. The purpose of this paper is to study the effect of this temperature-dependent coefficient on the hygrothermal stresses of two-dimensional composite or porous body by nonlinearly coupled hygrothermal theory. In this article, a powerful numerical method, consisting of discretizing the space domain by the finite element method, treating the time domain by Laplace and inverse Laplace transform, and handling the nonlinear term by direct Newton-Raphson iteration, is developed to study the nonlinear coupled transient problem. It can be found from a number of examples that the nonlinear and linear solutions have significant discrepancy in moisture distributions but only a small difference in temperature distributions. In the early stages of the transient period, the induced heat source by rate of moisture based on nonlinear theory is weaker than that based on linear theory. Therefore, the temperature distribution corresponding to linear theory is higher. However, in the latter stage of the transient period, the tendency is the reverse, and the temperature distribution predicted by the nonlinear theory becomes larger.

Introduction

Physically there exists a coupling effect between temperature and moisture in most materials. It has been verified that the influence of the coupling effect becomes significant as the ratio of thermal conductivity and moisture diffusivity approaches unity. For instance, the coupling effect has little influence for most metals whose values of thermal conductivity is much higher than that of moisture diffusivity. However, it becomes significant for some porous and composite materials whose thermal conductivity and moisture diffusivity have a closed value. G. S. Springer (1984) investigated the effects of environment (that includes temperature and moisture) on composite materials and obtained some basic data by experiment. C. D. Shirrell (1978) experimentally studied the interactive effect between thermal and moisture for some composite materials and obtained the data of some coefficients that are relevant to the coupling effect. Some investigators (Hartranft and Sih, 1980; Sih et al., 1980; Sin and Ogawa, 1982) utilized the previous experimental data to analyze the hygrothermal stresses of plate by the theory of coupled heat and moisture. Due to the mathematical difficulties encountered in these coupled terms, this kind of problem that admits to a closed-form solution was evidently scarce and was confined to one-dimensional problems only (Chang et al., 1992). However, if more complex geometries, multiple substances, and time-dependent boundary conditions are involved additionally in the analysis of the problem, numerical techniques, instead of analytical methods, have to be adopted. Due to the versatility of the finite element technique, considerable attention has been focused on this method in many engineering fields. Generally, the treatment of a time gradient in the finite element equations has been discretized by the time integration method (Prevost and Tao, 1983). Therefore, the solutions, at any time, shall be evaluated step by step from initial values, and an optimum algorithm for a time increment is required to achieve both numerical stability and rapid convergence (Huges and Liu, 1978a, 1978b). Due to this severe limitation on the interval of a time step, an excessive amount of computer time may be required to obtain the long-term transient solutions.

Contributed by the Applied Mechanics Division of THE AMERICAN SOCIETY OF MECHANICAL ENGINEERS for presentation at the International Mechanical Engineering Congress and Exhibition, the Winter Annual Meeting of The ASME, Chicago, IL, Nov. 6-11, 1994.

Discussion on this paper should be addressed to the Technical Editor, Professor Lewis T. Wheeler, Department of Mechanical Engineering, University of Houston, Houston, TX 77204-4792, and will be accepted until four months after final publication of the paper itself in the ASME JOURNAL OF APPLIED MECHANICS.

Manuscript received by the ASME Applied Mechanics Division, Jan. 15, 1993; final revision, Nov. 23, 1993. Associate Technical Editor: A. K. Noor.

Paper No. 94-WA/APM-7.

Copyright © 1994 by ASME
Downloaded 03 May 2010 to 171.66.16.20. Redistribution subject to ASME license or copyright; see http://www.asme.org/terms/Terms_Use.cfm

Recently, a general and efficient numerical procedure, by combining the finite element method, Laplace, and inverse Laplace transform techniques, was used to analyze the linear problems of coupled heat and moisture (Chen et al., 1992). In the present study, this method is further extended to analyze the nonlinear problems of coupled heat and moisture. The solid under consideration may be composed of composite materials with irregular geometry and subjected to arbitrary time-dependent hygrothermal loading conditions. The linearized governing equations are first formulated by the finite element technique in the Laplace transform domain. Then the solutions in the transformed domain are evaluated by direct Newton-Raphson iteration. From these transformed solution the response in the real-time domain at any time could be evaluated directly. Since the problems of coupled heat and moisture generally have a relatively long transient period, it is believed that this kind of problem is appropriate to be dealt with by the present numerical method. A number of examples are presented which demonstrates the accuracy and efficiency of the proposed method. It can be found from the numerical results that there exists a significant discrepancy between nonlinear and linear solutions in moisture distributions but only a small difference in temperature distributions for composite material T300/5208. Moreover, the transient period predicted by nonlinear coupled theory is much shorter than that by linear coupled theory.

Temperature and Moisture Distributions

Basic Equations. The derivation of the basic equations with coupled heat and moisture content in a solid has already been made and discussed (Hartranft and Sih, 1980). The associated equations of the second model described in a previous work can be expressed as follows:

$$\nabla \cdot (L \nabla T) - \frac{\partial}{\partial t}(T - \nu C) = 0 \tag{1}$$

$$\nabla \cdot (D(T) \nabla C) - \frac{\partial}{\partial t}(C - \lambda T) = 0 \tag{2}$$

where T is the temperature; C is the mass of moisture per unit volume of void space in the solid; λ is the coupling coefficient having the unit of mass per unit volume per unit temperature; ν is another coupling coefficient having the reciprocal unit of λ; and L and D are the equivalent diffusion coefficient of heat and moisture, respectively. When ν and λ vanish, Eqs. (1) and (2) reduce to the uncoupled theory. If the variation of temperature is not confined within a small range, the diffusivity of moisture D may no longer be regarded as a constant. According to the results of experimental data (Barrier, 1937; Loos and Springer, 1979; Shen and Springer, 1976; Whitney and Browning, 1978; Delasi and Whiteside, 1978; Shirrell, 1977), it reveals that the value of this coefficient for composite and porous materials is strongly dependent on temperature; generally, the higher the temperature, the larger the value of the coefficient. Its relationship with temperature can be expressed as

$$D(T) = D_0 \cdot \exp(-E_0/R_s T), \tag{3}$$

in which D_0 is a constant, E_0 is the activation energy, R_s is the gas constant, and T is the temperature measured on the Kelvin scale.

By introducing the dimensionless variables defined as

$$T^* = (T - T_i)/(T_f - T_i), \quad C^* = (C - C_i)/\lambda(T_f - T_i),$$

Eqs. (1) and (2) can then be converted to the following forms:

$$L \nabla^2 T^* = \frac{\partial}{\partial t}(T^* - \nu \lambda C^*) \tag{4}$$

$$\nabla \cdot (D(T) \nabla C^*) = \frac{\partial}{\partial t}(C^* - T^*) \tag{5}$$

where T_i and C_i are the reference temperature and moisture, respectively; T_f is the final equilibrium temperature.

The associated hygrothermal boundary conditions may be of the following types:

$$T^* = T_s^* \quad \text{on} \quad S_{h1} \tag{6a}$$

$$-K\frac{\partial T^*}{\partial n} = q_h \quad \text{on} \quad S_{h2} \tag{6b}$$

$$-K\frac{\partial T^*}{\partial n} = h_h(T^* - T_\infty^*) \quad \text{on} \quad S_{h3} \tag{6c}$$

$$C^* = C_s^* \quad \text{on} \quad S_{m1} \tag{6d}$$

$$-D_m\frac{\partial C^*}{\partial n} = q_m \quad \text{on} \quad S_{m2} \tag{6e}$$

$$-D_m\frac{\partial C^*}{\partial n} = h_m(C^* - C_\infty^*) \quad \text{on} \quad S_{m3} \tag{6f}$$

where the first three equations belong to the thermal boundary conditions while the last three denote the moisture boundary conditions. $S_{h1}(S_{m1})$ is the part of the boundary on which the temperature T^* (moisture C^*) is prescribed; $S_{h2}(S_{m2})$ is the part of the boundary on which the heat flux q_h (moisture flux q_m) is prescribed; $S_{h3}(S_{m3})$ is the part of the boundary on which the convective heat (moisture) transfer is prescribed. Each set of subsurfaces S_{h1}, S_{h2}, S_{h3}, (S_{m1}, S_{m2}, S_{m2}) forms the complete boundary surface S of the solid. K and D_m are the thermal conductivity and moisture diffusion coefficients, respectively.

The initial conditions are

$$T^*(x, y, 0) = T_0^*(x, y), \quad C^*(x, y, 0) = C_0^*(x, y). \tag{7}$$

Finite Element Formulation. The formulation associated with this initial boundary value problem of nonlinearly coupled theory is obtained in a standard way. The solid, under consideration, is divided into nonoverlapping finite elements and nodal points. Two sets of shape functions are introduced to approximate both the temperature and moisture fields on the element level.

$$T^* = \sum_{i=1}^{n} N_i T_i^* = [N]\{T^{*e}\} \tag{8}$$

$$C^* = \sum_{i=1}^{n} N_i' C_i^* = [N']\{C^{*e}\} \tag{9}$$

where $\{T^*\}$ and $\{C^*\}$ are the vectors of nodal point temperature and moisture, respectively; $[N]$ and $[N']$ are the shape functions for temperature and moisture, respectively; i is the node number; n is the number of nodes per element. In the following analysis, $[N]$ and $[N']$ are made identical to each other.

By substitution in integro-differential equations of variational form, which are derived from Eqs. (4) and (5), with Eqs. (8) and (9), the following equations expressed by matrices could be obtained:

$$\sum_{e=1}^{N}\left(\begin{bmatrix} [H] & \cdot & -\nu\lambda[H] \\ \cdot & \cdot & \cdot \\ -[H] & \cdot & [H] \end{bmatrix}\begin{Bmatrix} \{\dot{T}^{*e}\} \\ \cdots \\ \{\dot{C}^{*e}\} \end{Bmatrix} + \begin{bmatrix} L[K] & \cdot & 0 \\ \cdot & \cdot & \cdot \\ 0 & \cdot & [K'(T)] \end{bmatrix}\begin{Bmatrix} \{T^{*e}\} \\ \cdots \\ \{C^{*e}\} \end{Bmatrix} = \begin{Bmatrix} \{F_1^e\} \\ \cdots \\ \{F_2^e\} \end{Bmatrix}\right). \tag{10}$$

Downloaded 03 May 2010 to 171.66.16.20. Redistribution subject to ASME license or copyright; see http://www.asme.org/terms/Terms_Use.cfm

In Eq. (10), some matrices involving integrals are defined as

$$[H]=\int_V [N]^T[N]dV$$

$$[F_1]=\int_{S_{h2}} q_h[N]dS+\int_{S_{h3}} h_h T^*_\infty[N]dS$$

$$[K]=\int_V [M]^T[M]dV$$

$$[K'(T)]=\int_V D(T)[M]^T[M]dV$$

$$[F_2]=\int_{S_{m2}} q_m[N]dS+\int_{S_{m3}} h_m C^*_\infty[N]dS \qquad (11)$$

where $q_h(q_m)$ is the heat (moisture) flux along the boundary surface $S_{h2}(S_{m2})$; $h_h(h_m)$ is the heat (moisture) transfer coefficient; $S_{h3}(S_{m3})$ is the boundary surface wherein heat (moisture) convection is specified; $T^*_\infty(C^*_\infty)$ is the environment temperature (moisture).

Laplace Transform. The second of ordinary differential Eq. (10) is nonlinear due to the existence of nonlinear term $[K'(T)]\{C^{*e}\}$ and cannot be taken Laplace transform directly. Therefore, this equation shall be linearized first. In this article, the lineralization of equation is carried out by specifying the temperature of integral matrix $[K'(T)]$ with a known value obtained by previous iteration, which may be either the average temperature or the temperature at Gaussian points of the element.

Making application of the Laplace transform defined by

$$\bar{f}(s)=\int_0^\infty e^{-st}f(t)dt \qquad (12)$$

with respect to both sides of linearized Eq. (10), yields

$$\sum_{e=1}^{N}\left(\begin{bmatrix} s[H]+L[K] & \cdot & -s\nu\lambda[H] \\ \cdot & \cdot & \cdot \\ -s[H] & \cdot & s[H]+[K'(T^{i-1})] \end{bmatrix}\begin{Bmatrix} \{\bar{T}^{*e}\}^i \\ \cdots \\ \{\bar{C}^{*e}\}^i \end{Bmatrix}=\begin{Bmatrix} \{\bar{F}^e_1\} \\ \cdots \\ \{\bar{F}^e_2\} \end{Bmatrix}\right) \qquad (13)$$

where the superscripts i and $i-1$ denote the number of iteration; $\{\bar{T}^{*e}\}^i$ and $\{\bar{C}^{*e}\}^i$ are the ith approximation of the vectors of nodal point temperature and moisture in the transformed domain, respectively; T^{i-1} is the $i-1$th approximation of either the average temperature or the temperature at Gaussian points of the element. It reveals from numerical results that the numerical value of integral $[K'(T^{i-1})]$ will be more accurate and a more rapid convergence may be obtained in case the temperature at Gaussian points, instead of the average temperature of the element, is selected in calculation. This result is also well consistent with our estimations from the viewpoint of mathematical integration.

An accurate and efficient numerical inversion scheme for Laplace transform is adopted in this work. In accordance with the method of Durbin (1973), the relation between function in real time domain $f(t)$ and that in transform domain $f(s)$ can be expressed as

$$f(t)=\frac{e^{vt}}{\tau}\left[-\frac{1}{2}\mathrm{Re}\{\bar{f}(v)\}+\sum_{k=1}^{N}\mathrm{Re}\left\{\bar{f}\left(v+\frac{ik\pi}{\tau}\right)\right\}\cos\frac{k\pi t}{\tau}-\sum_{k=1}^{N}\mathrm{Im}\left\{\bar{f}\left(v+\frac{ik\pi}{\tau}\right)\right\}\sin\frac{k\pi t}{\tau}\right]-FI(v,t,\tau)+FA(N,v,t,\tau) \qquad (14)$$

where $FI(v, t, \tau)$ is the discretization error, and $FA(N, v, t, \tau)$ is the truncation error.

In this paper, an accurate and efficient numerical method known as Korrektur, proposed by Honig and Hirdes (1984), is used to obtain the inversion of the Laplace transform. The detail procedures to obtain solution at a specific time can be referred to (Chen and Weng, 1988).

The convergence criterion for nonlinear Eq. (10) is

$$\frac{\|\{T\}^i-\{T\}^{i-1}\|_2}{\|\{T\}^i\|_2}<\epsilon_T$$

$$\frac{\|\{C\}^i-\{C\}^{i-1}\|_2}{\|\{C\}^i\|_2}<\epsilon_C \qquad (15)$$

where $\{T\}^i$, $\{C\}^i$ and $\{T\}^{i-1}$, $\{C\}^{i-1}$ are the vectors of temperature and moisture obtained in the ith and $i-1$th iterations, respectively; $\|\ \|_2$ is used to denote the Euclidean norm of a vector; ϵ_T and ϵ_C are prescribed tolerances for temperature and moisture, respectively.

Hygrothermal Stress Distributions

The equations of motion can be expressed as

$$\sigma_{ij,j}+\rho b_i=\rho\ddot{u}_i \qquad (16)$$

where σ_{ij} are the components of stress tensor; ρ is the density; b_i is the body force vector; u_i are the components of displacement vector.

A shape function is introduced to approximate the displacement field on the element level

$$\{u\}=[N'']\{u^e\} \qquad (17)$$

where $\{u^e\}$ is the vector of nodal point displacement; $[N'']$ is the shape function for displacement. In the following analysis, $[N'']$ is identical to the shape function for temperature and moisture.

By substituting in integro-differential equations of variational form, which are derived from Eq. (16), with Eq. (17) and associated stress-strain relations, the following equations expressed by matrices could be obtained (Chen et al., 1992):

$$[M]\{\ddot{u}^e\}+[K_1]\{u^e\}+[K_2]\{T^{*e}\}+[K_3]\{C^{*e}\}=\{F^e\}. \qquad (18)$$

In Eq. (18), some matrices involving integrals are defined as

$$[M]=\int_V [N]^t\rho[N]dV$$

$$[K_1]=\int_V [B_1]^t[D_1][B_1]dV$$

$$[K_2]=\int_V [B_1]^t[E][N]dV$$

$$[K_3]=\int_V [B_1]^t[A][N]dV$$

$$\{F^e\}=\int_V [N]^t\rho\{b\}dV+\int_S [N]^t\{f\}dS \qquad (19)$$

in which

$$[B_1]=\begin{bmatrix} \frac{\partial N_1}{\partial x} & 0 & \cdot & \frac{\partial N_2}{\partial x} & 0 & \cdot & \cdot & \frac{\partial N_n}{\partial x} & 0 \\ 0 & \frac{\partial N_1}{\partial y} & \cdot & 0 & \frac{\partial N_2}{\partial y} & \cdot & \cdots & 0 & \frac{\partial N_n}{\partial y} \\ \frac{\partial N_1}{\partial y} & \frac{\partial N_1}{\partial x} & \cdot & \frac{\partial N_2}{\partial y} & \frac{\partial N_2}{\partial x} & \cdot & \cdot & \frac{\partial N_n}{\partial y} & \frac{\partial N_n}{\partial x} \end{bmatrix}$$

Downloaded 03 May 2010 to 171.66.16.20. Redistribution subject to ASME license or copyright; see http://www.asme.org/terms/Terms_Use.cfm

$$[D_1]=\frac{E(1-\mu)}{(1+\mu)(1-2\mu)}\begin{bmatrix}1 & \frac{\mu}{1-\mu} & 0\\ \frac{\mu}{1-\mu} & 1 & 0\\ 0 & 0 & \frac{1-2\mu}{2(1-\mu)}\end{bmatrix}$$

$$[E]=-\frac{\alpha' E}{1-2\mu}\begin{Bmatrix}1\\1\\0\end{Bmatrix}$$

$$[A]=-\frac{\beta' E}{1-2\mu}\begin{Bmatrix}1\\1\\0\end{Bmatrix} \tag{20}$$

where $\alpha'=(\alpha-\beta\omega)(T_f-T_i)$; $\beta'=\beta\omega(T_f-T_i)$.

Making Laplace transform of Eq. (18), it yields

$$([M]_s^2+[K_1])\{\bar{u}^e\}=\{\bar{F}^e\}-[K_2]\{\bar{T}^{*e}\}-[K_3]\{\bar{C}^{*e}\}. \tag{21}$$

Therefore, the displacement field in the real-time domain can also be evaluated through the application of Eq. (21) and the scheme of numerical inversion in the same manner as in the previous description. However, if the inertia term is disregarded, the displacement field can be directly evaluated by Eq. (18).

Numerical Applications

In order to make a comparison between the results predicted by nonlinear and linear theories, the same examples as our previous work (Chen et al., 1992) are enumerated in this article. In these examples, an eight-node isoparametric quadrilateral element is used for both temperature and displacement calculations. And the material is assumed to be homogeneous and isotropic. The evaluated values of an optimal free parameter for each nodal variable, in each example, are approximately ranged from 5.4 to 7.2. In order to accelerate the convergence of the Fourier series evenly in the domain considered, an assigned value of optimal parameter 6.4, by averaging the maximum and the minimum data, is selected as the basis of the optimal parameter for the whole domain. It could be found in the following examples that the solutions converge very well even if only a 15-term approximation of a Fourier series is used by adopting this assigned optimal parameter. Furthermore, in these examples, the effect of inertia term is insignificant and could be satisfactorily disregarded.

Example 1. Consider an infinitely long annular cylinder, having inner and outer radii r_1 and r_3, respectively, subjected to symmetrical hygrothermal loadings as follows:

$$T^*(r_1, t)=1, \quad t>0$$
$$T^*(r_3, t)=1, \quad t>0$$
$$C^*(r_1, t)=0, \quad t>0$$
$$C^*(r_3, t)=0, \quad t>0.$$

The initial conditions are

$$T^*(r, 0)=0, \quad r_1<r<r_3$$
$$C^*(r, 0)=0, \quad r_1<r<r_3.$$

The solutions are conveniently interpreted in terms of the following dimensionless variables:

$$R=\frac{r}{r_1}, \quad R_1=\frac{r_1}{r_1}=1, \quad R_3=\frac{r_3}{r_1},$$

$$\sigma_{ij}^*=\frac{\sigma_{ij}(1-2\mu)}{\alpha E(T_f-T_i)}, \quad t^*=\frac{Lt}{r_1^2}.$$

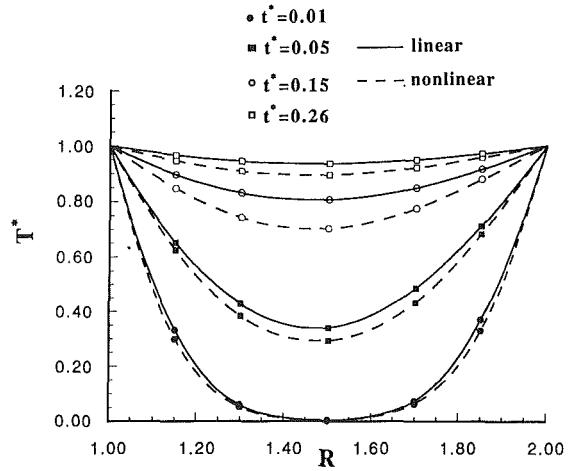


Fig. 1 Temperature T^* distributions for various times ($t^*=0.01$, 0.05, 0.15, 0.26)

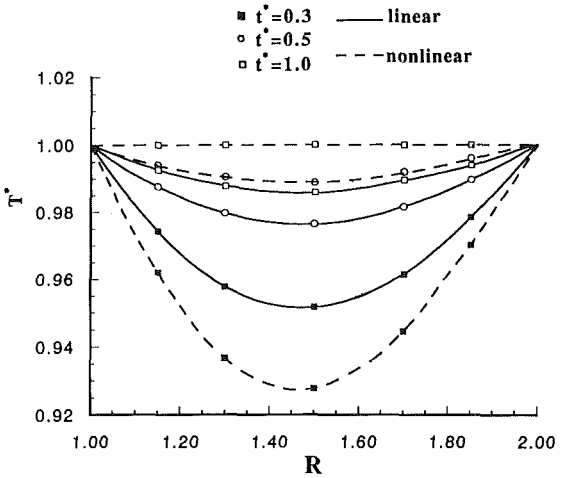


Fig. 2 Temperature T^* distributions for various times ($t^*=0.3$, 0.5, 1.0)

The numerical results are determined for a T300/5208 composite circular cylinder whose radius and material properties (Sih et al., 1986) and listed as follows:

$$R_3=2, \quad \alpha=31.3\times10^{-6}\ \text{cm/cm}\cdot{}^\circ\text{C},$$
$$\beta=2.68\times10^{-3}\ \text{cm/cm}\cdot\%\text{H}_2\text{O},$$
$$\mu=0.33, \quad D_0=1.53\times10^3\ \text{cm}^2/\text{hr}, \quad E_0=1.25\times10^4\ \text{cal/g-mole},$$
$$R_s=1.986\ \text{cal/g-mole}\cdot{}^\circ\text{C}, \quad E=64.3\ \text{GPa}, \quad \lambda=0.5\ \text{g/cm}^3\cdot{}^\circ\text{C},$$
$$\nu=0.5\ \text{cm}^3\cdot{}^\circ\text{C/g}, \quad L=7.78\times10^{-6}\ \text{cm}^2/\text{hr}.$$

The temperature and moisture distributions along the radial direction for various times are plotted in Figs. 1 to 3. The solid lines refer to the linear case, while the dashed lines refer to the nonlinear case. It can be seen from Eqs. (4) and (5) that the temperature distributions are affected by the moisture rate and the corresponding thermal boundary conditions. Furthermore, the moisture will play the role of heat source for the temperature distribution if the moisture rate is positive (i.e., $\partial C^*/\partial t^*>0$). It will act as a heat sink, however, if the moisture rate is negative (i.e., $\partial C^*/\partial t^*<0$). Similarly, the role of temperature, depending on the sign of the temperature, may be either a moisture source or a moisture sink. Since the diffusion coefficient of moisture for nonlinear theory increases very fast as the temperature rises, consequently, the total transient period for nonlinear case will be shorter than for linear case. Figure 3 indicates that the moisture will reach its max-

Downloaded 03 May 2010 to 171.66.16.20. Redistribution subject to ASME license or copyright; see http://www.asme.org/terms/Terms_Use.cfm

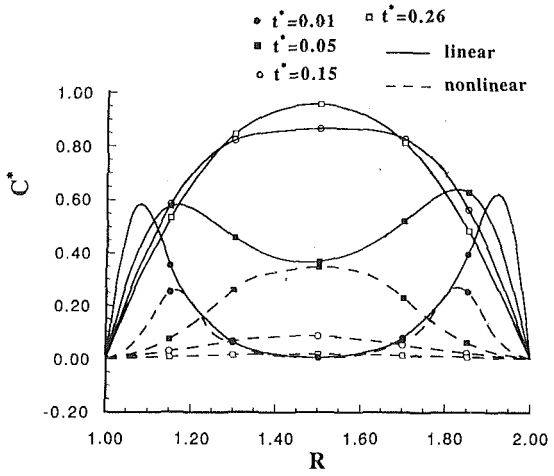


Fig. 3 Moisture C^* distributions for various times ($t^* = 0.01, 0.05, 0.15, 0.26$)

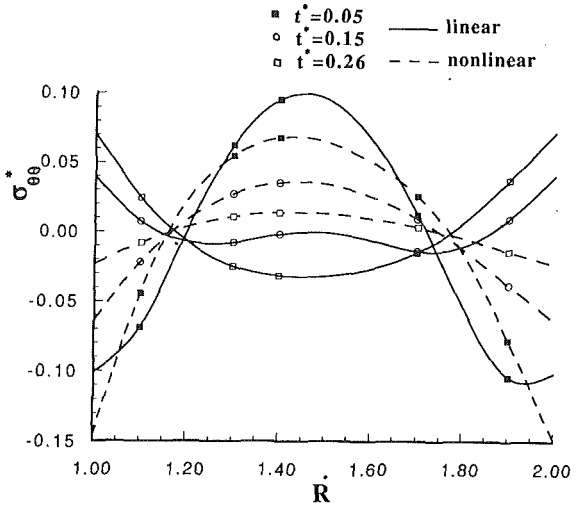


Fig. 4 Circumferential stress $\sigma^*_{\theta\theta}$ distributions for various times ($t^* = 0.05, 0.15, 0.26$)

imum value when $t^* = 0.26$ for a linear case, and $t^* = 0.05$ for a nonlinear case. It implies that $\partial C^*/\partial t^* > 0$ (heat source) when $t^* < 0.26$ for linear case and $t^* < 0.05$ for a nonlinear case, while $\partial C^*/\partial t^* < 0$ (heat sink) when $t^* > 0.26$ for a linear case and $t^* > 0.05$ for a nonlinear case. Moreover, compared with the situations of linear case, the variation of moisture for nonlinear case is small and then the induced strength of heat source or heat sink becomes weaker. Therefore, the temperature distributions, as shown in Figs. 1 and 2, for the nonlinear case are always lower than those for the linear case in the early stage of transient period. (It should be noted that the y coordinate, as shown in Fig. 2, has a very small range, i.e., 0.92–1.00; therefore, they only represent a small difference between the linear and nonlinear results.) However, in the later stage of transient period, the temperature distributions for nonlinear case will conversely be higher than for the linear case. In the same manner, the moisture distributions are also affected by the temperature rate and the boundary conditions of the moisture. Because the temperature rate remains positive at all times, the temperature will always play the role of moisture source. For both nonlinear and linear cases, at the beginning of the transient period, the temperature rate near the surfaces is greater than that near the core. This implies that the moisture source near the surfaces is stronger than that in the core region. Consequently, the moisture distributions will reveal double peaks near the inner and outer surfaces and will become concave around the core region. As the time increases, the temperature will gradually approach its steady value, and the temperature rate becomes small. Because of the diffusion of moisture through the boundary surfaces, the moisture distribution will gradually decrease and have only one peak around the core region. Finally, it becomes null everywhere in the steady state. Since the diffusion coefficient of moisture for nonlinear theory increases with increasing temperature, the moisture flux passing through the boundary is higher. Therefore, compared with the situations of linear case, the nonlinear case reflects a lower moisture peak and a shorter transient period. The distributions of circumferential stress for various times are plotted in Fig. 4. Under these thermal and moisture loading conditions it is seen that the circumferential stress for the nonlinear case always stays compressive near both surfaces and becomes tensile around the core region. However, this tendency is not always true for the linear case.

Example 2. A $d \times d$ square cylinder with elliptical hole, shown in Fig. 5, with semi-major and semi-minor axes a and b, respectively, is subjected to surface heating on its traction-free inner surface by sudden exposure to a temperature $T^* = 1.0$

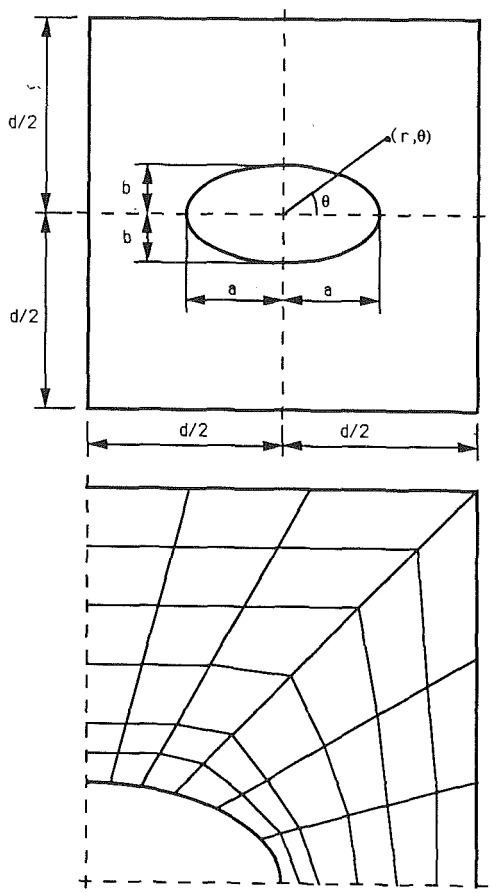


Fig. 5 Geometry of a square cylinder with an elliptical hole

at $t > 0$, and remains its original temperature on its traction-free outer surface. These boundary conditions could be expressed as follows:

$$T^* = H(t), \quad C^* = 0, \quad \text{at the inner surface when } t > 0$$

$$T^* = 0, \quad C^* = 0, \quad \text{at the outer surface when } t > 0.$$

The initial conditions are

$$T^* = 0, \quad C^* = 0, \quad \text{when } t = 0.$$

The solutions are conveniently interpreted in terms of the following dimensionless variables:

Downloaded 03 May 2010 to 171.66.16.20. Redistribution subject to ASME license or copyright; see http://www.asme.org/terms/Terms_Use.cfm

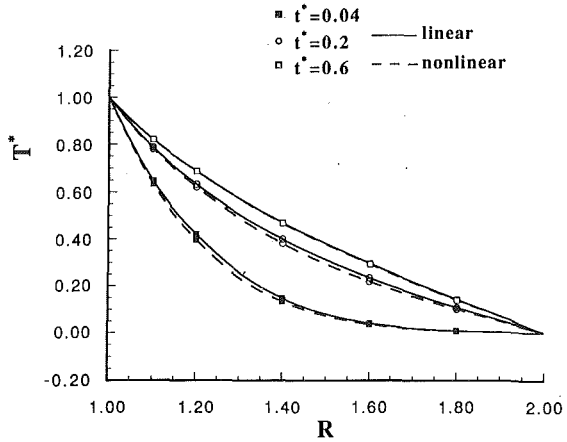


Fig. 6 Temperature T^* distributions along the direction $\theta = 0$ deg for various times ($t^* = 0.04, 0.2, 0.6$)

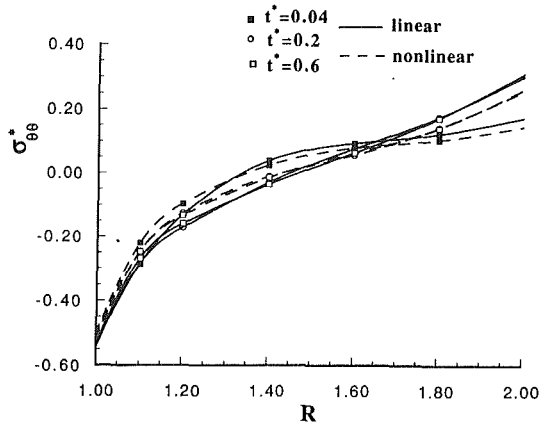


Fig. 7 Circumferential stress $\sigma^*_{\theta\theta}$ distributions along the direction $\theta = 0$ deg for various times ($t^* = 0.04, 0.2, 0.6$)

$$R = \frac{r}{a}, \quad t^* = \frac{Lt}{a^2}, \quad \sigma^*_{ij} = \frac{\sigma_{ij}(i-2\mu)}{\alpha E(T_f - T_i)}.$$

Suppose the selected material is the same as the previous example and the geometry of the cylinder is

$$\frac{a}{b} = 2, \quad \frac{d}{a} = 4.$$

The problem is symmetric about both the x and y axes. Thus only a quarter of the cylinder need to be considered. The temperature distributions for various times along the direction $\theta = 0$ deg are shown in Fig. 6. The circumferential stress distributions for various times along the same direction are plotted in Fig. 7. It is seen, in this example, that there still exists a significant discrepancy between nonlinear and linear solutions. The maximum hygrothermal stress is taken place at the inner surface of the semi-major axis.

Discussion and Conclusion

In this study, a general finite element method/Laplace transform model, that is originally restricted to deal with the linear transient problem only, is extended here to deal with the plane problems of nonlinearly coupled temperature and moisture. To illustrate the efficiency of the present method, two different examples are analyzed. Since the present model takes off the time dimension by the Laplace transform, the solution of a specific location at a specific time, that is either long or short, can be evaluated directly. This kind of approach is quite different from the conventional procedure that treats the time domain by the time integration method. The latter process will thus lead to a step-by-step or recurrence calculation and is appropriate to evaluate a short-time solution. The only shortcoming of the present method is concerned with the treatment of the numerical Laplace inversion, which required more computer time (generally, it is equivalent to take 15 times in solving equation if an optimal free parameter is given) than step-by-step integration schemes. However, it is believed that the present method is still more economical and better than the classical time-integration techniques in case a long-time solution is required, since several hundred or more time steps may be required to achieve this long-time solution by time-integration techniques. Furthermore, it can be seen in all the examples that the discrepancy in transient solution between nonlinear and linear theories is significant for the composite material T300/5208. Therefore, the nonlinear effect originated from the coefficient of moisture diffusion shall be considered in analysis in case the temperature variation of the body is not confined to a narrow range.

Acknowledgments

This work was supported by the National Science Council of Taiwan, R.O.C. (Grant No. NSC 82-0401-E-006-060).

References

Barrier, R. M., 1937, "Nature of the Diffusion in Rubber," *Nature*, Vol. 140, pp. 106–107.

Belystchko, T., and Mullen, R., 1978, "Stability of Explicit-Implicit Mesh Partitions in Time Integration," *Int. J. Num. Meths. Eng.*, Vol. 12, pp. 1575–1586.

Chang, W. J., Chen, T. C., and Weng, C. I., 1992, "Transient Hygrothermal Stresses in an Infinitely Long Annular Cylinder: Coupling of Heat and Moisture," *J. Therm. Stresses*, Vol. 14, pp. 439–454.

Chen, T. C., and Weng, C. I., 1988, "Generalized Coupled Transient Thermoelastic Plane Problems by Laplace Transform/Finite Element Method," ASME JOURNAL OF APPLIED MECHANICS, Vol. 55, pp. 377–382.

Chen, T. C., Weng, C. I., and Chang, W. J., 1992, "Transient Hygrothermal Stresses Induced in General Plane Problems by Theory of Coupled Heat and Moisture," ASME JOURNAL OF APPLIED MECHANICS, Vol. 59, pp. S10–S16.

Delasi, R., and Whiteside, J. B., 1978, "Effect of Moisture on Epoxy Resins and Composites," *Advanced Composite Materials—Environmental Effects*, J. R. Vinson, ed., ASTM-STP-658, pp. 2–20.

Dubin, F., 1973, "Numerical Inversion of Laplace Transform: An Effective Improvement of Nubner and Abate's Method," *Comput. J.*, Vol. 17, pp. 371–376.

Hartranft, R. J., and Sih, G. C., 1980, "The Influence of the Soret and Dufour Effects on the Diffusion of Heat and Moisture in Solids," *Int. J. Engng. Sci.*, Vol. 18, pp. 1375–1383.

Honig, G., and Hirdes, U., 1984, "A Method for the Numerical Inversion of Laplace Transform," *J. Comput. Appl. Maths.*, Vol. 10, pp. 00.113–132.

Hughes, T. J. R., and Liu, W. K., 1978, "Implicit-Explicit Finite Elements in Transient Analysis: Stability Theory," ASME JOURNAL OF APPLIED MECHANICS, Vol. 45, pp. 371–374.

Hughes, T. J. R., and Liu, W. K., 1978, "Implicit-Explicit Finite Elements in Transient Analysis: Implementation and Numerical Examples," ASME JOURNAL OF APPLIED MECHANICS, Vol. 45, pp. 375–378.

Loos, A. C., and Springer, G. S., 1979, "Moisture Absorption of Graphite/Epoxy Composites Immersed in Liquids and in Humid Air," *J. Composite Materials*, Vol. 13, pp. 131–147.

Shen, C. H., and Springer, G. S., 1976, "Moisture Absorption and Desorption of Composite Materials," *J. Composite Materials*, Vol. 10, pp. 2–20.

Shirrell, C. D., 1976, "Moisture Diffusion in Advanced Composite Resin Matrix Laminates," AFMU Progress Report, Bergamo Center.

Shirrell, C. D., 1978, *Diffusion of Water Vapor in Graphite/Epoxy Composites: Advanced Composite Materials—Environmental Effects*, J. R. Vinson, ed., ASTM, STP659, pp. 19–42.

Sih, G. C., Shih, M. T., and Chou, S. C., 1980, "Transient Hygrothermal Stresses in Composites: Coupling of Moisture and Heat with Temperature Varying Diffusivity," *Int. J. Engng. Sci.*, Vol. 18, pp. 19–42.

Sih. G. C., and Ogawa, A., 1982, "Transient Thermal Change on a Solid Surface: Coupled Diffusion of Heat and Moisture," *J. Therm. Stresses*, Vol. 5, pp. 265–282.

Sih, G. C., Michopoulos, J. G., and Chou, S. C., 1986, *Hygrothermoelasticity*, Kluwer Academic Publishers, Dordrecht, The Netherlands.

Springer, G. S., 1984, *Environmental Effects on Composite Materials*, Vol. 2, Technomic Publishing Company.

Whitney, J. M., and Browning, C. E., 1978, "Some Anomalies Associated with Moisture Diffusion in Epoxy Matrix Composite Materials," *Advanced Composite Materials—Environmental Effects*, J. R. Vinson, ed., ASTM STP-658, pp. 43–60.

Downloaded 03 May 2010 to 171.66.16.20. Redistribution subject to ASME license or copyright; see http://www.asme.org/terms/Terms_Use.cfm

Theoretical and Experimental Analysis of the Forced Response of Sagged Cable/Mass Suspensions

S.-P. Cheng
Research Assistant,
Assoc. Mem. ASME.

N. C. Perkins
Assistant Professor,
Mem. ASME.

Department of Mechanical Engineering
and Applied Mechanics,
The University of Michigan,
Ann Arbor, MI 48109-2125

This study examines the forced response of a sagged elastic cable supporting an array of discrete masses. Such systems arise, for instance, in ocean engineering applications employing cable hydrophone arrays. The excitation considered is harmonic and normal to the cable and may, for instance, approximate prescribed environmental loading. An asymptotic model is presented that describes the linear forced response of a cable/mass suspension having small equilibrium curvature. Closed-form expressions for the Green's function to an associated boundary value problem are obtained using a transfer matrix formulation. The derived Green's function is utilized to construct integral representations for steady-state response under boundary and/or domain excitation. Solutions obtained for a variety of domain loading distributions demonstrate the utility and efficiency of this solution strategy. The theoretical response predictions are verified through experimental measurements of the natural frequency spectrum and frequency response of laboratory cable/mass suspensions.

Introduction

Cables are lightweight, flexible structural elements capable of transmitting forces, carrying payloads and conducting signals over long distances. These distinctive characteristics make cables well suited to many engineering applications, particularly in the marine environment. There, for example, cables are used in the mooring of vessels and platforms and in the towing of hydrophones, underwater cameras, and other instruments. In applications, however, submerged cables are excited by a variety of sources and, in particular, by the fluid vortices shed by cross-flows. The vortex shedding may induce resonant cable response whenever the frequency of vortex shedding is close to a natural frequency of the cable. This resonant condition, commonly refer to as *strumming* (Griffin, 1985), increases cable drag forces and promotes cable fatigue. In addition, strumming may increase cable acoustic emissions and generate spurious readings from hydrophones.

For the purpose of predicting the dynamic behavior of cables and the onset of strumming, several studies focus first on the free response of cable suspensions. For sagged *bare* cable suspensions, the calculation of free response follows in a relatively straightforward manner using a well-established theory for linear cable dynamics (Irvine and Caughey, 1974; Triantafyllou, 1984). The calculation is greatly complicated by the addition of many (often hundreds of) attached masses (e.g., cable hydrophone arrays). In such cases, previous investigators (Rosenthal, 1981; Griffin and Rosenthal, 1985) have developed numerical strategies for analyzing the linear vibration characteristics of sagged cable/mass systems. These numerical methods, however, suffer from convergence difficulties that limit their application to relatively low-order vibration modes and small numbers of attached masses. An alternative strategy was developed by the authors and based upon an asymptotic model for cable/mass suspensions with small equilibrium curvature (Cheng, 1992). Closed-form transfer matrix methods were used to calculate the linear response of suspensions that support a single mass (Cheng and Perkins, 1992a) or numerous masses (Cheng and Perkins, 1992b). This strategy allows the determination of relatively high-order vibration modes even for arrays supporting large numbers of attached masses.

The present study provides an important extension to those above by considering the forced response of cable/mass suspensions. In doing so, this study also provides a simple means to validate the asymptotic model using laboratory measurements of frequency response. The excitation considered herein is, in general, distributed, harmonic, and normal to the cable. Such excitation might, for instance, represent an approximation to the distributed lift forces imparted to a suspension in a cross-flow.

This paper is organized as follows. First, an asymptotic

Contributed by the Applied Mechanics Division of THE AMERICAN SOCIETY OF MECHANICAL ENGINEERS for publication in the ASME JOURNAL OF APPLIED MECHANICS.

Discussion on this paper should be addressed to the Technical Editor, Professor Lewis T. Wheeler, Department of Mechanical Engineering, University of Houston, Houston, TX 77204-4792, and will be accepted until four months after final publication of the paper itself in the ASME JOURNAL OF APPLIED MECHANICS.

Manuscript received by the ASME Applied Mechanics Division, Jan. 29, 1993; final revision, June 15, 1993. Associate Technical Editor: F. Y. M. Wan.

Downloaded 03 May 2010 to 171.66.16.20. Redistribution subject to ASME license or copyright; see http://www.asme.org/terms/Terms_Use.cfm

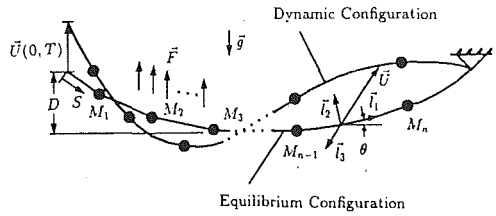


Fig. 1 Definition diagram for horizontally suspended sagged cable supporting an array of n attached masses (M_i, $i = 1, 2, \cdots n$). S denotes arc length coordinate measured along the planar equilibrium curve, and U denotes the displacement from equilibrium decomposed into components aligned with the Frenet triad (l_1, l_2, l_3). The masses M_i are located at $S = S_i$, $i = 1, 2, \cdots n$.

model is presented that describes the linear forced response of a cable/mass suspension having small equilibrium curvature. Closed-form expressions for the Green's function to an associated boundary value problem are then obtained using a transfer matrix formulation. The derived Green's function is utilized to construct integral representations for steady-state response under boundary and/or domain excitation. Solutions obtained for a variety of domain loading distributions demonstrate the utility and efficiency of this solution strategy. The theoretical predictions of the cable/mass system response are verified through experimental measurements of frequency response characteristics for laboratory cable suspensions. Natural frequency spectra and frequency response functions of a representative cable/mass system are obtained using experimental modal testing techniques.

Asymptotic Model

The present study considers a sagged elastic cable of length L supporting an arbitrary number (n) of discrete masses and suspended between two horizontal supports; refer to Fig. 1. Under gravity, the cable/mass suspension forms a planar equilibrium curve having maximum sag D. The masses M_i, $i = 1, 2, \cdots n$, are attached to the cable at positions $S = S_i$, $i = 1, 2, \cdots n$, respectively, where S denotes an arc length coordinate measured from the left support along the equilibrium profile. The three-dimensional displacement of the cable about equilibrium $U(S, T)$ is decomposed into the components $U_1(S, T)$, $U_2(S, T)$ and $U_3(S, T)$, resolved along the local tangential l_1, normal l_2, and binormal l_3 directions of the equilibrium curve. Due to the masses, equilibrium curve is piecewise smooth and the unit vectors l_1 and l_2 exist on the open subintervals defined by the mass locations. The right support at $S_{n-1} = L$ is fixed while the left support at $S_0 = 0$ may execute a prescribed three-dimensional displacement $U(0, T) = R_1(T)l_1 + R_2(T)l_2 + R_3(T)l_3$. Distributed external excitation applied in the cable domain is described by $F(S, T) = F_1 l_1 + F_2 l_2 + F_3 l_3$.

Following (Cheng and Perkins, 1992b), the equations of motion for an elastic cable supporting an array of discrete masses are derived from Hamilton's principle. Here, the asymptotic form of this model is presented which governs the linear response of sagged suspensions having small equilibrium curvature (sag) and level supports. Following nondimensionalization, the equation governing forced response in the (in-plane) normal direction becomes (Cheng and Perkins, 1992b)

$$v_t^2 u_{2,ss} - k^2 v_l^2 \left[1 + \sum_{i=1}^{n} m_i \delta(s - s_i)\right] \left[\int_0^1 u_2(\eta, t)\, d\eta + \sum_{i=1}^{n} m_i u_2(s_i, t)\right] + f_2 = \left[1 + \sum_{i=1}^{n} m_i \delta(s - s_i)\right] u_{2,tt}, \quad 0 < s < 1 \tag{1}$$

with boundary conditions

$$u_2(0, t) = r_2(t), \; u_2(1, t) = 0. \tag{2}$$

In arriving at (1), the excitation is considered to be normal the cable ($F_1 = R_1 = 0$) and the following nondimensional parameters are used

$$s = \frac{S}{L}, \; t = \frac{T}{\sqrt{L/g}}, \; f_2 = \frac{F_2}{\rho g L}, \; r_2 = \frac{R_2}{L}, \; u_j = \frac{U_j}{L}, \; j = 1,2,3$$

$$v_t^2 = \frac{1}{k} = \frac{P_o}{\rho g L}, \; v_l^2 = \frac{EA}{\rho g L}, \; s_i = \frac{S_i}{L}, \; m_i = \frac{M_i}{\rho L}, \; i = 1, 2, \cdots n, \tag{3}$$

where P_o is the horizontal component of the equilibrium cable tension and EA is the cable section stiffness. Note that the parameters v_t^2 and v_l^2 are measures of the speed of propagation of transverse and longitudinal waves, respectively. Note also that the equation of motion governing out-of-plane (bi-normal) response problem is a special case of that governing in-plane (normal) response (1) recovered in the limit of vanishing equilibrium curvature $k \to 0$. In this regard, solutions for out-of-plane response follow in a straightforward manner from those for in-plane response and are not pursued herein. Instead attention is presently focused on the (more complex) in-plane response problem.

Integral Solution for Harmonic Excitation. A general solution for in-plane response under harmonic domain and/or boundary excitation is obtained by first prescribing the excitation

$$f_2(s, t) = -p(s) e^{i\omega_f t} \tag{4}$$

and

$$u_2(0, t) = r(t) = \gamma e^{i\omega_f t}. \tag{5}$$

In the above, $p(s)$ is the amplitude of the excitation/length along the suspension domain, γ is the amplitude of the prescribed end displacement (at $s = 0$), and ω_f is the excitation frequency. The steady-state response of the suspension is described by the separable solution

$$u_2(s, t) = v(s) e^{i\omega_f t}, \tag{6}$$

where $v(s)$ represents the response amplitude of the cable/mass system.

Substitution of the (4)–(6) into (1) and (2) leads to the boundary value problem governing the response amplitude $v(s)$:

$$\mathbf{L}v = v'' + \Omega_f^2 \left[1 + \sum_{i=1}^{n} m_i \delta(s - s_i)\right] v - \lambda^2 \left[1 + \sum_{i=1}^{n} m_i \delta(s - s_i)\right] \times \left[\int_0^1 v(\eta)\, d\eta + \sum_{i=1}^{n} m_i v(s_i)\right] = \phi, \tag{7}$$

with boundary conditions

$$v(0) = \gamma, \; v(1) = 0. \tag{8}$$

In (7), $\mathbf{L}$ denotes the linear operator defining the left-hand side of the field equation and

$$\Omega_f = \frac{\omega_f}{v_t}, \; \phi(s) = \frac{p(s)}{v_t^2}, \; \lambda^2 = \frac{v_l^2}{(v_t^2)^3}. \tag{9}$$

Here, λ^2 is the *cable parameter* introduced by Irvine and Caughey (1974) which describes the geometric and material properties of the cable.

The inner product of the (as yet undetermined) Green's function $G(s, \xi)$ and $\mathbf{L}v$ over the cable segment yields, after integrating by parts,

$$\int_0^1 G\mathbf{L}v\, d\xi = (Gv' - G_{,\xi} v)\,|_0^1 + \int_0^1 v\mathbf{L}^* G\, d\xi, \tag{10}$$

where $\mathbf{L}^*$ is the formal adjoint operator of $\mathbf{L}$. Solution of the

Downloaded 03 May 2010 to 171.66.16.20. Redistribution subject to ASME license or copyright; see http://www.asme.org/terms/Terms_Use.cfm

boundary value problem (7) and (8) follows from selecting G such that

$$\mathbf{L}^* G(\xi, s) = \delta(\xi - s), \tag{11}$$

and

$$G(0, s) = G(1, s) = 0. \tag{12}$$

Note that as the operator $\mathbf{L}$ is formally self-adjoint ($\mathbf{L}^* = \mathbf{L}$), the Green's function is symmetric in its arguments (Stakgold, 1979). Thus, $G(\xi, s)$ satisfies

$$\mathbf{L}G(s, \xi) = \delta(s - \xi), G(0, \xi) = G(1, \xi) = 0, \tag{13}$$

and, from (10), the (steady-state) response solution is

$$v(s) = -G_{,\xi}(s, 0)\gamma + \int_0^1 G(s, \xi)\phi(\xi)d\xi. \tag{14}$$

The first and second terms on the right-hand side of (14) capture the response due to boundary and domain excitation, respectively.

Calculation of Green's Function. The Green's function can be computed by closed-form analysis in a manner similar to that used to compute the eigensolutions of (Cheng and Perkins, 1992b). To facilitate the calculation of the Green's function, the cable is divided into $n + 2$ subdomains defined by the mass locations $s = s_i$, $i = 1, 2, \cdots n$, the position of the delta distribution $s = \xi$, and the two boundaries, $s_0 = 0$ and $s_{n+1} = 1$. For $s_{j-1} < \xi < s_j$, $j = 1, 2, \cdots n + 1$, the new spatial parameters ξ_i are defined as

$$\xi_i = \begin{cases} s_i, & i = 0, \cdots, j-1 \\ \xi, & i = j \\ s_{i-1}, & i = j+1, \cdots, n+2 \end{cases} \tag{15}$$

and the length of each subdomain is given by $l_{\xi_i} = \xi_i - \xi_{i-1}$, $i = 1, 2, \cdots n + 2$. Furthermore, the subscripts for the attached masses are redefined as

$$m_{\xi_i} = \begin{cases} m_i, & i = 1, \cdots, j-1 \\ 0, & i = j \\ m_{i-1}, & i = j+1, \cdots, n+1. \end{cases} \tag{16}$$

With the above notation, the boundary value problem defining $G(s, \xi)$ becomes

$$\frac{d^2 G_i}{ds^2} + \Omega_f^2 G_i = c \text{ on } \xi_{i-1} < s < \xi_i \quad i = 1, 2, \cdots n+2, \tag{17}$$

with the boundary conditions

$$G_1(0, \xi) = 0, \quad G_{n+2}(1, \xi) = 0, \tag{18}$$

and the matching conditions at the locations of the attached masses

$$G_{i+1}(\xi_i) - G_i(\xi_i) = 0,$$

$$\frac{dG_{i+1}(\xi_i)}{ds} - \frac{dG_i(\xi_i)}{ds} + \Omega^2_f m_{\xi_i} G_i(\xi_i) = m_{\xi_i} c,$$

$$i = 1, \cdots, j-1 \text{ and } j+1, \cdots, n+1, \tag{19}$$

and the matching conditions at the location $s = \xi$

$$G_{j+1}(\xi_j) - G_j(\xi_j) = 0, \quad \frac{dG_{j+1}(\xi_j)}{ds} - \frac{dG_j(\xi_j)}{ds} = 1. \tag{20}$$

In the above equations, c represents a dynamic cable tension factor (Cheng and Perkins, 1992b) and is defined by

$$c = \lambda^2 \left[\int_0^1 G(\eta, \xi)d\eta + \sum_{i=1}^{n+1} m_{\xi_i} G_i(\xi_i, \xi) \right]. \tag{21}$$

The general solution of (17) is given by

$$G_i(s, \xi) = A_i \sin [\Omega_f (s - \xi_{i-1})] + B_i \cos [\Omega_f (s - \xi_{i-1})] + \frac{c}{\Omega_f^2},$$

$$\xi_{i-1} < s < \xi_i \quad i = 1, 2, \cdots n+2 \tag{22}$$

in terms of the constants of integration (A_i, B_i) for the ith subdomain. Substitution of (22) into (19) and (20) yields the recursion formulae for the constants of integration:

$$\begin{bmatrix} A_{i+1} \\ B_{i+1} \end{bmatrix} = \begin{bmatrix} \cos \Omega_f l_{\xi_i} - m_{\xi_i}\Omega_f \sin \Omega_f l_{\xi_i} & -\sin \Omega_f l_{\xi_i} - m_{\xi_i}\Omega_f \cos \Omega_f l_{\xi_i} \\ \sin \Omega_f l_{\xi_i} & \cos \Omega_f l_{\xi_i} \end{bmatrix} \begin{bmatrix} A_i \\ B_i \end{bmatrix}, \tag{23}$$

for all $i = 1, \cdots, J-1, J+1, \cdots, n+1$, and

$$\begin{bmatrix} A_{j+1} \\ B_{j+1} \end{bmatrix} = \begin{bmatrix} \cos \Omega_f l_{\xi_j} & -\sin \Omega_f l_{\xi_j} \\ \sin \Omega_f l_{\xi_j} & \cos \Omega_f l_{\xi_j} \end{bmatrix} \begin{bmatrix} A_j \\ B_j \end{bmatrix} + \begin{bmatrix} 1 \\ 0 \end{bmatrix}. \tag{24}$$

Use of the first boundary condition of (18) yields $B_1 = -c/\Omega_f^2$. It is then observed that all the coefficients A_i and B_i, $i = 2, 3, \cdots n + 2$, depend only on two unknowns A_1 and c which have to be chosen to satisfy the remaining boundary condition

$$G_{n+2}(1, \xi) = 0, \tag{25}$$

and the definition for c (21). These two unknowns can be evaluated by simultaneous solution of (25) and (21) using standard Newton-Raphson iteration.

As formulated above, the Green's function can be evaluated for any (nonresonant) frequency ω_f and any position $s = \xi$. By using the symmetry property; $G(s, \xi) = G(\xi, s)$, the complete Green's function over the two-dimensional (s, ξ) space can be determined in an efficient manner.

Theoretical and Experimental Results

To illustrate the characteristics of the Green's function, the example of (Cheng and Perkins, 1992b) is re-examined and consists of a cable supporting four equally spaced ($s_i - s_{i-1} = 0.2$, $i = 1, \cdots 5$), equal masses ($m_i = 0.1462$, $i = 1, \cdots 4$). In Fig. 2, the Green's function of this symmetric cable/mass suspension is illustrated over the entire domain of definition, $0 < s < 1$ and $0 < \xi < 1$, for the case: $\lambda/\pi = 2$, $\Omega_f/\pi = 4$. The surface $G(s, \xi)$ exhibits symmetry with respect to the (diagonal) plane $s = \xi$, as required. Furthermore, this Green's function is also symmetric to the (other diagonal) plane $s = 1 - \xi$. This latter symmetry, which results from the fact that this cable/mass system is symmetric with respect to the cable midspan is destroyed when the mass array is no longer symmetric (Cheng, 1992). Note that slope of the Green's function is discontinuous along $s = \xi$ and at the locations of the attached masses $s = s_i$ and $\xi = s_i$, $i = 1, \cdots 4$. Note also that the Green's function achieves its greatest values mainly in the neighborhood of the delivered excitation point, $s = \xi$. This is expected for this nonresonant case.

The derived Green's function above is presently employed to determine the steady-state response to harmonic end excitation by evaluating the first term in (14). As an example, Fig. 3 illustrates the response amplitude of the case considered in Fig. 2 ($\Omega_f = 4$, $\lambda/\pi = 2$). Figure 3 confirms that, for this nonresonant case, the response is greatest near the driven end.

Evaluation of the second term in (14) provides the amplitude of steady-state response due to harmonic domain excitation. To highlight this capability, three types of harmonic domain excitation are presently considered: (a) uniformly distributed excitation, (b) (equal) concentrated excitation applied at each attached mass, and (c) sinusoidally distributed excitation. Non-

Downloaded 03 May 2010 to 171.66.16.20. Redistribution subject to ASME license or copyright; see http://www.asme.org/terms/Terms_Use.cfm

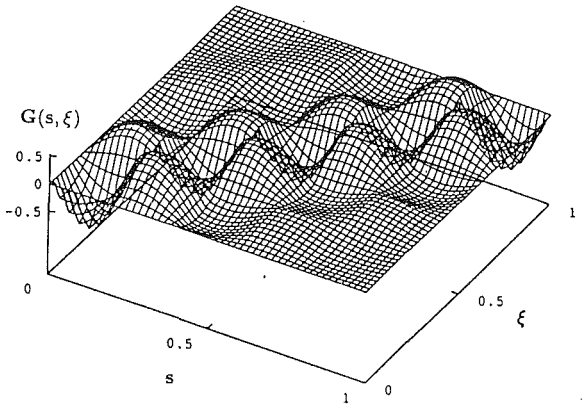


Fig. 2 The Green's function of a symmetric cable/mass suspension defined by $\lambda/\pi = 2$, $m_i = 0.1462$, $s_1 = 0.2$, $s_2 = 0.4$, $s_3 = 0.6$, $s_4 = 0.8$; refer to Cheng and Perkins (1992b). The Green's function is plotted over the domain $0 < s < 1$ and $0 < \xi < 1$ for a (nonresonant) case: $\Omega_f/\pi = 4$.

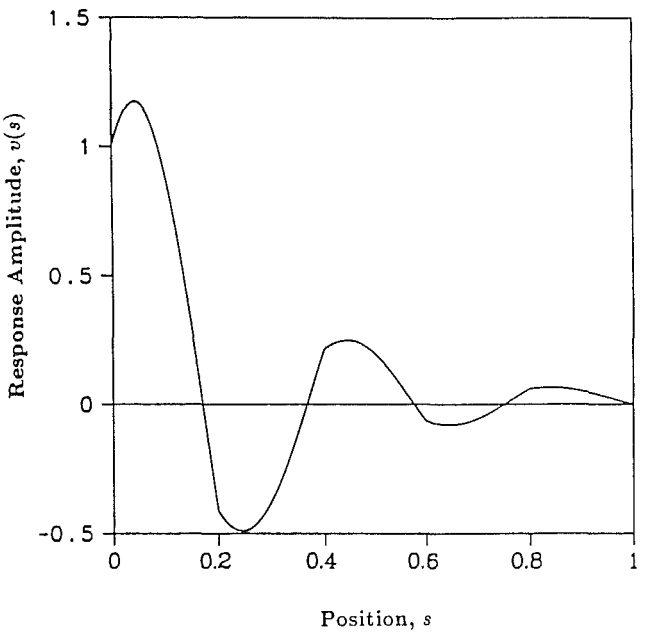


Fig. 3 The steady-state response amplitude under harmonic end excitation for the example (symmetric) suspension defined in Fig. 2

resonant harmonic excitations of frequency $\Omega_f/\pi = 4$ having the above distributions are applied to the symmetric four mass suspension considered in Fig. 2 ($\lambda/\pi = 2$). The resulting response amplitudes for the three excitation distributions are shown in Fig. 4. Note that the response amplitudes to the various excitation distributions retain the symmetry properties of the distributed excitation. In particular, the response due to the symmetric distributions, Cases a and b, are symmetric, while that due to the antisymmetric distribution, Case c, is antisymmetric. These symmetry properties are destroyed when the masses are no longer symmetrically distributed with respect to the cable midspan (Cheng, 1992).

The forced response predictions above provide a natural avenue to validate the asymptotic model through measurements of frequency response. To this end, a series of laboratory tests were conducted on a laboratory cable/mass suspension with parameters corresponding to those for the system of Fig. 2. Quantitative measurements of the response of the cable/mass suspensions were determined using standard modal testing techniques and using the cable test stand and instrumentation illustrated in the schematic of Fig. 5. Shown in Fig. 5 is a (two-axis) optical displacement probe that was used to

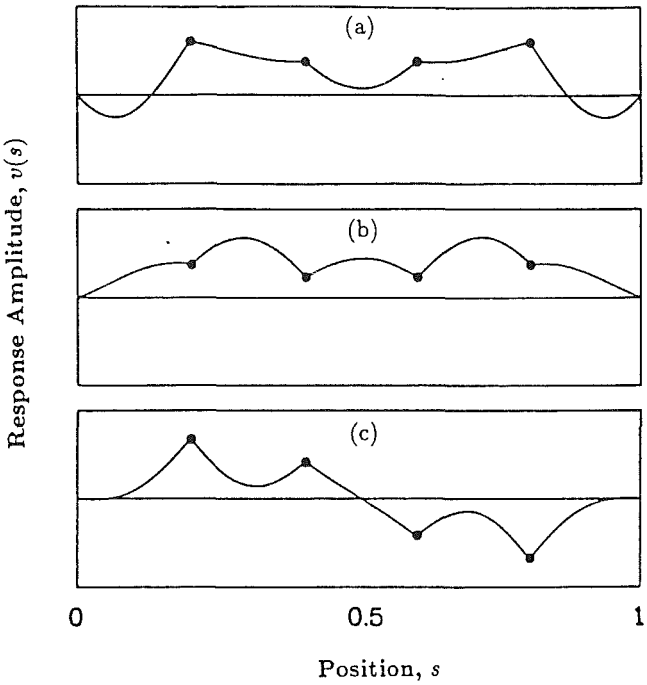


Fig. 4 The steady-state response amplitude under harmonic domain excitation for the example (symmetric) suspension defined in Fig. 2. The response amplitudes are illustrated for three excitation distributions: (*a*) uniform excitation, $\phi(s) = 1$; (*b*) equal concentrated excitation on each attached mass, $\phi(s) = \Sigma_{i=1}^{n} \delta(s - s_i)$; (*c*) sinusoidal excitation, $\phi(s) = \sin 2\pi s$.

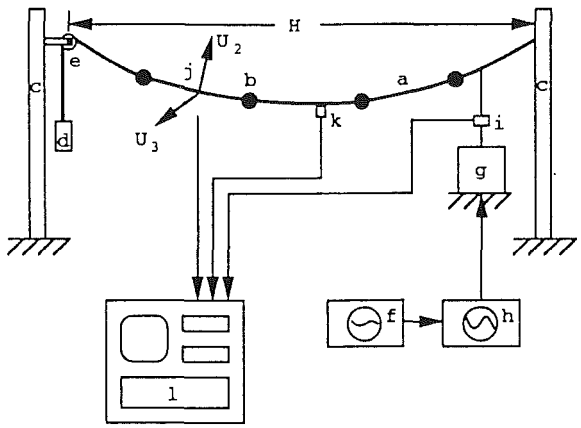


Fig. 5 Experimental test stand. (a) Cable—8 mm diameter, 2.5-m long amber surgical tubing filled with sand. $\rho = 72$ g/m, $EA = 118.56$ N. (b) Attached masses are lead weights of mass $M_i = 26.32$ g, $i = 1, 2, 3, 4$. (c) Columns—8 × 8 cm uni-strut, 1.5 m long; $0.5 < H < 5$ m. (d) Dead weights (1 N to 10 N). (e) Lockable pulley. (f) Vibration exciter controller—Brüel and Kjaer 1050. (g) Vibration exciter—Brüel and Kjaer 4809. (h) Power amplifier—Brüel and Kjaer 2712. (i) Load cell—Entran ELS 500-1. (j) Optical displacement probe. (k) Accelerometer—PCB 309A. (l) GEN-RAD 2515 Computer-Aided Testing System.

make noncontacting measurements of cable response along the normal U_2 and the bi-normal U_3 directions at a single location along the cable. The optical displacement probe was used to measure lower frequency/larger amplitude motions (0–14 Hz) while higher frequency/lower amplitude motions (14–22 Hz) were measured using two miniature accelerometers. The suspension was subjected to controlled harmonic excitation delivered at one point along the suspension by a voice-coil shaker. The measured response and excitation signals were recorded and reduced to provide frequency response measurements. A complete description of the test stand and procedure is given in Cheng (1992).

Downloaded 03 May 2010 to 171.66.16.20. Redistribution subject to ASME license or copyright; see http://www.asme.org/terms/Terms_Use.cfm

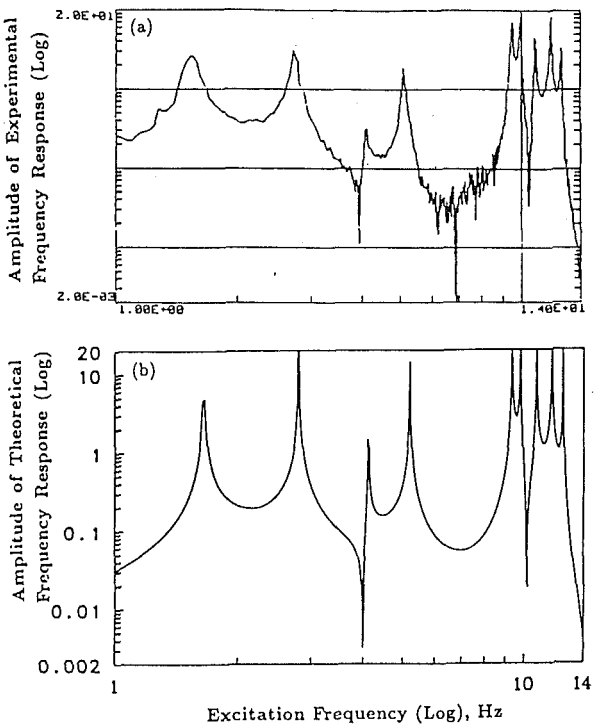


Fig. 6 Comparison of theoretical (a) and experimental (b) frequency response. Magnitude of the FRF shown versus (log scale) excitation frequency Ω_f for example array. Computed for response at $s = 0.679$ due to concentrated excitation at $\xi = 0.05$.

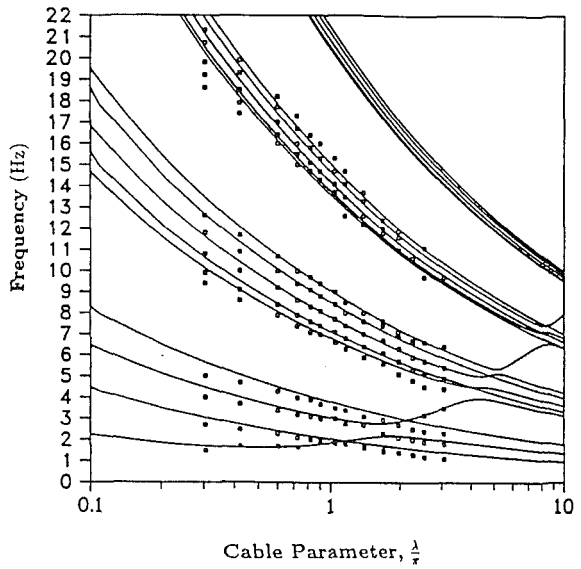


Fig. 7 Comparison of theoretical and experimental natural frequencies for the example array. The first 14 in-plane natural frequencies (in Hz) for 14 values of the cable parameter λ/π (see squares) are compared with the theoretical predictions (solid curves); refer to Cheng and Perkins (1982b).

A frequency response function (FRF) measured for the example (symmetric) system is illustrated in Fig. 6 together with that computed from the Green's function solution (14). Shown in Fig. 6(*a*) (experiment) and 6(*b*) (theory) is the amplitude of the FRF at $s = 0.679$ resulting from concentrated harmonic excitation at $\xi = 0.05$. Observe that the theoretical predictions of the FRF amplitude are quite accurate throughout the frequency range of interest. Predictable discrepancies exist at the resonant peaks, as the present theoretical model neglects damping in the model. Note also that the first four resonances (forming the first pass band) are well separated from the next five resonances (forming the second pass band) by a significant stop band (approx. 5–10 Hz). The stop band/pass band behavior for this example follows from the eigenstructure discussed in Cheng and Perkins (1992b).

The measured locations of these resonant peaks were also used to confirm the natural frequencies predicted by the eigensolutions obtained in Cheng and Perkins (1992b). In Fig. 6, the natural frequencies predicted by the asymptotic model (solid curves) are compared to those measured by experiment (squares) for the present example array and over a substantial range of the cable parameter λ/π. The first 14 in-plane natural frequencies, which fall within the first three pass bands discussed in Cheng and Perkins (1992b), were measured for various values of the cable parameter λ/π. Although modest discrepancies exist, the experimental results are in good overall agreement with the theoretical results over a range of values of the cable parameter that encompasses the first and second crossover regions; refer to Cheng and Perkins (1992b). The discrepancies observable for the smallest values of λ/π may attributed to errors in estimating Young's modulus for the cable. (The cable used is nonlinear in its material behavior, yet linear behavior is assumed.) Discrepancies for the highest values of λ/π are likely to derive from inaccuracies in measuring the associated cable tension which is very small in this range.

Summary and Conclusions

A closed-form analysis of the response of sagged cable/mass suspensions under harmonic excitation is pursued using transfer matrix methods. Integral representations for steady-state response under harmonic boundary and/or domain excitation are derived using closed-form expressions for the associated Green's function. Computed frequency response characteristics are compared to those obtained experimentally using modal testing techniques. Experimental results compare quite favorably with theoretical predictions of system frequency response and natural frequencies.

Acknowledgment

The authors gratefully acknowledge the support of the U.S.N. Office of Naval Research under grant number N00014-89-J-3159.

References

Cheng, S.-P., 1992, "Linear Dynamics of Sagged Cable/Mass Suspensions with Small Curvature," Ph.D. Dissertation, University of Michigan, Ann Arbor, MI.

Cheng, S.-P., and Perkins, N. C., 1992a, "Free Vibration of a Sagged Cable Supporting a Discrete Mass," *Journal of the Acoustical Society of America*, Vol. 91, No. 5, pp. 2654–2662.

Cheng, S.-P., and Perkins, N. C., 1992b, "Closed-form Vibration Analysis of Sagged Cable/Mass Suspensions," ASME JOURNAL OF APPLIED MECHANICS, Vol. 59, No. 4, pp. 923–928.

Griffin, O. M., 1985, "Vortex-Induced Vibrations of Marine Cables and Structures," Naval Research Laboratory, Memorandum Report No. 5600.

Griffin, O. M., and Rosenthal, R., 1985, "The Dynamics of Slack Marine Cables," Naval Research Laboratory Memorandum Report No. 5559.

Irvine, H. M., and Caughey, T. K., 1974, "The Linear Theory of Free Vibrations of a Suspended Cable," *Proc. Royal Soc. London*, Vol. A341, pp. 299–315.

Rosenthal, F., 1981, "Vibrations of Slack Cables with Discrete Masses," *J. Sound and Vibration*, Vol. 78, No. 4, pp. 573–583.

Stakgold, I., 1979, *Green's Function and Boundary Value Problems*, John Wiley and Sons, New York.

Triantafyllou, M. S., 1984, "The Dynamics of Taut Inclined Cables," *Quart. J. Mechanics and Applied Mathematics*, Vol. 37, pp. 421–440.

Downloaded 03 May 2010 to 171.66.16.20. Redistribution subject to ASME license or copyright; see http://www.asme.org/terms/Terms_Use.cfm

Bending Vibrations of Rotating Nonuniform Timoshenko Beams With an Elastically Restrained Root

Sen Yung Lee
Professor,
Mechanical Engineering Department,
National Cheng Kung University,
Tainan, Taiwan 701, R.O.C.

Shueei Muh Lin
Associate Professor,
Mechanical Engineering Department,
Kung Shan Institute of Technology,
Tainan, Taiwan 710, R.O.C.

Without considering the Coriolis force, the governing differential equations for the pure bending vibrations of a rotating nonuniform Timoshenko beam are derived. The two coupled differential equations are reduced into two complete fourth-order differential equations with variable coefficients in the flexural displacement and in the angle of rotation due to bending, respectively. The explicit relation between the flexural displacement and the angle of rotation due to bending is established. The frequency equations of the beam with a general elastically restrained root are derived and expressed in terms of the four normalized fundamental solutions of the associated governing differential equations. Consequently, if the geometric and material properties of the beam are in polynomial forms, then the exact solution for the problem can be obtained. Finally, the limiting cases are examined. The influence of the coupling effect of the rotating speed and the mass moment of inertia, the setting angle, the rotating speed and taper ratio on the natural frequencies, and the phenomenon of divergence instability (tension buckling) are investigated.

1 Introduction

Rotating beams, which have importance in many practical applications such as turbine blades, helicopter rotor blades, airplane propellers, long and flexible rotating space booms, and robot manipulators, was a textbook subject for a long time (Stodola, 1927; Myklestadt, 1944; Rao, 1992). An interesting review of the subject can be found in the review papers by Leissa (1981), Ramamurti et al. (1984), and Rao (1987).

Based on the Bernoulli-Euler beam theory, the governing characteristic differential equation for bending vibrations of rotating beams is a fourth-order ordinary differential equation with variable coefficients expressed in terms of the flexural displacement (Lo et al., 1960). The influence of tip mass, rotating speed, hub radius, setting angle, taper ratio, and elastic root restraints on the natural frequencies of transverse vibrations of a rotating beam were investigated by many investigators (Pnueli, 1972; Carlson and Wong, 1978; Hodges, 1979; Hodges and Rutkowski, 1981; Wright et al., 1982; Liu and Yeh, 1987; Storti and Aboelnaga, 1987; Lee and Kuo, 1991; Lee and Kuo, 1992a). The exact solution for the bending vibrations of a class of rotating nonuniform beams was given by Storti and Aboelnaga (1987). Combining the exact closed-form fundamental solutions for a self-adjoint fourth-order ordinary differential equation with variable coefficients given by Lee and Kuo (1992b) and the frequency equation for the bending vibrations of a rotating nonuniform beam given by Lee and Kuo (1992a), it reveals that exact solution for the bending vibrations of rotating nonuniform beams with bending rigidity and mass density varying in arbitrary polynomial forms can be obtained.

The effects of shear deformation and rotatory inertia on the bending vibrations of a rotating uniform beam have been studied by numerous authors (Carnegie, 1964; Krupka and Baumanis, 1969; Stafford and Giurgiutiu, 1975; Wang et al., 1976; Putter and Manor, 1978; Abbas, 1985; Yokoyama, 1988; Vyas and Rao, 1992). Recently, Ko (1989) studied the flexural vibration of a rotating sandwich tapered beam without considering the effect of setting angle and hub radius. From the existing literature, it reveals that the governing equations for the bending vibrations of a rotating nonuniform Timoshenko beam with setting angle and hub radius had never been derived. It was also well known that the governing differential equations for the bending vibrations of a nonrotating nonuniform Timoshenko beam are two coupled differential equations expressed in terms of two dependent variables: the flexural displacement and the angle of rotation due to bending. The exact solution for the problem had never been found except for the work recently done by Lee and Lin (1992a), who reduced the two coupled differential equations into one complete fourth-order differential equation in the angle of rotation due to bending, and gave an exact solution to the beams with bending rigidity in polynomial forms. As a result, no exact solution

Contributed by the Applied Mechanics Division of THE AMERICAN SOCIETY OF MECHANICAL ENGINEERS for presentation at the International Mechanical Engineering Congress and Exhibition, the Winter Annual Meeting of The ASME, Chicago, IL, Nov. 6–11, 1994.

Discussion on this paper should be addressed to the Technical Editor, Professor Lewis T. Wheeler, Department of Mechanical Engineering, University of Houston, Houston, TX 77204-4792, and will be accepted until four months after final publication of the paper itself in the ASME JOURNAL OF APPLIED MECHANICS.

Manuscript received by the ASME Applied Mechanics Division, Feb. 1, 1993; final revision, Nov. 5, 1993. Associate Technical Editor: P. D. Spanos.

Paper No. 94-WA/APM-8.

Copyright © 1994 by ASME
Downloaded 03 May 2010 to 171.66.16.20. Redistribution subject to ASME license or copyright; see http://www.asme.org/terms/Terms_Use.cfm

has been given to the bending vibrations of a rotating nonuniform Timoshenko beam.

In this paper, the governing differential equations for the bending vibrations of a rotating nonuniform Timoshenko beam with setting angle, hub radius, and rotating at a constant angular velocity are derived. The effect of Coriolies force is not considered. The beam considered is doubly symmetric such that the mass axis, the centroidal axis, and the elastic axis are coincident. The two coupled differential equations are reduced into two complete fourth-order ordinary differential equations with variable coefficients in the flexural displacement and in the angle of rotation due to bending, respectively. The explicit relations between the flexural displacement and the angle of rotation due to bending are established. The frequency equations of the beam with a general elastically restrained root are derived and expressed in terms of the four normalized fundamental solutions of the associated governing differential equations. If the geometric and material properties of the beam are in polynomial forms, then these four fundamental solutions are exact (Lee and Lin, 1992a). Consequently, the exact solution for the bending vibrations of the rotating beam can be obtained. Finally, the limiting cases are examined and examples are given to illustrate the validity and accuracy of the analysis. The influence of the coupling effect of the rotating speed and the mass moment of inertia, the setting angle and the rotating speed on the natural frequencies, and the phenomenon of divergence instability (tension buckling) (Lee and Kuo, 1991) are examined.

2 Analysis

Consider the flexural and the axial motions of an untwisted and doubly symmetric nonuniform Timoshenko beam elastically restrained, mounted with setting angle θ on a hub with radius R, rotating with constant angular velocity Ω, as shown in Fig. 1. The displacement fields of the beam are

$$u(x, t) = u_0(x, t) - z\Psi(x, t),$$
$$v = 0$$
$$w = w(x, t) \tag{1}$$

where u, v, and w denote the displacements of the beam in the x, y, and z-directions, respectively. Ψ is the angle of rotation due to bending, u_0 is the axial neutral displacement due to axial force. Here, the influence of the bending flexural on the axial neutral displacement u_0 is neglected.

The velocity vector of a point (x, y, z) in the beam is given by

$$\mathbf{V} = \left[\frac{du}{dt} + \Omega \sin\theta(z + w) - y\Omega \cos\theta\right]\mathbf{i} + [(x + R + u)\Omega \cos\theta]\mathbf{j} + \left[\frac{dw}{dt} - (x + R + u)\Omega \sin\theta\right]\mathbf{k}. \tag{2}$$

The potential energy and the kinetic energy of the beam are

$$U = \int_0^L \int_{-b/2}^{b/2} \int_{-h/2}^{h/2} \left(\frac{1}{2}\sigma_{xx}\epsilon_{xx} + \sigma_{xz}\epsilon_{xz}\right) dz dy dx + \frac{1}{2}K_\theta \Psi^2(0, t) + \frac{1}{2}K_T w^2(0, t), \tag{3}$$

and

$$T = \frac{1}{2}\int_0^L \int_{-b/2}^{b/2} \int_{-h/2}^{h/2} \mathbf{V}\cdot\mathbf{V}\rho dz dy dx, \tag{4}$$

respectively, where σ_{ij} and ϵ_{ij} are stresses and strains, respectively. K_θ and K_T are the rotating and the translational spring constants at the root of the beam, respectively. $\rho(x)$ is the mass density per unit volume and $b(x)$ and $h(x)$ are the breadth and the height of the beam, respectively.

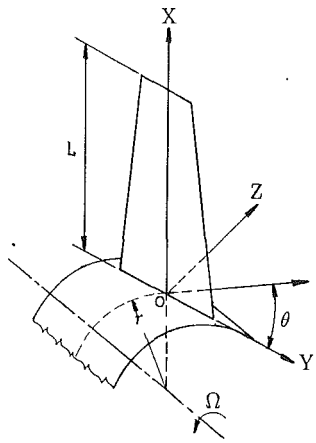


Fig. 1 Geometry and coordinate system of a rotating nonuniform beam with an elastically restrained root

Application of Hamilton's principle yields the following governing differential equations:

$$\rho A\left[\Omega^2(x + R + u_0) - 2\frac{\partial w}{\partial t}\Omega \sin\theta - \frac{\partial^2 u_0}{\partial t^2}\right] + \frac{\partial N}{\partial x} = 0, \tag{5}$$

$$J\left(\Psi\Omega^2 - \frac{\partial^2\Psi}{\partial t^2}\right) + \frac{\partial}{\partial x}\left(EI\frac{\partial\Psi}{\partial x}\right) + \kappa GA\left(\frac{\partial w}{\partial x} - \Psi\right) = 0, \tag{6}$$

$$\rho A\left(2\frac{\partial u_0}{\partial t}\Omega \sin\theta + w\Omega^2 \sin^2\theta - \frac{\partial^2 w}{\partial t^2}\right) + \frac{\partial}{\partial x}\left(N\frac{\partial w}{\partial x}\right) + \frac{\partial}{\partial x}\left[\kappa GA\left(\frac{\partial w}{\partial x} - \Psi\right)\right] = 0, \tag{7}$$

and the corresponding boundary conditions

at $x = 0$:

$$u_0 = 0,$$
$$-EI\frac{\partial\Psi}{\partial x} + K_\theta\Psi = 0,$$
$$K_T w - N\frac{\partial w}{\partial x} - \kappa GA\left(\frac{\partial w}{\partial x} - \Psi\right) = 0, \tag{8}$$

at $x = L$:

$$N = 0,$$
$$EI\frac{\partial\Psi}{\partial x} = 0,$$
$$\kappa GA\left(\frac{\partial w}{\partial x} - \Psi\right) = 0, \tag{9}$$

where $A(x)$ is the cross-sectional area, $E(x)$ is the Young's modulus, $G(x)$ is the shear modulus, $J(x)$ is mass moment of inertia per unit length, $N(x)$ is the centrifugal force, and κ is the shear correction factor. Here the coupling effect of the rotating speed and the mass moment of inertia, the term $J\Psi\Omega^2$ in Eq. (6), is considered.

2.1 Nonuniform Timoshenko Beams. For an inextensional beam, without taking account of the Coriolis forces effect, the centrifugal force in Eq. (5) can be expressed as

$$N = \int_x^L \rho A\Omega^2(\chi + R)d\chi. \tag{10}$$

In terms of following dimensionless quantities,

Downloaded 03 May 2010 to 171.66.16.20. Redistribution subject to ASME license or copyright; see http://www.asme.org/terms/Terms_Use.cfm

$$b(\xi)=E(\xi)I(\xi)/[E(0)I(0)], \quad g(\xi)=J(\xi)/J(0),$$

$$m(\xi)=\rho(\xi)A(\xi)/[\rho(0)A(0)], \quad n(\xi)=\alpha^2\int_\xi^1 m(\chi)(r+\chi)d\chi,$$

$$r=R/L, \quad s(\xi)=\kappa(\xi)G(\xi)A(\xi)/[\kappa(0)G(0)A(0)],$$

$$W=w/L, \quad \alpha^2=\rho(0)A(0)\Omega^2L^4/[E(0)I(0)],$$

$$\beta_T=K_TL^3/[E(0)I(0)], \quad \beta_\theta=K_\theta L/[E(0)I(0)],$$

$$\eta=J(0)/[\rho(0)A(0)L^2], \quad \mu=E(0)I(0)/[\kappa(0)G(0)A(0)L^2],$$

$$\xi=x/L, \quad \Lambda^2=\rho(0)A(0)\omega^2L^4/[E(0)I(0)], \tag{11}$$

the governing differential equations become

$$\frac{d}{d\xi}\left[n\frac{dW}{d\xi}+\frac{s}{\mu}\left(\frac{dW}{d\xi}-\Psi\right)\right]+m(\alpha^2\sin^2\theta+\Lambda^2)W=0, \tag{12}$$

$$\frac{d}{d\xi}\left(b\frac{d\Psi}{d\xi}\right)+\frac{s}{\mu}\left(\frac{dW}{d\xi}-\Psi\right)+g\eta(\alpha^2+\Lambda^2)\Psi=0, \quad \xi\in(0,1) \tag{13}$$

and the associated boundary conditions are

at $\xi = 0$:

$$\beta_TW-n\frac{dW}{d\xi}-\frac{1}{\mu}\left(\frac{dW}{d\xi}-\Psi\right)=0, \tag{14}$$

$$\beta_\theta\Psi=\frac{d\Psi}{d\xi}, \tag{15}$$

at $\xi = 1$:

$$\frac{d\Psi}{d\xi}=0, \tag{16}$$

$$\frac{dW}{d\xi}-\Psi=0. \tag{17}$$

To simplify the analysis, it is assumed that the mass density of the beam is a constant and the bending rigidity and shearing rigidity of the beam are third and first-order differentiable with respect to the dimensionless spatial variable ξ, respectively.

2.1.1 Governing Differential Equation in Terms of the Angle of Rotation due to Bending. Upon substituting Eq. (13) into Eq. (12), the dimensionless flexural displacement can be explicitly expressed in terms of the angle of rotation due to bending

$$W=\frac{1}{m(\alpha^2\sin^2\theta+\Lambda^2)}\frac{d}{d\xi}\left\{\left(1+\frac{\mu n}{s}\right)\frac{d}{d\xi}\left(b\frac{d\Psi}{d\xi}\right)+\left[g\eta\left(1+\frac{\mu n}{s}\right)(\alpha^2+\Lambda^2)-n\right]\Psi\right\}. \tag{18}$$

Substituting Eq. (18) back to Eq. (12) one obtains the governing characteristic differential equation of motion, which is a fourth-order ordinary differential equation with variable coefficients, in terms of the angle of rotation due to bending.

$$s\frac{d}{d\xi}\left\{\frac{1}{m(\alpha^2\sin^2\theta+\Lambda^2)}\frac{d}{d\xi}\left\{\left(1+\frac{\mu n}{s}\right)\frac{d}{d\xi}\left(b\frac{d\Psi}{d\xi}\right)+\left[g\eta\left(1+\frac{\mu n}{s}\right)(\alpha^2+\Lambda^2)-n\right]\Psi\right\}\right\}+\mu\frac{d}{d\xi}\left(b\frac{d\Psi}{d\xi}\right)+[\mu g\eta(\alpha^2+\Lambda^2)-q]\Psi=0, \quad \xi\in(0,1). \tag{19}$$

2.1.2 Governing Differential Equation in Terms of the Dimensionless Flexural Displacement. Equation (21) can be written as

$$\frac{d\Psi}{d\xi}=\frac{1}{s}\left\{\frac{d}{d\xi}\left[(s+\mu n)\frac{dW}{d\xi}\right]+\mu m(\alpha^2\sin^2\theta+\Lambda^2)W-\frac{ds}{d\xi}\Psi\right\}. \tag{20}$$

Upon substituting Eq. (20) into Eq. (13) and multiplying it by a factor μs^2, the angle of rotation due to bending is explicitly expressed in terms of the dimensionless flexural displacement

$$\Psi=\frac{1}{\zeta}\left\{\mu\left(2\frac{ds}{d\xi}b-s\frac{db}{d\xi}\right)\left[\frac{d}{d\xi}\left[(s+\mu n)\frac{dW}{d\xi}\right]+\mu m(\alpha^2\sin^2\theta+\Lambda^2)W\right]-\mu bs\frac{d}{d\xi}\left[\frac{d}{d\xi}\left[(s+\mu n)\frac{dW}{d\xi}\right]+\mu m(\alpha^2\sin^2\theta+\Lambda^2)W\right]-s^3\frac{dW}{d\xi}\right\}, \tag{21}$$

where $\zeta = \mu[2(ds/d\xi)^2b - sd(bds/d\xi)/d\xi + s^2g\eta(\alpha^2 + \Lambda^2)] - s^3$.

Substituting Eq. (21) into Eq. (12), the governing characteristic differential equation can be expressed in terms of the dimensionless flexural displacement

$$\frac{d}{d\xi}\left\{n\frac{dW}{d\xi}-\frac{s}{\zeta}\left[\left(2\frac{ds}{d\xi}b-\frac{db}{d\xi}s\right)\left(\frac{d}{d\xi}\left[(s+\mu n)\frac{dW}{d\xi}\right]+\mu m(\alpha^2\sin^2\theta+\Lambda^2)W\right)-bs\frac{d}{d\xi}\left(\frac{d}{d\xi}\left[(s+\mu n)\frac{dW}{d\xi}\right]+\mu m(\alpha^2\sin^2\theta+\Lambda^2)W\right)\right]+\frac{s}{\zeta}\left[2\left(\frac{ds}{d\xi}\right)^2b-s\frac{d}{d\xi}\left(\frac{ds}{d\xi}b\right)+s^2g\eta(\alpha^2+\Lambda^2)\right]\frac{dW}{d\xi}\right\}+m(\alpha^2\sin^2\theta+\Lambda^2)W=0, \quad \xi\in(0,1). \tag{22}$$

2.2 Uniform Timoshenko Beams. For a rotating uniform Timoshenko beam, $b = g = m = s = 1$. The governing characteristic differential Eqs. (19) and (22) are reduced to

$$(1+\mu n)\frac{d^4\Psi}{d\xi^4}+2\mu\frac{dn}{d\xi}\frac{d^3\Psi}{d\xi^3}+\left[\mu\left(\frac{d^2n}{d\xi^2}+\alpha^2\sin^2\theta+\Lambda^2\right)+\eta(\alpha^2+\Lambda^2)(1+\mu n)-n\right]\frac{d^2\Psi}{d\xi^2}+2\frac{dn}{d\xi}[\mu\eta(\alpha^2+\Lambda^2)-1]\frac{d\Psi}{d\xi}+[\mu\eta(\alpha^2+\Lambda^2)-1]\left(\frac{d^2n}{d\xi^2}+\alpha^2\sin^2\theta+\Lambda^2\right)\Psi=0, \quad \xi\in(0,1), \tag{23}$$

and

$$(1+\mu n)\frac{d^4W}{d\xi^4}+3\mu\frac{dn}{d\xi}\frac{d^3W}{d\xi^3}+\left[\mu\left(\alpha^2\sin^2\theta+\Lambda^2+3\frac{d^2n}{d\xi^2}+n\eta(\alpha^2+\Lambda^2)\right)-n+\eta(\alpha^2+\Lambda^2)\right]\frac{d^2W}{d\xi^2}+\frac{dn}{d\xi}[\mu\eta(\alpha^2+\Lambda^2)-1]\frac{dW}{d\xi}+[\mu\eta(\alpha^2+\Lambda^2)-1](\alpha^2\sin^2\theta+\Lambda^2)W=0, \quad \xi\in(0,1), \tag{24}$$

respectively. It should be noted that when $\theta = 0$ and $\pi/2$, Eq. (24) becomes the equation for the flapping motion and the lead-lag motion, respectively. These equations are the same as those given by Stafford and Giurgiutiu (1975).

Downloaded 03 May 2010 to 171.66.16.20. Redistribution subject to ASME license or copyright; see http://www.asme.org/terms/Terms_Use.cfm

2.3 Nonuniform Bernoulli-Euler Beams. For Bernoulli-Euler beams, both shear deformation and rotatory inertia are not considered. By letting $\mu = g\eta = 0$ in Eqs. (19) and (22), the equations yield to

$$\frac{d}{d\xi}\left\{\frac{1}{m(\alpha^2 \sin^2\theta+\Lambda^2)}\frac{d}{d\xi}\left[\frac{d}{d\xi}\left(b\frac{d\Psi}{d\xi}\right)-n\Psi\right]\right\} - \Psi = 0, \quad \xi\epsilon(0, 1). \quad (25)$$

and

$$\frac{d^2}{d\xi^2}\left(b\frac{d^2W}{d\xi^2}\right)-\frac{d}{d\xi}\left(n\frac{dW}{d\xi}\right) - m(\alpha^2 \sin^2\theta+\Lambda^2)W = 0, \quad \xi\epsilon(0, 1), \quad (26)$$

respectively. Equation (26) is exactly the same as the one given by Lo et al. (1960).

The boundary conditions for the nonuniform Timoshenko beam in terms of the angle of rotation due to bending and the flexural displacement can be obtained by substituting the relations between them, Eqs. (18), (20), and (21), into the boundary conditions (14)–(17). The associated boundary conditions for the uniform Timoshenko and the nonuniform Bernoulli-Euler beams can be reduced from the boundary conditions for nonuniform Timoshenko beams by taking a suitable limiting procedure.

3 Frequency Equation

The four linearly independent fundamental solutions $V_j(\xi)$, $j = 1, 2, 3, 4$ of the corresponding governing characteristic differential equation can be chosen such that they satisfy the following normalization conditions at the origin of the coordinate system:

$$\begin{bmatrix} V_1(0) & V_2(0) & V_3(0) & V_4(0) \\ V_1'(0) & V_2'(0) & V_3'(0) & V_4'(0) \\ V_1''(0) & V_2''(0) & V_3''(0) & V_4''(0) \\ V_1'''(0) & V_2'''(0) & V_3'''(0) & V_4'''(0) \end{bmatrix} = \begin{bmatrix} 1 & 0 & 0 & 0 \\ 0 & 1 & 0 & 0 \\ 0 & 0 & 1 & 0 \\ 0 & 0 & 0 & 1 \end{bmatrix}, \quad (27)$$

where primes indicate differentiation with respect to dimensionless spatial variable ξ. If the coefficients of the differential equation are in polynomial forms, then the closed-form power series solutions of the four fundamental solutions can be obtained (Lee and Lin, 1992a). Otherwise, the approximated solutions can be obtained by following the algorithm developed by Lee and Lin (1992b).

Substituting the homogeneous solution which is a linear combination of the four fundamental solutions into the associated boundary conditions, the frequency equation of the system is obtained,

$$\pi = 0. \quad (28)$$

The frequency equations in the angle of rotation due to bending and in the dimensionless flexural displacement for the Timoshenko beam with a general elastically restrained and clamped root are derived and tabulated in Appendix A and Appendix B, respectively.

4 Numerical Results

To illustrate the previous analysis and investigate the influence of the coupling effect of the rotating speed and the mass moment of inertia, the setting angle, the rotating speed, and the taper ratio on the bending frequencies of a rotating nonuniform Timoshenko beam, several numerical results are presented and discussed. In the following numerical analysis, the material properties and the width of the beam are assumed to be constants and the depth of the beam varied linearly with the taper ratio λ. Consequently, $m = s = (1+\lambda\xi)$, $b = g = (1+\lambda\xi)^3$.

In Table 1, the first four natural frequencies of a cantilever nonuniform beam are shown. It is observed that the natural frequencies of the Timoshenko and the Bernoulli-Euler beams determined by employing the frequency equation in the angle of rotation due to bending, given in Appendix A, are all the same as those determined by employing the frequency equation in the dimensionless flexural displacement, given in Appendix B. While comparing the natural frequencies of the Bernoulli-Euler beams with those given by Hodges and Rutkowski (1981) and by Lee and Kuo (1992a), it shows that the results are very consistent.

In Table 2, the first four natural frequencies of cantilever uniform Timoshenko beams with different setting angles are shown. The natural frequencies determined in the angle of rotation due to bending are all the same as those determined

Table 1 First four dimensionless frequencies for a nonuniform cantilever beam [$m = s = (1-0.5\,\xi)$, $b = g = (1-0.5\,\xi)^3$, $\theta = 0$, $r = 0$]

		Timoshenko		Bernoulli-Euler			
		$\eta = 0.0064$		$\eta = 0$			
α	Λ	$\mu = 0.01958$		$\mu = 0$			
		*	**	*	**	#	##
0	Λ_1	3.6500	3.6500	3.8238	3.8238	3.8238	3.8242
	Λ_2	15.022	15.022	18.317	18.317	18.317	18.320
	Λ_3	32.785	32.785	47.265	47.265	47.265	47.271
	Λ_4	53.341	53.341	90.450	90.450	—	—
3	Λ_1	4.8866	4.8866	5.0927	5.0927	5.0927	5.0927
	Λ_2	16.460	16.460	19.684	19.684	19.684	19.684
	Λ_3	34.458	34.458	48.619	48.619	48.619	48.620
	Λ_4	55.358	55.358	91.822	91.822	—	—
5	Λ_1	6.4712	6.4712	6.7434	6.7434	6.7345	6.7432
	Λ_2	18.744	18.744	21.905	21.905	21.905	21.905
	Λ_3	37.224	37.224	50.934	50.934	50.934	49.646
	Λ_4	58.730	58.730	94.206	94.206	—	—
10	Λ_1	10.991	10.991	11.502	11.502	11.502	11.501
	Λ_2	26.928	26.928	30.183	30.183	30.183	30.177
	Λ_3	47.883	47.883	60.564	60.564	60.564	60.555
	Λ_4	71.986	71.986	104.61	104.61	—	—

* in the angle of rotation due to bending
** in the dimensionless flexural displacement
\# given by Hodges and Rutkowski (1981)
\## given by Lee and Kuo (1992a)

Downloaded 03 May 2010 to 171.66.16.20. Redistribution subject to ASME license or copyright; see http://www.asme.org/terms/Terms_Use.cfm

Table 2 First four dimensionless frequencies for an uniform cantilever Timoshenko beam [$b = g = m = s = 1, r = 3, \alpha = 10$]

		$\eta=0.01,\ \mu=0.030588$				$\eta=0.0025,\ \mu=0.007647$			
θ	Λ	Λ_1	Λ_2	Λ_3	Λ_4	Λ_1	Λ_2	Λ_3	Λ_4
0	*	22.938	44.781	66.287	71.967	23.491	55.984	96.913	143.71
	**	22.938	44.781	66.287	71.967	23.491	55.984	96.913	143.71
	#	23.037	45.428	66.854	72.313	23.514	56.072	97.011	143.82
	##	23.050	45.598	67.716	73.076	23.524	56.105	97.188	144.49
45	*	21.873	44.550	66.200	71.792	22.411	55.575	96.693	143.57
	**	21.873	44.550	66.200	71.792	22.411	55.575	96.693	143.57
	#	21.974	45.194	66.793	72.146	22.436	55.662	96.792	143.67
	##	21.987	45.359	67.619	72.914	22.446	55.696	96.968	144.35
90	*	20.753	44.315	66.109	71.620	21.277	55.162	96.473	143.43
	**	20.753	44.315	66.109	71.620	21.277	55.162	96.473	143.43
	#	20.850	44.955	66.668	71.982	21.302	55.250	96.570	143.53
	##	20.867	45.115	67.520	72.756	21.313	55.284	96.747	144.21

* in the angle of rotation due to bending
** in the dimensionless flexural displacement
\# given by Wang et al. (1976)
given by Yokoyama (1988)

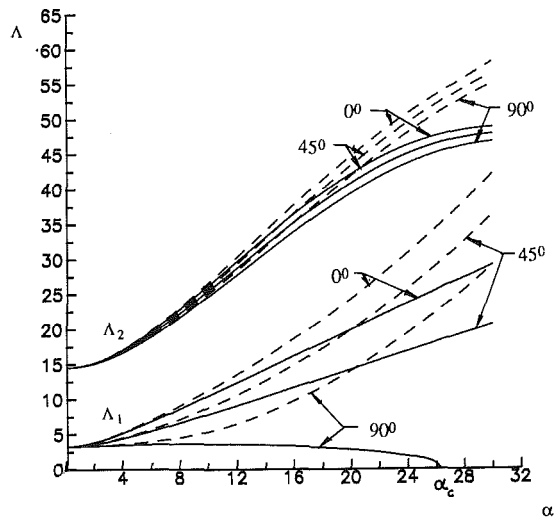


Fig. 2 Influence of the coupling effect and rotating speed on the first two natural frequencies of a nonuniform Timoshenko beam with different setting angles [$\lambda = -0.1, r = 0, \eta = 0.01, \mu = 0.030588$; —— : the coupling effect considered; ---: the coupling effect ignored]

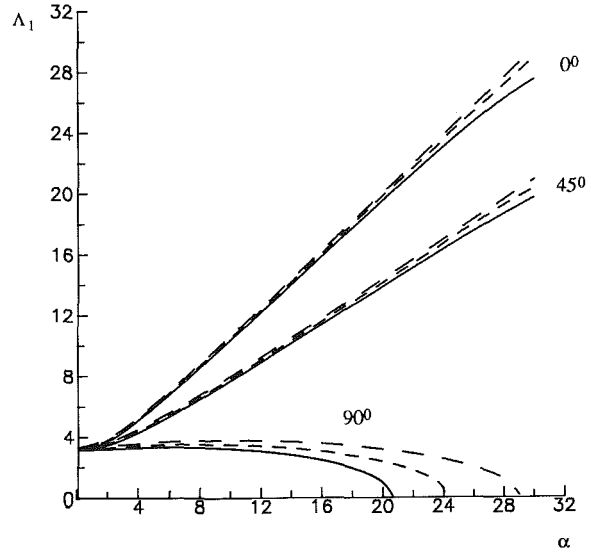


Fig. 3 Influence of taper ratio and rotating speed on the first natural frequency of a cantilever Timoshenko beam [$r = 0, \eta = 0.01, \mu = 0.030588$; —— : $\lambda = 0.2$; ---: $\lambda = 0$; ——: $\lambda = -0.2$]

in the dimensionless flexural displacement. Moreover, the results are very consistent with those given by Wang et al. (1976) using the extended Galerkin method and those obtained by Yokoyama (1988) using the finite element method.

In Fig. 2, the first two natural frequencies of a cantilever rotating nonuniform Timoshenko beam with various setting angles are shown. The dashed and real lines correspond to the natural frequencies with the coupling effect of the rotating speed and the mass moment of inertia ignored and considered, respectively. It can be observed that the setting angle has no influence on the natural frequencies of nonrotating beams. The natural frequencies of rotating beams will decrease as the setting angle is increased. The coupling effect of the rotating speed and the mass moment of inertia will decrease the natural frequencies. As the rotating speed is increased, the influence of the coupling effect of the rotating speed and the mass moment of inertia on the natural frequencies increases. It is also found that if the coupling effect is considered, the first natural frequency for the beam with setting angle being equal to 90 turns to be pure imaginary as the rotating speed is greater than the critical speed α_c. Consequently, the phenomenon of divergence instability occurs for the cantilever beam. This observation can be considered as a modification of the one revealed by Lee and Kuo (1991). They showed that the phenomenon of divergence instability will not occur if the beam is a cantilever Bernoulli-Euler beam. However, the phenomenon may occur as the translational rigidity of the root is relatively low. The difference in the observation for the Bernoulli-Euler beam and the Timoshenko beam is due to the ignorance of the coupling effect of the rotating speed and the mass moment of inertia in Bernoulli-Euler beam theory.

Figure 3 shows the influence of taper ratio and rotating speed on the first natural frequencies of cantilever nonuniform Timoshenko beams with different setting angles. It is observed that when the taper ratio is decreased, the natural frequency increases. The influence of taper ratio and rotating speed on the first natural frequency becomes significant when the phenomenon of divergence instability is about to occur.

5 Conclusions

In this paper, the governing differential equations for the pure bending vibrations of a rotating nonuniform Timoshenko beam are reduced into two complete fourth-order ordinary differential equations with variable coefficients in the dimensionless flexural displacement and in the angle of rotation due to bending, respectively. The frequency equations of the beam with a general elastically restrained root are expressed in terms

Downloaded 03 May 2010 to 171.66.16.20. Redistribution subject to ASME license or copyright; see http://www.asme.org/terms/Terms_Use.cfm

of the four normalized fundamental solutions of the associated governing differential equations. As a result, if the geometric and material properties of the beam are in polynomial forms, then the exact solution for the problem can be obtained. The influence of the coupling effect of the rotating speed and the mass moment of inertia, the setting angle, the rotating speed and taper ratio on the natural frequencies and the phenomenon of divergence instability of a rotating nonuniform Timoshenko beam are investigated. It is shown that

(1) The setting angle has no influence on the natural frequencies of nonrotating beams. The natural frequencies of rotating beams will decrease as the setting angle is increased.

(2) The coupling effect of the rotating speed and the mass moment of inertia will decrease the natural frequencies. As the rotating speed is increased, the influence of the coupling effect of the rotating speed and the mass moment of inertia on the natural frequencies increases.

(3) The observation on the phenomenon of divergence instability of a rotating cantilever beam is modified.

(4) When the taper ratio is decreased, the natural frequency increases. The influence of taper ratio and rotating speed on the first natural frequency becomes significant when the phenomenon of divergence instability is about to occur.

Acknowledgment

This research work was supported by the National Science Council of Taiwan, R. O. C. under grant NSC 81-0401-E006-577 and is gratefully acknowledged.

References

Abbas, B. A. H., 1985, "Dynamic Analysis of Thick Rotating Blades with Flexible Roots," *The Aeronautical Journal*, Vol. 89, pp. 10–16.

Abbas, B. A. H., 1986, "Dynamic Stability of a Rotating Timoshenko Beam with a Flexible Root," *Journal of Sound and Vibration*, Vol. 108, No. 1, pp. 25–32.

Carlson, R. M., and Wong, J. T., 1978, "An Exact Solution for the Static Bending of Uniform Rotating Beams," *Journal of the American Helicopter Society*, Vol. 23, No. 4, pp. 36–38.

Carnegie, W., 1964, "Vibrations of Pre-Twisted Cantilever Blading Allowing for Rotary Inertia and Shear Deflection," *Journal Mechanical Engineering Science*, Vol. 6, pp. 105–109.

Hodges, D. H., 1979, "Vibration and Response of Nonuniform Rotating Beams with Discontinuities," *Journal of the American Helicopter Society*, Vol. 24, pp. 43–50.

Hodges, D. H., and Rutkowski, M. J., 1981, "Free-Vibration Analysis of Rotating Beams by a Variable-Order Finite-Element Method," *AIAA Journal*, Vol. 19, No. 11, pp. 1459–1466.

Ko, C. L., 1989, "Dynamic Analysis for Free Vibrations of Rotating Sandwich Tapered Beams," *AIAA Journal*, Vol. 27, No. 10, pp. 1425–1433.

Krupka, R. M., and Baumanis, A. M., 1969, "Bending-Bending Mode of a Rotating Tapered-Twisted Turbomachine Blade Including Rotatory Inertia and Shear Deformation," ASME *Journal of Engineering for Industry*, Vol. 91, No. 4, pp. 1017–1024.

Lee, S. Y., and Kuo, Y. H., 1991, "Bending Frequency of a Rotating Beam With an Elastically Restrained Root," ASME JOURNAL OF APPLIED MECHANICS, Vol. 58, pp. 209–214.

Lee, S. Y., and Kuo, Y. H., 1992a, "Bending Vibrations of a Rotating Nonuniform Beam with an Elastically Restrained Root," *Journal of Sound and Vibration*, Vol. 154, No. 3, pp. 441–451.

Lee, S. Y., and Kuo, Y. H., 1992b, "Exact Solutions for the Analysis of General Elastically Restrained Nonuniform Beams," ASME JOURNAL OF APPLIED MECHANICS, Vol. 59, No. 2, pp. 205–212.

Lee, S. Y., and Lin, S. M., 1992a, "Exact Vibration Solutions for Nonuniform Timoshenko Beams with Attachments," *AIAA Journal*, Vol. 30, No. 12, pp. 2930–2934.

Lee, S. Y., and Lin, S. M., 1992b, "Free Vibrations of General Elastically Restrained Nonuniform Timoshenko Beams," *Recent Advances in Structural Mechanics*, ASME, New York, pp. 101–109.

Leissa, A., 1981, "Vibrational Aspects of Rotating Turbomachinery Blades," ASME *Applied Mechanics Reviews*, Vol. 34, pp. 629–635.

Liu, W. H., and Yeh, F. H., 1987, "Vibrations of Non-Uniform Rotating Beams," *Journal of Sound and Vibration*, Vol. 119, No. 2, pp. 379–384.

Lo, H., Goldberg, J. E., and Bogdanoff, J. L., 1960, "Effect of Small Hub-Radius Change on Bending Frequencies of a Rotating Beam," ASME JOURNAL OF APPLIED MECHANICS, Vol. 27, No. 3, pp. 548–550.

Myklestadt, N. O., 1944, *Vibration Analysis*, McGraw-Hill, Englewood Cliffs, NJ.

Pnueli, D., 1972, "Natural Bending Frequency Comparable to Rotating Frequency in Rotating Cantilever Beam," ASME JOURNAL OF APPLIED MECHANICS, Vol. 39, pp. 602–604.

Putter, S., and Manor, H., 1978, "Natural Frequencies of Radial Rotating Beams," *Journal of Sound and Vibration*, Vol. 56, No. 2, pp. 175–185.

Ramamurti, V., and Balasubramanian, P., 1984, "Analysis of Turbomachine Blades: A Review," Vol. 16, pp. 13–28.

Rao, J. S., 1987, "Turbomachine Blade Vibration," *The Shock and Vibration Digest*, Vol. 19, pp. 3–10.

Rao, J. S., 1992, *Advanced Theory of Vibration*, John Wiley and Sons, New York.

Stafford, R. O., and Giurgiutiu, V., 1975, "Semi-Analytic Methods for Rotating Timoshenko Beams," *International Journal of Mechanical Sciences*, Vol. 17, pp. 719–727.

Stodola, A., 1927, *Steam and Gas Turbines*, McGraw Hill, Englewood Cliffs, N.J.

Storti, D., and Aboelnaga, Y., 1987, "Bending Vibrations of a Class of Rotating Beams with Hypergeometric Solutions," ASME JOURNAL OF APPLIED MECHANICS, Vol. 54, No. 2, pp. 311–314.

Vyas, N. S., and Rao, J. S., 1992, "Equations of Motion of a Blade Rotating with Variable Angular Velocity," *Journal of Sound and Vibration*, Vol. 156, No. 2, pp. 327–336.

Wang, J. T. S., Mahrenholtz, O., and Bohm, J., 1976, "Extended Galerkin's Method for Rotating Beam Vibrations using Legendre Polynomials," *Solid Mechanics Archives*, Vol. 1, No. 4, pp. 341–365.

Wright, A. D., Smith, C. E., Thresher, R. W., and Wang, J. L. C., 1982, "Vibration Modes of Centrifugally Stiffened Beams," ASME JOURNAL OF APPLIED MECHANICS, Vol. 49, No. 1, pp. 197–202.

Yokoyama, T., 1988, "Free Vibration Characteristics of Rotating Timoshenko Beam," *International Journal of Mechanical Sciences*, Vol. 30, No. 10, pp. 743–755.

APPENDIX A

The Frequency Equation of Rotating Nonuniform Timoshenko Beams in the Angle of Rotation due to Bending

Case 1: Elastically Restrained Root. For this case, K_θ and K_T are constants and the frequency equation is

$$\pi = F_{14}G_{33}G_{41} + F_{11}G_{34}G_{43} + F_{13}G_{31}G_{44} - F_{14}G_{31}G_{43} - F_{11}G_{33}G_{44} - F_{13}G_{34}G_{41} + \beta_T(F_{14}G_{33}G_{42} + F_{13}G_{32}G_{44} + F_{12}G_{34}G_{43} - F_{14}G_{32}G_{43} - F_{13}G_{34}G_{42} - F_{12}G_{33}G_{44}) = 0,$$

where

$$F_{11} = \eta(\alpha^2+\Lambda^2)\{\beta_T[\mu(n'-ns') + (1+\mu n)g'] + (\alpha^2\sin^2\theta+\Lambda^2)(1+\mu n)\} - \beta_T n' - n(\alpha^2\sin^2\theta+\Lambda^2)|_{\xi=0},$$

$$F_{12} = (1+\mu n)[b'(\alpha^2\sin^2\theta+\Lambda^2) + \beta_T b'' + \beta_T\eta(\alpha^2+\Lambda^2)] + \beta_T[\mu b'(n'-ns') - n]|_{\xi=0},$$

$$F_{13} = (1+\mu n)(\alpha^2\sin^2\theta+\Lambda^2+2\beta_T b') + \beta_T\mu(n'-ns')|_{\xi=0},$$

$$F_{14} = \beta_T(1+\mu n)|_{\xi=0},$$

$$G_{3j} = V_j'(1),$$

$$G_{4j} = b(1)V_j''(1) + b'(1)V_j'(1) + g(1)\eta(\alpha^2+\Lambda^2)V_j(1), \quad j = 1,2,3,4.$$

Case 2. Clamped-Free. For this case, K_T and $K_\theta \to \infty$, the frequency equation is

$$\pi = F_{14}G_{33}G_{42} + F_{13}G_{32}G_{44} + F_{12}G_{34}G_{43} - F_{14}G_{32}G_{43} - F_{13}G_{34}G_{42} - F_{12}G_{33}G_{44} = 0,$$

where

$$F_{11} = \eta(\alpha^2+\Lambda^2)[\mu(n'-ns') + (1+\mu n)g'] - n'|_{\xi=0},$$

$$F_{12} = (1+\mu n)[b'' + \eta(\alpha^2+\Lambda^2)] + [\mu b'(n'-ns') - n]|_{\xi=0},$$

$$F_{13} = 2b'(1+\mu n) + \mu(n'-ns')|_{\xi=0},$$

$$F_{14} = 1 + \mu n(0),$$

Downloaded 03 May 2010 to 171.66.16.20. Redistribution subject to ASME license or copyright; see http://www.asme.org/terms/Terms_Use.cfm

$$G_{3j} = V_j'(1),$$
$$G_{4j} = b(1)V_j''(1) + b'(1)V_j'(1) + g(1)\eta(\alpha^2 + \Lambda^2)V_j(1),$$
$$j = 1,2,3,4.$$

APPENDIX B

The Frequency Equation of Rotating Nonuniform Timoshenko Beams in the Dimensionless Flexural Displacement

Case 1: Elastically Restrained Root. For this case, K_θ and K_T are all constants and the frequency equation is

$$\pi = \begin{vmatrix} F_{14} & F_{13} & F_{12} & F_{11} \\ F_{24} & F_{23} & F_{22} & F_{21} \\ G_{34} & G_{33} & G_{32} & G_{31} \\ G_{44} & G_{43} & G_{42} & G_{41} \end{vmatrix} = 0,$$

where

$$F_{11} = B_0/\mu + \beta_T\zeta|_{\xi=0}, \qquad F_{12} = (B_1 - \zeta)/\mu - n\zeta|_{\xi=0},$$
$$F_{13} = B_2/\mu|_{\xi=0}, \qquad F_{14} = B_3/\mu|_{\xi=0},$$
$$F_{21} = (\beta_\theta + s')B_0 - \mu(\alpha^2 \sin^2\theta + \Lambda^2)\zeta|_{\xi=0},$$
$$F_{22} = (\beta_\theta + s')B_1 - (s' + \mu n')\zeta|_{\xi=0},$$
$$F_{23} = (\beta_\theta + s')B_2 - (1 + \mu n)\zeta|_{\xi=0},$$
$$F_{24} = (\beta_\theta + s')B_3|_{\xi=0},$$
$$F_{31} = s'B_0 - \mu s(\alpha^2 \sin^2\theta + \Lambda^2)\zeta|_{\xi=1}, \qquad F_{32} = s'B_1 - (s' + \mu n')\zeta|_{\xi=1},$$
$$F_{33} = s'B_2 - (q + \mu n)\zeta|_{\xi=1}, \qquad F_{34} = s'B_3|_{\xi=1},$$
$$F_{41} = B_0/\mu|_{\xi=1}, \quad F_{42} = (B_1 - \zeta)/\mu|_{\xi=1}, \quad F_{43} = B_2/\mu|_{\xi=1}, \quad F_{44} = B_3/\mu|_{\xi=1},$$
$$B_0 = \mu^2(\alpha^2 \sin^2\theta + \Lambda^2)(2bms' - b'ms - bm's),$$
$$B_1 = \mu[(2bs' - b's)(s' + \mu n') - bs(s'' + \mu n'') - \mu bms(\alpha^2 \sin^2\theta + \Lambda^2)] - s^3,$$
$$B_2 = \mu(2\mu bs'n - 2\mu bsn' - \mu b'sn - b's^2),$$
$$B_3 = -\mu bs(s + \mu n),$$
$$G_{3j} = F_{34}V_j'''(1) + F_{33}V_j''(1) + F_{32}V_j'(1) + F_{31}V_j(1),$$
$$G_{4j} = F_{44}V_j'''(1) + F_{43}V_j''(1) + F_{42}V_j'(1) + F_{41}V_j(1), \quad j = 1,2,3,4.$$

Case 2: Clamped-Free. For this case, K_T and $K_\theta \to \infty$, the frequency equation is

$$\pi = F_{22}G_{33}G_{44} + F_{23}G_{34}G_{42} + F_{24}G_{32}G_{43} - F_{22}G_{34}G_{43} - F_{23}G_{32}G_{44} - F_{24}G_{33}G_{42} = 0,$$

where $F_{21} = B_0(0)$, $F_{22} = B_1(0)$, $F_{23} = B_2(0)$, $F_{24} = B_3(0)$ and the other parameters are the same as those of Case 1.

Downloaded 03 May 2010 to 171.66.16.20. Redistribution subject to ASME license or copyright; see http://www.asme.org/terms/Terms_Use.cfm

ERRATA

Errata on "On the Double Cantilever Beam Specimen for Mode-I Interface Delamination," by B. Balendran, published in the June 1994 issue of the ASME JOURNAL OF APPLIED MECHANICS, Vol. 61, pp. 471–473.

The following equations have typographical errors.

The correct equations (8*a*), (8*b*), and (10*b*) on page 473 are

$$C=\frac{6a}{5B}\left(\frac{1}{G_1h_1}+\frac{1}{G_2h_2}\right)+\frac{4a^3}{B}+\left(\frac{1}{E_1h_1^3}+\frac{1}{E_2h_2^3}\right)+\frac{D_1\alpha a^2}{B}\coth\alpha b,$$

$$G_{Ic}=\frac{6P_a^2a^2}{B^2}\left(\frac{1}{E_1h_1^3}+\frac{1}{E_2h_2^3}\right)+\frac{3P_c^2}{5B^2}\left(\frac{1}{G_1h_1}+\frac{1}{G_2h_2}\right)$$

$$+D_1\frac{\alpha aP_c^2}{B^2}\left(\coth\alpha b+\frac{\alpha a}{2\sinh^2\alpha b}\right). \quad (8a,b)$$

$$G_{Ic}=\frac{12P_c^2a^2}{EB^2h^3}+\frac{6P_c^2}{5GB^2h}\left(1+2\alpha a\coth\alpha b+\frac{\alpha^2a^2}{\sinh^2\alpha b}\right). \quad (10b)$$

Copyright © 1994 by ASME
Downloaded 03 May 2010 to 171.66.16.20. Redistribution subject to ASME license or copyright; see http://www.asme.org/terms/Terms_Use.cfm

Automation and Assessment of Augmented Lagrangian Algorithms for Frictional Contact Problems

T. A. Laursen
Assoc. Mem. ASME

V. G. Oancea

Department of Civil and Environmental Engineering, Duke University, Box 90287, Durham, NC 27708-0287

In recent work, the augmented Lagrangian approach to large deformation frictional contact problems has been advocated for finite element calculations. The resulting algorithms have been shown to facilitate accurate constraint enforcement in a robust manner, while providing an effective technique for removal of the nonsymmetry associated with most frictional constitutive laws. In this work, we examine automation schemes for the algorithm, such that multipliers can be determined to a specified degree of accuracy without user intervention. The performance of the resulting automatic augmentation algorithm is then examined, providing important information about practical attributes of the procedure.

Introduction

This work is concerned with the practical and efficient finite element simulation of large deformation processes in which mechanical contact and friction are observed. Such problems are common to our everyday experience, as evidenced for example by the wide variety of examples in metal forming, tribology, geomechanics, crashworthiness, and machine design.

Mathematically, these problems possess at least two sets of constraints associated with the contacting surfaces: impenetrability constraints, expressed as a set of complementarity (Kuhn-Tucker) conditions (see, e.g., Kikuchi and Oden, 1988), and frictional constraints, typically taken to be Coulomb-like in nature and conveniently written as equations of constrained evolution (e.g., Michaelowski and Mroz, 1978; Giannakopoulos, 1989). A common approach to solving a constrained problem of this type is to convert it from a variational inequality to an equality, via either Lagrange multipliers (e.g., Gallego and Anza, 1989; Rebelo, Nagtegaal, and Hibbitt, 1990) or the introduction of a penalty regularization (e.g., Oden and Pires, 1984; Benson and Hallquist, 1990). Although implementations of both types have been proposed and demonstrated, neither technique is completely free of difficulties. Implementation of Lagrange multiplier schemes can be unwieldy, particularly in frictional loading/unloading (i.e., slip reversal) situations. Convergent Lagrange multiplier treatments therefore often require simplifications to be made in the frictional characterization, such as approximation of the stick-slip transition or simplified loading-unloading conditions (see, e.g., Saran and Wagoner, 1991). Penalty regularizations do not require such simplifications, but are highly sensitive to the penalty selected (Luenberger, 1984), often making them somewhat unreliable in elastoplastic applications. In such cases, one may not know a priori whether or at what locations soft response (yielding) will occur, thereby introducing the risk of ill-conditioning by overpenalization. On the other hand, accuracy may depend crucially on adequate penalization taking place. It should be clear that use of the penalty method can require a great deal of trial and error on the part of the analyst.

It is largely in response to this situation that the method of augmented Lagrangians for contact problems has been proposed by several authors (Landers and Taylor, 1986; Simo and Laursen, 1992; Wriggers and Zavarise, 1993; Heegaard and Curnier, 1993). This method is perhaps best regarded as a compromise between Lagrange multipliers and the penalty method, and involves iterative improvement of the standard penalty regularization. In a significant improvement upon these efforts (Laursen and Simo, 1993a), the method has been extended to algorithmically symmetrize the (Coulomb) frictional problem. This latest development provides an algorithm in which only symmetric equations need be solved—an important practical consideration in the symmetry-dominated world of computational solid mechanics. Since frictional nonsymmetries generally arise from nonassociated frictional slip laws and not from the numerical algorithms applied to them, nonsymmetry is common to most earlier equation solving strategies (i.e., both Lagrange multiplier and penalty methods). Most previous symmetrization attempts centered on iterative schemes involving recursive treatments of the normal and tangential frictional constraints (Kikuchi and Oden, 1988; Mistakidis and Panagiotopoulos, 1993), with somewhat mixed results. The symmetrized augmented Lagrangian treatment appears to per-

Contributed by the Applied Mechanics Division of THE AMERICAN SOCIETY OF MECHANICAL ENGINEERS for presentation at the International Mechanical Engineering Congress and Exhibition, the Winter Annual Meeting of The ASME, Chicago, IL, Nov. 6–11, 1994.

Discussion on this paper should be addressed to the Technical Editor, Professor Lewis T. Wheeler, Department of Mechanical Engineering, University of Houston, Houston, TX 77204-4792, and will be accepted until four months after final publication of the paper itself in the ASME JOURNAL OF APPLIED MECHANICS.

Manuscript received by the ASME Applied Mechanics Division, July 16, 1993; final revision, Dec. 15, 1993. Associate Technical Editor: W. K. Liu.

Paper No. 94-WA/APM-5.

Copyright © 1994 by ASME
Downloaded 03 May 2010 to 171.66.16.20. Redistribution subject to ASME license or copyright; see http://www.asme.org/terms/Terms_Use.cfm

form well for a wide range of large deformation problems, while possessing the best attributes of penalty and Lagrange multiplier algorithms.

This paper addresses two aspects which are central to practical application and use of augmented Lagrangian algorithms. First, we discuss a technique for automation of the augmented Lagrangian update and solution process, such that multipliers (constraints) can be found (satisfied) to a prescribed degree of accuracy without user intervention. Second, through presentation of two examples, we quantify the performance of the resulting algorithm with a careful examination of the interrelationship between desired accuracy, prescribed penalty parameters, and economy of solution. We shall see that although the solution obtained is indeed insensitive to penalty parameter when solution tolerances are suitably small, the cost of obtaining these solutions is strongly affected by penalty selection. This paper therefore provides important practical information about the implementation and use of augmented Lagrangian contact algorithms.

2 Review of the Augmented Lagrangian Algorithm

Before discussing the Coulomb friction problem and its augmented Lagrangian treatment, some preliminary definitions need to be established. We assume that the quasi-static or dynamic motions of two deformable bodies $\Omega^{(1)}$ and $\Omega^{(2)}$ are to be determined over a time interval $I = [0, T]$. The motions $\varphi^{(i)}$ may be expressed via

$$\varphi^{(i)}: \bar{\Omega}^{(i)} \times I \to R^{n_{sd}},\ i = 1, 2, \tag{1}$$

where $\bar{\Omega}^{(i)}$ denotes the closure of an open subset $\Omega^{(i)}$ of $R^{n_{sd}}$, and $2 \le n_{sd} \le 3$ is the number of spatial dimensions. Subsurfaces $\Gamma^{(i)} \subset \partial\Omega^{(i)}$ are designated as *contact surfaces* for the two bodies, and are selected such that all prospective material points of contact are included. We arbitrarily select the surface $\Gamma^{(1)}$, and consider in the following the constraints governing the motion of points $\mathbf{X} \in \Gamma^{(1)}$ with respect to $\Gamma^{(2)}$.

A *gap* or *gauge* function $g(\mathbf{X}, t)$ is defined for any time $t \in I$ via the following *closest point projection* in the spatial configuration:

$$\left.\begin{aligned} g(\mathbf{X}, t) &= \text{sign}(g(\mathbf{X}, t))\, |g(\mathbf{X}, t)|, \text{ where} \\ |g(\mathbf{X}, t)| &= \min_{\mathbf{Y} \in \Gamma^{(2)}} \|\varphi^{(1)}(\mathbf{X}, t) - \varphi^{(2)}(\mathbf{Y}, t)\|, \text{ and} \\ \text{sign}(g(\mathbf{X}, t)) &= \begin{cases} -1 \text{ if } \varphi^{(1)}(\mathbf{X}, t) \text{ is admissible} \\ 1 \text{ otherwise} \end{cases} \end{aligned}\right\}. \tag{2}$$

Impenetrability requires that $g(\mathbf{X}, t) \le 0$. The point in $\Gamma^{(2)}$ achieving the minimization in (2) is denoted $\bar{\mathbf{Y}}(\mathbf{X}, t)$.

We note that the surface $\Gamma^{(2)}$ can be conceptualized as an $n_{sd} - 1$ dimensional manifold; accordingly, we assume it possesses suitable smoothness and give all points $\mathbf{Y} \in \Gamma^{(2)}$ a parametrization, so that $\mathbf{Y} = \Psi_0^{(2)}(\xi)$ for some point ξ in a parent domain $A^{(2)} \subset R^{n_{sd}-1}$. For a given point $\mathbf{X} \in \Gamma^{(1)}$ and at a given instant, we define $\bar{\xi} \in A^{(2)}$ such that $\bar{\mathbf{Y}} = \Psi_0^{(2)}(\bar{\xi})$. A *convected basis* in the spatial configuration is defined for each point $\mathbf{X} \in \Gamma^{(1)}$ as follows:

$$\tau_\alpha := \mathbf{F}_t^{(2)}(\bar{\mathbf{Y}}) \Psi_{0,\alpha}^{(2)}(\bar{\xi}),\ \alpha = 1, \ldots, n_{sd} - 1, \tag{3}$$

where the notation $(\cdot)_{,\alpha}$ symbolizes partial differentiation with respect to the components ξ^α of ξ. Vectors $\tau_\alpha = \mathbf{F}_t^{(2)} \cdot \mathbf{T}_\alpha$ (with $\mathbf{F}_t^{(2)}$ denoting the deformation gradient of body (2) and $\mathbf{T}_\alpha = \Psi_{0,\alpha}^{(2)}(\bar{\xi})$) are tangent vectors to the surface $\varphi^{(2)}(\Gamma^{(2)})$; together with the surface normal ν at $\varphi^{(2)}(\bar{\mathbf{Y}})$, they provide a basis in which the contact traction vector and kinematic measures can be defined and resolved.

The (dual) convected velocity of $\mathbf{X}$ relative to $\Gamma^{(2)}$ (see Laursen, 1993) is defined via

$$\mathbf{V}_T^\flat(\mathbf{X}, t) = V_{T_\alpha} \mathbf{T}^\alpha, \text{ where}$$

$$V_{T_\alpha} = M_{\alpha\beta} \dot{\bar{\xi}}^\beta \tag{4}$$

and $M_{\alpha\beta}$ is the metric in the convected representation, given by $M_{\alpha\beta} = \mathbf{T}_\alpha \cdot \mathbf{T}_\beta$. $\mathbf{V}_T^\flat$ provides the measure of slip velocity to be used in our characterization of the frictional problem.

2.1 Unregularized Coulomb Friction Problem. We now let φ denote the collection of motions $\varphi^{(1)}$ and $\varphi^{(2)}$; the particular configuration mapping obtained by fixing t is denoted by φ_t. Correspondingly, the collection of admissible material variations is written as $\overset{*}{\varphi}$. The (unregularized) Lagrange multiplier form of the problem has been long recognized (e.g., Duvaut and Lions, 1972), and is given using our current notation in Box 1, with λ_N and λ_T representing the normal and frictional Lagrange multipliers (contact tractions) on $\Gamma^{(1)}$.

BOX 1 Unregularized Coulomb friction problem

Find $\varphi^{(i)}$, $i = 1, 2$, λ_N and λ_T such that, for all $t \in I$:

$$G(\varphi_t, \overset{*}{\varphi}) + G_c(\varphi_t, \overset{*}{\varphi}) = 0 \tag{5}$$

where

$$G_c(\varphi_t, \overset{*}{\varphi}) := \int_{\Gamma^{(1)}} [\lambda_N \delta g + \lambda_{T_\alpha} \delta\bar{\xi}^\alpha] d\Gamma^{(1)}, \tag{6}$$

and for all $\mathbf{X} \in \Gamma^{(1)}$,

$$\left.\begin{aligned} &\lambda_N \ge 0 \\ &g \le 0 \\ &\lambda_N g = 0 \\ &V_{T_\alpha} - \zeta_\lambda \frac{\lambda_{T_\alpha}}{[\lambda_{T_\beta} M^{\beta\gamma} \lambda_{T_\gamma}]^{1/2}} = 0 \\ &\Phi(\lambda_{T_\alpha}, \lambda_N) := [\lambda_{T_\alpha} M^{\alpha\beta} \lambda_{T_\beta}]^{1/2} - \mu\lambda_N \le 0 \\ &\zeta_\lambda \ge 0,\ \Phi(\lambda_{T_\alpha}, \lambda_N)\zeta_\lambda = 0 \end{aligned}\right\}. \tag{7}$$

In (5), G is shorthand notation for the sum of the inertial virtual work, internal virtual work, and virtual work of the applied loads. Treatment of the contact virtual work G_c, with the indicated kinematic and dual constraints, is our primary interest here. In its expression, the summation convention is assumed on repeated Greek indices α, β, etc. (which run between 1 and $n_{sd} - 1$), and the notation $\delta(\cdot)$ denotes a *linearized variation*, or directional derivative in the direction $\overset{*}{\varphi}$.

We note in writing (5)–(7) that constraints on $\overset{*}{\varphi}$ due to the contact conditions (see, e.g., Kikuchi and Oden, 1988) have been removed through introduction of the multipliers, rendering a saddle point problem. Removal of these conditions on the variations has been achieved through introduction of additional variables (λ_N and λ_T) and extra governing equations (effectively those in (7)). These additional variables and equations may be removed via augmented Lagrangian regularization and subsequent iteration.

2.2 Regularization. The augmented Lagrangian regularization is as summarized in Box 2. The key observation is that the normal and frictional tractions are now represented by t_N and $\mathbf{t}_T$, which include a combination of Lagrange multiplier and penalty contributions as indicated in (9). In (9), ϵ_N and ϵ_T are the normal and tangential penalties, which penalize violations of the impenetrability and no reversible slip conditions, respectively. The latter penalization is achieved through introduction of an additional variable $\bar{\xi}_p^\beta$. This variable quantifies the inelastic slip, which is to exactly equal the relative velocity

Downloaded 03 May 2010 to 171.66.16.20. Redistribution subject to ASME license or copyright; see http://www.asme.org/terms/Terms_Use.cfm

when the Coulomb constraints (specifically $(7)_4$) are satisfied. In other words, the regularization introduces "elasticity" into the normal and tangential response, which must be removed if the Lagrange multiplier solution is to be obtained. If the multiplier contributions were discarded from Box 2, one would be left with a simple penalty method.

Importantly, the solution of the unregularized problem in Box 1 is the same as that of the augmented Lagrangian problem in Box 2 (see Luenberger, 1984, Chapter 13). This occurs because the solution of the unregularized problem will satisfy conditions (11), making the penalty contributions to t_N and t_{T_α} identically zero. Viewed from this perspective, solution of the problem in Box 2 is no easier than solution of the problem in Box 1; the multipliers and their corresponding extra equations are still present. The advantage of the augmented Lagrangian approach derives from the introduction of an iterative update scheme for the multipliers, which replaces constraints (11). The solution

BOX 2 Augmented Lagrangian regularization

Find $\varphi^{(i)}$, $i = 1, 2$, λ_N and λ_T such that, for all $t \in I$:

$$G(\varphi_t, \overset{*}{\varphi}) + \int_{\Gamma^{(1)}} [t_N \delta g + t_{T_\alpha} \delta \bar{\xi}^\alpha] d\Gamma^{(1)} = 0, \tag{8}$$

where for all $\mathbf{X} \in \Gamma^{(1)}$

$$\left.\begin{aligned} t_N &:= \langle \lambda_N + \epsilon_N g \rangle \\ t_{T_\alpha} &:= \lambda_{T_\alpha} + \epsilon_T M_{\alpha\beta}(\bar{\xi}^\beta - \bar{\xi}_p^\beta) \end{aligned}\right\}, \tag{9}$$

subject to

$$\left.\begin{aligned} M_{\alpha\beta}\dot{\bar{\xi}}_p^\beta &= \zeta \frac{t_{T_\alpha}}{[t_{T_\beta} M^{\beta\gamma} t_{T_\gamma}]^{1/2}} \\ \Phi(t_{T_\alpha}, \lambda_N) &:= [t_{T_\alpha} M^{\alpha\beta} t_{T_\beta}]^{1/2} - \mu t_N \le 0 \\ \zeta &\ge 0,\ \Phi(t_{T_\alpha}, \lambda_N)\zeta = 0 \end{aligned}\right\} \tag{10}$$

and conditions on the multipliers

$$\left.\begin{aligned} \lambda_N &\ge 0 \\ g &\le 0 \\ \lambda_N g &= 0 \\ V_{T_\alpha} - \zeta_\lambda \frac{\lambda_{T_\alpha}}{[\lambda_{T_\beta} M^{\beta\gamma} \lambda_{T_\gamma}]^{1/2}} &= 0 \\ \Phi(\lambda_{T_\alpha}, \lambda_N) &:= [\lambda_{T_\alpha} M^{\alpha\beta} \lambda_{T_\beta}]^{1/2} - \mu \lambda_N \le 0 \\ \zeta_\lambda &\ge 0,\ \Phi(\lambda_{T_\alpha}, \lambda_N)\zeta_\lambda = 0 \end{aligned}\right\} \tag{11}$$

of this iterative problem will only be identical to the unregularized problem in the limit as the iterative procedure converges.

2.3 Algorithmic Implementation. Box 3 contains a symmetric augmented Lagrangian algorithm for solution of the regularized problem in Box 2. Design of this algorithm is discussed more extensively in Laursen and Simo (1993a). The key aspect of the procedure is the iteration on the multipliers, indicated in Box 3 by the loop on (k), which replaces the constraints in (11). The benefit of the augmented Lagrangian regularization is now more readily apparent: it introduces a deformation-driven mechanism (constitutive law) for calculation of contact tractions in (14), with the induced constraint violations being iteratively removed through the multiplier updates in (15).

In the box, we consider the situation encountered in a typical finite element calculation, where we wish to step forward in an increment of time $[t_n, t_{n+1}] \subset I$. We have also written the problem in discretized fashion, with $\mathbf{d}$ representing the solution vector containing generalized nodal displacements, $\mathbf{M}$ representing the mass matrix, $\mathbf{F}^{\text{int}}$ representing the internal force vector, and $\mathbf{F}^{\text{ext}}$ denoting the external force vector. $\mathbf{R}_c$ is the contact force vector, obtained by performing the integration over $\Gamma^{(1)}$ indicated in Box 2. To provide concreteness, Newmark time integration has been assumed in the algorithm of Box 3; corresponding algorithms with different time integrators are readily conceived. Notably, symmetrization is achieved through use of the fixed multiplier $\lambda_{N_{n+1}}^{(k)}$ in $(14)_3$; this removes the dilatational component in the gradient of the slip function Φ and therefore preserves associativity of the slip rule. Consistent linearization of the equations in step 2 of Box 3 thus provides a symmetric tangent operator, which may be conveniently used in Newton-Raphson or quasi-Newton schemes for solution of these equations.

We note in passing that a key aspect of the algorithmic implementation, essentially omitted from this discussion, is the evaluation in the discrete setting of the contact virtual work. The approach used in this work is discussed at more length in Laursen and Simo (1993b), which should be consulted for details. To provide some insight, however, we consider the most general case of interest, where both $\Gamma^{(1)^h}$ and $\Gamma^{(2)^h}$ (finite-dimensional approximations of $\Gamma^{(1)}$ and $\Gamma^{(2)}$) deform and are described by parameterizations which are

BOX 3 Symmetric augmented Lagrangian algorithm

1 **Initialize** the augmented Lagrangian iteration counter k, and the initial guesses for the multipliers:

$$\left.\begin{aligned} \lambda_{N_{n+1}}^{(0)} &= \lambda_{N_n} \\ \lambda_{T_{n+1_\alpha}}^{(0)} &= \lambda_{T_{n_\alpha}} \\ k &= 0 \end{aligned}\right\}. \tag{12}$$

2 **Solve** for $\mathbf{d}_{n+1}^{(k)}$, corresponding to the fixed kth iterate for the multipliers,

$$\left.\begin{aligned} &\mathbf{M}\mathbf{a}_{n+1}^{(k)} + \mathbf{F}^{\text{int}}(\mathbf{d}_{n+1}^{(k)}) + \mathbf{R}_c(\mathbf{d}_{n+1}^{(k)}) = \mathbf{F}_{n+1}^{\text{ext}} \\ &\mathbf{d}_{n+1}^{(k)} = \mathbf{d}_n + \Delta t \mathbf{v}_n + \frac{\Delta t^2}{2}[(1-2\beta)\mathbf{a}_n + 2\beta \mathbf{a}_{n+1}^{(k)}] \\ &\mathbf{v}_{n+1}^{(k)} = \mathbf{v}_n + \Delta t[(1-\gamma)\mathbf{a}_n + \gamma \mathbf{a}_{n+1}^{(k)}] \end{aligned}\right\} \tag{13}$$

where the contact tractions on $\Gamma^{(1)}$ are governed by

$$\left.\begin{aligned} t_{N_{n+1}}^{(k)} &= \langle \lambda_{N_{n+1}}^{(k)} + \epsilon_N g_{n+1}^{(k)} \rangle \\ t_{T_{n+1_\alpha}}^{(k)} &= \lambda_{T_{n+1_\alpha}}^{(k)} + \epsilon_T \left\{ M_{\alpha\beta}[\bar{\xi}_{n+1}^{\beta(k)} - \bar{\xi}_n^\beta] - \zeta \frac{t_{T_{n+1_\alpha}}^{(k)}}{[t_{T_{n+1_\beta}}^{(k)} M^{\beta\gamma} t_{T_{n+1_\gamma}}^{(k)}]^{1/2}} \right\} \\ \Phi(t_{T_{n+1_\alpha}}^{(k)}, \lambda_{N_{n+1}}^{(k)}) &\le 0,\ \zeta \ge 0,\ \Phi(t_{T_{n+1_\alpha}}^{(k)}, \lambda_{N_{n+1}}^{(k)})\zeta = 0 \end{aligned}\right\}. \tag{14}$$

3 Update the Lagrange multipliers and iteration counter:

$$\left.\begin{aligned} \lambda_{N_{n+1}}^{(k+1)} &= \langle \lambda_{N_{n+1}}^{(k)} + \epsilon_N g_{n+1}^{(k)} \rangle \\ \lambda_{T_{n+1_\alpha}}^{(k+1)} &= \lambda_{T_{n+1_\alpha}}^{(k)} + \epsilon_T \left\{ M_{\alpha\beta}[\bar{\xi}_{n+1}^{\beta(k)} - \bar{\xi}_n^\beta] - \zeta_\lambda \frac{\lambda_{T_{n+1_\alpha}}^{(k+1)}}{[\lambda_{T_{n+1_\beta}}^{(k+1)} M^{\beta\gamma} \lambda_{T_{n+1_\gamma}}^{(k+1)}]^{1/2}} \right\} \\ \Phi(\lambda_{T_{n+1_\alpha}}^{(k+1)}, \lambda_{N_{n+1}}^{(k+1)}) &\le 0,\ \zeta_\lambda \ge 0,\ \Phi(\lambda_{T_{n+1_\alpha}}^{(k+1)}, \lambda_{N_{n+1}}^{(k+1)})\zeta_\lambda = 0 \\ k &\leftarrow k+1 \end{aligned}\right\}. \tag{15}$$

4 **Return** (if multipliers unconverged) to the solution phase.

only piecewise smooth (i.e., we have only C^0 continuity across element boundaries). The integral over $\Gamma^{(1)}$ required to compute $\mathbf{R}_c$ is approximated via quadrature; therefore, its discrete representation amounts to a sum of quadrature point evaluations

Downloaded 03 May 2010 to 171.66.16.20. Redistribution subject to ASME license or copyright; see http://www.asme.org/terms/Terms_Use.cfm

of the integrand. These contact quadrature points are usually taken to be nodes on the contact surface. Calculation of the needed contact kinematic quantities for a typical contact node then involves a searching algorithm consisting of two steps: (1) identification of the element in $\Gamma^{(2)^h}$ containing the closest point projection; and (2) calculation of the coordinates of the projection within this element. This latter calculation is done in terms of the parent (isoparametric) domain of the element edge, so that the element edge's parent domain is the (local) discrete counterpart of $A^{(2)}$. Steps (1) and (2) are fairly standard for computational treatment of contact problems; implementations along these lines may be found in Parish (1989), Benson and Hallquist (1990), and Wriggers, vu Van, and Stein (1990). The obvious problem in this approach is treatment of the frictional constraint near element boundaries, where the desired smoothness conditions do not hold. Some degree of approximation or reformulation is necessary in this case; research is ongoing to improve algorithmic robustness when this situation arises.

Steps 2–4 in Box 3 are generally repeated until all contact constraints are suitably enforced. In the following, we examine alternatives for specific definition of this convergence criterion, and evaluate their consequences.

3 Automation

When employing the algorithm in Box 3, one would like practical guidelines to avoid overaugmentation on one hand, and inadequate constraint enforcement on the other. In this section, we propose three possible criteria governing the repetition of steps 2–4 in Box 3. All can be automated, such that the multiplier updates, solves, and convergence checks are done without user intervention.

3.1 Convergence Criteria for Contact Constraints. In a finite element calculation the constraints of (14) are evaluated and enforced at a set of contact nodes, with the resulting set of forces comprising $\mathbf{R}_c$. Therefore, it is most expedient to base any type of multiplier convergence criterion on a summation over all such contact nodes, which comprise the discrete surface $\Gamma^{(1)^h}$. Although infinitely many criteria are certainly possible, we propose the following three, which are to be evaluated after step 3 in Box 3. In the event that the selected criterion is satisfied, the loop over steps 2–4 (i.e., the loop over (k)) is merely exited and solution proceeds to the next time step.

Criterion Number 1.

$$\left\{\frac{\Sigma_{\Gamma^{(1)^h}}[(\lambda_{N_{n+1}}^{(k+1)}-\lambda_{N_{n+1}}^{(k)})^2+\|\lambda_{T_{n+1}}^{(k+1)}-\lambda_{T_{n+1}}^{(k)}\|^2]}{\Sigma_{\Gamma^{(1)^h}}[\lambda_{N_{n+1}}^{(k+1)^2}+\|\lambda_{T_{n+1}}^{(k+1)}\|^2]}\right\}^{1/2}\leq \text{tol} \qquad (16)$$

Criterion Number 2.

$$\max_{\Gamma^{(1)^h}}\left\{\frac{|\lambda_{N_{n+1}}^{(k+1)}-\lambda_{N_{n+1}}^{(k)}|}{|\lambda_{N_{n+1}}^{(k+1)}|}+\frac{\|\lambda_{T_{n+1}}^{(k+1)}-\lambda_{T_{n+1}}^{(k)}\|}{\|\lambda_{T_{n+1}}^{(k+1)}\|}\right\}\leq \text{tol} \qquad (17)$$

Criterion Number 3.

$$\left\{\sum_{\Gamma^{(1)^h}}\frac{\langle g_{n+1}^{(k+1)}\rangle}{l_{\text{ref}}}+\sum_{\Gamma^{(1)^h}_{\text{stick}}}\|\mathbf{g}_{T_{n+1}}^{(k+1)}\|\right\}\leq \text{tol} \qquad (18)$$

The first two criteria test the convergence of the multipliers themselves, while the third tests directly for constraint enforcement. Note the appearance of $\Gamma^{(1)^h}_{\text{stick}}$ in (18); this is to indicate that the incremental tangential motions $\mathbf{g}_T$ are only to be added in for nodes detected to be sticking. Nodes that slip will obviously have finite tangential motions and cannot be expected to approach zero. All three tests are nondimensionalized; in the case of the third test, the tangential gaps $\mathbf{g}_T$ are evaluated in the dimensionless $A^{(2)}$ domain, while the normal gaps are nondimensionalized according to a reference dimension l_{ref} (typically taken to be a representative element length for one of the contacting elements).

Numerical tests were performed for all three criteria. The first, although less stringent than the other two, proved most effective in practical applications and is therefore the test considered in the examples of the next section. The second criterion is perhaps the most intuitively satisfying, since it ensures convergence of every single discrete multiplier in the problem to a prescribed degree of accuracy. This stringency tends to result in a great deal of expense for the algorithm, since unimportant multiplier changes in regions of very light contact are often observed to greatly extend the iteration process. Much the same could be said of the third criterion. Therefore, in quantifying the effects of various tolerances and penalties, the first criterion appears to the authors to be the most practical choice. Other criteria (or various combinations of these three) might be used just as profitably in other applications.

4 Assessment

With the algorithm and tolerancing strategy in hand, we shall quantify the performance of the algorithm through examination of two topics. First and most importantly, we wish to demonstrate the robust and accurate solution of frictional contact problems when using the augmented Lagrangian approach. Second, and of great interest in practical computing, we are interested in the sensitivity of the algorithm's performance on the choice of two user-prescribed quantities: the penalty parameters (i.e., ϵ_N and ϵ_T) and the tolerance in (16). The following examples will show that the constraints can be accurately enforced over a wide range of penalty values (addressing the first topic), and will provide evidence that the economy of the resulting solution algorithms depends quite strongly on penalty selection.

In the following we present the findings for an axisymmetric quasi-static sheet metal forming problem (Fig. 1) and a quasistatic pipe pinching problem (Fig. 2). Although the automation procedure has been successfully tested for dynamic problems also, we present quasi-static results only so that temporal accuracy of the time integration scheme is not a factor in evaluation of algorithmic performance. The incremental load method was employed, with the loads being displacement control of the spherical punch in the axisymmetric problem and displacement control of the plate ends in the pipe pinching problem. In each problem, the strategy was to select a modest value for the initial load increment, such that a calculation using this load increment throughout the quasi-static simulation would produce the same answer as calculations with smaller increments. After selection of this initial increment, an elementary automatic time-stepping procedure was then employed in the remainder of each simulation (Taylor and Govindjee, 1993), by which the load increment was increased when the number of Newton-Raphson equilibrium iterations in a given step was less than a lower threshold (indicating a relatively easy step), and was decreased if larger than an upper threshold (indicating more difficult convergence). If convergence could not be achieved in a given step, the state was automatically reset to the previously converged solution and the load increment was decreased. By repeating each calculation several times, with the same initial load increment but with different choices of the multiplier tolerance and penalties (ϵ_N and ϵ_T were taken to be equal in the calculations presented), one could readily observe the effect of these selections on the economy of solution.

In the forming problem, the metal sheet was discretized using 100 9-node finite strain elastoplastic elements (Simo, 1988), with the material properties being K = 63.48 GPa, G = 26.12 GPa, σ_y = 31. MPa, and H (the linear isotropic hardening rate) = $G/100$. The tooling was taken to be rigid. For the

Downloaded 03 May 2010 to 171.66.16.20. Redistribution subject to ASME license or copyright; see http://www.asme.org/terms/Terms_Use.cfm

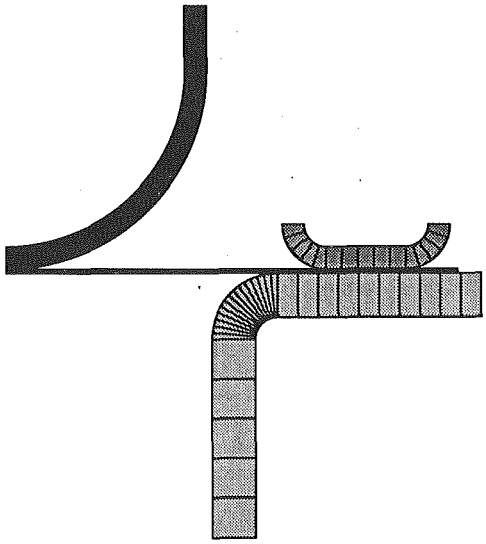


Fig. 1(*a*)

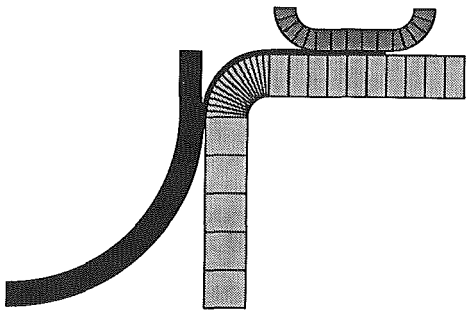


Fig. 1(*b*)

Fig. 1 Undeformed mesh (*a*) and final computed configuration (*b*) for the axisymmetric sheet-metal-forming problem

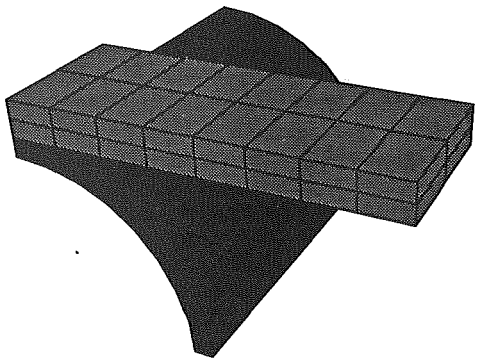


Fig. 2(*a*)

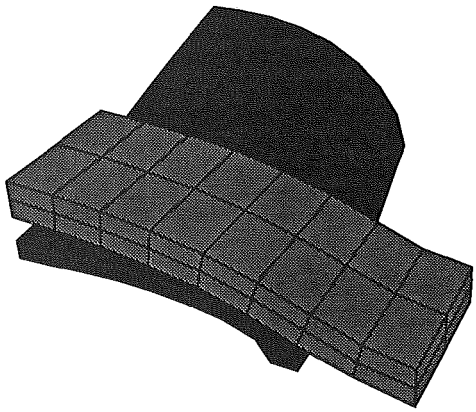


Fig. 2(*b*)

Fig. 2 Undeformed mesh (*a*) and final configuration (*b*) for the three-dimensional pipe pinching problem. Due to symmetry, only one-eighth of the geometry is modeled and shown.

three-dimensional problem the same material properties as above were used, with each plate comprised of 32 brick elements and each eighth of the pipe described by 112 elements. The coefficient of friction between the bodies in contact was prescribed as 0.1 in both problems.

Results for the drawing problem are presented in Fig. 3. In Fig. 3(*a*), the total number of linear (Newton-Raphson) solves necessary to solve the entire incremental problem is plotted as a function of prescribed penalties and tolerances. It is clear that for a given multiplier tolerance, both very small penalties (requiring excessive augmentations and associated solves) and very large penalties (requiring excessively small load increments in the presence of increasing ill-conditioning) are not efficient. Since linear equation solving tends to dominate the cost of larger implicit finite element calculations, the observed large variation in the number of required solves greatly influences the total solution cost. Figures 3(*b*) and 3(*c*) show that the number of time steps required increases with the penalty selected while the required amount of augmentation displays the opposite behavior. It is these competing factors which create the minimum in the number of solves (for a given multiplier tolerance) seen in Fig. 3(*a*).

Figure 3(*a*) also shows that the multipliers can be very accurately enforced over a wide range of penalties, by simply demanding a small tolerance. To demonstrate that the same solution was obtained in all cases, the load-displacement curves obtained from some additional calculations are presented in Fig. 4. In the first plot (Fig. 4(*a*)), results are shown in which the load increment was fixed, and the automated augmented Lagrangian procedure was employed for several different penalty parameters (using a moderate multiplier tolerance). In the other (Fig. 4(*b*)), a number of calculations using different, but constant load increments are shown. These load increments were selected to bracket the various load increments generated by the automatic time-stepping procedure used to generate Fig. 3. In both cases the results are seen to be insensitive to the parameter varied. This insensitivity was also observed when examining stresses and strains in the sheet. We can therefore have confidence that the vast differences in solution time indicated in Fig. 3 are not due to any artificial, numerically induced differences in the mechanical system itself, but are instead merely related to equation-solving difficulties induced by inauspicious choices of the penalty parameter.

An interesting issue to be examined is the sensitivity of the algorithm to the coefficient of friction. Figure 5 shows distributions of the frictional stresses on the workpiece/tooling interfaces at the final configuration for two different coefficients of friction: 0.1 (corresponding to the calculations reported above) and 0.5. Since at this state all contact interfaces are slipping, the pressures are merely proportional to the frictional stresses and are therefore not shown. It is clear that although some local details may be underresolved, the response is significantly different for the two cases. Interestingly, a sampling of the runs used to generate Fig. 4 shows that repeating them with $\mu = 0.5$ requires approximately 30 percent more linear solves to solve the entire incremental problem. This difference is mostly due to an increased number of augmentations required to achieve multiplier convergence in the presence of more friction. Although this extra expense is incurred, it is not exorbitant and seems to indicate that the algorithm is also effective for problems with significant friction.

Downloaded 03 May 2010 to 171.66.16.20. Redistribution subject to ASME license or copyright; see http://www.asme.org/terms/Terms_Use.cfm

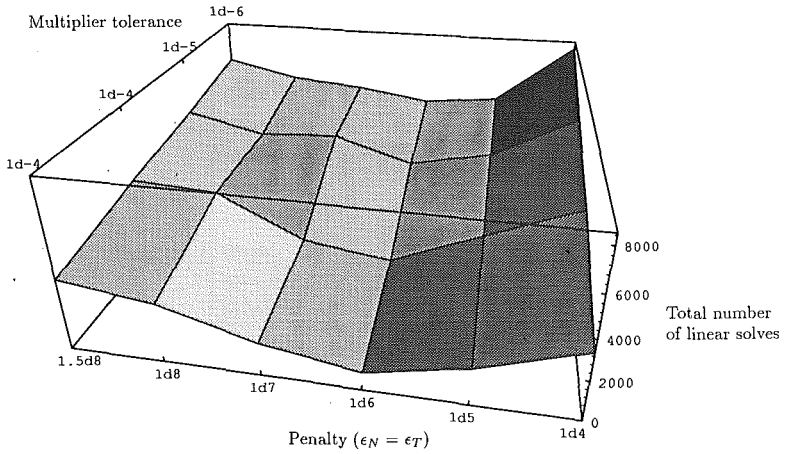


Fig. 3(*a*)

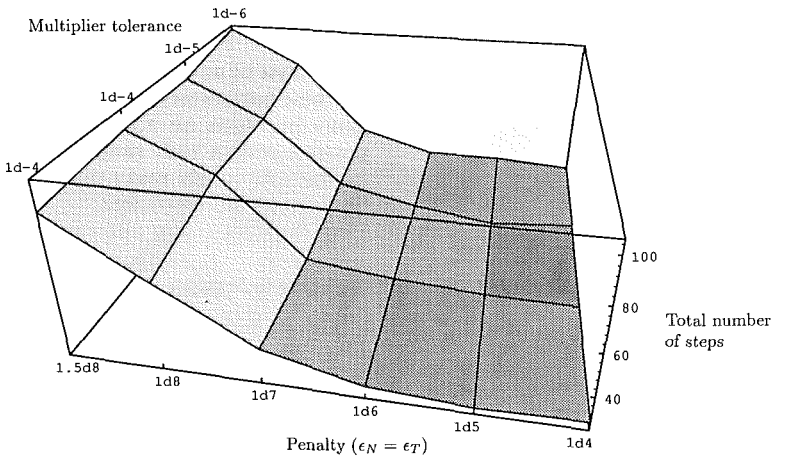


Fig. 3(*b*)

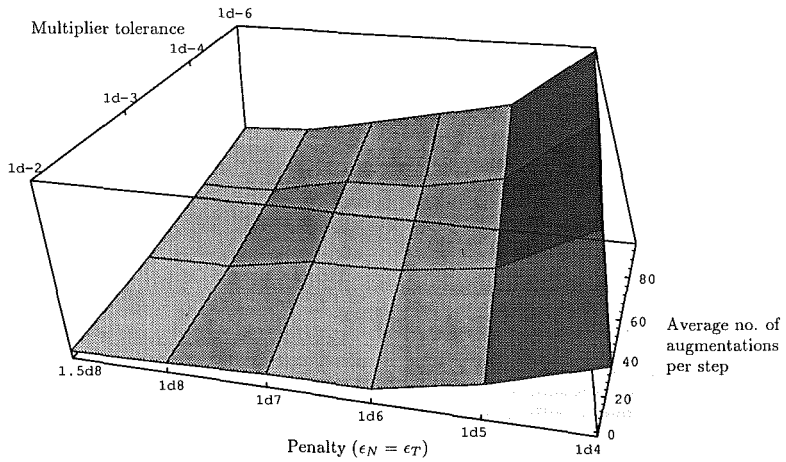


Fig. 3(*c*)

Fig. 3 Axisymmetric sheet metal forming results, showing (*a*) the total number of solves, (*b*) the total number of load increments, and (*c*) the average number of augmentations per load increment as functions of selected penalties and multiplier tolerance

Figure 6 shows the total number of solves versus contact input quantities for the three-dimensional problem, using both a Newton-Raphson solver (Fig. 6(*a*)) and the BFGS algorithm (Fig. 6(*b*)), as described in the landmark paper of Matthies and Strang (1979). One notes in Fig. 6(*a*) the same trends noted in the axisymmetric example. Although the BFGS results are preliminary, they demonstrate the importance of the symmetric augmented Lagrangian algorithm, since the BFGS quasi-Newton updates are suitable for symmetric systems only. The number of linear solves is much less in this case, since much of the convergence is achieved through the BFGS updates. It appears that the multiplier updates of step 3 in Box 3 can be effectively interwoven with the BFGS update scheme used to solve step 2; this could be crucial for efficient solution of large three-

Downloaded 03 May 2010 to 171.66.16.20. Redistribution subject to ASME license or copyright; see http://www.asme.org/terms/Terms_Use.cfm

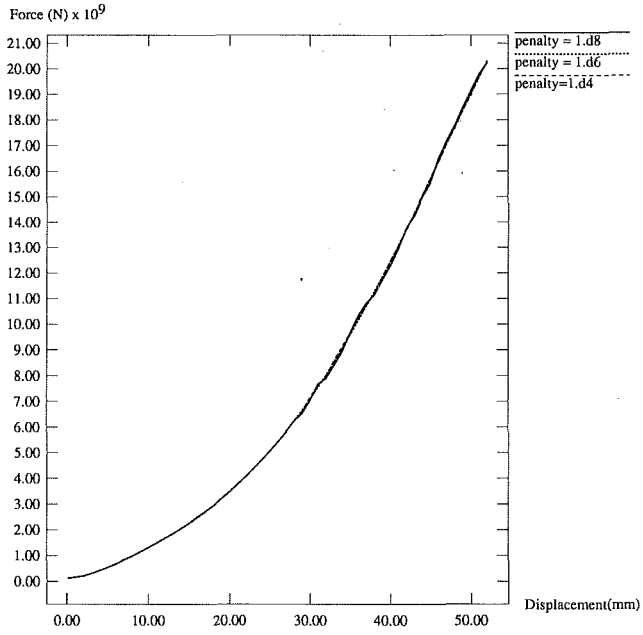


Fig. 4(*a*)

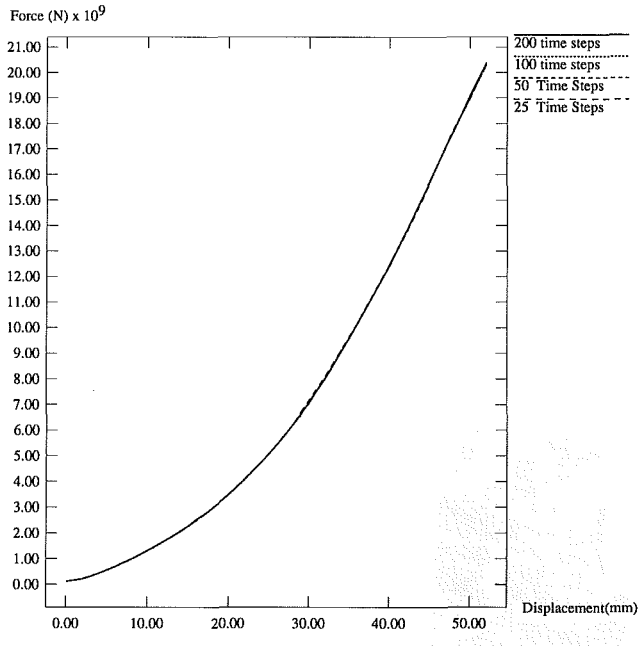


Fig. 4(*b*)

Fig. 4 Axisymmetric sheet-metal-forming load-displacement curves, showing insensitivity of results to (*a*) penalty selection, with 100 load increments and tol = 10^{-4}; and (*b*) load increment, with $\epsilon_N = \epsilon_T = 10^6$ and tol = 10^{-4}

dimensional problems and will be explored further in future work.

5 Summary and Conclusions

In this paper a fully automatic augmented Lagrangian algorithm for frictional contact problems has been introduced and evaluated. We have seen that although the algorithm removes penalty sensitivity as a concern in the accuracy of the numerical solution, the penalty values have an appreciable effect on the efficiency with which the governing constrained equations can be solved. Further work will explore alternatives for a priori estimation of optimal penalties, which would relieve the analyst of an often painstaking search for efficient choices for these parameters. It is to be emphasized, however, that for many problems an accurate determination of multipliers is possible over a wide range of penalties; optimal penalty selection will merely make the solution of the governing equations much more efficient.

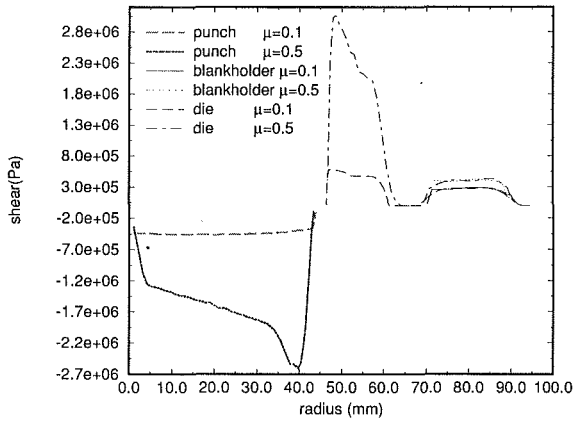


Fig. 5 Frictional interface stresses on the sheet in the axisymmetric sheet-metal-forming problem, for μ = 0.1 and μ = 0.5. Positive sign indicates stresses acting toward the outer edge of the sheet.

Acknowledgment

The authors wish to thank Dr. Brad N. Maker of Lawrence Livermore National Laboratory for several useful conversations on the subject of this paper.

References

Benson, D. J., and Hallquist, J. O., 1990, "A Single Surface Contact Algorithm for the Post-Buckling Analysis of Shell Structures," *Computer Methods in Applied Mechanics and Engineering*, Vol. 78, pp. 141–163.

Duvaut, G., and Lions, J. L., 1972, *Les Inequations en Mecanique et en Physique*, Dunod, Paris.

Gallego, F. J., and Anza, J. J., 1989, "A Mixed Finite Element Model for the Elastic Contact Problem," *International Journal for Numerical Methods in Engineering*, Vol. 28, pp. 1249–1264.

Giannakopoulos, A. E., 1989, "The Return Mapping Method for the Integration of Friction Constitutive Relations," *Computers and Structures*, Vol. 32, pp. 157–167.

Heegaard, J.-H., and Curnier, A., 1993, "An Augmented Lagrangian Method for Discrete Large-Slip Contact Problems," *International Journal for Numerical Methods in Engineering*, Vol. 36, pp. 569–593.

Kikuchi, N., and Oden, J. T., 1988, *Contact Problems in Elasticity: A Study of Variational Inequalities and Finite Element Methods*, SIAM, Philadelphia, PA.

Landers, J. A., and Taylor, R. L., 1986, "An Augmented Lagrangian Formulation for the Finite Element Solution of Contact Problems," NCEL Contract Report, Naval Civil Engineering Laboratory, Port Hueneme, CA.

Laursen, T. A., 1994, "The Convected Description in Large Deformation Frictional Contact Problems," *International Journal of Solids and Structures*, Vol. 31, pp. 669–681.

Laursen, T. A., and Simo, J. C., 1993a, "Algorithmic Symmetrization of Coulomb Frictional Problems Using Augmented Lagrangians," *Computer Methods In Applied Mechanics and Engineering*, Vol. 108, pp. 133–146.

Laursen, T. A., and Simo, J. C., 1993b, "A Continuum-Based Finite Element Formulation for the Implicit Solution of Multibody, Large Deformation Frictional Contact Problems," Vol. 36, pp. 3451–3485.

Luenberger, D. G., 1984, *Linear and Nonlinear Programming*, 2nd ed., Addison-Wesley, Reading, MA.

Matthies, H., and Strang, G., 1979, "The Solution of Nonlinear Finite Element Equations," *International Journal for Numerical Methods in Engineering*, Vol. 14, pp. 1613–1626.

Michalowski, R., and Mroz, Z., 1978, "Associated and Non-Associated Sliding Rules in Contact Friction Problems," *Archives of Mechanics*, Vol. 30, pp. 259–276.

Mistakidis, E. S., and Panagiotopoulos, P. D., 1993, "Numerical Treatment of the Nonmonotone (Zig-Zag) Friction and Adhesive Contact Problems with Debonding Approximation by Monotone Subproblems," *Computers and Structures*, Vol. 47, pp. 33–46.

Downloaded 03 May 2010 to 171.66.16.20. Redistribution subject to ASME license or copyright; see http://www.asme.org/terms/Terms_Use.cfm

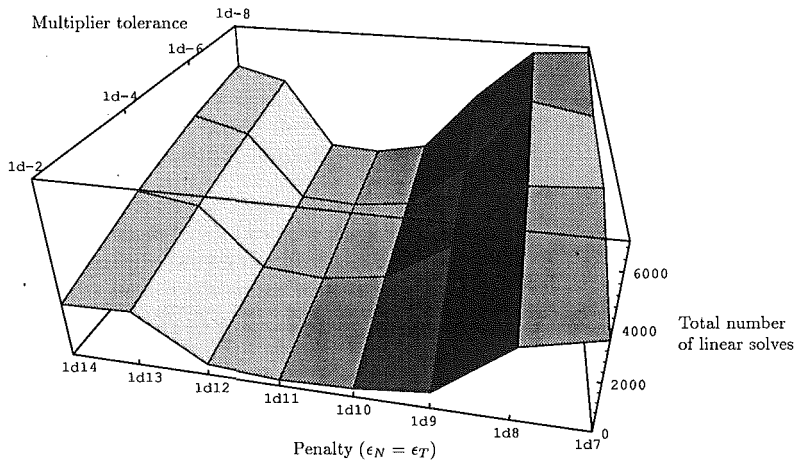


Fig. 6(*a*)

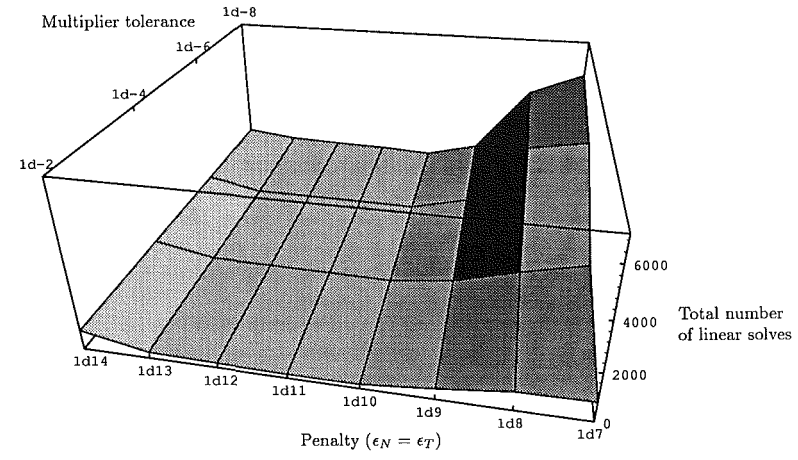


Fig. 6(*b*)

Fig. 6 Three-dimensional pipe pinching results, showing (*a*) total number of solves using Newton-Raphson iteration, and (*b*) total number of solves using BFGS updates, as functions of selected penalties and multiplier tolerance

Oden, J. T., and Pires, E. B., 1984, "Algorithms and Numerical Results for Finite Element Approximations of Contact Problems with Non-Classical Friction Laws," *Computers and Structures*, Vol. 19, pp. 137–147.

Rebelo, N., Nagtegaal, J. C., and Hibbitt, H. D., 1990, "Finite Element Analysis of Sheet Forming Processes," *International Journal for Numerical Methods in Engineering*, Vol. 30, pp. 1739–1758.

Saran, M. J., and Wagoner, R. H., 1991, "A Consistent Implicit Formulation for Nonlinear Finite Element Modeling with Contact and Friction: Part I—Theory," ASME JOURNAL OF APPLIED MECHANICS, Vol. 58, pp. 499–512.

Simo, J. C., 1988, "A Framework for Finite Strain Elastoplasticity Based on the Multiplicative Decomposition and Hyperelastic Relations. Part II: Computational Aspects," *Computer Methods in Applied Mechanics and Engineering*, Vol. 68, pp. 1–31.

Simo, J. C., and Laursen, T. A., 1992, "An Augmented Lagrangian Treatment of Contact Problems Involving Friction," *Computers and Structures*, Vol. 42, pp. 97–116.

Taylor, R. L., and Govindjee, S., 1993, unpublished research.

Wriggers, P., and Zavarise, G., 1993, "On the Application of Augmented Lagrangian Techniques for Nonlinear Constitutive Laws in Contact Interfaces," *Communications in Applied Numerical Methods*, submitted for publication.

Downloaded 03 May 2010 to 171.66.16.20. Redistribution subject to ASME license or copyright; see http://www.asme.org/terms/Terms_Use.cfm

Vibrations of Transversely Isotropic Finite Circular Cylinders

K. T. Chau
Department of Civil and Structural Engineering, Hong Kong Polytechnic, Hung Hom, Kowloon, Hong Kong
Mem. ASME.

This paper investigates the exact frequency equations for all the possible natural vibrations in a transversely isotropic cylinder of finite length. Two wave potentials are used to uncouple the equations of motion; the resulting hyperbolic equations are solved analytically for the vibration frequencies of a finite cylinder with zero shear tractions and zero axial displacement on the end surfaces and with zero tractions on the curved surfaces. In general, the mode shapes and the frequency equations of vibrations depend on both the range of the frequency and the elastic properties of the material. The vibration frequencies for sapphire cylinders are studied as an example. Two limiting cases are also considered: the long bar limit equals the frequency equation for the longitudinal vibration of bars obtained by Morse (1954) and by Lord Rayleigh (1945); and the frequency equation for thin disks (small length/radius ratio) is also obtained. The frequency for the first axisymmetric mode agrees with the experimental observation by Lusher and Hardy (1988) to within one percent. Natural frequencies for the first three longitudinal and circumferential modes are plotted for all cylinder geometries. The lowest frequency always corresponds to the first nonsymmetric mode regardless of the dimension of the cylinder. For axisymmetric vibration modes, numerical plots show that double roots exist in the frequency equations; such doublets were observed experimentally by Booker and Sagar (1971).

1 Introduction

Finite circular cylinders are commonly used as ultrasonic transducers and resonators; the natural frequency spectrum of such cylinders has to be calculated accurately for practical purposes (see, e.g., Lusher and Hardy, 1988). In addition, the natural frequencies of vibrations of a solid can also be used to determine the elastic constants of a material by using the resonating solid method (Schreiber et al., 1973; Heyliger et al., 1990). In particular, theoretical predictions for the natural frequencies of a specimen can be compared with the experimental measurements to give the best fitted elastic constants of the material. One of the typical specimen geometries used in the resonating solid method is a finite circular cylinder (Heyliger, 1991).

As summarized by Love (1944), the natural frequencies of an infinite vibrating cylinder was first obtained independently by Pochhammer and Chree. Morse (1954) extended Pochhammer-Chree's solution to a transversely isotropic infinite circular cylinder. Similar problems were also considered by Mirsky (1965), Chen and Wright (1966), and Xu and Datta (1991). Approximate solutions for the free vibrations of finite isotropic circular cylinders with zero-end tractions have been obtained by Mindlin and McNiven (1960) and by McNiven and Perry (1962). Hutchinson (1972) solved the same problem by using series solution. Grinchenko and Komissarova (1980) considered the problem differently: the natural frequencies of free vibrations were calculated based on the solutions of a vibrating cylinder under radial forcing. Other studies for the vibrations of isotropic finite circular cylinders include the works by Sheiba and Shlyapochnikov (1974), Imenitova et al. (1976), Chernyshev and Shegai (1977), and Fridman (1981). Lusher and Hardy (1988) had extended Hutchinson's method to consider the axisymmetric free vibrations of a transversely isotropic finite circular cylinder.

Numerical methods for the free vibrations of finite cylinders include: the finite difference method by McMahon (1964); the finite element method by Gladwell and Tahbildar (1972) and by Gladwell and Vijay (1975); and the Ritz method by Rumerman and Raynor (1971), Heyliger (1991), and Heyliger and Jilani (1992).

Except the finite element analysis by Gladwell and Vijay (1975) for isotropic cylinders and the Ritz analysis by Heyliger and Jilani (1992), all of the above analyses are, however, restricted to the axisymmetric modes of vibrations. Experimental observations for finite sapphire cylinders (Lusher and Hardy, 1988), however, suggest that the lowest natural frequency may be of nonaxisymmetric type depending on the actual geometry. In particular, Lusher and Hardy (1988) observed that the lowest vibration mode for a sapphire cylinder with roughly the same value for diameter and length is not axisymmetric.

Contributed by the Applied Mechanics Division of THE AMERICAN SOCIETY OF MECHANICAL ENGINEERS for publication in the ASME JOURNAL OF APPLIED MECHANICS.

Discussion on this paper should be addressed to the Technical Editor, Professor Lewis T. Wheeler, Department of Mechanical Engineering, University of Houston, Houston, TX 77204-4792, and will be accepted until four months after final publication of the paper itself in the ASME JOURNAL OF APPLIED MECHANICS.

Manuscript received by the ASME Applied Mechanics Division, Feb. 3, 1993; final revision, June 10, 1993. Associate Technical Editor: S. K. Datta.

Copyright © 1994 by ASME
Downloaded 03 May 2010 to 171.66.16.20. Redistribution subject to ASME license or copyright; see http://www.asme.org/terms/Terms_Use.cfm

In this study, we consider the exact frequency equations for all the possible vibration modes (including nonaxisymmetric ones) for a transversely isotropic circular cylinder of finite length. The most commonly adopted boundary conditions are the zero-traction conditions on both the end and the curved surfaces. However, for the sake of mathematical simplicity we consider in this study a mixed-end condition that allows the separation of variables to be applicable. In particular, we consider the vibrations of a finite cylinder subjected to zero shear tractions and zero axial displacement on the end surfaces. As a result, the evaluation of exact frequency equations becomes possible. Although this end condition differs from the commonly used traction-free end condition, the experimental configuration employed by Lusher and Hardy (1988) seems to agree well with this assumed end condition. More specifically, Lusher and Hardy (1988) found that their measured natural frequencies agree better with the theoretical predictions if the vibration modes are of small axial displacement on the end surfaces. That is, a zero displacement end condition seems to be more appropriate in modeling their experimental configuration.

In particular, two wave potentials, obtained by extending Hu's (1957) wave potentials to cylindrical coordinates, are used to uncouple the equations of motion for a transversely isotropic material; and a time harmonic vibration is considered.

2 Mathematical Formulations

We consider the natural vibrations of a finite circular cylinder of radius a and length L and governed by the following linear elastic transversely isotropic constitutive model:

$$\sigma_{rr}=C_{11}\epsilon_{rr}+C_{12}\epsilon_{\theta\theta}+C_{13}\epsilon_{zz},\quad \sigma_{\theta\theta}=C_{12}\epsilon_{rr}+C_{11}\epsilon_{\theta\theta}+C_{13}\epsilon_{zz},$$
$$\sigma_{zz}=C_{13}(\epsilon_{rr}+\epsilon_{\theta\theta})+C_{33}\epsilon_{zz},\quad \sigma_{r\theta}=(C_{11}-C_{12})\epsilon_{r\theta},$$
$$\sigma_{z\alpha}=2C_{44}\epsilon_{z\alpha}, \quad (1)$$

where $\alpha = r, \theta$ and (r, θ, z) are the cylindrical polar coordinates, σ is the Cauchy stress tensor, and ϵ is the strain tensor. The strain components are related to the displacement field (u_r, u_θ, u_z) by

$$\epsilon_{zz}=\frac{\partial u_z}{\partial z},\quad \epsilon_{rr}=\frac{\partial u_r}{\partial r},\quad \epsilon_{\theta\theta}=\frac{u_r}{r}+\frac{1}{r}\frac{\partial u_\theta}{\partial \theta},$$
$$\epsilon_{r\theta}=\frac{1}{2}\left(\frac{\partial u_\theta}{\partial r}+\frac{1}{r}\frac{\partial u_r}{\partial \theta}-\frac{u_\theta}{r}\right),\quad \epsilon_{\theta z}=\frac{1}{2}\left(\frac{1}{r}\frac{\partial u_z}{\partial \theta}+\frac{\partial u_\theta}{\partial z}\right),$$
$$\epsilon_{rz}=\frac{1}{2}\left(\frac{\partial u_r}{\partial z}+\frac{\partial u_z}{\partial r}\right). \quad (2)$$

Rewriting the equations of motion, $\nabla \cdot \sigma = \rho\partial^2\mathbf{u}/\partial t^2$ (where ρ and t are the density and time, respectively) for a transversely isotropic solid characterized by (1) in terms of the displacements gives

$$C_{11}\frac{\partial e}{\partial r}+(C_{11}-C_{12})\frac{1}{r}\frac{\partial \Omega_{r\theta}}{\partial \theta}+C_{44}\frac{\partial^2 u_r}{\partial z^2}$$
$$+(C_{13}-C_{11}+C_{44})\frac{\partial^2 u_z}{\partial r\partial z}=\rho\frac{\partial^2 u_r}{\partial t^2}, \quad (3)$$

$$C_{11}\frac{1}{r}\frac{\partial e}{\partial \theta}+(C_{11}-C_{12})\frac{\partial \Omega_{\theta r}}{\partial r}+C_{44}\frac{\partial^2 u_\theta}{\partial z^2}$$
$$+(C_{13}-C_{11}+C_{44})\frac{1}{r}\frac{\partial^2 u_z}{\partial \theta\partial z}=\rho\frac{\partial^2 u_\theta}{\partial t^2}, \quad (4)$$

$$(C_{31}+2C_{44})\frac{\partial e}{\partial z}+[C_{33}-C_{31}-2C_{44}]\frac{\partial^2 u_z}{\partial z^2}$$
$$+C_{44}\left[\frac{1}{r}\frac{\partial \Omega_{z\theta}}{\partial \theta}+\frac{1}{r}\frac{\partial}{\partial r}(r\Omega_{zr})\right]=\rho\frac{\partial^2 u_z}{\partial t^2}, \quad (5)$$

where $\Omega = [(\nabla\mathbf{u})^T - \nabla\mathbf{u}]/2$ and $e = \nabla \cdot \mathbf{u}$ are the spin tensor and the volumetric strain, respectively. We choose a cylindrical coordinate system such that the origin rests on the bottom of the cylinder and the z-axis coincides with the axis of symmetry. Thus, the boundary conditions are

$$u_z=0,\quad \sigma_{zr}=0,\quad \sigma_{z\theta}=0, \quad (6)$$

on $z = 0, L$; and

$$\sigma_{rr}=0,\quad \sigma_{rz}=0,\quad \sigma_{r\theta}=0, \quad (7)$$

on $r = a$. As mentioned in the Introduction, motivated by the experimental observation by Lusher and Hardy (1988) we assume a zero axial displacement on the end surfaces instead of a zero-normal traction.

3 Method of Solution

The static problems of a transversely isotropic solid can be solved analytically by using two displacement potentials introduced by Hu (1954); these potentials have also been extended by Chau (1993a, 1993b) to analyze the geometric bifurcations, including barrelling, buckling, and surface instabilities, for a finite transversely isotropic circular cylinder. For vibration problems, Hu (1957) proposed two wave potentials in Cartesian coordinates. In this study, we extend Hu's (1957) potentials to cylindrical polar coordinates:

$$u_r=\frac{\partial^2\Phi}{\partial r\partial z}+\frac{1}{r}\frac{\partial \Psi}{\partial \theta},\quad u_\theta=\frac{1}{r}\frac{\partial^2\Phi}{\partial\theta\partial z}-\frac{\partial\Psi}{\partial r},$$
$$u_z=\frac{1}{(C_{13}+C_{44})}\left[\rho\frac{\partial^2\Phi}{\partial t^2}-C_{11}\nabla_1\Phi-C_{44}\frac{\partial^2\Phi}{\partial z^2}\right] \quad (8)$$

where

$$\nabla_1=\frac{1}{r}\frac{\partial}{\partial r}\left(r\frac{\partial}{\partial r}\right)+\frac{1}{r^2}\frac{\partial^2}{\partial\theta^2}. \quad (9)$$

Note that if both Φ and Ψ are independent of time, these wave potentials reduce to the displacement potentials introduced by Hu (1954). By using the equations of motion, (3)–(5), two uncoupled governing equations for Φ and Ψ are obtained:

$$\left[\left(C_{11}\nabla_1+C_{44}\frac{\partial^2}{\partial z^2}-\rho\frac{\partial^2}{\partial t^2}\right)\left(C_{44}\nabla_1+C_{33}\frac{\partial^2}{\partial z^2}-\rho\frac{\partial^2}{\partial t^2}\right)\right.$$
$$\left.-(C_{13}+C_{44})^2\nabla_1\frac{\partial^2}{\partial z^2}\right]\Phi=0, \quad (10)$$

$$\left[\frac{1}{2}(C_{11}-C_{12})\nabla_1+C_{44}\frac{\partial^2}{\partial z^2}-\rho\frac{\partial^2}{\partial t^2}\right]\Psi=0. \quad (11)$$

These two partial differential equations can further be factored as

$$\left(\nabla_1-\nu_1^2\frac{\partial^2}{\partial z^2}-c_1^2\frac{\partial^2}{\partial t^2}\right)\left(\nabla_1-\nu_2^2\frac{\partial^2}{\partial z^2}-c_2^2\frac{\partial^2}{\partial t^2}\right)\Phi$$
$$=(1+\nu_1^2)(c_1^2\nu_2^2+c_2^2)\frac{\partial^4\Phi}{\partial z^2\partial t^2}, \quad (12)$$

$$\left(\nabla_1+\nu_3^2\frac{\partial^2}{\partial z^2}-c_3^2\frac{\partial^2}{\partial t^2}\right)\Psi=0, \quad (13)$$

where c_1, c_2, and c_3 are the reciprocal of the longitudinal shear wave speed, the reciprocal of the in-plane compressional wave speed, and the reciprocal of one of the two in-plane shear wave speed, respectively. More specifically, they are defined as

$$1/c_1=(C_{44}/\rho)^{1/2},\quad 1/c_2=(C_{11}/\rho)^{1/2},$$
$$1/c_3=[(C_{11}-C_{12})/(2\rho)]^{1/2}. \quad (14)$$

In addition, ν_1 and ν_2 satisfy the following equation:

$$A\nu_\alpha^4+B\nu_\alpha^2+C=0,\quad (\alpha=1, 2) \quad (15)$$

where

Downloaded 03 May 2010 to 171.66.16.20. Redistribution subject to ASME license or copyright; see http://www.asme.org/terms/Terms_Use.cfm

$$A = C_{11}C_{44}, \quad B = (C_{11}C_{33} - C_{13}^2 - 2C_{44}C_{13}), \quad C = C_{33}C_{44}; \tag{16}$$

while ν_3 is given by

$$\nu_3 = [2C_{44}/(C_{11} - C_{12})]^{1/2}. \tag{17}$$

Note that if a real root for ν_α ($\alpha = 1, 2$) exists for (15), shear band bifurcation (or strain localization) also becomes possible. To see this, we can rewrite (1) into a rate form, that is, σ and ϵ are replaced by $\dot{\sigma}$ (the material rate of the Cauchy stress) and $\mathbf{D}$ (the rate of deformation tensor), respectively; then the shear band analysis (Rudnicki and Rice, 1975; Rice, 1976) is applied. The characteristic equation for the components of the normal to the shear band, $g_z/(g_r^2 + g_\theta^2)^{1/2}$ (where $\mathbf{g}$ is the unit normal), is found equal to (15). Thus, a real root for ν_α means a real root for $g_z/(g_r^2 + g_\theta^2)^{1/2}$: that is, shear band localization is possible if the elastic material constants give a real ν_α. For the detail of this analysis we refer to Chau (1993a) and Chau and Rudnicki (1990). Therefore, we expect that there is no loss of ellipticity in the static problem; and only imaginary or complex roots are expected for (15). Table 1 summarizes the roots for $\nu_\alpha^2 (\alpha = 1, 2, 3)$ for various transversely isotropic minerals and crystals; and, as expected, all the roots for ν_1 or ν_2 are either purely imaginary or complex. The stress components in terms of the wave potentials, obtained by substituting (8) into (1) and (2), become

$$\sigma_{rr} = \left\{ \left[C_{12} - \frac{C_{13}C_{11}}{C_{13}+C_{44}} \right] \nabla_1 - \left[\frac{C_{13}C_{44}}{C_{13}+C_{44}} \right] \frac{\partial^2}{\partial z^2} \right\} \frac{\partial \Phi}{\partial z} + (C_{11} - C_{12}) \left[\frac{\partial^3 \Phi}{\partial z \partial r^2} + \frac{\partial}{\partial r} \left(\frac{1}{r} \frac{\partial \Psi}{\partial \theta} \right) \right] + \frac{C_{13}}{C_{13}+C_{44}} \rho \frac{\partial^2}{\partial t^2} \left(\frac{\partial \Phi}{\partial z} \right), \tag{18}$$

$$\sigma_{zz} = \left\{ \left[C_{13} - \frac{C_{33}C_{11}}{C_{13}+C_{44}} \right] \nabla_1 - \left[\frac{C_{33}C_{44}}{C_{13}+C_{44}} \right] \frac{\partial^2}{\partial z^2} \right\} \frac{\partial \Phi}{\partial z} + \frac{C_{33}}{C_{13}+C_{44}} \rho \frac{\partial^2}{\partial t^2} \left(\frac{\partial \Phi}{\partial z} \right), \tag{19}$$

$$\sigma_{rz} = \left\{ - \left[\frac{C_{44}C_{11}}{C_{13}+C_{44}} \right] \frac{\partial}{\partial r} \nabla_1 + \left[\frac{C_{13}C_{44}}{C_{13}+C_{44}} \right] \frac{\partial^3}{\partial r \partial z^2} \right\} \Phi + C_{44} \frac{1}{r} \frac{\partial^2 \Psi}{\partial \theta \partial z} + \frac{C_{44}}{C_{13}+C_{44}} \rho \frac{\partial^2}{\partial t^2} \left(\frac{\partial \Phi}{\partial r} \right), \tag{20}$$

$$\sigma_{z\theta} = \left\{ - \left[\frac{C_{44}C_{11}}{C_{13}+C_{44}} \right] \frac{1}{r} \frac{\partial}{\partial \theta} \nabla_1 + \left[\frac{C_{13}C_{44}}{C_{13}+C_{44}} \right] \frac{1}{r} \frac{\partial^3}{\partial \theta \partial z^2} \right\} \Phi - C_{44} \frac{\partial^2 \Psi}{\partial r \partial z} + \frac{C_{44}}{C_{13}+C_{44}} \rho \frac{\partial^2}{\partial t^2} \left(\frac{1}{r} \frac{\partial \Phi}{\partial \theta} \right), \tag{21}$$

$$\sigma_{r\theta} = (C_{11} - C_{12}) \left[\frac{\partial}{\partial r} \left(\frac{1}{r} \frac{\partial^2 \Phi}{\partial \theta \partial z} \right) + \frac{1}{2} \left(\frac{1}{r} \frac{\partial \Psi}{\partial r} + \frac{1}{r^2} \frac{\partial^2 \Psi}{\partial \theta^2} - \frac{\partial^2 \Psi}{\partial r^2} \right) \right]. \tag{22}$$

The expression for $\sigma_{\theta\theta}$ is given by (18) if the "plus" sign in front of $(C_{11} - C_{12})$ is replaced by a "minus." Note that the wave potentials method discussed here can, in general, be used to solve other dynamic problems for transversely isotropic solids if the general solutions for (12) and (13) are known for the initial and boundary conditions considered.

4 Vibration Modes and Frequency Equations

We consider the following form of the vibration modes:

$$\Phi = \phi(r) \sin(\eta z) \cos(n\theta) \exp(i\omega t),$$
$$\Psi = \psi(r) \cos(\eta z) \sin(n\theta) \exp(i\omega t), \tag{23}$$

where $\eta = m\pi/L$, $m = 1, 2, \ldots$ and $n = 0, 1, 2, \ldots$. Note that the axisymmetric vibration modes correspond to $n = 0$; the first nonsymmetric ones correspond to $n = 1$. The end boundary conditions, (6), are satisfied identically by (23). Substitution of (23) into (12) and (13) gives

$$(\nabla_2 - \beta_1^2)(\nabla_2 - \beta_2^2)\phi = 0, \quad (\nabla_2 + \beta_3^2)\psi = 0, \tag{24}$$

where

$$\nabla_2 = \frac{1}{r} \frac{d}{dr} \left(r \frac{d}{dr} \right) - \frac{n^2}{r^2}. \tag{25}$$

And β_α ($\alpha = 1, 2$) satisfies

$$\beta_\alpha^4 + \overline{B}\beta_\alpha^2 + \overline{C} = 0; \tag{26}$$

where

$$\overline{B} = \eta^2(\nu_1^2 + \nu_2^2) + \omega^2(c_1^2 + c_2^2),$$
$$\overline{C} = (\omega^2 c_2^2 - \eta^2 \nu_1^2 \nu_2^2)(\omega^2 c_1^2 - \eta^2), \tag{27}$$

and β_3 is given by

$$\beta_3^2 = \omega^2 c_3^2 - \eta^2 \nu_3^2. \tag{28}$$

The general solutions of (24) depend on the nature of the roots for β_α ($\alpha = 1, 2$) and on whether β_3^2 greater than zero. In particular, there are four possible solutions for the roots of (26): (1) all are complex (i.e., $\overline{B}^2 - 4\overline{C} < 0$ and $\overline{C} > 0$); (2) all are imaginary (i.e., $\overline{B}^2 - 4\overline{C} > 0$, $\overline{C} > 0$ and $\overline{B} > 0$); (3) two are real and two are imaginary (i.e., $\overline{C} < 0$); and (4) all are real (i.e., $\overline{B}^2 - 4\overline{C} > 0$, $\overline{C} > 0$ and $\overline{B} < 0$).

Equation (27) suggests that the nature of the roots for (26) depends on the range of the natural frequencies, ω. Similarly, the general solution of ψ depends on whether $\omega^2 c_3^2$ greater than $\eta^2 \nu_3^2$. However, we do not attempt to consider all the possible scenarios here. Because once the elastic constants are given, the general form for ϕ and ψ in different frequency ranges can be identified accordingly.

As an example, we consider a finite sapphire circular cylinder with the following parameters given by Wachtman et al. (1960): $C_{11} = 4.968$, $C_{33} = 4.981$, $C_{44} = 1.474$, $C_{12} = 1.636$, $C_{13} =$

Table 1 The values of $\nu_\alpha (\alpha = 1, 2, 3)$ for various minerals and crystals (results are based on the elastic constants from Payton (1983) and Wachtman et al. (1960))

Crystal	ν_1^2 and ν_2^2	ν_3^2	root type for ν_1 & ν_2
isotropic materials	-1.000,-1.000	1.0000	PI
apatite	-0.464±i0.789	0.8616	C
beryllium	-0.987±i0.420	1.2213	C
beryl	-0.348,-2.524	0.7514	PI
cadmium	-0.572±i0.336	0.5291	C
cobalt	-0.358,-3.255	1.0634	PI
ice (at 257K)	-0.386,-2.787	0.9057	PI
hafnium	-0.620,-1.755	1.0712	PI
magnesium	-0.508,-2.041	0.9791	PI
rhenium	-0.413,-2.702	0.9474	PI
sapphire	-0.429,-2.336	0.8848	PI
titanium	-0.635,-1.760	1.3343	PI
thallium	-0.519,-2.493	2.6889	PI
yttrium	-0.513,-1.926	0.9984	PI
zinc	-0.289±i0.541	0.5911	C

: PI = pure imaginary; C = complex

Downloaded 03 May 2010 to 171.66.16.20. Redistribution subject to ASME license or copyright; see http://www.asme.org/terms/Terms_Use.cfm

1.109 (all in units of 10^{11} Nm^{-2}), and $\rho = 3.986$ g/cm^3. For these material parameters, we find that, as expected, ν_1 and ν_2 are imaginary, as shown in Table 1. It can also be shown that $\overline{B}^2 - 4\overline{C} > 0$ for all positive $(\omega/\eta)^2$. Consequently, three different types of solutions for ϕ and ψ exist, depending on the value of ω, namely: (1) region I: $0 < (\omega/\eta)^2 < 1/c_1^2$; (2) region II: $1/c_1^2 < (\omega/\eta)^2 < (\nu_1\nu_2/c_2)^2$; and (3) region III: $(\nu_1\nu_2/c^2)^2 < (\omega/\eta)^2 < \infty$. Note that $(\nu_1\nu_2)^2$ equals 1.00284 for sapphire and $(\nu_1\nu_2)^2$ equals 1 for isotropic materials. The solution forms and the frequency equations for the three different regions are as follows.

(a) Region I. For $0 < (\omega/\eta)^2 < 1/c_1^2$, the solutions for (26) are $\beta_1 = \pm p$ and $\beta_2 = \pm q$. The general solution form for (24) becomes

$$\phi = A_1 I_n(pr) + A_2 I_n(qr), \quad \psi = A_3 I_n(\beta_3 r), \tag{29}$$

where I_n is the modified Bessel function of the first kind of order n; and A_1, A_2, and A_3 are constants. The parameters p, q, and β_3 are defined as

$$p^2 + q^2 = -\overline{B}, \quad p^2 - q^2 = (\overline{B}^2 - 4\overline{C})^{1/2}, \quad \beta_3^2 = \eta^2\nu_3^2 - \omega^2 c_3^2, \tag{30}$$

where $\overline{B}$ and $\overline{C}$ are defined in (27) and ν_3 is given by (17). Substitution of (23) and (29) into the curved boundary conditions, (7), gives three equations for A_1, A_2, and A_3. For nontrivial solutions, we require the determinant of the coefficients of A_1, A_2, and A_3 to vanish and this yields the following frequency equation:

$$W_1[Q(p)R(q) - Q(q)R(p)] + W_2[P(q)R(p) - P(p)R(q)] + W_3[P(p)Q(q) - P(q)Q(p)] = 0. \tag{31}$$

The following definitions have been used:

$$P(\xi) = \eta[2I_n(\xi a)\{\xi^2[C_{11}(C_{44} - C_{13}) + (C_{13} + C_{44})C_{12}] + 2(\eta^2 - c_1^2\omega^2)C_{13}C_{44}\}/(C_{13} + C_{44}) + (C_{11} - C_{12})\xi^2\{I_{n-2}(\xi a) + I_{n+2}(\xi a)\}], \tag{32}$$

$$Q(\xi) = \xi(C_{11}\xi^2 + \eta^2 C_{13} + \rho\omega^2)[I_{n-1}(\xi a) + I_{n+1}(\xi a)]/(C_{13} + C_{44}), \tag{33}$$

$$R(\xi) = -2n\eta\xi^2\left[I_{n-1}(\xi a) + I_{n+1}(\xi a) - \frac{2}{\xi a} I_n(\xi a)\right] \Big/ (\xi a), \tag{34}$$

$$W_1 = 2n(C_{11} - C_{12})\beta_3^2\left[I_{n-1}(\beta_3 a) + I_{n+1}(\beta_3 a) - \frac{2}{\beta_3 a} I_n(\beta_3 a)\right] \Big/ (\beta_3 a), \tag{35}$$

$$W_2 = 2n\eta\beta_3 \frac{I_n(\beta_3 a)}{(\beta_3 a)}, \tag{36}$$

$$W_3 = -\beta_3^2\left\{I_{n-2}(\beta_3 a) + I_{n+2}(\beta_3 a) + 2[1 + 2n^2/(\beta_3 a)^2]I_n(\beta_3 a) - \frac{2}{\beta_3 a}[I_{n-1}(\beta_3 a) + I_{n+1}(\beta_3 a)]\right\}. \tag{37}$$

(b) Region II. For $1/c_1^2 < (\omega/\eta)^2 < (\nu_1\nu_2/c_2)^2$, the roots for β_α become $\beta_1 = \pm p$ and $\beta_2 = \pm iq$, where $i = (-1)^{1/2}$. The general solution form for (24) becomes

$$\phi = A_1 I_n(pr) + A_2 J_n(qr), \quad \psi = A_3 J_n(\beta_3 r), \tag{38}$$

where J_n is the Bessel function of the first kind of order n; and p, q, and β_3 are defined as

$$p^2 + q^2 = (\overline{B}^2 - 4\overline{C})^{1/2}, \quad p^2 - q^2 = -\overline{B}, \quad \beta_3^2 = \omega^2 c_3^2 - \eta^2\nu_3^2. \tag{39}$$

Again, $\overline{B}$ and $\overline{C}$ are defined in (27). The curved boundary conditions yield

$$W_4[Q(p)U(q) - T(q)R(p)] + W_5[S(q)R(p) - P(p)U(q)] + W_6[P(p)T(q) - S(q)Q(p)] = 0, \tag{40}$$

where $P(\xi)$, $Q(\xi)$, and $R(\xi)$ are defined in (32)–(34); and $S(\xi)$, $T(\xi)$, $U(\xi)$, W_4, W_5, and W_6 are

$$S(\xi) = \eta[2J_n(\xi a)\{-\xi^2[C_{11}(C_{44} - C_{13}) + (C_{13} + C_{44})C_{12}] + 2(\eta^2 - c_1^2\omega^2)C_{13}C_{44}\}/(C_{13} + C_{44}) + (C_{11} - C_{12})\xi^2\{J_{n-2}(\xi a) + J_{n+2}(\xi a)\}], \tag{41}$$

$$T(\xi) = \xi(-C_{11}\xi^2 + \eta^2 C_{13} + \rho\omega^2)[J_{n-1}(\xi a) - J_{n+1}(\xi a)]/(C_{13} + C_{44}), \tag{42}$$

$$U(\xi) = -2n\eta\xi^2\left[J_{n-1}(\xi a) - J_{n+1}(\xi a) - \frac{2}{\xi a} J_n(\xi a)\right] \Big/ (\xi a), \tag{43}$$

$$W_4 = 2n(C_{11} - C_{12})\beta_3^2\left[J_{n-1}(\beta_3 a) - J_{n+1}(\beta_3 a) - \frac{2}{\beta_3 a} J_n(\beta_3 a)\right] \Big/ (\beta_3 a), \tag{44}$$

$$W_5 = 2n\eta\beta_3 \frac{J_n(\beta_3 a)}{(\beta_3 a)}, \tag{45}$$

$$W_6 = -\beta_3^2\left\{J_{n-2}(\beta_3 a) + J_{n+2}(\beta_3 a) - 2[1 - 2n^2/(\beta_3 a)^2]J_n(\beta_3 a) - \frac{2}{\beta_3 a}[J_{n-1}(\beta_3 a) - J_{n+1}(\beta_3 a)]\right\}. \tag{46}$$

(c) Region III. For $(\nu_1\nu_2/c_2)^2 < (\omega/\eta)^2 < \infty$, the roots for β_α becomes $\beta_1 = \pm ip$ and $\beta_2 = \pm iq$. The general solution form for ϕ and ψ is

$$\phi = A_1 J_n(pr) + A_2 J_n(qr), \quad \psi = A_3 J_n(\beta_3 r), \tag{47}$$

where p, q, and β_3 are defined as

$$p^2 - q^2 = (\overline{B}^2 - 4\overline{C})^{1/2}, \quad p^2 + q^2 = \overline{B}, \quad \beta_3^2 = \omega^2 c_3^2 - \eta^2\nu_3^2. \tag{48}$$

The zero tractions on the curved boundary yield the following frequency equation:

$$W_4[T(p)U(q) - T(q)U(p)] + W_5[S(q)U(p) - S(p)U(q)] + W_6[S(p)T(q) - S(q)T(p)] = 0, \tag{49}$$

where $S(\xi)$, $T(\xi)$, $U(\xi)$, W_4, W_5, and W_6 are given in (41)–(46).

Note that the above solutions for regions I, II, and III are also valid for isotropic circular cylinders by simply substituting $\nu_1^2 = \nu_2^2 = -1$ (as given in Table 1).

(d) Long Bar and Thin Disk Limits of the Frequency Equation. For very long cylinders, we set $a \to 0$ into (31) and the frequency equation is obtained by using the series representations of the Bessel functions. The frequency equation for the axisymmetric modes ($n = 0$) becomes

$$(\omega^2 c_1^2 - \eta^2)(C_{13} + C_{44})\{\omega^2(C_{11} + C_{12}) - \eta^2[C_{33}(C_{11} + C_{12}) - 2C_{13}^2]\} = 0. \tag{50}$$

Since $\omega^2 c_1^2 - \eta^2 < 0$ in region I, we have

$$\omega^2 = \frac{\eta^2}{\rho}\left[\frac{C_{33}(C_{11} + C_{12}) - 2C_{13}^2}{C_{11} + C_{12}}\right], \tag{51}$$

as the natural frequency for a long bar. To see the physical meaning of this term, we can invert (1) and set $\sigma_{rr} = \sigma_{\theta\theta} = 0$ (since for $a \to 0$ the stress state is basically one-dimensional). The axial strain becomes $\epsilon_{zz} = \sigma_{zz}/E_z$; and the Young's modulus in the axial direction is

$$E_z = \frac{C_{33}(C_{11} + C_{12}) - 2C_{13}^2}{C_{11} + C_{12}}. \tag{52}$$

Therefore, the lowest natural frequency ($m = 1$) becomes

$$\omega = (\pi/L)(E_z/\rho)^{1/2}. \tag{53}$$

Downloaded 03 May 2010 to 171.66.16.20. Redistribution subject to ASME license or copyright; see http://www.asme.org/terms/Terms_Use.cfm

Table 2 The natural frequencies ($\omega/2\pi$) for $n = 0$ and various m for a finite sapphire cylinder with $L/a = 1.9872894$

longitudinal mode number (m)	natural frequency, kHz	solution region (I, II, or III)
1	173.991	II
1	235.092	III
1	327.842	III
1	367.094	III
2	253.680	II
2	374.051	II
2	407.465	III
2	442.120	III
3	323.378	II
4	405.360	I

Table 3 The natural frequencies ($\omega/2\pi$) for $n = 1$ and various m for a finite sapphire cylinder with $L/a = 1.9872894$

longitudinal mode number (m)	natural frequency, kHz	solution region (I, II, or III)
1	78.543	I
1	211.003	III
1	231.061	III
1	362.725	III
2	180.198	I
2	281.698	II
2	352.596	II
2	431.128	III
3	280.453	I
3	361.543	II
3	431.884	II
4	379.562	I

This result is consistent with Morse's (1954) result for an infinite transversely isotropic cylinder; and the same frequency equation was also obtained by Rayleigh (1945) for the longitudinal vibration of a long bar.

The long bar limit ($a \to 0$) for the frequency equations for regions II and III, (40) and (49), also leads to (53); therefore, such limit does not depend on the relative value of ω/η comparing to $1/c_1$ and $\nu_1\nu_2/c_2$.

The thin disk limit ($a \to \infty$) of the frequency equation can be obtained by using the asymptotic expansion of the Bessel function with large argument; and we obtain

$$(\omega^2 c_1^2 - \eta^2)^{1/2}[\rho\omega^2 C_{11}(C_{44}+C_{13}) - \eta^2 C_{44}(C_{11}\nu_1^2 - C_{13})(C_{11}\nu_2^2 - C_{13})] + C_{11}(\omega^2 c_2^2 - \eta^2\nu_1^2\nu_2^2)^{1/2}[2C_{13}C_{44}\eta^2 + \rho\omega^2(C_{44}-C_{13})] = 0, \quad (54)$$

as the thin disk limit for region I. Note that (54) is independent of the circumferential mode number n and the radius a. However, similar consideration for the frequency equations for regions II and III does not yield such a simple form. In particular, the thin disk limits for these regions depends on both the radius a (even though $a \to \infty$) and the circumferential mode number n.

5 Numerical Results and Discussion

Since the experimental measurements by Lusher and Hardy (1988) are made between 150 kHz $< \omega/(2\pi) <$ 450 kHz, we give only those natural frequencies smaller than 450 kHz with $n = 0, 1$ in Tables 2-3. We find that only the first six circumferential modes ($n \leq 5$) have natural frequencies within this range. The elastic constants for sapphire are the same as those given in the previous section; and the radius and length of the cylinder are 1.4986 cm and 2.97815 cm, respectively. Table 2 shows the natural frequency spectrum for the axisymmetric modes ($n = 0$). Although the end boundary conditions used in this study do not correspond exactly to the experimental configuration used by Lusher and Hardy (1988), the lowest axisymmetric frequency (173.991 kHz) agrees with the experimental results (175.1 kHz and 175.2 kHz) by Lusher and Hardy (1988) to within one percent. The natural frequencies for the first nonsymmetric modes ($n = 1$) are given in Table 3. The lowest frequency is 78.542 kHz, which is outside the measurable range considered by Lusher and Hardy (1988). Therefore, the lowest frequency is not of axisymmetric type for this particular geometry ratio ($L/a = 1.9872894$). (Later numerical results suggest that this is true for all possible a/L.) One of the natural frequencies for vibration mode with $m = 2$ and $n = 2$ is 249.345 kHz comparing to 249.88 kHz observed by Lusher and Hardy (1988). For $m = 2$, u_r behaves as $\cos(2\pi z/L)$ and this deformation mode agrees with the mode shape depicted by Lusher and Hardy (1988) for this so-called "third odd mode."

Natural frequencies below 450 kHz are obtained for all possible n and m; there are totally 49 different natural frequencies found between 150 kHz and 450 kHz for this particular geometry. This result agrees with the observation by Lusher and Hardy (1988): they remarked that there are about 50 vibration modes in this range. However, the frequencies and the corresponding mode shapes for these 50 modes were not reported by Lusher and Hardy (1988); thus, more detailed comparison is not possible. Also, we do not find the nonaxisymmetric modes with frequencies of 163.3 kHz and 163.4 kHz reported by Lusher and Hardy (1988); instead we obtain two nonaxisymmetric modes with very close frequencies of 180.85 kHz (for $m = 1$, $n = 2$) and 180.198 kHz (for $m = 2$, $n = 1$). This discrepancy may result from the difference in the end boundary conditions between the experiments and our theoretical analysis. Another possible source of error is our assumption that sapphire is transversely isotropic (actually one elastic constant, C_{14}, of sapphire is neglected in this study). Further, a lack of axisymmetry in the manufactured cylinders may also attribute to this discrepancy. However, the effect of geometric imperfection on the vibration frequency of circular cylinders is not known; further studies on this possibility are required before a conclusive statement can be made. The frequencies given in Tables 2-3 are restricted to circular cylinders with $L/a = 1.9872894$. To study the dependence of ω on the geometric ratio of the cylinder, we plot the normalized frequency, $\omega a(\rho/C_{44})^{1/2}$, against L/a in Figs. 1-3 for very thin disks ($L/a \to 0$) to moderate geometry ratios ($L/a = 5$). In Figs. 1-3, we set $a = 0.014986$ m with a varying value of L. The frequency spectrum for the vibration modes with $n = 0$, 1, 2 are given in Figs. 1, 2, and 3 respectively. Only the first three longitudinal modes (i.e., $m = 1, 2, 3$) are shown. Note that there are more than one root for the natural frequency for a fixed set of n and m because of the nonlinearity of ω involved in the frequency equations.

For axisymmetric modes ($n = 0$), there are some points with double roots for a fixed n and m. For example, double-root points are found near $L/a = 1.3$ for $m = 1$, near $L/a = 1.8$ and 2.7 for $m = 2$, and near $L/a = 2.6$, 3.8, and 4.1 for m

Downloaded 03 May 2010 to 171.66.16.20. Redistribution subject to ASME license or copyright; see http://www.asme.org/terms/Terms_Use.cfm

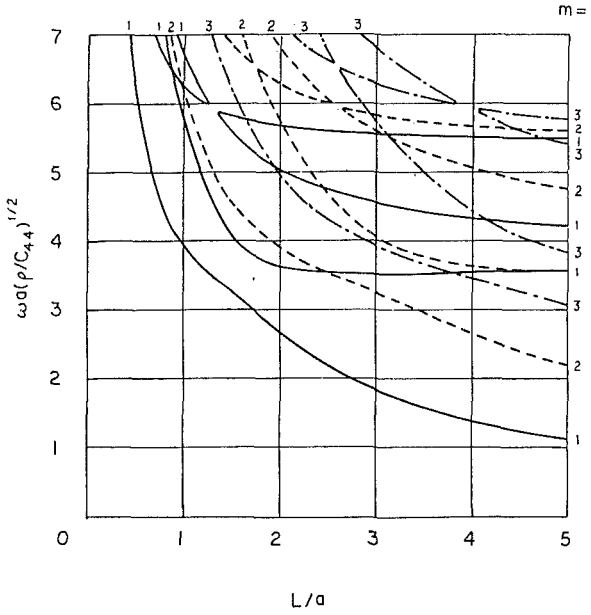


Fig. 1 Frequency spectrum with $\omega a(\rho/C_{44})^{1/2}$ against L/a for $n = 0$ and for $m = 1, 2, 3$ (the solid lines for $m = 1$, the dash lines for $m = 2$ and the broken lines for $m = 3$)

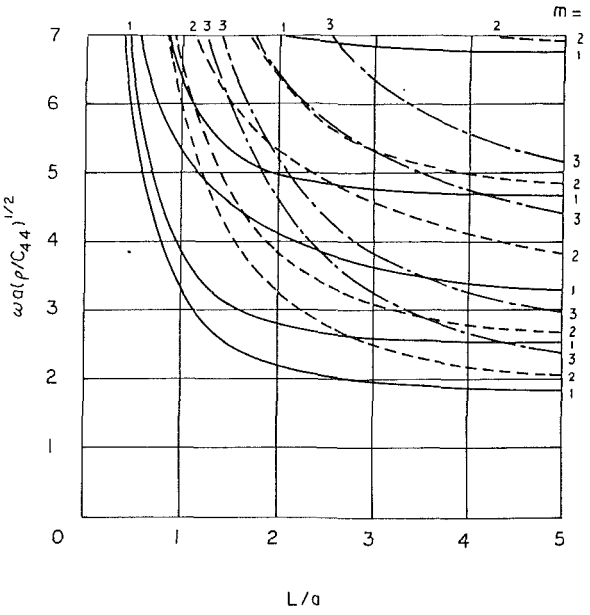


Fig. 3 Same as Fig. 1 for $n = 2$ and $m = 1, 2, 3$

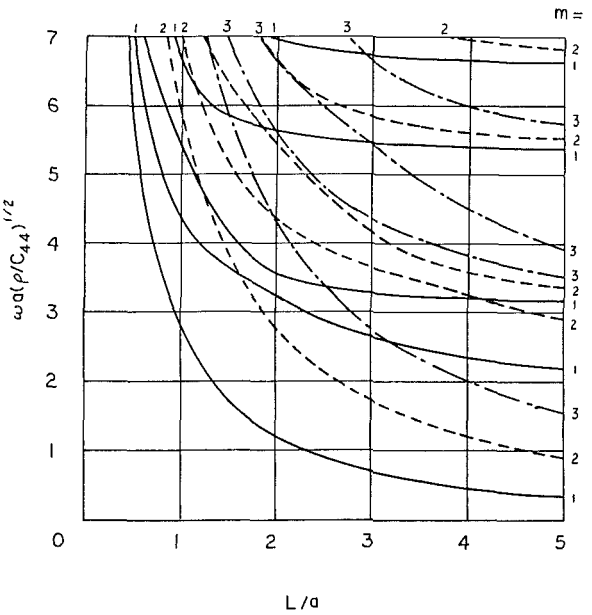


Fig. 2 Same as Fig. 1 for $n = 1$ and $m = 1, 2, 3$

$= 3$. Our numerical results for higher frequencies also show that these doublet points continue to appear as the frequency and the longitudinal mode number increase. These kind of doublet frequency points have been observed experimentally by Booker and Sagar (1971) for a number of cylindrical fused silica, aluminum, steel, and brass rods. They attributed these multiplets in frequency to the "end resonance effect" proposed by Oliver (1957) and examined by Zemanek (1962). However, Fig. 1 shows that doublets are predicted by the theoretical analysis even through our end boundary condition ($u_z = 0$, on $z = 0, L$) excludes the possibility of the end resonance (see Fig. 12 of Oliver, 1957).

In general, the proximity of some of the natural frequencies observed by Lusher and Hardy (1988) and by Booker and Sagar (1971) may due to: (1) two essentially different modes corresponding to the same frequency; and (2) the existence of double roots for the frequency equation as discussed above. To see the first possibility we find that there are many intersections between the frequency spectrum; if we superpose any two of Figs. 1-3, special care is required to separate them experimentally (see, e.g., Soedel and Dhar, 1978).

Figures 1-3 are restricted to small L/a. Actually, we also have plotted the frequency spectrum for all possible geometric ratios. Again, doublets are found in abundance for other frequency range and other geometric ratios. However, no double root is found for vibration modes with $n \geq 1$. Our numerical results also suggest that the lowest natural frequency always corresponds to the first nonaxisymmetric mode ($n = 1$) independent of the dimension of the specimen.

6 Conclusion

We have given a frequency analysis for a transversely isotropic finite circular cylinder. Hu's wave potentials (1957) for transversely isotropic materials have been extended to cylindrical polar coordinates; and two uncoupled partial differential equations are obtained as the governing equations. Analytic results of the frequency equations are obtained for sapphire as an example. Contrary to the previous studies, zero axial displacement is imposed instead of zero-normal traction on the end surfaces; and this choice is motivated by the experimental configuration used by Lusher and Hardy (1988).

The long bar ($a \to 0$) limit and the thin disk ($a \to \infty$) limit are considered as special cases of the exact frequency equation for sapphire. The former corresponds to the frequency equation obtained by Rayleigh (1945) and by Morse (1954) for the longitudinal vibrations of an infinite cylinder. The frequency for the lowest axisymmetric mode predicted by the theory agrees with the experimental data by Lusher and Hardy (1988) to within one percent. The complete frequency spectrum with $\omega/2\pi \leq 450$ kHz is obtained for the first three longitudinal and circumferential modes ($m, n = 1, 2, 3$) for sapphire cylinders of all geometry ratios (a/L). Numerical results show that double roots exist for the axisymmetric frequency equation only; and this provides a possible explanation for the doublets in natural frequencies observed by Booker and Sagar (1971) and by Lusher and Hardy (1988). In addition, numerical results show that the lowest frequency for a sapphire cylinder always corresponds to the first nonaxisymmetric one independent of its geometry.

Downloaded 03 May 2010 to 171.66.16.20. Redistribution subject to ASME license or copyright; see http://www.asme.org/terms/Terms_Use.cfm

More detailed experimental studies are required to examine the validity of the present theoretical analysis in modeling the experimental configuration by Lusher and Hardy (1988). Nevertheless, the present study provides a framework of the frequency analysis for transversely isotropic circular cylinders of materials other than sapphire.

Acknowledgment

The author is grateful to Prof. John W. Rudnicki of Northwestern University for his advice and support during the author's stay as a postdoctoral research fellow when this work was first formulated. This work was supported by National Science Foundation Grant No. MSS-8915607 to Northwestern University. The support by the Hong Kong Polytechnic through Grant No. 0340.538.A3.310 is also much appreciated.

References

Booker, R. E., and Sagar, F. H., 1971, "Velocity Dispersion of the Lowest Order Longitudinal Mode in Finite Rods of Circular Cross Section," *Journal of the Acoustical Society of America*, Vol. 49, pp. 1491–1498.

Chau, K. T., 1992, "Non-normality and Bifurcation in a Compressible Pressure-sensitive Circular Cylinder under Tension and Compression," *International Journal of Solids and Structures*, Vol. 29, pp. 801–824.

Chau, K. T., 1993a, "Antisymmetric Bifurcations in a Compressible Pressure-Sensitive Circular Cylinder under Axisymmetric Tension and Compression," ASME JOURNAL OF APPLIED MECHANICS, Vol. 60, pp. 282–289.

Chau, K. T., 1993b, "Buckling, Barrelling, and Surface Instabilities of a Finite Transversely Isotropic Circular Cylinder," *Quarterly of Applied Mathematics*, in press.

Chau, K. T., and Rudnicki, J. W., 1990, "Bifurcations of Compressible Pressure-sensitive Materials in Plane Strain Tension and Compression," *Journal of the Mechanics and Physics of Solids*, Vol. 38, pp. 875–898.

Chen, W. T., and Wright, T. W., 1966, "Frequency Equations for Wave Propagation in an Initially Stressed Circular Cylinder," *Journal of the Acoustical Society of America*, Vol. 39, No. 5, pp. 847–848.

Chernyshev, K. V., and Shegai, V. V., 1977, "Natural Vibrations of Solid Cylinders of Finite Length," *Soviet Applied Mechanics*, Vol. 23, No. 4, pp. 358–360.

Fridman, L. I., 1981, "Dynamic Problem of the Theory of Elasticity for a Cylinder of Finite Dimension," *Soviet Applied Mechanics*, Vol. 17, No. 3, pp. 234–239.

Gladwell, G. M. L., and Tahbildar, U. C., 1972, "Finite Element Analysis of the Axisymmetric Vibrations of Cylinders," *Journal of Sound and Vibration*, Vol. 22, pp. 143–157.

Gladwell, G. M. L., and Vijay, D. K., 1975, "Natural Frequencies of Free Finite-length Circular Cylinders," *Journal of Sound and Vibration*, Vol. 42, pp. 387–397.

Grinchenko, V. T., and Komissarova, G. L., 1980, "Analysis of Frequency Spectrum and Vibrational Modes of Long Cylinders," *Soviet Applied Mechanics*, Vol. 16, pp. 1–5.

Heyliger, P. R., Ledbetter, H., and Austin, M., 1990, "Resonating-orthotropic-cube Method for Elastic Constants," *Dynamic Elastic Modulus Measurements in Materials*, ASTM-STP 1045, ASTM, Philadelphia, PA, pp. 100–109.

Heyliger, P. R., 1991, "Axisymmetric Free Vibrations of Finite Anisotropic Cylinders," *Journal of Sound and Vibrations*, Vol. 148, pp. 507–520.

Heyliger, P. R., and Jilani, A., 1992, "The Free Vibrations of Inhomogeneous Elastic Cylinders and Spheres," *International Journal of Solids and Structures*, Vol. 29, pp. 2689–2708.

Hu, H.-C., 1954, "On the Three-dimensional Problems of the Theory of Elasticity of a Transversely Isotropic Body," *Acta Scientia Sinica*, Vol. 2, pp. 145–151.

Hu, H.-C., 1957, "On the Equilibrium and Vibration of a Transversely Isotropic Elastic Body," *Proceedings of the International Congress of Applied Mechanics*, Vol. 9, No. 7, pp. 485–496.

Hutchinson, J. R., 1972, "Axisymmetric Vibrations of a Free Finite-length Rod," *Journal of the Acoustical Society of America*, Vol. 51, pp. 233–240.

Imenitova, K. V., Chernyshev, K. V., and Shegai, V. V., 1976, "Calculation of the Free Oscillations of Elastic Cylinders of Finite Length," *Soviet Physics Doklady*, Vol. 21, No. 7, pp. 397–399.

Love, A. E. H., 1944, *A Treatise on the Mathematical Theory of Elasticity*, 4th ed., Dover, New York.

Lusher, C. P., and Hardy, W. N., 1988, "Axisymmetric Free Vibrations of a Transversely Isotropic Finite Cylindrical Rod," ASME JOURNAL OF APPLIED MECHANICS, Vol. 55, pp. 855–862.

McMahon, G. W., 1964, "Finite Difference Analysis of the Vibrations of Solid Cylinders," *Journal of the Acoustical Society of America*, Vol. 48, pp. 307–312.

McNiven, H. D., and Perry, D. C., 1962, "Axially Symmetric Waves in Finite, Elastic Rods," *Journal of the Acoustical Society of America*, Vol. 34, pp. 433–437.

Mindlin, R. D., and McNiven, H. D., 1960, "Axially Symmetric Waves in Elastic Rods," ASME JOURNAL OF APPLIED MECHANICS, Vol. 27, pp. 145–151.

Mirsky, I., 1965, "Wave Propagation in Transversely Isotropic Circular Cylinders, Part 1: Theory," *Journal of the Acoustical Society of America*, Vol. 37, pp. 1016–1021.

Morse, R. W., 1954, "Compressional Waves along an Anisotropic Circular Cylinder Having Hexagonal Symmetry," *Journal of the Acoustical Society of America*, Vol. 26, pp. 1018–1021.

Oliver, J., 1957, "Elastic Wave Dispersion in a Cylindrical Rod by a Wide Band Short-duration Pulse Technique," *Journal of the Acoustical Society of America*, Vol. 29, pp. 189–194.

Payton, R. G., 1983, *Elastic Wave Propagation in Transversely Isotropic Media*, Martinus Nijhoff, The Hague, The Netherlands.

Rayleigh, Lord, 1945, *Theory of Sound*, Vol. I, 2nd ed., Dover, New York, Chapter 7.

Rice, J. R., 1976, "The Localization of Plastic Deformation," *Proceedings of the Fourteenth International Congress of Theoretical and Applied Mechanics*, Vol. 1, pp. 207–220.

Rudnicki, J. W., and Rice, J. R., 1975, "Conditions for the Localization of Deformation in Pressure-sensitive Dilatant Materials," *Journal of the Mechanics and Physics of Solids*, Vol. 23, pp. 371–394.

Rumerman, M., and Raynor, S., 1971, "Natural Frequencies of Finite Circular Cylinders in Axially Symmetric Longitudinal Vibration," *Journal of Sound and Vibration*, Vol. 15, No. 4, pp. 529–543.

Schreiber, E., Anderson, O. L., and Soga, N., 1973, *Elastic Constants and Their Measurement*, McGraw-Hill, New York.

Sheiba, L. S., and Shlyapochnikov, S. A., 1974, "A Class of Natural Modes of an Elastic Cylinder," *Soviet Physics and Acoustics*, Vol. 20, No. 2, pp. 207–208.

Soedel, W., and Dhar, M., 1978, "Difficulties in Finding Modes Experimentally when Several Contribute to a Resonance," *Journal of Sound and Vibration*, Vol. 58, pp. 27–38.

Wachtman, J. B., Jr., Tefft, W. E., Lam, D. G. Jr., and Stinchfield, R. P., 1960, "Elastic Constants of Synthetic Single Crystal Corundum at Room Temperature," *Journal of Research of the National Bureau of Standards—A: Physics and Chemistry*, Vol. 64A, pp. 213–228.

Xu, P. C., and Datta, S. K., 1991, "Characterization of Fiber-Matrix Interface by Guided Waves: Axisymmetric Case," *Journal of the Acoustical Society of America*, Vol. 89, No. 6, pp. 2573–2583.

Zemanek, J., 1962, "An Experimental and Theoretical Investigation of Elastic Wave Propagation in a Cylinder," Doctor of Philosophy Dissertation, University of California, Los Angeles, CA.

Downloaded 03 May 2010 to 171.66.16.20. Redistribution subject to ASME license or copyright; see http://www.asme.org/terms/Terms_Use.cfm

Ven-Gen Lee
Assoc. Mem. ASME.

Toshio Mura
Fellow ASME.

Department of Theoretical and Applied Mechanics, Northwestern University, Evanston, IL 60208

Load Transfer From a Finite Cylindrical Fiber Into an Elastic Half-Space

Based on the equivalent inclusion method, the load transfer problem of a finite cylindrical fiber embedded in an elastic half-space of different elastic properties is presented. The equivalent condition of inhomogeneity and inclusion problems simulates the fiber to an inclusion with chosen eigenstrains, and the problem is formulated to a set of integral equations with the unknown strength of eigenstrains. A numerical procedure is developed using a discretizing scheme by which the set of integral equations is reduced to a system of algebraic equations.

Introduction

The analysis of an embedded bar in an elastic medium of different material properties has been the subject of research interests. An illustrative example related to this problem is the mechanics of a fiber pull-out process in fiber-reinforced composites. To assess the performance of fiber-reinforced composites, it is essential to have detailed knowledge of mechanical response such as stress distributions and the load diffusion behavior from the fiber to the matrix.

In general, the investigation of the pull-out process is considered as an inhomogeneity problem of an elastic bar embedded in a semi-infinite matrix of different material properties. The problem was first examined in the studies of load transfer in stiffened structural components and in geotechnical engineering. Due to the complexities of three-dimensionality and an inhomogeneous medium, the analysis of a three-dimensional load transfer problem generally requires various approximate treatments. One of the most important approaches was presented by Muki and Sternberg to investigate the load diffusion of an infinite bar into an elastic infinite continuum (1969) and of a bar into an elastic half-space (1970). The same method was recently used by Pak (1989) and Pak and Saphores (1991) in the study of the response of a bar under various loads. A rigid cylindrical body embedded in an elastic half-space was considered by Suriyamongkol et al. (1973) and Selvadurai and Rajapakse (1985). The rigid domain and the rest of the half-space are treated as a homogeneous half-space, which is subjected to distributed force applied on the boundary of the cylindrical body. The other noteworthy contributions include the works by Luco (1976), Luk and Keer (1979), Karasudhi et al. (1984), Slaughter and Sanders (1991), Lee and Mura (1993), etc.

The axisymmetric problem of load transfer from a finite cylindrical fiber to surrounding media of distinct elastic media is studied in the present paper. By utilizing the equivalent inclusion method the inhomogeneity problem is induced to a set of integral equations, and the kernels in the integral equations are the unknown eigenstrain distributions and their derivatives. A numerical analysis is proposed to reduce the system of integral equations into a set of algebraic equations. A numerical result for the load transfer is shown to compare with the approximate solutions given by Muki and Sternberg (1970). The distributions of the eigenstrain and stress field are also presented for various material parameters.

Formulation of Problem

Consider a finite cylindrical fiber Ω of length b and radius c in an elastic half-space $D - \Omega$ as shown in Fig. 1. The fiber is perfectly bonded to the surrounding matrix and is subjected to uniform stress $\sigma^0_{zz} = \sigma_0$ at the free end of the fiber. The elastic modulus of the fiber and matrix is denoted by $C^*_{ijkl}(E^*, \nu^*)$ and $C_{ijkl}(E, \nu)$, respectively.

Theory of Inclusion Problem. For a given eigenstrain, ϵ^*_{ij}, distributed in a subdomain Ω of an elastic solid D, the induced displacement can be shown as (see Mura, 1987)

$$u_i(\mathbf{x}) = -\int_\Omega G_{ij}(\mathbf{x}, \mathbf{x}')F_j(\mathbf{x}')d\mathbf{x}' \tag{1}$$

where F_j is the function of eigenstrain distribution. Since the geometry and loading under consideration are axisymmetric, the equivalent body force F_j can be expressed in terms of cylindrical coordinates

Contributed by the Applied Mechanics Division of THE AMERICAN SOCIETY OF MECHANICAL ENGINEERS for presentation at the International Mechanical Engineering Congress and Exhibition, the Winter Annual Meeting of The ASME, Chicago, IL, Nov. 6–11, 1994.

Discussion on this paper should be addressed to the Technical Editor, Professor Lewis T. Wheeler, Department of Mechanical Engineering, University of Houston, Houston, TX 77204-4792, and will be accepted until four months after final publication of the paper itself in the ASME JOURNAL OF APPLIED MECHANICS.

Manuscript received by the ASME Applied Mechanics Division, Apr. 15, 1993; final revision, Nov. 23, 1993. Associate Technical Editor: X. Markenscoff.

Paper No. 94-WA/APM-9.

Copyright © 1994 by ASME
Downloaded 03 May 2010 to 171.66.16.20. Redistribution subject to ASME license or copyright; see http://www.asme.org/terms/Terms_Use.cfm

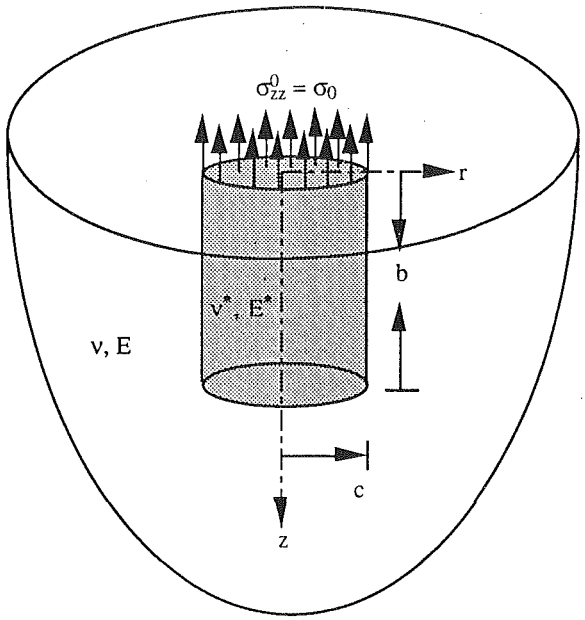


Fig. 1 A finite cylindrical fiber in a half-space with different elastic constants

$$F_r(\mathbf{x}) = (\lambda + 2\mu)\frac{\partial \epsilon^*_{rr}}{\partial r} + \lambda\frac{\partial \epsilon^*_{\theta\theta}}{\partial r} + \lambda\frac{\partial \epsilon^*_{zz}}{\partial r} + 2\mu\frac{\partial \epsilon^*_{rz}}{\partial z} + \frac{2\mu}{r}(\epsilon^*_{rr} - \epsilon^*_{\theta\theta}) \tag{2}$$

$$F_\theta(\mathbf{x}) = 2\mu\frac{\partial \epsilon^*_{r\theta}}{\partial r} + 2\mu\frac{\partial \epsilon^*_{\theta z}}{\partial z} + \frac{4\mu}{r}\epsilon^*_{r\theta} \tag{3}$$

$$F_z(\mathbf{x}) = \lambda\frac{\partial \epsilon^*_{rr}}{\partial z} + \lambda\frac{\partial \epsilon^*_{\theta\theta}}{\partial z} + (\lambda + 2\mu)\frac{\partial \epsilon^*_{zz}}{\partial z} + 2\mu\frac{\partial \epsilon^*_{rz}}{\partial r} + \frac{2\mu}{r}\epsilon^*_{rz} \tag{4}$$

where λ and μ are the Lamé constants. The Green's function, $G_{ij}(\mathbf{x}, \mathbf{x}')$, represents the displacement in the x_i direction at the point $\mathbf{x}$ due to a distributed ring force applied along the circle $\mathbf{x}' = (\rho, z')$ in the x_j direction. Here, the indices i and j stand for the components in the cylindrical coordinate system (r, θ, z).

For the concentrated ring loading F_i of unit intensity applied on the fictitious plane, $z = z'$, the continuity conditions of the displacement and the equilibrium conditions at the interface are

$$u_j|_{z=z'^+} = u_j|_{z=z'^-}, \quad j = r, \theta, z$$
$$\sigma_{zj}|_{z=z'^+} - \sigma_{zj}|_{z=z'^-} = -\delta_{ij}\delta(r-\rho) \tag{5}$$

where δ_{ij} is the Kronecker delta and $\delta(\ )$ is Dirac's delta function. The traction-free conditions at the free surface, $z = 0$, are

$$\sigma_{zz} = \sigma_{zr} = \sigma_{z\theta} = 0. \tag{6}$$

The Green's function can be derived based on the potential theory and the Hankel transforms. By solving potential functions that satisfy the prescribed boundary conditions, the Green's functions are obtained as

$$G_{rr}(\mathbf{x}, \mathbf{x}') = \frac{\rho}{8\mu(1-\nu)}\int_0^\infty J_1(\eta\rho)J_1(\eta r)\{[5 - 12\nu + 8\nu^2 - \kappa\eta(z+z') + 2zz'\eta^2]e^{-\eta(z+z')} + [\kappa - \eta|z-z'|]e^{-\eta|z-z'|}\}d\eta \tag{7}$$

$$G_{zr}(\mathbf{x}, \mathbf{x}') = \frac{\rho}{8\mu(1-\nu)}\int_0^\infty J_1(\eta\rho)J_0(\eta r)\{[-4 + 12\nu - 8\nu^2 - \kappa\eta(z-z') + 2zz'\eta^2]e^{-\eta(z+z')} + \eta(z'-z)e^{-\eta|z-z'|}\}d\eta \tag{8}$$

$$G_{\theta\theta}(\mathbf{x}, \mathbf{x}') = \frac{\rho}{2\mu}\int_0^\infty J_1(\eta\rho)J_1(\eta r)[e^{-\eta(z+z')} + e^{-\eta|z-z'|}]d\eta \tag{9}$$

$$G_{rz}(\mathbf{x}, \mathbf{x}') = \frac{\rho}{8\mu(1-\nu)}\int_0^\infty J_1(\eta r)J_0(\eta\rho)\{[-4 + 12\nu - 8\nu^2 + \kappa\eta(z-z') + 2zz'\eta^2]e^{-\eta(z+z')} - \eta(z'-z)e^{-\eta|z-z'|}\}d\eta \tag{10}$$

$$G_{zz}(\mathbf{x}, \mathbf{x}') = -\frac{\rho}{8\mu(1-\nu)}\int_0^\infty J_0(\eta\rho)J_0(\eta r)\{[5 - 12\nu + 8\nu^2 + \kappa\eta(z+z') + 2zz'\eta^2]e^{-\eta(z+z')} + [\kappa + \eta|z-z'|]e^{-\eta|z-z'|}\}d\eta. \tag{11}$$

Thus, the elastic field caused by an inclusion of distributed eigenstrains can be obtained from Eqs. (1)–(4) and the Green's functions.

Theory of Inhomogeneity Problem. When a subdomain of a material has elastic moduli different from those of the remainder (matrix), the subdomain is called an inhomogeneity. Due to external applied force, the inhomogeneity can result in stress disturbances. The stress-strain relation for the fiber and the matrix can be written as

$$\sigma^0_{ij} + \sigma_{ij} = C^*_{ijkl}(\epsilon_{kl} + \epsilon^0_{kl}) \quad \text{in } \Omega \tag{12}$$
$$\sigma^0_{ij} + \sigma_{ij} = C_{ijkl}(\epsilon_{kl} + \epsilon^0_{kl}) \quad \text{in } D - \Omega \tag{13}$$

where ϵ_{kl} is the strain disturbance due to the presence of the fiber, and ϵ^0_{kl} represents the strain field caused by the external load. To formulate a general inhomogeneity problem, Eshelby (1957) first pointed out that the inhomogeneity problem can be formulated into an equivalent inclusion problem of an inclusion with appropriate eigenstrains that can describe the stress disturbance due to the presence of inhomogeneity. Therefore, the inhomogeneity can be treated as the equivalent inclusion problem such that the stress field is

$$\sigma^0_{ij} + \sigma_{ij} = C_{ijkl}(\epsilon_{kl} + \epsilon^0_{kl} - \epsilon^*_{kl}) \quad \text{in } \Omega. \tag{14}$$

From Eqs. (12) and (14), the necessary and sufficient condition for the equivalency of stresses and strains between the inhomogeneity and inclusion problems gives

$$C^*_{ijkl}(\epsilon_{kl} + \epsilon^0_{kl}) = C_{ijkl}(\epsilon_{kl} + \epsilon^0_{kl} - \epsilon^*_{kl}) \quad \text{in } \Omega. \tag{15}$$

For an ellipsoidal inhomogeneity in an infinite elastic solid, the relation of the strain disturbance and eigenstrains can be obtained in closed form by using the Eshelby's tensors (Eshelby, 1957). In general, the strain disturbance, ϵ_{kl}, can be expressed in terms of the unknown eigenstrains, ϵ^*_{kl}, from Eq. (1) and Green's functions.

Using the theory of inclusion problem and substituting the corresponding strain, Eq. (15) can be rewritten as

$$\int_\Omega \left\{\lambda\left[A^r_i\frac{\partial \epsilon^*_{kk}}{\partial \rho} + A^z_i\frac{\partial \epsilon^*_{kk}}{\partial z'}\right] + 2\mu A^r_i\left[\frac{\partial \epsilon^*_{rr}}{\partial \rho} + \frac{\epsilon^*_{rr}}{\rho}\right] - 2\mu A^r_i\frac{\epsilon^*_{\theta\theta}}{\rho} + 2\mu A^z_i\frac{\partial \epsilon^*_{zz}}{\partial z'} + 2\mu\left[A^r_i\frac{\partial \epsilon^*_{rz}}{\partial z'} + A^z_i\left(\frac{\partial \epsilon^*_{rz}}{\partial \rho} + \frac{\epsilon^*_{rz}}{\rho}\right)\right]\right\}d\mathbf{x}' - \epsilon^*(\mathbf{x}) = f_i(\mathbf{x}) \quad i = 1\text{–}4 \tag{16}$$

where $\epsilon^*_{kk} = \epsilon^*_{rr} + \epsilon^*_{\theta\theta} + \epsilon^*_{zz}$, and

$$f_1(\mathbf{x}) = \epsilon^0_{rr}(\mathbf{x}) - \epsilon^0_{\theta\theta}(\mathbf{x}), \qquad f_2(\mathbf{x}) = \epsilon^0_{zz}(\mathbf{x}) - \epsilon^0_{\theta\theta}(\mathbf{x}),$$
$$f_3(\mathbf{x}) = \epsilon^0_{kk}(\mathbf{x}) + 2\Gamma_3\epsilon^0_{\theta\theta}(\mathbf{x}), \quad f_4(\mathbf{x}) = 2\epsilon^0_{rz}(\mathbf{x}) \tag{17}$$

Downloaded 03 May 2010 to 171.66.16.20. Redistribution subject to ASME license or copyright; see http://www.asme.org/terms/Terms_Use.cfm

with

$$\epsilon^*(\mathbf{x}) = \begin{Bmatrix} -\Gamma\epsilon^*_{rr} + \Gamma\epsilon^*_{\theta\theta}, & i=1 \\ \Gamma\epsilon^*_{\theta\theta} - \Gamma\epsilon^*_{zz}, & i=2 \\ -\Gamma_1\epsilon^*_{rr} - \Gamma_2\epsilon^*_{\theta\theta} - \Gamma_1\epsilon^*_{rr}, & i=3 \\ -2\Gamma\epsilon^*_{rz}, & i=4 \end{Bmatrix}. \quad (18)$$

The constants used in Eq. (18) are defined as follows:

$$\Gamma = \frac{1}{\frac{\mu^*}{\mu} - 1}, \quad \Gamma_1 = \frac{\lambda}{\lambda^* - \lambda}, \quad \Gamma_2 = \frac{\lambda + 2\mu}{\lambda^* - \lambda}, \quad \Gamma_3 = \frac{\mu^* - \mu}{\lambda^* - \lambda}. \quad (19)$$

The $A_i^p(\mathbf{x}, \mathbf{x}')$, $p = r, z$, is the function of Green's functions as

$$A_1^p(\mathbf{x}, \mathbf{x}') = -\frac{G_{rp}(\mathbf{x}, \mathbf{x}')}{r} + \frac{\partial G_{rp}(\mathbf{x}, \mathbf{x}')}{\partial r} \quad (20)$$

$$A_2^p(\mathbf{x}, \mathbf{x}') = -\frac{G_{rp}(\mathbf{x}, \mathbf{x}')}{r} + \frac{\partial G_{zp}(\mathbf{x}, \mathbf{x}')}{\partial z} \quad (21)$$

$$A_3^p(\mathbf{x}, \mathbf{x}') = \frac{(1+2\Gamma_3)}{r} G_{rp}(\mathbf{x}, \mathbf{x}') + \frac{\partial G_{rp}(\mathbf{x}, \mathbf{x}')}{\partial r} + \frac{\partial G_{zp}(\mathbf{x}, \mathbf{x}')}{\partial z} \quad (22)$$

$$A_4^p(\mathbf{x}, \mathbf{x}') = \frac{\partial G_{rp}(\mathbf{x}, \mathbf{x}')}{\partial z} + \frac{\partial G_{zp}(\mathbf{x}, \mathbf{x}')}{\partial r}. \quad (23)$$

It is noted that the vanishing eigenstrains are $\epsilon^*_{r\theta}$ and $\epsilon^*_{\theta z}$.

Numerical Analysis

Equation (16) is a set of integral equations with four unknown distributions of eigenstrain ϵ^*_{rr}, $\epsilon^*_{\theta\theta}$, ϵ^*_{zz}, and ϵ^*_{rz}. The notations ϵ^*_1, ϵ^*_2, ϵ^*_3, and ϵ^*_4 are used to refer to the eigenstrains ϵ^*_{rr}, $\epsilon^*_{\theta\theta}$, ϵ^*_{zz}, and ϵ^*_{rz}, respectively. To solve the unknown eigenstrains in Eq. (16), the fiber is first divided into $M \times N$ ring elements, which include M sections in the radial direction and N sections in the vertical direction. In addition, each ring element is assumed to sustain with the uniform eigenstrains. The element (m, n) is defined as $c_m \le r \le c_{m+1}$, $b_n \le z \le b_{n+1}$ with the collocation point located at the center of the element, i.e.,

$$(r^m, z^n) = \left(\frac{c_m + c_{m+1}}{2}, \frac{b_n + b_{n+1}}{2} \right).$$

Therefore, the eigenstrains in each element can be expressed as

$$\epsilon^*_k(m, n) = \overline{\epsilon^*_k}(m, n)[H(r - c_m) - H(r - c_{m+1})] \times [H(z - b_n) - H(z - b_{n+1})] \quad (k = 1, 2, 3, 4; \; m = 1, 2, \ldots, M; \; n = 1, 2, \ldots, N) \quad (24)$$

where $\overline{\epsilon^*_k}$ represents the magnitude of the eigenstrain in each element and the function $H(x)$ is the Heaviside function. Each of $M \times N$ elements has four unknown eigenstrains ϵ^*_k. From Eq. (24), the integration in Eq. (16) is split into

$$\int_\Omega \{\ \} d\mathbf{x}' = \sum_{m=1}^{M} \sum_{n=1}^{N} \left\{ \overline{\epsilon^*}(m, n) \int_{c_m}^{c_{m+1}} d\rho \int_{b_n}^{b_{n+1}} \{\ \} dz' \right\}. \quad (25)$$

Therefore, the system of integral equations can be modified to be

$$\sum_{j=1}^{4} \sum_{s=1}^{M} \sum_{t=1}^{N} \{[k^{st}_{ij}(r^m, z^n) + \delta_{sm}\delta_{tn}\alpha_{ij}]\overline{\epsilon}^*_j(s, t)\} = f_i(r^m, z^n) \quad (i = 1, 2, 3, 4; \; m = 1, 2, \ldots, M; \; n = 1, 2, \ldots, N) \quad (26)$$

where α_{ij} represents the elastic constants as

$$[\alpha_{ij}] = \begin{bmatrix} -\Gamma & \Gamma & 0 & 0 \\ 0 & \Gamma & -\Gamma & 0 \\ -\Gamma_1 & -\Gamma_2 & -\Gamma_1 & 0 \\ 0 & 0 & 0 & -2\Gamma \end{bmatrix}. \quad (27)$$

The corresponding $k^{st}_{ij}(r^m, z^n)$ can be shown as

$$k^{st}_{ij}(r^m, z^n) = \int_{c_s}^{c_{s+1}} d\rho \int_{b_t}^{b_{t+1}} R_{ij}(r^m, z^n, \rho, z') dz' \quad (28)$$

with

$$R_{i1}(\mathbf{x}, \mathbf{x}') = A_i^r \left[(\lambda + 2\mu) \frac{\partial}{\partial \rho} + \frac{2\mu}{\rho} \right] + \lambda A_i^z \frac{\partial}{\partial z'},$$

$$R_{i2}(\mathbf{x}, \mathbf{x}') = A_i^r \left(\lambda \frac{\partial}{\partial \rho} - \frac{2\mu}{\rho} \right) + \lambda A_i^z \frac{\partial}{\partial z'},$$

$$R_{i3}(\mathbf{x}, \mathbf{x}') = \lambda A_i^r \frac{\partial}{\partial \rho} + (\lambda + 2\mu) A_i^z \frac{\partial}{\partial z'},$$

$$R_{i4}(\mathbf{x}, \mathbf{x}') = 2\mu A_i^r \frac{\partial}{\partial z'} + 2\mu A_i^z \left(\frac{\partial}{\partial \rho} + \frac{1}{\rho} \right) \quad (i = 1, 2, 3, 4). \quad (29)$$

Therefore, a system of $4 \times M \times N$ algebraic equations is obtained, and the unknown eigenstrains can be solved numerically.

Result and Discussion

In this section, the numerical results are presented for stress distribution and load diffusion behavior. The ratio of Young's modulus is denoted by $\beta = E^*/E$. First, Figs. 2(*a*)–2(*c*) give the example of eigenstrain distributions for the case of $\nu = \nu^* = 0.25$, $\beta = 2$ and $b/c = 5$. The ϵ^*_{rr} and $\epsilon^*_{\theta\theta}$ distributions show similar variation and the magnitudes are positive. On the contrary, the ϵ^*_{zz} distribution presents negative values. All normal eigenstrain distributions become uniform along the radial direction at the bottom half of the fiber. The smooth variation of ϵ^*_{rz} distribution shows in Fig. 2(*c*). With the solved eigenstrains, the stress field can be obtained by introducing the eigenstrain and the strain disturbance to Eqs. (12) and (15).

In general, the load diffusion behavior is interpreted in terms of the resultant axial force along the axis of the fiber, that is

$$P(z) = 2\pi \int_0^c \sigma_{zz}^{(in)}(r, z) r dr. \quad (30)$$

The three-dimensional load transfer problem in a half-space was first examined by Muki and Sternberg (1970). In Muki and Sternberg's approximation, the inhomogeneity medium is decomposed into a homogeneous half-space and a one-dimensional fictitious bar. The Poisson effect of the fiber is neglected in their approach, and their solutions are restricted to the case of the fiber being stiffer than matrix. The effect of Poisson's ratio of the fiber on load transfer behavior can be seen in Fig. 3(*a*) for the case $\nu = 0.5$ and $b/c = 5$. The axial force is normalized by the applied force, $P_0 = \sigma_0 \pi c^2$. It is noted that the diffusion of applied loading tends to become slower with increasing β. Compared with Muki and Sternberg's results, the present result shows the differences caused by Poisson's ratio and their solution is close to the present result for $\nu^* = 0$ since the neglect of the Poisson effect is equivalent to set Poisson's ratio zero. The normalized resultant axial force for $\nu = 0.25$ and $b/c = 20$ is shown in Fig. 3(*b*). By comparing Figs. 3(*a*) and 3(*b*), it is observed that Muki and Sternberg's approximation and present results are closer as the length of fiber becomes longer.

When the elastic properties of fiber are identical to those of matrix, i.e., $\beta = 1$ and $\nu = \nu^*$, the problem is reduced to a homogeneous half-space subjected to applied pressure, σ^0_{33},

Downloaded 03 May 2010 to 171.66.16.20. Redistribution subject to ASME license or copyright; see http://www.asme.org/terms/Terms_Use.cfm

uniformly distributed over a circular domain on the free surface. From the equivalent condition, the solution of Eq. (16) appears to be trivial solutions, that is $\epsilon^*_{kl} = 0$, and the non-vanishing stress field can be obtained in close forms in terms of the integrals of Lipschitz-Hankel type

$$\sigma_{rr}/\sigma_0 = cI(1, 0; 0) - czI(1, 0; 1) + \frac{cz}{r} I(1, 1; 0) - \frac{c(1-2\nu)}{r} I(1, 1; -1) \quad (31)$$

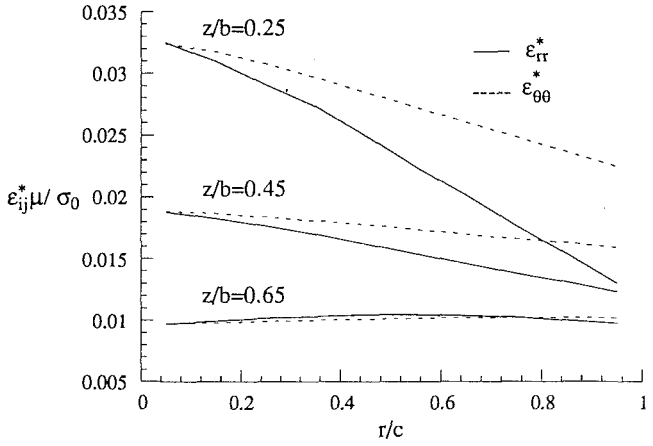


Fig. 2(*a*) ϵ^*_{rr} and $\epsilon^*_{\theta\theta}$ variation

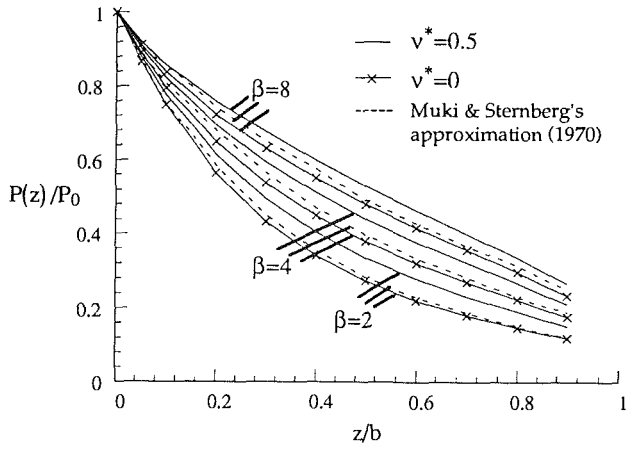


Fig. 3(*a*) Comparison of normalized resultant axial force for ν = 0.5 and *b/c* = 5

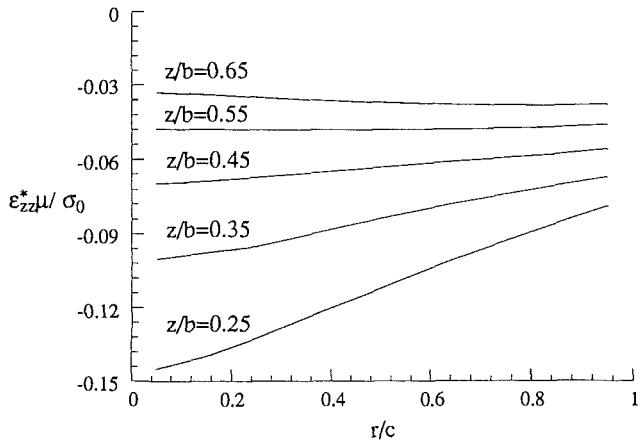


Fig. 2(*b*) ϵ^*_{zz} variation

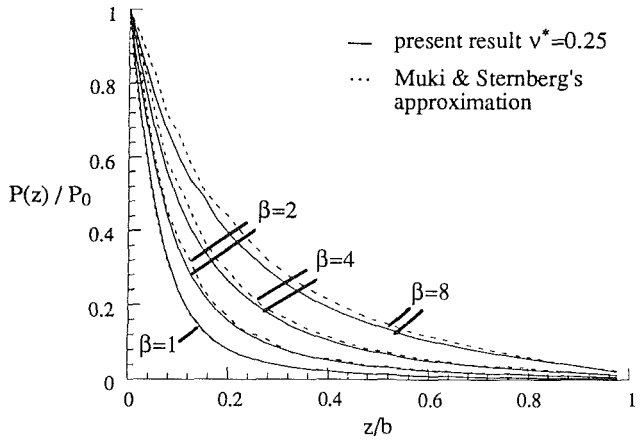


Fig. 3(*b*) Comparison of normalized resultant axial force for ν = 0.25 and *b/c* = 20

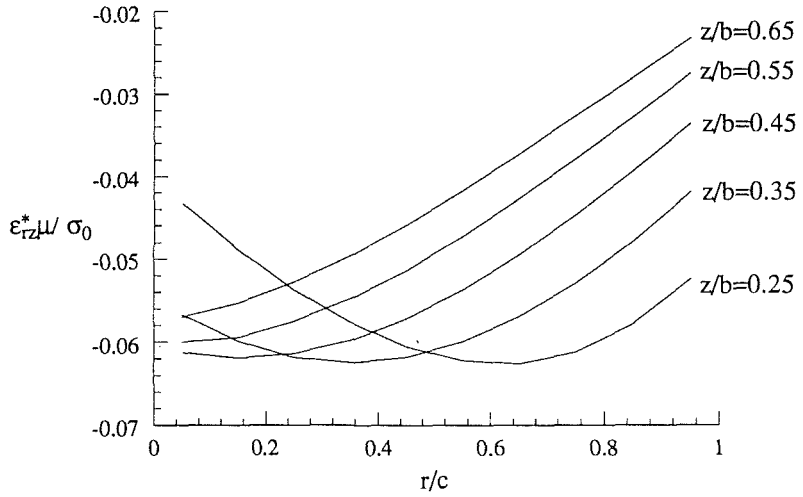


Fig. 2(*c*) ϵ^*_{rz} variation

Fig. 2 The eigenstrain distributions along *r*-direction for β = 2, $\nu = \nu^*$ = 0.25, and *b/c* = 5

Downloaded 03 May 2010 to 171.66.16.20. Redistribution subject to ASME license or copyright; see http://www.asme.org/terms/Terms_Use.cfm

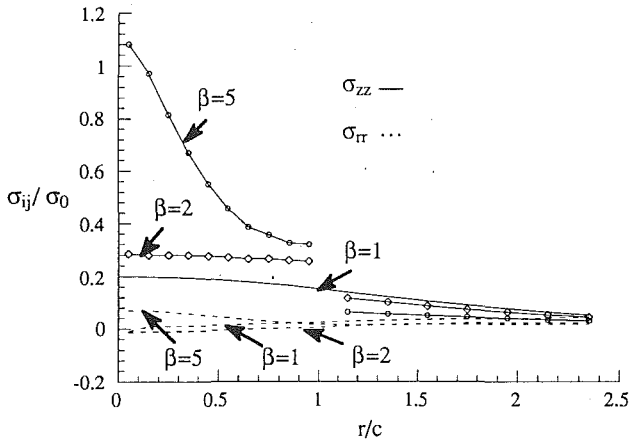


Fig. 4(*a*) The stress distribution for varied β at $z/b = 0.5$ for $\nu = \nu^* = 0.25$ and $b/c = 5$

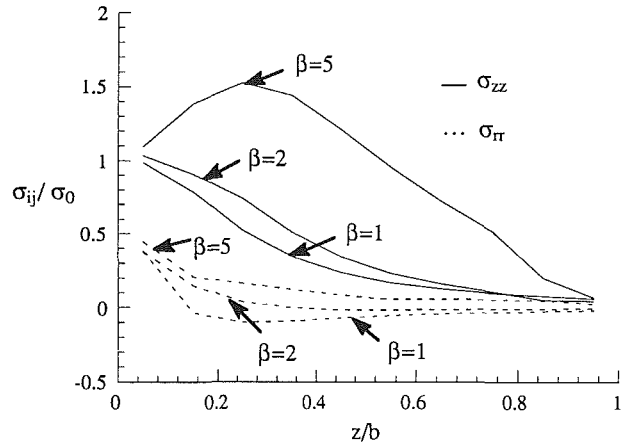


Fig. 4(*b*) The stress distribution for varied β at $r = 0$ for $\nu = \nu^* = 0.25$ and $b/c = 5$

$$\sigma_{\theta\theta}/\sigma_0 = 2\nu cI(1, 0; 0) - \frac{cz}{r} I(1, 1; 0) + \frac{c(1-2\nu)}{r} I(1, 1; -1) \tag{32}$$

$$\sigma_{zz}/\sigma_0 = cI(1, 0; 0) + czI(1, 0; 1) \tag{33}$$

$$\tau_{rz}/\sigma_0 = czI(1, 1; 1) \tag{34}$$

where the Lipschitz-Hankel integral is defined as

$$I(\alpha, \beta; \gamma) = \int_0^\infty J_\alpha(\eta c) J_\beta(\eta r) \eta^\gamma e^{-\eta z} d\eta. \tag{35}$$

The solution of a homogeneous half-space subjected to the uniform load distributed over a circular surface area was originally derived by Lamb in 1902. The stress distributions for varied β are presented in Fig. 4(*a*) (at $z/b = 0.5$) and Fig. 4(*b*) (at $r = 0$) with $\nu = \nu^* = 0.25$ and $b/c = 5$.

An analytic study for load transfer problem of a finite cylindrical fiber embedded in a half-space of different elastic moduli is presented based on the equivalent inclusion method. The equivalent inclusion formulation has been extended to the three-dimensional problem of a finite cylindrical inhomogeneity. Without using approximate approach, the present paper shows favorable results. It is noted that the formulation developed herein can be further applied to the multiphase inhomogeneity problems.

Acknowledgment

This research was supported by AFOSR-F49620-92-J-0319.

References

Eshelby, J. D., 1957, "The Determination of the Elastic Field of an Ellipsoidal Inclusion and Related Problems," *Proceedings of the Royal Society*, Vol. A241, pp. 376-396.

Karasudhi, P., Rajapakse, R. K. N. D., and Hwang, B. Y., 1984, "Torsion of a Long Cylindrical Elastic Bar Partially Embedded in a Layered Elastic Half Space," *Int. J. Solids Structures*, Vol. 20, pp. 1-11.

Lamb, H., 1902, "On Boussinesq's Problem," *Proc. London Math. Soc.*, Vol. 34, pp. 276-284.

Lee, V. G., and Mura, T., 1993, "Load Diffusion and Absorption Problems from a Finite Fiber to Elastic Infinite Matrix," ASME JOURNAL OF APPLIED MECHANICS, in press.

Luco, J. E., 1976, "Torsion of a Rigid Cylinder Embedded in an Elastic Half Space," ASME JOURNAL OF APPLIED MECHANICS, Vol. 43, pp. 419-423.

Luk, V. K., and Keer, L. M., 1979, "Stress Analysis for an Elastic Half Space Containing an Axially-Loaded Rigid Cylindrical Rod," *International Journal of Solids and Structures*, Vol. 15, pp. 805-827.

Muki, R., and Sternberg, E., 1969, "On the Diffusion of an Axial Load from an Infinite Cylindrical Bar Embedded in an Elastic Medium," *International Journal of Solids and Structures*, Vol. 5, pp. 587-605.

Muki, R., and Sternberg, E., 1970, "Elastostatic Load-Transfer to a Half-Space from a Partially Embedded Axially Loaded Rod," *International Journal of Solids and Structures*, Vol. 6, pp. 69-90.

Mura, T., 1987, *Micromechanics of Defects in Solids*, 2nd rev. ed., Martinus Nijhoff, The Netherlands.

Pak, R. Y. S., 1989, "On the Flexure of a Partially Embedded Bar Under Lateral Loads," ASME JOURNAL OF APPLIED MECHANICS, Vol. 56, pp. 263-269.

Pak, R. Y. S., and Saphores, J. M., 1991, "On the Response of a Partially Embedded Rod to Axial Load," ASME JOURNAL OF APPLIED MECHANICS, Vol. 58, pp. 599-602.

Selvadurai, A. P. S., and Rajapakse, R. K. N. D., 1985, "On the Load Transfer from a Rigid Cylindrical Inclusion into an Elastic Half Space," *International Journal of Solids and Structures*, Vol. 21, pp. 1213-1229.

Slaughter, W. S., and Lyell Sanders, J., 1991, "A Model for Load-Transfer from an Embedded Fiber to an Elastic Matrix," *International Journal of Solids and Structures*, Vol. 28, No. 8, pp. 1041-1052.

Downloaded 03 May 2010 to 171.66.16.20. Redistribution subject to ASME license or copyright; see http://www.asme.org/terms/Terms_Use.cfm

Journal of Applied Mechanics

Brief Notes

A Brief Note is a short paper that presents a specific solution of technical interest in mechanics but which does not necessarily contain new general methods or results. A Brief Note should not exceed 1500 words *or equivalent* (a typical one-column figure or table is equivalent to 250 words; a one line equation to 30 words). Brief Notes will be subject to the usual review procedures prior to publication. After approval such Notes will be published as soon as possible. The Notes should be submitted to the Technical Editor of the JOURNAL OF APPLIED MECHANICS. Discussions on the Brief Notes should be addressed to the Editorial Department, ASME, United Engineering Center, 345 East 47th Street, New York, N. Y. 10017, or to the Technical Editor of the JOURNAL OF APPLIED MECHANICS. Discussions on Brief Notes appearing in this issue will be accepted until two months after publication. Readers who need more time to prepare a Discussion should request an extension of the deadline from the Editorial Department.

Stagnation Point Flow With Suction: An Approximate Solution

P. D. Ariel[1]

1 Introduction

Approximate solutions of physical problems which are simple and reasonably accurate are handy tools in the hands of a scientist and an engineer. Though the advent of computers has opened new vistas for obtaining accurate numerical solutions of the problems of ever-increasing complexity, it has in no way diminished the utility of a judiciously produced approximate solution. In the present Note we present an approximate solution to the problem of the laminar two-dimensional flow of an incompressible, viscous fluid impinging on a wall from which the fluid is extracted at a uniform rate.

The classical problem of the two-dimensional stagnation point flow was first examined by Hiemenz (1911). It has been generalized in numerous ways to include various physical effects since then. Thus among the non-Newtonian fluids, its solution, for viscoelastic fluids, has been given by Rajeshwari and Rathna (1962), Beard and Walters (1964), Teipel (1986), Ariel (1992), and others; for power-law fluid by Djukic (1974); and for micropolar fluids by Nath (1975). In hydromagnetics this problem was chosen by Na (1979) to illustrate the solution of a third-order boundary value problem using the technique of finite differences. An approximate solution of the same problem has been recently provided by Ariel (1994).

Since the suction of the fluid is an acknowledged technique for controlling the undesirable features in the boundary layer theory, the effect of suction on the Hiemenz problem has been considered in the literature. Schlichting and Bussman (1943) gave the numerical results first. More detailed solutions were later presented by Preston (1946).

2 Equations of the Problem

The boundary value problem characterizing the flow of a viscous, incompressible fluid impinging normally to a wall from which the fluid is extracted at a uniform rate has been derived in the literature (see, for example, Rosenhead, 1963) and need not be rederived here again. In terms of the non-dimensional similarity variables f, a measure of the stream function and η, the distance normal to the wall, it is given by

$$f''' + ff'' + 1 - f'^2 = 0, \tag{1}$$

$$f(0) = A,\ f'(0) = 0,\ f'(\infty) = 1, \tag{2}$$

where A is the dimensionless suction velocity and a prime denotes the derivative with respect to η.

We now present an approximate solution of the problem based on the idea of stretching of the variables.

3 An Approximate Solution

We introduce α, an amplification factor for stretching both, the independent variable η, and the dependent variable f. The new variables

$$\zeta = \alpha\eta, \quad F = \alpha f, \tag{3}$$

transform the BVP (1) and (2) into

$$\alpha^2 \frac{d^3F}{d\zeta^3} + F\frac{d^2F}{d\zeta^2} + 1 - \left(\frac{dF}{d\zeta}\right)^2 = 0, \tag{4}$$

$$F(0) = \alpha A, \quad \frac{dF(0)}{d\zeta} = 0, \quad \frac{dF(\infty)}{d\zeta} = 1. \tag{5}$$

Now we choose the approximation

$$\frac{dF}{d\zeta} = 1 - e^{-\zeta}, \tag{6}$$

which satisfies both the boundary conditions on $dF/d\zeta$ in (5).

One advantage of this approximation, beside its simplicity, is that the parameter α can be directly identified with $f''(0)$, which is a measure of the skin friction at the wall.

Integration of Eq. (6) from 0 to ζ yields

$$F(\zeta) = \alpha A + \zeta - 1 + e^{-\zeta} \tag{7}$$

on taking into account the remaining boundary condition in (5).

The defect $R(\zeta;\ \alpha)$ in the differential Eq. (4) is given by

$$R(\zeta;\ \alpha) = (1 + \alpha A - \alpha^2)e^{-\zeta} + \zeta e^{-\zeta}. \tag{8}$$

The objective here is to minimize this defect in some sense

[1]Institut fur Mechanik, Universitat Hannover, Hannover, Germany. Current address: Head, Department of Mathematics, Engineering College, Kota, Rawatbhata Road, Akelgarh, Kota, 324010, India.

Contributed by the Applied Mechanics Division of THE AMERICAN SOCIETY OF MECHANICAL ENGINEERS for publication in the ASME JOURNAL OF APPLIED MECHANICS. Manuscript received by the ASME Applied Mechanics Division, Jan. 12, 1993; final revision June 1, 1993. Associate Technical Editor: S. Lichter.

Copyright © 1994 by ASME
Downloaded 03 May 2010 to 171.66.16.20. Redistribution subject to ASME license or copyright; see http://www.asme.org/terms/Terms_Use.cfm

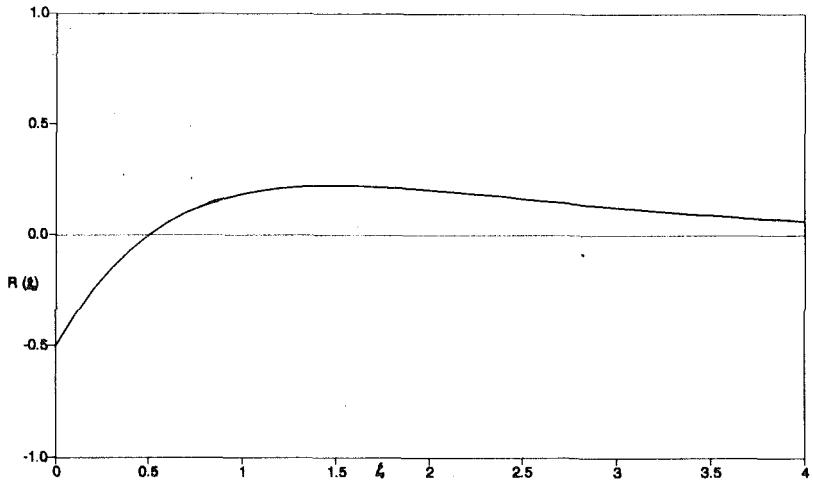


Fig. 1 Plot of the error distribution $R(\zeta)$ against ζ, the stretched independent variable

which then determines the value of the unknown α. Out of several possible choices, such as collocation method, moments method, sub-domain method, Galerkin's method, least-squares method, we decided to opt for the last-named method. Setting

$$\frac{\partial}{\partial \alpha} \int_0^\infty R^2(\zeta; \alpha) d\zeta = 0, \tag{9}$$

give the following cubic in α:

$$\alpha^3 - \frac{3}{2} A\alpha^2 + \frac{1}{2}(A^2 - 3)\alpha + \frac{3}{4} A = 0. \tag{10}$$

We are fortunate to find that $a - 1/2A$ is a factor of the cubic polynomial in (10). This factor can be safely discarded as it corresponds to the value of $1/2A$ for α, which does not describe the skin friction adequately either for small A ($A = 0$) or for large values of A ($A \to \infty$). Thus, on leaving out this factor, we are left with the quadratic

$$\alpha^2 - A\alpha - \frac{3}{2} = 0. \tag{11}$$

This gives two values of α, one of which is negative and must be evidently rejected; the remaining value is

$$\alpha = \frac{1}{2}(A + \sqrt{A^2 + 6}). \tag{12}$$

Hence, with the value of α as given by Eq. (12), the approximate solution for f and f' are

$$f(\eta) = A + \eta - \frac{1}{\alpha}(1 - e^{-\alpha\eta}), \quad f'(\eta) = 1 - e^{-\alpha\eta}. \tag{13}$$

The value of $f''(0)$ is, of course, α given in Eq. (12).

4 Results and Discussion

The accuracy of an approximation can be judged by several criteria. An obvious measure of error is the defect in the differential equation given by Eq. (8). The substitution of α from Eq. (11) into Eq. (8) leads to

$$R(\zeta) = \left(\zeta - \frac{1}{2}\right) e^{-\zeta}. \tag{14}$$

It is interesting to find the above expression for R to be independent of A in the stretched coordinate system. In Fig. 1, R is plotted against ζ. It has a maximum value when $\zeta = 3/2$. Thus

$$-0.5 \le R(\zeta) < 0.223130, \quad 0 \le \zeta < \infty. \tag{15}$$

This error bound is quite satisfactory considering the fact that only one parameter was used in obtaining the approximation solution. Using the more sophisticated extremal point collocation method involving an elaborate iterative numerical scheme Jain (1963) had a similar order of error bounds even though he took two parameters in his approximate solution.

Table 1 Illustrating the variation of $f''(0)$ with A

	$f''(0)$	
A	Exact Solution	Approximate Solution
0	1.232576	1.224745
0.1	1.290978	1.275765
0.2	1.351148	1.328821
0.5	1.541754	1.500000
1	1.889316	1.822876
2	2.678564	2.581139
5	5.359529	5.283822
10	10.193554	10.147815

Another commonly used measure of error is the minimized value of the integral of R^2. This value can be easily seen to be equal to $1/8$ for all values of A, the suction parameter.

In addition, a measure of accuracy can be provided by comparing the values of $f''(0)$ obtained by the exact numerical solution and by the least squares approximation given above. These are presented in Table 1 for various values of A, the suction parameter. It can be seen that the maximum relative error in the value of $f''(0)$ is reasonably small for the entire range of values of A. The worst error occurs when A is nearly equal to 1, when it is roughly 3 1/2 percent. It decreases monotonically as A is either increased or decreased from this value. Considering the small amount of error and the simplicity and elegance of the approximate formula, one can conclude that it can be used satisfactorily in most practical situations. It is possible to obtain more accurate results by using other approximate methods, but in terms of ease of use, it would be hard to get a better solution with comparable accuracy.

Acknowledgments

The author wishes to acknowledge his gratitude to DAAD (Deutscher Akademischer Austauschdienst) for the award of a visiting fellowship and to Moi University for providing the travel funds.

References

Ariel, P. D., 1992, "A Hybrid Method for Computing the Flow of Visco-Elastic Fluids," *International Journal for Numerical Methods in Fluids*, Vol. 14, pp. 757–774.

Ariel, P. D., 1994, "Hiemenz Flow in Hydromagnetics," *Acta Mechanica*, Vol. 103, pp. 31–43.

Beard, D. W., and Walters, K., 1964, "Elastico-viscous Boundary Layer Flows

Downloaded 03 May 2010 to 171.66.16.20. Redistribution subject to ASME license or copyright; see http://www.asme.org/terms/Terms_Use.cfm

I, Two Dimensional Flow near a Stagnation Point," *Proceedings of Cambridge Philosophical Society*, Vol. 60, pp. 667–674.

Djukic, D. S., 1974, "Hiemenz Magnetic Flow of Power-Law Fluids," ASME JOURNAL OF APPLIED MECHANICS, Vol. 40, pp. 822–823.

Hiemenz, K., 1911, "Die Grenzschicht in Einem in Dem Gleichförmingen Flüssigkeitsstrom Eingetauchten Gerade Kreiszylinder," *Dingler Polytechnic Journal*, Vol. 326, pp. 321–410.

Jain, M. K., 1963, "On Extremal Point Collocation Method for Fluid Flow Problems," *Applied Scientific Research*, Section A, Vol. 11, pp. 177–188.

Na, T. Y., 1979, *Computational Methods in Engineering Boundary Value Problems*, Academic Press, New York, pp. 107–121.

Nath, G., 1975, "Similar Solutions for the Incompressible Laminar Boundary Layer with Pressure Gradient in Micropolar Fluids," *Rheological Acta*, Vol. 14, pp. 850–857.

Preston, J. H., 1946, "The Boundary Layer Flow over a Permeable Surface through which Suction is Applied," Reports and Memoirs, British Aerospace Research Council, London, No. 2244.

Rajeshwari, G. K., and Rathna, S. L., 1962, "Flow of a Particular Class of Non-Newtonian Visco-elastic and Visco-inelastic Fluids near a Stagnation Point Flow," *Zeitschrift für Angewandte Mathematik und Physik*, Vol. 13, pp. 43–57.

Rosenhead, L., eds., 1963, *Laminar Boundary Layers*, Oxford, Clarendon Press, London, U.K., pp. 242–243.

Schlichting, H., and Bussmann, K., 1943, "Exakte Lösungen für die Laminare Grenzchicht mit Absaugung und Ausblasen," *Schriften der Deutschen Akademie der Luftfahrtforschung*, Series B, Vol. 7, pp. 25–69.

Teipel, I., 1986, "Die Rämliche Staupunktströmung für ein Visco-elastisches Fluid," *Rheological Acta*, Vol. 25, pp. 75–79.

Thermoelastic Problem of Dissimilar Anisotropic Solids With a Rigid Line Inclusion

C. K. Chao[2] and R. C. Chang[3]

A general solution to the thermoelastic problem of an interface rigid line inclusion between anisotropic dissimilar media is presented. The complex variable representation of plane elastic problem developed by Lekhnitskii is extended into anisotropic thermoelasticity, and a special technique of analytical continuation is introduced to deal with the dissimilar media problem. It is indicated that singularities of the thermal stresses induced by a rigid line inclusion are similar to the case of a slit crack. A numerical example for zirconia bonded to titanium composite under remote heat flux is also examined.

Introduction

The near-tip oscillatory behavior for an interface crack between two isotropic materials was first discovered by Williams (1959). Since then, a number of solutions for the interface crack problems have been obtained. Furthermore, the thermoelastic interface crack problems have been studied by Ting and Hwu (1991), Hwu (1992), Ting and Yan (1992). On the other hand, following the equivalent inclusion approach of Eshelby (1957) and the complex variable method of Muskhelishvili (1953), Wang et al. (1985) have considered the problem of a rigid line inclusion in an isotropic elastic body under uniform remote loading. Based on the Stroh's formalism (Stroh, 1958), a line inclusion in an anisotropic solid has been treated by Li and Ting (1989). Wu (1990) further examined the line inclusion problem in anisotropic bimaterial media.

The objective of the present paper is to provide a general solution to the thermoelastic problem of a rigid inclusion between dissimilar anisotropic media. The analysis is based upon the use of complex variable approach developed by Lekhnitskii (1963) and a special technique of analytical continuation which allow us to make the full-field solutions more compact and simple. The explicit expressions for the tractions along the interface ahead and behind the rigid inclusion are presented. A typical example of zirconia bonded to titanium associated with a rigid line inclusion is also considered in the present work.

Interface Inclusion Problem

For a two-dimensional problem, i.w., with geometry and external loading invariant in the direction normal to the xy-plane, the thermoelastic field can be represented in terms of four holomorphic functions including three stress functions $\phi_1(z_1)$, $\phi_2(z_2)$, $\phi_3(z_3)$ and a temperature function $\theta(z_4)$. The arguments are expressed as $z_j = x + \mu_j y$. With these holomorphic functions or complex potentials, the representation for stresses, σ_{ij}, and the derivative of displacement, u_i', can be written as

$$\sigma_{1i} = -2\mathrm{Re}\left\{\sum_{j=1}^{3} L_{ij}\mu_j\phi_j(z_j) + c_i\mu_4\theta(z_4)\right\},$$

$$\sigma_{2i} = 2\mathrm{Re}\left\{\sum_{j=1}^{3} L_{ij}\phi_j(z_j) + c_i\theta(z_4)\right\},$$

$$u_i' = 2\mathrm{Re}\left\{\sum_{j=1}^{3} A_{ij}\phi_j(z_j) + d_i\theta(z_4)\right\}, \quad (1)$$

where $u_i' = \partial u_i/\partial x$ and Re{ } denotes the real part of a complex function. The characteristic numbers μ_α and elastic constants L_{ij}, A_{ij} are derived by Lekhnitskii (1963) while the thermal coefficients c_i and d_i are defined by Chao and Chang (1993). Without loss of generality, we can present our solutions by the function vector $\boldsymbol{\phi}(z)$ defined as

$$\boldsymbol{\phi}(z) = [\phi_1(z_1), \phi_2(z_2), \phi_3(z_3)]^T. \quad (2)$$

In the present study, both the traction on the y-plane and displacement derivative need to satisfy the corresponding boundary value problem. They are

$$\mathbf{t} = \mathbf{L}\boldsymbol{\phi}(z) + \overline{\mathbf{L}\boldsymbol{\phi}(z)} + \mathbf{c}\theta(z) + \overline{\mathbf{c}\theta(z)},$$
$$\mathbf{u}' = \mathbf{A}\boldsymbol{\phi}(z) + \overline{\mathbf{A}\boldsymbol{\phi}(z)} + \mathbf{d}\theta(z) + \overline{\mathbf{d}\theta(z)}, \quad (3)$$

where the overbar denotes the complex conjugate. The subscripts of z are dropped for convenience. Once the solution is obtained for a given boundary value condition, a replacement of z_1, z_2, z_3, or z_4 should be made.

Consider a line inclusion of length $2a$ lying along the interface of two dissimilar anisotropic media subjected to an uniform heat flow h in the positive y-direction, as shown in Fig. 1. The notations S_1 and S_2 denote the corresponding domain of the dissimilar media that occupied the upper ($y>0$) and lower ($y<0$) space, respectively. The boundary condition on the inclusion surface is

$$\mathbf{u}_1(x) = \mathbf{u}_2(x) = 0 \quad (\text{or } \mathbf{u}_1'(x) = \mathbf{u}_2'(x) = 0), \quad |x| < a \quad (4)$$

and the condinuous conditions along the bonded portion of the interface are

$$\mathbf{t}_1(x) = \mathbf{t}_2(x), \quad \mathbf{u}_1(x) = \mathbf{u}_2(x) \quad (\text{or } \mathbf{u}_1'(x) = \mathbf{u}_2'(x)), \quad |x| > a \quad (5)$$

[2] Professor, Department of Mechanical Engineering, National Taiwan Institute of Technology, Taipei, Taiwan, 106, Republic of China.

[3] Associate Professor, Department of Mechanical Engineering, St. John's and St. Mary's Institute of Technology, Tamsui, Taipei, Taiwan, 251, Republic of China.

Contributed by the Applied Mechanics Division of THE AMERICAN SOCIETY OF MECHANICAL ENGINEERS for publication in the ASME JOURNAL OF APPLIED MECHANICS. Manuscript received by the ASME Applied Mechanics Division, Jan. 19, 1993; final revision, Sept. 15, 1993. Associate Technical Editor: R. Abeyaratne.

Downloaded 03 May 2010 to 171.66.16.20. Redistribution subject to ASME license or copyright; see http://www.asme.org/terms/Terms_Use.cfm

I, Two Dimensional Flow near a Stagnation Point," *Proceedings of Cambridge Philosophical Society*, Vol. 60, pp. 667–674.

Djukic, D. S., 1974, "Hiemenz Magnetic Flow of Power-Law Fluids," ASME JOURNAL OF APPLIED MECHANICS, Vol. 40, pp. 822–823.

Hiemenz, K., 1911, "Die Grenzschicht in Einem in Dem Gleichförmingen Flüssigkeitsstrom Eingetauchten Gerade Kreiszylinder," *Dingler Polytechnic Journal*, Vol. 326, pp. 321–410.

Jain, M. K., 1963, "On Extremal Point Collocation Method for Fluid Flow Problems," *Applied Scientific Research*, Section A, Vol. 11, pp. 177–188.

Na, T. Y., 1979, *Computational Methods in Engineering Boundary Value Problems*, Academic Press, New York, pp. 107–121.

Nath, G., 1975, "Similar Solutions for the Incompressible Laminar Boundary Layer with Pressure Gradient in Micropolar Fluids," *Rheological Acta*, Vol. 14, pp. 850–857.

Preston, J. H., 1946, "The Boundary Layer Flow over a Permeable Surface through which Suction is Applied," Reports and Memoirs, British Aerospace Research Council, London, No. 2244.

Rajeshwari, G. K., and Rathna, S. L., 1962, "Flow of a Particular Class of Non-Newtonian Visco-elastic and Visco-inelastic Fluids near a Stagnation Point Flow," *Zeitschrift für Angewandte Mathematik und Physik*, Vol. 13, pp. 43–57.

Rosenhead, L., eds., 1963, *Laminar Boundary Layers*, Oxford, Clarendon Press, London, U.K., pp. 242–243.

Schlichting, H., and Bussmann, K., 1943, "Exakte Lösungen für die Laminare Grenzchicht mit Absaugung und Ausblasen," *Schriften der Deutschen Akademie der Luftfahrtforschung*, Series B, Vol. 7, pp. 25–69.

Teipel, I., 1986, "Die Rämliche Staupunktströmung für ein Visco-elastisches Fluid," *Rheological Acta*, Vol. 25, pp. 75–79.

Thermoelastic Problem of Dissimilar Anisotropic Solids With a Rigid Line Inclusion

C. K. Chao[2] and R. C. Chang[3]

A general solution to the thermoelastic problem of an interface rigid line inclusion between anisotropic dissimilar media is presented. The complex variable representation of plane elastic problem developed by Lekhnitskii is extended into anisotropic thermoelasticity, and a special technique of analytical continuation is introduced to deal with the dissimilar media problem. It is indicated that singularities of the thermal stresses induced by a rigid line inclusion are similar to the case of a slit crack. A numerical example for zirconia bonded to titanium composite under remote heat flux is also examined.

Introduction

The near-tip oscillatory behavior for an interface crack between two isotropic materials was first discovered by Williams (1959). Since then, a number of solutions for the interface crack problems have been obtained. Furthermore, the thermoelastic interface crack problems have been studied by Ting and Hwu (1991), Hwu (1992), Ting and Yan (1992). On the other hand, following the equivalent inclusion approach of Eshelby (1957) and the complex variable method of Muskhelishvili (1953), Wang et al. (1985) have considered the problem of a rigid line inclusion in an isotropic elastic body under uniform remote loading. Based on the Stroh's formalism (Stroh, 1958), a line inclusion in an anisotropic solid has been treated by Li and Ting (1989). Wu (1990) further examined the line inclusion problem in anisotropic bimaterial media.

The objective of the present paper is to provide a general solution to the thermoelastic problem of a rigid inclusion between dissimilar anisotropic media. The analysis is based upon the use of complex variable approach developed by Lekhnitskii (1963) and a special technique of analytical continuation which allow us to make the full-field solutions more compact and simple. The explicit expressions for the tractions along the interface ahead and behind the rigid inclusion are presented. A typical example of zirconia bonded to titanium associated with a rigid line inclusion is also considered in the present work.

Interface Inclusion Problem

For a two-dimensional problem, i.w., with geometry and external loading invariant in the direction normal to the xy-plane, the thermoelastic field can be represented in terms of four holomorphic functions including three stress functions $\phi_1(z_1)$, $\phi_2(z_2)$, $\phi_3(z_3)$ and a temperature function $\theta(z_4)$. The arguments are expressed as $z_j = x + \mu_j y$. With these holomorphic functions or complex potentials, the representation for stresses, σ_{ij}, and the derivative of displacement, u_i', can be written as

$$\sigma_{1i} = -2\mathrm{Re}\left\{\sum_{j=1}^{3} L_{ij}\mu_j\phi_j(z_j) + c_i\mu_4\theta(z_4)\right\},$$

$$\sigma_{2i} = 2\mathrm{Re}\left\{\sum_{j=1}^{3} L_{ij}\phi_j(z_j) + c_i\theta(z_4)\right\},$$

$$u_i' = 2\mathrm{Re}\left\{\sum_{j=1}^{3} A_{ij}\phi_j(z_j) + d_i\theta(z_4)\right\}, \tag{1}$$

where $u_i' = \partial u_i/\partial x$ and Re{ } denotes the real part of a complex function. The characteristic numbers μ_α and elastic constants L_{ij}, A_{ij} are derived by Lekhnitskii (1963) while the thermal coefficients c_i and d_i are defined by Chao and Chang (1993). Without loss of generality, we can present our solutions by the function vector $\boldsymbol{\phi}(z)$ defined as

$$\boldsymbol{\phi}(z) = [\phi_1(z_1), \phi_2(z_2), \phi_3(z_3)]^T. \tag{2}$$

In the present study, both the traction on the y-plane and displacement derivative need to satisfy the corresponding boundary value problem. They are

$$\mathbf{t} = \mathbf{L}\boldsymbol{\phi}(z) + \overline{\mathbf{L}\boldsymbol{\phi}(z)} + \mathbf{c}\theta(z) + \overline{\mathbf{c}\theta(z)},$$
$$\mathbf{u}' = \mathbf{A}\boldsymbol{\phi}(z) + \overline{\mathbf{A}\boldsymbol{\phi}(z)} + \mathbf{d}\theta(z) + \overline{\mathbf{d}\theta(z)}, \tag{3}$$

where the overbar denotes the complex conjugate. The subscripts of z are dropped for convenience. Once the solution is obtained for a given boundary value condition, a replacement of z_1, z_2, z_3, or z_4 should be made.

Consider a line inclusion of length $2a$ lying along the interface of two dissimilar anisotropic media subjected to an uniform heat flow h in the positive y-direction, as shown in Fig. 1. The notations S_1 and S_2 denote the corresponding domain of the dissimilar media that occupied the upper ($y>0$) and lower ($y<0$) space, respectively. The boundary condition on the inclusion surface is

$$\mathbf{u}_1(x) = \mathbf{u}_2(x) = 0 \quad (\text{or } \mathbf{u}_1'(x) = \mathbf{u}_2'(x) = 0), \quad |x| < a \tag{4}$$

and the condinuous conditions along the bonded portion of the interface are

$$\mathbf{t}_1(x) = \mathbf{t}_2(x), \quad \mathbf{u}_1(x) = \mathbf{u}_2(x) \quad (\text{or } \mathbf{u}_1'(x) = \mathbf{u}_2'(x)), \quad |x| > a \tag{5}$$

[2] Professor, Department of Mechanical Engineering, National Taiwan Institute of Technology, Taipei, Taiwan, 106, Republic of China.

[3] Associate Professor, Department of Mechanical Engineering, St. John's and St. Mary's Institute of Technology, Tamsui, Taipei, Taiwan, 251, Republic of China.

Contributed by the Applied Mechanics Division of THE AMERICAN SOCIETY OF MECHANICAL ENGINEERS for publication in the ASME JOURNAL OF APPLIED MECHANICS. Manuscript received by the ASME Applied Mechanics Division, Jan. 19, 1993; final revision, Sept. 15, 1993. Associate Technical Editor: R. Abeyaratne.

Copyright © 1994 by ASME
Downloaded 03 May 2010 to 171.66.16.20. Redistribution subject to ASME license or copyright; see http://www.asme.org/terms/Terms_Use.cfm

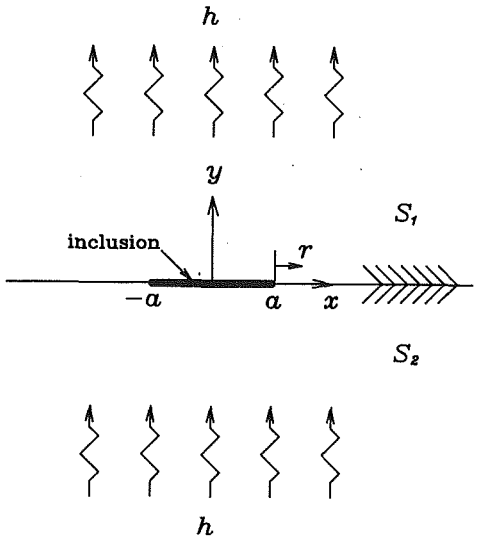


Fig. 1 An interface inclusion between dissimilar anisotropic media subjected to a remote heat flow

where the subscripts 1 and 2 stand for the upper and lower media, respectively. From Eqs. (4) and (5), it implies that the displacement derivative is continuous along the interface including the bonded and inclusion portion and the boundary condition in Eq. (4) can be put in the form

$$\mathbf{f}^+(x)+\overline{\mathbf{H}}^{-1}\mathbf{H}\mathbf{f}^-(x)-\mathbf{e}_1\theta_1^+(x)-\mathbf{e}_2\theta_2^-(x)=0, \quad |x|<a \tag{6}$$

where

$$\mathbf{f}(z)=\begin{cases} i\mathbf{H}^{-1}[(\mathbf{L}_1-\overline{\mathbf{L}}_2\overline{\mathbf{A}}_2^{-1}\mathbf{A}_1)\phi_1(z)+\mathbf{c}_3\theta_1(z)], & z\in S_1,\\ i\mathbf{H}^{-1}[(\mathbf{L}_2-\overline{\mathbf{L}}_1\overline{\mathbf{A}}_1^{-1}\mathbf{A}_2)\phi_2(z)+\mathbf{c}_4\theta_2(z)], & z\in S_2,\end{cases} \tag{7}$$

$$\mathbf{H}=i(\mathbf{L}_1\mathbf{A}_1^{-1}-\overline{\mathbf{L}}_2\overline{\mathbf{A}}_2^{-1}), \tag{8}$$

$$\mathbf{c}_3=(\mathbf{c}_1-\overline{\mathbf{L}}_2\overline{\mathbf{A}}_2^{-1}\mathbf{d}_1)-\frac{k_1}{k_2}(\overline{\mathbf{c}}_2-\overline{\mathbf{L}}_2\overline{\mathbf{A}}_2^{-1}\overline{\mathbf{d}}_2),$$

$$\mathbf{c}_4=(\mathbf{c}_2-\overline{\mathbf{L}}_1\overline{\mathbf{A}}_1^{-1}\mathbf{d}_2)-\frac{k_2}{k_1}(\overline{\mathbf{c}}_1-\overline{\mathbf{L}}_1\overline{\mathbf{A}}_1^{-1}\overline{\mathbf{d}}_1), \tag{9}$$

$$\mathbf{e}_1=i\mathbf{H}^{-1}\mathbf{c}_3-\mathbf{d}_1, \quad \mathbf{e}_2=i\overline{\mathbf{H}}^{-1}\mathbf{c}_4-\mathbf{d}_2. \tag{10}$$

The temperature functions $\theta_1(z)$ and $\theta_2(z)$ in Eq. (6) can be determined independently, that is (Chao and Chang, 1992)

$$\theta_1(z)=-\frac{h}{2k_1}\sqrt{z^2-a^2}+\frac{hz}{2k_1},$$

$$\theta_2(z)=-\frac{h}{2k_2}\sqrt{z^2-a^2}+\frac{hz}{2k_2}. \tag{11}$$

Substituting Eq. (11) into Eq. (6), leads to the following Hilbert problem (Muskhelishivili, 1953):

$$\mathbf{f}^+(x)+\overline{\mathbf{H}}^{-1}\mathbf{H}\mathbf{f}^-(x)=\mathbf{h}_0x+\mathbf{j}_0\sqrt{x^2-a^2}, \quad |x|<a, \tag{12}$$

where

$$\mathbf{h}_0=\left(\frac{\mathbf{e}_1}{2k_1}+\frac{\mathbf{e}_2}{2k_2}\right)h, \quad \mathbf{j}_0=\left(\frac{\mathbf{e}_2}{2k_2}-\frac{\mathbf{e}_1}{2k_1}\right)h. \tag{13}$$

In order to decouple Eq. (12), one considers the following eigenvalue problem (Suo, 1990):

$$\overline{\mathbf{H}}\mathbf{w}=e^{2\pi\epsilon}\mathbf{H}\mathbf{w}. \tag{14}$$

Since $\mathbf{H}$ is a 3×3 Hermitian matrix, there exists for the following three eigenpairs

$$(\epsilon,\ \mathbf{w}), \quad (-\epsilon,\ \overline{\mathbf{w}}), \quad (0,\ \mathbf{w}_3), \tag{15}$$

where ϵ is a real positive number and $\mathbf{w}$, $\mathbf{w}_3$ are corresponding to a complex and a real eigenvector, respectively. Using Eq. (14), $\mathbf{f}(z)$ can now be represented as a linear combination of the three eigenvectors, that is

$$\mathbf{f}(z)=f_1(z)\mathbf{w}+f_2(z)\overline{\mathbf{w}}+f_3(z)\mathbf{w}_3, \tag{16}$$

and Eq. (12) can be evaluated by residue theory and the final result becomes

$$f_1(z)=\frac{\chi(z)}{1+e^{-2\pi\epsilon}}\left\{h_{01}\left[\chi^{-1}(z)z-z^2-i2\epsilon az+\frac{1}{2}(1+2\epsilon^2)a^2\right]\right\}$$
$$+\{j_{01}[\chi^{-1}(z)\sqrt{z^2-a^2}-z^2-i2\epsilon az+(1+2\epsilon^2)a^2]\},$$

$$f_2(z)=\frac{\overline{\chi}(z)}{1+e^{2\pi\epsilon}}\left\{h_{02}\left[\overline{\chi}^{-1}(z)-z^2+i2\epsilon az+\frac{1}{2}(1+2\epsilon^2)a^2\right]\right\}$$
$$+\{j_{02}[\overline{\chi}^{-1}(z)\sqrt{z^2-a^2}-z^2+i2\epsilon az+(1+2\epsilon^2)a^2]\},$$

$$f_3(z)=\frac{\chi_0(z)}{2}\left\{h_{03}\left[\chi_0^{-1}(z)z-z^2+\frac{a^2}{2}\right]\right\}$$
$$+\{j_{03}[\chi_0^{-1}(z)\sqrt{z^2-a^2}-z^2+a^2]\}, \tag{17}$$

where the Plemelj functions are written as

$$\chi(z)=(z+a)^{-1/2-i\epsilon}(z-a)^{-1/2+i\epsilon},$$

$$\chi_0(z)=(z+a)^{-1/2}(z-a)^{-1/2}, \tag{18}$$

and

$$h_{01}=\frac{\overline{\mathbf{w}}^T\mathbf{H}\mathbf{h}_0}{\overline{\mathbf{w}}^T\mathbf{H}\mathbf{w}}, \quad h_{02}=\frac{\mathbf{w}^T\mathbf{H}\mathbf{h}_0}{\mathbf{w}^T\mathbf{H}\overline{\mathbf{w}}}, \quad h_{03}=\frac{\mathbf{w}_3^T\mathbf{H}\mathbf{h}_0}{\mathbf{w}_3^T\mathbf{H}\mathbf{w}_3},$$

$$j_{01}=\frac{\overline{\mathbf{w}}^T\mathbf{H}\mathbf{j}_0}{\overline{\mathbf{w}}^T\mathbf{H}\mathbf{w}}, \quad j_{02}=\frac{\mathbf{w}^T\mathbf{H}\mathbf{j}_0}{\mathbf{w}^T\mathbf{H}\overline{\mathbf{w}}}, \quad j_{03}=\frac{\mathbf{w}_3^T\mathbf{H}\mathbf{j}_0}{\mathbf{w}_3^T\mathbf{H}\mathbf{w}_3}, \tag{19}$$

Now, a general solution for the thermoelastic interface inclusion between dissimilar anisotropic media has been achieved. Having the stress and temperature functions, the full-field solutions of the stresses and displacements can be obtained from Eq. (1).

From Eq. (18), it is recognized that a square-root singularity with oscillatory behavior exists at the tip of the rigid line inclusion, similar to the case of a crack. For a more appropriate description of the stress singularity, the traction along the bonded interface with a distance r ahead of the inclusion tip is obtained by substituting the stress functions determined previously into Eq. (3) as follows:

$$\mathbf{t}(r)=\frac{(\mathbf{B}_1e^{\pi\epsilon}+\overline{\mathbf{B}}_1e^{-\pi\epsilon})Fr^{i\epsilon}\mathbf{w}+(\mathbf{B}_1e^{-\pi\epsilon}+\overline{\mathbf{B}}_1e^{\pi\epsilon})\overline{F}r^{-i\epsilon}\overline{\mathbf{w}}}{2(2\pi r)^{1/2}}$$
$$+\frac{(\mathbf{B}_1+\overline{\mathbf{B}}_1)F_3\mathbf{w}_3}{2(2\pi r)^{1/2}}, \tag{20}$$

where r is extremely small as compared with the inclusion geometry, i.e., $r\ll a$. The asymptotic coefficients F and F_3 appeared in Eq. (20) as defined as

$$F=2\sqrt{2\pi}e^{-\pi\epsilon}\lim_{z\to a^+}(z-a)^{1/2-i\epsilon}f_1(z),$$

$$F_3=2\sqrt{2\pi}\lim_{z\to a^+}(z-a)^{1/2}f_3(z), \tag{21}$$

and the bimaterial constant $\mathbf{B}_1$ is given by

$$\mathbf{B}_1=\mathbf{L}_1\mathbf{A}_1^{-1}. \tag{22}$$

In view of the eigenvalue problem shown in Eq. (14), the traction in Eq. (20) can also be represented as

$$\mathbf{t}(r)=\frac{(\mathbf{B}_2e^{-\pi\epsilon}+\overline{\mathbf{B}}_2e^{\pi\epsilon})Fr^{i\epsilon}\mathbf{w}+(\mathbf{B}_2e^{\pi\epsilon}+\overline{\mathbf{B}}_2e^{-\pi\epsilon})\overline{F}r^{-i\epsilon}\overline{\mathbf{w}}}{2(2\pi r)^{1/2}}$$
$$+\frac{(\mathbf{B}_2+\overline{\mathbf{B}}_2)F_3\mathbf{w}_3}{2(2\pi r)^{1/2}} \tag{23}$$

where $\mathbf{B}_2=\mathbf{L}_2\mathbf{A}_2^{-1}$.

Downloaded 03 May 2010 to 171.66.16.20. Redistribution subject to ASME license or copyright; see http://www.asme.org/terms/Terms_Use.cfm

Table 1 Thermoelastic material properties

	$E(\times 10^{11}\ Nm^{-2})$	ν	$\alpha(\times 10^{-6}\ K^{-1})$	$k(Wm^{-1}\ K^{-1})$
zirconia	2.00	0.23	13.0	2.20
titanium	1.15	0.32	8.60	7.79

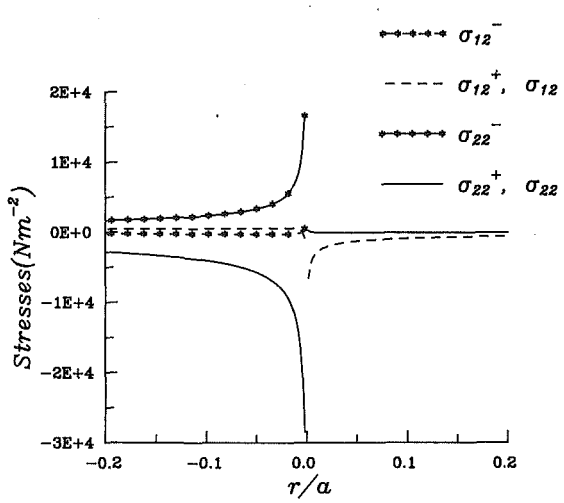


Fig. 2 Tractions along the interface of the vicinity of inclusion tip for zirconia-to-titanium composite

Similarly, the traction on the inclusion surface with a distance r behind of the inclusion tip is

$$\mathbf{t}^+(r) = \frac{i(\bar{\mathbf{B}}_1 - \mathbf{B}_1)(Fr^{i\epsilon}\mathbf{w} + \bar{F}r^{-i\epsilon}\bar{\mathbf{w}})}{2(2\pi r)^{1/2}} + \frac{i(\bar{\mathbf{B}}_1 - \mathbf{B}_1)F_3\mathbf{w}_3}{2(2\pi r)^{1/2}},$$

$$\mathbf{t}^-(r) = \frac{i(\mathbf{B}_2 - \bar{\mathbf{B}}_2)(Fr^{i\epsilon}\mathbf{w} + \bar{F}r^{-i\epsilon}\bar{\mathbf{w}})}{2(2\pi r)^{1/2}} + \frac{i(\mathbf{B}_2 - \bar{\mathbf{B}}_2)F_3\mathbf{w}_3}{2(2\pi r)^{1/2}}, \quad (24)$$

where the superscripts + and − denote the upper and lower surface, respectively. Note that, keeping with the physical meaning, the tractions that appear in Eqs. (20), (23), and (24) are all real.

Numerical Example

In order to illustrate the solutions derived in the previous sections for the fundamental nature of the interlaminar inclusion problem, a typical example of an inclusion lying along the interface between zirconia (S_1) and titanium (S_2) composite under a remote uniform heat flow is considered. The thermoelastic properties are listed in Table 1, where E, ν, α, k denote Young's modulus, Poisson's ratio, thermal expansion coefficient and thermal conductivity, respectively. Tractions along the interface ahead and behind of the inclusion tip ($z = a$) with $h = 1$ W/m^2 and $a = 10^{-2}$ m are shown in Fig. 2, where the dashed and solid lines denote the shear and normal stresses, respectively, and star symbols stand for the stresses on the lower surface of inclusion. It shows that the induced thermal stresses change sign across the inclusion surface and the shear stresses dominate on the bonded portion while the normal stresses dominate on the inclusion surface. Moreover, the induced thermal stresses on the inclusion surface are higher than those on the bonded interface. It is noted that the general solution derived in this study is only valid when the material behaves generally anisotropic. However, with a small perturbation of the material constants, the solutions presented above could give a good approximation for the case of degeneration of thermoelastic material properties. Another interesting aspect is that the oscillatory behavior of traction does not appear clearly in Fig. 2, since the scale of oscillation cycle is far smaller than the geometric length of inclusion.

Conclusion

A general solution for the thermoelastic interface inclusion between dissimilar anisotropic media has been obtained by taking advantage of the explicitness of Lekhnitskii's derivation and the method of analytical continuation. It shows that the stress field near the tip of a rigid line between dissimilar anisotropic media subjected to a remote heat flux exhibits $r^{-1/2\pm i\epsilon}$ singularity similar to the case of slit interface crack, where ϵ is a bimaterial constant. A typical example of zirconia bonded to titanium composite under remote heat flux is considered. The result shows that the induced thermal stresses on the inclusion surface are higher than those on the bonded surface.

References

Chao, C. K., and Chang, R. C., 1993, "Hygrothermal Stresses for a Plane Crack in a Generally Anisotropic Plate," *Engineering Fracture Mechanics*, Vol. 45, No. 6, pp. 831–841.

Chao, C. K., and Chang, R. C., 1992, "Thermal Interface Crack Problems in Dissimilar Anisotropic Media," *Journal of Applied Physics*, Vol. 72, pp. 2598–2604.

Eshelby, J. D., 1957, "The Determination of the Elastic Field of an Ellipsoid Inclusion and Related Problems," *Proceedings of the Royal Society, London*, Vol. A247, pp. 376–396.

Hwu, C., 1992, "Thermoelastic Interface Crack Problems in Dissimilar Anisotropic Media," *International Journal of Solids and Structures*, Vol. 29, pp. 2077–2090.

Lekhnitskii, S. G., 1963, *Theory of Elasticity of an Ansiotropic Elastic Body*, Holdenday, San Francisco, CA.

Li, Q., and Ting, T. C. T., 1989, "Line Inclusions in Anisotropic Elastic Solid," ASME JOURNAL OF APPLIED MECHANICS, Vol. 56, pp. 556–563.

Muskhelishivili, N. I., 1953, *Some Basic Problems of Mathematical Theory of Elasticity*, P. Noordhoff, Groningen, The Netherlands.

Stroh, A. N., 1958, "Dislocations and Cracks in Anisotropic Elasticity," *Philosophical Magazine*, Vol. 3, pp. 625–646.

Suo, Z., 1990, "Singularities, Interfaces and Cracks in Dissimilar Anisotropic Media," *Proceedings of the Royal Society, London*, Vol. A427, pp. 331–358.

Ting, T. C. T., and Hwu, C., 1991, "Effects of Heat Flow on Stress Singularities at the Interface Crack," *Mechanics of Composites at Elevated and Cryogenic Temperatures*, S. N. Singhal, W. F. Jones, and C. T. Herakovich, eds., ASME-AMD-Vol. 118, pp. 231–238.

Ting, T. C. T., and Yan, G., 1992, "The $r^{-1/2}(\ln r)$ Singularity at Interface Cracks in Anisotropic Bimaterials due to Heat Flow," *Journal of Thermal Stresses*, Vol. 15, pp. 85–99.

Wang, Z. Y., Zhang, H. Y., and Chou, Y. T., 1985, "Characteristics of the Elastic Field of a Rigid Line Inhomogeneity," ASME JOURNAL OF APPLIED MECHANICS, Vol. 52, pp. 818–822.

Williams, M. L., 1959, "The Stresses Around a Fault or Crack in Dissimilar Media," *Bulletin of the Seismological Society of America*, Vol. 49, pp. 199–204.

Wu, K. C., 1990, "Line Inclusion at Anisotropic Bimaterial Interface," *Mechanics of Materials*, Vol. 10, pp. 173–182.

Stability of Harmonic Waves in a Periodic System and the Radiation Condition

Paul E. Barbone[4]

1 Introduction

Even before the classic book by Brillouin (1946), it has been well known that the frequency response of a waveguide with

[4]Department of Applied Mathematics and Theoretical Physics, University of Cambridge, Cambridge, CB3 9EW, U.K. Current address: Department of Aerospace and Mechanical Engineering, Boston University, 110 Cummington Street, Boston, MA 02215.

Contributed by the Applied Mechanics Division of THE AMERICAN SOCIETY OF MECHANICAL ENGINEERS for publication in the ASME JOURNAL OF APPLIED MECHANICS. Manuscript received by the ASME Applied Mechanics Division, Aug. 31, 1992; final revision, Aug. 24, 1993. Associate Technical Editor: P. D. Spanos.

Downloaded 03 May 2010 to 171.66.16.20. Redistribution subject to ASME license or copyright; see http://www.asme.org/terms/Terms_Use.cfm

Table 1 Thermoelastic material properties

	$E(\times 10^{11}\ Nm^{-2})$	ν	$\alpha(\times 10^{-6}\ K^{-1})$	$k(Wm^{-1}\ K^{-1})$
zirconia	2.00	0.23	13.0	2.20
titanium	1.15	0.32	8.60	7.79

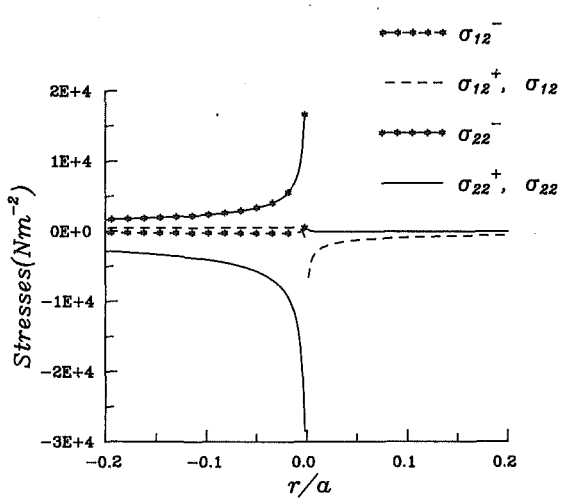


Fig. 2 Tractions along the interface of the vicinity of inclusion tip for zirconia-to-titanium composite

Similarly, the traction on the inclusion surface with a distance r behind of the inclusion tip is

$$\mathbf{t}^+(r)=\frac{i(\bar{\mathbf{B}}_1-\mathbf{B}_1)(Fr^{i\epsilon}\mathbf{w}+\bar{F}r^{-i\epsilon}\bar{\mathbf{w}})}{2(2\pi r)^{1/2}}+\frac{i(\bar{\mathbf{B}}_1-\mathbf{B}_1)F_3\mathbf{w}_3}{2(2\pi r)^{1/2}},$$

$$\mathbf{t}^-(r)=\frac{i(\mathbf{B}_2-\bar{\mathbf{B}}_2)(Fr^{i\epsilon}\mathbf{w}+\bar{F}r^{-i\epsilon}\bar{\mathbf{w}})}{2(2\pi r)^{1/2}}+\frac{i(\mathbf{B}_2-\bar{\mathbf{B}}_2)F_3\mathbf{w}_3}{2(2\pi r)^{1/2}}, \quad (24)$$

where the superscripts + and − denote the upper and lower surface, respectively. Note that, keeping with the physical meaning, the tractions that appear in Eqs. (20), (23), and (24) are all real.

Numerical Example

In order to illustrate the solutions derived in the previous sections for the fundamental nature of the interlaminar inclusion problem, a typical example of an inclusion lying along the interface between zirconia (S_1) and titanium (S_2) composite under a remote uniform heat flow is considered. The thermoelastic properties are listed in Table 1, where E, ν, α, k denote Young's modulus, Poisson's ratio, thermal expansion coefficient and thermal conductivity, respectively. Tractions along the interface ahead and behind of the inclusion tip ($z=a$) with $h=1$ W/m^2 and $a=10^{-2}$ m are shown in Fig. 2, where the dashed and solid lines denote the shear and normal stresses, respectively, and star symbols stand for the stresses on the lower surface of inclusion. It shows that the induced thermal stresses change sign across the inclusion surface and the shear stresses dominate on the bonded portion while the normal stresses dominate on the inclusion surface. Moreover, the induced thermal stresses on the inclusion surface are higher than those on the bonded interface. It is noted that the general solution derived in this study is only valid when the material behaves generally anisotropic. However, with a small perturbation of the material constants, the solutions presented above could give a good approximation for the case of degeneration of thermoelastic material properties. Another interesting aspect is that the oscillatory behavior of traction does not appear clearly in Fig. 2, since the scale of oscillation cycle is far smaller than the geometric length of inclusion.

Conclusion

A general solution for the thermoelastic interface inclusion between dissimilar anisotropic media has been obtained by taking advantage of the explicitness of Lekhnitskii's derivation and the method of analytical continuation. It shows that the stress field near the tip of a rigid line between dissimilar anisotropic media subjected to a remote heat flux exhibits $r^{-1/2\pm i\epsilon}$ singularity similar to the case of slit interface crack, where ϵ is a bimaterial constant. A typical example of zirconia bonded to titanium composite under remote heat flux is considered. The result shows that the induced thermal stresses on the inclusion surface are higher than those on the bonded surface.

References

Chao, C. K., and Chang, R. C., 1993, "Hygrothermal Stresses for a Plane Crack in a Generally Anisotropic Plate," *Engineering Fracture Mechanics*, Vol. 45, No. 6, pp. 831–841.

Chao, C. K., and Chang, R. C., 1992, "Thermal Interface Crack Problems in Dissimilar Anisotropic Media," *Journal of Applied Physics*, Vol. 72, pp. 2598–2604.

Eshelby, J. D., 1957, "The Determination of the Elastic Field of an Ellipsoid Inclusion and Related Problems," *Proceedings of the Royal Society, London*, Vol. A247, pp. 376–396.

Hwu, C., 1992, "Thermoelastic Interface Crack Problems in Dissimilar Anisotropic Media," *International Journal of Solids and Structures*, Vol. 29, pp. 2077–2090.

Lekhnitskii, S. G., 1963, *Theory of Elasticity of an Ansiotropic Elastic Body*, Holdenday, San Francisco, CA.

Li, Q., and Ting, T. C. T., 1989, "Line Inclusions in Anisotropic Elastic Solid," ASME Journal of Applied Mechanics, Vol. 56, pp. 556–563.

Muskhelishivili, N. I., 1953, *Some Basic Problems of Mathematical Theory of Elasticity*, P. Noordhoff, Groningen, The Netherlands.

Stroh, A. N., 1958, "Dislocations and Cracks in Anisotropic Elasticity," *Philosophical Magazine*, Vol. 3, pp. 625–646.

Suo, Z., 1990, "Singularities, Interfaces and Cracks in Dissimilar Anisotropic Media," *Proceedings of the Royal Society, London*, Vol. A427, pp. 331–358.

Ting, T. C. T., and Hwu, C., 1991, "Effects of Heat Flow on Stress Singularities at the Interface Crack," *Mechanics of Composites at Elevated and Cryogenic Temperatures*, S. N. Singhal, W. F. Jones, and C. T. Herakovich, eds., ASME-AMD-Vol. 118, pp. 231–238.

Ting, T. C. T., and Yan, G., 1992, "The $r^{-1/2}(\ln r)$ Singularity at Interface Cracks in Anisotropic Bimaterials due to Heat Flow," *Journal of Thermal Stresses*, Vol. 15, pp. 85–99.

Wang, Z. Y., Zhang, H. Y., and Chou, Y. T., 1985, "Characteristics of the Elastic Field of a Rigid Line Inhomogeneity," ASME Journal of Applied Mechanics, Vol. 52, pp. 818–822.

Williams, M. L., 1959, "The Stresses Around a Fault or Crack in Dissimilar Media," *Bulletin of the Seismological Society of America*, Vol. 49, pp. 199–204.

Wu, K. C., 1990, "Line Inclusion at Anisotropic Bimaterial Interface," *Mechanics of Materials*, Vol. 10, pp. 173–182.

Stability of Harmonic Waves in a Periodic System and the Radiation Condition

Paul E. Barbone[4]

1 Introduction

Even before the classic book by Brillouin (1946), it has been well known that the frequency response of a waveguide with

[4]Department of Applied Mathematics and Theoretical Physics, University of Cambridge, Cambridge, CB3 9EW, U.K. Current address: Department of Aerospace and Mechanical Engineering, Boston University, 110 Cummington Street, Boston, MA 02215.

Contributed by the Applied Mechanics Division of The American Society of Mechanical Engineers for publication in the ASME Journal of Applied Mechanics. Manuscript received by the ASME Applied Mechanics Division, Aug. 31, 1992; final revision, Aug. 24, 1993. Associate Technical Editor: P. D. Spanos.

Copyright © 1994 by ASME
Downloaded 03 May 2010 to 171.66.16.20. Redistribution subject to ASME license or copyright; see http://www.asme.org/terms/Terms_Use.cfm

simple periodic structure is divided into *pass bands* and *stop bands*. A pass band is an interval on the frequency axis in which waves propagate freely along the waveguide. A stop band, on the other hand, is an interval in which wave motion is entirely reflected, and thus waves are stopped.

Floquet's theorem (Ince, 1956) shows that a time-harmonic wave propagating in a periodic system necessarily has the form

$$u(x)e^{-i\omega t}=p_1(x)e^{i\lambda x-i\omega t}+p_2(x)e^{-i\lambda x-i\omega t}. \tag{1}$$

Here, the real part of $u(x)$ denotes a field quantity, say the displacement in the waveguide, $p_1(x)$ and $p_2(x)$ are periodic functions which have the same periodicity as the waveguide structure, ω is the frequency, and $\lambda=\alpha+i\gamma$ is the *Floquet wave number*. We assume, without loss of generality, $\alpha>0$, $\gamma\geq 0$.

With $\alpha>0$, the first term on the right of (1) seems to represent a wave propagating to the right, while the second term represents a left traveling wave. In terms of λ, the pass and stop bands correspond to frequencies in which $\gamma=0$ or $\gamma\neq 0$, respectively. When $\gamma\neq 0$, the first term in (1) represents a wave which decays in amplitude while propagating to the right, while the second term represents a wave which decays in amplitude while propagating to the left.

The existence of a solution of the form

$$u(x)=p_2(x)e^{-i\alpha x+\gamma x} \tag{2}$$

has caused some people to interpret these waves as unstable since they grow exponentially to the right (Kim and Ginsberg, 1992; Nayfeh and Nemat-Nasser, 1972; Schoenberg and Weitsman, 1975; Watanabe, 1984). In describing the origin of the instability, in each case an analogy was drawn between waves in periodic waveguides and the motion of a periodic oscillator with a parametric instability. It is interesting to note, however, that where the waves are said to be unstable, no attempt is made at applying a radiation condition. Thus, it was not determined whether the waves were *growing* (unstable) to the right, or actually *decaying* (stable) to the left.

It is intuitively clear that if a wave field is to grow as it propagates, energy must be provided to that wave field. The lack of energy sources in a passive periodic waveguide provoked Kim and Ginsberg (1992) to examine the claim of instability. These authors numerically integrated the equations of motion in time for various values of periodic waveguide parameters. In particular, in the regions of (potentially) maximum exponential growth, they found the *fastest exponential decay*. It was conjectured that the transience is somehow responsible for suppressing the unstable solution.

In order to integrate the equations of motion in time, however, Kim and Ginsberg necessarily imposed a causality condition. In fact, we will see that it is not the transience per se that suppresses the unstable solution, but the causality condition. This causality condition takes the form of a radiation condition in time-harmonic problems. In subsequent sections we show that the unstable solution does not exist in the steady-state response of a periodic waveguide, *once a radiation condition has been imposed.*

The purpose of this Note is to make two points. The first is that the analogy between harmonic oscillators and waveguides extends only as far as the governing differential equation. The difference between an initial value problem, on one hand, and a two-point boundary value problem, on the other, is quite distinct. The oscillator is the former and a waveguide is the latter.

The second objective of this Note is point out the role of the radiation condition in suppressing the "unstable" solution in the waveguide. Rigorously applying a radiation condition to solutions of the form (1) is difficult in very complicated problems (see, e.g., Braga and Herrmann, 1992). Often, applying the radiation condition is done in the ad hoc way that we have described above. For the purposes of this paper, we shall study a problem for which a rigorous application of the radiation condition already exists (Hood, 1985). Then we need only review the methodology rather than the precise proof, and we can be confident that our understanding is based upon sound results.

Section 2 describes a harmonic oscillator which exhibits parametric instability. In Section 3 we examine time-harmonic waves propagating on a semi-infinite string with masses attached periodically. We show that the waves are governed by the same differential equation as the oscillator. Then we describe how the application of the radiation condition eliminates the unstable solution. We end by considering the transient response of the string in a stop-band, and find exponential decay localized around the drive end, just as in the numerical calculations of Kim and Ginsberg (1992).

2 Periodically Excited Harmonic Oscillator

We consider a harmonic oscillator with mass M and restoring spring constant K, being kicked with an impulse of magnitude IY at times $T=nP$. The equation of motion governing such an oscillator is

$$M\frac{d^2}{dT^2}Y+KY+I\sum_{n=0}^{\infty}\delta(T-nP)Y=0. \tag{3}$$

The function $Y(T)$, the displacement of the oscillator from equilibrium, is subject to the *initial* conditions

$$Y(0)=Y_0 \qquad \frac{dY}{dT}(0)=\dot{Y}_0. \tag{4}$$

We now rescale the equations above by introducing the symbols y, t, k, η, y_0, $\dot{y}_0$ such that

$$t=T/P \qquad k^2=KP^2/M \qquad \eta=IP/M$$
$$y=Y/Y_0 \qquad y_0=1 \qquad \dot{y}_0P\dot{Y}_0/Y_0 \tag{5}$$

In terms of the new parameters, Eq. (3) and initial conditions (4) become

$$\frac{d^2}{dt^2}y+k^2y+\eta\sum_{n=0}^{\infty}\delta(t-n)y=0 \tag{6}$$

$$y(0)=y_0 \qquad \frac{dy}{dt}(0)=\dot{y}_0. \tag{7}$$

Differential Eq. (6) is a second-order linear differential equation. Its general solution can be written as a linear combination of two linearly independent solutions. We use Floquet theory (Ince, 1956) to find two such solutions of (6) and write the general solution as

$$y(t)=Ap_1(t)e^{i\lambda t}+Bp_2(t)e^{-i\lambda t}. \tag{8}$$

The constant λ is called the *Floquet* or *Bloch wave number* (Auld, 1990) and satisfies

$$2\cos\lambda=2\cos k-\frac{\eta}{k}\sin k. \tag{9}$$

We must restrict the branch of λ which we will take as the solution of (9). For our present purposes, however, it suffices to specify $\Re\lambda\geq 0$ and if $\Re\lambda=0$, then $\Im\lambda>0$. The functions $p_1(t)$ and $p_2(t)$ are periodic functions with unit period and are defined for $0\leq t<1$ as

$$p_1(t)=e^{-i\lambda t}\{[2ike^{ik}e^{i\lambda}-2ik-\eta]e^{ikt}+\eta e^{-ikt}\} \tag{10}$$

$$p_2(t)=e^{i\lambda t}\{\eta e^{ikt}+[2ik-2ike^{-ik}e^{-i\lambda}-\eta]e^{-ikt}\}. \tag{11}$$

The constants A and B in (8) are found by applying the initial conditions (7). From this calculation we note only that B is in general nonzero.

If the parameters (k,η) are such that the magnitude of the right-hand side of (9) is greater than two, then λ will be complex. We suppose that λ is pure imaginary, so that $\lambda=i\gamma$, $\gamma>0$. Then the displacement of the oscillator takes the form

Downloaded 03 May 2010 to 171.66.16.20. Redistribution subject to ASME license or copyright; see http://www.asme.org/terms/Terms_Use.cfm

$$y(t) = Ap_1(t)e^{-\gamma t} + Bp_2(t)e^{\gamma t}. \quad (12)$$

This situation corresponds to the case when the impulsive kicks to the oscillator provide a resonant excitation and so the solution grows with time. This is an example of an unstable solution describing an unstable physical system. The coefficient B multiplying the growing function $p_2(t)e^{\gamma t}$ is in general nonzero due to the choice of initial conditions.

3 Waves Propagating in a Periodic Medium

We shall now consider a string under tension F with lineal density ρ. The string supports equal point masses m at locations $X = nL$; $n = 0,1,2,\ldots$. The equation of motion of the string is thus

$$F\frac{\partial^2}{\partial X^2}U - \rho\frac{\partial^2}{\partial T^2}U - m\sum_{n=0}^{\infty}\delta(X-nL)\frac{\partial^2}{\partial T^2}U = 0. \quad (13)$$

Here, U is the normal displacement of the string from equilibrium. Equation (13) is a hyperbolic equation and as such is subject to two initial conditions at $T = 0$, and to two boundary conditions, one each at $X = 0$ and $X = \infty$. The condition at $X = \infty$ takes the form of a radiation condition which we will discuss presently.[2] We assume an excitation at $X = 0$ in the form

$$U(0,T) = U_0 e^{-i\omega_0 t} \quad (T > 0). \quad (14)$$

We prescribe the initial conditions as

$$U(X,0) = 0 \qquad \frac{\partial U}{\partial T}(X,0) = 0. \quad (15)$$

Equations (13)–(15) together with the radiation condition completely specify the solution U.

We shall now focus our attention on time-harmonic waves by taking $U(X,T)$ in the form

$$U(X,T) = \frac{1}{U_0}\int_{-\infty}^{+\infty} v(X,\omega)e^{-i\omega T}d\omega. \quad (16)$$

Substituting (16) into (13), multiplying by $e^{i\omega T}$ and integrating, we obtain

$$F\frac{\partial^2}{\partial X^2}v + \rho\omega^2 v + m\omega^2\sum_{n=0}^{\infty}\delta(X-nL)v = 0. \quad (17)$$

Equation (17) is analogous to Eq. (6) in the previous section. We complete the comparison of the equations of this section to those of the previous section by introducing x and redefining the symbols k, η, such that

$$x = X/L \qquad k^2 = \rho\omega^2 L^2/F \qquad \eta = m\omega^2 L/F. \quad (18)$$

We now use (18) in (17) to find that $v(x,\omega)$ satisfies

$$\frac{d^2}{dx^2}v + k^2 v + \eta\sum_{n=0}^{\infty}\delta(x-n)v = 0 \quad (19)$$

$$v(0,\omega) = v_0. \quad (20)$$

Equations (14)–(16) show that v_0 is

$$v_0(\omega) = \frac{1}{2\pi i(\omega - \omega_0)}. \quad (21)$$

Further, $v(x,\omega)$ is also subject to an appropriate radiation condition as $x \to \infty$.

The relation between Eqs. (6) and (19) is obvious. We keep the distinction between time t and distance x to remind us that one equation represents an initial value problem while the other represents a two-point boundary value problem. With reference to Eq. (8) we know that the general solution of the differential Eq. (19) is

$$v(x) = Cp_1(x)e^{i\lambda x} + Dp_2(x)e^{-i\lambda x}. \quad (22)$$

The periodic functions p_1 and p_2 and the constant λ are as discussed above. More will be said about λ in the next section.

To determine the values of the coefficients C and D, we need two conditions. One of those comes from the end point $x = 0$ (Eq. (21)) while the other is the radiation condition. We shall examine the form of the radiation condition now.

3.1 The Radiation Condition. The Floquet wave number λ is determined by Eq. (9). It is clear from (9) that if λ is a solution, then so is $\lambda + 2m\pi$, where m is an integer. We make λ unique by introducing the quantities κ and ϕ so that

$$k = 2m\pi + \kappa \qquad -\pi \le \kappa < \pi \quad (23)$$

$$\lambda = 2m\pi + \phi \quad (24)$$

Here, m is restricted to nonnegative integer values. Now we define ϕ by the relation

$$\phi = \mathrm{sgn}(\kappa)\cos^{-1}\left(\cos k - \frac{\eta}{2k}\sin k\right). \quad (25)$$

At pass band frequencies i.e., when κ is real, we take the principal root of the *arccos* function in (25). Thus when ϕ is real it is restricted to $-\pi \le \phi < \pi$. At stop band frequencies, i.e., when λ is complex, we take $\mathrm{sgn}(\kappa) = 1$ and so $\Im\phi \equiv \Im\lambda > 0$.

With λ defined as above, the two linearly independent solutions in (22) have very simple physical interpretations. To show this, we introduce $v_1(x,t)$ and $v_2(x,t)$ as

$$v_1(x,t) = p_1(x)e^{i\lambda x - i\omega t} \quad (26)$$

$$v_2(x,t) = p_2(x)e^{-i\lambda x - i\omega t}. \quad (27)$$

From (26) and (27) we see that $v_1(x,t)$ seems to correspond to a right traveling wave, while $v_2(x,t)$ seems to correspond to a left traveling wave.

That the two solutions v_1 and v_2 do indeed correspond to right and left traveling waves can be demonstrated by several arguments. For example, the simplest indication that this interpretation of the two solutions is correct can be found by taking the limit of $v_1(x,t)$ and $v_2(x,t)$ as $\eta \to 0$ (i.e., as the masses vanish.) A more convincing argument is that with λ so specified, positive λ yields a non-negative group velocity for all λ, as is obvious from the example in the figure.[3] Alternatively, $v_j(x,t)$ between any two masses is of the form

$$v_j(x,t) = A_j e^{ikx - i\omega t} + B_j e^{-ikx - i\omega t}. \quad (28)$$

Comparing of the relative magnitudes of A_j and B_j determines the sign of the energy flux in the solution, and shows that v_1 and v_2 are right and left going, respectively. Finally, these arguments can be made rigorous by including dissipation in the system, and taking the limit of zero dissipation. Proofs of these facts are presented by Hood (1985). Therefore, we do not repeat it here.

The radiation condition as $\chi \to \infty$ can now be applied easily. Simply, there can be no energy flux into the string from infinity. Since $v_2(x,t)$ represents a left traveling wave with a net energy flux to the left, then in (22) we must take

$$D = 0. \quad (29)$$

Independent of the condition at $x = 0$, Eq. (29) shows that the steady-state wave solution is of the form

$$v(x) = Cp_1(x)e^{i\lambda x}. \quad (30)$$

With λ defined as above, $v(x)$ is *always* bounded, even for λ nonreal. We find that the part of the general solution

[5] A radiation condition is not absolutely necessary for a proper problem statement involving this hyperbolic equation. In its place, we could have a restriction on the support of the initial data. The radiation condition becomes absolutely essential, however, in the time-harmonic problem where the disturbances extend to $\pm\infty$. The author is indebted to Dr. Danny Givoli for reminding him of this fact upon reviewing a preprint of this Note.

[6] We note here that the group velocity corresponds to the energy velocity only in regions of normal dispersion, as described by Sommerfeld in (Brillouin, 1960). Periodic structures, however, have many regions of anomalous dispersion.

Downloaded 03 May 2010 to 171.66.16.20. Redistribution subject to ASME license or copyright; see http://www.asme.org/terms/Terms_Use.cfm

$p_2(x)e^{-i\lambda x}$, which had the possibility of becoming unbounded is not admissible due to the *radiation condition* at infinity.

3.2 Transient Response of the String. Kim and Ginsberg (1992) examined the transient response of a system analogous to the one studied here (i.e., a one-dimensional wave bearing medium with periodic spatial variation). It was numerically demonstrated that in the "unstable" parameter regime, the response of the system was stable and consisted of two main contributions. At the forced end of the medium, a spatially decaying steady-state signal dominated, while a leading wave front propagated at the signal velocity into the still medium ahead. We shall now show that this behavior follows directly from the steady-state response derived above.

For convenience, we define $u(x,t)$ such that

$$u(x,t) = U(X/L,t). \tag{31}$$

Using (21), (22), and (29), we determine C to be

$$C = \frac{1}{2\pi i p_1(0,\omega)(\omega-\omega_0)}. \tag{32}$$

Then, we use (16), (22), and (32) to obtain

$$u(x,t) = \int_{-\infty}^{+\infty} \frac{U_0}{2\pi i p_1(0,\omega)(\omega-\omega_0)} p_1(x,\omega) e^{i\lambda(\omega)x - i\omega t} d\omega. \tag{33}$$

Causality dictates that the implied integration contour in (33) passes above the pole at $\omega=\omega_0$. Equation (33) determines the transient behavior of the string which is initially still, and is excited harmonically at one end starting at $t=0$.

We now examine the behavior of the system for large t (large $\omega_0 t$) but with x fixed and finite. Then the phase of the integrand has no stationary points and the dominant contribution comes from the pole. Thus, for $t\to\infty$ and x fixed:

$$u(x,t) \sim U_0[p_1(0,\omega_0)]^{-1} p_1(x,\omega_0) e^{i\lambda(\omega_0)x - i\omega_0 t}. \tag{34}$$

When the parameters of the problem are such that $\lambda=\alpha+i\gamma$, i.e., when the differential equation has "unstable" solutions, we see that $u(x,t)$ decays exponentially with x. Indeed, the more "unstable" the differential equation, i.e., the greater the value of γ, the faster the spatial decay, as noted by Kim and Ginsberg (1992).

4 Conclusions

We have examined two physical systems which are governed by a common differential equation. One of the systems we examined, namely the string with periodic scatterers, is analogous to problems discussed elsewhere where the stability of the system was in doubt. We showed that though the differential equation admits "unstable" solutions, the behavior of the system is stable. The form of the solution is crucially dependent on the type of boundary or initial conditions which must be imposed on the general solution of the differential equation.[4] For the case of the wave system, the overall equation is a hyperbolic partial differential equation. This fact determines the appropriate boundary conditions to be imposed on the time-reduced equation. The overall behavior of the physical system is as much determined by the boundary conditions as by the differential equation itself.

Acknowledgments

The author is grateful for the many helpful comments from Dr. Danny Givoli, Dr. Mark Spivack, Dr. C. J. Chapman, and anonymous referees. This work is supported financially by ONR grant N00014-92-J-1035 to University of Cambridge.

[7]This fact can likewise be seen in the more mundane example of the deflection of a beam on an elastic foundation. The homogeneous differential equation has solutions which grow and decay exponentially, but the magnitude of the solution is bounded by the end conditions imposed on the beam.

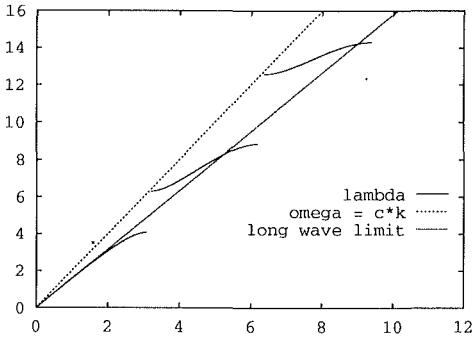


Fig. 1 Frequency ω versus the real part of λ. Also shown are the lines $\omega = ck$ (the zero scattering limit) and $\omega = [c^{-2} + \eta/\omega^2]^{-1/2}k$ (the long wavelength limit). The gaps in the plot of λ are the stop bands, where λ is complex, and are obviously regions of anomalous dispersion. In these regions, $\Re\lambda = m\pi$.

References

Auld, B. A., 1990, *Acoustic Waves and Fields in Solids*, Academic Press, New York.

Braga, A. M. B., and Herrmann, G., 1992, "Floquet Waves in Anisotropic Periodically Layered Composites," *J. Acoust. Soc. Am.*, Vol. 91, No. 3, pp. 1211–1227.

Brillouin, L., 1946, *Wave Propagation in Periodic Structures*, McGraw-Hill, New York.

Brillouin, L., 1960, *Wave Propagation and Group Velocity*, Academic Press, New York.

Hood, M. J., 1985, "A Uniqueness Problem for Wave Propagation in a Periodic Structure," *IMA Journal of Applied Mathematics*, Vol. 34, pp. 279–294.

Ince, E. L., 1956, *Ordinary Differential Equations*, Dover Publications, New York.

Kim, H. S., and Ginsberg, J. H., 1992, "Transient Wave Propagation in a Harmonically Heterogeneous Elastic Solid," ASME JOURNAL OF APPLIED MECHANICS, Vol. 59, pp. S145–S151.

Nayfeh, A. H., and Nemat-Nasser, S., 1972, "Elastic Waves in Inhomogeneous Elastic Media," ASME JOURNAL OF APPLIED MECHANICS, Vol. 39, pp. 696–702.

Schoenberg, M., and Weitsman, Y., 1975, "Wave Propagation and Parametric Instability in Materials Reinforced by Fibers with Periodically Varying Directions," ASME JOURNAL OF APPLIED MECHANICS, Vol. 42, pp. 835–831.

Watanabe, K., 1984, "Plane SH-Waves in Harmonically Inhomogeneous Elastic Media," *Wave Motion*, Vol. 6, pp. 477–488.

Rigid-Body Rotation and Crack-Tip Opening Displacement at the Tip of a Kinked Crack in an Infinite Plate

A. Bhattacharya[8]

Introduction

Several attempts have been made to study the phenomenon of crack kinking by using various analytical methods. From the integral equation technique based on Green's function, Karihaloo et al. (1980) obtained an almost closed-form solution at the tip of a kink. Hayashi and Nemat-Nasser (1981) investigated the kinking from a straight crack on the basis of the

[8]Department of Mechanical Engineering, Institute of Technology, Banaras Hindu University, Varanasi 221 005, India.

Contributed by the Applied Mechanics Division of THE AMERICAN SOCIETY OF MECHANICAL ENGINEERS for publication in the ASME JOURNAL OF APPLIED MECHANICS. Manuscript received by the ASME Applied Mechanics Division, July 5, 1991; final revision, Sept. 3, 1993. Associate Technical Editor: X. Markenscoff.

Downloaded 03 May 2010 to 171.66.16.20. Redistribution subject to ASME license or copyright; see http://www.asme.org/terms/Terms_Use.cfm

$p_2(x)e^{-i\lambda x}$, which had the possibility of becoming unbounded is not admissible due to the *radiation condition* at infinity.

3.2 Transient Response of the String. Kim and Ginsberg (1992) examined the transient response of a system analogous to the one studied here (i.e., a one-dimensional wave bearing medium with periodic spatial variation). It was numerically demonstrated that in the "unstable" parameter regime, the response of the system was stable and consisted of two main contributions. At the forced end of the medium, a spatially decaying steady-state signal dominated, while a leading wave front propagated at the signal velocity into the still medium ahead. We shall now show that this behavior follows directly from the steady-state response derived above.

For convenience, we define $u(x,t)$ such that

$$u(x,t) = U(X/L,t). \tag{31}$$

Using (21), (22), and (29), we determine C to be

$$C = \frac{1}{2\pi i p_1(0,\omega)(\omega-\omega_0)}. \tag{32}$$

Then, we use (16), (22), and (32) to obtain

$$u(x,t) = \int_{-\infty}^{+\infty} \frac{U_0}{2\pi i p_1(0,\omega)(\omega-\omega_0)} p_1(x,\omega) e^{i\lambda(\omega)x - i\omega t} d\omega. \tag{33}$$

Causality dictates that the implied integration contour in (33) passes above the pole at $\omega=\omega_0$. Equation (33) determines the transient behavior of the string which is initially still, and is excited harmonically at one end starting at $t=0$.

We now examine the behavior of the system for large t (large $\omega_0 t$) but with x fixed and finite. Then the phase of the integrand has no stationary points and the dominant contribution comes from the pole. Thus, for $t\to\infty$ and x fixed:

$$u(x,t) \sim U_0[p_1(0,\omega_0)]^{-1} p_1(x,\omega_0) e^{i\lambda(\omega_0)x - i\omega_0 t}. \tag{34}$$

When the parameters of the problem are such that $\lambda=\alpha+i\gamma$, i.e., when the differential equation has "unstable" solutions, we see that $u(x,t)$ decays exponentially with x. Indeed, the more "unstable" the differential equation, i.e., the greater the value of γ, the faster the spatial decay, as noted by Kim and Ginsberg (1992).

4 Conclusions

We have examined two physical systems which are governed by a common differential equation. One of the systems we examined, namely the string with periodic scatterers, is analogous to problems discussed elsewhere where the stability of the system was in doubt. We showed that though the differential equation admits "unstable" solutions, the behavior of the system is stable. The form of the solution is crucially dependent on the type of boundary or initial conditions which must be imposed on the general solution of the differential equation.[4] For the case of the wave system, the overall equation is a hyperbolic partial differential equation. This fact determines the appropriate boundary conditions to be imposed on the time-reduced equation. The overall behavior of the physical system is as much determined by the boundary conditions as by the differential equation itself.

Acknowledgments

The author is grateful for the many helpful comments from Dr. Danny Givoli, Dr. Mark Spivack, Dr. C. J. Chapman, and anonymous referees. This work is supported financially by ONR grant N00014-92-J-1035 to University of Cambridge.

[7]This fact can likewise be seen in the more mundane example of the deflection of a beam on an elastic foundation. The homogeneous differential equation has solutions which grow and decay exponentially, but the magnitude of the solution is bounded by the end conditions imposed on the beam.

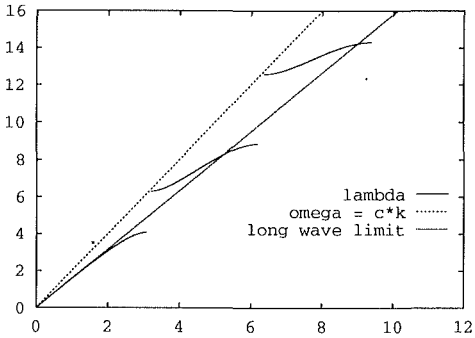


Fig. 1 Frequency ω versus the real part of λ. Also shown are the lines $\omega = ck$ (the zero scattering limit) and $\omega = [c^{-2} + \eta/\omega^2]^{-1/2}k$ (the long wavelength limit). The gaps in the plot of λ are the stop bands, where λ is complex, and are obviously regions of anomalous dispersion. In these regions, $\Re\lambda = m\pi$.

References

Auld, B. A., 1990, *Acoustic Waves and Fields in Solids*, Academic Press, New York.

Braga, A. M. B., and Herrmann, G., 1992, "Floquet Waves in Anisotropic Periodically Layered Composites," *J. Acoust. Soc. Am.*, Vol. 91, No. 3, pp. 1211–1227.

Brillouin, L., 1946, *Wave Propagation in Periodic Structures*, McGraw-Hill, New York.

Brillouin, L., 1960, *Wave Propagation and Group Velocity*, Academic Press, New York.

Hood, M. J., 1985, "A Uniqueness Problem for Wave Propagation in a Periodic Structure," *IMA Journal of Applied Mathematics*, Vol. 34, pp. 279–294.

Ince, E. L., 1956, *Ordinary Differential Equations*, Dover Publications, New York.

Kim, H. S., and Ginsberg, J. H., 1992, "Transient Wave Propagation in a Harmonically Heterogeneous Elastic Solid," ASME JOURNAL OF APPLIED MECHANICS, Vol. 59, pp. S145–S151.

Nayfeh, A. H., and Nemat-Nasser, S., 1972, "Elastic Waves in Inhomogeneous Elastic Media," ASME JOURNAL OF APPLIED MECHANICS, Vol. 39, pp. 696–702.

Schoenberg, M., and Weitsman, Y., 1975, "Wave Propagation and Parametric Instability in Materials Reinforced by Fibers with Periodically Varying Directions," ASME JOURNAL OF APPLIED MECHANICS, Vol. 42, pp. 835–831.

Watanabe, K., 1984, "Plane SH-Waves in Harmonically Inhomogeneous Elastic Media," *Wave Motion*, Vol. 6, pp. 477–488.

Rigid-Body Rotation and Crack-Tip Opening Displacement at the Tip of a Kinked Crack in an Infinite Plate

A. Bhattacharya[8]

Introduction

Several attempts have been made to study the phenomenon of crack kinking by using various analytical methods. From the integral equation technique based on Green's function, Karihaloo et al. (1980) obtained an almost closed-form solution at the tip of a kink. Hayashi and Nemat-Nasser (1981) investigated the kinking from a straight crack on the basis of the

[8]Department of Mechanical Engineering, Institute of Technology, Banaras Hindu University, Varanasi 221 005, India.

Contributed by the Applied Mechanics Division of THE AMERICAN SOCIETY OF MECHANICAL ENGINEERS for publication in the ASME JOURNAL OF APPLIED MECHANICS. Manuscript received by the ASME Applied Mechanics Division, July 5, 1991; final revision, Sept. 3, 1993. Associate Technical Editor: X. Markenscoff.

Copyright © 1994 by ASME
Downloaded 03 May 2010 to 171.66.16.20. Redistribution subject to ASME license or copyright; see http://www.asme.org/terms/Terms_Use.cfm

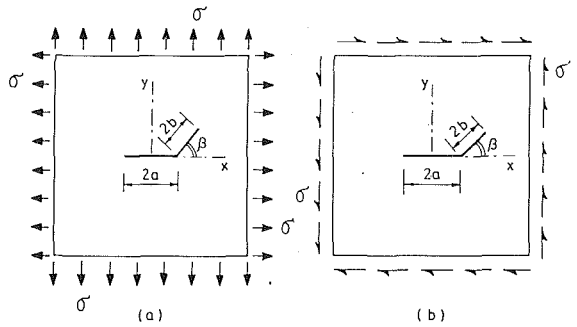


Fig. 1 Infinite plate containing a kinked crack under (*a*) uniform biaxial tension, (*b*) uniform shear

maximum energy release-rate criterion under the plane-strain condition. Sumi et al. (1983) used the first-order perturbation solution for a semi-infinite straight crack with slightly branched and curved extension. A solution method was given by including the effects of the geometry of finite outer boundaries and the crack length. Recently, Isida and Nishino (1990) also applied a perturbation method and obtained equations for the dimensionless stress intensity factors. The objective of present work is, however, not to evaluate the stress intensity factors but to study some aspects like the rigid-body rotation and crack-tip opening displacement at the tip of a short kinked crack.

The concept of rigid-body rotation near the crack tip and its relevance to a crack-tip opening displacement were reported in an earlier work by this author (Bhattacharya, 1990). In the present paper, the stress intensity factors K_I and K_{II} from the work of Isida and Nishino (1990) are used to obtain rigid-body rotation near the crack tip of a short kinked crack. The values of rotation are obtained by assuming a Dugdale plastic zone (Dugdale, 1960) near the crack tip. For the applied stresses which are small compared to the yield strength of plate material, the crack-tip opening displacement is shown to depend only on K_I. The crack-tip opening angle is found to be independent of K_I or K_{II}.

Analysis

An infinite plate containing a crack of length $2a$ and having a kink length $2b$ at an angle β is shown in Fig. 1. The plate is assumed to be loaded at infinity, and the stress σ is taken as reference. For the problem shown by Fig. 1, the rigid-body rotation ω_z is obtained as

$$\omega_z = \frac{4}{E'} Im\,[\phi'(z)], \tag{1}$$

where $\phi'(z)$ is a complex potential (Muskhelishvili, 1958) and E' denotes the elasticity modulus. Assuming that the crack tip of a kinked crack is subjected to combined mode I and mode II loading and setting polar coordinates (r, θ) near the crack tip, Eq. (1) can be used to obtain (Bhattacharya, 1990)

$$\omega_z = -\frac{2}{E'}\frac{1}{\sqrt{2\pi r}}\left[K_I \sin\frac{\theta}{2} + K_{II}\cos\frac{\theta}{2}\right]. \tag{2}$$

Using the expressions of K_I and K_{II} (Isida and Nishino, 1990), the rotation ω_z in Eq. (2) is written as

$$\omega_z = -\left(\frac{\sigma}{E'}\right)\sqrt{\frac{2}{f}}\left[\sin\frac{\theta}{2}\sum_{n=0}^{N} F^{(k)}_{I,n}\cdot\lambda^{m-1/2} + \cos\frac{\theta}{2}\sum_{n=0}^{N} F^{(k)}_{II,n}\cdot\lambda^{m-1/2}\right], \tag{3}$$

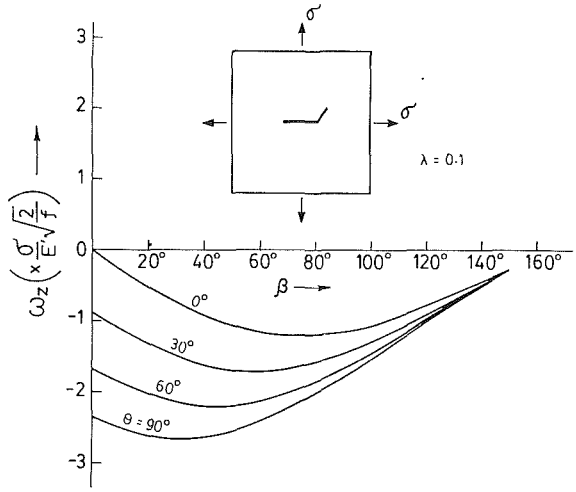


Fig. 2 ω_z versus β under the uniform biaxial tension

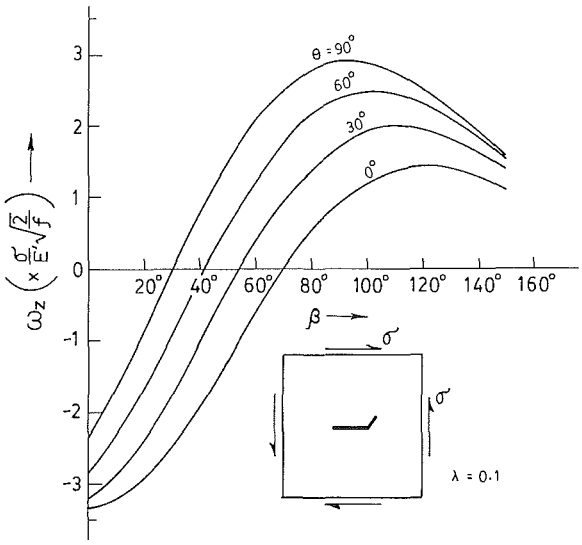


Fig. 3 ω_z versus β under uniform shear

where $f = r/b$, $\lambda = b/a$, $N = 2$ for a short kinked crack with $\lambda \leq 0.2$, and $m = n$ for $k = 1, 2$. Values of ω_z are determined from Eq. (3), and these are plotted in terms of $(\sigma/E')\sqrt{2/f}$ in Figs. 2 and 3 against the kink angle values from $\beta = 0$ to $\beta = 150$ deg and $\lambda = 0.1$. It may be observed in Fig. 2 that ω_z is always negative and it becomes maximum at a certain value of β. For the shear condition shown in Fig. 3, the rotation ω_z increases continuously until it attains the maximum positive value in the range, 70 deg $< \beta <$ 120 deg.

Crack-Tip Opening Displacement and ω_z at the Plastic Zone Distance

At a Dugdale plastic zone distance (Dugdale, 1960) $r = r_y = (\pi/8)\cdot(K_I^2/\sigma_y^2)$, where σ_y is the yield strength in tension, an equation of ω_z becomes

$$\omega_z^{(k)} = -\left(\frac{4}{\pi}\right)\left(\frac{\sigma_y}{E'}\right)\left[\sin\frac{\theta}{2} + \frac{K_{II}^{(k)}}{K_I^{(k)}}\cdot\cos\frac{\theta}{2}\right]. \tag{4}$$

For an applied stress $\sigma \ll \sigma_y$, the Dugdale plastic zone is small compared to kink length b. Hence, the tip of the crack may be assumed to be at the end of a wedge-shaped plastic zone and the rotation is obtained as $\omega_z = -(4/\pi)\cdot(\sigma_y/E')$, which is independent of stress intensity factors. Therefore, for small

Downloaded 03 May 2010 to 171.66.16.20. Redistribution subject to ASME license or copyright; see http://www.asme.org/terms/Terms_Use.cfm

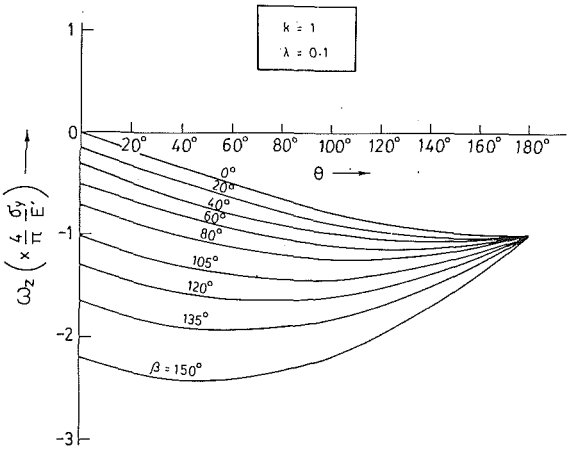


Fig. 4 ω_z versus θ under the uniform biaxial tension

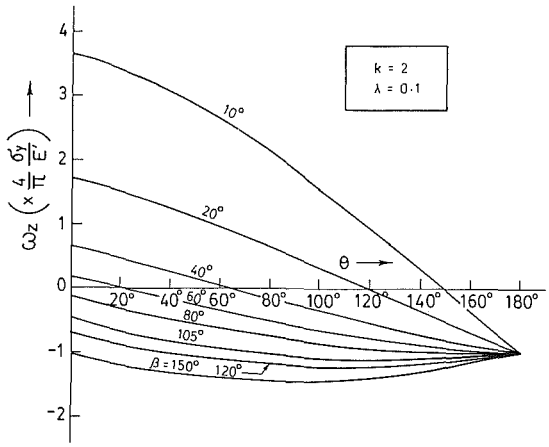


Fig. 5 ω_z versus θ under uniform shear

values of ω_z, the crack-tip opening displacement (CTOD) can be written as

$$\text{CTOD} = 2\left[\frac{4\sigma_y}{\pi E'}\right]\left[\frac{\pi}{8}\frac{K_I^2}{\sigma_y^2}\right] = \frac{K_I^2}{E'\sigma_y}, \tag{5}$$

which is often found in the literature.

Values of rotation in the plastic zone region are plotted in Figs. 4 and 5 for the two types of loading ($k = 1, 2$). It may be observed that, irrespective of the type of loading and kink angle value, the rotation at $\theta = 180$ deg is found as $\omega_z = -(4/\pi)\cdot(\sigma_y/E')$. The changes in ω_z at $\theta < 180$ deg represent the features of loading type and kink angle.

Conclusion

The values of rigid-body rotation ω_z in close vicinity of the crack tip are obtained against various kink angle values with $\lambda = 0.1$. It is shown that the crack-tip opening displacement can be determined from the rigid-body rotation at plastic zone distance near the crack tip. For small values of applied stresses "σ," the crack-tip opening angle depends on the material parameters only.

Acknowledgment

This work was supported by the Department of Science and Technology, Ministry of Science and Technology, Government of India, New Delhi 110 016.

References

Bhattacharya, A., 1990, "Rigid Body Rotation at the Tip of a Slant Crack in Infinite Plate," *International Journal of Fracture*, Vol. 44, pp. 209–219.

Dugdale, D. S., 1960, "Yielding of Steel Sheets Containing Slits," *Journal of Mechanics and Physics of Solids*, Vol. 8, pp. 100–108.

Hayashi, K., and Nemat-Nasser, S., 1981, "Energy-Release Rate and Crack Kinking Under Combined Loading," ASME JOURNAL OF APPLIED MECHANICS, Vo. 48, pp. 520–524.

Isida, M., and Nishino, T., 1990, "Formulae of Stress Intensity Factors at Tips of Kinked Cracks Under Various Loadings," *Engineering Fracture Mechanics*, Vol 36, pp. 697–711.

Karihaloo, B. L., Keer, L. M., and Nemat-Nasser, S., 1980, "Crack Kinking Under Non-Symmetric Loading," *Engineering Fracture Mechanics*, Vol. 13, pp. 879–888.

Muskhelishvili, N. I., 1958, "Some Basic Problems on the Mathematical Theory of Elasticity," Noordhoff, Leyden.

Sumi, Y., Nemat-Nasser, S., and Keer, L. M., 1983, "On Crack Branching and Curving in a Finite Body," *International Journal of Fracture*, Vol. 21, pp. 67–79.

Identification of Mechanical Parameters in a Porous Elastically Deformable Medium by Compression-Relaxation Test

S. Naïli,[9] O. Le Gallo,[9] and D. Geiger[9, 10]

1 Introduction

Biot (1941) formulated the basic theory of the deformation of a porous, isotropic, elastic solid, and saturated by a Newtonian fluid which is subject to a small strain. If each phase (structure and fluid) is incompressible, this theory requires the knowledge of four mechanical parameters—drained Young's modulus, drained Poisson's ratio, permeability of the structure, and the dynamic viscosity of the interstitial fluid—the terminology of Rice and Cleary (1976) being used.

There are two approaches for the determination of the mechanical parameters of a porous elastic solid saturated by a viscous fluid: (i) measurement of the radial displacement under one-dimensional axial tension with no variation of the fluid content (Coussy, 1991) and (ii) measurement of the velocity of acoustic waves in the sample (Bourbié et al., 1987), following the work of Biot (1956).

In the present work, we focus on the case in which the constituents are incompressible separately. A simple method is proposed for the determination of drained Young's modulus and drained Poisson's ratio, the permeability of the structure and the dynamic viscosity of the fluid determined as usual (Bourbié et al., 1987). A standard tension compression test machine is used in order to investigate the asymptotic behavior of a cylindrical sample subject to compressive loading and relaxation. The method further imposes the determination of the compression and relaxation vertical force of the sample, by an analytical approach using spectral decomposition with orthogonal eigenvectors. The analysis of the vertical force (particularly the asymptotic behavior of the vertical force during compression) shows that the ordinate of the origin is a measure of the drained Poisson's ratio and the slope of the curve yields

[9]Laboratoire de Mécanique Physique, Faculté des Sciences et Technologie, Université Paris XII, Av. du Général De Gaulle, 94010 Crétiel Cedex, France.
[10]Mem. ASME.

Contributed by the Applied Mechanics Division of THE AMERICAN SOCIETY OF MECHANICAL ENGINEERS for publication in the JOURNAL OF APPLIED MECHANICS. Manuscript received by the ASME Applied Mechanics Division, June 4, 1993; final revision, Nov. 4, 1993. Associate Technical Editor: J. W. Rudnicki.

Downloaded 03 May 2010 to 171.66.16.20. Redistribution subject to ASME license or copyright; see http://www.asme.org/terms/Terms_Use.cfm

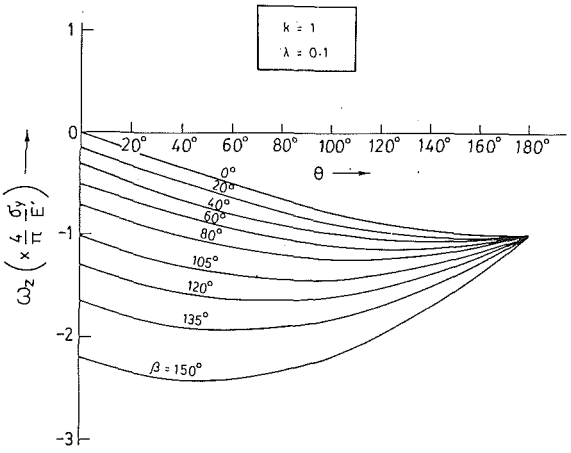


Fig. 4 ω_z versus θ under the uniform biaxial tension

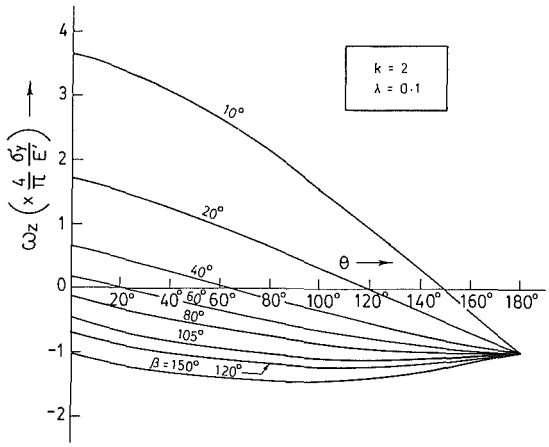


Fig. 5 ω_z versus θ under uniform shear

values of ω_z, the crack-tip opening displacement (CTOD) can be written as

$$\text{CTOD} = 2\left[\frac{4\sigma_y}{\pi E'}\right]\left[\frac{\pi}{8}\frac{K_I^2}{\sigma_y^2}\right] = \frac{K_I^2}{E'\sigma_y}, \tag{5}$$

which is often found in the literature.

Values of rotation in the plastic zone region are plotted in Figs. 4 and 5 for the two types of loading ($k = 1, 2$). It may be observed that, irrespective of the type of loading and kink angle value, the rotation at $\theta = 180$ deg is found as $\omega_z = -(4/\pi)\cdot(\sigma_y/E')$. The changes in ω_z at $\theta < 180$ deg represent the features of loading type and kink angle.

Conclusion

The values of rigid-body rotation ω_z in close vicinity of the crack tip are obtained against various kink angle values with $\lambda = 0.1$. It is shown that the crack-tip opening displacement can be determined from the rigid-body rotation at plastic zone distance near the crack tip. For small values of applied stresses "σ," the crack-tip opening angle depends on the material parameters only.

Acknowledgment

This work was supported by the Department of Science and Technology, Ministry of Science and Technology, Government of India, New Delhi 110 016.

References

Bhattacharya, A., 1990, "Rigid Body Rotation at the Tip of a Slant Crack in Infinite Plate," *International Journal of Fracture*, Vol. 44, pp. 209–219.

Dugdale, D. S., 1960, "Yielding of Steel Sheets Containing Slits," *Journal of Mechanics and Physics of Solids*, Vol. 8, pp. 100–108.

Hayashi, K., and Nemat-Nasser, S., 1981, "Energy-Release Rate and Crack Kinking Under Combined Loading," ASME JOURNAL OF APPLIED MECHANICS, Vo. 48, pp. 520–524.

Isida, M., and Nishino, T., 1990, "Formulae of Stress Intensity Factors at Tips of Kinked Cracks Under Various Loadings," *Engineering Fracture Mechanics*, Vol 36, pp. 697–711.

Karihaloo, B. L., Keer, L. M., and Nemat-Nasser, S., 1980, "Crack Kinking Under Non-Symmetric Loading," *Engineering Fracture Mechanics*, Vol. 13, pp. 879–888.

Muskhelishvili, N. I., 1958, "Some Basic Problems on the Mathematical Theory of Elasticity," Noordhoff, Leyden.

Sumi, Y., Nemat-Nasser, S., and Keer, L. M., 1983, "On Crack Branching and Curving in a Finite Body," *International Journal of Fracture*, Vol. 21, pp. 67–79.

Identification of Mechanical Parameters in a Porous Elastically Deformable Medium by Compression-Relaxation Test

S. Naïli,[9] O. Le Gallo,[9] and D. Geiger[9, 10]

1 Introduction

Biot (1941) formulated the basic theory of the deformation of a porous, isotropic, elastic solid, and saturated by a Newtonian fluid which is subject to a small strain. If each phase (structure and fluid) is incompressible, this theory requires the knowledge of four mechanical parameters—drained Young's modulus, drained Poisson's ratio, permeability of the structure, and the dynamic viscosity of the interstitial fluid—the terminology of Rice and Cleary (1976) being used.

There are two approaches for the determination of the mechanical parameters of a porous elastic solid saturated by a viscous fluid: (i) measurement of the radial displacement under one-dimensional axial tension with no variation of the fluid content (Coussy, 1991) and (ii) measurement of the velocity of acoustic waves in the sample (Bourbié et al., 1987), following the work of Biot (1956).

In the present work, we focus on the case in which the constituents are incompressible separately. A simple method is proposed for the determination of drained Young's modulus and drained Poisson's ratio, the permeability of the structure and the dynamic viscosity of the fluid determined as usual (Bourbié et al., 1987). A standard tension compression test machine is used in order to investigate the asymptotic behavior of a cylindrical sample subject to compressive loading and relaxation. The method further imposes the determination of the compression and relaxation vertical force of the sample, by an analytical approach using spectral decomposition with orthogonal eigenvectors. The analysis of the vertical force (particularly the asymptotic behavior of the vertical force during compression) shows that the ordinate of the origin is a measure of the drained Poisson's ratio and the slope of the curve yields

[9]Laboratoire de Mécanique Physique, Faculté des Sciences et Technologie, Université Paris XII, Av. du Général De Gaulle, 94010 Crétiel Cedex, France.
[10]Mem. ASME.

Contributed by the Applied Mechanics Division of THE AMERICAN SOCIETY OF MECHANICAL ENGINEERS for publication in the JOURNAL OF APPLIED MECHANICS. Manuscript received by the ASME Applied Mechanics Division, June 4, 1993; final revision, Nov. 4, 1993. Associate Technical Editor: J. W. Rudnicki.

Copyright © 1994 by ASME
Downloaded 03 May 2010 to 171.66.16.20. Redistribution subject to ASME license or copyright; see http://www.asme.org/terms/Terms_Use.cfm

the drained Young's modulus. Thereby the measurement of the radial displacement is not necessary and the variation of fluid content is irrelevant. With the usual methods, the measurement of the radial displacement is, indeed, difficult to carry out when dealing with soft materials like foam rubber or biological materials, and no variation of the fluid content must occur.

2 Behavior of a Poroelastic Medium

We consider the quasi-static behavior of an isotropic poroelastic medium with constant porosity, saturated by a Newtonian fluid. If the constitutents are separately incompressible, and, the structure only subjected to small strain, the constitutive equations are described by

$$\epsilon = \frac{1+\nu}{E}\,\sigma - \frac{\nu}{E}\,\{\text{Tra }\sigma\}\,\mathbf{I} + \frac{1-2\nu}{E}\,p\mathbf{I}, \tag{1}$$

$$\theta = \text{Tra }\epsilon \tag{2}$$

where ϵ denotes the symmetrical strain tensor for small strains, σ the symmetrical tensor of total stress, Tra the trace operator of the tensor, $\mathbf{I}$ the identity tensor, p the pore fluid pressure, θ the variation of the relative fluid content of the structure, E its drained Young's modulus, and ν its drained Poisson's ratio.

By writing the equilibrium equation of the structure, ignoring the body force per unit mass and inertia force, and by combining Darcy's law with the mass conservation equation for the fluid, we obtain a system of displacement and pressure coupled equations, assuming that the scalar, vector, and tensor fields are "smooth" enough to differentiate

$$\frac{E}{2(1+\nu)}\left[\Delta U + \frac{1}{1-2\nu}\,\textit{Grad}\,(\text{Div }U)\right] - \textit{Grad}\,p = \mathbf{0} \tag{3}$$

$$\frac{\partial}{\partial t}\,(\text{Div }U) = \frac{\kappa}{\mu}\,\Delta p. \tag{4}$$

In these equations, U denotes the structure displacement vector, κ the permeability of the structure, and μ the dynamic viscosity of the fluid.

3 Method for the Identification of the Mechanical Parameters

3.1 Theoretical Model. Consider a cylindrical laterally unconfined structure, formed by an incompressible sample whose axis parallels the vertical axis z, and placed on an impermeable rigid base. The structure is loaded along the direction z, with an impermeable plate; it is saturated with an incompressible Newtonian fluid and placed in a tank. This tank is already filled with the same fluid, and is large enough to avoid boundary and surface effects. The height and radius of the sample are denoted as h and a.

Changes in the structure are described in cylindrical coordinates. Given its axial symmetry, the problem is two dimensional in r and z. The boundary conditions can be written as follows:

- at $z=0$ the vertical displacement is zero: $U\cdot z=0$,
- at $z=h$ the displacement is imposed and is considered to be small in comparison with h: $U\cdot z=-vt$,
- at $r=a$ the pressure is zero and there is no radial stress: $p=0$ and $\sigma n=0$ where n is the unit outer normal vector along the boundary $r=a$,
- at $z=0$ and h "the boundaries are impermeable,": $\partial p/\partial z=0$.

To these boundary conditions, the initial condition must be added at $t=0$: Div $U=0$.

3.2 Compression and Relaxation Test: Kinematics Conditions. The test involves two steps. In the first one, during a finite duration t_0, the sample is subjected to a compression at constant strain rate v. In the second step, the sample relaxes at a constant strain. For each step, the displacement of the top surface of the sample is given by

$$U\cdot z = -vt,\ \forall t\epsilon]0,\ t_0],\ \text{and}\ U\cdot z = 0,\ \forall t \geq t_0.$$

3.3 Hypothesis. For a small strain, due to the geometry and loading of the medium, we assume that the displacement vector $U=(U_r,\ U_\theta,\ U_z)$ can be written as

$$U \doteq U_r(r,\ t)\ \boldsymbol{e}_r + U_z(z,\ t)\boldsymbol{e}_z$$

where $(\boldsymbol{e}_r,\ \boldsymbol{e}_\theta,\ \boldsymbol{e}_z)$ is the local basis in cylindrical coordinates.

In addition, we shall assume that strain and pressure do not dependent on z. Therefore, the stress tensor σ is only a function of r or t.

3.4 Compression Step. Following the results obtained in Cartesian geometry (Naïli et al., 1992), the solution of the consolidation equation, in its general form, can be written as

$$\theta(r,\ t) = f(r) + \xi t + g(r)\cdot e^{-st}$$

where the scalar functions f and g and the ξ and s scalars are unknown.

We have developed the necessary tools to solve such a problem in the case of a simple geometry, by using a "spectral method" as initiated by Mandel (1953). With this method, we have thereby determined the following fields: displacements, strains, stresses, pressure, flow, and vertical force.

After some algebra, we can determine the compression stress σ_{zz}; finally, the vertical forces at $z=h$, during compression, is obtained by calculating the following integral:

$$F(t) = \int_{S_h} \sigma_{zz}\, dS$$

where S_h is the cross-section of the sample at $z=h$. This integral give.

$$F(t) = \pi a^2 E\,\frac{v}{h}\,t + F_0\,(1-2\nu)^2 - \pi a^2 \sum_{k=0}^{\infty} A_k \left[\frac{2E}{(1+\nu)\omega_k a}\,J_1(\omega_k a) - \frac{\mu c}{\kappa}\,J_0\,(\omega_k a)\right]\cdot e^{-s_k t},\ \forall t\epsilon\ [0,\ t_0] \tag{5}$$

where $F_0=\pi a^4\ (\nu/h)\ (\mu/8\kappa)$, J_0 and J_1 are the zero and first-order Bessel function of the first kind, and A_k is given by

$$A_k = -\frac{(1-2\nu)v}{ch\omega_k^2}\,\frac{\omega_k a J_0(\omega_k a) - 2J_1(\omega_k a)}{\omega_k a[J_0^2(\omega_k a) + J_1^2(\omega_k a)] - 2J_0(\omega_k a)J_1(\omega_k a)}.$$

The ω_k are the roots of $\omega a(1-\nu)J_0(\omega a) = (1-2\nu)J_1(\omega a)$. The number of these roots, which are distinct and strictly positive, is infinite. The s_k are given by $\omega_k^2 = s_k/c$, where c is the consolidation constant given by

$$c = \frac{\kappa}{\mu}\,\frac{E(1-\nu)}{(1+\nu)(1-2\nu)} = \frac{a^2}{\mathfrak{I}}.$$

In this equation, $\mathfrak{I}$ is the characteristic (or consolidation) time, and it is given by

$$\mathfrak{I} = \frac{(1-2\nu)(1+\nu)}{(1-\nu)}\,\frac{a^2\mu}{E\kappa}. \tag{6}$$

3.5 Relaxation Step. The relaxation step is studied by imposing $\epsilon_{zz} = vt_0/h,\ \forall t \geq t_0$. The continuity of the fields gives the initial condition at $t=t_0$, which corresponds to the passage from the compression and relaxation steps, and especially the continuity of the field of the variation of the relative fluid content of the structure.

Downloaded 03 May 2010 to 171.66.16.20. Redistribution subject to ASME license or copyright; see http://www.asme.org/terms/Terms_Use.cfm

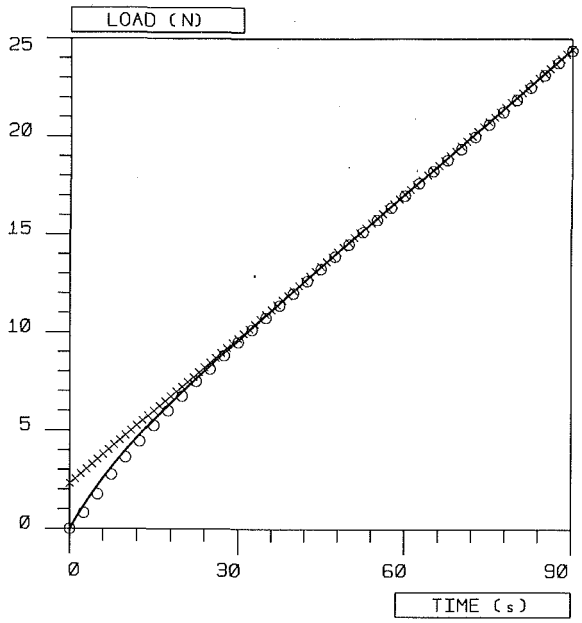


Fig. 1 Vertical force versus time during compression. Foam rubber geometry parameters are height $h = 30$ mm, radius $a = 50$ mm, and mechanical characteristics $E \sim 28500$ N•m^{-2}, $\nu \sim -0.3$, $\kappa = 0.3 \times 10^{-11}$m^2; viscosity of water $\mu = 10^{-3}$Pa•s; crushing rate $v = 3.4 \times 10^{-2}$mm•s^{-1}; duration of compression step $t_0 = 90$ s. o o o: experiment, × × ×: asymptotic behavior ——— : theory.

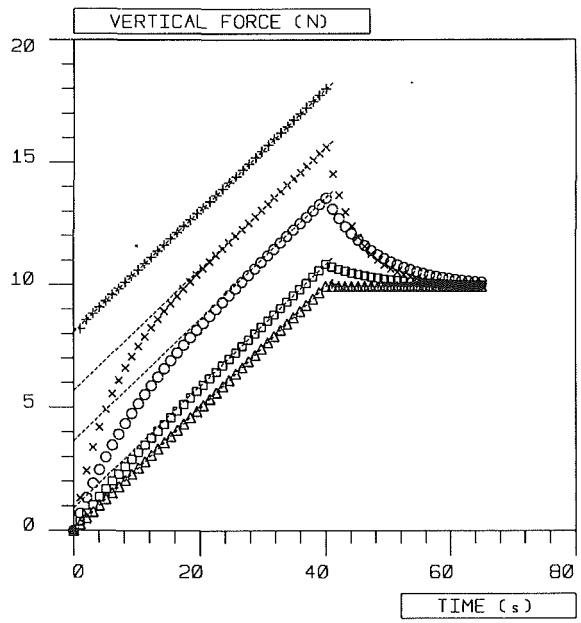


Fig. 2 Evolution with time of the vertical force during compression and relaxation for various values of drained Poisson's ratio. Duration of compression step $t_0 = 40$ s. In both cases --- represents the asymptotic behavior; drained Poisson's ratio: + + + ($\nu = -0.999$), × × × ($\nu = -0.75$), o o o ($\nu = -0.5$), □ □ □ ($\nu = 0$), △ △ △ ($\nu = 0.499$).

We need $\theta(r, t)$ in the form of $\theta = j(r) + l(r) \cdot e^{-st}$, where the scalar functions j and l and the scalar s must be determined.

After some more algebra, we determine the stresses during relaxation, and finally, the vertical force at $z = h$ as

$$F(t) = \pi a^2 \{E\epsilon_{zz} - \frac{c\mu}{\kappa} \sum_{k=0}^{\infty} B_k J_0(\omega_k a) \cdot e^{-s_k t}\}, \ \forall t \geq t_0 \quad (7)$$

where B_k is given by $B_k = A_k (1 - e^{s_k t_0})$.

4 Analysis and Discussion

After a period of time of the order of the consolidation time $\mathfrak{I}$, but greater, the strength given by Eq. (5) reduces to the following simplified expression:

$$F(t) = \pi a^2 E \frac{v}{h} t + (1 - 2\nu)^2 F_0. \quad (8)$$

This is the equation of a straight line whose ordinate at the origin enables us to measure ν, if μ and κ have been previously determined, and whose slope gives E. Therefore, during the compression test, we have only to record the vertical force versus time curve. This method has the advantage of enabling the measurement of the drained Poisson's ratio without having to determine the radial displacement. However, it requires a good accuracy in the measurement of the permeability κ of the structure, in order to obtain a good estimation of the drained Poisson's ratio ν.

It is worth noting that, in this approach, the transient step is not used in order to characterize the medium. The measured coefficients are derived from the steady-state asymptotic behavior of the structure, assuming the medium to be poroelastic, although the test itself cannot determine whether or not this is the case.

The vertical force during compression predicted by the model when using these values for ν and E in Eq. (8), must be checked against the vertical force measured in the transient step. Further, the relaxation step makes it possible to verify the measurement of drained Young's modulus because the asymptotic behavior of the vertical force during relaxation given by Eq. (7) yields the value of this parameter.

Figure 1 shows the vertical force versus time curve during the compression of the water-saturated foam-rubber test sample. The permeability κ of the structure and μ, the dynamic viscosity of the fluid, were measured prior to the test. The constitutents (foam rubber and water) of this experiment are clearly incompressible. The undrained Poisson's ratio is then equal to 1/2 (Duvaut, 1990). Circles denote test points. The crosses show the asymptotic behavior of the sample, which yields its drained Young's modulus and drained Poisson's ratio, as described above. In this experiment, we obtained $\nu \sim -0.3$, $E \sim 285090 N \cdot m^{-2}$ and $\mathfrak{I} \sim 25s$. The solid line represents the theoretical behavior from Eq. (5) obtained with these experimental values.

The results based on the theoretical formulation are in good agreement with experimental observations. A negative value of the drained Poisson's ratio can be surprising, but this result is within the allowed theoretical variation of this ratio, $[-1, 0.5]$ (Auriault and Sanchez-Palencia, 1977). Moreover, a negative drained Poisson's ratio can tentatively be explained by the alveolar interstitial structure of the foam (Lakes, 1987).

The drained Poisson's ratio has a great influence on the overall behavior of the medium. The consolidation time $\mathfrak{I}$, given by Eq. (6), characterizes the speed with which the structure consolidates, i.e., from the moment after which the transient step become negligible. Therefore, it is interesting to investigate the effect of the above parameters on $\mathfrak{I}$, particularly the influence of drained Poisson's ratio. It is worth pointing out that $\mathfrak{I}$ has the same value—i.e., $\mathfrak{I} = 0$—in the limits $\nu \to -1$ and $\nu \to 0.5$. In other words, the transient step does not occur for such values. The consolidation time is maximum when $\nu = 0$.

Figure 2 shows the vertical force versus time curves during compression and relaxation, given by Eqs. (5) and (7), for various values of drained Poisson's ratio. In these curves, the duration of compression step t_0 is equal to 40s; the geometry parameters and the mechanical characteristics are the same as in the experiment. It is interesting to consider the variation of

Downloaded 03 May 2010 to 171.66.16.20. Redistribution subject to ASME license or copyright; see http://www.asme.org/terms/Terms_Use.cfm

the $F(t)$ with respect to the drained Poisson's ratio. $F(t)$ is found to decrease monotonically in the interval considered above. Since its maximum value for $\nu \to -1$ corresponds to $\mathfrak{I}$ equal to zero, then $F(t)$—as given by Eq. (5)—undergoes a sudden upward jump. Likewise, $F(t)$—as expressed by Eq. (7)—is subjected in the same limit to a downward jump when the relaxation step of the test begins. The explanation of the latter phenomenon is that the speed of filtration becomes infinite. When $\nu \to 0.5$, both $\mathfrak{I}$ and the ordinate at the origin are equal to zero. The function $F(t)$—as expressed both by Eqs. (5) and (7)—is equal to its asymptotes in each time interval (compression, relaxation). This may be interpreted as a purely elastic behavior. In this case, the radial displacement of the solid skeleton has the same velocity as the fluid flow and, as a result, there is simply no filtration.

In can also be shown that when the speed of the piston is doubled, the slopes of the asymptotic behavior of the vertical force versus time curve changes and the ordinate at the origin changes proportionally. Similarly, for radial stress versus strain, the ordinate at the origin varies also in the same manner, the slopes remaining equal for the two speeds. From such curves, it is therefore not possible to dintinguish a porous medium from a medium described with a viscoelastic behavior admitting two parameters, such as in the Kelvin-Voigt model.

Now, if the radius of the cylinder is doubled, the slopes of the curves in the asymptotic behavior region are in the ratio 1 to 16, while the ordinate at the origin changes only in the ratio 1 to 4. For radial stress versus strain, the slope remains identical for the two radii, while the ordinate at the origin varies in the ratio 1 to 4. This shows that the behavior of the porous medium cannot be described in terms of a Kelvin-Voigt model, for which the characteristic coefficients are not dependent on geometry.

5 Conclusion

The proposed test makes possible the validation of the model of a "poroelastic"—i.e., a porous deformable medium saturated by a Newtonian fluid—medium with separately incompressible constitutents. By using a standard tension compression test machine, this method allows the determination of the mechanical coefficients of the structure from its asymptotic behavior. However, for a very long consolidation time, this approach may be inappropriate if a standard tension compression test machine is used. In that case, sinusoidal tests would be a better approach.

References

Auriault, J. L., and Sanchez-Palencia, E., 1977, "Etude du Comportement Macroscopique d'un Milieu Poreux Saturé Déformable," *Journal de Mécanique*, Vol. 16, No. 4, pp. 577–603.

Biot, M. A., 1941, "General Theory of Three Dimensional Consolidation," *Journal of Applied Physics*, Vol. 12, pp. 155–165.

Biot, M. A., 1946, "Theory of Propagation of Elastic Waves in a Fluid Saturated Porous Solid, Parts I and Parts II," *Journal of the Acoustical Society of America*, Vol. 28, No. 2, pp. 168–191.

Bourbié, T., Coussy, O., and Zinszner, B., 1987, *Acoustics of Porous Media*, Editions Technip.

Coussy, O., 1991, *Mécanique des Milieux Poreux*, Editions Technip.

Duvaut, G., 1990, *Mécanique des Milieux Continus*, Masson.

Lakes, R., 1987, "Foam Structures With a Negative Poisson's Ratio," *Science*, No. 235, pp. 1038–1040.

Mandel, J., 1953, "Etude Mathématique de la Consolidation des Sols," *Géotechnique 3*, pp. 287–299.

Naïli, S., Le Gallo, O., and Geiger, D., 1992, "Characterization of a Porous Elastically Deformable Medium by a Compression-Relaxation Test," C.R. Acad. Sci. Paris, t. 315, Série II, pp. 1439–1444.

Rice, J. R., and Cleary, M. P., 1976, "Some Basic Diffusion Solutions for Fluid-Saturated Elastic Porous Media With Compressible Constitutents," *Reviews of Geophysics and Space Physics*, Vol. 14, No. 2, pp. 227–241.

Zero Drag of a Thin Wing Moving in an Elastic Medium at the Rayleigh Speed[11]

G. P. Cherepanov[12]

The goal of the present technical Note is to prove the following theorem.

Theorem

The drag of an arbitrary thin rigid wing steadily moving in an elastic medium at the Rayleigh speed equals zero. Absorption or emission of energy, particularly at the nose of the wing and in the cavity far behind the wing, equals zero, too.

Proof

Consider the following complex potentials, $\varphi_1'(z_1)$ and $\varphi_2'(z_2)$:

$$\varphi_1'(z_1) = \frac{\beta_4(1-2\nu)}{2\pi i \beta_1^2(\beta_4-1)} \int_0^\infty \frac{f'(x)dx}{x-z_1}; \tag{1}$$

$$\varphi_2'(z_2) = \frac{(1-2\nu)}{2\pi i(1-\beta_4)} \int_0^\infty \frac{f'(x)dx}{x-z_2}. \quad (f(0)=0). \tag{2}$$

Here $z_1 = x + i\beta_1 y$, $z_2 = x + \beta_2 y$

$$\beta_1^2 = 1 - \frac{1-2\nu}{2-2\nu} m_R^2, \quad \beta_2^2 = 1 - m_R^2, \quad \beta_3 = 1 + \frac{\nu m_R^2}{2-2\nu},$$

$$\beta_4 = 1 - \frac{1}{2} m_R^2, \quad m_R = \frac{c_R}{c_2}, \quad c_1^2 = \frac{\lambda+2\mu}{\rho}, \quad c_2^2 = \frac{\mu}{\rho} \tag{3}$$

$$2\mu = E/(1+\nu), \quad \lambda = \nu E(1+\nu)^{-1}(1-2\nu)^{-1}$$

(ρ, the density; E, Young's modulus; ν, Poisson's ratio).

The value of m_R is the real root of the Rayleigh equation

$$R(m_R) \equiv \beta_1\beta_2 - \beta_4^2 = 0. \tag{4}$$

The functions, $\varphi_1'(z_1)$ and $\varphi_2'(z_2)$, describe a certain two-dimensional steady-state dynamical elastic field propagating in the direction opposite to that of the x-axis with the Rayleigh speed, c_R, and defined as follows (Cherepanov, 1979):

$$\frac{\partial u_x}{\partial x} = \frac{2}{1-2\nu} Jm[\beta_1\varphi_1'(z_1) + \beta_2\varphi_2'(z_2)] \tag{5}$$

$$\frac{\partial u_y}{\partial x} = \frac{2}{1-2\nu} \mathrm{Re}[\beta_1^2\varphi_1'(z_1) + \varphi_2'(z_2)] \tag{6}$$

$$\sigma_x = \frac{2E}{(1+\nu)(1-2\nu)} Jm[\beta_1\beta_3\varphi_1'(z_1) + \beta_2\varphi_2'(z_2)] \tag{7}$$

$$\sigma_y = -\frac{2E}{(1+\nu)(1-2\nu)} Jm[\beta_1\beta_4\varphi_1'(z_1) + \beta_2\varphi_2'(z_2)] \tag{8}$$

$$\tau_{xy} = \frac{2E}{(1+\nu)(1-2\nu)} \mathrm{Re}[\beta_1^2\varphi_1'(z_1) + \beta_4\varphi_2'(z_2)]. \tag{9}$$

[11]The work was supported by NASA grant 59204.

[12]Department of Mechanical Engineering, College of Engineering and Design, Florida International University, Miami, FL 33199. Mem. ASME.

Contributed by the Applied Mechanics Division of THE AMERICAN SOCIETY OF MECHANICAL ENGINEERS for publication in the ASME JOURNAL OF APPLIED MECHANICS. Manuscript received by the ASME Applied Mechanics Division, Aug. 16, 1993; final revision, Nov. 11, 1993. Associate Technical Editor: S. A. Berger.

Downloaded 03 May 2010 to 171.66.16.20. Redistribution subject to ASME license or copyright; see http://www.asme.org/terms/Terms_Use.cfm

the $F(t)$ with respect to the drained Poisson's ratio. $F(t)$ is found to decrease monotonically in the interval considered above. Since its maximum value for $\nu \to -1$ corresponds to $\mathfrak{I}$ equal to zero, then $F(t)$—as given by Eq. (5)—undergoes a sudden upward jump. Likewise, $F(t)$—as expressed by Eq. (7)—is subjected in the same limit to a downward jump when the relaxation step of the test begins. The explanation of the latter phenomenon is that the speed of filtration becomes infinite. When $\nu \to 0.5$, both $\mathfrak{I}$ and the ordinate at the origin are equal to zero. The function $F(t)$—as expressed both by Eqs. (5) and (7)—is equal to its asymptotes in each time interval (compression, relaxation). This may be interpreted as a purely elastic behavior. In this case, the radial displacement of the solid skeleton has the same velocity as the fluid flow and, as a result, there is simply no filtration.

In can also be shown that when the speed of the piston is doubled, the slopes of the asymptotic behavior of the vertical force versus time curve changes and the ordinate at the origin changes proportionally. Similarly, for radial stress versus strain, the ordinate at the origin varies also in the same manner, the slopes remaining equal for the two speeds. From such curves, it is therefore not possible to dintinguish a porous medium from a medium described with a viscoelastic behavior admitting two parameters, such as in the Kelvin-Voigt model.

Now, if the radius of the cylinder is doubled, the slopes of the curves in the asymptotic behavior region are in the ratio 1 to 16, while the ordinate at the origin changes only in the ratio 1 to 4. For radial stress versus strain, the slope remains identical for the two radii, while the ordinate at the origin varies in the ratio 1 to 4. This shows that the behavior of the porous medium cannot be described in terms of a Kelvin-Voigt model, for which the characteristic coefficients are not dependent on geometry.

5 Conclusion

The proposed test makes possible the validation of the model of a "poroelastic"—i.e., a porous deformable medium saturated by a Newtonian fluid—medium with separately incompressible constitutents. By using a standard tension compression test machine, this method allows the determination of the mechanical coefficients of the structure from its asymptotic behavior. However, for a very long consolidation time, this approach may be inappropriate if a standard tension compression test machine is used. In that case, sinusoidal tests would be a better approach.

References

Auriault, J. L., and Sanchez-Palencia, E., 1977, "Etude du Comportement Macroscopique d'un Milieu Poreux Saturé Déformable," *Journal de Mécanique*, Vol. 16, No. 4, pp. 577–603.

Biot, M. A., 1941, "General Theory of Three Dimensional Consolidation," *Journal of Applied Physics*, Vol. 12, pp. 155–165.

Biot, M. A., 1946, "Theory of Propagation of Elastic Waves in a Fluid Saturated Porous Solid, Parts I and Parts II," *Journal of the Acoustical Society of America*, Vol. 28, No. 2, pp. 168–191.

Bourbié, T., Coussy, O., and Zinszner, B., 1987, *Acoustics of Porous Media*, Editions Technip.

Coussy, O., 1991, *Mécanique des Milieux Poreux*, Editions Technip.

Duvaut, G., 1990, *Mécanique des Milieux Continus*, Masson.

Lakes, R., 1987, "Foam Structures With a Negative Poisson's Ratio," *Science*, No. 235, pp. 1038–1040.

Mandel, J., 1953, "Etude Mathématique de la Consolidation des Sols," *Géotechnique 3*, pp. 287–299.

Naïli, S., Le Gallo, O., and Geiger, D., 1992, "Characterization of a Porous Elastically Deformable Medium by a Compression-Relaxation Test," C.R. Acad. Sci. Paris, t. 315, Série II, pp. 1439–1444.

Rice, J. R., and Cleary, M. P., 1976, "Some Basic Diffusion Solutions for Fluid-Saturated Elastic Porous Media With Compressible Constitutents," *Reviews of Geophysics and Space Physics*, Vol. 14, No. 2, pp. 227–241.

Zero Drag of a Thin Wing Moving in an Elastic Medium at the Rayleigh Speed[11]

G. P. Cherepanov[12]

The goal of the present technical Note is to prove the following theorem.

Theorem

The drag of an arbitrary thin rigid wing steadily moving in an elastic medium at the Rayleigh speed equals zero. Absorption or emission of energy, particularly at the nose of the wing and in the cavity far behind the wing, equals zero, too.

Proof

Consider the following complex potentials, $\varphi_1'(z_1)$ and $\varphi_2'(z_2)$:

$$\varphi_1'(z_1) = \frac{\beta_4(1-2\nu)}{2\pi i \beta_1^2(\beta_4-1)} \int_0^\infty \frac{f'(x)dx}{x-z_1}; \tag{1}$$

$$\varphi_2'(z_2) = \frac{(1-2\nu)}{2\pi i(1-\beta_4)} \int_0^\infty \frac{f'(x)dx}{x-z_2}. \quad (f(0)=0). \tag{2}$$

Here $z_1 = x + i\beta_1 y$, $z_2 = x + \beta_2 y$

$$\beta_1^2 = 1 - \frac{1-2\nu}{2-2\nu} m_R^2, \quad \beta_2^2 = 1 - m_R^2, \quad \beta_3 = 1 + \frac{\nu m_R^2}{2-2\nu},$$

$$\beta_4 = 1 - \frac{1}{2} m_R^2, \quad m_R = \frac{c_R}{c_2}, \quad c_1^2 = \frac{\lambda+2\mu}{\rho}, \quad c_2^2 = \frac{\mu}{\rho} \tag{3}$$

$$2\mu = E/(1+\nu), \quad \lambda = \nu E(1+\nu)^{-1}(1-2\nu)^{-1}$$

(ρ, the density; E, Young's modulus; ν, Poisson's ratio).

The value of m_R is the real root of the Rayleigh equation

$$R(m_R) \equiv \beta_1\beta_2 - \beta_4^2 = 0. \tag{4}$$

The functions, $\varphi_1'(z_1)$ and $\varphi_2'(z_2)$, describe a certain two-dimensional steady-state dynamical elastic field propagating in the direction opposite to that of the x-axis with the Rayleigh speed, c_R, and defined as follows (Cherepanov, 1979):

$$\frac{\partial u_x}{\partial x} = \frac{2}{1-2\nu} Jm[\beta_1\varphi_1'(z_1) + \beta_2\varphi_2'(z_2)] \tag{5}$$

$$\frac{\partial u_y}{\partial x} = \frac{2}{1-2\nu} \mathrm{Re}[\beta_1^2\varphi_1'(z_1) + \varphi_2'(z_2)] \tag{6}$$

$$\sigma_x = \frac{2E}{(1+\nu)(1-2\nu)} Jm[\beta_1\beta_3\varphi_1'(z_1) + \beta_2\varphi_2'(z_2)] \tag{7}$$

$$\sigma_y = -\frac{2E}{(1+\nu)(1-2\nu)} Jm[\beta_1\beta_4\varphi_1'(z_1) + \beta_2\varphi_2'(z_2)] \tag{8}$$

$$\tau_{xy} = \frac{2E}{(1+\nu)(1-2\nu)} \mathrm{Re}[\beta_1^2\varphi_1'(z_1) + \beta_4\varphi_2'(z_2)]. \tag{9}$$

[11]The work was supported by NASA grant 59204.

[12]Department of Mechanical Engineering, College of Engineering and Design, Florida International University, Miami, FL 33199. Mem. ASME.

Contributed by the Applied Mechanics Division of THE AMERICAN SOCIETY OF MECHANICAL ENGINEERS for publication in the ASME JOURNAL OF APPLIED MECHANICS. Manuscript received by the ASME Applied Mechanics Division, Aug. 16, 1993; final revision, Nov. 11, 1993. Associate Technical Editor: S. A. Berger.

Copyright © 1994 by ASME

Downloaded 03 May 2010 to 171.66.16.20. Redistribution subject to ASME license or copyright; see http://www.asme.org/terms/Terms_Use.cfm

Here σ_x, σ_y and τ_{xy} are components of the stress tensor and u_x and u_y are the displacement components. The $\varphi_1'(z_1)$ and $\varphi_2'(z_2)$ are analytic outside the cut along $y = 0\ x > 0$ where these functions are discontinuous.

Using the Sokhotsky-Plemeli equation,

$$\lim_{\substack{y\to\pm 0\\ x>0,}} \frac{1}{\pi i}\int_0^\infty \frac{f'(x)\,(dx)}{x-z} = \pm f'(x) + \frac{1}{\pi i}\,P.V.\int_0^\infty \frac{f'(x_1)dx_1}{x_1-x} \tag{10}$$

and Eq. (5) we find

$$\lim_{\substack{y\to\pm 0\\ x>0.}} u_y(x, y) = \pm\int_0^x f'(x)\,(dx) = \pm f(x). \tag{11}$$

Hence, the complex potentials $\varphi_1'(z_1)$ and $\varphi_2'(z_2)$ describe the elastic field produced by a symmetrical wing profile of the arbitrary thickness, $2f(x)$, moving at the Rayleigh speed in the direction opposite to that of the x-axis.

Using Eqs. (4), (8), (9), and (10), we find as well that

$$\text{when } x>0, \quad y\to\pm 0: \quad \sigma_y=\tau_{xy}=0. \tag{12}$$

Thus, the normal and shear tractions acting upon the arbitrary wing profile are zero at all the points of contact with an elastic medium, that is, the drag is zero. From the proof, it follows that the wing itself can be a part of the contour, $\pm f(x)$, on the positive x-axis, or the wing can be even inside the cavity of the thickness $2f(x)$, with the banks free of tractions.

Let us now prove that the energy flux rate at the nose, $z = 0$, and at infinity equals zero.

Suppose that (i) the angle of a nose opening of a wing or cavity is acute or right:

$$\alpha = \lim_{x\to+0} \arctan f'(x) \le \frac{\pi}{2}; \tag{13}$$

(ii) the opening at infinity and the nose is inside a certain parabola:

$$\lim f(x) \le C\sqrt{x}, \text{ when } x\to+\infty \text{ or } x\to+0 \tag{14}$$

(C is a positive constant).

The energy flux rate, Γ_x, of a steady dynamic elastic field is calculated by means of the invariant integral resulted in the following equations (Cherepanov, 1979):

$$\text{when } z\to 0, \text{ and } \alpha<\frac{\pi}{2}: \quad \Gamma_x=0 \tag{15}$$

$$\text{when } z\to\infty \text{ and } \lim f(x) < C_1 x^{\delta}\left(\delta<\frac{1}{2}\right): \quad \Gamma_x=0; \tag{16}$$

(C_1, a constant)

$$\text{when } z\to 0 \text{ or } z\to\infty \text{ and } \lim f(x) = Cx^{1/2}:$$

$$\Gamma_x = \frac{K_I^2(1+\nu)m^2\beta_1(m)}{8ER(m)} \quad (m = V/c_2). \tag{17}$$

Here V is the velocity of propagation of a steady-state elastic field ($V < c_2$), and the stress intensity factor, K_I, is

$$K_I = \lim(\sigma_y\sqrt{2\pi x})$$

$$\text{when } x\to+\infty \text{ or } x\to+0. \tag{18}$$

The value of K_I and C in Eq. (17) is generally different for $z \to 0$ or $z \to \infty$. Use the known asymptotic property of the Cauchy integrals (1) and (2),

$$\text{if } f'(x)\to\frac{1}{2}Cx^{-1/2} \text{ when } x\to+0 \text{ or } x\to+\infty,$$

$$\text{then } \varphi_1'(z_1)\to\frac{\beta_4(1-2\nu)C}{4\beta_1^2(\beta_4-1)\sqrt{z_1}}, \text{ when } z\to 0 \text{ or } z\to\infty, \tag{19}$$

$$\text{and } \varphi_2'(z_2)\to\frac{(1-2\nu)C}{4(1-\beta_4)\sqrt{z_2}}, \text{ when } z\to 0 \text{ or } z\to\infty. \tag{20}$$

Substituting φ_1' and φ_2' in Eq. (8) by Eqs. (19) and (20), we find K_I by means of Eq. (18):

$$\text{when } y=0\ x\to+0 \text{ or } x\to+\infty \text{ and } f(x)\to Cx^{1/2}$$

$$K_I = \frac{CER(m)}{2(1+\nu)\beta_1(1-\beta_4)}, \tag{21}$$

and hence Γ_x because of Eq. (17) equals

$$\Gamma_x = \frac{m^2C^2ER(m)}{32(1+\nu)\beta_1(1-\beta_4)^2}. \tag{22}$$

According to this equation the steady-state dynamic elastic field, propagating at a sub-Rayleigh speed and forming a parabolic nose near $z = 0$ or a parabolic cavity at infinity, loses an energy at the sink $z = 0$ (like a static crack-tip) and absorbs the energy at infinity. If $c_R < V < c_2$, a parabolic nose emanates an energy (an energy source at $z = 0$) and the elastic field emits the energy to infinity. When $V = c_R$, $\Gamma_x = 0$ according to Eq. (22), that is absorption or emission of energy at the nose and infinity equals zero. All other points of the elastic field described by potentials (1) and (2) are nonsingular, so that zero absorption or emission of energy at these points follows from the theory of elasticity.

The theorem is proven. The theorem is valid as well for a steady field nonsymmetrical with respect to the x-axis.

The two-dimensional condition of a field around a moving wing projectile is analogous to that in the aerofoil theory (Cherepanov, 1993).

The theorem may have some interesting engineering applications. From the theorem it follows that a thin plane cavity, the banks of which are free of tractions, can propagate in an elastic medium without limits in space and time at the Rayleigh speed. Let us refer to the specific internal solitary wave formed by the elastic field constructed, as the rayleighon. According to the theorem, the rayleighon neither emits nor absorbs the energy and its cavity shape is arbitrary (within the limits of the usual requirement, $|f'(x)| \ll 1$, following from the linear theory of elasticity). Therefore, a projectile inside a rayleighon cavity moving at the same Rayleigh speed can also travel in an elastic medium without limits in space and time.

This paradoxical result can probably explain the mysterious phenomenon of superdeep penetration (at hypervelocity impact) of some solid particles, the remains of which were discovered sometimes on depths thousand or ten thousand times greater than the initial diameter of particles (Kozorezov et al., 1981; Andilevko et al., 1979; Romanov et al., 1988; Altshuler et al., 1989; etc.). One can imagine a lot of significant practical applications of the phenomenon, from superdeep implantation to underground travel (Cherepanov, 1995).

References

Altshuler, L. V., Andilevko, S. K., Romanov, G. S., and Usherenko, S. M., 1989, "On a Model of Superdeep Penetration," *Pisma v Zhurnal Technicheskoi Fiziki* (*Letters to ZhTF*), Vol. 15, No. 5, pp. 55–57.

Andilevko, S. K., Roman, O. V., Romanov, G. S., and Usherenko, S. M., 1987, "Implantation of a Powder into a Metal," *Poroshkovaia Metallurgia* (*Soviet Powder Metallurgy and Metal Ceramics*), Vol. 11, pp. 6–11.

Cherepanov, G. P., 1979, *Mechanics of Brittle Fracture*, McGraw-Hill, New York, pp. 102–104, 252, 857–858.

Cherepanov, G. P., 1993, "An Introduction to Singular Integral Equations in Aerodynamics," *Method of Discrete Vortices*, by S. M. Belotserkovsky and I. K. Lifanov, CRC Press, London, pp. 1–16.

Cherepanov, G. P., 1995, "Superdeep Penetration," *Fracture: A Topical Encyclopedia of Current Knowledge Dedicated to Alan Arnold Griffith*, G. P. Cherepanov, ed., Krieger Publishing Co., Melbourne, FL, pp. 679–724.

Kozorezov, K. I., Maksimenko, V. N., and Usherenko, S. M., 1981, "Study of Interaction of Micro-Particles with Solid Materials," *Some Problems of Modern Mechanics, Proceedings of Moscow State University*, Vol. 1, pp. 12–36 (in Russian).

Romanov, G. S., Usherenko, S. M., and Yurin, S. E., 1988, "Effect of Initial

Downloaded 03 May 2010 to 171.66.16.20. Redistribution subject to ASME license or copyright; see http://www.asme.org/terms/Terms_Use.cfm

Temperature of Iron on the Superdeep Penetration," *Trudy Vsesouznogo Soveshania po Detonatcii, (Proceedings of All-Union Meeting on Detonation, Chernogolovka)*, pp. 152–157 (in Russian).

Influential Functions for a Layered Medium Subjected to a Finite Distributed Source

Ruichong Zhang[13] and Yan Yong[14]

Introduction

A Green's function is defined as a response field of a continuum medium subjected to a unidirectional unit impulse at a particular point (localized precisely in both space and time; Aki and Richards, 1980). For a typical source finitely distributed in a volume or on a surface, the response solution is an integration of infinite Green's functions that account for excitations all over the source region. Closed-form solutions are only found in special cases like a semi-infinite uniform medium with a circular source area (Pak, 1987). In many other cases such as an inhomogeneous medium or irregular source geometry, seeking Green's functions requires considerable efforts even if they do exist. Thus, determination of response solutions has mainly relied on numerical computations (Bouchon and Aki, 1979; Luco and Apsel, 1983; Kennett, 1983; Zhang et al., 1991). The computations are usually pursued by dividing the source region into subsections. The contribution of each subsection to the total response is represented by a Green's function of numerical form such that the response solution becomes a linear composition rather than an integration of Green's functions. Such computational scheme is equivalent to discretization of the source into a series of point sources evenly distributed in the source region.

A different decomposition scheme is proposed in this Note. A typical finitely distributed source is decomposed into a series of so-called fundamental sources, each of which is continuously distributed over the source region with a simple spatial variation. The numerical computation required in this approach is expected to be less time-consuming than the conventional Green's function approach. Such advantage appears prominent when responses in the near field are required. The reason for this is quite straight forward: responses at those locations close to the source area are usually sensitive to source spatial variations, and influence functions defined in this Note have a better ability to represent such variations compared to Green's functions. The merit of the current approach may be seen clearly in some inverse problems (Yong et al. 1994).

Formulation of the Problem

Consider a layered medium with a finitely distributed source buried in one of its layers, say, layer j. Each layer contains a linearly elastic, isotropic, and uniform medium. Since any motion can be expanded into time-harmonic components through the Fourier integral transformation, displacement $\mathbf{u}$ and traction $\mathbf{t}$ can be expressed in the frequency domain as

$$\mathbf{u}(r, \varphi, z, \omega) = \mathbf{u}_r\mathbf{e}_r + \mathbf{u}_\varphi\mathbf{e}_\varphi + \mathbf{u}_z\mathbf{e}_z$$

$$\mathbf{t}(r, \varphi, z, \omega) = \tau_{rz}\mathbf{e}_r + \tau_{\varphi z}\mathbf{e}_\varphi + \tau_{zz}\mathbf{e}_z \quad (1)$$

where $\mathbf{e}_r$, $\mathbf{e}_\varphi$ and $\mathbf{e}_z$ are unit vectors in the r, φ and z directions, respectively.

Continuity conditions at each layer-to-layer interface require that displacement $\mathbf{u}$ and traction $\mathbf{t}$ be continuous across the interface. Boundary conditions can be either finite or infinite. At a finite boundary, one half of the displacement and traction components are constrained. For instance, a free surface is associated with $\mathbf{t}(r, \varphi, z, \omega)|_{z=0} = \mathbf{0}$. A layered medium with an infinite boundary embodies one layer of infinite depth. Any wave traveling into this layer can never be bounced back. A buried source in a layered medium usually falls into one of the following kinds:

$$\mathbf{u}(r, \varphi, z, \omega)|_{z=z_s^+} - \mathbf{u}(r, \varphi, z, \omega)|_{z=z_s^-} = \Delta\mathbf{u}(r, \varphi, \omega), \quad r \le a(\varphi) \quad (2)$$

$$\mathbf{t}(r, \varphi, z, \omega)|_{z=z_s^+} - \mathbf{t}(r, \varphi, z, \omega)|_{z=z_s^-} = \Delta\mathbf{t}(r, \varphi, \omega), \quad r \le a(\varphi) \quad (3)$$

where $a(\varphi)$ is the boundary of a source area. It is noted that these two kinds of discontinuity sources cannot take place simultaneously; the physics will be violated otherwise.

In a conventional approach, the response to a finitely distributed source is calculated from the following integration:

$$G_{\eta\xi}(r, \varphi, z, \omega) = \int_0^{2\pi}\int_0^{a(\varphi)} g_{\eta\xi}(r, \varphi, z, \omega; r_s, \varphi_s, z_s) S_\xi(r_s, \varphi_s, \omega) r_s dr_s d\varphi_s, \quad \xi, \eta = r, \varphi, z \quad (4)$$

where $G_{\eta\epsilon}$ is a displacement or stress response component in the η-direction responding to source $S_\xi(r, \varphi, \omega)$, which is the ξ-th component of a finitely distributed source representing either $\Delta\mathbf{u}$ or $\Delta\mathbf{t}$, and $g_{\eta\xi}$ is a Green's function in the η-direction due to point excitation $S_\xi(r_s, \varphi_s, \omega)/|S_\xi(r_s, \varphi_s, \omega)|$. Green's function $g_{\eta\xi}$ can be obtained by solving the equation of motion along with constitutive equations, continuity conditions and boundary conditions (e.g., Aki and Richards, 1980). However, $g_{\eta\xi}$ usually has a complicated representation for an inhomogeneous medium. A closed-form integral in Eq. (4) is very difficult to obtain, if not impossible. As a result, an expensive numerical computation is required to calculate the integration in Eq. (4). Also, the computational scheme is equivalent to the discretization of a distributed source into a series of point sources evenly distributed in the source region.

Instead of adopting the representation in Eq. (4) and the associated numerical treatment, an alternative approach is proposed, which begins with a series expansion of a typical finitely distributed source. Without loss of generality, we only consider the symmetric part of the distributed source. The antisymmetric part can be treated in the same way.

A typical symmetrical source with respect to $\varphi = 0$, either $\Delta\mathbf{u}$ or $\Delta\mathbf{t}$, can be represented by

$$\mathbf{S}(r_s, \varphi_s, \omega) = \sum_j \sum_l \sum_{\xi=r,\varphi,z} a_\xi^{jl}\, \Phi_\xi^{jl}(r_s, \varphi_s)\mathbf{e}_\xi; \quad 0 \le r_s \le a(\varphi_s),\ 0 \le \varphi_s \le 2\pi \quad (5)$$

in which

$$\Phi_\xi^{jl}(r_s, \varphi_s) = \begin{cases} r_s^l \cos(j\varphi_s) & \text{if } \xi = r, z \\ r_s^l \sin(j\varphi_s) & \text{if } \xi = \varphi \end{cases} \quad (6)$$

is called the fundamental source distribution. In Eq. (5) a_ξ^{jl}, $\xi = r, \varphi, z$, are constant coefficients with proper units. Ap-

[13]Research Associate, Department of Civil Engineering and Operations Research, Princeton University, Princeton, NJ 08544. Assoc. Mem. ASME.

[14]Associate Professor, Center for Applied Stochastics Research and Ocean Engineering Department, Florida Atlantic University, Boca Raton, FL 33431.

Contributed by the ASME Applied Mechanics Division of THE AMERICAN SOCIETY OF MECHANICAL ENGINEERS for publication in the ASME JOURNAL OF APPLIED MECHANICS. Manuscript received by the ASME Applied Mechanics Division, June 29, 1992; final revision, Jan. 3, 1994. Associate Technical Editor: X. Markenscoff.

Downloaded 03 May 2010 to 171.66.16.20. Redistribution subject to ASME license or copyright; see http://www.asme.org/terms/Terms_Use.cfm

Temperature of Iron on the Superdeep Penetration," *Trudy Vsesouznogo Soveshania po Detonatcii, (Proceedings of All-Union Meeting on Detonation, Chernogolovka)*, pp. 152–157 (in Russian).

Influential Functions for a Layered Medium Subjected to a Finite Distributed Source

Ruichong Zhang[13] and Yan Yong[14]

Introduction

A Green's function is defined as a response field of a continuum medium subjected to a unidirectional unit impulse at a particular point (localized precisely in both space and time; Aki and Richards, 1980). For a typical source finitely distributed in a volume or on a surface, the response solution is an integration of infinite Green's functions that account for excitations all over the source region. Closed-form solutions are only found in special cases like a semi-infinite uniform medium with a circular source area (Pak, 1987). In many other cases such as an inhomogeneous medium or irregular source geometry, seeking Green's functions requires considerable efforts even if they do exist. Thus, determination of response solutions has mainly relied on numerical computations (Bouchon and Aki, 1979; Luco and Apsel, 1983; Kennett, 1983; Zhang et al., 1991). The computations are usually pursued by dividing the source region into subsections. The contribution of each subsection to the total response is represented by a Green's function of numerical form such that the response solution becomes a linear composition rather than an integration of Green's functions. Such computational scheme is equivalent to discretization of the source into a series of point sources evenly distributed in the source region.

A different decomposition scheme is proposed in this Note. A typical finitely distributed source is decomposed into a series of so-called fundamental sources, each of which is continuously distributed over the source region with a simple spatial variation. The numerical computation required in this approach is expected to be less time-consuming than the conventional Green's function approach. Such advantage appears prominent when responses in the near field are required. The reason for this is quite straight forward: responses at those locations close to the source area are usually sensitive to source spatial variations, and influence functions defined in this Note have a better ability to represent such variations compared to Green's functions. The merit of the current approach may be seen clearly in some inverse problems (Yong et al. 1994).

Formulation of the Problem

Consider a layered medium with a finitely distributed source buried in one of its layers, say, layer j. Each layer contains a linearly elastic, isotropic, and uniform medium. Since any motion can be expanded into time-harmonic components through the Fourier integral transformation, displacement $\mathbf{u}$ and traction $\mathbf{t}$ can be expressed in the frequency domain as

$$\mathbf{u}(r, \varphi, z, \omega) = \mathbf{u}_r\mathbf{e}_r + \mathbf{u}_\varphi\mathbf{e}_\varphi + \mathbf{u}_z\mathbf{e}_z$$

$$\mathbf{t}(r, \varphi, z, \omega) = \tau_{rz}\mathbf{e}_r + \tau_{\varphi z}\mathbf{e}_\varphi + \tau_{zz}\mathbf{e}_z \quad (1)$$

where $\mathbf{e}_r$, $\mathbf{e}_\varphi$ and $\mathbf{e}_z$ are unit vectors in the r, φ and z directions, respectively.

Continuity conditions at each layer-to-layer interface require that displacement $\mathbf{u}$ and traction $\mathbf{t}$ be continuous across the interface. Boundary conditions can be either finite or infinite. At a finite boundary, one half of the displacement and traction components are constrained. For instance, a free surface is associated with $\mathbf{t}(r, \varphi, z, \omega)|_{z=0} = \mathbf{0}$. A layered medium with an infinite boundary embodies one layer of infinite depth. Any wave traveling into this layer can never be bounced back. A buried source in a layered medium usually falls into one of the following kinds:

$$\mathbf{u}(r, \varphi, z, \omega)|_{z=z_s^+} - \mathbf{u}(r, \varphi, z, \omega)|_{z=z_s^-} = \Delta\mathbf{u}(r, \varphi, \omega), \quad r \le a(\varphi) \quad (2)$$

$$\mathbf{t}(r, \varphi, z, \omega)|_{z=z_s^+} - \mathbf{t}(r, \varphi, z, \omega)|_{z=z_s^-} = \Delta\mathbf{t}(r, \varphi, \omega), \quad r \le a(\varphi) \quad (3)$$

where $a(\varphi)$ is the boundary of a source area. It is noted that these two kinds of discontinuity sources cannot take place simultaneously; the physics will be violated otherwise.

In a conventional approach, the response to a finitely distributed source is calculated from the following integration:

$$G_{\eta\xi}(r, \varphi, z, \omega) = \int_0^{2\pi}\int_0^{a(\varphi)} g_{\eta\xi}(r, \varphi, z, \omega; r_s, \varphi_s, z_s) S_\xi(r_s, \varphi_s, \omega) r_s dr_s d\varphi_s, \quad \xi, \eta = r, \varphi, z \quad (4)$$

where $G_{\eta\epsilon}$ is a displacement or stress response component in the η-direction responding to source $S_\xi(r, \varphi, \omega)$, which is the ξ-th component of a finitely distributed source representing either $\Delta\mathbf{u}$ or $\Delta\mathbf{t}$, and $g_{\eta\xi}$ is a Green's function in the η-direction due to point excitation $S_\xi(r_s, \varphi_s, \omega)/|S_\xi(r_s, \varphi_s, \omega)|$. Green's function $g_{\eta\xi}$ can be obtained by solving the equation of motion along with constitutive equations, continuity conditions and boundary conditions (e.g., Aki and Richards, 1980). However, $g_{\eta\xi}$ usually has a complicated representation for an inhomogeneous medium. A closed-form integral in Eq. (4) is very difficult to obtain, if not impossible. As a result, an expensive numerical computation is required to calculate the integration in Eq. (4). Also, the computational scheme is equivalent to the discretization of a distributed source into a series of point sources evenly distributed in the source region.

Instead of adopting the representation in Eq. (4) and the associated numerical treatment, an alternative approach is proposed, which begins with a series expansion of a typical finitely distributed source. Without loss of generality, we only consider the symmetric part of the distributed source. The antisymmetric part can be treated in the same way.

A typical symmetrical source with respect to $\varphi = 0$, either $\Delta\mathbf{u}$ or $\Delta\mathbf{t}$, can be represented by

$$\mathbf{S}(r_s, \varphi_s, \omega) = \sum_j \sum_l \sum_{\xi=r,\varphi,z} a_\xi^{jl}\, \Phi_\xi^{jl}(r_s, \varphi_s)\mathbf{e}_\xi; \quad 0 \le r_s \le a(\varphi_s),\ 0 \le \varphi_s \le 2\pi \quad (5)$$

in which

$$\Phi_\xi^{jl}(r_s, \varphi_s) = \begin{cases} r_s^l \cos(j\varphi_s) & \text{if } \xi = r, z \\ r_s^l \sin(j\varphi_s) & \text{if } \xi = \varphi \end{cases} \quad (6)$$

is called the fundamental source distribution. In Eq. (5) a_ξ^{jl}, $\xi = r, \varphi, z$, are constant coefficients with proper units. Ap-

[13]Research Associate, Department of Civil Engineering and Operations Research, Princeton University, Princeton, NJ 08544. Assoc. Mem. ASME.

[14]Associate Professor, Center for Applied Stochastics Research and Ocean Engineering Department, Florida Atlantic University, Boca Raton, FL 33431.

Contributed by the ASME Applied Mechanics Division of THE AMERICAN SOCIETY OF MECHANICAL ENGINEERS for publication in the ASME JOURNAL OF APPLIED MECHANICS. Manuscript received by the ASME Applied Mechanics Division, June 29, 1992; final revision, Jan. 3, 1994. Associate Technical Editor: X. Markenscoff.

Copyright © 1994 by ASME
Downloaded 03 May 2010 to 171.66.16.20. Redistribution subject to ASME license or copyright; see http://www.asme.org/terms/Terms_Use.cfm

parently, the variation of φ_s for the source representation was expanded using the finite Fourier transform while the variation of r_s was represented, or more precisely fitted, by a polynomial. The response to the finitely distributed source in the ηth direction can then be simply expressed as

$$G_{\eta\xi}(r, \varphi, z, \omega) = \sum_j \sum_l a_\xi^{jl} G_{\eta\xi}^{jl}(r, \varphi, z, \omega); \quad \eta, \xi = r, \varphi, z \tag{7}$$

where $G_{\eta\xi}^{jl}$ is the response to basic loading $\Phi_{\eta\xi}^{jl}\,\mathbf{e}_\xi$, called influence frequency response function or simply influence function. It is noted that in the numerical computation, only finite terms are needed in the series, say, $j = 0, \ldots, M-1$ and $l = 0, \ldots, N-1$. Given a set of influence functions, the response is only related to $M \times N$ constants a_ξ^{jl} that characterize the source distribution. In a forward problem, $S(r_s, \varphi_s, z)$ is known and the corresponding coefficients can be determined using such approach as the least squares. In an inverse problem, the distribution of $S(r_s, \varphi_s, z)$ is unknown and the coefficients can be determined by solving $M \times N$ simultaneous algebraic equations that are obtained through evaluating Eq. (7) at $M \times N$ different locations. It is noted that in many engineering problems a source with large spatial variation usually results in a response with small spatial variation, and vice versa. Typical examples may be found as an indentation by a flat-ended cylinder and crack opening or shear dislocation in an elastic medium. The former is associated with the soil-structure interaction problem while the latter with eruption mechanism of a seismic source. In general, $M \times N$ is not expected to be large in leading to accurate results (Yong et al., 1993).

In what follows, influence functions are formulated to constitute a vector

$$\mathbf{G}_\xi^{jl}(r, \varphi, z, \omega) = G_{r\xi}^{jl}(r, \varphi, z, \omega)\mathbf{e}_r + G_{\varphi\xi}^{jl}(r, \varphi, z, \omega)\mathbf{e}_\varphi + G_{z\xi}^{jl}(r, \varphi, z, \omega)\mathbf{e}_z; \quad \xi = r, \varphi, z \tag{8}$$

that responds to the fundamental source defined by

$$\zeta_\xi = \delta_{\xi r}\Phi_r^{jl}\mathbf{e}_r + \delta_{\xi\varphi}\Phi_\varphi^{jl}\mathbf{e}_\varphi + \delta_{\xi z}\Phi_z^{jl}\mathbf{e}_z \tag{9}$$

where δ is a generalized Kroneck Delta function, being equal to one if the two subindexes are the same and zero otherwise.

Representation of Influence Functions

Following Takeuchi and Saito (1972), it is shown that displacement $\mathbf{u}$ and traction $\mathbf{t}$ can be expanded as

$$\mathbf{u}(r, \varphi, z, \omega) = \frac{1}{2\pi}\sum_{m=-\infty}^{\infty}\sum_{n=1}^{\infty}\frac{2}{[r_T J_m'(k_n r_T)]^2}(W_R\mathbf{R}_{k_n}^m + W_S\mathbf{S}_{k_n}^m + W_T\mathbf{T}_{k_n}^m); \quad r \le r_T$$

$$\mathbf{t}(r, \varphi, z, \omega) = \frac{\omega}{2\pi}\sum_{m=-\infty}^{\infty}\sum_{n=1}^{\infty}\frac{2}{[r_T J_m'(k_n r_T)]^2}(F_R\mathbf{R}_{k_n}^m + F_S\mathbf{S}_{k_n}^m + F_T\mathbf{T}_{k_n}^m); \quad r \le r_T \tag{10}$$

where r_T denotes the truncated radius, m is the azimuthal order, k_n is wave number determined based on transcendental equation $J_m(k_n r_T) = 0$ for a given m, and orthogonal vector harmonics are

$$\mathbf{R}_{k_n}^m = Y_{k_n}^m(r, \varphi)\mathbf{e}_z; \quad \mathbf{S}_{k_n}^m = \frac{1}{k_n}\frac{\partial Y_{k_n}^m}{\partial r}\mathbf{e}_r + \frac{1}{k_n r}\frac{\partial Y_{k_n}^m}{\partial \varphi}\mathbf{e}_\varphi;$$

$$\mathbf{T}_{k_n}^m \frac{1}{k_n r}\frac{\partial Y_{k_n}^m}{\partial \varphi}\mathbf{e}_r - \frac{1}{k_n}\frac{\partial Y_{k_n}^m}{\partial r}\mathbf{e}_\varphi \tag{11}$$

in which $Y_{k_n}^m = J_m(k_n r)e^{im\varphi}$. The orthogonality is interpreted in terms of a double integration of two dotted vectors within $(0, r_T)$ and $(0, 2\pi)$. Such integration in fact is a finite Fourier Hankel transformation. It can be shown (Kennett, 1983) that $\mathbf{w} \equiv \{W_R, W_S\}^T$ and $\mathbf{f} \equiv \{F_R, F_s\}^T$ are associated with the motion of P-SV waves, whereas $w \equiv W_T$ and $f \equiv F_T$ are associated with the motion of SH waves.

Performing the finite Fourier Hankel transform on Eq. (9), we obtain

$$Z_{R\xi}^{jl} = \int_0^a r dr \int_0^{2\pi} d\varphi\, \zeta_\xi^{jl} \cdot (\mathbf{R}_{k_n}^m)^* = \delta_{\xi z}\mathbf{I}(m, l+1)\pi\delta_{|m|j}$$

$$Z_{S\xi}^{jl} = \int_0^a r dr \int_0^{2\pi} d\varphi\, \zeta_\xi^{jl} \cdot (\mathbf{S}_{k_n}^m)^* = \left\{\frac{a^{l+1}}{k_n}[J_m(k_n a) - J_m(0)]\,\delta_{\xi r} - \frac{(l+1)\delta_{\xi r} + |m|\delta_{\xi\varphi}}{k_n} I(m, l)\right\}\pi\delta_{|m|j}$$

$$Z_{T\xi}^{jl} = \int_0^a r dr \int_0^{2\pi} d\varphi\, \zeta_\xi^{jl} \cdot (\mathbf{T}_{k_n}^m)^* = i\left\{\mathrm{sig}(m)\frac{a^{l+1}}{k_n}[J_m(k_n a) - J_m(0)]\delta_{\xi\varphi} - \frac{\mathrm{sig}(m)(l+1)\delta_{\xi\varphi} + m\delta_{\xi r}}{k_n} I(m, l)\right\}\pi\delta_{|m|j} \tag{12}$$

where Z's are ΔW's or $\omega\Delta F$'s if ζ^ξ represents displacement or stress discontinuities accordingly, a is the radius of a circular source and $I(m, l) = \int_0^a r^l J_m(k_n r)dr$. When $l \pm m$ is a positive odd integer,

$$I(l, 2m+1) = \frac{a^{2m+l-1}}{k_n}(m-1)! \times \sum_{j=0}^{m-1}\left(\frac{-2}{k_n a}\right)^j \frac{J_{l+j+1}(k_n a)}{(m-j-1)!}; \quad m = 1, 2, \ldots \tag{13}$$

Otherwise, it can be represented by Bessel, Gamma, and Lommel functions.

With the representation of the fundamental source in the transformed domain, it can be proved (Yong and Lin, 1992) that the corresponding responses at depth z_o are

$$\begin{Bmatrix} w \\ f \end{Bmatrix} = \begin{bmatrix} \mathbf{M}_u(i) & \mathbf{M}_d(i) \\ \mathbf{N}_u(i) & \mathbf{N}_d(i) \end{bmatrix} \begin{Bmatrix} \mathbf{I} \\ R(b_u, o) \end{Bmatrix} \times [\mathbf{I} - \mathbf{R}(s^-, z_o)\mathbf{R}(b_u, o)]^{-1}\mathbf{T}(o, s^-)\mu_u(s^-), \quad \text{if } z_{i-1}^+ \le z_o \le z_i^- \le z_s^- \tag{14}$$

where $\mu_u(s^-)$ is a wave vector generated by a seismic source at z_s. In Eq. (14), $\mathbf{I}$ denotes the identity matrix, $\mathbf{M}(i)$ and $\mathbf{N}(i)$ are functions of material properties of the ith layer such as P and S wave speeds and material density, $\mathbf{R}(m, n)$ and $\mathbf{T}(m, n)$ represent the reflection and transmission matrices in the medium bounded by z_m and z_n, where subscript m and n may be i, b_u, b_d, o, and s, representing locations associated with a layer-to-layer interface, top boundary, bottom boundary, observation site and source, respectively. Closed-form matrices $\mathbf{M}$, $\mathbf{N}$, $\mathbf{R}$, and $\mathbf{T}$ are given in Zhang et al. (1991). Substituting influence functions in the transformed domain, i.e., Eq. (14), into Eq. (10), we obtain the influence functions in the frequency space domain.

Downloaded 03 May 2010 to 171.66.16.20. Redistribution subject to ASME license or copyright; see http://www.asme.org/terms/Terms_Use.cfm

Examples and Verification With Existent Analytical Solutions

To show the merit of this new analytical approach, we present the following two examples of different source loadings. Response solutions determined using the current approach are verified with existing analytical solutions.

Example 1: Distributed Discontinuities of Vertical Components. A discontinuity in the z direction is corresponding to $a_r^{jl} = a_\varphi^{jl} = 0$ (cf. Eq. (5)). When $j = l = 0$, the source is axisymmetric and associated with a distributed vertical external load or an opening crack. In particular, a uniformly distributed vertical load on a circle with radius a can be expressed as $\Delta \mathbf{u} = 0$ and $\Delta \mathbf{t} = \mathbf{e}_z/\pi a^2$. The discontinuity across the depth z_s in the transformed domain (cf. Eq. (12)) can be found as follows:

$$\Delta F_R = -\frac{2}{\omega}\frac{J_1(k_n a)}{k_n a}; \quad \Delta F_S = \Delta F_T = \Delta W_R = \Delta W_S = \Delta W_T = 0. \tag{15}$$

The corresponding displacement responses in frequency domain then can be expressed as (cf. Eq. (10))

$$u_r(r, \varphi, z, \omega) = -\sum_{n=1}^{\infty} \frac{2}{r_T^2[J_0'(k_n r_T)]^2}\frac{1}{2\pi} W_S J_1(k_n r)$$

$$u_\varphi(r, \varphi, z, \omega) = 0$$

$$u_z(r, \varphi, z, \omega) = \sum_{n=1}^{\infty} \frac{2}{r_T^2[J_0'(k_n r_T)]^2}\frac{1}{2\pi} W_R J_0(k_n r) \tag{16}$$

where W_S and W_R are obtained from Eq. (14). Consider a degenerated case of a uniform half-space. When $r_T \to \infty$, $\Sigma\, 2/[r_T J_0'(k_n r_T)]^2$ approaches to $\int_0^\infty dk$. It is interesting to note that Eq. (16) is the same as Eq. (35) in Pak (1987). Solutions in Pak (1987) were obtained through the method of potentials.

Example 2: Distributed Discontinuities of Horizontal Components. In this case $a_z^{jl} = 0$. If $a_r^{jl} = -a_\varphi^{jl}$ for $j = 1$ or $a_r^{jl} = a_\varphi^{jl}$ $j = -1$, the discontinuity in displacement in fact represents a dislocation in the x-direction (also called pure shear slip); the discontinuity in stresses is associated with a horizontal force applying in the x-direction. This is a special case of a uniformly distributed shear slip associated with $a_r^{10} = -a_\varphi^{10} = D/(\pi a^2)$, where D is the permanent slip in the x direction. Its counterpart in the transformed domain can be found from Eq. (12) as

$$\Delta F_R = \Delta F_S = \Delta F_T = \Delta W_R = 0; \quad \Delta W_S = \pm\frac{D J_1(k_n a)}{k_n a},$$

$$\Delta W_T = -i\frac{D J_1(k_n a)}{k_n a}; \quad m = \pm 1. \tag{17}$$

It can be verified that as radius a approaches to zero, the response solutions reduce to those obtained by Kennett (1983). It is noted that Kennett's results were obtained by solving the equation of motion with replacement of a shear slip by equivalent double-couple body forces.

Acknowledgments

The research reported in this Note was supported by the National Science Foundation under grant BCS-9057052. This support is gratefully acknowledged.

References

Aki, K., and Richards, P. G., 1980, *Quantitative Seismology—Theory and Methods*, Vol. 1 and 2, W. H. Freeman and Company.

Bouchon, M., and Aki, K., 1977, "Discrete Wave-Number Representation of Seismic-Source Wave Fields," *Bull. Seis. Soc. Am.*, Vol. 67, No. 2, pp. 259–277.

Kennett, B. L. N., 1985, *Seismic Wave Propagation in Stratified Media*, Cambridge University Press, New York.

Luco, J. E., and Apsel, R. J., 1983, "On the Green's Functions for a Layered Half-Space, Part I," *Bull. Seis. Soc. Am.*, Vol. 73, No. 4, pp. 909–929.

Pak, R. Y. S., 1987, "Asymmetric Wave Propagation in an Elastic Half-Space by a Method of Potentials," ASME JOURNAL OF APPLIED MECHANICS, Vol. 54, pp. 121–126.

Takeuchi, H., and Saito, M., 1972, "Seismic Surface Waves," *Methods in Computational Physics*, Vol. 11, pp. 217–295.

Yong, Y., and Lin, Y. K., 1992, "Dynamic Response Analysis of Trust-Type Structural Networks—A Wave Propagation Approach," *Journal of Sound and Vibration*, Vol. 156, No. 1, pp. 27–45.

Yong, Y., Yu, J., and Zhang, R. C., 1994, "Soil-Structure Interaction under Earthquake Excitations," *Proceedings of the 5th U.S. National Conference on Earthquake Engineering*, Chicago, IL, July 10–14, pp. 15–24.

Zhang, R. C., Yong, Y., and Lin. Y. K., 1991a, "Earthquake Ground Motion Modeling I: Deterministic Point Source; II: Stochastic Line Source," *J. Eng. Mech.*, Vol. 117, No. 9, pp. 2114–2148.

The Complete Stress Field due to a Dislocation Located Anywhere in Two Bonded Quarter Planes

P. Kelly,[15] D. A. Hills,[15] and D. Nowell[15]

1 Introduction

In a paper by the authors (Kelly et al., 1993a), the state of stress arising *along* the interface between two dissimilar quarter planes induced by a dislocation situated *on* the interface was given. It has now proved possible to develop the method to deal with the (more general) state of stress arising *anywhere* within the two quarter planes induced by a dislocation situated *anywhere* within the quarter planes, and hence provide the means of solving the problem of a crack lying anywhere within the quarter planes. This problem is of some practical importance as the fracture resistance of interfaces between ceramics and metals is often greater than that of the ceramic component. Thus crack propagation often occurs within the ceramic component rather than on the interface itself (Evans et al., 1985). The method of solution and nomenclature employed is exactly as that used in Kelly et al. (1993a).

2 Method of Solution

The general problem posed is shown in Fig. 1(*a*) where the dislocation is located, without loss of generality, in Region "1" at position (a, ϕ) while the resulting state of stress is to be obtained at a general position (r, θ) which may lie within either quarter plane (θ is measured counterclockwise from the interface, ϕ counterclockwise from the free edge of Region "1").

As in Kelly et al. (1993a), the complete stress field $\sigma(r, \theta)$ is obtained as follows: First, the stress field due to a dislocation having resolved Burgers vector components b_x and b_y, situated at position (a, ϕ) in Region "1" of two bonded half-planes (see Fig. 1(*b*)), is evaluated. The next step is to clear the line $\theta = \mp\pi/2$ of tractions, thus creating a free surface—the faces

[15]Department of Engineering Science, Oxford University, Parks Road, Oxford, OX1 3PJ, England.

Contributed by the Applied Mechanics Division of THE AMERICAN SOCIETY OF MECHANICAL ENGINEERS for publication in the ASME JOURNAL OF APPLIED MECHANICS. Manuscript received by the ASME Applied Mechanics Division, Sept. 20, 1993; final revision, Sept. 20, 1993. Associate Technical Editor: D. M. Barnett.

Downloaded 03 May 2010 to 171.66.16.20. Redistribution subject to ASME license or copyright; see http://www.asme.org/terms/Terms_Use.cfm

Examples and Verification With Existent Analytical Solutions

To show the merit of this new analytical approach, we present the following two examples of different source loadings. Response solutions determined using the current approach are verified with existing analytical solutions.

Example 1: Distributed Discontinuities of Vertical Components. A discontinuity in the z direction is corresponding to $a_r^{jl} = a_\varphi^{jl} = 0$ (cf. Eq. (5)). When $j = l = 0$, the source is axisymmetric and associated with a distributed vertical external load or an opening crack. In particular, a uniformly distributed vertical load on a circle with radius a can be expressed as $\Delta \mathbf{u} = 0$ and $\Delta \mathbf{t} = \mathbf{e}_z/\pi a^2$. The discontinuity across the depth z_s in the transformed domain (cf. Eq. (12)) can be found as follows:

$$\Delta F_R = -\frac{2}{\omega}\frac{J_1(k_n a)}{k_n a}; \quad \Delta F_S = \Delta F_T = \Delta W_R = \Delta W_S = \Delta W_T = 0. \tag{15}$$

The corresponding displacement responses in frequency domain then can be expressed as (cf. Eq. (10))

$$u_r(r, \varphi, z, \omega) = -\sum_{n=1}^{\infty} \frac{2}{r_T^2[J_0'(k_n r_T)]^2}\frac{1}{2\pi} W_S J_1(k_n r)$$

$$u_\varphi(r, \varphi, z, \omega) = 0$$

$$u_z(r, \varphi, z, \omega) = \sum_{n=1}^{\infty} \frac{2}{r_T^2[J_0'(k_n r_T)]^2}\frac{1}{2\pi} W_R J_0(k_n r) \tag{16}$$

where W_S and W_R are obtained from Eq. (14). Consider a degenerated case of a uniform half-space. When $r_T \to \infty$, $\Sigma\, 2/[r_T J_0'(k_n r_T)]^2$ approaches to $\int_0^\infty dk$. It is interesting to note that Eq. (16) is the same as Eq. (35) in Pak (1987). Solutions in Pak (1987) were obtained through the method of potentials.

Example 2: Distributed Discontinuities of Horizontal Components. In this case $a_z^{jl} = 0$. If $a_r^{jl} = -a_\varphi^{jl}$ for $j = 1$ or $a_r^{jl} = a_\varphi^{jl}$ $j = -1$, the discontinuity in displacement in fact represents a dislocation in the x-direction (also called pure shear slip); the discontinuity in stresses is associated with a horizontal force applying in the x-direction. This is a special case of a uniformly distributed shear slip associated with $a_r^{10} = -a_\varphi^{10} = D/(\pi a^2)$, where D is the permanent slip in the x direction. Its counterpart in the transformed domain can be found from Eq. (12) as

$$\Delta F_R = \Delta F_S = \Delta F_T = \Delta W_R = 0; \quad \Delta W_S = \pm\frac{D J_1(k_n a)}{k_n a},$$

$$\Delta W_T = -i\frac{D J_1(k_n a)}{k_n a}; \quad m = \pm 1. \tag{17}$$

It can be verified that as radius a approaches to zero, the response solutions reduce to those obtained by Kennett (1983). It is noted that Kennett's results were obtained by solving the equation of motion with replacement of a shear slip by equivalent double-couple body forces.

Acknowledgments

The research reported in this Note was supported by the National Science Foundation under grant BCS-9057052. This support is gratefully acknowledged.

References

Aki, K., and Richards, P. G., 1980, *Quantitative Seismology—Theory and Methods*, Vol. 1 and 2, W. H. Freeman and Company.

Bouchon, M., and Aki, K., 1977, "Discrete Wave-Number Representation of Seismic-Source Wave Fields," *Bull. Seis. Soc. Am.*, Vol. 67, No. 2, pp. 259–277.

Kennett, B. L. N., 1985, *Seismic Wave Propagation in Stratified Media*, Cambridge University Press, New York.

Luco, J. E., and Apsel, R. J., 1983, "On the Green's Functions for a Layered Half-Space, Part I," *Bull. Seis. Soc. Am.*, Vol. 73, No. 4, pp. 909–929.

Pak, R. Y. S., 1987, "Asymmetric Wave Propagation in an Elastic Half-Space by a Method of Potentials," ASME JOURNAL OF APPLIED MECHANICS, Vol. 54, pp. 121–126.

Takeuchi, H., and Saito, M., 1972, "Seismic Surface Waves," *Methods in Computational Physics*, Vol. 11, pp. 217–295.

Yong, Y., and Lin, Y. K., 1992, "Dynamic Response Analysis of Trust-Type Structural Networks—A Wave Propagation Approach," *Journal of Sound and Vibration*, Vol. 156, No. 1, pp. 27–45.

Yong, Y., Yu, J., and Zhang, R. C., 1994, "Soil-Structure Interaction under Earthquake Excitations," *Proceedings of the 5th U.S. National Conference on Earthquake Engineering*, Chicago, IL, July 10–14, pp. 15–24.

Zhang, R. C., Yong, Y., and Lin. Y. K., 1991a, "Earthquake Ground Motion Modeling I: Deterministic Point Source; II: Stochastic Line Source," *J. Eng. Mech.*, Vol. 117, No. 9, pp. 2114–2148.

The Complete Stress Field due to a Dislocation Located Anywhere in Two Bonded Quarter Planes

P. Kelly,[15] D. A. Hills,[15] and D. Nowell[15]

1 Introduction

In a paper by the authors (Kelly et al., 1993a), the state of stress arising *along* the interface between two dissimilar quarter planes induced by a dislocation situated *on* the interface was given. It has now proved possible to develop the method to deal with the (more general) state of stress arising *anywhere* within the two quarter planes induced by a dislocation situated *anywhere* within the quarter planes, and hence provide the means of solving the problem of a crack lying anywhere within the quarter planes. This problem is of some practical importance as the fracture resistance of interfaces between ceramics and metals is often greater than that of the ceramic component. Thus crack propagation often occurs within the ceramic component rather than on the interface itself (Evans et al., 1985). The method of solution and nomenclature employed is exactly as that used in Kelly et al. (1993a).

2 Method of Solution

The general problem posed is shown in Fig. 1(*a*) where the dislocation is located, without loss of generality, in Region "1" at position (a, ϕ) while the resulting state of stress is to be obtained at a general position (r, θ) which may lie within either quarter plane (θ is measured counterclockwise from the interface, ϕ counterclockwise from the free edge of Region "1").

As in Kelly et al. (1993a), the complete stress field $\sigma(r, \theta)$ is obtained as follows: First, the stress field due to a dislocation having resolved Burgers vector components b_x and b_y, situated at position (a, ϕ) in Region "1" of two bonded half-planes (see Fig. 1(*b*)), is evaluated. The next step is to clear the line $\theta = \mp\pi/2$ of tractions, thus creating a free surface—the faces

[15]Department of Engineering Science, Oxford University, Parks Road, Oxford, OX1 3PJ, England.

Contributed by the Applied Mechanics Division of THE AMERICAN SOCIETY OF MECHANICAL ENGINEERS for publication in the ASME JOURNAL OF APPLIED MECHANICS. Manuscript received by the ASME Applied Mechanics Division, Sept. 20, 1993; final revision, Sept. 20, 1993. Associate Technical Editor: D. M. Barnett.

Copyright © 1994 by ASME
Downloaded 03 May 2010 to 171.66.16.20. Redistribution subject to ASME license or copyright; see http://www.asme.org/terms/Terms_Use.cfm

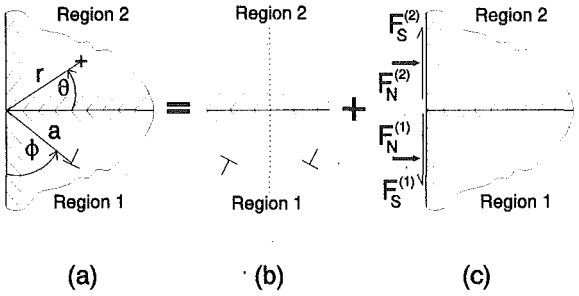


Fig. 1 Geometry of the problem; (*a*) the problem to be solved, (*b*) dislocation and its image present in two bonded half-planes, and (*c*) the surface stresses needed to render the intended free surface traction-free

of the quarter planes. To effect this, an image dislocation (i.e., a dislocation having resolved Burgers vector components $-b_x$ and $-b_y$ at position $(a, -\phi)$) is employed. The stress field due to both the dislocation with Burgers vector component b_x and its image, $-b_x$, gives rise to zero normal tractions on the line $\theta = \mp\pi/2$. Similarly, the stress field due to both the dislocation with Burgers vector component b_y and its image generates no shear tractions on $\theta = \mp\pi/2$. Thus, an analytic solution is found, denoted by $\tilde{\sigma}(r, \theta)$, i.e., which comprises the stress field due to both the dislocation and its image, and which clears the intended faces of the quarter planes of *one* set of tractions for each of the Burgers vector components of the dislocation in question.

Finally, a third solution must be superimposed. This is the "clearing" traction stress field $\bar{\sigma}(r, \theta)$, which clears the line $\theta = \mp\pi/2$ of any remaining tractions, as shown in Fig. 1(*c*), and which constitutes the stress field arising in two bonded quarter planes, when the faces are loaded by tractions equal and opposite to those arising from the image dislocation solution described above. Thus, the complete stress field, $\sigma(r, \theta)$, is given by

$$\sigma(r, \theta) = \tilde{\sigma}(r, \theta) + \bar{\sigma}(r, \theta). \tag{1}$$

The stress field induced by a dislocation at position (a, ϕ) in two bonded half-planes (Fig. 1(*b*)) may be derived from the Airy stress function for a dislocation given by Dundurs and Mura (1964) (see, for example, Kelly et al., 1993b). The stress field due to the image dislocation may also be obtained from this solution, giving $\tilde{\sigma}(r, \theta)$.

3 Influence of Clearing Tractions

The principal new results which we wish to include here are the influence of the clearing tractions, Fig. 1(*c*). These are found by the Mellin transform technique, using Eq. (8) of Kelly et al. (1993a). From recipes given by Erdélyi et al. (1954), the results are:

For Region 2:

$$\frac{(\kappa_1+1)}{4b_y a^{s+1}\mu_1}\hat{F}^{(2)}_{N_e} = \frac{1+\alpha}{1-\beta^2}\left\{\beta\frac{\sin[(s+1)\phi]}{\sin[(s+1)\pi]} - \frac{\cos[(s+1)\phi]}{\sin[(s+1)\pi]} \times ((s+1)(1-\beta)\cos\phi\ \sin\phi)\right\}$$

$$\frac{(\kappa_1+1)}{4b_y a^{s+1}\mu_1}\hat{F}^{(2)}_{N_o} = \frac{1+\alpha}{1-\beta^2}\left\{-\frac{\sin[(s+1)\phi]}{\sin[(s+1)\pi]} \times (s+1)[2\beta+(1-\beta)\sin^2\phi]\right\}$$

$$\frac{(\kappa_1+1)}{4b_x a^{s+1}\mu_1}\hat{F}^{(2)}_{S_e} = \frac{1+\alpha}{1-\beta^2}\left\{\beta\frac{\sin[(s+1)\phi]}{\sin[(s+1)\pi]} + \frac{\cos[(s+1)\phi]}{\sin[s+1)\pi]}((s+1)(1-\beta)\cos\phi\ \sin\phi)\right\} \tag{2,a-d}$$

$$\frac{(\kappa_1+1)}{4b_x a^{s+1}\mu_1}\hat{F}^{(2)}_{S_o} = \frac{1+\alpha}{1-\beta^2}\left\{+\frac{\sin[(s+1)\phi]}{\sin[(s+1)\pi]} \times (s+1)[2\beta+(1-\beta)\sin^2\phi]\right\}$$

and, for Region 1:

$$\frac{(\kappa_1+1)}{4b_y a^{s+1}\mu_1}\hat{F}^{(1)}_{N_e} = +(s+1)\sin\phi\ \cos\phi\left[\frac{\cos[(s+1)(\pi-\phi)]}{\sin[(s+1)\pi]} - \frac{\beta-\alpha}{1+\beta}\frac{\cos[(s+1)\phi]}{\sin[(s+1)\pi]}\right] + \frac{\sin[(s+1)\phi]}{\sin[(s+1)\pi]} \times \left[\frac{-\beta(1+\alpha)}{1-\beta^2} - 2\frac{\beta-\alpha}{1+\beta}(s+1)^2\cos^2\phi\right]$$

$$\frac{(\kappa_1+1)}{4b_y a^{s+1}\mu_1}\hat{F}^{(1)}_{N_o} = (s+1)\left[-\sin^2\phi\frac{\sin[(s+1)(\pi-\phi)]}{\sin[(s+1)\pi]} + \frac{\beta-\alpha}{1+\beta}(s+1)\sin 2\phi\frac{\cos[(s+1)\phi]}{\sin[(s+1)\pi]} + \frac{\beta-\alpha}{1+\beta}(2\cos^2\phi+\sin^2\phi)\frac{\sin[(s+1)\phi]}{\sin[(s+1)\pi]}\right] \tag{3,a-d}$$

$$\frac{(\kappa_1+1)}{4b_x a^{s+1}\mu_1}\hat{F}^{(1)}_{S_e} = -(s+1)\sin\phi\ \cos\phi\left[\frac{\cos[(s+1)(\pi-\phi)]}{\sin[(s+1)\pi]} - \frac{\beta-\alpha}{1+\beta}\frac{\cos[(s+1)\phi]}{\sin[(s+1)\pi]}\right] + \frac{\sin[(s+1)\phi]}{\sin[(s+1)\pi]} \times \left[\frac{-\beta(1+\alpha)}{1-\beta^2} - 2\frac{\beta-\alpha}{1+\beta}(s+1)^2\cos^2\phi\right]$$

$$\frac{(\kappa_1+1)}{4b_x a^{s+1}\mu_1}\hat{F}^{(1)}_{S_o} = (s+1)\left[+\sin^2\phi\frac{\sin[(s+1)(\pi-\phi)]}{\sin[(s+1)\pi]} + \frac{\beta-\alpha}{1+\beta}(s+1)\sin 2\phi\frac{\cos[(s+1)\phi]}{\sin[(s+1)\pi]} - \frac{\beta-\alpha}{1+\beta}(2\cos^2\phi+\sin^2\phi)\frac{\sin[(s+1)\phi]}{\sin[(s+1)\pi]}\right]$$

where α and β are Dundurs' constants. If the value of ϕ is specialized to $\pi/2$, these equations reduce to Eqs. (9) of Kelly et al. (1993a). Substituting these values into equations (3.14, 3.15) of Bogy (1970) yields the stress field $\hat{\sigma}(s, \theta)$, from which the "clearing" traction solution $\bar{\sigma}(r, \theta)$ may be obtained by application of the inverse Mellin transform integral.

The solution generated thus provides a Green's function which may be used as the kernel in an integral equation formulation for the solution of cracks adjacent as well as on the interface, and either buried or breaking the free surface.

References

Bogy, D. B., 1970, "On the Problem of Edge Bonded Elastic Quarter Planes Loaded at the Boundary," *International Journal of Solids and Structures*, Vol. 6, pp. 1287–1313.

Dundurs, J., and Mura, T., 1964, "Interaction Between an Edge Dislocation and a Circular Inclusion," *Journal of Mechanics and Physics of Solids*, Vol. 12, pp. 177–189.

Erdélyi, A., Magnus, W., Oberhettinger, F., and Tricomi, F. G., 1954, *Tables of Integral Transforms*, Vol. I, McGraw-Hill, New York, pp. 307–311.

Evans, A. G., Ruhle, M., and Turwitt, M., 1985, "On the Mechanics of Failure in Ceramic/Metal Bonded Systems," *Journal de Physique*, Vol. 46, No. C4, pp. 613–625.

Kelly, P. A., Hills, D. A., and Nowell, D., 1993a, "The Stress Field due to a Dislocation on the Interface Between Two Quarter Planes," ASME JOURNAL OF APPLIED MECHANICS, Vol. 60, pp. 743–748.

Kelly, P. A., Hills, D. A., and Nowell, D., 1993b, "The Stress Concentration Produced by a Hole Near an Interface or Joint," *Proceedings IMechE Part C: Journal of Mechanical Engineering Science*, Vol. 207, pp. 239–246.

Downloaded 03 May 2010 to 171.66.16.20. Redistribution subject to ASME license or copyright; see http://www.asme.org/terms/Terms_Use.cfm

A Note on Interface Cracks With and Without Friction in Contact Zone

X. Deng[16]

A complete set of Comninou's bimaterial interface crack-tip fields with and without friction in the contact zone (Comninou, 1977a,b) is given in terms of several arbitrary analytic functions. When the bimaterial becomes homogeneous, the complex function representation fully describes the crack-tip field for a cracked body under conditions of crack surface contact and slip, which can occur when the body is subjected to combined compression and shear loadings.

Introduction

For a stationary interface crack between two homogeneous, isotropic, and linearly elastic solids, the two-dimensional crack-tip field under conditions of zero crack surface tractions, physically correct when there is no predicted interpenetration, can be put in a simple format with several arbitrary analytic functions (Rice, 1988), which is equivalent to a full Williams-type (Williams, 1957) series expansion. The leading term of the expansion, first obtained by Williams (1959), has oscillatory singularity and, as pointed out by England (1965), predicts crack surface interpenetration in a near-tip region, which is inconsistent with its underlying open-crack assumption. To overcome this inconsistency in the near-tip region, Comninou (1977a) introduced a crack-tip field that takes crack surface contact into consideration. By treating the contact as frictionless, she showed that the crack-tip singular field resembles that of the classical mode II problem. The crack-tip field and its singularity for the case of frictional crack surface contact was also given by Comninou (1977b).

In this Note, we report, in terms of several arbitrary analytic functions, a general representation of Comninou's interface crack-tip fields *with and without friction* in the contact zone, in a form similar to that used by Rice (1988), which corresponds to complete Williams-type series expansions of the crack-tip fields. We will make observations about certain connections existing between the interface crack-tip fields with crack surface contact and those without contact, and about how they compare with counterpart crack-tip fields in homogeneous solids. When the two component materials are identical, these analytic functions completely represent the stress and deformation fields around a crack whose surfaces are in frictionless or frictional contact, probably caused by combined compression and shear loadings. It turns out that the resulting singular field is exactly the same as that of the classic mode II problem, hence governed by a similarly defined stress intensity factor K_{II}, which relates to a nonzero *crack-tip* energy release rate even in the case of frictional crack surface contact.

Full Representations of Comninou's Interface Crack-Tip Fields

Consider an interface crack lying along the negative x-axis of a rectangular xy-coordinate system (with its origin at the crack tip and the x-axis pointing to the right). Assume that material 1 occupies the half-space above the x-axis and material 2, the half-space below the axis. Making use of Muskhelishvili's complex function formulation, one can express the stress and displacement fields for each of the two component materials in terms of two analytic functions, $\phi(z)$ and $\Omega(z)$, where $z=x+iy$ is the complex variable, through

$$2\mu(u_x+iu_y)=\kappa\phi(z)+(\bar{z}-z)\overline{\phi}'(\bar{z})-\overline{\Omega}(\bar{z})$$
$$\sigma_{xx}+\sigma_{yy}=2[\phi'(z)+\overline{\phi}'(\bar{z})]$$
$$\sigma_{yy}-\sigma_{xx}+2i\sigma_{xy}=2[(\bar{z}-z)\phi''(z)-\phi'(z)+\Omega'(z)] \quad (1)$$

where μ is the shear modulus; κ is related to the Poisson's ratio ν and equals $3-4\nu$ for plane strain $(3-\nu)/(1+\nu)$ for plane stress, a bar over an complex quantity denotes its complex conjugate; and $\phi'(z)=d\phi/dz$, and so on. The asymptotic boundary conditions to be satisfied by the analytic functions, namely $\phi_1(z)$ and $\Omega_1(z)$ for material 1, and $\phi_2(z)$ and $\Omega_2(z)$ for material 2 (whenever necessary, subscripts 1 and 2 will be used to signify quantities for materials 1 and 2, respectively), are as follows. Along the positive x-axis, tractions and displacements must be continuous across the material interface:

$$(\sigma_{xy})_1=(\sigma_{xy})_2,\ (\sigma_{yy})_1=(\sigma_{yy})_2;$$
$$(u_x)_1=(u_x)_2,\ (u_y)_1=(u_y)_2. \quad (2)$$

And along the negative x-axis, the crack surfaces must be either in frictionless contact

$$(\sigma_{xy})_1=(\sigma_{xy})_2=0,\ (\sigma_{yy})_1=(\sigma_{yy})_2\le 0;\ (u_y)_1=(u_y)_2 \quad (3)$$

or in frictional contact

$$(\sigma_{xy})_1=(\sigma_{xy})_2=-\rho(\sigma_{yy})_1,\ (\sigma_{yy})_1=(\sigma_{yy})_2\le 0;\ (u_y)_1=(u_y)_2 \quad (4)$$

where ρ equals the positive or negative value of the coefficient of kinetic friction depending on the relative sliding direction of the two crack faces. Specifically, $\rho>0$ when $d(u_x)_1/dt-d(u_x)_2/dt>0$ and $\rho<0$ when $d(u_x)_1/(dt-du_x)_2/dt<0$, where $d()/dt$ denotes time derivative.

It can be shown, with the method of analytic continuation, that the most general forms of $\phi_1(z)$, $\Omega_1(z)$, $\phi_2(z)$, and $\Omega_2(z)$ that obey (2) and (3) (frictionless contact) can be written as

$$\phi_1'(z)=\frac{z^{-1/2}f(z)+f^*(z)}{c_1-\eta}+\frac{2c_2g(z)}{c_1+c_2}$$
$$\Omega_1'(z)=\frac{z^{-1/2}\overline{f}(z)+f^*(z)}{c_2+\eta}-\frac{2c_2\overline{g}(z)}{c_1+c_2} \quad (5)$$

$$\phi_2'(z)=\frac{z^{-1/2}f(z)+f^*(z)}{c_2+\eta}+\frac{2c_1g(z)}{c_1+c_2}$$
$$\Omega_2'(z)=\frac{z^{-1/2}\overline{f}(z)+f^*(z)}{c_1-\eta}-\frac{2c_1\overline{g}(z)}{c_1+c_2} \quad (6)$$

where $f(z)$, $f'(z)$, and $g(z)$ are entire functions (analytic in the whole plane), and the elastic constants c_1 and c_2 and the mismatch constant η are given by

$$c_1=(\kappa_1+1)/\mu_1,\ c_2=(\kappa_2+1)/\mu_2,\ \eta=(1/\mu_1)-(1/\mu_2). \quad (7)$$

Note that $f(z)$ and $f^*(z)$ are restricted by $\overline{f}(z)=-f(z)$ and $\overline{f^*}(z)=f^*(z)$ but are otherwise arbitrary, where $\overline{f}(z)$ denotes the complex conjugate of $f(\bar{z})$, and so on.

Similarly, the most general forms of $\phi_1(z)$, $\Omega_1(z)$, $\phi_2(z)$ and $\Omega_2(z)$ that obey (2) and (4) (frictional contact) can be written as

[16]Asst. Professor, Department of Mechanical Engineering, University of South Carolina, Columbia, SC 29208. Associate Mem. ASME.

Contributed by the Applied Mechanics Division of THE AMERICAN SOCIETY OF MECHANICAL ENGINEERS for publication in the ASME JOURNAL OF APPLIED MECHANICS. Manuscript received by the ASME Applied Mechanics Division, June 28, 1993; final revision, Jan. 26, 1994. Associate Technical Editor: C. F. Shih.

Copyright © 1994 by ASME
Downloaded 03 May 2010 to 171.66.16.20. Redistribution subject to ASME license or copyright; see http://www.asme.org/terms/Terms_Use.cfm

$$\phi_1'(z)=\frac{z^{-1/2+\delta}f(z)+(1+i\rho)f^*(z)}{c_1-\eta}+\frac{2c_2g(z)}{c_1+c_2}$$
$$\Omega_1'(z)=\frac{z^{-1/2+\delta}\bar{f}(z)+(1-i\rho)f^*(z)}{c_2+\eta}-\frac{2c_2\bar{g}(z)}{c_1+c_2} \quad (8)$$
$$\phi_2'(z)=\frac{z^{-1/2+\delta}f(z)+(1+i\rho)f^*(z)}{c_2+\eta}+\frac{2c_1g(z)}{c_1+c_2}$$
$$\Omega_2'(z)=\frac{z^{-1/2+\delta}\bar{f}(z)+(1-i\rho)f^*(z)}{c_1-\eta}-\frac{2c_1\bar{g}(z)}{c_1+c_2}. \quad (9)$$

The exponent $\delta(-1/2<\delta<1/2)$ in the above can be determined from

$$\tan \pi\delta=\rho\beta,\ \beta=\frac{\mu_1(\kappa_2-1)-\mu_2(\kappa_1-1)}{\mu_1(\kappa_2+1)+\mu_2(\kappa_1+1)} \quad (10)$$

where β is a mismatch parameter originally defined by Dundurs (1969). It is apparent that solutions in (5) and (6) for the interface crack with frictionless contact can be recovered from those in (8) and (9) by setting ρ and δ to zero.

As pointed out by Rice (1988), a full Williams-type series expansion of the crack-tip fields can be obtained by expression the three entire functions $f(z)$, $f^*(z)$, and $g(z)$ in terms of complex Taylor series. (The coefficients for these Taylor series will be imaginary for $f(z)$, real for $f^*(z)$ and complex for $g(z)$.) The leading term from $f(z)$ will give the singular stress field, with one arbitrary constant, which was first determined by Comninou (1977a, b) using Williams' eigen-expansion technique. It is clear that the only possible stress singularity at the crack tip is of the type $r^{-1/2+\delta}$, where r is the distance to the crack tip. Although $\delta=0$ when there is no friction, it can be either positive or negative, depending on loading history, when friction is present between the contacting crack surfaces (Comninou, 1977b; Dundurs and Comninou, 1979). The constant terms of the stress field will come from the leading terms in both $f^*(z)$ and $g(z)$, which contain two, instead of three, arbitrary constants. In general, it can be concluded from Eqs. (5), (6), (8), and (9) that the crack-tip stress field expansion will be composed of terms $r^{-1/2+\delta+n}$ $(n=0, 1, 2, \ldots)$, which come from $z^{-1/2+\delta}f(z)$ with *one* set of arbitrary constants, and terms r^n $(n=0, 1, 2, \ldots)$, which come from both $f^*(z)$ and $g(z)$ with *three* sets of arbitrary constants.

Observation and Discussion

For easy observation and comparison, we list here, with minor rearrangement, the complete crack-tip field representation derived by Rice (1988) for the interface crack with crack surface separation:

$$\phi_1'(z)=\frac{2e^{-\pi\epsilon}z^{-1/2-i\epsilon}f(z)}{c_1+c_2}+\frac{2c_2g(z)}{c_1+c_2}$$
$$\Omega_1'(z)=\frac{2e^{\pi\epsilon}z^{-1/2+i\epsilon}\bar{f}(z)}{c_1+c_2}-\frac{2c_2\bar{g}(z)}{c_1+c_2} \quad (11)$$
$$\phi_1'(z)=\frac{2e^{\pi\epsilon}z^{-1/2-i\epsilon}f(z)}{c_1+c_2}+\frac{2c_1g(z)}{c_1+c_2}$$
$$\Omega_2'(z)=\frac{2e^{-\pi\epsilon}z^{-1/2+i\epsilon}\bar{f}(z)}{c_1+c_2}-\frac{2c_1\bar{g}(z)}{c_1+c_2} \quad (12)$$

where $\epsilon=(1/2\pi)\ln[(1-\beta)/(1+\beta)]$.

An immediate observation from comparing (11) and (12) with (5) and (6), and (8) and (9), is that the different interface crack-tip fields share the same arbitrary entire function $g(z)$ in identical forms, which implies that a large portion of the series expansions of these fields at the crack tip are identical. This is not a mere coincidence. In fact, a close examination reveals that the entire function $g(z)$ represents a crack-tip field whose displacements are fully continuous in the whole plane and whose stresses are such that the tractions along the entire x-axis are zero, which means that it satisfies the boundary conditions specified in all three problems (interface cracks without contact and those with contact but with and without friction in the contact zone) at the same time.

Another observation is that when the bimaterial becomes homogeneous (hence $c_1=c_2$ and $\epsilon=\delta=\beta=\eta=0$), the fields given by (11) and (12) recovers completely the classic mixed-mode crack-tip fields in plane strain and plane stress, whereas those given by (5) and (6) (or (8) and (9) with $\rho=0$) will lose all symmetric terms of the type $r^{-1/2+n}$ $(n=0, 1, 2, \ldots)$ but they will gain extra symmetric terms of the type r^n $(n=0, 1, 2, \ldots)$. However, it is easy to see that when the bimaterial becomes homogeneous the classic mixed-mode fields can be recovered by multiplying the entire function $f^*(z)$ in (5)–(9) by $z^{-1/2}$. It is interesting to note that $f^*(z)$ represents a crack-tip field whose displacements and two stress components σ_{yy} and σ_{xy} are fully continuous in the whole plane, such that along the x-axis, $u_y=\rho u_x$ and $\sigma_{xy}=-\rho\sigma_{yy}$.

A related observation can be made about the solution in (8) and (9) for interface cracks with friction in the contact zone. When the bimaterial becomes homogeneous but still with frictional crack surface contact, the fields given by (8) and (9), although differing from those for classic mixed mode I and II problems when $\rho=0$, can be used to deal with practical situations where crack surface contact and slip exist due to combined compression and shear loadings. It is noted that in this case the crack-tip fields are completely represented by (8) and (9) with $c_1=c_2$ and $\delta=\eta=0$, and the stress singularity is identical to that of the classic mode II problem, hence still governed by the traditional stress intensity factor K_{II}. Naturally, when there is no friction between the contacting crack surfaces, the energy release rate, as expressed by the conventional J-integral, will be path-independent, and when there is friction between the crack surfaces, the energy release rate must be evaluated at the crack tip. In either case, K_{II} is expected to relate to the energy release rate in the usual manner.

Finally, when an interface crack is subjected to a combined *tension* and shear loading, the region of dominance for (5) and (6) or (8) and (9) is expected to shrink to zero when the bimaterial tends to the homogeneous limit. In this case the dominant solution is given by (11) and (12), which as mentioned earlier recovers the classic mixed-mode solution at the limit. However, as alluded to in the above, when the interface crack is subjected to a combined *compression* and shear loading, it appears that the solution represented by (5) and (6) or (8) and (9), rather than (11) and (12), is the valid one at the homogeneous material limit. This is because compression is expected to induce crack contact and hence renders the classic crack-tip fields unsuitable.

References

Comninou, M., 1977a, "The Interface Crack," ASME JOURNAL OF APPLIED MECHANICS, Vol. 44, pp. 631–636.

Comninou, M., 1977b, "Interface Crack With Friction in the Contact Zone," ASME JOURNAL OF APPLIED MECHANICS, Vol. 44, pp. 780–781.

Dundurs, J., 1969, discussion, ASME JOURNAL OF APPLIED MECHANICS, Vol. 36, pp. 650–652.

Dundurs, J., and Comninou, M., 1979, "Some Consequences of the Inequality Conditions in Contact and Crack Problems," *Journal of Elasticity*, Vol. 9, pp. 71–82.

England, A. H., 1965, "A Crack Between Dissimilar Media," ASME JOURNAL OF APPLIED MECHANICS, Vol. 32, pp. 400–402.

Rice, J. R., 1988, "Elastic Fracture Mechanics Concepts for Interfacial Cracks," ASME JOURNAL OF APPLIED MECHANICS, Vol. 55, pp. 98–103.

Williams, M. L., 1957, "On the Stress Distribution at the Base of a Stationary Crack," ASME JOURNAL OF APPLIED MECHANICS, Vol. 24, pp. 109–114.

Williams, M. L., 1959, "The Stresses Around a Fault or Crack in Dissimilar Media," *Bulletin of the Seismological Society of America*, Vol. 49, pp. 199–204.

Downloaded 03 May 2010 to 171.66.16.20. Redistribution subject to ASME license or copyright; see http://www.asme.org/terms/Terms_Use.cfm

Exact Stresses Between Axisymmetric Bodies in Contact Having Quartic Profiles

Chin-Tu Lu[17] **and M. D. Bryant**[18]

Introduction

Hamilton and Goodman (1966) solved stresses for axisymmetric parabolically shaped bodies in sliding contact. Bryant and Keer (1982), Sackfield and Hills (1983a, 1983b, 1988a, 1988b) and Hills and Sackfield (1985, 1987a, 1987b) extended the work to sliding contacts between various shaped indenters with dissimilar elastic constants.

Evolving thermal deformations in frictionally and/or electrically heated contacts can flatten initially parabolic surfaces (Yune and Bryant, 1994)—strictly parabolic profiles with concomitant stresses are poor approximations. Large-scale stress computations (Lu, 1993) for thermal mounding, accurate when the surface profile and contact radius evolve with temperature, are greatly simplified by higher order profiles coupled with appropriate solutions.

With $r=(x^2+y^2)^{1/2}$, $E'=[1-\nu_1^2/E_1+1-\nu_2^2/E_2]^{-1}$, Young's modulus E, Poisson's ratio ν (subscripts 1, 2 index bodies), and contact radius a, Steuermann found the contact pressure $p_n(r)$ and contact force F_n for terms $c_n r^{2n}$ in the profile $f(r)=\sum_{n=1}^{N} c_n r^{2n}$ (see Johnson, 1985). The total contact pressure p and force F sum over N components.

Quartic Components

For $N=2$, $f(r)=c_1r^2+c_2r^4$, $p(r)=4E'/\pi\ [c_1+8/9\ c_2(a^2+2r^2)]\sqrt{a^2-r^2}$, and $F=8E'a^3/3\ (c_1+8/5\ c_2a^2)$. Cartesian stresses derived via potential functions of Green (1949) and Hamilton and Goodman (1966) over $z\geq 0$ are in equilibrium and decay at remote points. On $z=0$, all tractions vanish except $\sigma_{zz}=\dfrac{\sigma_{xz}}{\mu}=-p(r)$ within the contact $r\leq a$. In the following list of stresses for the pure quartic profile, any stress not specified is zero.

(a) Normal Load.

For $z>0$:

$$\sigma_{xx}=p_0[(X^2+2\nu Y^2)S_1+X^2S_2+S_4+9/2\ (1-\nu)Y^2ZS_0]$$
$$\sigma_{yy}=p_0[(Y^2+2\nu X^2)S_1+Y^2S_2+S_4+9/2\ (1-\nu)X^2ZS_0]$$
$$\sigma_{zz}=p_0[S_5-6Z^3S_0];$$
$$\sigma_{xy}=p_0XY[S_2+(1-2\nu)S_1-9/2\ (1-\nu)ZS_0]$$
$$\sigma_{xz}=\frac{X}{Y}\sigma_{yz}=p_0X[S_6+9Z^2S_0]. \tag{1}$$

On $z=0$ and $r\leq a$:

$$\sigma_{xx}=p_0[(X^2+2\nu Y^2)Q_1-Q_2];\quad \sigma_{yy}=p_0[(Y^2+2\nu X^2)Q_1-Q_2]$$
$$\sigma_{zz}=-p_0Q_3;\qquad \sigma_{xy}=p_0(1-2\nu)XYQ_1. \tag{2}$$

On $z=0$ and $r>a$:

$$\sigma_{xx}=-\sigma_{yy}=p_0\left[\frac{3}{5R^4}(1-2\nu)(X^2-Y^2)\right];$$
$$\sigma_{xy}=p_0\left[\frac{6}{5R^4}(1-2\nu)XY\right]. \tag{3}$$

On $r=0$:

$$\sigma_{xx}=\sigma_{yy}=p_0\left[\frac{3}{2(1+Z^2)}-(2+\nu)Q_4\right];$$
$$\sigma_{zz}=p_0\left[-\frac{3}{1+Z^2}+2Q_4\right]. \tag{4}$$

(b) Tangential Load.

For $z>0$:

$$\sigma_{xx}=\mu p_0X[X^2S_7+X^2S_8+S_9+S_{10}+3/8\ (Q_5-42Z^2-6\nu Z^2)S_0]$$
$$\sigma_{yy}=\mu p_0X[Y^2S_7-X^2S_8+ZS_1-3S_{11}+3/8\ (3\nu R^2+2\nu X^2-6Z^2-18\nu Z^2)S_0]$$
$$\sigma_{zz}=\mu p_0X[S_6+9Z^2S_0]$$
$$\sigma_{xy}=\mu p_0Y[ZS_1-S_3+S_{11}+X^2S_7+X^2S_8+3/8\ (Q_6-18Z^2+6\nu Z^2)S_0]$$
$$\sigma_{xz}=\mu p_0[S_{12}+X^2S_2+ZS_3-3Z/8\ (15R^2+6X^2-20Z^2)S_0]$$
$$\sigma_{yz}=\mu p_0XY[S_2-9Z/4\ S_0]. \tag{5}$$

On $z=0$ and $r\leq a$:

$$\sigma_{xx}=-\mu p_0\left[\frac{3\pi X}{16}Q_5\right];\qquad \sigma_{yy}=-\mu p_0\left[\frac{3\pi\nu X}{16}(3R^2+2X^2)\right]$$
$$\sigma_{xy}=-\mu p_0\left[\frac{3\pi Y}{16}Q_6\right];\qquad \sigma_{xz}=-\mu p_0Q_3. \tag{6}$$

On $z=0$ and $r>a$:

$$\sigma_{xx}=\mu p_0X\{[6Q_7+\nu(3Q_7-Q_8)]Q_9-Q_5Q_{10}\}$$
$$\sigma_{yy}=\mu p_0\nu X[(3Q_7+Q_8)Q_9-(3R^2+2X^2)Q_{10}]$$
$$\sigma_{xy}=\mu p_0Y\{[3Q_7-\nu(Q_7+Q_8+16R^2)]Q_9-Q_6Q_{10}\}. \tag{7}$$

On $r=0$:

$$\sigma_{xz}=\mu p_0\left[\frac{3}{2(1+Z^2)}-\frac{5}{2}Q_4\right]. \tag{8}$$

Here $R=r/a$, $X=x/a$, $Y=y/a$, $Z=z/a$, $R_2=\sqrt{R^2+Z_2^2}$, $Z_2=Z+i$, $i=\sqrt{-1}$, contact pressure at the origin $p_0=32\ c_2a^3E'/(9\pi)$, and S_i and Q_i are given in the Appendix.

When evaluated, expressions agreed to at least four digits with Sackfield and Hills (1988a), who used quadratures to approximate certain integrals.

Results and Discussion

The von Mises parameter $J_2=\sigma_{xy}^2+\sigma_{xz}^2+\sigma_{yz}^2+1/6\ [(\sigma_{xx}-\sigma_{yy})^2+(\sigma_{xx}-\sigma_{zz})^2+(\sigma_{yy}-\sigma_{zz})^2]$ and largest principal tensile stress σ_p were calculated for $\nu=0.3$.

For a pure quartic profile $f(r)=c_2r^4$ and $a=[15F/(64c_2E')]^{1/5}$. The maximum contact pressure $p_{\max}=32\sqrt{2}\ c_2a^3E'/(9\pi)>p_0$ occurs at $r/a=1/\sqrt{2}$. In Fig. 1, contours of $\sqrt{J_2}/p_{\max}$ are plotted on $y=0$. For $\mu=0$ in Fig. 1(*a*), maximum $\sqrt{J_2}/p_{\max}\approx 0.348$ is located at $(x/a, z/a)\approx(\pm 0.74, 0.33)$. As μ increases to 0.5 in Fig. 1(*b*), the maximum J_2 increases and approaches $z=0$ near $x/a=-1$. This is similar to Hamilton and Goodman (1966) for parabolic profiles, but here the peak value $[9/50\ (1-2\nu)^2+9\pi\mu/80\ (1-2\nu)(3-2\nu)+9\pi^2\mu^2/512\ (12-6\nu+7\nu^2)]^{1/2}$ is about 1.5 times larger.

[17]Department of Mechanical Engineering, Nan-Tai College, One Nantai Street, Yungkang, Tainan, Taiwan 71008, R.O.C.

[18]Department of Mechanical Engineering, The University of Texas at Austin, Austin, TX 78712-1063. Assoc. Mem. ASME.

Contributed by the Applied Mechanics Division of THE AMERICAN SOCIETY OF MECHANICAL ENGINEERS for publication in the ASME JOURNAL OF APPLIED MECHANICS. Manuscript received by the ASME Applied Mechanics Division, June 28, 1993; final revision, Oct. 11, 1993. Associate Technical Editor: X. Markenscoff.

Copyright © 1994 by ASME
Downloaded 03 May 2010 to 171.66.16.20. Redistribution subject to ASME license or copyright; see http://www.asme.org/terms/Terms_Use.cfm

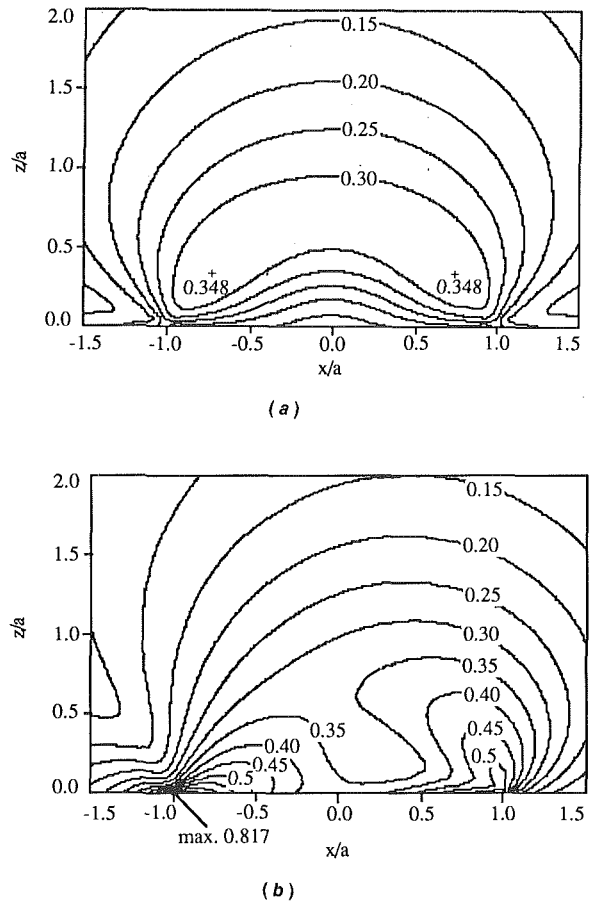


Fig. 1 Contours of $\sqrt{J_2}/p_{max}$ on $y=0$ for pure quartic profiles: (a) $\mu=0$ and (b) $\mu=0.5$

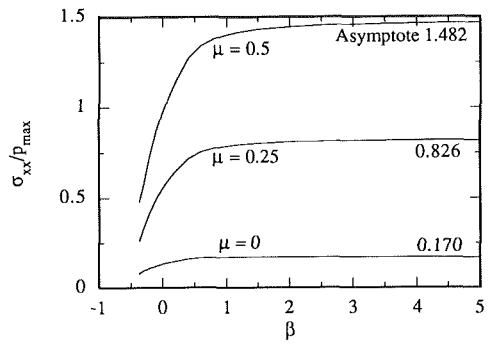


Fig. 2 Maximum tensile stress on $z=0$ varies with $\beta = c_2a^2/c_1$ for a range of μ

Maximum σ_{xx}/p_{max} is plotted versus $\beta = c_2a^2/c_1 \geq -3/8$ (otherwise $p(r) < 0$) in Fig. 2. For a parabolic profile $\beta \to 0$, while $\beta \to \infty$ for a quartic profile. The peak σ_p for the quartic profile is about 1.5 times larger than Hertzian contacts. The maximum $\sigma_{xx}/p_{max} = 1/\sqrt{2}\ [3/5\ (1-2\nu) + 3\pi/16\ \mu(6+\nu)]$ occurs at $y = z = 0$ and $x/a = -1$, coincides with σ_p, monotonically increases with β and μ, and for large β is bounded by the value corresponding to a pure quartic profile. For $\beta = -3/8$, the maximum is half the value corresponding to a parabolic profile.

Acknowledgments

National Science Foundation grant MEA-8410524 (Tribology) is gratefully acknowledged.

References

Bryant, M. D., and Keer, L. M., 1982, "Rough Contact Between Elastically and Geometrically Identical Curved Bodies," ASME JOURNAL OF APPLIED MECHANICS, Vol. 49, pp. 345–352.

Green, A. E., 1949, "On Boussinesq's Problem and Penny-Shaped Cracks," *Proceedings of the Cambridge Philosophical Society*, Vol. 45, pp. 251–257.

Hamilton, G. M., and Goodman, L. E., 1966, "The Stress Field Created by a Circular Sliding Contact," ASME JOURNAL OF APPLIED MECHANICS, Vol. 33, pp. 371–376.

Hills, D. A., and Sackfield, A., 1985, "Sliding Contact Between Dissimilar Elastic Cylinders," ASME *Journal of Tribology*, Vol. 107, pp. 463–466.

Hills, D. A., and Sackfield, A., 1987a, "The Stress Field Induced by Normal Contact Between Dissimilar Spheres," ASME JOURNAL OF APPLIED MECHANICS, Vol. 54, pp. 8–14.

Hills, D. A., and Sackfield, A., 1987b, "The Stresses Induced in a Half-Space by an Arbitrary Axisymmetric Pressure Distribution," ASME *Journal of Tribology*, Vol. 109, pp. 630–633.

Johnson, K. L., 1985, *Contact Mechanics*, Cambridge University Press, New York, pp. 114–118.

Lu, C. T., 1993, "Thermal and Mechanical Behavior and Failure of Carbon and MetalGraphite Brushes in Sliding Electrical Contacts," Ph.D. Dissertation, The University of Texas at Austin, Austin, Texas.

Sackfield, A., and Hills, D. A., 1983a, "Some Useful Results in the Classical Hertz Contact Problem," *Journal of Strain Analysis*, Vol. 18, pp. 101–105.

Sackfield, A., and Hills, D. A., 1983b, "Some Useful Results in the Tangentially Loaded Hertz Contact Problem," *Journal of Strain Analysis*, Vol. 18, pp. 107–110.

Sackfield, A., and Hills, D. A., 1988a, "Sliding of a General Axisymmetric Point Contact," ASME *Journal of Tribology*, Vol. 110, pp. 492–498.

Sackfield, A., and Hills, D. A., 1988b, "Sliding Contact Between Dissimilar Elastic Bodies," ASME *Journal of Tribology*, Vol. 110, pp. 592–596.

Yune, Y. G., and Bryant, M. D., 1994, "Thermoelastic Evolution of Hot Spots in Thermally Nonlinear Carbon Graphite Sliders," *Journal of Thermal Stresses*, Vol. 17, pp. 45–61.

Appendix

Re{•} denotes real part. Singularities in $1/R_2$ at $z = 0$ and $r = a$ were removed by recognizing that $Z/R_2 = 0$.

$$S_0 = \mathrm{Re}\{i \log(R_2 + Z_2)\}$$

$$S_1 = \mathrm{Re}\left\{\frac{3}{80(R_2+Z_2)^2}(-32 - 16\,iR_2 - 64\,R_2^2 + 32\,iR_2^3 + 21\,iZ - 2\,R_2Z + 19\,iR_2^2Z + 106\,Z^2 - 94\,iR_2Z^2 - 77\,iZ^3)\right\}$$

$$S_2 = \mathrm{Re}\left\{\frac{3Z}{16R_2(R_2+Z_2)^2}(16 - 15\,iR_2 + 6\,R_2^2 - 9\,iR_2^3 + 34\,R_2Z - 38\,iR_2^2\,Z - 25\,iR_2Z^2)\right\}$$

$$S_3 = \mathrm{Re}\left\{\frac{3}{32(R_2+Z_2)}(-5 - 15\,iR_2 - 9\,R_2^2 - 3\,iR_2^3 - 17\,iZ + 34\,R_2Z - 55\,iR_2^2\,Z - 25\,Z^2 - 25\,iR_2Z^2 + 35\,iZ^3)\right\}$$

$$S_4 = \mathrm{Re}\left\{\frac{1+2\nu}{160(R_2+Z_2)}(-96i - 96R_2 + 96\,iR_2^2 - 64\,R_2^3 + 64\,iR_2^4 + 21\,Z + 63\,iR_2Z + 57\,R_2^2Z + 19\,iR_2^3Z - 159\,iZ^2 + 318\,R_2Z^2 - 441\,iR_2^2Z^2 - 231\,Z^3 - 231\,iR_2Z^3 + 189\,iZ^4)\right\} + ZS_3 - \frac{3Z}{4}(9R^2 + 3\nu R^2 - 8Z^2 - 4\nu Z^2)S_0$$

$$S_5 = \mathrm{Re}\left\{\frac{3Z}{R_2} + iR_2(3 + 2\,R_2^2 - 6\,iZ + 6\,Z^2)\right\}$$

Downloaded 03 May 2010 to 171.66.16.20. Redistribution subject to ASME license or copyright; see http://www.asme.org/terms/Terms_Use.cfm

$$S_6=\mathrm{Re}\left\{\frac{3Z}{2R_2(R_2+Z_2)}\,(2-2\,iR_2+4\,R_2^2 - 4\,iR_2^3-R_2Z-iR_2^2Z+5\,iR_2Z^2)\right\}$$

$$S_7=\mathrm{Re}\left\{\frac{3Z}{20R_2(R_2+Z_2)^3}\,(20-28\,iR_2-24\,R_2^2+8\,iR_1^3 - 11\,R_2Z+9\,iR_2^2Z+3\,iR_2Z^2)\right\}$$

$$S_8=\mathrm{Re}\left\{\frac{\nu}{80(R_2+Z_2)^3}\,(145-15\,iR_2+105\,R_2^2-55\,iR_2^3+237\,iZ + 546\,R_2Z-297\,iR_2^2Z+369\,Z^2-381\,iR_2Z^2-147\,iZ^3)\right\}$$

$$S_9=\mathrm{Re}\left\{\frac{3}{80(R_2+Z_2)^2}\,(25i-50R_2+120\,iR_2^2+30\,R_2^3+15\,iR_2^4 - 156\,Z-58\,iR_2Z-592\,R_2^2Z+386\,iR_2^3Z+273\,iZ^2-176\,R_2Z^2 + 457\,iR_2^2Z^2+618\,Z^3-332\,iR_2Z^3-406\,iZ^4)\right\}$$

$$S_{10}=\mathrm{Re}\left\{\frac{3\nu}{160(R_2+Z_2)^2}\,(115i-30R_2+120\,iR_2^2+50\,R_2^3+5\,iR_2^4 + 44\,Z-38\,iR_2Z-272\,R_2^2Z+206\,iR_2^3Z+48\,iZ^2-346\,R_2Z^2 + 422\,iR_2^2Z^2-72\,Z^3+278\,iR_2Z^3+49\,iZ^4)\right\}$$

$$S_{11}=\mathrm{Re}\left\{\frac{\nu}{160(R_2+Z_2)^2}\,(65i+70R_2-120\,iR_2^2-10R_2^3-25\,iR_2^4 + 164Z-18\,iR_2Z+528\,R_2^2Z-374\,iR_2^3Z-372\,iZ^2 - 6R_2Z^2-378\,iR_2^2Z^2-672\,Z^3+378\,iR_2Z^3+399\,iZ^4)\right\}$$

$$S_{12}=\mathrm{Re}\left\{\frac{R_2}{2}\,(6i+4\,iR_2^2+3\,Z-15\,iZ^2)\right\}$$

$$Q_1=\frac{3}{5R^4}\,[2-(2+R^2+2R^4)(1-R^2)^{1/2}];\qquad Q_2=\frac{1+2\nu}{5R^2}\,[3-(3+2R^2)(1-R^2)^{3/2}]$$

$$Q_3=(1+2R^2)(1-R^2)^{1/2};\quad Q_4=1-3Z^2+3Z^3\tan^{-1}(1/Z)$$

$$Q_5=6R^2+3\nu R^2-2\nu X^2;\quad Q_6=3R^2-\nu R^2-2\nu X^2$$

$$Q_7=2R^4+3R^6;\quad Q_8=X^2(32+4R^2+6R^4)-24R^2$$

$$Q_9=\frac{\sqrt{R^2-1}}{8R^6};\quad Q_{10}=\frac{3}{8}\tan^{-1}(1/\sqrt{R^2-1})$$

Post-buckling Behavior of Stiffened Cross-Ply Cylindrical Shells

M. Savoia[19] and J. N. Reddy[20]

The post-buckling of stiffened, cross-ply laminated, circular cylinders under uniform axial compression is investigated to determine the effects of shell lamination scheme and stiffeners on the reduced load-carrying capacity. The effect of geometric imperfection is also included. The analysis is based on the layerwise shell theory of Reddy, and the "smeared stiffener" technique is used to account for the stiffener stiffness. Numerical results for stiffened and unstiffened cylinders are presented, showing that imperfection-sensitivity is strictly related to the number of nearly simultaneous buckling modes.

1 Introduction

It is generally accepted that the reduced load-carrying capacity of axially loaded cylinders is strictly related to the presence of simultaneous or nearly simultaneous modes. Reddy and Savoia (1992) have shown that thin isotropic cylinders of finite length usually have more than 100 modes characterized by a buckling load about ten percent higher than the minimum buckling load; moreover, the level lines of the eigenvalue map were shown to be very similar to the Koiter circles (Koiter, 1945). In this case, a buckling mode superposition analysis needs a very large number of terms to achieve good estimates of the load-carrying capacity of thin isotropic cylinders. For fiber-reinforced laminated cylinders, the buckling maps are substantially different from those of isotropic cylinders, and usually very few modes are nearly the same (Reddy and Savoia, 1992).

The paper by Reddy and Savoia (1992) was concerned with the post-buckling of unstiffened circular cylindrical shells, whereas the present study deals with the post-buckling behavior of stiffened, cross-ply laminated circular cylindrical shells. For the modeling of the skin, the layerwise shell theory of Reddy (1992) is used.

2 Formulation

In the layerwise theory of Reddy (1992), the displacements and the radial imperfection of the cylinder are expressed as

$$[u_1,\,u_2,\,u_3,\,\hat{u}_3](x,\,y,\,z)=\sum_{i=1}^{S+1}[u_i,\,v_i,\,w_i,\,\hat{w}_i](x,\,y)\Phi^i(z) \qquad (1)$$

where S is the number of numerical layers, $(u_i,\,v_i,\,w_i)$ and $\hat{w}_i$ are interface displacements and imperfections, respectively, and $\Phi^i(z)$ are layerwise continuous functions of the thickness coordinate. Here $(x,\,y,\,z)$ denotes an orthogonal reference frame, where x is taken along the cylinder axis and y along the circumferential direction. In the present study, linear (finite element) interpolation functions are used for Φ^i.

[19]Assistant Professor, Istituto di Tecnica delle Costruzioni, Universita di Bologna, Bologna, Italy.

[20]Oscar S. Wyatt Chair Professor, Department of Mechanical Engineering, Texas A&M University, College Station, TX 77843-3123.

Contributed by the Applied Mechanics Division of The American Society of Mechanical Engineers for publication in the ASME Journal of Applied Mechanics. Manuscript received by the ASME Applied Mechanics Division, Mar. 25, 1993; final revision, Oct. 25, 1993. Associate Technical Editor: L. T. Wheeler.

Downloaded 03 May 2010 to 171.66.16.20. Redistribution subject to ASME license or copyright; see http://www.asme.org/terms/Terms_Use.cfm

$$S_6 = \mathrm{Re}\left\{\frac{3Z}{2R_2(R_2+Z_2)}\,(2-2\,iR_2+4\,R_2^2 - 4\,iR_2^3 - R_2Z - iR_2^2Z + 5\,iR_2Z^2)\right\}$$

$$S_7 = \mathrm{Re}\left\{\frac{3Z}{20R_2(R_2+Z_2)^3}\,(20-28\,iR_2-24\,R_2^2+8\,iR_1^3 - 11\,R_2Z+9\,iR_2^2Z+3\,iR_2Z^2)\right\}$$

$$S_8 = \mathrm{Re}\left\{\frac{\nu}{80(R_2+Z_2)^3}\,(145-15\,iR_2+105\,R_2^2-55\,iR_2^3+237\,iZ + 546\,R_2Z-297\,iR_2^2Z+369\,Z^2-381\,iR_2Z^2-147\,iZ^3)\right\}$$

$$S_9 = \mathrm{Re}\left\{\frac{3}{80(R_2+Z_2)^2}\,(25i-50R_2+120\,iR_2^2+30\,R_2^3+15\,iR_2^4 - 156\,Z-58\,iR_2Z-592\,R_2^2Z+386\,iR_2^3Z+273\,iZ^2-176\,R_2Z^2 + 457\,iR_2^2Z^2+618\,Z^3-332\,iR_2Z^3-406\,iZ^4)\right\}$$

$$S_{10} = \mathrm{Re}\left\{\frac{3\nu}{160(R_2+Z_2)^2}\,(115i-30R_2+120\,iR_2^2+50\,R_2^3+5\,iR_2^4 + 44\,Z-38\,iR_2Z-272\,R_2^2Z+206\,iR_2^3Z+48\,iZ^2-346\,R_2Z^2 + 422\,iR_2^2Z^2-72\,Z^3+278\,iR_2Z^3+49\,iZ^4)\right\}$$

$$S_{11} = \mathrm{Re}\left\{\frac{\nu}{160(R_2+Z_2)^2}\,(65i+70R_2-120\,iR_2^2-10R_2^3-25\,iR_2^4 + 164Z-18\,iR_2Z+528\,R_2^2Z-374\,iR_2^3Z-372\,iZ^2 - 6R_2Z^2-378\,iR_2^2Z^2-672\,Z^3+378\,iR_2Z^3+399\,iZ^4)\right\}$$

$$S_{12} = \mathrm{Re}\left\{\frac{R_2}{2}\,(6i+4\,iR_2^2+3\,Z-15\,iZ^2)\right\}$$

$$Q_1 = \frac{3}{5R^4}\,[2-(2+R^2+2R^4)(1-R^2)^{1/2}];\qquad Q_2 = \frac{1+2\nu}{5R^2}\,[3-(3+2R^2)(1-R^2)^{3/2}]$$

$$Q_3 = (1+2R^2)(1-R^2)^{1/2};\quad Q_4 = 1-3Z^2+3Z^3\tan^{-1}(1/Z)$$

$$Q_5 = 6R^2+3\nu R^2-2\nu X^2;\quad Q_6 = 3R^2-\nu R^2-2\nu X^2$$

$$Q_7 = 2R^4+3R^6;\quad Q_8 = X^2(32+4R^2+6R^4)-24R^2$$

$$Q_9 = \frac{\sqrt{R^2-1}}{8R^6};\quad Q_{10} = \frac{3}{8}\tan^{-1}(1/\sqrt{R^2-1})$$

Post-buckling Behavior of Stiffened Cross-Ply Cylindrical Shells

M. Savoia[19] and J. N. Reddy[20]

The post-buckling of stiffened, cross-ply laminated, circular cylinders under uniform axial compression is investigated to determine the effects of shell lamination scheme and stiffeners on the reduced load-carrying capacity. The effect of geometric imperfection is also included. The analysis is based on the layerwise shell theory of Reddy, and the "smeared stiffener" technique is used to account for the stiffener stiffness. Numerical results for stiffened and unstiffened cylinders are presented, showing that imperfection-sensitivity is strictly related to the number of nearly simultaneous buckling modes.

1 Introduction

It is generally accepted that the reduced load-carrying capacity of axially loaded cylinders is strictly related to the presence of simultaneous or nearly simultaneous modes. Reddy and Savoia (1992) have shown that thin isotropic cylinders of finite length usually have more than 100 modes characterized by a buckling load about ten percent higher than the minimum buckling load; moreover, the level lines of the eigenvalue map were shown to be very similar to the Koiter circles (Koiter, 1945). In this case, a buckling mode superposition analysis needs a very large number of terms to achieve good estimates of the load-carrying capacity of thin isotropic cylinders. For fiber-reinforced laminated cylinders, the buckling maps are substantially different from those of isotropic cylinders, and usually very few modes are nearly the same (Reddy and Savoia, 1992).

The paper by Reddy and Savoia (1992) was concerned with the post-buckling of unstiffened circular cylindrical shells, whereas the present study deals with the post-buckling behavior of stiffened, cross-ply laminated circular cylindrical shells. For the modeling of the skin, the layerwise shell theory of Reddy (1992) is used.

2 Formulation

In the layerwise theory of Reddy (1992), the displacements and the radial imperfection of the cylinder are expressed as

$$[u_1, u_2, u_3, \hat{u}_3](x, y, z) = \sum_{i=1}^{S+1} [u_i, v_i, w_i, \hat{w}_i](x, y)\Phi^i(z) \qquad (1)$$

where S is the number of numerical layers, (u_i, v_i, w_i) and $\hat{w}_i$ are interface displacements and imperfections, respectively, and $\Phi^i(z)$ are layerwise continuous functions of the thickness coordinate. Here (x, y, z) denotes an orthogonal reference frame, where x is taken along the cylinder axis and y along the circumferential direction. In the present study, linear (finite element) interpolation functions are used for Φ^i.

[19]Assistant Professor, Istituto di Tecnica delle Costruzioni, Universita di Bologna, Bologna, Italy.

[20]Oscar S. Wyatt Chair Professor, Department of Mechanical Engineering, Texas A&M University, College Station, TX 77843-3123.

Contributed by the Applied Mechanics Division of THE AMERICAN SOCIETY OF MECHANICAL ENGINEERS for publication in the ASME JOURNAL OF APPLIED MECHANICS. Manuscript received by the ASME Applied Mechanics Division, Mar. 25, 1993; final revision, Oct. 25, 1993. Associate Technical Editor: L. T. Wheeler.

Copyright © 1994 by ASME
Downloaded 03 May 2010 to 171.66.16.20. Redistribution subject to ASME license or copyright; see http://www.asme.org/terms/Terms_Use.cfm

The "smeared stiffener" approach (Hutchinson and Amazigo, 1967) is adopted for the stiffeners. This approach is very effective when the stiffeners have identical cross-section and their spacing is small when compared to the buckling wave length. In the framework of a stability analysis this means that no skin wrinkling before general instability is assumed to take place. The kinematic description of the stiffeners is based on the Euler-Bernoulli beam theory. Axial and ring stiffeners are assumed to deform in the x-y and the y-z planes, respectively.

The total potential energy functional II of the stiffened shell can be expressed in terms of the functions u_i, v_i and w_i (see Reddy, 1992; Reddy and Savoia, 1992). The nonlinear problem derived from the principle of minimum total potential energy is solved by means of the Rayleigh-Ritz method for simply-supported edge conditions at ($x = 0$, L).

3 Numerical Results

A three-layer, cross-ply laminated cylindrical shell subjected to axial compression is chosen to study the effect of axial and/or ring stiffeners on the post-buckling behavior. The cylinder has the following geometric parameters, $L = 300$ cm, $R = L/\pi = 95.49$ cm and total thickness $h = 1$ cm. The individual layers have equal thicknesses $h_i = h/3$, and the elastic coefficients are those typical of a high-modulus graphite-epoxy composite: $E_L = 150$ GPa, $E_T = 7$ GPa, $G_{LT} = 3.5$ GPa, $G_{TT} = 1.4$ GPa, $\nu_{LT} = \nu_{TT} = 0.3$, where subscripts L and T denote the directions along the length and transverse to the fibers, respectively. The lamination scheme used is [0/90/0]. Since the extensional modulus in the fiber direction E_L is large with respect to that in the transverse direction E_T, the cylinder turns out to be reinforced in the axial direction. Moreover, equally spaced outside stiffeners are considered. The geometric and material characteristics of the I-shaped steel stiffeners adopted here are $E_a = E_c = 210$ GPa, $G_a = G_c = 80.8$ GPa, $A_a = A_c = 1.2$ cm^2, $\bar{I}_a = \bar{I}_c = 7.2$ cm^4, $J_a = J_c = 0.004$ cm^4 $\bar{z}_a = \bar{z}_c = 3.5$ cm. Uniformly distributed axial loads are used here.

The full nonlinear post-buckling analysis has been performed for the cylinder $N1$ in order to evaluate the influence of stiffening on the reduced load-carrying capacity due to geometrical imperfections, as well as on the minimum post-buckling load. The nonlinear system of equations has been solved by making use of the Riks-Wempner incremental iterative method. The linearized eigenvalue analysis was previously performed (Reddy, 1992) in order to select the modes that dominate the pre-buckling state and those having smallest buckling loads. Up to 12 buckling modes have been included in the multimode analysis. In all the cases examined here, the addition of more terms did not change significantly the results obtained. Note that the maximum load can be reached for very small geometric imperfections only.

For the unstiffened cylinder (see Fig. 1), the maximum buckling load $q_{\max}$ and the minimum post-buckling load q_{mpb} are almost coincident, and are approximately 60 percent of the linear buckling load q_b obtained through eigenvalue analysis. The post-buckling path is related to the coupling of modes (4, 7) and (4, 8), and its stiffness in the axial direction is approximately one-half of the membrane stiffness. For the axially stiffened cylinder (figure not included here) the reduction in the load-carrying capacity due to the smaller geometrical imperfection is found to be only 20 percent. But unlike the previous case, q_{mpb} is found to be considerably lower than $q_{\max}$, and the post-buckling branch is characterized by a stiffness which is comparable to that of the pre-buckling path; this is essentially due to the very high bending rigidity of the shapes involved during buckling (i.e., modes (1, 4), (1, 5), (1, 6)). The ring-stiffened cylinder (results not shown here) showed the highest reduction of the load-carrying capacity, namely, 44 percent of the buckling load. Moreover, its deformed shape

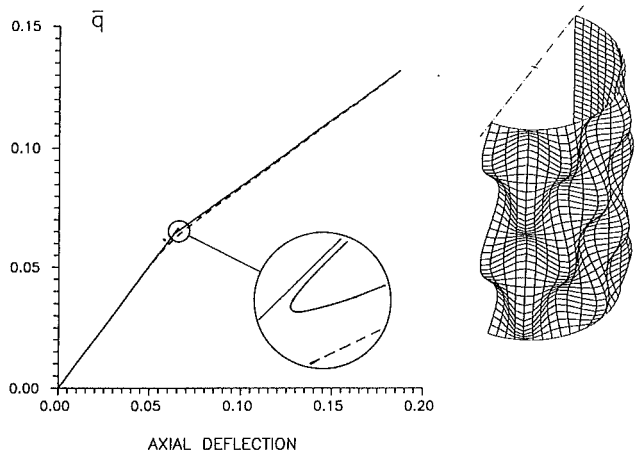


Fig. 1 Plot of applied axial load versus axial deflection (at $x = L/2$, $y = 0$, $z = h/2$) for unstiffened cylinder, for different values of the mode imperfection (——: ${}^3\hat{\Delta}_i^{mn} = 10^{-5}$ cm; · · · : ${}^3\hat{\Delta}_i^{mn} = 10^{-2}$ cm)

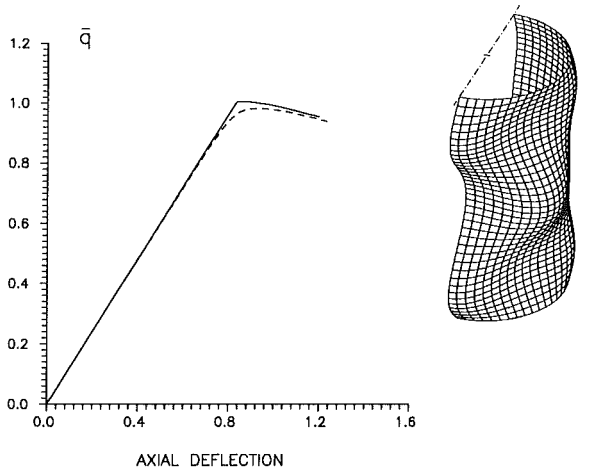


Fig. 2 Plot of applied axial load versus axial deflection (at $x = L/2$, $y = 0$, $z = h/2$) for stiffened cylinder with 20 ring and 40 axial stiffeners, for different values of the mode imperfection (——: ${}^3\hat{\Delta}_i^{mn} = 10^{-5}$ cm; · · · : ${}^3\hat{\Delta}_i^{mn} = 10^{-2}$ cm)

is almost axisymmetric, with a high number of axial waves (modes (14, 1), (14, 2) and (14, 3)); in this case, no minimum post-buckling load is reached. Higher values of the maximum load have been obtained for very small values of the geometrical imperfections[3] $\Delta_i^{mn} < 10^{-7}$ cm. Then, in this case the linearized buckling analysis cannot yield any information about the real load-carrying capacity of the cylinder. Moreover, even the b-factor initial post-buckling analyses (Koiter, 1945) are valid in the neighborhood of the maximum load for small values of geometrical imperfections only, so that they cannot be used to predict this decreasing behavior. When axial and ring stiffeners are used (see Fig. 2), not only the buckling load is rapidly increased, but also a low imperfection sensitivity occurs, and the reduction in the load-carrying capacity is approximately 20 percent.

Acknowledgments

The first author was supported by the (Italian) Ministry of University and Scientific Technological Research (MURST) and the National Council of Research (CNR-contr. 92.03045.07). The second author was supported by the Army Research Office grant DAL03-90-G-0134.

Downloaded 03 May 2010 to 171.66.16.20. Redistribution subject to ASME license or copyright; see http://www.asme.org/terms/Terms_Use.cfm

References

Hutchinson, J. W., and Amazigo, J. C., 1967, "Imperfection-Sensitivity of Eccentrically Stiffened Cylindrical Shells," *AIAA Journal*, Vol. 5, pp. 392–401.

Koiter, W. T., 1945, "On the Stability of Elastic Equilibrium," Thesis, Delft, The Netherlands, (Engl. Transl. issued as NASA TT-F10833, 1967).

Reddy, J. N., 1992, "A Layer-Wise Shell Theory with Applications to Buckling and Vibration of Cross-Ply Laminated Circular Cylindrical Shells," Research Report CCMS-92-01, Center for Composite Materials and Structures, Virginia Polytechnic Institute and State University, Blacksburg, VA.

Reddy, J. N., and Savoia, M., 1992, "The Layer-Wise Shell Theory for Post-Buckling of Circular Cylindrical Shells," *AIAA Journal*, Vol. 30, pp. 2148–2154.

Savoia, M., and Reddy, J. N., 1993, "Buckling and Post-Buckling Behavior of Eccentrically Stiffened Laminated Cylinders," *Mechanics of Composite Materials—Nonlinear Effects*, M. W. Hyer, ed., AMD-Vol. 159, New York, pp. 127–142.

Analytical Solution of Hill's Equation

Y. Pala[21]

Introduction

In this study, the analytical solution to the famous Hill's equation concerning the plastic deformations of a bar subjected to bending and twisting together is given. It is required to find the critical combinations of moments and torques which render the members fully plastic and the corresponding distribution of stresses. Assumptions concerned and the other details can be found in papers by Handelman (1944), Hill (1948), Steel (1954), and Hill and Siebel (1953). Hill's equation was originally derived by Handelman (1944). The same equation was also derived by Hill using his maximum plastic work principle (Hill, 1948). Numerical solutions to this differential equation have been attempted by Steel (1954), Hill and Siebel (1953), Steel (1954), Gaydon and Nuttall (1957) and Imegwu (1962a, 1962b). So far as the author knows, an analytical solution to this nonlinear partial differential equation has not appeared in the literature.

Handelman Equation

Handelman equation is given by (Steel, 1954)

$$\frac{\partial}{\partial x}\left[y\frac{\partial u}{\partial x}\left[1-\left(\frac{\partial u}{\partial x}\right)^2-\left(\frac{\partial u}{\partial y}\right)^2\right]^{-1/2}\right]+\frac{\partial}{\partial y}\left[y\frac{\partial u}{\partial y}\left[1-\left(\frac{\partial u}{\partial x}\right)^2+\left(\frac{\partial u}{\partial y}\right)^2\right]^{-1/2}\right]+A=0 \quad (1)$$

where $A=(2/\sqrt{3})(\dot{\theta}/\dot{\rho})$. On the other hand, stress field and bending moment M and twisting moment T are given by (Handelman, 1944; Imegwu, 1962a)

$$\tau_{xz}=-k\frac{\partial u}{\partial y},\ \tau_{yz}=k\frac{\partial u}{\partial x},\ \sigma_z=\mp\sqrt{3}k\sqrt{1-\left(\frac{\partial u}{\partial x}\right)^2-\left(\frac{\partial u}{\partial y}\right)^2}$$

$$M=\sqrt{3}\iint y\sqrt{1-u_x^2-u_y^2}\,dxdy \qquad T=2k\iint u dxdy \quad (2)$$

Solution

In order to solve Eq. (1), we will make use of the transformation

$$\frac{\partial\phi}{\partial x}=yu_x\,[1-u_x^2-u_y^2]^{-1/2},\ \frac{\partial\phi}{\partial y}=yu_y\,[1-u_x^2-u_y^2]^{-1/2}. \quad (3)$$

Thus, Eq. (1) gives

$$\frac{\partial^2\phi}{\partial x^2}+\frac{\partial^2\phi}{\partial y^2}+A=0. \quad (4)$$

By putting $\phi=\phi_1-(A/4)(x^2+y^2)$ in Eq. (6), we have

$$\frac{\partial^2\phi_1}{\partial x^2}+\frac{\partial^2\phi_1}{\partial y^2}=0. \quad (5)$$

This is a well-known Laplace differential equation whose solutions are harmonic functions.

Rating two equations in (3), we obtain $\phi_y/\phi_x=u_y/u_x$. Here, we adopt the notations $\phi_x=\partial\phi/\partial x$, $\phi_y=\partial\phi/\partial y$. In the same way, finding u_x in terms of θ_x/θ_y, we have from (3) that

$$u_x=\frac{1}{\sqrt{1+\left(\frac{\phi_y}{\phi_x}\right)^2+\frac{y^2}{(\phi_x+\phi_y)^2}\left[1+\frac{\phi_y}{\phi_x}\right]^2}}$$

$$u_y=\frac{\phi_y/\phi_x}{\sqrt{1+\left(\frac{\phi_y}{\phi_x}\right)^2+\frac{y^2}{(\phi_x+\phi_y)^2}\left[1+\frac{\phi_y}{\phi_x}\right]^2}}.$$

Since ϕ can readily be found from Eq. (5), ϕ_x and ϕ_y can also easily be found. Thus, nonzero stress terms τ_{xz}, τ_{yz}, σ_{zz}, bending moment M and twisting moment T can be found from Eq. (2).

In order that the torque T be integrated, the function u must be expressed in a functional form. It is possible to do this under the condition $u=0$. Indeed, by the nature of the problem, torque T can be written in the form

$$T=2k\iint u dxdy=2k\iint\frac{\partial u}{\partial x}x dxdy, \qquad u=0. \quad (7)$$

Since $\partial u/\partial x=u_x$ can readily be determined without finding the open form of u, twisting moment T can be put in a form which can be solved numerically or analytically.

Now, let us look at how we can find the function u. It is known that the solutions of Eq. (5) are harmonic functions. That is, real and imaginary parts of the complex function $z=(x+iy)^n$ which will be found for the integer values of $n=1, 2,\ldots, n$, satisfies the above differential equation. For example, real parts x^2-y^2, $(n=2)$, x^3-3xy^2, $(n=3)$, are the solutions to Eq. (5). Let us take x^2-y^2 as a solution. Thus, we can write $\phi_1=m(x^2-y^2)$. Putting this expression into the expression for ϕ, we have

$$\phi=m(x^2-y^2)-\frac{A}{4}(x^2+y^2) \quad (8)$$

where m is a constant to be determined. Taking partial derivatives of the above equation, we obtain

$$\phi_x=\frac{1}{2}(4m-A)x, \qquad \phi_y=-\frac{1}{2}(4m+A)y. \quad (9)$$

Since $u_y/u_x=\phi_y/\phi_x$, we can write $(u_y/u_x)=(-4m+A)y/((4m-A)x)$. Substituting this expression into (2) and (6), we can readily determine the partial derivatives u_x, u_y and bending and twisting moments.

Boundary Conditions

Although the twisting moment T has been written such that

[21]Assistant Professor, University of Uludag, Engineering Faculty, Gorukle, Bursa, Turkey.

Contributed by the Applied Mechanics Division of THE AMERICAN SOCIETY OF MECHANICAL ENGINEERS for publication in the ASME JOURNAL OF APPLIED MECHANICS. Manuscript received by the ASME Applied Mechanics Division, Mar. 1, 1992; final revision, Mar. 14, 1994. Associate Technical Editor: R. M. McMeeking.

Downloaded 03 May 2010 to 171.66.16.20. Redistribution subject to ASME license or copyright; see http://www.asme.org/terms/Terms_Use.cfm

References

Hutchinson, J. W., and Amazigo, J. C., 1967, "Imperfection-Sensitivity of Eccentrically Stiffened Cylindrical Shells," *AIAA Journal*, Vol. 5, pp. 392–401.

Koiter, W. T., 1945, "On the Stability of Elastic Equilibrium," Thesis, Delft, The Netherlands, (Engl. Transl. issued as NASA TT-F10833, 1967).

Reddy, J. N., 1992, "A Layer-Wise Shell Theory with Applications to Buckling and Vibration of Cross-Ply Laminated Circular Cylindrical Shells," Research Report CCMS-92-01, Center for Composite Materials and Structures, Virginia Polytechnic Institute and State University, Blacksburg, VA.

Reddy, J. N., and Savoia, M., 1992, "The Layer-Wise Shell Theory for Post-Buckling of Circular Cylindrical Shells," *AIAA Journal*, Vol. 30, pp. 2148–2154.

Savoia, M., and Reddy, J. N., 1993, "Buckling and Post-Buckling Behavior of Eccentrically Stiffened Laminated Cylinders," *Mechanics of Composite Materials—Nonlinear Effects*, M. W. Hyer, ed., AMD-Vol. 159, New York, pp. 127–142.

Analytical Solution of Hill's Equation

Y. Pala[21]

Introduction

In this study, the analytical solution to the famous Hill's equation concerning the plastic deformations of a bar subjected to bending and twisting together is given. It is required to find the critical combinations of moments and torques which render the members fully plastic and the corresponding distribution of stresses. Assumptions concerned and the other details can be found in papers by Handelman (1944), Hill (1948), Steel (1954), and Hill and Siebel (1953). Hill's equation was originally derived by Handelman (1944). The same equation was also derived by Hill using his maximum plastic work principle (Hill, 1948). Numerical solutions to this differential equation have been attempted by Steel (1954), Hill and Siebel (1953), Steel (1954), Gaydon and Nuttall (1957) and Imegwu (1962a, 1962b). So far as the author knows, an analytical solution to this nonlinear partial differential equation has not appeared in the literature.

Handelman Equation

Handelman equation is given by (Steel, 1954)

$$\frac{\partial}{\partial x}\left[y\frac{\partial u}{\partial x}\left[1-\left(\frac{\partial u}{\partial x}\right)^2-\left(\frac{\partial u}{\partial y}\right)^2\right]^{-1/2}\right]+\frac{\partial}{\partial y}\left[y\frac{\partial u}{\partial y}\left[1-\left(\frac{\partial u}{\partial x}\right)^2+\left(\frac{\partial u}{\partial y}\right)^2\right]^{-1/2}\right]+A=0 \quad (1)$$

where $A=(2/\sqrt{3})(\dot{\theta}/\dot{\rho})$. On the other hand, stress field and bending moment M and twisting moment T are given by (Handelman, 1944; Imegwu, 1962a)

$$\tau_{xz}=-k\frac{\partial u}{\partial y},\ \tau_{yz}=k\frac{\partial u}{\partial x},\ \sigma_z=\mp\sqrt{3}k\sqrt{1-\left(\frac{\partial u}{\partial x}\right)^2-\left(\frac{\partial u}{\partial y}\right)^2}$$

$$M=\sqrt{3}\iint y\sqrt{1-u_x^2-u_y^2}\,dxdy \qquad T=2k\iint u dxdy \quad (2)$$

[21]Assistant Professor, University of Uludag, Engineering Faculty, Gorukle, Bursa, Turkey.

Contributed by the Applied Mechanics Division of THE AMERICAN SOCIETY OF MECHANICAL ENGINEERS for publication in the ASME JOURNAL OF APPLIED MECHANICS. Manuscript received by the ASME Applied Mechanics Division, Mar. 1, 1992; final revision, Mar. 14, 1994. Associate Technical Editor: R. M. McMeeking.

Solution

In order to solve Eq. (1), we will make use of the transformation

$$\frac{\partial\phi}{\partial x}=yu_x\,[1-u_x^2-u_y^2]^{-1/2},\ \frac{\partial\phi}{\partial y}=yu_y\,[1-u_x^2-u_y^2]^{-1/2}. \quad (3)$$

Thus, Eq. (1) gives

$$\frac{\partial^2\phi}{\partial x^2}+\frac{\partial^2\phi}{\partial y^2}+A=0. \quad (4)$$

By putting $\phi=\phi_1-(A/4)(x^2+y^2)$ in Eq. (6), we have

$$\frac{\partial^2\phi_1}{\partial x^2}+\frac{\partial^2\phi_1}{\partial y^2}=0. \quad (5)$$

This is a well-known Laplace differential equation whose solutions are harmonic functions.

Rating two equations in (3), we obtain $\phi_y/\phi_x=u_y/u_x$. Here, we adopt the notations $\phi_x=\partial\phi/\partial x$, $\phi_y=\partial\phi/\partial y$. In the same way, finding u_x in terms of θ_x/θ_y, we have from (3) that

$$u_x=\frac{1}{\sqrt{1+\left(\frac{\phi_y}{\phi_x}\right)^2+\frac{y^2}{(\phi_x+\phi_y)^2}\left[1+\frac{\phi_y}{\phi_x}\right]^2}}$$

$$u_y=\frac{\phi_y/\phi_x}{\sqrt{1+\left(\frac{\phi_y}{\phi_x}\right)^2+\frac{y^2}{(\phi_x+\phi_y)^2}\left[1+\frac{\phi_y}{\phi_x}\right]^2}}.$$

Since ϕ can readily be found from Eq. (5), ϕ_x and ϕ_y can also easily be found. Thus, nonzero stress terms τ_{xz}, τ_{yz}, σ_{zz}, bending moment M and twisting moment T can be found from Eq. (2).

In order that the torque T be integrated, the function u must be expressed in a functional form. It is possible to do this under the condition $u=0$. Indeed, by the nature of the problem, torque T can be written in the form

$$T=2k\iint u dxdy=2k\iint\frac{\partial u}{\partial x}x dxdy, \qquad u=0. \quad (7)$$

Since $\partial u/\partial x=u_x$ can readily be determined without finding the open form of u, twisting moment T can be put in a form which can be solved numerically or analytically.

Now, let us look at how we can find the function u. It is known that the solutions of Eq. (5) are harmonic functions. That is, real and imaginary parts of the complex function $z=(x+iy)^n$ which will be found for the integer values of $n=1, 2,\ldots, n$, satisfies the above differential equation. For example, real parts x^2-y^2, $(n=2)$, x^3-3xy^2, $(n=3)$, are the solutions to Eq. (5). Let us take x^2-y^2 as a solution. Thus, we can write $\phi_1=m(x^2-y^2)$. Putting this expression into the expression for ϕ, we have

$$\phi=m(x^2-y^2)-\frac{A}{4}(x^2+y^2) \quad (8)$$

where m is a constant to be determined. Taking partial derivatives of the above equation, we obtain

$$\phi_x=\frac{1}{2}(4m-A)x, \qquad \phi_y=-\frac{1}{2}(4m+A)y. \quad (9)$$

Since $u_y/u_x=\phi_y/\phi_x$, we can write $(u_y/u_x)=(-4m+A)y/((4m-A)x)$. Substituting this expression into (2) and (6), we can readily determine the partial derivatives u_x, u_y and bending and twisting moments.

Boundary Conditions

Although the twisting moment T has been written such that

Copyright © 1994 by ASME
Downloaded 03 May 2010 to 171.66.16.20. Redistribution subject to ASME license or copyright; see http://www.asme.org/terms/Terms_Use.cfm

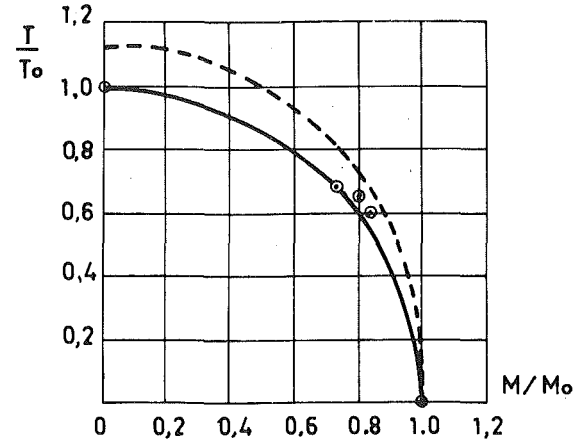


Fig. 1 Interaction curve for a circular cross-section

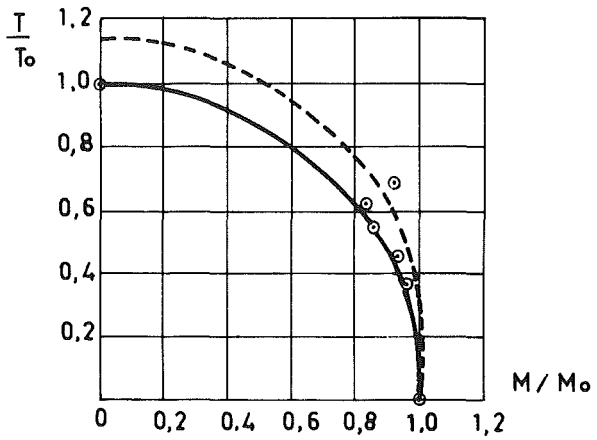


Fig. 2 Interaction curve for an elliptical cross-section

the boundary condition $u=0$ on the surface of the bar would be satisfied, we have still not used this condition when finding the expression of M, u_x and u_y. We will now use this condition. Since $u(x,y)=0$ on the surface, it is possible to write

$$du=\frac{\partial u}{\partial x}\,dx+\frac{\partial u}{\partial y}\,dy=0, \text{ or } \frac{(u_x)}{(u_y)}=-\frac{(dy)}{(dx)}. \tag{10}$$

But, on the other hand, since $\phi_x/\phi_y=u_x/u_x$, we obtain $(-dy/dx)=(\phi_x/\phi_y)$. This is the condition that makes u constant but not necessarily zero. This shows that another method must be found so as to be sure that u is indeed zero on the surface. To do this, we can consider the contour integration of u. If $u=0$, then $\oint du$ must also be zero. With a little reflection, it can be seen that $u_x(1+(\phi_y/\phi_x)\ (dy/dx))=0$. Since τ_{xz} is supposed to be different than zero and u_x cannot be zero, we can write $\phi_x/\phi_y=-dy/dx$. This is the condition that makes u zero on the surface. Thus, any function chosen as solution must satisfy this equality on the boundary curve.

Application

As an application, a bar of elliptical cross-section will be considered. In order to find the constant m, we take the equation of ellipse into account $(x^2/a^2+y^2/b^2=1)$, where a and b are the principal axes. Differentiating this equation, we have $(dy/dx)=(-b^2/a^2)(x/y)$. Since the condition $u=0$ requires $\phi_x/\phi_y=-dy/dx$, we have $m=((A/4)(a^2+b^2))/(a^2-b^2)$. Thus, the equation of ϕ is given by

$$\phi=\frac{A}{4}\left[\frac{a^2+b^2}{a^2-b^2}(x^2-y^2)-(x^2+y^2)\right]. \tag{11}$$

We also note that $b=0$ gives a solution for an infinitely thin plate subjected to bending and twisting together. For the circular cross-section ($a=b$), m must be taken as zero. Indeed, if we take the equation of circle, $x^2+y^2=r^2$ (r=radius) into account we find that $m=0$.

In order to find the yield surface, Eqs. (2) and (7) were integrated. It is seen from Figs. 1 and 2 that the yield surface are not very much dependent upon the cross-section, as pointed out by Imegwu (1962a, 1962b). Some points found outside the lower and upper bounds arises from the error made in numerical calculations.

Discussion

In this study, we have dealt with the analytical solution of the famous Hill's equation and have shown that the analytical solution can be given for the beams of elliptical and circular cross-sections. Different solutions can be given for different cross-sections. The selection of the functional form of ϕ_1 that satisfies the Laplace equation must be made such that m can always be obtained as a constant value. It is seen from the preceding sections that this is not very easy and depends on the author's ability to think.

References

Gaydon, F. A., and Nuttall, H., 1957, "Combined Plastic Loading," *Journal of the Mechanics and Physics of Solids*, Vol. 6, pp. 17.

Handelman, G. H., 1944, "A Variational Principle for a State of Combined Plastic Stress," *Quarterly Journal of Mechanics and Applied Mathematics*, Vol. 1, pp. 351–353.

Hill, R., 1948, "A Variational Principle of Maximum Plastic Work in Classical Plasticity," *Quarterly Journal of Mechanics and Applied Mathematics*, pp. 18.

Hill, R., and Siebel, M. P. L., 1953, "On the Principle of Maximum Plastic Work," *Journal of the Mechanics and Physics of Solids*, Vol. 1, pp. 207.

Imegwu, E. O., 1962a, "Plastic Flexure and Torsion," *Journal of the Mechanics and Physics of Solids*, Vol. 8, pp. 141–146.

Imegwu, E. O., 1962b, "Combined Plastic Bending and Torsion," *Journal of the Mechanics and Physics of Solids*, Vol. 10, pp. 277–282.

Steel, M. C., 1954, "The Plastic Bending and Twisting of Square Section Members," *Journal of the Mechanics and Physics of Solids*, Vol. 3, pp. 156.

Materials With Negative Poisson's Ratio: A Qualitative Microstructural Model

N. Phan-Thien[22] and B. L. Karihaloo[23]

Materials with negative Poisson's ratio are peculiar in that they expand laterally when stretched. Examples of such type of

[22]Department of Mechanical Engineering, University of Sydney, NSW 2006, Australia.

[23]School of Civil and Mining Engineering, University of Sydney, NSW 2006, Australia. Mem. ASME.

Contributed by the Applied Mechanics Division of THE AMERICAN SOCIETY OF MECHANICAL ENGINEERS for publication in the ASME JOURNAL OF APPLIED MECHANICS. Manuscript received by the ASME Applied Mechanics Division, Feb. 10, 1992; final revision, June 8, 1994. Associate Technical Editor: R. M. McMeeking.

Downloaded 03 May 2010 to 171.66.16.20. Redistribution subject to ASME license or copyright; see http://www.asme.org/terms/Terms_Use.cfm

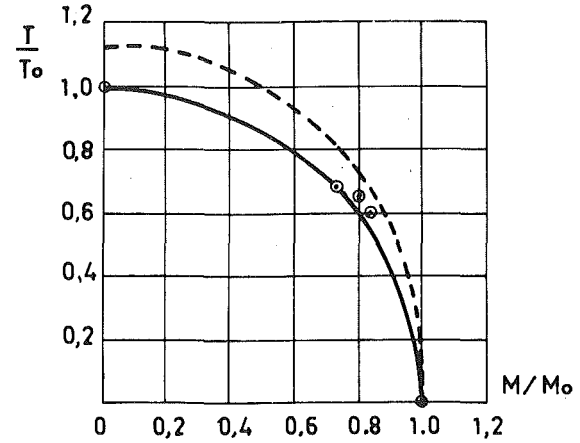


Fig. 1 Interaction curve for a circular cross-section

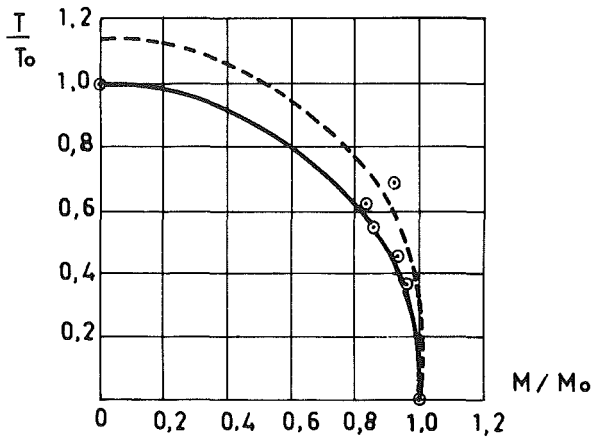


Fig. 2 Interaction curve for an elliptical cross-section

the boundary condition $u=0$ on the surface of the bar would be satisfied, we have still not used this condition when finding the expression of M, u_x and u_y. We will now use this condition. Since $u(x,y)=0$ on the surface, it is possible to write

$$du=\frac{\partial u}{\partial x}\,dx+\frac{\partial u}{\partial y}\,dy=0, \text{ or } \frac{(u_x)}{(u_y)}=-\frac{(dy)}{(dx)}. \tag{10}$$

But, on the other hand, since $\phi_x/\phi_y=u_x/u_x$, we obtain $(-dy/dx)=(\phi_x/\phi_y)$. This is the condition that makes u constant but not necessarily zero. This shows that another method must be found so as to be sure that u is indeed zero on the surface. To do this, we can consider the contour integration of u. If $u=0$, then $\oint du$ must also be zero. With a little reflection, it can be seen that $u_x(1+(\phi_y/\phi_x)\ (dy/dx))=0$. Since τ_{xz} is supposed to be different than zero and u_x cannot be zero, we can write $\phi_x/\phi_y=-dy/dx$. This is the condition that makes u zero on the surface. Thus, any function chosen as solution must satisfy this equality on the boundary curve.

Application

As an application, a bar of elliptical cross-section will be considered. In order to find the constant m, we take the equation of ellipse into account $(x^2/a^2+y^2/b^2=1)$, where a and b are the principal axes. Differentiating this equation, we have $(dy/dx)=(-b^2/a^2)(x/y)$. Since the condition $u=0$ requires $\phi_x/\phi_y=-dy/dx$, we have $m=((A/4)(a^2+b^2))/(a^2-b^2)$. Thus, the equation of ϕ is given by

$$\phi=\frac{A}{4}\left[\frac{a^2+b^2}{a^2-b^2}(x^2-y^2)-(x^2+y^2)\right]. \tag{11}$$

We also note that $b=0$ gives a solution for an infinitely thin plate subjected to bending and twisting together. For the circular cross-section ($a=b$), m must be taken as zero. Indeed, if we take the equation of circle, $x^2+y^2=r^2$ (r=radius) into account we find that $m=0$.

In order to find the yield surface, Eqs. (2) and (7) were integrated. It is seen from Figs. 1 and 2 that the yield surface are not very much dependent upon the cross-section, as pointed out by Imegwu (1962a, 1962b). Some points found outside the lower and upper bounds arises from the error made in numerical calculations.

Discussion

In this study, we have dealt with the analytical solution of the famous Hill's equation and have shown that the analytical solution can be given for the beams of elliptical and circular cross-sections. Different solutions can be given for different cross-sections. The selection of the functional form of ϕ_1 that satisfies the Laplace equation must be made such that m can always be obtained as a constant value. It is seen from the preceding sections that this is not very easy and depends on the author's ability to think.

References

Gaydon, F. A., and Nuttall, H., 1957, "Combined Plastic Loading," *Journal of the Mechanics and Physics of Solids*, Vol. 6, pp. 17.

Handelman, G. H., 1944, "A Variational Principle for a State of Combined Plastic Stress," *Quarterly Journal of Mechanics and Applied Mathematics*, Vol. 1, pp. 351–353.

Hill, R., 1948, "A Variational Principle of Maximum Plastic Work in Classical Plasticity," *Quarterly Journal of Mechanics and Applied Mathematics*, pp. 18.

Hill, R., and Siebel, M. P. L., 1953, "On the Principle of Maximum Plastic Work," *Journal of the Mechanics and Physics of Solids*, Vol. 1, pp. 207.

Imegwu, E. O., 1962a, "Plastic Flexure and Torsion," *Journal of the Mechanics and Physics of Solids*, Vol. 8, pp. 141–146.

Imegwu, E. O., 1962b, "Combined Plastic Bending and Torsion," *Journal of the Mechanics and Physics of Solids*, Vol. 10, pp. 277–282.

Steel, M. C., 1954, "The Plastic Bending and Twisting of Square Section Members," *Journal of the Mechanics and Physics of Solids*, Vol. 3, pp. 156.

Materials With Negative Poisson's Ratio: A Qualitative Microstructural Model

N. Phan-Thien[22] and B. L. Karihaloo[23]

Materials with negative Poisson's ratio are peculiar in that they expand laterally when stretched. Examples of such type of

[22]Department of Mechanical Engineering, University of Sydney, NSW 2006, Australia.

[23]School of Civil and Mining Engineering, University of Sydney, NSW 2006, Australia. Mem. ASME.

Contributed by the Applied Mechanics Division of THE AMERICAN SOCIETY OF MECHANICAL ENGINEERS for publication in the ASME JOURNAL OF APPLIED MECHANICS. Manuscript received by the ASME Applied Mechanics Division, Feb. 10, 1992; final revision, June 8, 1994. Associate Technical Editor: R. M. McMeeking.

Copyright © 1994 by ASME
Downloaded 03 May 2010 to 171.66.16.20. Redistribution subject to ASME license or copyright; see http://www.asme.org/terms/Terms_Use.cfm

behavior have been discovered with foams by Lakes (1987); however, it is only recently that isotropic materials with negative Poisson's ratio have been shown by Milton (1992) to exist within the framework of classical theory of elasticity. In this Note, we demonstrate qualitatively that a composite material with a reentrant microstructure can also have a negative Poisson's ratio, even though the composite may be isotropic owing to a completely random distribution of the microstructure.

1 Introduction

Most ordinary engineering materials contract laterally when subjected to an axial tension, which corresponds to a positive Poisson's ratio. Recently, however, Lakes (1987) has been able to fabricate an isotropic foam material which exhibits a negative Poisson's ratio. Subsequently, Lakes (1991) outlined some microstructures which he believed could result in negative Poisson's ratios. The key requirement of these microstructures seems to be the presence of reentrant corners, and nonaffine kinematics or noncentral forces combined with preloading.

Prior to the foam produced by Lakes (1987), other structures exhibiting negative Poisson's ratios have been proposed: the two and three-dimensional structures consisting of hinges, springs, and sliding collars by Almgren (1985), the inverted honeycomb frame by Kolpakov (1985), and by Gibson and Ashby (1988). These model structures are not strictly elastic continua and therefore the fundamental question arises as to whether an elastic continuum with a negative Poisson's ratio can exist within the framework of the classical theory of elasticity.

From the definition of Poisson's ratio for an isotropic material, a negative value would correspond to low bulk and high shear moduli. Milton (1992) has called such a material dilational. He showed that a periodic, two-dimensional two-phase material can have its Poisson's ratio bounded between -1 and an upper bound which depends on the microstructural geometry, and the (assumed) common Poisson's ratio of the two phases. The bounds were found by using the classical variational principles with ingenious choices of the trial strain and stress fields. In particular, he showed that with a proper choice of the geometry, the upper bound on Poisson's ratio can be made negative, and as close to -1 as desired. Finally, Milton (1992) showed an easily manufacturable two-phase laminate structure with a negative Poisson's ratio.

In this Note we describe a composite microstructural model which is made up of a rigid phase suspension in an elastic matrix, and show that its effective Poisson's ratio is also negative. The material is, however, anisotropic unless the distribution of the rigid phase is purely random. In contrast to the bounding techniques employed by Milton (1992), we derive the full constitutive equation for the composite for which we use work done before, in connection with suspension mechanics, for example, by Batchelor (1970), Russell (1973), Phan-Thien and Huilgol (1980), and with the kinetic theory of macromolecules, for example, by Bird et al. (1987). The central feature of the microstructure is the presence of reentrant corners, which has been already mentioned by Lakes (1987, 1991).

2 A Reentrant Microstructural Model

A reentrant structure, adapted from Fig. 3 of Lakes (1987), is shown in Fig. 1. If such a structure is stretched in one of the principal directions, then it will produce lateral forces in the remaining directions. Lakes' reentrant structure is, however, more complicated than need be. Figure 2 shows a two-dimensional sketch of a three-dimensional microstructure that has essentially the same physical features. It is made up of a three-pronged fiber structure, AB, BC, and BD; BD is perpendicular to AC. Joint B is not rigid so that AC can be stretched due to a deformation imposed on it. As it does so, the fiber BD will be displaced relative to the matrix along its length. We assume for simplicity that the aspect ratios of the three prongs are the same, and equal to $A = l/d$, where l and d are the length and the diameter of the three prongs, respectively.

We now consider a dilute suspension of such a microstructure ($\Phi \ll 1$, Φ is the volume fraction of the microstructure) in an elastic matrix so that the deformation of each microstructure can be considered in isolation. This simplification will limit the validity of the proposed model, but will not alter its qualitative features. Under a homogeneous deformation (we assume that the length scale of the deformation is considerably larger than the length scale of the microstructure, l),

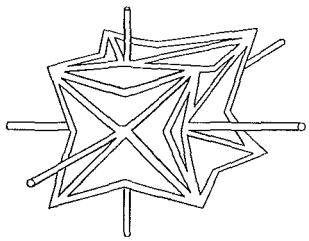


Fig. 1 The reentrant structure produced by the symmetrical collapse of a 24-sided polyhedron, after Lakes (1987).

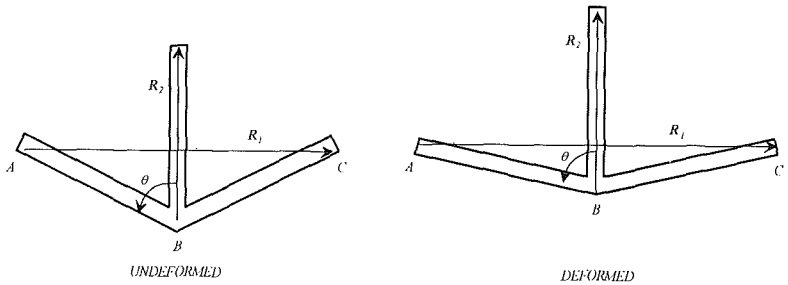


Fig. 2 A simple reentrant microstructure in the undeformed, and in the deformed state. The fiber segments AB, BC, and BD are nearly rigid fibers. As AC is stretched due to the imposed deformation, BD will be displaced along its length relative to the matrix and so produces a lateral force along this direction.

Downloaded 03 May 2010 to 171.66.16.20. Redistribution subject to ASME license or copyright; see http://www.asme.org/terms/Terms_Use.cfm

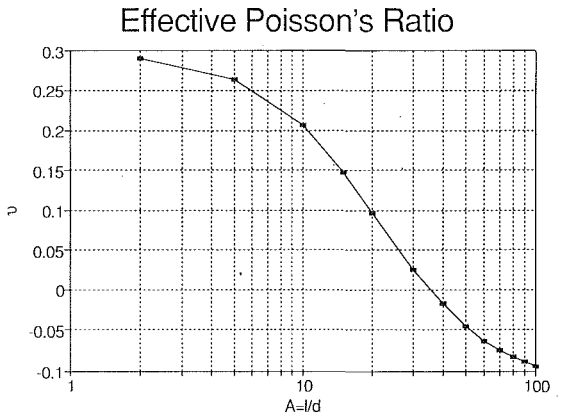


Fig. 3 The effective Poisson's ratio for the case where $\nu_m = 0.3$, $\Phi = 0.02$, $\theta = 45$ deg at different aspect ratios. Note that the theory may not be valid at high aspect ratios, if ΦA^2 is $O(1)$ or higher.

the microstructure is stretched, and the vector $\mathbf{R}_1$ is carried to $\mathbf{r}_1$ (Fig. 2). The relative displacement of AC is $\mathbf{u} = \mathbf{r}_1 - \mathbf{R}_1$.

Due to the near rigidity of the fibers, the relative displacement of the fiber BD along its length is $(\mathbf{u} \cdot \mathbf{pq} \tan\theta)/2$, where $\mathbf{p}$ is the unit vector along $\mathbf{r}_2$, $\mathbf{q}$ is a unit vector along $\mathbf{r}_2$, θ is the angle between AB and BD, and we have assumed an infinitesimal displacement field.

To calculate the forces acting on the microstructure, it is necessary to solve a complex boundary value problem (for given displacement of the structure). However, if the forces arising from the translational motion of the fiber segments are dominant, then a quick estimate of the forces involved can be obtained by regarding the microstructure as consisting of two segments: the fiber segment BD and the segment AC. Undoubtedly this is a simplistic model, but for nearly rigid slender fibers this should yield a realistic estimate of the forces. The approximation will be the better the nearer θ is to 90 deg (but it should not be equal to 90 deg). Small values of θ are also excluded (see below). Quantitative improvement of the model can be made by a detailed study of the deformation involved (perhaps by numerical means).

Due to a relative displacement $\mathbf{u}$ between A and C, the force acting on the whole structure is thus

$$\mathbf{F} = \mathbf{F}_1 + \mathbf{F}_2 = \zeta_1 \, \mathbf{u} - \frac{1}{2} \zeta_2 \, \mathbf{u} \cdot \mathbf{pq} \tan\theta, \tag{1}$$

where ζ_1 is a resistance coefficient due to the motion of AC (the resistance felt by the fibers AB and BC), and ζ_2 is the resistance coefficient due to the relative motion of the fiber BD. From the slender body theory of Russell (1973), these coefficients can be estimated as

$$\zeta_1 \approx \frac{2\pi\mu_m (2l \sin\theta)}{\ln 2A}, \quad \zeta_2 \approx \frac{2\pi\mu_m l}{\ln 2A}. \tag{2}$$

The effective stress tensor is given by

$$\mathbf{S} = (1 - \Phi)\mathbf{S}_m + \mathbf{S}_f, \tag{3}$$

where $\mathbf{S}_m = \lambda_m \mathrm{tr}\gamma \mathbf{1} + \mu_m (\gamma + \gamma^T)$ is the matrix stress tensor, and $\mathbf{S}_f$ is the fiber-contributed stress, which is given by (cf. Bird et al., (1987))

$$\mathbf{S}_f = \frac{N}{2} < \mathbf{F}_1\mathbf{r}_1 + \mathbf{r}_1\mathbf{F}_1 + \mathbf{F}_2\mathbf{r}_2 + \mathbf{r}_2\mathbf{F}_2 >, \tag{4}$$

where N is the number density of the microstructure, and the angular brackets denote an ensemble average with respect to the distribution of the orientation of the microstructure.

In an homogeneous deformation with deformation gradient $F = \mathbf{1} + \gamma$, $\mathbf{r}_1 = \mathbf{R}_1 + \gamma\mathbf{R}_1$, and thus $\mathbf{u} = \gamma\mathbf{R}_1 = 2l\sin\theta\gamma\mathbf{P}$, where $\mathbf{P}$ is the unit vector along AC.

The fiber contributed stress is, using our estimate of $\zeta_{1,2}$, and up to leading terms in $|\gamma|$,

$$\mathbf{S}_f = \frac{16\Phi A^2}{3 \ln 2A} \mu_m \left\langle 2\sin^3\theta(\gamma\mathbf{PP} + \mathbf{PP}\gamma^T) - \frac{1}{2} \tan\theta \sin\theta\gamma : \mathbf{PPQQ} \right\rangle, \tag{5}$$

where $\mathbf{Q}$ is the unit vector along $\mathbf{R}_2$ (BD). The definition of the number density has been used in deriving (5).

The resulting constitutive law for the composite is anisotropic; the anisotropy depends on the initial distribution of the microstructure. The maximum effect will therefore be realized when the microstructure is fully aligned. If we assume that this is so and that $\mathbf{P} = (1, 0, 0)$, $\mathbf{Q} = (0, 1, 0)$, then in an elongational deformation where $\gamma = \mathrm{diag}(\alpha, \beta, \beta)$, the effective stresses in the 11 and 22-directions from (3) and (5) are

$$S_{11} = (1 - \Phi)[\lambda_m(\alpha + 2\beta) + 2\mu_m\alpha] + \frac{64\Phi A^2}{3 \ln 2A} \mu_m \, \alpha \, \sin^3\theta,$$

$$S_{22} = (1 - \Phi)[\lambda_m(\alpha + 2\beta) + 2\mu_m\beta] - \frac{8\Phi A^2}{3 \ln 2A} \mu_m \, \alpha \tan\theta \sin\theta.$$

The stress in the 11-direction increases over and above the matrix value due to the added resistance of the microstructure in this direction. Furthermore, the lateral contraction in the 22-direction ($= -\beta/\alpha$) is obtained by setting S_{22} to zero. This lateral contraction can be regarded as the effective Poisson's ratio in the 22-direction. With $\Phi A^2 = 2.5$, $A = 50$, $\Phi = 0.002$, $\theta = 45$ deg, and $\nu_m = 0.3$, we find that the effective Poisson's ratio is -0.109. The reason for this negative Poisson's ratio is clear: as the microstructure is stretched in the 11-direction, it produces lateral forces in the 22-direction causing a positive displacement in this direction.

Suppose now that we have a random distribution of the microstructure so that

$$\langle P_i P_j \rangle = \frac{1}{3}\delta_{ij},$$

$$\langle P_i P_j Q_k Q_l \rangle = \frac{1}{30} (4\delta_{ij}\delta_{kl} - \delta_{ik}\delta_{jl} - \delta_{il}\delta_{jk}).$$

The last result is derived by expressing $\langle \mathbf{PPQQ} \rangle$ as a linear combination of fourth-order isotropic tensors and requiring that the contraction of relevant pairs of indices produce either $\mathbf{1}/3$ or zero. From (5), the fiber-contributed stress is

$$\mathbf{S}_f = \frac{8\Phi A^2}{45 \ln 2A} \mu_m \left\{ -4 \cos\theta \, \mathrm{tr}\gamma \mathbf{1} + (20 \sin^3\theta + \frac{1}{2} \tan\theta \sin\theta)(\gamma + \gamma^T) \right\}. \tag{6}$$

When combined with (3), we find that the composite material is isotropic, as it should be. The effective Lamé constants can be determined, whence the effective Poisson's ratio and bulk modulus are given by, respectively,

$$\nu_e = \frac{(1 - \Phi)\nu_m - \frac{8\Phi A^2(1 - 2\nu_m)}{45 \ln 2A} \tan\theta \sin\theta}{1 - \Phi + \frac{8\Phi A^2(1 - 2\nu_m)}{45 \ln 2A} (20 \sin^3\theta - 3/2 \cos\theta)}, \tag{7}$$

$$\kappa_e = (1 - \Phi)\kappa_m + \frac{16\Phi A^2}{27 \ln 2A} (4 \sin^3\theta - \frac{1}{2} \tan\theta \sin\theta)\mu_m, \tag{8}$$

where κ_m is the bulk modulus of the matrix. To ensure that the effective bulk modulus satisfies the condition $\kappa_e > \kappa_m$,

Downloaded 03 May 2010 to 171.66.16.20. Redistribution subject to ASME license or copyright; see http://www.asme.org/terms/Terms_Use.cfm

which is a consequence of Voigt-Reuss and Hashin-Shtrikman bounds, θ must exceed a certain value (about 11 deg for $A = 50$ and $\nu_m = 0.3$). With $A = 50$, $\Phi = 0.02$, $\theta = 45$ deg, and $\nu_m = 0.3$, we find that the effective Poisson's ratio is about -0.044. There is a significant cancellation effect due to the random distribution. At high aspect ratios, the magnitude of the negative effective Poisson's ratio increases, see Fig. 3. Note, however, that the theory is not expected to be valid at high values of ΦA^2.

In summary, we have been able qualitatively to demonstrate on an example of a composite solid with a reentrant microstructure that its effective Poisson's ratio is negative, even though the composite is overall isotropic. The main feature of the microstructure is its ability to produce a lateral force when stretched. This feature is seen to be sufficient to produce a small negative effective Poisson's ratio. For larger negative values closer to -1, one has to dispense with the dilute limit and consider large volume fractions. This would require complicated numerical simulations which are beyond the scope of this Note.

References

Almgren, R. F., 1985, "An Isotropic Three-Dimensional Structure with Poisson's ratio = −1," *J. Elasticity*, Vol. 15, pp. 427–430.

Batchelor, G. K., 1970, "The Stress System in a Suspension of Force-Free Particles," *J. Fluid Mechanics*, Vol. 41, pp. 545–570.

Bird, R. B., Curtiss, C. F., Armstrong, R. C., and Hassager, O., 1970, *Dynamics of Polymeric Liquids*, 2nd ed., John Wiley, New York, pp. 64–71.

Gibson, L. J., and Ashby, M., 1988, *Cellular Solids Structure and Properties*, Pergamon, New York, pp. 72–82.

Kolpakov, A. G., 1985, "Determination of the Average Characteristics of Elastic Frameworks," *PMM J. Applied Mathematics and Mechanics USSR*, Vol. 49, pp. 739–745.

Lakes, R., 1987, "Foam Structures with a Negative Poisson's Ratio," *Science*, Vol. 235, pp. 1038–1040.

Lakes, R., 1991, "Deformation Mechanisms in Negative Poisson's Ratio Materials: Structural Aspects," *J. Material Science*, Vol. 26, pp. 2287–2292.

Milton, G. W., 1994, "Composite Materials with Poisson's Ratios Close to −1," *J. Mechanics and Physics of Solids*, in press.

Phan-Thien, N., and Huilgol, R. R., 1980, "A Miocromechanic Theory of Chopped-Fiber-Reinforced Materials," *Fibre Science and Technology*, Vol. 13, pp. 423–433.

Russel, W. B., 1973, "On the Effective Moduli of Composite Materials: Effect of Fiber Length and Geometry at Dilute Concentrations," *Zeitschrift für angewandte Methematik und Physik*, Vol. 23, pp. 434–464.

Downloaded 03 May 2010 to 171.66.16.20. Redistribution subject to ASME license or copyright; see http://www.asme.org/terms/Terms_Use.cfm

Journal of Applied Mechanics

Discussion

A Conservation Theorem for Constrained Multibody Systems[1]

J. G. Papastavridis.[2] In Wang (1993), a laudable effort is made to remove the theoretical shortcomings of Kane and Levinson (1988). However, in the process Wang misrepresents the far more general exposition of Papastavridis (1991); he also introduces a number of fundamental errors which render his paper physically meaningless.

Let us begin with the latter. Wang states and proves (sic) that the power equation of *every* constrained mechanical system, under *arbitrary* forces, integrates to a corresponding first integral (constant) of motion of that system; i.e., that *every* constrained mechanical system has an energy integral! But, in general, the power of *nonpotential* forces does *not* equal the $(\cdots)$ derivative of a scalar energetic function; i.e., *the corresponding elementary work in general, is not the exact (or total) differential of a potential (or work) function.* Calling a power-like quantity $\dot{Z}$, Eq. (53), and then integrating it to Z, Eq. (54), is mathematically impermissible and physically meaningless—in general, *no Z exists.* (Similar remarks apply to the generally *nonexistent* Q, Eqs. (57)–(59).) Contrary to Wang's implication, power equations, in general, do *not* lead to energy/conservation theorems. A first integral of motion is a (first-order) algebraic relation among time, positions, and velocities holding for any system motion. Of course, *after* the problem has been solved and a particular motion has been found, Wang's $\dot{Z}$, $\dot{Q}$, etc., become *known functions of time* (or of equivalent path parameters), and can be integrated to yield Z, Q, etc., *but that doesn't make them integrals of motion.* Therefore Wang's transition from Eqs. (57)–(58) to Eq. (59), the centerpiece of his paper, is, generally, invalid.

Incidentally: (i) Wang's "definition" (56) is well known; (ii) while his allegedly new definition of the Hamiltonian, Eqs. (98), (99), can be found in most advanced dynamics expositions (e.g., Gantmacher (1970), Greenwood (1976), and Papastavridis (1991), Eqs. (12), (13), (14), (55)); (iii) Wang's terminology Eq. (34), ". . . $\dot{Q}$ is the net power flowing into the system" confuses the first law of thermodynamics with the purely mechanical law of kinetic energy, e.g., Langhaar (1962), Fox (1967), according to which the rate of change of the sum $K + V =$ Total Energy equals the power of *nonpotential* external *and* internal forces; and the integral of $\dot{Q}$ is neither a constant, nor "the first integral of motion of the system."

Next, analytical dynamics is about *impressed* forces and forces of *constraint* (reactions); whereas "elementary" mechanics is about external and internal forces. Contrary to Wang's claims: (i) Papastavridis (1991), whose equations easily specialize to multibody systems, obtains power equations *with* constraint reactions in *holonomic* variables, Eqs. (11)–(15); and, *purposely*, *without* constraint reactions in *nonholonomic* variables, Eqs. (57)–(71); and indicates how to connect them and obtain reaction power equations in nonholonomic variables, if needed (Remark on Eq. (52)). The absence of constraint reactions in Eqs. (57), (58), (71) is an advantage; but if one wants, he/she can easily do that as shown there; or by applying the well-known theorem of kinetic energy Eqs. (11), (136–139.2). Hence Wang's statement". . . this useful information is not provided by the power equation given by Papastavridis (1991)" is a misrepresentation. And "this useful information" is not provided by Wang's Eqs. (52), (53) either, but by his Eqs. (67), (89); and there are general equivalents to both sets of equations in Papastavridis (1991).

In sum: The power equations of Papastavridis (1991) are based on the fundamental division of forces into *impressed* and *constraint reactions.* On the other hand, the law of kinetic energy involves *all* forces, external and internal. Hence, comparing power equations based on such different force classifications, as Wang does, leads, in general, to meaningless, or flawed, results. One cannot expect to obtain the power of constraint forces from equations of motion specifically formulated to exclude them (even though Papastavridis (1991) treats both cases). And if Papastavridis' speculation on the root causes of the Kane and Levinson (1988) limitations is invalid, then Wang should show the precise physical meaning of the absence of satisfaction of Kane and Levinson's conditions; and exactly how that affects Wang's Z, Eq. (53).

References

Fox, E. A., 1967, *Mechanics*, Harper and Row, New York, pp. 92–97.

Gantmacher, F., 1970, *Lectures in Analytical Mechanics*, Mir, Moscow, pp. 48–51.

Greenwood, D. T., 1976, *Classical Dynamics*, Prentice-Hall, Englewood Cliffs, NJ pp. 66–78.

Kane, T. R., and Levinson, D. A., 1988, "A Method for Testing Numerical Integrations of Equations of Motion of Mechanical Systems," ASME JOURNAL OF APPLIED MECHANICS, Vol. 55, pp. 711–715.

Langhaar, H. L., 1962, *Energy Methods in Applied Mechanics*, John Wiley and Sons, New York, pp. 10–13.

Papastavridis, J. G., 1991, "On Energy Rate Theorems for Linear First-Order Nonholonomic Systems," ASME JOURNAL OF APPLIED MECHANICS, Vol. 58, pp. 536–544.

Author's Closure[3]

I find that Professor Papastavridis' discussion adds nothing but confusion to the paper under discussion. To set the record straight I am responding to his comments, including that I "misrepresented" his work, and that my paper has "a number of fundamental errors," below.

1 I could not agree with him that the paper under discussion "is made to remove the theoretical shortcomings of Kane and Levinson (1988)." The so-called "shortcomings" were reme-

[1]By J. T. Wang and published in the Dec. 1993 issue of the JOURNAL OF APPLIED MECHANICS, Vol. 60, pp. 962–969.

[2]Associate Professor, School of Mechanical Engineering, Georgia Institute of Technology, Atlanta, GA 30332-405.

[3]J. T. Wang, Staff Research Engineer, Engineering Mechanics Department, GM R&D Center, 30500 Mound Road, Box 9055, Warren, MI 48090-9055.

Copyright © 1994 by ASME
Downloaded 03 May 2010 to 171.66.16.20. Redistribution subject to ASME license or copyright; see http://www.asme.org/terms/Terms_Use.cfm

Journal of Applied Mechanics

Book Review

Biomechanics: Mechanical Properties of Living Tissues, 2nd ed., by Y. C. Fung. Springer-Verlag, New York, 1993. 568 pages.

REVIEWED BY S. C. COWIN[1]

This book is the second edition of the first volume in a series of three volumes by Y. C. Fung on biomechanics. The first edition was published in 1981. The second volume in the series was *Biodynamics: Circulation* (1984) and the third was *Biomechanics: Motion, Flow, Stress, and Growth* (1990). In these three books Professor Fung describes the constitutive behavior of biological tissues, the functional mechanics of the body's organs and related engineering problems. The series of three volumes summarizes the application of an enormously wide spectrum of mechanics and thermodynamics to physiology and the engineering of biologically related problems. The mechanics applied includes rigid-body mechanics, mechanical vibration theory, viscous and perfect fluid theory, linear and nonlinear elasticity and viscoelasticity, wave propagation in fluid and solid media, multiphase mixture theory, chemical thermodynamics, and numerous subtopics of mechanics. The problems addressed cover the spectrum from birds flying and fish swimming to oxygen transport, human impact tolerance, cell behavior, and the engineering of activities at the cellular level.

The reviews of the first edition of this volume were "rave" reviews. In this journal (*Journal of Applied Mechanics*, 1982, Vol. 49, p. 464) Richard Skalak wrote that "Professor Fung is one of the few people who has kept up with the development of biomechanics on so many different fronts in the last decade and could single-handedly write this book for us." James McElhaney closed his review (*Medical Physics*, Vol. 9, 1982) with "For those of you interested in analysis of the mechanical properties of biologically derived tissues, this book is a must buy. Professor Fung has organized, consolidated, and unified this difficult field in an elegant and erudite textbook." In the dozen years between the first and second edition of this book Professor Fung has both widened and deepened his knowledge of the field of biomechanics and that enhanced vision is reflected in this new edition. The accolades appropriate for the first edition should be increased by 1/3 and applied to the second edition, for the second edition is 4/3 times the length of the first edition. This review is focused on the new 135 pages and the rewriting of the original 433 pages as the excellent and positive reviews of James McElhaney and Richard Skalak more than adequately covered the 1st edition.

Although Chapter 1 is rewritten and its length is increased by only four percent, the title of Chapter 1 is unchanged and remains "Introduction: A Sketch of the History and Scope of the Field"; similarly the titles of chapters 2 and 3, "The Meaning of Constitutive Equations" and "The Flow Properties of Blood", respectively, are unchanged although their content has been refined and their lengths are increased by ten percent. Chapter 4, formerly entitled "Red Blood Cells and Their Deformability" has become "Mechanics of Erythrocytes, Leukocytes and Other Cells" and now, 47 percent greater in size, includes not only the mechanics of the red blood cell (the erythrocyte), but also recent work on the basic cell mechanisms (e.g., adhesion) and other cells (e.g., leukocytes). Chapter 5, "The Rheology of Blood in Microvessels" has become "Interaction of Red Cells with Vessel Wall, and Wall Shear with Endothelium" and the chapter length has increased by 57 percent. Much of the new material concerns the endothelium and the transmission of the blood shear load to more solid structures in the body and models of the endothelial cell. Chapter 6 on "Bioviscoelastic Fluid" is unchanged in length while Chapter 7 on "Bioviscoelastic Solids," is 21 percent longer. Much of the new material on bioviscoelastic solids is concerned with the strain energy function in Professor Fung's finite deformation theory of the pseudo-elasticity for soft tissue behavior. Chapter 8 entitled "Mechanical Properties and Active Remodeling of Blood Vessels" is 73 percent longer than the same chapter in the previous edition where the chapter title did not contain the phrase "and Active Remodeling." Most of the increase in the chapter's length is associated with the material on active remodeling of the blood vessel, a technical area that Professor Fung has contributed to extensively in the last decade. Chapter 9 on "Skeletal Muscle" is 30 percent greater than in the first edition due to the inclusion of material on the cross-bridge hypothesis of the interaction of actin and myosin filaments. Chapter 10 on "Heart Muscle" has been extensively extended, reorganized and rewritten; it is now 50 percent longer than in the first edition. Chapter 11 on "Smooth Muscles" is 21 percent longer than in the first edition due to material on the active contraction of ureteral muscle and other smooth muscle organs. Chapter 12 on "Bone and Cartilage" is 32 percent longer with more information on the mechanical behavior of bone, articular cartilage, tendons, and ligaments.

The changes between the first and second edition of this volume reflect the exponential growth of significant research results in biomechanics during the past 12 years. The first edition was focused on the development of phenomenological constitutive equations for biological tissues and the only cell receiving significant attention was the red blood cell. In the second edition that focus is now joined with the development of microstructurally based constitutive equations and the broad application of mechanics to cellular level mechanisms.

I paraphrase the advice of James McElhaney in stating that for those of us interested in analysis of the mechanical properties of biologically derived tissues, this book is a must buy. In particular this update is significant and first editions should be replaced by the second edition.

[1]The City College, City University of New York, 107 West 86th Street, New York, NY 10024.

Copyright © 1994 by ASME
Downloaded 03 May 2010 to 171.66.16.20. Redistribution subject to ASME license or copyright; see http://www.asme.org/terms/Terms_Use.cfm